

7th European Workshop on Thermal Protection Systems & Hot Structures

ESA-ESTEC, Noordwijk, The Netherlands, 8-10 April 2013

Monday 8 April (all sessions as plenary in Newton 1&2)

Registration	10:00	In front of meeting rooms		
Session 1 - Opening		Co-chairs: Olivier Pin & Rafael Bureo (ESA-ESTEC)		
	11:00	Workshop Opening	C. Stavrinidis	ESA-ESTEC
	11:20	The IXV Development Status and Perspectives	G. Tumino	ESA-HQ
	11:45	ExoMars - Status of the Entry Descent and Landing Demonstrator Module (EDM)	O. Bayle	ESA-ESTEC
	12:10	Sample Return Missions Requirements for Earth Re-entry Capsules Thermal Protection System	D. Rebuffat	ESA-ESTEC
	12:35	ESA technology roadmaps - ongoing and planned developments	H. Ritter	ESA-ESTEC
Lunch break	13:00 - 14:10			
Session 2 - Applications		Co-chairs: Pierre Omary (CNES) & Jose Longo (ESA-ESTEC)		
	14:10	An insight into the Heatshield Development for the ExoMars 2016 Entry, Descent and Landing demonstrator	Y. Mignot	Astrium Bordeaux
	14:35	Zefiro 40 Solid Rocket Motor Nozzle Development and Innovations	R. Marocco	AVIO
	15:00	Testing of DLR C/C-SiC for HIFiRE 8 Scramjet Combustor	Th. Reimer	German Aerospace Center (DLR)
	15:25	Overall Preliminary Design of the Thermal Protection System for a Long Range Hypersonic Rocket-powered Passenger Vehicle (Spaceliner)	N. Garbers	German Aerospace Center (DLR)
Coffee break	15:50 - 16:20			
Session 3 - SHEFEX - The German Sharp Edge Flight Experiments		Co-chairs: Ali Gülhan (DLR) & Heiko Ritter (ESA-ESTEC)		
	16:20	SHEFEX II, 2nd Flight within DLR's Re-Entry Technology and Flight Test Program	A. Gülhan	German Aerospace Center (DLR)
	16:45	ASTRIUM's TPS & HS Materials on SHEFEX II - Experiment Description & Flight Evaluation -	W. Fischer	Astrium GmbH
	17:10	SHEFEX III - Assessment of Cooling Concepts for Sharp Leading Edges	C. Dittert	German Aerospace Center (DLR)
Session 4 - Heatshield Concepts		Co-chairs: Ali Gülhan (DLR) & Heiko Ritter (ESA-ESTEC)		
	17:35	Characterization of Actively Cooled Porous C/C Wall Segments According to Pressure Loss and Internal Temperature Distribution under Heat Loads Generated by IR Radiation	S. Schweikert	Institute of Aerospace Thermodynamics, University of Stuttgart
	18:00	RASTAS SPEAR : Radiation-Shapes-Thermal Protection Investigations for High Speed Earth Re-entry	J-M. Bouilly	Astrium Space Transportation
	18:25	FP7/SPACE PROJECT "HYDRA" Hybrid Ablative Development for Re-entry in Planetary Atmospheric Thermal Protection	J. Barcena	Tecnalia Research & Innovation

Tuesday 9 April (separate morning sessions, afternoon session as plenary in Newton 1&2)

Session 5 - Modelling of Ablation and Gas-Surface Interaction (part 1)		Co-chairs: Tom van Eekelen (LMS Samtech) & Luca Ferracina (ESA-ESTEC)		
	9:00	Ablator Response Model Development & Challenges	Th. Magin	VKI
Newton 1 only	9:25	Numerical Simulation of Ablative-Material Response - Code and Model Comparisons: Ablation Test-case Series #3	T. van Eekelen	LMS Samtech
	9:50	Modeling of Volume Averaged Surface Recession on a Charring Ablator	A. Martin	University of Kentucky
	10:15	Computational Analysis of Hypersonic Flows Including Finite Rate Ablation Thermochemistry	D. Bianchi	Sapienza University of Rome
Coffee break	10:40 - 11:10			

Session 6 - Modelling of Ablation and Gas-Surface Interaction (part 2)		Co-chairs: Alexandre Martin (University of Kentucky) & Luca Ferracina (ESA-ESTEC)		
	11:10	Gas-Surface Interactions modelling	B. Chanetz / J. Vos	Onera / CFS
Newton 1 only	11:35	A Numerical Comparison of high- and low-Fidelity Radiation Models for Conduction-Radiation Coupling in (Charring) Ablators	G. Pinaud	ASTRIUM ST
	12:00	High Speed Entry Ablation-Flight Mechanics Coupling Effects	A. Bourgoing/ N. de Champvallins	Astrium Space Transportation
	12:25	Ground to Flight Investigations of Hayabusa with Ablation Effects	E. Fahy	University of Queensland
Session 7 - Advanced high temperature ceramics		Co-chairs: Thomas Reimer (DLR) & Laurent Pambaguian (ESA-ESTEC)		
	9:00	TOUGH CERAM	M. Sardou	SARDOU SA
Newton 2 only	9:25	Oxidation Behavior of Laminate Ceramics belonging to SiC-ZrB2 System	C. Badini	Politecnico di Torino
	9:50	Active/Passive Oxidation Transition and Active Oxidation Kinetics for C/SiC Composites in IXV Re-Entry Conditions	M. Balat-Pichelin	PROMES-CNRS
	10:15	Catalycity and Emissivity of ZrB2-SiC Based UHTC in Air Plasma Flow at High Temperatures	M. Balat-Pichelin	PROMES-CNRS
Coffee break		10:40 - 11:10		
Session 8 - Advanced joining techniques		Co-chairs: Wolfgang Fischer (Astrium) & Christopher Semprimoschnig (ESA-ESTEC)		
	11:10	FP7/Space Project "SMARTTEES". Towards a New TPS Reusable Concept for Atmospheric Reentry from Low Earth Orbit	J. Barcena	Tecnalia Research & Innovation
Newton 2 only	11:35	Joining of Ceramic Matrix Composites to high and ultra high Temperature Ceramics for Thermal Protection Systems	K. Mergia	National Centre for Scientific Research "Demokritos"
	12:00	Overview of the TPS Activities within the "RASTAS SPEAR" Project	G. Vekinis	NCSR Demokritos
	12:25	Morphological Study and Characterization of Carbon Composites for Hot Structures Applications	A.V. Nenarokomov	Moscow Aviation Institute
Lunch break		12:50 - 14:10		
Session 9 - IXV - The Intermediate Experimental Vehicle		Co-chairs: Samantha Ianelli (ASI) & Gandolfo di Vita (ESA-HQ)		
	14:10	TPS Design, Development and Verification Approach for IXV Program	E. Brach Prever	Thales Alenia Space
Newton 1 & 2	14:35	Design Solutions for Integration of TPS Assemblies on IXV	M.T. Signorelli	Thales Alenia Space
	14:50	CMC TPS Technology for the IXV Manufacturing and Qualification Status	T. Pichon	Herakles, SAFRAN Group
	15:15	Development and Qualification of the Thermal Protective Seal of IXV's hot Structure Control Surface Actuator ROD	F. Infed	MT Aerospace AG
	15:40	Qualification of In-Flight Experimentation for the IXV Re-Entry Vehicle	C. Pereira	RUAG Space
	16:05	Preparatory Activities for the IXV TPS&HS Subsystem PWT Tests	M.T. Signorelli	Thales Alenia Space
Bus departure for dinner cruise		16:50		
Wednesday 10 April (all sessions as plenary in Newton 1&2)				
Session 10 - Ablative materials		Co-chairs: Volker Liedtke (AAC) & David Agnolon (ESA-ESTEC)		
	9:00	AEROFAS: Development of Innovative Thermal Protections	J-M. Bouilly	Astrium Space Transportation
	9:25	ASTERM: Maturation of a new Low Density Ablative Material	J-M. Bouilly	Astrium Space Transportation
	9:50	Carbon Phenolic Ablators Industrial Status and Potential Applications	T. Pichon	Herakles, Safran group
	10:15	Ablative Materials Thermal Properties Estimating	A.V. Nenarokomov	Moscow Aviation Institute
Coffee break		10:40 - 11:10		
Session 11 - Plasma testing capabilities		Co-chairs: Jean-Marc Bouilly (Astrium) & Lionel Marraffa (ESA-ESTEC)		
	11:10	Characterization of new high Heat Flux Test Conditions in L3K	B. Esser	DLR
	11:35	TPS Testing in the Plasmatron Facility for Super-Orbital Re-Entry	O. Chazot	VKI

	12:00	Characterization of a 50 kW Inductively Coupled Plasma Torch for use in Testing of Ablative Materials	M. MacDonald	Ecole Centrale Paris
	12:25	High speed gas turbine exhaust facility for TPS materials testing	P. Bonfà / A. Petrini	Aero Sekur S.p.A.
Lunch break		12:50 -14:10		
Session 12 - Sensor development and heat flux derivation		Co-chairs: Olivier Chazot (VKI) & Helmut Frühholz (ESA-ESTEC)		
	14:10	Experimental Investigation of Photogrammetric Surface Analysis of Heat Shield Materials during Plasma Wind Tunnel Testing	S. Loehle	Institut für Raumfahrtssysteme (IRS)
	14:35	Combined Sensor Assembly COMARS for EXOMARS EDM Demonstrator	A. Guelhan	DLR
	14:50	Measurement of Temperature and Heat Flux in Ablative TPS	C. Pereira	RUAG Space Switzerland
	15:15	A New Calibration-Based Inverse Method for Estimating Surface Heat Flux	J.I. Frankel	University of Tennessee
	15:40	In-Flight Experiment Design and Ground Testing for TPS Development	I. Sakraker	von Karman Institute for Fluid Dynamics

ExoMars 2016

Status of the

EDL Demonstrator Module

(EDM)

Olivier Bayle
ExoMars EDM System Engineer
ESA - ESTEC

ExoMars Programme Mission Architecture

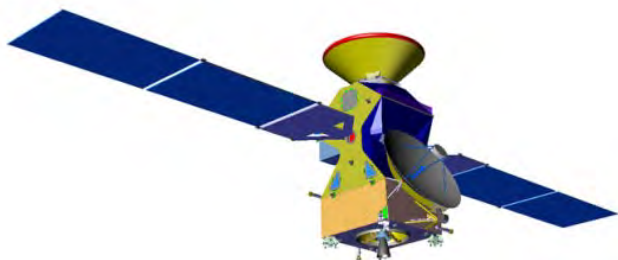
ExoMars Programme: two missions launched in 2016 and 2018.

- The 2016 mission consists of the Trace Gas Orbiter (TGO) and the EDL Demonstrator Module (EDM)
- The 2018 mission consists of the Rover, accommodated inside a Descent Module (DM) and carried to Mars by a Carrier Module (CM)
- Large international cooperation with Roscosmos and some contributions from NASA

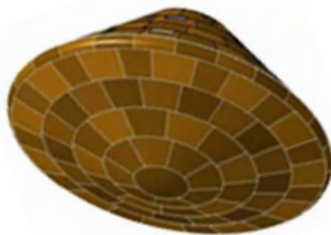
2016 Mission



Proton



Trace Gas Orbiter (TGO)



EDL Demonstrator Module (EDM)



2018 Mission



Proton



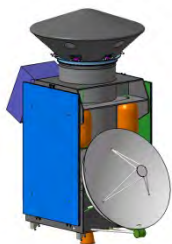
Carrier Module & Descent Module



Rover + Landed Platform

ExoMars 2016 Mission Overview

LAUNCH

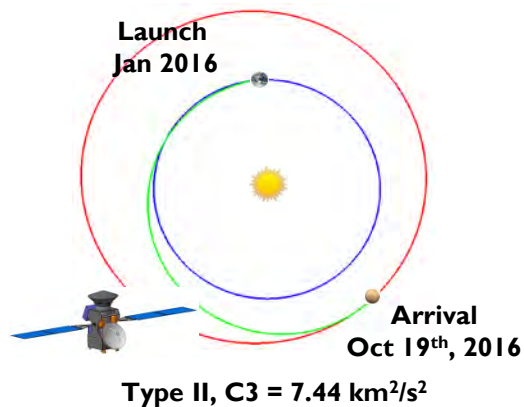


ExoMars SCC in launch configuration

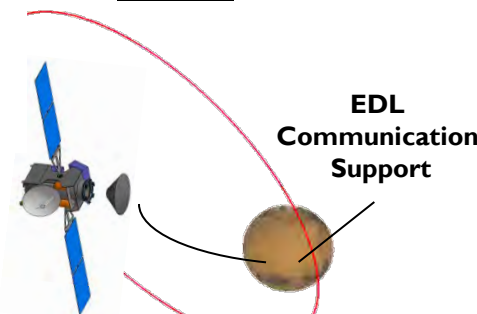


Proton

INTERPLANETARY CRUISE

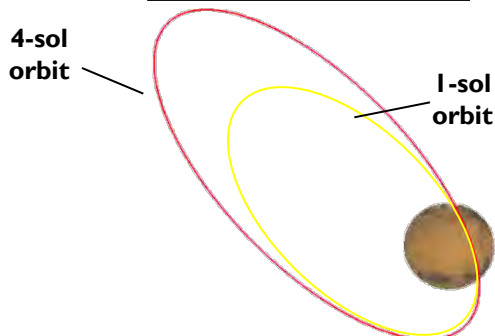


APPROACH, EDM RELEASE & MOI



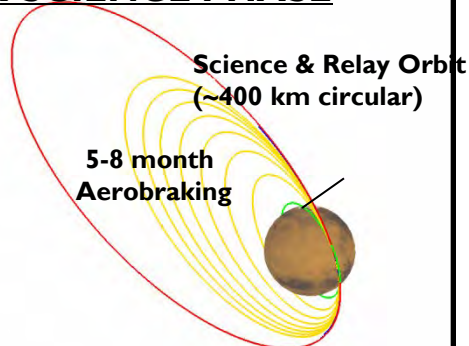
- (1) EDM released from the hyperbolic approach 3 days before MOI
- (2) Orbiter performs retargeting and MOI into 4 sol orbit (inclination compatible with target landing site)

EDM RELAY & TRANSITION TO I-SOL ORBIT



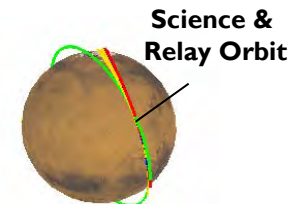
- (1) Inclination change to that of science orbit ($74^\circ \pm 10^\circ$)
- (2) Apoares reduction to 1 sol

AEROBRAKING & SCIENCE PHASE



- (1) Aerobroke to final orbit
- (2) Start of Science Phase

DATA RELAY PHASE



- (1) Data relay for 2018 Rover starts in Jan 2019
- (2) Data relay capability for future Mars surface assets throughout 2022

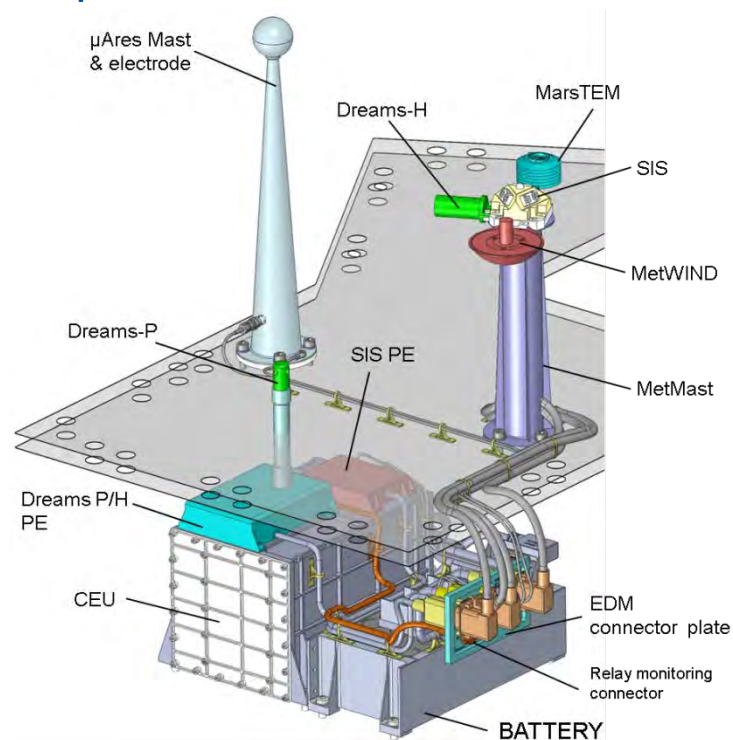
EDM Technology Objectives

- **Design, develop and flight-demonstrate key technologies to land a Payload on Mars:**
 - Heat shield
 - Parachute system
 - Doppler Radar system
 - Liquid propulsion system
 - Impact attenuation system

- **Measure and transmit back to Earth engineering data for post-flight analysis**
 - EDM shall provide flight measurements allowing reconstruction of:
 - Flown trajectory
 - Thermo-mechanical loads during EDL
 - Performance of the EDL subsystems
 - EDM mission shall allow for data transmission to Earth

EDM Scientific Objectives

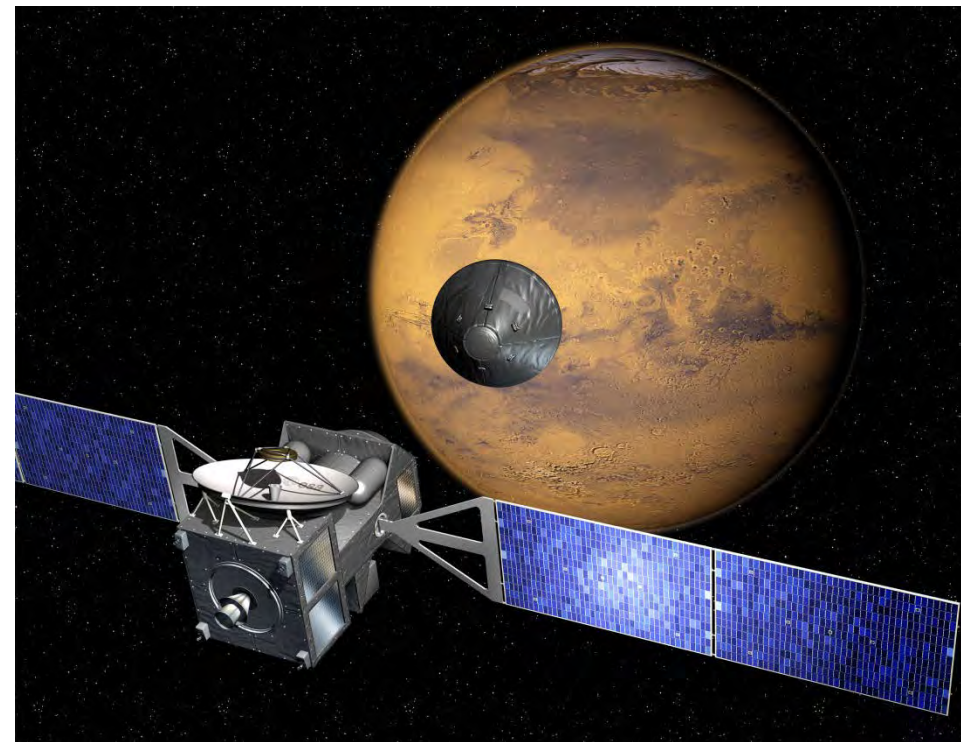
- ❑ EDM offers limited resources for science instruments (3.6 kg) and a short lifetime on Mars surface (4 sols) because of its lack of long-term power supply
- ❑ DREAMS scientific instruments will be operated on Mars surface
 - Provide in-situ measurements of Mars atmospheric characteristics during the Global Dust Storm Season:
 - Temperature
 - Pressure
 - Winds
 - Humidity
 - Electric field
 - Dust
 - Improve our understanding of temporal and spatial variability of the Mars atmosphere



EDM Mission Scenario (1)

Coast Phase

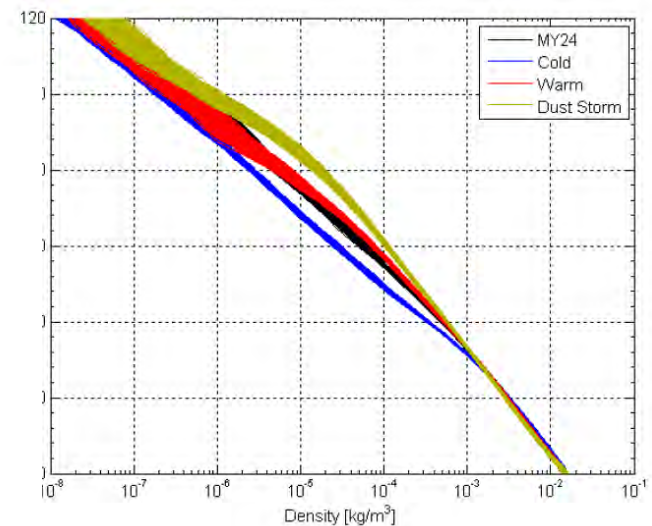
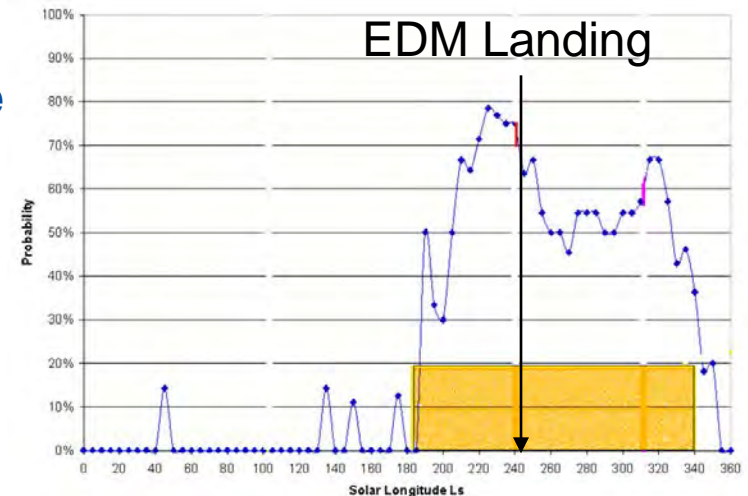
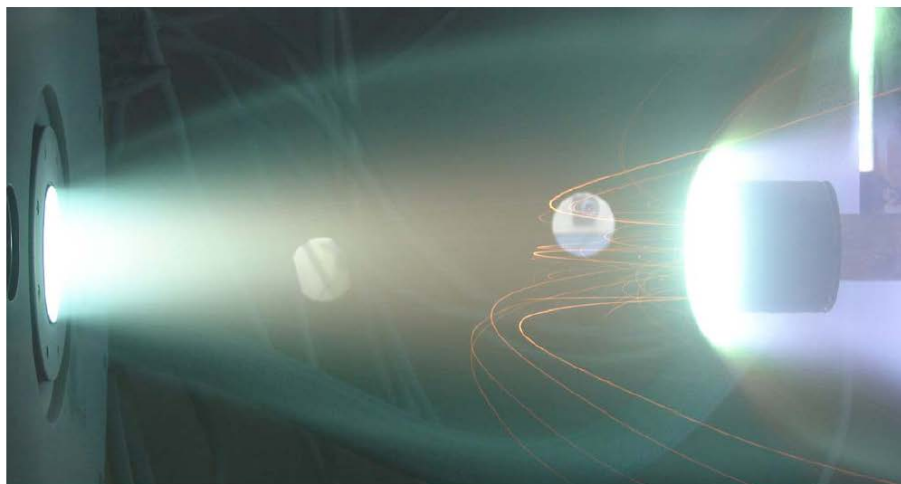
- ❑ **Coast Phase is the autonomous EDM flight between separation from the TGO and entry in Mars atmosphere**
- ❑ **EDM is separated from the TGO by a 3-point spin-up mechanism, that provides 2.75 rpm spin rate**
- ❑ **Coast phase duration = 3 days:**
 - EDM systems move to Hibernation shortly after separation in order to save electrical power
 - EDM awaken about 1 hour before entry, needs to rebuild inertial attitude reference (dedicated sun sensor)



EDM Mission Scenario (2)

EDL in Global Dust Storm Season

- ❑ T2 transfer in 2016 implies arrival at Mars at solar longitude $L_s=244$, i.e. in the middle of the Global Dust Storm Season
- ❑ High probability to encounter Global Dust Storm is accounted for in the EDM design:
 - Larger variability in Atmospheric density and temperature
 - Erosion of Front shield accounted in TPS sizing (several WTT were performed in DLR-L2K)



EDM Mission Scenario (3)

Entry and Descent

- ❑ **Target Landing Site in Meridiani Planum (6.1°W-1.8°S)**
- ❑ **Entry conditions**
 - Maximum relative velocity = 5.83 km/s
 - Entry FPA = -12.4 deg
 - Entry corridor > 0.8 deg (dispersions at entry +/- 0.3 deg)
- ❑ **12 m DGB deployed at Mach [1.8-2.1]**
- ❑ **Front shield jettisoned on timer**
- ❑ **Doppler Radar acquires ground relative position and velocity**



EDM Mission Scenario (4)

Landing

- ❑ EDM Surface Platform separates from Backshell at about 1200 m altitude
- ❑ Final braking by 9 hydrazine thrusters (Astrium CHT-400), operated in pulse-modulation
- ❑ Thrusters shut down 1.5 m from terrain
- ❑ Final free fall and impact attenuated by a layer of crushable material
- ❑ Crushable material was selected:
 - Low mass and cost
 - Simple design
 - Leaves platform close to the ground for surface access to scientific instruments (or rover egress for future missions)



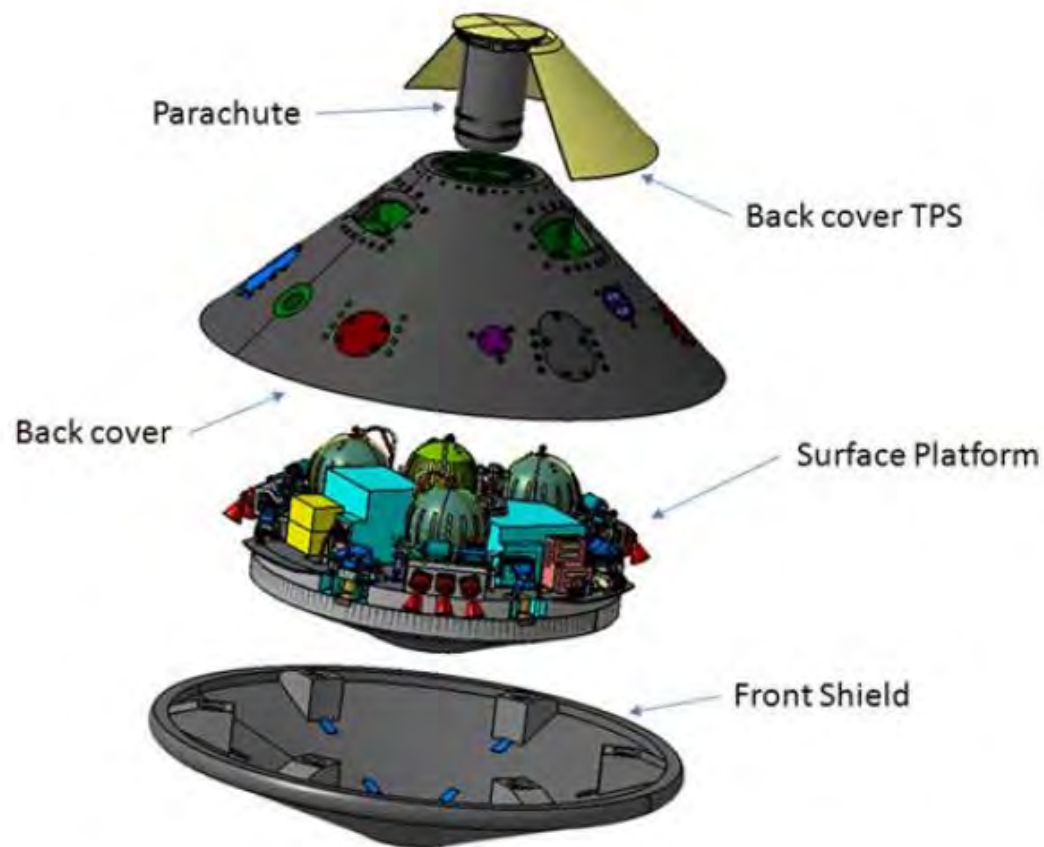
EDM Configuration

□ Mass properties:

- EDM = 600 kg
- Surface Platform = 300 kg
- Propellant = 39 kg
- CoM < 27%.Diameter

□ Main dimensions:

- EDM Diameter = 2.4 m
- Surface Platform = 1.7 m
- Front cone = 70 deg
- Back cone = 47 deg



EDM Development Status

Critical Technologies

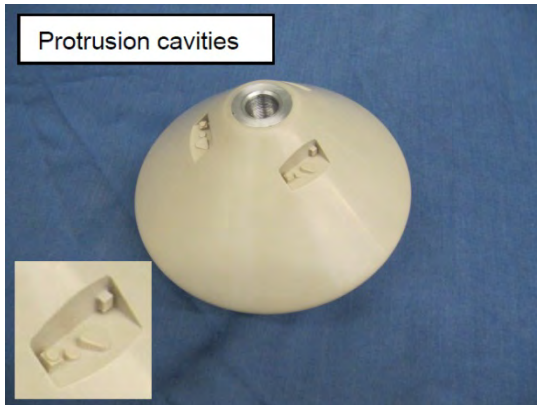
1. **Aerothermodynamics**
2. **Heat Shield**
3. **Parachute System**
4. **Propulsion System**
5. **Radar Doppler Altimeter**
6. **Landing System**

EDM Technology Development Status

1- Aerothermodynamics

- ❑ **Aerothermal verification: Backshell heat flux distribution and effect of singularities**

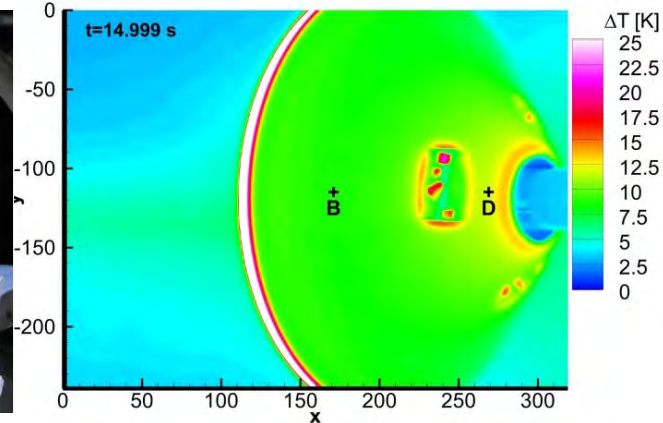
Manufacturing of high-fidelity model



Test Campaign in DLR H2K Wind Tunnel



Correlation with CFD Results

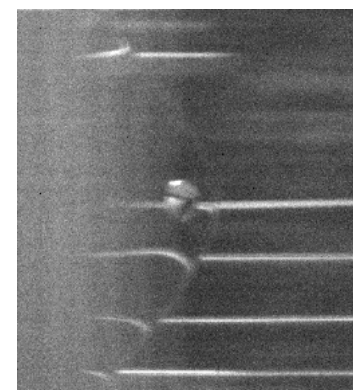


- ❑ **Aerodynamic verification: Stability in low supersonic regime (Mach 1:3)**

Manufacturing of instrumented models



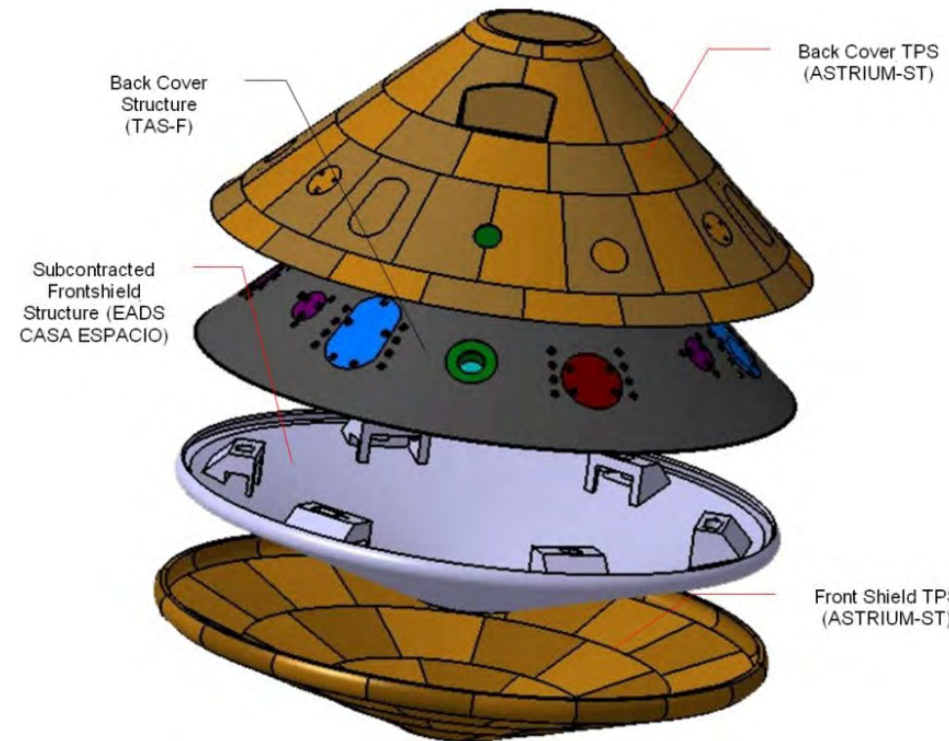
*Free-flight campaign in ISL
Powder Gun
Picture at Mach 2.2*



EDM Technology Development Status

2- Heat Shield - TPS

- ❑ TPS material (Norcoat-Liege) successfully tested in Astrium SIMOUN wind tunnel
 - Qualification limit increased to 2 MW/m²
 - Air and CO₂ flows comparison
 - Detailed ablation model obtained
 - Bonding / filling material qualified
 - External Single Layer Insulation tested successfully



Before Test

After Test



Front Shield TPS Tile Test

Heat Flux = 2 MW/m² – Sample dimension = 420 mm x 150 mm

EDM Technology Development Status

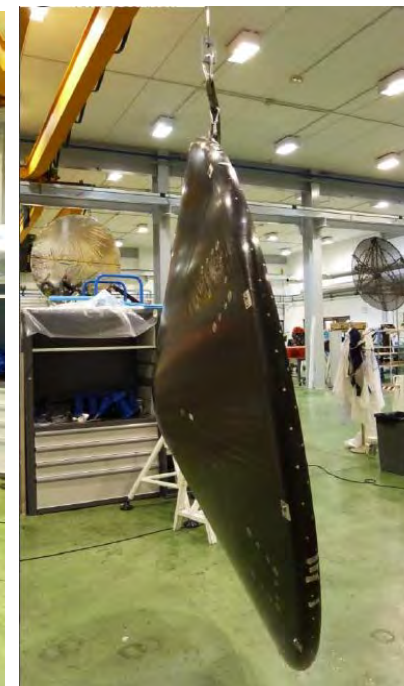
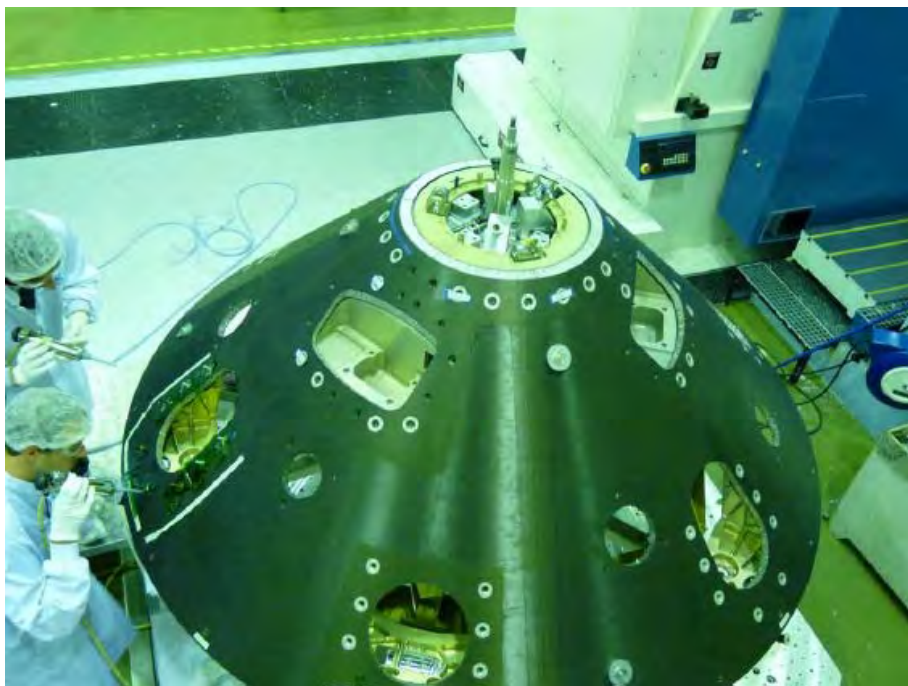
2- Heat Shield - Structure

❑ Backcover Structure (TAS-F):

- Structural Model completed
- Flight Model manufacturing on-going

❑ Front Shield Structure (EADS CASA):

- Structural Model completed
- Flight Model manufactured and under test



EDM Technology Development Status

3- Parachute System (PAS)

- ❑ Parachute geometry scaled from Huygens design - 12 m diameter
- ❑ Mortar deployed at Mach [1.8-2.1]
- ❑ Break-out Patch (BoP) decelerated by drogue parachute
- ❑ Tests performed:
 - Mortar tests (PDD)
 - Confirmed ejection velocity
 - Supersonic WTT in GRC 10x10ft
 - Low Altitude Drop Test for Break-out Patch drogue
 - Confirmed no recontact with probe



BoP drogue test

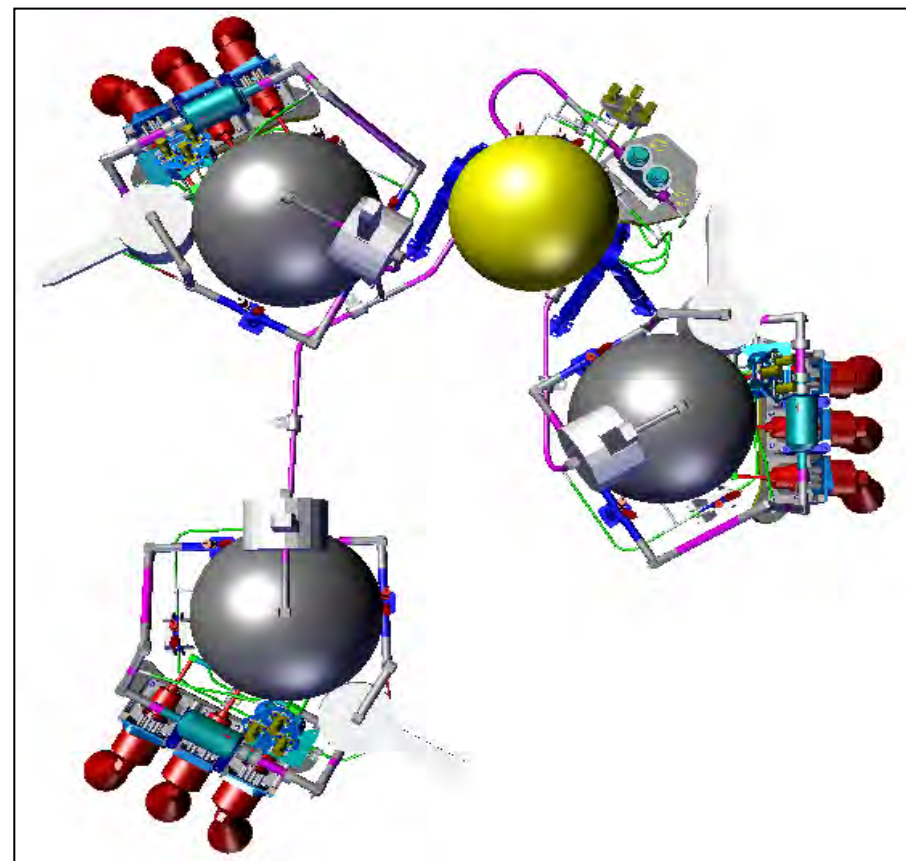


Parachute Deployment Tests

EDM Technology Development Status

4- Propulsion System

- ❑ **Based on 9 hydrazine thrusters operated in pulse modulation**
 - CHT400 from ASTRIUM
 - 400 N thrust
 - 3 clusters of 3 thrusters
 - 5 Hz operation
- ❑ **Designed with 3 independent PIA branches:**
 - No coupling between clusters
 - No propellant migration
 - Simpler AIV
- ❑ **All components are off-the-shelf or require minor modification (e.g. propellant tank diameter tuning) or delta-qualification**



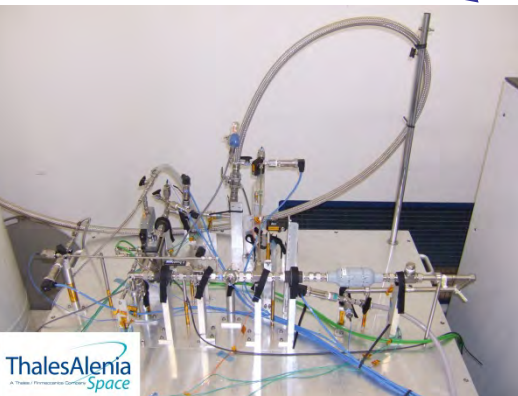
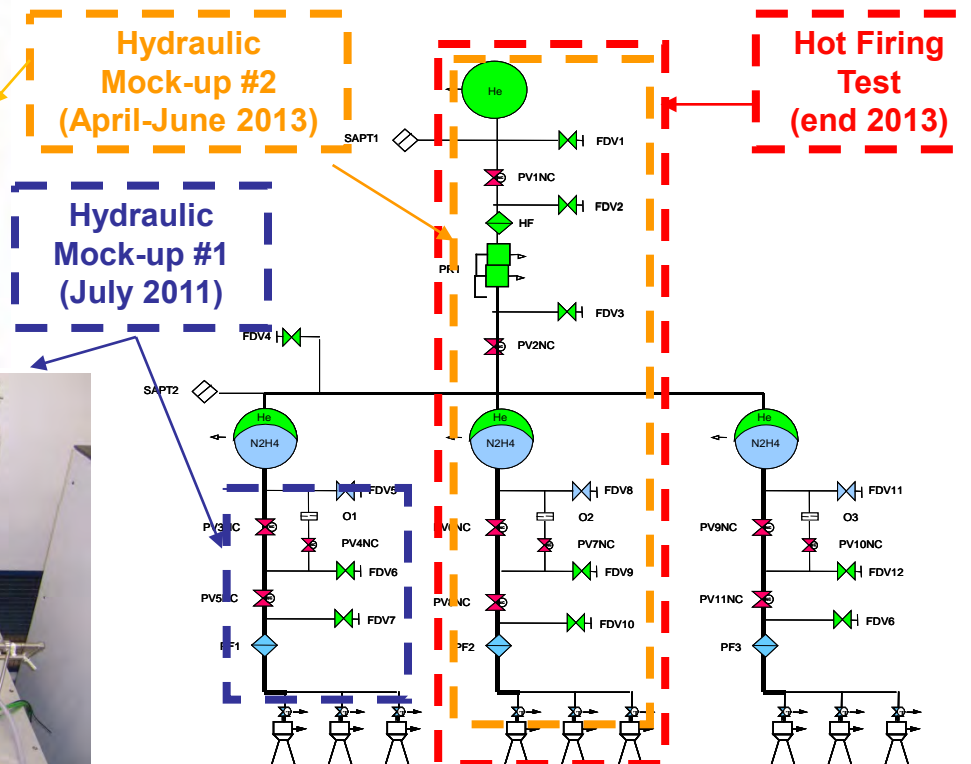
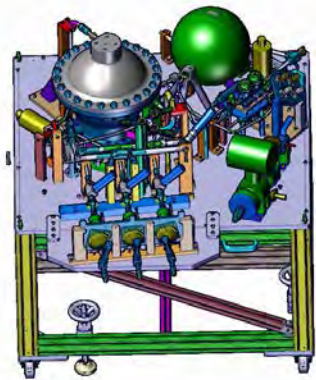
EDM Technology Development Status

4- Propulsion System Verification

- Development tests on component level successfully finalised in 2012 (e.g. CHT400 Firing test, PV shock test, He tank burst test, PR high flow tests)
- Incremental verification approach for the complete RCS



CHT400 Test hot firing

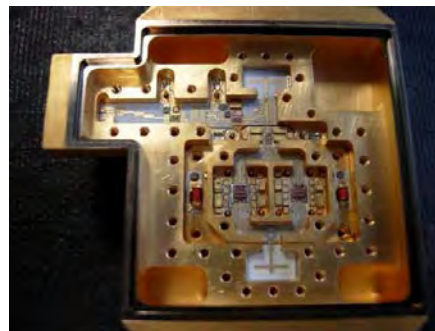


EDM Technology Development Status

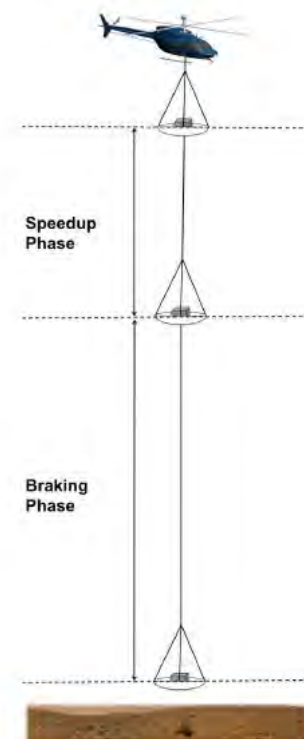
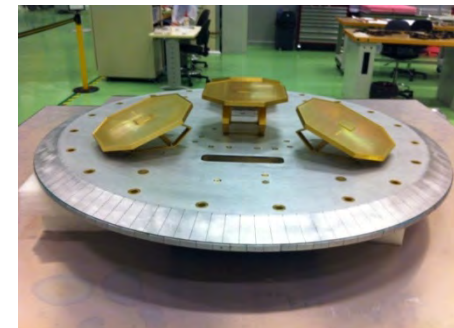
5- Radar Doppler Altimeter

- ❑ **Breadboard tests completed**
 - Solid State Power Amplifier
 - Digital section
 - Tx blanking
 - Antenna
- ❑ **Sub-assembly CDRs on going**
- ❑ **Structural Model completed and delivered in May 2012**
- ❑ **Engineering Model Field test on-board a helicopter planned in September 2013**
 - High speed descent tests
 - Captive carry tests

RDA SSPA Breadboard



Antenna Assembly

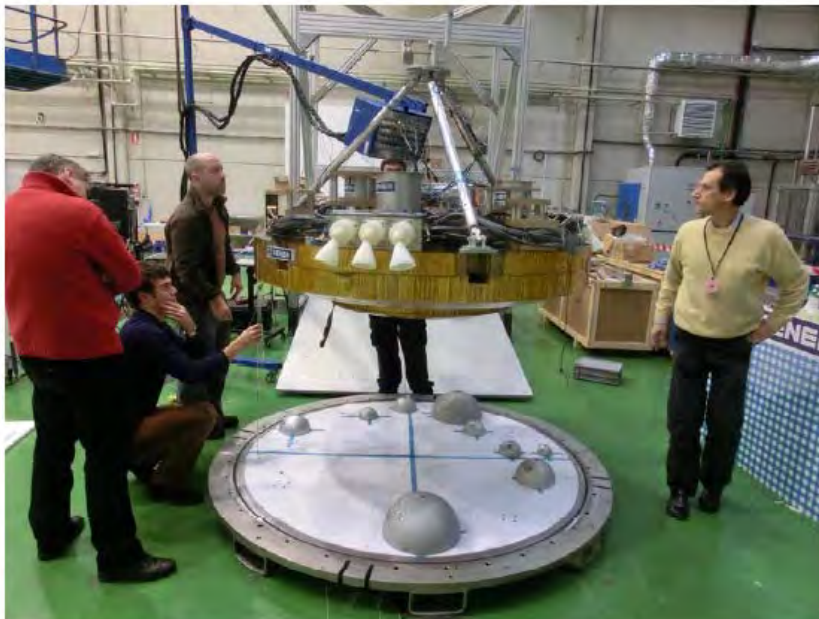
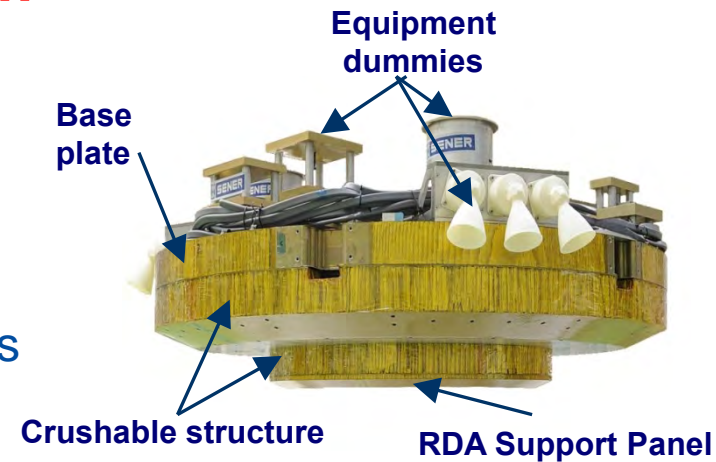


EDM Technology Development Status

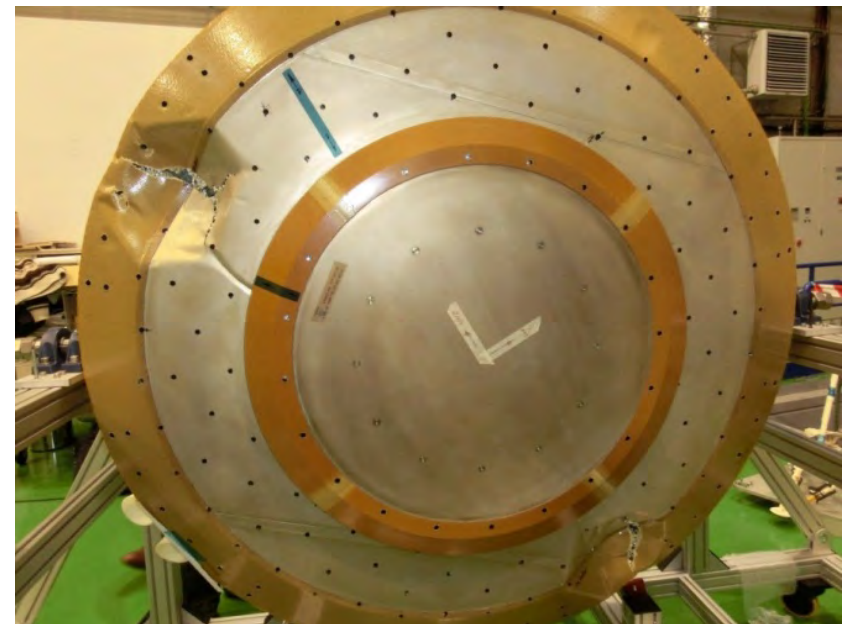
6- Landing System

❑ Surface Platform Full Scale drop test campaign:

- Vertical drops
- Drops with horizontal velocity onto slopes
- Flat impact, centre rock, rock garden
- Fully equipped SPSSM with equipment dummies



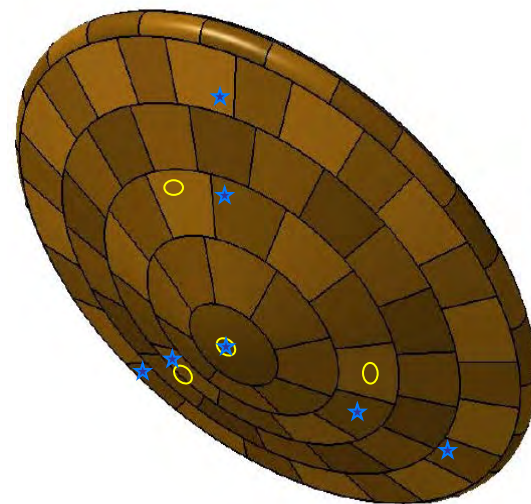
Surface Platform on Rock Garden



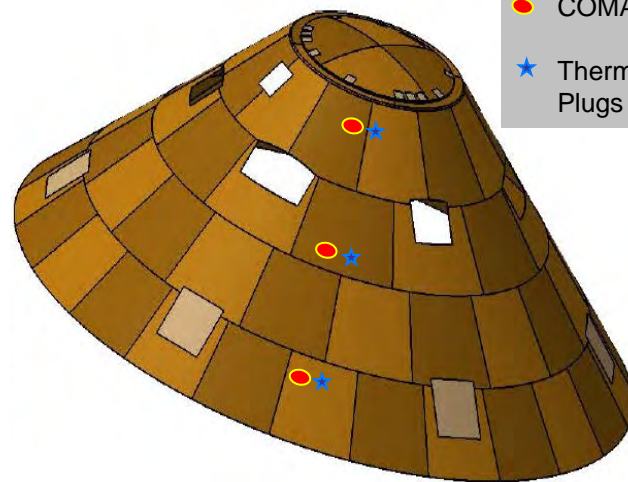
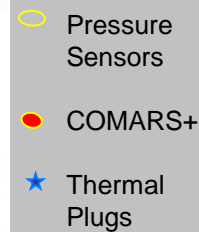
Crushable Structure after Vertical Drop

EDL Engineering Sensors

- ❑ **Flight Dynamics measured by GNC sensors**
 - IMU → Accelerations & angular rates
 - Radar Doppler Altimeter → Ground-relative motion
 - Sun Sensor → Inertial attitude before Entry
- ❑ **Aerothermodynamics & TPS Sensors**
 - Pressure sensors on Front Shield (x4)
 - COMARS+ (x3) to measure Pressure, Convective Heat Flux and Radiative Heat Flux
TPS Sensors
(DLR and CNES in-kind contribution)
 - Thermal plugs embedded in Front Shield (x7) and Back Shield (x3) TPS
- ❑ **Parachute Inflation loads measured by IMU
(100 Hz acquisition frequency)**
- ❑ **Impact loads measured by dedicated accelerometers**

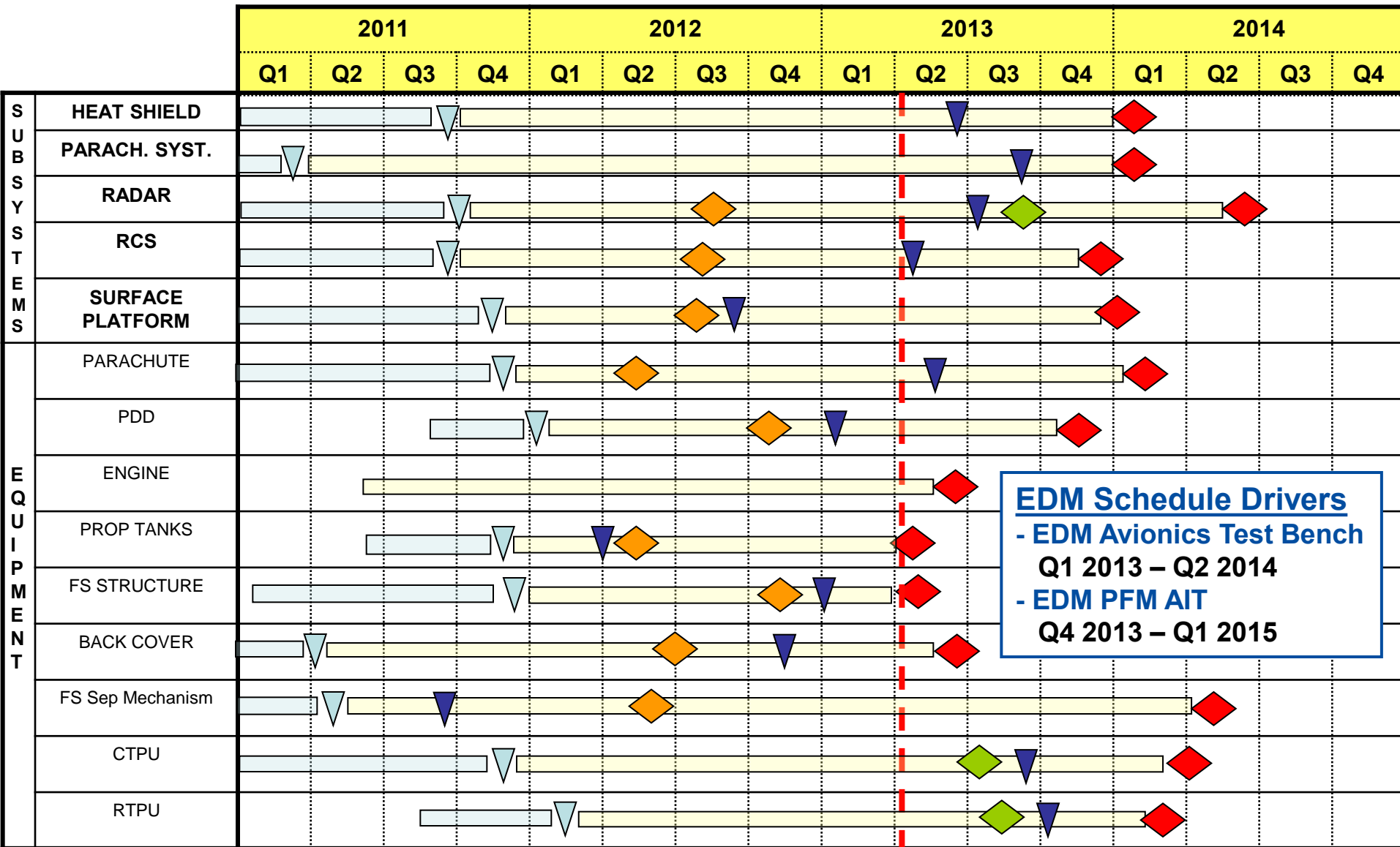


Front Shield Instrumentation



Back Shield Instrumentation

EDM Schedule Overview



EDM Schedule Drivers
 - EDM Avionics Test Bench
 Q1 2013 – Q2 2014
 - EDM PFM AIT
 Q4 2013 – Q1 2015

ExoMars EDM Structural Model (SM) during Leak Test



ExoMars EDM Structural Model (SM) during Sine Test



Conclusion – Next Steps

- ❑ All EDL technologies are progressing very well
- ❑ Subsystems CDRs are on-going, all will be completed within 2013
- ❑ EDM CDR planned in November 2013
- ❑ Significant test campaigns planned in 2013
 - Propulsion System HMU#2 and Firing Tests
 - Aeroshell static tests
 - Avionics Test bench Tests
 - Radar Doppler Altimeter Field Test
 - Parachute High Altitude Drop Test

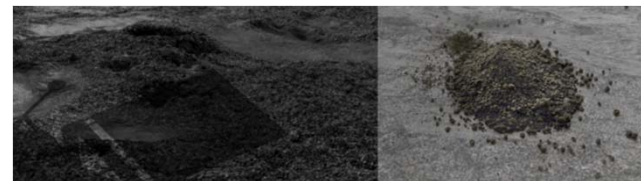
Sample Return Missions Requirements for Earth Re-entry Capsules TPS

D. REBUFFAT, ESA SRE-FP

ESA sample return mission studies featuring an ERC: Status



- **Phootprint:** sample return from the Mars moon Phobos
 - Science characterisation, static landing, sample acquisition and return to the Earth
 - Includes an Earth Re-entry Capsule that carries the sample container with 100g sample
 - CDF and 2 short industrial contracts in 2012
- **Marco Polo R:** sample return from a Near Earth Asteroid
 - Science characterisation, “touch and go” sampling and return to the Earth
 - Includes an Earth Re-entry Capsule that carries the sample container with 100g sample
 - 2 parallel industrial contracts on-going
- **Mars Sample Return Orbiter: an element of the MSR campaign**
 - Performs the Rendezvous and capture of the Sample Container in Mars orbit, then brings it back to the Earth following biosealing operations
 - Includes an Earth Re-entry Capsule that carries the biocontainer with 500g Mars sample
 - 2 parallel contracts completed in 2012



Phootprint mission main features

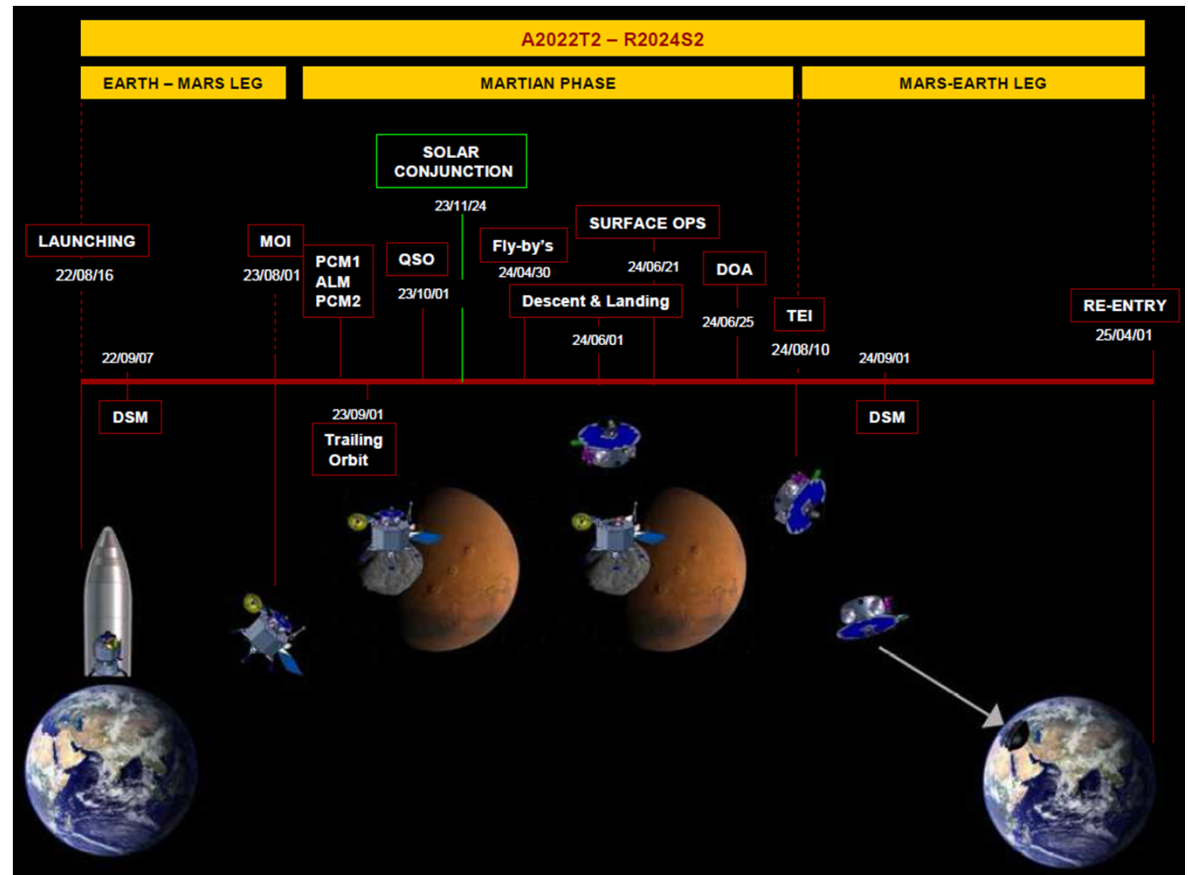


Mission profile:

1. Ariane 5 launch from Kourou in Direct escape in August 2022
2. Transfer to Mars (11 months)
3. 9 months around Phobos/Mars dedicated to science observations and sampling.
4. Departure from Mars in August 2024 – return to Earth (8 months)
5. ERC release and EDL in April 2025

Main features:

- < 3 years mission
- Composite composed of: Lander, Earth Return Vehicle, Earth Re-entry Capsule
- 3.9t launch mass
- Technological challenges: Descent and Landing GNC, landing gear & lander stability on low gravity body, sample acquisition and handling, high speed entry ERC



Marco Polo R mission main features

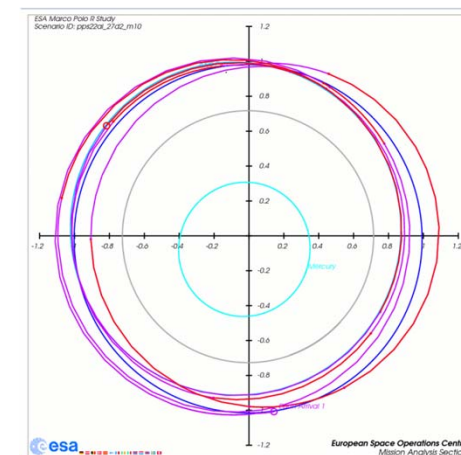
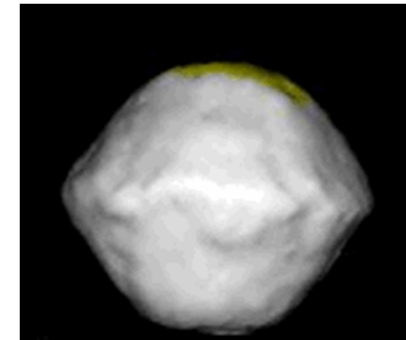


Mission profile:

1. Soyuz launch from Kourou, Direct escape in December 2022 with backup in 2023, 2024
2. Transfer to near-Earth asteroid 2008 EV5 via electric propulsion (Smart 1 engines)
3. 6 months around the asteroid, global characterization at 5 km distance, then local characterization at 250 m altitude for 5 sampling sites candidates, then sampling attempts (up to 3)
4. Departure in July 2025, return to Earth in June 2027, landing in Woomera, Australia

Main features:

- 2008 EV5 ~ 400 m diameter, ~ 1 AU to Sun
- < 4.5 year mission
- Main spacecraft + Earth Re-entry Capsule
- < 1650 kg launch mass
- Technological challenges: Asteroid descent GNC, touch and go system, sampling and sample transfer/containment, high speed re-entry (TPS + aero + crushable)

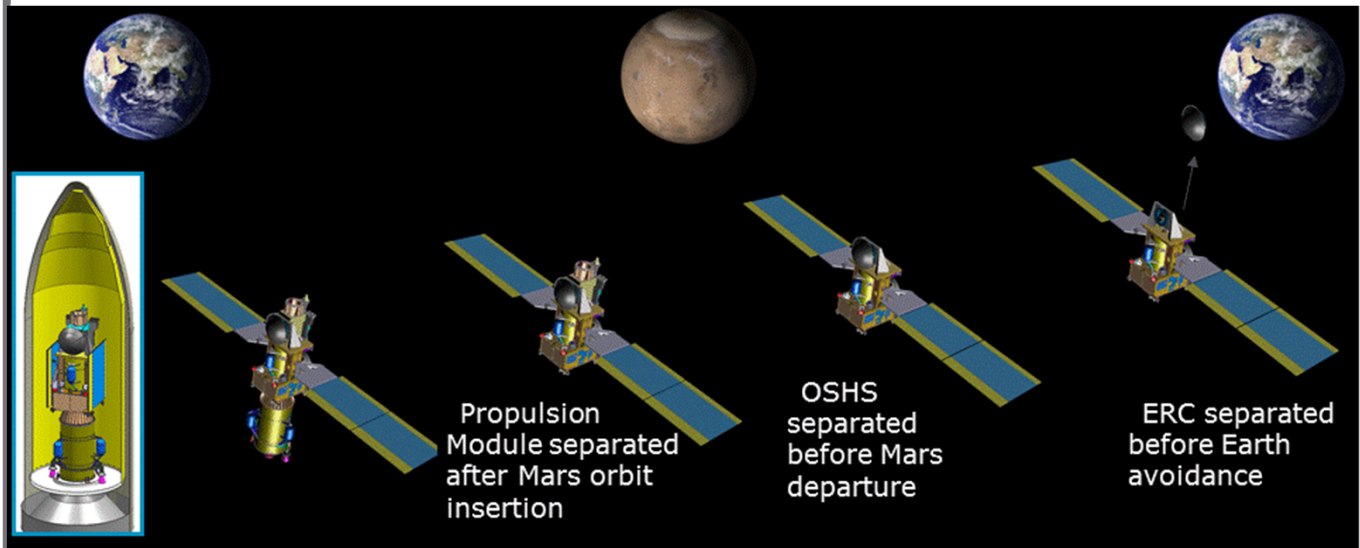


MSR-O mission main features



Mission profile:

1. Launch by Ariane 5 ECA
2. Direct escape or intermediate HEO
3. Transfer to Mars (11 months)
4. Mars insertion followed by aerobraking (1 year)
5. Communication relay to MSR surface elements (6 months)
6. Rendezvous and Capture of the OS after MAV launch (10 days)
7. Return to the Earth (10 months)
8. ERC release and EDL



The MSR-O spacecraft configuration evolves during the mission: staging allows to optimise mass

- Mission duration 5 years
- 4.4t launch mass
- Mission key challenges:
 - **Planetary Protection:** samples biosealing and safe return to Earth
 - **Rendezvous and Capture** in Mars orbit requiring a robust and autonomous GNC
 - **Earth Re-entry Capsule:** high speed re-entry and hard landing, reliability in line with Planetary Protection
 - **Mass** can be critical for certain launch dates

ERC TPS-related analyses for system studies



Sizing criterion:

- max heat flux **14-15 MW/m²** (TPS material and PWT facility performance limitation)
- max temperature at TPS / FS structure interface (**170deg C** for a CFRP – Al sandwich) -> TPS thickness & mass

Design loop (iteration) between

➤ Trajectory analysis

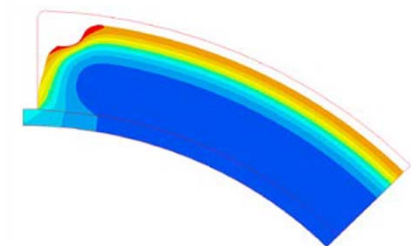
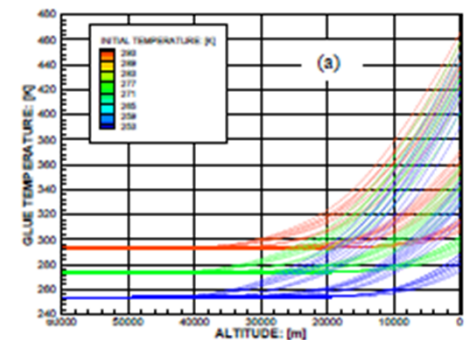
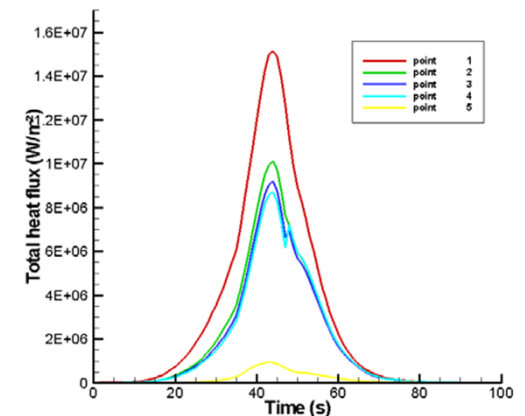
- 3 and 6 DoF calculations (Ventry, FPA, ballistic coef)

➤ Heat flux computation

- (convective and radiative) heat flux correlation
- For typical 11-12 Km/s re-entry velocities radiative flux is about 30% of the total flux (before applying margins)
- Margins of 20% (convective) and 100% (radiative) are applied

➤ TPS thermal analyses

- Thermal Mathematical Model (TMM) for TPS sizing including ablative behaviour (AblaTherM, SAMCEF/Amarylis)
- Specific analyses for MSRO for micrometeoroid-perforated TPS thermal behaviour (Axis symmetrical or 2D damage FEM with SAMCEF/Amarylis, including recession)

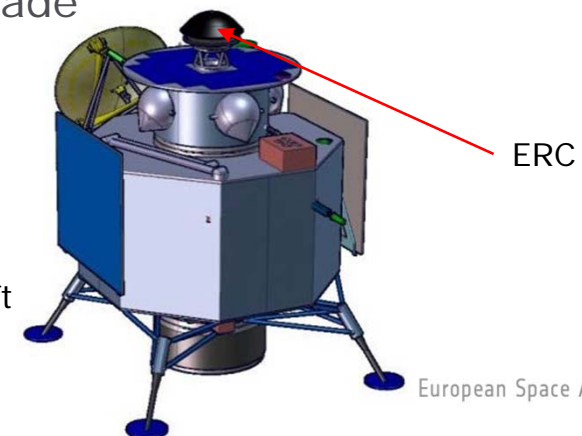


Phootprint ERC: System requirements



- Fully passive re-entry, no parachute
- Carries a Sample Container (SC) with ~100g sample (<2Kg) and an RF beacon for recovery
- Sample temperature to be kept below 40degC
 - Impact on the thermal load path to the sample
- SC g-loads at landing 2000g max (TBC ; target 800g) / science-driven
 - Drives the required stroke and ERC size
- Stability during re-entry / limited oscillations in subsonic for a good landing
- Relative entry velocity between 11 and 12.3 Km/s depending arrival date (timeframe: 2025 to 2029) and prograde vs retrograde
- 14-15 MW/m² peak heat flux
- 80g max deceleration peak during re-entry

Phootprint spacecraft

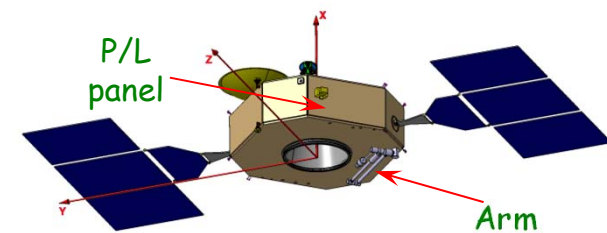
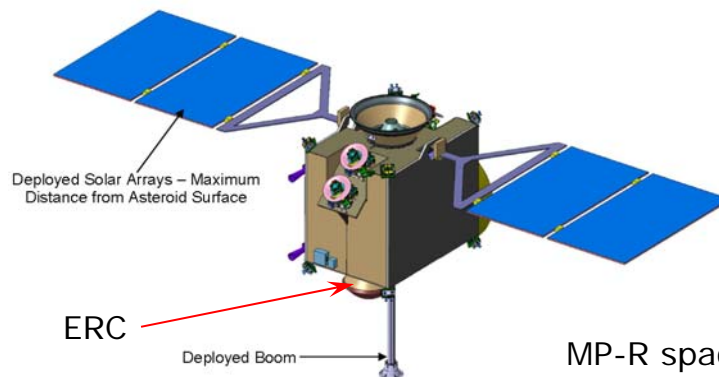


European Space Agency

Phootprint & MP-R ERC: System requirements



- Footprint compatible with Woomera area / to be minimised for easy recovery
 - Steep entry preferable
- Mass minimisation
 - TPS thickness minimisation privileges a steep entry
 - But FPA limited by TPS performance and ERC deceleration
- MarcoPolo-R has very similar requirements for ERC as Phootprint, e.g. fully passive re-entry, no parachute, sample mass, sample temperature, etc.

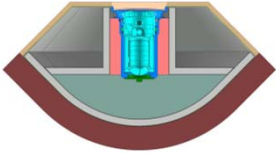
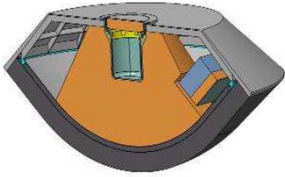


MP-R spacecraft (2 concepts)

European Space Agency

Phootprint ERC: Main features (very similar for MP-R)



	Astrium	TAS
General architecture	 <p>Hayabusa shape 45deg cone angle Diam 650 mm Mass 24 Kg CoG 29% D RN/D=0.5</p>	 <p>Hayabusa shape 45deg cone angle Diam 795 mm Mass 39 Kg CoG 30% D RN/D=0.5</p>
TPS material	FS: ASTERM* 0.28 g/cm ³ BS: Norcoat Liege 0.45 g/cm ³	FS: ATLAS** 0.25 g/cm ³ (target) BS: ATLAS
Entry conditions	V= 12.3 Km/s, FPA= -9.1deg	V=11.75 Km/s, FPA=-10.5deg
Peak heat flux incl margins (for FS)	15 MW/m ² @ stagnation point	14.9 MW/m ² @ stagnation point
TPS thickness	FS: 56mm BS: 11 mm	FS: 50mm BS: 3 to 9mm
TPS support structure (TPS glued)	FS: CFRP+Al sandwich BS: Al 2mm thick	FS: CFRP+Al sandwich BS: Al 1.5mm + ribs
Max temperature at TPS/FS structure I/F	170 degC	161 degC

* Phenolic resin impregnated carbon felt

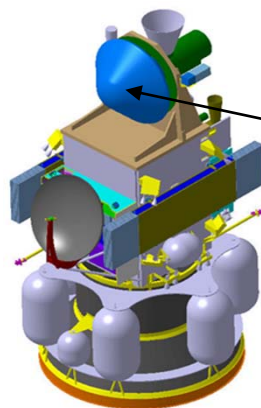
** Carbon fibres impregnated with phenolic resin

Mars Sample Return ERC: System requirements



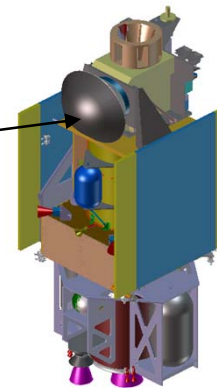
- Very high reliability due to Planetary Protection (PP) requirements
- Fully passive re-entry, no parachute
- Carries a Biocontainer with the sample (35 cm diameter / 15 Kg) and an RF beacon
- Sample temperature to be kept below 20degC except short excursions
 - Impact on the thermal load path to the sample
- Biocontainer g-loads at landing 500g max (PP-driven)
 - Drives the required stroke and ERC size
- Stability / limited oscillations in subsonic for a good landing
- Relative entry velocity between 11 and 12.7 Km/s depending arrival date and prograde vs retrograde (timeframe: 2027 to 2031)
- Mass minimisation due to high snowball effect on the ERC (preference for light density TPS)

Astrium design



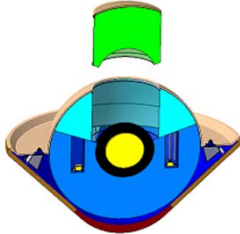
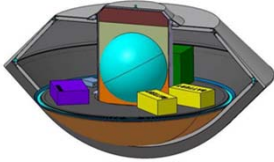
ERC

TAS design



Mars Sample Return ERC: Main features



	Astrium	TAS
General architecture	 <p>EVD shape 45deg cone angle Diam 1400 mm Mass 130 Kg CoG 29% D RN/D=0.25</p>	 <p>Hayabusa shape 45deg cone angle Diam 1400 mm Mass 120 Kg CoG 30% D RN/D=0.495</p>
TPS material	FS: ASTERM 0.42 g/cm ³ BS: Norcoat Liege 0.45 g/cm ³	FS: ATLAS 0.25 g/cm ³ (target) BS: ATLAS
Entry conditions	V=12.1 Km/s, FPA=-8.2deg	V=12 Km/s, FPA=-12deg
Peak heat flux incl margins (for FS)	15 MW/m ² @ stagnation point	13 MW/m ² @ stagnation point
TPS thickness	FS: 65mm BS: 13mm	FS: 50mm BS: 12mm
TPS support structure (TPS glued)	FS: Ti sandwich BS: metallic (Al or Ti)	FS: CFRP+Al sandwich BS: CFRP+Al sandwich
Max temperature at TPS/FS structure I/F	190 degC	170 degC

ESA Technology Roadmaps ongoing and planned developments

H. Ritter; L. Marraffa; L. Ferracina; J. Longo

7th European Workshop on
Thermal Protection Systems & Hot Structure

8 April 2013

- Recently ESA promoted a road mapping activity on Exploration Technologies, coordinating inputs from all concerned ESA Directorates and European Industry.
- A set of technology roadmaps has been compiled illustrating, for a timeframe beyond the Ministerial Council 2012, the technologies needed for space exploration.
- Following the outcome of the Ministerial Council in Nov. 2012, these roadmaps are currently refined.
- The roadmaps will then be used for the preparation of a consistent procurement plan for space exploration technologies in Europe.
- Optimum coordination of funding sources is needed from corporate R&D, ESA Exploration Programmes, and exploiting synergies with technology investments by other (ESA & non-ESA) programmes.

Technology Roadmaps

Exploration Technology Areas



Mars Robotic Exploration Programme (MREP) has studied four mission candidates for the post-Exomars launch slots:

- INPIRE: A Mars network science mission with three 300kg-class landers (considered as 2024-2026 candidate)
- Precision lander (< 10 km with hazard avoidance) with sampling/fetching rover (possible candidate after 2024 frame)

Heatshield building on heritage of ExoMars 2016 EDM. However, performance enhancement might be required.

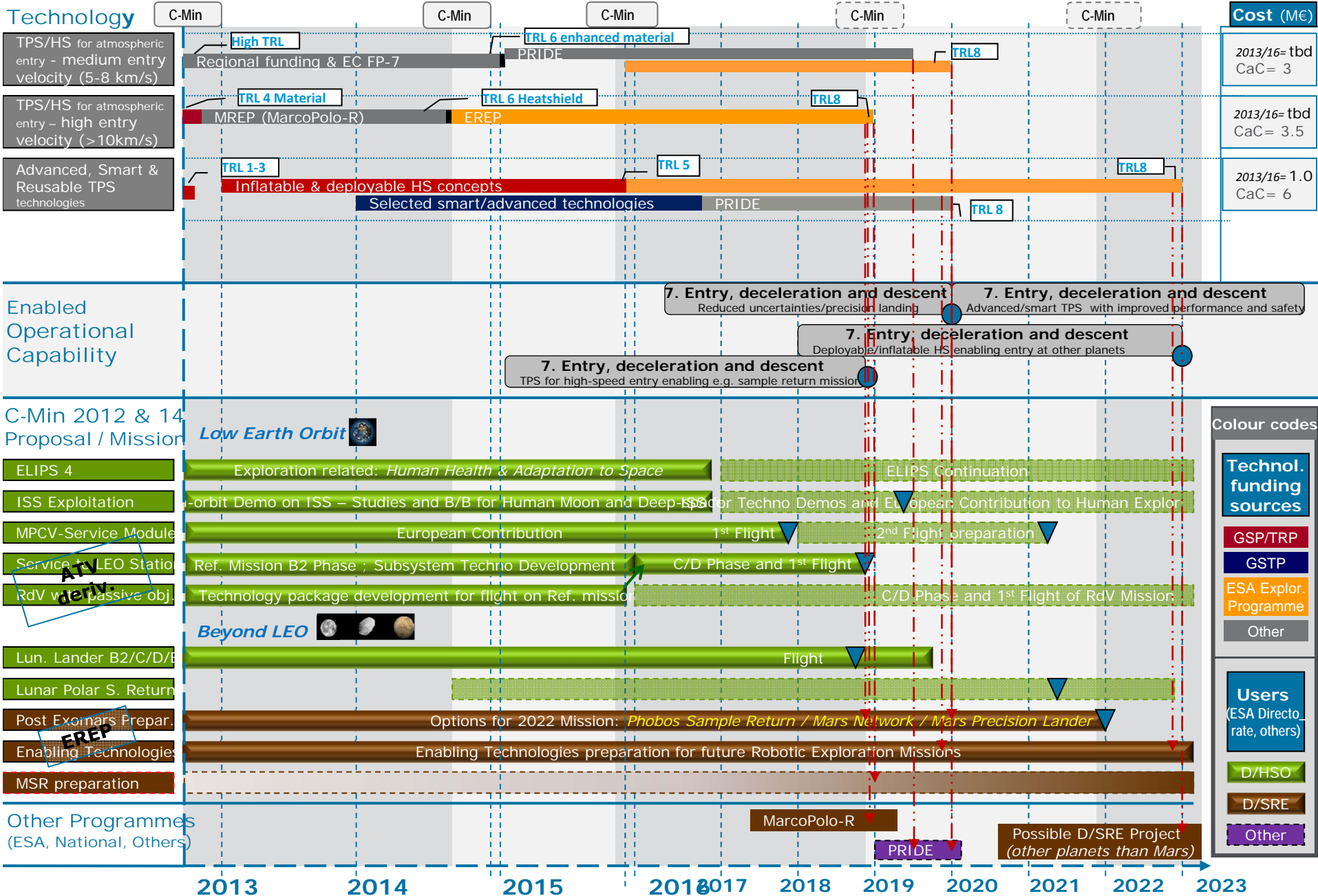
- PHOOTPRINT: sample return from the Mars moon Phobos (considered as 2024-2026 candidate)
- MSR orbiter (considered as long-term candidate)

Include an ERC to bring samples back to Earth. Critical technologies include:

- TPS for heat fluxes up to about 14 MW/m²
- Shock-absorbing structure for hard landing
- Planetary protection

In addition, Cosmic Vision program is re-assessing

- MarcoPolo-R aiming to bring back a sample from a near-Earth asteroid



Slide 1 - Explanatory Notes (1/2)

- **TPS/HS for atmospheric entry – medium entry velocity (5-8 km/s)**
 - Existing solutions available with high TRL for Earth and Mars entry
 - Ensure long-term availability (at low production rates)
 - Performance enhancement of existing materials (thermal performance, reduced and more homogeneous recession, resistance to ablation)
 - Optimise/tailor materials towards different environments (e.g. CO₂, high pressure, high shear, backcover)
 - Improved ablative systems (e.g. based on advanced materials or combined ablative-structural systems)
 - Complete databases for improved modelling
- **TPS/HS for atmospheric entry – high entry velocity (>10 km/s)**
 - Complete development and qualification of European material(s) able to withstand 10-20 MW/m²
 - Optimise/tailor materials towards different environments (e.g. CO₂, high pressure, high shear)
 - Reliability enhancement
 - Ensure long-term availability (at very low production rates)
 - Complete database for improved sizing analysis
 - Material consolidation up to TRL6 already covered in MREP

Slide 1 - Explanatory Notes (2/2)

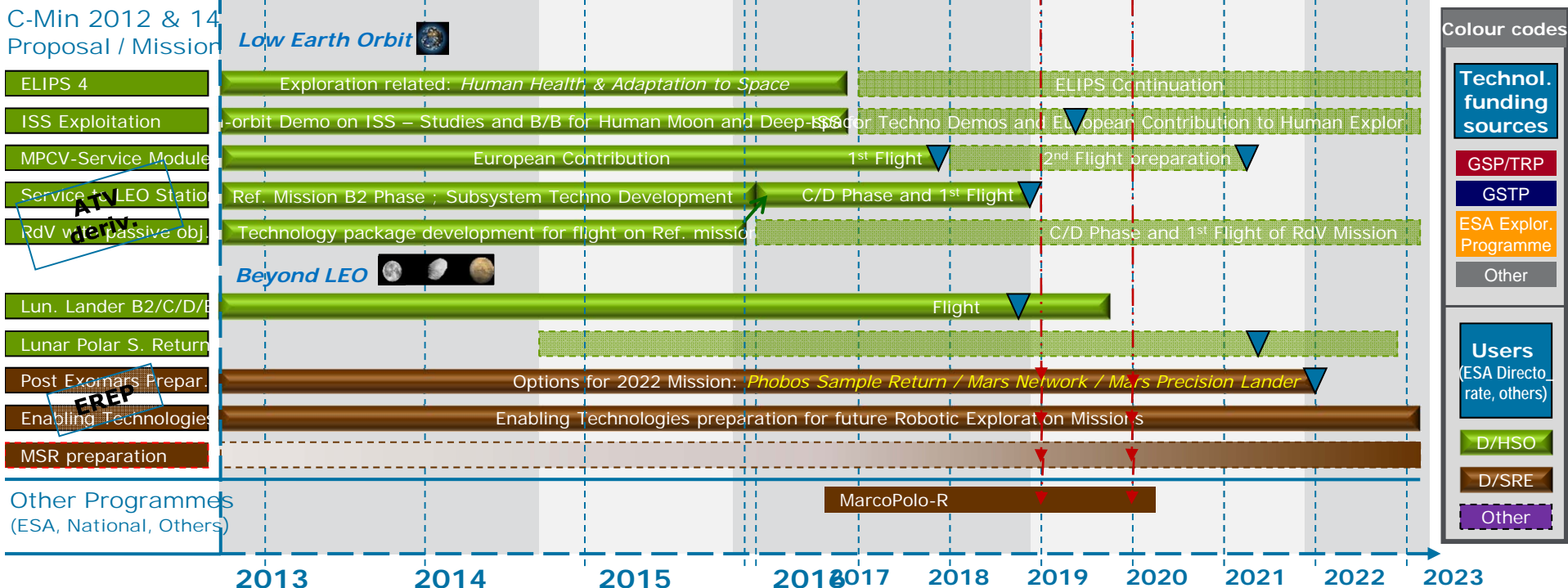
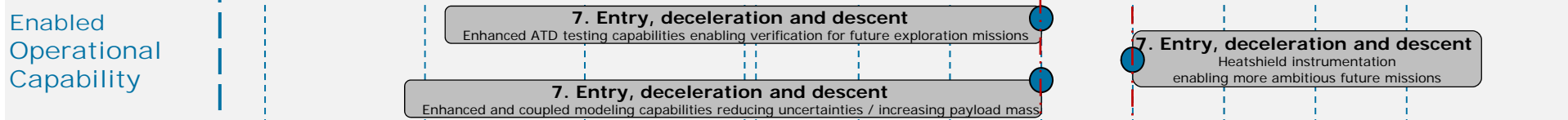
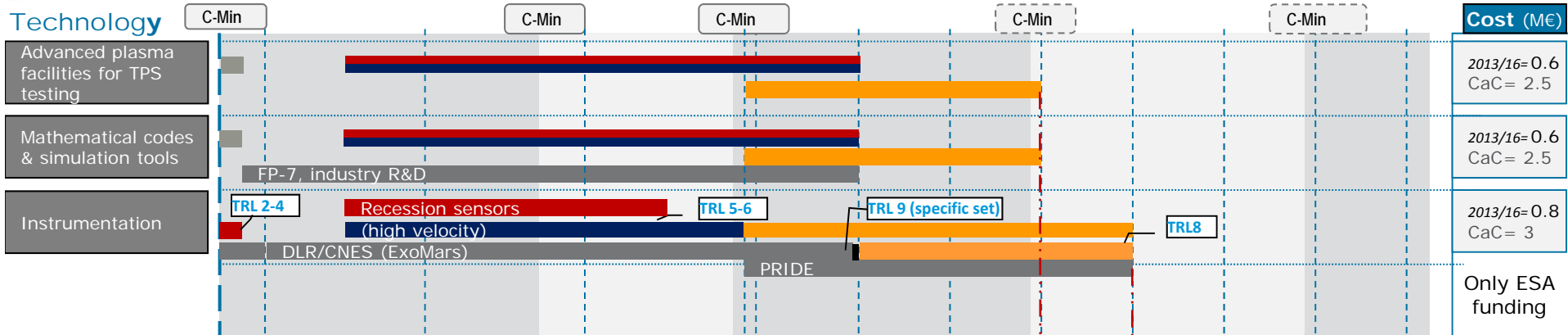
- **Advanced, Smart & Reusable TPS technologies**

- Deployable and/or inflatable heatshield & aero-braking concepts
 - Such technology might enable future planetary exploration missions which are not feasible today, e.g. high masses towards Venus, Saturn, Uranus and Neptune, but also to currently unreachable areas on Mars. By cutting down the ballistic coefficient, the heat flux, heat load and pressure are significantly reduced.
 - System study is required to assess the benefits/potential for new missions, trade-off deployable versus inflatable systems and assess the potential to develop the key technologies, including flexible TPS solutions and inflatable and/or deployable decelerator structures.
- Advanced overall heatshield design concepts (ablator on top of hot structure, crushable systems, ...)
- Smart systems, i.e. able to adapt to the environment or to adapt the aerodynamic shape
- Self-healing capabilities, secondary protections & in-orbit repair technologies
- Integrated active cooling systems
- Integrated micro-meteorite/radiation protection
- Reusable TPS for very high temperatures (>2000degC) using e.g. UHTC



5
3

Application Area: Thermal, TPS & Aerothermodynamics Aspects
 Technology Subject: Thermal Protection Systems (2/2)

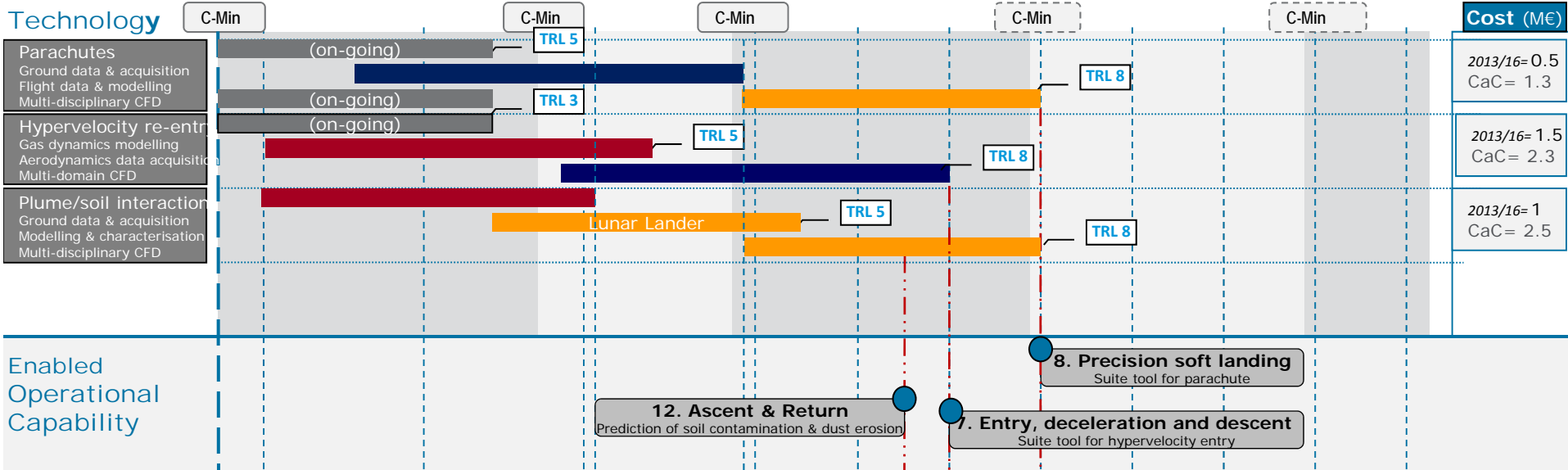


Slide 2 - Explanatory Notes

- **Advanced plasma facilities for TPS testing**
 - Capabilities at extreme heat fluxes (15-25 MW/m²) in air and CO₂
 - Capabilities to simulate also radiative fluxes
 - Capabilities to test sub-assemblies at more representative conditions
 - Calibration and diagnostics methodologies (standard cases, reduced uncertainties)
 - Improved facility instrumentation
- **Mathematical codes & simulation tools**
 - Improved modelling capabilities (ablation, pyrolysis, oxidation, in-depth heat transfer, ...)
 - Coupled analysis capabilities (ablation, flow-material interaction, radiation)
 - Enhanced capabilities for high velocity (radiation, Mollier at very high temperature, ...)
 - Rebuilding, correlation, verification with test cases
 - Implementation towards heatshield assemblies (3D-capabilities)
- **Instrumentation**
 - Development of advanced (combined) sensor systems (temperature, pressure, heat flux, radiation)
 - Ablation recession sensors
 - Health monitoring systems
 - Related mathematical tools (e.g. inverse methods to derive surface heat flux from in-depth temperatures)

5
4

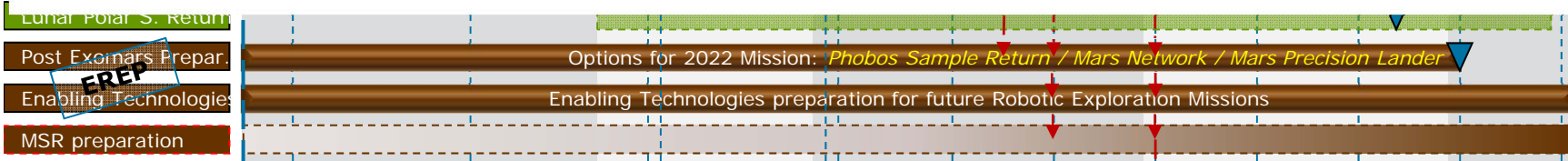
Application Area: Thermal, TPS & Aerothermodynamics Aspects
 Technology Subject: *Aerothermodynamics design tools for entry, descent, landing and take-off*



C-Min 2012 & 14

Hypervelocity re-entry Suite Tool.

- Development of a shock tunnel for hypervelocity gas dynamics characterisation and the corresponding measurement system (on-going).
- Upgrade of a shock tunnel for aerodynamic characterisation of hypervelocity re-entry and the corresponding measurement system.
- High fidelity multi-disciplinary multi-domain design tool for hypervelocity re-entry (with emphasis in aerodynamic instability due to shape change by ablation).



Colour codes

Technol. funding sources

- GSP/TRP
- GSTP
- ESA Explor. Programme
- Other

Users
(ESA Directorate, others)

- D/HSO
- D/SRE
- Other

- TRP activities:
 - European ablative materials (similar to US PICA) developed (DEAM)
 - Validation of aerothermochemistry models (two studies)
 - Models for Ablation-Radiation coupling under development
 - PARADE (Plasma Radiation Database) & CFD validation
 - In-flight heatshield sensors (LISE study)
 - ESA kinetic shock tube under development
 - European facilities upgraded for extremely high fluxes and pressures: VKI, DLR, IRS, CIRA (within AURORA)
- ESA WG on ablation, ESA/CNES WG on Radiation

Recently initiated & planned TDA's

TPS high entry velocity



Delta-development and Pre-qualification of a European lightweight Ablative material for sample return missions (DEAM-2)

- Objectives / planned work
 - Consolidation of material definition and related manufacturing process
 - Complete material characterisation
 - Extensive plasma testing
 - Pre-qualification including plasma tests on assemblies with interfaces
 - Large-scale TPS demonstrator manufacturing
- Goal: TRL-6 by 2014
- Status: Recently started, test campaigns in preparation
- Prime contractor: Astrium (F)
- Baseline material: ASTERM STD (density 280 kg/m³)



Recently initiated & planned TDA's

TPS high entry velocity



Characterization of TPS materials of High-density for High Heat flux re-entry applications (CT3H)

- Objectives
 - Characterize and test in laboratory and plasma environment samples of an existing European ablative heatshield material which has flight track records and which is suited to withstand the Earth re-entry conditions of a sample return mission such as MSR
 - Assess the reliability of the material for such mission under consideration of the particular planetary protection requirements
- Background: Planetary protection
- Goal: TRL-4 by 2014
- Status: Under negotiation

Recently initiated & planned TDA's

TPS medium / high entry velocity



Ablative Material Optimisation and Definition of Material Families adaptable to various Applications (AMOF)

- Objectives / planned work
 - Determine the limits of an existing reference ablative material when varying its key material parameters (e.g. density, mixing ratio and/or additive components)
 - Derive tailoring guidelines allowing to optimise the material definition and manufacturing process towards the requirements coming from a new mission application
 - Define optimised material definitions and manufacturing processes for selected new application types
 - Manufacture and test optimised material samples
- Status: Contract signed
- Prime contractor: HPS (D) with Astrium (F) for material development
- Baseline material: ASTERM STD (density 280 kg/m³)

Recently initiated & planned TDA's Advanced TPS/heatshield technologies



1. Material development for crushable TPS for the ERC

- Objectives / planned work
 - Develop a material that:
 - will be attached to an ablative material and to a cold structure
 - will absorb the impact energy and limit the acceleration loads on the payload to acceptable values.
 - will act as thermal insulation between the hot ablative material and the cold structure
- Status: Recently started (requirements review and screening on cellular/crushable materials ongoing)
- Contractor: Magna Parva (UK) with Manufacturing Technology Centre as sub-co

2. Design of a crushable TPS for the ERC

- Objectives / planned work
 - Investigate ways of building a multifunctional crushable TPS structure that not only acts as a heat shield for planetary re-entry but also brings structural integrity and mechanical shock damping capability for hard landing
 - Build and test breadboard models and perform detailed material characterisation
- Status: Under negotiation

Recently initiated & planned TDA's

Advanced & smart heatshield technology



Maxus International Nacelle to Investigate IRENE capabilities (MINI IRENE)

- Background
 - In 2010/2011 ASI has promoted and financed the feasibility study for the low-cost capsule "IRENE" with the objective to return payloads from the ISS to Earth and to perform short scientific missions or Earth observation activities from LEO.
 - Preliminary platform design was developed and potential heatshield materials tested.
 - Six-months "bridging phase" under ESA contract (phase A) to identify a low cost future demonstration mission as piggy-back payloads in a sub-orbital Maxus sounding rockets
- Objectives under new GSTP
 - Phase B design of Mini-IRENE capsule (flight demonstrator), including structure, heatshield, deployment mechanism and electronic subsystems
 - Development and testing of a scaled technology ground demonstrator (breadboard) of the variable geometry umbrella-like heatshield of IRENE capsule, the Mini-IRENE
- Status: In preparation

Recently initiated & planned TDA's

Advanced plasma facilities



Characterisation of high enthalpy facilities (CHEF)

- Objectives / planned work
 - Characterization of the flow field parameters at relevant locations in the facility (reservoir, arc generator, plenum chamber, nozzle and test region), using conventional and advanced measurement techniques
 - Quantification and reduction of uncertainties on the knowledge of the main drivers for material testing (convective and radiative heat flux, pressure, enthalpy, flow composition, radiation...), including gradients over the article surface
 - Establishment of standard procedures for calibration and tests, transferable to other facilities
 - Correlation of physico-chemical and numerical models with experimental results obtained at different locations of the facility
- Status: Started
- Prime contractor: DLR

Recently initiated & planned TDA's

Mathematical codes & Simulation tools



Aerothermodynamics of light ablative TPS

- Objectives / planned work
 - Prepare a catalogue of the existing European heat shield materials, defining the current performance envelope and extending the envelope where feasible.
 - Development of an ablation code suitable for classical and future ablation materials.
 - Develop 3D radiative transfer codes for the prediction of radiative fluxes around an entry vehicle or a payload/launcher element.
 - Miniaturization of Electron Beam Fluorescence for hypersonic-flow in-flight characterisation to perform local, non intrusive, steady and unsteady measurements of density, vibrational and rotational temperatures and velocity in low density hypersonic flows.
- Status: Planned (ITT expected end 2013)

Recently initiated & planned TDA's

Mathematical codes & Simulation tools



Catalytic properties of Ablators

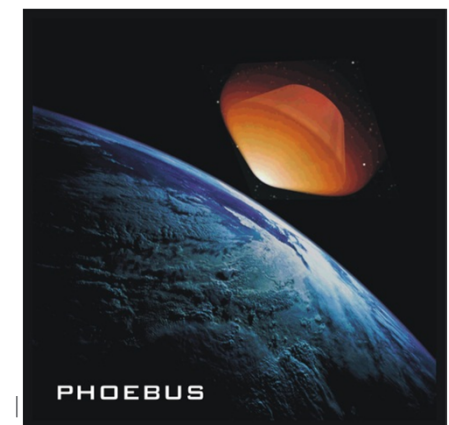
- Objectives / planned work
 - Determine the catalytic properties of ablator materials and derive corresponding physical models for implementation in CFD codes
 - Stringent requirements on cleanliness apply
- Status: Under preparation

Conclusion



- Technology roadmaps have been defined identifying the global development need for future exploration missions.
- Consolidation of these roadmaps, following the C-Min from Nov. 2012, and preparation of procurement plans is on-going.
- A number of relevant TDA's was recently initiated or is in preparation.
- Development needs over recent years have shifted with a stronger focus again on ablative materials, particularly for high-speed entry.
- European Ablation Working Group has prepared relevant numerical test cases for code assessment. Progress is slower than wanted due to limited budget.
- In-flight demonstration for high-speed Earth re-entry is considered highly relevant. PHOEBUS was studied to assess high-speed Earth entry: New TPS materials, radiative flux (particularly VUV), ablation-radiation interaction.

7th European Workshop on Thermal Protection Systems & Hot Structures | Noordwijk | 8-10 April 2013 |



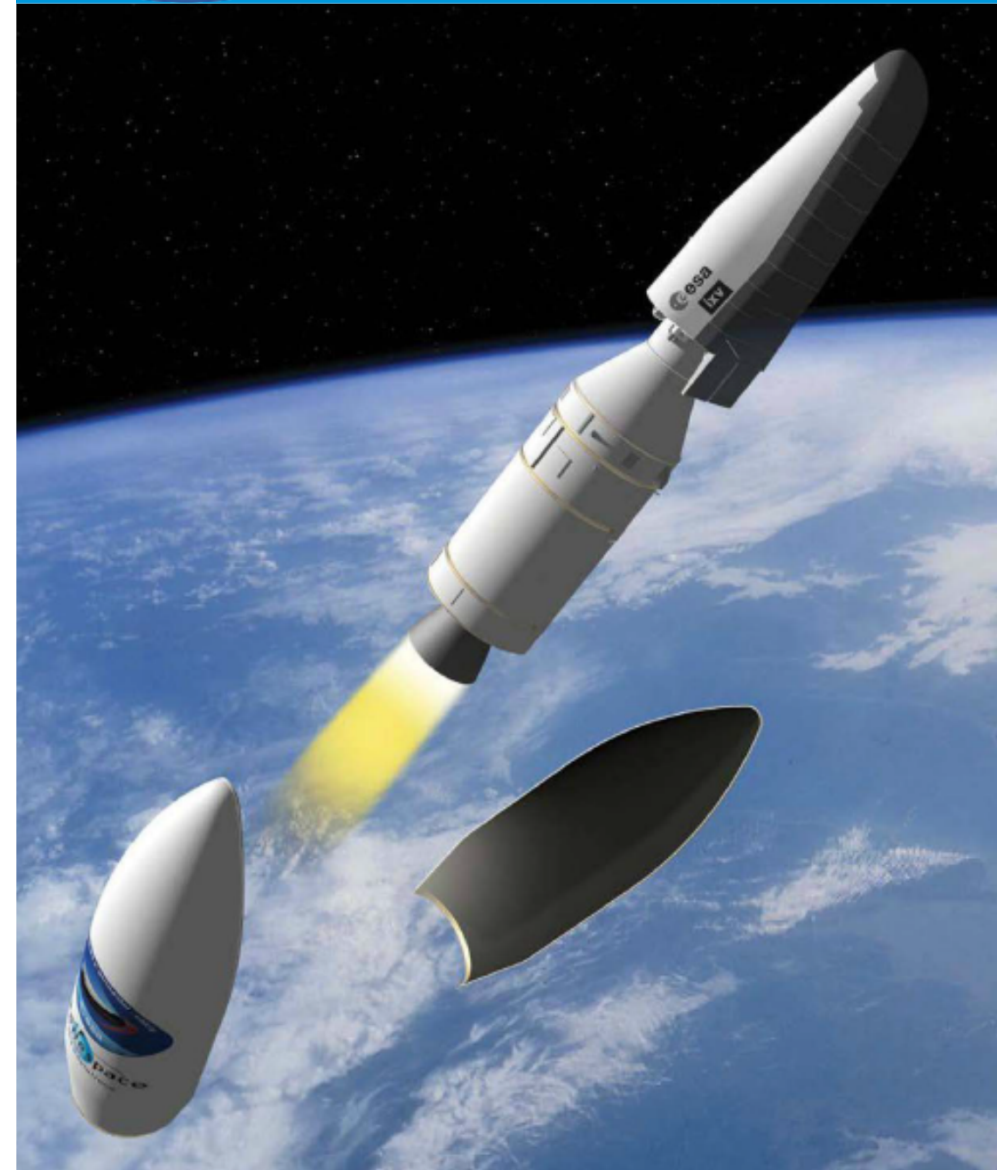
European Space Agency



The IXV Development Status and Perspectives

*Giorgio Tumino
Directorate of Launchers
European Space Agency*

7th European Workshop on TPS-HS, Noordwijk (NL), 8th April 2013





The IXV Development Status and Perspectives



Contents of the Presentation:

- **The Mission**
- **The Flight Segment**
- **The Ground Segment**
- **The Launch Campaign**
- **The Plan-at-Completion**
- **The Short-term Perspectives**
- **The Long-term Perspectives**



The Mission

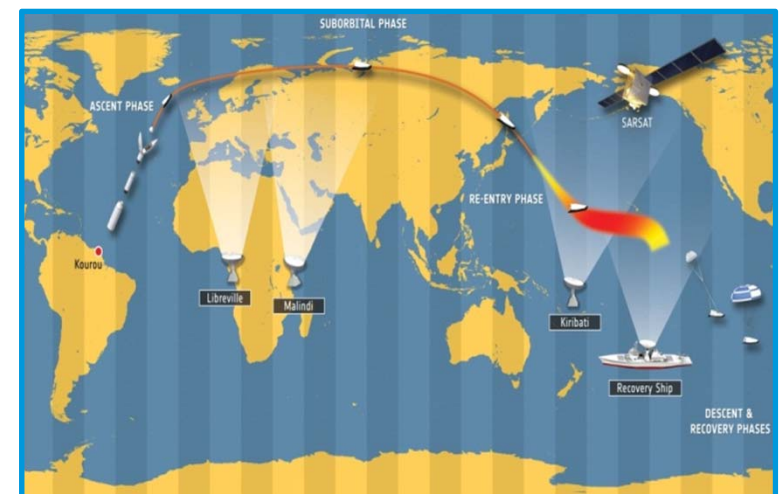


Objective:

The IXV is the “**intermediate**” element of a European roadmap enabling future operational system developments for a wide range of space applications at limited risks for Europe. The main mission objective is to perform the step forward with respect to the precursor **ARD**, by verifying in-flight the critical re-entry technologies performance (e.g. **TPS and HS**) against a **wider re-entry corridor**, while increasing the system performance in manoeuvrability, operability and precision landing.

Description:

The trajectory is equatorial, to comply with the minimization of the experimental flight over inhabited regions, and the maximisation of the VEGA launcher performance and its stages fall-out, where the IXV maximum altitude is set above 400 km, providing an entry velocity at the impact with the atmosphere of 7.5 km/s, **fully representative of LEO return mission**.





The Flight Segment

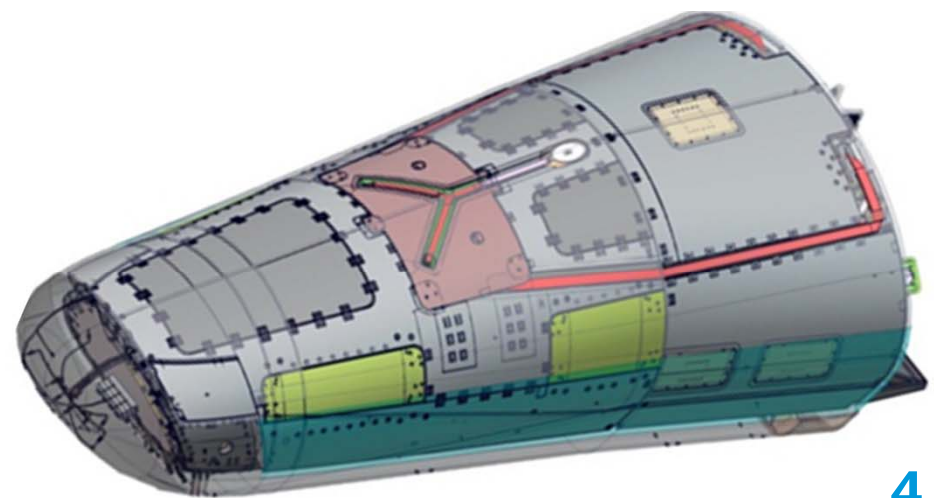
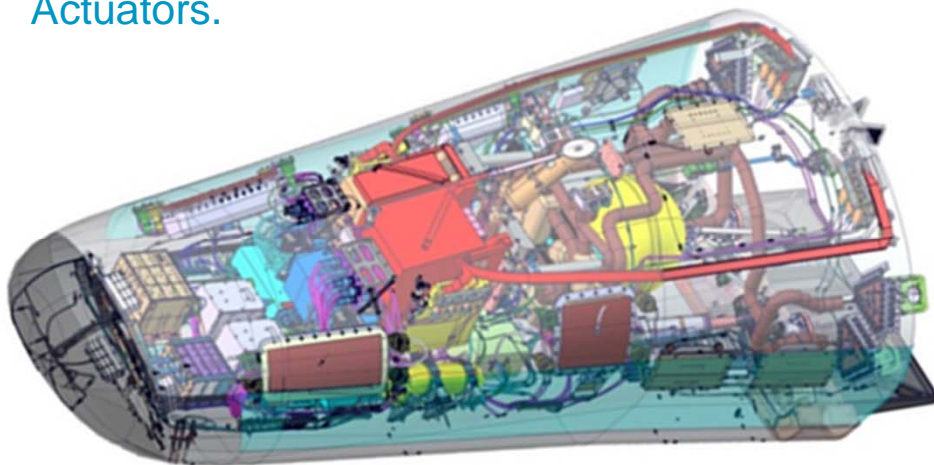
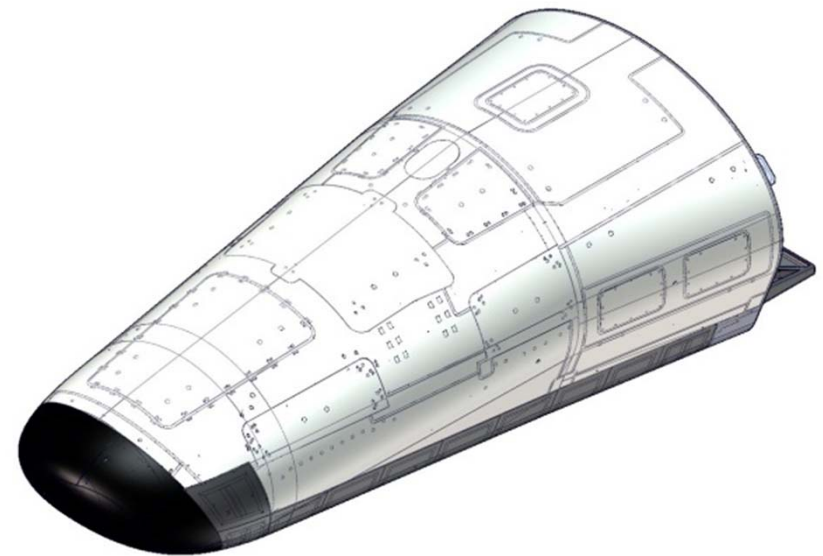


Spacecraft Configuration:

The spacecraft configuration is stable and characterized by a length of **5.0 m**, width of **2.2 m**, height of **1.5 m**.

From the outer to the inner layers, it includes the TPS and HS, the Structural Panels, the various Equipments.

From the front to the back compartments, it includes the Avionics, the Parachute, the Propulsion Panel, the Thrust Cylinder, the Control Actuators.





The Flight Segment



TPS and HS Subsystems Activities:



The thermal protection architecture is based on ceramic material for the nose, windward, hinge and body flaps, and ablative material for the lateral, leeward and base areas.

The windward area is protected by ceramic matrix composite **C-SiC panels** (shingles), with **lightweight ceramic insulations** (alumina/silica), and specific attachments made of **superalloy bolts**, **flexible stand-offs**, **ceramic thermal barrier washers**, and **ceramic fibres seals**. The nose assembly is derived from the windward technology to maximise synergies.

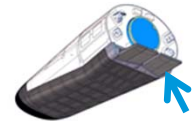




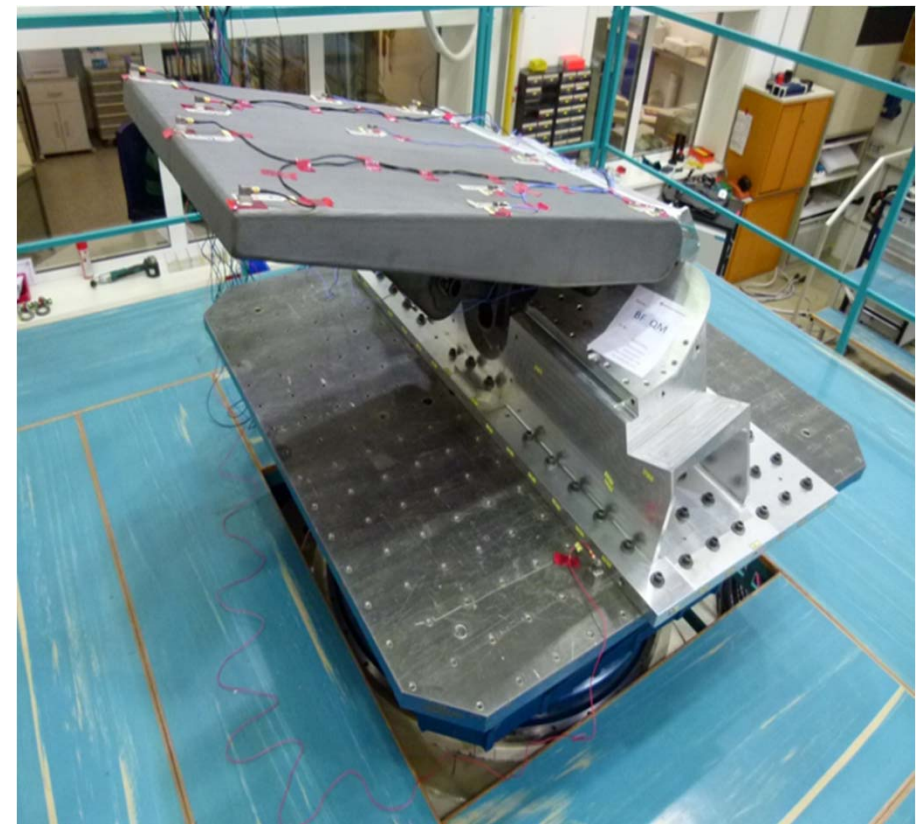
The Flight Segment



TPS and HS Subsystems Activities:



The design of the hinge and body flap assembly is based on ceramic **Keraman® C/SiC**, providing **highly integral components** complying with combined thermal, mechanical and vibration loads, interfaces and mass constraints.





The Flight Segment



TPS and HS Subsystems Activities:



The lateral, leeward and base areas are protected by ablative TPS, with an external **coating providing antistatic properties and proper thermo-optical characteristics**. The bonding of the tiles on the cold structure is assured through an **epoxy-based structural adhesive**. The gaps between adjacent plates are sealed with a filler made of the same adhesive used for bonding with addition of cork granules. This avoids thermal bridge effects among the different tiles.





The Flight Segment

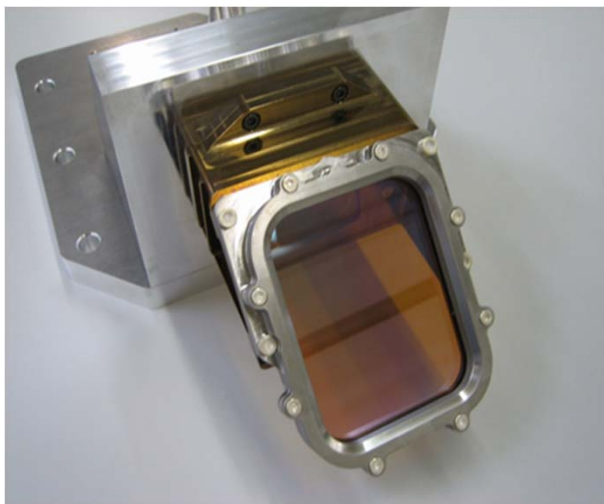


In-Flight Experimentation Activities:



The technological objectives of the IXV mission are met by flying a large number of experiments that have been chosen among a wide range of European proposals. Since each experiment required a specific set of measurements, several synergies and commonalities were exploited to identify a global set of sensors covering all experimentation requirements.

Sensors are split into **conventional** (i.e. 37 pressure ports, 194 thermocouples, 12 displacement sensors, 48 strain gauges) and **advanced** (i.e. infra-red camera).

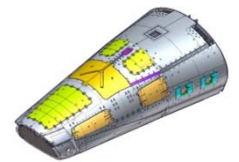




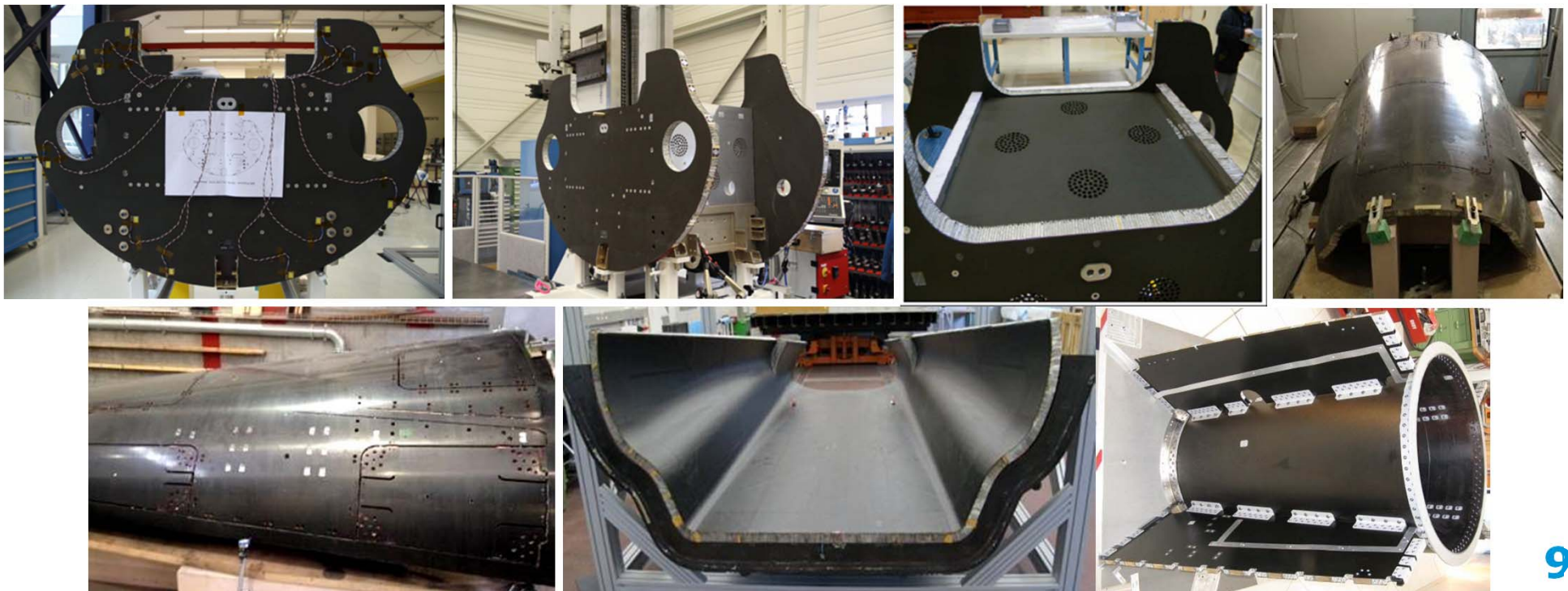
The Flight Segment



Structural Subsystem Activities:



The structure of the vehicle is based on carbon fiber reinforced plastics (CFRP), whose matrix is based on a high temperature resin selected in order to withstand the high temperature reached by the structure during the re-entry, with the design compliant with the challenging VEGA launcher requirements on stiffness, and mission requirements on strength induced by the sea landing impact.

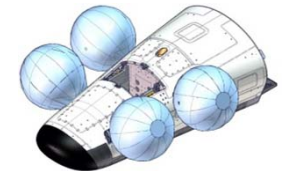




The Flight Segment



Mechanisms Subsystem Activities:



The mechanisms of the vehicle includes the **panel jettisoning** for the descent and recovery system deployment, and the **umbilical connectors** between the spacecraft and the launcher.

The panels jettisoning mechanisms **avoid the use of pyro-cords** thanks to the avionics architecture which is compatible with the implemented **non-explosive actuators**.

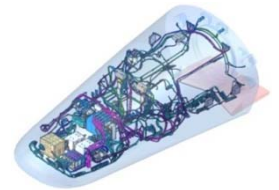




The Flight Segment



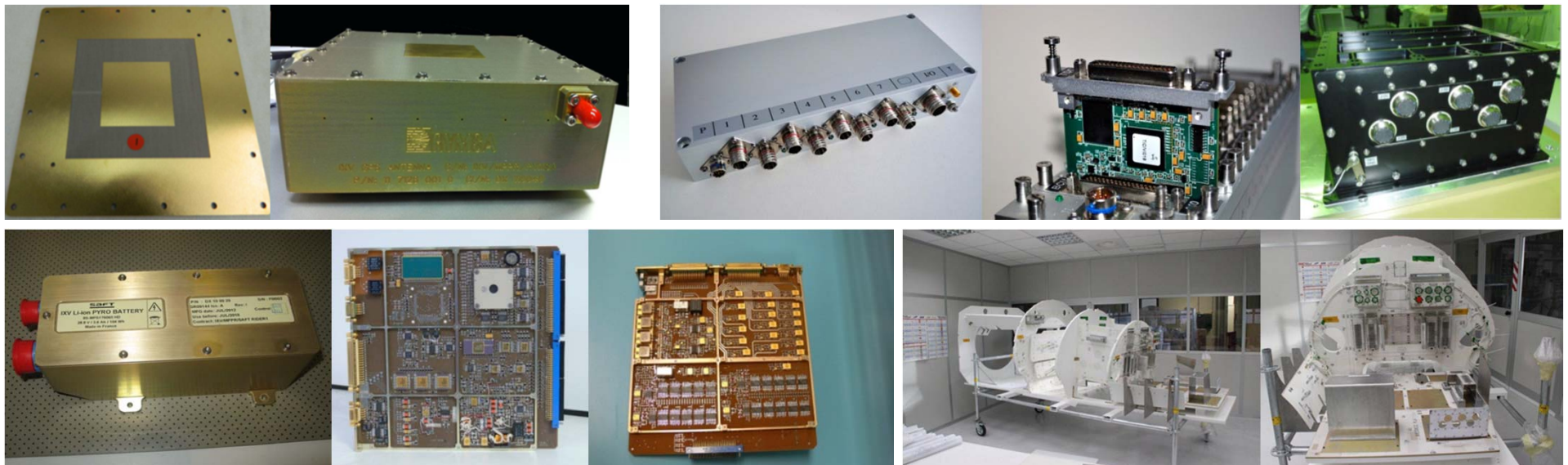
Electrical and Avionics Subsystems Activities:



The Power subsystem is based on a 28V main bus, maximizing off-the-shelves equipment, with protected outputs, performing DC/DC conversion to 55V for the Inertial Measurement Unit, with dedicated pyrotechnic section.

The Data Handling subsystem provides vital layer and experimental data acquisition, storage, recording, real time and delay transmission to the ground stations.

The Radio Frequency Telemetry subsystem is based on two independent chains for vital layer and experiment telemetries. It implements frequency and polarization diversity techniques for maximum coverage and data download capability.





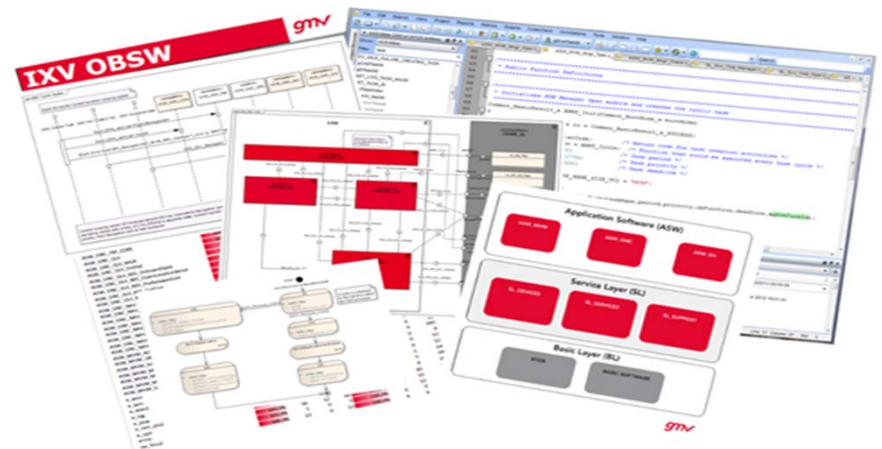
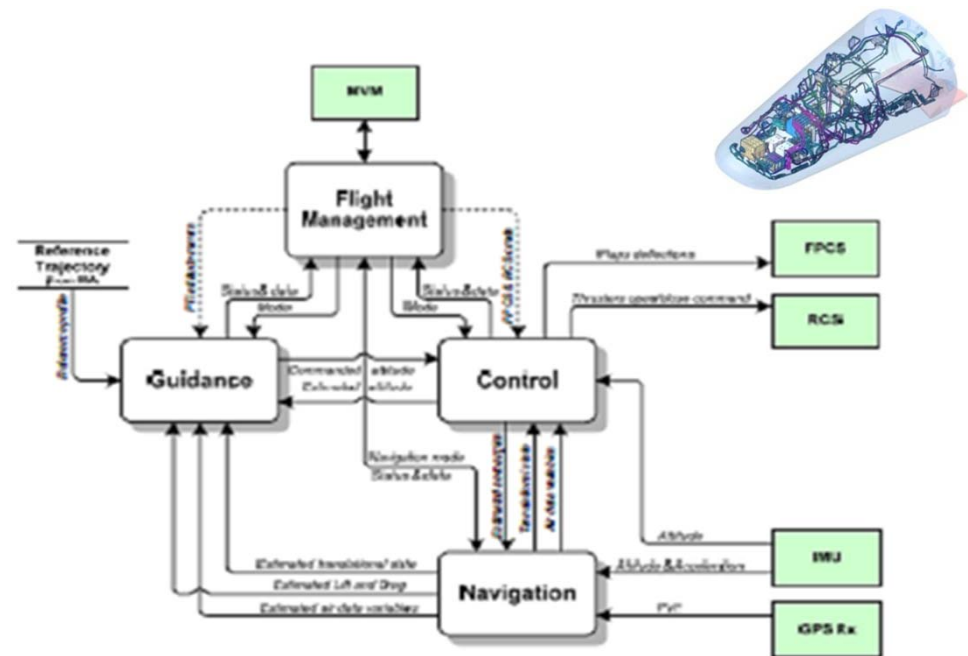
The Flight Segment



GNC and Software Activities:

The spacecraft GNC covers the three main mission phases (i.e. orbital, re-entry, descent), thanks to the **Flight Management** function which interfaces on one side with the **MVM** (Mission and Vehicle Management), and on the other side with the three **specific GNC functions** (i.e. guidance, navigation and control).

The SW activities include the **application SW** (i.e. the Mission and Vehicle Management SW), the **GNC SW**, the **SW embedded in the equipment's** (IMU, GPSR, FPCS), and, last but not least, **SW for the descent and landing system synthesis test**.





The Flight Segment



Descent and Recovery Subsystems Activities:



The descent and recovery function is assured by two dedicated subsystems, the parachute subsystem for the descent phase, and the floatation subsystem for the recovery phase.

The descent subsystem is based on a **four stages parachute** with consolidated technology, including one supersonic pilot, one supersonic ribbon drogue, one subsonic ribbon drogue, and one ringsail main parachute, with a **mortar** to extract the supersonic pilot and **strap-cutters**, and to separate the various parachute stages and the main parachute from the spacecraft after splash-down.





The Flight Segment



Descent and Recovery Subsystems Activities:



The recovery subsystem is also based on consolidated technology, including **inflation** devices (i.e. gas bottles, valves, hoses), **floatation** devices (i.e. balloons), and **localization** devices (i.e. beacons).

With the objective to mitigate the risk of failures occurring in the critical descent and landing phases, a dedicated Descent and Landing System Synthesis Test is planned in April 2013, where a system prototype shall be launched from a 3.0 Km altitude by an helicopter in a test range in Sardinia (I), and shall verify the last phases of the IXV mission, including descent, water splash-down, balloons inflation, floatation and recovery operations.

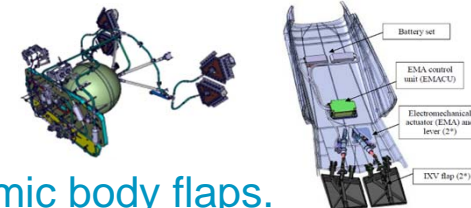




The Flight Segment



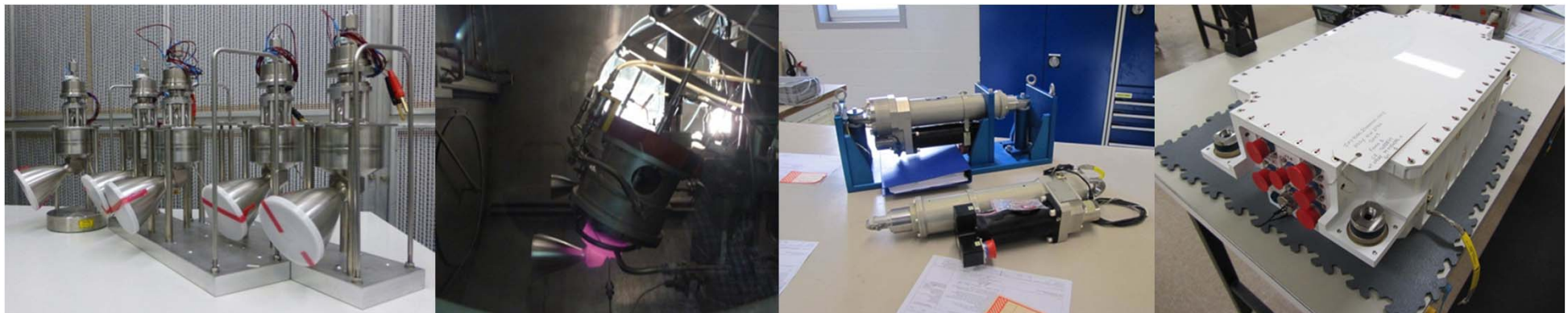
Flight Control Subsystems Activities:



The flight control is assured by means of four 400N thrusters and two aerodynamic body flaps.

The thrusters, inherited from the ARIANE 5 SCA, are located at the base of the vehicle to control the **attitude around the three axes during the orbital phase**, the **yaw during the atmospheric re-entry**, and providing **additional control authority to the body flaps in pitch and roll during the re-entry phase**, if required.

The flaps are also located at the base of the vehicle to **trim the vehicle on the longitudinal (symmetrical deflections) and lateral (unsymmetrical deflections) axes during the atmospheric re-entry phase**. These are actuated by two electro-mechanical-actuators (EMA), whose technology is inherited from the VEGA Zefiro thrust vector control system.





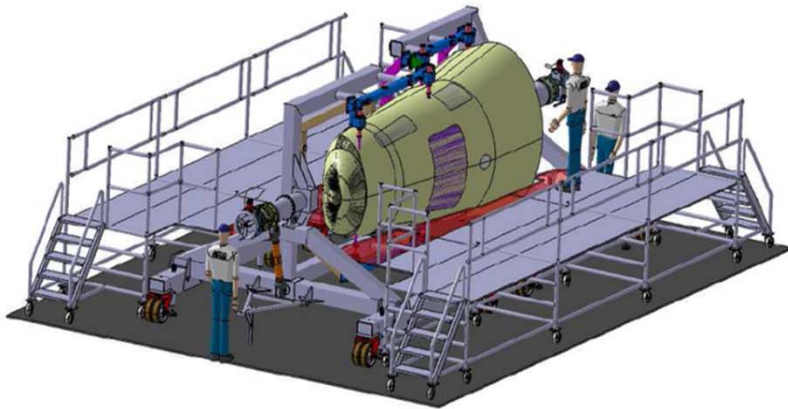
The Flight Segment



Ground Support Equipment Activities:

With the objective to minimize the financial efforts of the programme, several GSE elements have been reused from past ESA programmes, such as **HERSCHEL-PLANCK** (Anti-Seismic Racks and Mains Insulation Transformer Units), **XMM** (Vertical Support Stand), **GOCE** (Mechanical Test Adaptor, Test & Handling Clamp Band, Structure Panel Container), **CRYOSAT** (Spacecraft Container).

For what concerns the MGSE under development within the IXV activities, this includes the **Handling Adaptor**, the **Spreader Beam**, the **Mass Dummies Structures**, the **Panel Hoisting Device**, the **Trolleys and Access Platform**, the **Tilting and Lifting Device**, and the **Physical Properties Adaptor Plate**.





The Flight Segment



Ground Support Equipment Activities:

For what concerns the EGSE under development within the IXV activities, this includes the RF (Radio Frequency) Suitcase, the Battery Simulator SCOE, the Umbilical SCOE, the Overall Check-Out Equipment.





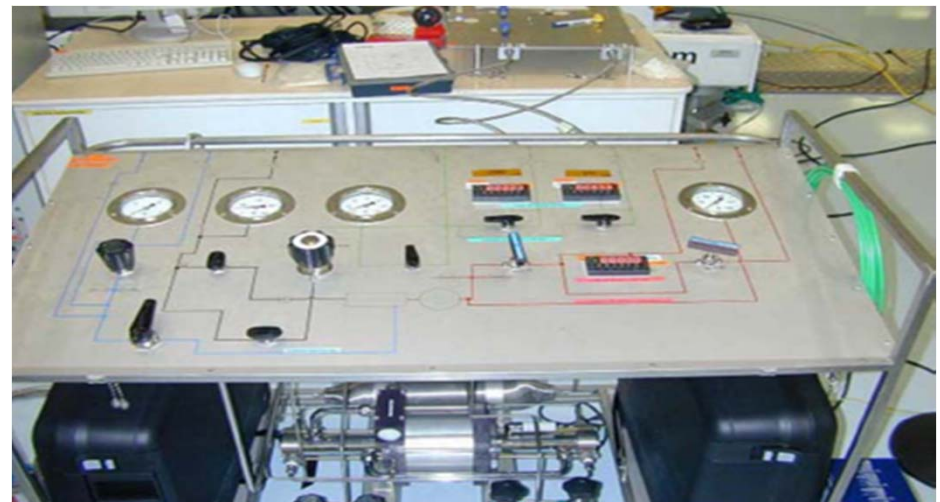
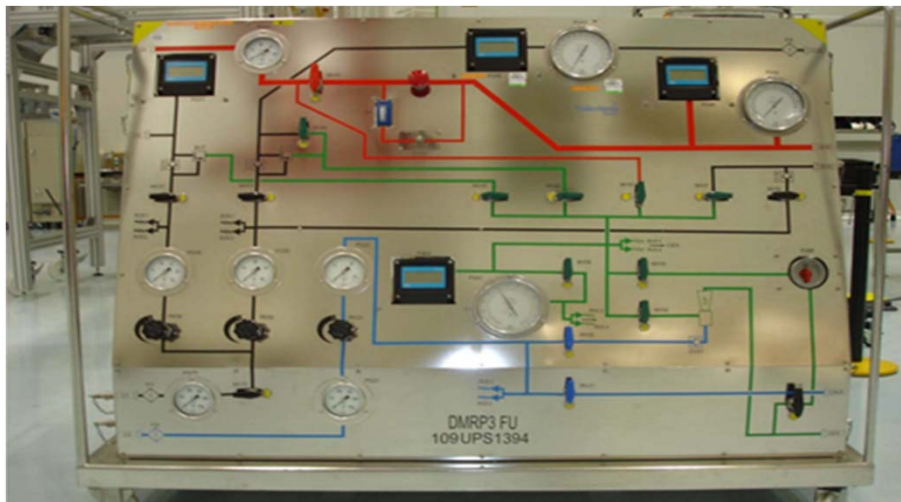
The Flight Segment



Ground Support Equipment Activities:

For what concerns the FGSE, this will make maximum use of equipment available at industrial premises. More specifically, it consists of:

- the parts owned by TAS-F, such as the existing **DMRP** (Dispositif Mobile de Remplissage et Pressurization), which will be used for the filling of the IXV tanks, and the **PTD** (Pressure Testing Device), which will be transferred to Turin at the start of the RCS integration in Q2-2013;
- the part owned by TAS-I, such as the **portable equipment** adapted to the IXV recovery operation's needs, which will be refurbished and tested in Turin during the integration campaign.





The Ground Segment



The Mission Control Centre:



The MCC development activities are well progressing, and the MCC is ready to undergo the qualification tests, including integrated testing with the telecommunication network and the telemetry system.





The Ground Segment



The Ground Stations:



For what concerns the telemetry system, the kit is ready to undergo qualification tests, and the first shelter structure is available and its acceptance was successfully performed.



For what concerns the antennas, the naval transportable antenna with scan-feed tracking to be embarked on-board the recovery ship is currently under manufacturing, while the ground transportable antenna to be installed in the Archipelagos of Kiribati is planned to be rented.





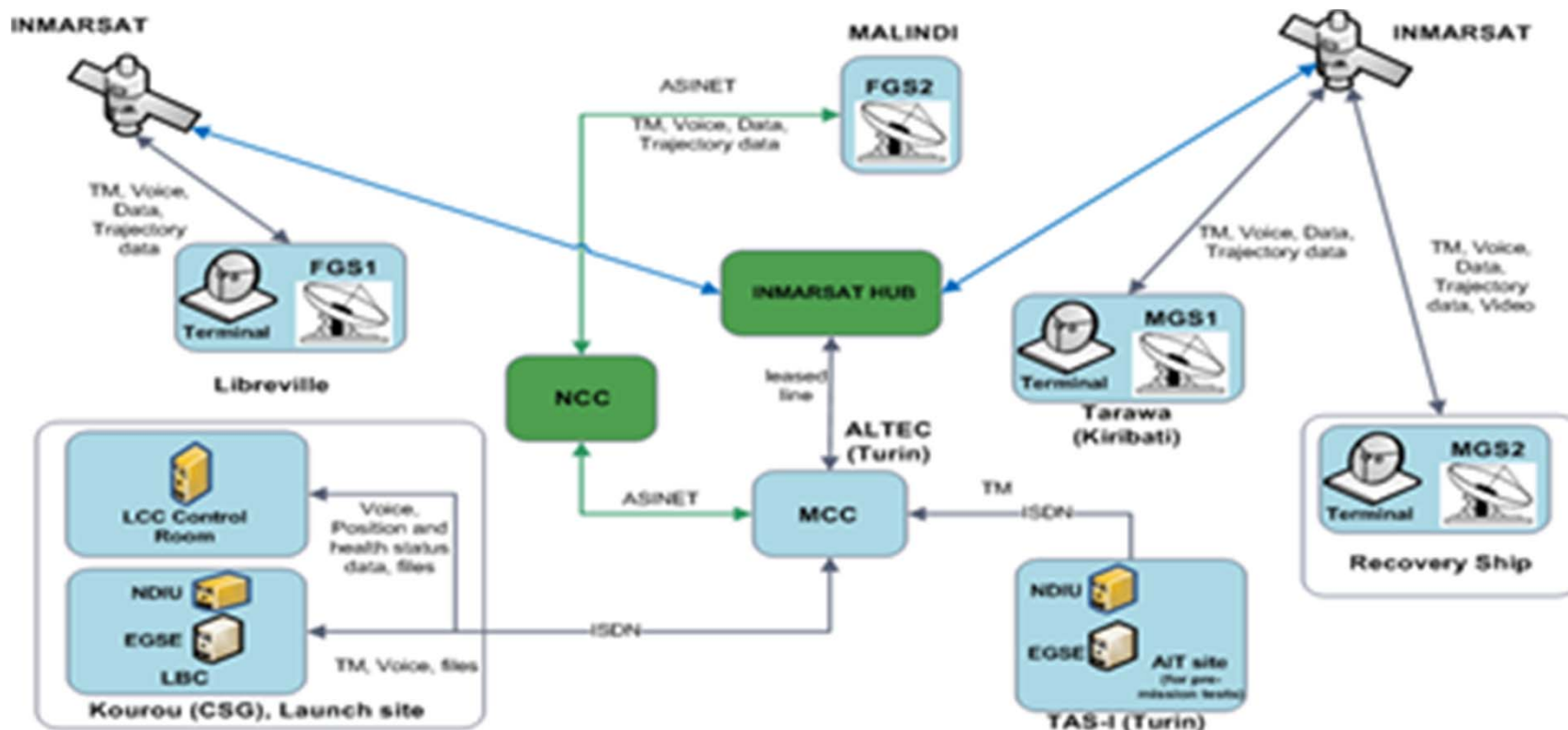
The Ground Segment



The Communication Network:



The telecommunication network is ready to undergo the qualification tests, including the integrated testing with the MCC and the telemetry system.





The Launch Campaign

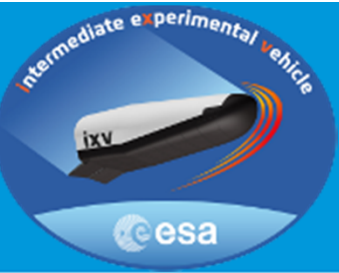


Arianespace Activities:

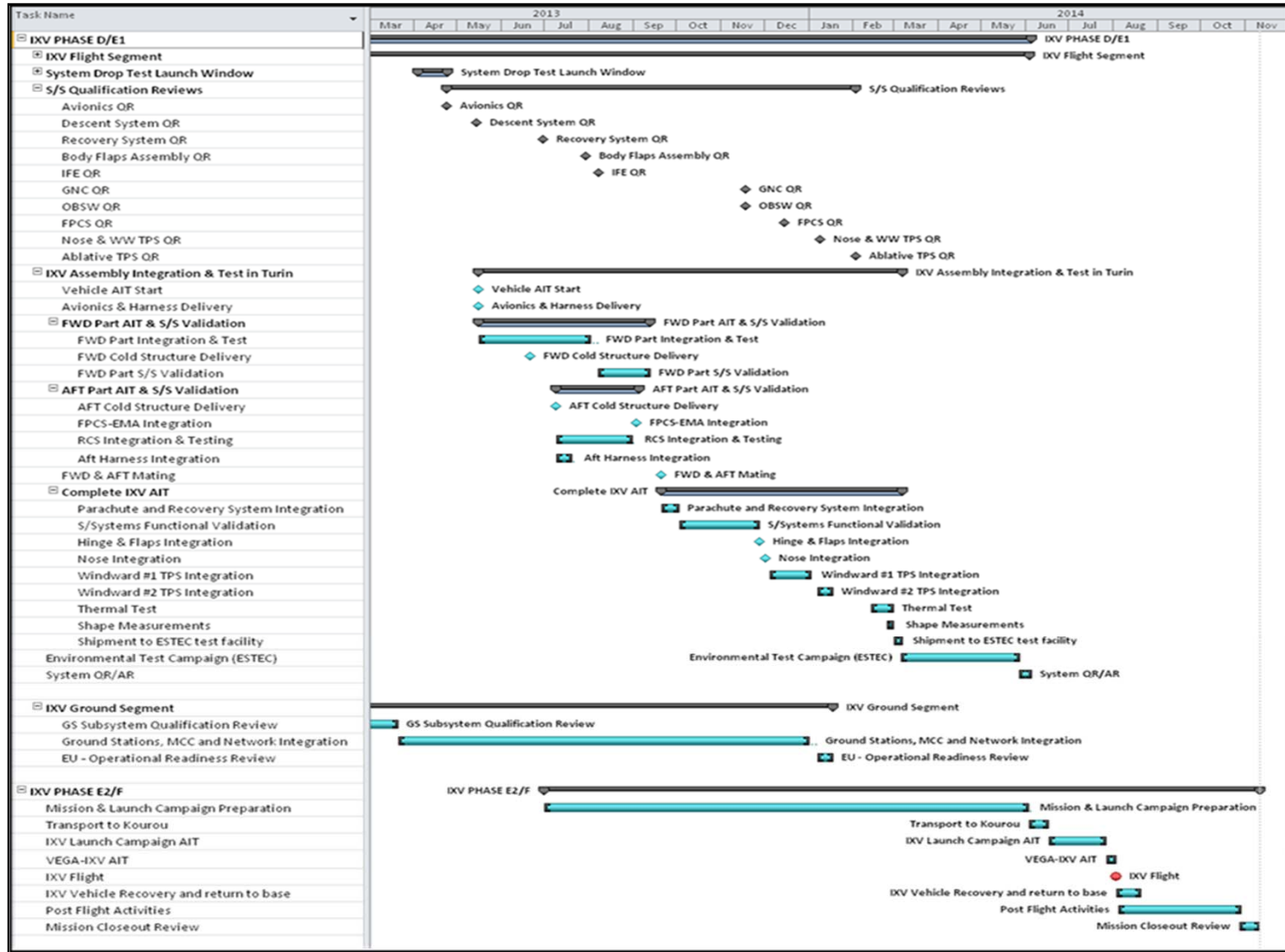
The launch campaign preparatory activities are also progressing, with the 1st Operations Meeting and Kourou Site Survey successfully held from 25th February to 1st March 2013, with the participation of Arianespace, CNES, ESA and TAS-I, addressing in details:

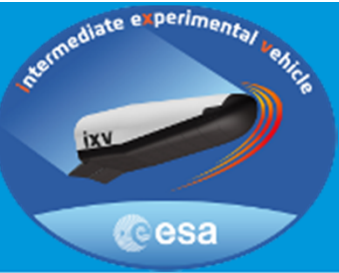
- IXV Launch Campaign Transportation and Logistics Aspects in Kourou;
- IXV Launch Site Operational Plan and Operational Needs;
- VEGA-IXV Launch Site Combined Operations and Chronology;
- VEGA-IXV Interfaces, including Interfaces to IXV Ground Segment;
- VEGA-IXV Safety Submissions Process.





The Plan-at-Completion

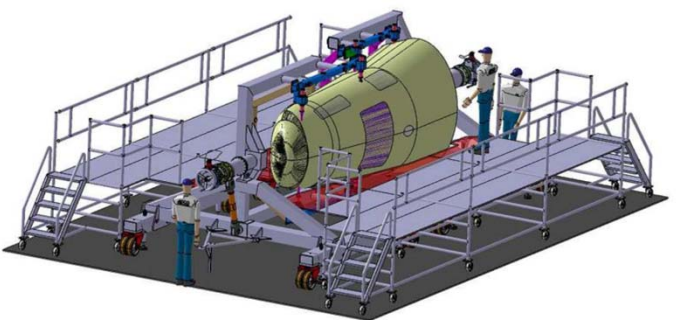




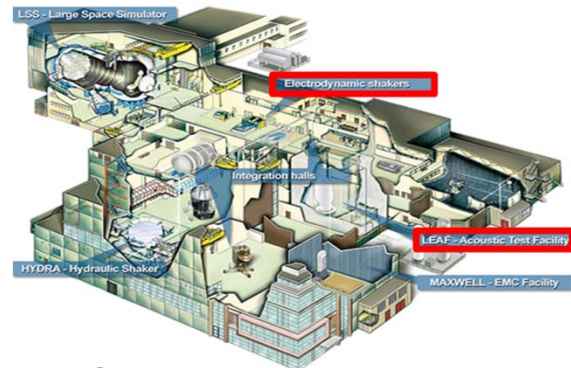
The Short-term Perspectives



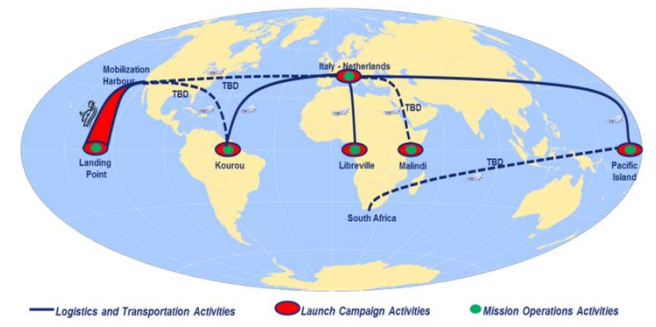
Sequence of Activities:



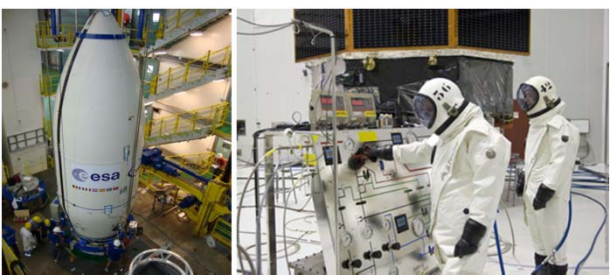
1. System Integration
(Turin, May '13)



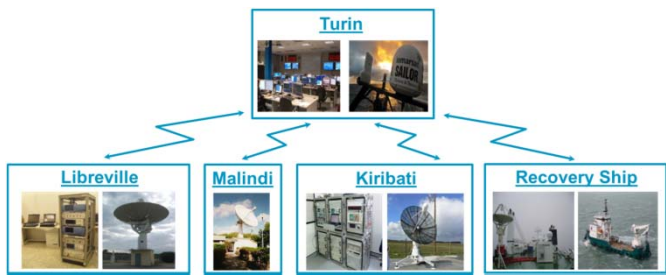
2. System Environmental Tests
(Noordwijk, March '14)



3. Flight and Ground Segment Deployment
(Worldwide, June '14)



4. Flight Segment Launch Campaign
(Kourou, July '14)



5. Ground Segment Launch Campaign
(Worldwide, July '14)



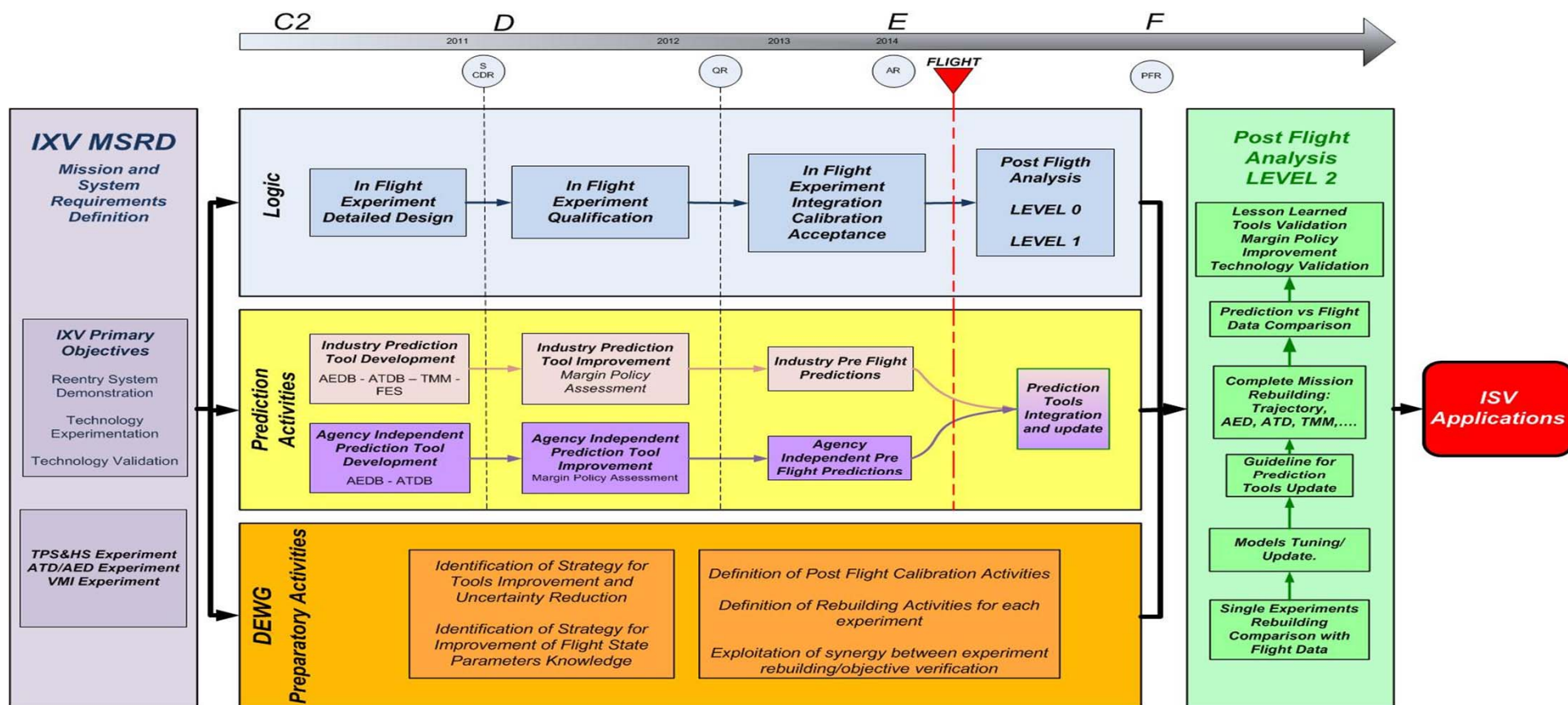
6. Launch and Mission into Space
(August '14)



The Short-term Perspectives



Post Flight Analysis:





The Long-term Perspectives



The PRIDE Programme:

From the IXV High Level Requirements:

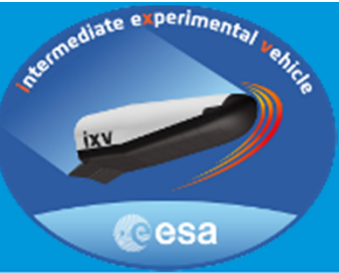
- Launcher: VEGA
- Mission Type: Suborbital
- Objectives: Demonstration & Experimentation
- Flight Regime: Hypersonic
- Landing: Sea splash-down
- Re-usability/Re-flyability: No



To the PRIDE-ISV High Level Requirements:

- Launcher: VEGA
- Mission Type: Orbital
- Objectives: Operational Prototype with Multi Purpose Cargo Bay
- Regime: Hypersonic, Supersonic, Subsonic
- Landing: Ground in conventional runway
- Re-usability/Re-flyability: Yes





THANKS TO



ThalesAlenia Space
THALES
 SAFRAN
 Snecma Propulsion Solide
 DASSAULT AVIATION
 ONERA

ACRA CONTROL

ThalesAlenia Space
QinetiQ
 S.A.B.C.A.

R.Tech Research & Technology
 TERMA
 NLR

EADS Astrium
 MT AEROSPACE

ZODIAC AEROSPACE
 PIONEER AEROSPACE

ISQ

RUAG
 Aerospace Defence Technology
 APCO TECHNOLOGIES SA
 ETH
 Eidgenössische Technische Hochschule Zürich
 Swiss Federal Institute of Technology Zurich
 CFS Engineering
 Computational Fluids & Structural Engineering

SENER
 gtm
 RYMSA
 deimos SPACE
 gtd

ThalesAlenia Space
 AleniaAermacchi
 A Finmeccanica Company
 CIRA
 LA SAPIENZA
 AERO SEKUR
 ALTEC
 SELEX Sistemi Integrati
 TELESPAZIO
 A Finmeccanica / Alcatel Company
 OHB
 CBS
 Avio

Overall Preliminary Design of the Thermal Protection System for a Long Range Hypersonic Rocket-Powered Passenger Vehicle (SpaceLiner)

Nicole Garbers

*German Aerospace Center (DLR)
Space Launcher System Analysis (SART) of the Institute of Space Systems
Robert-Hooke-Str. 7, 28359 Bremen, Germany
nicole.garbers@dlr.de*

ABSTRACT

The long range hypersonic passenger transportation system SpaceLiner has been proposed by the Space Launcher Systems Analysis Group (SART) of the German Aerospace Center (DLR) and investigated in the frame of the European Commission project FAST20XX. The SpaceLiner is a two-stage fully reusable vehicle powered by rocket engines. It should carry about 50 passengers from Australia to Europe within 90 minutes. To accomplish a safe return to earth for all passengers in case of an emergency, the SpaceLiner passenger capsule can be separated from the rest of the vehicle and is then able to fly autonomously back to Earth. The focus of the paper is the sizing of both stages as well as the capsule's passive thermal protection system.

The SpaceLiner's Thermal Protection System (TPS) has to withstand several different heat loads according to nominal flight and different abort cases. To be able to determine the heat loads for a full vehicle surface along different trajectories, fast engineering methods have to be used. The external heat flux was calculated by a fast code for preliminary flow analyses in hypersonic regime based on modified Newtonian surface inclination techniques and by using the Fay-Ridell equation close to the stagnation point and the Zoby-Moss-Sutton approach further downstream. The thicknesses of the different materials were optimized by using a 1D thermal conduction model. They depend heavily on the allowed temperature of the back-structure. According to the functional task and the chosen material, the structure is allowed to heat up to different maximum temperatures.

Depending on the maximum temperature for the subdivided surface regions, different reusable materials were considered: CMC, TABI, AETB, AFRSI and FRSI. The TPS of the capsule, which is not part of the orbiter's outer shell, is subject to high heat flux and has no need for re-usability. Therefore, an ablative thermal protection is preferred for stagnation and bottom areas with low system complexity, thus guaranteeing high safety. As an example, Avcoat was chosen.

The paper shows the overall preliminary design of the TPS for a long range hypersonic rocket-powered passenger vehicle, comparing different materials and different back-structure temperatures.

ABBREVIATIONS

AETB	Alumina Enhanced Thermal Barrier Tiles with TUF1 Coating
AFRSI	Advanced Flexible Reusable Surface
CHATT	Cryogenic Hypersonic Advanced Tank Technologies
CMC	Ceramic Matrix Composite
FAST	Future High-Altitude High-Speed Transport
FRSI	Felt Reusable Surface Insulation
HRSI	High-temperature Reusable Surface Insulation
LRSI	Low-temperature Reusable Surface Insulation
MECO	Main Engine Cut-Off
RCC	Reinforced Carbon-Carbon
SART	Space Launcher Systems Analysis Group
TABI	Tailorable Advanced Blanket Insulation
TOP	Thermal protection system Optimization Program
TUF1	Toughened Uni-Piece Fibrous Insulation

NOMENCLATURE

A	Area	[m ²]
$\delta_{m\&b}$	TPS thickness which is melted and burnt	[m]
δ_{min}	TPS thickness which not melted	[m]
q_V	Heat of vaporization	[MJ/m ³]
q_T	Total heat load	[MJ/m ²]
δ_{total}	Total thickness of ablative TPS layer	[m]
δ_{AVC}	Avcoat's density	[kg/m ³]

INTRODUCTION

The long range hypersonic passenger transportation system, SpaceLiner, was proposed by the Space Launcher Systems Analysis Group (SART) of the German Aerospace Center (DLR) in 2005 and further investigated in the frame of the European Commission project FAST20XX and CHATT [1 – 4]. It is a two stage reusable launch vehicle, consisting of a passenger stage (so called “orbiter”) and a booster stage which is separated after the booster’s main engine cut-off (MECO) and returns to ground (Fig. 1, Fig. 2). The orbiter continues its flight with its own rocket propulsion until all propellants have been burnt and then change into a hypersonic gliding mode without any additional propulsion. In this way, it will be possible to carry about 50 untrained passengers from Australia to Europe within 90 minutes. In contrast to other hypersonic transportation concepts, the SpaceLiner does not incorporate radically new or unproven technologies. Nevertheless, due to the comparatively low reliability of rocket launcher systems in comparison with conventional turbofan propelled passenger aircrafts, the passengers are not sitting directly in the orbiter but in a passenger capsule which is integrated in the orbiter. In the case of a critical emergency, the passenger capsule can be ejected autonomously from the main orbiter stage to bring the passengers safely back to earth.

So, a thermal protection system has to be designed for the booster, the orbiter and the passenger rescue capsule. The MECO of the orbiter stage occurs at about 70 km altitude with a velocity of more than 7 km/s. The subsequent gliding trajectory profile of the orbiter with Mach numbers well beyond 20 leads to heat fluxes higher than those encountered, for example, on the SpaceShuttle, thus requiring very thick thermal protection systems. In stagnation point regions heat fluxes can be so high that currently available TPS materials are unable to survive. In these regions some form of active cooling must be implemented. For the SpaceLiner, transpiration cooling using liquid water has been proposed in [5] and further developed in [6].

The focus of the paper is on the sizing of both stages as well as the capsule’s passive thermal protection system. Depending on the maximum temperature for the subdivided surface regions, different reusable materials were considered: Ceramic Matrix Composite (CMC), Tailorable Advanced Blanket Insulation (TABI), Alumina Enhanced Thermal Barrier Tiles with TUF1 Coating (AETB), Advanced Flexible Reusable Surface (AFRSI) and Felt Reusable Surface Insulation (FRSI). The TPS of the capsule, which is not part of the orbiter’s outer shell, is subject to high heat flux and has no need for re-usability. Therefore, as an ablative thermal protection Avcoat was chosen. The paper begins with a short description of the materials’ main characteristics. Then, the fast engineering methods, which have been used to determine the heat loads for a full vehicle surface along the different trajectories (nominal and abort cases), are described in more detail. This is followed by itemized results of the booster, orbiter and capsule’s thermal protection systems.

MATERIAL

The Thermal Protection System is, with exception of the nose area, a passive system consisting of materials selected for stability at high temperatures and weight efficiency.

In the high temperature zones a CMC cover has been selected with insulation material ZIRCAR Alumina mat. The multi-layer CMC-Alumina insulation is a composite of a ceramic matrix composite and fibres. Typically the fibres are carbon and the matrix is siliciumcarbide. The CMC used in the SpaceLiner is derived from the REX Free Flyer, which itself was a development from the Shefex experimental vehicle. The CMC was first developed in [7]. The insulation material ZIRCAR Sali used in the Rex Free Flyer is replaced by a ZIRCAR Alumina mat, due to its low density and low conductivity. For protection of the areas with intermediate temperatures TABI (< 1400 K) and AETB (< 1600K) were



Fig. 1 Artist’s impression of the SpaceLiner launch configuration

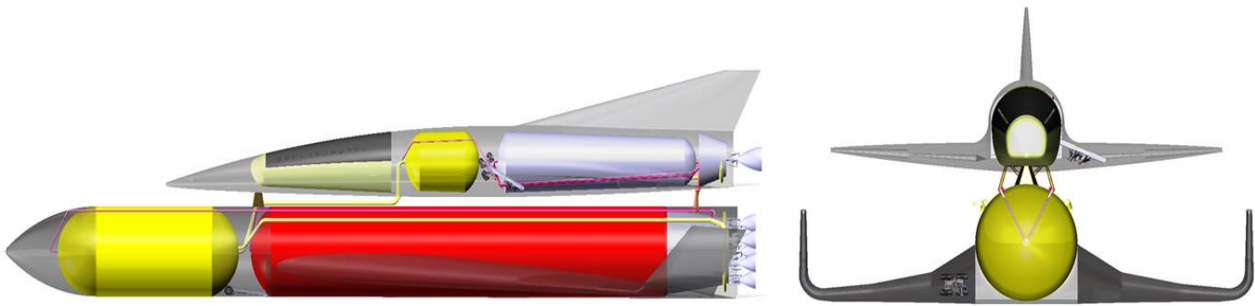


Fig. 2 Sketch of SpaceLiner launch configuration with passenger stage on top and booster stage at bottom

used. The AETB ceramic tile with TUF1 coating was developed at the NASA Ames Research Center as an improvement to the LI- 900 tile. The AETB tiles demonstrate higher strength and added durability. TABI was developed by the NASA Ames Research Center as an improvement to the AFRSI currently certified on the Space Shuttle orbiter. Integrally woven corrugations provide higher strength and a higher operational temperature than AFRSI and are attached to the structure with RTV adhesive.

For the lower temperature areas, AFRSI and FRSI were chosen. FRSI consists of a NOMEX blanket which is coated with a silicon elastomer for waterproofing. FRSI is very lightweight and can be used up to temperatures of 672 K on the wing's top surfaces exposed to lower temperatures. As an alternative for areas with intermediate temperatures, CRI (Ceramic Reusable Insulation) was also considered, but proved to be too heavy and therefore unfavorable in all cases.

The TPS of the capsule, which is not part of the orbiter's outer shell, is subject to high heat flux and has no need for re-usability. Therefore, an ablative thermal protection is preferred in stagnation and bottom areas with low system complexity, thus guaranteeing high safety. As an example, Avcoat was chosen. This material has previously been used for the heat shield on NASA's Apollo Command Module.

FAST ENGINEERING METHOD

The TPS has to withstand several different heat loads according to nominal flight and also for different abort cases. To be able to determine the heat loads for a full vehicle surface along different trajectories, fast engineering methods have to be used.

Starting from the flight trajectories, a sufficiently large number of flight points (e.g. 30) are chosen from each trajectory. The flight characteristics from each flight point (Mach Number, altitude, angle of attack) are used successively by the in-house tool HOTSOSE to calculate the heat fluxes at each mesh point of the vehicle surface for a certain flight point. HOTSOSE is a fast code for preliminary flow analyses in hypersonic regime based on modified Newtonian surface inclination techniques. Friction drag is estimated for each panel with the classical analytical methods for compressible laminar or turbulent flow of van Driest and White-Christoph. The surface temperatures are calculated under assumption of an adiabatic wall in radiation equilibrium. Heat fluxes are determined by using the Fay-Ridell equation close to the stagnation point and the Zoby-Moss-Sutton approach further downstream. The real gas effects on the gas dynamic and transport properties can be considered in the calculation for chemically reacting air in equilibrium. A fully turbulent flow along the flight path has been assumed for the TPS dimensioning as a conservative assumption. By this approach a heat flux profile over time is obtained for the complete vehicle surface.

Optimizing the material thickness for each of the thousands of mesh points on the vehicle would be excessively computationally intensive. Additionally, this would yield a design without sufficient margin on the TPS thickness which would be unpractical for manufacturing. Therefore, the vehicle surface is divided into a number of different regions, depending on the overall maximum temperature for all nominal and abort trajectories. At each time step, the highest heat flux of a region is identified and assumed to be the external heat flux for all mesh grid points in this region. Using subsequently the MATLAB-based in-house tool TOP, the TPS thickness for a certain region can be determined, using this region-based heat flux profile and the maximum acceptable temperature of the back-structure as input. Thereby, the TPS thickness optimization in TOP is based on a 1D thermal conduction model. As shown later, it can be optimized for different optimization goals, for example "thin" or "light". Due to physical space restrictions, sometimes, the thinner version is preferable over the lighter version.

Validation of the fast engineering methods

TOP has been validated by comparison with several literature-based examples; one of them was the Space Shuttle re-entry [8-10]. The space shuttle is composed of numerous materials, but the main structure is mostly made of 2024-T6 aluminium and graphite-epoxy. Both of these materials can only endure temperatures up to 448 K. So, in our test, it is assumed that the structure temperature is not allowed to exceed 400K.

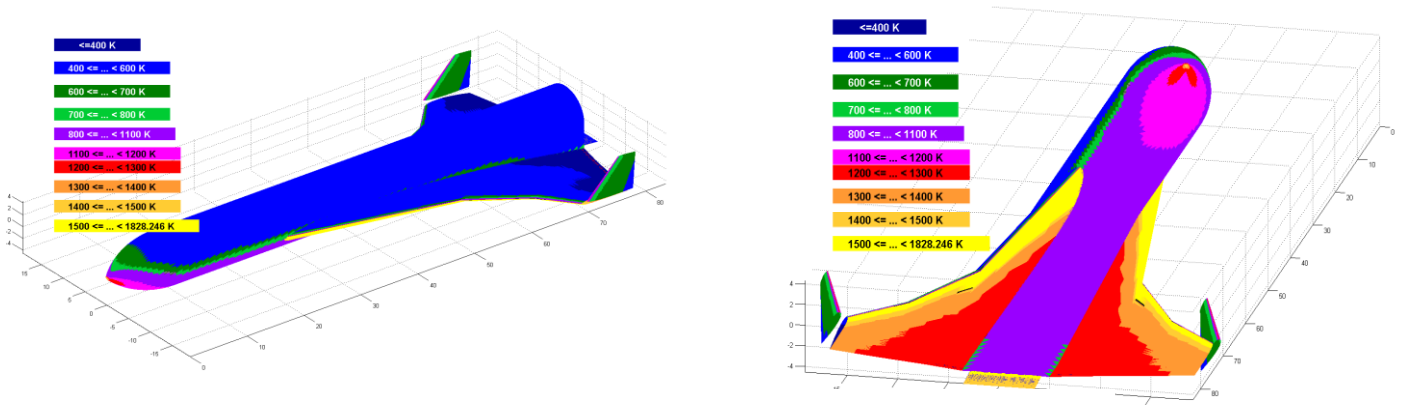


Fig. 3 Maximum temperatures of nominal and abort trajectories (Booster stage)

The original Space Shuttle TPS is composed of four main materials: Reinforced Carbon-Carbon (RCC), Low-temperature Reusable Surface Insulation (LRSI), High-temperature Reusable Surface Insulation (HRSI) and Felt Reusable Surface Insulation (FRSI). We will focus here on the results for FRSI (max. temperature < 390K), LRSI (max. temperature: 390 – 500K) and RCC (max. temperature > 1300 K) to give an impression of the order of accuracy for our fast engineering model. For the temperature area with a max temperature less than 390K, our method delivers a thickness of 1.21 cm (literature: 1.62 cm). Significantly less deviation to the literature value (2.853 cm) was obtained to the range with a maximum temperature between 390K and 500K with a calculated value of 2.5 cm. The accuracy can be further enhanced for the range with a maximum temperature of more than 1300K: 7.9 cm (calculated) in comparison to 8.9 cm (literature). This corresponds to a deviation of only about 12 %. The average deviation of all temperature ranges is about 20%. This is partly due to the simplicity of the model, but also to the fact that for our calculations the nominal re-entry trajectory was used, which is probably not the most critical one that has been the basis for real case dimensioning. Therefore, it can be assumed that the accuracy can be further improved if all dimensioning trajectories are well known, as is the case in our preliminary design process. Thus, the fast engineering method meets well our two oppositional requirements. On the one hand, it delivers fast results but on the other hand the results are precise enough for a preliminary design process.

BOOSTER THERMAL PROTECTION SYSTEM

For the booster stage the nominal ballistic and reentry flight has to be considered. Abort cases and off-nominal maneuvers have not been taken into account. The maximum heat loads can be found at the nose area and the underside of the wing edges. The TPS material has to be fully reusable. It is to be dimensioned in a way that the internal structure temperature nowhere exceeds 400 K because an aluminum Al2219 substructure is assumed.

As can be seen in Fig. 3, there is no need for TPS in the rear area of the upper wing surface, Most of the remaining part of the upper half is exposed to a maximum temperature of 600 K. For this area, FRSI is chosen which has a thickness between 1.44 cm and 2.39 cm, depending on the localization at the surface. The materials TABI, AETB-8 and AETB-12 were also considered, but for this temperature range, they all had a worse ratio of surface density to thermal conductivity which results in a higher mass, and therefore they were not selected.

The lower half becomes much hotter: the underside of the wing edges reaches up to 1828 K. For this area, starting from 1600 K, CMC was chosen. With a thickness of 16.4 and 16.9 cm it is much thicker than the AETB-8, which is used for 1400 – 1600 K. It measures a maximum of 6.7 cm. For the average temperature range of 900 - 1400 K, TABI was selected. Details can be found in Table 1.

Table 1 TPS (Booster)

Max. Temp. [K]	Material	Area [m ²]	Total Thickness [m]	Mass [kg]
< 400	No need	194.31	0.000	0.00
401 – 500	FRSI	1169.21	0.014	2874
501 – 600	FRSI	407.04	0.024	1380
601 – 700	AFRSI	265.32	0.029	1057
701 – 800	AFRSI	141.23	0.034	629
801 – 900	AFRSI	113.61	0.038	550
901 – 1000	TABI	286.89	0.053	1794
1001 – 1100	TABI	319.99	0.058	2155
1101 – 1200	TABI	66.75	0.063	481
1201 – 1300	TABI	324.39	0.066	2428
1301 – 1400	TABI	197.40	0.070	1562
1401 – 1500	AETB_8	51.82	0.066	473
1501 – 1600	AETB_8	19.45	0.067	180
1601 – 1700	CMC	87.55	0.164	1482
1701 – 1850	CMC	6.79	0.169	116
sum				17161

PASSENGER STAGE THERMAL PROTECTION SYSTEM

The Passenger Stage TPS has to be dimensioned for the heat loads of the nominal trajectory as well as for the abort cases without separation of the rescue capsule. We assume the most critical flight phases with respect to maximum heat load to be the abort shortly after booster separation and the abort at highest point are the most critical ones according to the maximum heat loads. That is why they are considered exemplarily for all abort cases. The total maximum temperature and the total maximum heat flux along the different flight trajectories are shown in Fig. 4. It should be kept in mind is that the capsule's upper half is part of the orbiter's outer shell. To avoid double counting, this part is not considered here but rather in the passenger cabin's calculation to take into account the reduction of the maximum inner temperature to 293K – 400K for passenger areas.

For the booster stage calculation an aluminum structure was assumed and therefore only the case of a maximum internal structure temperature of 400K was considered. For the passenger stage, it could be interesting to choose another material with sufficient strength at elevated temperature (up to 530K) like Titanium or the polymer PEEK. This could lead to a reduction of the insulation thickness and hence the TPS. To see the impact of the different maximum structure temperatures, the cases of 400K, 480K and 530K were considered and compared.

The fin is only dimensioned for the nominal flight because in the abort cases an increased angle of attack-flight is necessary in which the fin is protected by the fuselage and wing.

It can be seen that in the case of simulation until landing, the total mass of 34.25 tons (400K) is reduced by 16.2 % to 28.7 tons for a structure temperature of 480 K and by 25.2 % to 25.6 tons for a structure temperature of 530 K.

The second impact factor apart from the maximum structure temperature is the simulation of the flight time. If we set a buffer of 300 or 600 seconds to the landing time in which the maximum structure temperature should not be exceeded, the TPS mass increases slightly. In the case of a structure temperature of 400K, the total mass of 34.25 tons (simulation until landing) increases by 1.09 % to 34.6 tons for simulation until landing plus 300 seconds and by 2.28 % to 35.0 tons for simulation until landing plus 600 seconds.

A detailed mass analysis for the different temperature areas can be found in Table 3. It shows the different materials and thicknesses for the case of a structure temperature of 530 K and a simulation time of landing plus 600 seconds.

For the intermediate temperature areas up to 1400 K, TABI and AFRSI were used. These areas cover the whole upper half and large parts of the lower half. (Fig. 5) The thickness varies between 3.4 cm and 15.3 cm. Between 1400 K - 1600 K, AETB-12 was used. It has a lower thickness of maximum 9.3 cm. This shows the influence of the different optimization possibilities. Here, a mass optimization option was chosen that the mass had to be optimized. As an alternative, the thickness could be minimized, for example, if there insufficient space due to structure constraints. In this case, it would be possible to use AETB also for lower temperature areas for which TABI is used now. This would lead to a lower thickness but simultaneously to a higher mass.

Table 2 TPS Mass for different simulation scenarios (Passenger stage)

Mass [kg]	until landing	until landing + 300 s	until landing + 600 s
400 K	34249	34624	35032
480 K	28700	29243	29255
530 K	25605	25969	26181

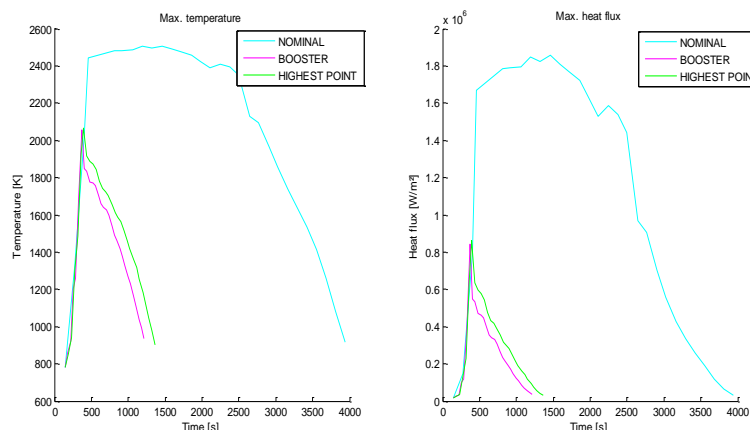


Fig. 4 Max. temperature and max. heat flux (Passenger Stage)

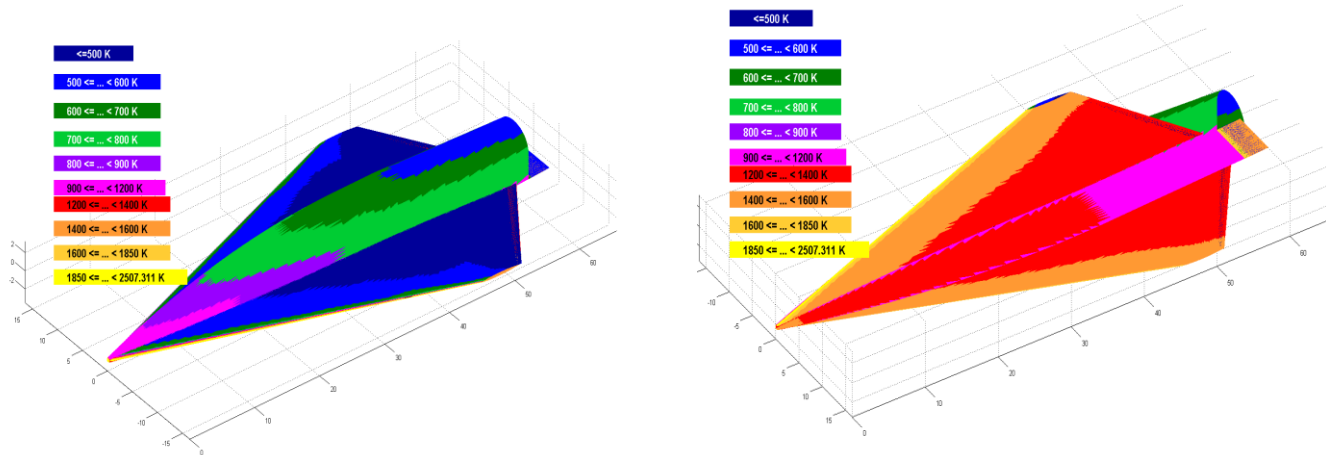


Fig. 5 Maximum temperatures of nominal and abort trajectories (Passenger stage)

The high thickness and mass of the SpaceLiner thermal protection system in comparison to the one of the Space Shuttle is not surprising if one has in mind that the thermal loads are still beyond those of the Space Shuttle orbiter at reentry.

PASSENGER CABIN THERMAL PROTECTION SYSTEM

The SpaceLiner's capsule Thermal Protection System (TPS) has the particularity that it has to be dimensioned for the nominal flight and the abort cases in which it is integrated in the passenger stage and also for the abort cases in which it is separated. In the course of this investigation, it has to be distinguished which areas of the capsule (i.e. the nose area, upper half or lower half) are considered. During nominal flight, the capsule is considered to be part of the orbiter. This means that the lower half and nose are protected by the orbiter structure and its TPS. They are therefore, not subjected to the external heat load until the capsule is separated in an abort case. In contrast, the capsule's upper half is part of the orbiter's outer shell and so is heated up during nominal flight. These differences lead to different starting conditions regarding initial temperature after abort separation. The upper half of the TPS is required to be dimensioned for the nominal mission Australia to Western Europe.

To guarantee passenger safety and comfort, the temperature inside the passenger capsule should not exceed habitable

Table 3 Detailed TPS (Passenger Stage, structure temperature 530 K, simulation time: landing plus 600s)

Temperature [K]	optimization: thin (530 K, until landing + 600 s)		
	Material	Thickness [m]	Mass [kg]
< 530	no need		
530 – 600	TABI	0.034	908
600 – 700	AFRSI	0.045	1134
600 – 700 (FIN)	AFRSI	0.044	229
700 – 800	AFRSI	0.059	1978
700 – 800 (FIN)	AFRSI	0.058	730
800 – 900	AFRSI	0.073	843
800 – 900 (FIN)	AFRSI	0.071	171
900 – 1000	TABI	0.096	843
900 -1000 (FIN)	TABI	0.089	15
1000 – 1100	TABI	0.109	487
1000 – 1100 (FIN)	TABI	0.095	21
1100 – 1200	TABI	0.123	1518
1100 – 1200 (FIN)	TABI	0.100	2
1200 – 1300	TABI	0.139	2155
1300 – 1400	TABI	0.153	7751
1400 – 1500	AETB-12	0.088	4788
1500 – 1600	AETB-12	0.093	1720
1600-1700	CMC	0.288	527
1700 – 1850	CMC	0.285	221
1850 - 2508			140
sum			26181

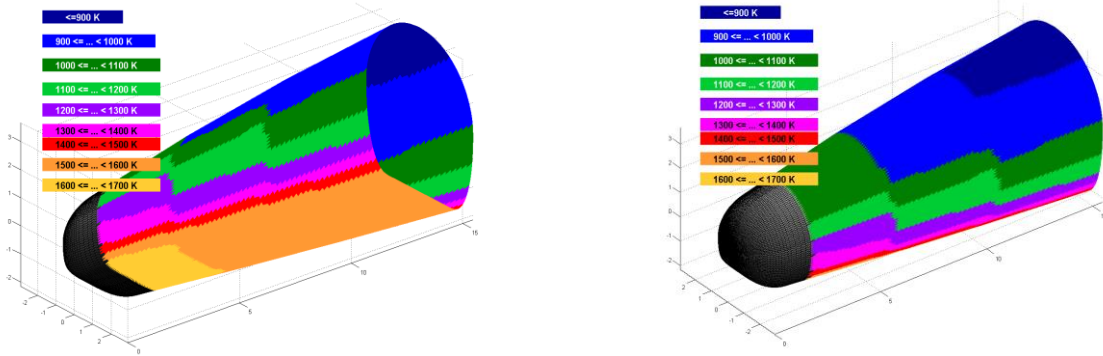


Fig. 6 Maximum temperatures of nominal and abort trajectories (Passenger cabin)

room temperatures. Hence, for the predesign of the capsule's TPS, four different scenarios were considered to see the impact on the TPS mass: an inside structure temperature of 293 K, 298 K 303 K and 400 K. The capsule itself includes an air-conditioning system, e.g. a ventilation system, necessary, which again has an impact on the mass. It was not considered in further detail, but has to be kept in mind for a detailed comparison in the future.

Ablative Nose

The high heat flux and ability to use a non-reusable TPS in the nose (as it is only required during an abort scenario) allows for the use of an ablative thermal protection system. The low system complexity of an ablative TPS helps guarantee high safety and reliability. The chosen material is Avcoat 5026-39/HC-6, which has already been used on other spacecraft such as the Apollo capsule. An ablative TPS cannot be calculated by the in-house program TOP, but is estimated as proposed in [11]. The thickness is determined by two different duties. One part is melted and burnt ($\delta_{m\&b}$); the other part is used to decrease the temperature from ablation temperature of approximately 922 K to an acceptable value for the human beings inside the capsule (δ_{min}). The critical flight trajectory is given by an emergency case during MECO. Here, the ablative temperature is immediately reached and continues for approximately 800 s. The total heat load q_T can be calculated by integration of the heating rate which is equal to the area under the maximum heat flux curve bounded by $t_1 = 0\text{ s}$ and $t_2 = 800\text{ s}$. This lead to $q_T = 900.8\text{ MJ/m}^2$. The heat of vaporization of the ablative material is given by $q_V = 1.46 \cdot 10^4\text{ J/m}^3$. It results in a recession layer thickness of $\delta_{m\&b} = 0.062\text{ m}$.

The minimum TPS thickness has to remain until the end of the ablation period to protect the inner structure. A good guess for the required thickness can be taken from the Apollo TPS. That leads to the assumption of $\delta_{min} = 0.07112\text{ m}$. The material properties are taken from [11] for an internal temperature of approximately 303 K. Even if this test case does not exactly fit the internal structure temperature we have considered for the rest of the body, it gives us a good idea of a reasonable TPS mass assumption for the nose region. Thus, the total thickness is calculated by $\delta_{total} = 0.133\text{ m}$. The considered nose area is given by $A = 19.1574\text{ m}^2$ (1.7m from the top) and Avcoat's density $\delta_{AVC} = 528.6\text{ kg/m}^3$. Therefore, the ablative TPS mass is 1347kg for a structure temperature of approximately 303K.

Reusable TPS-Areas

It is assumed for the lower half of the capsule (similar to the nose area) that the thermal protection system of the orbiter provides the heat protection for this area until the time of an emergency separation. This means that the capsule's TPS does not have a thermal load history and its initial temperate can be set to 290 K. Due to the fact that in a case of capsule separation, re-usability of the TPS is not required, an ablative TPS is able to be considered for the lower half of the capsule. However for a first approximation, only non-ablative materials, as used for the upper side, are considered. The upper half of the capsule is designed to act as part of the combined orbiter's structure and therefore is required to withstand the heat load of the nominal trajectory, as well as the thermal conditions of the three different abort scenarios. Table 5 shows a detailed mass analysis for two different optimizations (both: structure temperature 303 K, simulation time: landing + 300s). On the left hand, the thinnest materials (AETB-12, CMC) were chosen, on the right hand the lightest ones (AFRSI, TABI, AETB-12, CMC). The thinnest version has an additional mass of 461.09 kg (10.18 %) compared to the lightest version.

An overview about the other simulation cases can be found in Table 4.

Table 4 TPS Mass for different simulation scenarios (Passenger capsule)

Mass [kg]	until landing		until landing + 300 s		until landing + 600 s	
	light	thin	light	thin	light	thin
293 K	4858	5107	5017	5327	5164	5455
298 K	4595	5030	4701	5197	4764	5306
303 K	4429	4753	4530	4991	4633	5227
400 K	3558	3859	3632	3932	3697	4059

Table 5 Detailed mass analysis (Passenger cabin, structure temperature 303 K, simulation time: landing plus 300s)

Temperature	thin			light		
	Material	Thickness [m]	Mass [kg]	Material	Thickness [m]	Mass [kg]
(303 K) until landing + 300						
< 900 K (Upper half)	AETB-12	0.102	260	AFRSI	0.141	211
900 – 1200 K (Upper half)	AETB-12	0.102	1961	TABI	0.160	1611
< 1200 K (Lower half)	AETB-12	0.057	166	TABI	0.098	151
1200 – 1300 K (Lower half)	AETB-12	0.060	189	TABI	0.108	177
1300 – 1400 K (Lower half)	AETB-12	0.063	149	TABI	0.116	145
1400 – 1500 K (Lower half)	AETB-12	0.0659	113	AETB-12	0.066	113
1500 – 1600 K (Lower half)	AETB-12	0.067	568	AETB-12	0.067	568
1600 – 1700 K (Lower half)	CMC	0.220	198	CMC	0.220	198
1700 – 1850 K (Lower half)	CMC	0.220	10	CMC	0.220	10
Nose section	AVCOAT	0.133	1347	AVCOAT	0.133	1347
Sum			4961			4531

CONCLUSION

Only strong simplifications (e.g. Newtonian surface inclination techniques for preliminary flow analyses, assumption of only 1D heat-flux) enable a complete vehicle consideration for different trajectories and trade-offs.

The one-dimensional Thermal protection system Optimization Program TOP has been described in detail and some validation examples are given. The most recent design of the SpaceLiner’s TPS was introduced extensively, including the Booster, Passenger Stage and Passenger Cabin thermal protection systems.

After analyzing the effects of several flight scenarios and structure materials, it has been shown that the choice of the structure material plays a major role in the TPS predesigning process. A well-considered structure material can lead to an enormous TPS mass reduction (up to 25 %), but mostly to an increasing structure mass. So, these two effects have to be taken into account in more detail in the consequent design processes.

Furthermore, due to limited space it may be necessary to adapt the TPS to the available space. Therefore, the lightest as well as the thinnest TPS versions have to be considered to find the optimum design.

ACKNOWLEDGEMENT

Part of this work has been performed within the FAST20XX project. FAST20XX ‘Future High-Altitude High-Speed Transport 20XX’ project, investigating high-speed transport systems, coordinated by ESA-ESTEC, and supported by the EU within the 7th Framework Programme Theme7 Transport, Contract no.: ACP8-GA-2009-233816.

Further information on FAST20XX can be found on <http://www.esa.int/fast20xx>.

REFERENCES

- [1] M. Sippel, “Comparative Study on Options for High-Speed Intercontinental Passenger Transports: Air-Breathing-vs. Rocket-Propelled,” *56th International Astronautical Congress*, IAC-05-D2.4.09, October 2005
- [2] M. Sippel, “Introducing the SpaceLiner Vision,” *7th International Symposium on Launcher Technologies*, Barcelona, April 2-5, 2007
- [3] M.Sippel and A. van Foreest, “SpaceLiner Rocket-Powered High-Speed Passenger Transportation Concept Evolving in FAST20XX,” *61st International Astronautical Congress*, IAC-10-D2.4.06, Prague, September 2010
- [4] M. Sippel, T. Schwanekamp, C.Bauer, N. Garbers, A. van Foreest, U. Tengzelius and A. Lentsch, “Technical Maturation of the SpaceLiner Concept,” *18th AIAA International Space Planes and Hypersonic Systems and Technologies Conference*, AIAA 2012-5850 Tours, September 2012
- [5] A. van Foreest, A. Gülhan, B. Esser, M. Sippel, B. Ambrosius and K. Sudmeijer, “Transpiration Cooling Using Liquid Water,” *AIAA journal of thermophysics and heat transfer*, vol.23-2009, issue 4
- [6] M. Sippel, C. Bauer, N. Garbers, T. Schwanekamp, A. Kopp and Magni Johansson, „SpaceLiner 7 subsystem integration including CAD lay-out and vehicle mass breakdown,“, *ACP8-GA-2009-233816*, FAST20XX, 2013
- [7] B. Tong Minh, “Design of the SpaceLiner Thermal Protection System,” *SART TN-002/2011*, DLR, Bremen, 2001
- [8] P.F. Bradley and D.A. Throckmorton, “Space Shuttle orbiter flight heating rate measurement sensitivity to thermal protection system uncertainties,” *NASA STI/Recon Technical Report N 05/1981*, NASA Langley Research Center, Hampton, VA
- [9] D. Scott, “Effects of Nonequilibrium and Catalysis on Shuttle Heat Transfer,” *18th AIAA Thermophysics Conference*, AIAA-83-1485, Montreal, June, 1983
- [10] D.A. Stewart, J. V. Rakich and M. J. Lanfranco, „Catalytic surface effects on space thermal protection system during Earth entry of flights STS-2 through STS-5,“ *Prog. In Astronautics and Aeronautics*, Vol. 82, pp. 248 272, 1982
- [11] W.-L. Ko, L. Gong, and R.D. Quinn, “Reentry Thermal Analysis of a Generic Crew Exploration Vehicle Structure,” *Technical report*, NASA Dryden Flight Research Center, 2007

Overall Preliminary Design of the Thermal Protection System for a Long Range Hypersonic Rocket-powered Passenger Vehicle (Spaceliner)

*7th European Workshop on Thermal Protection Systems and Hot Structures
8th April 2013*

*Nicole Garbers
Space Launcher Systems Analysis (SART), DLR, 28359 Bremen, Germany*

Knowledge for Tomorrow

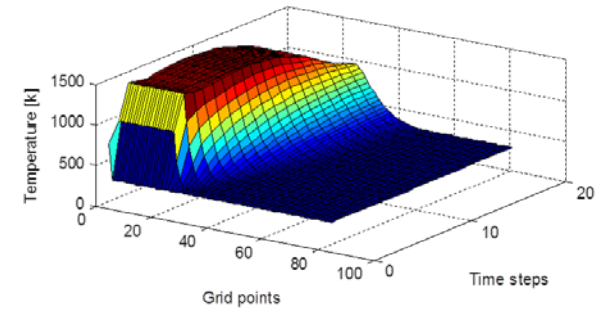


Overview

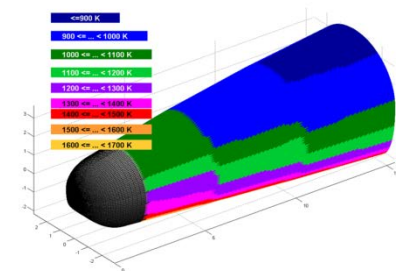
- SpaceLiner



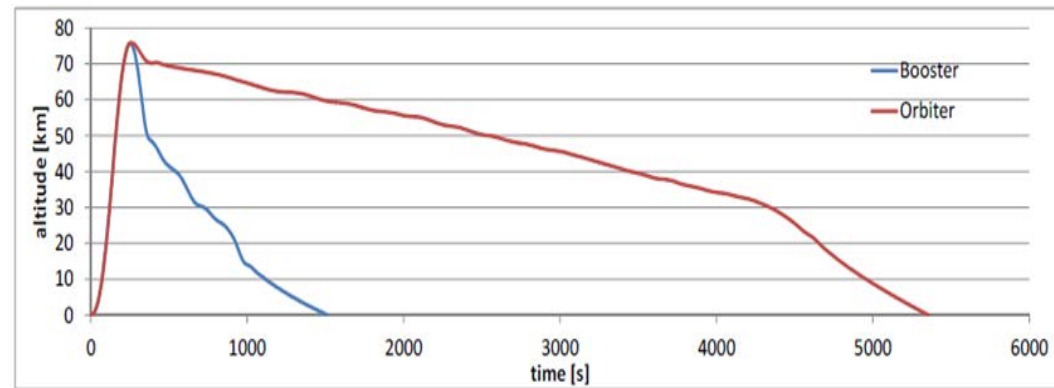
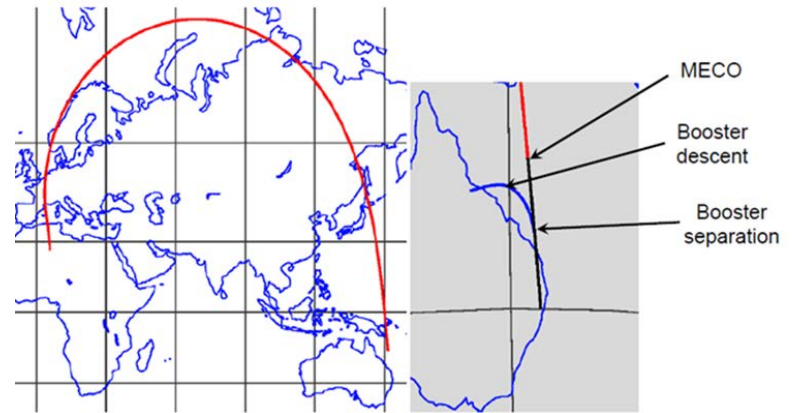
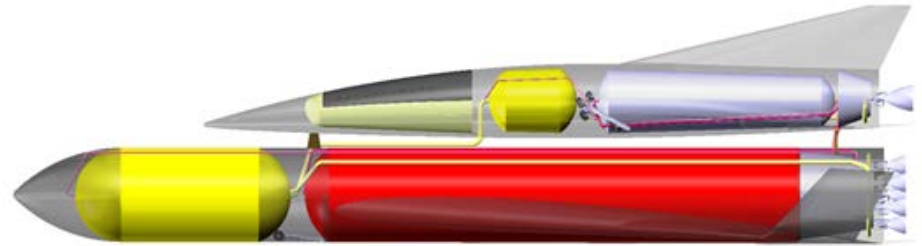
- TPS designing tool TOP



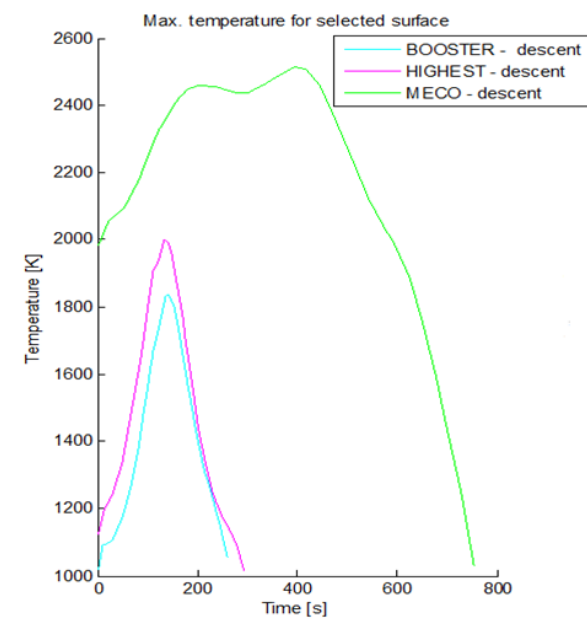
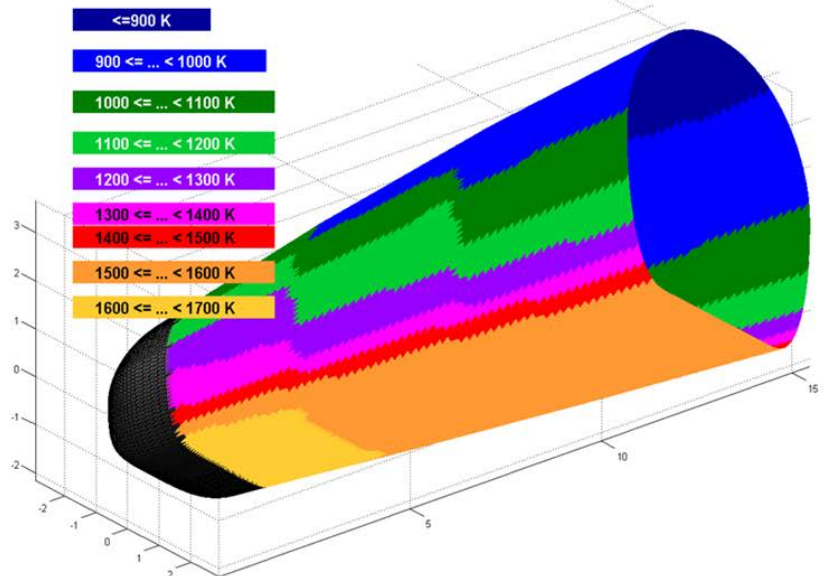
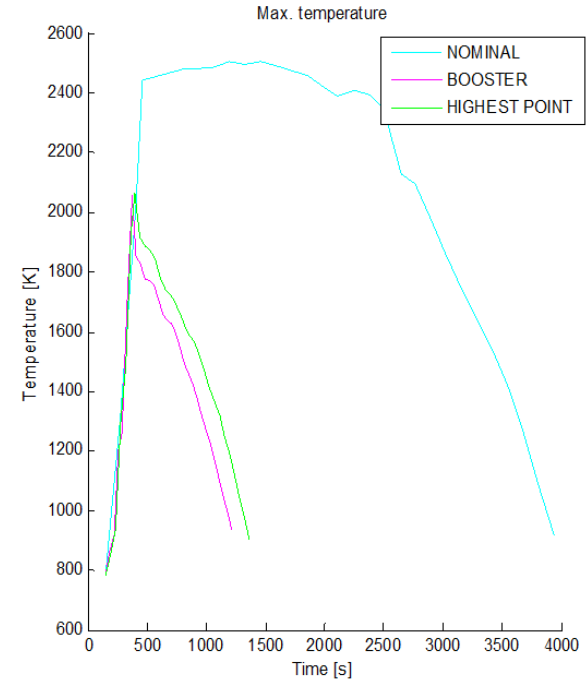
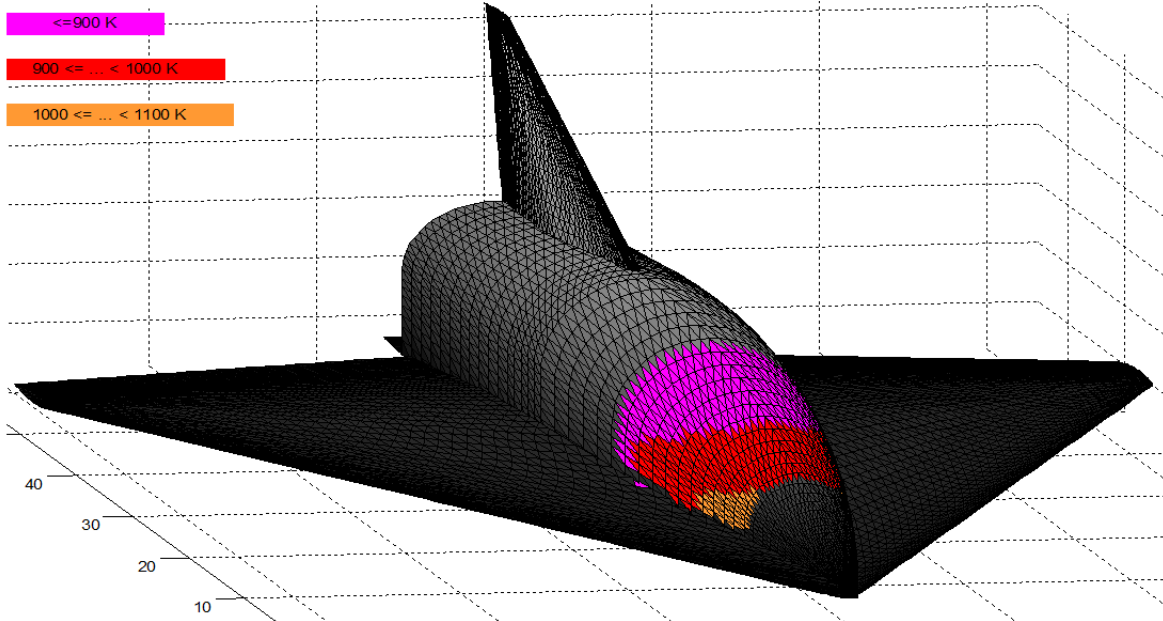
- Preliminary TPS design passenger capsule (SpaceLiner)



SpaceLiner



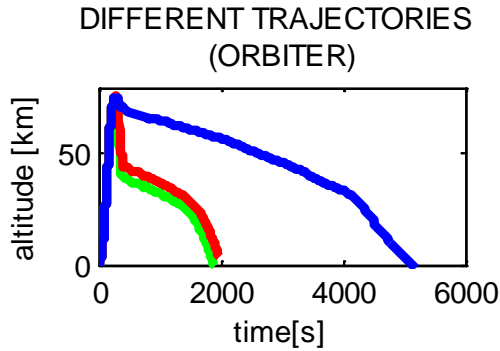
Preliminary design needs fast engineering methods



Physical Modell

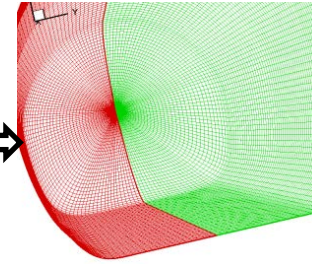
Flight trajectories (nominal & abort)

~ 30 flight points
per trajectory



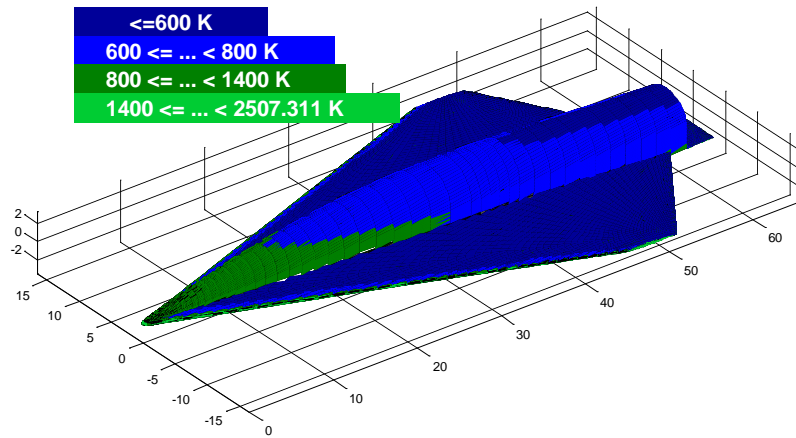
Mach Number
altitude
angle of attack

HOTSOSE

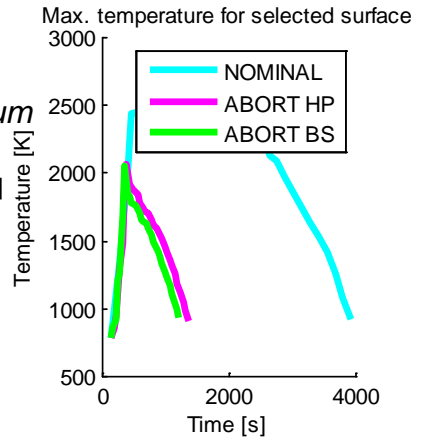


temperature at each
grid point for
selected flight points

Recall for each
trajectory



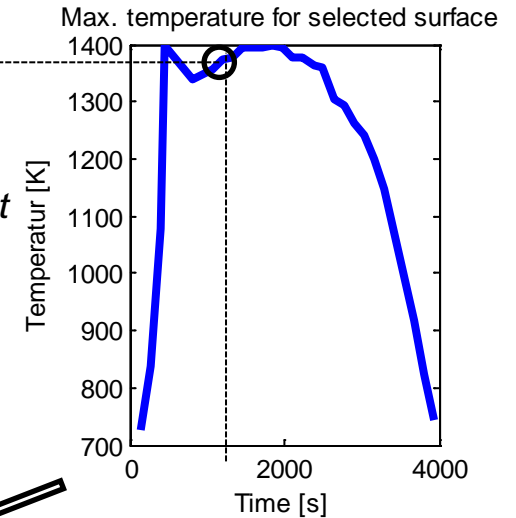
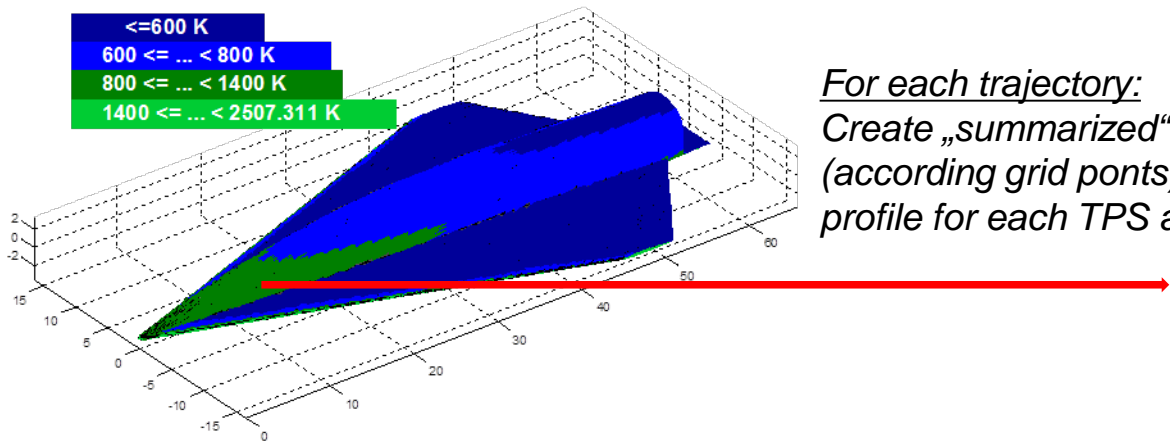
overall maximum
temperature



time-dependent
temperature
profile for each grid
point

Physical Modell

Example for one trajectory:



Grid points

1 ... 10

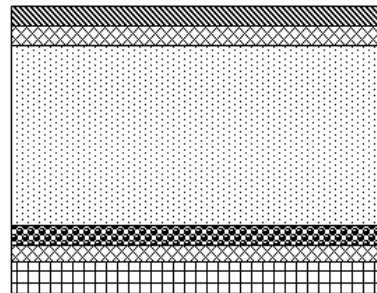
11...20

21...50

51...60

61...70

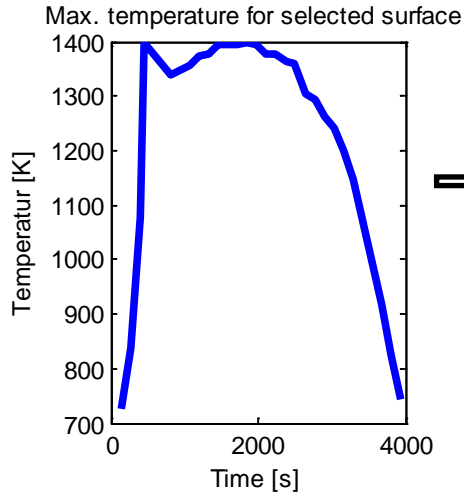
71...80



C9 (Coating)	(2.54E-04 m)
Outer Fabric (AB312)	(2.29E-04 m)
Q-fiber Felt Insulation	(to be adapted)
Inner Fabric (AB312)	(2.29E-04 m)
RTV Adhesive	(2.29E-04 m)
Structure (Aluminium)	(2.00E-02 m)

Physical Modell

(only conduction, 1D)



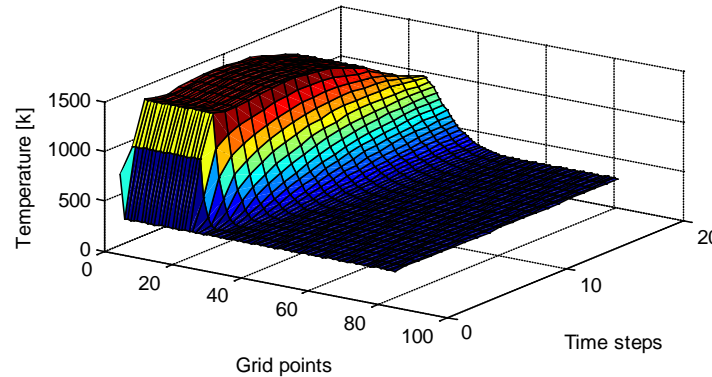
$$\frac{\partial}{\partial x} \left(\lambda \frac{\partial T}{\partial x} \right) = \rho c_p \frac{\partial T}{\partial t}$$

User-given/ adapted

- Material properties
- => First guess of thickness
- Max. allowed structure temperature

MATLAB => pdepe

Solve initial-boundary value problems for parabolic-elliptic PDEs in 1-D

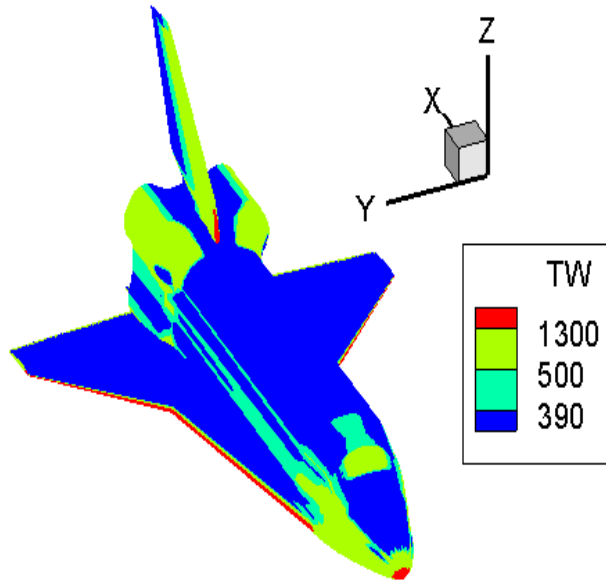


Max. structure temperature ~ max. allowed structure temperature

NO

Time-dependent boundary conditions for heat equation

Validation of the physical modell: Space Shuttle



FRSI (blue, < 390 K)

literature: 1.62 cm

calculated: 1.21 cm

LRSI (turquoise, 390 – 500 K)

literature: 2.853 cm

calculated: 2.5 cm

RCC (red, > 1300 K)

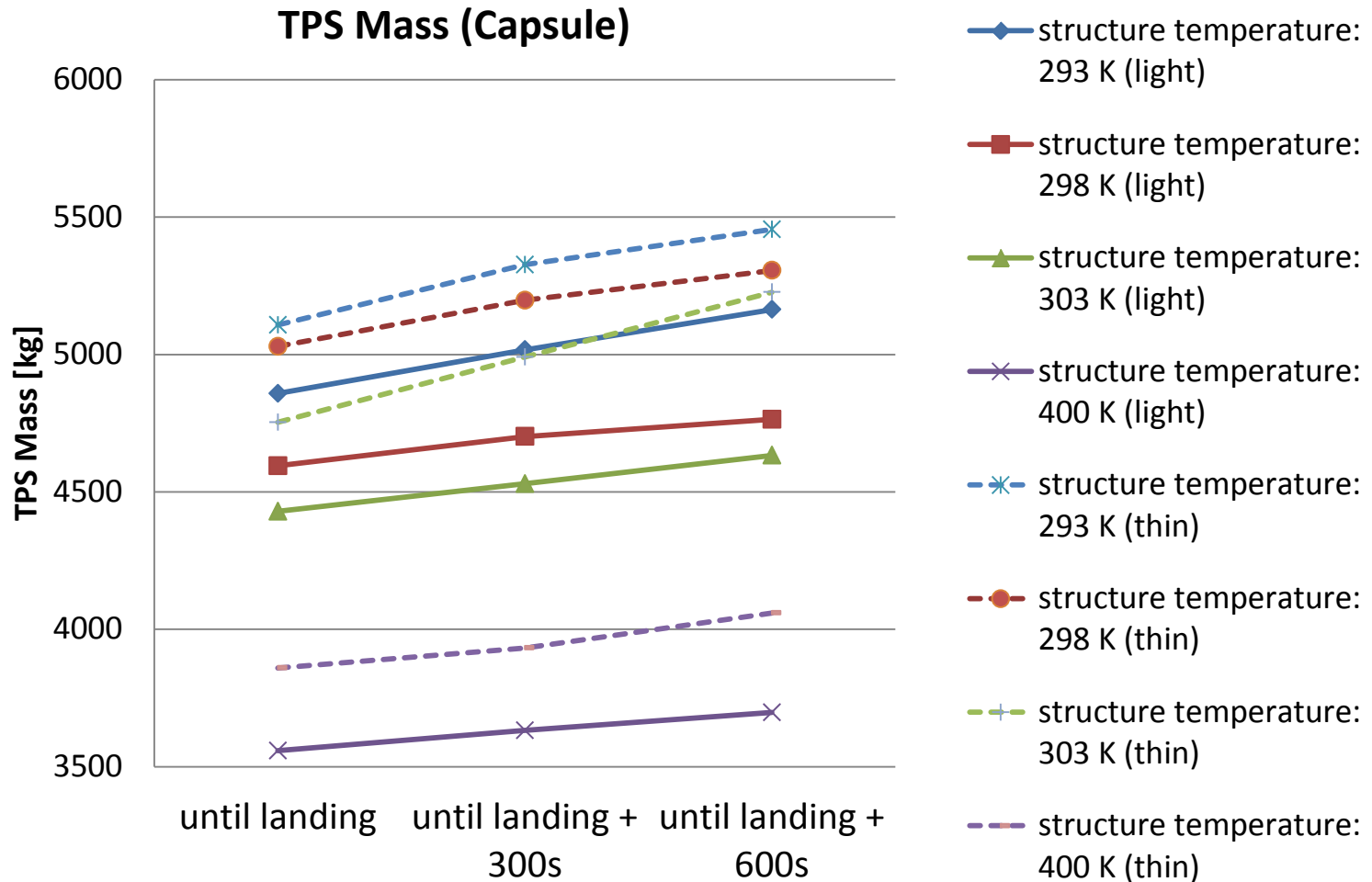
literature: 8.9 cm

calculated: 7.9 cm

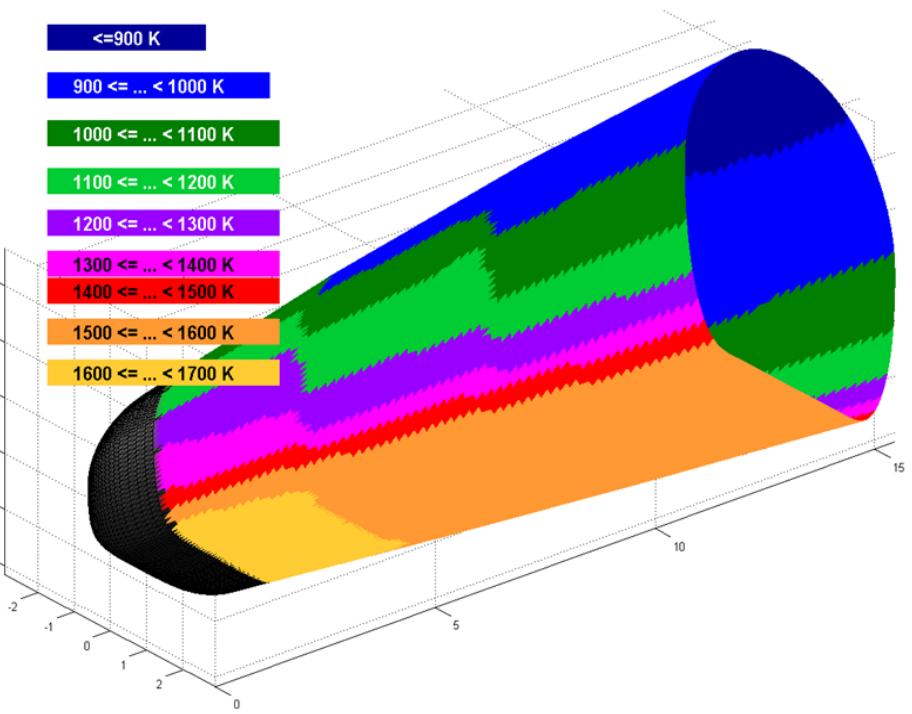
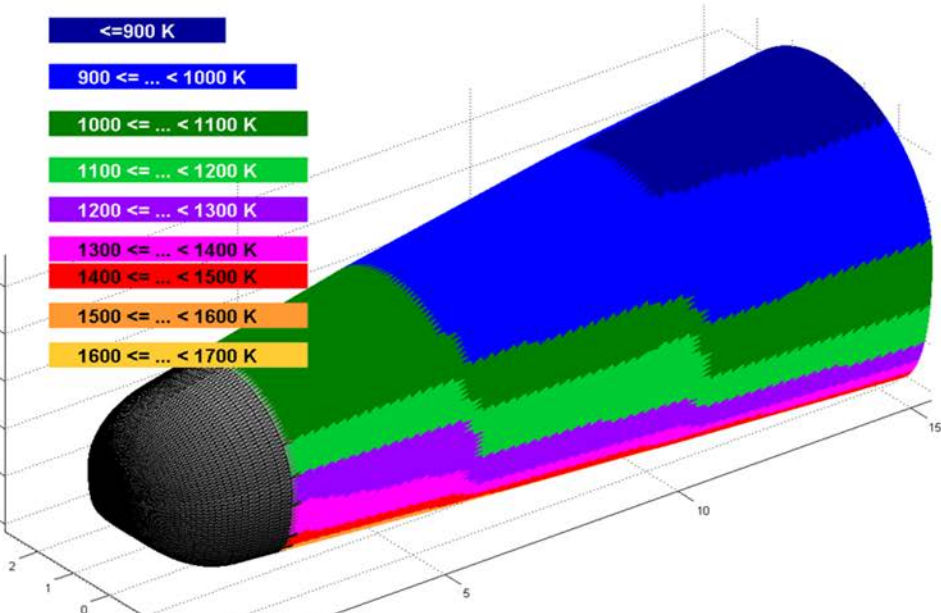
Difference due to

- use of nominal trajectory for calculation (not the critical one which would be basis for real case)
- only assumption of 1D heat flux

Simulation scenarios for passenger capsule



Passenger capsule



Temperature	optimization:thin		
	Material	Thicknes s [m]	Mass [kg]
(303 K) until landing + 300			
Upper half < 900 K	AETB-12	0.1021	289.50
Upper half 900 – 1200 K	AETB-12	0.1021	1961.48
Lower half < 1200 K	AETB-12	0.0566	165.99
Lower half 1200 – 1300 K	AETB-12	0.0600	189.18
Lower half 1300 – 1400 K	AETB-12	0.0627	149.17
Lower half 1400 – 1500 K	AETB-12	0.0659	113.12
Lower half 1500 – 1600 K	AETB-12	0.0674	567.71
Lower half 1600 – 1700 K	CMC	0.2198	197.83
Lower half 1700 – 1850 K	CMC	0.2198	10.01
Nose section	AVCOAT	0.1330	1347
Sum			4991.0



Summary

- Fast engineering modell works well for TPS predesigning process !
 - => acceptable validation done
 - => fast enough to analyse hugh number of modells during predesign

- TPS Spaceliner
 - => TPS mass is a critical factor in the designing process
 - => Material thickness has to be a compromise between „thin“ and „light“
 - => combination between a air-condition cooling system and a passive TPS can be useful.



Testing of DLR C/C-SiC for HIFiRE 8 Scramjet Combustor

7th European Workshop on Thermal Protection Systems and Hot Structures

8-10 April 2013

ESA/ESTEC, Noordwijk, The Netherlands

David E. Glass

MS 190, NASA Langley Research Center, Hampton, VA 23681 USA
david.e.glass@nasa.gov

Diego P. Capriotti

MS 168, NASA Langley Research Center, Hampton, VA 23681 USA
diego.p.capriotti@nasa.gov

Thomas Reimer and Marius Kütemeyer

Deutsches Zentrum für Luft- und Raumfahrt (DLR), Pfaffenwaldring 38-40, Stuttgart, Germany
thomas.reimer@dlr.de and marius.kuetemeyer@dlr.de

and

Prof. Michael Smart

The University of Queensland, Brisbane, Australia
m.smart@uq.edu.au

Ceramic Matrix Composites (CMCs) have been proposed for use as light-weight hot structures in scramjet combustors. Previous studies have calculated significant weight savings by utilizing CMCs (active and passive) versus actively cooled metallic scramjet structures. Both a C/C and a C/C-SiC material fabricated by DLR (Stuttgart, Germany) are being considered for use in a passively cooled combustor design for HIFiRE 8, a joint Australia / AFRL hypersonic flight program, expected to fly at Mach 7 for ~ 30 sec, at a dynamic pressure of 55 kPa. Flat panels of the DLR C/C and the C/C-SiC materials were installed downstream of a hydrogen-fueled dual-mode ramjet combustor and tested for several minutes at conditions simulating flight at Mach 5 and Mach 6. Gaseous hydrogen fuel was used to fuel the ramjet combustor. The test panels were instrumented with embedded Type K and Type S thermocouples. Zirconia felt insulation was used during some of the tests to reduce heat loss from the back surface and thus increase the heated surface temperature of the C/C-SiC panel ~ 177°C (350°F). The final C/C-SiC panel was tested for 3 cycles totaling over 135 sec at Mach 6 enthalpy. Slightly more erosion was observed on the C/C panel than the C/C-SiC panels, but both material systems demonstrated acceptable recession performance for the HIFiRE 8 flight.

INTRODUCTION

The HIFiRE Program is a collaboration between the Defence Science & Technology Organisation (DSTO) of Australia and the United States Air Force through its Air Force Research Laboratory (AFRL). The primary objectives of the HIFiRE program are to investigate fundamental hypersonic phenomena and to develop and demonstrate component technologies which enable the sustained operation of aerospace systems within the atmosphere at speeds greater than Mach 5. The current manifest of the HIFiRE program includes nine flights yielding basic scientific data with analyses relevant to the design of future aerospace systems.

Completed flights in the HIFiRE program, such as HIFiRE 1, have produced significant data on high-speed boundary layer transition. The launch technology used in HIFiRE is based around the sounding rocket approach developed during the HyShot Program at The University of Queensland [1]. Thus far, HIFiRE test technology has been used to test partially complete scramjet flowpaths that remain attached to the second stage booster. Furthermore, the trajectory for the tests have been ballistic, with the scramjet experiment conducted upon re-entry to the atmosphere at very high flight path angles. In contrast, the HIFiRE 8 vehicle, shown in Figure 1, is intended to cruise at Mach 7 under scramjet power for 30 seconds at approximately zero flight path angle. A significant upgrade in the use of high-temperature materials is required for key components of HIFiRE 8 (relative to earlier HIFiRE flights), including the scramjet combustor.



Figure 1: Schematic of the HIFiRE 8 flight vehicle

State-of-the-art scramjet combustors utilize actively cooled metallic structures. However, ceramic matrix composites (CMC), due to their high-temperature capabilities, have the potential to provide a passive alternative for at least a portion of the flowpath. Due to the relatively short flight time (~30 sec) and single use nature of the HIFiRE 8 flight, a scramjet combustor constructed using a passive CMC material is being considered. Toward this end, flat panels of the DLR C/C-SiC were tested in the NASA Langley Direct Connect Supersonic Combustion Test Facility (DCSCTF) [2] using the Durable Combustor Rig (DCR) test article. In addition to the C/C-SiC, the DLR C/C material was also tested.

TEST FACILITY & TEST ARTICLE

Tests of the DLR test articles were conducted in the Direct Connect Supersonic Combustion Test Facility (DCSCTF). The facility is located in a 16- by 16- by 52-ft test cell within Building 1221D at the NASA Langley Research Center in Hampton, Virginia. The facility has historically been used to test ramjet and scramjet flow paths at stagnation enthalpies duplicating that of flight at Mach numbers between 3.5 and 7.5. The facility is of a direct-connect, or connected-pipe, configuration such that the entire facility test gas mass flow passes through the flow path model; the flow at the exit of the facility nozzle simulates the flow entering the isolator of a ramjet or scramjet in flight. The stagnation enthalpy necessary to simulate the flight Mach number for the test is achieved through hydrogen-air combustion with oxygen replenishment to obtain a test gas with the same oxygen mole or mass fraction as atmospheric air (0.2095 or 0.2314, respectively).

CHARACTERIZATION OF THE TEST FLOW CONDITIONS

Using the inflow conditions, the amount of fuel added ($\phi_{H_2} = 0.58$), and estimates of the viscous drag and heat loss, the 1-D flow properties in the duct can be calculated. In the region where the CMC panel was installed ($x = 43$ in.), the total temperature of the flow was $T_t = 3900^\circ\text{R}$ (2167K), the static temperature was $T = 3200^\circ\text{R}$ (1778K), the static pressure was $P = 15$ psia (103 kPa) and the Mach number was $M = 1.35$. Based on a calculation of the facility boundary layer performed using the Van Driest II method, the heat load applied to a wall at $T_w = 540^\circ\text{R}$ (300K) in the region of the CMC panel was $q_{\text{dot}} (T_w=300\text{K}) \sim 1.4$ MW/m². Due to the higher total enthalpy, more fuel could be added in the combustor without disrupting the test, and typical fueling was at $\phi_{H_2} = 1.01$. At $x = 43$ in., the 1-D flow properties for these tests were $T_t = 4500^\circ\text{R}$ (2500K), $T = 3800^\circ\text{R}$ (2111K), $P = 14$ psia (96 kPa) and $M = 1.35$. The estimated heat load seen by the CMC panel in this case was estimated to be $q_{\text{dot}} (T_w=300\text{K}) \sim 1.9$ MW/m².

FABRICATION OF DLR C/C-SiC COMPOSITE PANELS

Ceramic matrix composites have been proposed for use as thermal protection materials and hot structures. At the Institute of Structures and Design of DLR in Stuttgart, a specific CMC variant, C/C-SiC has been developed consisting mainly of carbon fibers embedded in a silicon carbide matrix [3]. The fabrication of C/C-SiC CMC composites at DLR is divided into three steps, as indicated in Figure 2. In the first step, a carbon fiber reinforced plastic (CFRP) component is produced which can be performed in different ways. The preferred approach is resin transfer molding (RTM) or using autoclave technology, but warm pressing or filament winding are also acceptable processes. After the curing, the composites are tempered for 4 hr at 240°C to complete the polymerization of the matrix. It is essential to use a resin (e.g. phenolic) with high carbon yield in this step to create a matrix with sufficient carbon content in the subsequent step.

In the second step, the CFRP composite is carbonized under inert atmosphere (nitrogen) at a temperature of 1650°C to convert the polymer matrix to amorphous carbon. The result is a C/C component. The pyrolysis results in a macroscopic shrinkage of about 10% mainly in thickness and a microscopic network of cracks within the C/C composite is formed. The fiber bundles remain practically intact.

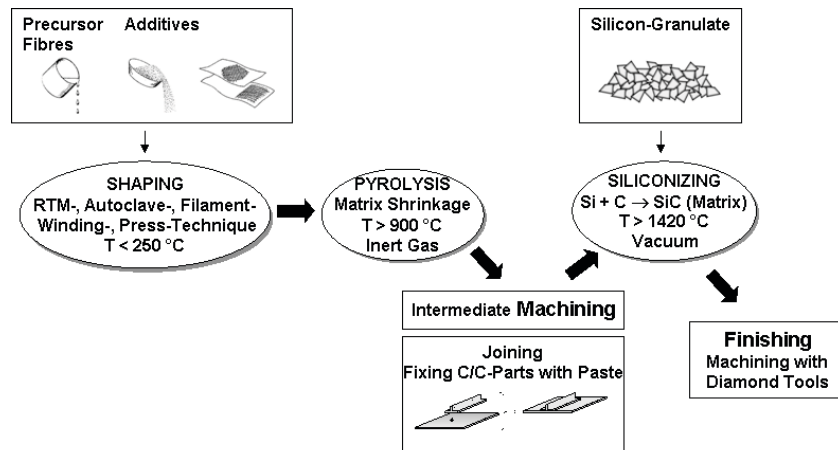


Figure 2: Schematic diagram of fabrication process

In the third step, the C/C component is siliconized via melt infiltration. The component is placed into a coated graphite crucible and solid silicon is added as granulated pure metal. After heating up to over 1420°C (melting of silicon) the porous C/C component is filled with liquid silicon due to the capillary effect of the micro-cracks and the low viscosity of the molten silicon. In an exothermic reaction between the molten silicon and the carbon matrix, silicon carbide is formed along the micro cracks encapsulating the carbon fiber bundles. The siliconizing is carried out under vacuum at a temperature of 1650°C. The resulting C/C-SiC composites contain three material phases. These are the carbon phase consisting of carbon fibers and residual carbon matrix, silicon carbide as the main matrix constituent and a small share of unreacted free silicon.

TEST RESULTS

The test matrix is shown in Table 1. Three C/C-SiC and one C/C panels were tested, with multiple tests per panel. The test hardware was allowed to cool for approximately 20 minutes between tests. The facility run number is shown, followed by the simulated flight Mach number, either Mach 5 or 6. The actual (aerodynamic) Mach number of the flowfield within the DCR was ~ Mach 2. As mentioned previously, two TC's were embedded in the panel from the back surface. In each of the panels tested, there was one Type K and one Type S thermocouple installed. Shown in the table are the temperatures of the TC at the end of each test. The facility total temperature and pressure are also shown in the table, along with the equivalence ration (ER) of the injected hydrogen fuel. Finally, the fuel-on time and the total test duration are shown.

Table 1: Test Matrix

Panel	Run No.	Simulated Flight Mach No.	Temperature at end of Test, °R		P ₀ [psia]	T ₀ [°R]	ER	Fuel-on Time [sec]	Total Test Duration [sec]
			Type K	Type S					
C/C HP635-7	68	5	859	858	96.1	2131		n/a	20
	69	5	1507	1450	96.1	2117	0.556	35	40
	70	5	1611	1548	95.9	2130	0.741	35	40
	71	6	1002	1031	89.4	2546		n/a	20
	72	6	1878	1796	91.8	2611	0.986	40	45
	73	6	1026	1015	88.8	2558		n/a	20
	74	6	1987	1800	91.6	2594	1.003	39	44
	75	6	2051	1835	90.8	2626	1.023	39	44
C/C-SiC #4	52	5	1005	972	92	1939		n/a	20
	53	5	1248	1193	91.6	1957		n/a	40
	54	5	997	971	91.8	1989		n/a	20
	55	5	1214	1329	92.6	2020	0.53	14	20
	56	5	1044	1062	94.2	2035		n/a	20
	57	5	1737	1834	94.5	2070	0.58	32.5	38.5
	60	5	1076	1087	94.2	2070		n/a	20
C/C-SiC #3	62	6	1010	999	94.6	2059		n/a	20
	62	6	1281	1291	90.6	2624		n/a	20
	63	6	1295	1319	90.7	2647		n/a	20
C/C-SiC #1	64	6	2025	2206	90.6	2648	1.01	30	40
	76	6	1382	1317	89.6	2591		n/a	20
	77	6	2352	2515	91.9	2599	1.009	39	44
	78	6	2342	2504	91.2	2639	1.039	39.5	44.5
	79	6	2336	2462	91.9	2654	1.047	39.5	44.5

In an effort to increase the hot surface temperature on the final test panel (Runs 76-79), zirconia insulation was placed on the cool surface of the panel (backside). The insulation increased the hot surface temperature by $\sim 177^{\circ}\text{C}$ (350°F).

A plot of the data from the two embedded TC's is show in Figure 3 (for Run 79). The Type S TC reads a higher temperature, and was located upstream of the Type K TC. The facility total pressure (PTOTAL1) and fuel supply pressure (FUEL1P) are also shown on the figure. A photograph of the test panel post-test is also shown on the figure.

After the final run, the test panel was removed from the carbon steel fixture. Despite the high heating that the panel was subjected to during the last test and the melting of the steel sidewalls, the panel showed practically no damage, just a slight stain where the melted steel came into contact with the panel.

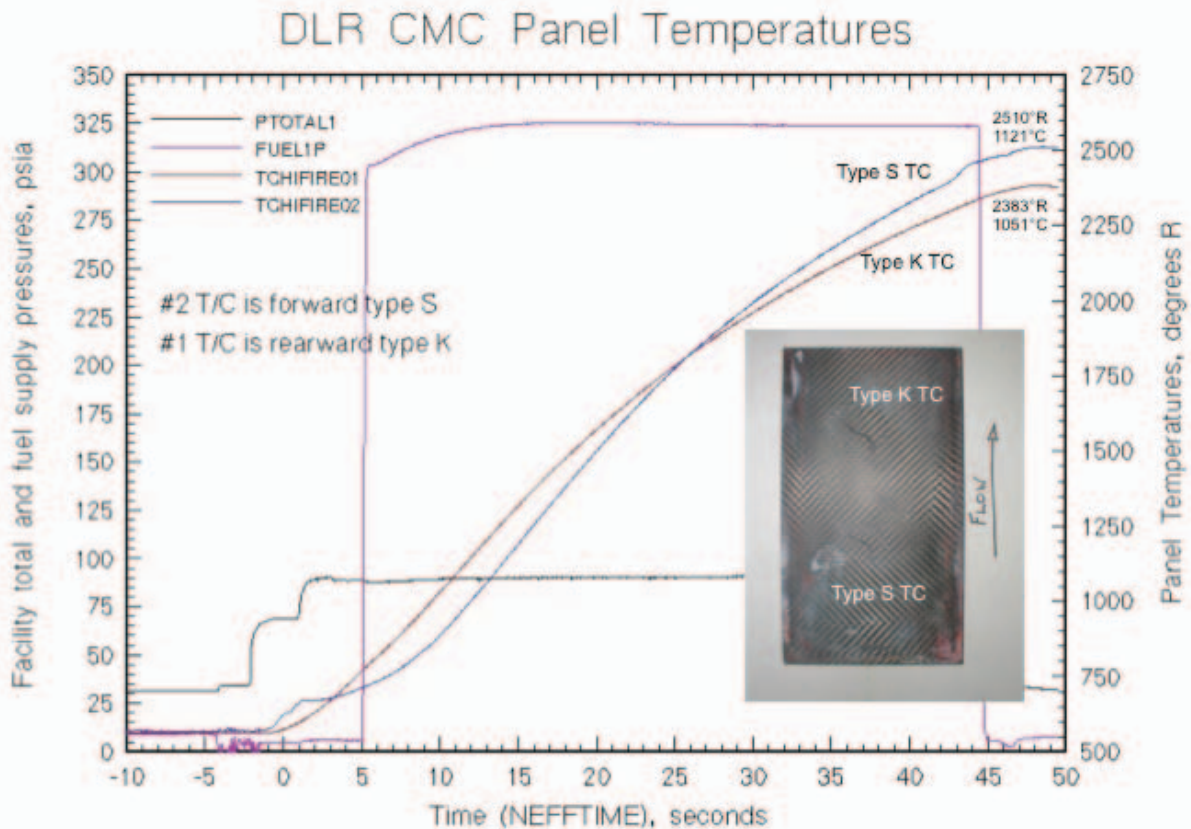


Figure 3: C/C-SiC panel test temperatures during Run 79

Very little recession was measured on the test panels. The largest recession was 0.051 mm. Several locations have zero recession. Table 2 shows the pre- and post-test thickness measurements, taken prior to the first run with panel C/C-SiC #1 and taken again after the last run with C/C-SiC #1. As indicated by the recession measurements and the post-test photographs of the panel, the panel survived the series of tests with negligible deterioration.

Table 2: Pre-and post-test thickness measurements for C/C-SiC panel #1

	Thickness (mm) / Measurement location							
	1	2	3	4	5	6	7	8
Pre-test	8.026	8.052	8.052	8.103	8.306	8.280	8.052	8.052
Post-test	8.026	8.001	8.026	8.077	8.306	8.255	8.026	8.052

After the C/C-SiC panels were tested, a single C/C panel from DLR was also tested. A plot of the two embedded TC's is show in Figure 4. The Type S TC reads a higher temperature, and was located upstream of the Type K TC. The facility total and fuel supply pressures are also shown on the figure. A photograph of the test panel post-test is also shown on the figure.

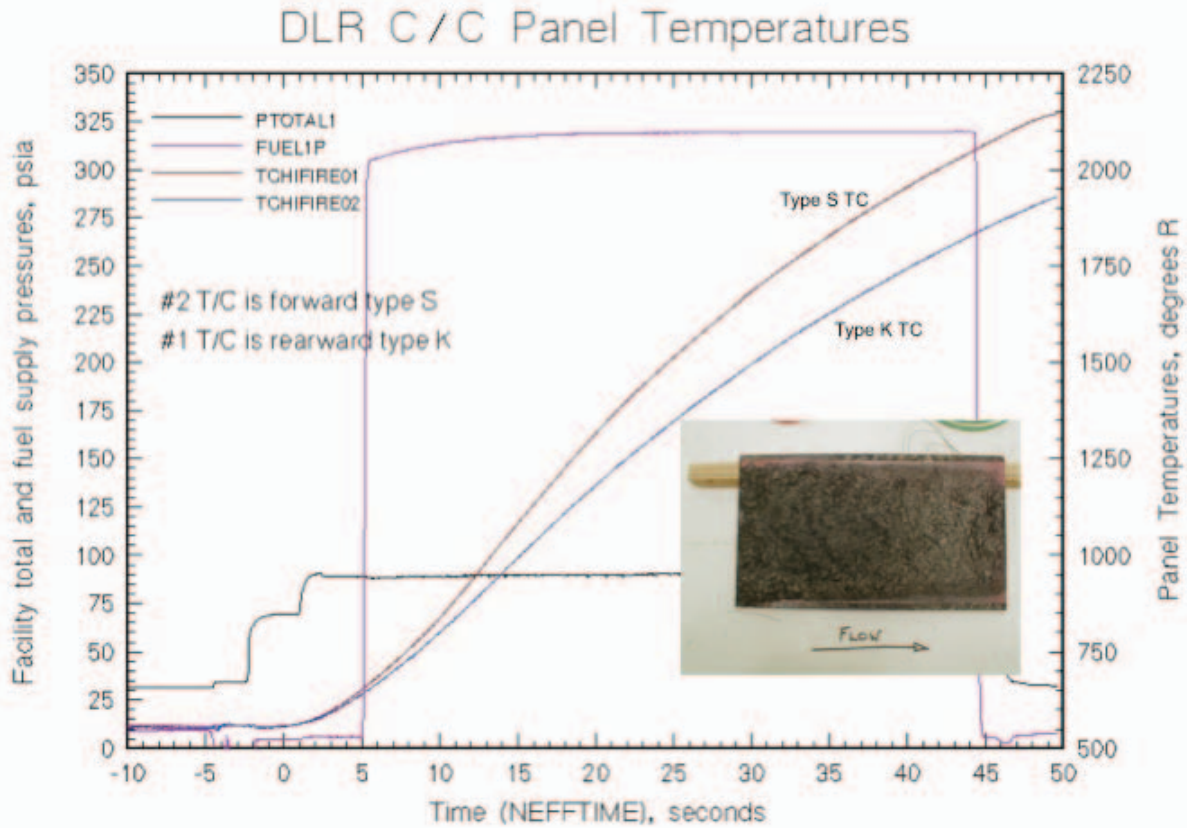


Figure 4: C/C panel test temperatures during Run 75

As shown in Table 1, the panel was tested for 100 seconds at Mach 5 conditions, and 193 seconds at Mach 6 conditions. The measured recession data is shown in Table 3.

Table 3: Pre-and post-test thickness measurements for C/C panel HP635-7

	Thickness (mm) / Measurement location							
	1	2	3	4	5	6	7	8
Pre-test	10.008	10.008	10.008	10.008	10.084	10.109	9.957	9.931
Post-test	9.881	9.881	9.957	9.881	9.830	9.627	9.855	9.881

POST-TEST INVESTIGATION OF C/C-SiC PANELS

Several of the test panels were fabricated from C/C-SiC material as described previously. The surface that was to be exposed to the exhaust flow of the combustor was intentionally not machined in order not to remove the as-fabricated SiC layer that forms as the result of the material processing. The backside of the panels was machined and grooves for thermocouple installation were created. Post-test investigations were performed with samples from all three tested C/C-SiC panels. Since the findings were consistent between the three panels, the process is described for panel #1 only.

A number of samples were prepared on the centerline of the panel and on a line that was 20 mm from the side edge of the panel. The panel was cut into 19 pieces, and each piece was numbered accordingly. The samples were prepared for investigations in the SEM, i.e. they were embedded in a packing material and the surface to be investigated was ground and polished. For the investigations presented here, two samples from each panel were prepared. These were the cut-outs #5 and #17 from the centerline, as shown in Figure 5. Cut-out #5 was upstream on the panel closest to the combustor. Cut-out #17 was on the downstream end of the panel close to the nozzle exit.

Figure 6 shows a scanning electron microscope (SEM) image with the typical C/C-SiC microstructure. Carbon fiber bundles are separated by crack volumes that are filled with SiC at the boundaries, and Si in the case when the width of the pore or crack is comparatively large. The surface of the sample is not flat due to the fact that it was not machined, so the topology of the fiber textile is seen. The area on the top part of the image where numerous bright spots appear is the packing material used for embedding the sample.

There is no evidence of significant oxidation which might have resulted in degraded fibers or matrix near the surface. What can be seen is a thin bright layer on the surface that was identified as silicon dioxide (or silica) using electron diffraction spectroscopy (EDX) analysis.

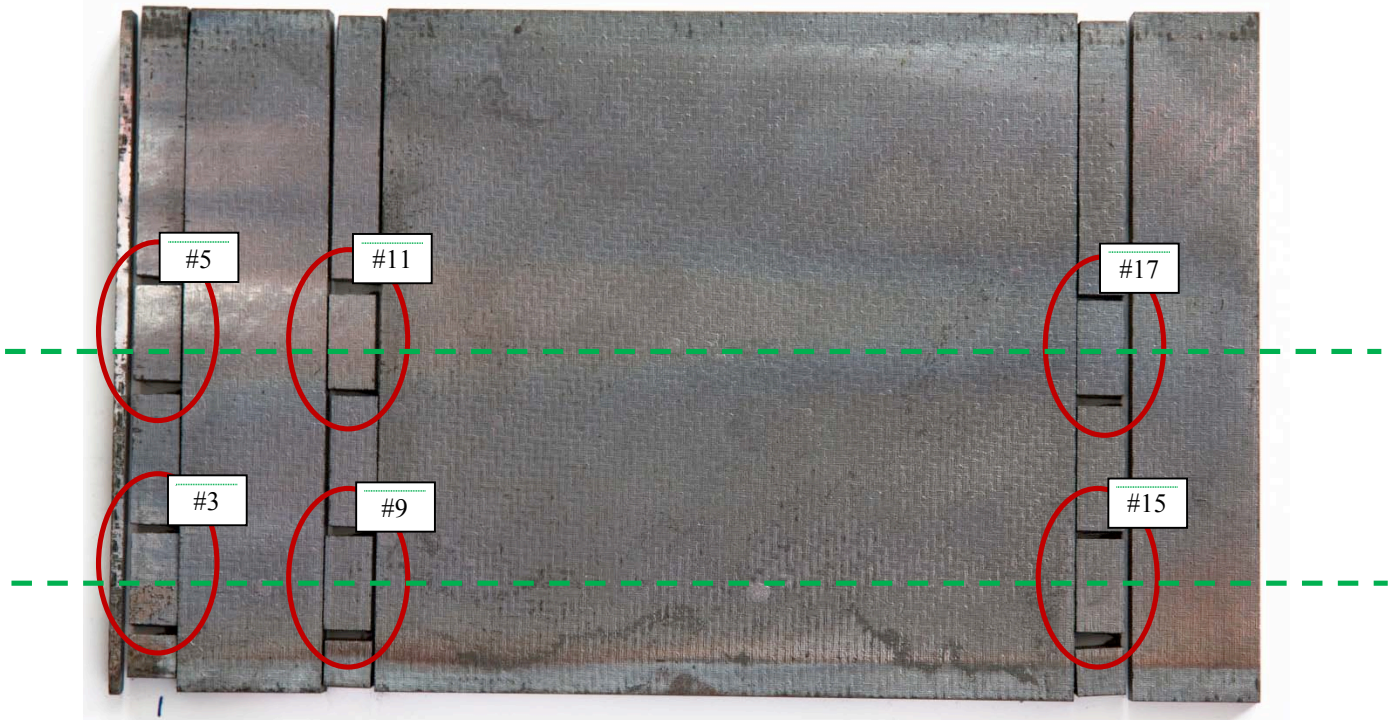


Figure 5: Panel 1 with cut pattern for the sample preparation

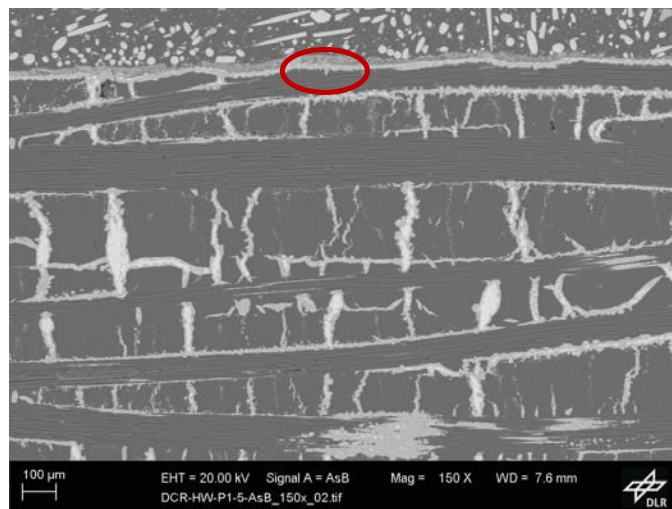
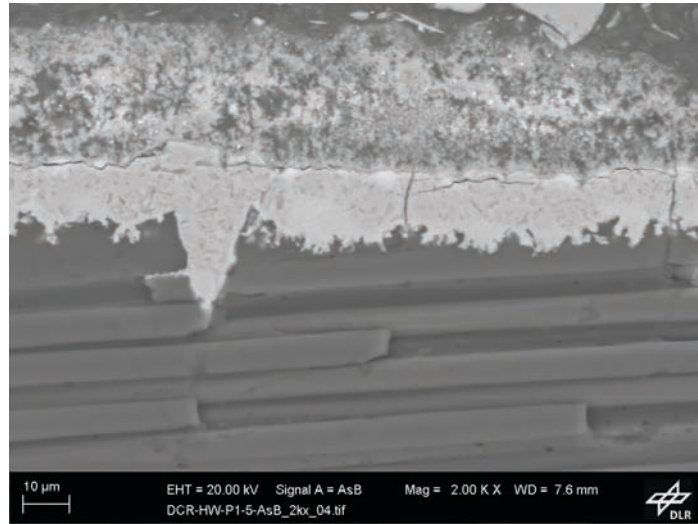


Figure 6: SEM image of sample #5 from panel 1. There is a thin layer on the surface that is identified as silica. The circle indicates the area that is shown in higher magnification in Figure 7.

The close-up of the detail highlighted in Figure 6 is shown in Figure 7. The different material phases can be distinguished very well. There is a fiber bundle with silicon carbide on the surface. On the surface, above the silicon carbide is a thin layer of silica of around 20 μm thickness. The SiO₂ layer on the surface does not have a constant thickness in every location over the sample. There are some spots where no SiO₂ layer can be found and there are locations with a thinner layer compared to Figure 7, but in general, there is a SiO₂ layer over most of the sample.



Silicon dioxide, SiO₂

Silicon carbide

Carbon fibers and carbon matrix

Figure 7: SEM image of the SiO₂ scale on top surface of the sample

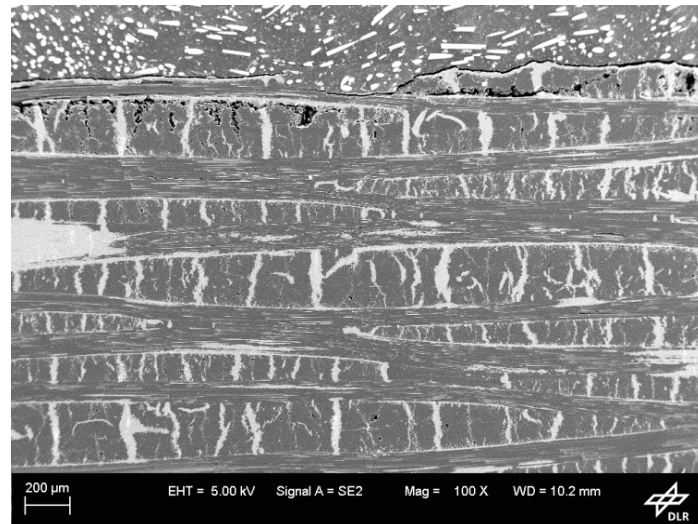


Figure 8: SEM overview image of sample #17 from panel 1, exposed surface is on the top

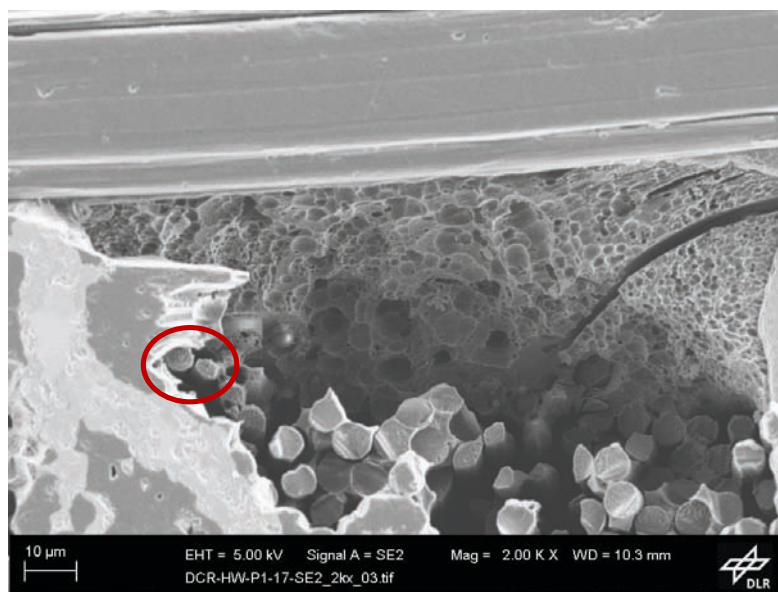


Figure 9: Close-up SEM image showing some indication of matrix oxidation in the pore.

Figure 8 shows the surface of sample #17 from the end of the panel. There are a few cracks and pores in the two topmost layers. These could be the result of oxidation of the carbon since close-up images show signs of oxidation

in the pores at fiber ends and on the matrix; however, the amount of pores was significantly smaller in other samples, so in part they can also be the result of sample preparation as there is a tendency of sample material to break out at the edges due to the relative softness of the surrounding packaging. Figure 9 shows a close-up SEM image showing some indication of matrix oxidation in the pore. Note the clean-cut ends of most of the fibers as the result of the preparation. The circle indicates the region detailed in Figure 10.

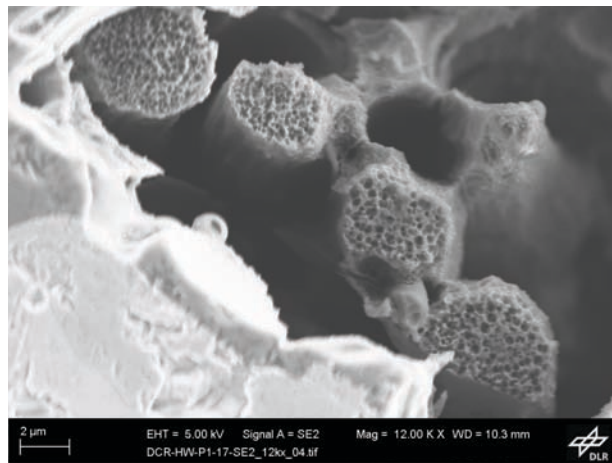


Figure 10: SEM image of fiber ends that have a rough cross-section which is interpreted as the effect of oxidation.

The conclusion is that there was some oxidation on the surface of the panel, but limited to only the topmost one or two layers, with no significant degradation of the panel.

CONCLUDING REMARKS

The DLR C/C and C/C-SiC materials were tested at NASA Langley Research Center in a high-enthalpy direct-connect test facility at conditions simulating flight at Mach 5 and Mach 6 for several minutes. The C/C-SiC survived the high-temperature scramjet combustor environment with very little erosion. The C/C material experienced slightly more erosion, but still only a small amount. SEM analysis of the tested panels indicated very little oxidation of the exposed surface. The HIFiRE 8 flight, for which the materials were tested, is planned for Mach 7 for ~ 30 sec. Due to the successful performance of the test panels, the DLR C/C-SiC material is being considered for use as a passive combustor on the HIFiRE 8 flight vehicle.

ACKNOWLEDGEMENT

The technical effort reported herein was sponsored by the Hypersonic International Flight Research and Experimentation (HIFiRE) Program Office under an international collaboration between the Air Force Research Laboratory (AFRL) and the Australian Defence Science and Technology Organisation (DSTO). Specific Authority was secured under the terms and conditions of Project Arrangement (PA) AF-06-0046, and subject to terms and conditions secured under the joint US DoD-DoD Australia Memorandum of Understanding (MOU) for Co-operative and Collaborative Research, Development and Engineering.

REFERENCES

1. Smart, M.K., Hass, N.E. and Paull, A., "Flight Data Analysis of the HyShot 2 Flight Experiment", AIAA Journal, Vol. 44, No. 10, pp 2366-2375, 2006.
2. Guy, R.W.; Rogers, R.C.; Puster, R.L.; Rock, K.E.; and Diskin, G.S.: *The NASA Langley Scramjet Test Complex*, (AIAA-96-3243), AIAA, ASME, SAE, and ASEE, Joint Propulsion Conference and Exhibit, 32nd, Lake Buena Vista, FL, July 1-3, 1996.
3. Krenkel, W.: *Ceramic Matrix Composites*, ISBN 978-3-527-31361-7 – Wiley-VCH, Weinheim, 2008

Z40 Solid Rocket Motor nozzle development and innovations

7th European Workshop on Thermal Protection Systems and Hot Structures
8-10 April 2013
ESA/ESTEC, Noordwijk, The Netherlands

R. Marocco⁽¹⁾, P. Perugini⁽¹⁾, A. Pascucci⁽¹⁾
S. Cifani⁽²⁾, E.A. Squeo⁽²⁾, G. Greti⁽²⁾
L. Nele⁽³⁾, F. Brunaccini⁽³⁾

⁽¹⁾⁽²⁾AVIO S.p.A.

Via Ariana km 5.2, Colleferro (Rome), Italy

Email: renato.marocco@aviogroup.com

pierluigi.perugini@aviogroup.com

alessandro.pascucci@aviogroup.com

silvia.cifani@aviogroup.com

ericaanna.squeo@aviogroup.com

gilberto.greti@aviogroup.com

⁽³⁾Università degli Studi di Napoli "Federico II", Italy

Dipartimento di Ingegneria Chimica, dei Materiali e della Produzione Industriale

Email: nele@unina.it

brunaccinifederico@gmail.com

ABSTRACT

In the frame of VEGA Evolution Program Zefiro 40 is a solid rocket motor (at the moment in development phase) whose design and manufacturing is AVIO responsibility. Main objective is the development of technological innovations able to increase VEGA Launcher performances and reduce fixed costs. Part of technological development concerns nozzle design and manufacturing. Z40 nozzle is submerged with expansion ratio equal to 37. It shall sustain max actuation of 7°. Major innovations with respect to similar AVIO products are the development of self-protected flexible joint and manufacturing of divergent composite thermal protection by resin infusion technology. Both technologies aim to optimise performances/costs ratio. Self protected FJ design shall withstand mechanical and thermal loads and at the same time decrease stiffness (and mass) allowing to use lightweight actuators. This is obtained by synthetic soft rubber pads and hybrid composite structural reinforcements. Resin infusion manufacturing process adopted for divergent TP allows to avoid typical defects for pre-preg tape-wrapped items (wrinkles, delaminations) and reduce process and machining time.

INTRODUCTION

VEGA Launch Vehicle is the small European expandable launcher, developed by Prime Contractor ELV (a company established by Avio S.p.A. and Italian Space Agency in December 2000), designed to deliver from 300 to 2500 kg payloads into Polar and low Earth orbits and successfully flown on 13th of February 2012 from Guyana Space Center of Kourou during its Maiden Flight [1].

VEGA is a 30 m tall single body launcher, with a maximum diameter of 3 m and a weight of 137 tons. It consists of three solid rocket stages, the P80 FW first stage, the Zefiro 23 second stage, the Zefiro 9 third stage and a liquid bipropellant rocket upper module called AVUM (see Fig. 1). In the frame of VEGA Evolution Program several launcher architecture changes were investigated in order to improve the launcher performance, the payload comfort and to reduce the launch cost. In particular the first stage propellant increase to about 120 tons and the second stage propellant increase to about 40 tons would represent an important initial enhancing step for payload mass.

For this reason ELV and Avio S.p.A. started defining a series of functional requirements for a 40 tons propellant solid rocket motor, named Zefiro 40, to be used as second stage motor of VEGA Evolution Launcher (see Fig. 1) and prototype for new technologies introduction, with direct benefits on present Vega engines and fruitful also for next generation launchers development.

ZEFIRO 40 SOLID ROCKET MOTOR OVERVIEW

Zefiro 40 Motor, derived from Zefiro 16, Zefiro 23 and Zefiro 9 experience, has been designed in order to comply with very challenging requirements defined at system level.

Zefiro 40 SRM will be a very high mass fraction (ratio between propellant and total mass) motor with about 36 tons of HTPB composite propellant. Zefiro 40 length and maximum thrust will be comparable with Zefiro 23 ones, while diameter and combustion time will be greater.

It will implement advanced technologies (as automated tape laying for skirt fabrication, nozzle self-protected flexible joint for thrust orientation, etc) and high performance materials (as Avio own made composite material for structural Case, a new low density material for Thermal Protection, etc.) able to fulfil the challenging mass fraction requirement and to improve the production capability of several processes.

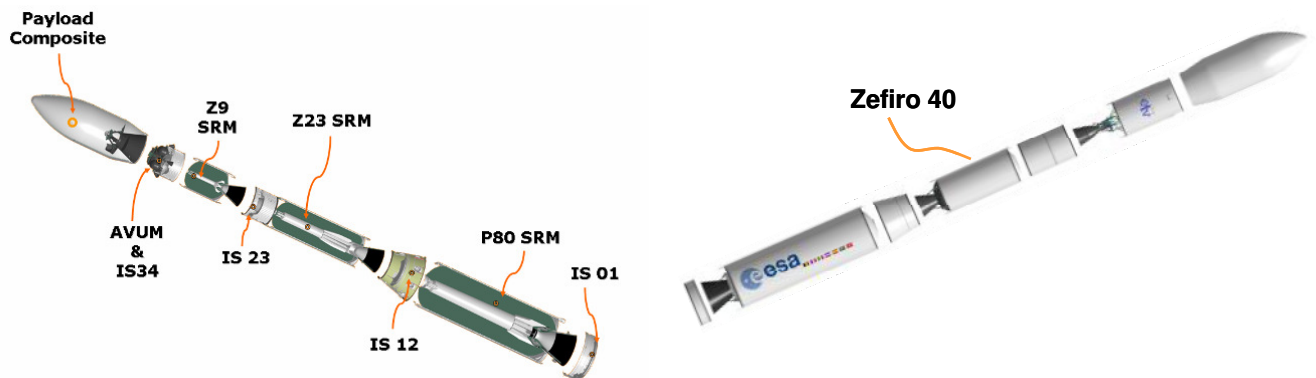


Fig. 1: VEGA launcher stage motors and Possible VEGA launcher evolution with Zefiro 40 motor

ZEFIRO 40 NOZZLE

Description

The nozzle is the motor component which accelerates the combustion gas products in order to generate thrust. [2] Special technological improvements will be introduced in Zefiro 40 nozzle, which will be the largest one ever produced in Avio facilities. Nozzle configuration is characterised by the main following elements (see Fig. 2):

- an interface structure with Solid Rocket Motor (SRM) case (Stationary Shell); the internal surface is protected from the combustion gas by means of an internal thermal protection
- a low torque self-protected Flexible-Joint to allow the required deflection of the movable part by light actuator;
- a Nozzle Movable Part constituted by:
 - Throat Insert made in carbon-carbon to dissipate part of thermal energy coming from hot flow by ablation in the most thermally loaded convergent and throat area of nozzle and to guarantee the respect of the throat erosion requirement
 - Nose Cap items made in carbon-phenolic to thermally protect the movable ring of flexible joint and its junction with the metallic divergent
 - Insulators made in carbon phenolic to thermally protect the forward metallic divergent from the items in contact with
 - Divergent made in carbon phenolic with fibers oriented at 10° w.r.t. nozzle axis to thermally protect the forward metallic divergent in the first portion of divergent
 - Metallic Divergents to ensure mechanical stiffness to the divergent channel
 - Divergent thermal protections to thermally protect both metallic divergents

The Z40 Nozzle design already passed Preliminary Design Review.

Technological developments

Main technological developments implemented in Z40 nozzle are self protected flexible joint and forward divergent thermal protection manufactured by Liquid resin Infusion (LRI). [3]

A self-protected flexible joint (FJ) is in development phase. Trade off activity has been performed in order to choose best composite materials for reinforcement shims. Very stringent requirement on FJ stiffness and component encumbrance demanded an effort from calculation point of view in order to assess materials behaviour in different geometrical configurations. This led to choose a hybrid composite configuration and technological necessity to adapt FJ manufacturing process cycle. Hybrid composite shims shall be produced by hand layup and autoclave curing. Even FJ manufacturing process is subjected to trade off activity. Rubber transfer molding is considered the baseline because this is the process used at the moment for Zefiro FJ. Likely problems can occur in homogenous heating of liquid rubber during mold penetration due to low thermal diffusivity of composite shims.

Composite and rubber post-cured bonding is considered a backup process. Technical and cost problems can arise due to necessity of several equipment to ensure correct and centered adhesion between rubber pads and composite shims and need to test correct adhesive agents based on cold or hot bonding process.

Technology of LRI will be applied for the production of divergent thermal protection at lower diameters, where more defects usually occur. The standard technology currently used in the production of the conical divergent parts of the nozzles consists in wrapping tapes of composite prepreg material (carbon phenolic) on a suitable mandrel, followed by the application of vacuum bag, hydroclave cycle and machining to obtain the final piece.

Wrinkles on the outer surface are likely to appear due to the compacting of the material during the thermal and pressure cycle. These defects induce deformations in the fibers geometry and resin bubbles thickening which reduce the mechanical strength of the final item. On the contrary, LRI technology shall allow to avoid wrinkle defects with a significant reduction in manufacturing cost and time.

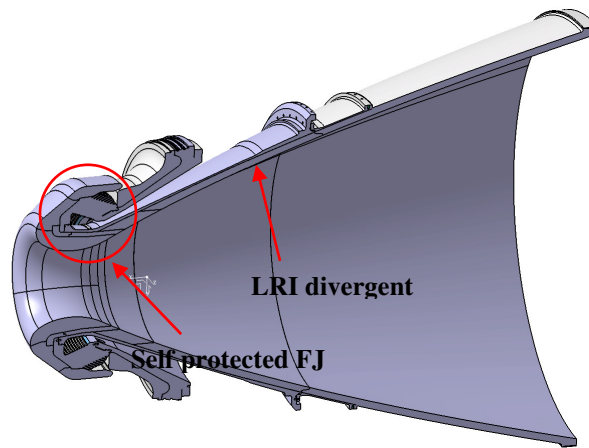


Fig. 2: Zefiro 40 Nozzle scheme

SELF-PROTECTED FLEXIBLE JOINT

Description

Self protected FJ have been designed and used in SRM for years. [4],[5],[6]

It consists of two interface rings (one fixed and the other one movable) and a series of thinner rings (composite reinforcement shims) alternated with synthetic low module rubber layers. Synthetic rubber shows more stable mechanical properties if compared with natural rubber. Shims in composite material will allow to strongly reduce FJ mass (also because of absence of further thermal protections parts) and FJ stiffness. Self-protected FJ allows to avoid manufacturing and integration of dedicated thermal protections by protruding composite shims beyond rubber pads in order to withstand thermal loads coming from combustion gas. Examples of self protected FJ can be found in [4], [5], [7]. Main differences between classical FJ and self-protected FJ are shown in Fig. 3. In self protected FJ composite shims protrude out of rubber pads to act as thermal protection, where classical FJ show only metallic reinforcements to be covered by dedicated thermal protection. Self-protected FJ show limited margins to high pressure stability. A self protected FJ shows no or limited cone angle in order reduce stress on reinforcements when pressure and actuation act simultaneously. Anyway this geometrical configuration is the most “volume consuming” in terms of nozzle envelope and involve substantial decrease of stiffness when FJ is pressurised (as reported for example in [8]).

Requirements and design

Zefiro 40 self-protected flexible joint design has been guided by following requirements:

- low FJ stiffness (<3000 Nm/°) by acting on rubber modulus and pad thickness
- thermal resistance for 100 sec of composite reinforcements

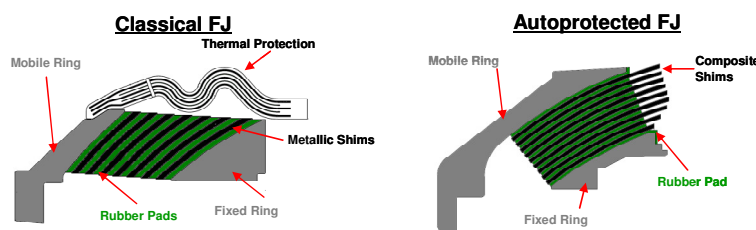


Fig. 3: Classical and autoprotected FJ

- mechanical resistance to loads induced by max pressure of 100 bar and max actuation of 7°
 - mechanical stability at high pressure
- Z40 nozzle FJ design is a compromise between very low torque requirements and high pressure conditions stability. The principal geometrical characteristics (see Fig. 4) of this configuration are:
This configuration is the result of a long trade off activity aimed to answer all requirements while minimising mass and encumbrance.

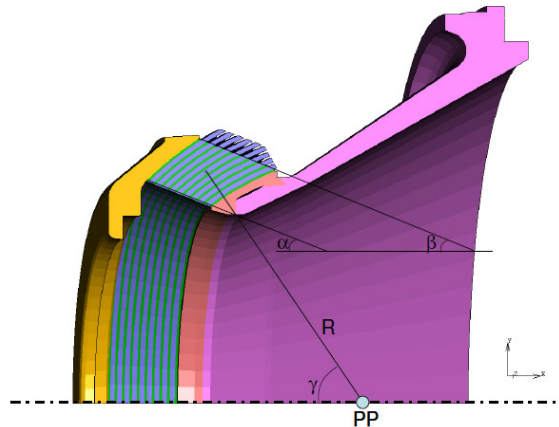


Fig. 4: Geometric configuration of Z40 nozzle FJ

FJ technology

Technological development plan and manufacturing activity up to delivery of FJ qualification item is outlined in Fig. 5. Two parallel activities shall be carried out during technological development: composite shims manufacturing and FJ manufacturing. Due to necessities to withstand simultaneously high mechanical loads on low diameters and high thermal loads in aggressive combustion chamber environment in higher diameters, reinforcement shims are made by hybrid composite: layered carbon –epoxy and glass-epoxy in low diameter zone in order to stiffen and strengthen most mechanically loaded area, glass-epoxy in contact with hot gas.

Transition from carbon/glass –epoxy area up to just glass-epoxy is achieved by ply drop and it is studied in order to provide suitable stiffness to overall FJ (in order to have margins with respect to high pressure stability) and to keep constant shim thickness along its length. Aspect ratio of external part of shims (length of shims/gap between shims) is high enough to avoid recirculation of hot gas and quick heating of rubber.

Hybrid composite shims will be manufactured by manual stratification of stripes of fabric pre-preg and curing in autoclave (tow winding technology feasibility has been evaluated but problems in achievable fibres angles and shims thickness tolerances did not allow to use this technology).

Two different prototypes will be produced at Z23 scale in order to set up and optimise manufacturing process (the first prototype is visible in Fig. 6), set up acceptance controls and define dimensional threshold for acceptable defects.

In the meanwhile a low module-high strain synthetic rubber is in development phase. This rubber is an evolution of rubber used at the moment in the Zefiro 9 and 23 FJs.

A preliminary trade off between two different components formulations has been performed by tension, compression and shear testing at RT. The best performing rubber has been chosen to be subjected to:

- molding process setup
- FJ blank transfer molding tests
- complete thermo-mechanical characterisation foreseen for hyperelastic materials at room temperature (RT) up to 300°C

Then shims at Z40 scale will be produced and used to manufacture self protected FJ prototype without adhesive between composite and rubber in order to check suitability of mold process cycle and to perform controls on shims and pads. If the blank test provides positive results (in terms of thickness, complete rubber reticulation, etc.), a FJ mold with adhesive is performed in order to obtain first self-protected FJ. This first development item shall be subjected to acceptance tests of pressurisation and actuation on dedicated cold test bench. Complete development plan is summarised in Fig. 5.

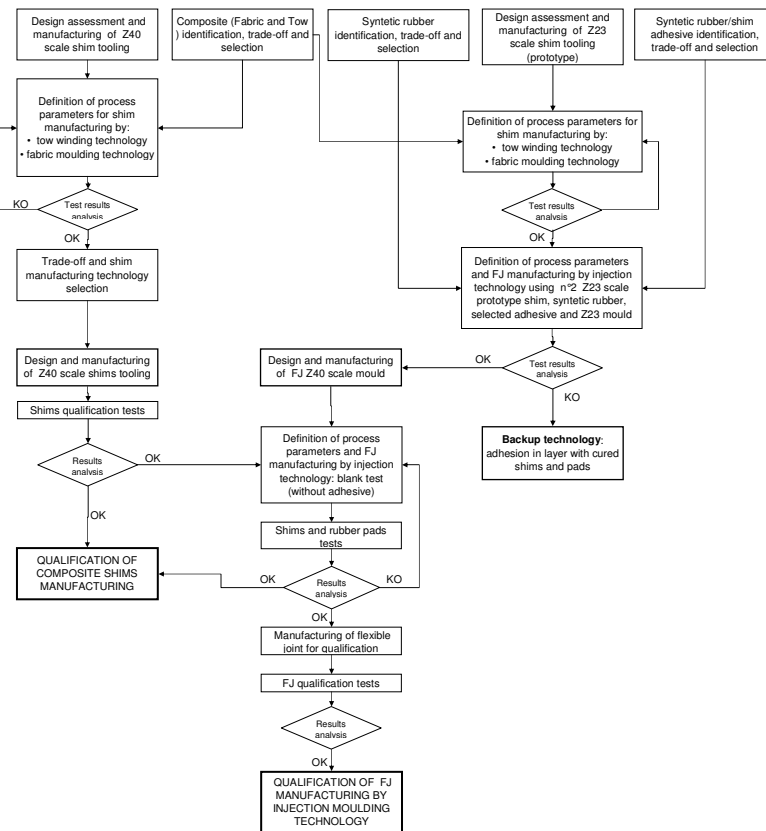


Fig. 5: Z40 Nozzle FJ Technological test plan



Fig. 6: 1st prototype of hybrid composite spherical reinforcement shims at Z23 scale

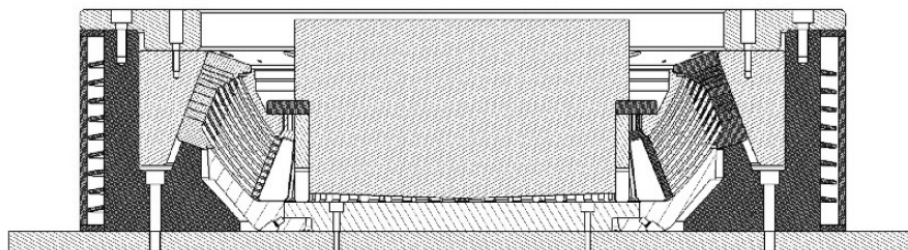


Fig. 7: Self protected flexible joint mold preliminary design

DIVERGENT IN RESIN INFUSION

Description

LRI technology is an alternative and relatively recent technology to manufacture long fibers composite items. A highly porous fiber structure (generally 2D, but even 3D for simple geometries) is subjected to resin injection in temperature. Resin in liquid phase fills in voids between fibers when depressurisation is applied under vacuum bag and cures by proper temperature cycle (see Fig. 8).

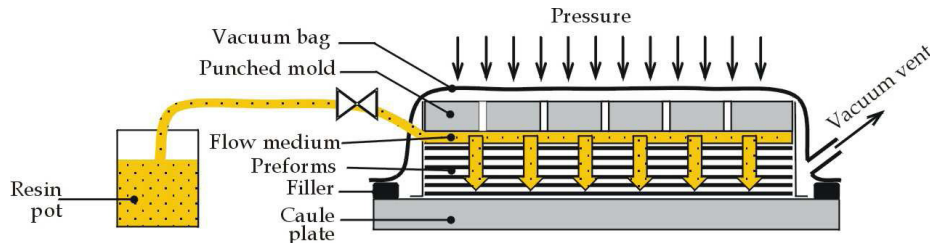


Fig. 8: Resin infusion technological set up

In last years similar technology process involving infusion under pressure [Resin Transfer Molding (RTM)] has been used to manufacture parts for jet engines, engine nacelles, air ducts and weight-saving components, even nozzles components. [9], [10]

LRI technology is simpler and cheaper involving only vacuum pumps and bags. If a low viscosity resin (or an injection process at minimum resin viscosity temperature) can be used, no fiber structure deformation is foreseen during impregnation process. In order to have more stable and cost effective process, this technology has been preferred to RTM for divergent manufacturing. (numerical and experimental analysis on LRI can be found in [11])

It allows to substitute parts for various metal alloy components and composite components produced by tape wrapping [For example nozzle Carbon Fiber Reinforced Polymer (CFRP) components for solid propellant rockets] with lightweight high strength composites by low cost process. [9],[12],[13],[14].

Requirements and design

Z40 nozzle is constituted by two divergent thermal protections components. The divergent at lowest diameter will be manufactured in LRI. This technology applied to divergent thermal protection allows to avoid wrinkle problems typical in technology of tape wrapping and curing under pressure (especially for cones at low diameters) and avoid final machining since finite item can be achieved.

This process consists of following three main steps:

1. lay-up of a nozzle divergent fibre preform;
2. impregnation of the preform with a specifically developed resin under a vacuum bag set-up;
3. curing of impregnated preform;

Zefiro 40 divergent thermal protection design has been guided by following requirements:

- good thermal ablative resistance to hot combustion gas
- thermal insulation for 100 sec in order to avoid temperatures over 100°C at metallic structure interface
- thermo-mechanical resistance to loads induced by pressure, temperature and actuation.

Classical divergent protection components are manufactured by tape wrapping at angle 0° to 30° w.r.t. nozzle axis with fibres arranged at angle ψ w.r.t. circumferential direction [2] (AVIO nozzles use $\psi = 0^\circ$ up to 45°). Preliminary design of LRI divergent foresees θ equal to inclination of internal divergent profile (due to braid structure process) and $\psi = \pm 45^\circ$ braid angle.

Divergent technology

Development of LRI technology and manufacturing of composite divergent TP by LRI foresees the following steps, already partially performed:

1. Trade off for suitable heat resistant resins and carbon fibres and preliminary tests on 4 resins and 2 fibre systems
2. Choice of most suitable resin (viscosity vs temperature and thermogravimetric behaviour are stringent requirements) and fiber after testing on samples
3. Braiding machine setup for manufacturing of fibres structure to achieve correct orientations, density, thickness, shape
4. Small scale braided fiber structure manufacturing
5. Resin infusion process set up in fibres structure (by simulations and tests) [Small scale specimens are planned in order to verify the mechanical properties and absence of defects, then the full scale process setup will be performed]
6. Resin infusion of selected resin in small scale braided fibre structure to manufacture divergent to be fire tested.
7. Study to scale up technology, equipments, machines and manufacturing cycles

8. Manufacturing of full scale divergent to be tested on Z40 QM nozzle

First feasibility technological tests and studies have been performed at small scale level:

- Braiding process set up for carbon fibers braids on cylindrical mandrels (see Fig. 9) has been achieved with 100% cover factor and different braid angles ($\pm 45^\circ$, $\pm 60^\circ$, $\pm 75^\circ$)
- Resins trade off (phenolic, bismaleimide, epoxy and epoxy-phenolic) by chemical, rheological and thermal tests has been almost completed (an example of TGA curves for different resins is reported in Fig. 12). Phenolic resin seems to be best performing according to main requirements on char residual at high temperatures and viscosity minimum value to due processability.
- Braided fibers on squared mandrels have been produced and are ready to be infused with phenolic resin directly on mandrel in order to avoid fibers deformation during resin injection (see Fig. 10). Samples shall be extracted to be tested in tension, shear and compression.
- First assessments on braiding process on conical mandrels at small scale level (Fig. 11) are ongoing. Analytical braiding models (as described for example in [14]) are being used in order to find a compromise between maximum cover factor and braid angle able to guarantee suitable stiffness and strength for item in operative conditions.
- At the same time FE models on small scale divergent are being setup. Models with several braid angle distributions in axisymmetric and 3D configurations have been subjected to thermomechanical loads. They provide slightly different stress results due to presence of balanced but non symmetric laminate stratification for multilayer braided structure model. This configuration induces on conical geometries some torque stresses that cannot be modelled only with axisymmetric model. Anyway effect of different braid angles seems not to be so important on final thermomechanical performances of small scale conical divergent.

This technology seems very promising in order to reduce manufacturing time and dependence from operator and increase process automation compared with tape wrapping technology.



Fig. 9 Carbon fibers braiding at 60° on cylindrical mandrel



Fig. 10: Braiding on squared mandrel



Fig. 11: Small scale conical mandrel

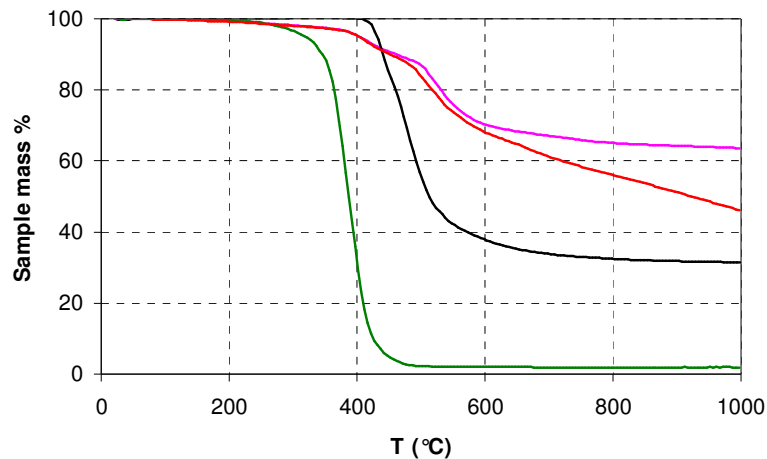


Fig. 12: Trade off resins thermogravimetric measures

CONCLUSIONS

Z40 SRM nozzle development is an opportunity for AVIO to introduce alternative manufacturing technologies. In the present article self-protected FJ and LRI divergent designs and technological developments have been presented. Development process is ongoing at the moment. Classical solutions and technological improvements have been compared from design, technological and manufacturing point of view. Both technologies development are scheduled to be completed within march 2015 when first Z40 SRM bench test is foreseen.

REFERENCES

- [1] M. Angelone, F. Mascanzoni, C. Milana, *Technological and programmatic development of Zefiro 40 Solid Rocket Motor*, AIAA/ASME/SAE/ASEE Joint Propulsion conference and Exhibit, AIAA 2012-4213
- [2] Solid Rocket Motor nozzles, NASA SP-8115
- [3] D. Scoccimarro, P. Perugini, M. Fabrizi, *Future launch vehicle new technologies for solid propulsion*, Space Access 2011-50, 21-23 Sept. 2011, Paris, France
- [4] Hoyt Sherard, *Development of advanced flex joint technology*, AIAA/SAE 9th Propulsion conference, AIAA Paper n° 73-1262
- [5] Prins, William S., Meyer, Scott A., Cox, Paul D., *Advanced solid rocket motor nozzle thrust vector control flexseal development status*, AIAA, SAE, ASME, and ASEE, Joint Propulsion Conference and Exhibit, 28th, Nashville, TN, July 6-8, 1992. 9 p.
- [6] Donat, James R., *Solid rocket motor nozzle flexseal design sensitivity*, AIAA, AHS, and ASEE, Aerospace Design Conference, Irvine, CA, Feb. 16-19, 1993, 11 p.
- [7] Descamps C., Gautronneau E., Rousseau G., Daurat M., *P80 SRM low torque flex-seal development – thermal and chemical modeling of molding process*, Progress in Propulsion Physics 1 (2009) 141-152
- [8] WANG Chun-guang¹, SHI Hong-bin², WANG Xue-kun¹, LI Jiang¹, SHA Bao-lin¹, *Numerical analysis of deflection torque of flexible joint with high pressure*, Journal of Propulsion Technology, 2011-02
- [9] Freitas G., *High Reliability, Low-Cost RTM Preforms for Solid Rocket Motor Nozzles*, NAS08-39844
- [10] Berdoyer M., Dauchier M., Just C., *A New Ablative Material Offering Nozzle Design Breakthroughs*, 47th AIAA/ASME/SAE/ASEE Joint Propulsion Conference & Exhibit 31 July - 3 August 2011
- [11] J. Bruchon, D. Pino-Muñoz, F. Valdivieso, and S. Drapier, *Numerical and experimental analyses of resin infusion manufacturing processes of composite materials*, Journal of the American Ceramics Society, 95(8) : 2398 – 2405, 2012
- [12] Strobel, Forrest, King, Belinda, *ASRM nozzle thermal analysis*, Final Report Aerotherm Corp., Huntsville, AL.
- [13] Summerscales J., Searle T.J., *Low pressure (vacuum infusion) techniques for moulding large composite structures*, Advanced Composite Manufacturing Centre, School of Engineering, Univ. of Plymouth, Proc. IMech.E Vol219 Part I, Journal of Materials: Design and Applications
- [14] Guang-Wu Du, Frank K. Ko, *Analysis and design of 2D braided preforms for composite reinforcement*, ICCM/9 Proceedings, Composite Design, Vol. IV, pag.532-540

Zefiro 40 SRM Nozzle

Development and Innovations

Renato Marocco



SUMMARY

- **Zefiro 40 Program objectives**
- **VEGA perspective configurations**
- **Zefiro 40 nozzle**
- **Self protected FJ design and technologies**
- **LRI divergent design and technologies**
- **Zefiro 40 Program Macro-planning**

Zefiro 40 program objectives

Zefiro 40 SRM is conceived as the future second stage of VEGA E launcher.

The Z40 development is performed introducing innovative technological aspects useful for the new generation of SRM.

In particular the aim is to develop and qualify on a full scale prototype new technologies and materials for the development of a SRM with improved performance and reduced inert masses and recurring costs

The technologies, materials and processes developed in the frame of the Zefiro 40 Program have the following potential returns:

- ***Development of a new first stage (P120) for the Vega Consolidated Launcher (VEGA C)***
- ***New filament wounded cases for Large sizing SRM/SRB for applications on future Ariane 6***

VEGA perspective configurations

VEGA Consolidated (VEGA C) launcher vs actual VEGA:

- **P120 SRM as first stage instead of P80 SRM**

The VEGA Evolution (VEGA E) Launcher vs VEGA C:

- **Zefiro 40 as second stage alternative to Zefiro 23;**
- **cryogenic upperstage (MYRA) instead of Z9 + AVUM**

In analogy to P80 SRM Development, the Zefiro 40 Program originally born as Technology Demonstrator for innovative materials (propellant, ultra-light thermal protections), technologies and process (carbon fibers pre-preg, etc.) could evolve in the development of innovative SRM/SRB.



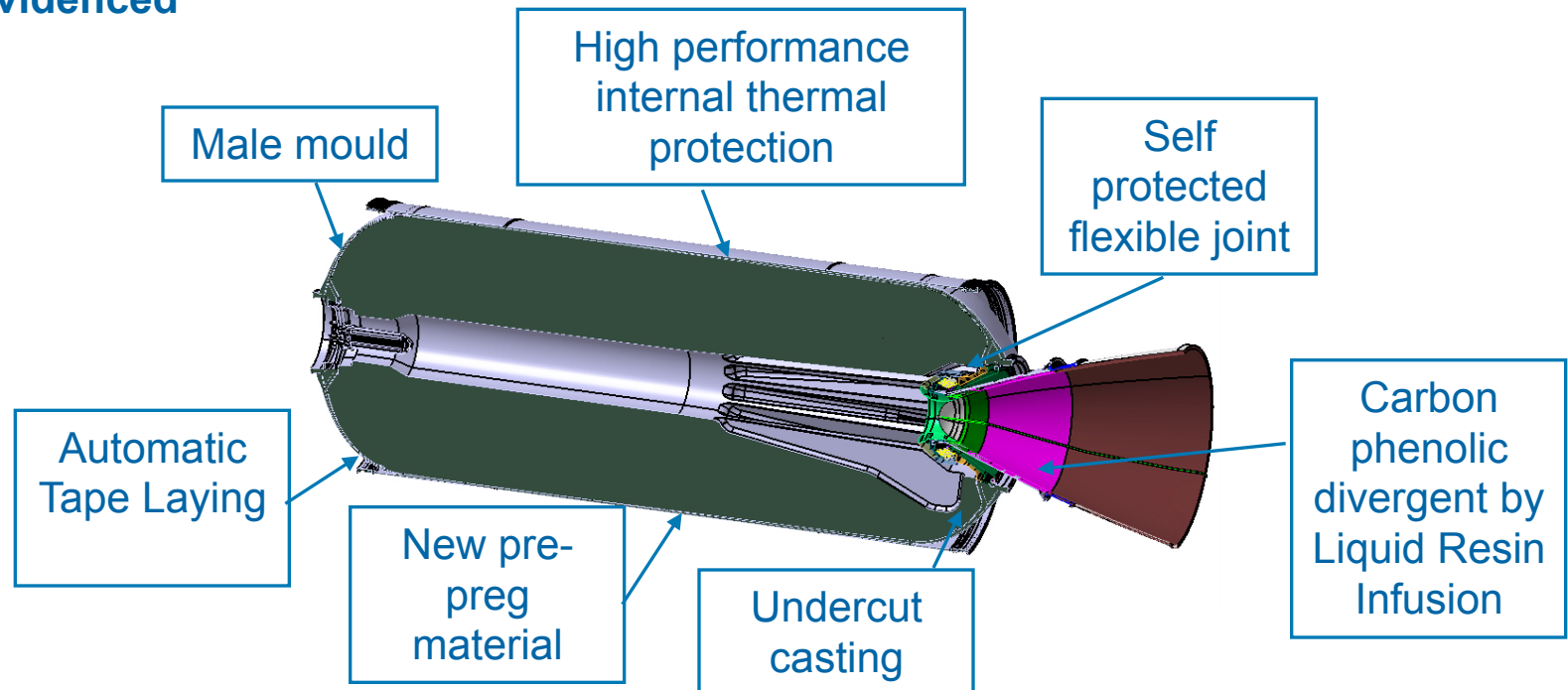
Z40

Z40 SRM

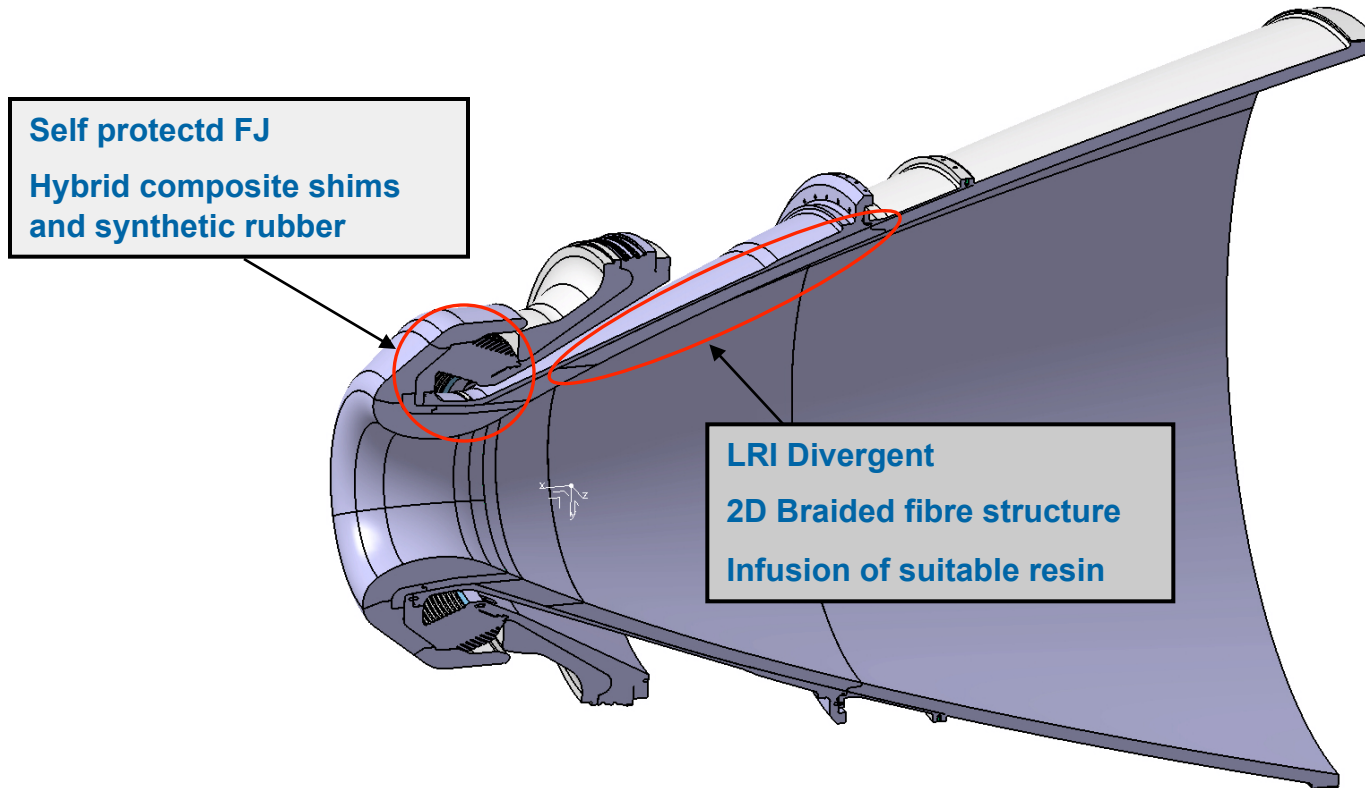
Development of new manufacturing technologies and processes are aimed to:

- cost reduction
- performance improvements
- materials supplier policy problems solution

The figure shows a sketch of Z40 SRM in which the new technologies/materials are evidenced



Z40 SRM Nozzle



- Throat diameter ~ 300 mm
- Expansion ratio ~ 37
- MEOP ~ 110 bar
- Combustion time ~ 100 sec

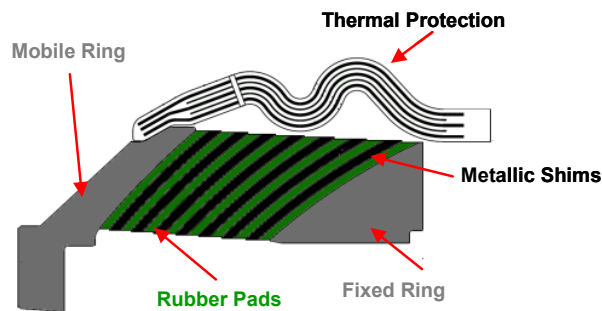
- Biggest nozzle manufactured by AVIO
- Few components design
- Low stiffness self protected FJ
- LRI on braided divergent

Z40 SRM Nozzle – Flexible Joint

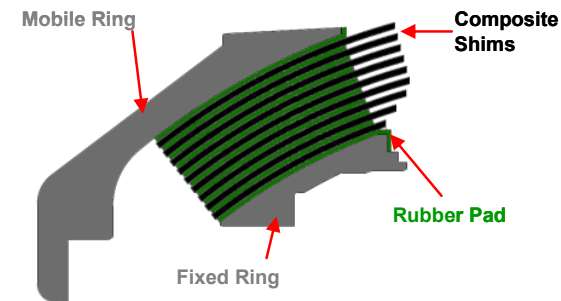
- The self protected FJ is produced with synthetic rubber layers and spherical composite shims needed to act as structural reinforcements and thermal protection.
- Stringent FJ stiffness requirements led to adopt pad thickening and cone angle
- Instability at high pressure --> stiff shims manufactured by hybrid carbon-glass epoxy composite

Technological challenges of :

- Hybrid composite shims (allow to strongly reduce FJ mass: composite vs metal, no further thermal protections)
- Synthetic rubber (more stable properties than natural, low stiffness)
- Self protected FJ manufacturing: transfer molding process is baseline, hot/cold components bonding is backup solution



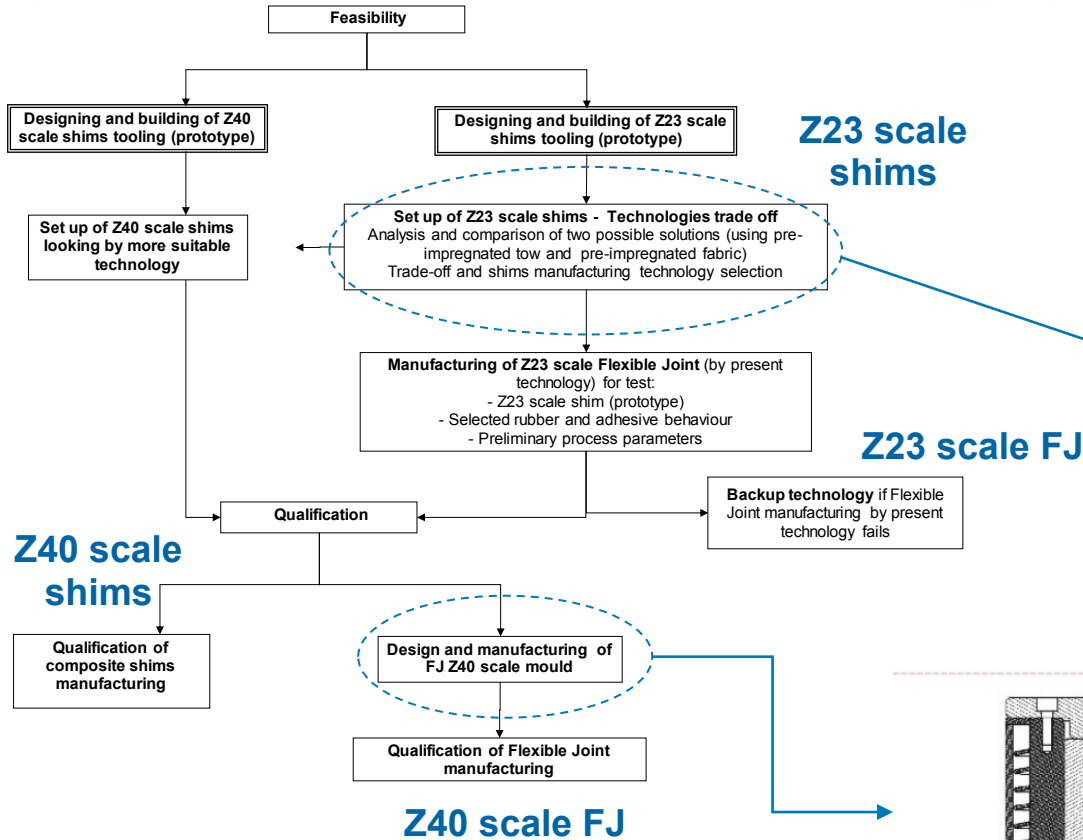
CLASSICAL PROTECTED FLEXIBLE JOINT



SELF-PROTECTED FLEXIBLE JOINT

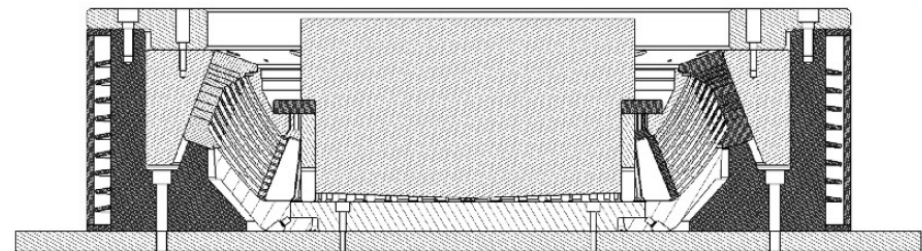
Z40 SRM Nozzle FJ Technological Development Plan

SELF PROTECTED FJ MAIN ACTIVITIES FLOWCHART



Z23 scale shims

Z23 scale FJ



Design phase for FJ Z40 mould (LLI)

In scale test bomb hosting a FJ mockup simulator is in design phase

Z40 SRM Nozzle - LRI Divergent

- AVIO present technology for the carbon phenolic divergent manufacturing consist in
 - winding tapes of composite pre-preg material (carbon phenolic) on a suitable mandrel
 - application of vacuum bag
 - hydroclave cycle
 - final machining to obtain the final piece

In order to minimize defects occurring divergent manufacturing (especially wrinkles), the technology of Liquid Resin Infusion will be applied for the production of this components.

This technology will be implemented in the following three main steps:

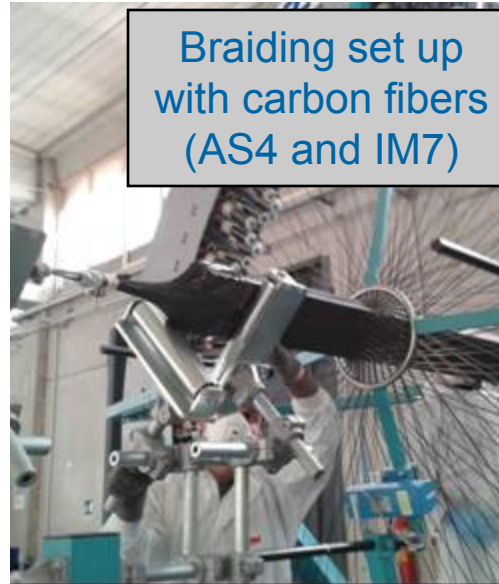
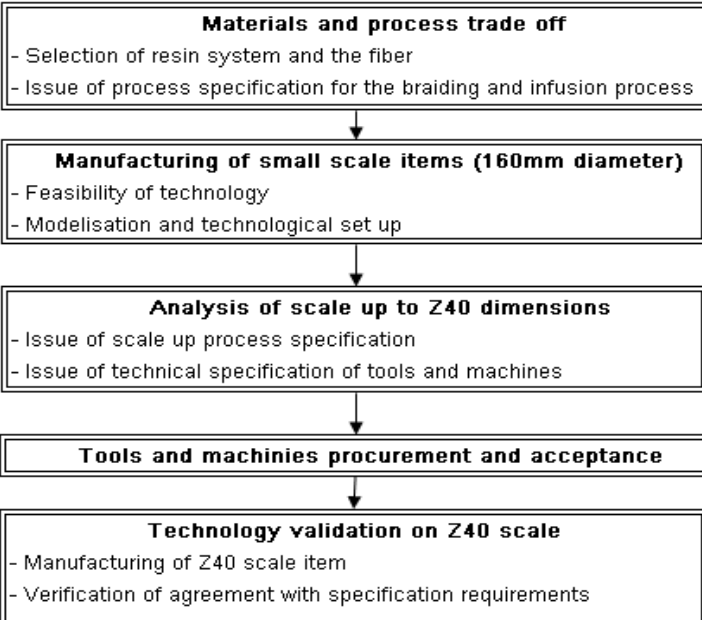
1. lay-up of pre-formed fibers structure on conical mandrel (braiding process)
2. impregnation of the preform with a suitable resin under a vacuum bag set-up (infusion process);
3. curing of impregnated preform.



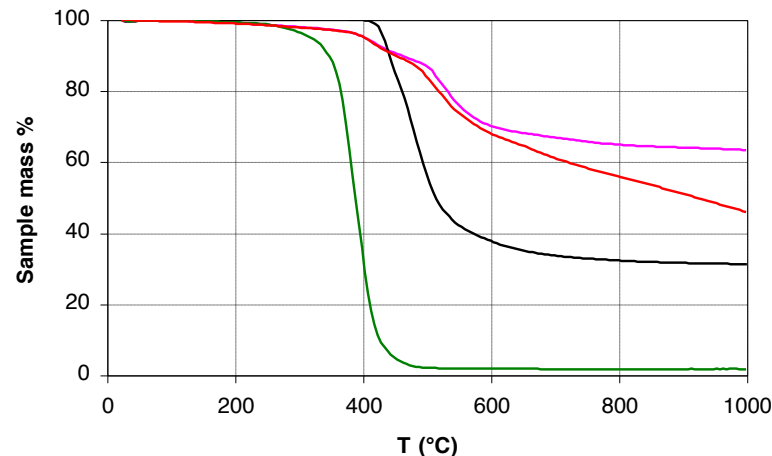
At the moment this process is in development phase in collaboration with external aeronautical company and University of Naples

Z40 SRM Nozzle LRI Divergent Technological Development Plan

LRI DIVERGENT MAIN ACTIVITIES



At the moment infusion tests are ongoing.
Process simulation has been setup.
Cover factor vs braing angle on conical geometries is under study



Phenolic, Epoxy, Hybrid epoxy-phenolic and BMI resins subjected to trade off tests

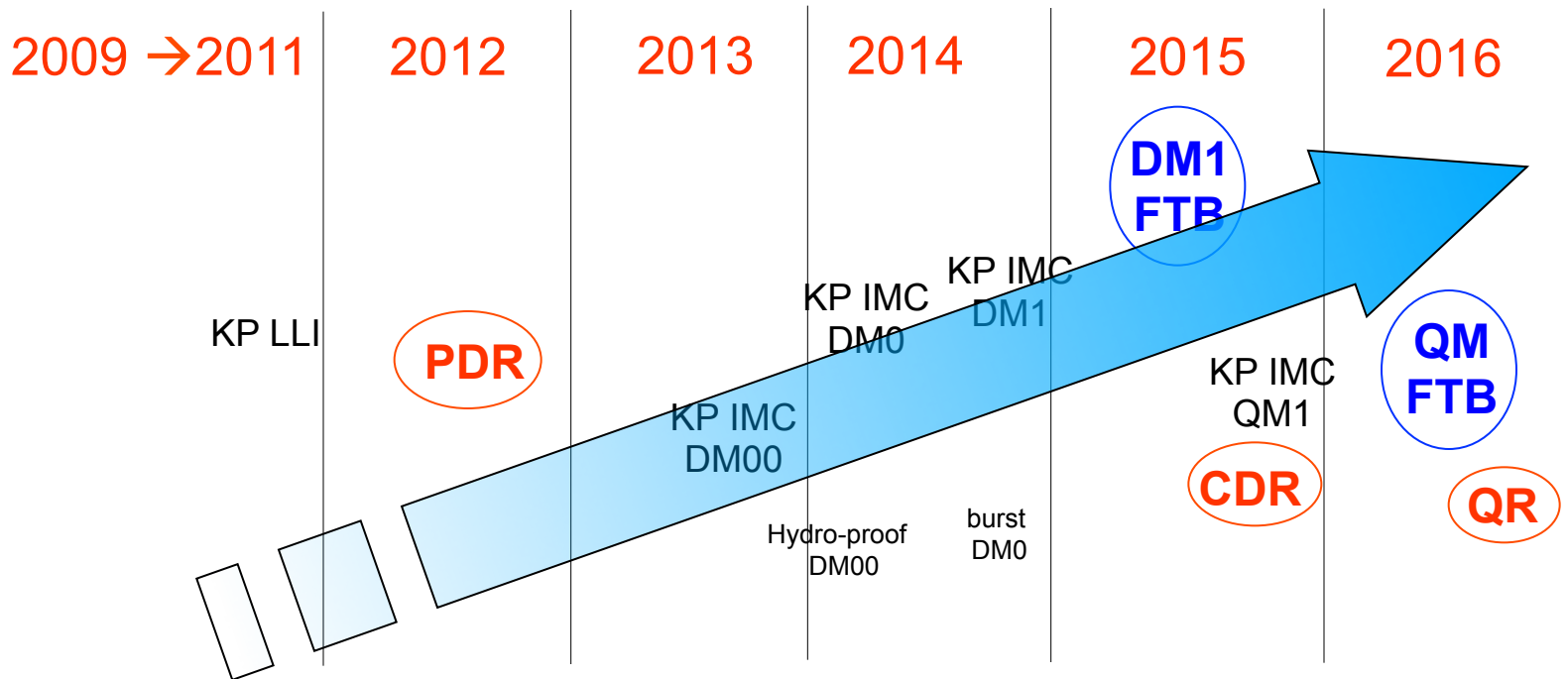
Zefiro 40 Program macro-Planning

Zefiro 40 Program start: 2009

Preliminary design up to LLI definition: December 2011 (mandrel, forgings, etc.)

Materials trade-off completion (selection of propellant, carbon fibers and nozzles materials): June 2012

PDR: September 2012



THANKS



ESA TPS WORKSHOP – 7th edition

An insight into EXOMARS EDM HS development

ASTRIUM // 2013-04-08

*Yann Mignot **, *Cédric Plaindoux **, *Christophe Balemboy **, *Emilie Boulier **, *G. Pinaud **, *Michel Boquet **, *Roberto Velasco ***, *Yolanda Camacho ***, *Carlos Samartin ***

* ASTRIUM Space Transportation - BP 20011, 33 165 Saint-Médard_en-Jalles Cedex, France

Email: yann.mignot@astrium.eads.net

** ASTRIUM CASA Espacio - Avenida de Aragon, Madrid, Spain

Email: roberto.velasco@astrium.eads.net

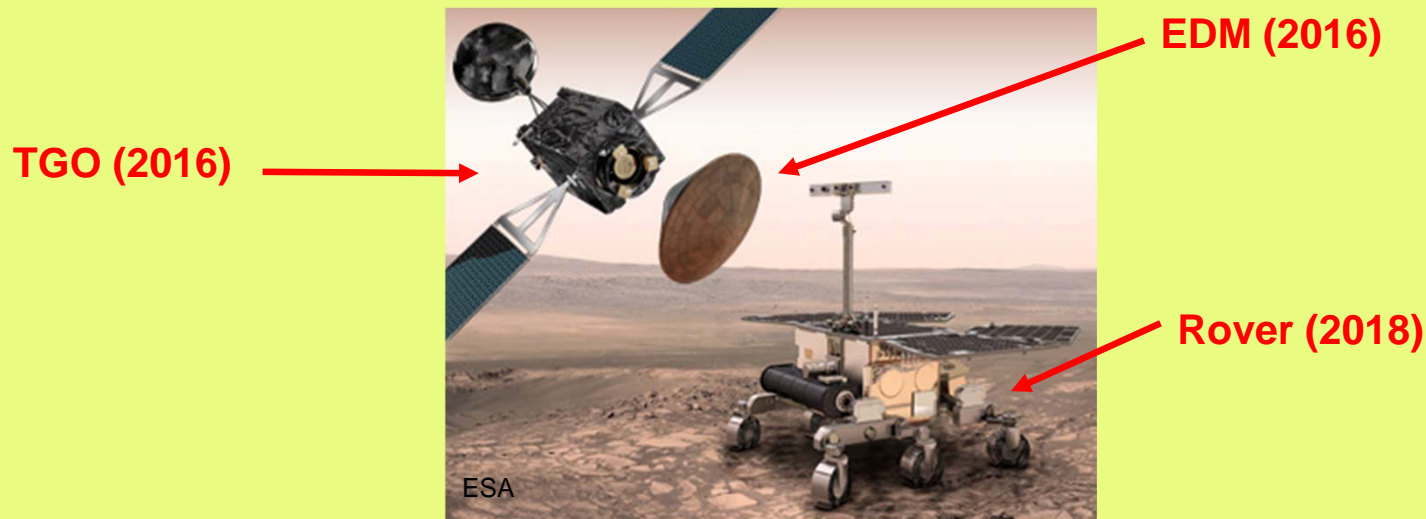
All the space you need



EXOMARS MISSIONS OVERVIEW

14/03/2013 : signature by ESA and ROSCOSMOS of a comprehensive agreement for 2 EXOMARS missions

- **launcher for both missions : PROTON**
- **2016 mission with ESA lead :**
Trace Gaz Orbiter (TGO)
& Entry & Descent Demonstrator Module (EDM)
- **2018 mission with ROSCOSMOS lead:**
Russian Entry & Descent Module & ESA rover



EXOMARS OBJECTIVES :

1- **Exobiology** : searching for signs of life whether past or present:

- TGO will search for gas in the atmosphere like methane that could indeed be signatures of biological processes
- The rover will be the main asset, notably with its drilling device capable of going down to a 2m depth

2- **Technology demonstration** : the EDM will land on Mars to prove key entry, descent and landing technologies

3- **Deployment on Martian soil of an environmental and meteorological unit** : DREAMS (Dust Characterization, Risk Assessment, and Environment Analyzer on Martian Surface)



EXOMARS HS

EXOMARS Frontshield

- 2.4m in diameter
- ~80kg
- first frequencies above 100Hz
- 7.8t pressure during Entry
- [-110°C;+180°C] temperature range for the Frontshield Structure (FSS)
- [-110°C;1750°C] temperature range for the TP
- 90 tiles, 7 types of tiles
- Outgassed Norcoat Liège TP bonded with ESP495 silicone glue
- Bioseal/Heatseal
- flight instrumentation : 7 thermoplugs, 4 pressure sensors, 7 thermistors



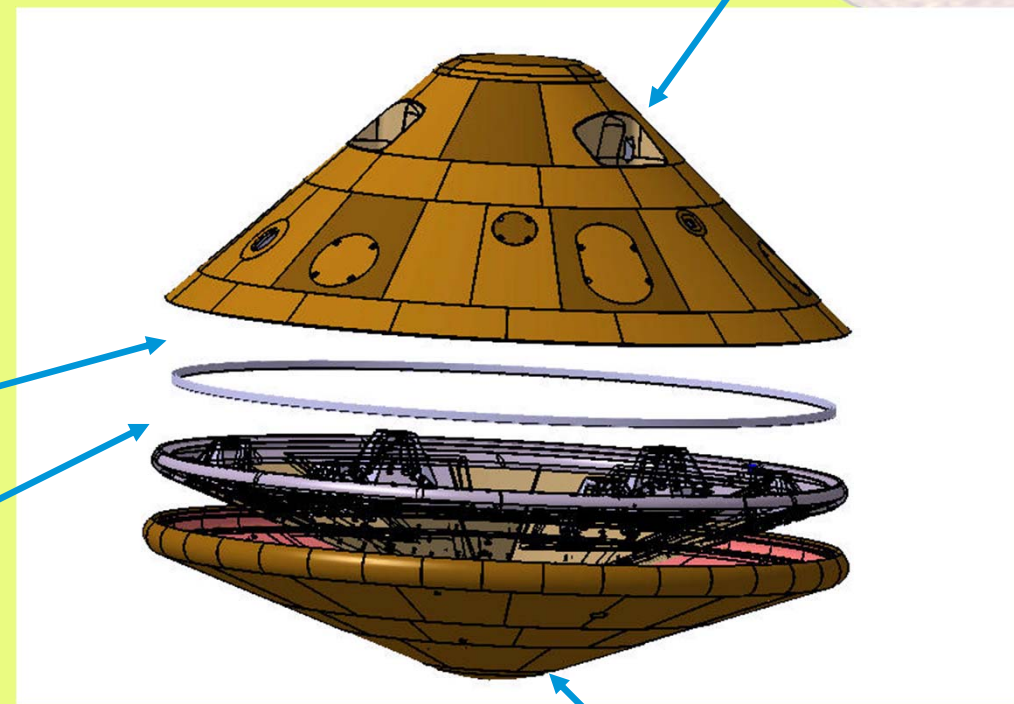
EXOMARS Backshield (=BCV TPS + flight instrumentation)

- ~20kg
- 93 tiles, 12 types of tiles, 3 thermoplugs, 3 thermistors
- Outgassed Norcoat Liège TPS + N4011 (antenna) bonded with ESP495 silicone glue
- [-110°C;710°C] temperature range

Backshield

Bioseal /
heatseal

FSS



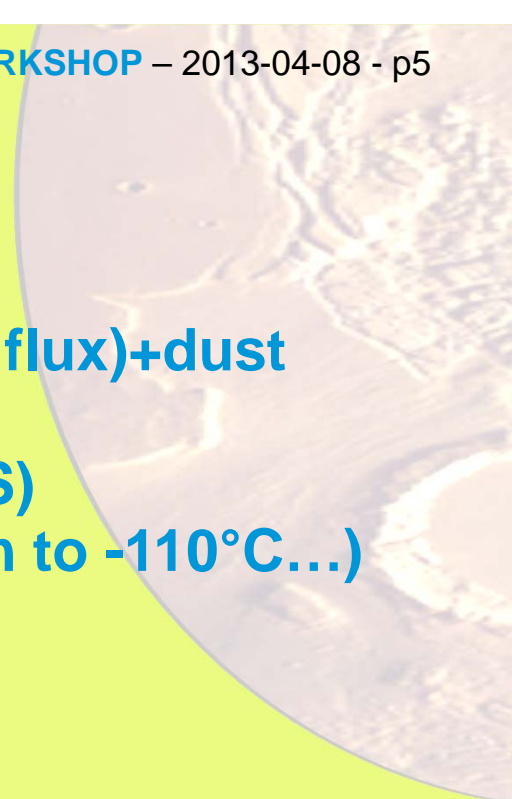
Frontshield TPS

Stringent requirements to match:

- Mass
- stiffness
- Aerothermal Entry environment (1800 KW/m² heat flux)+dust erosion
- Mechanical Entry environment (~8t applying on FS)
- Space Environment (irradiation, temperature down to -110°C...)
- Planetary Protection constraints

→as a consequence, EXOMARS HS development characterized by :

- a high level of interactions between design, justification & test activities
- a high attention paid to FS structure and TPS mass management
- dedicated test and design activities to address ageing and PP aspects
- a significant aerothermal qualification campaign



Strong interactions between design & test activities

Thermal characterization & Aerothermal tests

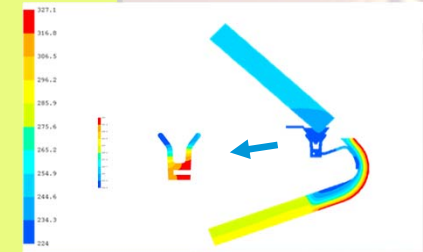


Mechanical tests



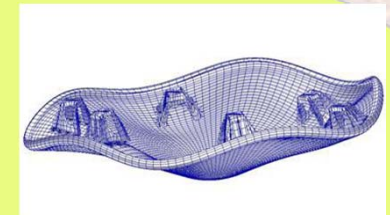
HS Requirements

Thermal design & justification analyses

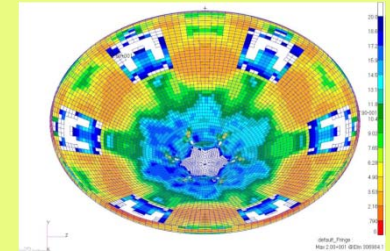


Structural design & justification analyses

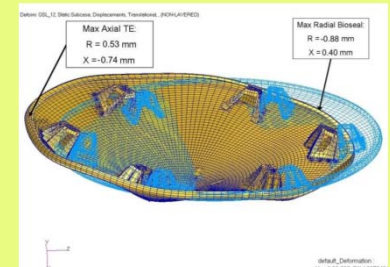
Frequency analyses



Strength analyses



Static stiffness analyses



Taking into account ageing

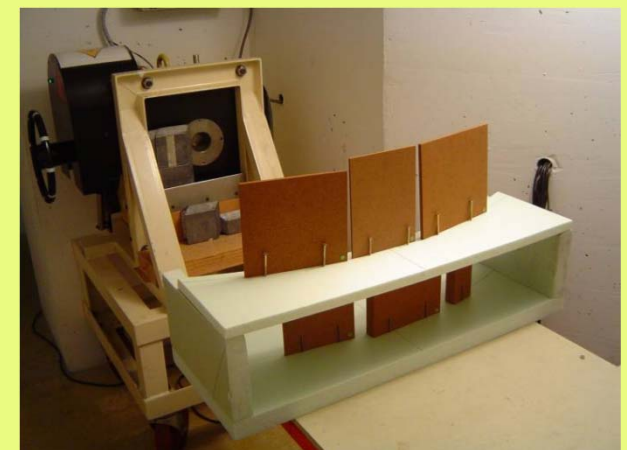
Specimens (for characterization or qualification) are undergoing an extensive ageing :



Fast depressurization tests



Thermal cycling tests
[-110°C; +80°C]

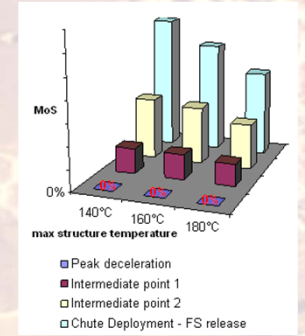


Irradiation



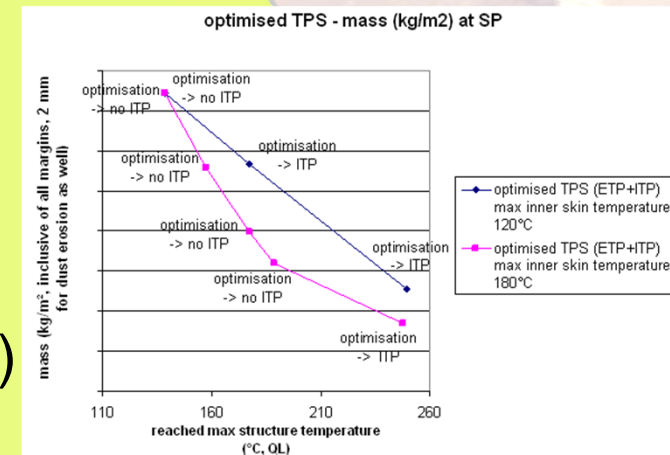
Matching stringent mass requirements : 1- FSS mass

A fruitful management of mass has been achieved through:



1- Relevant decisions early in the project
 AST SPACE TRANSPORTATION “structure temperature trade-off” in 2009 concluded (in the specific case of EXM) on:

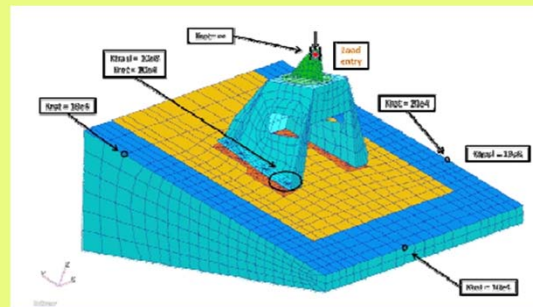
- the compatibility of a standard “cold structure” (epoxy) with a max 180°C structure temperature during Entry
- a relatively low mass gain to be expected with a FS with a “hot structure” (BMI,...) compared to the induced risks (low TRL&IRL& tight schedule)



2- ASTRIUM CASA ESPACIO design & justification supported by an extensive characterization campaign



Shear failure on M40J/M18 MD specimens at 180°C



IF test correlation



Insert specimens before compression test at 130°C

Matching stringent mass requirements : 2- TPS mass

Early in the project, considering the strong pressure on mass, 2 important decisions were taken by AST-ST wrt TPS:

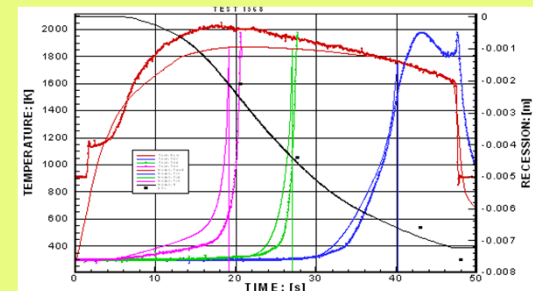
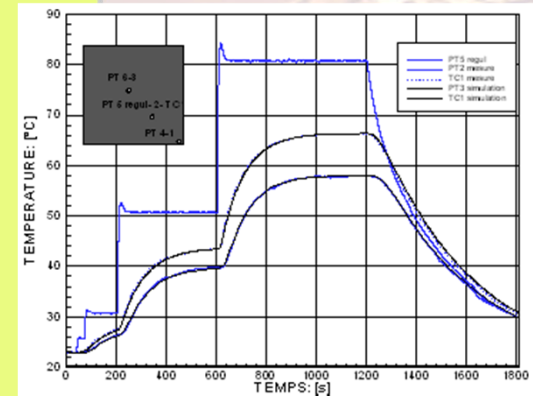
- **Evolutionary TPS thickness on the FS**
- **Deep revisiting of outgassed NL thermal mathematical model for Entry (and not a simple adjustment)**

Via:

- a re-characterization of virgin materials conductivity and thermal capacity (hot guarded plates, diffusivity by flash method, inverse methods) + TGA measurements
- an extensive analysis of several Plasma tests for both FS (high heat flux: $2\text{MW/m}^2 \pm 10\%$) and BCV (low heat flux: $70\text{-}120\text{ KW/m}^2$)

A significant enhancement has been achieved:

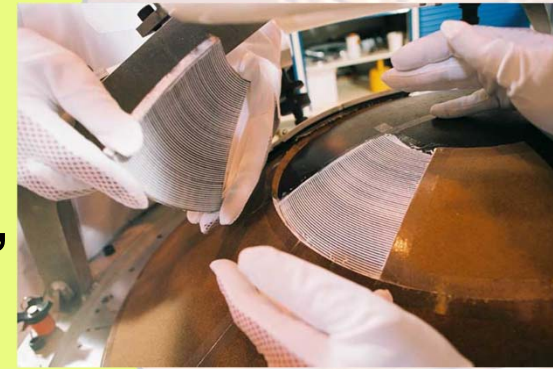
- Introducing a 2-step-Arrhenius law
- Discriminating between chemical recession and mechanical recession



→ **Recent assessment at iso Requirements : TPS mass gain : 8-9%**

PP constraints – impact on HS development

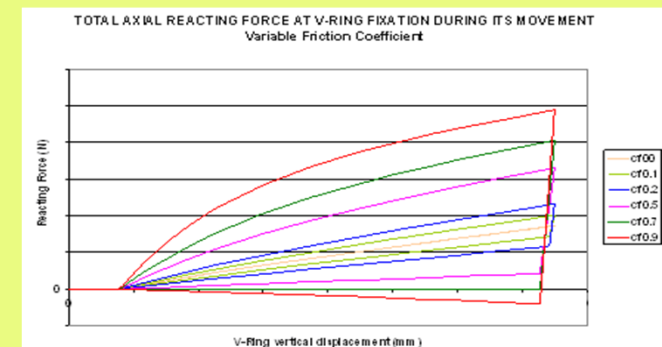
Before being a significant constraint for MAIT teams, PP has deep implications in HS development



- The final Dry Heat Microbial Reduction cycle (125°C – 30 hours) implies a pre-treatment for all tested specimens : mechanical, thermal and aerothermal specimens
- Once assembled in class 10000 after the separate sterilization of all subassemblies, the bioseal/heatseal between the Frontshield and the BCV has to fulfill a major role : contributing in the non contamination of the inner EDM.

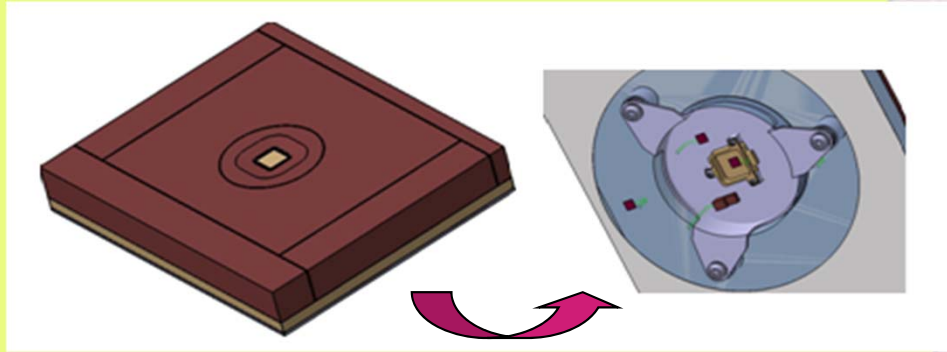
The development of the Bioseal/Heatseal is a challenging one considering the antagonist requirements to match :

- providing a sufficient tightness on ground & during Entry
- not preventing FS jettisoning



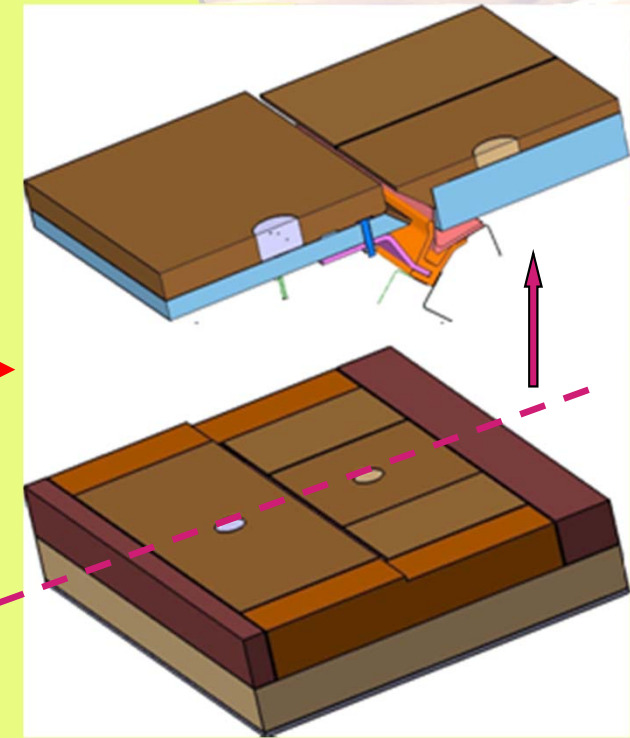
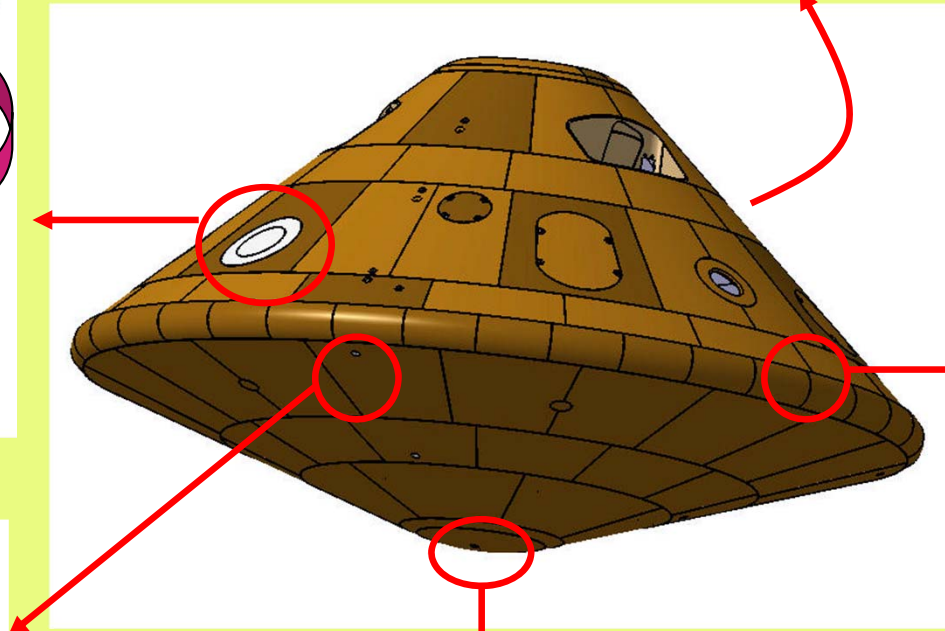
transient mechanical FE analysis
of loads at Bioseal IF during
FS/BCV separation

TPS AEROTHERMAL QUALIFICATION



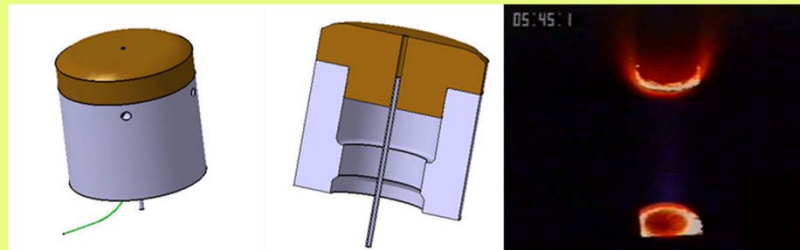
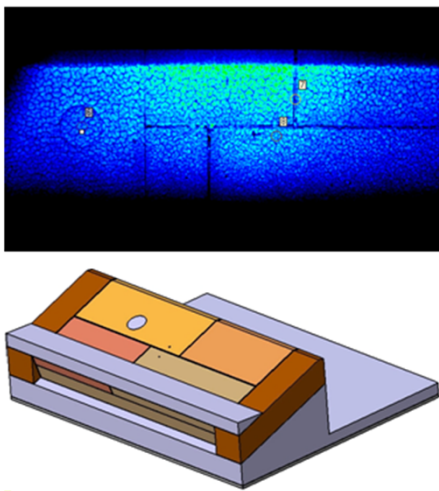
BCV Sun Sensor specimen (**)

BCV antenna specimen (**)



FS/BCV IF specimen (**)

2 FS specimen (**)



2 stagnation point specimens (*)

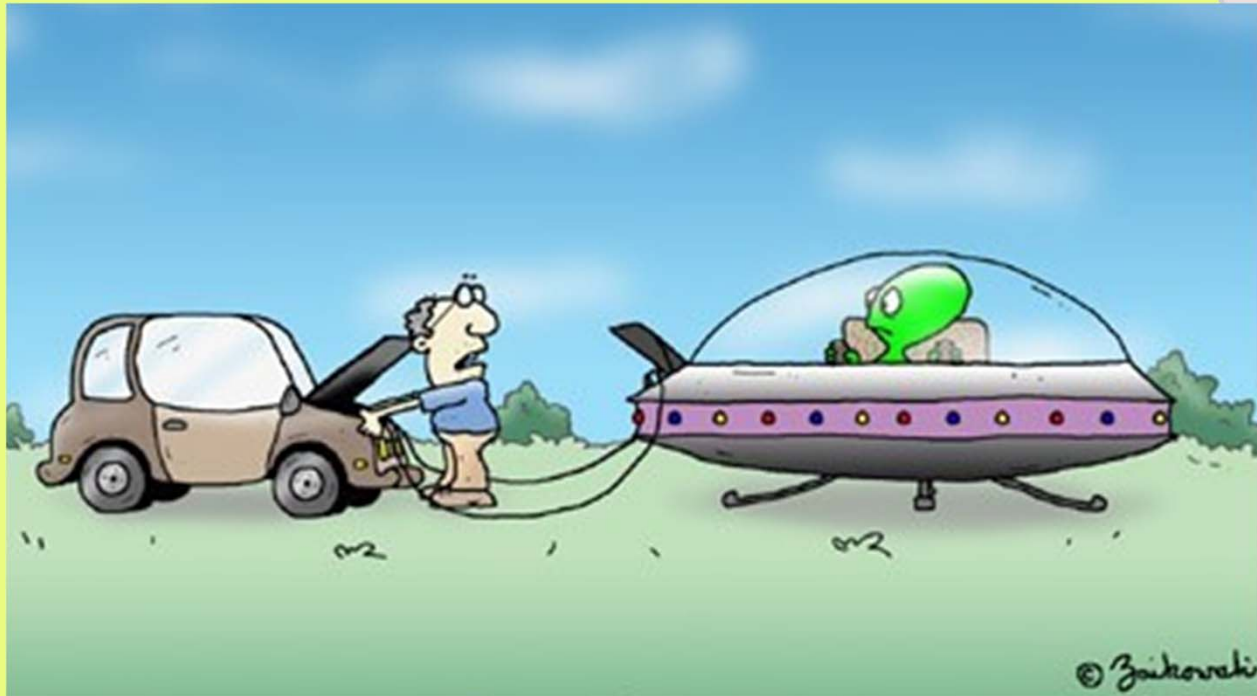
- (*) Comète subsonic inductive plasma test
- (**) Simoun supersonic arcjet plasma test

CONCLUSION : status on HS activities

- **FSS CDR passed successfully in December 2012, PFM FSS ready for sine acceptance tests before delivery to AST-ST in Bordeaux**
- **HS development quasi completed – CDR before summer 2013**
- **HS CoG of activities is moving surely towards TPS MAIT activities :**
 - **Mid-May to end of summer : bonding tool and procedure validation on full scale FSS and BCV models**
 - **September-February 2014 : PFM HS activities**



**FSS mockup unpacking in
AST-ST cleanroom in Bordeaux**



Questions welcome



Testing of DLR C/C-SiC for HIFiRE 8 Scramjet Combustor

David E. Glass and Diego P. Capriotti
NASA Langley Research Center
Hampton, VA USA

Thomas Reimer and Marius Kütemeyer
German Aerospace Center
Stuttgart, Germany

and

Michael Smart
University of Queensland
Brisbane, Australia

Outline



◆ Introduction

- HiFIRE 8
- DCR

◆ Test

◆ Post-test SEM investigations

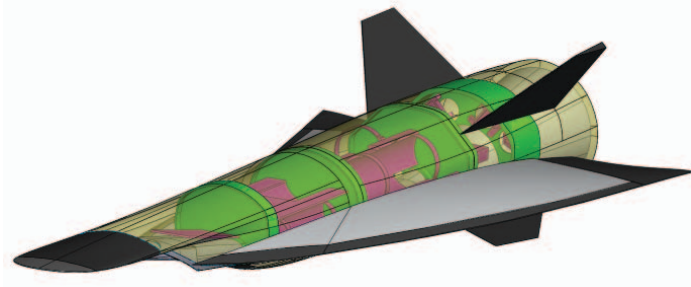
◆ Concluding remarks

HIFiRE Program



“The main goal of the HIFiRE Program is to develop the technology for sustained flight at Mach 8”

- Jointly run by DSTO and the US Air Force
- Sounding rocket based launch
- 9 flights over 5 years (first flight was in March 2009 – HIFiRE 0)
- Combination of fundamental hypersonic flow experiments and scramjet flights
- *Culminating in a sustained flight (30 second engine operation) of an autonomous vehicle - HIFiRE 8.*

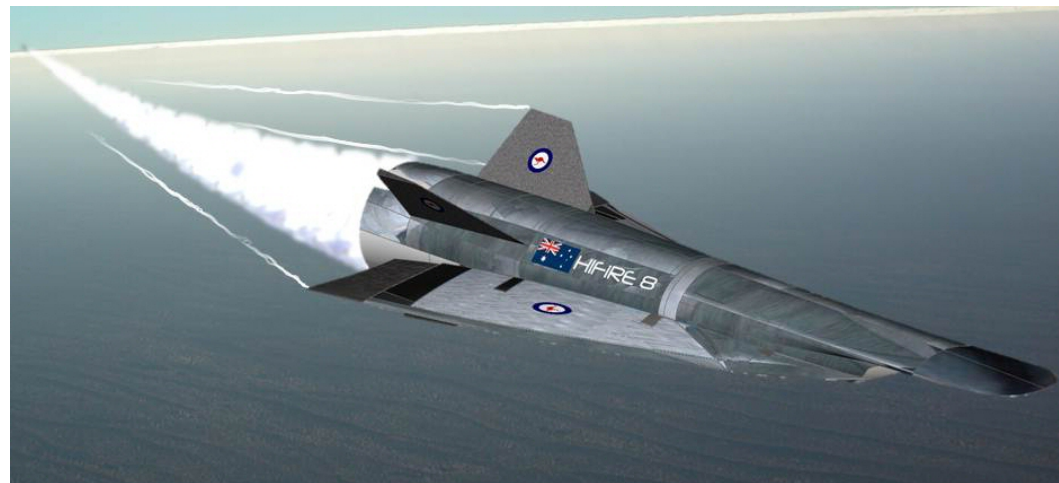


HIFiRE 8



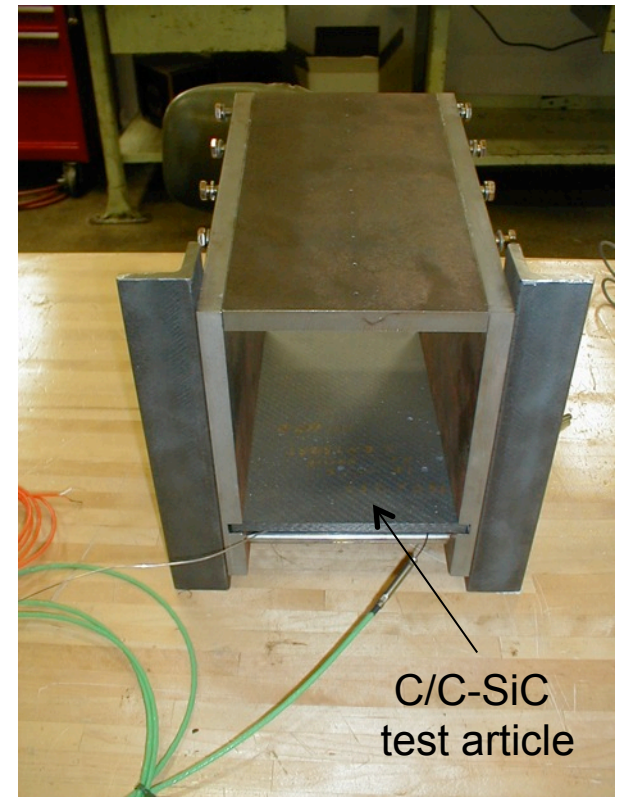
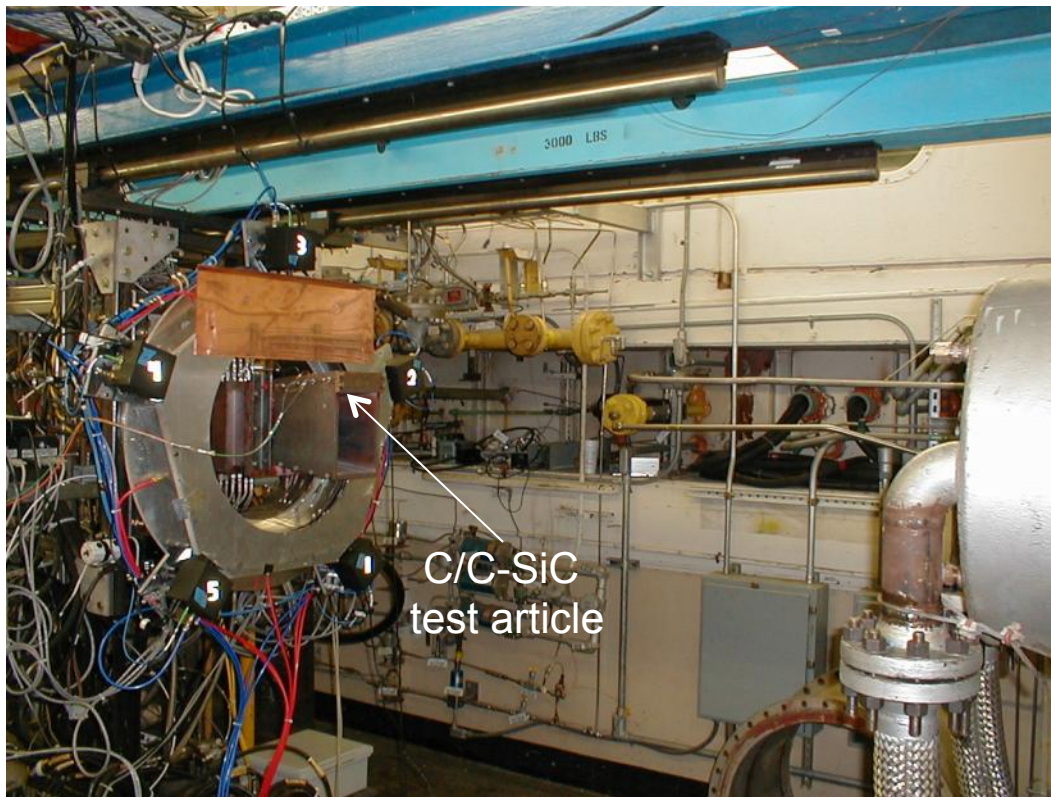
Motivation for CMC Panel Test

- HIFiRE 8 Objective is to demonstrate 30 seconds of horizontal scramjet powered flight at Mach 7 and 1000 psf (55 kPa) dynamic pressure.
- Desire to avoid the complexity, weight, and cost of an actively cooled combustor.
- Decision made to examine the possibility of un-cooled CMC combustor.
- DLR C/C-SiC fins flying on other HIFiRE flights.
- *Decided to evaluate the performance of the DLR C/C-SiC (also C/C) at scramjet combustor conditions.*



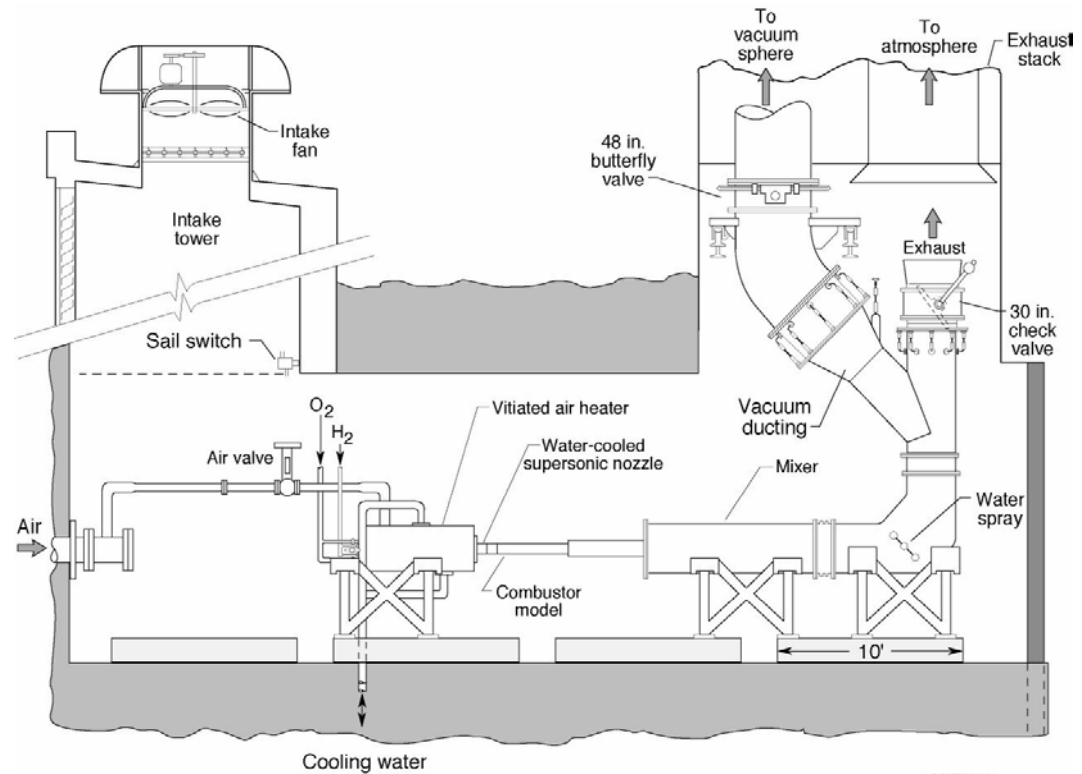
Durable Combustor Rig (DCR)

- ◆ **Simulated Mach 6 conditions**
 - Actual flow velocity ~ Mach 2
- ◆ **$q = 1000$ psf (479 hPa)**
- ◆ **$H = 793$ Btu/lb (1.846 MJ/kg)**
- ◆ **Hydrogen fuel**



Direct Connect Supersonic Combustion Test Facility (DCSCTF)

- ◆ Simple, older facility used for basic testing of scramjet combustors
 - Mixing of a combusting fuel stream with the hot test gas
- ◆ H_2 /Air/ O_2 combustion heated, wet (contains water) test gas
- ◆ $M_\infty = 3.5$ to 7.5 by varying H_2 /Air/ O_2
- ◆ Match total enthalpy, test gas O_2 content, $P_{isolator}$
- ◆ 16 x 16 x 52-foot ventilated test cell (4.87 x 4.87 x 15.85 m)



Simulated Flight Mach Number (at 1000 psf 478 hPa)	Facility Total Pressure (psia)	Facility Total Temperature ($^{\circ}$ R)	Facility Total Enthalpy (BTU/lb _m)	Facility Nozzle Exit Mach number	Facility Nozzle Exit Pressure (psia)	Facility Mass Flow Rate (lb _m /s)	Test gas water mole fraction
5	94.8 (6.53 bar)	2103 (895 $^{\circ}$ C)	574 (1.34 MJ/kg)	2.12	10.0 (690 hPa)	8.08 (3.7 kg/s)	12.7
6	91.4 (6.3 bar)	2721 (1238 $^{\circ}$ C)	793 (1.85 MJ/kg)	2.10	10.0 (690 hPa)	6.73 (3.1 kg/s)	18.5

Outline

◆ Introduction



◆ Test

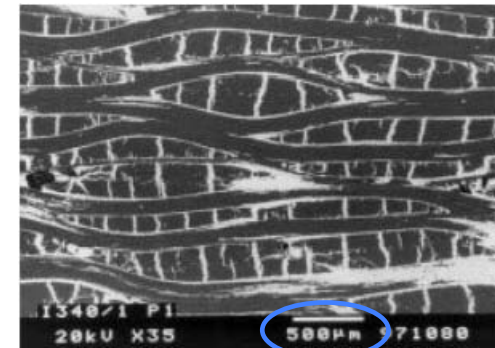
◆ Post-test SEM investigations

◆ Concluding remarks

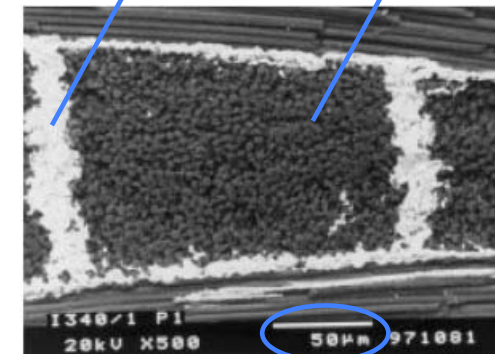
DLR C/C-SiC

◆ Under development since the 1980's

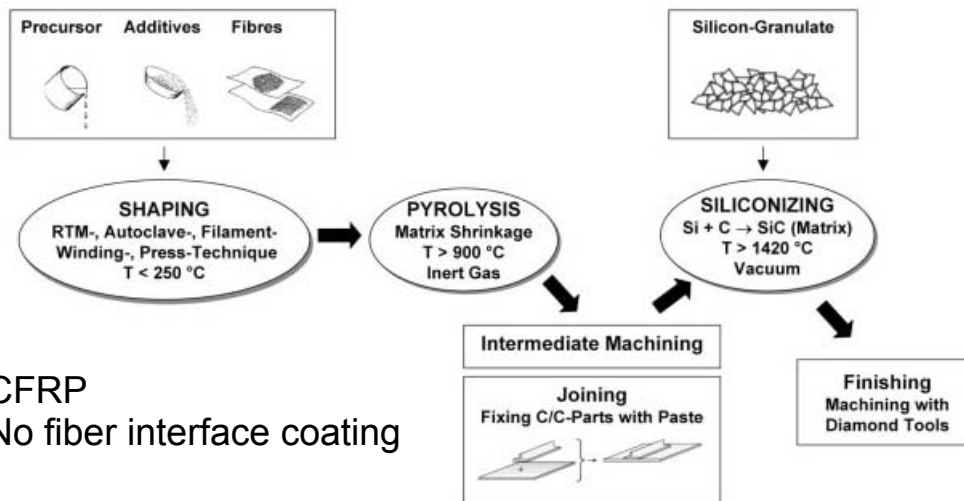
HYTEX	National hypersonic technology program. Development of a C/C-SiC intake ramp
CETEX	Manufacture of a C/C-SiC thermal protection system for the reentry capsule Express
Hot structures	Technology program for the development of joining technologies for fibre reinforced ceramics
FESTIP	Development of a C/C-SiC thermal protection system for a single-stage space vehicle
TETRA	Development of a thermally extremely loaded ($T_{max} = 3272^{\circ}\text{F}$, 1800°C) C/C-SiC nose cap for the NASA experimental space craft X-38
FOTON	Development and reentry test of a new concept of a C/C-SiC thermal protection system for spacecraft
SHEFEX	Development of an extremely loaded ($T_{max} = 3452^{\circ}\text{F}$, 1900°C), cost efficient thermal protection system on the basis of flat C/C-SiC panels
EXPERT	Development of a C/C-SiC nose cap (current project)



SiC matrix C fibers



SEM of 3002°F (1650°C) heat treatment C/C-SiC



- CFRP
- No fiber interface coating

LSI (liquid silicon infiltration) process for C/C-SiC

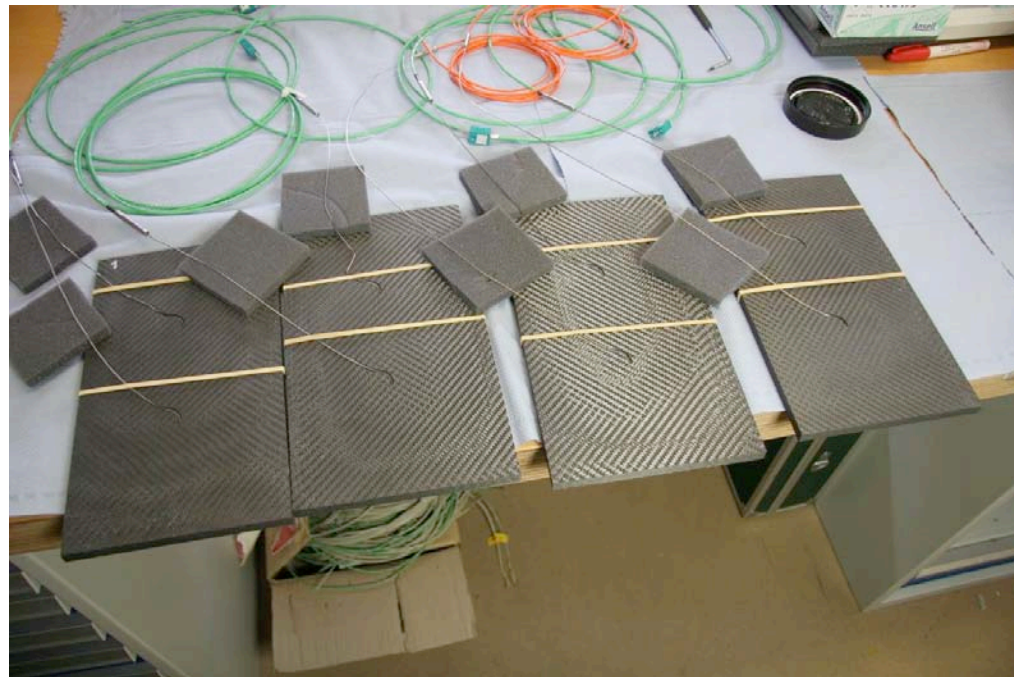
Dieter Jacob, editor, et al., "Basic Research and Technologies for Two-Stage-To-Orbit Vehicles", Final Report of the Collaborative Research Centres 253, 255, and 259, Wiley-VCH Verlag GmbH & Co. KGaA, 2005.

Test Panels

- ◆ Size: 254 mm x 145 mm x 8 mm
- ◆ Mass: ~ 550 g
- ◆ Instrumentation
 - Embedded TC's
 - 2 mm below the cool surface (6 mm below hot surface)

???	???	???	???
?	?	?	???
?	?	?	???
?	?	?	???
?	?	?	???

Not tested



Test Matrix

Panel	Run No.	Simulated Flight Mach No.	Temperature at end of Test, °R		P ₀ [psia]	T ₀ [°R]	ER (ramp + film)	ER (S3)	Fuel-on Time [sec]	Total Test Duration [sec]
			Type K	Type S						
C/C HP635-7	68	5	859	858	96.1	2131			n/a	20
	69	5	1507	1450	96.1	2117	0.556		35	40
	70	5	1611	1548	95.9	2130	0.741		35	40
	71	6	1002	1031	89.4	2546			n/a	20
	72	6	1878	1796	91.8	2611	0.986		40	45
	73	6	1026	1015	88.8	2558			n/a	20
	74	6	1987	1800	91.6	2594	1.003		39	44
	75	6	2051	1835	90.8	2626	1.023		39	44
C/C-SiC #4	52	5	1005	972	92	1939			n/a	20
	53	5	1248	1193	91.6	1957			n/a	40
	54	5	997	971	91.8	1989			n/a	20
	55	5	1214	1329	92.6	2020	0.53		14	20
	56	5	1044	1062	94.2	2035			n/a	20
	57	5	1737	1834	94.5	2070	0.58		32.5	38.5
	58	5	1076	1087	94.2	2070			n/a	20
	59	5	1319	1421	93.7	2073	0.53	0.36	13/5*	20
	60	5	1010	999	94.6	2059			n/a	20
	61	5	2126	2142	95.3	2063	0.52	0.32	29.5/19.5*	39.5
C/C-SiC #3	62	6	1281	1291	90.6	2624			n/a	20
	63	6	1295	1319	90.7	2647			n/a	20
	64	6	2025	2206	90.6	2648	1.01		30	40
C/C-SiC #1	76	6	1382	1317	89.6	2591			n/a	20
	77	6	2352	2515	91.9	2599	1.009		39	44
	78	6	2342	2504	91.2	2639	1.039		39.5	44.5
	79	6	2336	2462	91.9	2654	1.047		39.5	44.5

C/C-SiC Panel #1, Tests 76-79

◆ Insulation added to back surface to increase hot-surface temperature

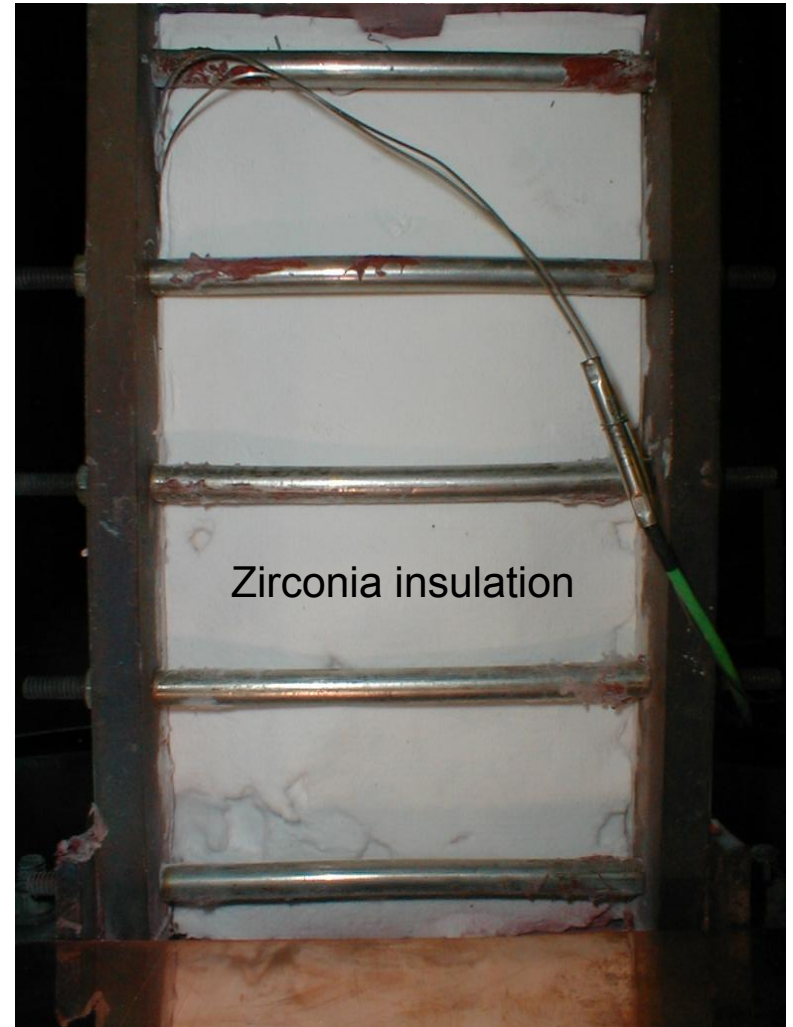
- Zirconia felt, type ZYF-100, 4 layers, 0.1" each
- ~350°F higher TC reading than with no insulation
- No significant erosion from the 3 fueled tests (3 x 44 sec)

◆ Mach 6

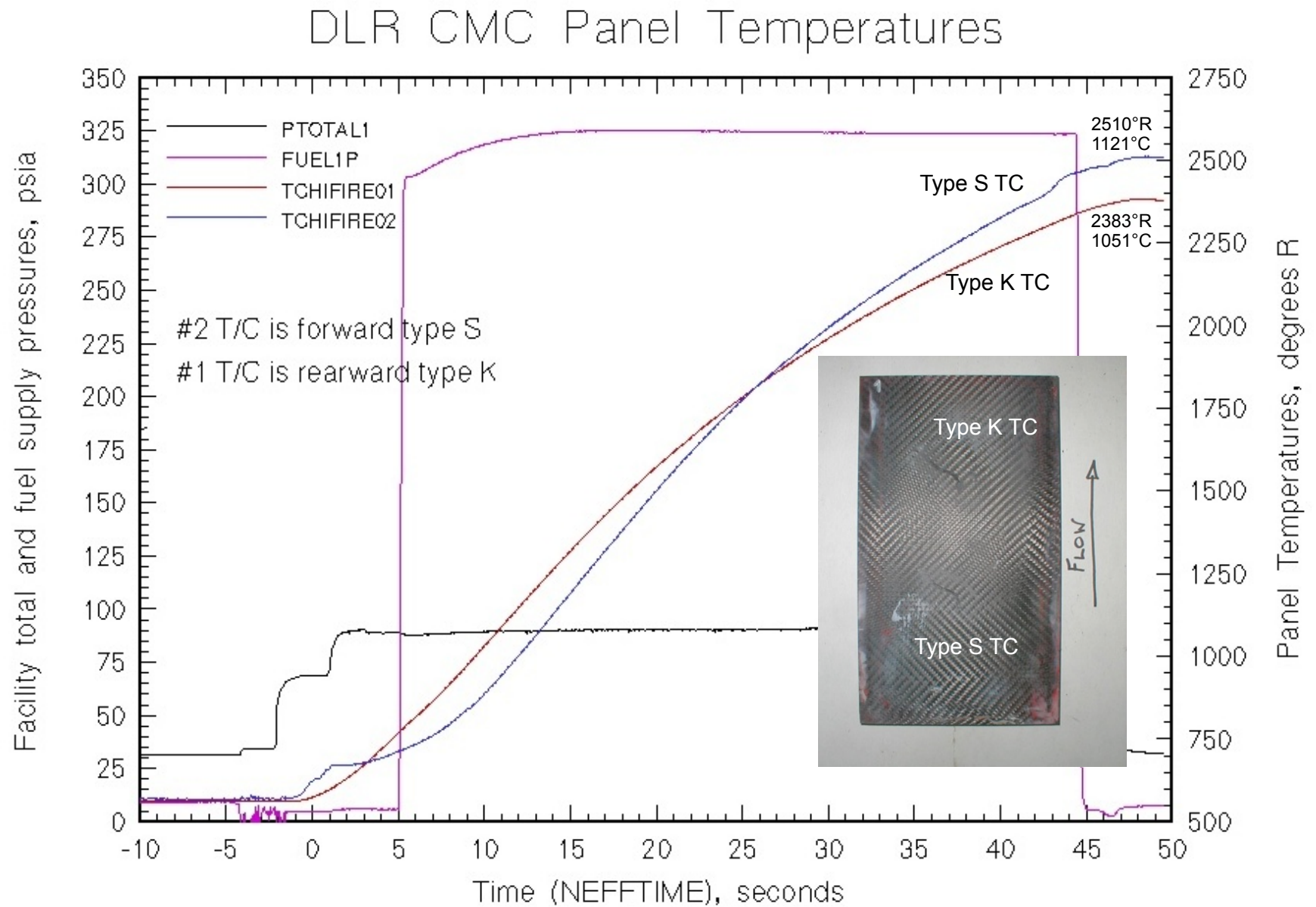
- Enthalpy, $H_{t0} = 793 \text{ Btu/lb}_m$
- Dynamic pressure, $q = 1000 \text{ psf}$
- Fuel injectors 24" upstream of C/C-SiC leading edge

◆ RTV used to seal panel

- High temperature silicone sealant
- $T_{\text{max}} \sim 650^\circ\text{F}$
- Overheated and burned



Panel Temperatures (Run 79)



Carbon Steel Fixture After Panel #1 Tests

- ◆ Steel sidewalls melted and metal can be seen exiting the duct during video



Fixture with panel removed

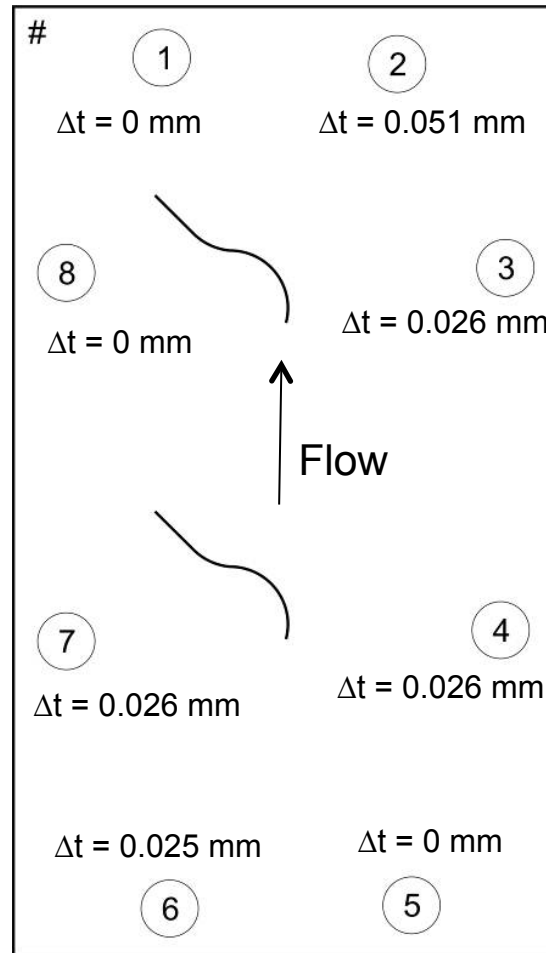


Melted carbon steel sidewalls. Slot for panel shown.

C/C-SiC Panel #1 Post Test

- ◆ 4 tests
- ◆ M ~ 6 enthalpy
- ◆ 20 sec tare (no fuel)
- ◆ 3 x 44 sec fueled tests

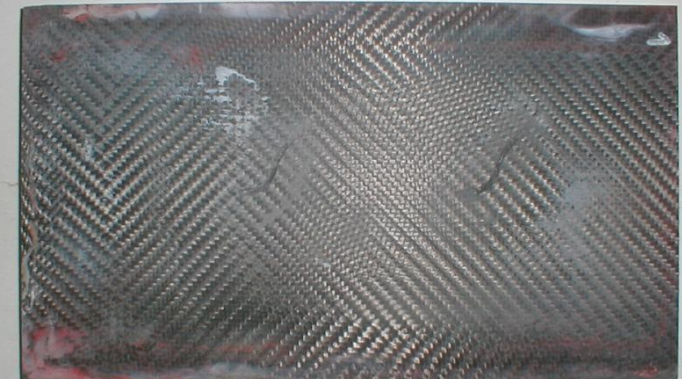
Locations for thickness measurements, ~ 0.003" uncertainty



Hot surface, post test



Cool surface, post test



	Thickness (mm) / Measurement location							
	1	2	3	4	5	6	7	8
Pre-test	8.026	8.052	8.052	8.103	8.306	8.280	8.052	8.052
Post-test	8.026	8.001	8.026	8.077	8.306	8.255	8.026	8.052

Pre- and Post-Test 79 Photographs



Discoloration due to melting
of carbon steel fixturing

Photograph During C/C-SiC Panel #1, Run 79



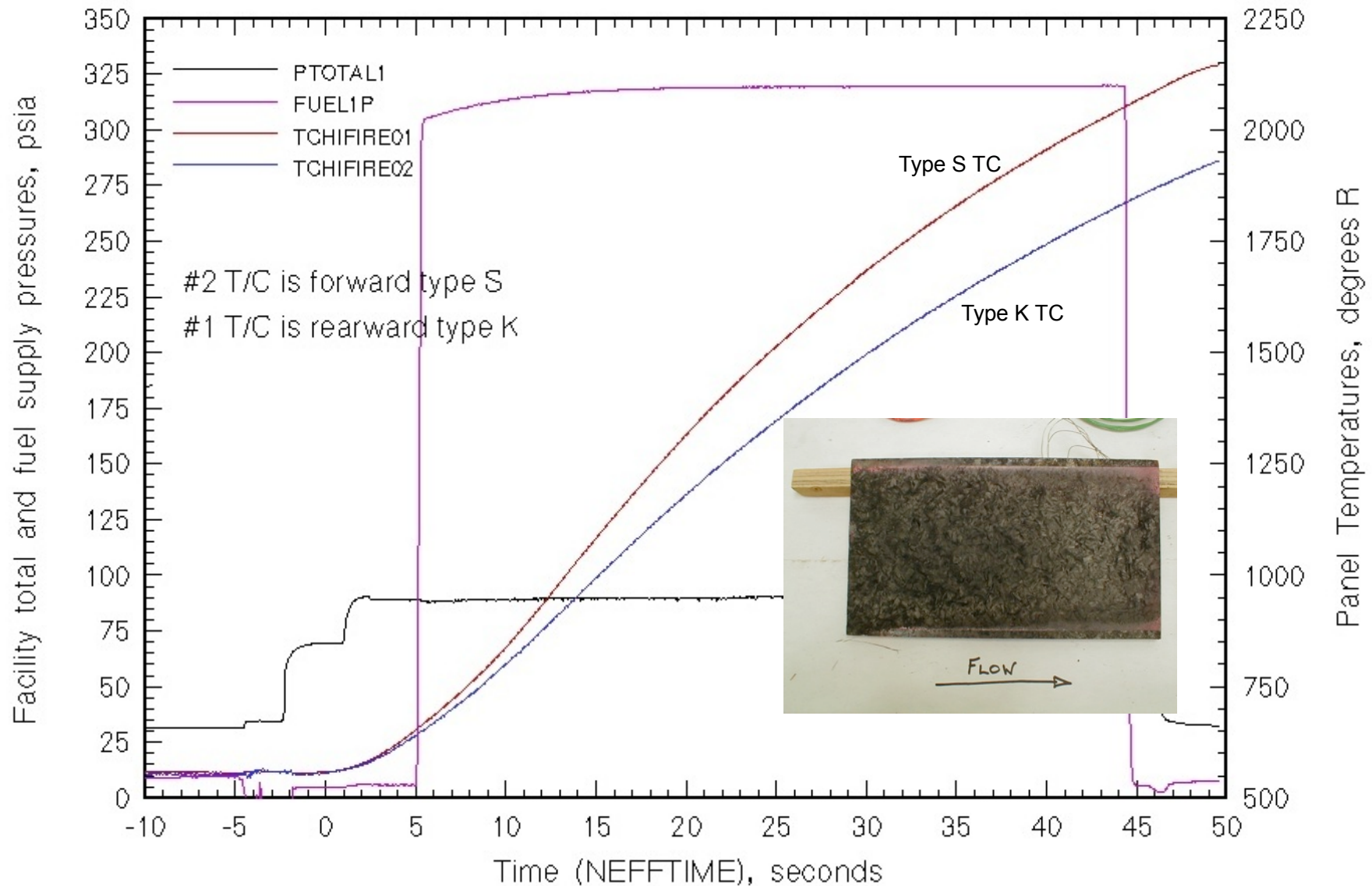
Approved For Public Release

Test Matrix

Panel	Run No.	Simulated Flight Mach No.	Temperature at end of Test, °R		P ₀ [psia]	T ₀ [°R]	ER (ramp + film)	ER (S3)	Fuel-on Time [sec]	Total Test Duration [sec]
			Type K	Type S						
C/C HP635-7	68	5	859	858	96.1	2131			n/a	20
	69	5	1507	1450	96.1	2117	0.556		35	40
	70	5	1611	1548	95.9	2130	0.741		35	40
	71	6	1002	1031	89.4	2546			n/a	20
	72	6	1878	1796	91.8	2611	0.986		40	45
	73	6	1026	1015	88.8	2558			n/a	20
	74	6	1987	1800	91.6	2594	1.003		39	44
	75	6	2051	1835	90.8	2626	1.023		39	44
C/C-SiC #4	52	5	1005	972	92	1939			n/a	20
	53	5	1248	1193	91.6	1957			n/a	40
	54	5	997	971	91.8	1989			n/a	20
	55	5	1214	1329	92.6	2020	0.53		14	20
	56	5	1044	1062	94.2	2035			n/a	20
	57	5	1737	1834	94.5	2070	0.58		32.5	38.5
	58	5	1076	1087	94.2	2070			n/a	20
	59	5	1319	1421	93.7	2073	0.53	0.36	13/5*	20
	60	5	1010	999	94.6	2059			n/a	20
	61	5	2126	2142	95.3	2063	0.52	0.32	29.5/19.5*	39.5
C/C-SiC #3	62	6	1281	1291	90.6	2624			n/a	20
	63	6	1295	1319	90.7	2647			n/a	20
	64	6	2025	2206	90.6	2648	1.01		30	40
C/C-SiC #1	76	6	1382	1317	89.6	2591			n/a	20
	77	6	2352	2515	91.9	2599	1.009		39	44
	78	6	2342	2504	91.2	2639	1.039		39.5	44.5
	79	6	2336	2462	91.9	2654	1.047		39.5	44.5

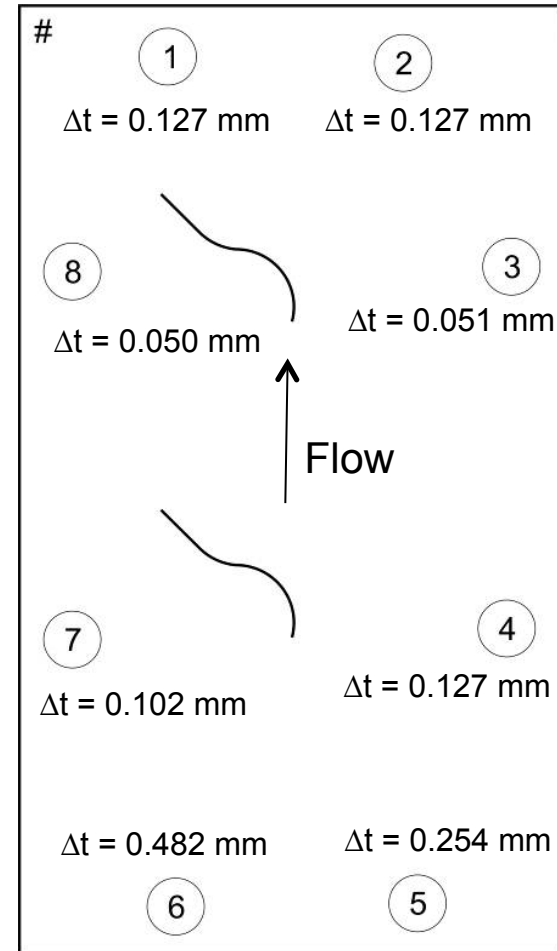
C/C Panel Temperatures, Run 75

DLR C/C Panel Temperatures



C/C Panel Test Post Test

- ◆ 100 sec, M ~ 5 conditions
- ◆ 193 sec, M ~ 6 conditions



	Thickness (mm) / Measurement location							
	1	2	3	4	5	6	7	8
Pre-test	10.008	10.008	10.008	10.008	10.084	10.109	9.957	9.931
Post-test	9.881	9.881	9.957	9.881	9.830	9.627	9.855	9.881

Outline

◆ Introduction

◆ Test

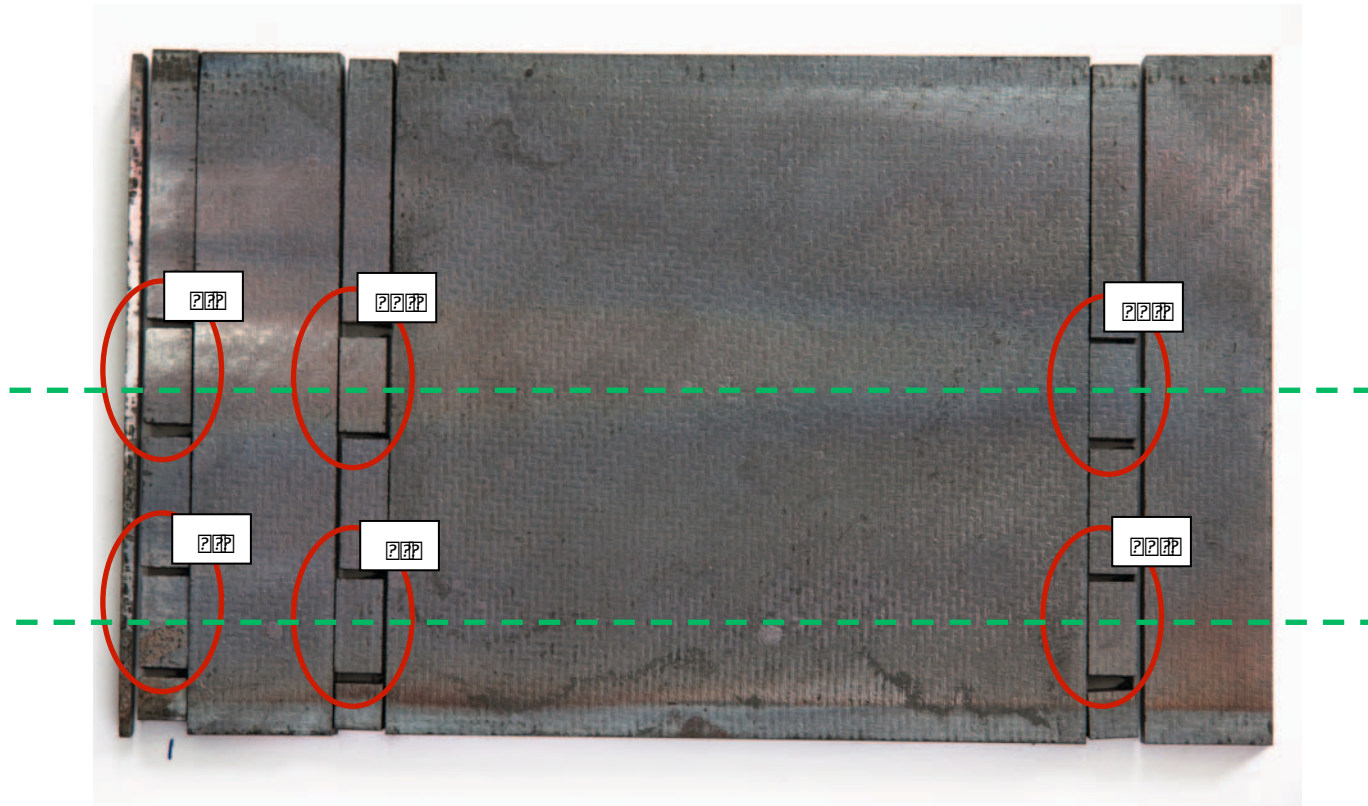


◆ **Post-test SEM investigations**

◆ Concluding remarks

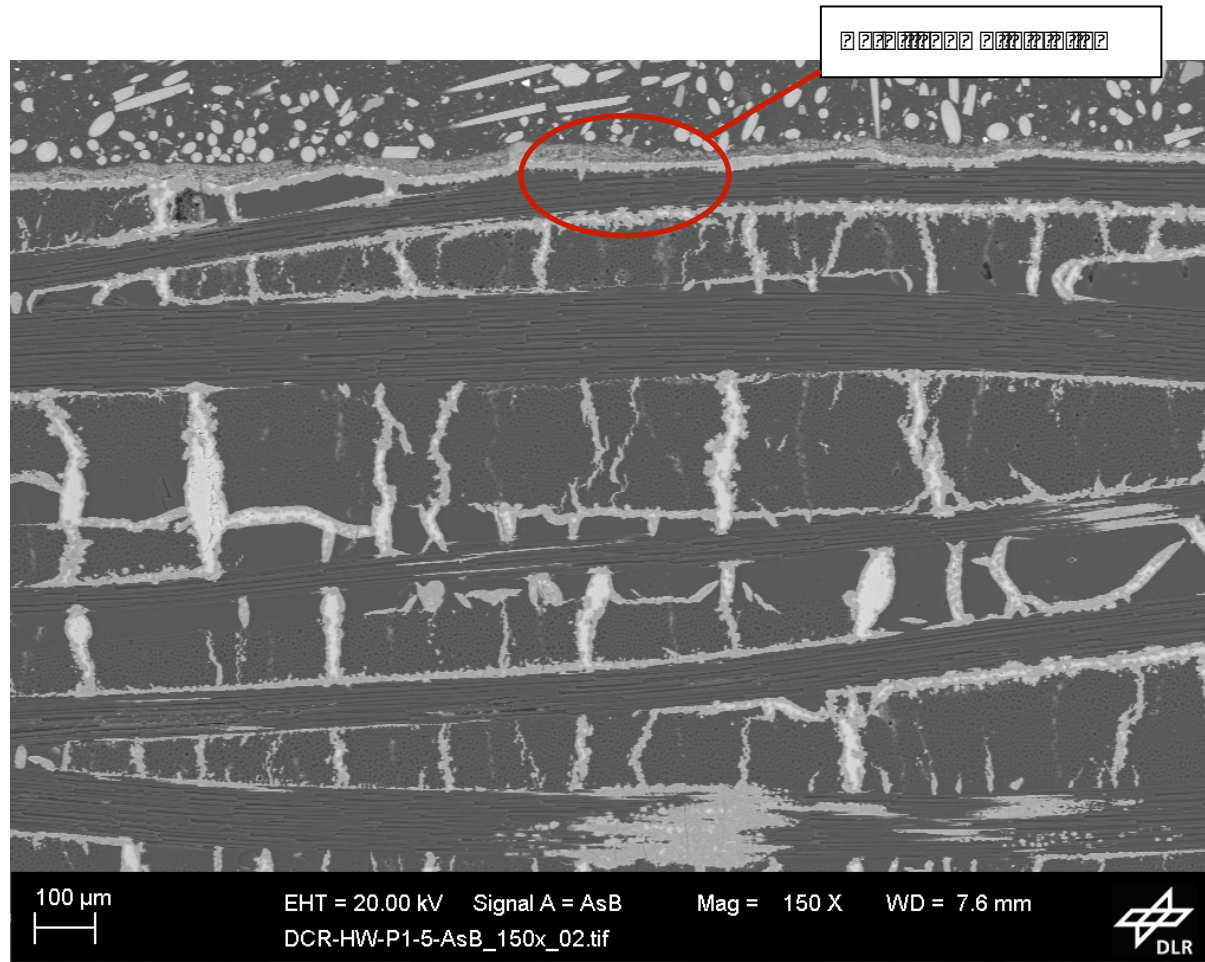
Post-Test SEM Investigations

- ◆ SEM investigations done at DLR with C/C-SiC panels
- ◆ Results shown for panel 1 centerline samples #5 and #17



Post-Test SEM Investigations

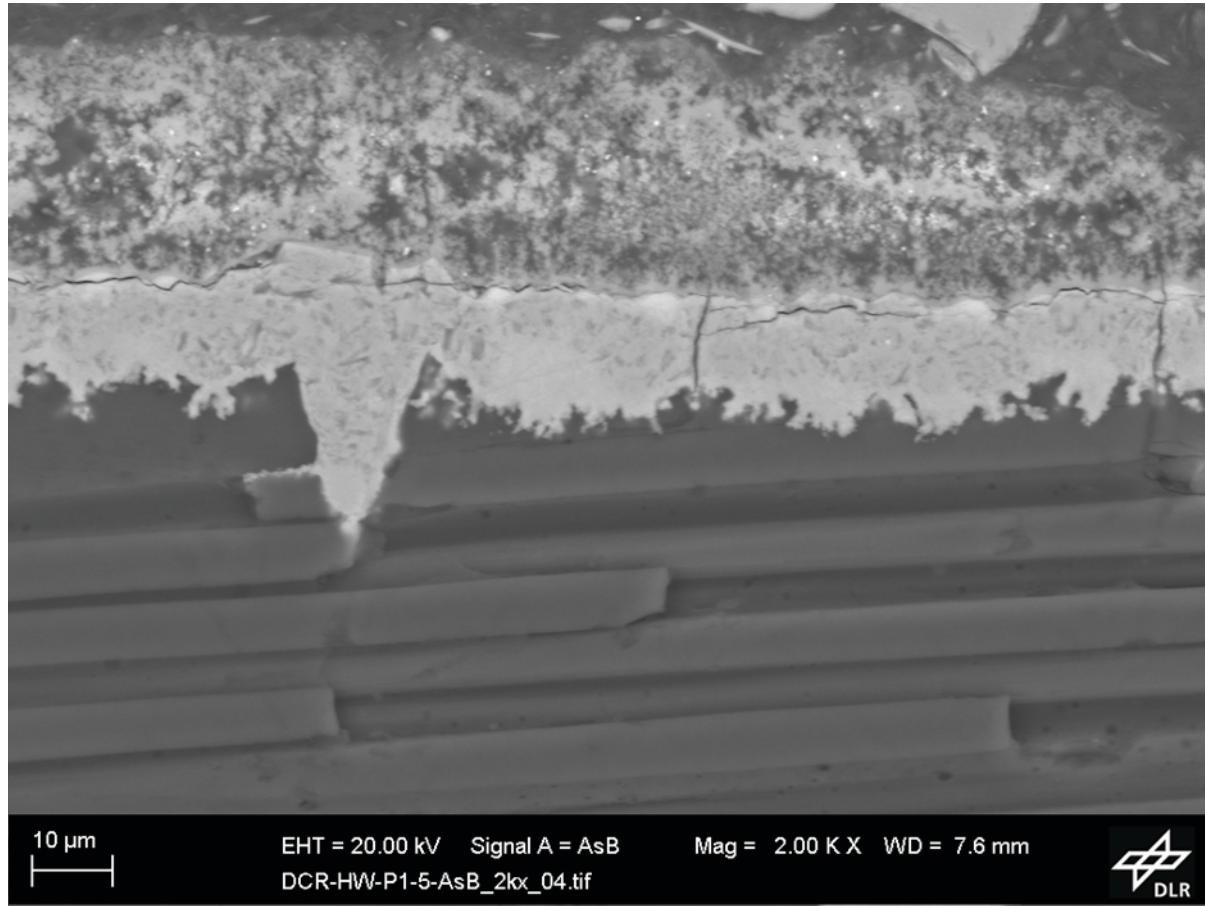
- ◆ SiO₂ layer on top of the sample
- ◆ No other signs of oxidation or erosion



Sample # 5

Post-Test SEM Investigations

◆ EDX analysis to confirm constitution of the top layer



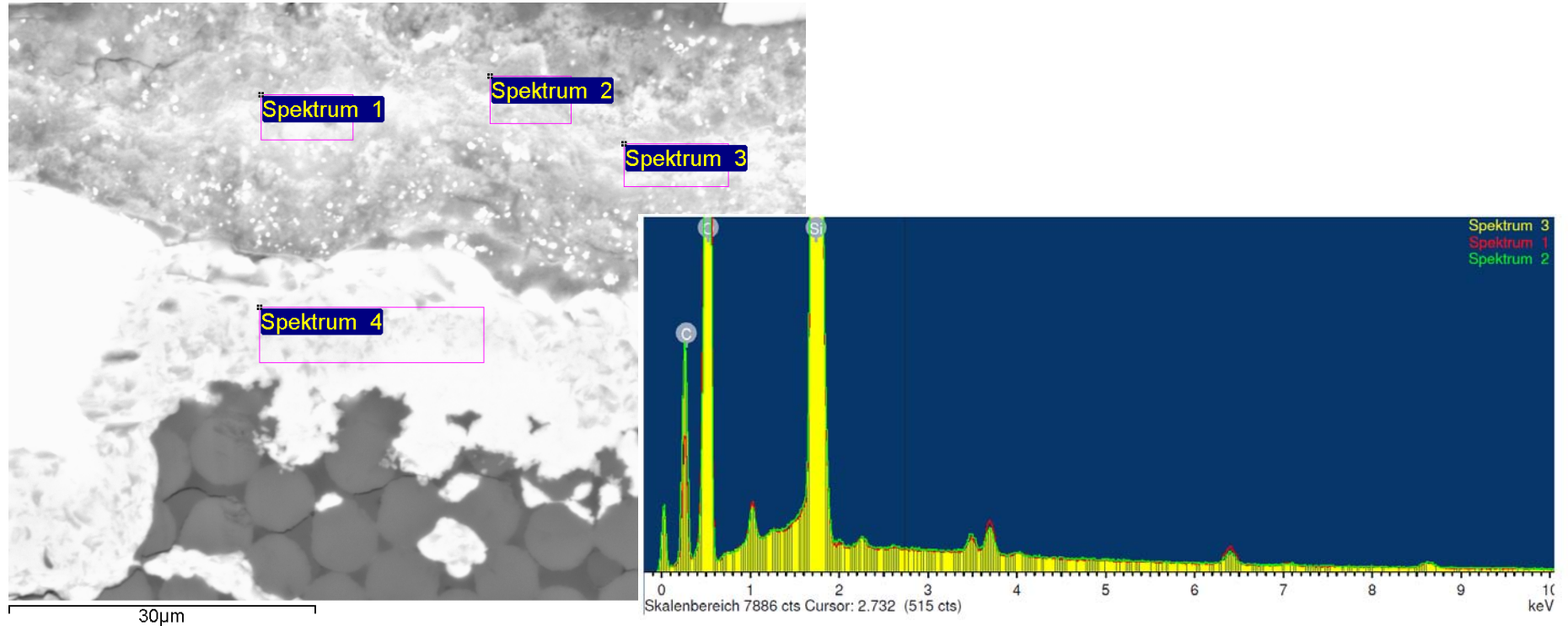
Silicon dioxide

Silicon carbide

Carbon fibers and
carbon matrix

Post-Test SEM Investigations

◆ EDX analysis to confirm constitution of the top layer



Prozessoption: Alle Elemente analysiert (Normalisiert)

Spektrum	In Stat...	C	O	Si	P	In	Sn
Spektrum 1	Ja	28.98	51.82	19.20			
Spektrum 2	Ja	39.13	43.54	17.34			
Spektrum 3	Ja	37.52	46.24	16.25			
Spektrum 4	Ja	50.40	0.88	48.10	0.10	0.18	0.35

Max.		50.40	51.82	48.10	0.10	0.18	0.35
Min.		28.98	0.88	16.25	0.10	0.18	0.35

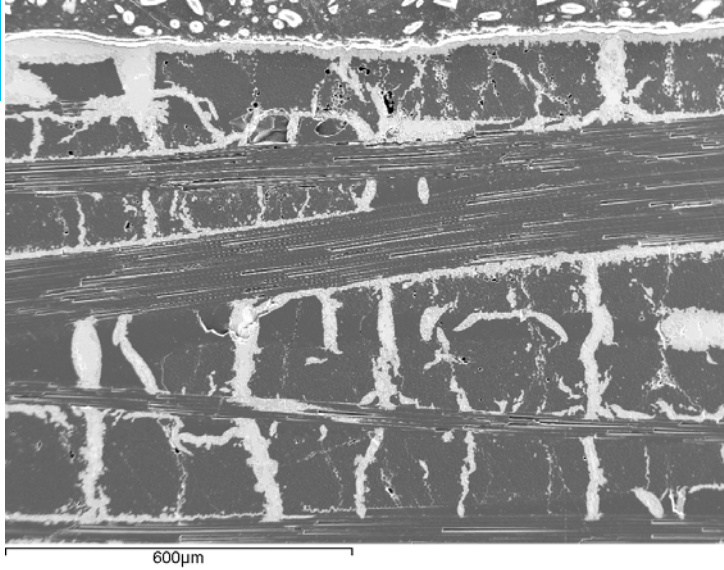
Alle Resultate in Atom%

Approved For Public Release

Post-Test SEM Investigations

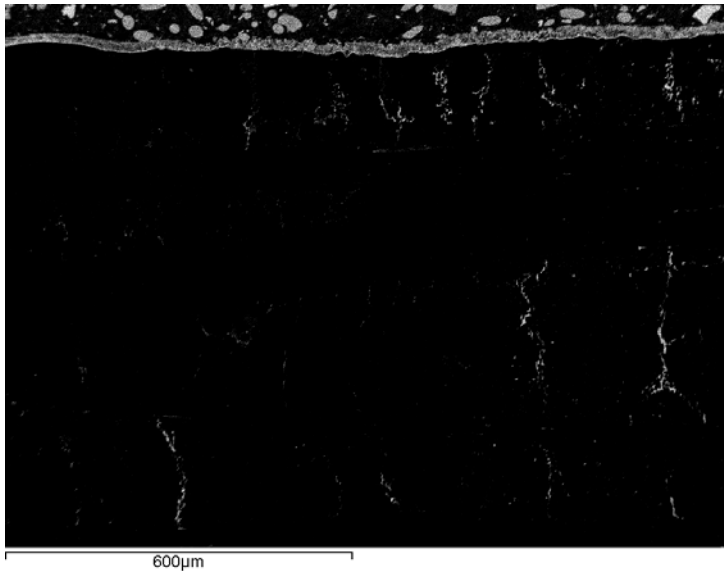
◆ EDX element mapping looking for oxygen distribution (sample # 5)

image



C

O



Si

Outline

◆ Introduction

◆ Test

◆ Post-test SEM investigations



◆ Concluding remarks

Concluding Remarks

◆ DCR performed very well

- Has since been mothballed

◆ DLR C/C-SiC

- Performed very well with very little erosion
- Tested at M ~ 6 flight conditions for several minutes
- Flight is M ~ 7, ~ 30 sec.
- SEM investigations show little effect of oxidation
- Mass loss and thickness reduction negligible

◆ Overall Conclusion

- Under the given conditions the performance was excellent
- Being considered for flight vehicle

Assessment of Cooling Concepts for SHEFEX III Leading Edge

7th European Workshop on Thermal Protection Systems and Hot Structures
8-10 April 2013
ESA/ESTEC, Noordwijk, The Netherlands

Christian Dittert⁽¹⁾, Hannah Böhrk⁽²⁾

^{(1),(2)} *Institute of Structures and Design, German Aerospace Center (DLR)
Space Systems Integration
Pfaffenwaldring 38-40, D-70569 Stuttgart, Germany
Christian.Dittert@dlr.de
Hannah.Boehrk@dlr.de*

1. INTRODUCTION

Sharp leading edges offer advantages in aerodynamic performance as they are known to induce minimum drag, require low thrust during ascent and achieve high cross-range during re-entry leading to larger re-entry windows. However, they are subject to severe aerothermodynamic load. The shock formed ahead of the vehicle upon re-entry into the atmosphere stands ahead of blunt shapes but may be attached to pointed shapes. Blunt bodies are therefore commonly used in order to increase the shock distance from the thermal protection system (TPS) and reduce the thermal load. However, the recent progress in material development and the improvement of layout and design calculation methods allows for a reconsideration of sharp leading edge concepts for hypersonic flight. Development of a feasible concept is, among other objectives, pursued in the re-entry flight program SHEFEX (Sharp Edge Flight Experiment).

Two SHEFEX flights I and II have shown successful performance of a ceramic matrix composite (CMC) sharp leading edge with a radius <1 mm for re-entry Mach numbers 6.5 and 10. The flight at higher velocity, SHEFEX II as shown on the left side in Fig. 1 recorded and transmitted data down to an altitude of 30 km. A thermocouple just 20 mm behind the leading edge measured a temperature of 1121K at this trajectory point and temperatures above 2275K are expected at altitudes below that [1].

SHEFEX III as presented on the right side in Fig. 1 will perform return flight at a velocity up to 5.5 km/s, thus a Ma number around 20 will be reached [2]. Even higher thermal response of the sharp leading edge is, thus, expected, resulting in temperatures above the generic heat shield material's capabilities. New material and cooling concepts for the thermal protection system, therefore, have to be considered. A possible solution to face these high heat loads has already been investigated during SHEFEX II flight. The AKTiV experiment on SHEFEX II has successfully cooled down the material by transpiration cooling with gaseous nitrogen [3]. The present paper is to compare this concept to radiation cooled high temperature material.

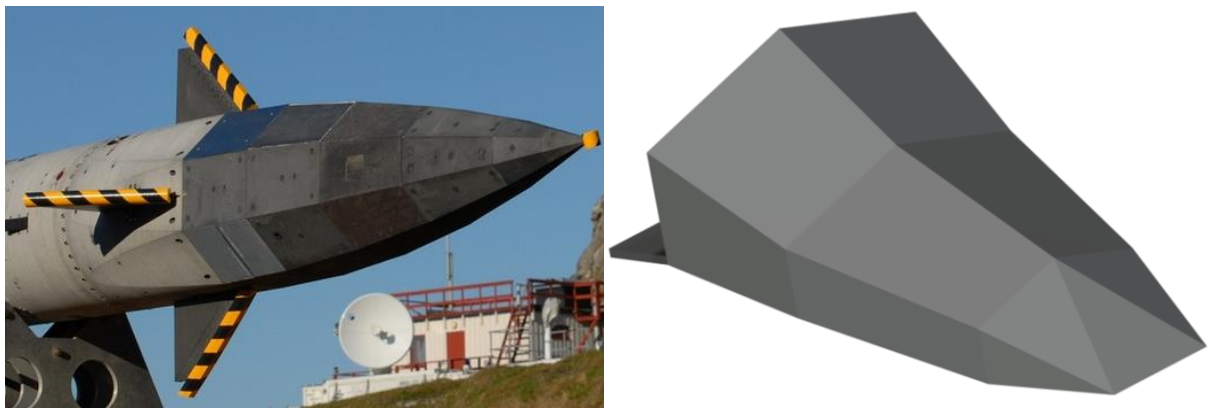


Fig. 1. Left: SHEFEX II, right: model of SHEFEX III

After presenting the investigated cooling and material concepts, the SHEFEX III trajectory, the present paper described the utilized numerical methods, tools and models. Finally, the thermal response of each investigated concept will be described and related and all concepts will be evaluated with respect to suitability for the SHEFEX III sharp leading edge.

2. INVESTIGATED COOLING CONCEPTS

In this study the focus lies on three different cooling concepts and their appropriate materials. The presented concepts are chosen because of their ability to face high heat load, especially those at sharp leading edges. Initially a radiation cooled wedge with the properties of the DLR (German Aerospace Center) material C/C-SiC is investigated. The reason to start an approach with C/C-SiC is that the material investigated and developed for a long time, so the material behaviour is well predictable. Furthermore the material has been successfully tested during re-entry flight as a part of the SHEFEX II TPS concept [1] shown in Fig. 1.

For the second concept a new approach regarding the material is chosen. Contrarily to the standard C/C-SiC ceramic matrix composite, a ceramic matrix composite with a pitch fiber instead of the basic carbon fiber can be used so the material behavior changed to a material with very high thermal conductivity. The idea behind is to transport the heat away from the tip to a region with lower heat flux and more material by using the benefit of the high thermal conductivity.

Compared to the two passively cooled concepts also one actively cooled concept is investigated. For that transpiration cooling seems to be a good choice to avoid high heat loads to the material. Transpiration cooling works in a way that a fluid flows through a porous material where first in the material heat convectively transferred to the fluid and secondly a protective film is developing on the surface. Therefore a porous material like Carbon/Carbon (C/C) is required. Furthermore a lot of knowledge with transpiration cooling was accumulated through the AKTiV experiment flown on SHEFEX II [3]. In this experiment a TPS-tile from SHEFEX II made of porous C/C was transpiration cooled by nitrogen and first results are indicating a very good cooling effect. For the investigated cooling concepts special ceramic materials are required, a material overview is listed in Table 1.

Table 1. Material properties

Material	λ_{II} / W/mK	λ_{\perp} / W/mK	ϵ
C/C-SiC	17	8	0,85
Pitch fiber ceramic*	150	50	0,85
C/C	14	2	0,85

* theoretical values

3. SHEFEX III TRAJECTORY

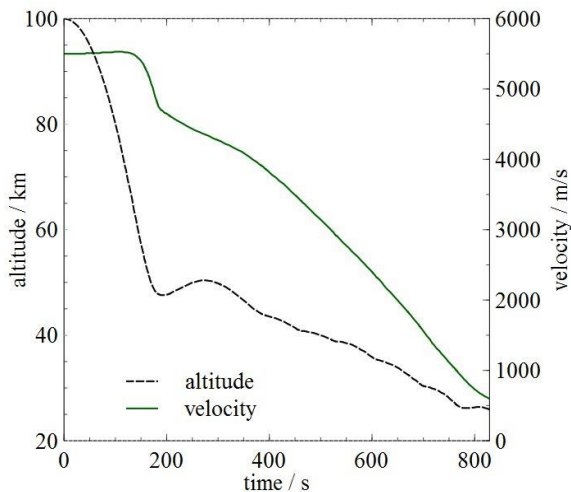


Fig. 2. SHEFEX III trajectory

The incoming heat load during a re-entry flight is affected by two major characteristics. Firstly the vehicles shape is one parameter which determines the incoming heat load and the heat flux at a sharp leading edge is much higher than the heat flux at blunt leading edges. Secondly the given trajectory has a huge effect on the heat flux. By changing for example the re-entry velocity or the angle of attack the heat flux can be in- or decreased. A possible SHEFEX III trajectory is presented in Fig. 2. The re-entry starts at an altitude of about 100km with a velocity of 5.5km/s [2]. Consequently SHEFEX III is twice as fast as SHEFEX II and also the heat load will increase to a much higher level compare to the SHEFEX II mission.

4. HEAT TRANSFER

The tool HEATS has been developed in order to determine transient wall heat flux to a material wall [4, 5]. Analytical equations for the oblique shock and expansion fans are used to determine the state variables in the vicinity of the vehicle. This approach was demonstrated in a former and validated by comparison to the CFD-data of a particular available SHEFEX II trajectory point [3]. These state variables of the atmospheric gas aerodynamically heating the surface are used as input data to HEATS.

The heat equation

$$\rho_{mat} c_{mat} \frac{\partial T}{\partial t} = \lambda_y \frac{\partial^2 T}{\partial y^2} + \lambda_x \frac{\partial^2 T}{\partial x^2} \quad (1)$$

is used to determine transient heat flux with a boundary condition for the surface of third type with

$$\dot{q}_{conduction} = \lambda_y \left(\frac{\partial T}{\partial y} \right)_w + \lambda_x \left(\frac{\partial T}{\partial x} \right)_w \quad (2)$$

and a boundary condition of second type at the rear side and the edges of

$$\lambda_y \left(\frac{\partial T}{\partial y} \right)_w = 0 \text{ and } \lambda_x \left(\frac{\partial T}{\partial x} \right)_w = 0, \quad (3)$$

i.e. assuming that these sides are adiabatic.

The method HEATS is based on a heat balance between wall material and surrounding hot gas. The heat balance for the surface in the present case of pure aerodynamic heating yields

$$\dot{q}_{convection} = \dot{q}_{conduction} + \dot{q}_{radiation} \quad (4)$$

By means of the heat equation and a heat balance for the boundary condition, thermal response of a thermal protection material to aerodynamic heating is modeled. Aerodynamic heating is determined from the gas properties with

$$\dot{q}_{convection} = h(T_{recovery} - T_{wall}) \quad (5)$$

as transferred from the hot gas to the wall through convection with the convection heat transfer coefficient h and the recovery temperature $T_{recovery}$. These parameters are functions of the flow properties and can be expressed as

$$h = St \rho u c_p \quad (6)$$

and

$$T_{recovery} = T_\infty \left(1 + r \frac{\kappa - 1}{2} Ma_\infty^2 \right). \quad (7)$$

The recovery temperature is the temperature that the total air temperature is approximated by because of the incomplete recovery of the kinetic energy of the air by the temperature probe.

The two commonly unknown variables of (6) and (7) are the Stanton number St and the recovery factor r . They must be determined for each flow condition, be it laminar or turbulent. This is done based on known models of Crocco and van Driest [4, 6, 7]. A general approach to determine the local Stanton number and the recovery factor for a laminar flow is given by van Driest for a flat plate with the equation

$$St_x = 0.332 Pr^{-\frac{2}{3}} Re_x^{-\frac{1}{2}}. \quad (8)$$

In a first approximation, the recovery factor for laminar flow over a flat plate is commonly defined as $r = \sqrt{Pr}$.

As a result of the advanced evolution of SHEFEX, the design changed to a lifted body concept with sharp edges contrary to the axisymmetric SHEFEX II body. Hence the nose geometry in order to determine the heat transfer between nose and surrounding flow is estimated as simple wedge geometry. In order to calculate the heat flux between wall and flow it is necessary to know the heat transfer coefficient h and the recovery temperature $T_{recovery}$ given by (6) and (7). Furthermore the velocity u , the density ρ and the heat capacity c_p behind the oblique shock have to be calculated to determine the heat transfer coefficient in (6). The solution for the heat transfer coefficient and the recovery temperature is presented in Fig. 3. As a first result it can be assumed that the heat flux based on (5) is achieving a maximum between 180s and 400s.

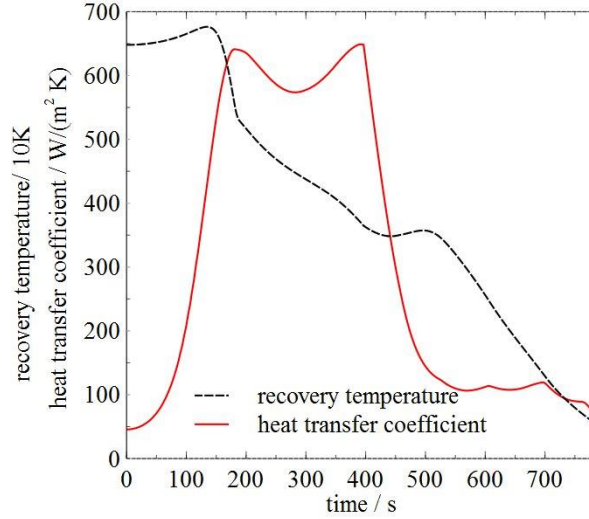


Fig. 3. Heat transfer coefficient and recovery temperature

Because of the increase of velocity and flight duration for SHEFEX III, it can be assumed that the heat load for the material is much higher than for SHEFEX II. Hence it is necessary to make a new approach in respect to cooling methods. In that case HEATS has the ability to determine transient wall temperatures for transpiration cooled surface conditions [4, 5]. Therefore the heat equation (1) is extended by a term describing the convective heat transfer between fluid and material [8]. Hence the heat equation is expanded to

$$\rho_{mat} c_{mat} \frac{\partial T}{\partial t} = \left(\lambda_y \frac{\partial^2 T}{\partial^2 y^2} + \lambda_x \frac{\partial^2 T}{\partial^2 x^2} \right) + h_v (T_{fluid} - T_{material}). \quad (9)$$

In this equation the volumetric heat transfer coefficient h_v is unknown and has to be defined by a model developed by Florio [9]. During transpiration cooling a thin film layer develops on the surface. To solve the heat balance at the surface it is necessary to determine the film layer, this is done with an approach after Goldstein [10].

For the calculation in HEATS, a 2D model of a wedge or a flat plate with a grid as laid down in Fig. 4 is used. To compute the equations (1) to (9), HEATS is used an explicit solver.

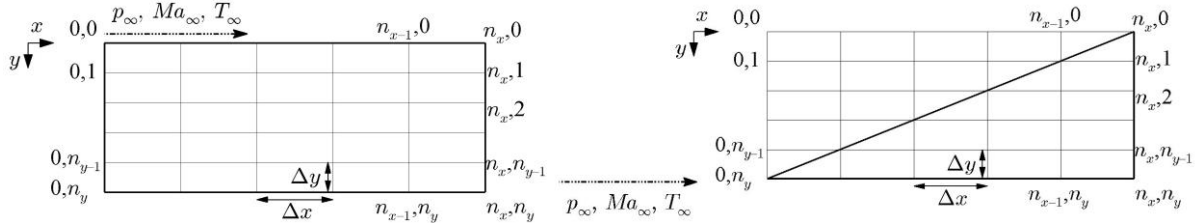


Fig. 4 Possible grid configurations

5. NUMERICAL SETUP AND MODEL

For these very first simulations the SHEFEX III nose geometry is replaced by a simple wedge as displayed in Fig. 5 with an opening angle of 32° and a length of 150mm. Furthermore for reasons of clarity all results are given in reference to the defined reference points 1 to 4. These points are located at the very tip (RP1) and then in distance of 20mm (RP2), 50mm (RP3) and 100mm (RP4) from the tip 2mm below the surface.

For all calculations with focus on radiation cooling a wedge grid as presented in Fig. 4 is used. Furthermore the simulations done by HEATS are validated with help of a commercial FEM tool. To reduce the boundary conditions for the FEM simulations the mean instead of the local heat transfer coefficient is used. The mean heat transfer

coefficient based on the overall amount of heat being transferred between initial point 0 and x. It is based on the mean Stanton number which is defined for a flat plate as just twice the local value at a given position [11]. The difference between local and mean heat transfer coefficient for the thermal response is shown in Fig. 6 left side. It is important to know, by using the local heat transfer coefficient the temperatures are more realistic and much higher at the very tip then using the mean heat transfer coefficient. In the opposite direction at the rear the temperatures are lower than the one calculated with the mean transfer coefficient.

The calculations done for transpiration cooling are based on a flat plate model and grid as presented in Fig. 4 on the left side with the dimensions of 156mm x 10mm, thus the surface length is equal to the wedge surface. Unfortunately it is necessary to change the model because the HEATS transpiration code is so far not able to calculate wedge geometry. Nevertheless it is possible to compare the results between these two models. In Fig. 6 on the right hand temperatures presented for the wedge and the flat plate at same position and they are almost the same. That mean the heat which has to be cooled away is in both cases the same. Hence for a first estimation it is acceptable to use two different models.

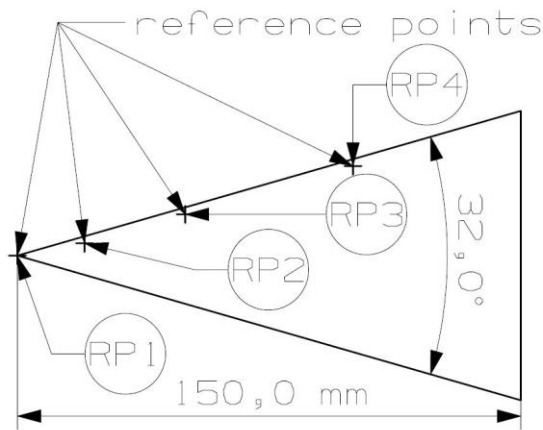


Fig. 5. Simplified nose model

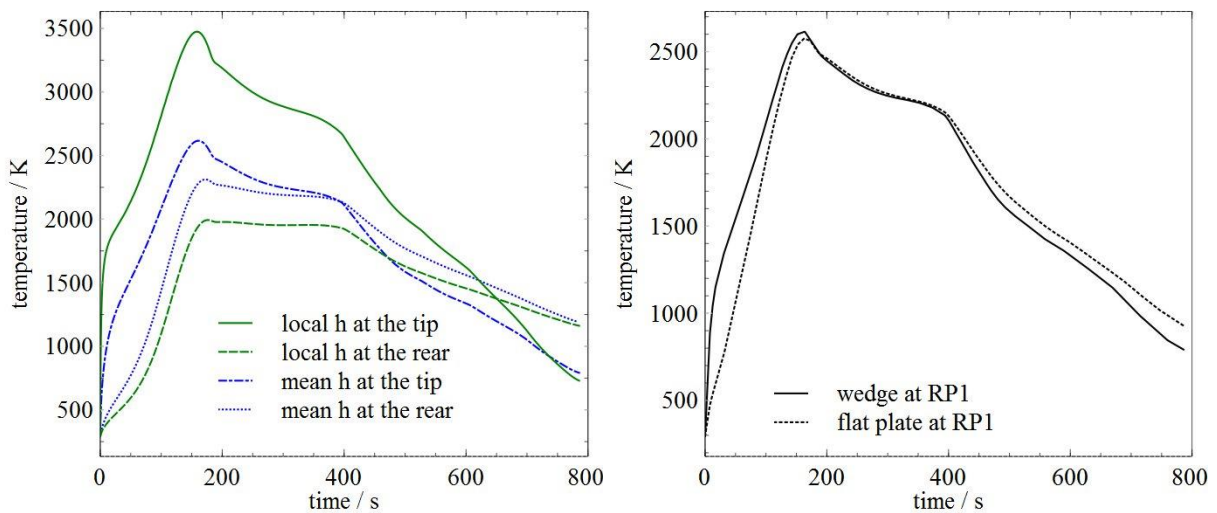


Fig. 6. Left: compared local- and mean heat transfer coefficient, right: thermal response of the two calculation models

6. RESULTS

6.1. Radiation Cooled Concepts

The results for the investigated radiation cooled concepts are presented in Fig. 7. The two diagrams at the top and the one at the bottom on the left show wall temperature for different reference points presented in Fig. 5. Furthermore all simulations are done with the in Fig. 3 presented mean heat transfer coefficient and recovery temperature, so the temperatures at the very tip are lower than equivalent temperatures calculated with a local heat transfer coefficient. Besides the emissivity for all materials is set to $\epsilon=0.85$. The temperature responses are shown for the C/C-SiC and the pitch fiber material in the two diagrams at the top and the one below on the left side. Especially at the very tip of the nose (RP1) the temperatures are identical between 180s-400s. Moreover the maximum is reached in all cases after 180s with a temperature of about 2600K. Surprising is the temperature distribution in the bottom left diagram, because of an additionally boundary condition (a constant wall temperature of about 480K is set on the rear side) a smaller maximum temperature was expected. In the diagram at the right bottom the temperature distributions at the very tip are compared for all cases. As mentioned before the temperatures are the same in all cases between 180s-400s with their maximum at 180s. Compared to the diagram representing the heat transfer coefficient Fig. 3 it appears reasonable that the heat load between 180s and 400s is dictating the wall temperature. However, after 400s in the diagram at the bottom right Fig. 7 an influence on the wall temperature caused by the chosen material and boundary conditions is clearly visible. Finally the wall temperatures develop at the nose due to the calculated heat transfer coefficient are too high for presented material. Generally it will be assumed that the maximum working temperature for the presented CMC is about 2000K.

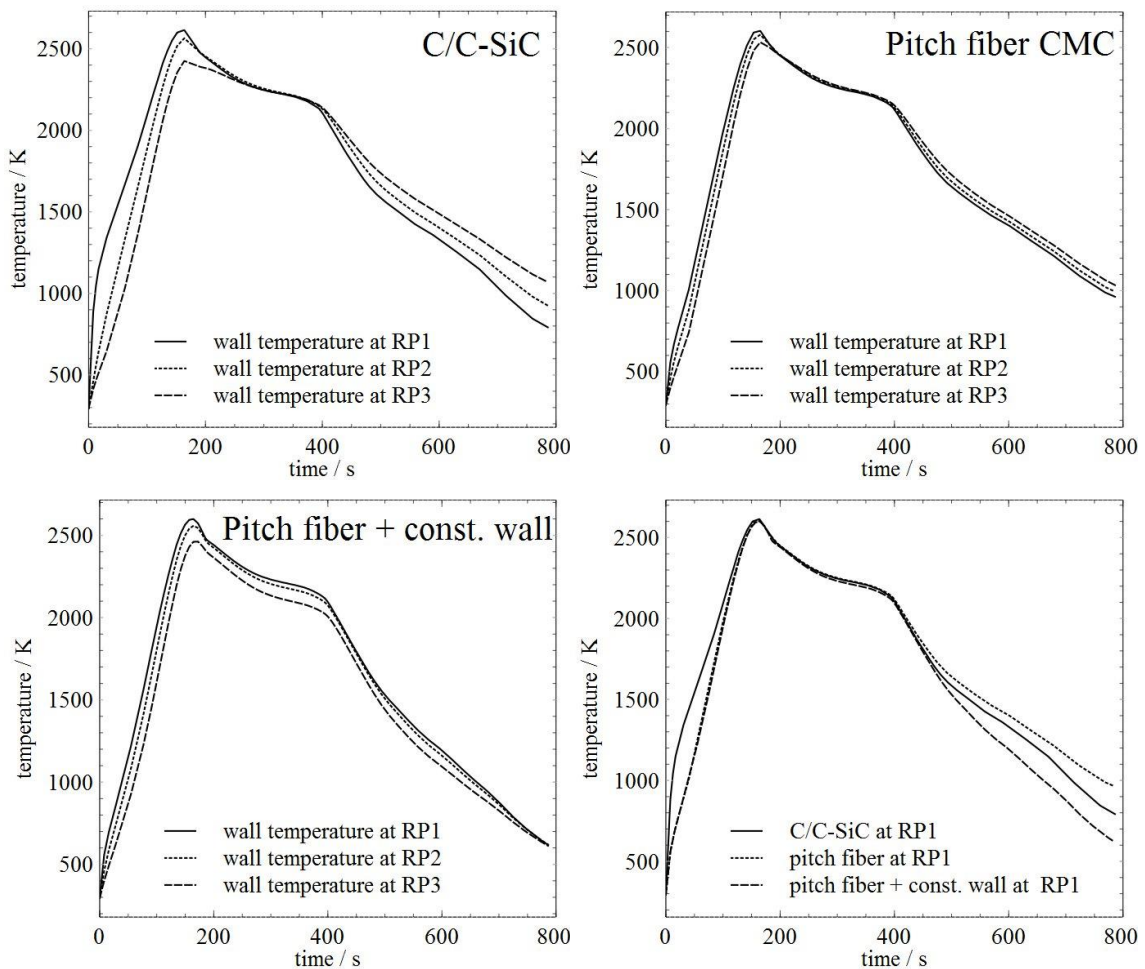


Fig. 7. Results for radiation cooled concepts

6.2. Transpiration Cooled Concept

As mentioned before transpiration cooling has the potential to protect a structure and material from high heat load. Hence in a first attempt a transpiration cooled nose with nitrogen as cooling gas and cooling between 120s-300s was simulated. The presented results in Fig. 8 are determined with the local heat transfer coefficient, so the temperatures at the very tip are higher than equivalent temperatures calculated with a mean heat transfer coefficient. As nose material porous C/C with an emissivity of $\epsilon=0.85$ is used. For a mass flow of 4g/s the results are indicating a significant and immediate reduction of the wall temperature. Hence contrary to radiation cooling, transpiration cooling has the ability to lock out the heat by developing a thin protective film layer at the surface so the temperature can be reduced as shown in Fig. 8 up to 1000K compared to uncooled conditions. Moreover to optimize the transpiration cooling it is possible to control the cooling effect by changing parameters like mass flow or cooling time. The results of such a variation of parameters are presented in Fig. 9. In the left hand diagram the mass flow was varied between 4g/s and 0.4g/s at constant cooling time. Especially at the reference point 2mm below the surface (RP2) the wall temperature increases up to 300K for reducing the cooling mass flow to 0.4g/s. The right hand diagram in Fig. 9 is showing the thermal response for different cooling time frames. As a result of the time and mass flow variation it is possible to find an optimal working point for transpiration cooled systems. Furthermore transpiration cooling can be used to reduce the heat load at specific points along the trajectory, so it is not necessary to cool the entire re-entry time.

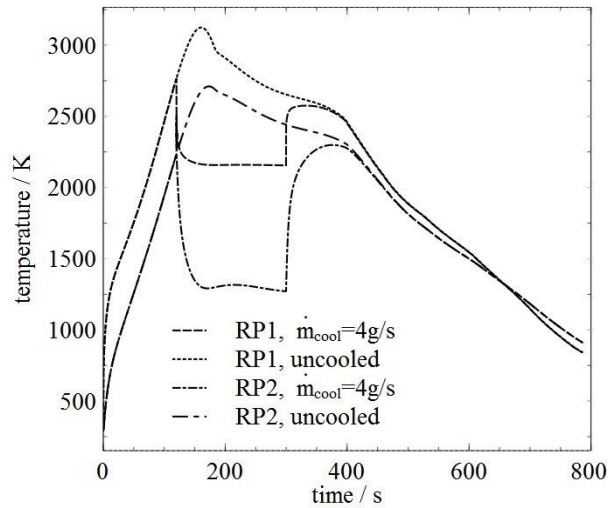


Fig. 8. Transpiration cooled porous C/C for SHEFEX III nose

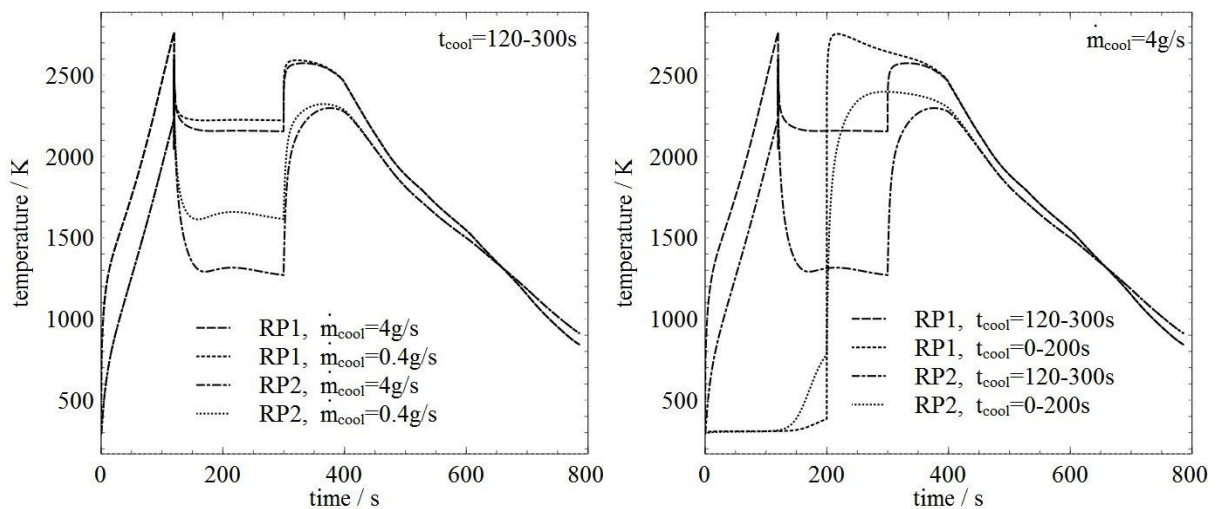


Fig. 9. Variation of mass flow and cooling time

7. ASSESSMENT OF THE PRESENTED COOLING CONCEPTS AND NEXT STEPS

Considering the high heat load calculated for the SHEFEX III re-entry Fig. 3, only the transpiration cooled concept has clearly the potential to compete with this high heat load, especially around the stagnation point. Moreover with the AKTiV experiment on SHEFEX II the operational work, of transpiration cooling was successfully proven. However just like every active concept, the complexity rises as does the possible failure risk.

The radiation cooled concept based on C/C-SiC is the concept which has been investigated for the longest period of time. Hence the material behaviour is well understood. The material itself has been used many times as a part of the thermal protection systems for example on SHEFEX I and II. However for the SHEFEX III nose the heat load might be too high for the material but in regions with lower heat flux C/C-SiC will be part of the thermal protection system.

At this point in time the pitch fiber based ceramic has the lowest potential to be part of a thermal protection system. The material development just started and the material characteristics as presented in Table 1 are not reached yet. Especially the concept for a radiation cooled sharp leading edge based on a pitch fiber ceramic seems unrealistic due to the high heat loads since the material is saturated very fast so the heat cannot be transported away. But for lower heat fluxes a regenerative cooling concept based on a pitch fiber ceramic as implied for the case with the constant wall temperature at rear side can be an opportunity for future investigation.

For future development of the SHEFEX III nose it is necessary to continue the investigation particularly in reference to the transpiration cooling. Therefore it is essential to expand the HEATS transpiration code for wedge geometry and to do a lot more calculations with a variation in parameters. Finally all investigated cooling concepts have to be verified in arc jet facilities by experiments.

8. REFERENCES

- [1] H. Böhrk, T. Thiele, C. Dittert, "Thermal Testing of the Sharp Leading Edge of SHEFEX II", *18th AIAA/3AF International Space Planes and Hypersonic Systems and Technologies Conference*, Tours, France, Sep 2012
- [2] J. Telaar, H. Strauch, J. Sommer, "SHEFEX III Flight Control System," *4th International ARA-Days*, Arcachon, France, Mai 2013.
- [3] H. Böhrk, M. Kuhn, H. Weihs, "Concept of the Transpiration Cooling Experiment on SHEFEX II," *2nd International ARA-Days*, Arcachon, France, Oct. 2008.
- [4] H. Böhrk, O. Piol, M. Kuhn, "Heat Balance of a Transpiration-Cooled Heat Shield," *Journal of Thermophysics and Heat Transfer*, vol. 24, No. 3, 2010, pp. 581–588.
- [5] H. Böhrk, A. Herbertz, M. Ortelt, "Heat Balance of a Transpiration-Cooled Ceramic Combustion Chamber," *Space Propulsion 2010*, San Sebastian, Spain, May 2010.
- [6] E.R. van Driest, "Investigation of Laminar Boundary Layer in Compressible Fluids using the Crocco Method," *Tech. Rep. NACA TN-2597*, NACA, 1952.
- [7] E.R. van Driest, "The Problem of Aerodynamic Heating," *Aeronautical Engineering Review*, Vol. 15, No. 10, 1956, pp. 26–41.
- [8] M. Kaviany, "Principles of Heat Transfer in Porous Media," *Springer Verlag*, New York, 1991.
- [9] J. Florio, J.B. Henderson, F.L. Test and R. Hariharan "Experimental Determination of Volumetric Heat Transfer Coefficients in Decomposing Polymer Composites," *Porous Media, Mixtures and Multiphase Heat transfer (ASME Winter Annual Meeting, SanFrancisco, CA)*, 1989, HTD-Vol. 117, pp. 51–60.
- [10] R.J. Golstein, "Film Cooling," *Advances in Heat Transfer*, Irvin, T.F and Hartnett, J.P. Eds., Academic Press, New York, 1971, pp. 321–379.
- [11] L. F. Crabtree, J. G. Woodley and R. L. Dommett, "Estimation of Heat Transfer to Flat Plates, Cones and Blunt Bodies," *Reports and memoranda No. 3637*, Ministry of Thecnology, Aeronautical Research Council, 1970

SHEFEX III - Assessment of Cooling Concepts for Sharp Leading Edges

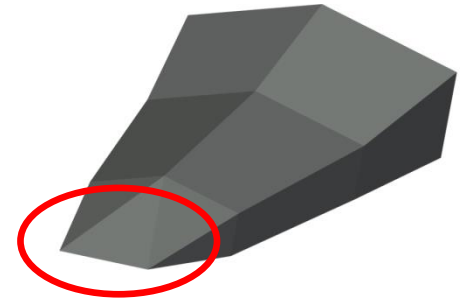
C. Dittert
H. Böhrk
German Aerospace Center
Stuttgart



Knowledge for Tomorrow



Outline



- SHEFEX III geometry and mission profile
- HEATS
- Investigated cooling concepts
 - Radiation cooled leading edge (C/C-SiC)
 - Radiation cooled leading edge (pitch fiber)
 - Transpiration cooled leading edge (C/C)
- Assessment
- Next steps



SHEFEX Development Strategy



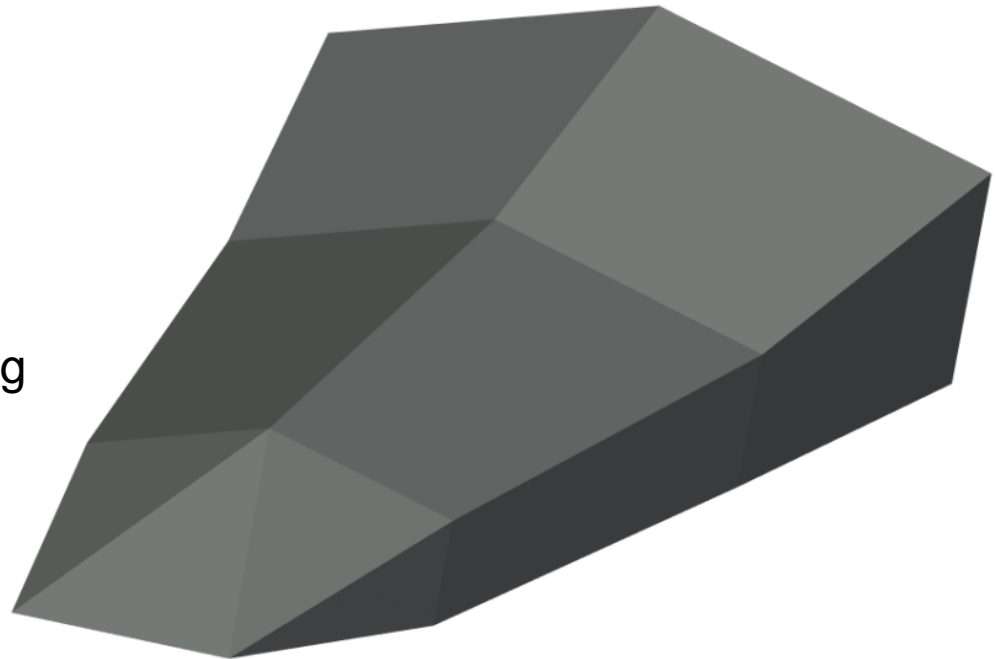
SHEFEX III dimensions

length: 1500mm

width: max. 1040mm

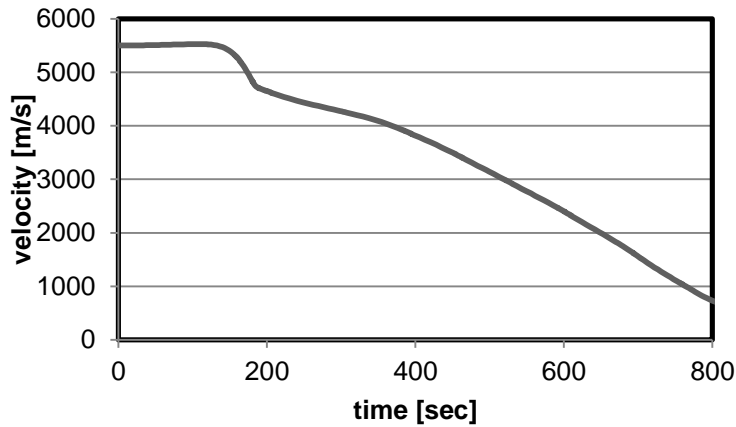
height: max. 470mm

mass: complete ~500kg

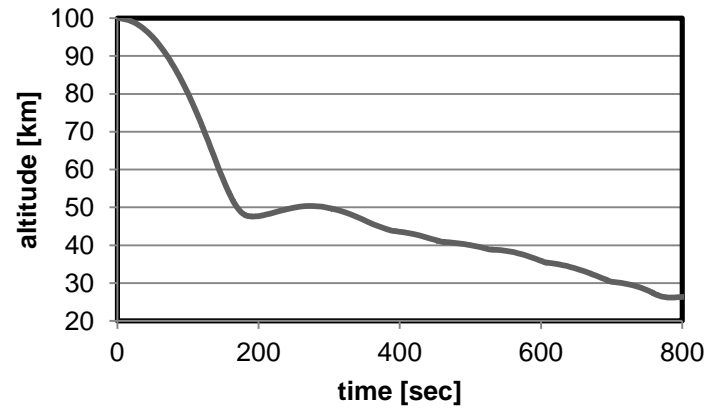


SHEFEX III – a possible trajectory

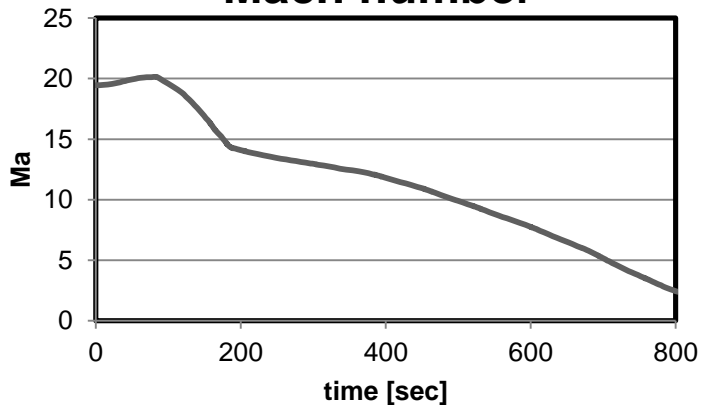
Velocity



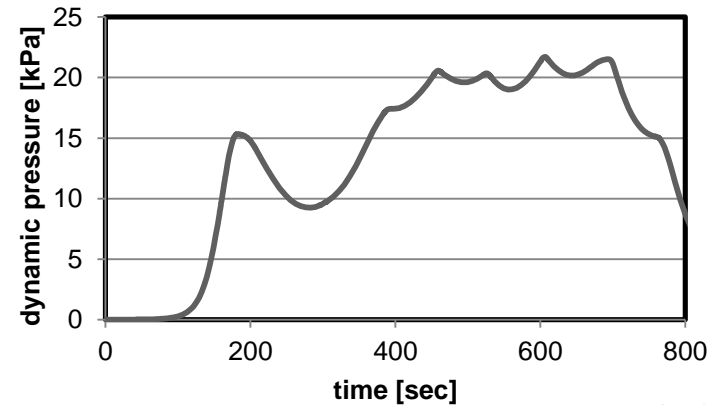
Altitude



Mach number



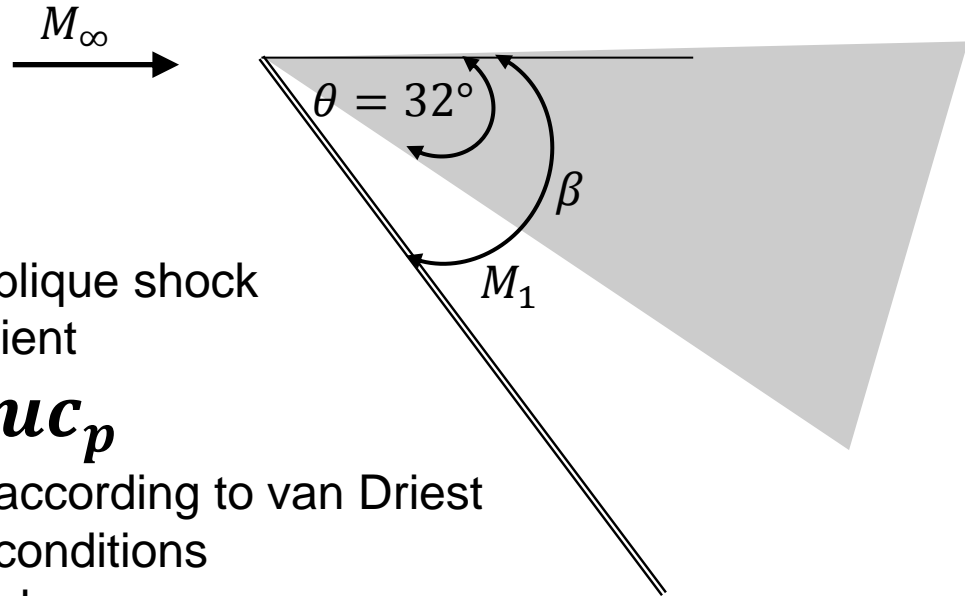
Dynamic pressure



source: Astrium



Heat transfer

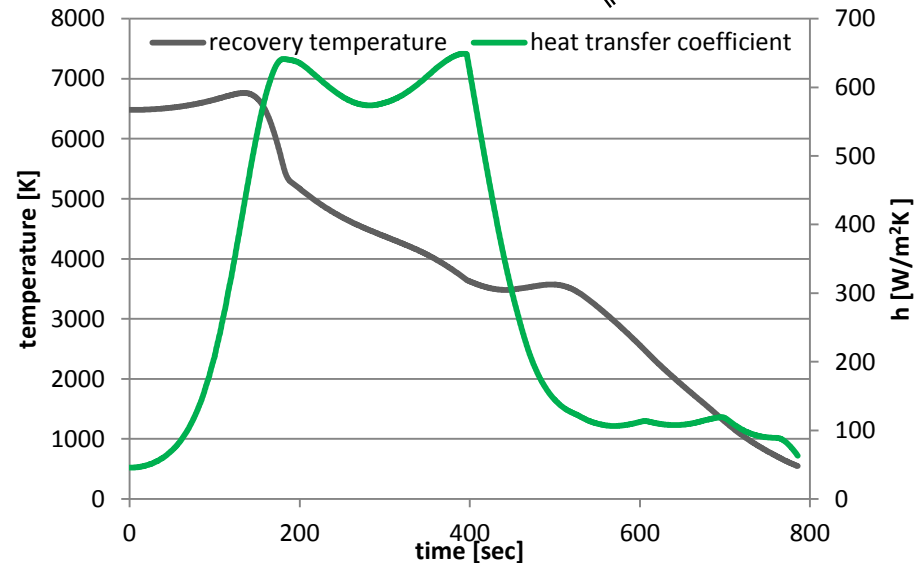


- determine conditions behind oblique shock
- determine heat transfer coefficient

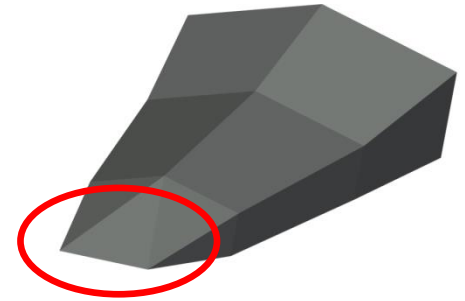
$$h = St\rho u c_p$$

- Stanton number is calculated according to van Driest for laminar and turbulent flow conditions
- ρ , u , c_p and T_r are given behind the shock
- calculated h and T_r define the heat transfer between flow and wall

$$\dot{q}_{conv} = h(T_r - T_{wall})$$



HEATS*



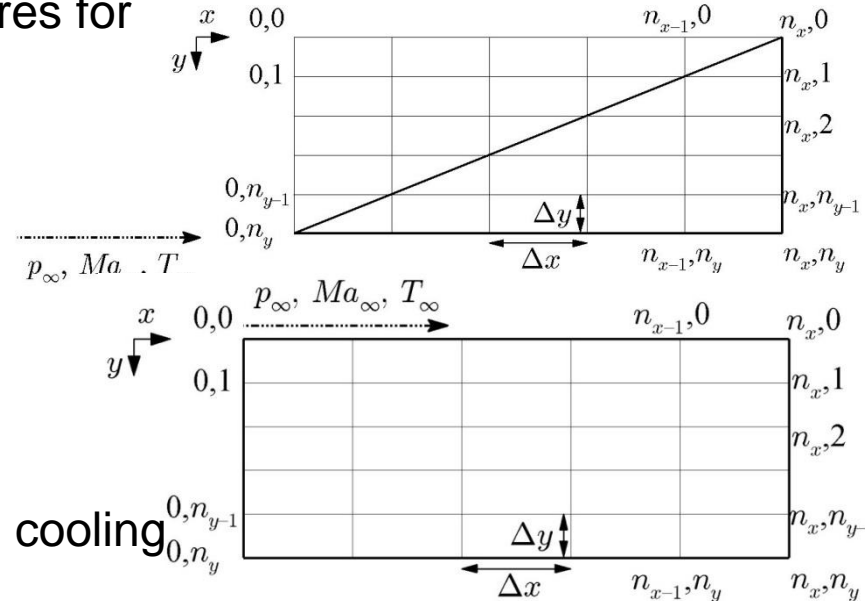
- developed for the layout of transpiration cooled systems

- determines transient wall temperatures for

- transpiration-cooled,
- film-cooled,
- uncooled surface conditions

- different models are used:

- Van Driest: aerodynamic heating
- Goldstein: film-cooling
- Florio, Henderson: transpiration cooling



* Journal of Thermophysics and Heat Transfer; Heat Balance of a Transpiration-Cooled Heat Shield; H.Böhrk et. al



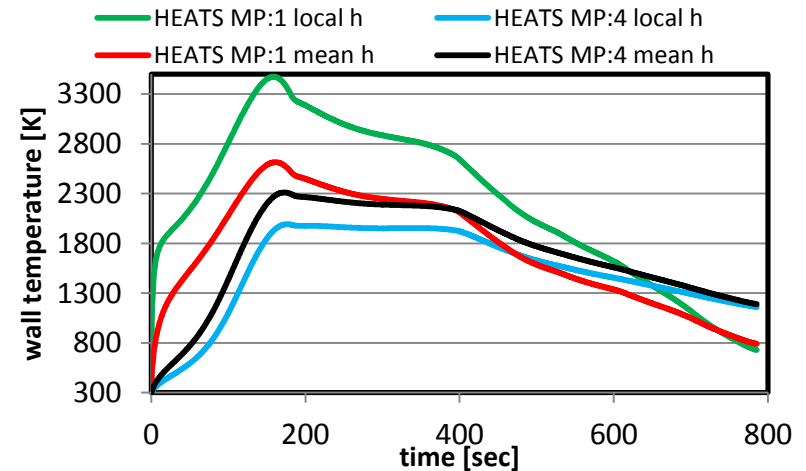
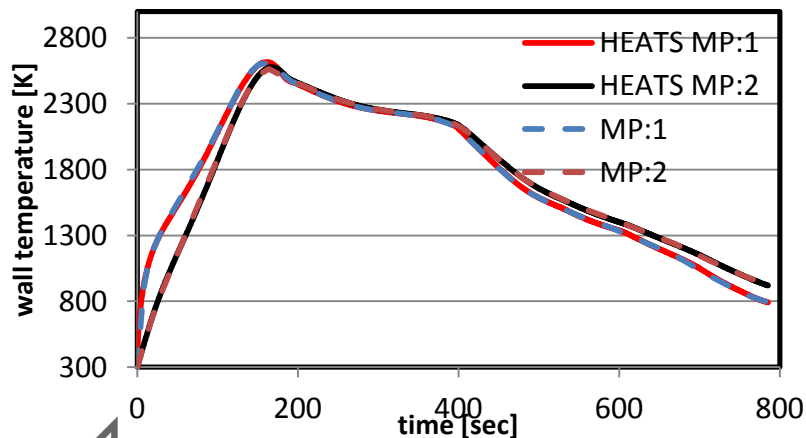
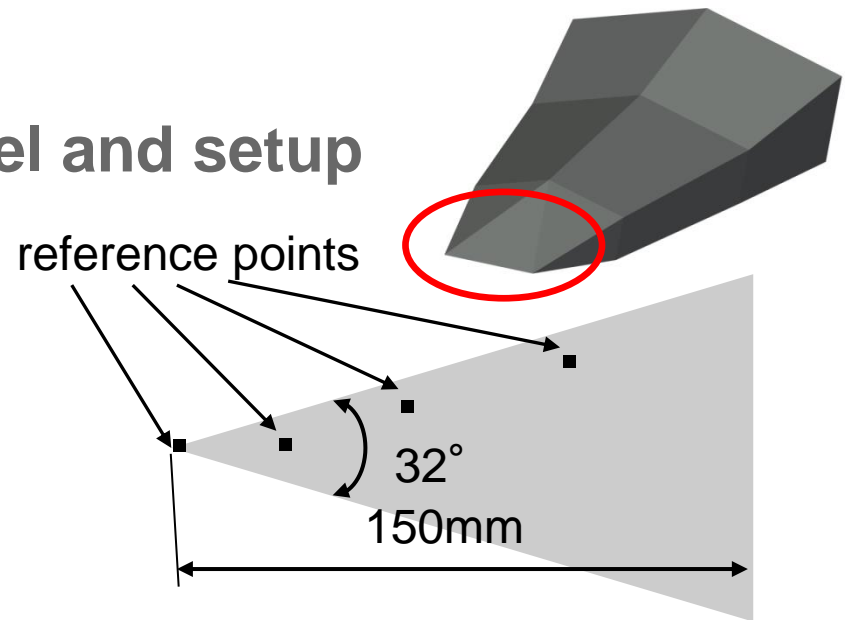
HEATS – numerical model and setup

HEATS is validated by ANSYS

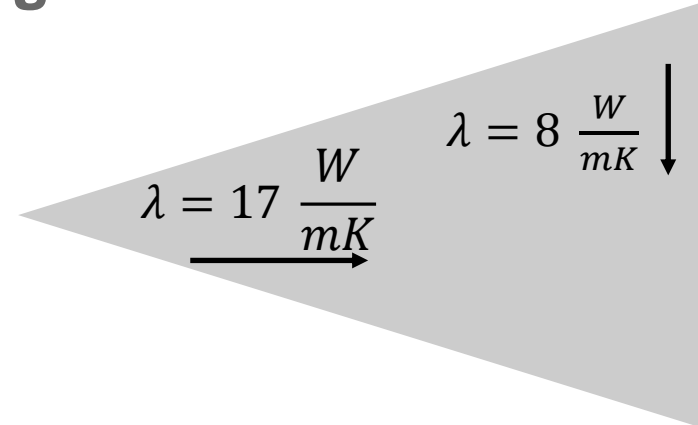
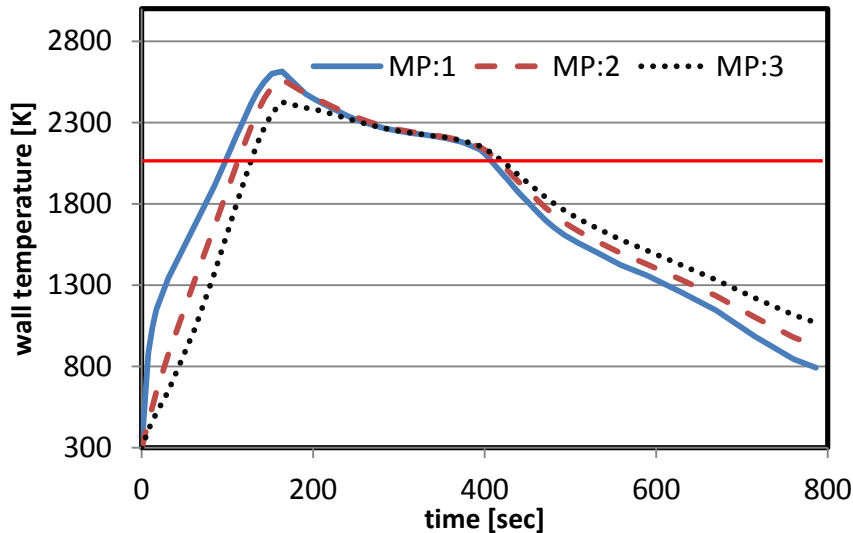
- constraint: mean instead of local heat transfer coefficient is used

Reference points are:

- MP1: at the tip
- MP2, 3, 4 are 2mm below the surface in a distance of 20mm, 50mm and 100mm from the tip



Radiation cooled leading edge: C/C-SiC



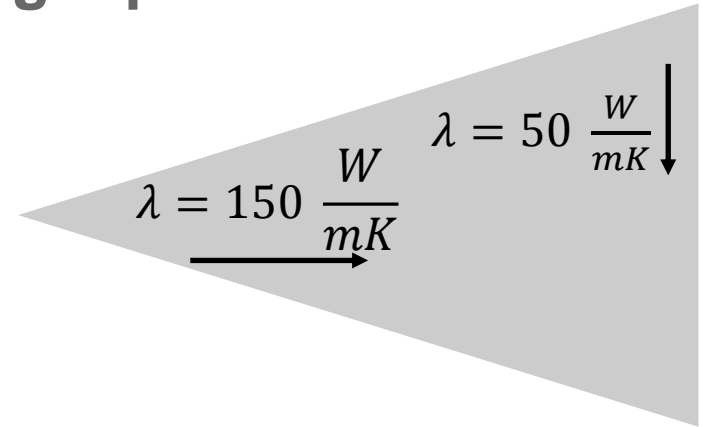
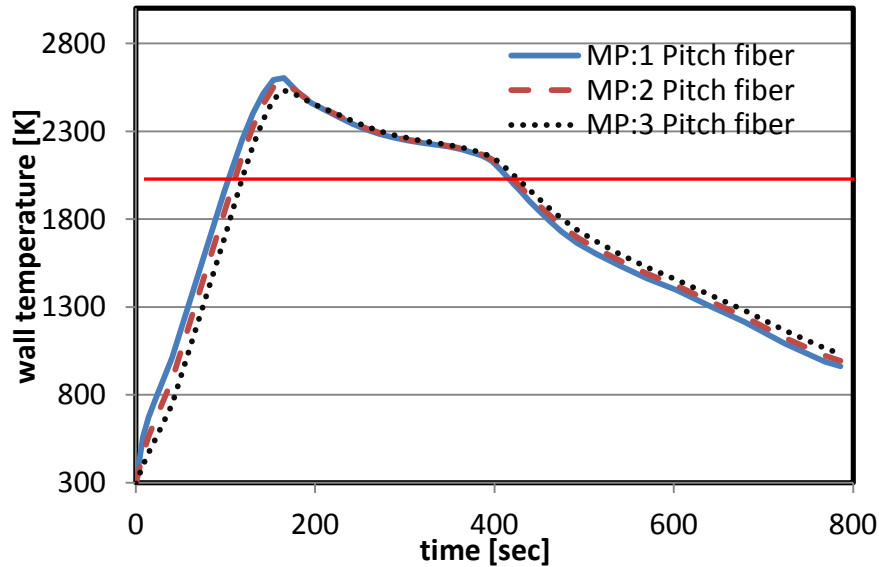
- standard material at DLR Stuttgart
- already used in flight as heatshield (TPS) on SHEFEX II

Boundary conditions are:

- convection, mean h and T_r
- radiation, $\epsilon = 0,85$



Radiation cooled leading edge: pitch fiber



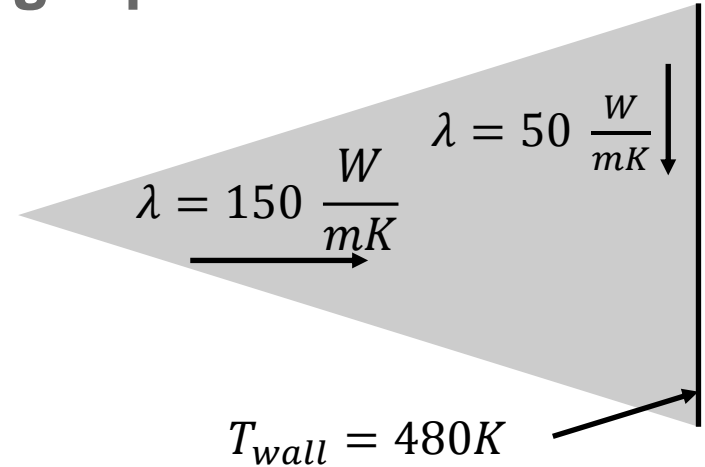
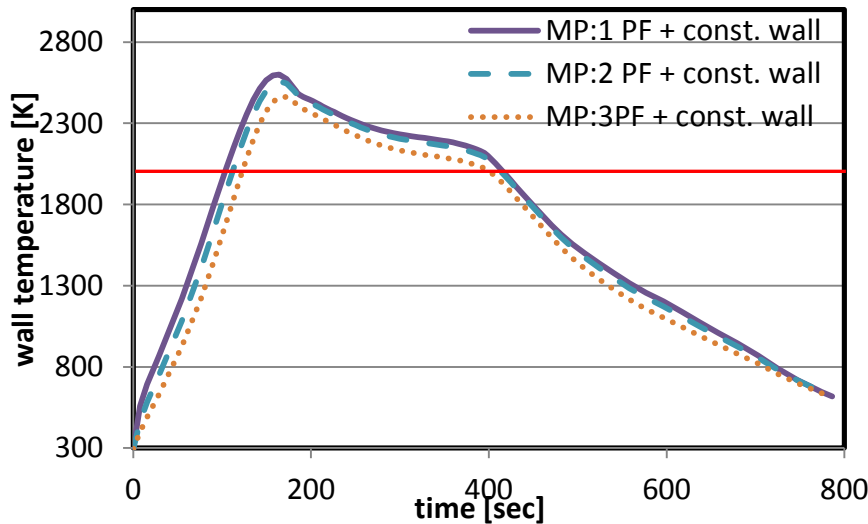
Idea: transport the heat away from the tip using the very high thermal conductivity

Boundary conditions are:

- convection, mean h and T_r
- radiation, $\varepsilon = 0,85$



Radiation cooled leading edge: pitch carbon fiber



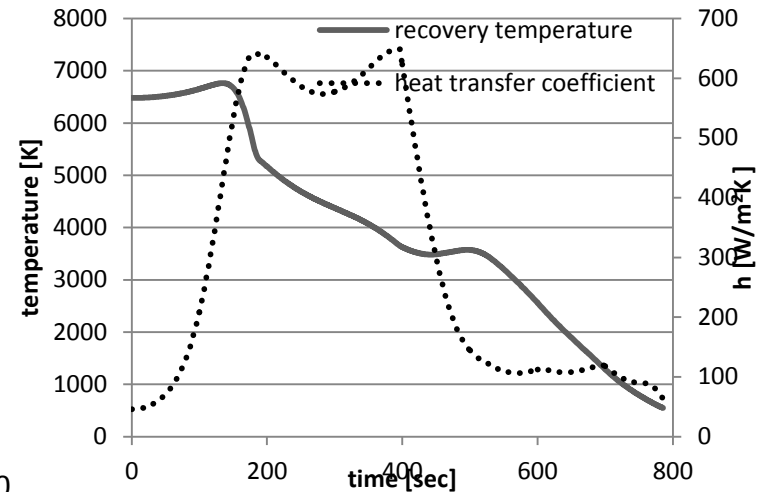
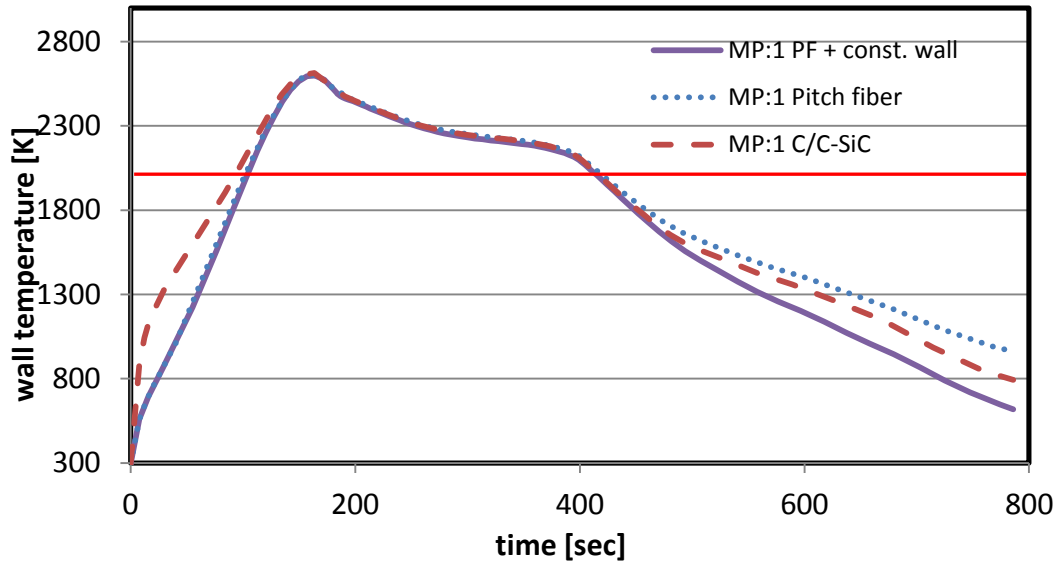
Idea: transport the heat away from the tip using the very high thermal conductivity

Boundary conditions are:

- convection, mean h and T_r
- radiation, $\varepsilon = 0,85$



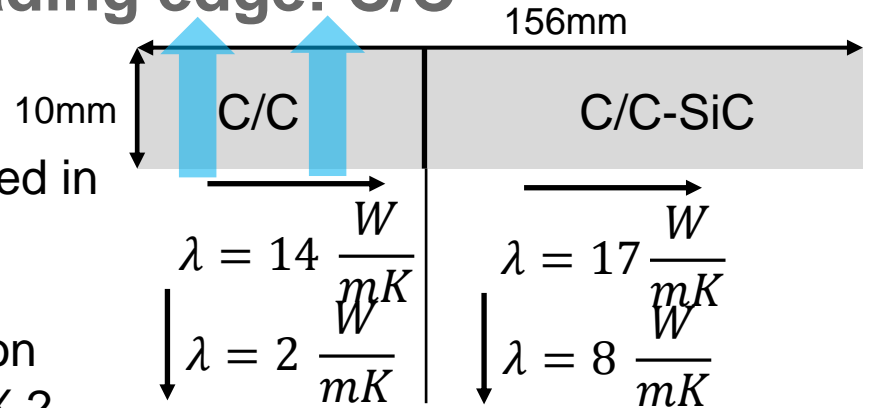
Radiation cooled leading edge: comparison



- no effect between 180s-400s
- heat loads during this time dictate the temperature
- material properties show their effect after 400s



Transpiration cooled leading edge: C/C

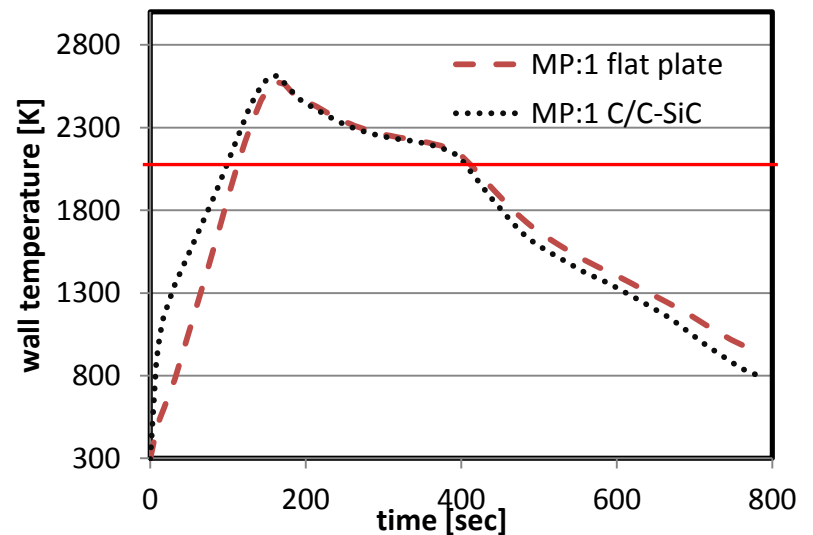


- transpiration cooling already tested in arc jet facilities
- AKTIV experiment: a transpiration cooled C/C tile flown on SHEFEX 2

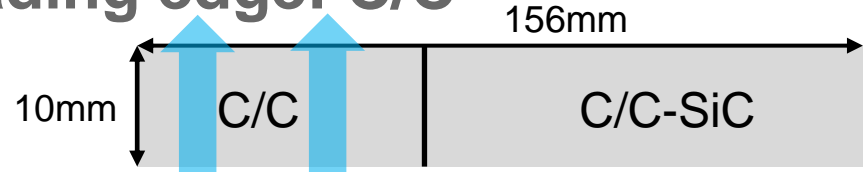
- model simplified to a flat plate
- max. temperatures are the same

Boundary conditions are:

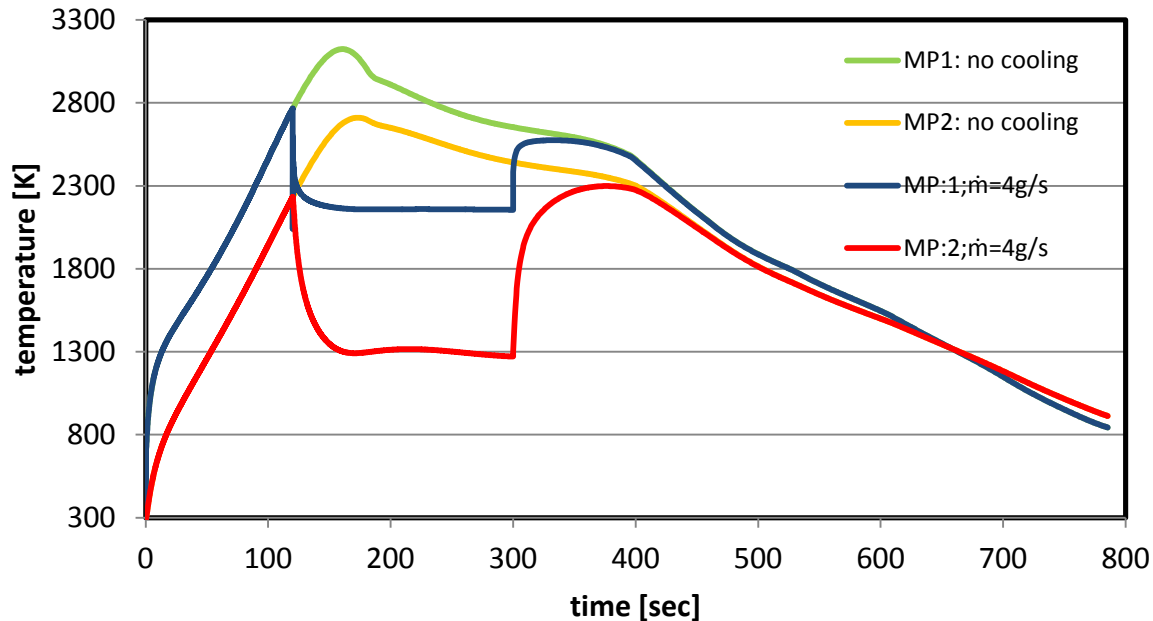
- convection, mean h and T_r
- radiation, $\varepsilon = 0,85$



Transpiration cooled leading edge: C/C



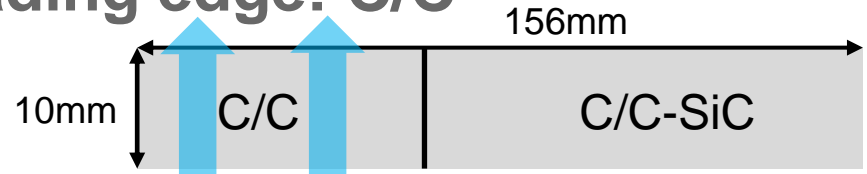
- cooling from 120s-300s
- cooling gas is nitrogen with 4g/s
- wall temperatures determined with local heat transfer coefficient



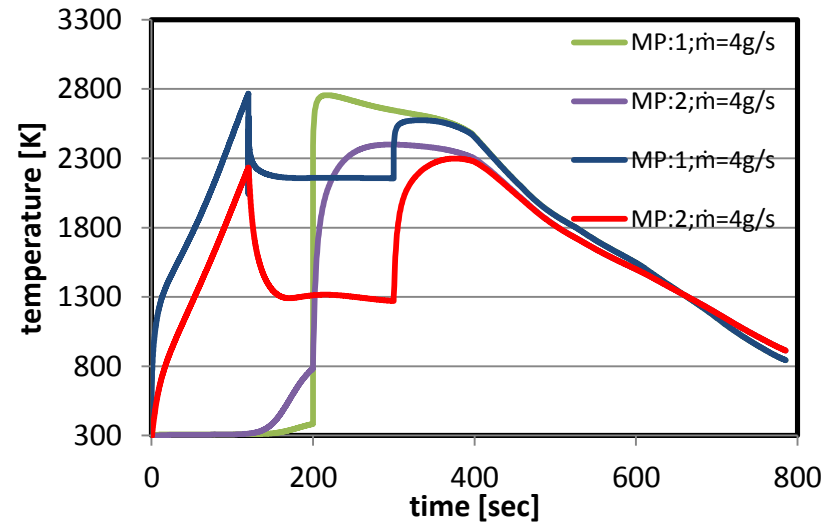
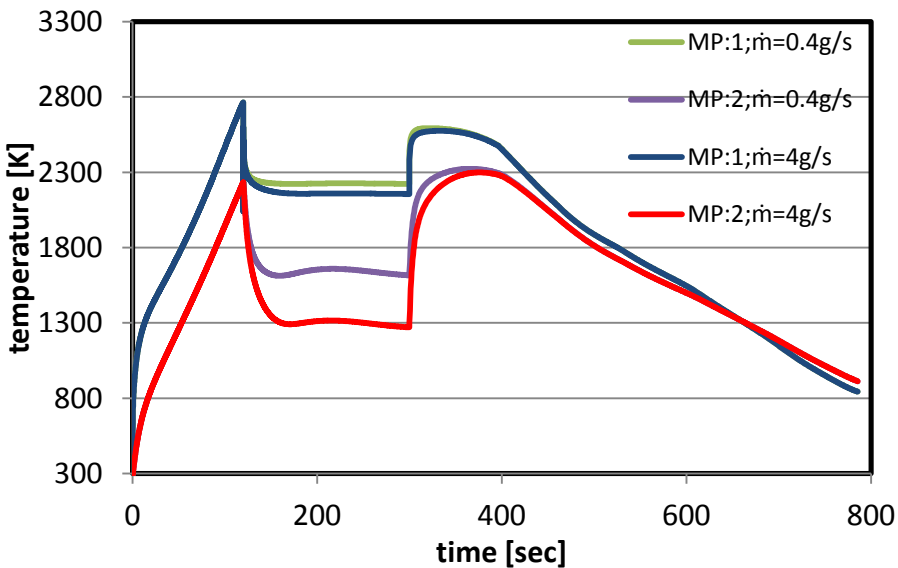
- transpiration cooling reduce the wall temperature immediately



Transpiration cooled leading edge: C/C



- cooling effect can be controlled by different parameters e.g. mass flow, or cooling time



Assessment and Problems

Radiation cooled leading edge: C/C-SiC

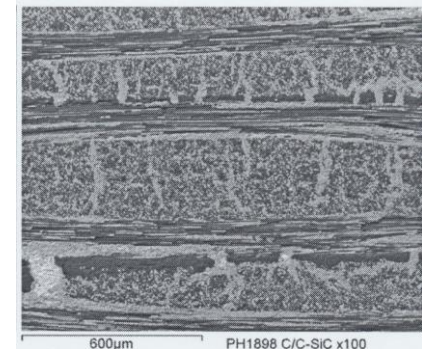
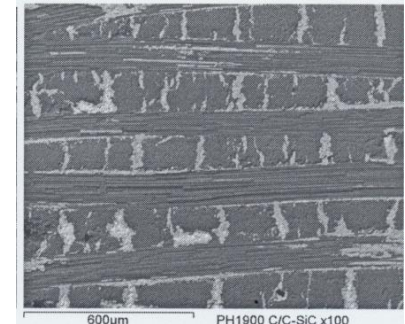
- pro: material investigated, already used as TPS
- contra: heat loads might be to high

Radiation cooled leading edge: pitch fiber

- pro: effect to transport the heat is clearly visible for constant wall temperature
- contra: heat loads might be to high, and material development just started

Transpiration cooled leading edge: C/C

- pro: has the ability to face these high heat loads
- pro: material and concept investigated and tested in flight
- contra: cooling system more complex, higher failure risk



Source:
Dr. Jens Schmidt
DLR, 2010



Next steps

- HEATS transpiration code should be expanded for wedge geometry
- more calculations with variation of parameters
- design update
- material and cooling concept test in arc jet facilities



Thank you for listening!

Do you have any questions?



ASTRIUM's TPS & HS Materials on SHEFEX II - Experiment Description & Flight Evaluation -

Wolfgang P.P. Fischer

*ASTRIUM GmbH - Space Transportation
Airbus-Allee 1
29199 BREMEN, Germany
Email: wolfgang.fischer@astrium.eads.net*

INTRODUCTION

SHEFEX II (SH II) test bed has flown recently a Ma 12 trajectory on top of a sounding rocket launched from Andoya, Norway.

On this vehicle ASTRIUM has tested several TPS and HS materials under real flight conditions.

The work started some years ago with the selection of materials and the design and analyses of in total 4 experiments. Materials selected are based on C/SiC (fiber reinforced ceramic composite) for high temperature applications, oxide ceramic composite for medium temperature and metallic components for moderate temperatures.

Taking into account the specific conditions for SH II the experiments have been manufactured and integrated on the SHII capsule. Flight acceptance has been performed successfully.

The launch campaign took place in June 2012 in Andoya, Norway with a successful flight towards the north pole and landing in sea south west Svalbard.

Telemetry data for the vehicle as well as for the experiments were successful acquired during flight.

This paper provides a description of the ASTRIUM experiments and gives some information about the SHEFEX II flight.

LOCATIONS OF ASTRIUM'S EXPERIMENTS ON SH II

The experiments are located as follows:

- SICTEX → panel B2
- MetTPS → panels E1 & E2
- SPFI → panel d2
- C/SiC → panel B3

The locations are depicted in Fig. below.

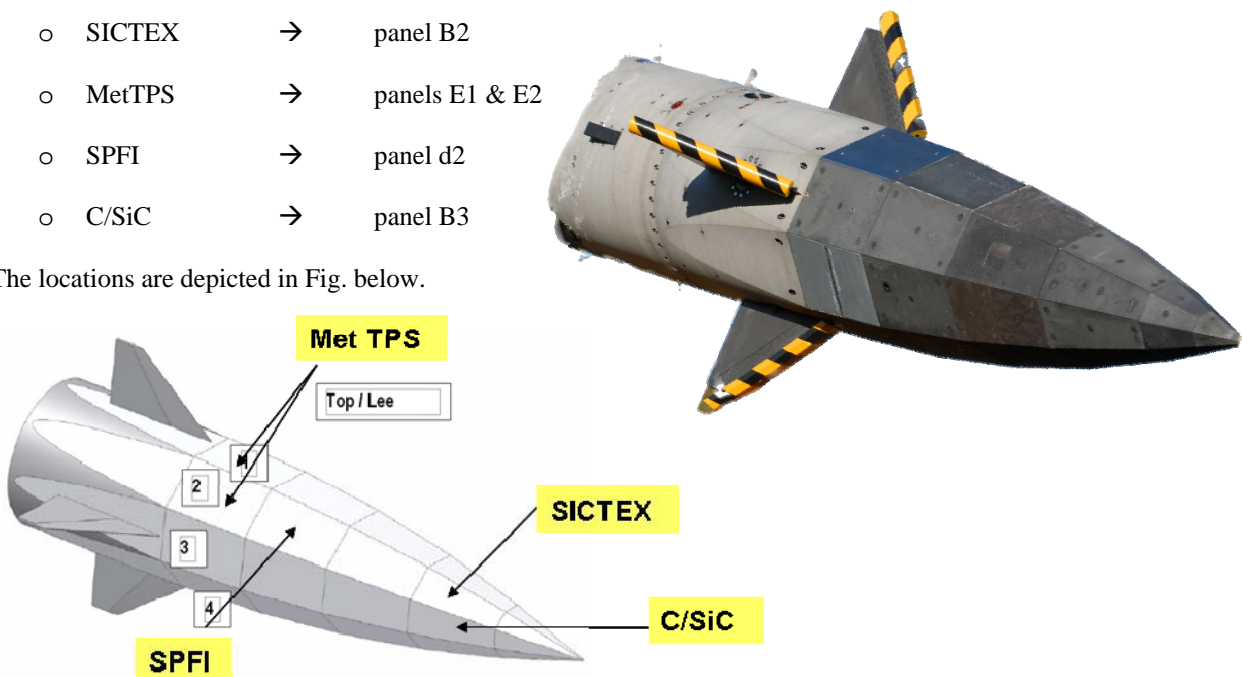


Fig. 1: Locations of ASTRIUM's TPS Experiments

DESCRIPTIONS OF EXPERIMENTS

SPFI Ox/Ox Ceramic TPS Experiment

SPFI TPS-Panel Technology

SPFI is based on an FEI-1100 blanket whose components (fabrics, threads, felt) consist of ABS ceramic materials. The outer surface of this blanket is covered by a thin CMC (Ceramic Matrix Composite) sheet to provide aerodynamic smoothness as well as pressure tightness. On the outer surface of this sheet a coating is applied to protect the CMC against the degrading environment and to provide adequate thermo-optical properties (i.e. absorptance, emittance). Depending on mission requirements the interior of the SPFI as well as the external surface can be water-proofed to minimize water absorption during mission preparation and launch of the vehicle. The SPFI is glued to the substructure of the vehicle to be protected by a room temperature vulcanizing adhesive. This supports easy integration and maintenance of this TPS.

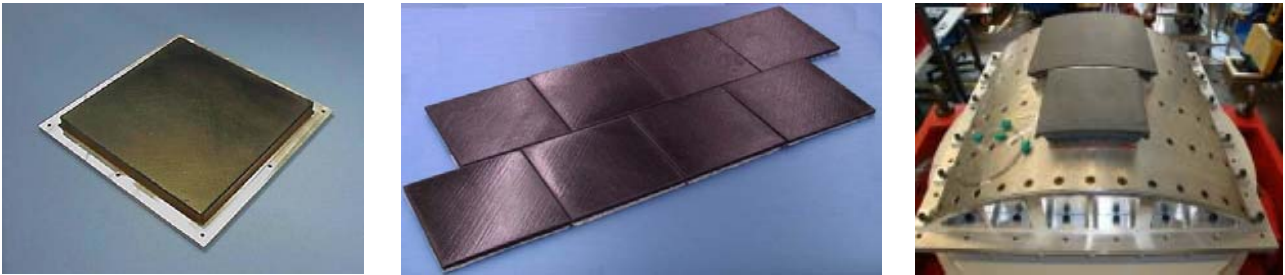


Fig: 2: Pictures of SPFI Panels and Arrays.

SPFI Experiment Design

The SPFI experiment design comprises a flat panel of trapezoidal shape with a thickness of 30mm. This panel will be glued directly to the aluminum substructure panel of SH II. The shape of the panel is depicted in Fig. below.

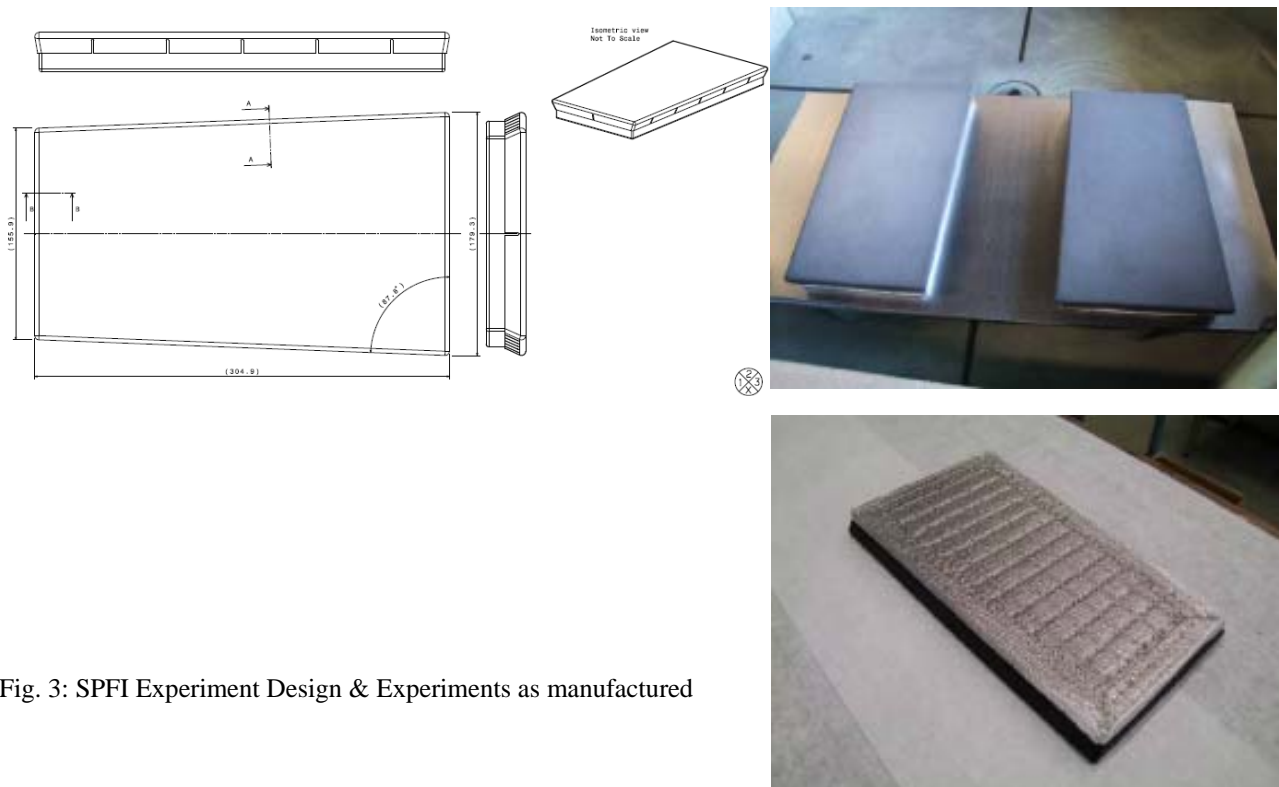


Fig. 3: SPFI Experiment Design & Experiments as manufactured

MetTPS Experiment on the Basis of the MERIT-Concept

MetTPS-Panel Technology

The sketch depicted below shows all parts of the chosen MERIT metallic TPS panel assembly design without micro-fibre insulation and sneak flow seal.

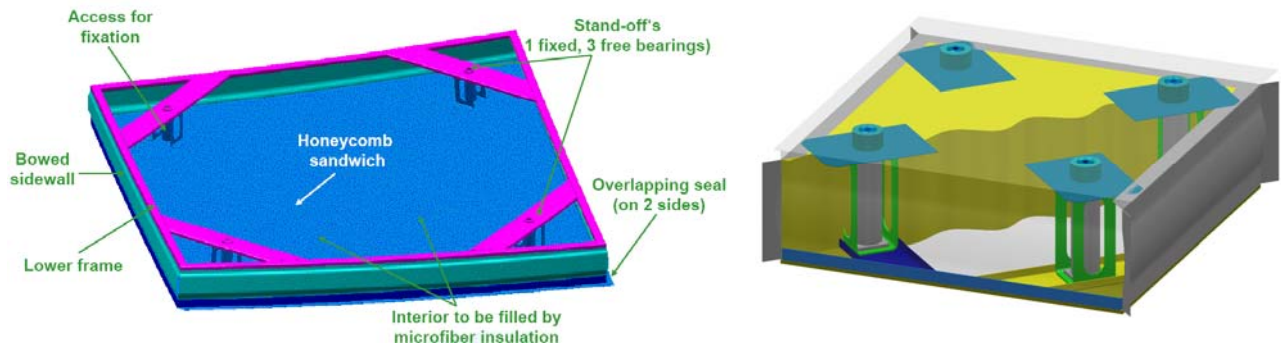


Fig. 4: Layout of metallic TPS

The honeycomb panel overlaps the neighbouring TPS panels at 2 sides with the outer face sheet. At the stand-off (S/O) locations inserts are brazed to the honeycomb (HC). These inserts are for the closure caps which enable access of tools to the screws for panel fixation.

So-called Ω -stand-off's (S/O's) were selected in order to compensate relatively large thermal expansions in the lateral direction. In the perpendicular direction higher stiffness is required to guarantee the outer aerodynamic shape of the panel. These S/O's are fixed to the inner face sheet of the HC via patches reinforcing this area. At the lower end the S/O's are screwed to the substructure of the vehicle.

All high temperature parts like HC, S/O, inserts and closure caps are made from β -21S material.

The lower frame, made from Titanium is a lightweight thin-walled foil and spot-welded construction. It serves to fix the side and back wall as well as provides a rigid interface (I/F) to the substructure of the vehicle.

Between the lower frame and the substructure a silicon-foam seal is clamped acting as a sneak flow barrier and providing certain structural damping characteristics.

The side and back walls are made of thin-walled Nickel foils since they are also subjected to high temperatures and are fixed to the HC and lower frame. Thin foils are needed here in order to minimise the heat flux from the HC to the substructure.

The entire interior of the panel is filled by a micro fibre insulation especially developed and optimized by ASTRIUM, Bremen.

Underneath the overlapping between adjacent TPS panels seals made of ceramic fabric sleeves filled by the same micro fibre insulation as for the panel but with higher density are incorporated. These seals should avoid hot gas ingress.

MetTPS Experiment Design

The MetTPS experiment design comprises two flat panels of trapezoidal shape with a thickness of 30mm. Between the panels a sealing system is incorporated to avoid hot gas ingress. These panels will be screwed directly to the aluminum substructure panel of SH II. The shape of the experiment is depicted in Fig. below.

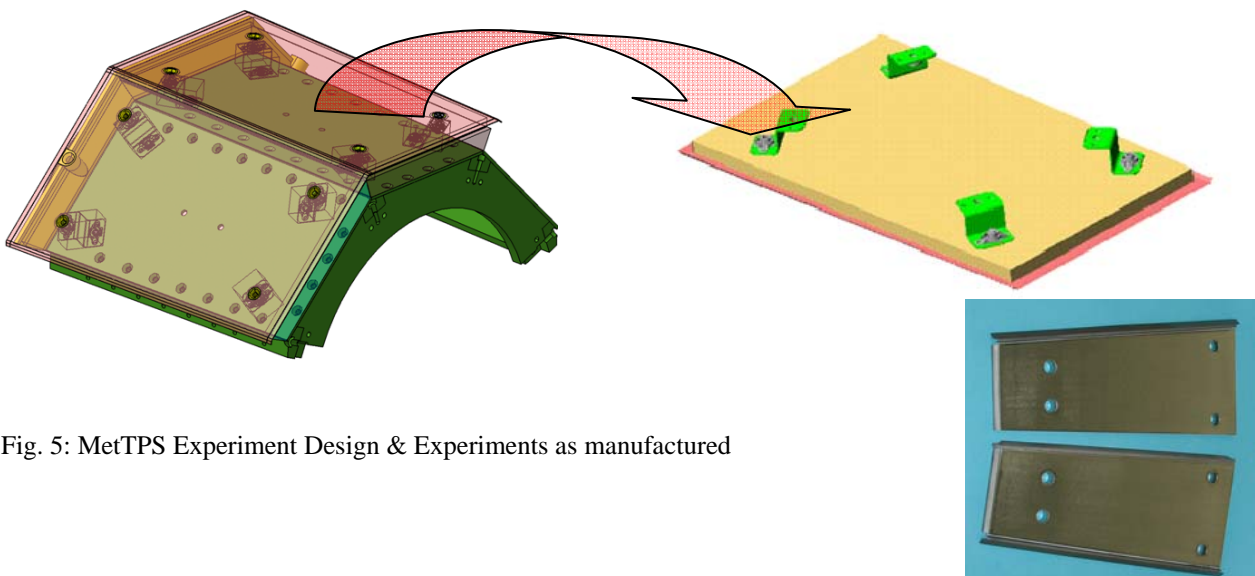


Fig. 5: MetTPS Experiment Design & Experiments as manufactured

C/SiC-Ceramic TPS experiment

C/SiC-Ceramic TPS-Panel Technology

C/SiC TPS is a CMC generally used for high temperature applications. This TPS is being developed/investigated into for use on the nose cone and wings leading edge of RLV as it retains high strength and stiffness at high temperatures. C/CiS is manufactured from Ceramic Silicon Carbide. It is fabricated as a single piece that is, no connection is needed between the panel and standoff as they are apart of the same structure and are made from the same material. It has a constant thickness of 2.4mm throughout and is fixed to the substructure through five stand-offs. The empty space between the panel and the structure is filled with micro fibre insulation to limit the temperature (during the experimental phase) below 100°C. Some examples of different panels used in previous programs are given in Fig. below.

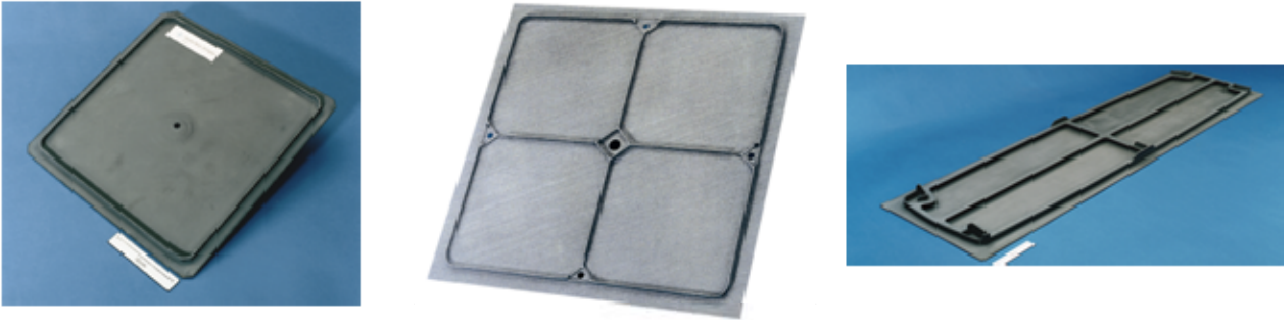


Fig. 6: Examples of different C/SiC Panels

C/SiC Ceramic Experiment Design

The C/SiC Ceramic experiment design comprises one flat panel of trapezoidal shape with a total thickness of 30mm. The panel will be screwed directly to the aluminum substructure panel of SH II. The shape of the experiment is depicted in Fig. below.

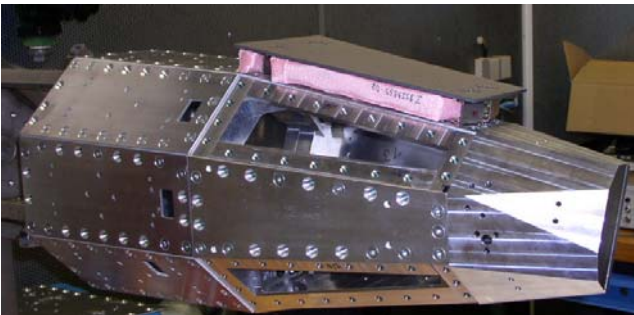
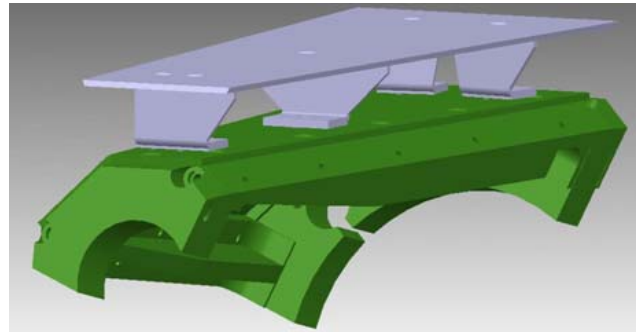
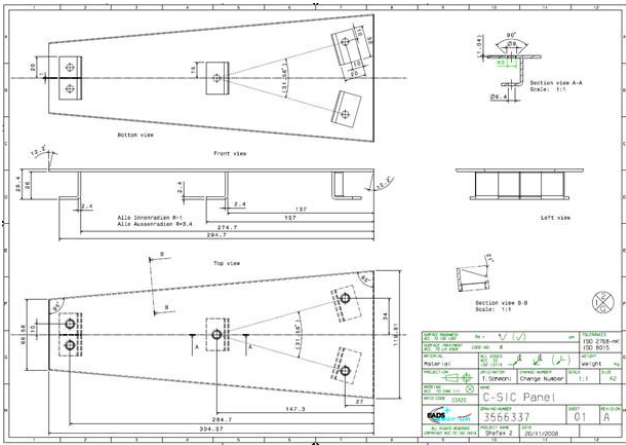


Fig. 7: C/SiC Ceramic Experiment Design & Experiment as manufactured and integrated on SH II

SICTEX-Ceramic TPS experiment

SICTEX -Ceramic TPS-Panel Technology

SICTEX is an advanced 3D C/SiC. It's manufactured via braiding & stitching. For attachment to SH II substructure the DLR standard attachment system is used.



Fig. 8: SICTEX 3-D panel & Application Example as Engine Nozzle

SICTEX Ceramic Experiment Design

The SICTEX Ceramic experiment design comprises one flat panel of trapezoidal shape with a total thickness of 30mm. The panel will be screwed directly to the aluminum substructure panel of SH II using standard (DLR) interfaces. The shape of the experiment is depicted in Fig. below.

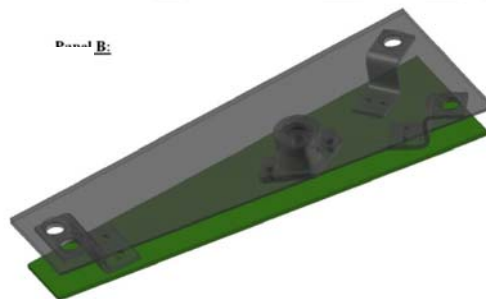


Fig. 9: SICTEX Ceramic Experiment Design (standard panel & DLR attachment design)

EXPERIMENT INTEGRATION ON SH II

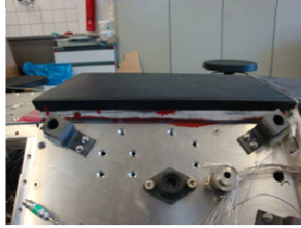
The integration of the ASTRIUM experiments on the SH II capsule took place in the SH II integration room at DLR Stuttgart in two campaigns. The experiments were fixed to the capsules outer surface using different attachment systems (see design description above). Instrumentation by thermocouples was done and the sensors were connected to the SH II internal data acquisition system.

Before launch the capsule together with experiments were put on top of the launcher in the Andoya rocket range preparation facility.

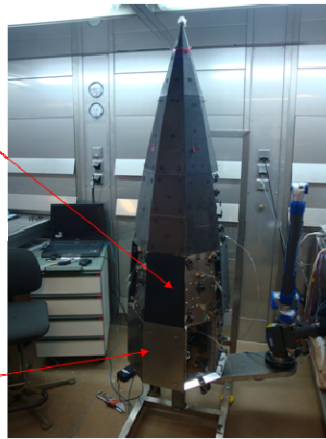
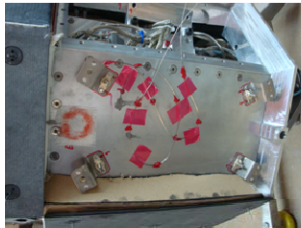
Some pictures showing integration details in Stuttgart and Andoya are given below.

DLR, Stuttgart

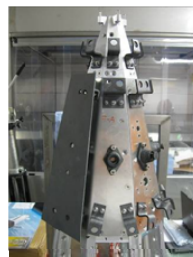
SPFI



MetTPS



SICARBON



SICTEX



Rocket Range, Andoya

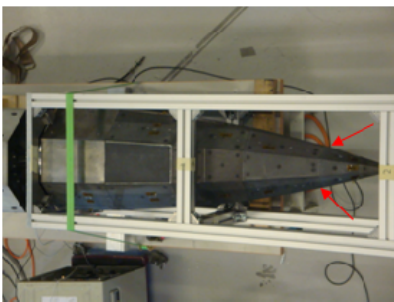


Fig. 10: Integration of ASTRIUM Experiments at DLR, Stuttgart and Andoya Rocket Range

SH II FLIGHT

The experiment flight of SH II took place on the evening of June 22nd 2012 from Andoya rocket range in Norway. The trajectory was heading towards the North Pole and landing site was around 1000 km away from Andoya. The flight duration was about 10 min and sea landing took place south-west of the island Svalbard.

The max. altitude was around 180 km and the flight velocity was exceeding Ma 12. Experimental time for the re-entry simulation was around 48s.

Unfortunately telemetry signal was lost shortly before parachute phase leading finally to a situation where it was not possible to recover the vehicle from sea.

Nevertheless all flight data especially during the experiment phase could be acquired and are currently under investigations.

Some pictures of the successful launch are given below.



Fig. 11: SHEFEX II Launch from Andoya Rocket Range

CONCLUSION

ASTRIUM has successfully performed the design, analyses, manufacturing and integration of 4 TPS experiments flown on SHEFEX II in June 2012 from Andoya, Norway.

Preliminary evaluation shows a successful overall performance of all the four different TPS & HS experiments.

Since the flight evaluation is still ongoing the original intention to present in this paper already flight evaluation data must be shifted unfortunately to a later date.

REFERENCES

- [1] Wolfgang P.P. Fischer et al; SPFI - A New TPS for Re-entry Vehicles; International Conference on Environmental Systems; Denver, CO, USA, July 1999
- [2] Wolfgang P.P. Fischer, Burkhard Behrens: "Development Status of TPS Candidates for Future RLV's", 3rd International Symposium Atmospheric Reentry Vehicles and Systems, Arcachon March 2003
- [3] Fischer, Wolfg. P.P., Metallic Thermal Protection System for Future RLV's, ICES Conf. 2002, San Antonio, TX, SAE-ICES paper 2002-01-2548
- [4] Fischer, Wolfg. P.P. et al, Metallic Thermal Protection System for Future RLV's. Design and thermo-mech. Analyses, ICES Conf. 2003, Vancouver, CA, SAE-ICES paper 2003-01-2469
- [5] B.Behrens, U.Rieck, W.D.Ebeling, FEI on X-38, ICES Conf. 1999, Denver, CO, USA, SAE-ICES paper 1999-01-2167
- [6] Fischer, Wolfg. P.P., ULTIMATE: Metallic Thermal Protection System for Future RLV's -Current Status of the Development, 5th European Workshop on Hot Structures and TPS, 2006, Noordwijk, The Netherlands
- [7] Fischer, Wolfg. P.P. et al, Metallic Thermal Protection System for Future RLV's -Design and Performance Verification Approach, ICES Conf. 2004, Colorado, Col, SAE-ICES paper 2004-01-2566
- [8] Fischer, Wolfg. P.P., Plasma Wind Tunnel Tests on a new TPS Material, 4th European Workshop on Hot Structures and TPS, 2002, Palermo, Italy
- [9] Fischer, Wolfg. P.P., ASTRIUM's TPS Experiments on SHEFEX II, 6th European Workshop on Hot Structures and TPS, 2009, Stuttgart, Germany

SUBMISSION REQUIREMENTS

Publication of a paper in the proceedings of the **7th European Workshop on Thermal Protection Systems and Hot Structures** is contingent upon the receipt of the electronic version of the paper in **PDF format by 26 April 2013**.

Papers are to be delivered by mail to the editor:

Esa.conference.bureau@esa.int

Contact Details

If you have any questions about preparing your paper, please contact the editor:

ESA Conference Bureau

Reference: Proceeding Editor TPS2013

Email: esa.conference.bureau@esa.int

All other questions concerning conference arrangements, fees, accommodation, etc., should be addressed to the ESA Conference Bureau, esa.conference.bureau@esa.int.

PAPER PREPARATION

Each paper is limited to a **maximum of 8 (eight) single-sided pages**. Prepare your paper using the following guidelines:

Margins: In order to achieve a paper-format independent print area of 17x23.4 cm (6.7x9.21 inches), please adjust your word processor to the following margins shown in Table 1.

Table 1. Recommended margins for the paper

Paper format:	US LETTER		A4	
Unit:	Inch	cm	inch	cm
Margin LEFT	0.90	2.29	0.79	2.00
Margin RIGHT	0.90	2.29	0.79	2.00
Margin TOP	1.00	2.54	1.00	2.54
Margin BOTTOM	0.79	2.00	1.48	3.76
PRINT Area Width	6.70	17.02	6.69	17.00
PRINT Area Height	9.21	23.39	9.21	23.40

Text: The text shall be organised in a **single column**, left and right justified. Use single spacing in the body of the text and double spacing between sections.

Font:
Text: Times New Roman
Variable: Times New Roman italic
Symbol: True Type Symbol font

Size:
Paper title: 12 pt bold (**TITLE**)
Author(s): 10 pt bold (**Author**)
Affiliation(s): 10 pt bold italic (*Affiliation*)
Normal text: 10 pt (regular text)
Text in tables: 9 pt
Symbols: 12 pt ($\Omega \cong \phi$)
Sub/super-script: 7 pt (x^y)

Tabs: Set the first three levels of tabs at 1 cm (0.39"), 2 cm (0.79") and 3 cm (1.18"). Set a right tab stop at 17 cm (6.69") for "flush-right" adjustment of equation numbers. Set a centre tab at 8.5 cm (3.55").

Headings: Chapter headings should be left aligned, double-spaced (one blank line before and after the heading) and printed in bold "**ALL CAPS**". Sub-headings should be left aligned and double-spaced in bold text with the main words capitalised ("**Title Case**"). Sub-sub-heads are left aligned in italic font with the main words capitalised ("*Title Case*").

Colour: **The proceedings will be produced in colour (CD ROM).**

Header/footer: The use of header/footer or footnotes is not recommended. Only NAVITEC 2008 shall appear as a footer as appears in this document

Title and Author Affiliation

The paper title, author(s) name(s), affiliation, complete mailing address and email should be centred at the top of the first page using the font as indicated above. If there are several authors, the complete affiliation should be given for each of them using superscript⁽¹⁾ in the authors⁽²⁾ list⁽³⁾ to refer to them.

Equations

Should be centred and number equations consecutively with equation numbers in parentheses flush with the right margin. To make your equations more compact, you may use the solidus (/), the exp function, or appropriate exponents. Italicise Roman and Greek symbols for quantities and variables. Use a long dash rather than a hyphen for a minus sign. Use parentheses to avoid ambiguities in denominators. Punctuate equations with commas or periods when they are part of a sentence. Be sure that the symbols in your equation have been defined before the equation appears or immediately following. Use “(1)” not “Eq. (1)” nor “equation (1)” except at the beginning of a sentence, then use “Equation (1) is....”. An example for an equation is:

$$T_s = \frac{T_b}{1 + (\lambda T_b / \alpha) \ln \varepsilon} \quad (1)$$

Figures and Tables

Position figures and tables at the top and bottom of pages. Figure captions should be below the figures; table captions should be above the tables. Avoid placing figures and tables before first mentioned in the text. Use the abbreviation “Fig.1,” even at the beginning of a sentence. All images must be embedded into your document. The type of graphics you include will affect the quality and size of your electronic paper.

An example for an image embedded in the document is given in Fig. 1. (Courtesy EUMETSAT)

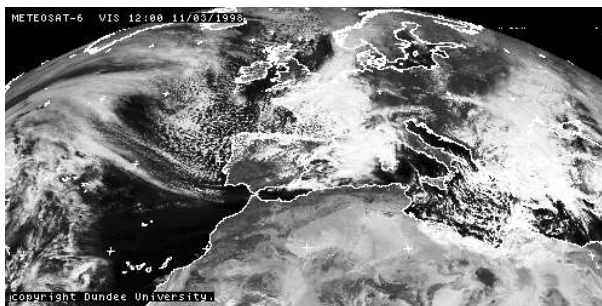


Fig. 1. Meteosat Visible channel showing clouds over Europe

Abbreviations and Acronyms

Define abbreviations and acronyms the first time they are used in text, even after they have been defined in the abstract. Abbreviations such as TTC, TM, TC, ac and dc do not have to be defined. Do not use abbreviations in the title unless they are unavoidable.

Page Numbering

Do not number the electronic paper.

REFERENCES

Number citations consecutively in square brackets [1]. The sentence punctuation follows the brackets [2]. Refer simply to the reference number, as in [3]. Do not use “Ref.[3]” or “reference [3]” except at the beginning of a sentence: “Reference [3] was the first....” The title of the book or the name of the journal shall be typed in italic.

Give all authors' names; do not use "et al" unless there are six authors or more. Papers that have not been published, even if they have been submitted for publication, should be cited as "unpublished" [4]. Papers that have been accepted for publication should be cited as "in press" [5]. For papers published in translation journals, please give the English citation first, followed by the original foreign-language citation [6].

Sample References

- [1] G. Eason, B. Noble, and I.N. Sneddon, "On certain integrals of Lipschitz-Hankel type involving products of Bessel functions," *Phil. Trans.. Roy. Soc. London*, vol. A247, pp. 529-551, April 1955.
- [2] J. Clerk Maxwell, *A Treatise on Electricity and Magnetism*, 3rd ed., vol. 2. Oxford: Clarendon, pp. 68-73, 1892.
- [3] I.S. Jacobs and C.P. Bean, "Fine Particles, Thin Films and Exchange Anisotropy," in *Magnetism*, vol. III. G.T. Rado and H. Suhl, Eds. New York: Academic, pp. 271-350, 1963.
- [4] K. Elissa, "Title of paper," unpublished.
- [5] R. Nicole, "Title of Paper," in press.
- [6] Y. Yorozu, M. Hirano, K. Oka, and Y. Tagawa, "Electron spectroscopy studies on magneto-optical media and plastic substrate interface," *IEEE Transl. J. Magn. Japan*, vol. 2, pp. 740-741, August 1987.

ASTRIUM's TPS & HS Materials on SHEFEX II



7th European Workshop on TPS & HS
ESTEC, Noordwijk, The Netherlands
Wolfgang P.P. Fischer // 08.-10. April 2013

This document and its content is the property of Astrium [Lu/SAS/GrmbH] and is strictly confidential. It shall not be communicated to any third party without the written consent of Astrium [Lu/SAS/GrmbH].

All the space you need



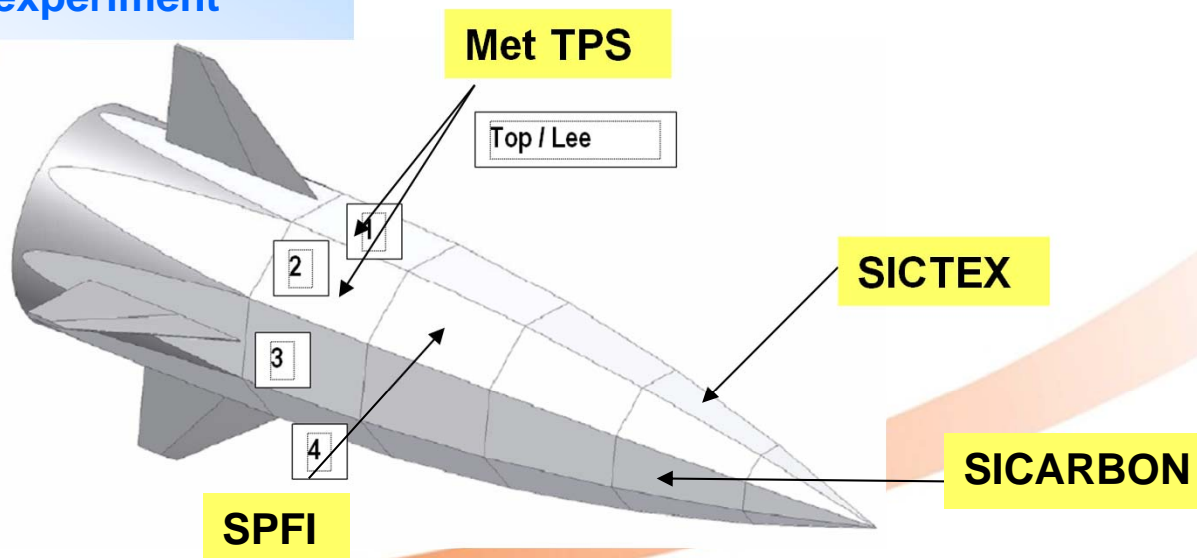
Outline

- **ASTRIUM EXPERIMENT LOCATIONS ON SH II**
- **EXPERIMENT DESCRIPTION (SPFI, MetTPS, SiCarbon, SICTEX)**
 - TPS & HS Technology
 - Experiment Design
 - Experiment Manufacturing
 - Experiment Location & Instrumentation
- **EXPERIMENT ANALYSES**
 - Thermal
 - Thermo-Mechanical
- **EXPERIMENT INTEGRATION**
- **SHEFEX II FLIGHT**
- **PRELIMINARY FLIGHT DATA**
- **ACKNOWLEDGEMENTS**



ASTRIUM Experiment Locations

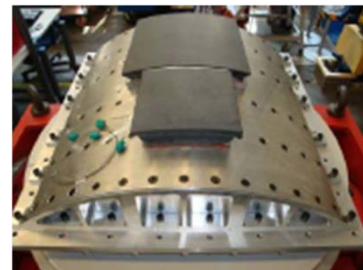
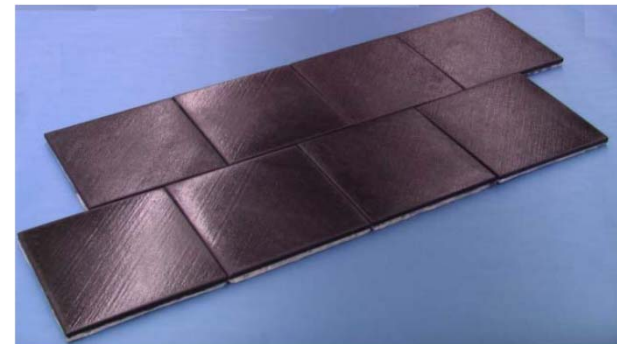
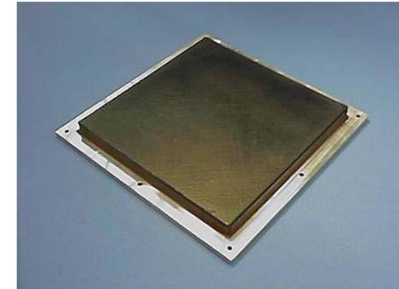
- SICTEX-ceramic TPS experiment
- MetTPS experiment on the basis of the MERIT-concept
- SPFI Ox/Ox ceramic TPS experiment
- SiCarbon-ceramic TPS experiment



Experiment Description

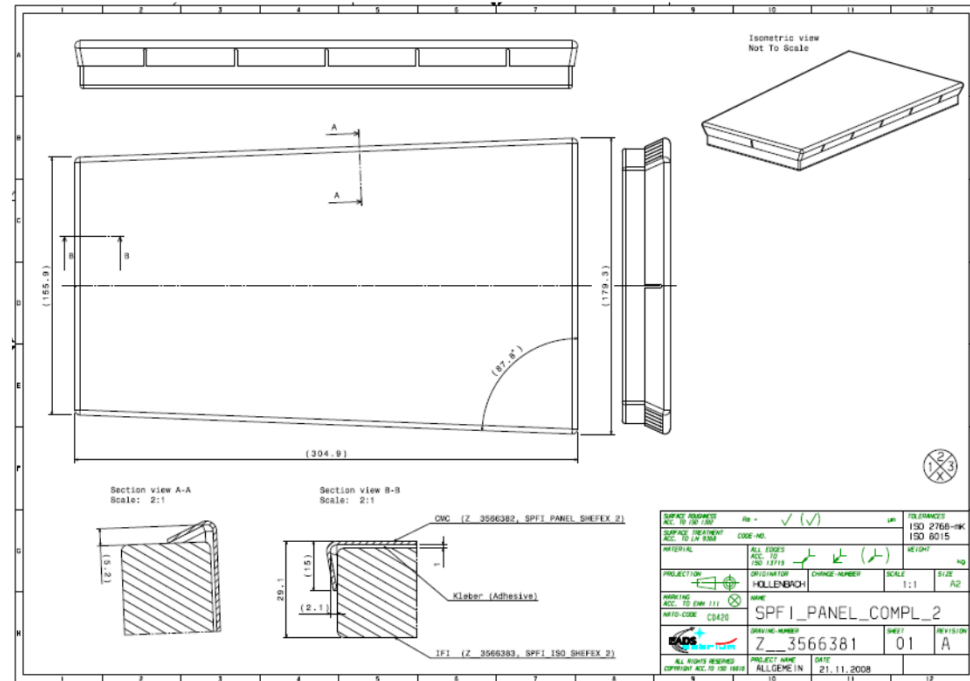
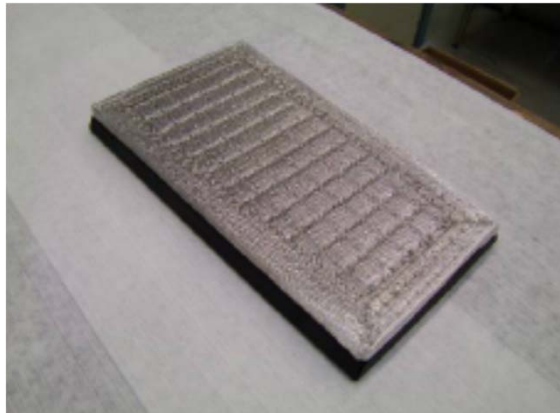
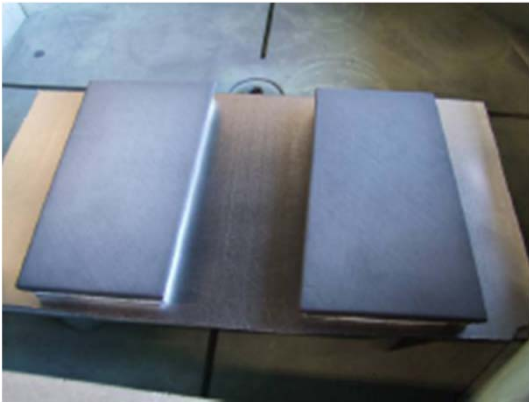
SPFI TPS-Panel Technology

- A thin CMC layer makes the underlying insulation blanket pressure-tight and provides a smooth aero-dynamical surface
- a coating on SIB6 basis generates corresponding thermo-optical properties
- The micro-fibre blanket provides the required insulation properties
- the SPFI panel is glued to the vehicle substructure by an RTV adhesive



Experiment Description

SPFI TPS Experiment Design

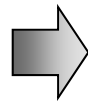


Experiment Description

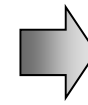
SPFI TPS Experiment Manufacturing



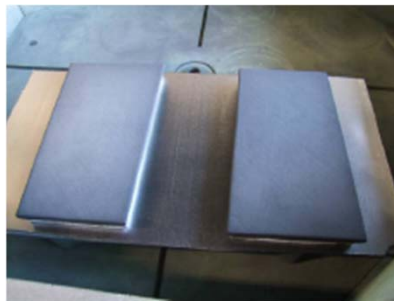
green body



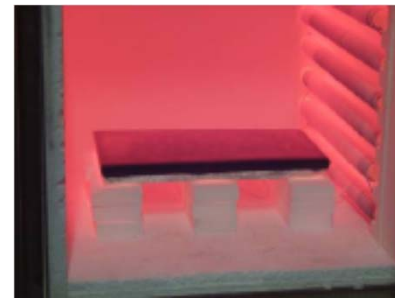
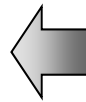
after pyrolysis



after coating



ready

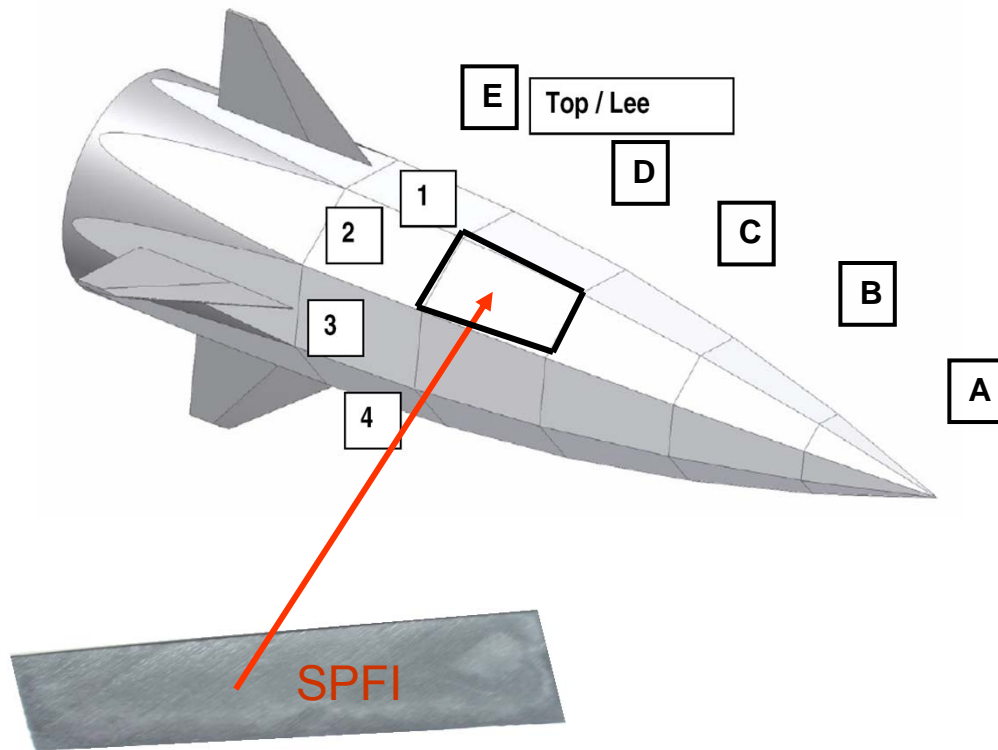


activation

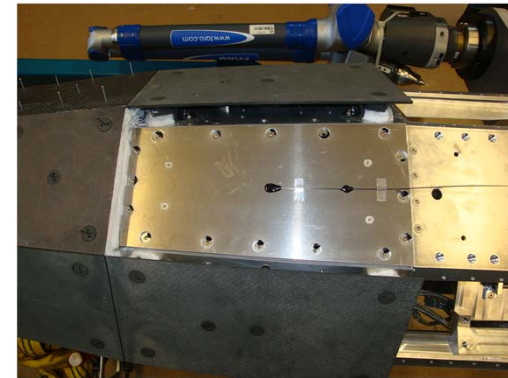


Experiment Description

SPFI TPS Experiment Location & Instrumentation



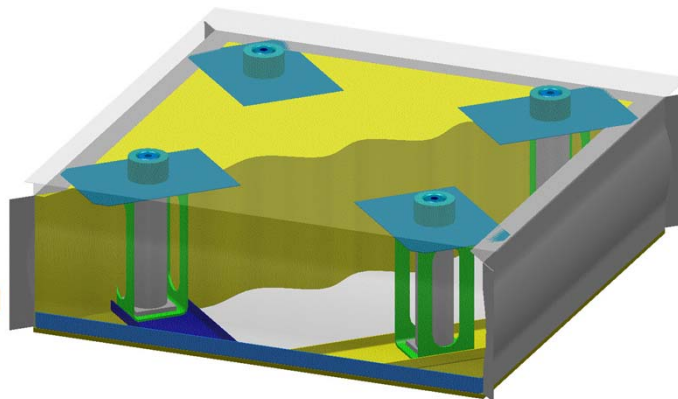
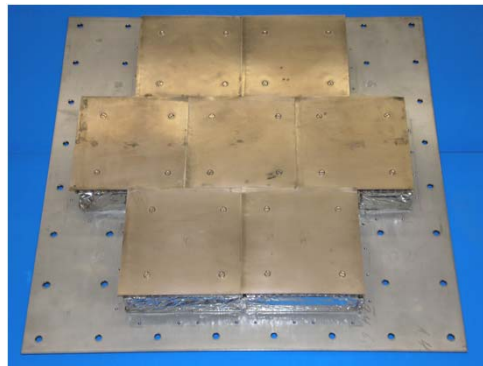
1 TC on substructure



2 TC's underneath CMC cover

Experiment Description

Metallic TPS-Panel Technology (Basis MERIT)

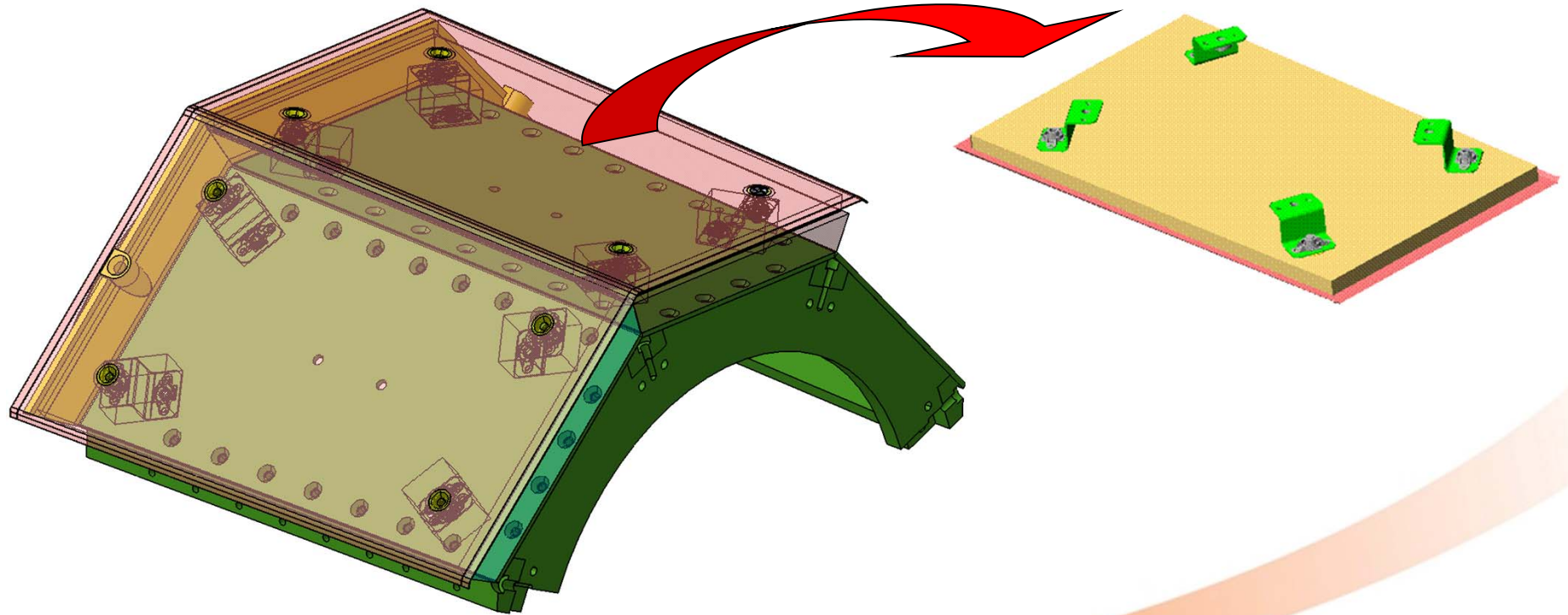


- based on honeycomb made from Ti beta 21S for up to 950° C
- all high temperature components are made from this material, rest is from aerospace Ti
- Each panel is fixed by S/O's to the substructure of the vehicle
- space between honeycomb and substructure is filled by a micro-fibre insulation



Experiment Description

Metallic TPS-Panel Experiment Design

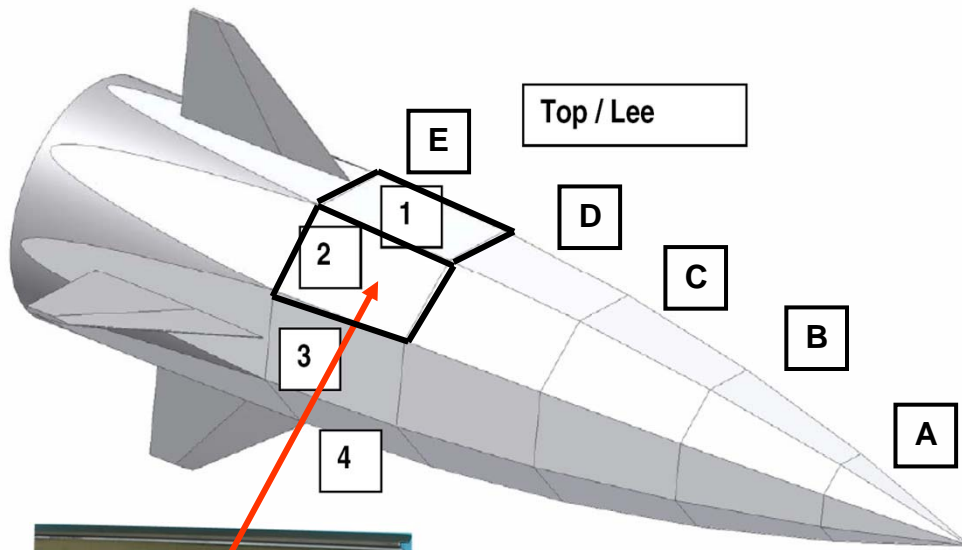


This document and its content is the property of Astrium [Lu/SAS/GmbH] and is strictly confidential. It shall not be communicated to any third party without the written consent of Astrium [Lu/SAS/GmbH].

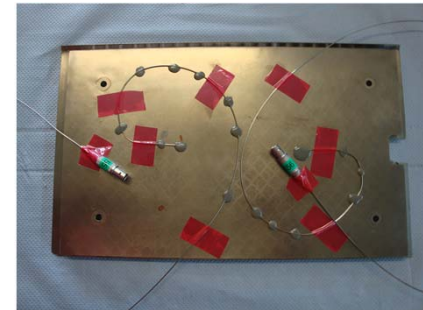


Experiment Description

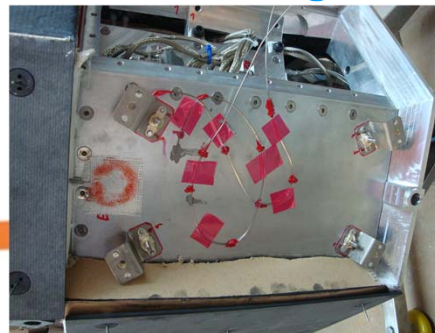
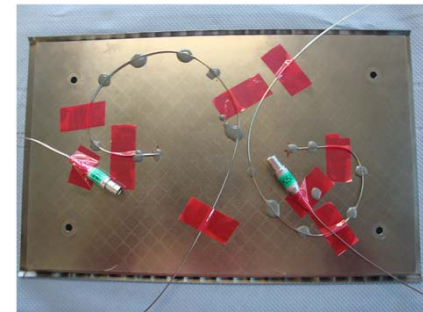
Metallic TPS Experiment Location & Instrumentation



1 TC on right forward S/O
1 TC close to right forward S/O



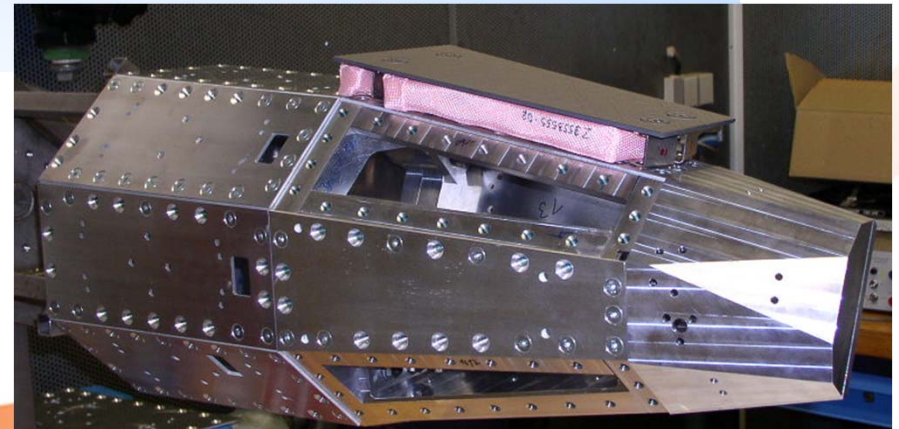
2 TC's underneath honeycomb



Experiment Description

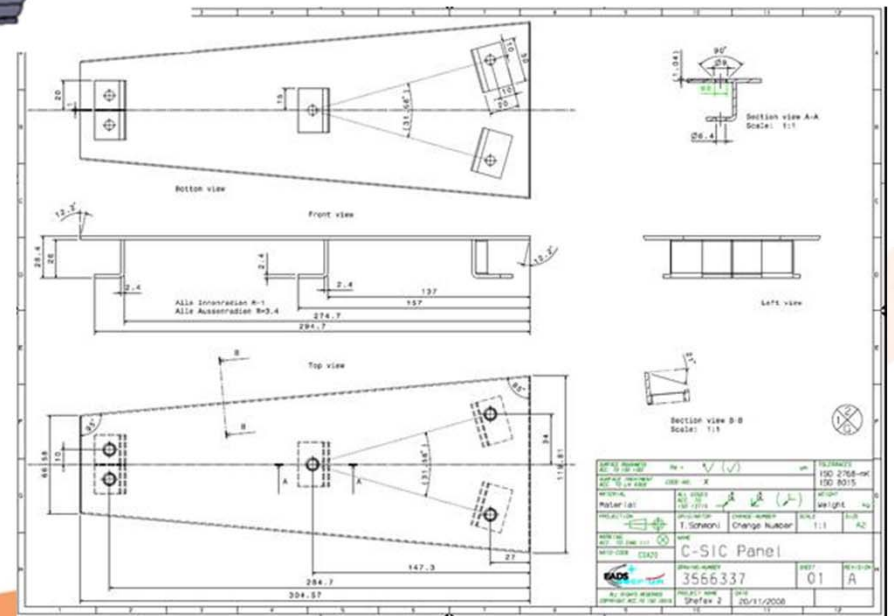
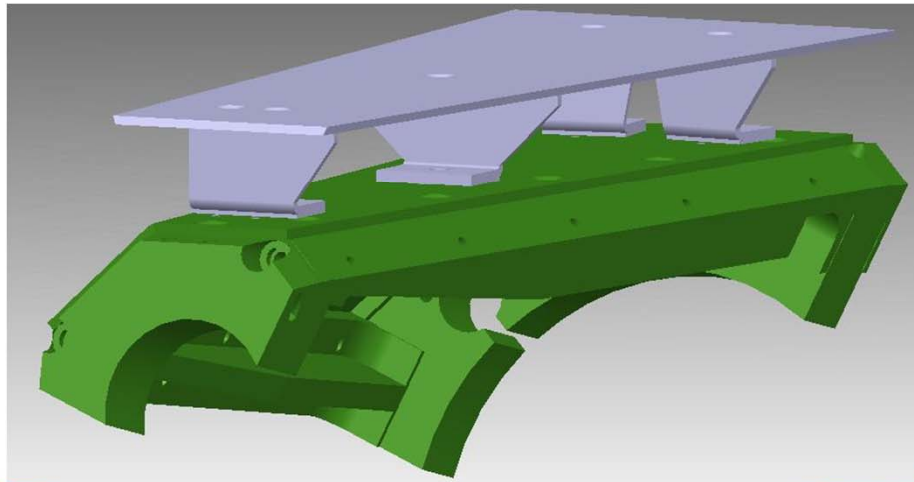
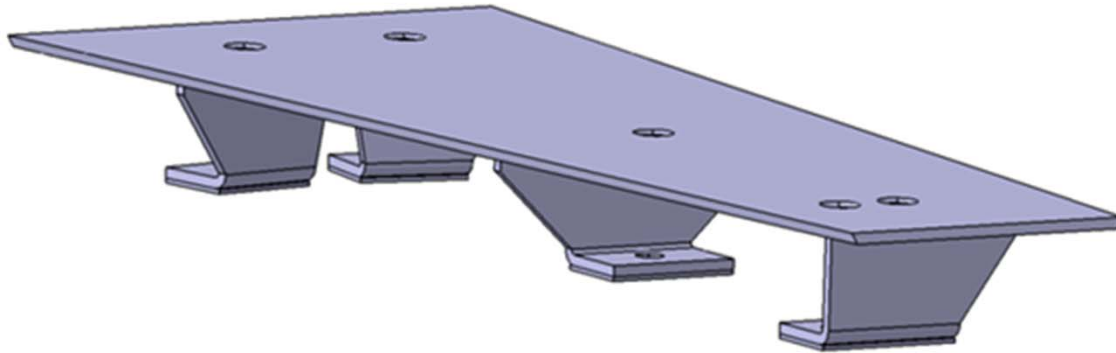
C/SiC TPS-Panel Technologie (SiCARBON®)

- Standard C/SiC CMC for HS & Panel TPS with 2.4mm thickness (applied already on SHEFEX I, X-38, et cet.)
- Made by LPI with deposition on rovings
- integral C/SiC attachment system with closure caps (external access) and metallic screws on substructure
- Standard SiC coating
- Sealing: DLR Whipox Seal



Experiment Description

SICARBON Experiment Design



This document and its content is the property of Astrium [LufSAS/GmbH] and is strictly confidential. It shall not be communicated to any third party without the written consent of Astrium [LufSAS/GmbH].

Experiment Description

SICARBON Experiment Manufacturing



green body (prepregs)
winding and lamination



after pyrolysis

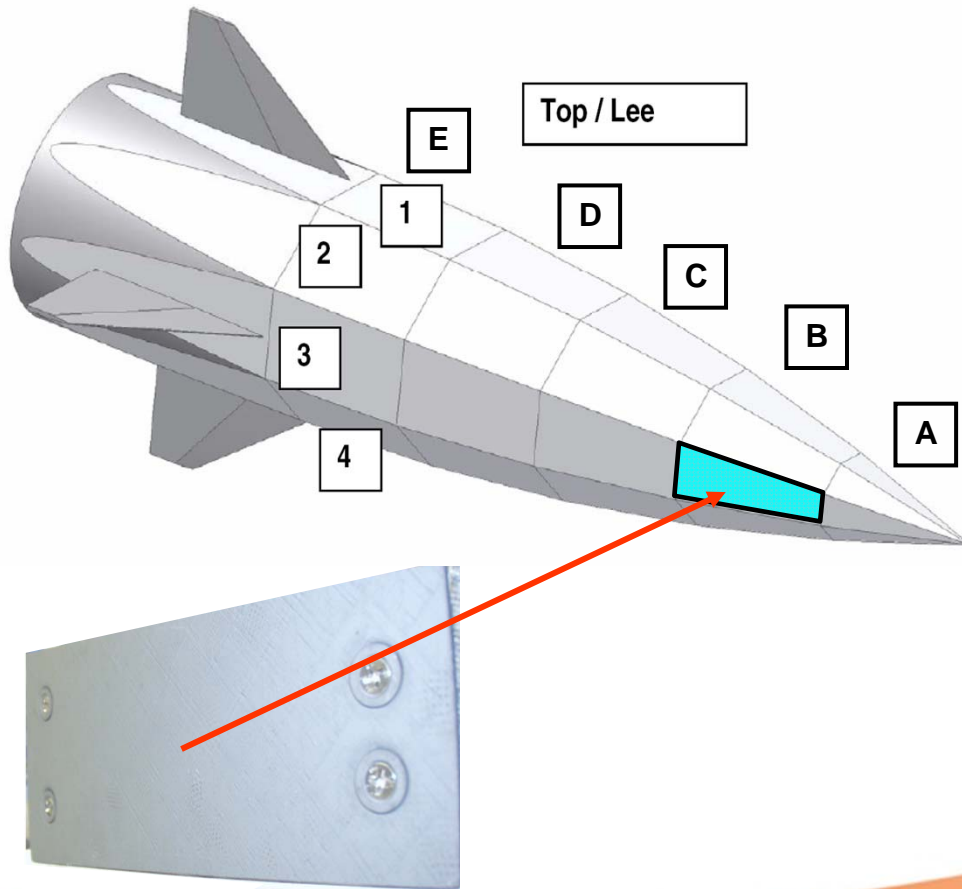


after machining & coating
incl. fixation elements

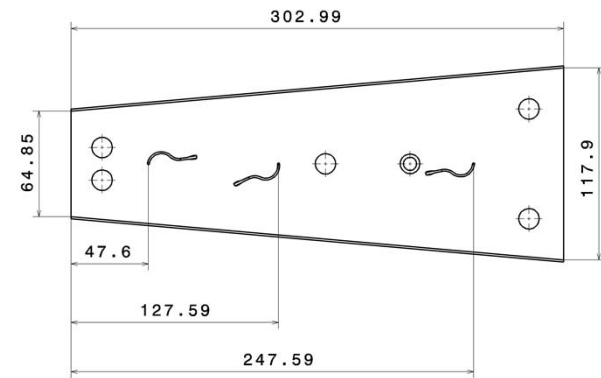


Experiment Description

SICARBON Experiment Location & Instrumentation



KeramikkacheIn B Thermoelement-Positionen (DLR)
Maßstab: 1:2



3 TC's within CMC (in grooves)

1 TC on substructure



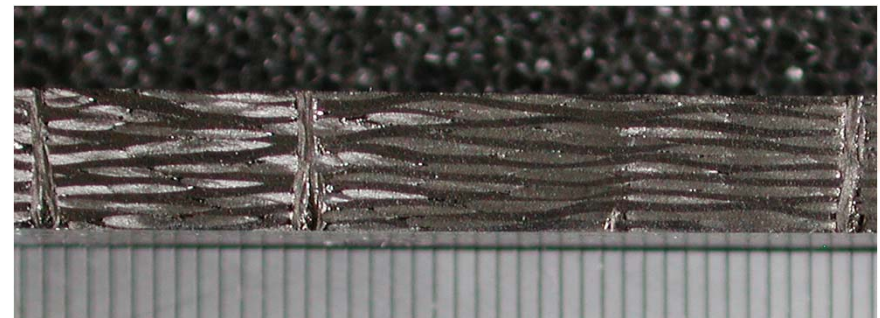
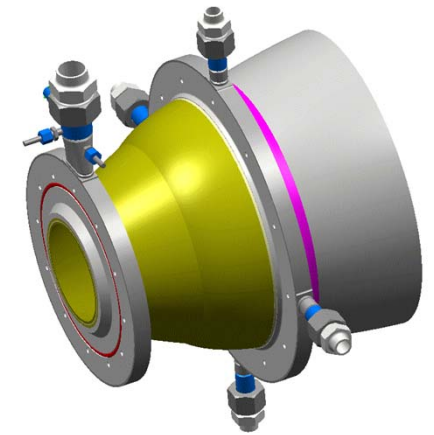
Experiment Description

SICTEX TPS-Panel Technology

- new 3D C/SiC CMC material for TPS
- application field for propulsion systems
- manufactured via braiding & stitching
- followed by resin infiltration and LSI
- elevated mechanical performance due to fabrication process and 3D reinforcements
- standard SiC coating



Exemplary image of braided structures for the Fuel-Cooled-Ceramic-Nozzle (FCCN) in Dual-Bell contour

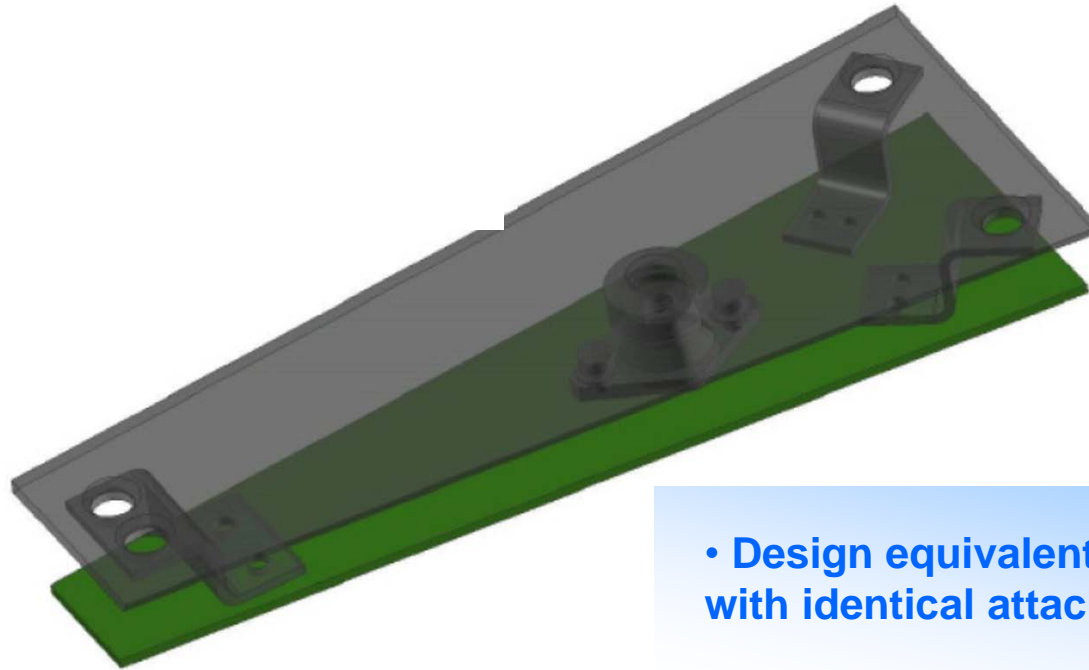


3D standard SICTEX specimen, side view



Experiment Description

SICTEX Experiment Design

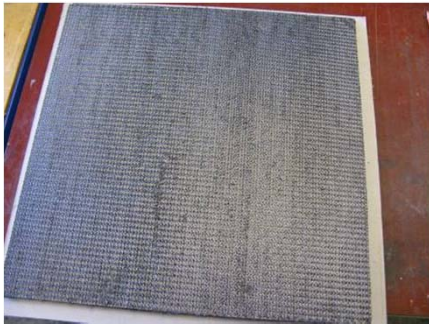


- Design equivalent to DLR ceramic-panels with identical attachment

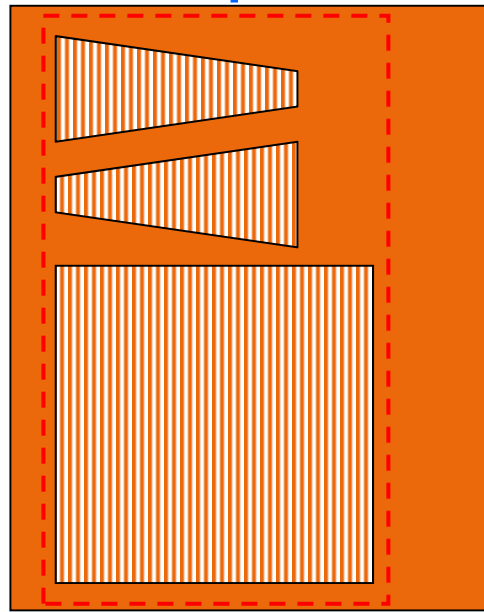
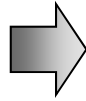


Experiment Description

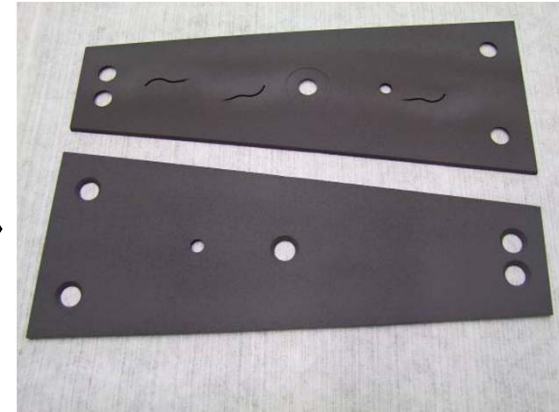
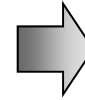
SICTEX Experiment Manufacturing



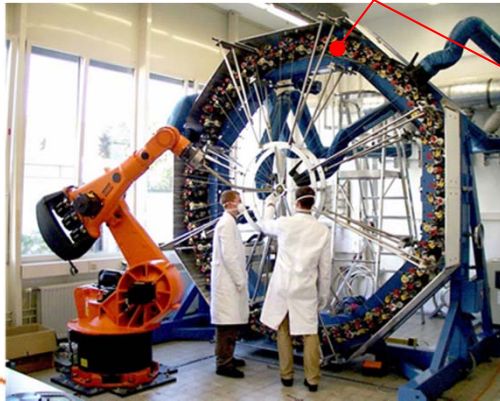
textile 3D-preform
Robotic-supported knitting,
Lay-up and sewing



cutting

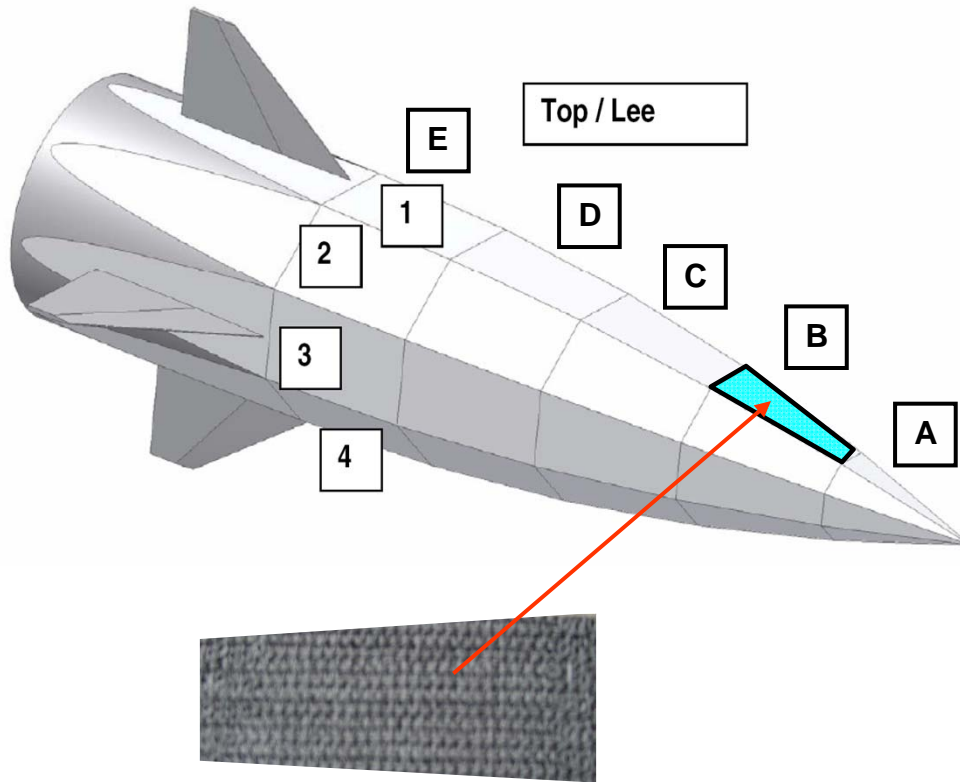


after liquid-phase siliconizing
& coating

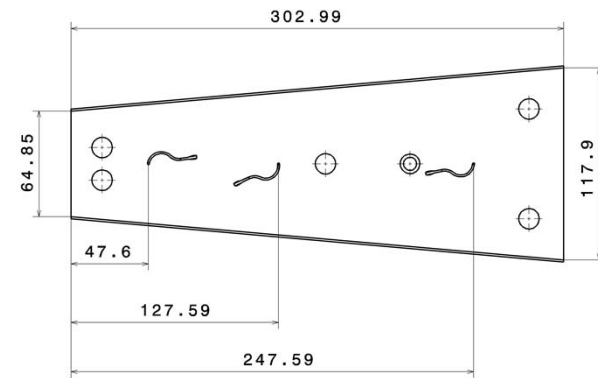


Experiment Description

SICTEX Experiment Location & Instrumentation



Keramikkacheln B Thermoelement-Positionen (DLR)
Maßstab: 1:2



3 TC's within CMC (in grooves)

1 TC on substructure

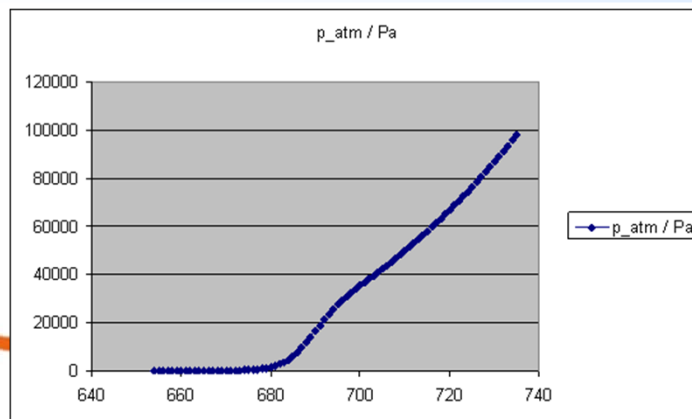
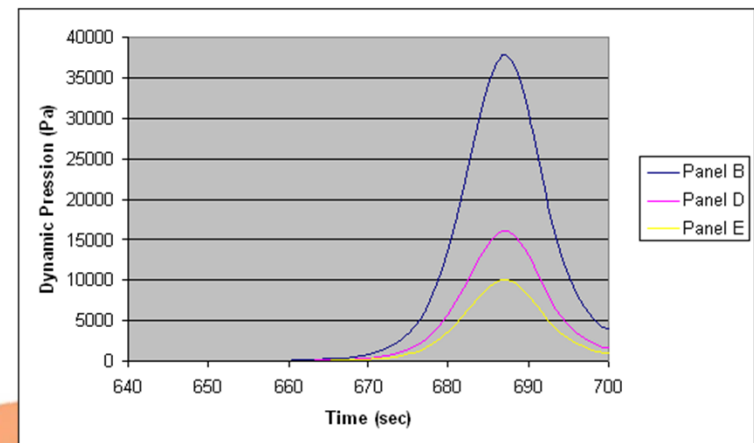
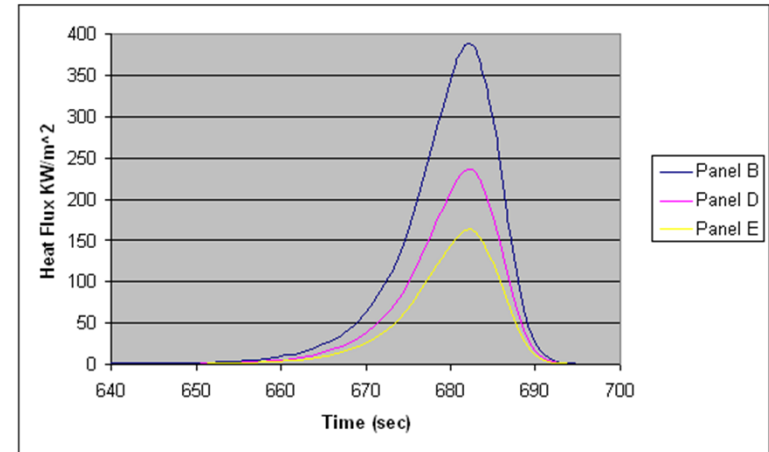


Experiment Analyses

Thermal Analysis

Boundary conditions

- Start temperature: 20° C
- Radiation background: 200K
- Experimental phase from t=650s to 685s
- Adiabatic I/F underneath substructure

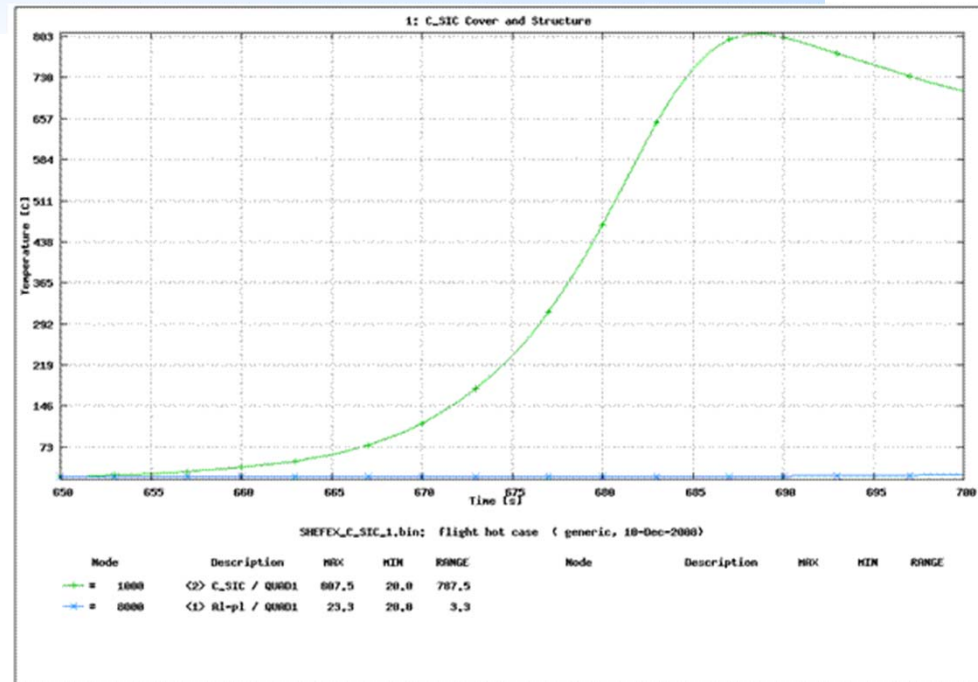
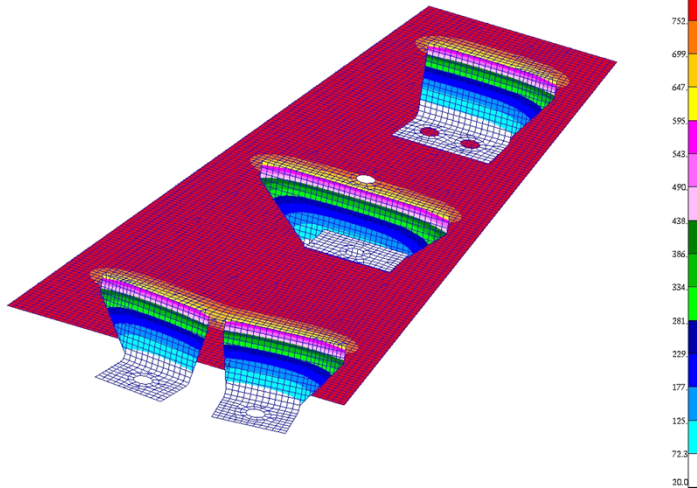


Experiment Analyses

TPS Experiment Thermal Analysis (exemplarily shown for SICARBON)

- maximum temperature on CMC cover sheet is **808° C** at 687s
- max. substructure temperature is far below the allowed temperature of 100° C.

MD Patran 2006 27-Jan-09 09:49:20
Scale: Temperature:Temperature Plot



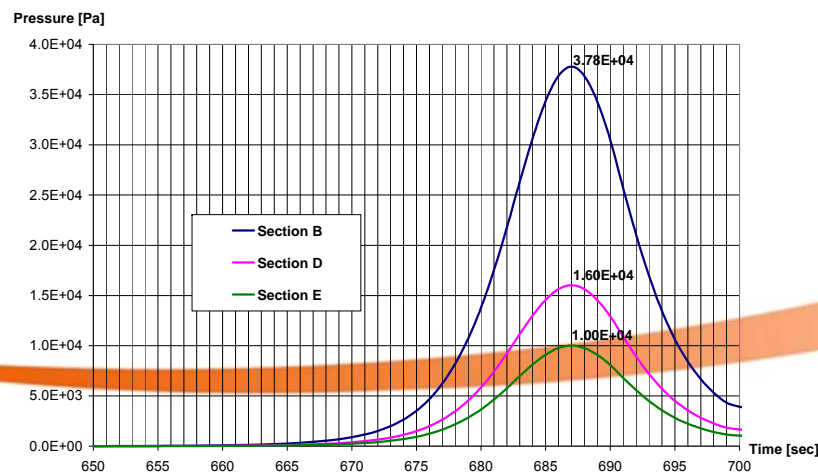
Experiment Analyses

Thermo-mechanical Analysis

Boundary conditions

- Ascent: 50g, simultaneously for all 3 axis
- Experimental phase: combination of max. pressure and max. thermal loads

Analysis comprises modal- and deformation calculations

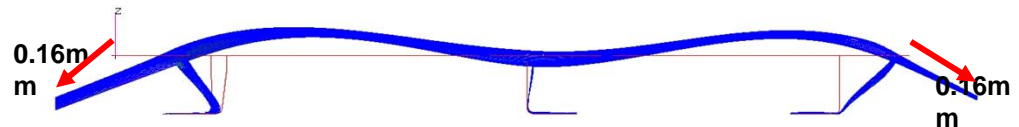
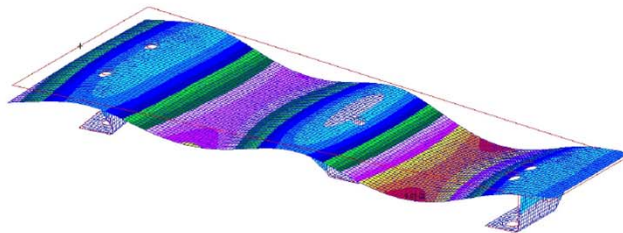


Experiment Analyses

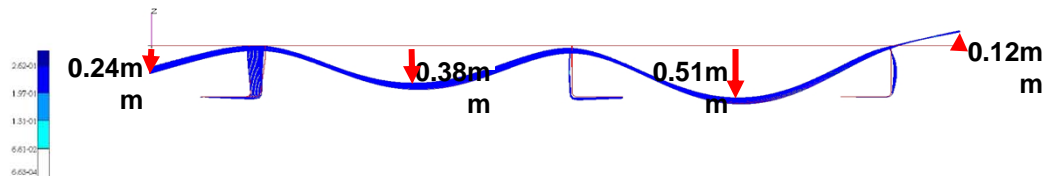
TPS Experiment Thermo-mechanical Analysis (exemplarily shown for SICARBON)

- Modal analysis showed 1. Eigenfrequency at **470 Hz**, this is significantly above the required 150 Hz
- Deformation analysis showed uncritical deformations especially at the panel circumference in the order of some tens of a millimeter

MD Patran 2006 26-Jan-09 17:27:44
Fringe: TEMP_689SEC.SC4, A1:Static Subcase, Displacements, Translational, Magnitude, (NON-LAYERED)



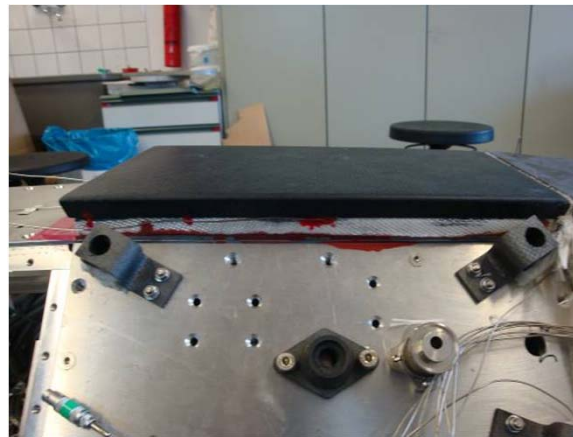
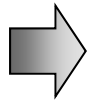
MD Patran 2006 26-Jan-09 17:28:26
Fringe: 0.378BAR.SC5, A1:Static Subcase, Displacements, Translational, Magnitude, (NON-LAYERED)



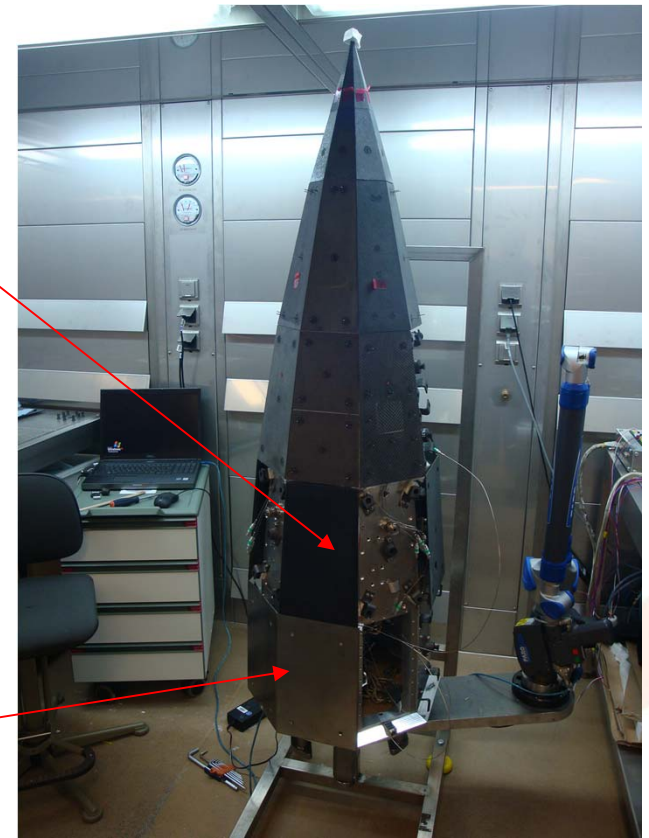
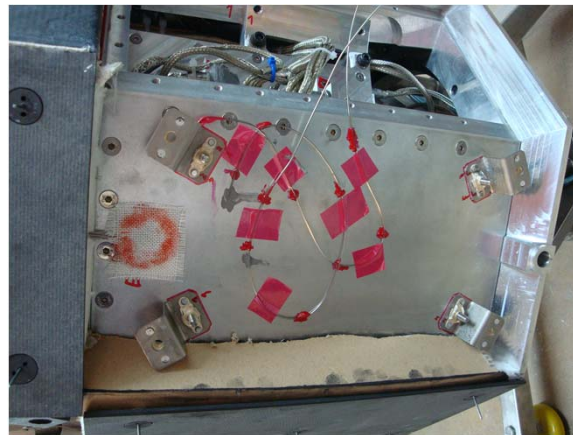
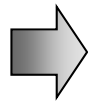
Experiment Integration

DLR, Stuttgart

SPFI



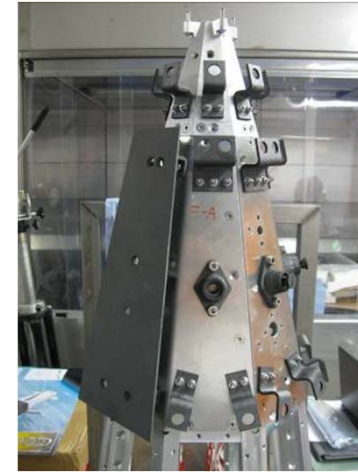
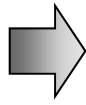
MetTPS



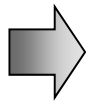
Experiment Integration

DLR, Stuttgart

SICARBON

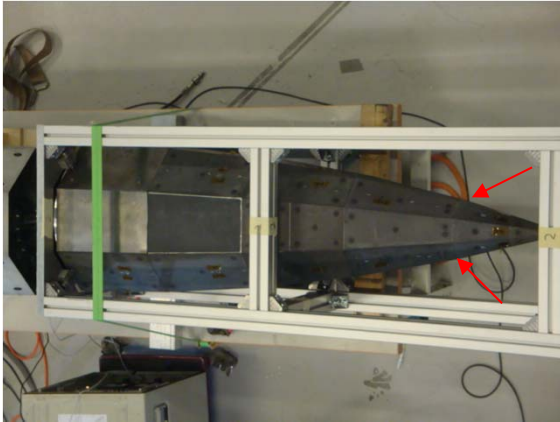


SICTEX



Experiment Integration

Rocket Range, Andoya

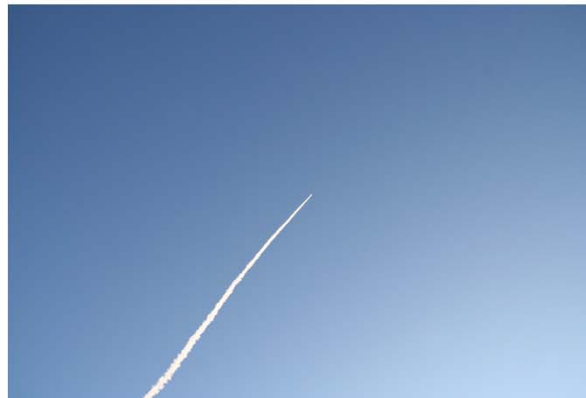




SHEFEX II Flight



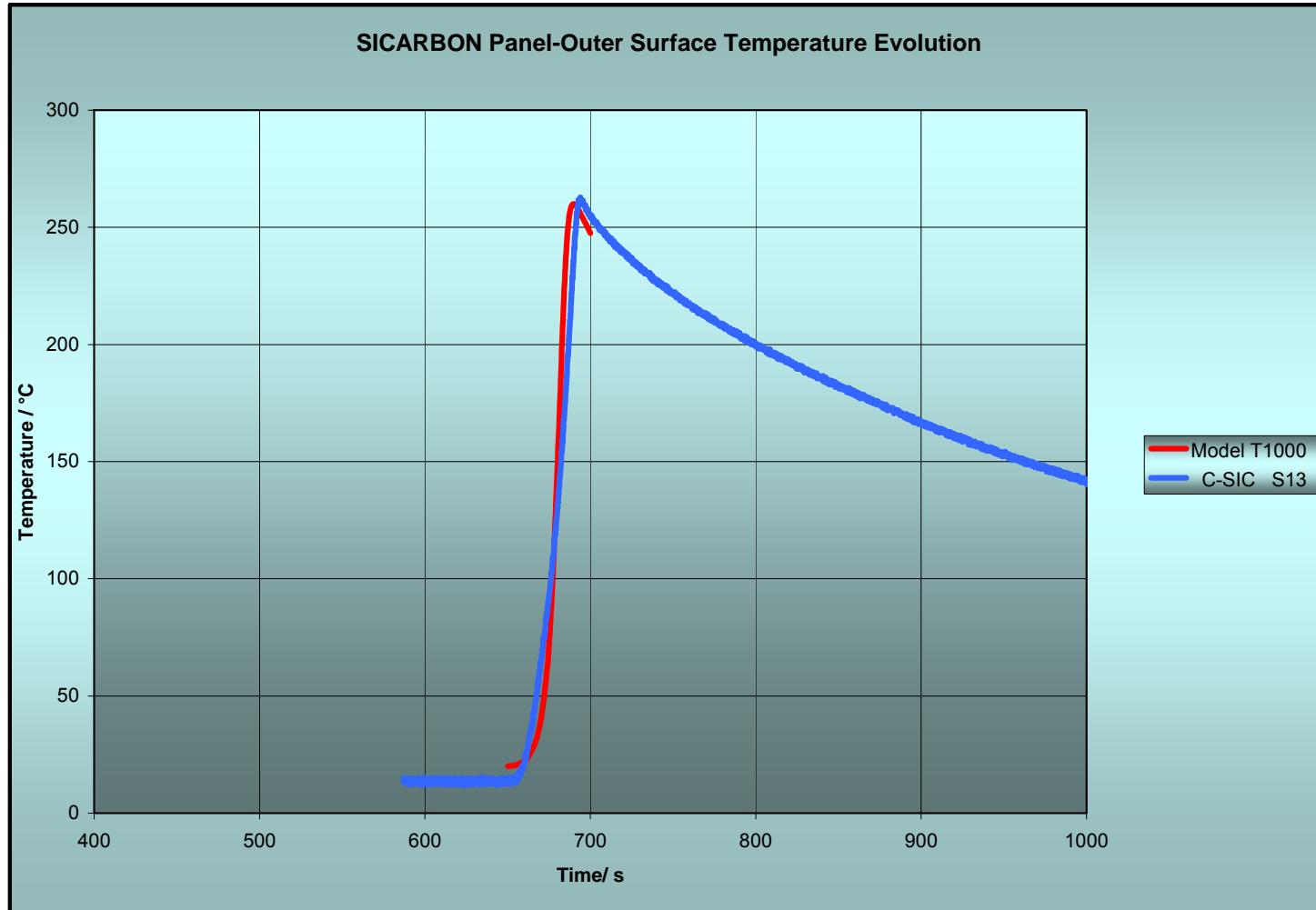
from Rocket Range, Andoya to southwest of Svalbard (water landing)



This document and its content is the property of Astrium [Lu/SAS/GmbH] and is strictly confidential. It shall not be communicated to any third party without the written consent of Astrium [Lu/SAS/GmbH].



Preliminary Flight Data

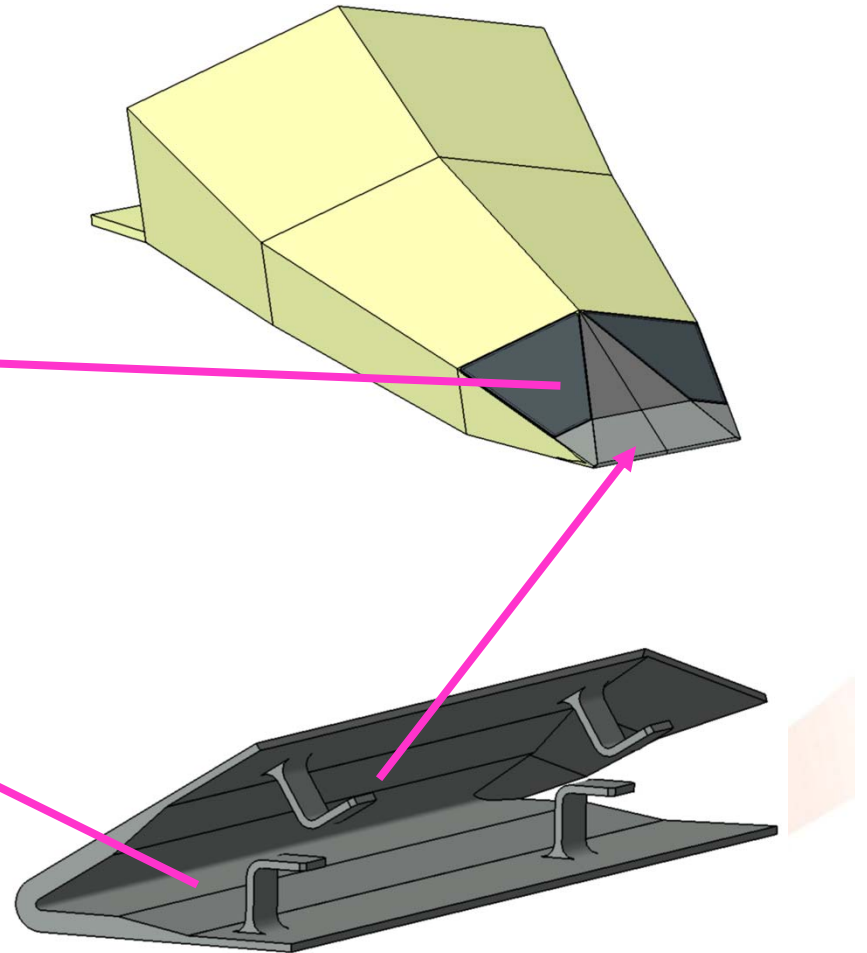
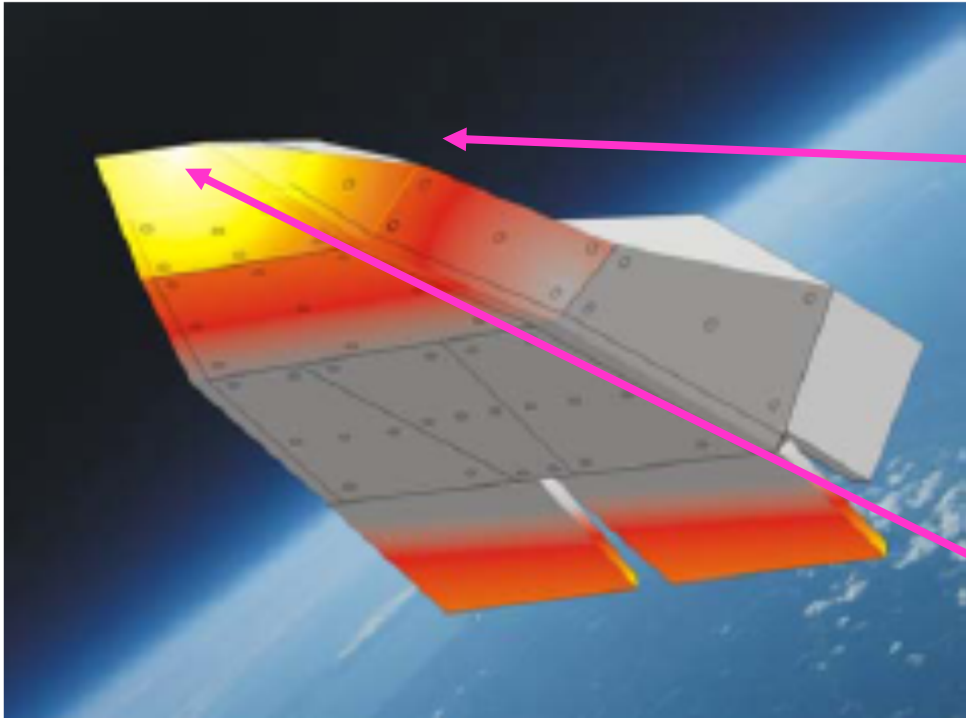


This document and its content is the property of Astrium [LuftSAS/GmbH] and is strictly confidential. It shall not be communicated to any third party without the written consent of Astrium [LuftSAS/GmbH].



Next SH III Flight

■ SHEFEX III AST TPS proposal



This document and its content is the property of Astrium [Lu/SAS/GmbH] and is strictly confidential. It shall not be communicated to any third party without the written consent of Astrium [Lu/SAS/GmbH].



Acknowledgements

Afore described experiments were financed by ASTRIUM R&T

Many thanks to:

- **WERNER BECK** from FormTech, Weyhe-Dreye for MetTPS experiment manufacturing
- my colleague **CHRISTIAN WILHELMI** from EADS IW, Ottobrunn for ceramic experiments manufacturing
- my colleagues in ASTRIUM, Bremen, contributing to the design, analyses & integration
- **HENDRIK WEIHS**, DLR SHEFEX II project manager



SHEFEX II

2nd Flight within DLR's Re-Entry Technology and Flight Test Program

The SHEFEX Team

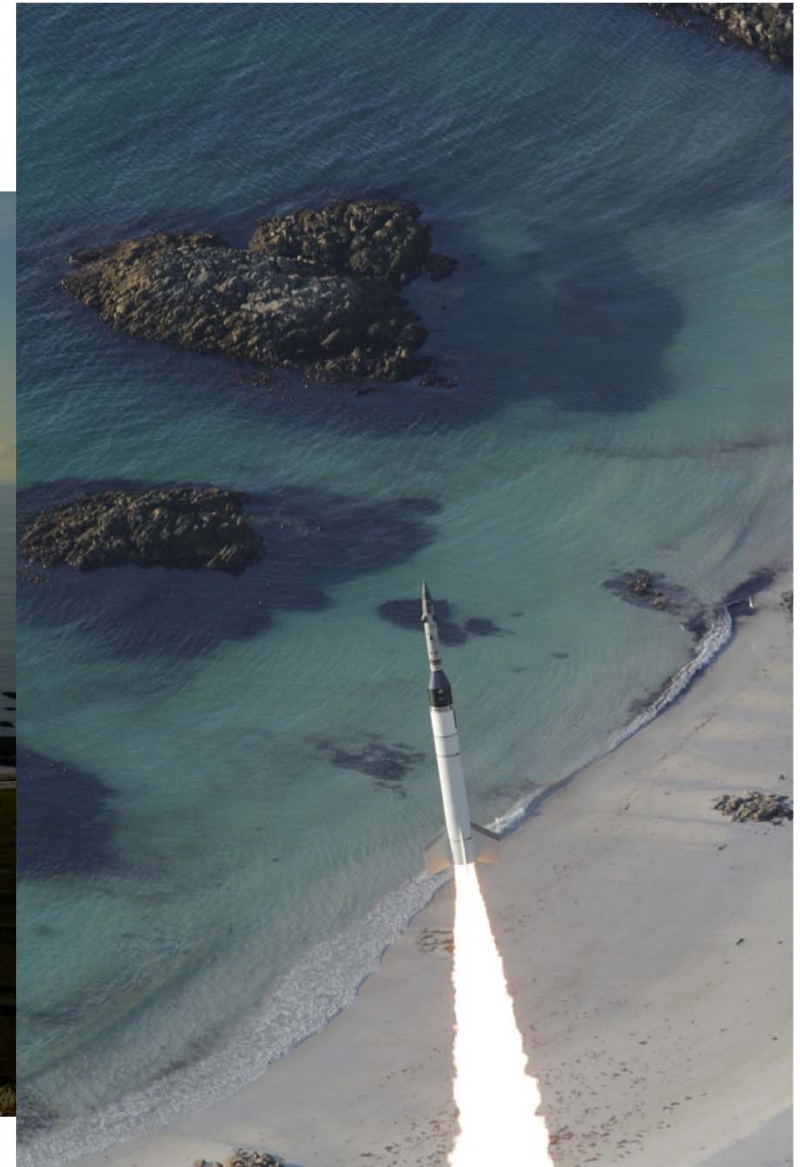


Knowledge for Tomorrow



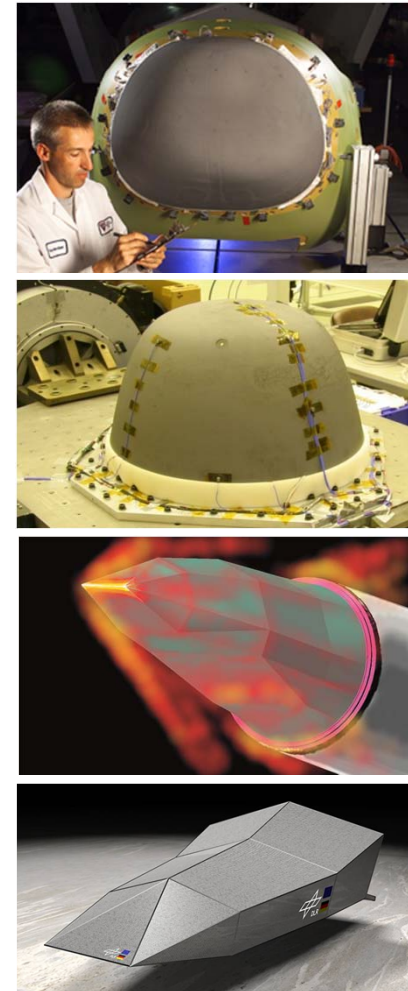
Andoya, Norway

June, 22nd 2012, 21.19 CEST

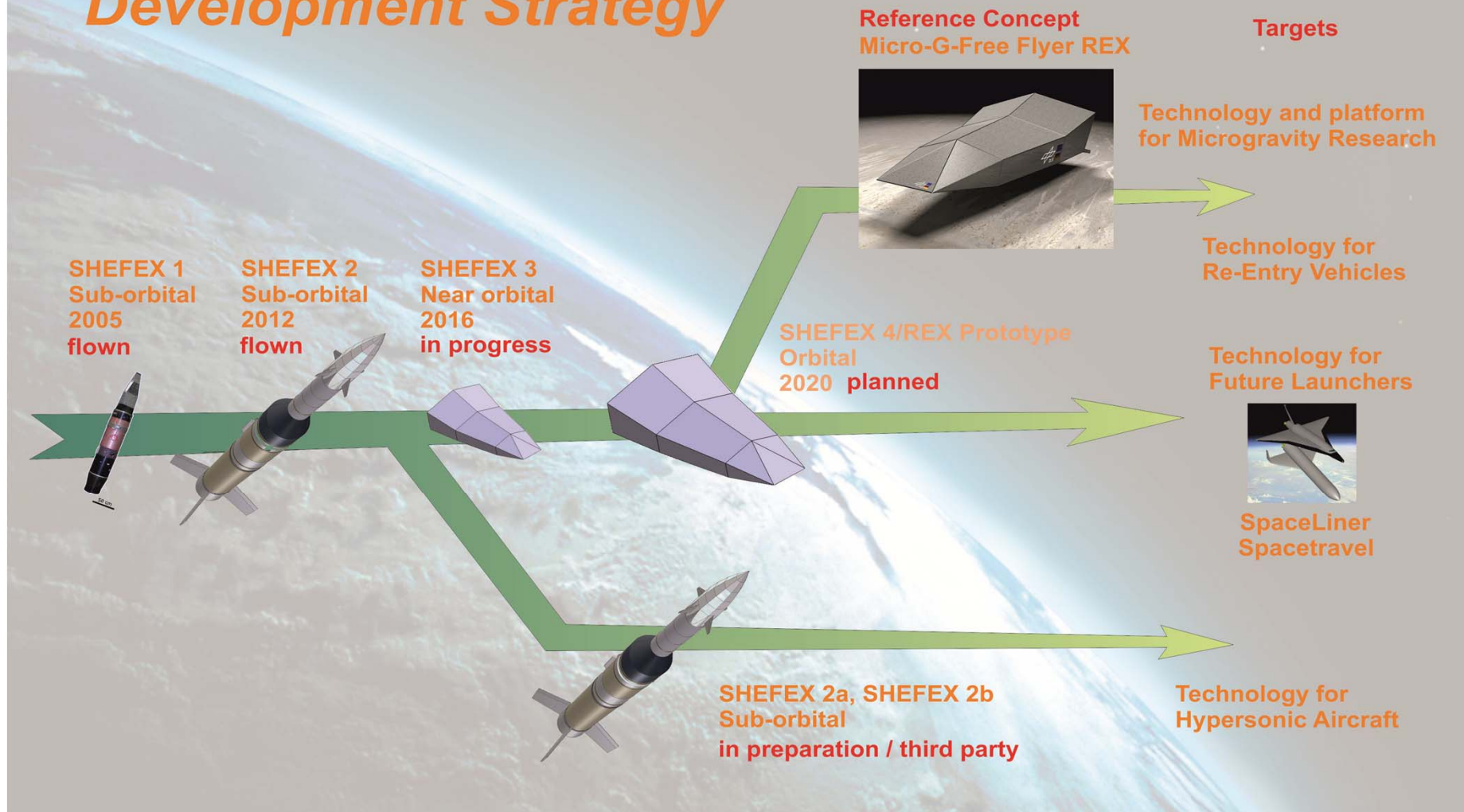


DLR`s Re-Entry Program, Why?

- Re-entry or return technology respectively, is a strategic key competence which becomes obvious after retirement of the Space Shuttle fleet.
- Currently, the German industry and DLR is well experienced and prepared within all related disciplines due to a lot of recent development programs.
- Within DLR CMC based thermal protection systems are available up to a technology readiness level of 6 to 7
- Within the SHEFEX/REX Development program all related scientific disciplines like materials and structures, TPS, flight control, GNC and aerodynamics are linked together to develop and test in flight new technologies for innovative space crafts with enhanced re-entry capability.



SHEFEX Development Strategy



Location of DLR Competences for SHEFEX

Bremen:

**Mission analysis, Navigation technology,
Avionics**

Braunschweig:

**Aerodynamic vehicle layout, aerodynamic
control system,**

Göttingen:

Hypersonic Wind Tunnel Tests

Köln:

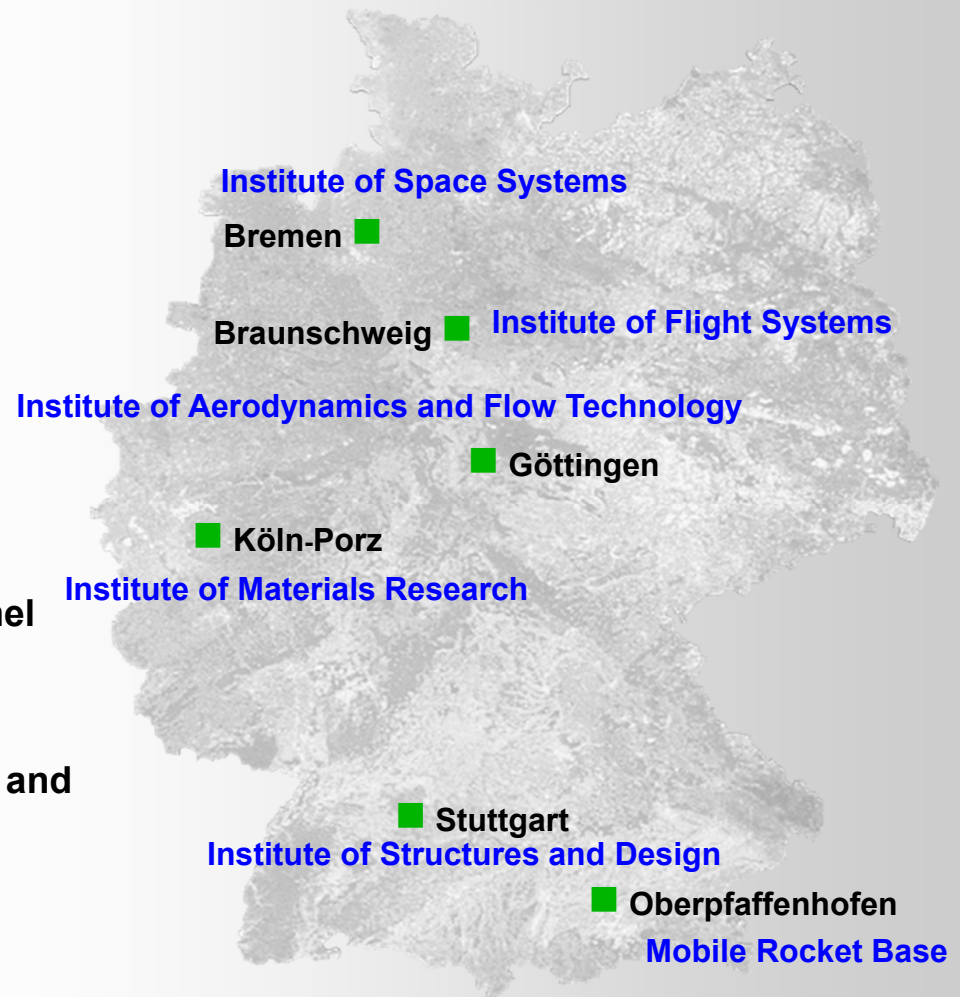
**Instrumentation and Hypersonic Wind Tunnel
Tests, oxide based TPS**

Stuttgart:

**Program coordination, Vehicle design, TPS and
Hot Structures, Fairing and fin structures**

Oberpfaffenhofen:

**Rocket Design, Subsystems, RCS-Control,
Launch Operation**



Partners of SHEFEX II



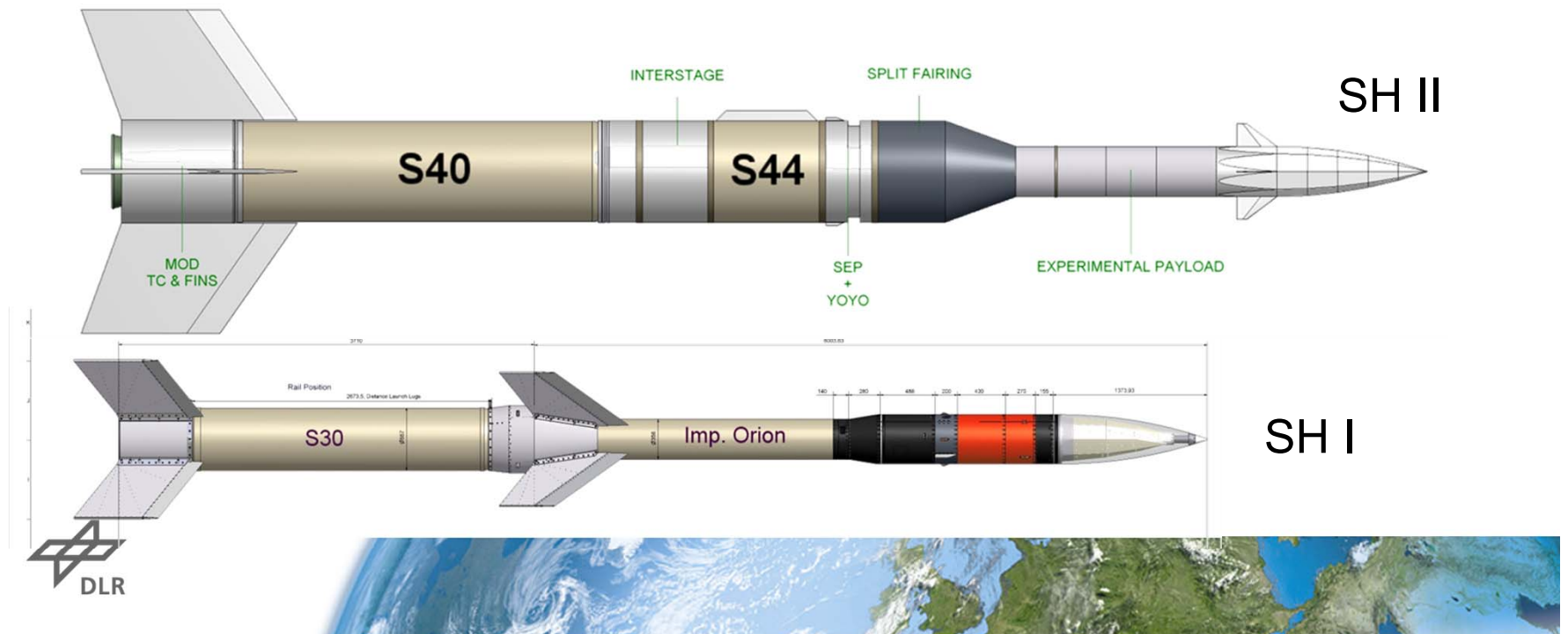
Australian Government

Department of Defence
Defence Science and
Technology Organisation

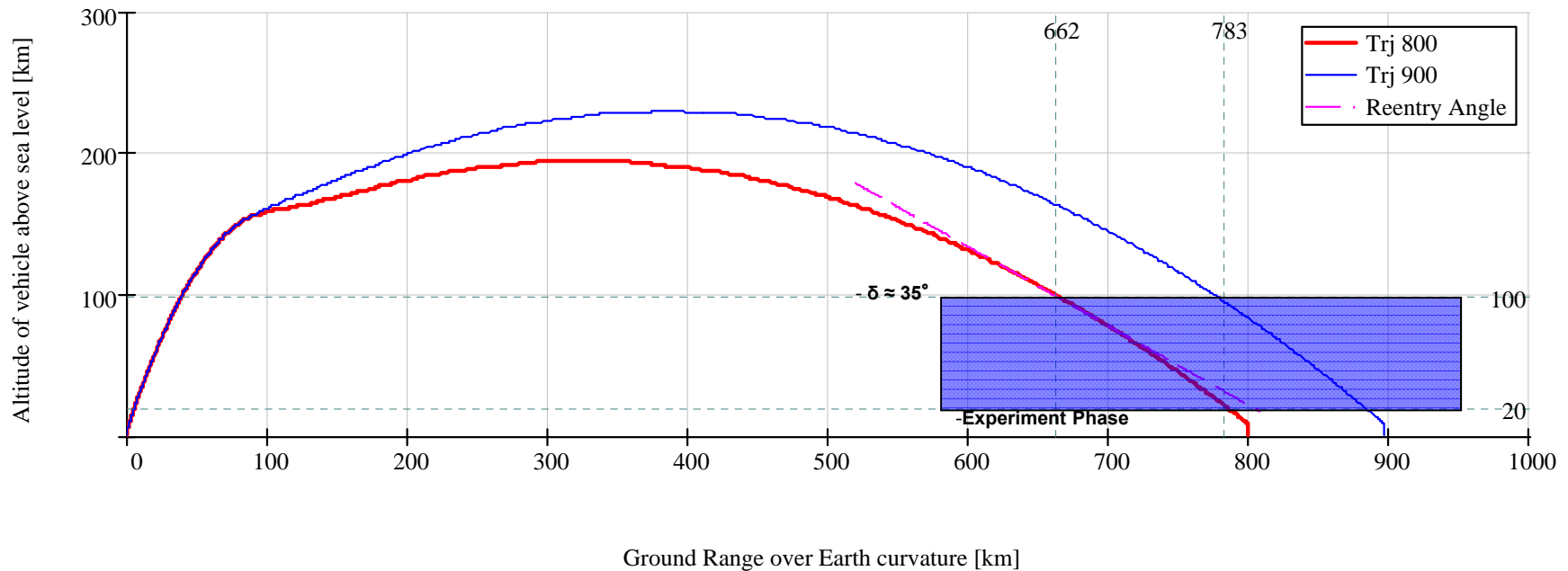


SHEFEX I versus SHEFEX II

- Re-entry velocity rises from 1.4 km/s to 2.8 km/s
- Experiment duration rises from 15 s to 50 s
- Active flight control during entry phase (100-20 km)
- Faceted, symmetric payload tip
- Measurement also during ascent phase
- Extension of instrumentation and experiments



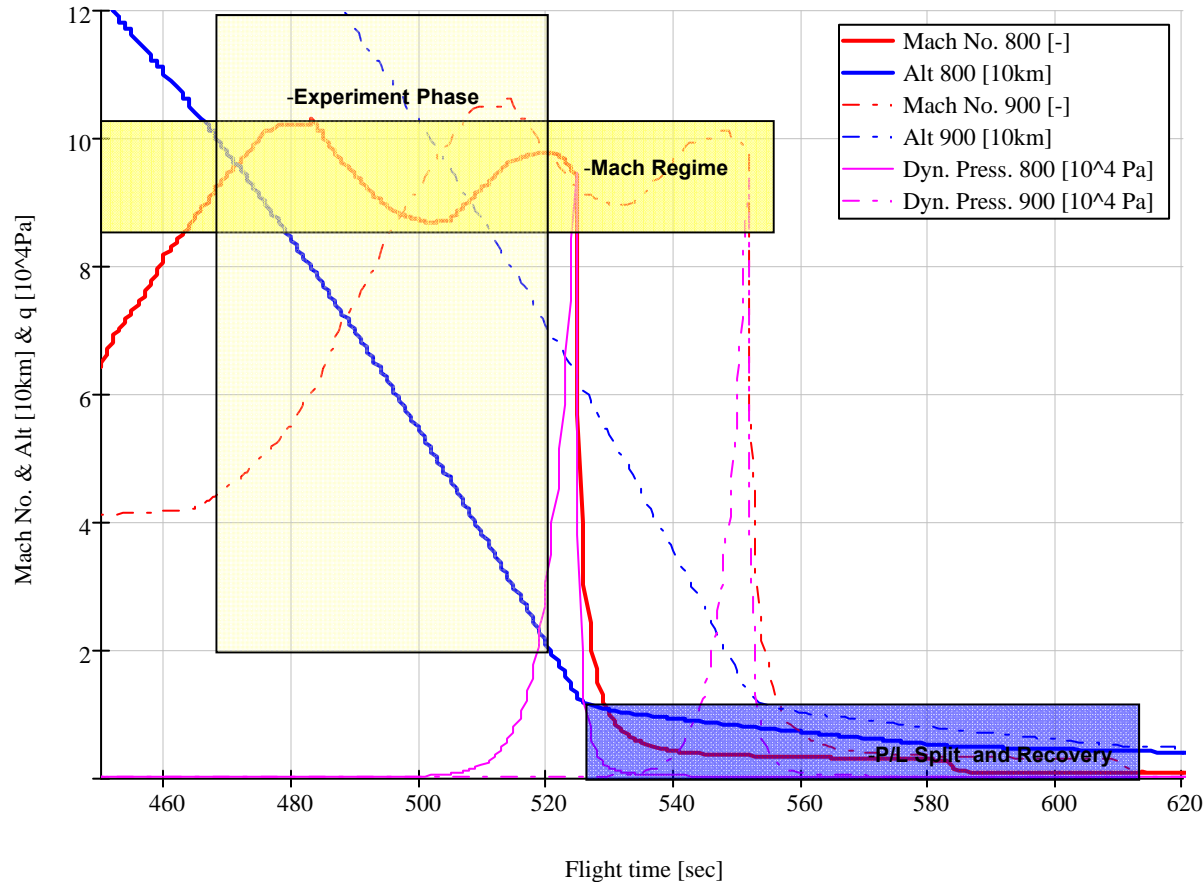
SHEFEX 2 Preliminary Altitude vs. Ground Range



- Apogee Trj800 (Baseline) $h \approx 194$ km
- Ground range GR ≈ 800 km
- Reentry angle $\delta \approx 35^\circ$
- Ground range Experiment Phase $GR_{exp} \approx 120$ km



SHEFEX 2 Predicted Reentry Parameter



- Mach No. regime
M ≈ 10.3 to 8.7
- Experiment time from
100 to 20km $t_{exp} \approx 53\text{sec}$
- Max. dynamic pressure up to
900 kPa at P/L split
- P/L split at $h \approx 15\text{km}$ (M ≈ 9)
- Begin of both recovery
sequences at $h \approx 4.6\text{km}$



Complete Vehicle Layout - Overview



- Vehicle consists of S40/S44 motor combination w/ modified tail can and fins
- Interstage adapter with active stage separation system
- Motor adapter equipped w/ destruct and separation system
- Experiment fins covered by CFK split fairing (l= 1.6m)
- Total length l= 12.741m
- Total mass m≈ 6800kg

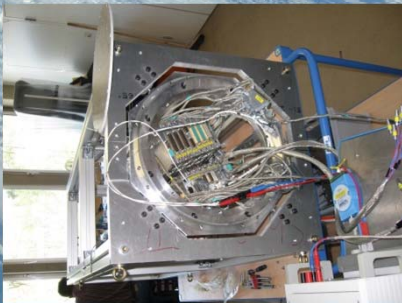


Experiments on SHEFEX II

Hybrid navigation system



Instrumentation, TC, Heatflux, pressure, Pyrometer, Compare (IRS)



New ablative fin structure



Aerodynamic control



Hybrid CMC/Metallic Canards

Windtunnel testing

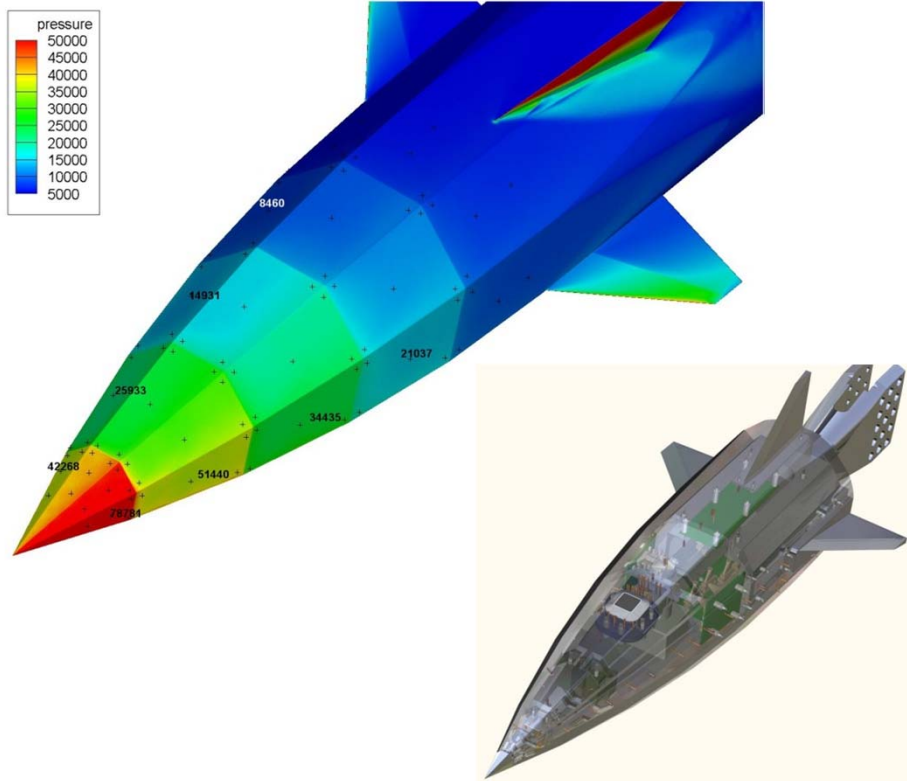


9 TPS Systems (ASTRIUM, MT-A, AFRL, DLR)

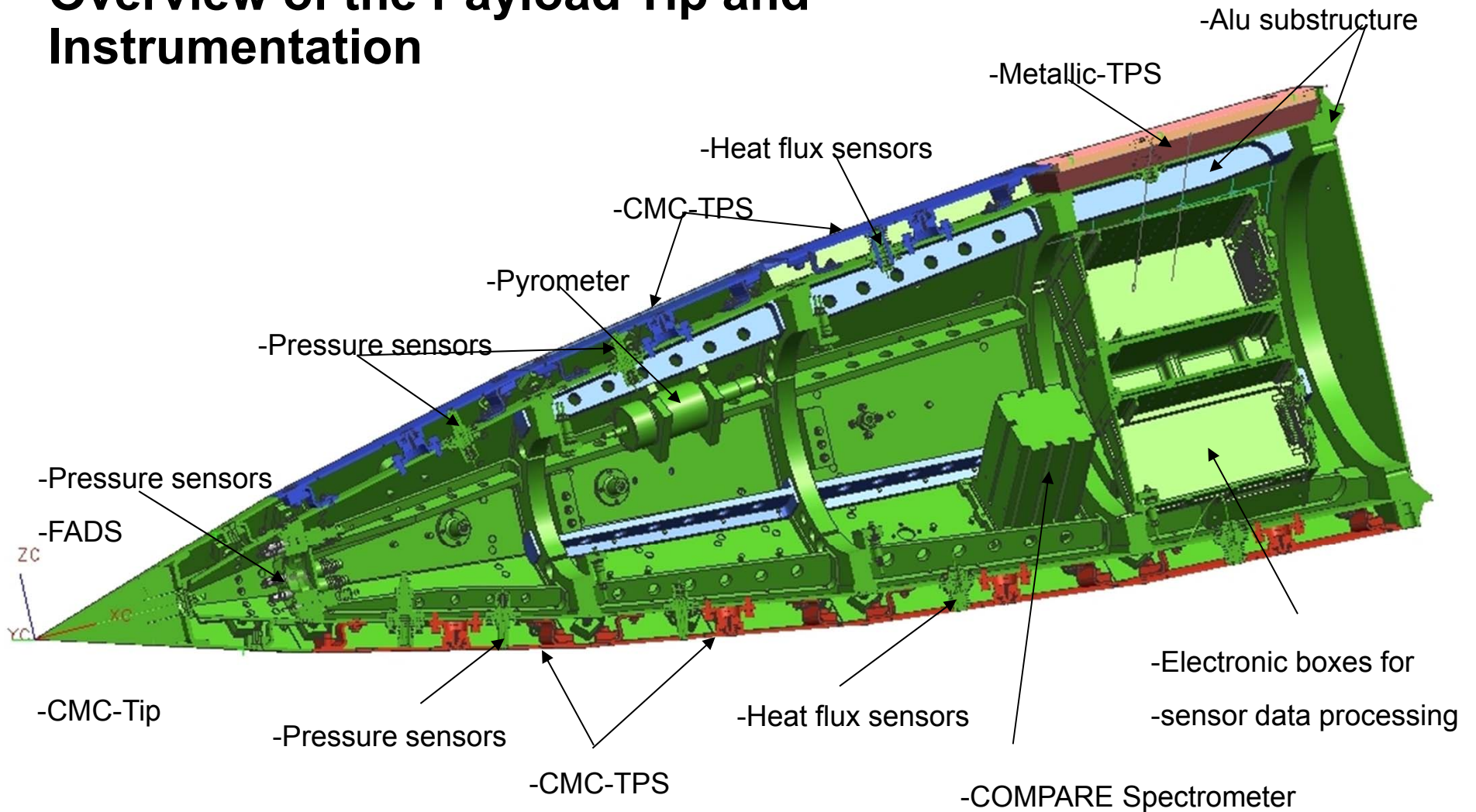
1 actively cooled segment
4 „Hot“ Antennas



SHEFEX II: Determination of Aerodynamic Data Base (numerical and wind tunnel testing)



Overview of the Payload Tip and Instrumentation

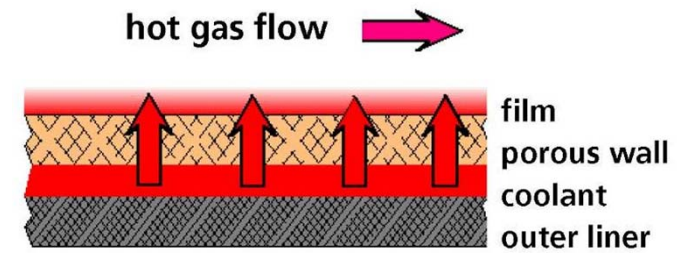


Material and Thermal Protection Experiments

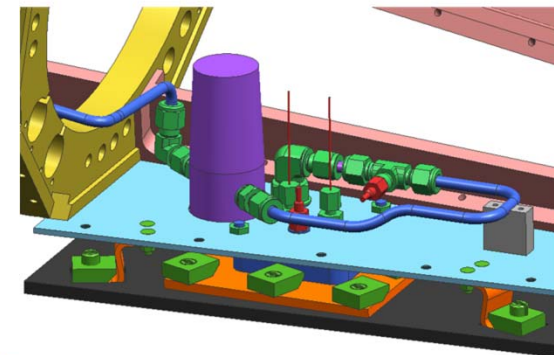
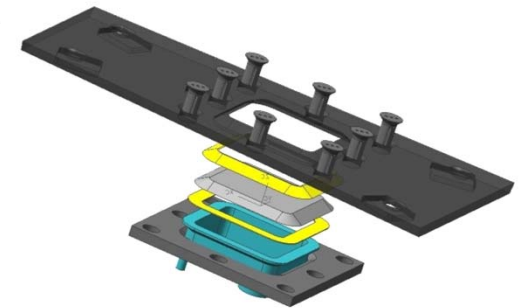
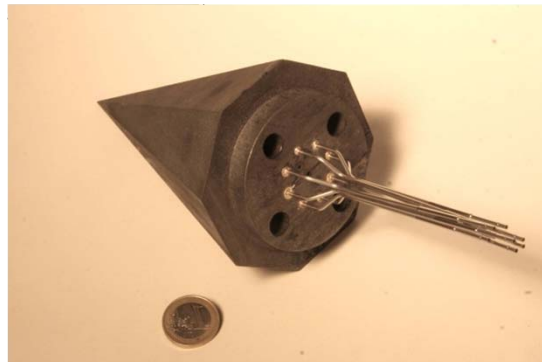
Oxide based CMC Elements for Antenna Inserts



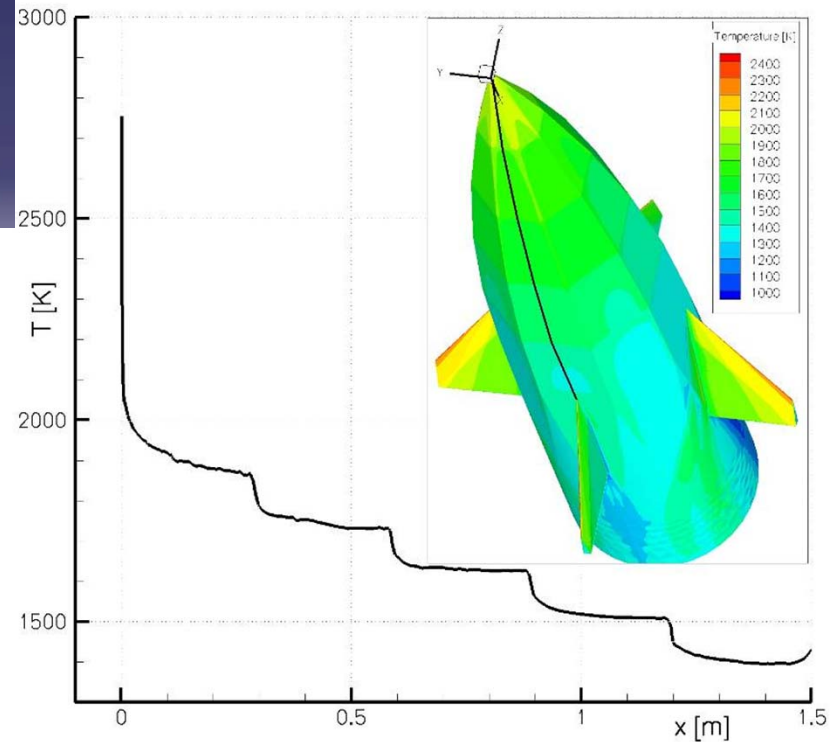
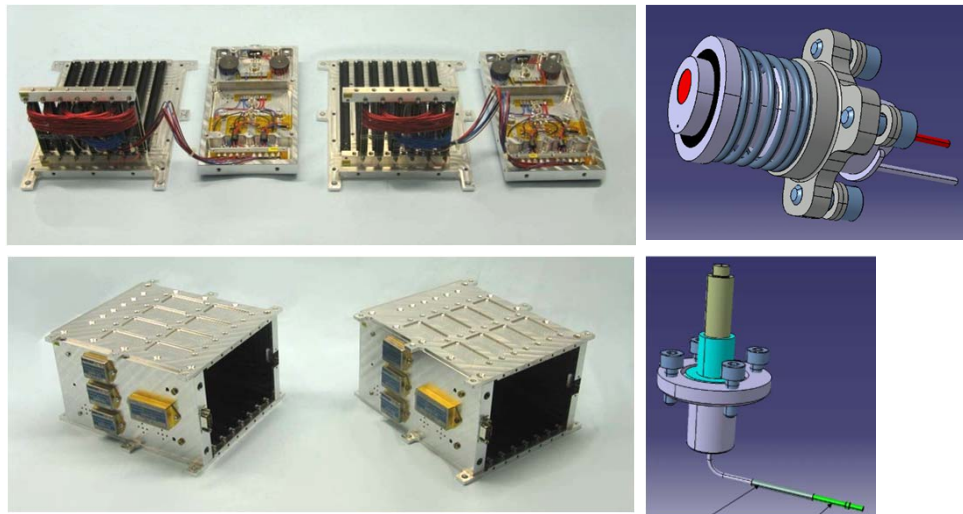
Actively cooled TPS Element



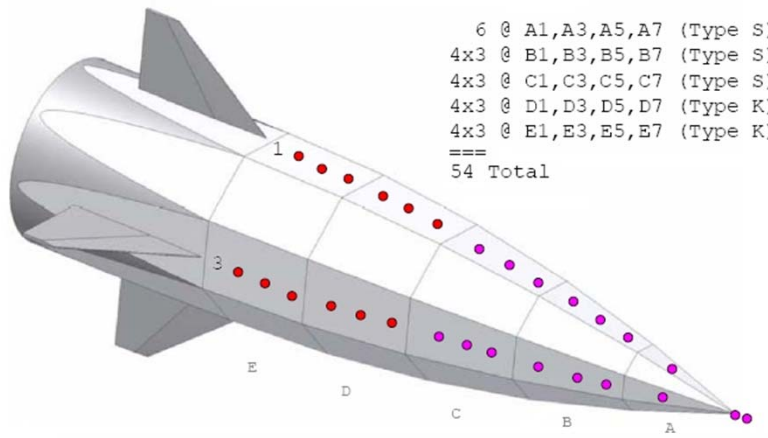
CMC Nose Tip including Pressure ports for FADS



Instrumentation



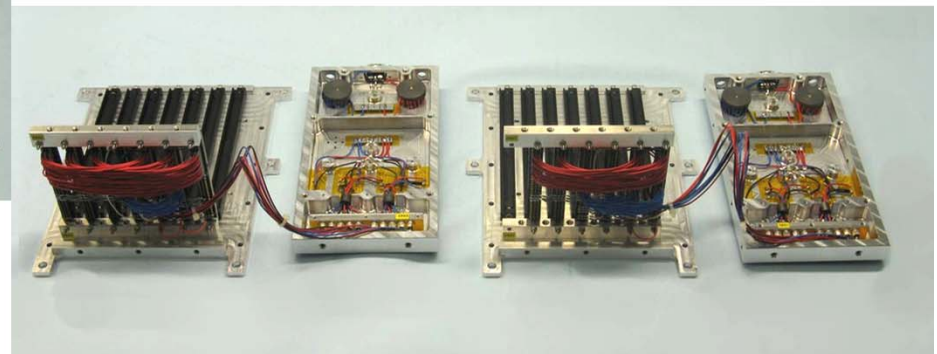
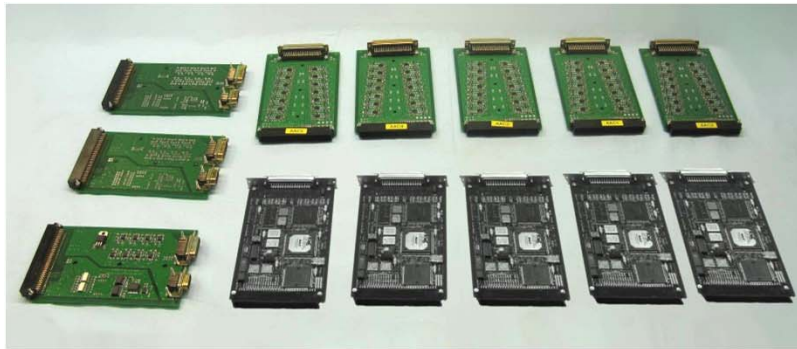
-Surface thermocouples



**Temperature distribution of the vehicle using radiation adiabatic boundary condition
turbulent boundary layer, Alt 20 km, Ma 8, $\alpha = 2.5^\circ$**

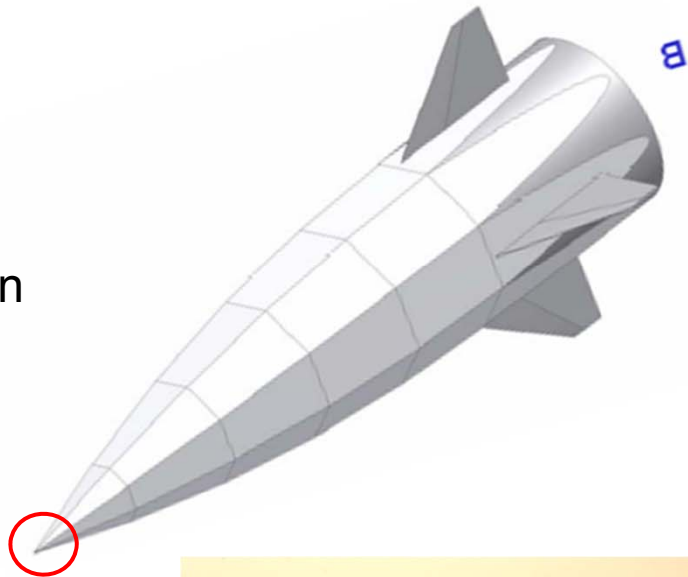


SHEFEX II, Hardware: Instrumentation

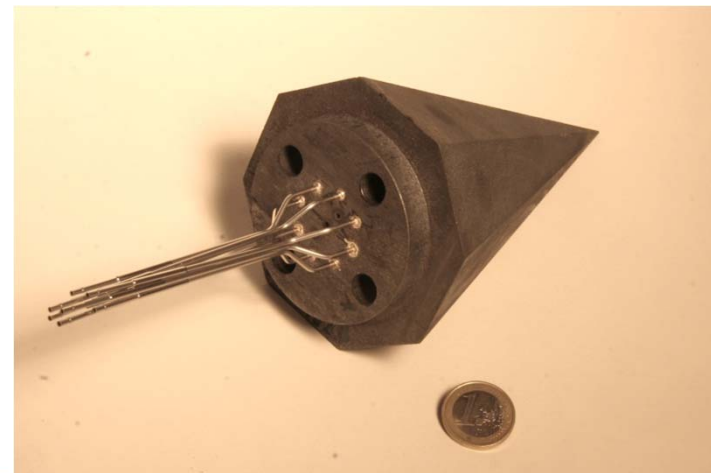
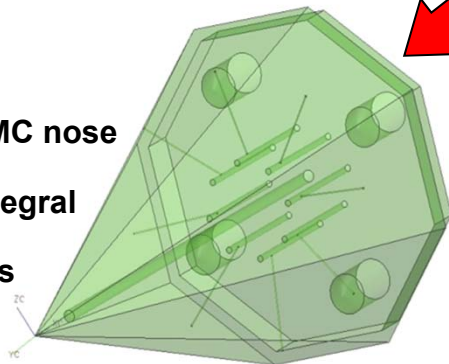


Flush air data system (FADS) experiment

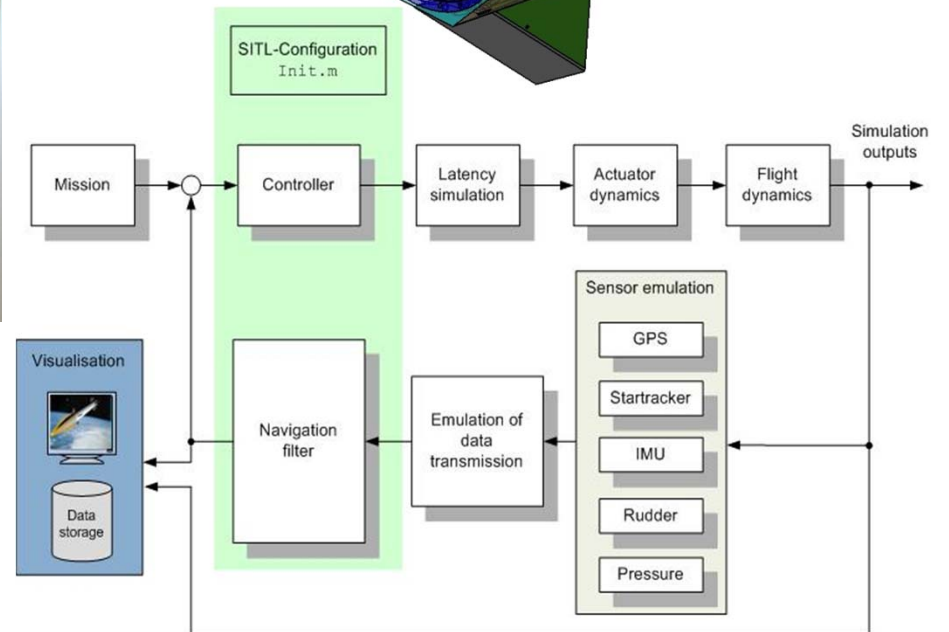
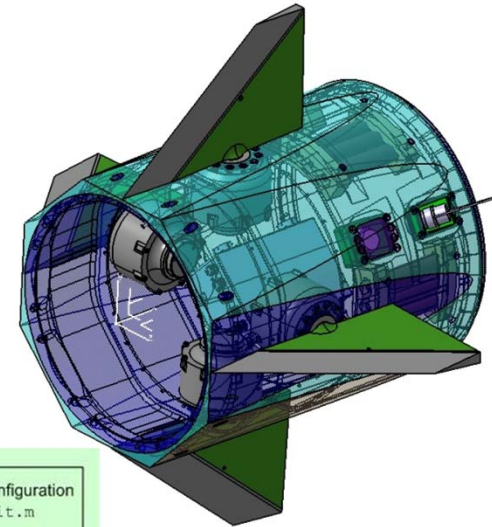
- > Measurement of static pressure at 8 locations
- > Development of algorithm for determination of gas flow orientation
- > Calibration within hypersonic wind tunnel facility
- > Comparison to navigation platform results



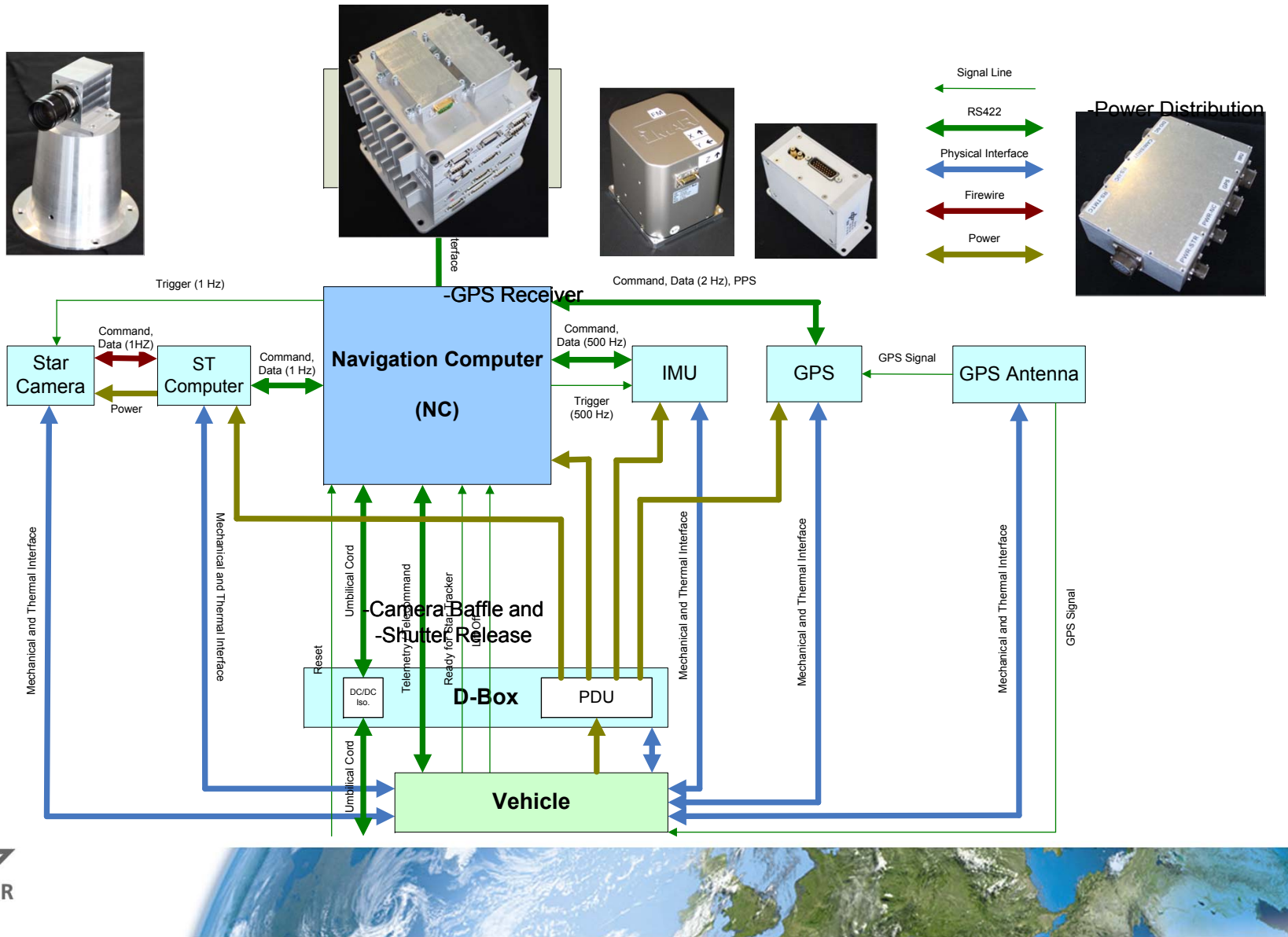
Monolithic CMC nose insert with integral pressure ports



SHEFEX II: Aerodynamic Flightcontrol



Hardware: Hybride Navigation System (Experiment)



SHEFEX: Secondary structural Experiments

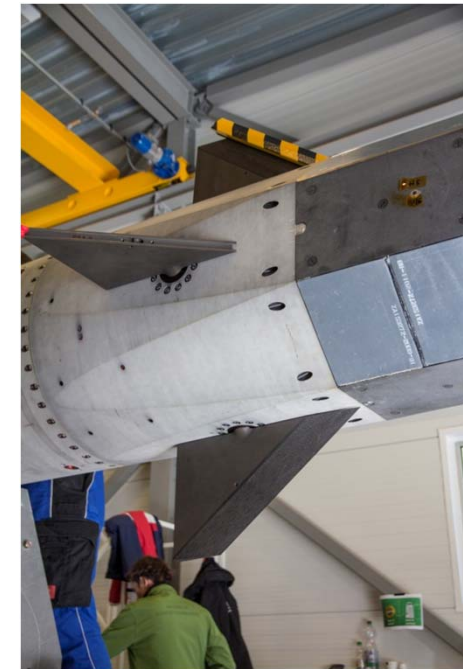
Ablative stabilizer fins



Hybrid Al/CFRP stabilizer fins



CFRP Fairing with integrated ablative TPS



Hybrid TI/CMC Canards



Andoya Rocket Range, Norway

payload assembly hall

control center

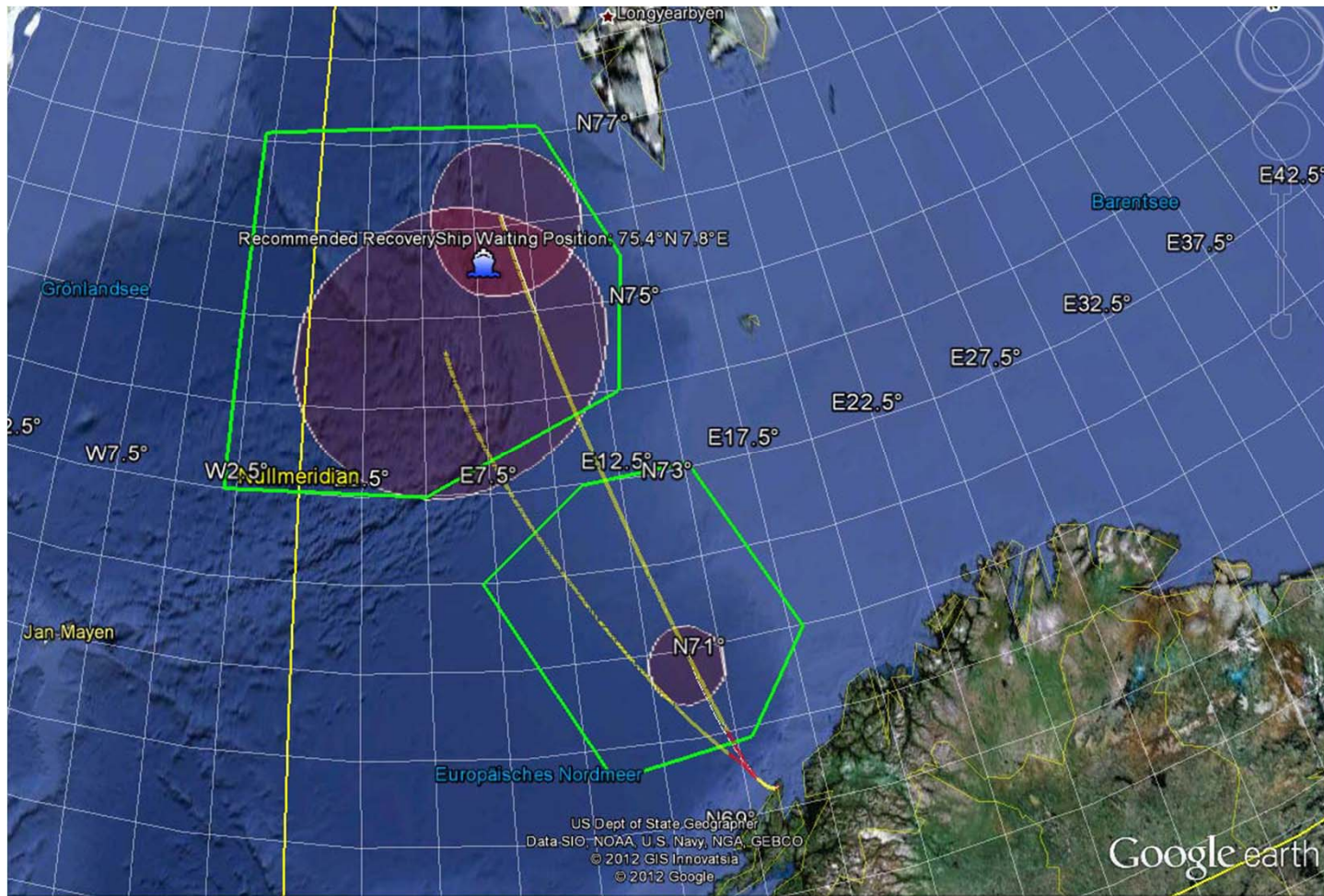
rocket assembly hall

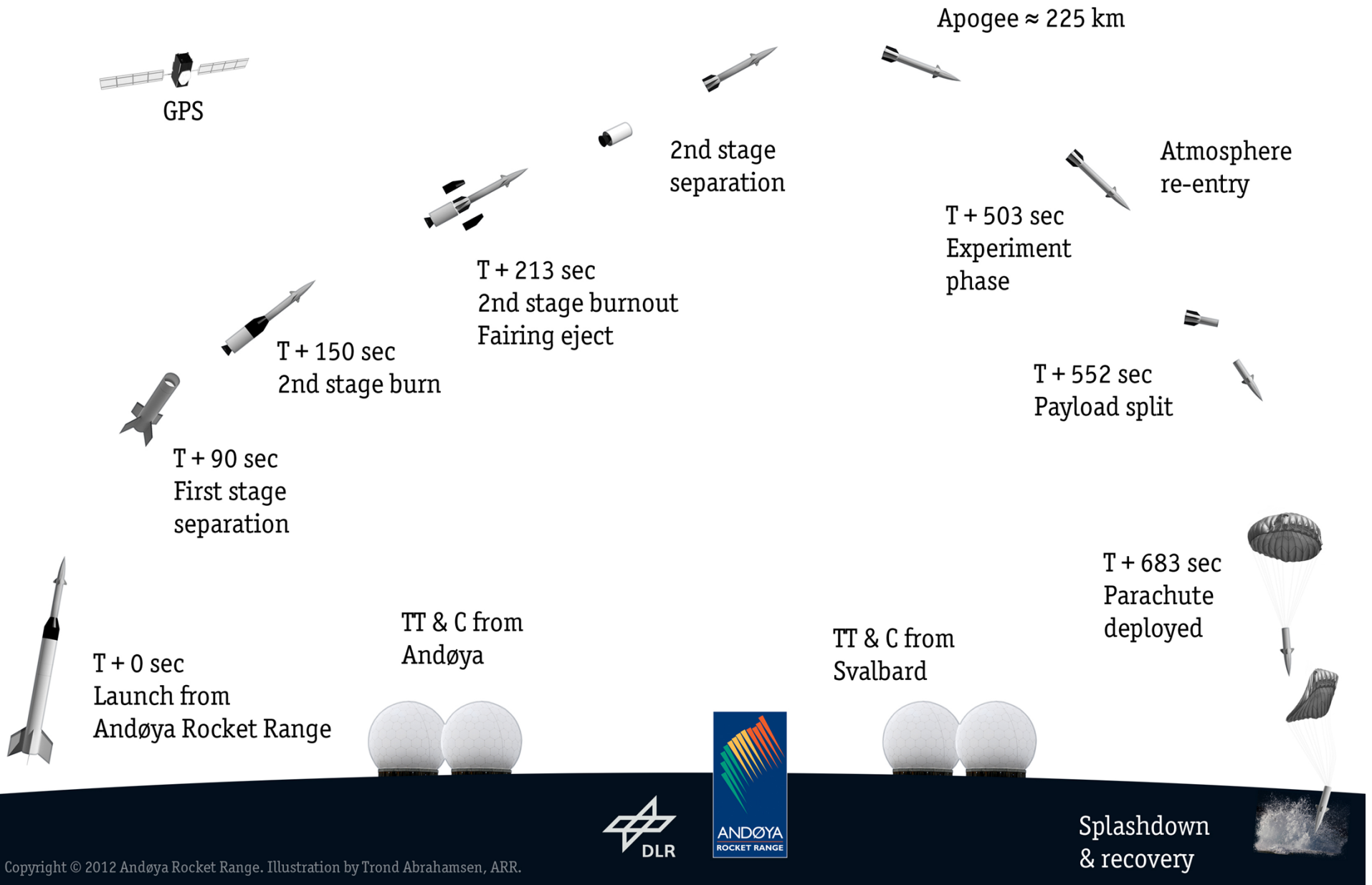
block house

launch pad



SHEFEX II Trajectory and Impact areas





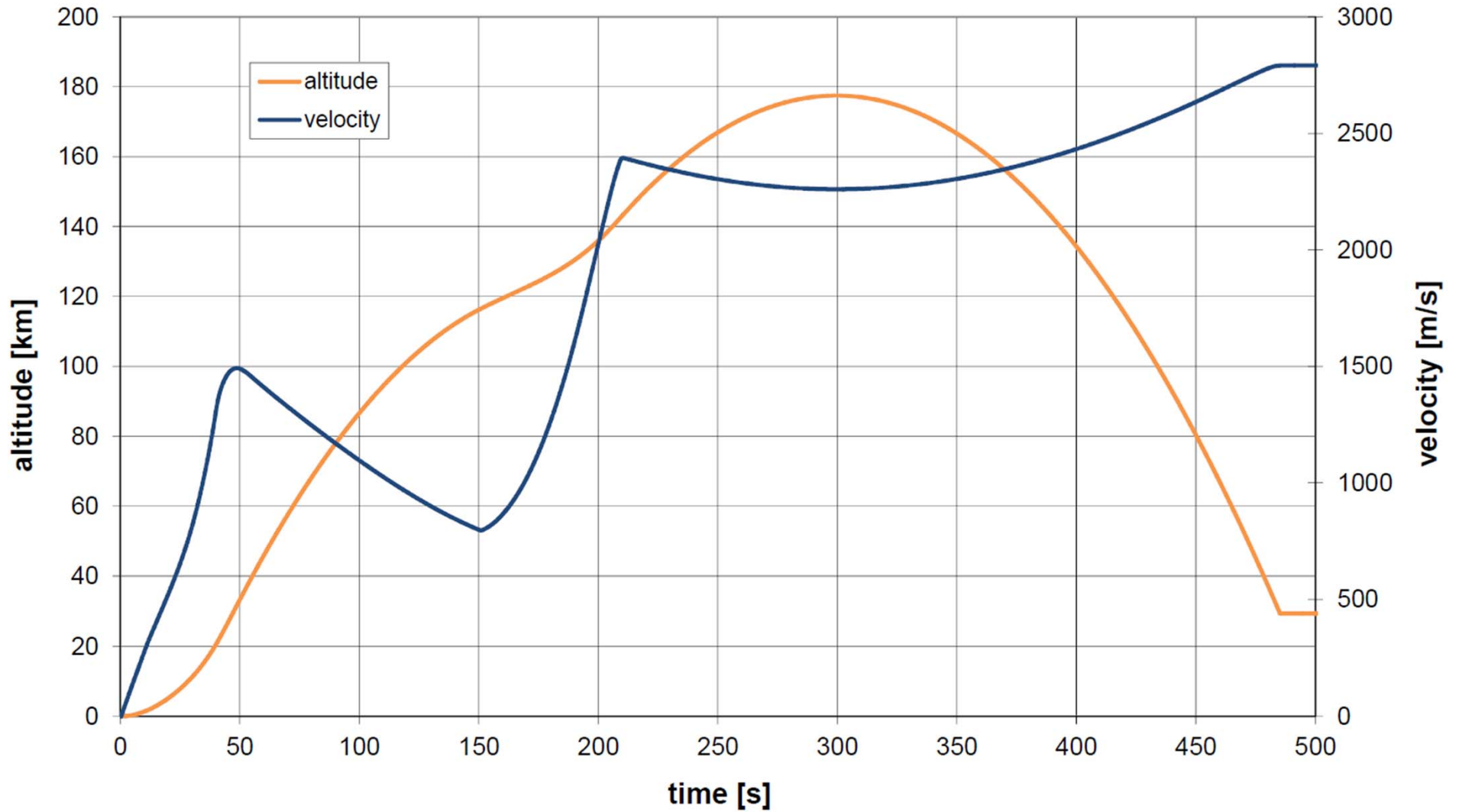
Preparing the launcher



3 , 2, 1, ignition ...



Shefex II flown Trajectory, GPS Data

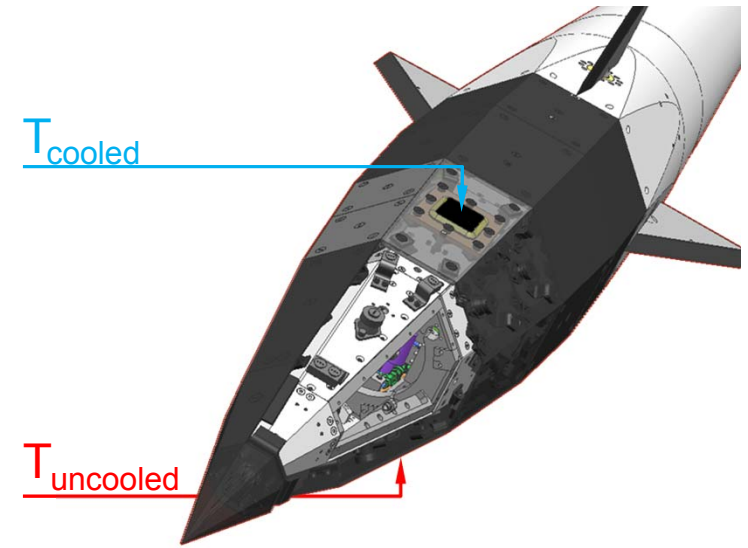
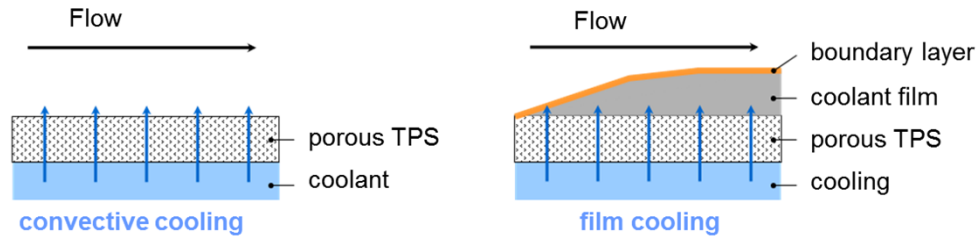




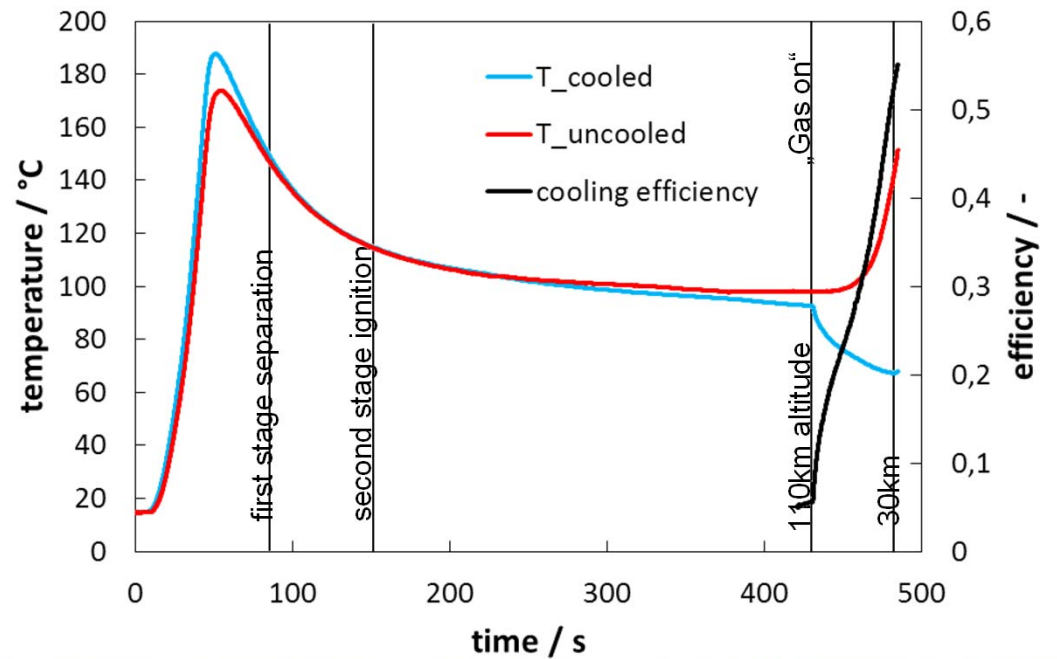
-AKTIV Panel



Results: AKTiV



- cooling effect visible during return flight
- cooling efficiency $\eta = (1 - T_c / T_{uc})$ up to ~50%





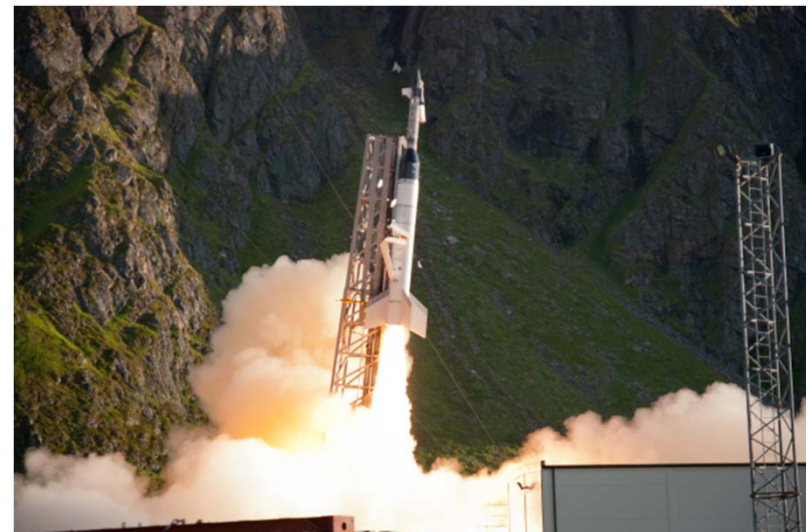
SHEFEX II Mission Accomplished

First results

- Trajectory flown as planned (deviation <1%)
- All vehicle maneuvers successful
- All experiments got data during ascent and re-entry
- Max. velocity 2.8 km/s
- Assessment of flight data will cover the next years

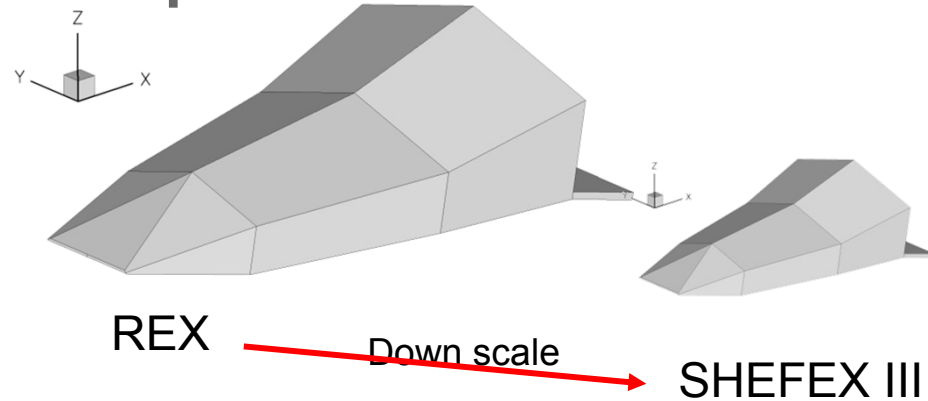
However

- Hardware is lost due to changing weather conditions at landing site

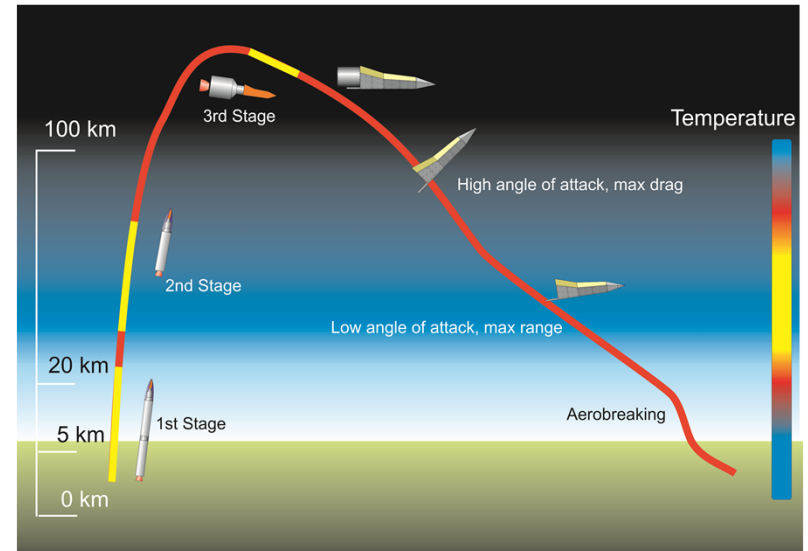


SHEFEX-Program, next Step

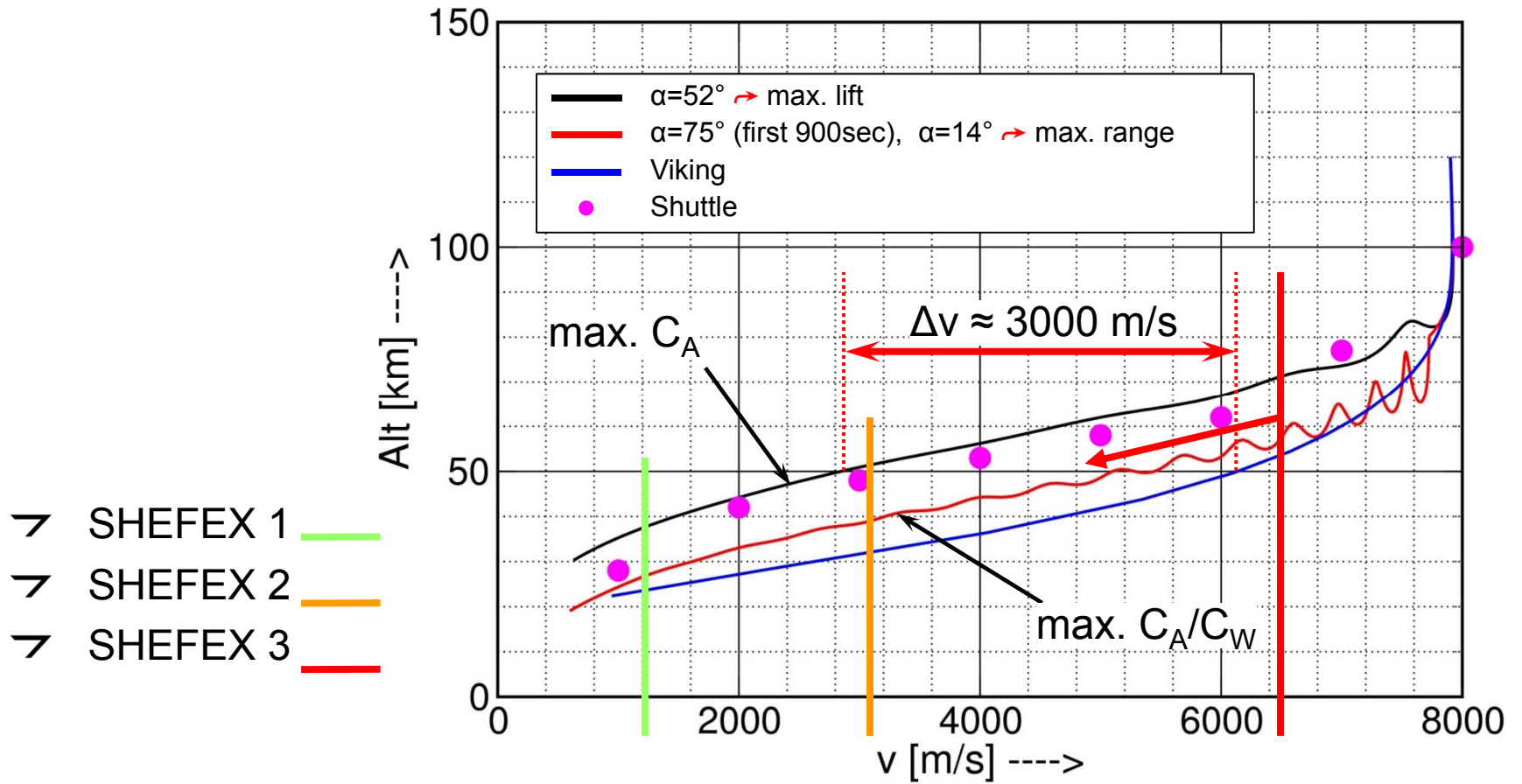
- SHEFEX I
- SHEFEX II
- SHEFEX III






- Suborbital Mission
- Demonstrating an optimized trajectory
- Rocket system VLM-1 (brasil.)
- Mass approx. 500kg
- Velocity approx. Ma 20
- Re-Entry duration approx. 15 Min
- In preparation
- DLR lead, ASTRIUM Cooperation partner



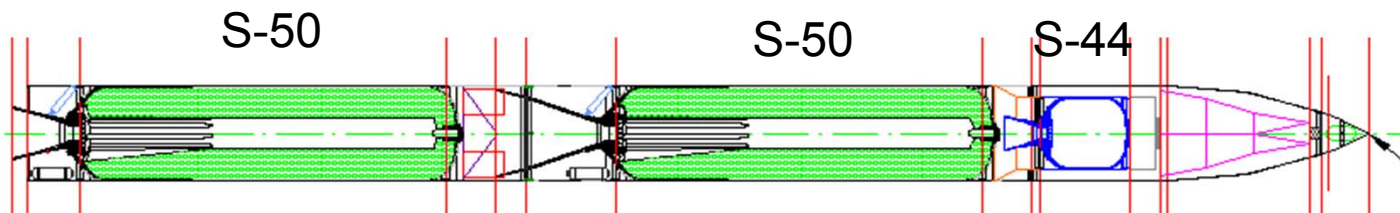
Flight regime



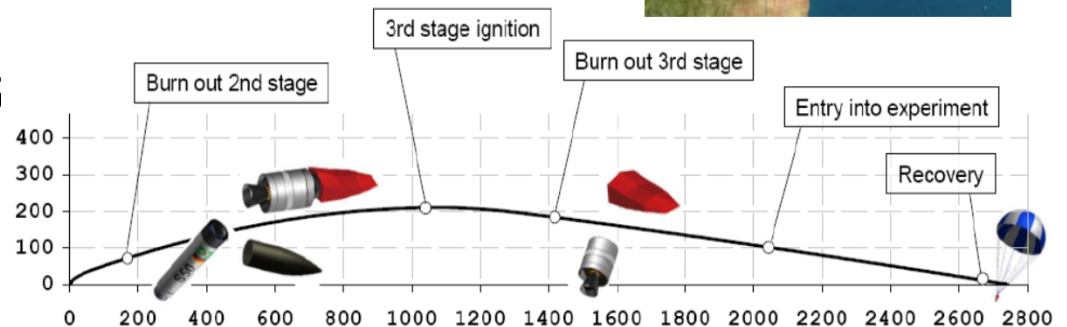
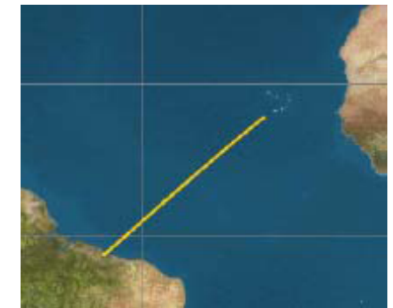
- SHEFEX 1 
- SHEFEX 2 
- SHEFEX 3 



VLM: Launch vehicle for SHEFEX III



- Length: ~18 m, Diameter: 1.4 m, Mass: ~26 tons
- **Launch Site:**Alcantara(Brazil)
- **Impact:** North east of Cap Verdean Islands
- **Re-Entry Capacity:**
- ~ 570 kg @ 100km Altitude @ 6.5 km/sec



FP7/Space Project “HYDRA” Hybrid Ablative Development for Re-Entry in Planetary

Atmospheric Thermal Protection

J. Barcena⁽¹⁾, S. Florez⁽¹⁾, B. Perez⁽¹⁾, J.-M. Bouilly⁽²⁾, G. Pinaud⁽²⁾, W. P. P. Fischer⁽³⁾, A. de Montbrun⁽⁴⁾, M. Descamps⁽⁴⁾, D. Lorrain⁽⁴⁾, C. Zuber⁽⁵⁾, W. Rotaermel⁽⁵⁾ and H. Hald⁽⁵⁾, P. Portela⁽⁶⁾, K. Mergia⁽⁷⁾, G. Vekinis⁽⁷⁾, A. Stefan⁽⁸⁾, C. Ban⁽⁸⁾, D. Bernard⁽⁹⁾, V. Leroy⁽⁹⁾, R. Wernitz⁽¹⁰⁾, A. Preci⁽¹⁰⁾ and G. Herdrich⁽¹⁰⁾

⁽¹⁾*Tecnalia Research & Innovation.
Industry and Transport Division*

*Mikeletegi Pasealekua, 2, Donostia-San Sebastian, Spain
Email: jorge.barcena@tecnalia.com*

⁽²⁾*Astrium SAS.*

*TEA213: Thermal & Thermomechanical
BP 11, Saint Medard en Jalles, France
Email: JEAN-MARC.BOUILLY@astrium.eads.net*

⁽³⁾*Astrium GmbH*

*Thermodynamics Department
Airbusalle 1, Bremen, Germany
Email: Wolfgang.Fischer@astrium.eads.net*

⁽⁴⁾*Société des Lièges HPK*

*Rue de Lasserens, 47230, France
Email: ademontbrun@lieges-hpk.com*

⁽⁵⁾*DLR – German Aerospace Center*

*Institute of Structures and Design
Pfaffenwaldring 38-40, D-70569 Stuttgart
Email: Waldemar.Rotaermel@dlr.de*

⁽⁶⁾*HPS – High Performance Structures Lda*

*Rua Doutor Roberto Frias, 4200 465 Porto, Portugal
Email: pedro.portela@hps-lda.pt*

⁽⁷⁾*N.C.S.R. "Demokritos"*

*Aghia Paraskevi, 15310 Athens, Greece
Email: kmergia@ipta.demokritos.gr*

⁽⁸⁾*INCAS - National Institute for Aerospace Research "Elie Carafoli"*

*Aerospace Special Materials Laboratory
Iuliu Maniu 220 Sector, 061121 Bucharest, Romania
Email: adriana@incas.ro*

⁽⁹⁾*ICMCB-CNRS Centre National de la Recherche Scientifique*

*Ferroelectrics Materials, Ceramics and Composites
87 av. du Dr A. Schweitzer, F-33608 PESSAC, France
Email: bernard@icmcb-bordeaux.cnrs.fr*

⁽¹⁰⁾*University of Stuttgart.*

*Institute of Space Systems (IRS).
Pfaffenwaldring 31, D-70569 Stuttgart
Email: herdrich@irs.uni-stuttgart.de*

INTRODUCTION

Original approaches based on ablative materials and novel TPS solutions are required for space applications where resistance in extreme oxidative environments and high temperatures are required. The atmospheric entry of space vehicles from high-energy trajectories requires high-performance thermal protection systems that can withstand extreme heat loads [1].

A new scenario has appeared due to a worldwide change in space mission planning strategies with entry vehicles going back to capsule designs and ablators are re-gaining attention. Consequently, the development of new, more efficient materials and systems is a must. Such developments, nevertheless, have to be subject to extensive experimental investigations using suitable facilities to obtain the desired maturity level and optimization [2]. In this view, the investigation and development of new materials based on ablative and ceramic thermo-structural concepts is crucial. A new (hybrid) concept based on the combination of both type of TPS materials is proposed. The advantage of the ceramic for this function is the low density compared to ablative material and the excellent thermal performance in this heat load range, as well as the stability of the shape of TPS which is an advantage for the aerodynamic of the re-entry vehicle.

Another asset comes from the reliability and safety point of view. The underneath ceramic core offers extra thermal protection in case of the failure or underestimated design of the ablative external protections (see reference of the Galileo's Probe). An accompanying effect is also the lower contamination during all mission phases and especially during re-entry.

SCOPE OF THE PROJECT

The concept of the project is based on the development of a novel hybrid heatshield, based on the integration of an external ablative part with a ceramic matrix composite (CMC) thermostructural core (see Fig. 1a). This will be carried out by the integration of dissimilar materials.

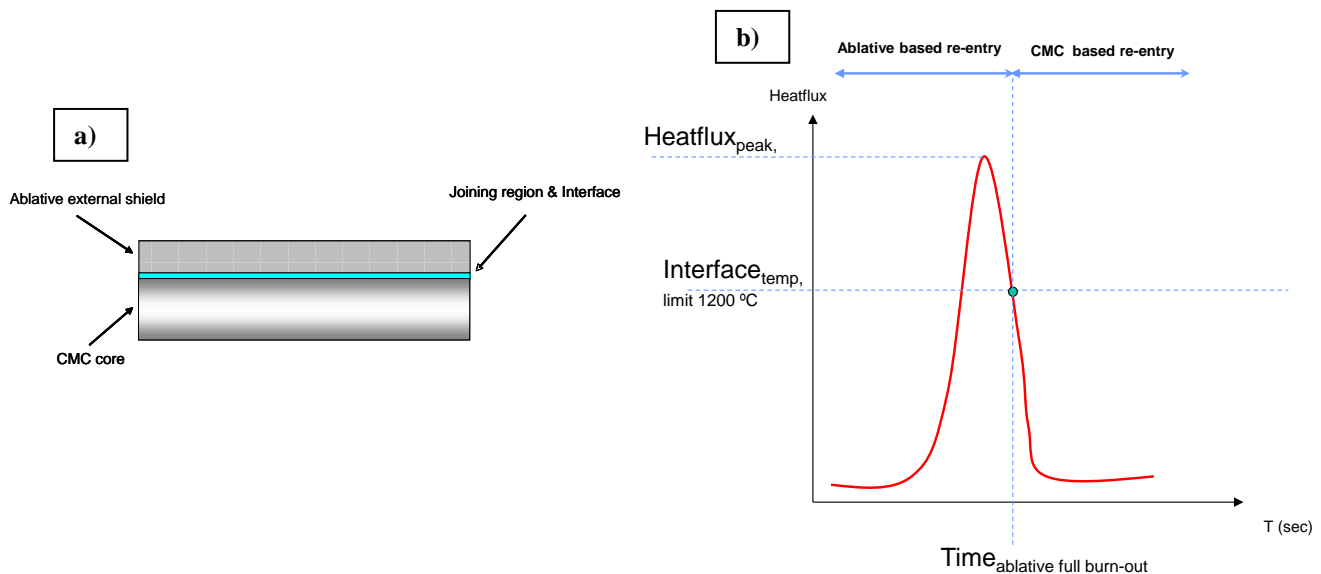


Fig. 1. Scheme with the hybrid concept: a) Thin ablative layer on top of a ceramic composite thermostructure, and b) The peak heat load profile of very fast re-entry scenario

The main advantage of a hybrid TPS heat-shield is based on the capability of the ablative layer of the hybrid TPS of bearing higher heat loads than the ceramic layer underneath while the tough ceramic composite underneath provides structural support.

The main challenge is to achieve a sound bonding between the two parts. This will be carried-out by employing advanced bonding technologies. The development of new adhesives solutions with improved mechanical and insulating characteristics will be investigated. The use of advanced high temperature adhesives and hybrid solutions in combination with mechanical attachments will be assessed, as well as other existing hybrid solutions.

From this point of view the HYDRA system will offer improved mechanical properties as well as better robustness during the entry. Besides, the new moon or interplanetary planned missions create higher heat loads during earth re-entry than ceramic or metallic TPS can withstand. Since these heat loads are characterized by a peak profile (Figure 1b) the ablator can dissipate the high heat loads during the peak. For that, a comparatively thin layer of ablative material is thought to be sufficient.

The HYDRA project started at the beginning of 2012 and it will have a duration of three years. The core group of the project is composed of 10 public and private organisations giving an excellent balance between large industries (Astrium-GmbH and Astrium SAS), SMEs (HPK and HPS - Portugal), Public research entities and Universities (NCSR, INCAS, ICMCB and IRS) and private research centres (TECNALIA, DLR). The partners are coming from five different European countries: France, Greece, Germany, Romania and Spain. The project consists of seven different technical workpackages dealing with: the selection of a reference mission and specifications, definition of the current state-of-the-art and materials trade-off, procurement of ablator and CMC parts, study of the ablator to CMC attachment, simulation & design and characterisation at relevant environment to achieve a TRL 4 at the end of the project.

ENVISAGED MISSION AND REQUIREMENTS

A deep analysis of the current mission and European roadmaps for planetary re-entry has been carried-out by Astrium SAS. Various types of missions have been analysed such as Earth atmospheric re-entry from Moon, Earth re-entry missions from LEO / ISS (ARV), Interplanetary exploration missions (Exomars, MPL on Mars, Venus & Titan long term) and sample return missions (Marco polo, ERC for MSR or MMSR...) among others. Exploratory missions are out of interest due to too high or too low thermal environments. Earth re-entry has been chosen: return from LEO/ISS or Moon, respectively named as CTV/ARV (Crew Transfer Vehicle / Advanced Re-Entry Vehicle) [3] and CSTS (Crew Space Transportation System) [4]. See Fig. 2 for the external aspect of the envisaged vehicles.

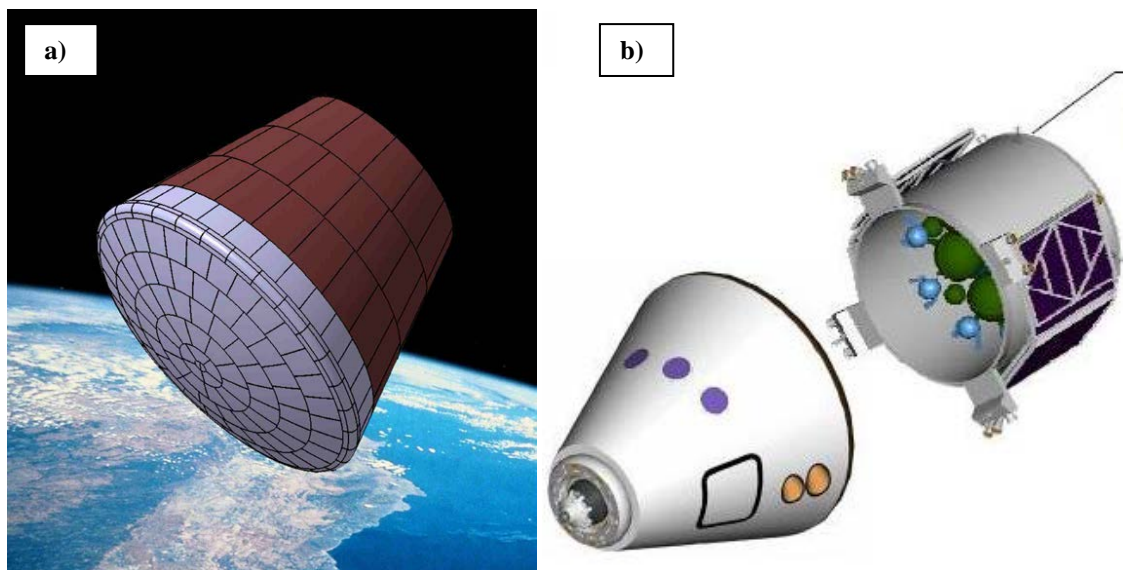


Fig. 2. Envisaged vehicles a) CTV/ ARV (Credit Astrium SAS) and b) CSTS (Credit Astrium GmbH)

In addition, mission specifications and requirements have been collected, including a list of the main requirements criteria (entry environment, materials requirements, mechanical requirements, interface requirements and so on). Table 1 shows the main re-entry parameter of the envisaged missions as compared with a sample return vehicle.

Table 1. Main-re-entry parameter for envisaged missions

Mission	Convective flux (max – kW/m ²)	Radiative flux (max – kW/m ²)	Total flux (max – kW/m ²)	Max Stagnation Pressure (Pa)	Total Heat Load (MJ/m ²)
CSTS (LLO)	4300	2280	5700	60600	416
CTV / ARV	700 - 1700	N/A	700 - 1700	~15000 to 20000	140 - 270
Sample Return (EVD)	9520	4300	13800	81700	209

Based on these parameters an iterative loop has started to correlate them with a robust hybrid concept and a selection of the specimen and conditions at the plasma wind tunnel facilities.

STATE-OF-THE-ART, TRADE-OFF AND MATERIALS PROCUREMENT

A careful review of ablative material systems at worldwide level with emphasis on European suppliers has been carried out, which has included the location of the project partners in this state-of-the-art (Astrium and DLR). The state-of-the-art revision also referred to the analysis of previous “hybrid” concepts: SEPCORE® [5] (Herakles Group, high density ablator on top) and SPA or “Surface Protected Ablator” [6] (Astrium GmbH, CMC on top). Both solutions are depicted in Fig. 3. Another hybrid system (‘Hybrid TPS’) has also been studied with some support from ESA by the NCSR group [7] which consists of a high temperature ceramic porous framework filled with a phenolic ablator, but it has not yet been taken beyond TRL2.

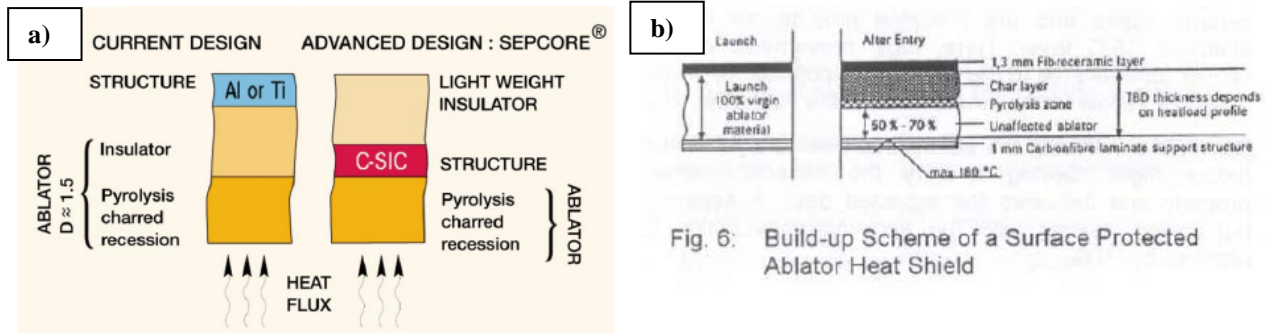


Fig. 3. Main previous hybrid concepts a) SEPCORE® (Herakles and b) SPA (Astrium GmbH)

The materials trade-off has taken into consideration relevant ablative TPS materials at worldwide level, where a TPS material selection matrix has been elaborated. Then after establishing the trade-off criteria (Related to Aerothermodynamic, Mass and Thermal Performance, Ablation, Design and Manufacture, Mechanical, Interface, Environmental, Physical,...) a materials ranking has been the output and finally the partners were located in the ranking.

Two types of ablators and two types of thermostructural core have been considered and the project partners have procured enough quantity to satisfy all the materials needs for the whole duration of the project. The two ablators consist of two different families of phenolic matrix composites based on carbon fibres and cork particles, with trade names ASTERM® [8] and NORCOAT FI® [9], respectively, both owned by Astrium SAS. On the other hand two types of thermostructural ceramic matrix composites (carbon fibre reinforced silicon carbide) were procured by Astrium GmbH and DLR, respectively under the commercial names SICARBON® [10] and C/C-SiC® [11]. The four materials are depicted in Fig. 4.

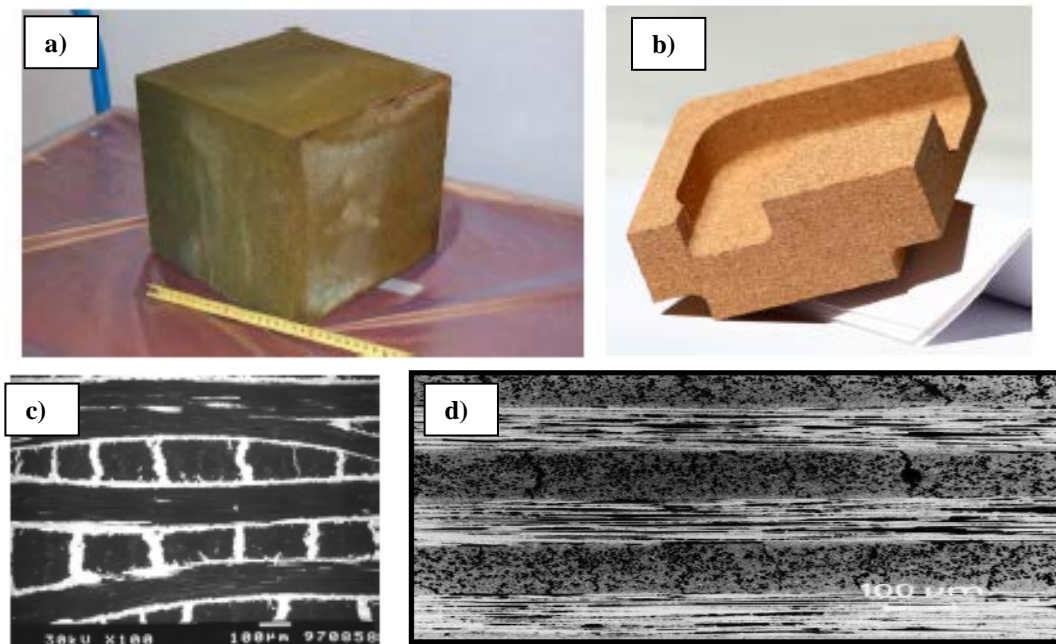


Fig. 4. Materials procured by HYDRA's partners: a) ASTERM® (Astrium SAS), b) NORCOAT FI® (Astrium SAS/HPK Liéges), c) SEM micrograph of C/C-SiC® (DLR) and d) SEM micrograph of SICARBON® (Astrium GmbH)

BONDING AND TPS ASSEMBLY

Two families of material combinations are envisaged. The first family consists of an ASTERM[®] thin layer on top of a SICARBON[®] substructure; this combination has been envisaged for the front shield of the vehicle. The second material family is based on a layer of NORCOAT[®] on top of a C/C-SiC[®] core, to be located at the backshield. The proposed solutions are depicted in Fig. 5.

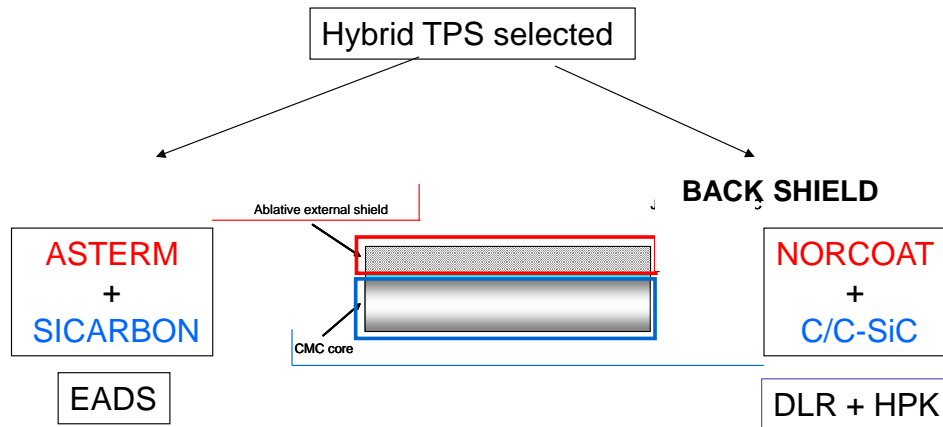


Fig. 5. Material families combinations: ASTERM[®] + SICARBON[®] and NORCOAT FI[®] + C/C-SiC[®]

The critical aspect of the bonding is the selection of a suitable adhesive at the ablator/CMC interface, as it has to withstand a temperature peak of 1200 °C and still perform when the ablator is fully charred. Therefore, the solution must be based on the use of inorganic adhesives. For the selection of the appropriate adhesive the following are taken into account:

- Performance at the different phases (launching, ascent, re-entry)
- Nature of the inorganic filler (alumina, zirconia, graphite, etc..)
- Wettability with the surfaces of the base materials
- Curing temperature
- Ablator/ceramic interface temperature (aided by modeling)
- Thermal properties (CTE, thermal conductivity)

The bonding study has been extended as well to ablator/ablator interfaces, where in this case the use of organic adhesives is envisaged.

SIMULATION AND TPS DESIGN

Simulation includes activities at different levels of the structure. The first level refers to microstructure scale and to the thermo-chemical effects, where a performance in the micro/nano range is necessary. This kind of modeling is aided by 3D model technologies by the use of a nano-tomographic system (by ICMCB-CNRS). Few examples on both type of ablators are depicted in Fig. 6.

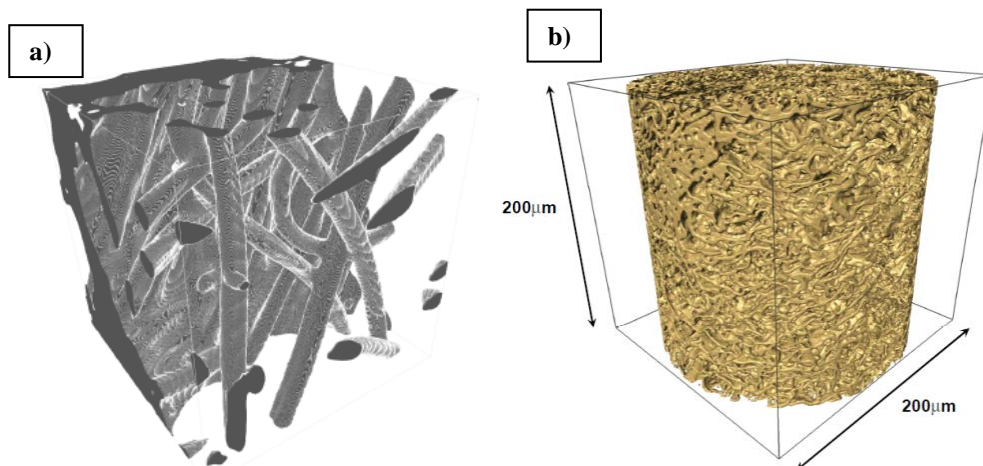


Fig. 6. Local model on ablators: a) Carbon fibre based and b) Cork particles based

In parallel, an empirical model is applied in order to predict the behavior of the ablator at the macroscale and aid design decisions. This is based on a 1D Thermal ablation model (by Astrium SAS) and is helping to assess ablator thickness and interfacial temperature [12]. As an example, in correlation with mission requirement, several control points were selected at the front and back shield, as depicted in Fig. 7a. Initial simulation envisaged to the CT /ARV capsule has allowed to calculate first design parameters; such as thicknesses and recession vs. temperature at the interface (see Fig. 7b). In addition, an extension to a 2D model will enable a thermal analysis of the hybrid solution.

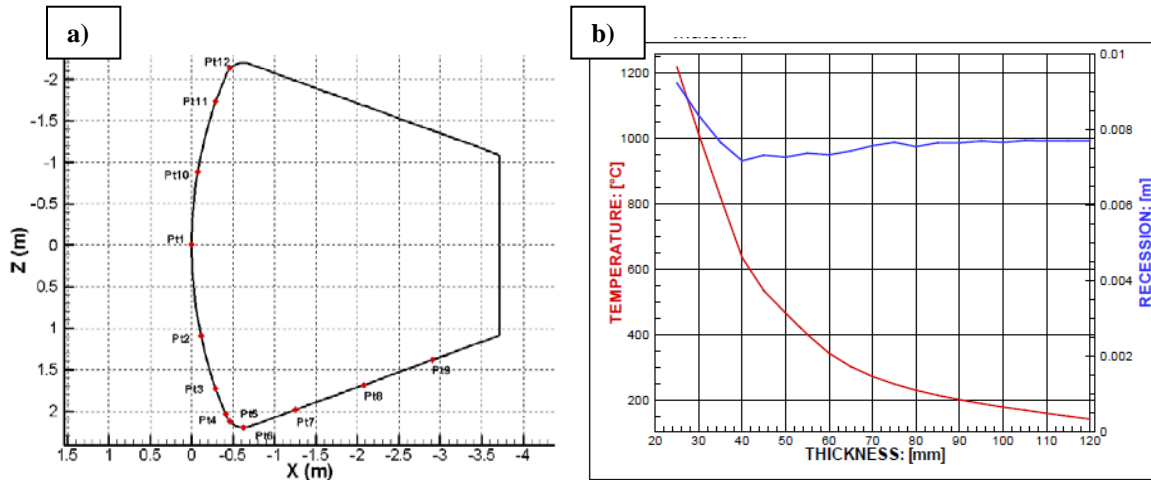


Fig. 7.1D modelling: a) Control points on front and back shield (CTV /ARV) b) Preliminary design analyses: recession and thickness vs ablator/ceramic interface temperature

Regarding further activities for design, a tile breadboard of 100 mm x 100 mm (planar) has been envisaged, which includes ablator/ablator joints and ablator/ceramic bonding. Moreover, mass saving calculation will be performed with respect to a complete capsule vehicle (i.e. CTV/ARV).

CHARACTERISATION AND VERIFICATION PLAN

The characterization activities are structured at three levels: (1) Characterization of materials and bonded structures, (2) Cyclic test at INDUTHERM (DLR Stuttgart) and (3) Final test of the breadboard at the PWT (IRS Stuttgart).

The materials and bonding characterisation includes a full plan for the measurement of the properties of ASTERM: mechanical (tensile, compressive and flexural strength, including cryogenic temperatures) and thermo-physical (Emissivity, coefficient of thermal expansion, specific heat, thermal diffusivity and conductivity). The bonding characterization will include the selection of the most suitable adhesive, where a first screening is running based on bonding results and shear strength test. A second screening will run based on thermal shock [13] (QST-2 at INCAS, see Fig 8a) and cyclic test at INDUTHERM [14] (DLR Stuttgart, see Fig. 8b). Final selection based on the performance and the plasma wind tunnel facilities at IRS [15]. A correlation with the specifications above mentioned with the plasma wind tunnel conditions is on-going (see Fig. 8c).

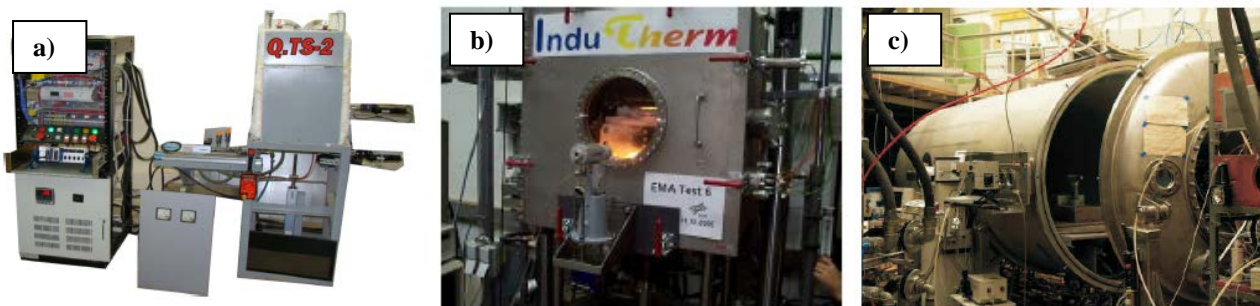


Fig. 8 View of few facilities used for the characterisation/verification plan a) QST-2 at INCAS, b) INDUTHERM at DLR-Stuttgart and c) PWK1 facility at IRS

MAIN CONCLUSIONS AND FUTURE WORK

HYDRA project explores a new TPS concept that combines a low density ablator and a underneath hot substructure. Main anticipated advantages are focused on mass reduction as compared with a solution based on a single ablator solution, while increasing the temperature limits as compared with a re-usable system. The project is running for one third of its total duration, the mission is selected, the requirements are set and the characterisation/verification plan is ready. The materials trade-off is almost finished and the materials have been procured to the partners. The simulation phase and bonding study has been initiated. Future effort will include the selection of the adhesive based on a complete screening study (2nd year) and the execution of the verification plan (3rd year) including characterisation under Plasma Wind Tunnel conditions. A mass saving analysis will be carried-out with regards to a full shield concept. For more details see www.hydra-space.eu

ACKNOWLEDGMENTS

This work has been performed within the framework of the European Project ‘‘HYDRA’’ (G.A. n. 283797) with the financial support by the European Community. The author specially thanks the strong support received EADS-IW (C. Wilhelmi) and ESA (M. Bottacini and B. Jeusset), IRS (T. Marynowski) and Astrium SAS (Y. Aspa)

REFERENCES

- [1] B. Laub and E. Venkatapathy, ‘‘Thermal Protection System Technology and Facility Needs for Demanding Future Planetary Missions’’. International Workshop on Planetary Probe Atmospheric Entry and Descent Trajectory Analysis and Science, Lisbon, Portugal, 6-9 October 2003.
- [2] J.-M. Bouilly, L. Dario, F. Leleu, ‘‘Ablative thermal protections for atmospheric entry. An overview of past missions and needs for future programmes’’, 5th European Workshop on TPS and Hot Structures – ESTEC Noordwijk – 17-19 May 2006
- [3] T. Salmon, X. Vo and M. Bottacini, ‘‘TPS Architecture on ARV’’ Proceedings of the 7th European Symposium on Aerothermodynamics, by Ouwehand, L. Noordwijk, Netherlands: European Space Agency, 2011, id.120.
- [4] M. Caporicci, ‘‘European Atmospheric Re-entry Activities Status and Perspectives’’, 3rd ARA Days – Arcachon, May 2011.
- [5] A. Lacombe and T. Pichon, ‘‘SEPCORE®: An Advanced Modular TPS Integral Structure’’ International Symposium on Atmospheric Re-entry Vehicles and Systems, March 16-18, 1999 Arcachon (France).
- [6] H. Stockflet, ‘‘Development, Performance and Application Potential of the Surface Protected Ablator concept used for the MIRKA Reentry Capsule Heatshield, 3rd European Workshop on Thermal Protection Systems – ESTEC Noordwijk – March 1998.
- [7] G. Vekinis and G. Xanthopoulou ‘‘Plasmatron Testing of Hybrid-TPS’’, 6th International Planetary Probe Workshop Conference Proceedings June 21-27, 2008 Atlanta, Georgia, USA
- [8] H. Ritter, O. Bayle, Y. Mignot, E. Boulier, P. Portela, J.-M. Bouilly et al. ‘‘Ongoing European Developments on Entry Heatshields and TPS Materials’’, 8th International Probe Workshop, June 6-10, Portsmouth –USA,
- [9] G. Pinaud, A.J. van Eekelen*, and J.-M. Bouilly,, ‘‘Aerofast: Development Of Cork TPS Material And A 3d Comparative Thermal/Ablation Analysis Of An Apollo & A Biconic Sled Shape For An Aerocapture Mission’’, 8th International Probe Workshop, June 6-10, Portsmouth –USA, 2011.
- [10] G. Motz, S. Schmidt and S. Beyer, ‘‘The PIP - process: Precursor Properties and Applications’’ in: ‘‘Ceramic matrix Composites, edited by Walter Krenkel, Wiley, pp. ,165-186, 2008
- [11] B. Heidenreich, ‘‘Melt Infiltration Processes’’ in: ‘‘Ceramic matrix Composites, edited by Walter Krenkel, Wiley, pp. ,113-139, 2008.
- [12] G. Pinaud and T. van. Eekelen, ‘‘A numerical comparison of high- and low-fidelity radiation models for conduction-radiation coupling in (charring) ablators’’, 7th European Workshop on Thermal Protection Systems and Hot Structures, 8 – 10 April 2013, ESA-ESTEC, Noordwijk, The Netherlands.
- [13] A. Stefan, D. Bojin, Victor Manoliu, ‘‘Ceramic Layers As Thermal Barrier’’, U.P.B. Sci. Bull., Series B, Vol. 69, No. 3, 2007
- [14] M. Ortel, H. Weihs, I. Fischer, M. Dogigli, ‘‘Thermo-Mechanical Qualification Tests of Complex CMC Re-Entry Structures’’ 27th Annual Cocoa Beach Conference on Advanced Ceramics and Composites: B: Ceramic Engineering and Science Proceedings, Volume 24, Issue 4, pp.281 - 287
- [15] G. Herdrich, M. Fertig and S. Löhle, ‘‘Experimental Simulation of High Enthalpy Planetary Entries’’ The Open Plasma Physics Journal, 2009, 2, 150-164.



FP7/SPACE PROJECT “HYDRA” Hybrid Ablative Development For Re-Entry In Planetary Atmospheric Thermal Protection

J. Barcena¹, S. Florez¹, B. Perez¹, J-M. Bouilly², G. Pinaud², W. P. P. Fischer³, A. de Montbrun⁴, M. Descomps⁴, D. Lorrain⁴, C. Zuber⁵, W. Rotaermel⁵ and H. Hald⁵, P. Portela⁶, K. Mergia⁷, G. Vekinis⁷, A. Stefan⁸, C. Ban⁸, D. Bernard⁹, V. Leroy⁹, R. Wernitz¹⁰, A. Preci¹⁰ and G. Herdrich¹⁰

¹Tecnalia Research & Innovation, ²Astrium SAS (France), ³Astrium GmbH(Germany), ⁴Liège HPK SA (France), ⁵DLR (Germany), ⁶High Performance Structures – HPS (Portugal), ⁷N.C.S.R "Demokritos" (Greece), ⁸INCAS (Romania), ⁹ICMCB-CNRS (France), ¹⁰IRS – University of Stuttgart (Germany)

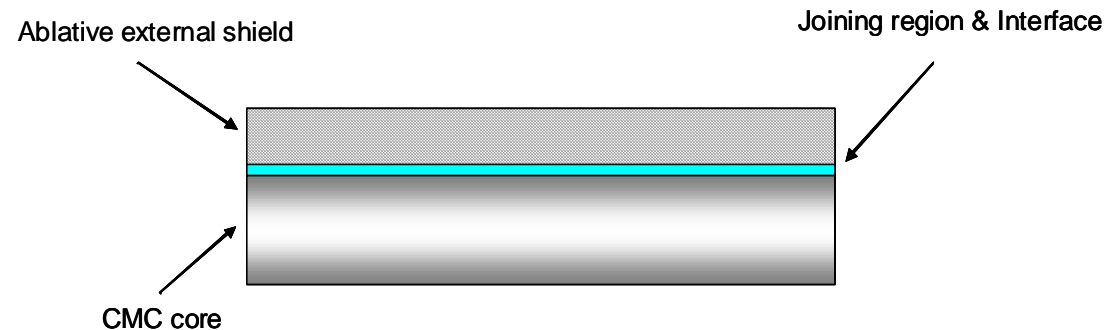


The research leading to these results has received funding from the European Union Seventh Framework Programme (FP7/2007-2013) under grant agreement n° 283797

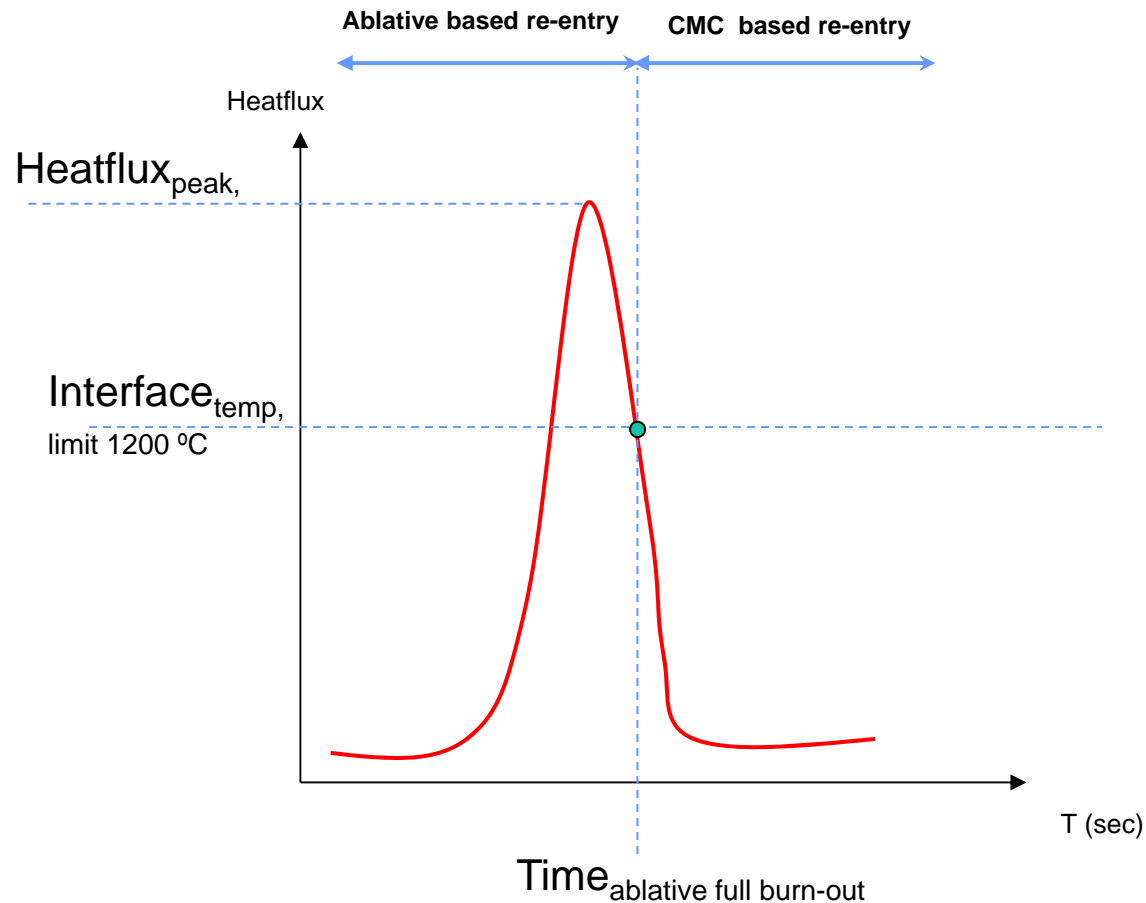
- INTRODUCTION AND MOTIVATION
- CONCEPT OF THE PROJECT
- CONSORTIUM, SCHEDULE AND WPs LOGIC
- MISSION REVIEW AND TPS SPECIFICATIONS
- MATERIALS STATE OF THE ART AND TRADE-OFF
- MATERIALS SELECTION AND PROCUREMENT
- BONDING & TPS ASSEMBLY
- SIMULATION AND TPS DESIGN
- CHARACTERISATION & VERIFICATION PLAN
- SUMMARY AND MAIN CONCLUSIONS
- ACKNOWLEDGMENTS

- **Original approaches** based on ablative materials and novel TPS solutions are required for space applications where resistance in extreme oxidative environments and high temperatures are required. The atmospheric entry of space vehicles from high-energy trajectories requires high-performance **thermal protection systems that can withstand** extreme heat loads.
- A new scenario has appeared due to a worldwide change in space mission planning strategies with entry vehicles going back to **capsule designs and ablators are re-gaining attention**.
- Consequently, the development of **new, more efficient materials and systems is a must**. Such developments, nevertheless, have to be subject to extensive experimental investigations using suitable facilities. In this view, **the investigation and development of new materials** based on ablative and thermostructural concepts is crucial. A new (hybrid) concept based on the combination of both type of TPS materials is proposed.
- The **advantage** of the ceramic for this function is the **low density compared to ablative material** and the excellent thermal performance in this heat load range, as well as the stability of the shape of TPS which is an advantage for the aerodynamic of the re-entry vehicle.
- **Another asset** comes from the **reliability and safety point of view**. The underneath ceramic core offers extra thermal protection in case of the failure or underestimated design of the ablative external protections (see reference of the Galileo's Probe). **An accompanying effect** is also the **lower contamination** during all mission phases and especially during re-entry.

- The concept of the project is based on the development of a novel hybrid heatshield, based on the **integration of an external ablative parts with a CMC thermostructural core**. This will be carried out by the **integration of dissimilar materials**.
- The **main advantage** of a hybrid TPS heat-shield is based on the **capability of the ablative layer** of the hybrid TPS of **bearing higher heat loads** than the ceramic layer underneath.



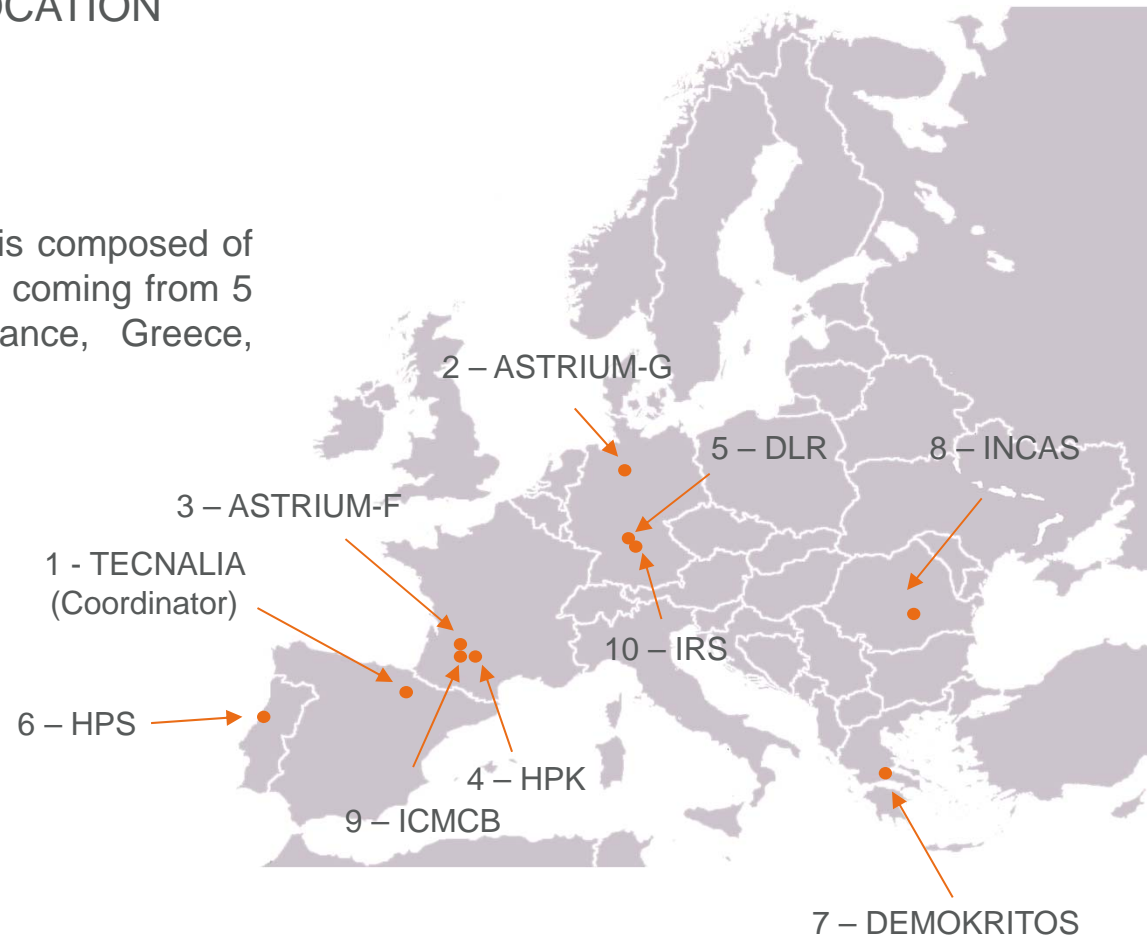
- The main challenge is to achieve a **sound bonding among the two parts**. This will be carried-out by advanced bonding technologies. This will be carried out by the study and development of **new adhesives solutions**, with improved mechanical and insulating characteristics. The use of advanced high temperature adhesives and hybrid solutions in **combination with mechanical attachments** will be assessed, as well as other **existing hybrid solutions**.



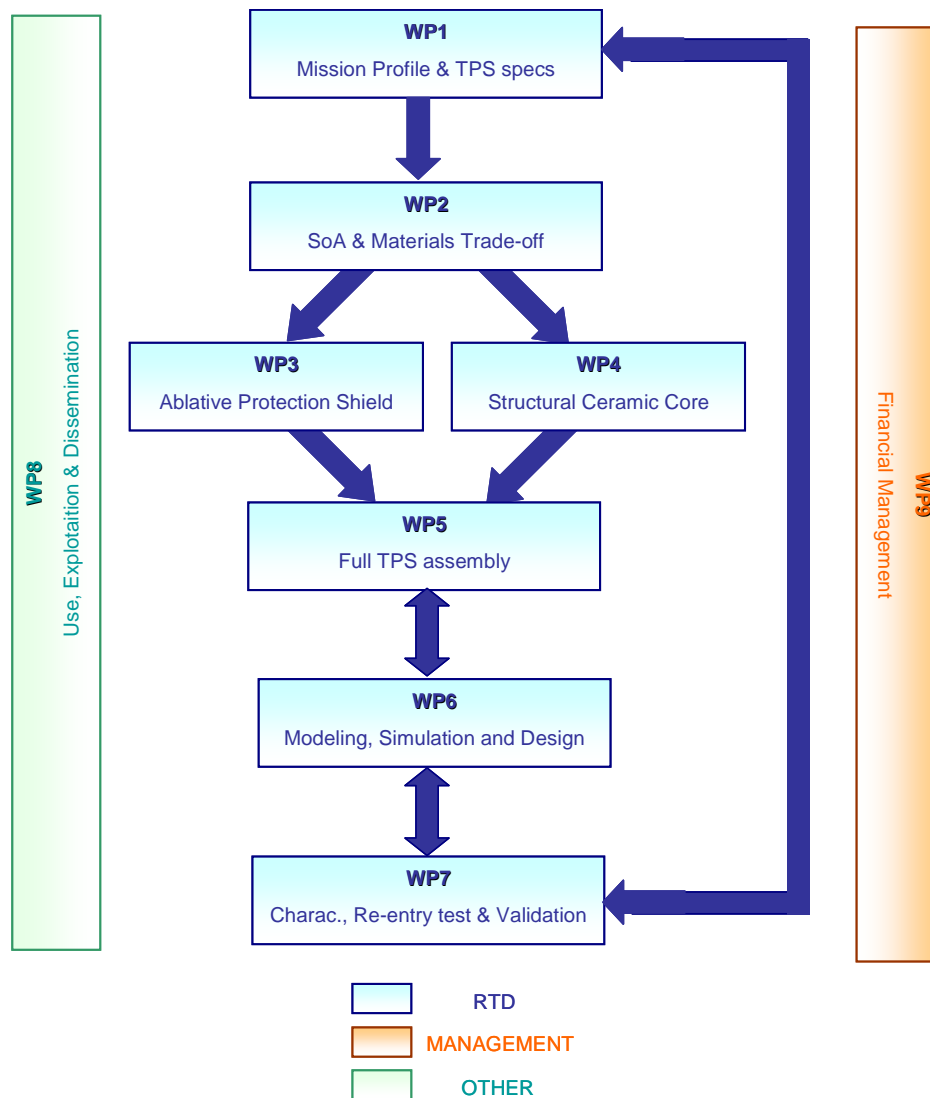
- From this point of view it will offer **improved mechanical properties as well as higher robustness** during the entry. Besides, the new moon or interplanetary missions planned cause higher heat loads during earth re-entry than ceramic or metallic TPS can withstand, since these heat loads are characterized by a peak profile the **ablator can bear the high heat loads during the peak**. For that a comparatively thin layer of ablative material is sufficient. **The large integral loads will then be overtaken by the ablative/ceramic interfacial layer.**

CONSORTIUM MEMBERS LOCATION

The core group of HYDRA project is composed of 10 public and private organisations coming from 5 different European countries: France, Greece, Germany, Romania and Spain.



Part.No.	Part. Short Name	Profile	Relevant expertise for the project	Role in the project	WPs Involvement
1	TECNALIA	Research centre	Ceramic composite materials design, processing, bonding terisation. Background on disseminations and technology transfer.	Coordination, materials developer, materials joining, centre in charge of dissemination actions.	WP2, WP5, WP8, WP9. Technical coordination in (WP1, WP3, WP4, WP6, Wp7)
2	ASTRIUM-G	End user, large company, large system integrator	CMC material development, design, analysis, manufacturing & flight/ground testing as well as application	Developing, designing, manufacturing and characterization testing of C/SiC CMC's.	WP4, WP8
3	ASTRIUM-F	End user, large company	Knowledge of management of atmospheric entry programs. Competence in heatshield thermal protection materials : development, production, characterisation, modelling and analysis	Mission specification, Material developer and producer, heatshield analysis	WP1, WP3, WP6, WP8
4	HPK	SME, material supplier	Cork composite materials (formulations and manufacturing), tooling, bonding, moulding and prototyping	Ablative cork materials and TPS breadboard part supplier.	WP3, WP8
5	DLR	Research centre, space systems manufacturer,	DLR is the German space agency. CMC material development and charactersiation	Developing, designing, manufacturing and characterization testing of C/C-SiC CMC's. Characterisation of hybrid joints.	WP4, WP5, WP6, WP7, WP8
6	HPS	SME, technology provider	TPS technology provider. Konow-how on materials selection.	Technology advisory. Engineering consulting.	WP2, WP5, WP6, WP7, WP8
7	NCSR D	Research centre	Ablative-ceramic joining. Ceramic composite materials characterization & coatings.	Materials joining and characterization.	WP3, WP4, WP5, WP7, WP8.
8	INCAS	Research centre	Composite materials CFRP, C-C composite and partially ceramic matrix design, processing, thermo-mechanical characterisation and morfostructural investigation	Characterisation of space materials	WP7, WP8
9	ICMCB	Research centre	Numerical modeling of coupled phenomenon occurring at local scale, 3D imaging of multi materials	Modelling and characterisation	WP6, WP7, WP8
10	IRS	University	Characterisation of TPS comments and hot structures.	Ground re-entry characterisation and validation of the technology sample	WP1, WP7, WP8




SCHEDULE STATUS

WP No.	Year 1												Year 2												Year 3																					
	February 2012	March 2012	April 2012	May 2012	June 2012	July 2012	August 2012	September 2012	October 2012	November 2012	December 2012	January 2013	February 2013	March 2013	April 2013	May 2013	June 2013	July 2013	August 2013	September 2013	October 2013	November 2013	December 2013	January 2014	February 2014	March 2014	April 2014	May 2014	June 2014	July 2014	August 2014	September 2014	October 2014	November 2014	December 2014	January 2015	February 2015									
WP1 Mission review, trade-off, selection and TPS specs						M1																																								
WP1.1 Mission Profile																																														
WP1.2 TPS specifications																																														
WP2 State-of-the-art & Materials trade-off															M2																															
WP2.1 State-of-the-art																																														
WP2.2 Materials trade-off																																														
WP3 Ablative protection shield																													M3																	
WP3.1 Advanced ablative materials based on resins																																														
WP3.2 Advanced ablative materials based on cork																																														
WP3.3 Manufacture of heat-shield parts																																														
WP4 Structural ceramic core																													M4																	
WP4.1 Ceramic core development & characterization																																														
WP4.2 Ceramic core concept verification & demonstr.																																														
WP5 Full protection system assembly																																														
WP5.1 Definition of bonding processes																																														
WP5.2 Ablative/ceramic frames joining																																														
WP5.3 Fabrication of TPS breadboard																																														
WP5.4. Testing & characterisation of the joint																																														
WP6 Modelling, simulation & TPS design																																														
WP6.1 Simulation of the oxidation																																														
WP6.2 Hybrid thermal modelling of the hybrid concept																																														
WP6.3 TPS final design																																														
WP7 Characterisation, re-entry and validation																																														M7
WP7.1 Microstructural and Thermo-mechanical chara.																																														
WP7.2 Re-entry testing																																														
WP7.3 Validation of the envisaged TPS concept																																														
WP8 Use, exploitation and dissemination																																														
WP8.1 Dissemination activities plan																																														
WP8.2 Use plan																																														
WP9 Financial management, coord. and reporting																																														
WP9.1 Administrative																																														
WP9.2 Financial																																														


Status
at
M13


MANUFACTURE

WP3 & WP4

 AST-F Manufacture of 10 ASTERM plates (550 x 550 x 70 mm)

 HPK Manufacture of 10 NORCOAT LIEGES plates (550 x 550 x 70 mm)


 AST-G Manufacture of SICARBON samples
1 m² in different pannels, 5mm


 DLR Manufacture of C-C/SiC samples
1 m² in different pannels, 5mm




ASSEMBLY

WP5

 NCRSD
Additional testing & surface treatments (K. Mergia)
Ablative-ablative interfaces (G. Veknis)

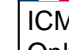
 TECNALIA
•Materials machining
•Basic Thermal & Mechanical Characterisation
•Gluing & Joining
• Materials & Breadboard store


 HPK
"in-situ" Cork Composite manufacture on top of a CMC plate





CHARACTERISATION


WP7

 ICMCB - Thermal Characterisation:
Only ablators
Laser Flash (RT - 1100)
Linear Dilatometry (RT-1600 °C).
(No. samples & Dimension TBD)

 NCRSD
Neutron Tomography
20 samples, Ø 40 x 40 mm aprox (special assembly). Before and after PWT

 INCAS – Thermo-mechanical:
Compression & Flexural (RT)
Thermal shock QST2 (RT-1500 °C)
Microstructural study
< 75 samples & 30 x 50 x 10 mm

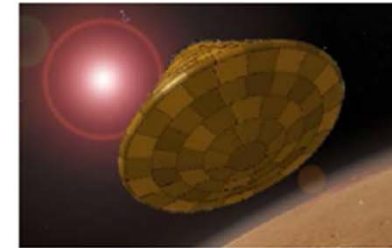
 DLR
Thermo-mechanical at INDUTHERM facility (RT-2000°C)
X-Ray tomography
45 samples - 60x 60 x 60

 IRS
Plasma Wind Tunnel.
20 samples, Ø 39.8 x 40 mm aprox (special assembly)
Emissivity (few samples are possible)

➤ **Mission review and trade-off (by Astrium SAS): analysis of the current mission and European roadmaps for planetary re-entry**

– Various types of missions have been analyzed

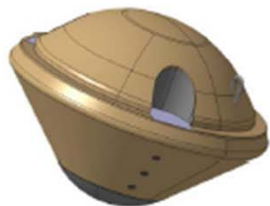
- Earth atmospheric re-entry from Moon
- Earth re-entry missions from LEO / ISS (ARV)
- Interplanetary exploration missions (Exomars, MPL on Mars, Venus & Titan long term)
- Sample return missions (Marco polo, ERC for MSR or MMSR...)
- Earth High speed return demo (Radflight/Phoebus)
- Others...



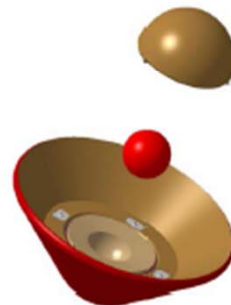
ExoMars (2016 / 2018)



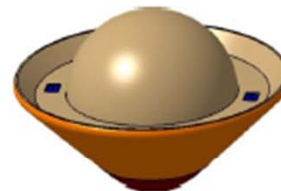
MPL
(< 10 years)



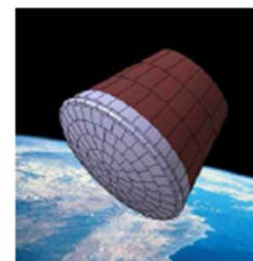
Radflight/Phoebus
(< 10 years)



Marco Polo &
sample return
(< 10 years)



ERC MSRO
(> 10 years)

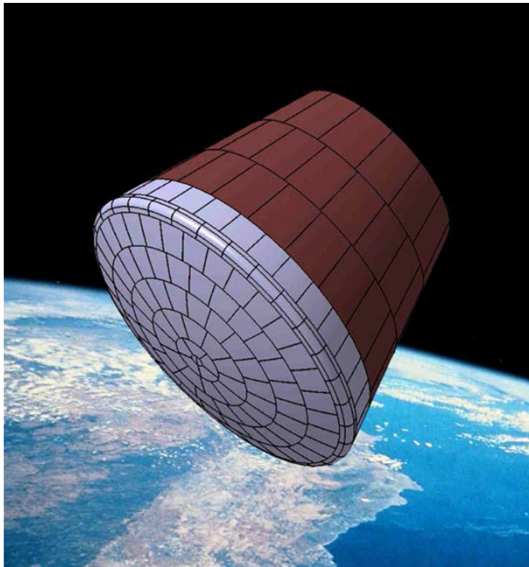


ARV
(ISS servicing)

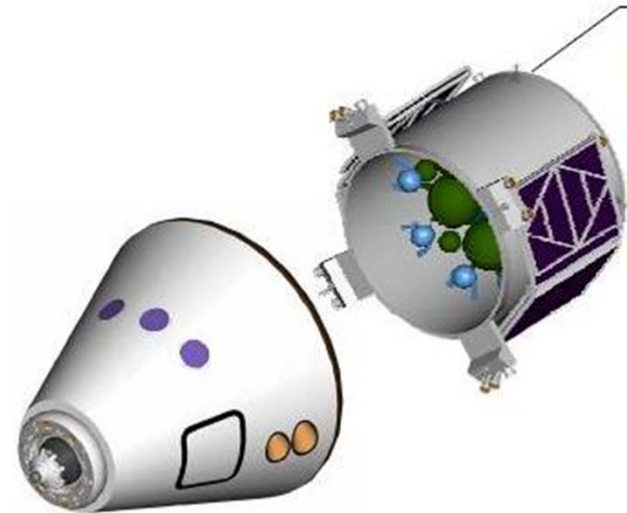


Titan exploration
(> 15 years)

- Final selection based on Earth re-entry: CSTS (from Low lunar orbit) and CTV/ARV (from ISS)



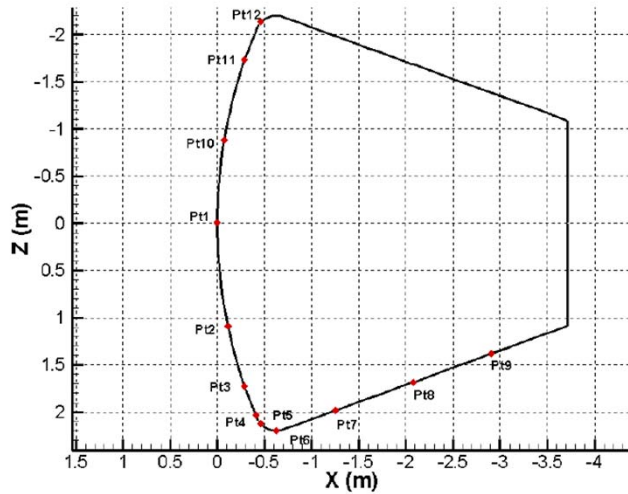
CTV/ ARV (Credit Astrium SAS)



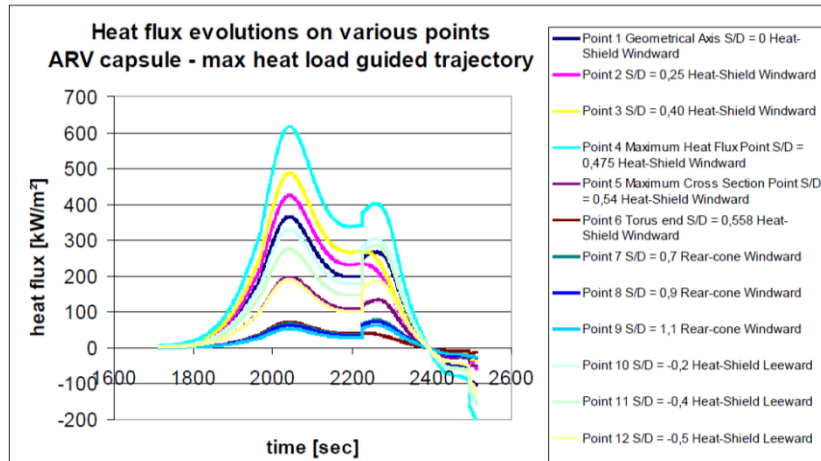
CSTS (Credit Astrium GmbH)

Mission	Convective flux (max – kW/m ²)	Radiative flux (max – kW/m ²)	Total flux (max – kW/m ²)	Max Stagnation Pressure (Pa)	Total Heat Load (MJ/m ²)
CSTS (LLO)	4300	2280	5700	60600	416
CTV / ARV	700 - 1700	/	700 - 1700	~15000 to 20000	140 - 270
Sample Return (EVD)	9520	4300	13800	81700	209

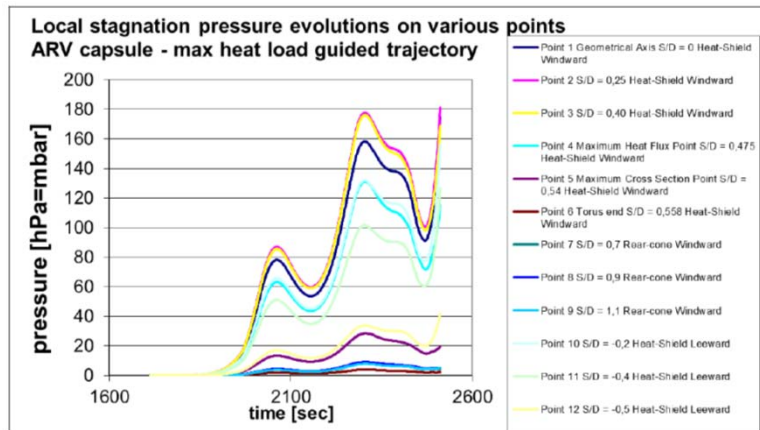
CTV/ARV (CREW TRANSFER VEHICLE / ADVANCED RE-ENTRY VEHICLE)



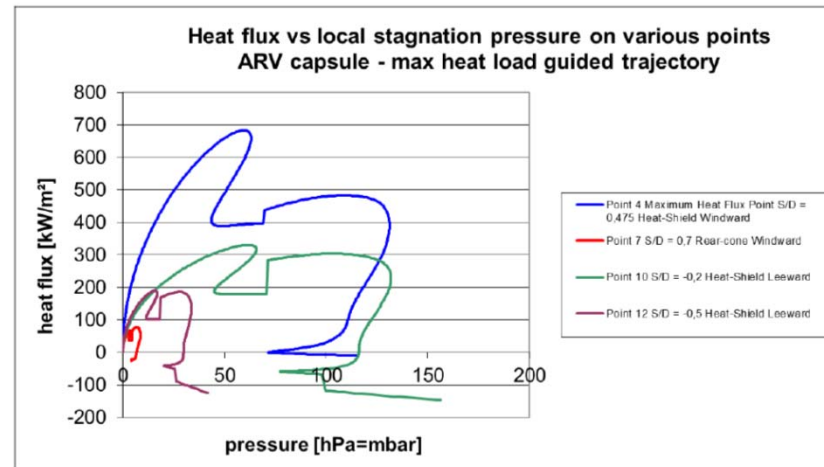
Control Points



Heatflux evolution

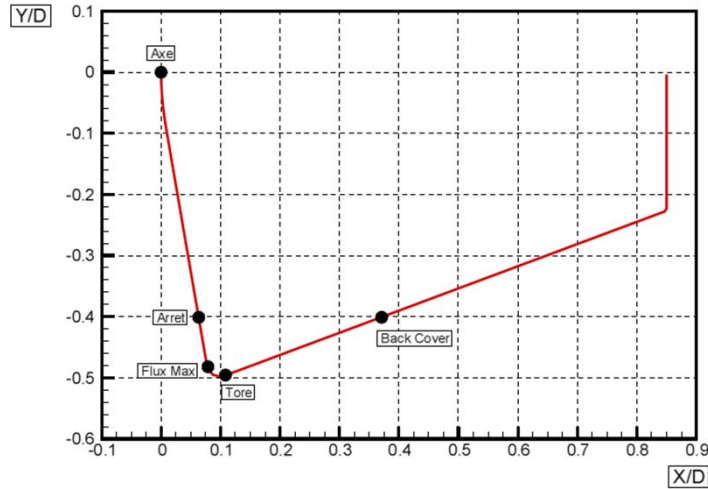


Local stagnation pressure

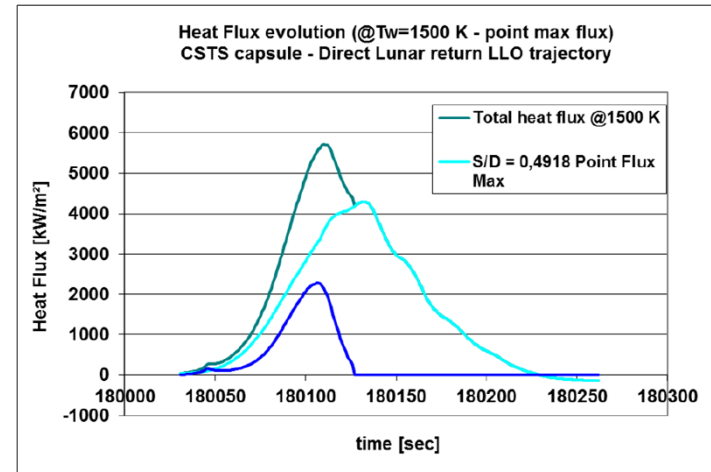


Heat-flux vs. Local stagnation pressure

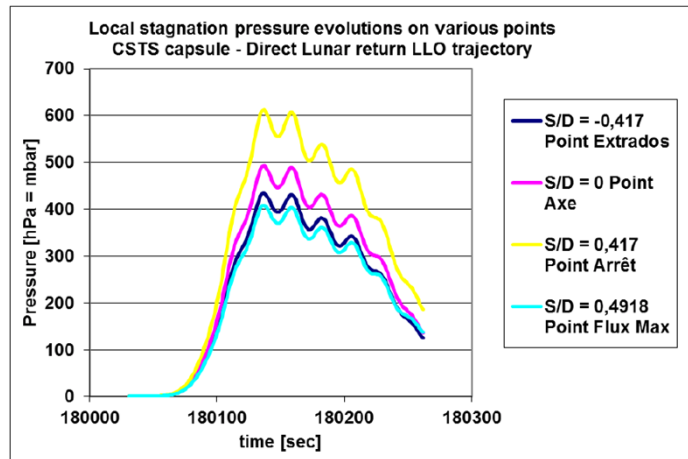
CSTS (CREW SPACE TRANSPORTATION SYSTEM)



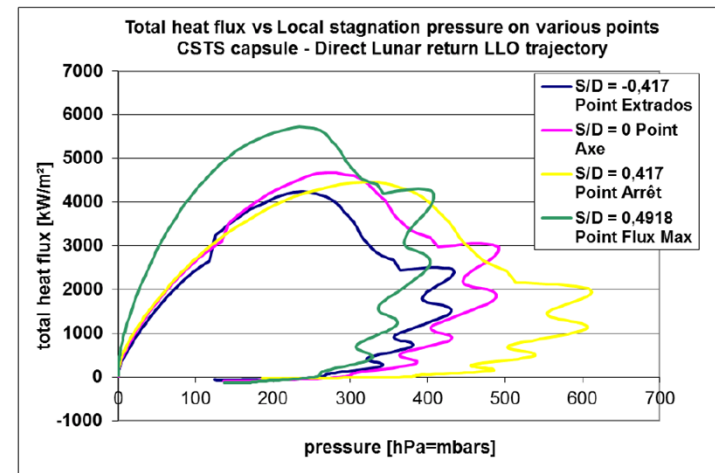
Control Points



Heatflux evolution



Local stagnation pressure



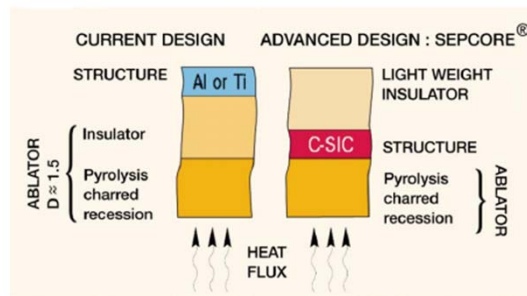
Heat-flux vs. Local stagnation pressure

- Set of requirements defined with regards to the following criteria:

ATD :	Entry Environment	Heat Flux, Pressure, Atmosphere
PER :	Mass & Thermal Performance	Minimal TPS mass
ABL :	Ablation Performance (if any)	Predictable, homogeneous, minimal
MEC :	Mechanical Requirements	Strength, Vibration, depressurisation
MAT :	Material Requirements	Outgassing, Space ageing, cleanliness
INT :	Interface Requirements	Structure, fixation, coating
ENV :	Environmental Requirements	Vacuum, micrometeoroids, temperature, thermal cycle, radiation, UV
PHY :	Physical Requirements	Emissivity, no transparency, ESD
PA :	Product Assurance	REACH, Export Control free, lifetime, flammability, no hazard
DES :	Design Requirements	Thickness, curvature, dimensions
PRO :	Programmatic Requirements	Availability, TRL, European, flexible process

➤ State of the art considering:

- ❖ Analysis of previous “hybrid” concepts: SEPCORE® (ablator on top), SPA (CMC on top), HybridTPS (Porous ceramic infiltrated).
- ❖ Review of ablative materials at worldwide level with emphasis on European supplier.
- ❖ Locate the project partners in this state-of-the-art



SEPCORE® (Herakles)

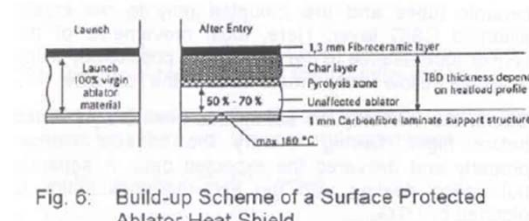


Fig. 6: Build-up Scheme of a Surface Protected Ablator Heat Shield

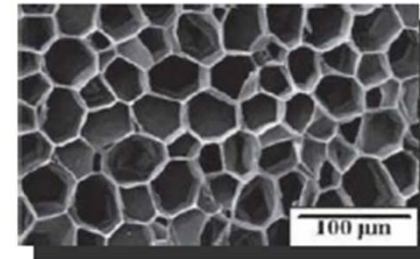
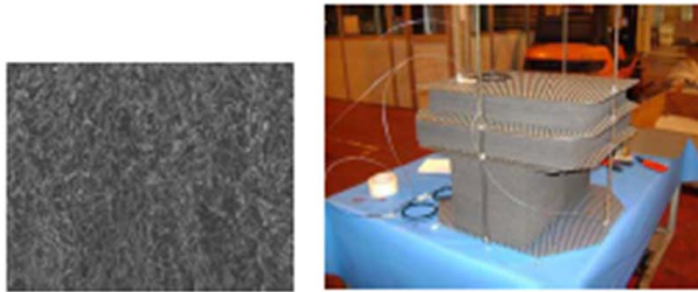
SPA (Astrium GmbH)

➤ Trade-off

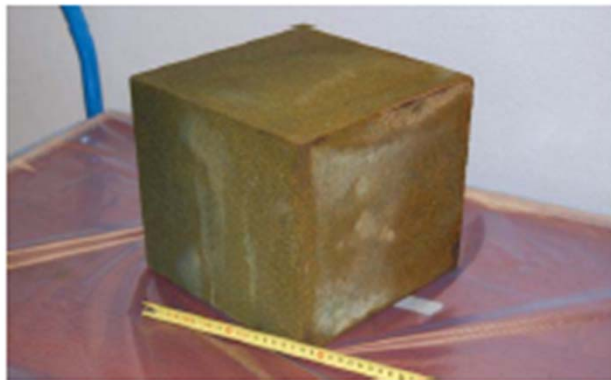
- ❖ Consider relevant ablative TPS materials at worldwide level.
- ❖ Elaborate a TPS material selection matrix -> Trade-off criteria
- ❖ Establish a materials ranking
- ❖ Locate project partner in the ranking
- ❖ Tailor this selection matrix to mission definition from WP1

➤ Two types of phenolic ablator envisaged for the project:

- ❖ Cork based materials: NORCOAT FI (backshield)
- ❖ Graphite based materials: ASTERM (frontshield)



Microscopic Cork cells view



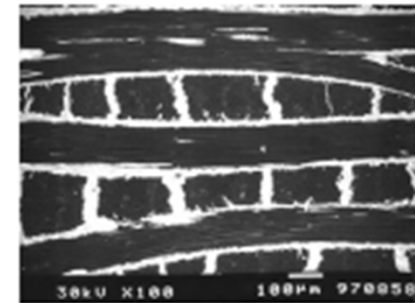
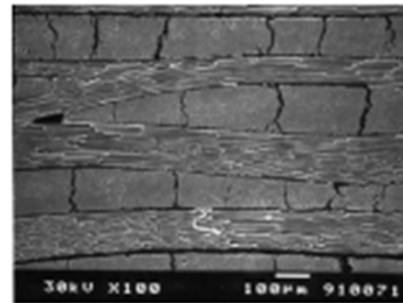
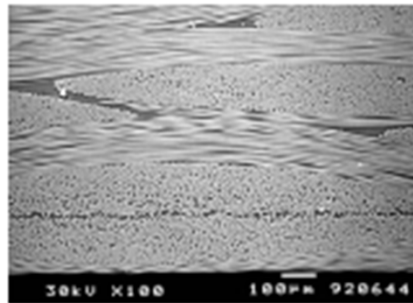
ASTERM
(Astrium SAS)



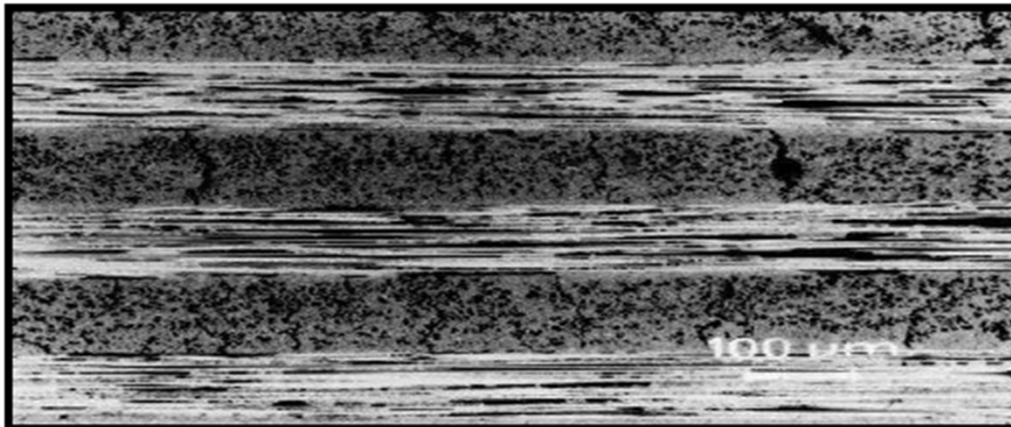
NORCOAT
(HPK Liéges)

➤ Two manufacturers CMC (Cf/SiC) envisaged for the project:

- ❖ C/C-SiC (from DLR stuttgart).
- ❖ SiCARBON© (EADS)



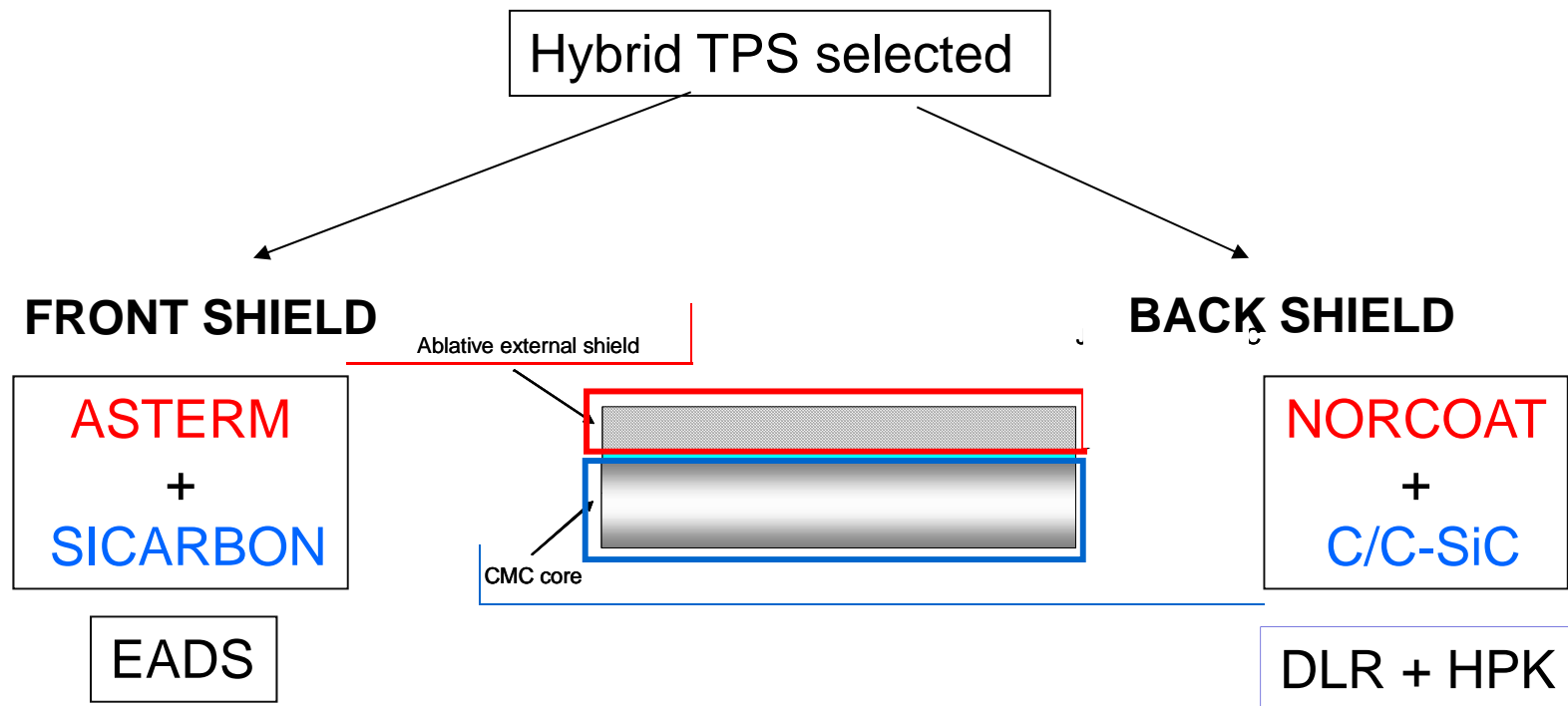
C/C-SiC
(DLR)



SiCARBON™

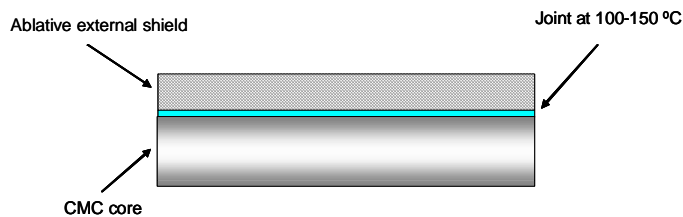
(EADS)

➤ Selection of materials combination

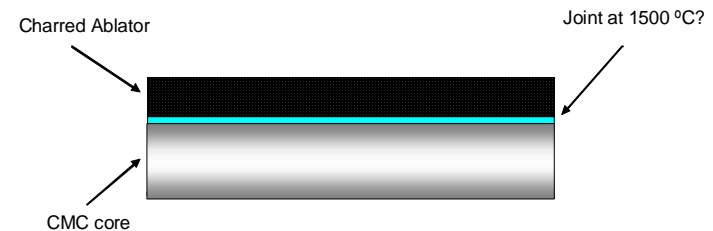


➤ Selection of adhesive:

- ❖ Inorganic based adhesive for the ablator/ceramic joint
- ❖ Organic adhesive for the ablator/ablator interface
- ❖ Criteria of selection:
 - Performance at the different phases (launching, ascent, re-entry)
 - Nature of the inorganic filler (alumina, silica, graphite, etc..)
 - Wettability with the surfaces
 - Curing temperature
 - Ablator/ceramic interface temperature (aided by modeling)
 - Thermal properties (CTE, Thermal conductivity)



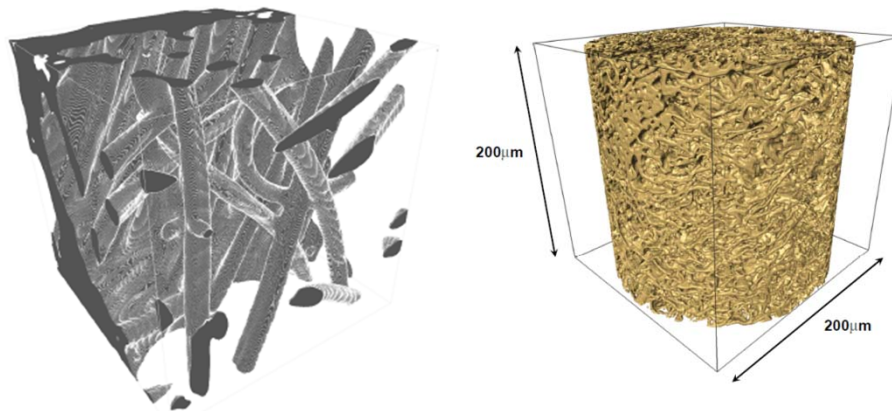
First stage of the re-entry



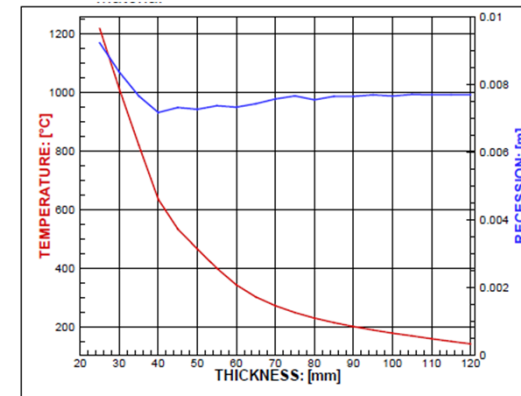
Second stage of the re-entry

➤ Simulation at different levels:

- ❖ Local thermo-chemical model
 - At the micro/nano range
 - Aided by 3D model technologies by the use of a nano-tomographic system (ICMCB)
- ❖ 1D Thermal ablation model (Astrium SAS) -> Assessment of ablator thickness and interfacial temperature -> Lecture by G. Pinaud.
- ❖ Thermal analysis (2D model) -> Materials properties as input



Local model on ablators



1D model (thickness vs. interface temperature and recession)

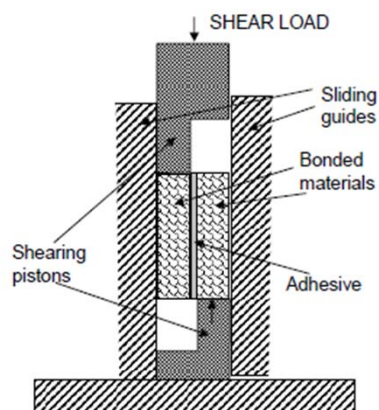
➤ TPS Design

- ❖ Tile breadboard:
 - Foreseen dimensions of 100 mm x 100 mm (planar)
 - Including ablator/ablator joints and ablator/ceramic bonding.
- ❖ Further mass saving calculation wrt a whole capsule vehicle (i.e. CTV/ARV)

➤ Characterization of materials and bonded structures:

- ❖ ASTERM ablator. Full characterization of thermal and mechanical properties
 - Emissivity, coefficient of thermal expansion, specific heat, thermal diffusivity and conductivity
 - Tensile, compressive and flexural strength (including cryogenic temperatures)
- ❖ Adhesive:
 - First screening based on bonding results and shear strength test
 - Second screening based on thermal shock (QST-2 at INCAS) and cyclic test at INDUTHERM (DLR Stuttgart)
 - Final selection based on the performance and the plasma wind tunnel (correlation with WP1 specifications).
- ❖ Final test of the breadboard at the PWT (IRS, Stuttgart). Comparison of performance vs. requirements.

Shear tests:

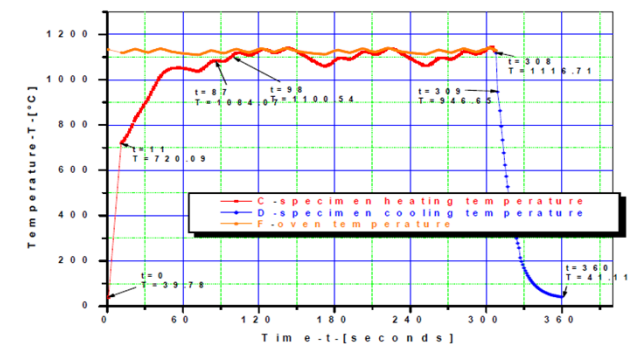


Shear test at NCSR "Demokritos"



Thermal shock furnace at INCAS

Typical heat-up and cool-down rates in QTS2 installation at 1100°C, TBC specimen



➤ Cyclic test at INDUTHERM (DLR Stuttgart)



Heating elements	Graphite	C/C-SiC
Max. heating temperature	2000°C	1700°C
El. power	50 kW	50 kW
Max. sample temperature (depending on sample geometry)	Approx. 1700°C	Approx. 1600°C
Atmosphere	Air up to 200 mbar, Nitrogen	Air, Nitrogen

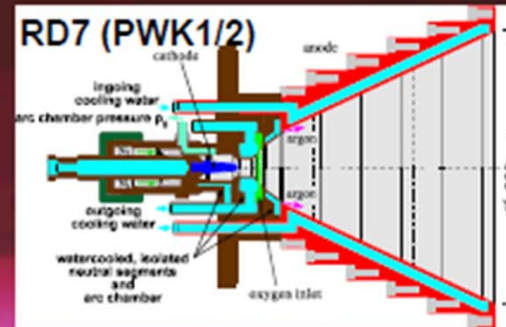
- Pressure range: 0.1 - 950 hPa, adjustable between 0.2 - 900 hPa
- Max. mechanical load: 250 kN
- Inner chamber dimensions (usable): 750 x 750 x 550 mm³
- Data acquisition: Digital



➤ Final test of the breadboard at the PWT (IRS Stuttgart):

MPG driven PWK1 / PWK2

- length 6m, \varnothing 2m
- specific Enthalpies: 2-150 MJ/kg
- total pressures: 1-100 hPa
- Working gases: N_2+O_2 , Ar, Ar+ O_2 , N_2 , H_2 , N_2+CH_4 , Ar+ CO_2 , He
- RD5 nozzle exit \varnothing 125mm, RD7 nozzle exit \varnothing 320mm

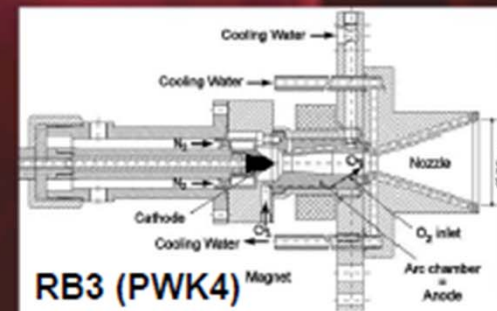
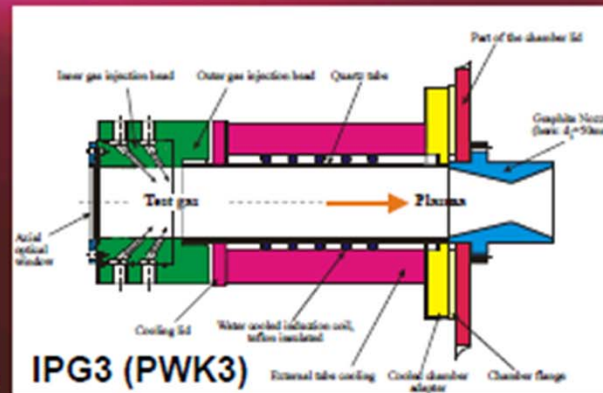


TPG driven PWK4

- length 6m, \varnothing 2m
- specific Enthalpies: 1-80 MJ/kg
- Total pressures: 1-15 hPa (air) / 50 hPa (O_2)
- Working gases: any, e.g. N_2 , O_2 , Ar, H_2 , CO_2 or combinations

IPG driven PWK3

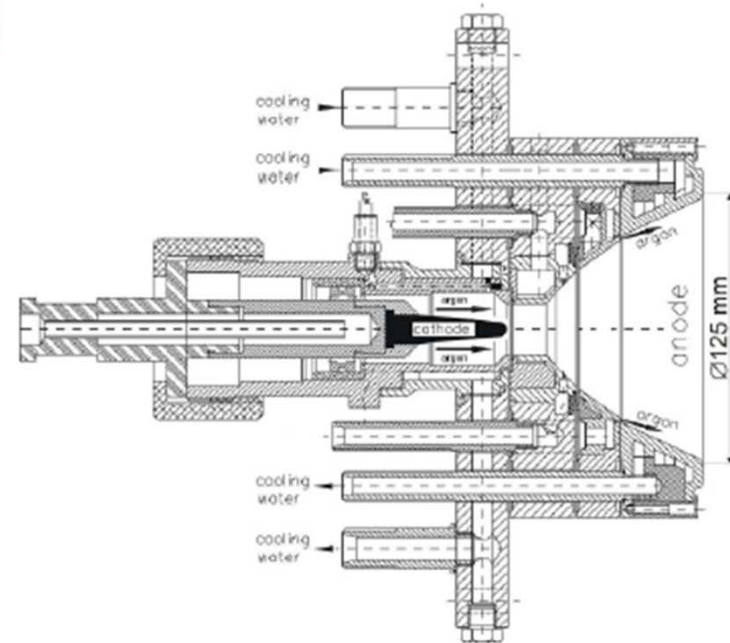
- length 2m, \varnothing 1.6m
- specific Enthalpies: 1-30 MJ/kg
- Total pressure: 1-1000 hPa
- Working gases: N_2+O_2 , Ar, Ar+ O_2 , N_2 , H_2 , N_2+CH_4 , Ar+ CO_2 , H_2+O_2 , He



➤ Final test of the breadboard at the PWT (IRS Stuttgart):

- Facility PWK2 for CTV/ARV conditions
- Facility PWK1 for CSTS, using either RD5 or RD7 as plasma source for 5.7 MW/m² condition

IRS Facility PWK1 (MPD driven)



- Steady state testing possible (up to several hours)
- Length: 6 m
- Diameter: 2 m
- 3 cylindrical water cooled segments
- Trajectory simulation by maneuverable 4-axis positioning system
- Plasma jet accessible by optical measurement devices on its whole length
- Plasma source flanged to the movable lid (on rails)
- Magneto-plasmadynamic generator MPG RD5
- Nozzle exit diameter: 125 mm
- Working gas types: Ar, N₂, N₂/O₂
- Pressure domain: up to 5000 Pa
- Enthalpy domain: up to 150 MJ/kg (air)
- Heating of the plasma by thermal energy of the arc
- Additional acceleration of the plasma through Lorentz forces

- HYDRA is a new TPS concept that combines a low density ablator and a underneath hot substructure.
- Main advantages are:
 - 1) Mass reduction as compared with a solution based on a single ablator solution, while
 - 2) Increase the temperature limits as compared with a re-usable system
- The project is running for one third of the total duration, the mission is selected, the requirements complied and the characterisation/verification plan is ready.
- The materials trade-off is almost finished and the materials are have been just procured to the partners. The simulation phase and bonding study has been initiated.
- Future effort will include the selection of the adhesive based on a complete screening study (2nd year) and the execution of the verification plan (3rd Year) including characterisation under Plasma Wind Tunnel conditions.
- A mass saving analysis will be carried-out with regards to a full shield concept.

- European Space Agency (M. Bottacini and B. Jeusset)
- European Commission
- Research Executive Agency (C. Ampatzis)
- EADS-Innovation Works (C. Wilhelmi).
- NCSRD (K. Triantou).
- IRS (T. Marynowski)
- ASTRIUM SAS (Y. Aspa)

RSS Feed
Google Custom Search

April 4, 2012 | 2:42 pm



Hybrid ablative development for re-entry in planetary atmospheric thermal protection



[HOMEPAGE](#)
[OBJECTIVES](#)
[PROJECT STRUCTURE](#)
[PARTNERS](#)
[DOCUMENTS](#)
[NEWS & EVENTS](#)
[CONTACT US](#)



Original approaches based on ablative materials and novel TPS solutions are required for space applications where resistance in extreme oxidative environments and high temperatures are required. The atmospheric entry of space vehicles from high-energy trajectories requires high-performance thermal protection systems that can withstand extreme heat loads. On missions like a sample return to earth or an entry into the atmosphere of a gas giant planet as e.g. Jupiter, thermal loads can be two to three orders of magnitude larger than those for earth re-entry from low earth orbit (LEO). Such missions are extremely mass critical and therefore very hard to realize.

The most challenging missions, such as the Pioneer Venus Probe missions and the Jupiter probe Galileo, were performed using the high density versions based on heritage carbon phenolic, which is the most efficient ablation material. However, the material is derived from developments that are more than 20 years old and the procurement is at present doubtful. In addition, a new scenario has appeared due to a worldwide change in space mission planning strategies with entry vehicles going back to capsule designs and ablators are re-gaining attention.

Consequently, the development of new, more efficient systems is a must. Such developments have to be subject to extensive experimental investigations using suitable facilities. The investigation and development of new materials based on ablative and thermostructural concepts is crucial.

HYDRA aims the development of hybrid thermal protection systems (TPS) for their use in space applications with extreme oxidative environments and high temperature resistance, such as hot parts of space vehicles for orbital entry, planetary probes and NEO exploration.

PRIVATE AREA

MAILING LIST

NEWS & EVENTS

HYDRA at the 7th ESA TPS workshop

[ESA News](#)

6 month progress meeting



PROJECT PARTNERS



















© 2012 HYDRA: Hybrid ablative development for re-entry in planetary atmospheric thermal protection
 & | 2012 | [CSS](#) - [Developed by tecnalia.intellicube](#)

For more details visit the Project webpage: www.hydra-space.eu

**END OF
PRESENTATION**

**Many thanks for
your attention**

RASTAS SPEAR : RADIATION-SHAPES-THERMAL PROTECTION INVESTIGATIONS FOR HIGH SPEED EARTH RE-ENTRY

J-M. Bouilly⁽¹⁾, A. Pisseloup⁽¹⁾, O. Chazot⁽²⁾, G. Vekinis⁽³⁾, A. Bourgoing⁽⁴⁾, B. Chanetz⁽⁵⁾, Z. Skorupka⁽⁶⁾

⁽¹⁾ EADS Astrium Space Transportation - BP 20011, 33 165 Saint-Médard_en-Jalles Cedex, France
e-mail : jean-marc.bouilly@astrium.eads.net, aurelien.pisseloup@astrium.eads.net

⁽²⁾ Von Karman Institute, Aeronautics & Aerospace Dept, Ch De Waterloo 72, 1640 Rh-St-Genese, Belgium

⁽³⁾ Institute of Materials Science, NCSR "Demokritos", 15310, Aghia Paraskevi Attikis, Greece

⁽⁴⁾ EADS Astrium Space Transportation, Route de Verneuil, 78133 Les Mureaux CEDEX, France

⁽⁵⁾ ONERA, 8 rue des Vertugadins, 92 190 Meudon, France

⁽⁶⁾ Institute of Aviation - Landing Gear Department, Al. Krakowska 110/114, 02-256 Warsaw, Poland

ABSTRACT / INTRODUCTION

An important step for Space Exploration activities and for a more accurate knowledge of the Earth, universe and environment is to develop the capability to send vehicles into space, which collect and return to Earth samples from solar system bodies. To return these samples, any mission will end by high-speed re-entry in Earth's atmosphere. This requires strong technological bases and a good understanding of the environment encountered during the Earth re-entry. Investment in high speed re-entry technology development is thus appropriate today to enable future Exploration missions such as Mars Sample Return. Rastas Spear project started in September 2010, with the main objective to increase Europe's knowledge in high speed re-entry vehicle technology to allow for planetary exploration missions in the coming decades.

The research leading to these results has received funding from the European Union Seventh Framework Programme (FP7/2007-2013) under grant agreement n° 241992.

The project's main objective can be derived in sub-objectives as follows:

- **OBJ1:** To better understand phenomena during high speed re-entry enabling more precise Capsule sizing and reduced margins.
- **OBJ2:** To identify the ground facility needs for simulation
- **OBJ3:** To master heat shield manufacturing techniques and demonstrate heat shield capabilities.
- **OBJ4:** To master damping at ground impact and flight mechanics and thus ensure a safe return of the samples.

This study has been carried out by a consortium of European companies and institutes : VKI (B), Kybertec (Cz), Demokritos (Gr), IoA (Pl), CIRA (I), CFS (CH), MSU (Ru), CNRS and ONERA (F), and coordinated by Astrium (F).

After shortly reminding the organisation and objectives of the RASTAS SPEAR project, the scope of this paper is to present its main achievements, aiming at enhancing the basic capabilities on some specific topics such as:

- Aeroshape stability
- High speed aerothermal environment
- Sub-system / equipment : Thermal protection, Crushable material

1. SCOPE

1.1 - PROJECT OVERVIEW

This project has been funded from the European Union Seventh Framework Programme (FP7/2007-2013) under grant agreement n° 241992. It was approved within EC FP7 second call, as part of the following topics:

- Activity 9.2 – strengthening of space foundations / research to support space science exploration
- SPA.2009.2.1.01 Space Exploration

This project started in September 2010 with a planned duration of 26 months. After a necessary 6-month extension, the end of the study is now scheduled at the end of April 2013.

The total budget is about 2.3 M€ including about 1.6 M€ grant from the European Commission.

The team is composed of 10 partners from 8 European Countries (see Table 1), Astrium being the coordinator.

More information can be found on the project website at www.rastas-spear.eu.

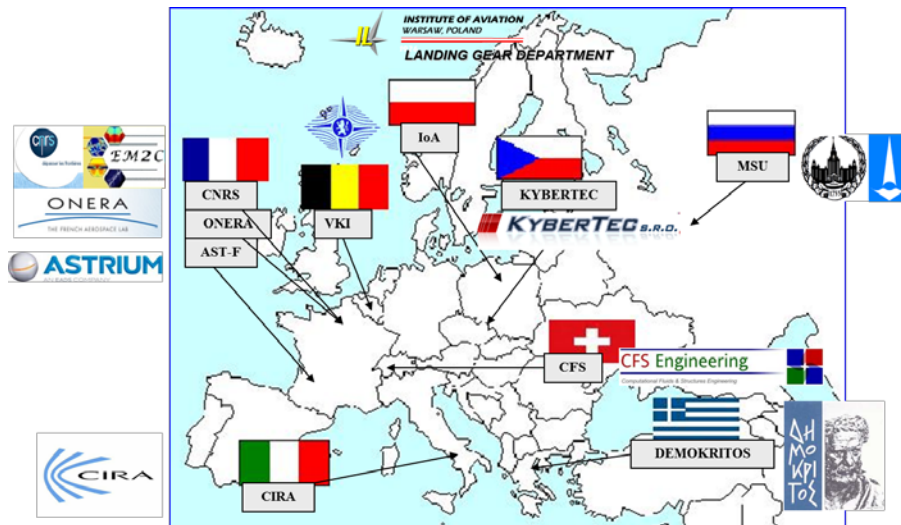


Figure 1: Partners involved in Rastas Spear project

2. WP1 : REVIEW OF SYSTEM REQUIREMENTS

This task was conducted at the very beginning of the project, with the aim to provide with general inputs for any other WP of the project. As detailed in [2,3], general system requirements for high-speed entry capsules were defined, through the following main sub-tasks:

- **Atmosphere modelling:** reference atmospheric models were consolidated for Earth and Venus
- **Trajectories:** generic aeroshapes were identified with respect to candidate exploration missions, with focused attention towards Earth entry. Trajectories have been computed including usual design criteria and flight domain has been determined with classical constraints on several parameters (max heat flux, max heat load, max g-load,...)
- **Aerodynamics and Aerothermodynamics:** Aerothermal environment (convective and radiative heat flux) was determined for the identified trajectories
- **Vehicle design:** aimed at a preliminary designing the generic ERC (Earth Return Capsule) (see Figure 3).

Preliminary requirements related to TPS for other WP have also been established thanks to 1 or 2D thermal models of the capsule: surface recession, mass loss, position of centre of gravity, temperature evolution, gas flow rate,...

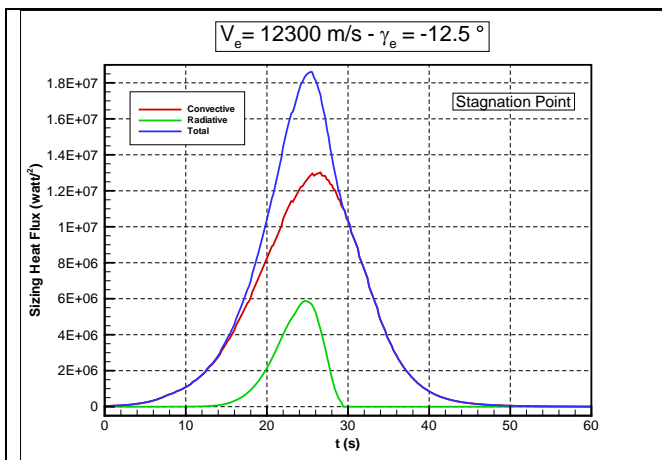


Figure 2: Determination of convective & radiative heat flux

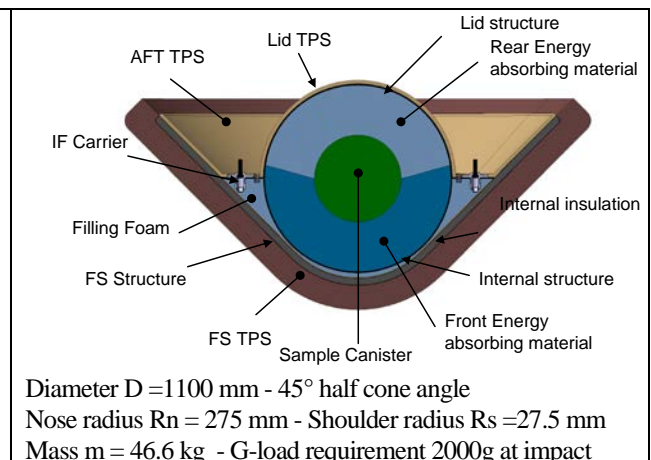


Figure 3 : preliminary ERC design

3. WP2 : GROUND FACILITIES FOR HIGH-SPEED RE-ENTRY TESTING

The severe aerothermodynamics environment encountered by a space vehicle during a planetary re-entry has to be reproduced at best in ground-based facilities to allow a precise understanding of the flow properties around the vehicle and an accurate evaluation of the Thermal Protection System (TPS) performances. In such situation dedicated ground testing capabilities appear as a strong requirement for TPS design. Firstly, they represent a first convenient step in the testing procedure at reduced cost compared with the launch of a mission. Secondly, the ground tests allow a better control of the environment and the measurement techniques to investigate TPS properties and to develop qualification tests. However, as well known, a complete experimental simulation of hypersonic conditions on a model, in a ground test facility, is almost impossible to achieve or at best impractical in a laboratory [4]. Nevertheless on one hand methodologies have been elaborated with specific high-enthalpy facilities to duplicate the features of the post shock environment for high-speed entry [5, 6]. On the other hand plasma wind tunnels have been developed to address the aerothermodynamic testing of TPS for critical points of space vehicles in typical re-entry conditions [7-9]. Those plasma facilities provide testing conditions with relevant heat-flux level but where the radiation heating remains a small amount of the total heat-flux.

However space exploration program requires the development of space vehicles able to manage a safety return through the Earth atmosphere. Mars sample return which is the main focus of the RASTAS SPEAR project will lead to very severe conditions. Those high speed re-entry conditions are an issue for the current ground testing simulation due to their important radiation features and the coupling phenomena they involved. In this context a review on the existing ground based facilities for high speed re-entry and TPS qualifications has been completed. In one hand it appears that only few ground based facilities are able to cover the typical super orbital re-entry conditions of the RASTAS SPEAR project. On top of that, considering hyper-velocities wind tunnels none of these facilities are located in Europe. They represent an essential tool to study the mission and investigate the re-entry environment that will need to be simulated in the frame of the TPS design. In the other hand the European plasma wind tunnels dedicated to the qualification of TPS offer suitable testing conditions regarding the typical heat-flux levels along the high speed re-entry been considered. In parallel to the worldwide facility review the measurement techniques for flow characterization have been listed for each of the high enthalpy and plasma wind tunnels. It appears that European facilities are generally well equipped with specific instruments that allow to cover a large spectrum for flow diagnostics.

In response to the lack of testing capabilities for super-orbital flight in Europe a preliminary design of an expansion tube has been investigated. This facility aims to offer a testing envelope for high speed re-entry conditions corresponding to the Rastas Spear project. A series of 1D numerical simulations were performed in order to achieve the optimal configuration leading to the target free stream conditions. All the elements of the expansion tube, from the driver to the test section have been calculated based on the X facilities operating in Australia.

Finally a test strategy combining the two types of facilities has been discussed. It would follow the use of high enthalpy facilities and plasma wind tunnels independently to determine specific radiation and gas surface interaction modelling thanks to dedicated measurement and suitable physical analysis of the phenomena occurring during the tests. The testing methodology could be represented as in the Figure 4. The models obtained from the database, generated with the two type of testing facility, are used in CFD tools. The coupling phenomena are realized through the numerical computations that serve as input to the thermo-structural analysis for the final TPS sizing.

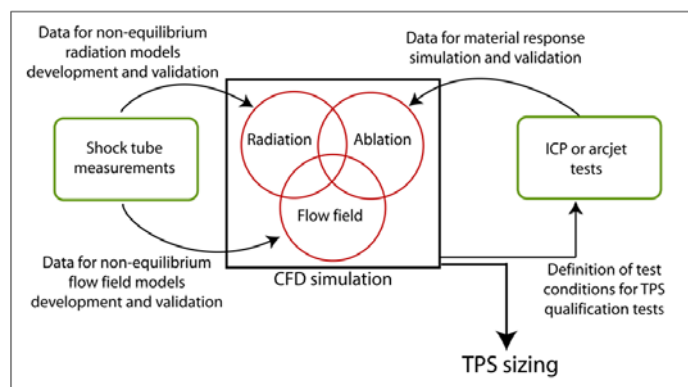


Figure 4: Testing methodology for high speed re-entry TPS sizing

4. KEY TECHNOLOGIES FOR HIGH SPEED ENTRY (WP3)

This activity about technologies that need to be developed for the ERC was led by NCSR Demokritos. Specifically, the main objectives of WP3 were to investigate and develop new and innovative methods, materials and systems for joining the ablative blocks together and to the substructure, to produce a complete Thermal Protection System (TPS) for sample-return missions. Another topic was also considered, related to the crushable material which would absorb the impact forces during the probe's hard landing on Earth.

4.1 TPS and Joints (WP 3.1 to 3.3)

General approach

The TPS can be sorted in 3 main components: the thermal protection material itself, the joint material to be positioned between different tiles or blocks, and the bonding process to fix the TP material on the underlying substructure.

Appropriate thermal protection materials are available: based on outcomes from WP1, the low density carbon-phenolic ablator "ASTERM" has been selected as baseline for the project. But the gap/seam materials are still to identify, which is one main goal of this WP3 activity [12], with the main following sub-tasks:

- Elaboration of a relevant set of criteria: Among the various considerations, a comparable but slightly higher recession than that of the surrounding material is searched. Another important consideration is the interest for relatively simple and cheap processing methods.
- Selection and elementary testing of appropriate joint materials
- Plasma testing of samples with Asterm + most promising joint materials
- Manufacturing of a technological breadboard

These different topics are summarized in the following sections.

Screening and Trade-off for gap-seam material

Based on above-mentioned requirements, screening tests were applied to various commercially available adhesives : evaluation of their out-gassing, volatility, low temperature (-196°C) mechanical behaviour, ease of handling, cost, ease of bonding to a fibrous substrate, curing conditions (time, humidity, air effect), ablation behaviour under propane gas flame.

Investigations were performed on 9 adhesives, among which CV1142 and another 2 adhesives (Mega Grey ("MG") and Mega Copper ("MCu") passed all thresholds and were selected for bond testing (tensile, shear and bending) in following step.

- CV1142 (made by NUSIL) used on Beagle 2 was chosen as reference material for comparative bond testing in this project
- MG and MCu are both inexpensive, commercial HT gasket silicones in the UK and USA. These RTV (room temperature vulcanizing) silicones cure into a silicone rubber that maintains long term durability and flexibility to make formed-in-place gaskets. They are all used for high temperature gasketing applications. According to their technical specifications, they have similar composition to CV1142

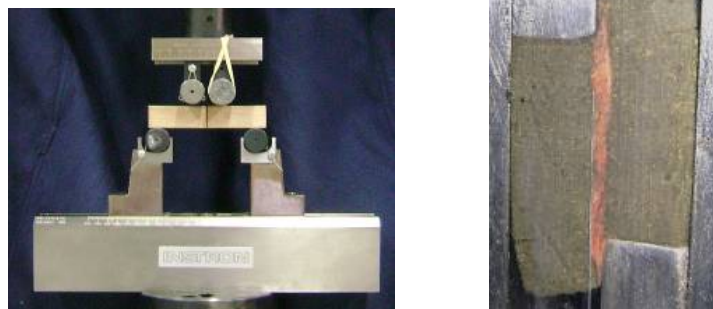


Figure 5: Bending and Shear Testing

Mechanical testing was carried out under direct shear, as mentioned above. It was found that in all cases, the adhesive joint is stronger than the ASTERM material: fracture occurred through the ASTERM in all cases.

The partial conclusion after mechanical testings is that MG and MCu indeed both offer a potentially viable alternative to CV1142, at least as far as their bonding and mechanical properties are concerned. Their curing behaviour and non-use of primer appears to also offer advantages for manufacturability of a shield. These adhesives were therefore selected for the next phase consisting of Plasma-jet tests.

Manufacturing of samples for plasma tests

After selection of appropriate silicone glues as above mentioned, this task consisted of two main parts:

- Actual production of samples to be tested in plasma test campaigns planned in WP3.2.
- Expertise of the samples after they have been tested (described in following section).

A first series of samples was produced for testing at Scirocco. Their geometry has been identified by CIRA and Astrium as a flat-top cone of plasma-facing diameter about 65mm. The samples are first machined from ASTERM and then cut and re-joined using a total of 4 joints each with a different adhesive (see Figure 6). CV1142 is used as reference and MG and MCu are used alone or mixed with various quantities of powdered ASTERM.

After reorientation of the test campaign (see next section), a new batch of samples was produced, each with 4 different adhesive joints as before (see Figure 7). In order to fit with DLR L3K facility, sample dimension was smaller (diameter 50 mm) than those for Scirocco. In the meantime, it was also decided to include a new candidate in the panel of tested adhesives: ESP495, which is the product used for ExoMars heatshield.

Arc Jet tests with different tiles accommodation (WP3.2)

This task consisted of an experimental assessment of the identified concepts, with the aim to consolidate the selection of the best joint materials. Arc-jet testing was undertaken, as the most satisfactory simulation wrt actual flight conditions. The initial rationale for the tests was the following:

- Performance of four plasma tests on the Scirocco facility of CIRA at moderate heat flux (5 MW/m²)
- Analysis of the results and selection of the two most promising gap/seam materials
- Performance of two tests at higher heat flux (15 MW/m²)

Testing at Scirocco

A first test campaign took place at CIRA in October-November 2011 where two runs were performed. During this first campaign, two sample holders broke off.

Only the first test at 5 MW/m² had a sufficient duration of 12 sec to allow some expertise of the sample. However, it was damaged due to the breakage of the supporting graphite arm. One of the MCu adhesive joints survived intact and showed good behaviour. Figure 6 shows pictures of the sample before and after test.



Figure 6: ASTERM TPS before and after Scirocco arc jet test

After this test campaign, the Scirocco facility was unavailable for a long time in 2012. The logic had thus to be totally reshuffled and it was decided in Autumn 2012 to shift the remaining tests to another arcjet test facility in Europe, at DLR, Köln, Germany.

Test campaign at DLR L3K

A new test plan was established for testing on the L3K facility of DLR, with proposed test conditions already experienced in former studies.

- 15 tests in total were carried out on samples with various joints materials.
- 9 tests at 6.1 MW/m², with different durations of 25 and 30 sec for comparison
- 6 tests at 13.6 MW/m², also with different durations of 10 and 15 sec, finally reduced to 9 and 12 sec, after the first test had to be stopped after 14 sec due to excessive erosion.

As these tests were completed quite late in the study, very little time was remaining for the expertise of the samples. A pretty satisfactory analysis was however achieved, the main conclusions of which are summarized below:

- CV1142 and ESP495 display good erosion resistance at 6 MW/m² (see Figure 7).
- At 13.6 MW/m², erosion becomes more important for these two adhesives, while it is unacceptable for the two other MCu and MG.
- The interest of adding Asterm powder to the adhesive as reinforcement is demonstrated.

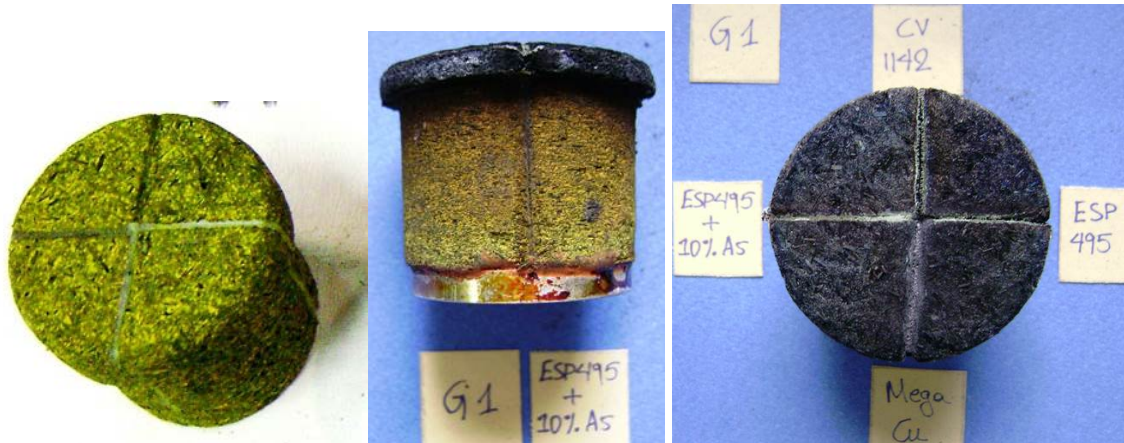


Figure 7: ASTERM TPS with joints, before and after arc jet test at 6 MW/m² on DLR L3K facility

Breadboard manufacturing (WP3.3)

This task consisted of the design and manufacturing of a technological breadboard representative of a TPS shield for a sample-return mission. The objective was to demonstrate the effective and efficient feasibility of the proposed TPS shield concept, with relevant geometry and dimensions, to be as representative as possible of the targeted application.

The Demonstrator Heat Shield was built in two stages. Design of the tiles on the shield was firstly completed (including FEM) and formed the basis of the dimensioning and manufacturing of the tiles. Considering the available amount of ASTERM material, a maximum diameter of about 90cm was proposed. This represents a reduction of about only 18% from the reference shape designed in WP1 (see Figure 3), which is considered fairly representative, as the overall shape and the total TPS thickness of 56 mm are applied.

In order to investigate a low cost approach, it was decided to manufacture this prototype following a predominantly manual process. Specifically, tiles of approximate dimensions are cut with the right angles on carpenter's circular saw which are then shaped by manual shaping with suitable sand paper against the truncated cone substrate and 3 special truncated cone rings at suitable positions. Once all the tiles (3 layers of 12 tiles each) are prepared, they are glued onto the substrate and joined between them, with bond and joints of about 1 to 1.5 mm thick max. In the next stage the totality of the 36 tiles bonded onto the substrate are "shaved" in one operation using a rotating "shaving tool" to the required thickness, thereby ensuring exact radial symmetry of the whole structure. Finally, the nose piece is also shaped using a spherical arc tooling guide and then bonded onto the prepared cone.

All these operations were described in a specific procedure established as preparatory work. As a precaution and to optimise the manufacturing method, it was decided to first develop the whole process using a simulating material (high density expanded polyurethane HDEPU) with which a complete demo was made. Once all the stages are completed and well-tuned, the actual DEMO breadboard was built using the ASTERM material, with an actual final diameter of 92.5cm.

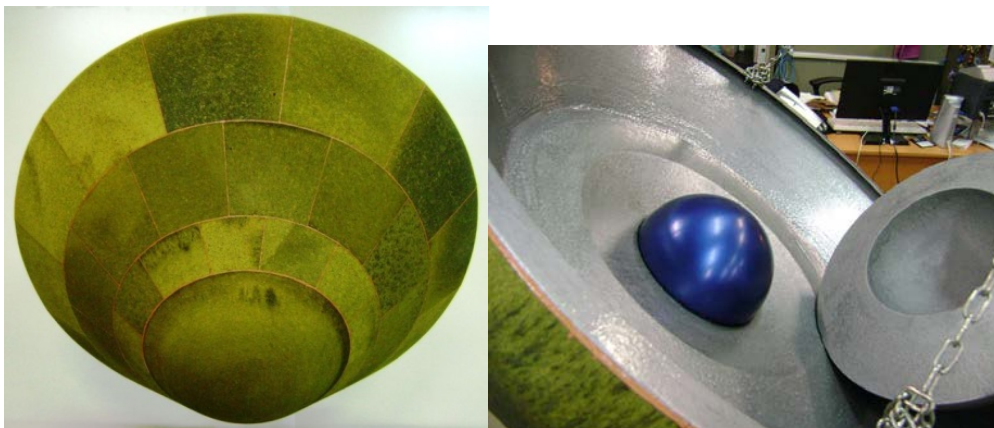


Figure 8: Demonstrator with ASTERM TPS ; Crushable material insert and sample sphere

Capability for actual implementation of such a low cost manual process is relevant, as there is for sure potential for further improvement, using greater precision tooling. This might become an attractive alternative to usual methodology, provided current dimensional tolerances are relaxed to some extent

4.2 Crushable structure (WP 3.4)

General approach

This activity about crushable structures was managed by IoA Warsaw, with the following main objectives:

- Propose a suitable impact absorbing material for future application in sample-return re-entry vehicles.
- Provide numerical simulation, calculations and analysis, which will lead to right choice of crushable structure. Identify an appropriate mathematical model of the material behaviour to picture the phenomenon
- Select the final material and provide the method and material for assembly on demonstrator.

Figure 9 depicts the progressive approach initially planned for this activity. After procurement of candidate materials, a step by step selection was undertaken relying on three types of tests: static, low speed dynamic, crush test.

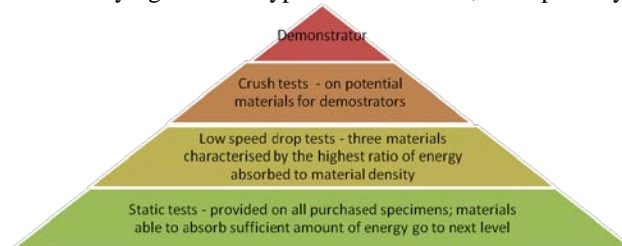


Figure 9: Step by step approach for crushable materials

Material screening

The activity started with investigations carried out about state of knowledge, technology readiness and commercial applications of this type of materials.

This prospective relied on a set of requirements established in WP1: lightweight material, good energy absorber during crush, quasi isotropic, thermally stable and insulator, compatible with vacuum, reproducible manufacturing process.

Figure 10 presents a few crushable materials resulting from the screening, covering various types of materials such as polymeric, metallic and brittle foams, as well as different ranges of density.

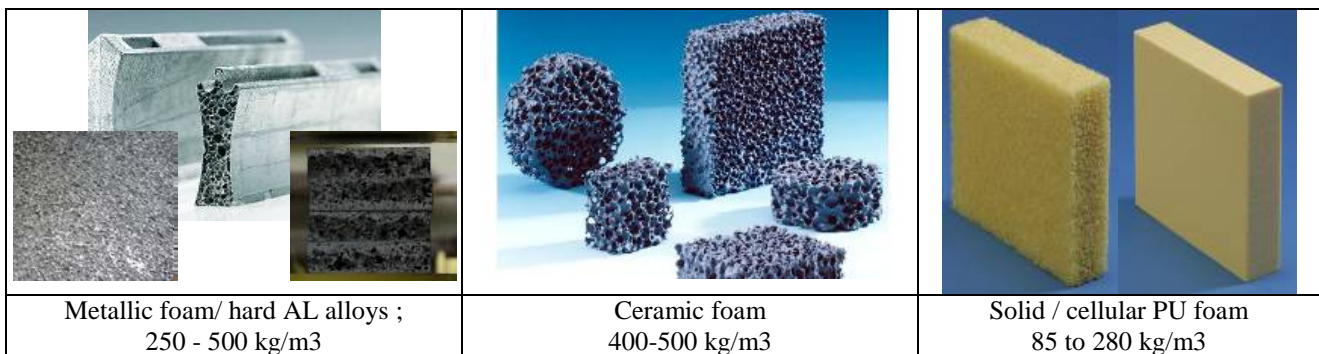


Figure 10: Typical crushable materials identified within the activity

Static tests

Based on the above-mentioned screening, a total of 20 different energy absorbing materials were tested. The shape of the tested specimens was finalised as cubes of side 100mm (see Figure 8). This series of quasi-static tests was performed on a 40 T hydraulic press available in Landing Gear department of IoA.

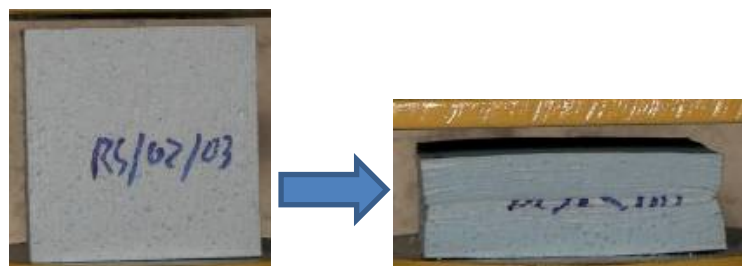


Figure 11: Typical material deformation during static test

These tests allowed determining the strength behaviour and capability for energy absorption for the considered materials. Comparative results in Figure 12 show that different behaviours are observed, making possible an optimised selection depending on required strength and deceleration capability.

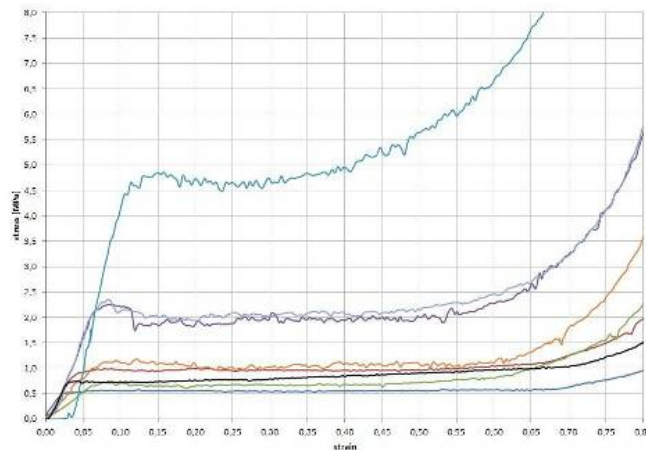


Figure 12: Comparative stress-strain characteristics determined for various materials

Low speed dynamic tests

A few tests were actually performed following the approach initially defined, and using the 10T drop test machine available at IoA. However, it turned out that it was uneasy to get satisfactory measurements. It was then preferred to rely only on a 2-step approach based on static tests and high speed tests.

High speed dynamic tests (samples)

During the first year of the project, a crash test stand had been designed and prepared. Preliminary tests and analysis showed problems with dissipating energy accumulated during acceleration phase. Additionally, projected (quoted) costs for the systems needed for this original design exceeded available resources.

A new test approach was therefore defined using a different technique: a horizontal pneumatic cannon. The cannon system was purchased after completion of the design that required further analyses. Development, assembly, calibration and implementation of most appropriate measurements was then successfully undertaken, though it turned out to be more tricky than anticipated. Following this important preparatory phase, tests using cannon with a high speed projectile (45 m/s) were carried out from April to July 2012.

Based on the results from the two previous test stages, those further tests were performed on eight most promising materials.

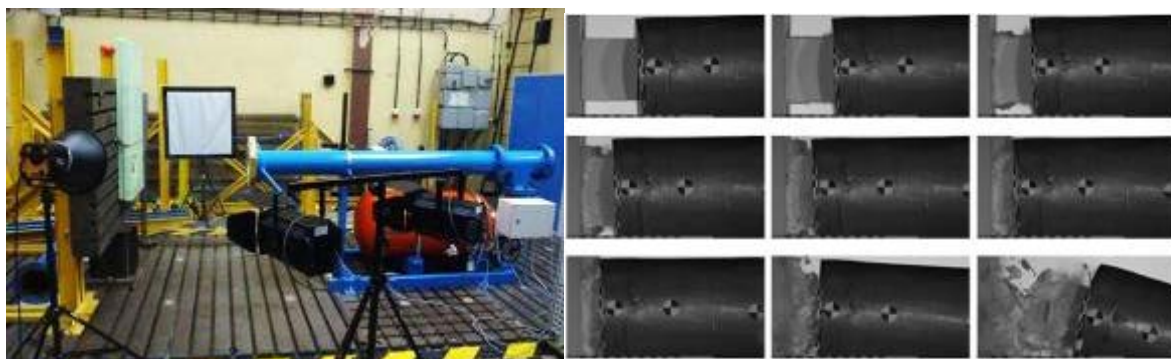


Figure 13: Air cannon and pictures from high speed camera during test

A numerical rebuilding of tests was then performed, using the LS-Dyna code, and taking into account as inputs material data obtained from static tests. As an example, the Figure 14 shows a pretty good comparison obtained for the PU foam SR10 between the FEM model and the experiment data.

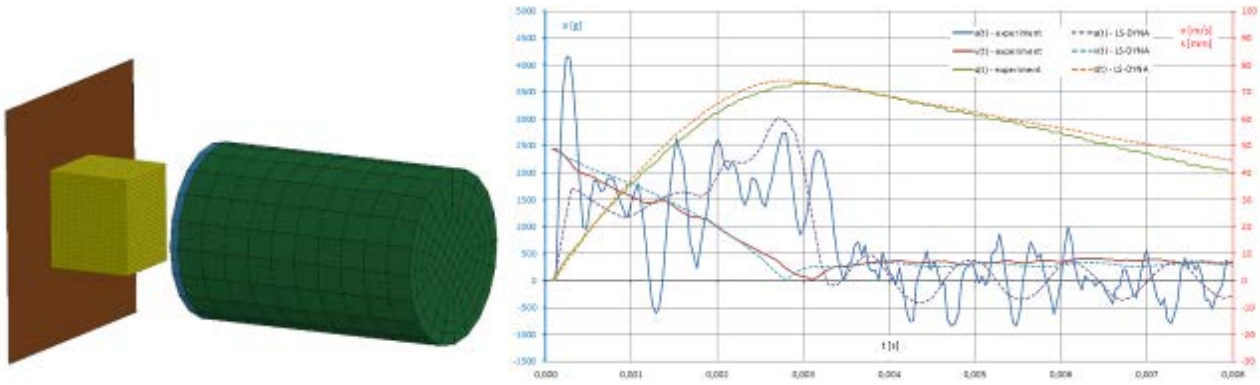


Figure 14: Comparison of experiment and numerical data for SR10 material

High speed dynamic tests (scale 1)

The following step consisted of high speed tests at larger scale. As it had been proven to be successful, the same technique with the air cannon was used again. A scale one specimen was considered, featuring appropriate dimensions for the foam block and for the bullet representing the container (see Figure 15). Three different densities of the PU foam Puren were used for these tests. The demonstrated interest of PU foam, as well as the possible procurement of large blocks, were the main reasons for this choice.



Figure 15: Cannon and 5.5 kg bullet (top) – Impacted foam block (bottom)

As in previous step, a numerical rebuilding of tests was then performed with the LS-Dyna code. Again, a good comparison was obtained between the FEM model and the experiment data.

Numerical Simulations

A scale one simulation was finally performed, including only the foam and the sample container, not the whole capsule. A sensitivity analysis showed a very limited influence of the foam initial velocity (zero, or same as the one of container).

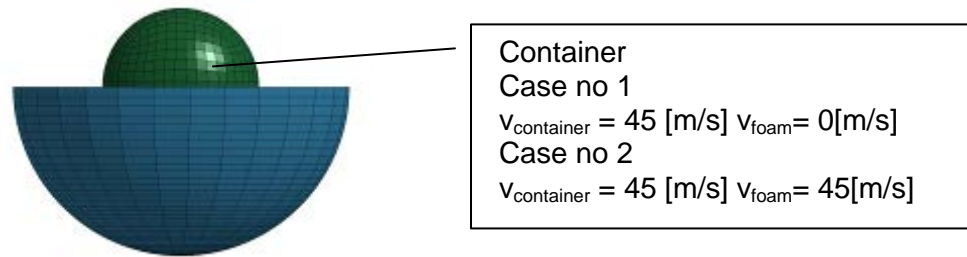


Figure 16: FEM model for scale 1 simulation

Demonstrator

After final selection of materials for crushable structure, a technology demonstrator was made. It is made of Puren 145, and manufactured according to dimensions given by Demokritos in order to fit to the TPS demonstrator described in a former section. IoA made also a demonstrator of Payload which is an aluminum sphere. Both Crushable Structure and Payload Breadboards are shown in Figure 17 below.

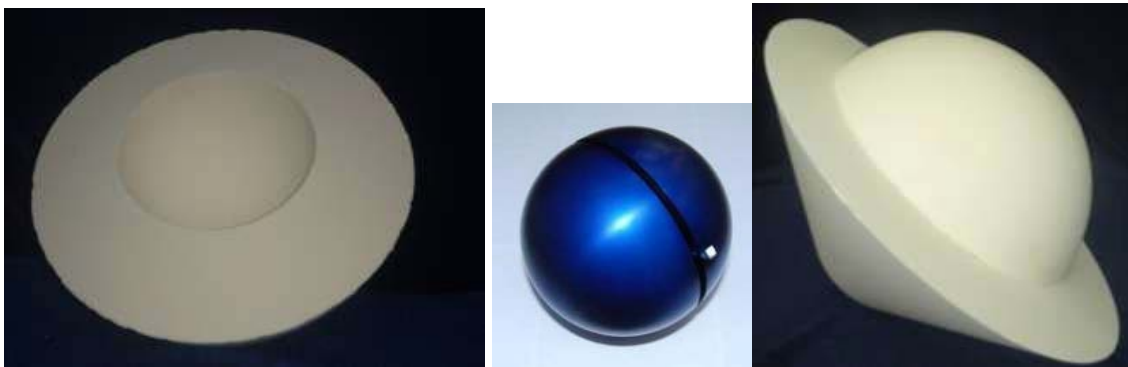


Figure 17: Crushable and payload breadboard – for integration with TPS demonstrator by Demokritos

Conclusion of activities on crushable materials

This activity on crushable materials results in several valuable outcomes, which can be summarized as follows:

- An efficient methodology has been elaborated, based on a two-step experimental approach
 - Static tests that provide strength behaviour and capability for energy absorption for the considered materials.
 - Impact tests using the air cannon technique.
- Numerical simulations of impact tests with LS-Dyna, using static tests results as inputs, give a good correlation between experimental and computed data
 - Validity has been demonstrated for PU foams, and should be further verified for other types of materials
 - It is possible numerically to simulate various geometries based only on static test results
- After setup pneumatic cannon test procedure turns out to be a very efficient methodology, which allows to perform 10 – 12 tests per day –
 - High speed camera and picture analysis software works perfectly with project application
 - A high mastery of the measurements is essential, because the use of pneumatic cannon for dynamic test gives important energy differences with small velocity variation
- Finally, the material identified as the most promising was selected for delivery of a representative breadboard to be integrated within the technological demonstrator.

5. ABLATION - FIGHT MECHANICS COUPLING ASSESSMENT (WP4) [11]

5.1 Implementation and assessment of coupled tool (WP 4.1 and 4.2)

High surface recession is expected on high-speed Earth entry capsule with impact on the aeroshape modification, the centre-of-gravity displacement and possibly on aerodynamic stability and the drag performances.

The main objective of this task was to assess the impact of massive ablation on aerodynamic performances and stability along the entry trajectory path. High TPS recession might occur during high-speed entries and it is necessary to identify which recession level could be tolerated with respect to capsule aerodynamic performances and stability requirements.

Astrium ST coupled tool

In order to address this topic, it is necessary to use an approach that couples aeroshape aerodynamic, trajectory and stability, aerothermal environment, TPS material thermal response and recession determination resulting in aeroshape modification. Such a coupled tool has been developed by Astrium ST : its main requirements and assumptions are discussed hereafter.

This tool has been developed following four main requirements.

- **Modularity:** this deals with the general architecture of the coupling tool. Basically the tool is constituted by two general entities: Functional Class Tools and Modules. A functional class tool is an interface between a generic task (Aerodynamics, Thermal response, Trajectory...) and a module attached to specific software chosen by the user. A functional class manages all the inputs/outputs needed for the functioning of all the modules in the coupling tool.
- **Robustness:** This requirement of robustness is particularly important for high speed entry where strong gradients (recession rate, temperature, mass loss...) can occur during the computation of a whole trajectory. This requirement has an impact on the choice of the module (software) employed inside a Functional Class.
- **Evolutionary Tool:** This is a basic but not to neglect requirement for scientific software. This is also an important requirement to keep the tool easily adaptable, also facilitated by its modular architecture.
- **12 CPU hours** is the target duration to perform a complete trajectory.

For the present study the coupling tool is constituted by 6 specific Functional classes associated with 6 modules, the main assumptions of which are sum up in the following table:

Trajectory tool	3 DoF mode
Aero-thermodynamics engineering tool	Aerodynamic coefficients, Convective and radiative heat flux, transition criteria...
Material response tool	Pyrolysis module: Arrhenius laws Ablation module: Chemical tables Boundary conditions: Convective + radiative heat fluxes Blockage effect: Only on convective heat flux $f(M_{\text{gas injected}}/M_{\text{air}}, T, P, \text{regime})$
Ablated Aeroshape Rebuilding Tool	This tool data processes the Material Response Tool output as recession and Mass loss per m^2 into ablated profile coordinates and global mass loss as input for MCI Tool and CFD Tool.
CFD Tool	- Inviscid - Gas at chemical equilibrium - Hypersonic/ supersonic regime from $2 < \text{Mach} < 42$
Mass Centering Inertia Tool	Outputs: updated mass table used for the next loop of the trajectory tool and the displacement of CoG due to shape and mass change. The initial position of the X_{CoG} capsule is -0.296m (26.9% of L_{ref})

Table 1 – Functional classes and main assumptions of the corresponding modules

Another assumption is worth being mentioned: The drag coefficients on modified aeroshape employed to update the trajectory are determined by an additive correction of the Drag coefficients on the nominal aeroshape from the initial aerodynamic data base. This correction is determined on both ablated/ non ablated aeroshape thanks to the CFD tool.

This correction is applied on the hypersonic/supersonic domain from Mach 42 to 2 which corresponds to an altitude range from 71km to 30km. Neither transonic/subsonic correction nor rarefied aerodynamics has been done at present, which could be a relevant task for further enhancement.

The global functioning is described in the flow chart presented in Figure 18.

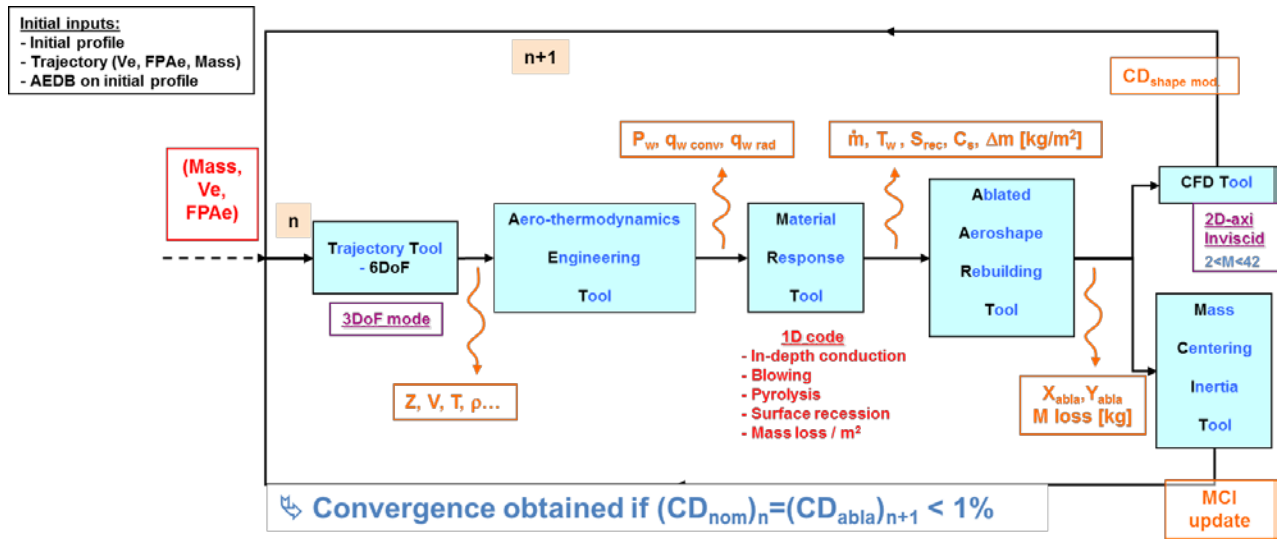


Figure 18 - Flow chart of the coupling tool

Preliminary coupling assessments

The application case for identification of aeroshape modification / mass change coupling has been done on the ERC aeroshape (see Table 2) for two selected trajectories described here below (see Table 3).



Sphero-conical capsule	
Diameter	$D = 1100 \text{ mm}$
Half cone angle	45°
Nose radius	$R_n = 275 \text{ mm}$ ($R_n / D = 0.25$)
Shoulder radius	$R_s = 27.5 \text{ mm}$ ($R_s / D = 0.025$)
S_{ref}	0.95 m^2

Table 2 – ERC shape and dimensions

	Traj. 1	Traj. 2
Entry Velocity at 120km	12.3km/s	12.3km/s
Flight path angle (FPAe)	-12.5°	-16.8°
Initial mass	66.7kg	66,7kg

Table 3 – Trajectory characteristics at entry

The observed impacts on trajectory parameters compared with no coupling case (nominal) for the two trajectories can be summarised as in Table 4.

Considering the model employed for the material response tool, the trajectory conditions and the nominal aeroshape, the aeroshape modification due to ablation in the high velocity domain is weak which can produce a low effect on trajectory but it has been found that on maximum heat flux trajectory the shape coupling has an effect of about 1km in the final range and therefore on the precision at impact. Due to aeroshape change the Center of Gravity of the heatshield moves backward of about 4-5mm which is also weak.

Parameters	Effects / nominal case	Maximum levels difference	% vs. nominal case	Criticality
Velocity	↕	50 ⇔ 75m/s	~1%	Low
Mach	↕	0.15 ⇔ 0.25	~1%	Low
Deceleration	↗	-0.5 ⇔ 1g	1% ⇔ 1.5%	Low
Dynamic pressure	↕	1.2 ⇔ 1.7kPa	~3% ⇔ 3.5%	Medium
Stagnation pressure	↕	2 ⇔ 3kPa	~2.5% ⇔ 4%	Medium
Heat Fluxes	↕	<100W/m ²	~0%	Negligible
Heat Load	↕	1.5 ⇔ 2.5MJ/m ²	1% ⇔ 2%	Medium
Range	↕	0.8 ⇔ 1.4km	~0.3%	Medium

Table 4 – Coupling effect comparisons on trajectory parameters

The first objective of this preliminary works was successfully achieved, which was to develop the coupling tool, and to test its ability to reach the main initial requirements.

Potential further work is identified on a few points, in order to continue enhancing the methodology:

- Massive ablation due to higher level of entry velocity could produce more important aeroshape modification and therefore stronger impact on trajectory, precision, MCI ... Further evaluation on more demanding trajectories is therefore appropriate to assess this aspect.
- The aeroshape modification in Transsonic/Subsonic domain cannot be taken into account in this version. This should be a relevant improvement, for which the use of NS computations seems the best way. However, this would result in strong investment on mesh activities, with increase of CPU time and potential impact on robustness.

5.2 Engineering modelling correction by CFD (WP 4.3)

As the modules constituting the coupled tools are essentially engineering codes based on simplified correlations, one way of improvement is to refine these correlations, relying on results from detailed CFD analyses. This activity was undertaken within WP4.3, and a series of computations was carried out, addressing the following items:

- Mass blowing influence on convection and radiation (8 points B1 to B8, selected to get a good coverage of the entire trajectory, as illustrated on Figure 19),
- Aeroshape modification influence on aerodynamics and aerothermodynamics (6 points M1 to M6),
- Non-equilibrium radiation (12 points R1 to R12).

These items have been split into four different sub-tasks [11]. CIRA was in charge of flow-field computations while radiation was analysed by CNRS.

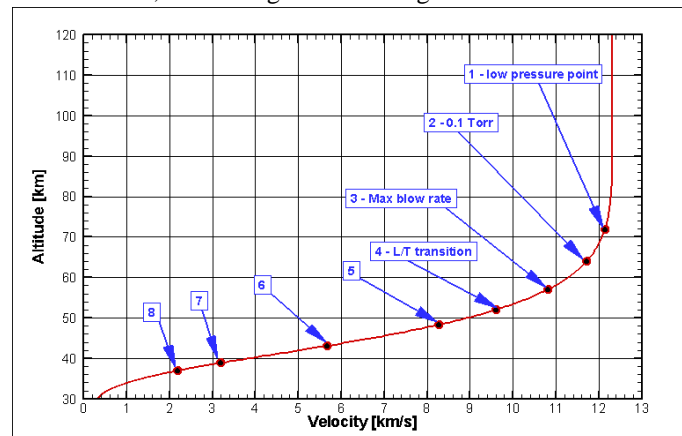


Figure 19: The 8 trajectory points considered for Blowing assessment

After checking the results obtained from a first run of these complex CFD analyses, it turned out that further consolidation was required. Although this could be achieved only partially within the resources of the project, following recommendations about the different correlations can already be derived from the partial conclusions obtained so far.

- Aerodynamic coefficient
 - CFD computations show that current correlations are valid (to be consolidated for high velocities)
- Convective heat flux
 - Correlations used for coupling tool are kept by conservatism

- No firm trend may be derived from current CFD computations, which require further consolidation
- Radiative heat flux
 - Correlation can be updated, as a reduction of shock stand-off distance on stagnation line is observed.
 - A subsequent reduction of level of radiative heat flux is thus anticipated.
 - This would require to be extended for a larger range of entry velocities.
 - Finally, the interest for actually coupled flowfield /radiation computations remains high.

5.3 Experimental assessment of radiating species around ablating materials (WP4.4 - CNRS)

Products ablated from the protective shield of a superorbital velocity re-entering vehicle may react with the incoming air plasma flow, thus producing chemical species such as C, C₂, C₃, CN, CO, CO₂, ... that can couple with those contained in the incoming air flowfield. These products may affect the absorption and emission properties of the boundary layer, thus potentially affecting the radiative heat flux to the surface of the superorbital velocity vehicle.

Thanks to remaining resources, it was proposed as additional work to complement the numerical simulations of WP4.3 by performing an experimental assessment of the feasibility of measuring these products in the 50 kW plasma torch facility of EM2C. The following tasks have been successfully completed:

- Installation of the plasma torch facility shown in Figure 21
- Implementation of the optical emission spectroscopy system depicted in Figure 22 (Nov 2011-Sept 2012)
 - Two surface T° measurements, using one single color and one two-color pyrometers
 - One low resolution broadband Spectrometer OceanOptics USB2000+
 - One high resolution spectrometer Acton SpectraPro 2750
- Design and building of an ablative layer holder (March-June 2012) designed to support a cylindrical ablator coupon (ASTERM, CBCF, ...) in the plasma stream (see **Figure 20**)
 - Water-cooled sting holds a 5 mm thick, 40 mm diameter copper disk
- First tests of plasma torch facility in air and adjustments (Sept-Nov 2012)
- Characterization of torch operating conditions in air: spectroscopic measurements of plasma temperature and calorimetric measurements of specific heat. Tests of ablator holder system (Dec. 2012 – Jan 2013)
- Experiments with ASTERM ablating material exposed to air plasma: measurements of ablator surface temperature, of heat flux to the ablator surface, of low and high resolution emission spectra. Analysis of results.
- Material temperature and species concentration profiles were measured in the boundary layer, showing spallated particles, sodium emission, plasma recombination.



Figure 21: plasma torch facility

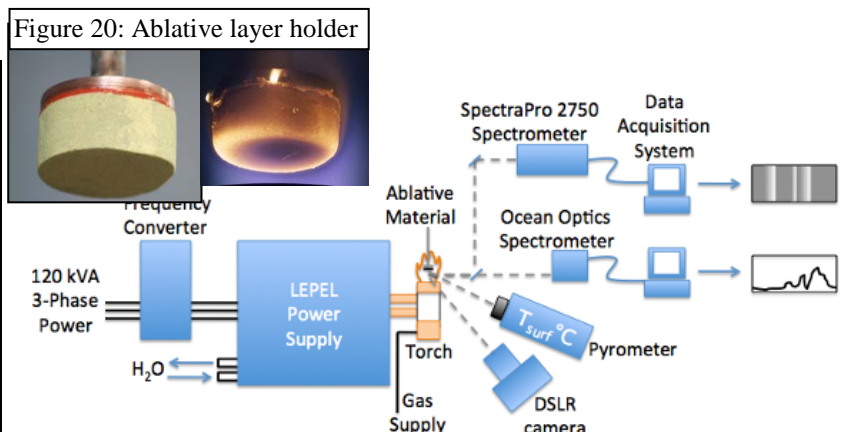


Figure 22: Optical emission spectroscopy system

The facility is now fully operational and ready for more testing and experimental research work such as:

- Investigation of material behaviour under test conditions with higher power and heat flux
- Search for more species (C, C₂, C₃)

6. GAS-SURFACE INTERACTION MODELLING (WP5)

6.1 An experiment to simulate the coupling between ablation and pyrolysis products

It is well known that during re-entry, and in particular for high speed re-entry, the TPS surface degradation results in rough surfaces that enhance dramatically the turbulent heating. In case of high gas surface blowing due to massive ablation, blowing might encompass roughness-induced over-heating. The general objective of the present work package is to carry out an experimental investigation of the coupling between surface roughness and blowing due to ablation and pyrolysis products and to identify possible margins saving.

The ONERA Meudon center R2Ch wind tunnel was used for the experiments. R2Ch wind tunnel is a blow-down facility (test duration between 15 and 30 seconds) equipped with its Mach 5 nozzle for this test campaign.

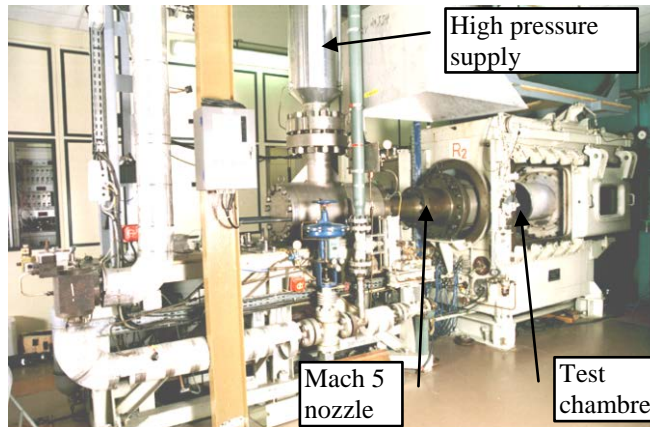


Figure 23: ONERA R2Ch facility

A flat plate model with a sharp leading edge was used for those experiments at 0° incidence. An exploded view of the set-up in the R2Ch test-chamber is shown in Figure 24, the flow direction being from the nozzle on the left to the right. The model was equipped with two inserts: one made out of steel (isotan) and one made out of ceramics represented in green on Figure 24. Furthermore, in order to reproduce the real effect of an ablated wall, the model was pressurized, and pressurized air was blown through the porous wall from a tank located under the insert.

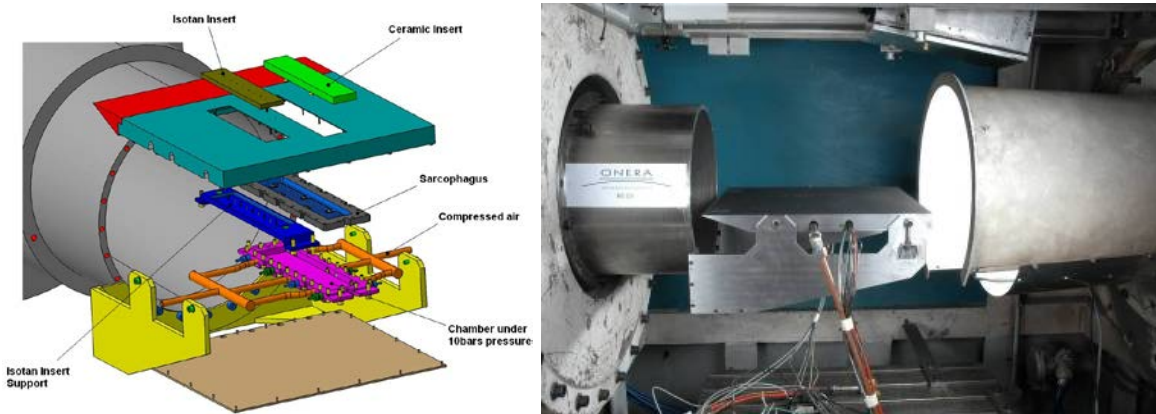


Figure 24: Exploded view (left) of the experimental set-up in the R2Ch test-chamber (right)

It has been chosen to reproduce an academic configuration (flat plate with regular roughness) in order to have the possibility to perform calculation. Indeed irregular roughness – as those obtained in reality during a reentry flight – could not easily be taken into account by a model. So it was decided to reproduce a regular pattern constituted by pyramidal roughness.

It was also required to use a material which simulates the deterioration of the wall surface state and the blowing effects. The wall in the experimental device was thus made out of porous rough ceramics in order to blow through the wall and hence to simulate the blowing due to ablation in reality.

Two porous ceramic inserts (one with and one without roughness) were manufactured by the firm CTI in Salindres in the south of France. The main features of such insert are a porosity of 48 %, and a roughness distribution made of regular truncated pyramids joined in alternate rows as shown in Figure 25.

The final insert was obtained after several uneasy iterations, and a detailed inspection enabled to determine its key parameters: the truncated pyramid height is $176 \pm 34 \mu\text{m}$, with a base of $550 \mu\text{m}$. Its overall dimension was also finally reduced from $220 \times 40 \text{ mm}$ to $100 \times 400 \text{ mm}$, in order to limit mechanical efforts during the pressurised tests.

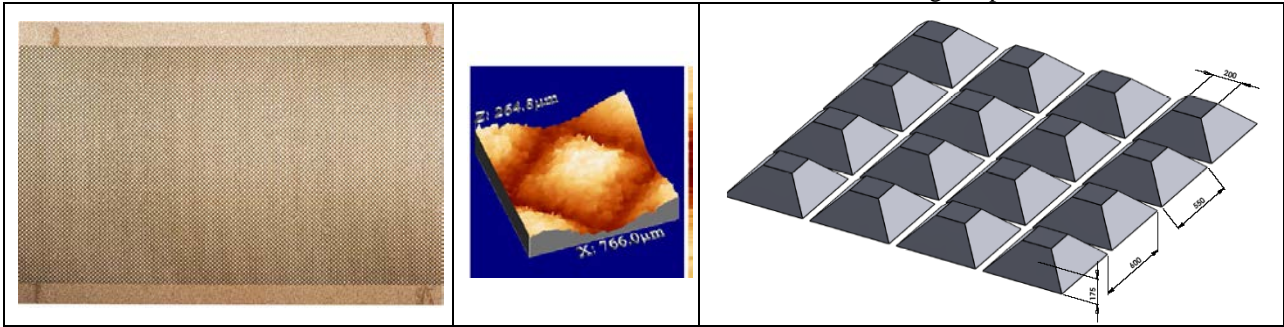


Figure 25 – Photograph of pyramid distribution on the insert (left) – microphotograph of the surface (centre) – pattern used for modelling (right)

During the tests, Schlieren photographs of the flow are made, as well as heat flux measurements using infrared thermography technique. Successive thermograms are recorded at a frequency of 50 Hz and, for a known local heat capacity of the wall, the analysis of successive thermograms yields the heat flux on the investigated surface. Two parallel measurements are performed on the ceramic insert and on the reference Isotan insert located nearby. In addition, four thermocouples are implemented at the wall of the Isotan insert in order to check the infrared results.

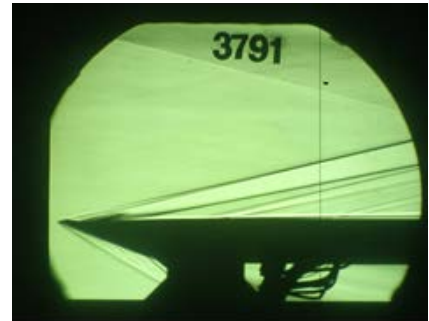


Figure 26 – Schlieren photograph during one of the runs

6.2 Experimental Results

Thirty-one documented runs (see Table 5) were performed in the hypersonic R2Ch wind tunnel for various conditions

- porous and rough wall
- with and without blowing : The mass flow rate level was determined in order to have a simulation in agreement with the reality along a classical re-entry trajectory. Tests were also run with an intermediate value corresponding approximately to the half of the highest mass flow rate.
- different stagnation pressures from $p_{st} = 7 \cdot 10^{*5} \text{ Pa}$ to $p_{st} = 50 \cdot 10^{*5} \text{ Pa}$, which corresponds to unit Reynolds number from $Re_L = 5.95 \cdot 10^{*6}$ to $Re_L = 42.5 \cdot 10^{*6}$ with $T_{st} = 650 \text{ K}$

A few tests were also duplicated at the beginning in order to demonstrate the good repeatability of the tests conditions.

surface	Mass flow [kg/m ² /s]	Stagnation pressure [Bar]		
		7	28	50
Smooth	0	3757 NT	-	3756 NT
		3764 NT		3763 NT
		3778 NT - BL		3759 NT - BL
	0.6	3780 TT	-	3774 NT - BL
		3779 TT - BL		3782 TT
		3772 NT		3775 NT - BL
1.12	3781 TT	3768 NT	3807 TT	
	3770 NT		3767 NT	
	3784 TT		3787 TT	
rough	0	3790 TT	-	3791 TT
		3802 NT		3792 TT
		3804 TT BL		
	0.66	3798 TT	-	3794 TT
		3799 TT		
		3803 NT		
1.15	3805 TT BL	-	3800 TT	

Table 5 : Synthesis of R2ch runs

NT: natural transition TT: tripped transition BL: Boundary layer measurements

The heat-fluxes have been deduced from the evolution of temperature – detected by infrared thermography - during the first seconds of the run. These heat-fluxes have been corrected by considering the variation of pressure during the run. The Stanton numbers have been deduced from these values by the following formula:

$$St = \Phi / \rho_{inf} U_{inf} C_p (T_{st} - T_w)$$

where Φ is the heat-flux in W/m², ρ_{inf} and U_{inf} are respectively the density and the velocity delivered by the nozzle, T_{st} the stagnation temperature and T_w the wall temperature and C_p is the calorific coefficient at constant pressure equal to 1003 J/kg/K.

The Figure 27 presents the evolution of the Stanton number along the X-axis for two different runs. The first abscissa X = 140 mm corresponds to the position of the two inserts at 140 mm from the leading edge. The green curve is relative to the Stanton numbers deduced from the infrared results obtained onto the ceramics insert. The red curve is relative to the Stanton numbers obtained onto the isotan insert. These last results are in excellent agreement with the Stanton numbers – represented with the blue points - deduced from the thermocouples implemented inside the isotan inserts. The eventual difference between the two curves has then to be corrected with an adjustment of surface emissivity and temperature of the ceramic insert.

At low pressure ($p_{st} = 7 \times 10^5$ Pa – left), an increase of the heat flux is observed which is the sign of the transition of regime from laminar to turbulent. At high pressure, ($p_{st} = 50 \times 10^5$ Pa – right), the flow is fully turbulent on the entire insert.

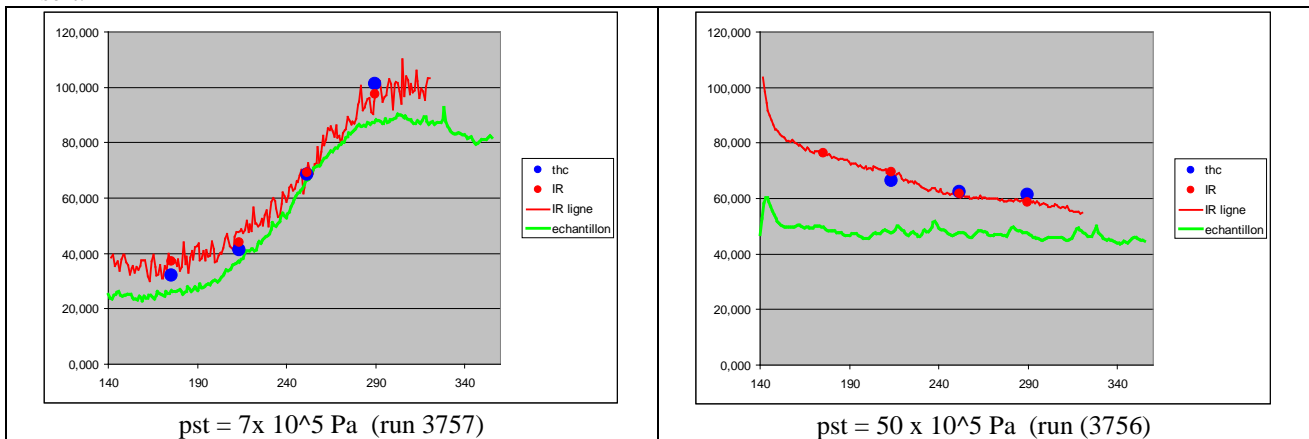


Figure 27 – Evolution of the Stanton number along the X-axis

Comparison between the different runs enables the identification of typical key behaviours.

- **Smooth wall with blowing:** Figure 28 shows the decrease of Stanton number along the ceramic insert with a smooth wall, when blowing is increased. The observed reduction is about 55-60% for the intermediate mass blow rate (0,6kg/m²/s) and 70-80% for the maximum mass rate which is rather important.

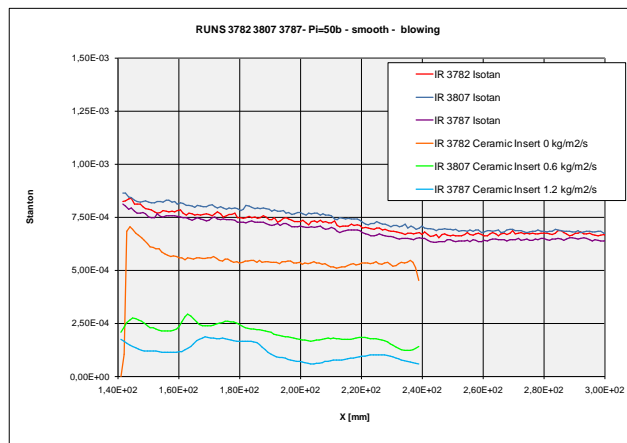


Figure 28 – Effect of blowing on Stanton number at 50bar

- Rough wall without blowing:

The experiment over rough surface without blowing gives an unexpected decrease of Stanton number whereas an increase is expected (see Figure 29).

Presently no satisfactory explanation is available to understand this point.

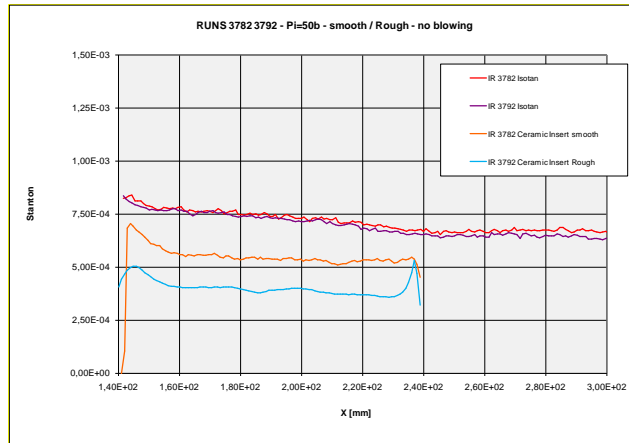


Figure 29 – Stanton number comparisons for smooth and rough cases without blowing

6.3 Gas-surface Interaction Modelling

Review of surface roughness and blowing influence (WP 5.1)

A review of surface roughness and blowing influence on aerothermodynamics has been performed by Astrium-ST and MSU, with a complementary support by Onera through a review concerning roughness effects. This work was completed by a review of blowing effects by MSU, which was in particular constructively extended based on research works performed in Russia.

Thanks to these elements, MSU worked on a model description and concluded that it is possible to take blowing effects into account by changing a velocity profile from a logarithmic one. After scientific discussion with Onera experts, the idea has been polished to obtain a robust approach.

The selected model was implemented by Onera in a boundary layer solver and by CFS in a Navier- Stokes code (NSMB).

Boundary layer calculations (WP 5.2.3)

This part of the work consisted in a numerical rebuilding of the experiments carried out in WP5.2. It was performed by ONERA using a Boundary Layer code.

Among all the documented runs, some were disregarded either because they correspond to a total pressure of 28×10^5 Pa for which no way to estimate where the transition takes place is available or to a total pressure of 7×10^5 Pa and are highly polluted by transition effects. Finally, seventeen runs were computed. With various hypotheses on wall temperature and transition location and various turbulence models with some variants, this led to a total of 244 different computations, which brings into evidence the interest of a boundary layer code to be able to investigate so many cases at a reasonable cost.

The analysis of the model predictions for the runs over the smooth surface pointed out the importance of the transition on the flow structure. Without tripping, the transition takes place close to the inserts at the highest total pressure and ends just at the beginning of the insert. At the lowest total pressure, the transition process extends all over the insert. With tripping, the transition takes place some distance after the rough trip for the lowest total pressure and still affects the flow on the insert. This led to favour the highest total pressure cases to investigate turbulent flow modelling.

The investigation of the smooth wall runs also evidenced two problems. The Stanton number measurements on the Isotan insert could quite easily be reproduced, while it was necessary to significantly increase the wall temperature to reproduce those on the ceramic insert.

The small blowing mass flow run is rather well predicted by all models. The strong blowing mass flow run points out the need for a blowing correction in the Spalart and Allmaras model. Cebeci's correction for wall blowing seems to be too strong.

The investigation of runs over rough surfaces without blowing evidences a sorting between roughness models. Krogstadt's, Boeing's and Wilcox' corrections predict stronger roughness effects than Rotta's, Blanchard's and ONERA's ones. The puzzling point is that there were not such differences between models in low speed test cases, for the same

range of reduced roughness heights for much closer predictions between Boeing and ONERA corrections. This is suspected to be due to the coupling between the way the roughness correction acts and the density gradients in the wall region.

The prediction of runs over rough surface is very problematic as experiments give an unexpected decrease of the Stanton number on rough surfaces while models predict an increase, as usual. The fact that the roughness elements are porous, while models were developed and validated for solid roughness elements, does not seem to be enough to explain this discrepancy.

At last, investigation of runs coupling wall roughness and blowing brought the unexpected result that the roughness model ranking obtained without wall blowing is completely reversed in presence of wall blowing. An open question is whether or not model should account for near-wall turbulence enhancement by both blowing and roughness effects. Unfortunately, these runs did not really allow selecting the best model.

6.4 CFD Modelling (WP5.3 - CFS)

CFD Code Adaptation (WP5.3.1)

The NSMB CFD code used in this project was extended with rough surface turbulence models. The well-known 1-equation turbulence model of Spalart-Allmaras was extended to rough surfaces using the method proposed by Bertrand Aupoix of ONERA. In addition, the $k-\omega$ family of turbulence models was extended to rough surfaces using the method proposed by Wilcox, and using the method proposed by Knopp (which is based on the work of Bertrand Aupoix for the Spalart Allmaras turbulence model). The $k-\omega$ family of models was also extended for blowing using the method proposed by Wilcox.

Validation simulations were carried out for two rough surface experiments, and for one experiment with blowing.

Wind Tunnel Test reconstruction (WP5.3.2)

The objective of this task was the CFD rebuilding of the wind tunnel experiments carried out in WP5.2. CFD simulations were performed using the adapted code as described above.

A reduced selection of six runs was considered for Navier Stokes CFD calculations, as reminded in Table 6. The results of the CFD calculations were compared with the experimental results and with results of Euler-boundary layer computations made at ONERA. The results of the Navier Stokes calculations show a good agreement with the results of the Euler-boundary layer simulations, and a reasonable agreement with the experimental results.

Case	1	2	3	4	5	6
Run#	3782	3807	3787	3792	3794	3800
Blowing rate	0	2.6 g/s (~0.6 kg/m ² /s)	4.8 g/s (~1.2 kg/m ² /s)	0	2.63 g/s (~0.6 kg/m ² /s)	4.6g/s (~1.2 kg/m ² /s)
Roughness	Smooth	Smooth	Smooth	176µm	176µm	176µm

Table 6 : Experiments selected for Navier Stokes CFD simulations

As an example, Figure 30 shows typical comparisons of the Stanton number for the case with a smooth insert with blowing at 0.6 kg/m²/s (Case 2 – Run 3807). Until the start of the Ceramic insert (at $x=0.138m$) the computed Stanton number is very close to the results for the case without blowing, as expected. On the Ceramic insert the computed Stanton number using the Spalart Allmaras turbulence model is slightly higher than the one computed using the $k-\omega$ Menter Shear Stress model. For the Spalart Allmaras turbulence model there is also a good agreement between the Navier Stokes and boundary layer calculations. Both Navier-Stokes and boundary layer calculations slightly underestimate the measured Stanton number in the middle of the ceramic insert.

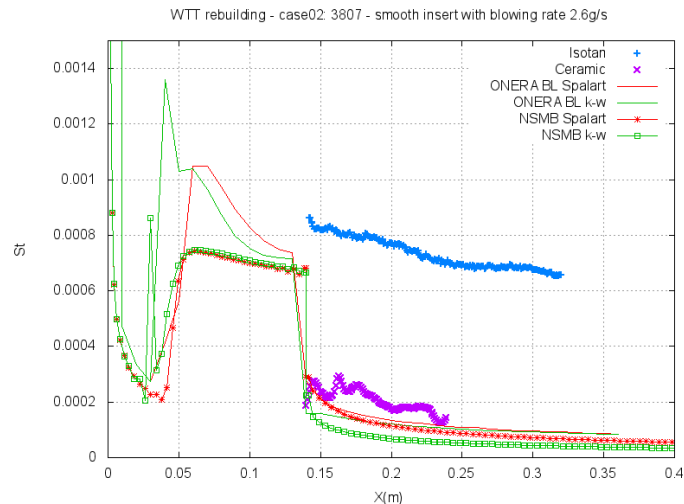


Figure 30 – Evolution of the Stanton: smooth wall , blowing rate 0.6 kg/m²/s

Earth Re-entry vehicle computations (WP5.3.3)

This last part of the activity consisted of an application to the entire capsule, also including most of the improvements implemented based on previous tasks. The grid for the Re-entry vehicle was based on the one used by CIRA within WP4. It was modified at CFS Engineering to permit the use of shock adaptation technique to improve the quality of the solution. For three selected trajectory points, two different roughness heights and two different turbulence models were considered. The influence of the ablation of the TPS material was simulated through the injection of mass (blowing) at the solid wall. For each trajectory point the mass flow rate was provided by Astrium at different locations along the capsule geometry. The NSMB code was modified to permit the reading of the mass flow rate data files and to interpolate the prescribed values on the CFD mesh. The change in geometry due to the ablating TPS material was not taken into account in these CFD simulations.

After discussion of the initial results it was decided to complete these calculations by sensitivity studies for one of the considered conditions. Additional calculations were made for a smooth wall, for a wall without mass injection, for a laminar flow and using the $k-\omega$ Wilcox turbulence model using different roughness models.

6.5 Summary status for WP5

The main outcomes of the activities carried out within this WP5 “Gas-surface interactions modelling” are summarized hereafter.

After a preparation work requiring several adjustments, the characteristics of the ground experiment were appropriately fixed, and a series of wind tunnel tests was then carried out.

- A good repeatability of the run has been evidenced,
- Lot of valuable experimental data have been acquired.

After implementation of both roughness and blowing effects in different solvers, computations and comparison with the experimental data were undertaken. A good agreement between the different solvers was observed: Boundary Layer Euler solver (ONERA) and NSMB - Navier-Stokes Multi-Blocks (CFS). The main conclusions of these comparisons are as follows:

- Wall blowing : Correct agreement of CFD simulations
 - Small blowing : the important observed heat flux decrease is well predicted by all models
 - Strong blowing mass flow case evidences the lack of a blowing correction for the Spalart and Allmaras mode
- Wall roughness : a key issue is highlighted
 - Models predict heat flux increase, while experiment show heat flux decrease. This remains unexplained (porosity of the insert, repeat tests with a much higher roughness?)
- Wall roughness + blowing cases are more complicated to simulate

- Models which cannot account for wall blowing (Spalart, $k-\omega$) predict too low levels
- No obvious best choice between Spalart and $k-\omega$ models

7. GENERAL CONCLUSION

Rastas Spear was a typical R&D project, carried out thanks to the funding of European Community Framework Programme n°7 (FP7).

A well-defined framework was applied for the study, with a focus on a passive Earth Return Capsule. The project was completed by end of April 2013, with a successful achievement of overall project objectives, in particular.

- Increase TRL for key technologies such as crushable materials, or joints for thermal protection material,
- A relevant state of art of ground testing facilities for simulation of high speed entry was done, with a proposed concept for high enthalpy expansion tube, recognized as a currently missing facility.
- Development of suitable facilities, such as the air cannon for high speed testing of crushable materials, the plasma torch for investigation of coupled ablation-radiation phenomena, the rough and porous insert to experimentally address the Gas-Surface Interaction issues,
- Establishment of methodologies and tools, such as testing strategy proposed for super-orbital reentry, coupled tool developed for analysis of capsule entry, enhanced thermochemical models and turbulence models accounting for blowing and roughness to be included in CFD codes.
- However, a few points show that further enhancement is still required, such as CFD modeling of complex coupled phenomena, and detailed understanding of combined influence of blowing and roughness on aerothermodynamic environment.

The outcomes of this project can be considered as a highly valuable step towards an actual flight mission, and especially for the following target missions currently under investigation at ESA : MarcoPolo-R, PhoPrint, MSR...

REFERENCES

- [1] www.rastas-spear.eu
- [2] J-M. Bouilly et al, RASTAS SPEAR: Radiation-Shapes-Thermal Protection Investigations for High Speed Earth Re-entry, 9th International Planetary Probe Workshop IPPW9, June 18 - 22, 2012, Toulouse
- [3] J-M. Bouilly et al, RASTAS SPEAR: Radiation-Shapes-Thermal Protection Investigations for High Speed Earth Re-entry, 8th International Planetary Probe Workshop IPPW8, June 18 - 22, 2011, Portsmouth
- [4] Neumann R.D., Experimental Methods for Hypersonics: Capabilities and Limitations, 2nd Joint Europe-US Short Course on Hypersonic: GAMNI-SMAI and Uni. Of Texas at Austin, USAF Academy, Colorado springs, CO 80840, January 1989.
- [5] Fay, J.A., Riddell, F.R., Theory of stagnation point heat transfer in dissociated air, Journal of Aeronautical Sciences, Vol. 25, No. 2, February 1958, p. 73-85.
- [6] Lees L., Laminar heat transfer over blunt-nosed bodies at hypersonic flight speed, Jet Propulsion, Vol. 26, April 1956, pp. 259-269.
- [7] Kolesnikov A.F., Condition of simulation of Stagnation Point heat transfer from High enthalpy flow, Fluid Dynamics, Plenum, (tr. From Russian), 1993, v.28, No. 1, pp 131-137.
- [8] Kolesnikov, A. Extrapolation from high enthalpy tests to flight based on the concept of LHTS. Belgium. RTO-VKI Special course. Measurement Techniques for High Enthalpy and Plasma Flows, October 1999.
- [9] Chazot O., R. Régnier and A. Garcia Muñoz, Simulation Methodology in Plasmatron Facility and Hypersonic Wind Tunnels, 12th International Conference on Method of Aerophysical Research, Akademgorodok, Novosibirsk, Russia, June 28 – July 4, 2004.
- [10] Chantetz B., Vos J., Bourgoing A., Gas-Surface Interactions modeling, 7th European Workshop on TPS & Hot Structures - Noordwijk (NL), 2013, April 8-10
- [11] Bourgoing A., DeChampvallins N, High Speed Entry Ablation-Flight Mechanics Coupling Effects, 7th European Workshop on TPS & Hot Structures - Noordwijk (NL), 2013, April 8-10
- [12] Vekinis G., Overview of the TPS Activities within the RASTAS SPEAR Project, 7th European Workshop on TPS & Hot Structures - Noordwijk (NL), 2013, April 8-10
- [13] Laux C., Mc Donald M., Characterization of a 50 kW Inductively Coupled Plasma Torch for use in Testing of Ablative Materials, 7th European Workshop on TPS & Hot Structures - Noordwijk (NL), 2013, April 8-10

*Radiation-Shapes-Thermal Protection Investigations
for High Speed Earth Re-entry*

RASTAS SPEAR : Radiation-Shapes-Thermal Protection Investigations for High Speed Earth Re-entry

**7th European Workshop on TPS & Hot Structures - Noordwijk (NL)
2013, April 8-10 - Session "Heatshield Concepts"**

J-M BOUILLY, A. PISSELOUP - EADS Astrium - Saint-Médard-en-Jalles, France

O. CHAZOT - Von Karman Institute, Rhode-St-Genese, Belgium

G. VEKINIS - Institute of Materials Science, NCSR "Demokritos", Greece

Z. SKORUPKA - Institute of Aviation – IoA Warsaw, Poland

A. BOURGOING - EADS Astrium Space Transportation, Les Mureaux, France

B. CHANETZ - ONERA, Meudon, France



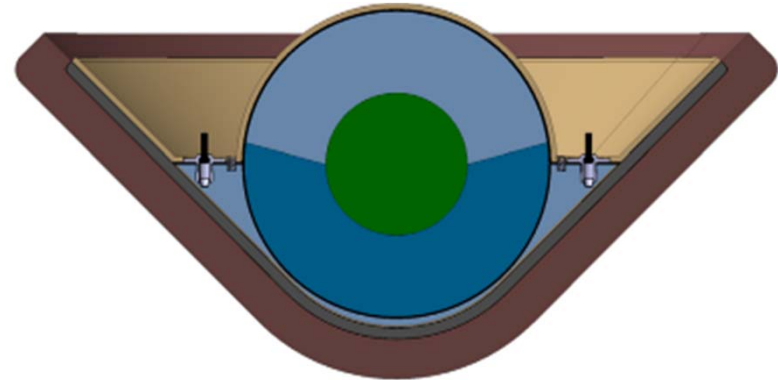
The research leading to these results has received funding from the European Union
Seventh Framework Programme (FP7/2007-2013) under grant agreement n° 241992

Overview

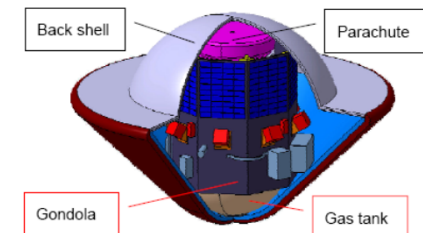
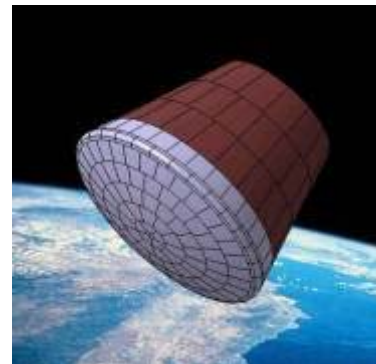
- Introduction
 - Objectives
 - WBS
- Overview of technical activities
 - Review of System Requirements
 - Ground Facilities Improvement
 - Key Technologies for High Speed Entry
 - Ablation – flight mechanics coupling assessment
 - Gas-surface interactions modeling
- Next Steps / Conclusion

General Objective

- Sample Return Missions : an important step for Solar System Exploration
 - After collecting samples, any return mission will end by high-speed re-entry in Earth's atmosphere.
 - This requires strong technological bases and a good understanding of the environment encountered during the Earth re-entry.
 - Investment in high speed re-entry technology development is thus appropriate today
 - to enable future planetary exploration missions in the coming decades.
 - Phobos Sample Return, Marco Polo, ..., Mars Sample Return
- Rastas Spear project
- to increase Europe's knowledge in high speed re-entry vehicle technology



Main focus : Sample Return Capsule



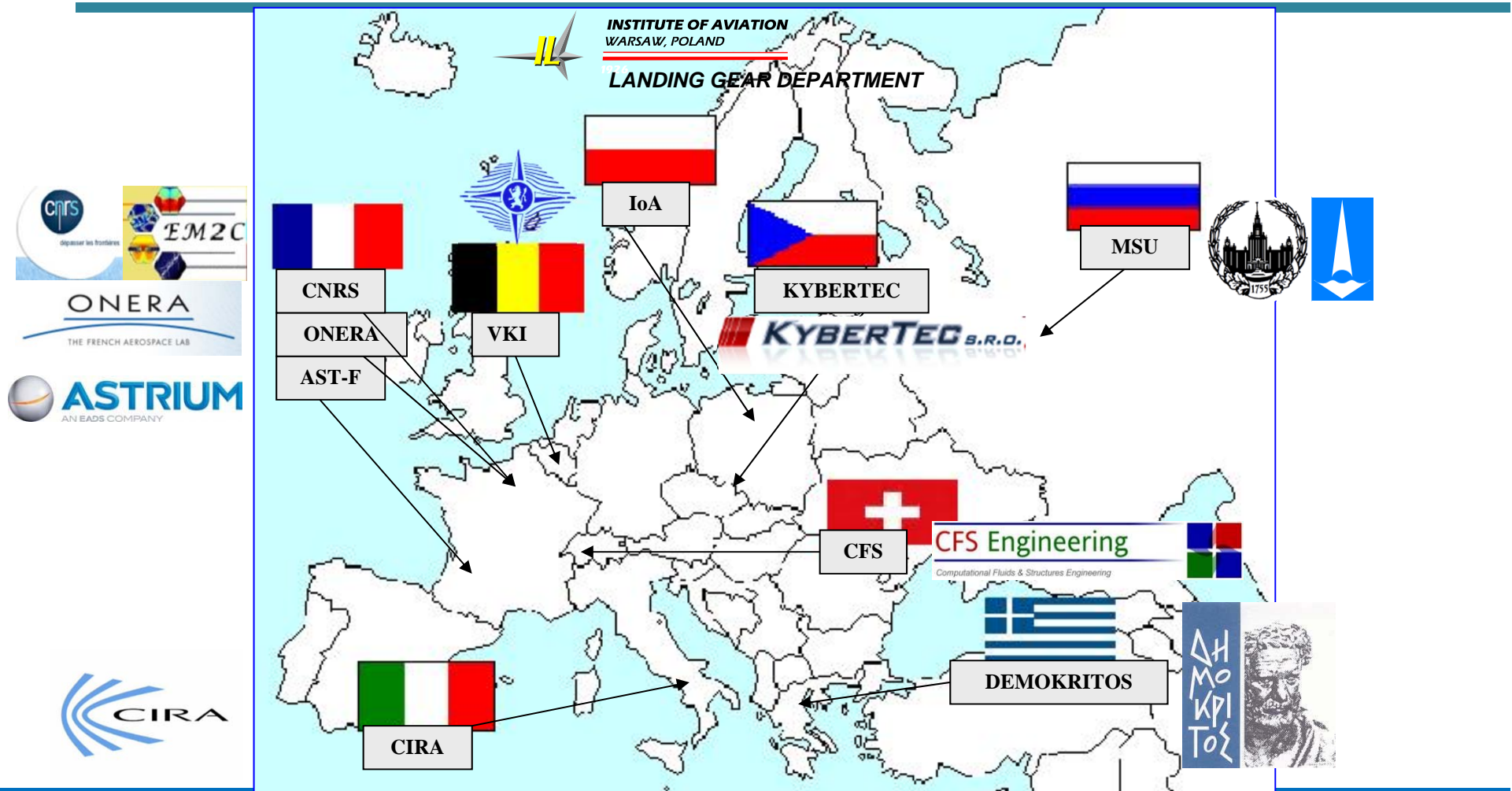
Other potential applications : ARV, Venus

Introduction /Acknowledgement

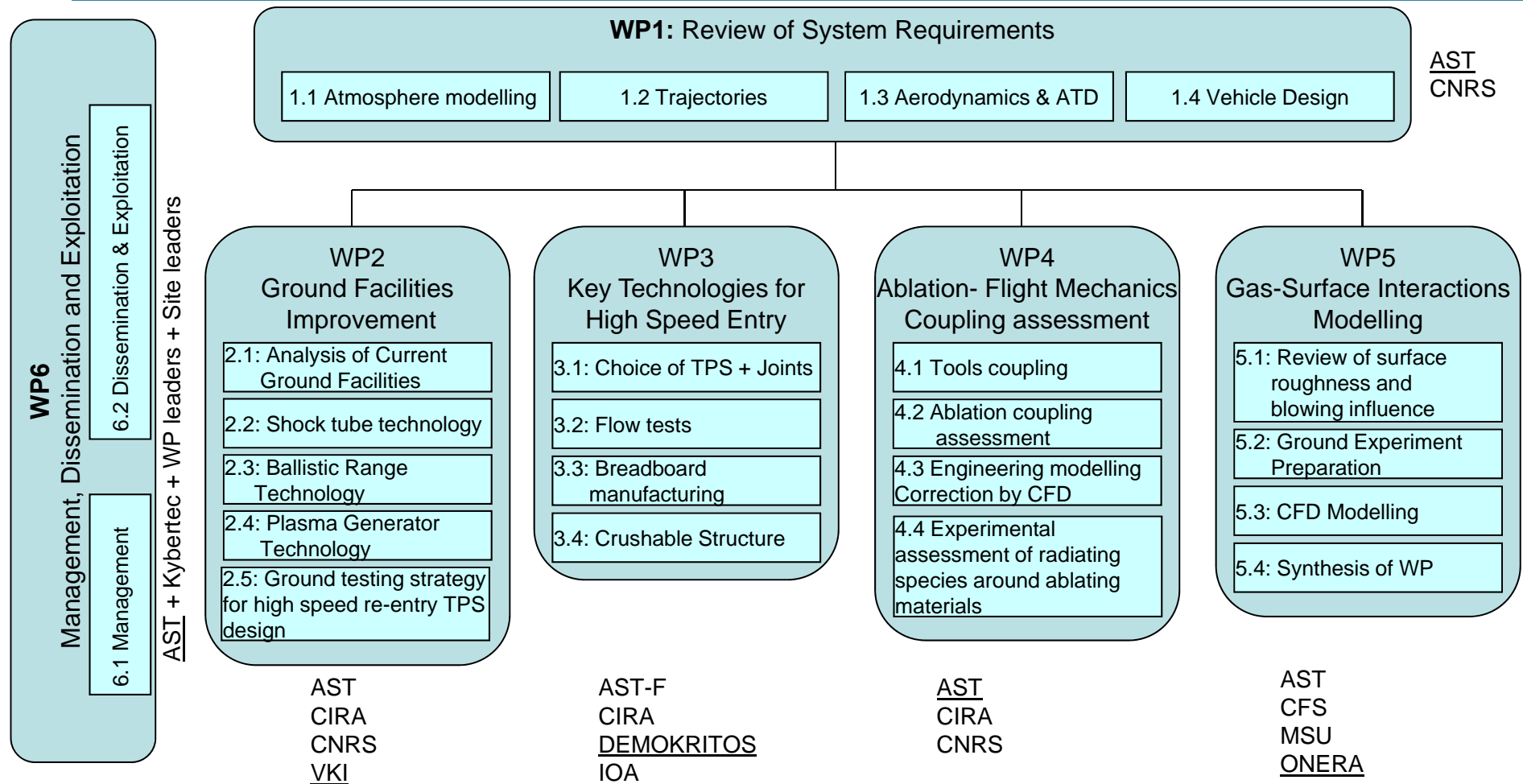
- In the frame of EC FP7 second call
 - Activity 9.2 – strengthening of space foundations / research to support space science exploration
 - SPA.2009.2.1.01 Space Exploration
- Duration
 - Sep 2010 – Apr 2013 (*)
() after 6-month extension*
- Status :
 - Team composed of 10 partners
 - Astrium is the coordinator
- Budget
 - total : 2.3 M€
 - including 1.6 M€ EU grant
- More at www.rastas-spear.eu



10 partners from 8 European countries



WBS



Several Rastas Spear presentations

Session “Modelling of Ablation and Gas- Surface Interaction (part 2)”

Tuesday, April 9, morning

- 11:10 “Gas-Surface Interactions modelling”
B. Chanetz, Onera ; J. Vos, CFS
- 12:00 “High Speed Entry Ablation-Flight Mechanics Coupling Effects”
A. Bourgoing, Astrium Space Transportation



Session “Advanced joining techniques “

Tuesday, April 9, morning

- 12:00 "Overview of the TPS Activities within the RASTAS SPEAR Project"
G. Vekinis, NCSR Demokritos



Session “Plasma testing capabilities”

Wednesday, April 10, morning

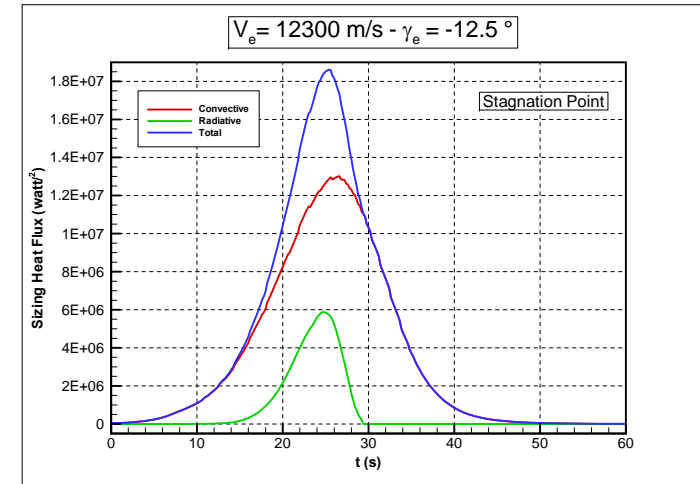
- 12:00 "Characterization of a 50 kW Inductively Coupled Plasma Torch for use in Testing of Ablative Materials"
M. MacDonald, Ecole Centrale Paris



WP 1 results: Review of System Requirements

- WP 1.1: Atmosphere modelling
 - Atmosphere compositions for Earth and Venus,
- WP 1.2: Trajectories
 - Identification of generic aeroshapes with respect to candidate exploration missions.
 - Investigation focused on Earth entry,
 - Flight domain determined with constraints on:
 - max heat flux, max heat load, max g-load
- WP 1.3: Aerodynamics & Aerothermodynamics
 - Convective and radiative heat flux
- WP 1.4: Vehicle design
 - Preliminary design of the generic capsule, and determination of TPS thickness
 - Definition of the Mass Centering and Inertia (MCI)
 - Preliminary TPS related requirements for other WP : surface recession, mass loss, temperature evolution, gas flow rate,...

→ See details on IPPW8 poster and paper



Sphere cone 45°
Diameter D = 1100 mm
Nose radius Rn = 275 mm
Mass m = 46.6 kg

D2.1 : Review on High Enthalpy Facilities



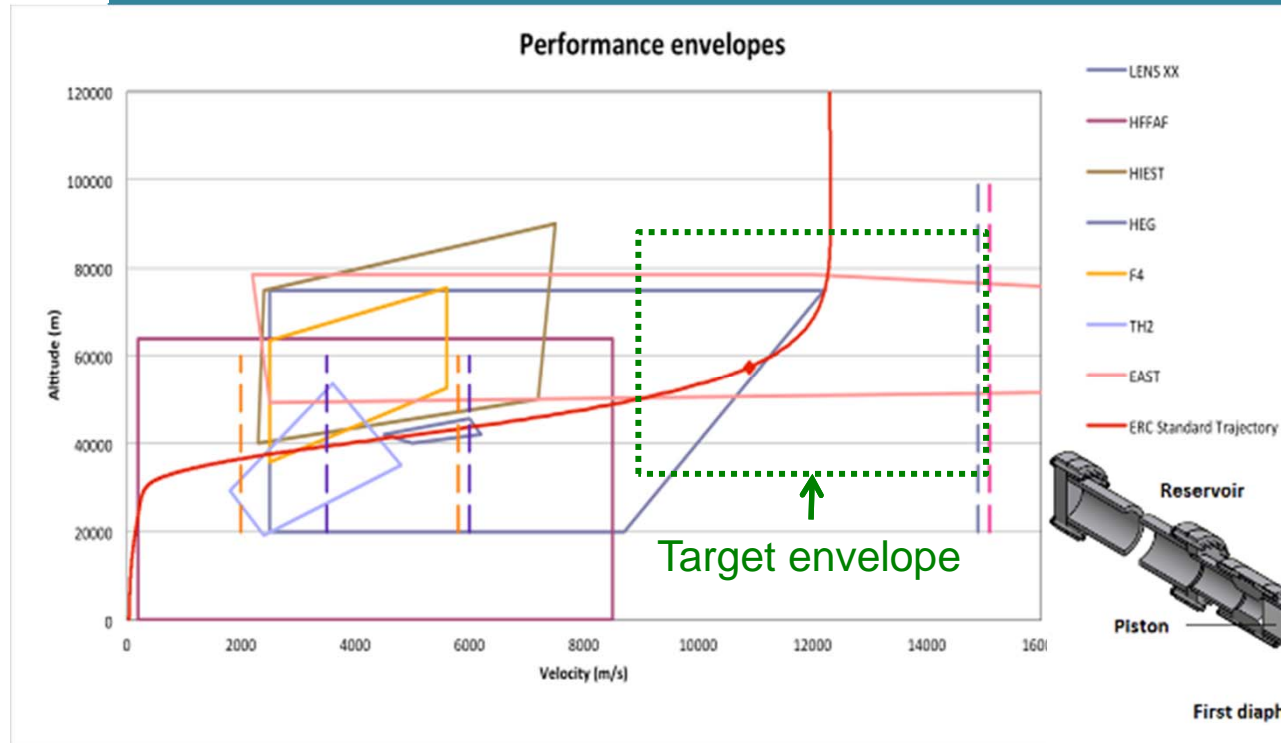
Only few facilities (in blue) are able to duplicate super orbital reentry conditions

Reports are available on website www.rastas-spear.eu

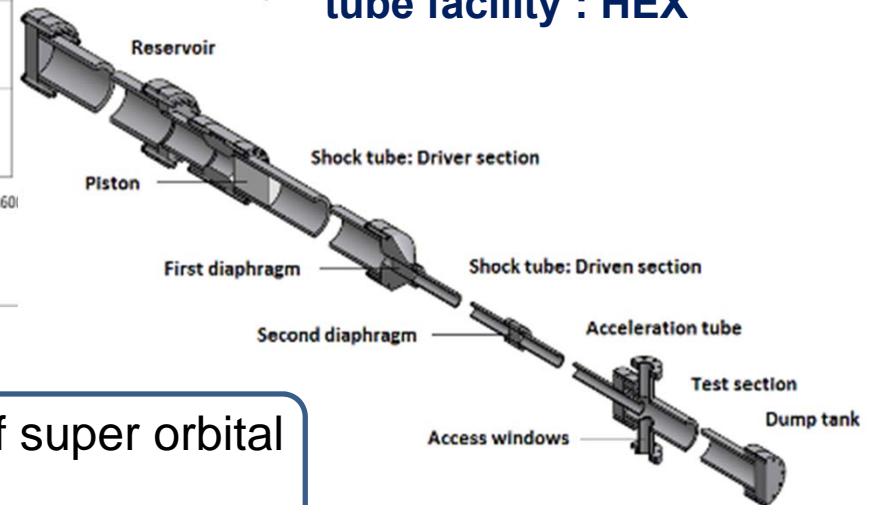


D2.4 Synthesis

Pre-design of hyper velocity facility



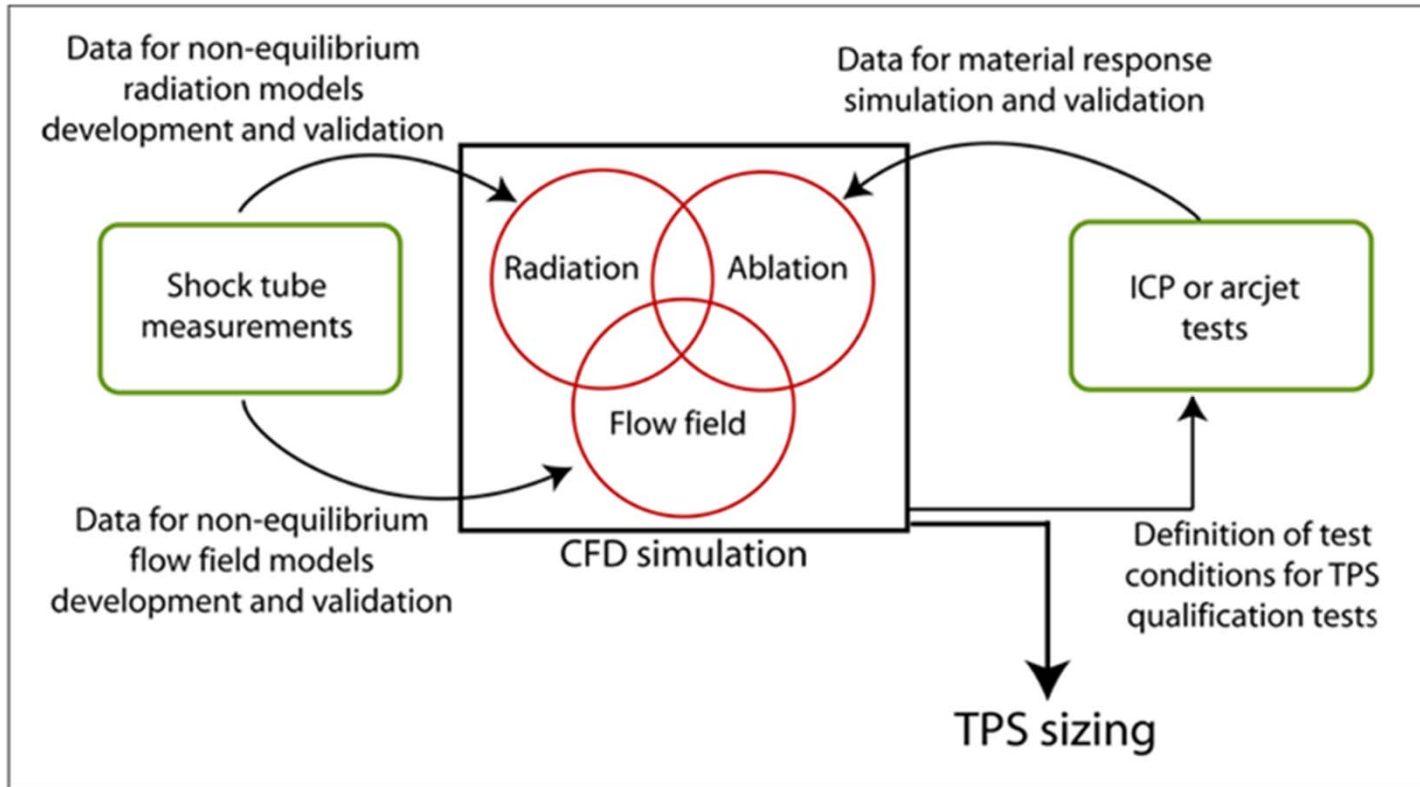
**Preliminary design for an
high Enthalpy Expansion
tube facility : HEX**



→ The designed facility targets duplication of super orbital testing condition

D2.5 Synthesis

Testing strategy for super-orbital reentry



The testing strategy involved **hyper velocity facility** together with **plasma wind tunnel** to developed **radiation** and **GSI** models to be coupled with CFD tools.

WP3: Key Technologies for High Speed Entry

Choice of TPS + joints



WP3.1 : choice of TPS + joints

- Based on ASTERM material
- Elaboration of a relevant set of criteria
- Screening of adhesives
 - → 2 products compared with ref CV1142
- Elementary characterisation
 - (shear, bending, tensile)



Bending test



Shear test

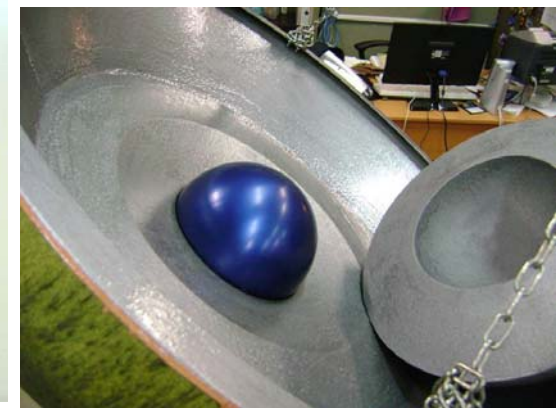
WP3.3

- Manufacturing of a demonstrator
 - Final diameter 92.5cm
 - Bonds and joints about 1-1.5mm max.
 - Outer surface finished in one operation
 - TPS thickness 56mm
- Manual methodology
 - low cost prototype
- Potential for further improvement, using greater precision tooling
- Capability for actual implementation, provided current dimensional tolerances are relaxed to some extent

Demonstrator with ASTERM TPS



Crushable material insert and sample sphere



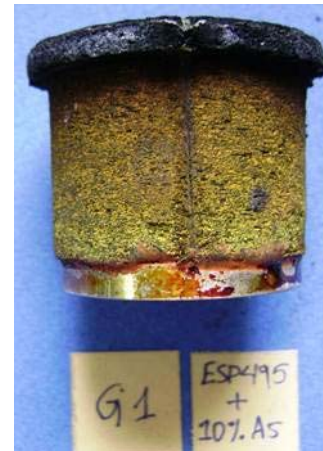


WP3: Key Technologies for High Speed Entry

Choice of TPS + joints

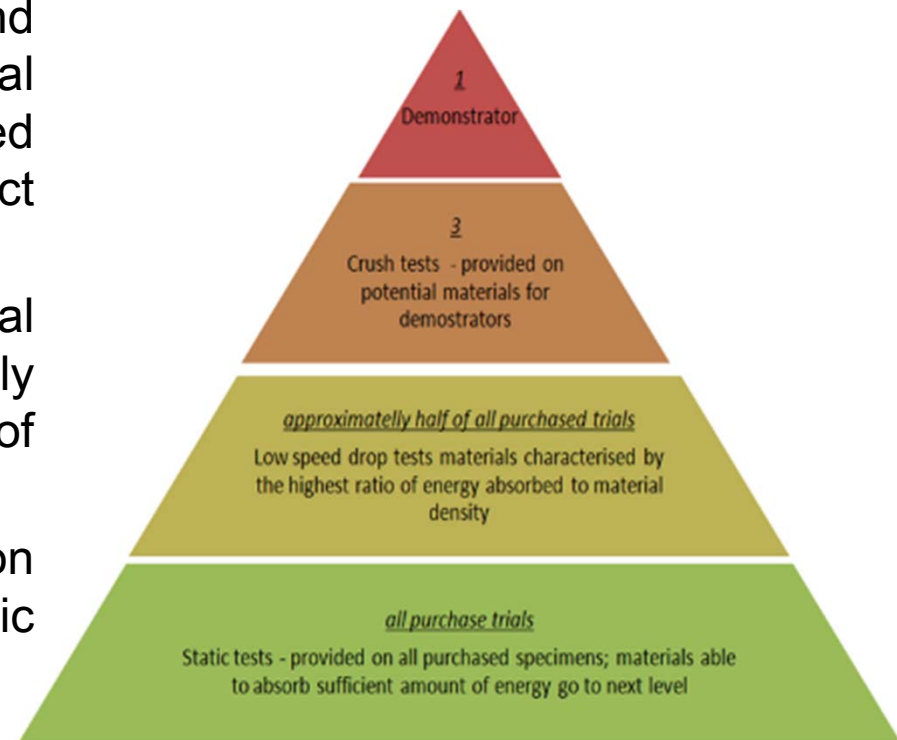
WP3.2

- Manufacturing of samples for testing on Scirocco
 - One test done, at 5 MW/m²
 - Then, campaign stopped due to unavailability of facility
- New test campaign had to be prepared on DLR L3K
 - 15 tests performed with various joint materials
 - Tests at 6 and 13.6 MW/m²
- Then analysis of the tests results
 - CV1142 and ESP495 display good erosion resistance at 6 MW/m²
 - At 13.6 MW/m², erosion becomes more important
 - Interest to add Asterm powder to the adhesive as reinforcement



WP3.4. Crushable Structures General overview

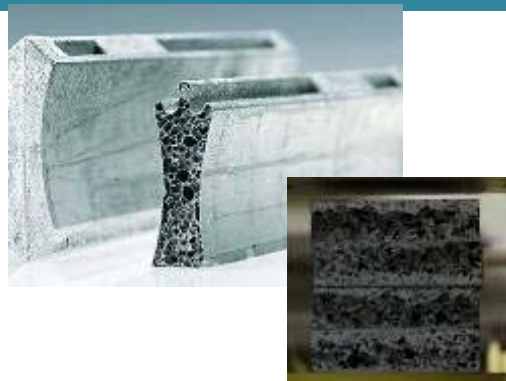
- Main task of the research: developing methodology for selection and evaluation of energy absorbing material based on numerical simulations coupled with simple shape specimens impact tests
- Selection of energy absorbing material for max. deceleration approximately 2000 g, and a defined set of requirements
- Developed methodology based on complementary static and dynamic tests



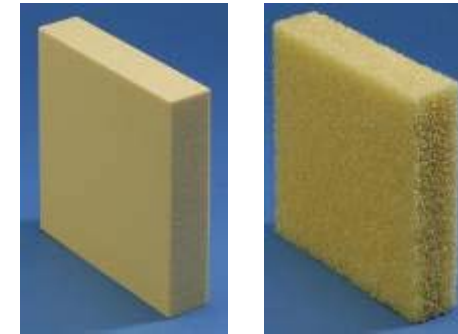
WP3.4. Crushable Structures Material screening (examples)



Soft PU foam with Al coating ; 30-40 kg/m³



Metallic foam/ hard ALSi alloy ; 500 kg/m³



Solid / cellular PU foam
85 to 280 kg/m³



Metallic foam/ hard ALCaTi alloy 250 kg/m³



Ceramic foam
400-500 kg/m³



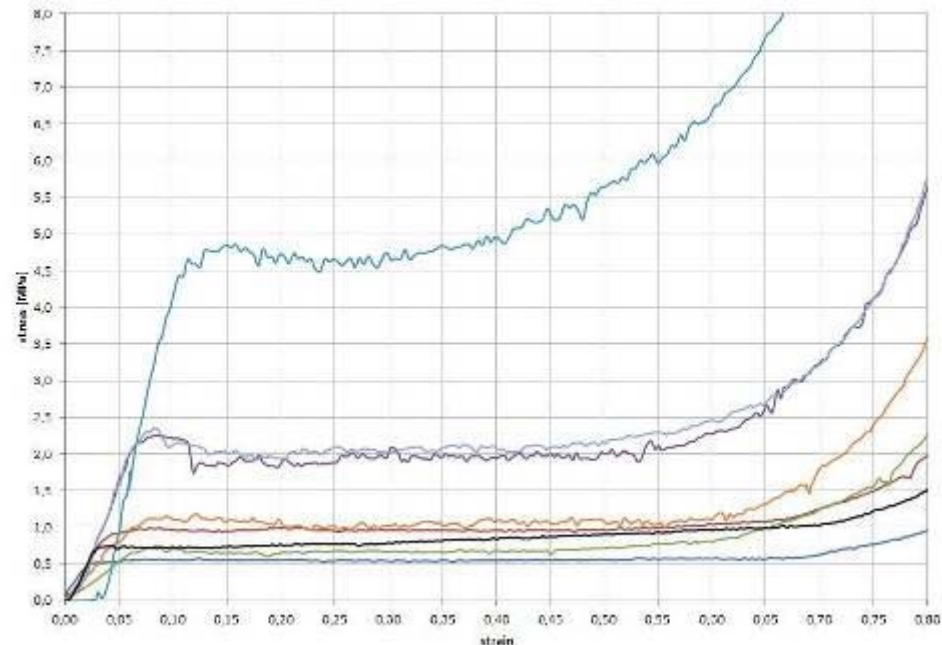
Polymeric foam/ medium Extruded Polystyrene (XPS)
45 kg/m³

WP3.4. Crushable Structures

Static tests



- Static tests on cubic samples 100 x 100 x 100 mm
 - Determination of stress-strain characteristics
- static experimental data then used as inputs for dynamic numerical simulations

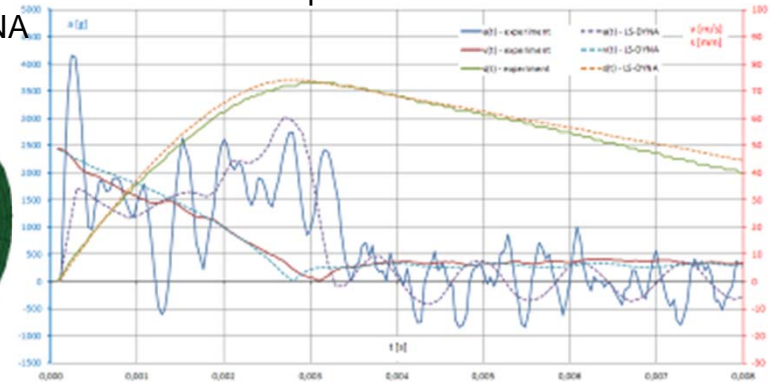
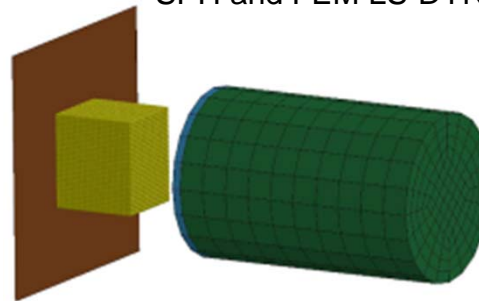
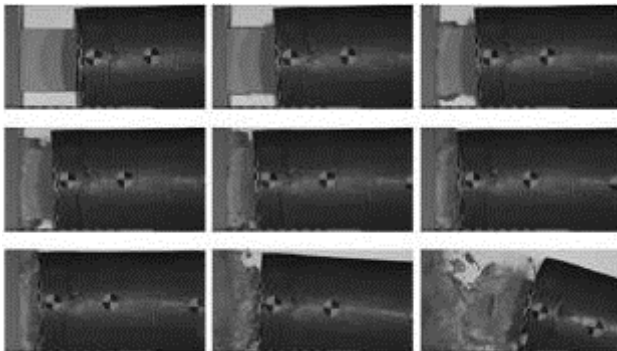


Comparative stress-strain characteristics
determined for various materials

WP3.4. Crushable Structures High Speed Tests



- Final calibration for impact tests (high-speed camera settings, lighting, position etc.)
- First-stage high-speed camera tests for finding optimal experiment setup
- Cubic samples 100 x 100 x 100 mm
- Air canon calibration and testing using 1.6 kg bullet
- Selected impact velocity at 45 m/s
- Image analysis using TEMA motion → position vs time
- Improved numerical SPH and FEM LS-DYNA model for testing crushable foam materials
- Good correlation between numerical and experiment data numerical SPH and FEM LS-DYNA

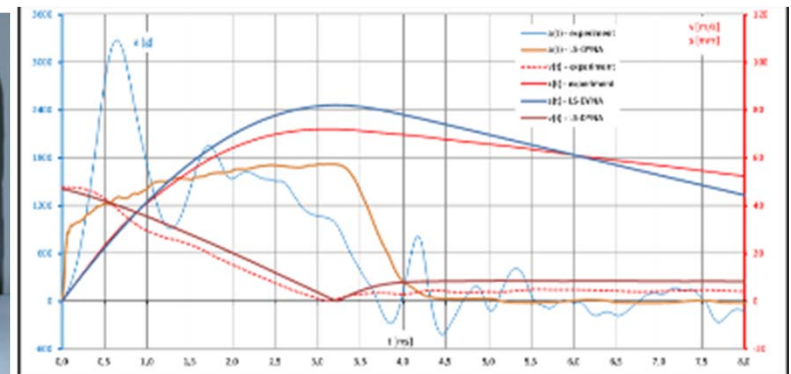
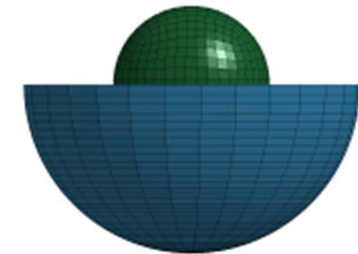


Comparison of experiment and numerical data for SR10 material

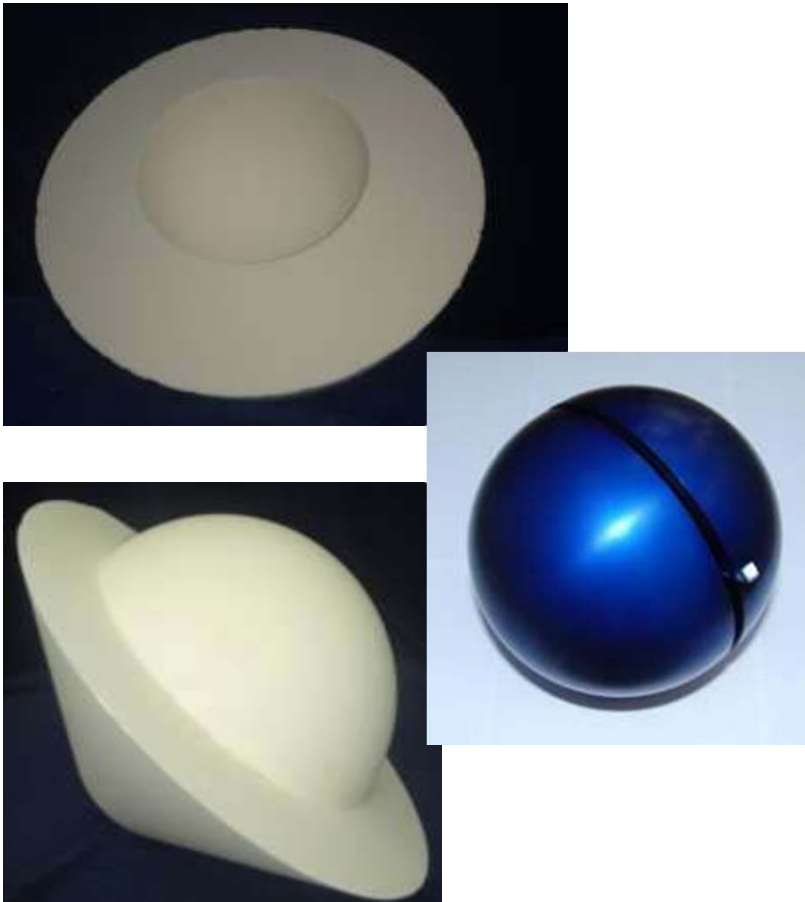
WP3.4. Crushable Structures High Speed Tests – full scale



- Full-scale impact test of chosen material for:
 - bullet mass $m=5$ [kg]
 - impact velocity $v= 45$ [m/s]
 - material thickness $t = 0.115$ [m]
- Test data analysis and excellent comparison with numerical simulation



WP3.4. Crushable Structures Conclusions

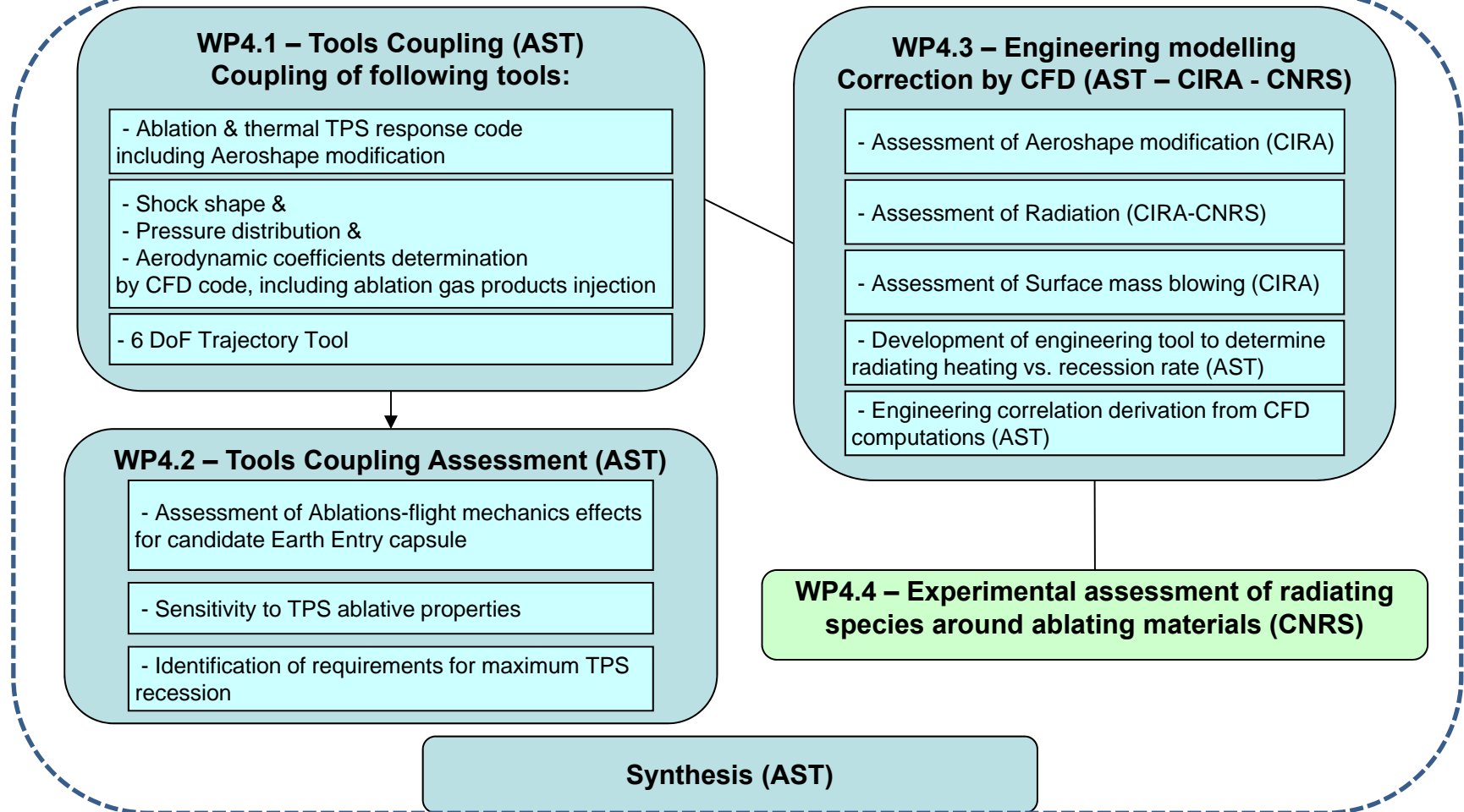


- Efficient methodology based on a two-step experimental approach
- Numerical simulation using static tests results giving good correlation between static and dynamic simulations
 - Validity demonstrated for PU foams – other types of materials should be verified
 - It is possible numerically to simulate various geometries based only on static test results
- High speed camera and picture analysis software works perfectly with project application
- After setup pneumatic cannon test procedure allows to perform 10 – 12 tests per day – efficient methodology
 - Using pneumatic cannon for dynamic test gives important energy differences with small velocity variation
- Finally, delivery of a representative breadboard to be integrated within the technological demonstrator

WP4: Ablation – flight mechanics coupling assessment

Work logic

Based on WP1 results as inputs :
flight environment, vehicle configuration



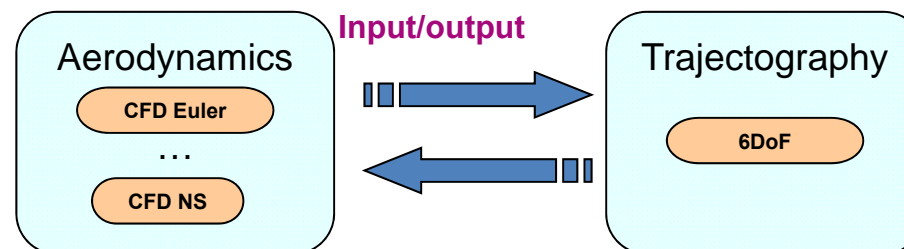
WP 4.1 – Tools coupling

Main Objectives

- To assess impact of massive ablation on aerodynamic performances and stability along the entry trajectory path.
- To elaborate and validate a coupled engineering tool

Main requirements:

- Modular tool:



↳ To permit easily the change of module (software) inside a functional class

- Robustness:

↳ **High requirement of robustness is needed for high speed entry**

- Evolutionary tool:

↳ **Basic requirement for software**

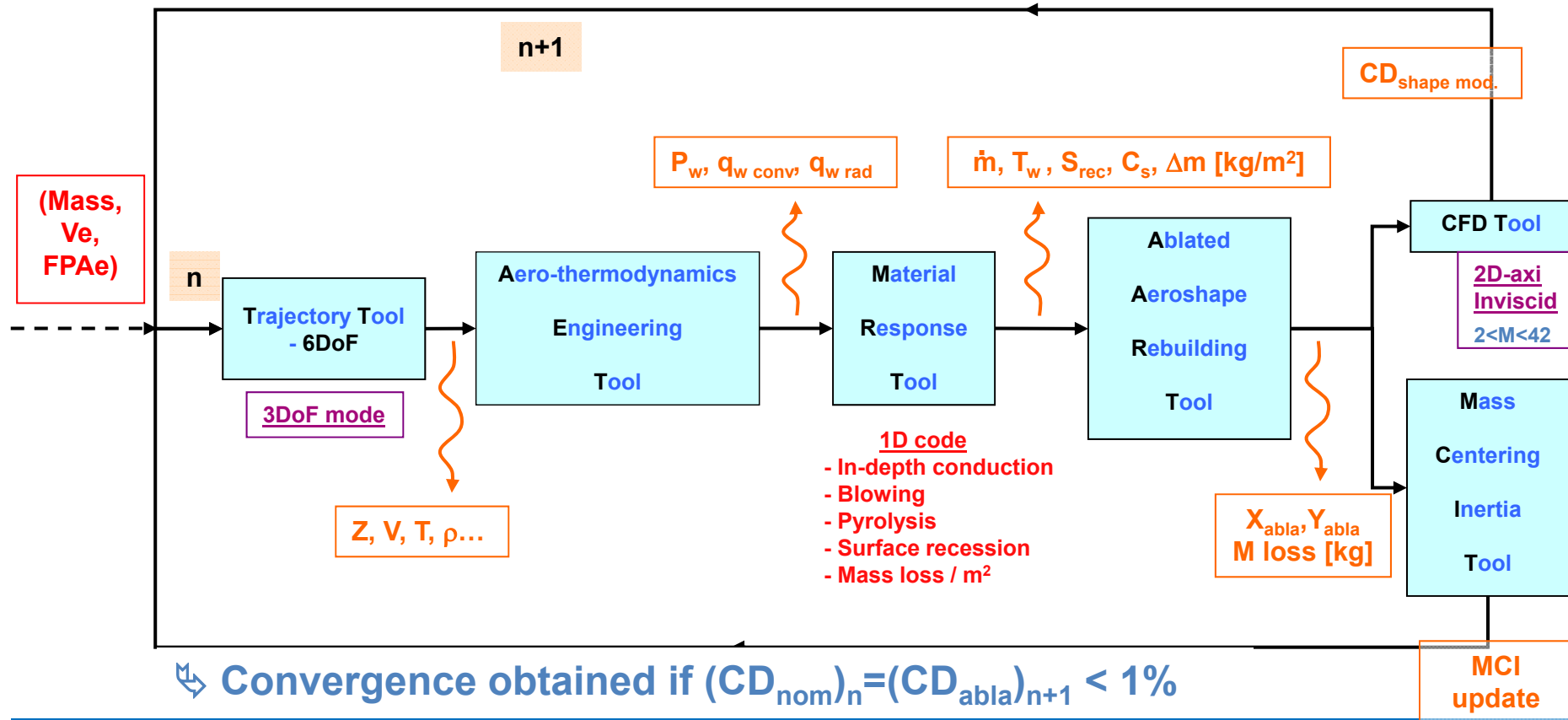
- To perform a complete trajectory within 12 CPU hours

↳ **To keep the Engineering tool spirit**

WP 4.1 – Tools coupling

Initial inputs:

- Initial profile
- Trajectory (Ve, FPAe, Mass)
- AEDB on initial profile



WP 4.2 – Ablation coupling assessment

- Trajectory analysis – Summary

Parameters	Effects compared with nominal case	Maximum levels difference	% vs nominal case	Criticality
Velocity	↘	50 ⇔ 75m/s	~1 %	Low
Mach	↘	0.15 ⇔ 0.25	~1 %	Low
Deceleration	↗	-0.5 ⇔ 1g	1 % ⇔ 1.5 %	Low
Dynamic pressure	↘	0.9 ⇔ 1.3kPa	3 % ⇔ 3.5 %	Medium
Stagnation pressure	↘	2 ⇔ 3kPa	2.5 % ⇔ 4 %	Medium
Heat Fluxes	↘	<100W/m ²	~0 %	Negligible
Heat Load	↘	1.5 ⇔ 2.5MJ/m ²	1 % ⇔ 2 %	Medium
Range	↘	0.8 ⇔ 1.4km	~0.3 %	Low

Assessment of tools coupling:

On the considered Rastas Spear trajectories (12.3 km/s), the aeroshape modification due to ablation is limited, and hence a low influence is observed on trajectory, heat fluxes and MCI

WP4.3 – Engineering Modelling Correction by CFD

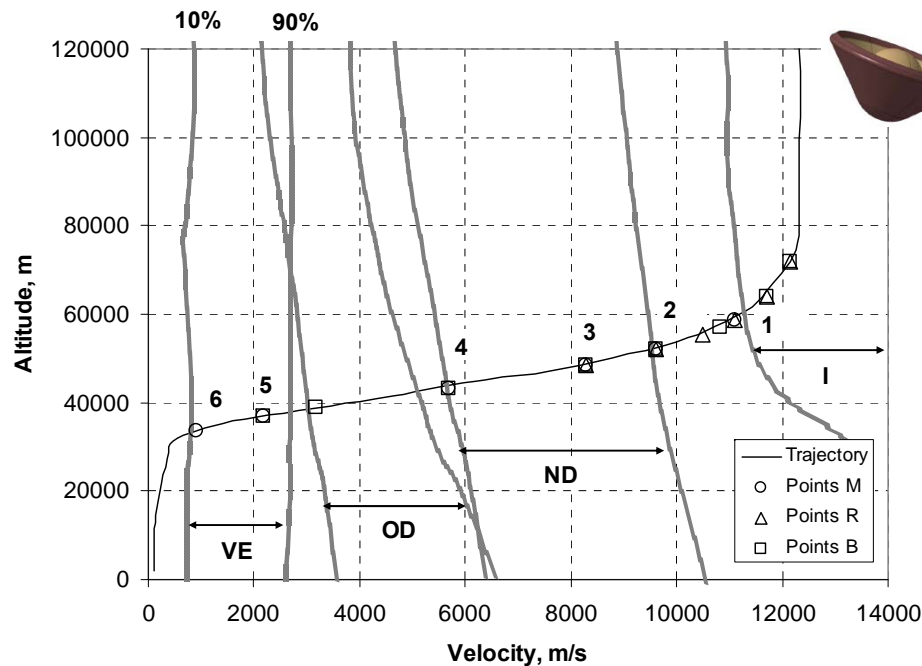
Task # 1: Assessment of aeroshape modification (M)

Task # 2: Assessment of Radiation Coupling (R)

Task # 3: Assessment of Surface Mass Blowing (B)



Re-entry Trajectory @ FPAe=-12.5 deg



- Complex CFD analyses were run to assess these various aspects

- Not all results were satisfactory, and consolidation is required for several points

- Aerodynamic coefficient

- CFD computations show that current correlations are valid (to be consolidated for high velocities)

Convective heat flux

- Correlations used for coupling tool are kept by conservatism
- No firm trend may be derived from current CFD computations, which require further consolidation

Radiative heat flux

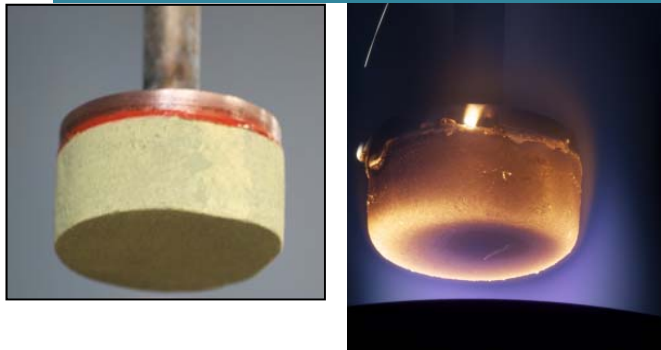
- Correlation can be updated (confirmed reduction of shock stand-off distance on stagnation line)
- Anticipated reduction of level of radiative heat flux
- To be extended for a larger range of entry velocities

Synthesis

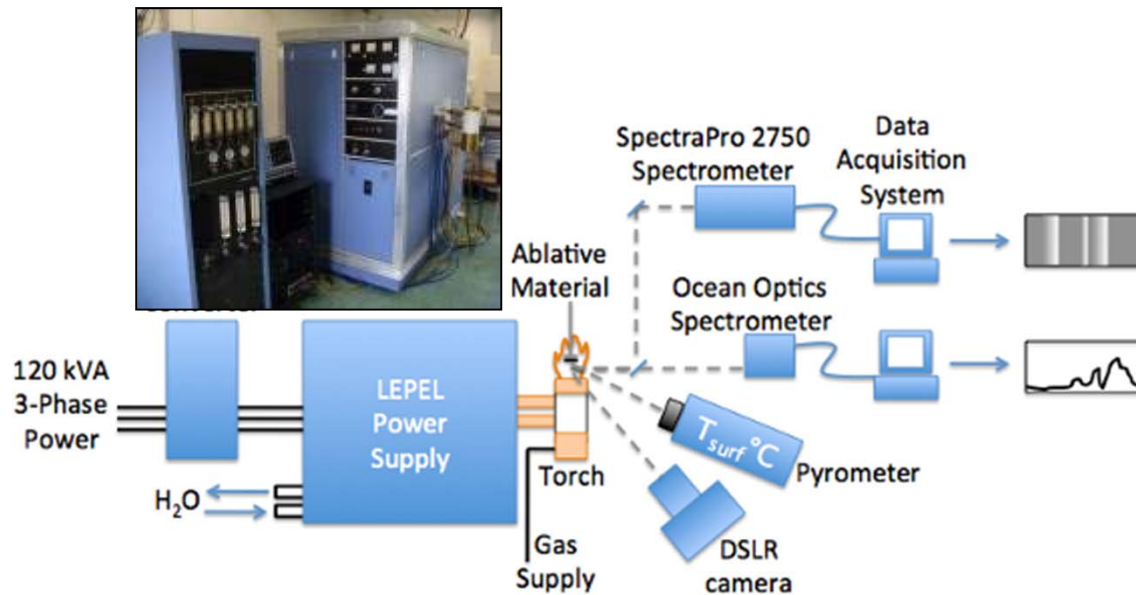
- Tools coupling:
 - A first version of the coupling tool is available and has been used for assessment tasks in WP4.2 activities
 - All the requirements are completed
 - Further work needed on following points
 - The aeroshape modification in Transsonic/Subsonic domain cannot be taken into account in this version \Rightarrow the use of NS computations seems to be the best way \Rightarrow strong investment on mesh activities, CPU time \Rightarrow and impact on robustness
 - Rarefied domain must be examined

- Assessment of tools coupling:
 - Low influence observed on considered trajectories
 - High interest to evaluate the tool for more severe trajectories

WP4.4 – Experimental assessment of radiating species around ablating materials



- RF plasma torch facility and associated optical diagnostics implemented at CNRS
- Designed to support cylindrical ablator coupon (ASTERM, CBCF, ...) in the plasma stream
 - Water-cooled sting holds a 5 mm thick, 40 mm diameter copper disk
- Two surface T° measurements and two spectrometers
 - Acton SpectraPro 2750
 - OceanOptics USB2000+
- Material temperature and species concentration profiles have been measured in the boundary layer, showing spallated particles, sodium emission, plasma recombination
- Fully operational facility ready for more testing
 - Higher power and heat flux
 - Search for more species (C, C₂, C₃)



WP5: Gas-surface interactions modeling

- WP 5.1 Review of surface roughness
 - Bibliography about roughness and blowing (Onera/MSU)
 - Turbulence model recommendations (MSU/Onera)
 - Critical analysis from real flight (Astrium/MSU)



- WP 5.2 Ground experiment
 - Tests in Mach 5 blow down wind tunnel (Onera)
 - Test analyses (Euler + boundary layer)



- WP 5.3 CFD modeling
 - Implementation of turbulence models on rough surface (from WP5.1)
 - WTT reconstruction and validation
 - Earth re-entry vehicle computation



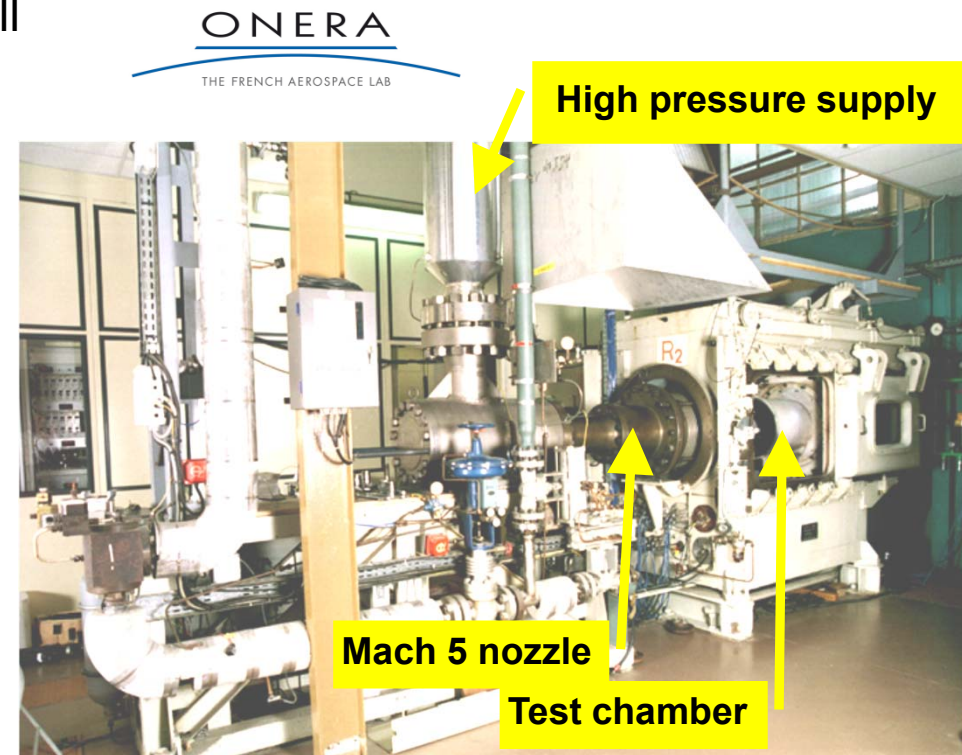
- WP 5.4 Synthesis



WP5: Gas-surface interactions modeling

Experiments in the blow down wind tunnel R2Ch

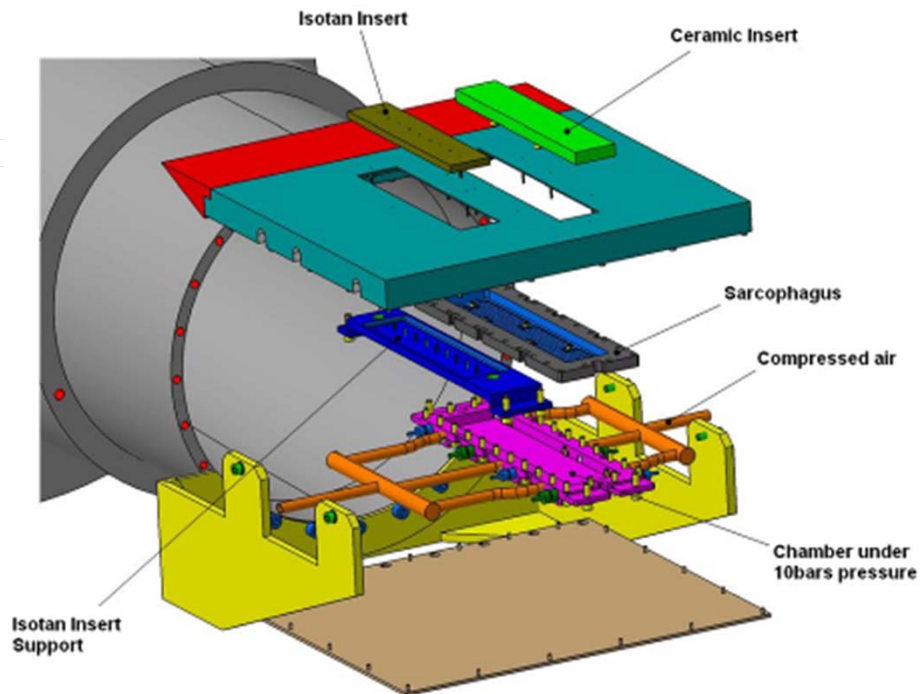
- **Test Objective** : qualification of the wall heat-flux with roughness effects and different blowing rates
- Performance of 31 runs with various test conditions
 - without blowing (reference case)
 - with a moderate blowing (0,6 kg/m²/s)
 - with a maximal blowing (1,2 kg/m²/s)
- On smooth or rough samples
- **Wind tunnel characteristics** :
 - Mach 5 nozzle with an
 - exit diameter : 326 mm
 - p_{st} : from $7 \cdot 10^5$ Pa to $50 \cdot 10^5$ Pa ; $T_{st} = 650$ K
 - Re (L=1 m) = from $5.95 \cdot 10^6$ to $42.5 \cdot 10^6$



WP5: Gas-surface interactions modeling

Experiments in the blow down wind tunnel R2Ch

Exploded view of the test set-up



- **Model** : Flat plate with a sharp leading edge, already available from a prior test campaign

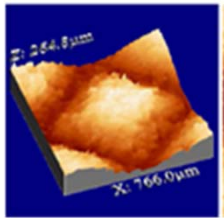
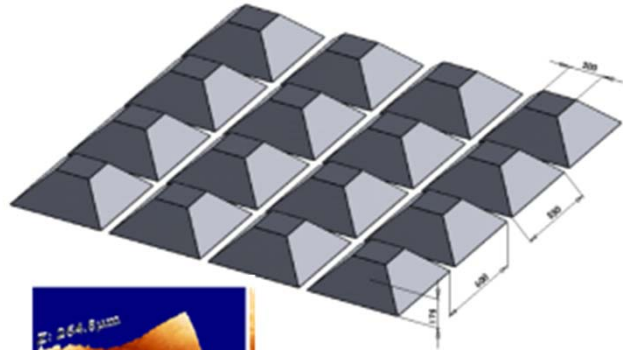
ONERA
THE FRENCH AEROSPACE LAB



During tests :

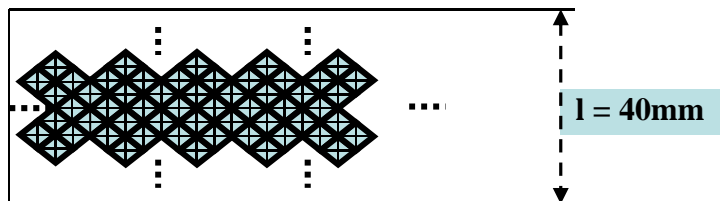
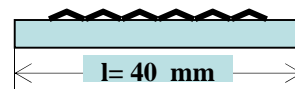
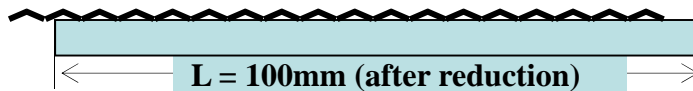
- Heat flux measurements by infrared thermography,
- Schlieren photographs

WP5: Gas-surface interactions modeling



Two porous ceramic insert (porosity 48 %)

- without roughness
- with roughness r1 (pyramid height $176 \pm 34 \mu\text{m}$)
- characteristics of the roughness : truncated pyramids (base $\sim 550 \mu\text{m}$) in staggered rows



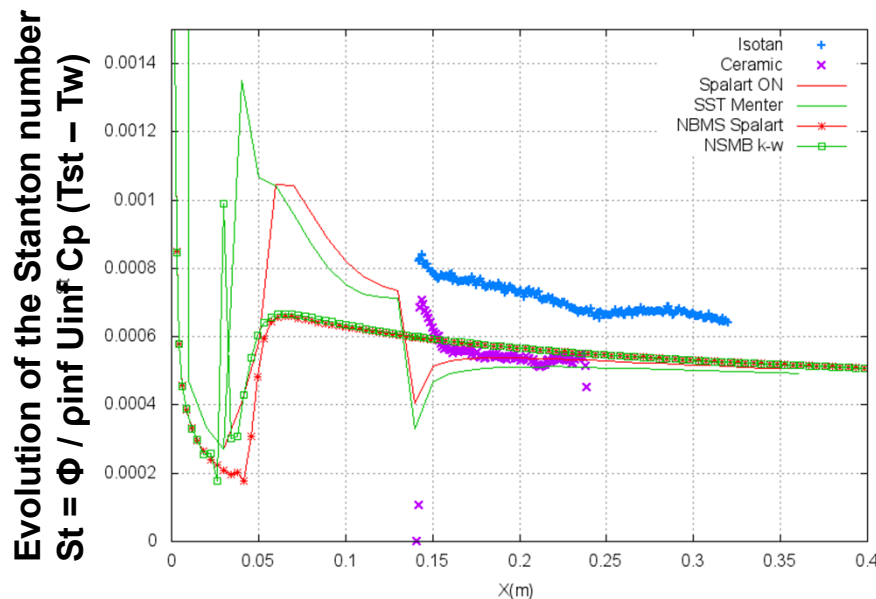
Top view of the rough insert

WP5: Gas-surface interactions modeling

WTT reconstruction and validation (CFD & BL)

Example of reconstruction

Run 3782: no blowing, no roughness



- Lot of valuable experimental data have been acquired
- Computations and comparison with the experimental data, after implementation of both roughness and blowing effects in different solvers.
- Good agreement between the different solvers
 - Boundary Layer Euler solver (ONERA)
 - NSMB - Navier-Stokes Multi-Blocks (CFS)
- No obvious best choice between Spalart and k-w models
- Wall blowing : Correct agreement of CFD simulations
 - Small blowing mass flow case well predicted by all models
 - Strong blowing mass flow case evidences the lack of a blowing correction for the Spalart and Allmaras model
- Wall roughness
 - Key issue: models predict heat flux increase, while experiment show heat flux decrease. Remains unexplained.
- Wall roughness + blowing cases are more complicated to simulate
 - Models which cannot account for wall blowing (Spalart, k-w) predict lower (too low?) levels

Conclusion

- Rastas Spear is a typical R&D project
 - Part of European Community Framework Programme n°7 (FP7)
- Well defined framework for the study
 - Focus on passive Earth Return Capsule
 - Target missions MarcoPolo-R, Phootprint, MSR...
- Successful achievement of the objective to increase the TRL of
 - Key technologies
 - Methodologies
- Completion of overall project objectives by end of April 2013
 - Finalization of the last actions and documents until end of study
- Highly valuable step towards an actual flight mission

Thank you for your attention

More at www.rastas-spear.eu

Characterization of Actively Cooled Porous C/C Wall Segments According to Pressure Loss and Internal Temperature Distribution

Sven Schweikert⁽¹⁾, Jens von Wolfersdorf⁽¹⁾, Markus Selzer⁽²⁾ and Hermann Hald⁽²⁾

⁽¹⁾ *Institute of Aerospace Thermodynamics (ITLR), University of Stuttgart
Pfaffenwaldring 31, 70569 Stuttgart, Germany
Email: sven.schweikert@itlr.uni-stuttgart.de*

⁽²⁾ *Institute of Structures and Design (IBK), German Aerospace Center (DLR)
Pfaffenwaldring 38-40, 70569 Stuttgart, Germany
Email: markus.selzer@dlr.de*

Aerospace components exposed to extremely high heat loads require the use of effective thermal protection systems. Transpiration cooling applied to porous high-temperature fiber ceramics is a promising technique in this regard. In this study, two test facilities are utilized to assess the aero-thermal behaviour of transpiration cooled carbon/carbon materials. Two different species of this ceramic are investigated as reference material to characterize the certain material class of ceramic matrix composites. The pressure loss and internal temperature distribution of the porous materials are monitored during experiments under heat loads. The application of the respective test benches enable the study of the material characteristics under aerodynamic or radiative heating. The measurements concerning the internal temperature distributions are compared with analytical models derived on the basis of the coupled set of energy equations, tolerating thermal non-equilibrium of fluid and solid phase of the material. The solutions are obtained applying temperature boundary conditions. To estimate the increased pressure losses of actively cooled porous ceramics under heat loads, a modified Darcy-Forchheimer equation is applied and compared to experimental data. Both models show a good agreement with the measured data. The aero-thermal behaviour of porous carbon/carbon turned out to be independent of the utilized heat source. Both facilities were operated with air as gaseous coolant.

INTRODUCTION

One of the key technologies of today's aerospace applications is the effective protection of thermally heavy loaded components, like the inner walls of combustion chambers or the heat shields of re-entry vehicles. This issue might become even more important for prospective missions, where considerably increased energy densities are expected. To serve the arising demand for powerful thermal protection systems, recent studies by DLR indicate the great potential of actively cooled porous high-temperature fibre ceramics (e.g. [1–3]). This active cooling technique is commonly known as transpiration cooling. Although the general feasibility of transpiration cooling applied to state of the art porous ceramics have been proven already by DLR's technology demonstration projects KSK (*Keramische Schubkammer* - ceramic thrust chamber) or AKTiV (*Aktive Kühlung im Versuch* - active cooling experiment) on SHEFEX II (e.g. [4, 13]), there is still a need to improve the understanding of the involved physical transport mechanisms and, based on that, to develop adequate design tools for future aerospace applications.

Considering transpiration cooling as a combination of internal cooling effects of heat exchange within the porous structure and external effects of coolant injection into a thermal boundary layer, the conducted studies focus on the internal mechanisms. In this regard, one of the first investigations can be traced back to the mid of last century, when Weinbaum and Wheeler [5] published an analytical solution for the internal temperature distribution for fluid and solid phase of porous sintered metal. The temperature characteristics are estimated tolerating thermal non-equilibrium of the two phases of the porous matrix and are solved using temperature boundary conditions. In the following years, this procedure had been adapted and validated by other authors, examining as well the effect of the applied boundary conditions (e.g. [6–8]). In the same period the question arose, to what extent the assumption of thermal equilibrium between fluid and solid phase of the porous material is valid (e.g. [10]). In doing so, the solution for the internal temperature distribution of porous structures can be simplified to only one differential equation of second order. Although the great potential of transpiration cooling had been obvious those days (e.g. [9]), the early studies were faced with a lack of proper materials, withstanding the high loads of possible aerospace applications [11]. Progress in the field of high-temperature ceramics technically reactivated this cooling technique and lead to recent investigations mainly focused on combustion chamber cooling (e.g. [1, 11–15]).

Also addressing this field of application, a discussion based on analytical studies, concerning the effect of enhanced coolant side heat transfer on the internal temperature characteristics, was presented by von Wolfersdorf [16]. Most recently, a theoretical model describing the temperature distribution within porous fibre ceramics under the assumption of thermal equilibrium was applied by Langener et al. [14]. The approach derived in this study is compared to experimental data gained by aerodynamic heating of actively cooled porous ceramic matrix composite (CMC) wall segments.

A further aspect to determine the internal aero-thermal characteristics of porous materials is the pressure loss caused by the coolant through flow. A quantification is commonly done considering the Darcy equation, based on studies achieved in the 19th century [17]. Besides inertia effects, pressure loss due to drag shall also be accounted for. Therefore, a quadratic term needs to be added completing this original formulation to the well-known Darcy-Forchheimer approach [18]. Recent investigations concerning pressure loss of porous media under heat load were conducted e.g. by Gascoin [19]. In this study, the material intrinsic permeabilities are used to identify the temperature dependency of the fluid viscosity. In contrast, Langener et al. [15] used the temperature dependent fluid properties to describe the increased pressure losses while heat loads are apparent. To correct the fluid properties, a linear temperature distribution within the porous material is suggested.

The work presented in this paper attempts to support the general understanding of the involved thermodynamic transport mechanisms of porous CMC materials under heat loads with respect to internal temperature distribution and pressure loss.

EXPERIMENTAL PROCEDURE & MATERIAL

Investigated Material

The porous high-temperature fibre ceramic C/C (carbon/carbon) was investigated during these studies. Designed and manufactured at DLR's Institute of Structure and Design (IBK), porous C/C samples are considered as reference material for the specific material class of CMC. The ceramic is manufactured via resin transfer moulding and pyrolysis, in which the resin matrix is changed into carbon. This process leads to a shrinking of the matrix volume, which creates micro dimensional cracks within the fabric. These cracks are interconnected and define the porosity as well as the permeability, which is essential for active through flows. The small size of these passages form a large internal surface, which is the basis for the significant internal heat transfer characteristics of this material. Depending on the resins and the fibres, material intrinsic properties like porosity, permeability as well as thermal conductivity can be triggered during the manufacturing process. Table 1 summarizes the material properties for the investigated C/C wall segments. The general geometry of the C/C samples is characterized by a thickness of 15 mm and an actively cooled area of $61 \times 61 \text{ mm}^2$. Besides the relative through flow direction within the segments, the material intrinsic parameters separate the investigated C/C samples in two different material species. The denotation of these species is chosen according to the internal through flow direction with respect to the fibre orientation in parallel and perpendicular samples. Figure 1 shows the top view of a perpendicular (a) and a parallel (b) wall segment as well as a micrograph (c), where the through flow directions are indicated. Further details concerning the manufacturing process as well as the characterisation of the material intrinsic properties are given in [20].

Test Facilities & Instrumentation

To estimate the aero-thermal behaviour of transpiration cooled C/C by precise and extensive sensor arrangements, the maximum applied heat loads are typically limited by the temperature durability of the used measurement equipment.

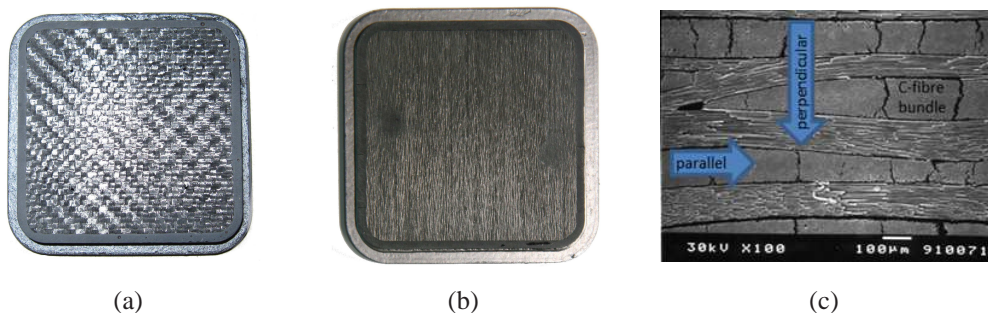


Figure 1: Investigated C/C wall segments: (a) Sample 1; (b) Sample 2; (c) Photomicrograph of C/C

Table 1: Thermophysical properties of the investigated C/C wall segments

		Sample 1	Sample 2
Coolant flow orientation		perpendicular	parallel
Porosity	ε [%]	12.4	11.1
Permeability	K_D [m^2]	$1.448 \cdot 10^{-13}$	$3.571 \cdot 10^{-13}$
	K_F [m]	$1.074 \cdot 10^{-8}$	$5.165 \cdot 10^{-8}$
Thermal conductivity	k_{eff} [W/mK]	1.4	13.5

These thermal loads are usually well below the ones real aerospace applications are exposed to. In doing so, the detailed study of involved physical mechanisms is addressed rather than the behaviour of an application in realistic environments. Following this approach, two different test facilities had been utilized for the conducted experiments. The first one is ITLR's hot gas test facility, which already had been used in previous studies of transpiration cooling (e.g. [14, 15, 21]). This test bench is originally designed to study supersonic combustion problems and consists of a two-staged screw compressor and an assembly of electrical heaters. A detailed description of this test bench is given e.g. in Scheuermann et al. [22]. For the performed experiments, compressed and dehumidified air is accelerated to Mach numbers up to 0.5 and heated up to gas temperatures between 420 K and 520 K. This hot gas stream is lead into a rectangular wind tunnel, where the porous sample is installed at one of the side walls. The pressurized coolant plenum, mounted at the back side of the C/C wall, supplies the porous sample with coolant and establishes the transpiration through flow. A cross sectional view of the wind tunnel, porous sample and coolant supply is given in Fig. 2 (a). The pressure within the coolant plenum is monitored with a Newport Omega PAA33X-C-15 pressure transducer, operating with an accuracy of 400 Pa. The coolant pressure is directly connected to the coolant mass-flow, which ranges from none to 6.0 g/s and is adjusted by a Teledyne-Hastings HFC-303 thermal mass-flow controller (accuracy: 0.048 g/s) for the conducted investigations. The coolant temperature in the plenum is measured by two thermocouples (Newport Omega, SuperOMEGACLAD™, accuracy: 1.1 K, K type, grounded). Ten additional thermocouples (TCs) of the same type are installed within the C/C sample. Four of them are flush mounted with the heated surface and the remaining TCs are fixed with carbon glue in different mounting depths, enabling the acquisition of the internal temperature characteristics at certain positions within the porous specimen. Details regarding the characterization of the hot gas stream as well as additional information of the wind tunnel system are given by Langener et al. [14, 15].

Although the hot gas test facility is run at moderate conditions, it's operation is respectively expensive and an alternative way to heat up the porous material became desirable. A suitable way was identified by the application of an infra-red (IR) heater. In this regard, the heated side of the C/C wall is considered as system boundary, where the heat loads are examined as net heat flux independent of the applied source. Since the external effects of coolant injection into a hot gas boundary layer are not captured by this approach, the focus of the investigations is exclusively set on the internal cooling mechanisms with radiative or aerodynamic net heat flux. The realization of this concept is achieved by the application of an Elstein SHTS/100 ceramic IR-radiator. This radiator electrically heats a $96 \times 96 \text{ mm}^2$ sized ceramic surface to temper-

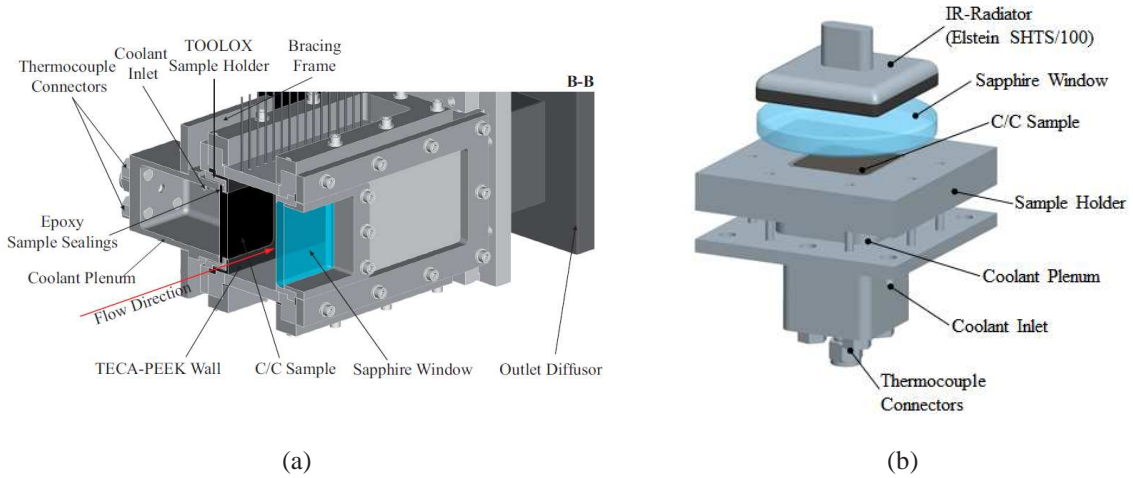


Figure 2: Experimental setup: (a) Cross sectional view of the hot gas test facility; (b) Radiative test facility

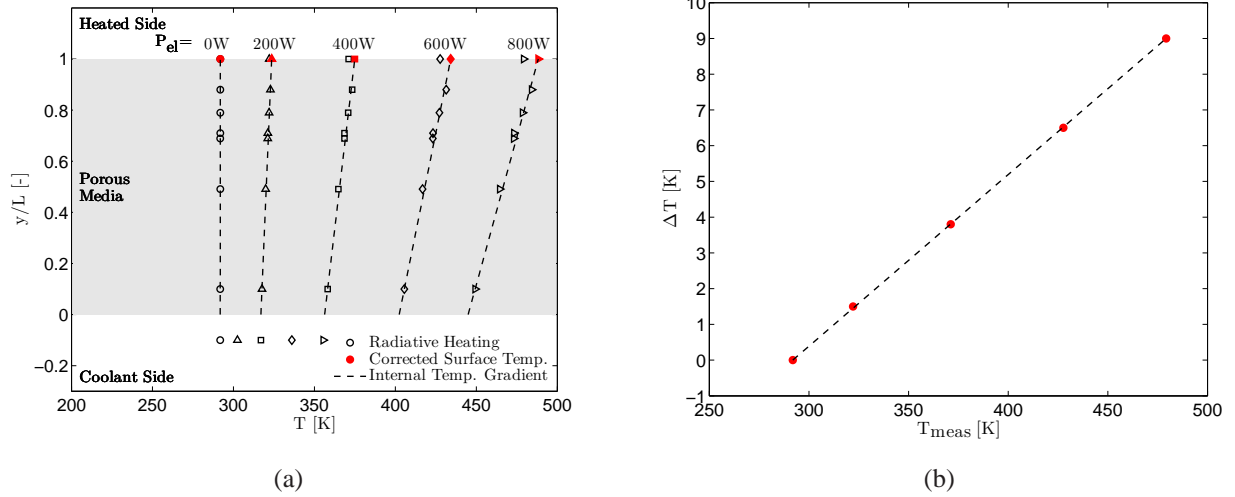


Figure 3: Radiative heating: (a) Internal temperature distribution w/o blowing; (b) Temperature correction characteristic

atures of up to 1173 K, which results in a nominal emitted heat flux of $80 \text{ kW}/\text{m}^2$. To separate the coolant exhalation from the hot surface of the IR-heater a sapphire window is installed in between. A schematic illustration of this second test facility is given in Fig. 2 (b). The coolant plenum, the sample integration concept as well as the complete measurement equipment are identical to the ones used at the hot gas test facility, ensuring a meaningful comparison of the collected data by the two test benches. Both facilities are operated with air as gaseous coolant.

Hot Gas Side Surface Temperature Correction

For radiative heating, the temperatures detected by the surface flush mounted TCs need to be corrected due to different absorption coefficients of C/C and nickel based metallic sheathed surface thermocouples at the heated side of the porous wall segment. Assuming the problem as one-dimensional with temperature independent material properties, the internal temperature distribution is linear for the cases without blowing according to Fourier's law. This assumption is affirmed by the good agreement with the measured internal temperatures of the C/C sample (Fig. 3 (a)). Based on that, the temperature gradient within the C/C is extrapolated to the heated side of the sample. Figure 3 (a) illustrates this procedure for varied power levels of the IR-heater. The unfilled black symbols indicate the TC measurements before the correction. The filled red symbols refer to the corrected surface temperatures based on an extrapolation of the internal temperature gradient. In Fig. 3 (b) the TC measured surface temperature T_{meas} is plotted versus the temperature difference ΔT , which needs to be considered due to the different absorption coefficients. The resulting correction characteristic appears to be linear for the considered temperature range. Since the established heat loads are pure radiative at the IR-heater test bench and existing differences are caused by different absorption coefficients, the application of this correction is also valid for the cases with blowing. However, the linear internal temperature distribution is not given any more when blowing is apparent. For those cases the heated side surface temperature is adjusted by an interpolation of the correction characteristic plotted in Fig. 3 (b), which is determined for the measurements without blowing at different temperature levels.

MODEL APPROACH

To reduce complexity, the investigated characteristics are determined considering the problem as one-dimensional. In this regard, the studies by Langener et al. [14, 15] have proven the validity of this assumption and form the basis of the following approaches. Figure 4 illustrates schematically the situation to be analysed. The *Coolant Side* refers to all parameters describing the coolant within the plenum. It is characterized by a certain temperature T_c , pressure p_c and coolant mass-flow \dot{m}_c . The *Heated Side* describes the aero-thermal situation at the sample where the heat load is apparent. Index h refers to the variables defining this location. In between the *Porous Media* is located. When dealing with porous structures two energy equations need to be solved, since a solid and a fluid phase need to be considered. Therefore, the dash-dotted red line schematically describes an internal temperature distribution $T_s(y)$ of the solid phase and the dashed blue line describes a possible temperature distribution $T_f(y)$ of the fluid phase.

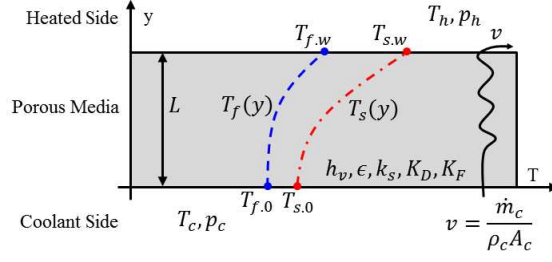


Figure 4: Schematic thermodynamic 1D situation of the C/C wall segment

Internal Temperature Distribution

To estimate the internal temperature distribution, the steady one-dimensional energy equations for actively cooled porous materials are solved. As preliminarily mentioned, the two phases of the porous problem require one energy equation for the solid phase and one the fluid phase. This set of coupled differential equations can be formulated as Eqn. (1) for the fluid phase and as Eqn. (2) for the solid phase (e.g. [16]).

$$-k_f \epsilon \frac{d^2 T_f}{dy^2} + \rho_f c_{p,f} v \frac{dT_f}{dy} = h_v (T_s - T_f) \quad (1)$$

$$-k_s (1 - \epsilon) \frac{d^2 T_s}{dy^2} = h_v (T_f - T_s) \quad (2)$$

Since the thermal conductivity of the fluid k_f is usually rather small, the first term on the left hand side of Eqn. (1) is neglected for the derived approaches. For porous materials, the thermal conductivity of the solid phase k_s needs to be corrected to also account for the fluid portion of the volume. This is achieved by the incorporation of the porosity in Eqn. (2) with $k_s (1 - \epsilon)$, which results in an effective thermal conductivity k_{eff} of the material compound (e.g [23]). These considerations lead to a further reduced formulation of the coupled energy equations as shown in Eqn. (3) for the fluid and in Eqn. (4) for the solid.

$$\rho_f c_{p,f} v \frac{dT_f}{dy} = h_v (T_s - T_f) \quad (3)$$

$$-k_{eff} \frac{d^2 T_s}{dy^2} = h_v (T_f - T_s) \quad (4)$$

The coupling of these differential equations takes place by the volumetric heat transfer coefficient h_v . This coefficient, or respectively it's combination with the temperature difference between solid and fluid phase, can be seen as source term in the energy equations, quantifying the internal heat transfer within the porous structure.

According to Weinbaum and Wheeler [5], substituting Eqn. (4) as well as it's differentiation with respect to y into Eqn. (3), results in a third order differential equation describing the solid temperature characteristic (Eqn. (5)).

$$\frac{d^3 T_s}{dy^3} + \frac{h_v}{\rho_f c_{p,f} v} \frac{d^2 T_s}{dy^2} - \frac{h_v}{k_{eff}} \frac{dT_s}{dy} = 0 \quad (5)$$

The general solution of this ordinary differential equation can be formulated as

$$T_s(y) = C_1 e^{\lambda_1 y} + C_2 e^{\lambda_2 y} + C_3 \quad (6)$$

with

$$\lambda_{1,2} = -\frac{h_v}{2\rho_f c_{p,f} v} \pm \sqrt{\left(\frac{h_v}{2\rho_f c_{p,f} v}\right)^2 + \frac{h_v}{k_{eff}}} \quad (7)$$

Differentiating twice and substituting the obtained temperature distribution $T_s(y)$ into Eqn. (4) determines the solution for the internal fluid temperature characteristic given in Eqn. (8) (e.g. [7]).

$$T_f(y) = C_1 \left(1 - \frac{\lambda_1^2 k_{eff}}{h_v}\right) e^{\lambda_1 y} + C_2 \left(1 - \frac{\lambda_2^2 k_{eff}}{h_v}\right) e^{\lambda_2 y} + C_3 \quad (8)$$

Here, C_1 , C_2 and C_3 of Eqn. (6) and Eqn. (8) are integration constants, which need to be determined by appropriate boundary conditions.

Boundary Conditions

At first instance and since these values are available as measured data, it was chosen to use temperature boundary conditions at the heated side ($y = L$) as well as at the coolant side ($y = 0$) of the porous specimen. The thermocouples detecting the temperatures at the C/C sample are assumed to measure the solid temperature at the respective location. In this respect, the boundary conditions to determine the three integration constants are given for the coolant side by

$$T_s|_{y=0} = T_b \quad \text{and} \quad T_f|_{y=0} = T_c, \quad (9)$$

where T_b represents the measured temperature directly at the coolant side of the C/C sample and T_c the measured temperature of the coolant within the plenum. The third boundary condition at $y = L$ is given by

$$T_s|_{y=L} = T_w, \quad (10)$$

where T_w refers to the measured surface temperature at the heated side of the C/C segment. A determination of the integration constants is achieved by an insertion of these boundary conditions in the derived solution for the internal temperature distribution of the solid (Eqn. (5)) as well as the fluid (Eqn. (8)) and can be written as

$$C_1 = \frac{T_w - T_b + (T_c - T_b) \frac{h_v}{k_{eff} \lambda_2^2} e^{\lambda_2 L} + (T_b - T_c) \frac{h_v}{k_{eff} \lambda_2^2}}{e^{\lambda_1 L} - \left(\frac{\lambda_1}{\lambda_2}\right)^2 e^{\lambda_2 L} + \left(\frac{\lambda_1}{\lambda_2}\right)^2 - 1}, \quad (11)$$

$$C_2 = \frac{(T_b - T_c) h_v}{k_{eff} \lambda_2^2} - C_1 \left(\frac{\lambda_1}{\lambda_2}\right)^2 \quad \text{and}$$

$$C_3 = T_b + (T_c - T_b) \frac{h_v}{k_{eff} \lambda_2^2} + C_1 \left[\left(\frac{\lambda_1}{\lambda_2}\right)^2 - 1 \right].$$

Volumetric Heat Transfer Coefficient

The quantification of the volumetric heat transfer coefficient is fairly hard to assess. There are some promising methods available (e.g. [24, 25]), which are quite difficult to be applied for the rather low porosity and homogeneous but highly irregular inner structure of C/C. For quantification, a segmentation of h_v in area specific heat transfer coefficient h and volume specific inner surface S is commonly used according to Eqn. (12) (e.g. [23]).

$$h_v = hS \quad \text{with} \quad S = \frac{A}{V} \quad (12)$$

Considering the large amount of micro dimensional interconnected cracks within C/C (Fig. 1 (c)), it becomes apparent that as a first guess, the specific inner surface can be assumed in the order of $S \approx 10^6 \text{ 1/m}$. Consequently, the volumetric heat transfer coefficient is estimated to $h_v > 10^6 \text{ W/m}^3\text{K}$. A precise determination of the volumetric heat transfer coefficient for C/C has been not possible. Therefore, the conducted studies are performed, using a constant volumetric heat transfer coefficient of $h_v = 10^6 \text{ W/m}^3\text{K}$. This assumption implies the rather coarse simplification of h_v being independent of the applied coolant mass flow.

Pressure Loss

To describe the pressure loss over the porous specimen, the Darcy-Forchheimer approach is usually applied as shown in Eqn. (13) (e.g. [18]).

$$\frac{dp}{dy} = - \left(\frac{\mu}{K_D} v + \frac{\rho}{K_F} v^2 \right) \quad (13)$$

To correctly describe the pressure loss for cases with heat loads, the Darcy-Forchheimer equation needs to be considered with temperature dependent fluid properties (e.g. [15]). This is done using a general power law formulation for the temperature dependent viscosity $\mu = \mu_{ref}(T/T_{ref})^n$ and in order to account for the temperature dependent density, by using the measured coolant mass flow $\dot{m}_c = \rho_c v A_c$ instead of the transpiration velocity v . These considerations and gaseous coolant, treated as ideal gas, result in a Darcy-Forchheimer formulation given by Eqn. (14).

$$p \frac{dp}{dy} = -R \left(\frac{1}{K_D} \frac{\dot{m}_c}{A_c} \frac{\mu_{ref}}{T_{ref}^n} T(y)^{n+1} + \frac{1}{K_F} \frac{\dot{m}_c^2}{A_c^2} T(y) \right) \quad (14)$$

The reference quantities of the general power law are taken from the NIST fluid property database REFPROP [26]. To estimate the temperature dependency of the coolant, the solution for the internal fluid temperature distribution $T_f(y)$ according to Eqn. (8) is considered.

RESULTS & DISCUSSION

Figure 5 illustrates the internal temperature distributions of the two investigated C/C species for different coolant mass flows. Figures 5 (a) and (c) describe the cases with aerodynamic heating and Fig. 5 (b) and (d) the ones with radiative heat loads. For the cases with radiative heating, the surface temperature correction is applied and the data of the four surface TCs are matched to one corrected temperature like it is described in the previous chapter. Sample 1 refers to C/C wall segments with perpendicular coolant through flows and sample 2 to segments with parallel through flow orientation. The respective material properties are given in Tab. 1. While no blowing is apparent, the heat fluxes are adjusted to establish heated side wall temperatures of $T_{w,0} \approx 500 \text{ K}$ for sample 1 and $T_{w,0} \approx 410 \text{ K}$ for sample 2. All temperatures are normalized by $T_{w,0}$, which is the highest temperature in the investigated system. Besides the experimental data, the solutions of the two energy equations are plotted. The dash-dotted red lines refer to the solution of the internal solid temperature and the dashed blue ones to the solutions of the fluid. These theoretical slopes are obtained by the application of temperature boundary conditions like it is described in the previous chapter. To maintain a clear arrangement of Fig. 5 the uncertainties are not plotted. Calculated according to the uncertainty analysis for single sample experiments suggested by Moffat [27], the normalized temperatures $T(y)/T_{w,0}$ are illustrated including an uncertainty of up to 0.5% and the TC positions y related to sample thickness L of up to 10%. The high uncertainty of the TC positions is based on a rather insecure installation accuracy of the TCs, which is conservatively assumed to be 1 mm.

A comparison of the general characteristics underlines the ability to create equivalent temperature distributions by the two test facilities. The lower temperature levels for the cases with blowing indicate lower net heat fluxes under radiative heating. A circumstance, which can be explained by not completely similar test conditions. Since the derived models address the general internal characteristics and are therefore not affected by the differing net heat fluxes, this issue can be seen as less relevant for the conducted studies.

For the parallel C/C species of sample 2 in Fig. 5 (c) and (d), a rather linear temperature distribution is measured for all blowing rates. The TC measurements of the perpendicular sample in Fig. 5 (a) and (b) identify a strong temperature gradient close to the heated side of the porous segment. For the cases with increased coolant mass flow this observation is even more pronounced. Since these characteristics are as well indicated by the derived solutions, for which the effective thermal conductivity is the only material connected parameter, this behaviour can be explained by the ten times higher thermal conductivity of the parallel C/C samples. Thermal non-equilibrium is indicated for the cases with low blowing rates at the coolant side and for higher coolant mass flows at the heated side of the porous sample. At the coolant side, the non-equilibrium is defined by the temperature boundary condition for the fluid. This temperature was chosen to be coolant temperature, which represents the extreme case of an adiabatic coolant side wall. At the heated side of the sample, the resulting differences between fluid and solid temperature are caused by the coupling of the describing energy equations and are quantified by the selected volumetric heat transfer coefficient.

In general it can be stated that the theoretical solutions are in good accordance with the measurements. However, significant deviations are apparent for temperatures measured by the internal TCs close to the coolant side of the C/C sample. Directly at the coolant side, measured temperatures and model approach are matching again, which is a boundary condition for the solutions of the coupled energy equations. Especially for the parallel material this offset is distinctive. The more homogeneous installation of the TCs over the material thickness intensifies this observation for the parallel specimen. Searching for physical reasons of this behaviour, the assumption of TCs exclusively detecting the solid temperature

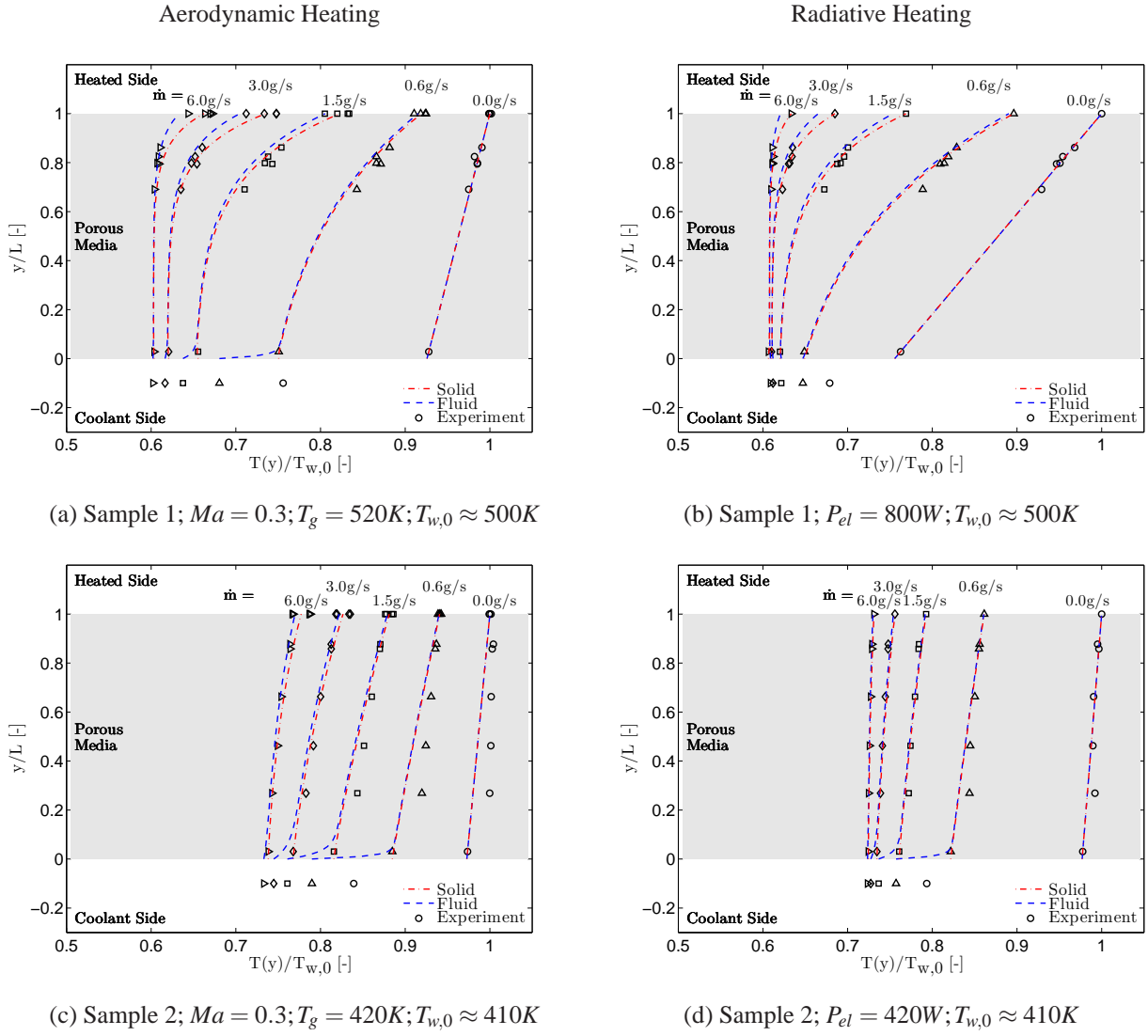


Figure 5: Internal temperature distributions

can be addressed. Even though the TCs are fixed with a carbon glue at their respective installation position, it cannot be ensured that the measuring tip of the TCs do not monitor fractions of fluid temperature. Although the investigated material is of quite low porosity, and therefore a possible detected fluid temperature portion of rather low influence, a consideration of this effect would lead to increased solid temperatures in the system. Following this approach, a suitable adjustment of the applied solid boundary conditions would shift the theoretical temperature distribution in the direction of measured values. As a second possible aspect in this regard, the consideration of the coolant side mounted TCs as surface increasing element can be named. The higher heat transferring surface would directly lead to locally augmented heat fluxes at the positions where the TCs exit the porous material. In order to cover as well for this possible effect, there would be a need to increase the coolant side temperature boundary condition of the solid. This adaptation would again result in a better match of model approach and experimental data. In this respect, further studies need to be conducted to clarify the thermo-physical situation at this location.

To describe the pressure losses of the investigated materials under heat loads, the solutions of the fluid temperature distributions $T_f(y)$ is used to account for the temperature dependency of the Darcy-Forchheimer approach. Details of this model assumption are given in the previous chapter. The comparison of this approach with the experimental data is illustrated in Fig. 6. All sub-plots of Fig. 6 refer to the respective temperature characteristic pictured in Fig. 5. Again, Fig. (a) and (c) describe the situation for aerodynamic heat loads and Fig. (b) and (d) refer to data measured at the radiative test bench. The pressure drops Δp are normalized by the sample thickness L and are plotted versus the transpiration velocity

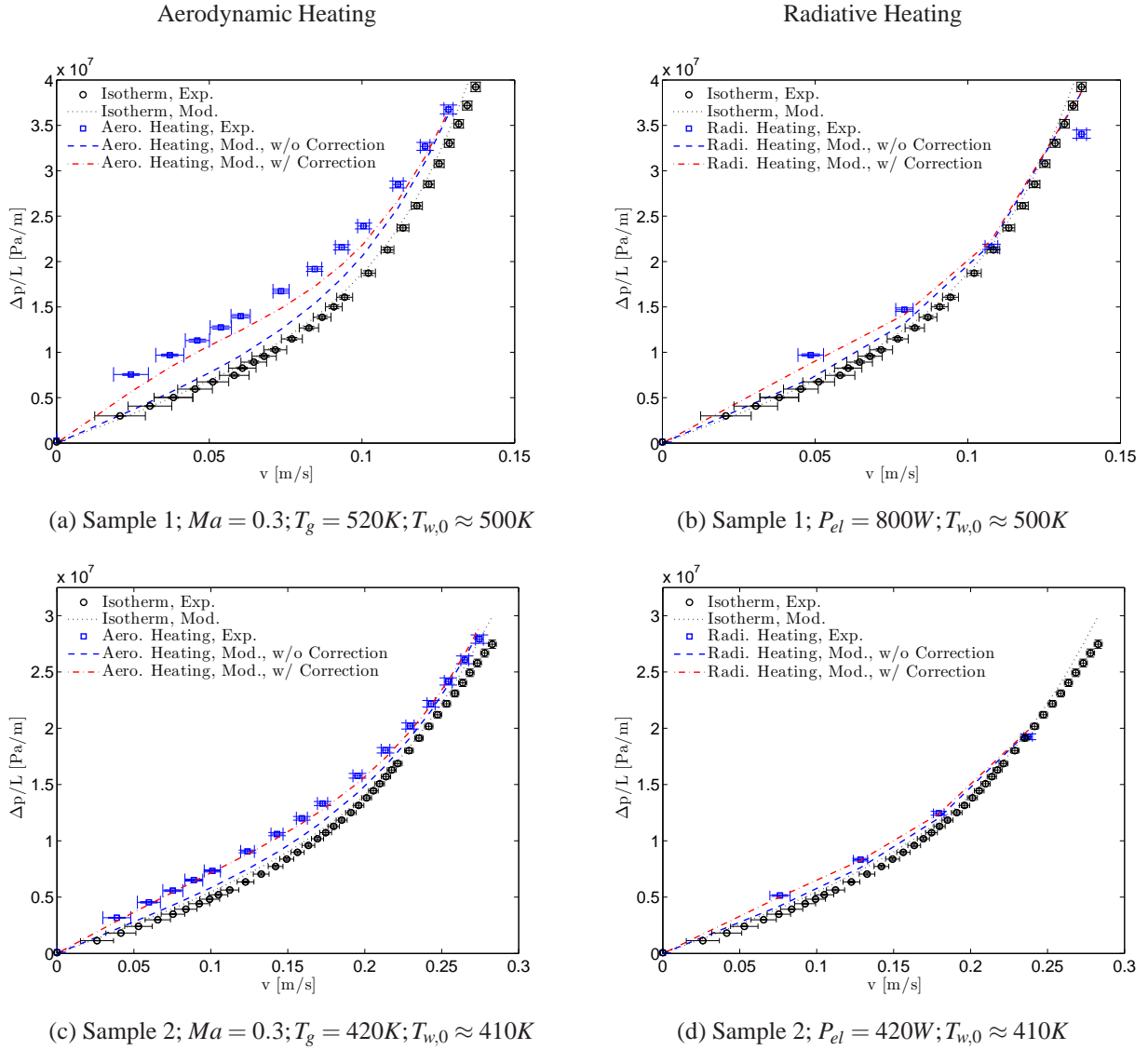


Figure 6: Pressure loss characteristics

$v = \dot{m}_c / (\rho_c A_c)$. For small transpiration velocities, the measurement uncertainty ranges up to 40% due to a low accuracy of the mass flow controller in the lower blowing regime. The uncertainty of the normalized pressure loss $\Delta p/L$ is limited to a maximum of 1.5%. The measurement uncertainties are calculated according to [27]. For all diagrams, experimental data are plotted as symbols and model approaches are given as lines. The blue dashed lines refer to solutions of the Darcy-Forchheimer formulation without temperature dependency and the dash-dotted red ones to the derived approach according to Eqn. (14). To underline the pressure loss augmentation caused by heat loads, isothermal (without heating) data are additionally illustrated as black symbols and dotted lines.

Information of Fig. 6 (b) is uncertain due to a leakage at the coolant plenum during the measurements under radiative heating. Retrospectively, this issue questions as well the internal temperature distribution of the same case given in Fig. 5 (b). For an isolated consideration of the internal temperature the leakage is not noticeable. This circumstance underlines the need to consider internal temperature as well as pressure loss characteristics simultaneously for a proper study of the porous material behaviour.

All other figures demonstrate the general feasibility of the derived model to account for heat load induced pressure losses for active through flows. Although the applied radiative net heat fluxes, and therefore also the increased pressure losses, are smaller than those of the aerodynamically heated cases, the proper match between model and experiment proves the comparability of the two test facilities as well for the pressure loss characteristics. Noticeable deviations between model and experiment are apparent for the aerodynamically heated perpendicular C/C sample in Fig. 6 (a). With respect to the

experimental values of this case, the theoretical approach predicts slightly lower pressure losses. Considering the indications above discussed for increased coolant side solid temperatures and adopting these on the pressure loss would again result in a better fit of theoretical and experimental data.

CONCLUSIONS

In this study, transpiration cooling applied to two species of porous C/C has been investigated. To describe the aero-thermal behaviour of this certain material, internal temperature distribution and pressure loss under heat load were chosen for characterization. The applied head loads were adjusted to the order of several kW/m^2 by two independent test facilities, establishing heated side surface temperatures of up to 500 K for the cases without blowing. Experimental data were collected for different coolant mass flows under aerodynamic or radiative heating and compared to analytical models. To theoretically describe the internal temperature distributions of the porous material, the coupled set of energy equations for fluid and solid phase were solved using temperature boundary conditions and tolerating thermal non-equilibrium. Pressure loss was modelled using a modified Darcy-Forchheimer equation, considering temperature dependent coolant properties to account for increased pressure losses under head load. To determine these temperature related parameters, the solution for the internal fluid temperature distribution was utilized. Both approaches consider the investigated problem as one-dimensional.

In general it can be stated that the theoretical models are in good agreement with the experimental data and independent of the applied heat source. In this regard, a closed model-based description for the aero-thermal behaviour of actively cooled C/C becomes feasible by the application of the derived fluid temperature solution, accounting for the increased pressure loss under heat load.

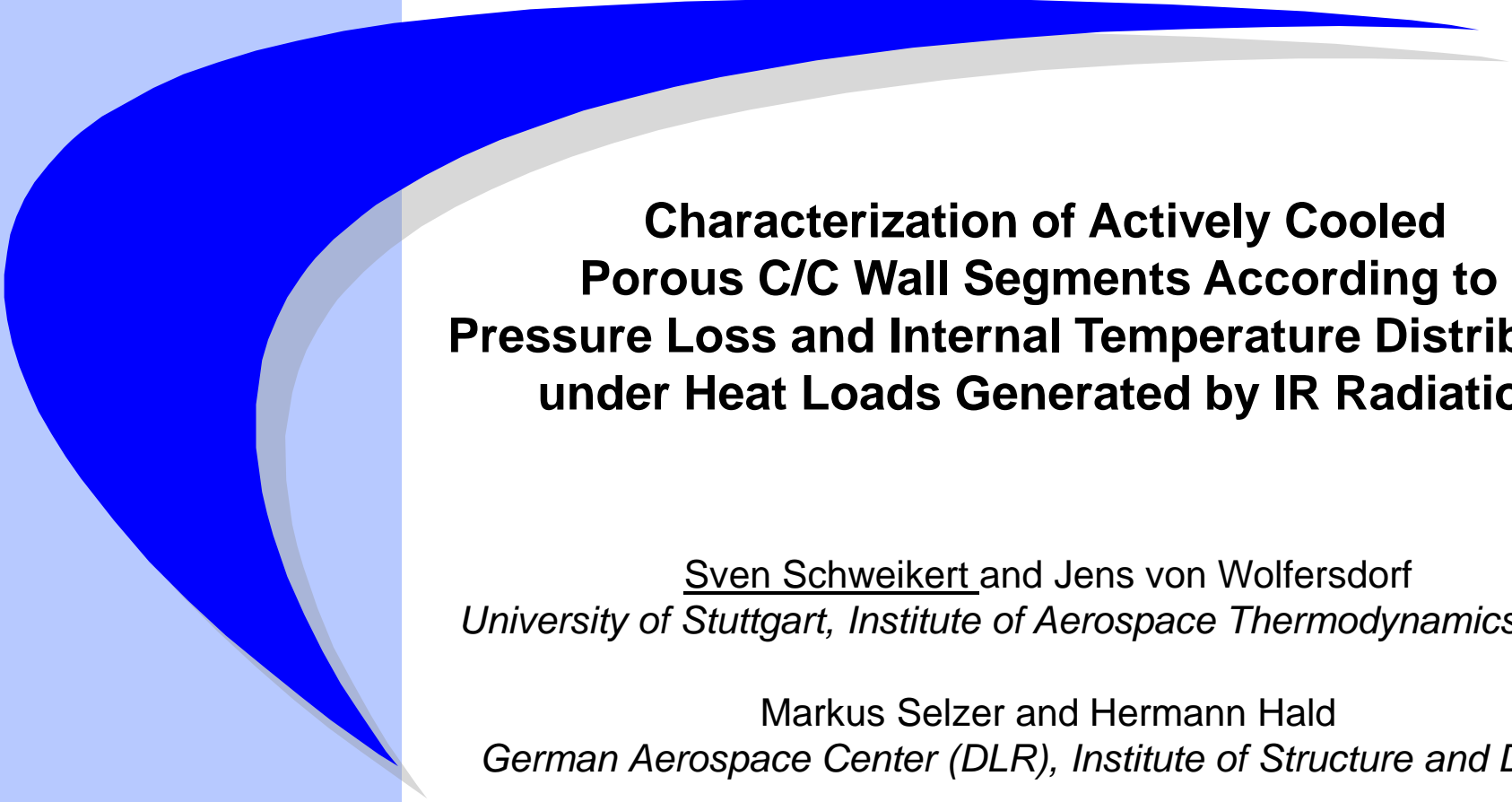
ACKNOWLEDGEMENTS

The present work has been carried out under financial support by the HGF-Allianz DLR@UniST and by the German Research Foundation in the framework of the Collaborative Research Centre Transregio 40. We would like to acknowledge this support gratefully.

REFERENCES

- [1] A. Herbertz, M. Ortelt, I. Müller and H. Hald, "A Transpiration-Cooled Ceramic Thrust Chamber Applicability for High-Thrust Rocket Engines", *48th Joint Propulsion Conference*, Atlanta, USA, 2012.
- [2] H. Böhrk, V. Wartemann, T. Eggers, J. M. Schramm, A. Wagner and K. Hannemann, "Shock Tube Testing of the Transpiration-Cooled Heat Shield Experiment AKTiV", *18th AIAA/3AF International Space Planes and Hypersonic Systems and technologies Conference*, Tours, France, 2012.
- [3] M. Kuhn, H. Hald, A. Gülhan, B. Esser and H. Olivier, "Experimental Investigation of Transpiration Cooled CMC's in Supersonic Plasma Flows", *Proceedings of the 5th European Workshop on Thermal Protection Systems and Hot Structures*, Noordwijk, The Netherlands, 2006.
- [4] H. Weihs, "SHEFEX II - 2nd Flight within DLR's Re-Entry Technology and Flight Test Program", *18th AIAA/3AF International Space Planes and Hypersonic Systems and technologies Conference*, Tours, France, 2012, oral presentation.
- [5] S. Weinbaum and H. L. Wheeler, Jr., "Heat Transfer in Sweat-Cooled Porous Metals", *Journal of Applied Physics*, 20, 1949, pp. 113-122.
- [6] N. Elsner, "Wärmedurchgang durch poröse Körper bei gleichzeitigem Stoffdurchsatz", *Wissenschaftlich Zeitschrift der HfV Dresden* 3, Nr.2, 1955, p. 129-157.
- [7] R. S. Colladay and F. S. Stepka, "Examination of Boundary Conditions for Heat Transfer Through a Porous Wall", *NASA Technical Note*, D-6405, 1971.
- [8] M. R. L'Ecuyer and R. S. Colladay, "Influence of Porous-Wall Thermal Effectiveness on Turbulent-Boundary-Layer Heat Transfer", *NASA Technical Note*, D-6837, 1972.

- [9] E. R. G. Eckert and N. B. Livingood, "Comparison of Effectiveness of Convection-, Transpiration- and Film-Cooling Methods with Air as Coolant", *NACA Technical Report*, 1182, 1954.
- [10] E. Mayer and J. G. Bartas, "Transpiration Cooling in Porous Metals Walls", *Jet Propulsion*, 1953, p. 366-368.
- [11] J. Meinert, "Haftreibung und Wärmeübergang in einer turbulenten Grenzschicht bei Fremdgasstranspiration", *Fortschritt-Berichte VDI, Reihe 7: Strömungstechnik*, Nr. 402, 2000.
- [12] H. Hald, A. Herbertz, M. Kuhn and M. Ortelt, "Technological Aspects of Transpiration Cooled Composite Structures for Thrust Chamber Application", *16th AIAA/DLR/DGLR International Space Planes and Hypersonic Systems and Technologies Conference*, Bremen, Germany, 2009.
- [13] A. Herbertz and M. Selzer, "Analysis of Coolant Mass Flow Requirements for Transpiration Cooled Ceramic Thrust Chambers", *29th International Symposium on Space Technology and Science*, Nagoya, Japan, 2013, in press.
- [14] T. Langener, J. von Wolfersdorf, M. Selzer and H. Hald, "Experimental investigations of transpiration cooling applied to C/C material", *International Journal of Thermal Sciences*, 54, 2012, pp. 70-81.
- [15] T. Langener, J. von Wolfersdorf, and J. Steelant, "Experimental Investigations on Transpiration Cooling for Scramjet Applications Using Different Coolants", *AIAA Journal*, 49, 2011, pp. 1409-1419.
- [16] J. von Wolfersdorf, "Effect Of Coolant Side Heat Transfer on Transpiration Cooling", *Heat Mass Transfer*, 41, 2005, pp. 327-337.
- [17] H. Darcy, "Les Fontaines Publiques de la Ville de Dijon", 1856, Paris: Victor Dalmont.
- [18] D. Nield and A. Bejan, "Convection in Porous Media", 3rd ed., 2006, Springer, Berlin.
- [19] N. Gascoïn, "High Temperature and Pressure Reactive Flows Through Porous Media", *International Journal of Multiphase Flow*, 37, 2011, pp. 24-35.
- [20] M. Selzer, T. Langener, H. Hald and J. von Wolfersdorf, "Production and Characterization of Porous C/C Material", *Collaborative Research Centre, SFB/TRR40*, annual report, 2009.
- [21] T. Langener, J. von Wolfersdorf, T. Laux and J. Steelant, "Experimental Investigation of Transpiration Cooling with Subsonic and Supersonic Flows at Moderate Temperature Levels", *44th AIAA/ASME/SAE/ASEE Joint Propulsion Conference and Exhibit*, Hartford, USA, 2008.
- [22] T. Scheuermann, J. Chun and J. von Wolfersdorf, "Experimental Investigation of Scramjet Combustor Characteristics", *15th AIAA/DLR/DGLR International Space Planes and Hypersonic Systems and Technologies Conference*, Dayton, USA, 2008.
- [23] D. A. S. Rees and I. Pop, "Local Thermal Non-Equilibrium in porous Medium Convection", *Transport Phenomena in Porous Media*, 3, 2005, pp. 147-173
- [24] B. Mayer, H. Gomma, B. Weigand and Y. B. Zudin, "An Analytical Model to Evaluate Heat Transfer Characteristics in Porous Media by a Periodic Quasi Steady-State Technique", *International Symposium on Transport Phenomena and Dynamics of Rotating Machinery*, 14, Honolulu, USA, 2012.
- [25] T. Jeng, M. Wang, G. Hwang and Y. Hung, "A Semi-Empirical Model for Predicting Heat Transfer Characteristics in Porous Channels", *Experimental Thermal and Fluid Science*, 29, 2004, pp. 9-21.
- [26] E. Lemmon, M. Huber and M. McLinden, "REFPROP - Reference Fluid Thermodynamic and Transport Properties", *NIST Standard Reference Database*, 23, 2007, Version 8.0.
- [27] R. Moffat, "Describing the Uncertainties in Experimental Results", *Experimental Thermal and Fluid Science*, 1, 1988, pp. 3-17.



**Characterization of Actively Cooled
Porous C/C Wall Segments According to
Pressure Loss and Internal Temperature Distribution
under Heat Loads Generated by IR Radiation**

Sven Schweikert and Jens von Wolfersdorf
University of Stuttgart, Institute of Aerospace Thermodynamics (ITLR)

Markus Selzer and Hermann Hald
German Aerospace Center (DLR), Institute of Structure and Design



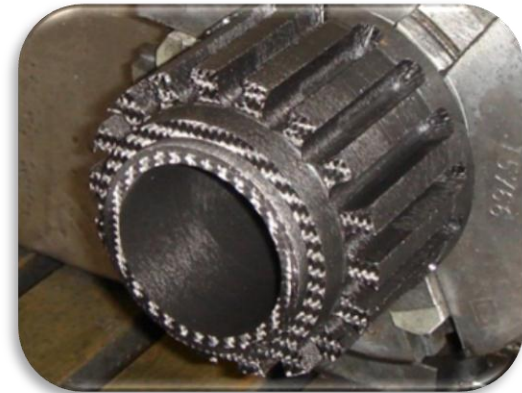
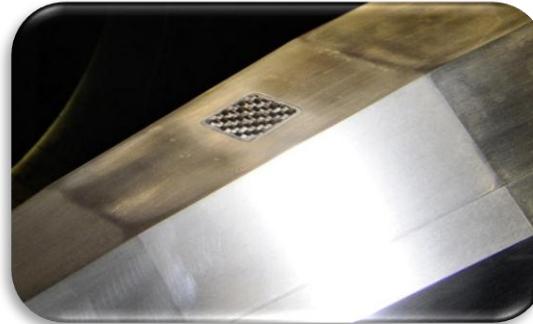
DLR's idea of transpiration cooling applied to porous high temperature fiber ceramics demonstrated as promising cooling

DLR's technology demonstrators:

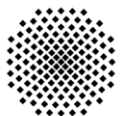
- SHEFEX II (AKTiV)
- KERBEROS

Expensive testing e.g.:

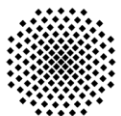
- Flight experiments
- Ground testing
- Plasma & shock wind tunnel



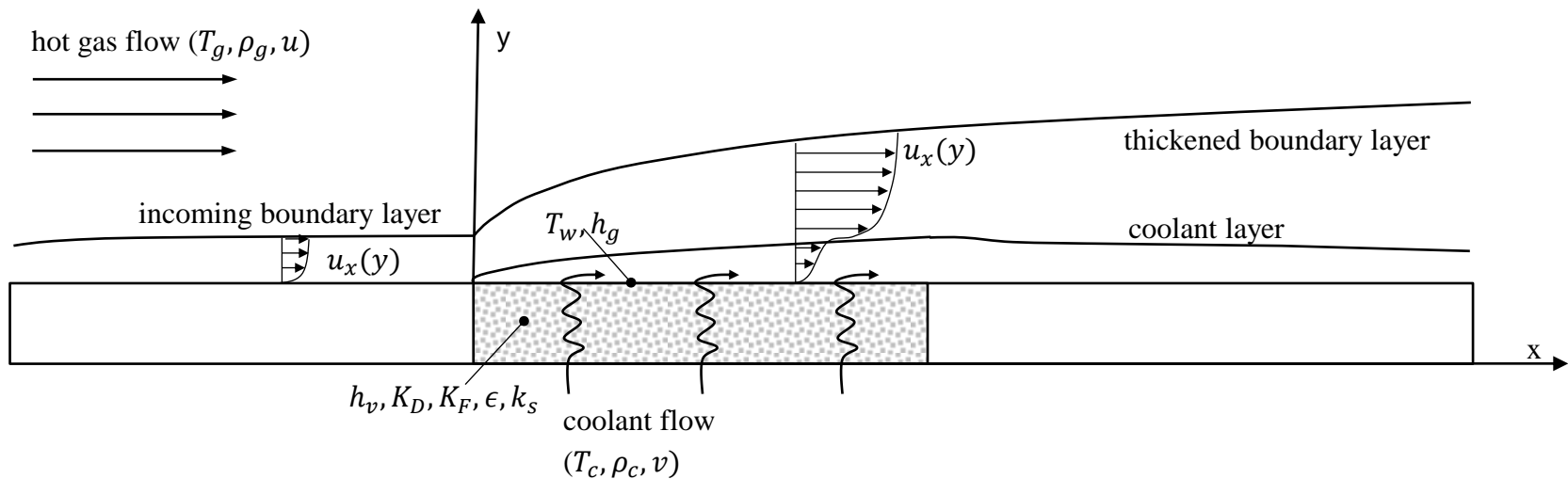
<http://www.dlr.de>



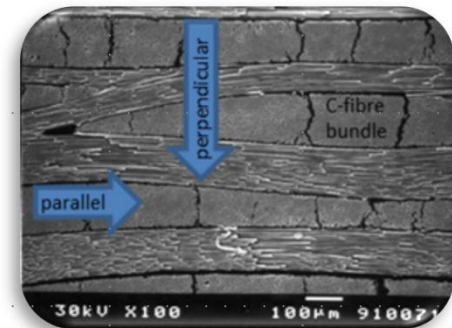
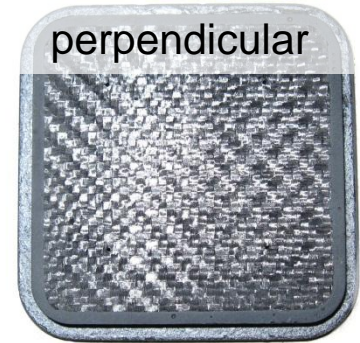
- Transpiration Cooling
- Investigated Material
- Test Facilities and Experimental Setup
- Internal Temperature Distribution
- Pressure Loss under Head Load



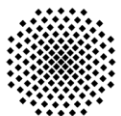
- Effective active cooling technique
- Internal mechanism – huge heat transferring surface
- External mechanism – coolant injection into boundary layer
- Continuously refreshed coolant layer

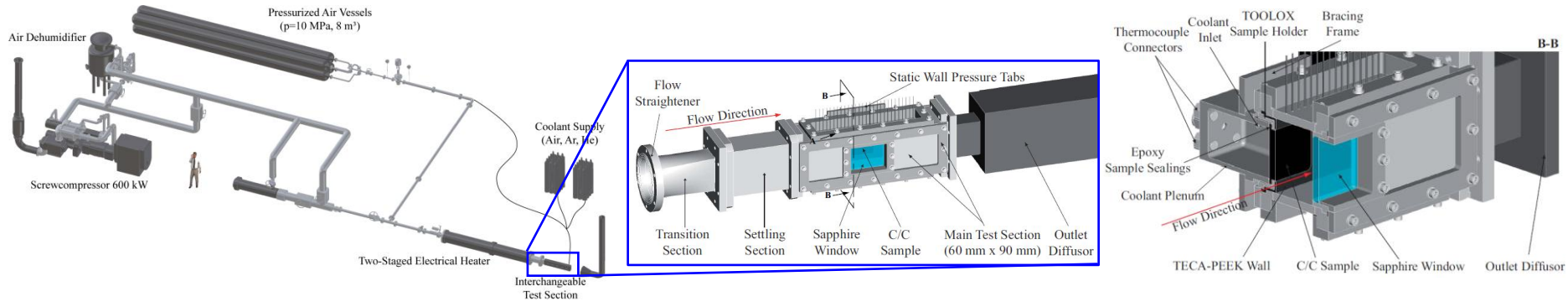


- ☞ Porous high temperature fiber ceramic (CMC) – C/C
- ☞ Invented and manufactured at DLR's IBK
- ☞ Reference material for transpiration cooled CMC concepts
- ☞ Definable material characteristics
 - Porosity
 - Permeability
 - Thermal conductivity



		Sample 2	Sample 4
Flow Orientation		perpendicular	parallel
Porosity	ϵ	12.4%	11,1%
Permeability	K_D	$1.448 \cdot 10^{-13} \text{m}^2$	$3.571 \cdot 10^{-13} \text{m}^2$
	K_F	$1.074 \cdot 10^{-8} \text{m}$	$5.165 \cdot 10^{-8} \text{m}$
Conductivity	k_S	1.4W/mK	13.5W/mK



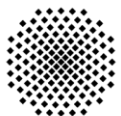
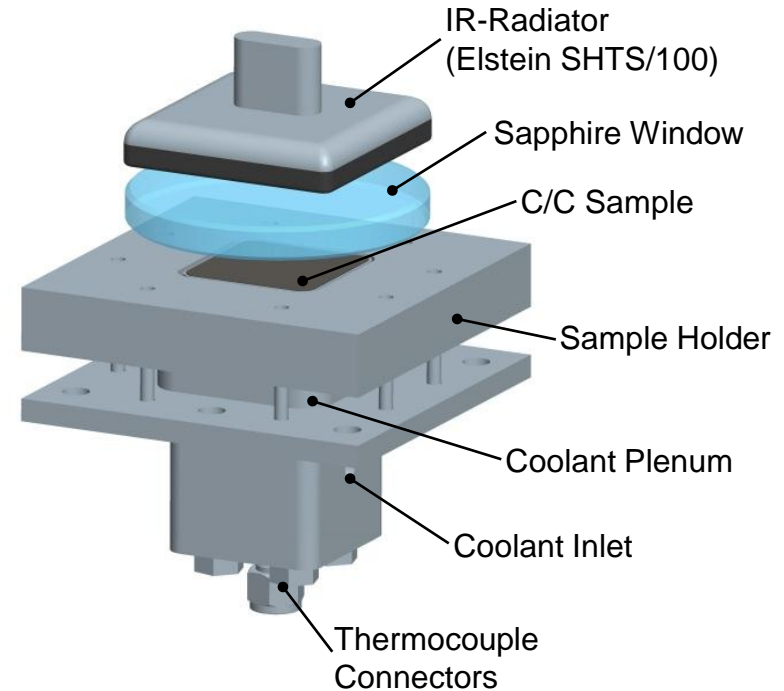


ITLR's hot gas test facility

- \dot{m}_g : 0.4 kg/s to 0.9 kg/s
- T_g : 360 K to 520 K
- M : 0.2 to 0.5

ITLR's IR-radiation test facility

- P_{el} : up to 800 W
- \dot{q}_{rad} : up to $\sim 80 \text{ kW/m}^2$



Temperature:

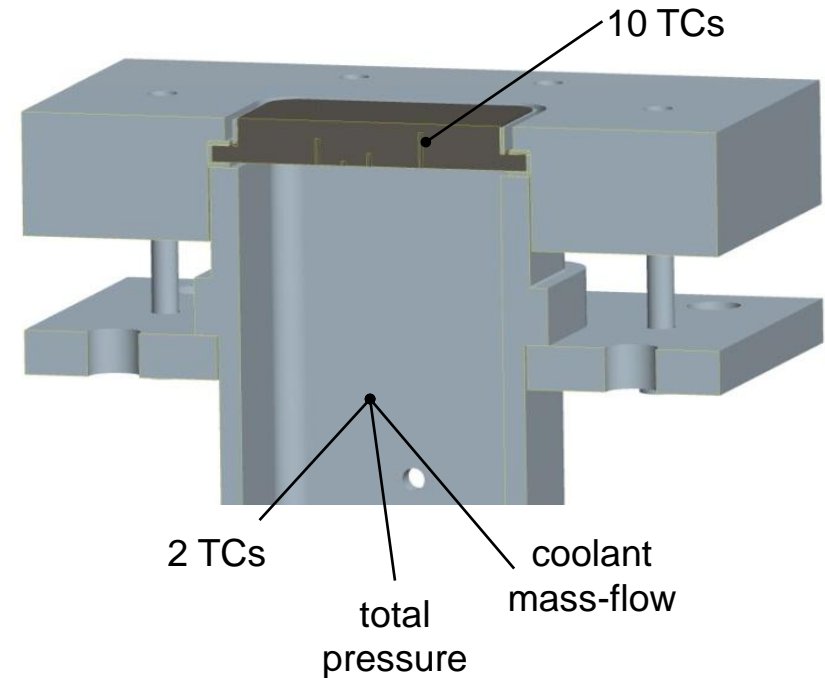
- 3 TCs for hot gas
- 2 TCs for coolant
- 10 TCs within the C/C sample

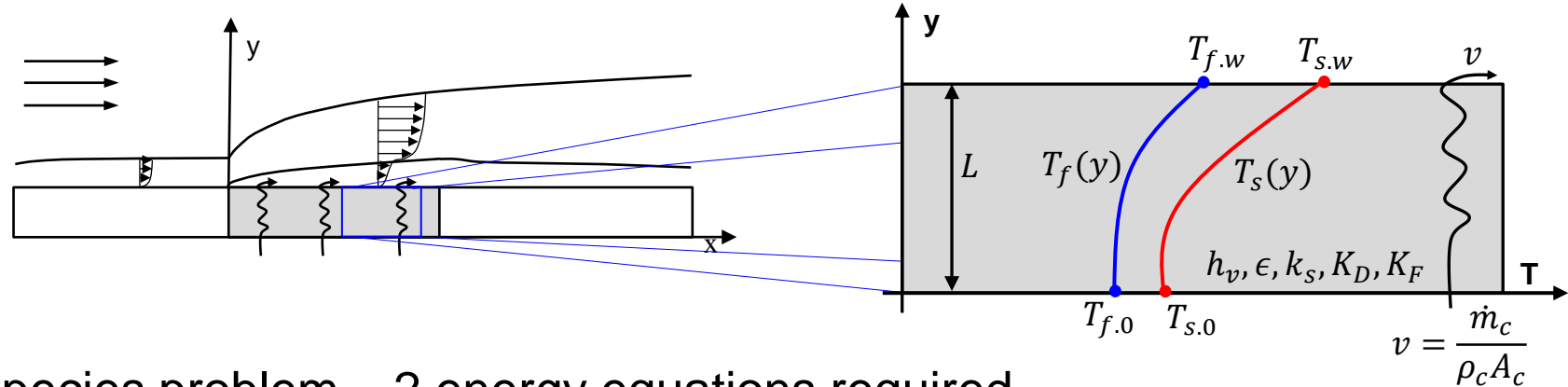
Pressure:

- Static pressure on heated side
- Total pressure on coolant side

Mass-flow:

- Vortex meter for hot gas
- Thermal mass-flow controller for coolant





2 species problem – 2 energy equations required

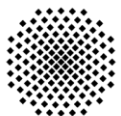
- Solid: $k_s(1 - \epsilon) \frac{d^2 T_s}{dy^2} = h_v(T_s - T_f)$
- Fluid: $\rho_c c_{p,c} v \frac{dT_s}{dy} = h_v(T_s - T_f)$

3 integration constants need to be determined by BCs

Chosen BCs:

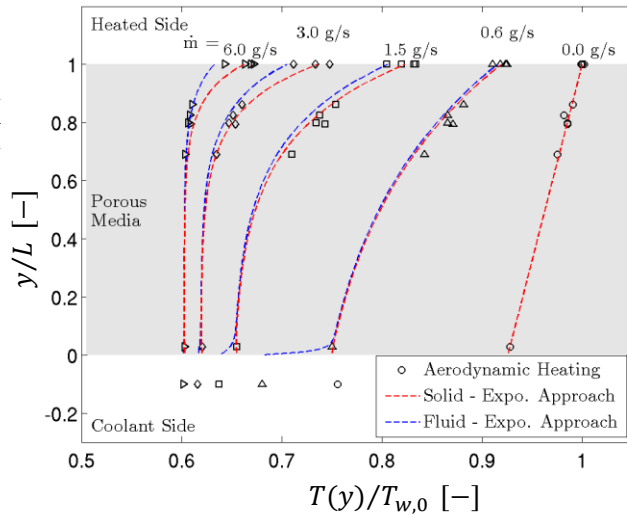
- Coolant side: $T_s|_{y=0} = T_b$ and $T_f|_{y=0} = T_c$
- Heated side: $T_s|_{y=L} = T_w$

$h_v = 10^6 \text{ W/m}^3 \text{ K}$
const. for all cases

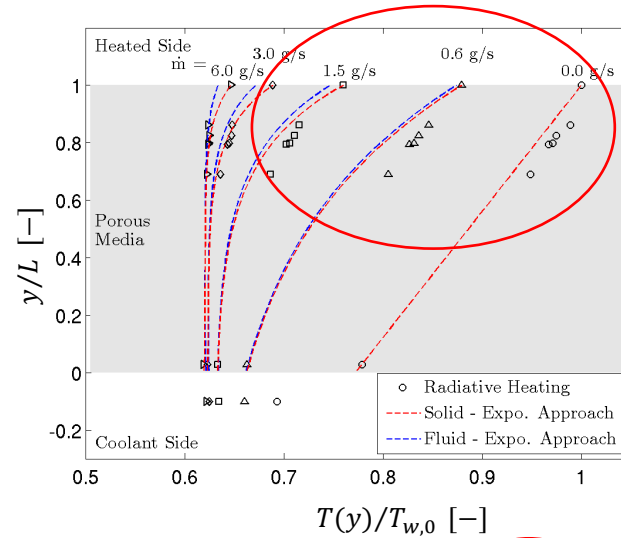


Internal Temperature Distribution

Sample 2
 $M = 0.3$
 $T_g = 520K$
 $T_{w,0} \sim 500K$



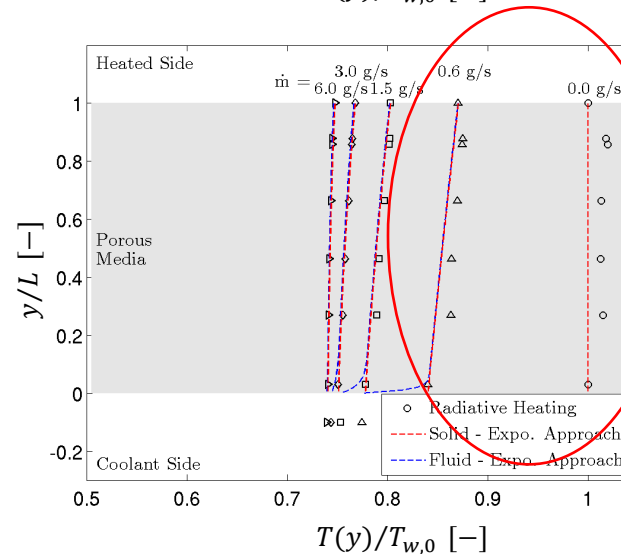
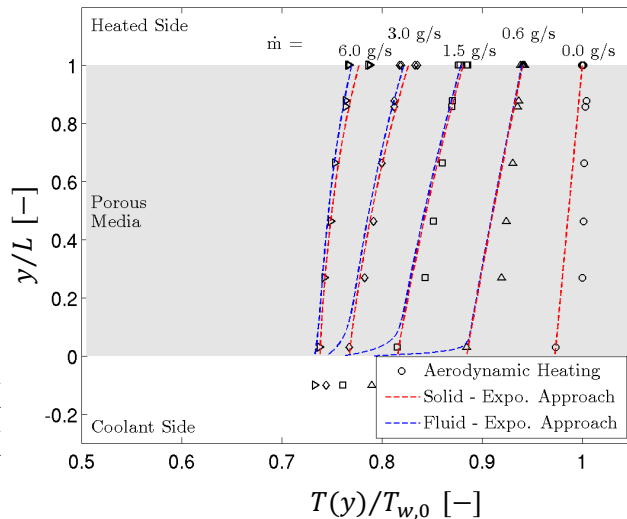
Sample 2
 $P_{el} = 800W$
 $T_{w,0} \sim 500K$



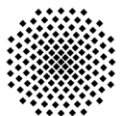
Radiative Heating

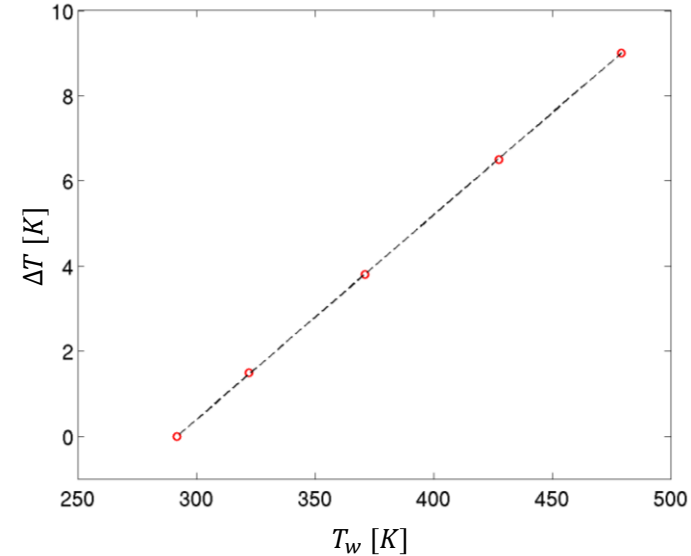
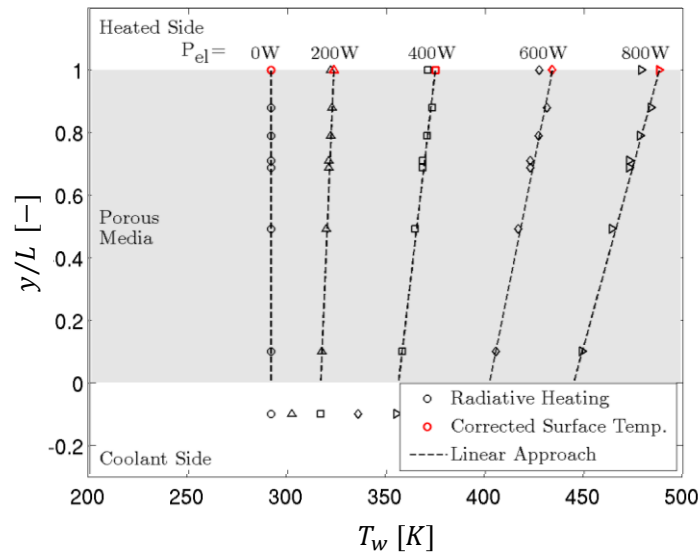
Aerodynamic Heating

Sample 4
 $M = 0.3$
 $T_g = 420K$
 $T_{w,0} \sim 410K$

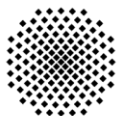


Sample 4
 $P_{el} = 415W$
 $T_{w,0} \sim 410K$





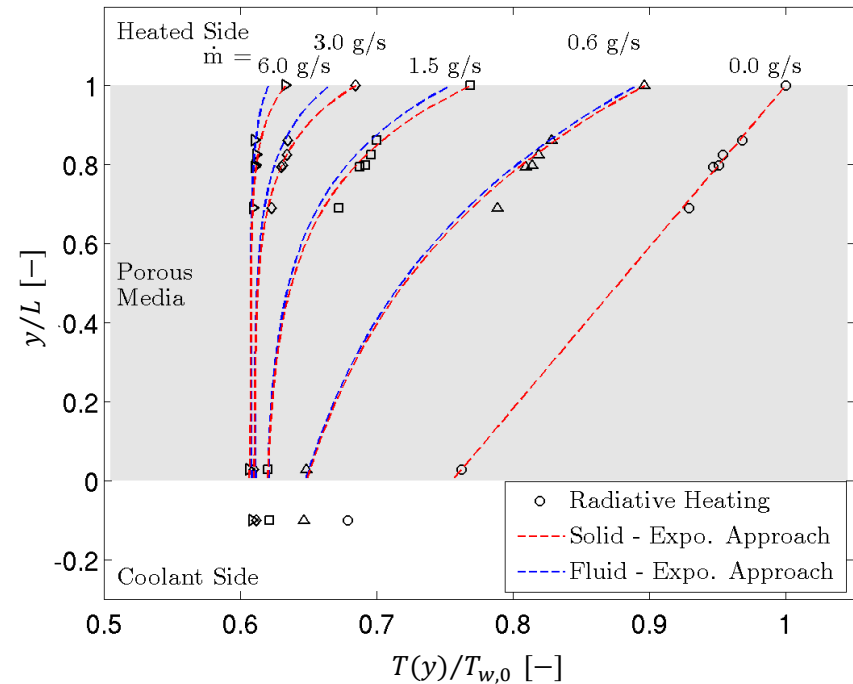
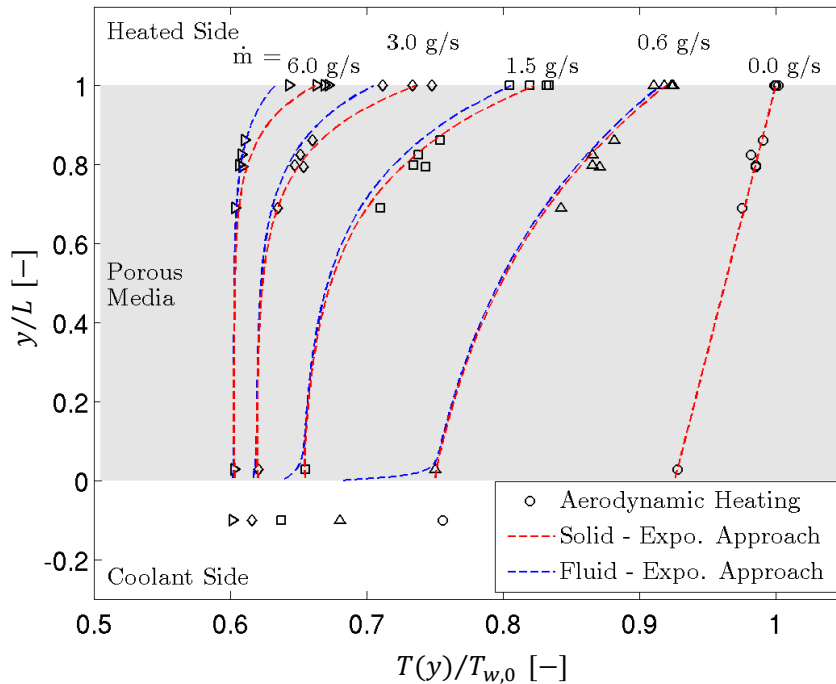
- Absorption coefficients: $\alpha_{C/C} > \alpha_{TC}$
- According to Fourier: linear internal temperature distribution w/o blowing
- Extrapolation of internal temperature gradient:
 - $$-k_s \left. \frac{dT_s}{dy} \right|_{0 < \frac{y}{L} < 1} = -k_s \left. \frac{dT_s}{dy} \right|_{\frac{y}{L} = 1}$$
- Surface temperature correction without blowing



Sample 2

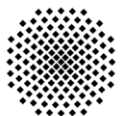
Aerodynamic Heating:
 $M = 0.3$; $T_g = 520\text{K}$; $T_{w,0} \sim 500\text{K}$

Radiative Heating:
 $P_{el} = 800\text{W}$; $T_{w,0} \sim 500\text{K}$



Coolant side: $T_s|_{y=0} = T_b$ and $T_f|_{y=0} = T_c$

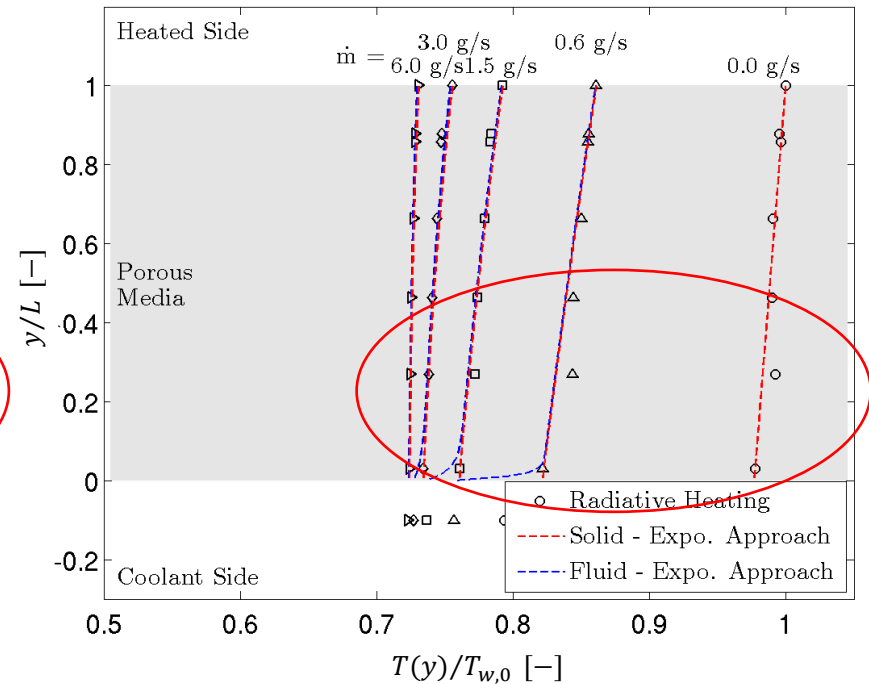
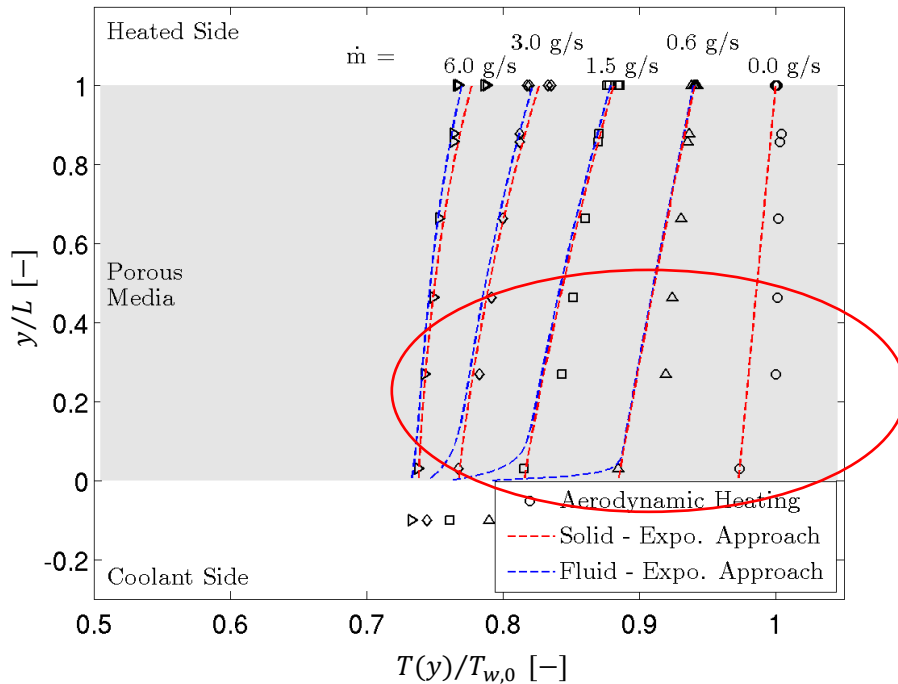
Heated side: $T_s|_{y=L} = T_w$ (+ ΔT if heated by radiation)



Sample 4

Aerodynamic Heating:
 $M = 0.3$; $T_g = 420\text{K}$; $T_{w,0} \sim 410\text{K}$

Radiative Heating:
 $P_{el} = 415\text{W}$; $T_{w,0} \sim 410\text{K}$



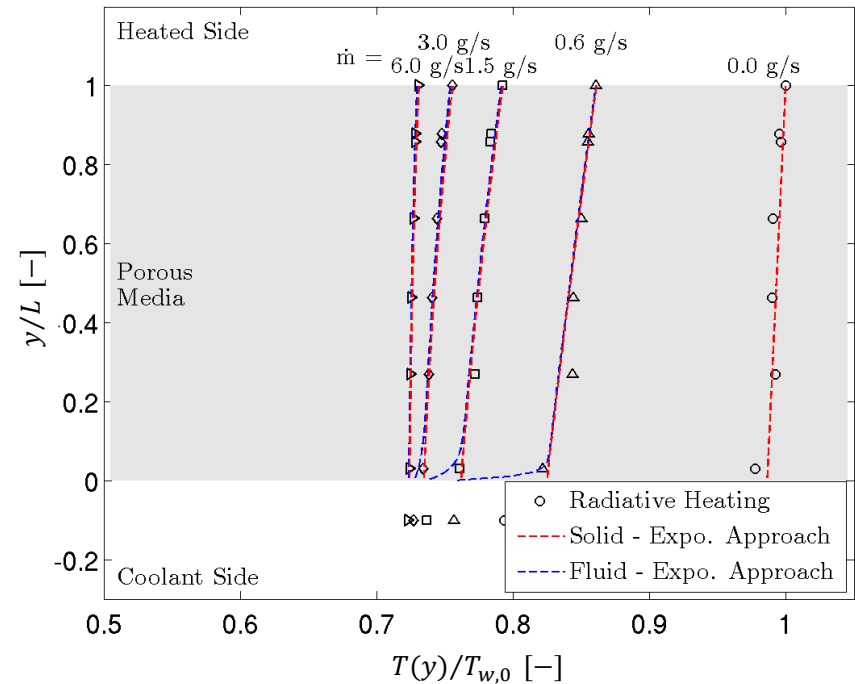
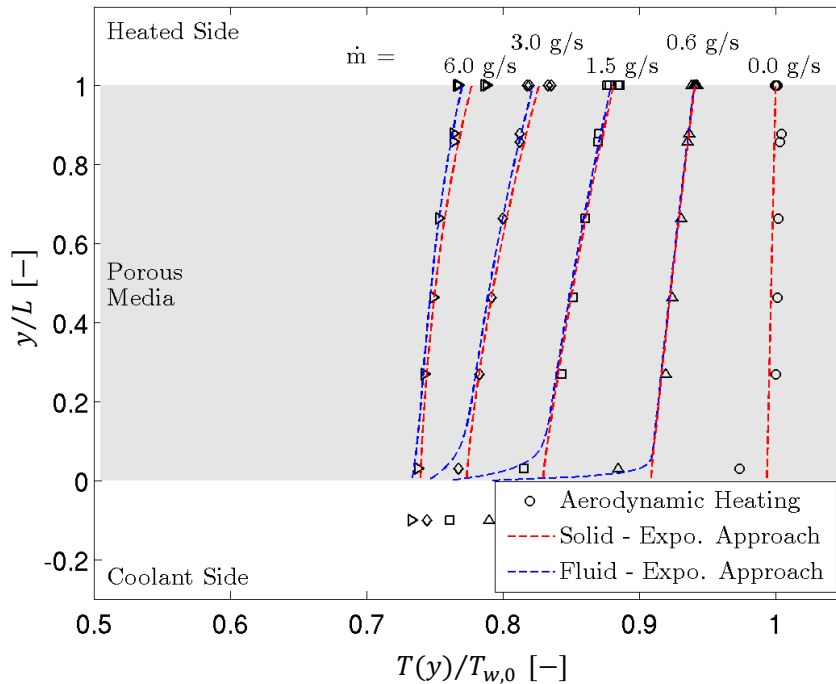
Coolant side: $T_s|_{y=0} = T_b$ and $T_f|_{y=0} = T_c$

Heated side: $T_s|_{y=L} = T_w$ (+ ΔT if heated by radiation)

Sample 4

Aerodynamic Heating:
 $M = 0.3$; $T_g = 420\text{K}$; $T_{w,0} \sim 410\text{K}$

Radiative Heating:
 $P_{el} = 415\text{W}$; $T_{w,0} \sim 410\text{K}$



Coolant side: $T_s|_{y=0} > T_b$ and $T_f|_{y=0} = T_c$

Heated side: $T_s|_{y=L} = T_w$ (+ ΔT if heated by radiation)

'Pin Fin' characteristic of TC at coolant side or detection of T_s and T_f mixture

Darcy-Forchheimer

- $$\frac{dp}{dy} = - \left(\frac{\mu}{K_D} v + \frac{\rho}{K_F} v^2 \right)$$

Temperature dependent coolant properties

- $\mu(T)$ and $\rho(T)$

Considering these in Darcy-Forchheimer

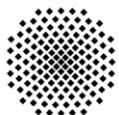
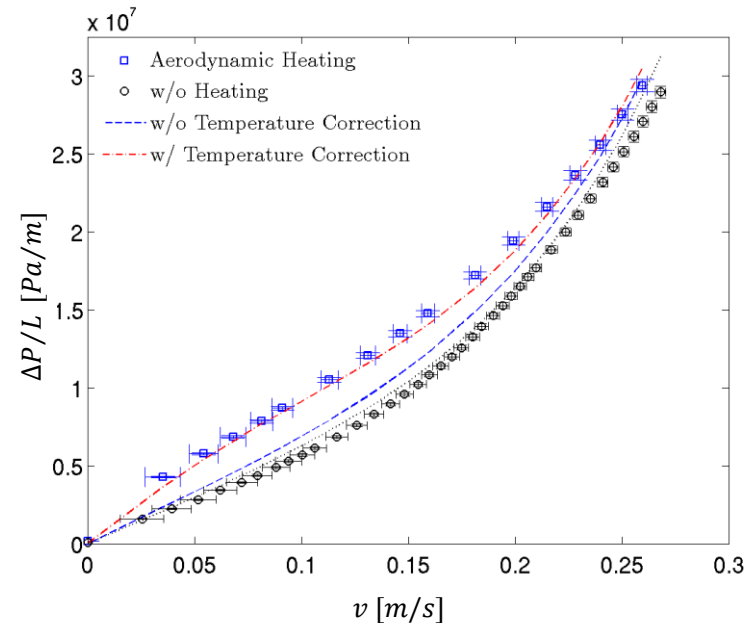
- $$p \frac{dp}{dy} = -R \left(\frac{\mu(T) \dot{m} T}{K_D A} + \frac{1}{K_F} \frac{\dot{m}^2 T}{A^2} \right)$$

Sutherland for $\mu(T)$

- $$p \frac{dp}{dy} = -R \left(\frac{1}{K_D} \frac{\dot{m} \mu_{ref}}{A T_{ref}} T(y)^{n+1} + \frac{1}{K_F} \frac{\dot{m}^2}{A^2} T(y) \right)$$

Application of model for internal fluid temperature distribution

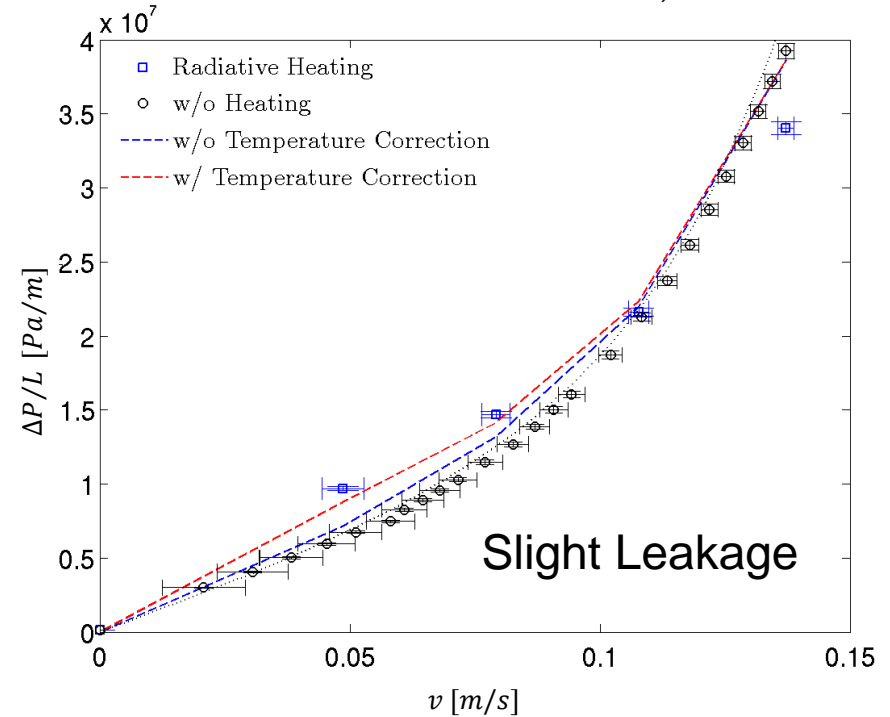
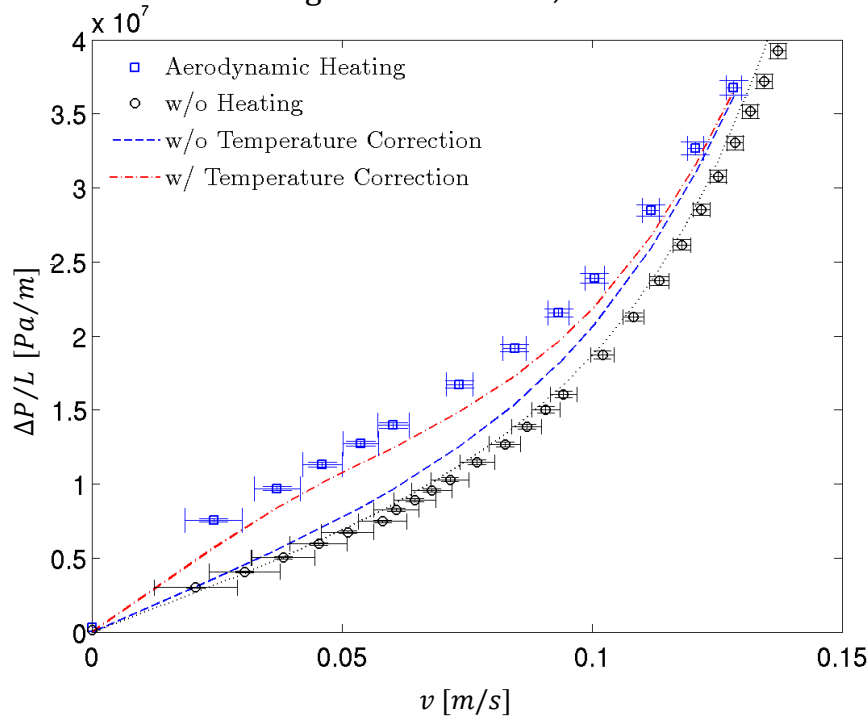
- $$T(y) = T_f(y) = C_1 \left(1 - \frac{k_s \lambda_1^2}{h_v} \right) e^{\lambda_1 y} + C_2 \left(1 - \frac{k_s \lambda_2^2}{h_v} \right) e^{\lambda_2 y} + C_3$$



Sample 2

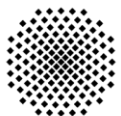
Aerodynamic Heating:
 $M = 0.3$; $T_g = 520\text{K}$; $T_{w,0} \sim 500\text{K}$

Radiative Heating:
 $P_{el} = 800\text{W}$; $T_{w,0} \sim 500\text{K}$



Temperature dependent coolant properties adapted by $T(y) = T_f(y)$

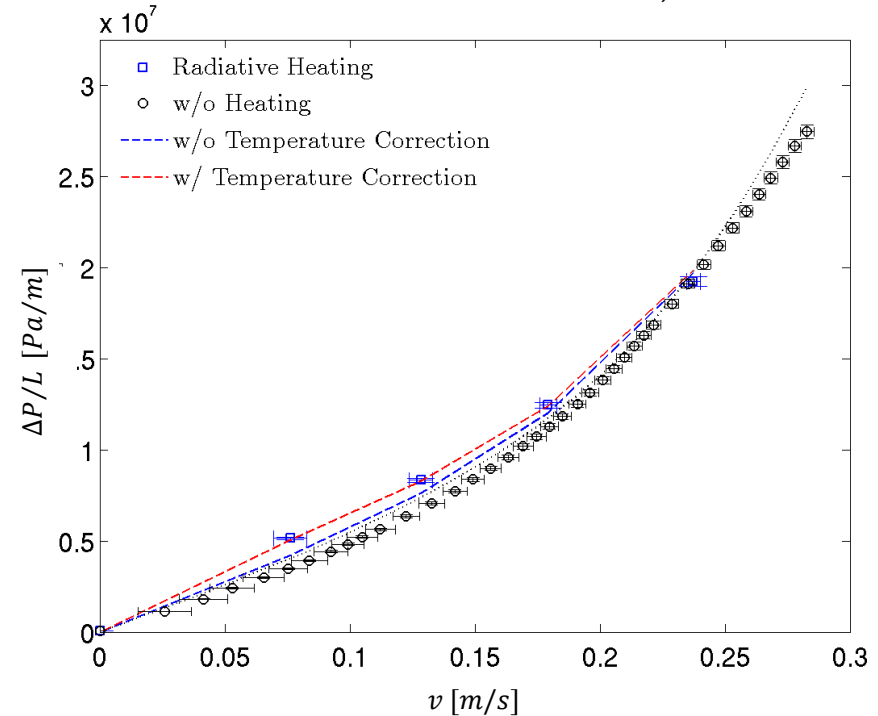
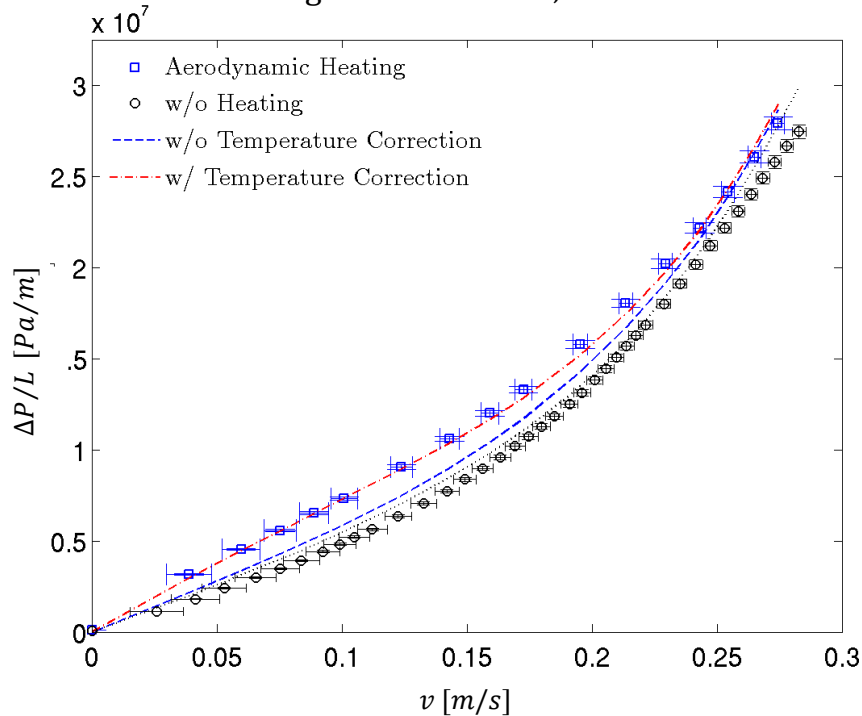
BCs: $T_s|_{y=0} = T_b$, $T_f|_{y=0} = T_c$ and $T_s|_{y=L} = T_w (+\Delta T \text{ if heated by radiation})$



Sample 4

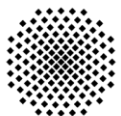
Aerodynamic Heating:
 $M = 0.3$; $T_g = 420\text{K}$; $T_{w,0} \sim 410\text{K}$

Radiative Heating:
 $P_{el} = 415\text{W}$; $T_{w,0} \sim 410\text{K}$



Temperature dependent coolant properties adapted by $T(y) = T_f(y)$

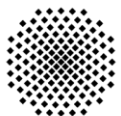
BCs: $T_s|_{y=0} = T_b$, $T_f|_{y=0} = T_c$ and $T_s|_{y=L} = T_w (+\Delta T \text{ if heated by radiation})$



- ☞ Good agreement of theoretical models and measurements
- ☞ Independent of the type of head load generation
- ☞ Respectively low costs of operation for IR heating

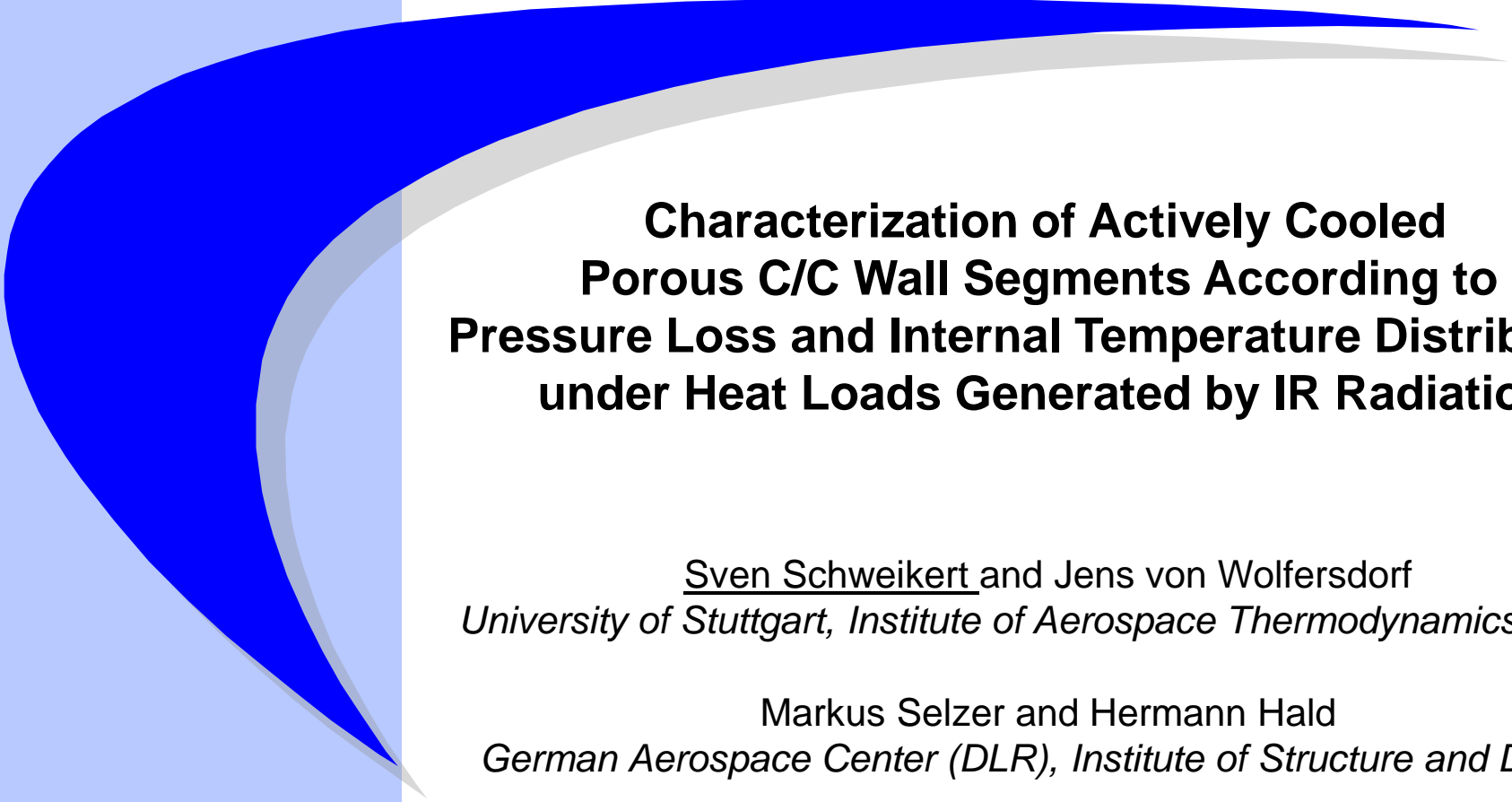
Outlook:

- ☞ Application of more general BCs
- ☞ Details about the thermo-physical properties of porous fiber ceramics
- ☞ Application on higher head loads



**Thank you for
your attention.**

7th European Workshop on Thermal Protection Systems & Hot Structures
ESA-ESTEC, Noordwijk, The Netherlands, 8-10 April 2013



**Characterization of Actively Cooled
Porous C/C Wall Segments According to
Pressure Loss and Internal Temperature Distribution
under Heat Loads Generated by IR Radiation**

Sven Schweikert and Jens von Wolfersdorf
University of Stuttgart, Institute of Aerospace Thermodynamics (ITLR)

Markus Selzer and Hermann Hald
German Aerospace Center (DLR), Institute of Structure and Design



Universität Stuttgart
Germany

Institute of Aerospace
Thermodynamics



Radiation-Shapes-Thermal Protection Investigations

for High Speed Earth Re-entry

RASTAS SPEAR :

Radiation-Shapes-Thermal Protection Investigations for High Speed Earth Re-entry

Overview of the TPS activities

A MARINOU¹, G VEKINIS¹ and J-M BOUILLY²

¹Institute of Advanced Materials PPNM, NCSR "Demokritos", 15310, Aghia Paraskevi Attikis, Greece

²EADS Astrium Space Transportation - BP 20011, 33 165 Saint-Médard_en-Jalles Cedex, France

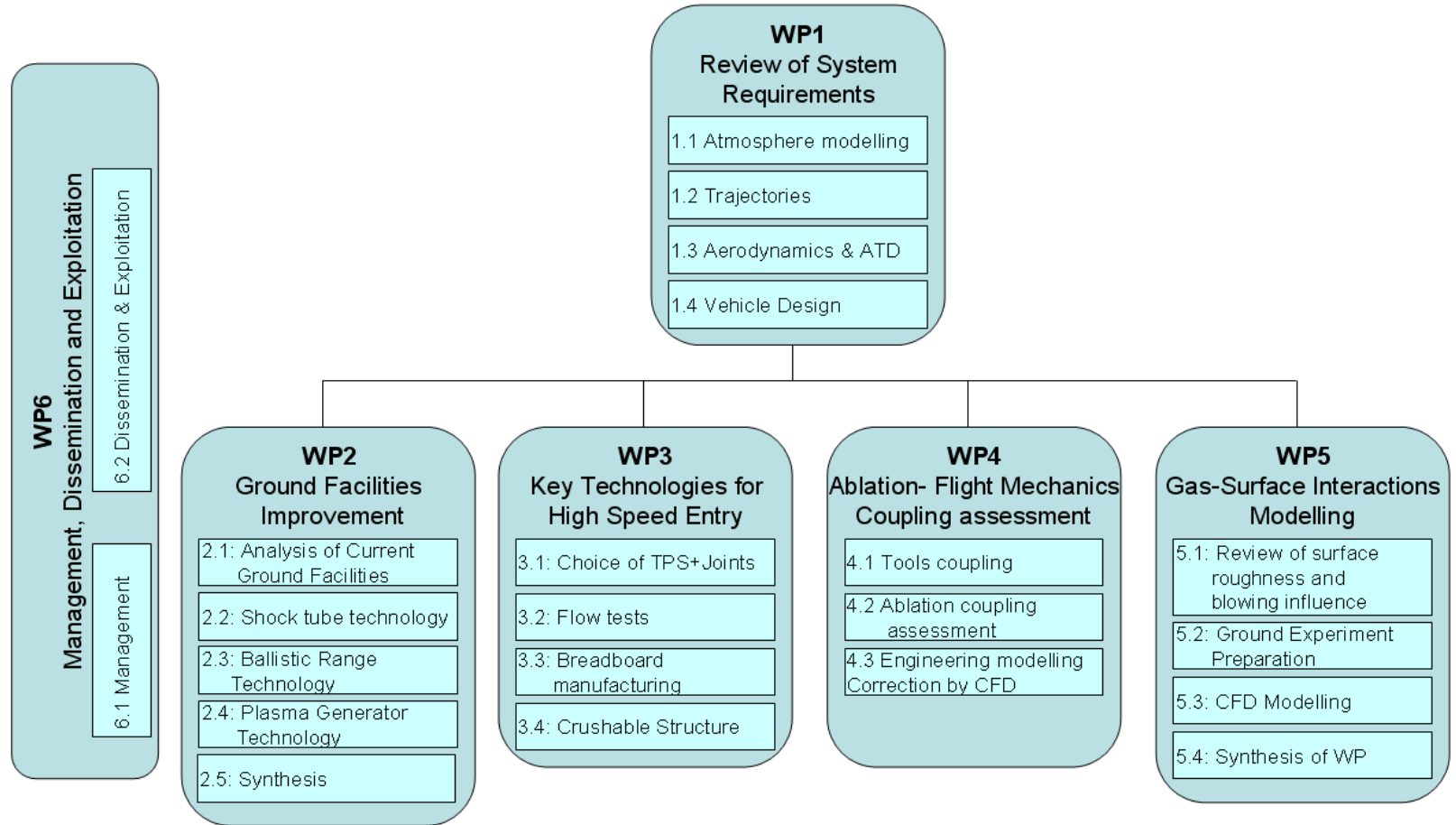
7th European Workshop on TPS-HS – ESA/ESTEC, 8-10 April 2013

www.rastas-spear.eu



The research leading to these results has received funding from the European Union Seventh Framework Programme (FP7/2007-2013) under grant agreement n° 241992

Rastas-Spear – Review and development of necessary technologies for sample-return missions



Rastas Spear Consortium




Von Karman Institute for Fluid Dynamics
<https://www.vki.ac.be/>





Astrium SAS
<http://www.astrium.eads.net/>


CNRS/EM2C
<http://www.em2c.ecp.fr/>


Office National d'Etudes et de Recherches Aéropatiales
<http://www.onera.fr/english.php>



Centro Italiano Ricerche Aerospaziali
<http://www.cira.it/it>



Lomonosov Moscow State University
<http://www.msu.ru/en/>



Institute of Aviation
<http://ioa.edu.pl/>



Kybertec
<http://kybertec.cz/>



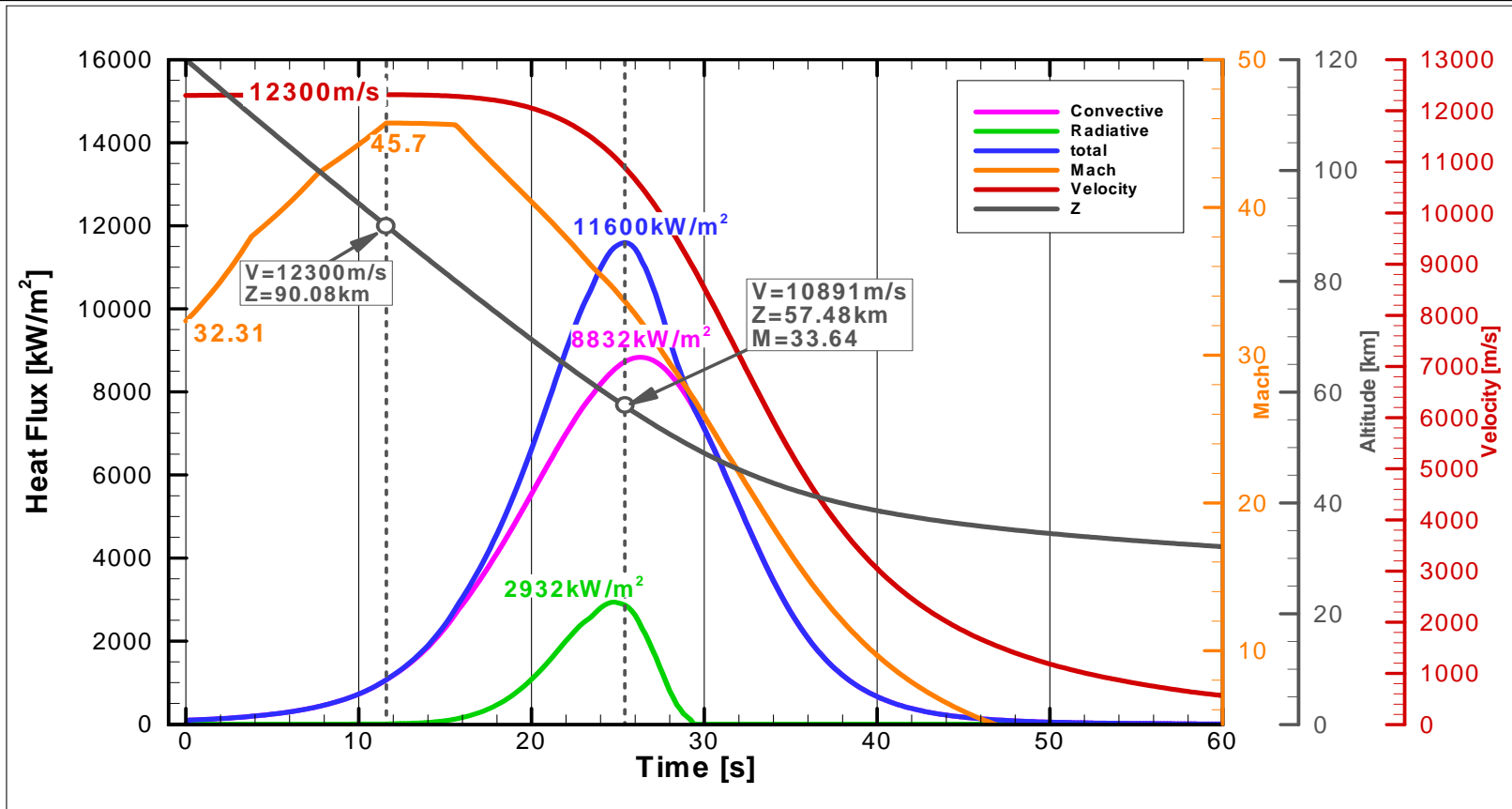
CFS Engineering
<http://www.cfse.ch/cfse/site/home.php>



NCSR Demokritos
<http://www.demokritos.gr/default.aspx?lang=en>

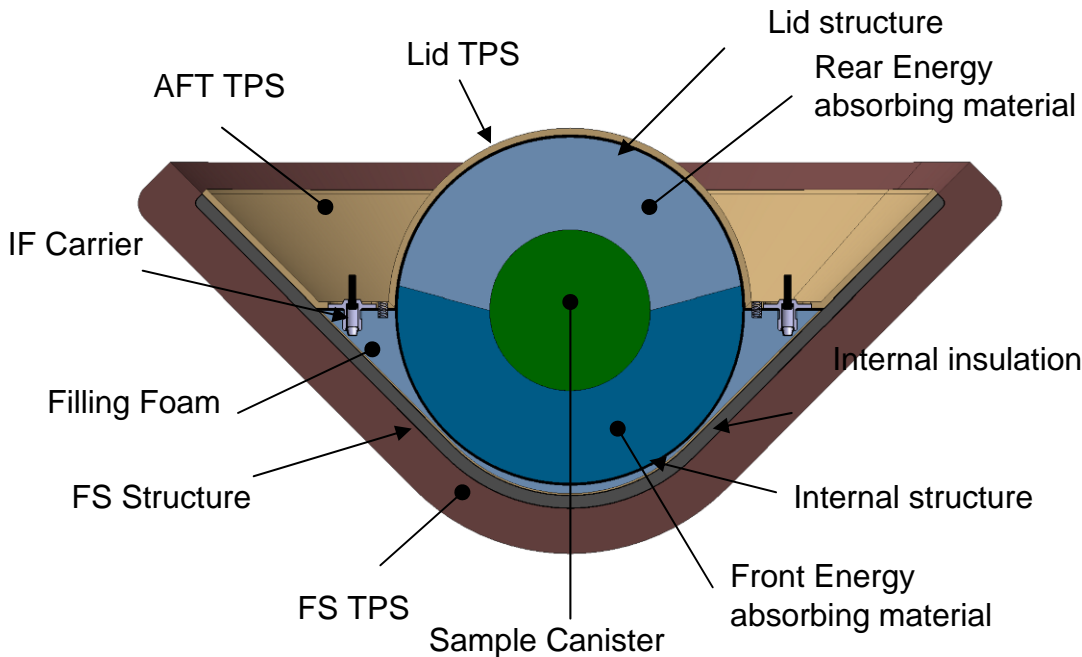



Rastas-Spear – Characteristics of the passive re-entry



Main characteristics of the RS passive re-entry. *Effective max. total heat flux is about 11.6MW/m², max. velocity 12.3km/sec (47.5Mach), total heat energy about 250MJ/m².*

Passive Earth Re-entry Capsule – Hayabusa design



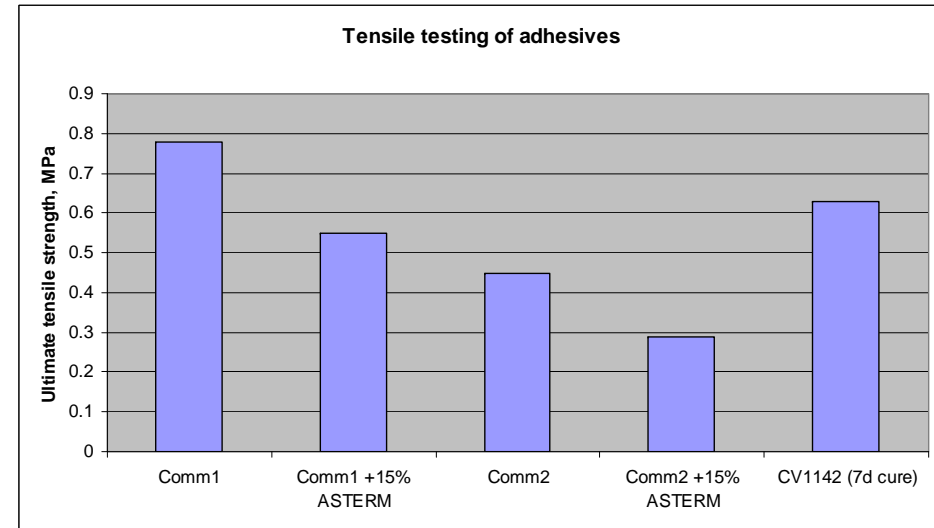
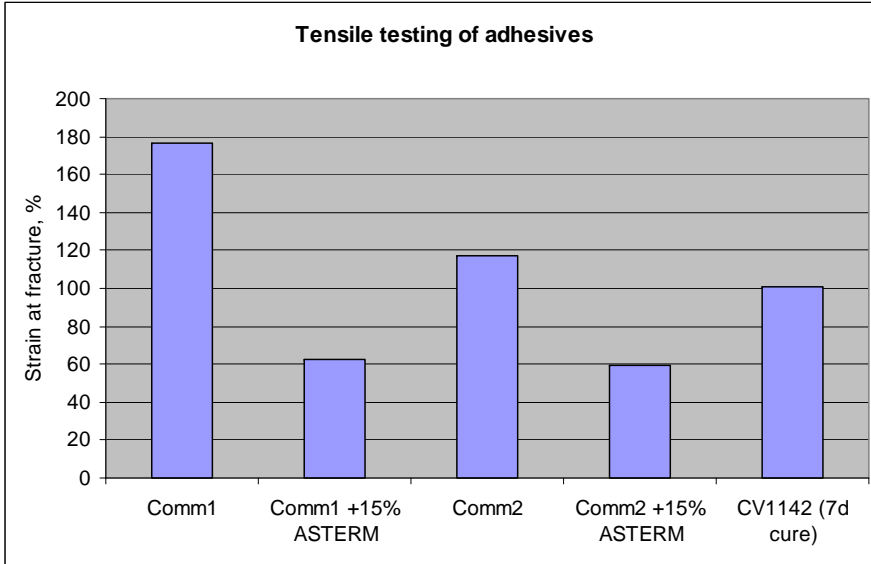
A 45° cone, spherical nose design for 12.3km/sec re-entry.

Maximum diameter 110cm, front radius of curvature 27.5cm and front HS TPS thickness of 56mm.

Main TPS activities in Rastas-Spear

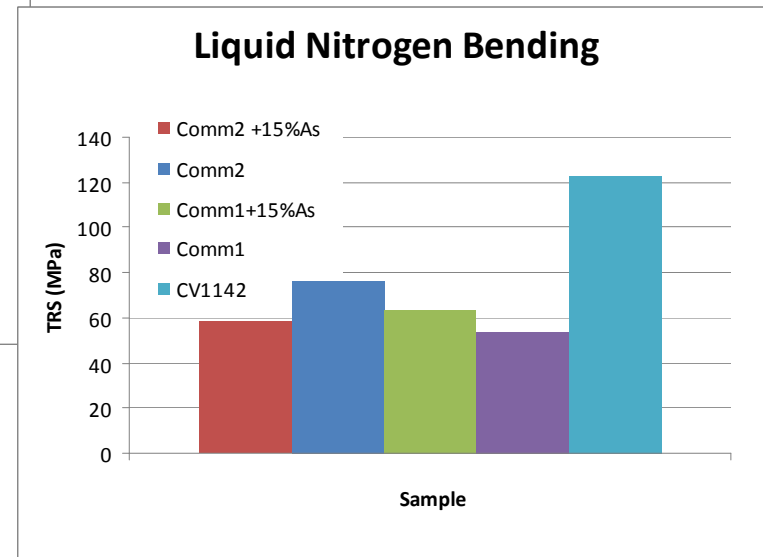
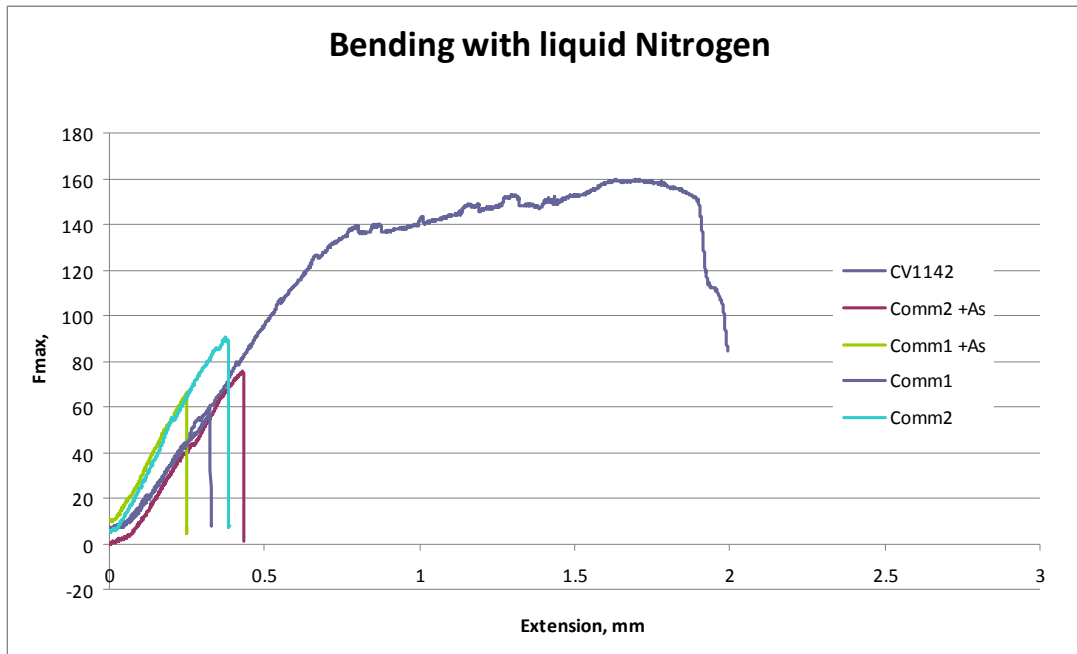
- Adhesive tests and shield development based on the ASTERM carbon-phenolic ablator, made by EADS/Astrium
- Screening and testing of a range of commercial adhesives for joining of ASTERM and bonding with various substrates. Main screening parameters: outgassing, curing behaviour and remanent elasticity at -196°C
- Two commercial adhesives selected and compared with CV1142 heritage adhesive (and with ESP495 for the DLR plasma tests).
- Comparison tests carried out included: mechanical strength of ASTERM joints and bonds, plasma-jet tests (CIRA/Scirocco and DLR/L3K at 5MW/m² and 6.1MW/m² / 13.6MW/m² respectively) up to about 200MJ/m²
- Manufacturing of a front heat shield demonstrator breadboard using an alternative low-cost, manual method.

Mechanical behaviour of adhesives at RT



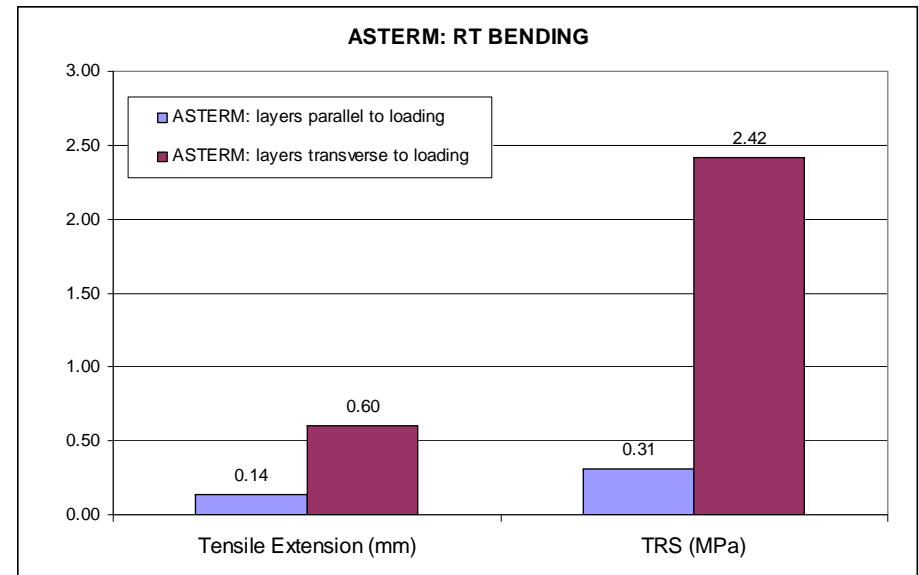
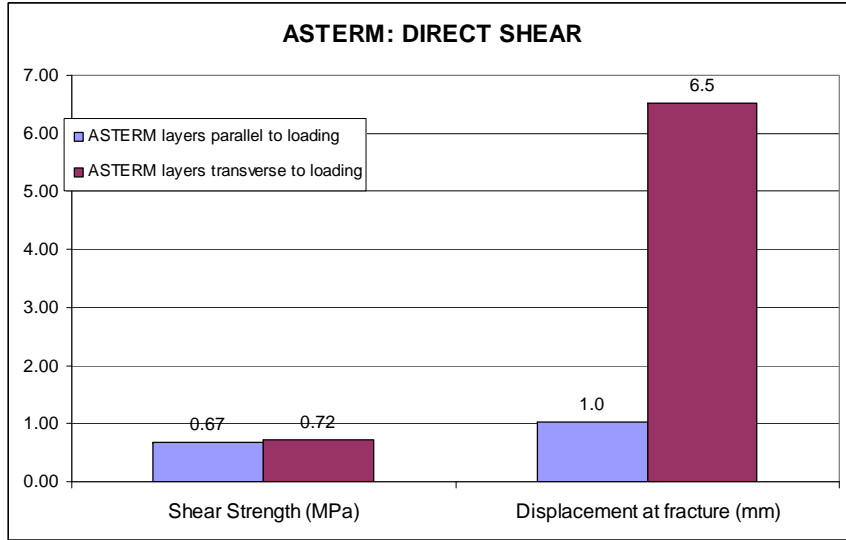
Mechanical behaviour in tension at RT is comparable for all adhesives, including those containing some Asterm powder. In all cases all adhesives are stronger than the Asterm ablator.

Mechanical behaviour of the adhesives at -196°C



All adhesives tested show remanent elasticity at -196°C but CV1142 is much stronger in bending

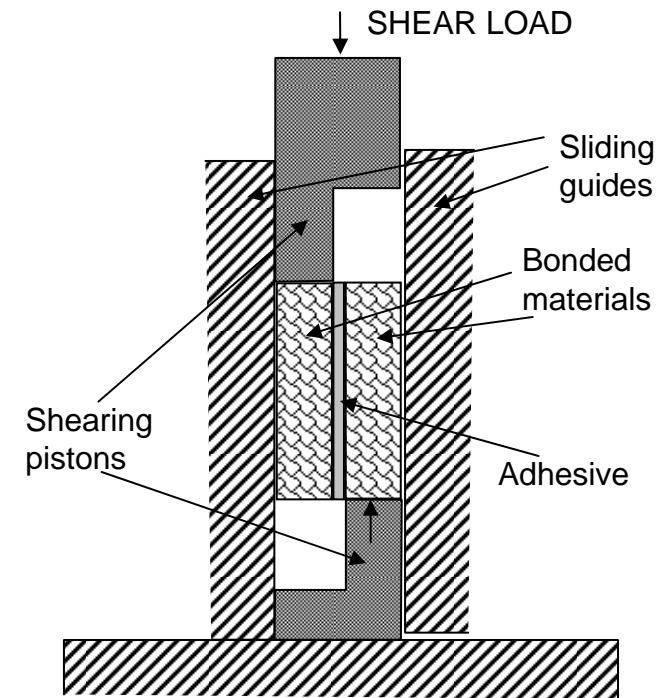
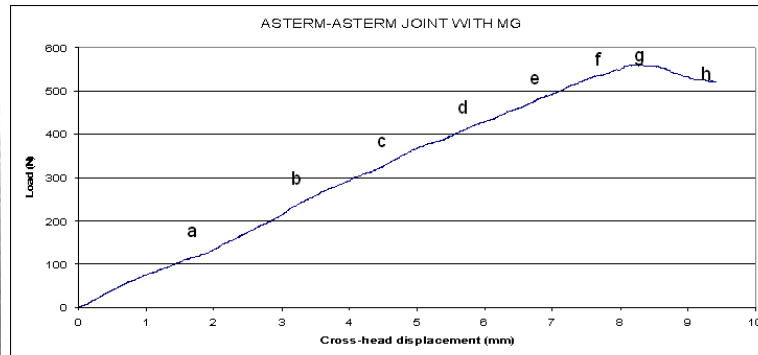
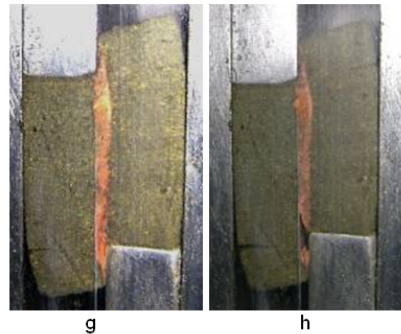
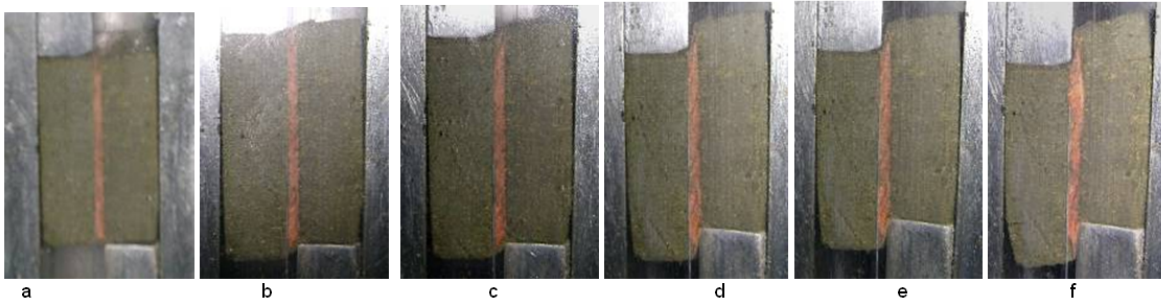
ASTERM: Shear and bending strength



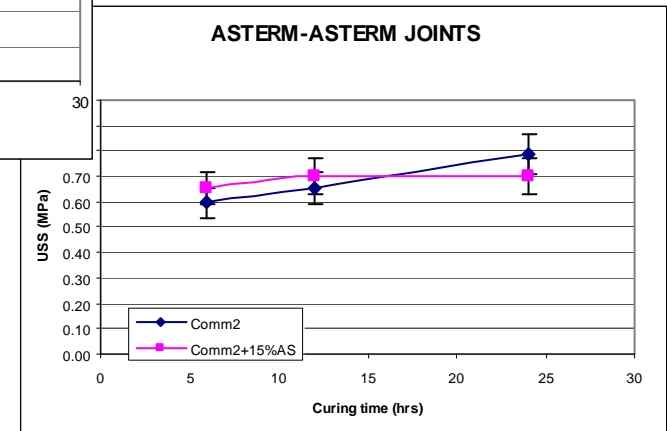
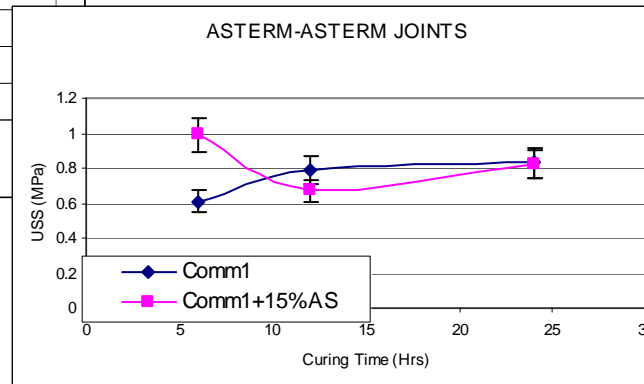
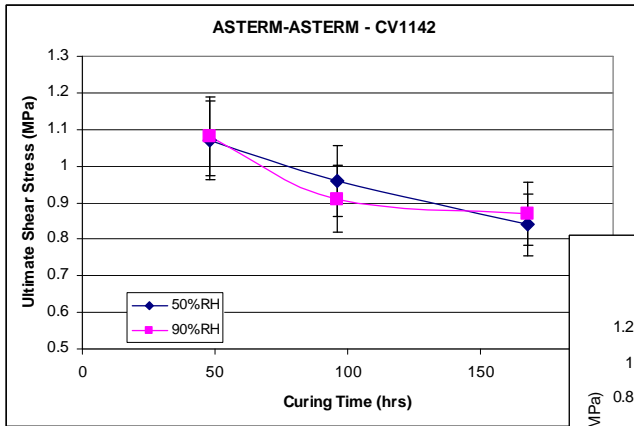
Shear strength in shear is independent of fibre direction but bending strength is highly dependent on it. Displacement at fracture is always much larger when the fibre layers are parallel to loading direction

ASTERM-ASTERM joints: Mechanical properties

Shear strength and fracture behaviour of joints and bonds

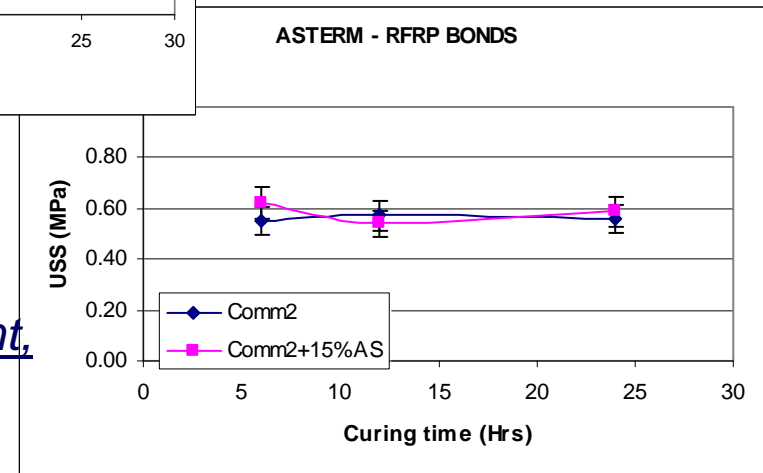
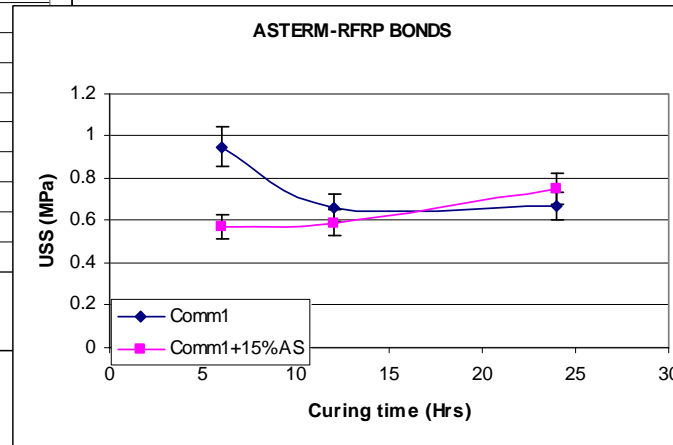
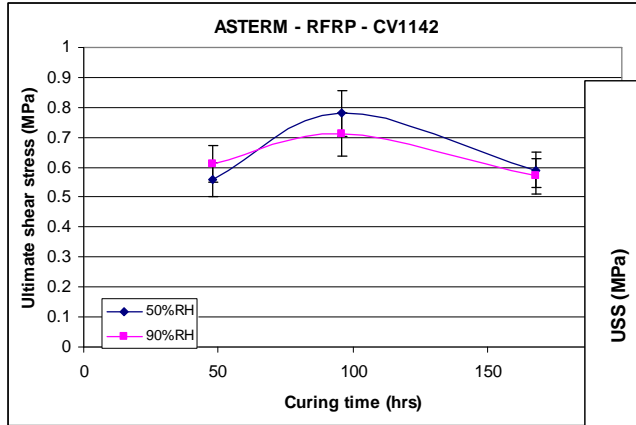


ASTERM-ASTERM joints: Shear strength



Shear strength and fracture behaviour of joints were similar for all adhesives tested.

ASTERM-CFRP bonds: Shear strength



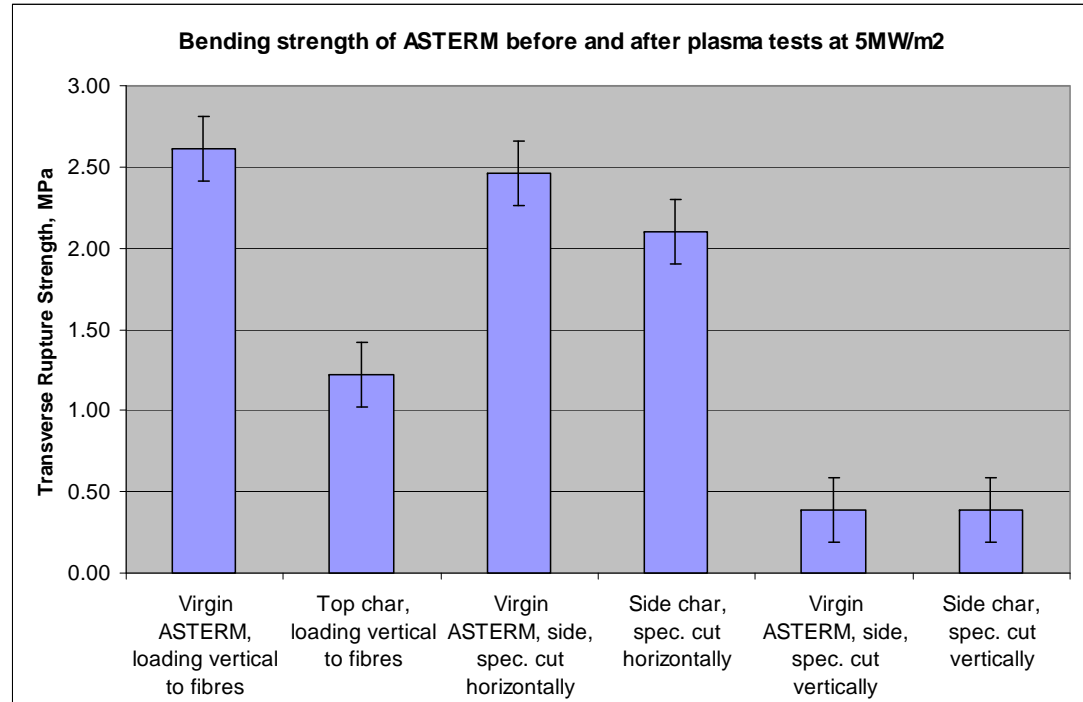
For both joints and bonds, beyond a certain minimum strength and strain at failure, the mechanical behaviour of the adhesive is irrelevant, since the weak link is the ablator in every case.

ASTERM joints: Plasma jet tests – CIRA/Scirocco

CIRA/Scirocco test:
5Mw/m², 12 seconds, 4Mach



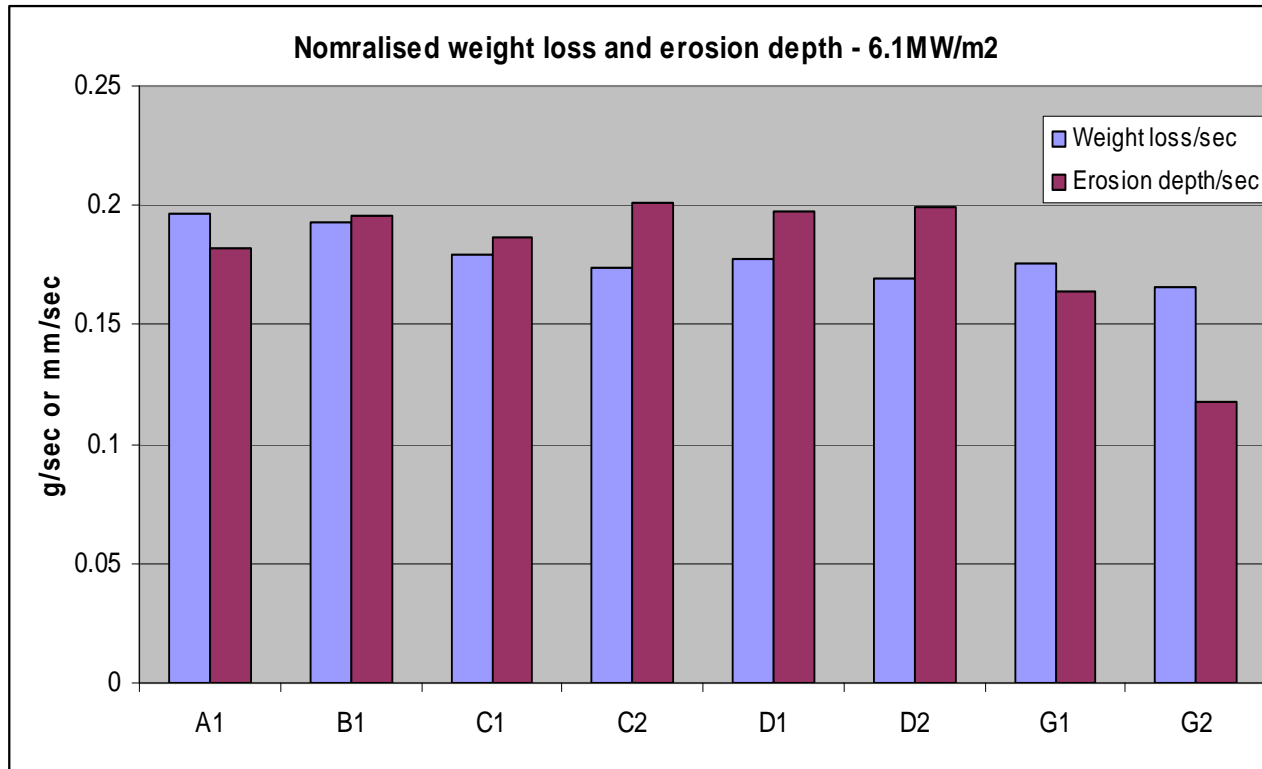
Total uniform recession about 2mm,
top char 12mm, side char about
6mm.



Good remanent strength after plasma-jet test

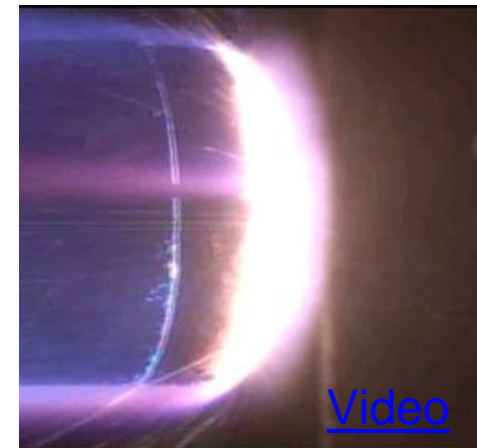
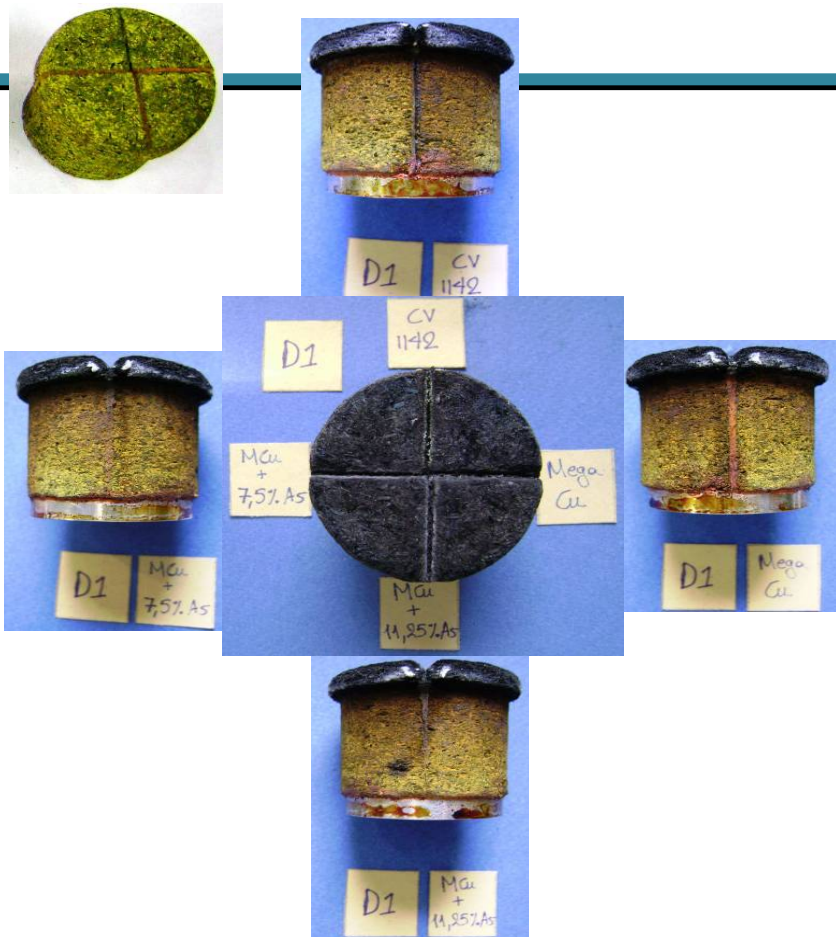
ASTERM joints: Plasma jet tests – DLR/L3K

DLR/L3K tests at 6.1Mw/m², 25-31 seconds



All adhesives eroded deeper than ablator.
Average erosion rate 0.12-0.2mm/sec.

ASTERM joints: Plasma jet tests – DLR/L3K



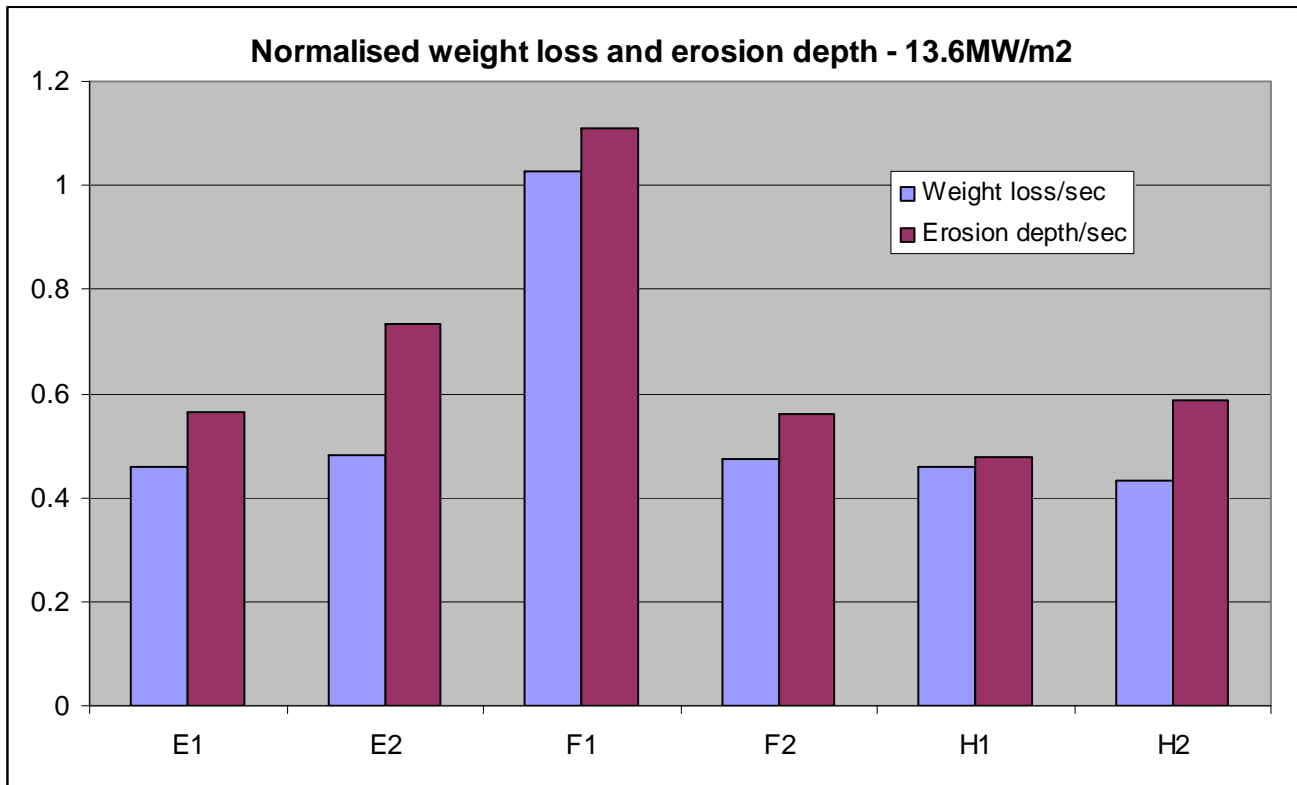
[Video](#)

Video of the D1 test at
6.1MW/m² for 25.3 seconds

All adhesives eroded more than ablator. Average erosion rate about 0.12-0.2mm/sec.
Mixing ASTERM powder with adhesive increases erosion resistance.

ASTERM joints: Plasma jet tests – DLR/L3K

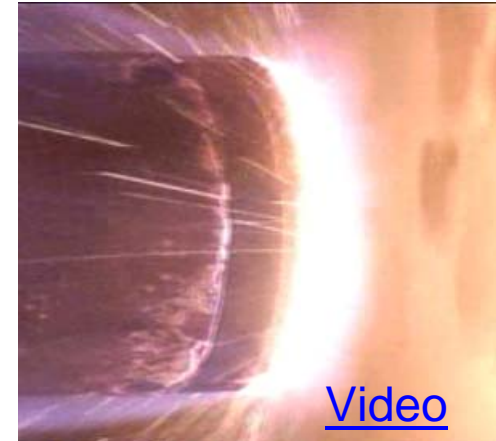
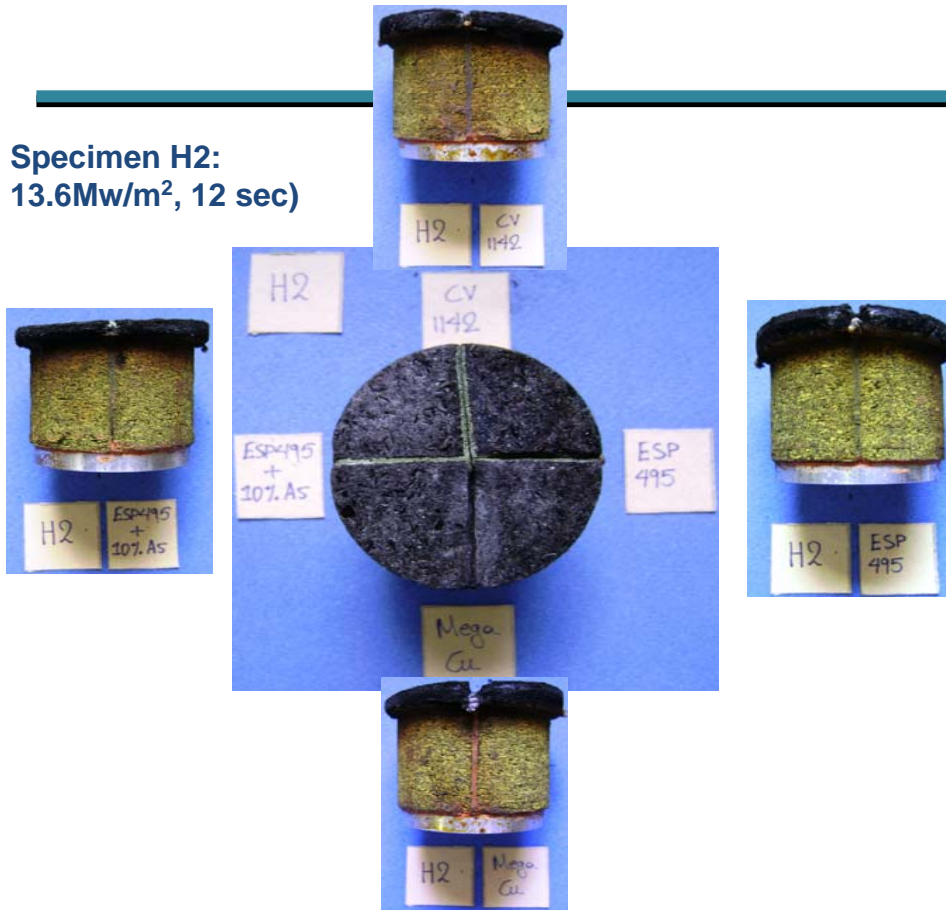
DLR/L3K tests at 13.6Mw/m², 9-14 seconds



All adhesives eroded deeper than ablator. Mostly uniform erosion with an average rate of about 0.6mm/sec for the ablator and about 0.8mm/sec for the adhesives.

ASTERM joints: Plasma jet tests – DLR/L3K

Specimen H2:
13.6Mw/m², 12 sec)



Video of the H2 test at
13.6MW/m² for 14 seconds

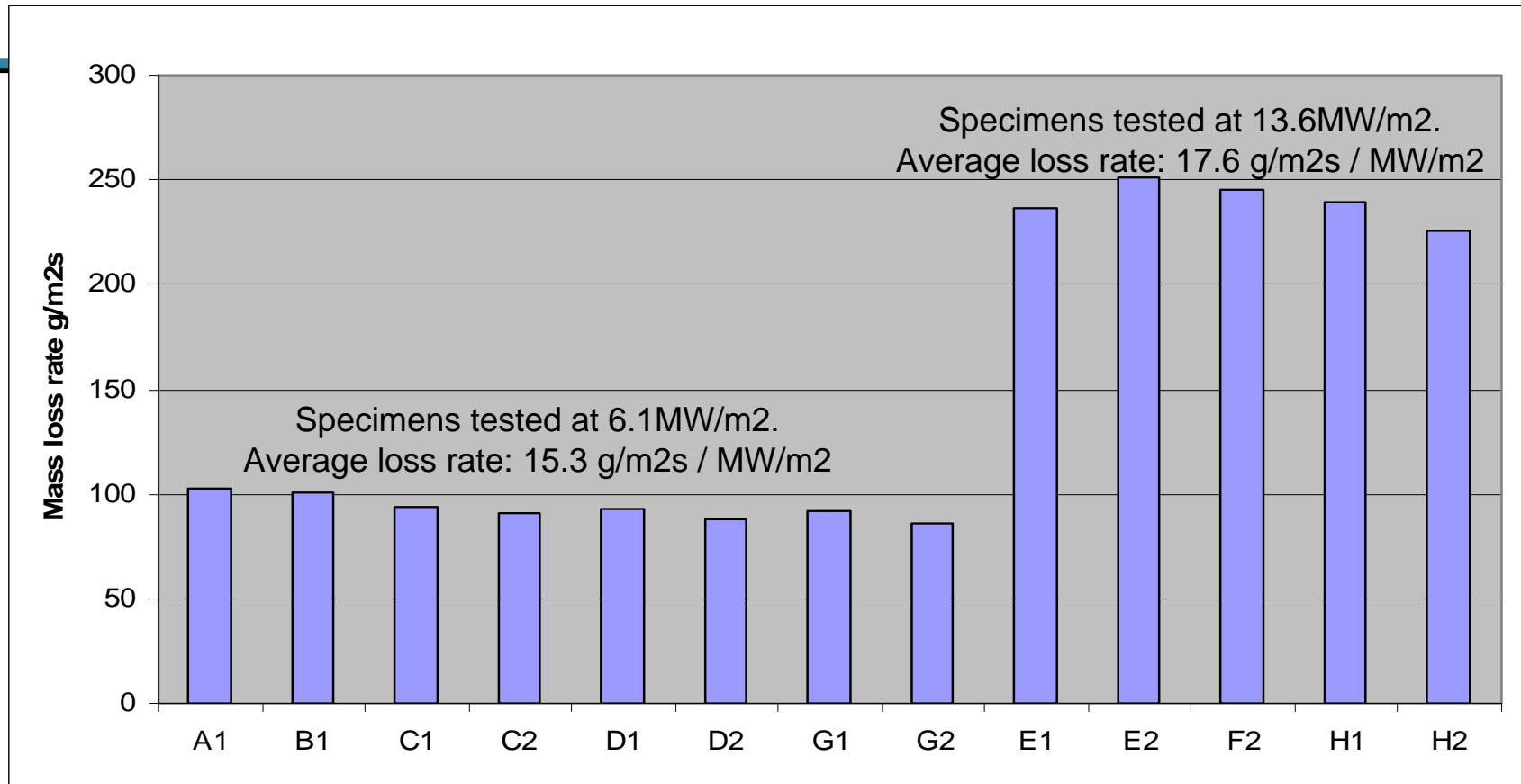
Heritage adhesives CV1142 and ESP495 displayed about 30% less erosion than the commercial adhesive tested. Mixing ASTERM powder with any adhesive increases erosion resistance.

ASTERM joints: Plasma jet tests – DLR/L3K

Sample	Joint 1				Joint 2				Joint 3				Joint 4			
	ASTERM		Gap		ASTERM		Gap		ASTERM		Gap		ASTERM		Gap	
	1a	1b	1a	1b	2a	2b	2a	2b	3a	3b	3a	3b	4a	4b	4a	4b
A1	4.5	5.6	5.5	6.3	4.5	5.5	6	7.9	4.6	6	6.5	8.5	4.6	6.1	6.2	8.3
B1	4.5	5.5	5.3	7.1	4.3	5.3	5.6	6.9	4.3	5.6	5.6	8.2	4.5	6	5.4	8.3
C1	4.6	5.5	5.4	7.1	4.4	5.2	6.2	8.5	4.5	5.6	6.2	8.4	4.5	5.6	6.3	9.5
C2	6	6.8	7	8.2	5.9	6.8	7.1	9.3	6.1	7.4	8.1	10.7	6	7.5	8.1	10.1
D1	4.4	5.1	4.9	7.1	4.4	5.5	6.1	7.5	4.7	5.8	5.9	8.8	4.6	5.6	5.8	9.3
D2	5.8	6.5	6.5	8.1	5.7	6.8	7.1	9.3	5.8	6.9	6.6	10.4	5.8	6.9	7.1	10.1
G1	4.2	4.9	5	6.5	4.5	5.2	4.9	6	4.5	5.8	5.3	8.1	4.4	5.4	4.5	6.1
G2	5.6	6.6	6.8	9.2	5.6	6.4	6.1	7.5	5.8	6.9	7.5	10.1	5.5	7	5.6	7.4
E1	7.7	6.8	9.6	10.9	8.1	6.6	12	13.5	8.6	8.6	12.8	15.5	8.5	9.1	10.7	12.4
E2	4.9	4.2	8.5	5.2	5.6	4.7	12	8.8	6	6	9.5	13.9	6.6	6.2	7.5	8.9
F2	7.6	5.4	11.5	8.7	8.1	6.5	10.8	12.2	8.3	7.7	10.7	13.1	8	7.5	13.1	12.7
H2	6.8	6.7	7.1	7.5	5.3	4.7	8.6	6.5	6.5	5.5	10.1	8.6	6.9	7.7	8.3	8.6
H1	5.4	5.2	5.4	5.9	4.6	4.2	8.5	6.9	5.4	5.1	8.4	8.5	5.9	6.7	6.8	7.8
X	5.5	6.9	5.8	8.5	6	6.4	6.4	8	6	6.4	8	11	5.8	7.4	6.8	9.8

CV1142 displayed least erosion wrt ASTERM followed by ESP495 and the commercial silicones with ASTERM powder.

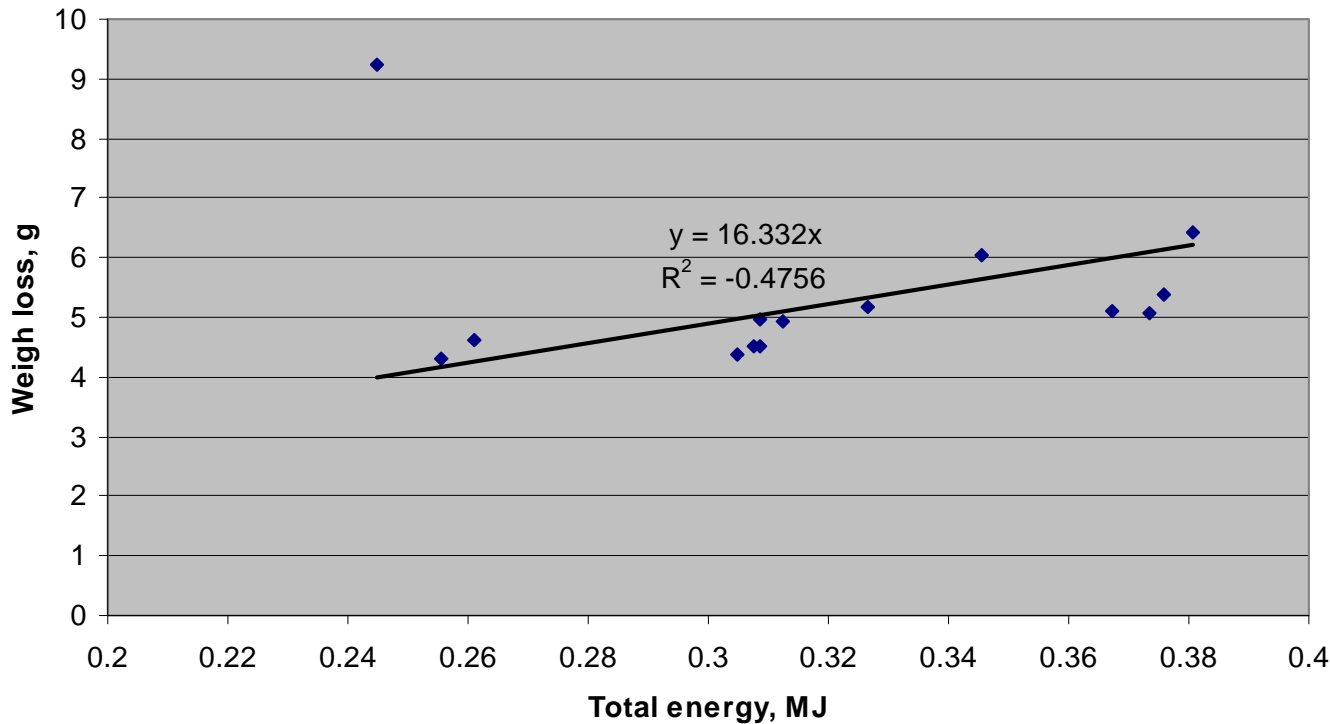
ASTERM joints: Plasma jet tests – DLR/L3K



The apparent acceleration of the mass loss rate with increasing heat flux level is possibly related to the plasma jet encroaching onto the sides of the specimen at extreme levels of erosion (aberrant result for F1 not shown).

ASTERM joints: Plasma jet tests – DLR/L3K

Weight loss against total energy for all specimens



Linear relationship of weight loss vs total plasma energy. Gradient gives 60kJ per g of material removed mainly by ablation, agreeing with independent plasma torch tests.

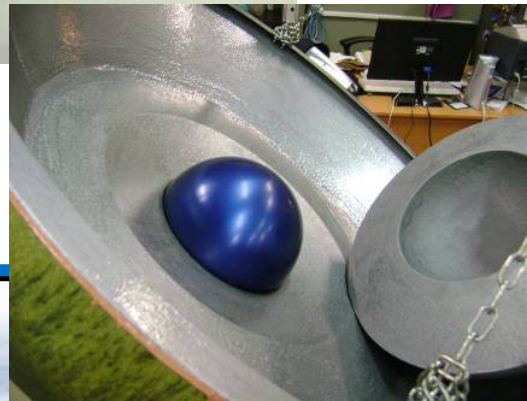
Rastas Spear: Front Heat Shield Breadboard



A front Heat Shield Breadboard Demonstrator was constructed with ASTERM and a commercial adhesive by a mainly manual, low-cost method, with a single, top surface finishing operation.

Maximum diameter 92.5cm, ablator thickness 56mm, joint and bond thickness about 1-1.2mm.

The method is flexible and can be adapted for any symmetric shape. It can be used to produce actual heat shields as long as the current dimensional tolerances are relaxed to some extent.



The inside of the breadboard Demo with the sample canister demonstrator in the crushable material made of rigid PU foam(made by IoL)

Rastas Spear: Main conclusions of the TPS tasks

- Space-qualified RTV silicone CV1142 as well as low-outgassing, low-cost, commercial RTV silicones were used for producing ASTERM joints and bonds with various substrates.
- Mechanical properties of joints and bonds were measured in shear and bending at -196°C
- ASTERM joints and bonds loaded in shear always failed through the ASTERM for all silicone adhesives examined and in both parallel and transverse loading directions.
- CV1142 displayed higher strength but similar elasticity at -196°C to commercial silicones. However, the higher strength cannot be leveraged as failure occurs through the ablator.
- Plasma-jet testing of various joints at 5.0 - 13.6MW/m² for up to 30 and 14sec respectively showed that ASTERM always displayed less recession than all joints tested, including CV1142 and ESP495 joints which were however better than commercial silicones.
- The use of ablator powder mixed-in with all silicones increases erosion resistance closer to that of ASTERM, potentially reducing irregularities on the charred surface.
- A tiled demonstrator front heat shield was manufactured satisfactorily using an alternative flexible manual method at much lower cost – this may be applicable for producing low-cost heat shields if the geometric tolerances on production method can be relaxed somewhat.

Thank you for your attention

Any questions?

More info at www.rastas-spear.eu

COMPUTATIONAL ANALYSIS OF HYPERSONIC FLOWS INCLUDING FINITE RATE ABLATION THERMOCHEMISTRY

Daniele Bianchi, Francesco Nasuti, Renato Paciorri, and Marcello Onofri

*“Sapienza” University of Rome
Department of Mechanical and Aerospace Engineering, Via Eudossiana 18, 00184, Rome, Italy
Email: daniele.bianchi@uniroma1.it*

Abstract

The design and correct sizing of thermal protection systems of re-entry bodies requires reliable simulation tools that can compute surface recession rate and temperature histories under general heating conditions. A formulation of a finite-rate surface boundary conditions for carbonaceous material ablation with pyrolysis gas injection is developed and implemented in a 3-D reacting Navier-Stokes equation solver, to predict ablation response of carbon and carbon-phenolic heat shields on reentry space vehicles. Validation of the approach is carried out by comparison with literature experimental data. Results show a satisfactory agreement with data and emphasize that including nitridation reaction may yield a significant overprediction of graphite mass blowing rate.

1. INTRODUCTION

One of the most challenging aspects of thermal protection system (TPS) design is to predict the desired coupling between the material response and the external flow. The present state of the art in fluid-material coupling is represented by loose coupling of a high-fidelity CFD flow solver with a material thermal response code [1]. Nevertheless, two major restrictions are still present in these state of the art coupled solutions. The ablation models are currently largely based on the surface equilibrium assumption and the effects and importance of non-equilibrium ablation models are only beginning to be explored in both reentry and propulsive applications [2, 3, 4, 5, 6, 7, 8]. The convective heating and surface recession rate predicted by the chemical equilibrium surface chemistry is usually reasonably conservative and is considered to be sufficient when the nonequilibrium computation is too expensive or unlikely to be achieved. Tables are established by solving the chemical equilibrium relations and the elemental species balance equations with thin-film transfer theory. If the chemical species concentrations, such as a chemical nonequilibrium shock layer with the presence of radiation, must be precisely defined in the flow simulation, then the chemical equilibrium surface conditions are no longer sufficient. Attempts were made to modify tables to include some nonequilibrium effects and to better fit ablation data, but the gas-phase nonequilibrium ablation products cannot be determined without a finite rate simulation. Moreover, the coupling between CFD solver and material response code is currently made considering non-ablating flowfield solutions [1]. This means that the effect on the flowfield solution of the ablation and pyrolysis gas injection and of variable surface temperature are treated only approximately, relying on the use of mass and energy transfer coefficients and semi-empirical relations. The limits and the errors introduced by these approximations are discussed in [9, 10, 11].

The objective of this work is the study of hypersonic re-entry flows coupled with gas-surface interaction phenomena occurring at the interface between TPS-materials and boundary-layer. The main goal is to couple a CFD solver (in-house) with gas-surface interaction modeling to allow surface ablation and surface temperature distributions to be determined as part of a solution that also contains more sophisticated ablation models based on finite-rate surface chemistry. Carbon-based materials are selected as the heat-shield materials in this study because their interactions with air are better understood. As more is known about the interactions of other heat-shield materials with ambient gases, this same computational methodology can be applied for other ablators. Because the entire flowfield is to be solved, the thin-film theory assumption made in establishing the classical B' equilibrium thermochemical tables is no longer needed, and all of the problems associated with the approximation of transfer coefficient and recovery enthalpy are avoided.

2. THEORETICAL MODEL

Modeling of both gas and surface chemical reactions is described in this section. Before going into details it is useful to remind that as long as gas-surface interactions are concerned, two different classes of TPS materials have to be considered: non-pyrolyzing materials and pyrolyzing materials. In non-pyrolyzing materials (e.g. carbon-carbon, graphite...), mass loss only occurs at the surface (thermochemical and/or mechanical erosion). Pyrolyzing materials (Fig. 1) are composites

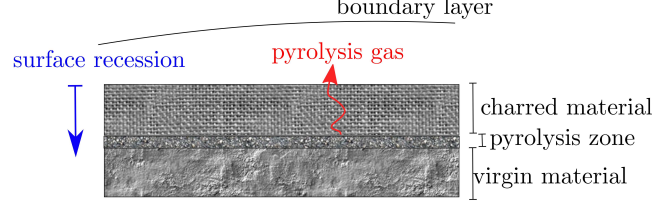


Figure 1: Pyrolyzing materials

of fiber or fabric reinforcement in a resin matrix (e.g. carbon-phenolic, silica-phenolic...). When heated, the resin experiences a series of chemical reactions that release gaseous by products (pyrolysis) leaving a layer of char or residue. Then the char itself can recede due to chemical or mechanical action by the boundary layer. In this work, attention will be focused on carbon-based charring and non-charring ablative materials such as graphite and carbon-phenolic, which are widely used for many reentry applications.

2.1. Gas/surface interaction model

If it is assumed that no material is being removed in a condensed phase (solid or liquid), then the general conservation laws at the gas-solid interface for a pyrolyzing material can be written as [12, 13]:

$$\text{Mass:} \quad (\rho v)_w = \dot{m}_g + \dot{m}_c = \dot{m} \quad (1)$$

$$\text{Species:} \quad -\rho D_{im} \nabla y_i + (\rho v)_w y_{i_w} = \dot{m}_c y_{i_c} + \dot{m}_g y_{i_g} \quad i = 1, N \quad (2)$$

$$\text{Energy:} \quad k \nabla T + \sum h_i \rho D_{im} \nabla y_i + \dot{m}_c h_c + \dot{m}_g h_g - \dot{m} h_w + \alpha \dot{q}_r - \sigma \epsilon T_w^4 - \dot{q}_s = 0 \quad (3)$$

where v_w stands for the radial velocity in the gas phase due to ablation products injection (both the pyrolysis gas and the char-oxidation product species) while $\dot{m}_c y_{i_c}$ is the rate of production/destruction of gas-phase species i at the surface due to heterogeneous reactions between the boundary layer hot gases and the solid char. The term $y_{i,g}$ represents the chemical composition of the pyrolysis gas which is injected in the boundary layer. Radiation absorption and emission terms are also included. The conduction term \dot{q}_s is represented by a closed expression available assuming steady state ablation:

$$\dot{q}_s = \dot{m}_c h_c + \dot{m}_g h_g - (\dot{m}_c + \dot{m}_g) h_{v_i} \quad (4)$$

which is a function of char/pyrolysis gas mass flow rate and enthalpy and takes into account the energy absorbed by the matrix decomposition process and the energy consumed in sensible enthalpy changes of the solid and of the pyrolysis gas. The steady-state ablation approximation is a reasonable assumption when high heating rate conditions are encountered [12]. At this point, substituting Eq. (4) into Eq. (3), the final steady-state surface energy balance becomes:

$$k \nabla T + \sum h_i \rho D_{im} \nabla y_i - \dot{m} (h_w - h_{v_i}) + \alpha \dot{q}_r - \sigma \epsilon T_w^4 = 0 \quad (5)$$

It is interesting to note that Eq. (5), which is in a convenient form for numerical implementation, can be cast into a more appealing form where each term has a more immediate physical significance, obtained substituting the species equation (2) into the energy equation (3):

$$\underbrace{k \nabla T}_{\text{convective}} - \underbrace{\sum \dot{m}_c y_{i_c} h_i + \dot{m}_c h_c}_{\text{chemical}} + \underbrace{\alpha \dot{q}_r - \sigma \epsilon T_w^4}_{\text{radiative}} - \dot{q}_s = 0 \quad (6)$$

distinguishing convective, chemical, radiative, and conductive heat flux, where the chemical heat flux represents the energy absorbed by the heterogeneous surface reactions which consume the charred material.

2.2. Finite-rate thermochemical ablation model

The rate of production/consumption of the generic gas-phase species i participating in heterogeneous reactions with carbon at the surface, $\dot{m}_c y_{i,c}$, appearing in both the species and energy balances, has to be estimated on the basis of the heat-shield material and the atmosphere composition. The non-equilibrium gas/surface interaction model for carbon in air studied in this work is the one developed by Park [14] consisting of two oxidation reactions, one nitridation reaction, and one sublimation reaction. The carbon mass blowing rates due to these gas-surface reactions are:

$$\begin{aligned}\dot{m}_1 &= \rho y_O \hat{\nu}_O (\beta_O/4) (M_C/M_O) && (\text{O} + \text{C}_s \Rightarrow \text{CO}) \\ \dot{m}_2 &= 2\rho y_{O_2} \hat{\nu}_{O_2} (\beta_{O_2}/4) (M_C/M_{O_2}) && (\text{O}_2 + 2\text{C}_s \Rightarrow 2\text{CO}) \\ \dot{m}_3 &= \rho y_N \hat{\nu}_N (\beta_N/4) (M_C/M_N) && (\text{N} + \text{C}_s \Rightarrow \text{CN}) \\ \dot{m}_4 &= \rho (y_{C_3,eq} - y_{C_3}) \hat{\nu}_{C_3} \beta_{C_3}/4 && (3\text{C}_s \Leftrightarrow \text{C}_3) \\ \dot{m}_c &= \dot{m}_1 + \dot{m}_2 + \dot{m}_3 + \dot{m}_4 = \rho_c \dot{s}\end{aligned}$$

Here, $\hat{\nu}_i = \sqrt{8kT_w/\pi m_i}$ is the mean molecular speed of the ablation-product species and ρ_c is the char density. The term β is the efficiency of each surface reaction [15, 16]. The rate of production/consumption of the i th gas-phase species at the wall, $\dot{m}_c y_{i,c}$, can be easily derived from the carbon mass blowing rates by the generic surface reaction and the mass balance available once the species molecular weights and the stoichiometry of the surface reactions are known. The surface mass and energy balances are intimately coupled, and therefore they must be solved jointly: with the wall pressure coming from the flow-field (assuming zero-pressure gradient at the wall) and with the wall temperature computed from the surface energy balance, Eq. (5), the chemical composition at the surface and the net char blowing rate can be obtained from Eq. (2), using an iterative algorithm.

2.3. Pyrolysis gas model

When heated, the resin experiences a series of chemical reactions that release gaseous by products (pyrolysis) leaving behind a porous residue, which is a carbonaceous char reinforced with the carbon fiber. During the matrix decomposition process, the gaseous pyrolysis products are forced by the pressure gradient to flow through the residual charred material. In the present model, the pyrolysis gas itself is assumed to be in chemical equilibrium as it passes through the char and before injection into the nozzle flow-field. Under this reasonable assumption [13, 4, 17] its chemical composition can be calculated by a series of equilibrium chemistry solutions, provided that the elemental make-up of the gas is known. The equilibrium species concentrations of pyrolysis gas, as a function of pressure and temperature, are computed using a chemical equilibrium code [18] and stored in a database for computational efficiency.

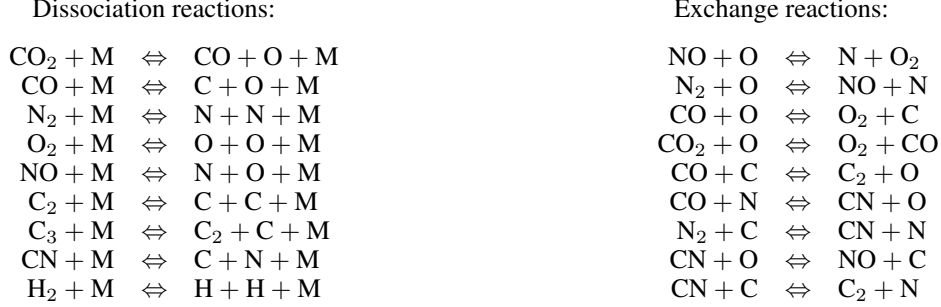
The elemental mass fractions in the pyrolysis gas are considered to be 37.5% C, 46.3% O, and 16.2% H, which are the values accepted in the community [19]. The computed equilibrium species concentrations of pyrolysis gas are mostly CO, H₂, and H. Moreover, for the actual pressure and temperature range, the pyrolysis gas composition is weakly influenced by temperature and the effect of pressure is almost negligible. Finally, it has also to be noted that although the pyrolysis gas is injected into the boundary layer at a well defined composition, the injected species can modify the boundary-layer as well as the mixture composition at the wall and thus influence the surface mass and energy balances.

3. NAVIER-STOKES SOLVER

A Navier-Stokes solver with integrated gas/surface interaction models and surface balances is used to simulate high-speed high-temperature flows over ablating materials. The developed tool is a finite-volume solver for three-dimensional compressible flows which is able to predict the surface recession, temperature, and the convective heat flux distributions of carbon-based heat shields on reentry vehicles. The code solves the time-dependent conservation equations of mass, momentum, and energy for the chemical nonequilibrium flowfield and adopts a standard finite volume Godunov-type formulation. It is second order accurate in both space and time and uses multi-block structured meshes. The system of equations is approximated by a cell-centered finite volume scheme. The viscous fluxes are approximated by centered differencing, whereas the convective fluxes are computed by means of the solution of a Riemann problem whose left

and right states are reconstructed by an interpolation procedure which uses the minmod limiter. The system of ordinary differential equations is advanced in time by means of an explicit Runge-Kutta integration. In addition, the code has been parallelized using the OpenMP directives and it can run on SMP computers.

A total of 13 gas-phase species have been considered in the analysis: N_2 , O_2 , NO , N , O , CO_2 , CO , C , C_2 , C_3 , CN , H_2 , and H . Five of the species are for air, and the rest are for ablation products. The gas-phase chemical reactions implemented in the CFD code are taken from the work of Olynick et al. [20] for Stardust earth entry simulation and are mainly derived from the work of Park [21, 22]. The total number of reactions is 18, including 9 dissociation reactions and 9 exchange reactions.



The thermodynamic properties for individual species are approximated by seventh-order polynomials of temperature and the transport properties are approximated by fourth-order polynomials [18]. Mixture properties for conductivity and viscosity are derived from Wilke's rule. The diffusion model is based on an effective diffusion coefficient obtained assuming a constant Schmidt number of 0.7.

Property	Value
Velocity	5354 [m/s]
Density	0.003 [kg/m ³]
Temperature	1428 [K]
Mass concentrations	
O ₂	0.0001
N ₂	0.6169
NO	0.0046
N	0.1212
O	0.2572

Table 1: Freestream condition for graphite test case.

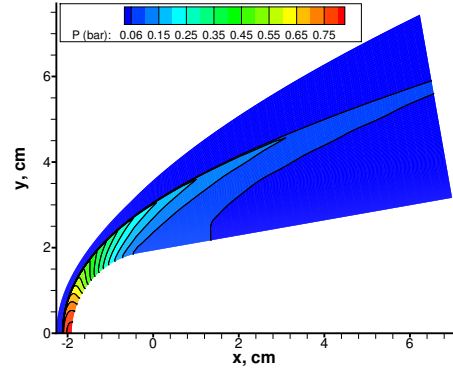


Figure 2: Pressure contours in the flowfield.

4. RESULTS AND DISCUSSION

The general finite rate carbon-phenolic ablation model without pyrolysis gas injection ($\dot{m}_g = 0$) can be used to simulate graphite ablation. The analyzed test case is a study of the interaction between a graphite model and an arc-jet stream, conducted in the Interaction Heating Facility (IHF) at the NASA Ames Research Center. Numerical simulations were performed to reproduce the experimental results which have been presented in two works by Chen and Milos [4], and Chen et. al. [23]. According to the data of Ref. [4] and [23], the first series of arc-jet tests were conducted with a Mach number of 6, a stream enthalpy of 27 MJ/kg and a stagnation point cold-wall heat flux of 2100 W/cm². The stagnation pressure is 0.8 atm according to [4]. The length of the heat pulse is 30 sec. The graphite model is a 10 half angle sphere-cone with nose radius of 1.905 cm. The total length of the model is 8.89 cm. Freestream quantities are reported in Ref. [4] and are listed in Table 1. Surface temperature distribution was measured using an infrared camera and pyrometers.

Two-dimensional axisymmetric simulations have been performed to numerically reproduce this test case. A single-block grid composed of 30×80 grid points in the axial and normal directions, respectively, is adopted. The grid is constructed such to ensure orthogonality at the surface and is adapted to the Mach contours to achieve proper grid alignment to the shock. In the normal direction, meshes are clustered near the body surface such to accurately capture the near wall phenomena. A grid convergence analysis is also performed to ensure that results are grid independent, performing simulations on a coarse 15×40 and a fine 60×160 grid. All the computations presented are at steady-state condition. Flowfield pressure contours are reported in Fig. 2.

The surface temperature and pressure profiles are shown in Fig. 3. Predicted carbon mass blowing rate distributions over the model surface are shown in Fig. 4. The solid and dotted lines are the results of Park's surface kinetics with and without the nitridation surface reaction ($N + C_s \Rightarrow CN$), respectively. With the nitridation reaction, the model overpredicts the graphite mass blowing rate by almost 40% with respect to arc-jet data at the stagnation point and by 30% at 45 from the stagnation point (assuming a graphite emissivity of 0.9). Without the nitridation reaction, the model underpredicts the graphite mass blowing rate by 7% (stagnation point) and by 15% (45 from stagnation point). The nitridation reaction is shown to have a significant effect on the total mass blowing rate. Surface temperature, instead, is only marginally affected by surface nitridation (Fig. 3); this is because the net energy exchange due to the surface nitridation reaction is small. Figure 5 presents the chemical species distributions along the stagnation streamline for Park's finite rate model with and without nitridation. When surface nitridation is activated, N is fully consumed at the surface and the ablation species CN is produced. The produced CN is soon dissociated into C and N as it diffuses in the hot boundary-layer. As shown in Fig. 6, the sublimation species C_3 peaks at the stagnation point, due to the maximum wall temperature which enhance the sublimation process, and then goes to zero in the conical region. Differently, CN and CO are present all along the wall. When nitridation is considered, the oxidation product CO is decreased at the surface with respect to the case without nitridation. This is because the nitridation reaction contributes to oxygen depletion in the boundary-layer. In fact, the atomic carbon produced by CN dissociation reacts with atomic oxygen in the boundary-layer producing CO and reducing the atomic oxygen available for surface oxidation.

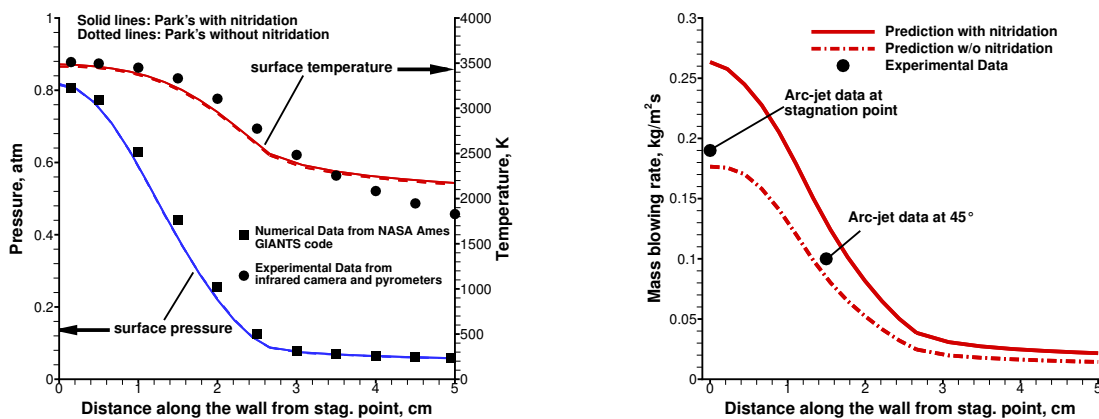


Figure 3: Surface temperature and pressure distributions. Figure 4: Predicted carbon mass blowing rate distributions.

To show the strong coupling which exists between gas-surface reactions and gas-phase chemistry, results with full gas-phase chemistry and with reduced gas-phase chemistry are compared. The reduced gas-phase chemistry model only includes the air chemistry, while it neglects the ablation species chemistry. This means that, with the reduced chemistry model, the ablation products are not allowed to react with each other or with the air species, as they are diffusing across the boundary layer. Figures 7 and 8 show the predicted carbon mass blowing rate distributions with the full and reduced gas-phase chemistry for the case with and without the nitridation reaction, respectively. The total ablation mass flux can be separated into a sublimation mass flux (orange line), an oxidation mass flux (red line), and a nitridation mass flux (blue line). The comparison of the results of Figs. 7 and 8 shows that, with the full gas-phase chemistry, the nitridation reaction significantly reduces the oxidation mass rate. However, if the reduced gas-phase chemistry model is used, the nitridation product CN is not allowed to dissociate in the boundary-layer and the oxygen depletion mechanism is hence inhibited. This produces a significant increase of the total carbon mass blowing rate. Differently, when the nitridation reaction is not considered (Fig. 8), the effect of the gas-phase chemistry on the ablation prediction is much smaller. As the use of the nitridation reaction is giving results which are significantly overestimating the experimental data (both with the full and the reduced gas-phase chemistry model), it will be not included in the following analysis.

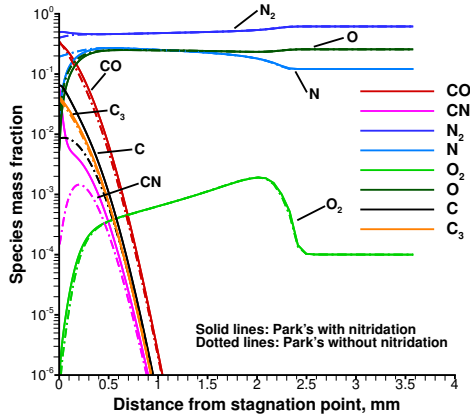


Figure 5: Chemical species distributions along the stagnation streamline.

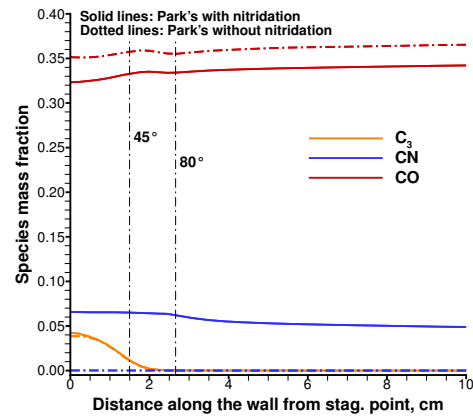


Figure 6: Ablation products wall mass fraction distributions.

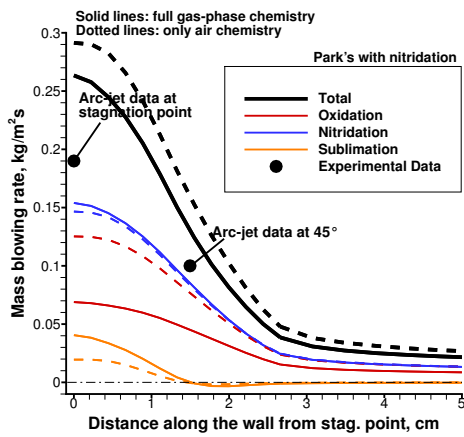


Figure 7: Mass blowing rate distributions with the nitridation reaction with different gas-phase chemistry models.

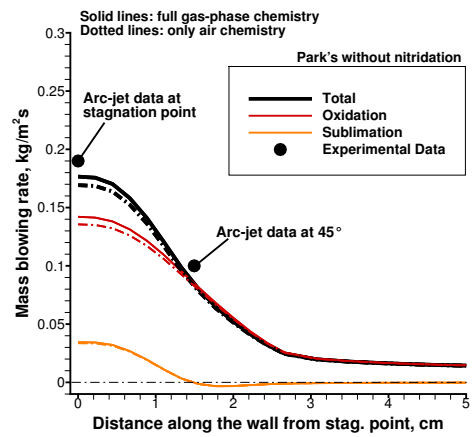


Figure 8: Mass blowing rate distributions without the nitridation reaction with different gas-phase chemistry models.

Figures 9 and 10 show the effect of the graphite emissivity (ranging from 0.7 to 0.9) on the carbon mass blowing rate and wall temperature distributions. As shown in Fig. 10, a change in the material emissivity directly affects the surface energy balance and hence the surface temperature. As Fig. 9 clearly shows, the surface temperature change is significantly affecting the sublimation mass rate while it is only slightly affecting the oxidation mass rate. This is because carbon oxidation is diffusion-limited in this test case (with oxygen being completely consumed at the surface due to the high wall temperature level) and hence it is practically insensitive to the wall temperature variation. This sensitivity analysis shows that, as long as the wall temperature is correctly reproduced, the model is able to predict the mass blowing rate with good accuracy.

Finally, Figs 11 and 12 show a comparison of the results obtained assuming a different TPS material: carbon-phenolic. In addition to the assumptions made in energy balance of Eq. (5), the pyrolysis gas injection rate, at steady-state, can be expressed by $\dot{m}_g/\dot{m}_c = (\rho_v/\rho_c - 1)$, where ρ_v and ρ_c are the virgin and char material density, respectively. Thus, assuming a PICA-like carbon-phenolic material, the pyrolysis gas injection rate is around 21% of the carbon char mass blowing rate [4]. When a carbon-phenolic material is assumed, due to the blowing effect of the pyrolysis gas injection, both the sublimation and the oxidation mass rates are reduced (Fig 11) as well as the surface temperature (Fig 12). It is interesting to see that the sublimation mass rate is more significantly reduced due to the combined effect of the pyrolysis gas blowing effect and the surface temperature reduction. Despite the oxidation and sublimation mass rate reduction, the total mass rate is increasing due to the added pyrolysis mass rate.

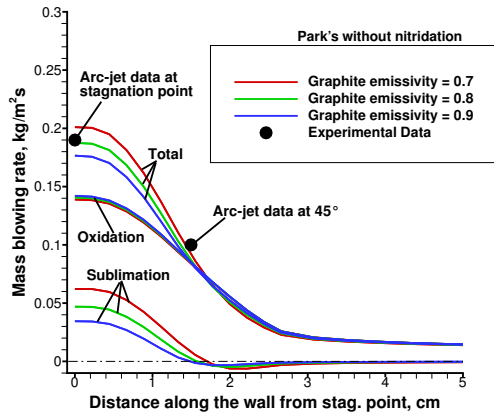


Figure 9: Carbon mass blowing rate distributions for different graphite emissivities.

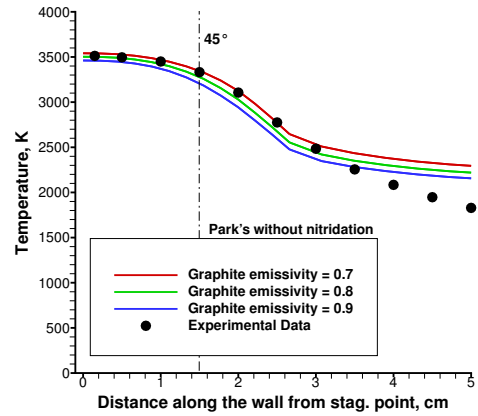


Figure 10: Surface temperature distributions for different graphite emissivities.

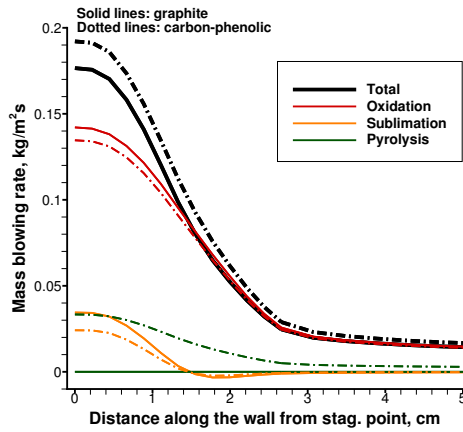


Figure 11: Mass blowing rate distributions for different materials.

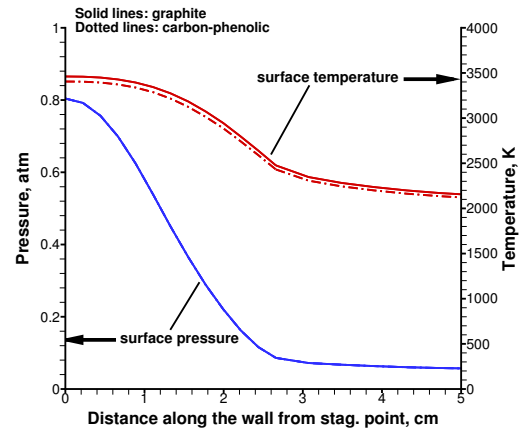


Figure 12: Surface temperature distributions for different materials.

5. CONCLUSIONS

The formulation of a finite-rate surface boundary conditions for carbon-based material ablation with pyrolysis gas injection has been developed for a 3-D reacting Navier-Stokes equation solver, to predict ablation response of carbon-based heat shields on reentry space vehicles. Solutions for an arc-jet test case, using Park's finite rate ablation model and a 18-species gas-phase chemical reaction model, have been obtained and compared with experimental data. With the nitridation reaction, the model overpredicts the graphite mass blowing rate by almost 40% with respect to arc-jet data at the stagnation point and by 30% at 45 from the stagnation point, assuming a graphite emissivity of 0.9. Without the nitridation reaction, the model underpredicts the graphite mass blowing rate by 7% with respect to arc-jet data at the stagnation point and by 15% at 45 from the stagnation point. The agreement with the surface temperature is also satisfactory, especially in the spherical part of the body where the heat fluxes are higher and hence the steady-state ablation approximation represents a suitable assumption. Moreover, if the graphite emissivity is varied to obtain a better agreement with the experimental temperature, the agreement with the experimental mass blowing rate is improved. Therefore, when the wall temperature is correctly predicted, the model is able to predict the mass blowing rate with satisfactory accuracy.

ACKNOWLEDGMENTS

This study was performed in the frame of the Contract No. 4200 104 697 on *Hypersonic Flow Analysis with Gas-Surface Interaction Modeling* with the European Space Agency ESA-ESTEC Centre.

REFERENCES

- [1] Y. K. Chen, F. Milos, and T. Gokcen. Loosely coupled simulation for two-dimensional ablation and shape change. *Journal of Spacecraft and Rockets*, 47(5), 2010.
- [2] A. Beeman, M. Lewis, R. Starkey, and B. Cybyk. Significance of nonequilibrium surface interactions in stardust return capsule ablation modeling. *Journal of Thermophysics and Heat Transfer*, 23(3), 2009.
- [3] D. Bianchi, F. Nasuti, and M. Onofri. Aerothermodynamic analysis of reentry flows with coupled ablation. AIAA Paper 2011-2273, 2011. doi: 10.2514/6.2011-2273.
- [4] Y. K. Chen and F. S. Milos. Navier-stokes solutions with finite rate ablation for planetary mission earth reentries. *Journal of Spacecraft and Rockets*, 42(6), 2005.
- [5] D. Bianchi, F. Nasuti, M. Onofri, and E. Martelli. Thermochemical erosion analysis for graphite/carbon-carbon rocket nozzles. *Journal of Propulsion and Power*, 27(1):197–205, 2011. doi: 10.2514/1.47754.
- [6] D. Bianchi and F. Nasuti. Carbon-carbon nozzle erosion and shape change in full-scale solid-rocket motors. *Journal of Propulsion and Power*, 28(4):820–830, 2012. doi: 10.2514/1.58842.
- [7] D. Bianchi and F. Nasuti. Numerical analysis of nozzle material thermochemical erosion in hybrid rocket engines. *Journal of Propulsion and Power*, 29(3):547–558, 2013. doi: 10.2514/1.B34813.
- [8] A. Turchi, D. Bianchi, F. Nasuti, and M. Onofri. A numerical approach for the study of the gas-surface interaction in carbon-phenolic solid rocket nozzles. *Aerospace Science and Technology*, 27(1):25–31, 2013. doi: 10.1016/j.ast.2012.06.003.
- [9] C. O. Johnston, P. A. Gnoffo, and A. Mazaheri. A study of ablation-flowfield coupling relevant to the orion heat-shield. AIAA Paper 2009-4318, 2009.
- [10] D. Bianchi, F. Nasuti, E. Martelli, and M. Onofri. A numerical approach for high-temperature flows over ablating surfaces. AIAA Paper 2007-4537, 2007. doi: 10.2514/6.2007-4537.
- [11] D. Bianchi, F. Nasuti, and E. Martelli. Navier-stokes simulations of hypersonic flows with coupled graphite ablation. *Journal of Spacecraft and Rockets*, 47(4):554–562, 2010. doi: 10.2514/1.47995.
- [12] F. S. Milos and D. J. Rasky. Review of numerical procedures for computational surface thermochemistry. *Journal of Thermophysics and Heat Transfer*, 8(1), 1994.
- [13] R. M. Kendall, E. P. Bartlett, R. A. Rindal, and C. B. Moyer. An analysis of the chemically reacting boundary layer and charring ablator. part i: Summary report. NASA CR 1060, 1968.
- [14] C. Park and H. K. Ahn. Stagnation-point heat transfer rates for pioneer-venus probes. *Journal of Thermophysics and Heat Transfer*, 13(1), 1999.
- [15] C. Park. *Nonequilibrium Hypersonic Aerothermodynamics*. Wiley, New York, 1990.
- [16] C. Park. Stagnation-point ablation of carbonaceous flat disks, part 1: Theory. *AIAA Journal*, 21(11):1588–1594, 1983.
- [17] Y. K. Chen and T. Gokcen. Effect of non-equilibrium surface thermochemistry in simulation of carbon based ablaters. AIAA Paper 2012-2747, 2012.
- [18] S. Gordon and B. J. McBride. Computer program for calculation of complex chemical equilibrium compositions and applications. NASA RP 1311, 1994.
- [19] C. Park. Calculation of stagnation-point heating rates associated with stardust vehicle. *Journal of Spacecraft and Rockets*, 44(1), 2007.
- [20] D. Olynick, Y. K. Chen, and M. E. Tauber. Aerothermodynamics of the stardust sample return capsule. *Journal of Spacecraft and Rockets*, 36(3), 1999.
- [21] C. Park. Review of chemical-kinetics problems of future nasa missions, i: Earth entries. *Journal of Thermophysics and Heat Transfer*, 7(3), 1993.
- [22] C. Park, J. T. Howe, and R. L. Jaffe. Review of chemical-kinetics problems of future nasa missions, ii: Mars entries. *Journal of Thermophysics and Heat Transfer*, 8(1), 1994.
- [23] Y. K. Chen, F. S. Milos, D. C. Reda, and D. A. Stewart. Graphite ablation and thermal response simulation under arc-jet flow conditions. AIAA Paper 03-4042, 2003.

Investigations about gas-surface interactions modelling for high speed earth re-entry

8-10 April 2013

ESA/ESTEC, Noordwijk, The Netherlands

B. Aupoix⁽¹⁾, A. Bourgoing⁽²⁾, B. Chanetz⁽¹⁾, D. Coponet⁽¹⁾, B. Rey⁽³⁾ and J. Vos⁽³⁾

⁽¹⁾Onera

Chemin de la Hunière, 91761 Palaiseau, France

Email: aupoix@onera.fr ; chanetz@onera.fr

⁽²⁾Astrium Space Transportation

51-61 route de Verneuil 78130 Les Mureaux, France

Email: ALEXIS.BOURGOING@astrium.eds.net

⁽³⁾CFS Engineering

PSE-A, 1015 Lausanne, Switzerland

Email: benoit.rey@cfse.ch ; jan.vos@cfse.ch

ABSTRACT/INTRODUCTION

Re-entry capsules in general use an ablative Thermal Protection System (TPS) because it reduces the heat load to the internal structure due to the effect of blowing at the wall. However, the ablating TPS leads to rough walls, and it is well known that rough walls have the effect to increase the heat load. The objective of the research presented in this paper is to better understand these physical phenomena in order to reduce margins on the Thermal Protection System (TPS). An experimental study was performed to test smooth and rough surfaces with and without blowing in order to reproduce what happens in reality on the TPS when a massive ablation occurs during an atmospheric re-entry. One wanted to analyse precisely the likely antagonist effects on the heat flux level due to the surface roughness after pyrolysis and the blowing effect due precisely to the pyrolysis effects. The experimental study was carried out in a cold wind tunnel at Onera. So it was required to use a material that simulates the deterioration of the wall surface state. For this purpose the wall in the experimental device was made out of rough porous ceramics in order to reproduce the real surface after ablation and also to blow air through the wall in order to simulate the real blowing due to ablation in reality. The experimental results thus obtained have been compared with numerical results from both boundary layer and Navier-Stokes approaches.

1) THE EXPERIMENTAL STUDY

The ONERA Meudon center R2Ch wind tunnel was used for the experiments. R2Ch wind tunnel is a blow-down facility (test duration between 15 and 30 seconds) equipped for these tests with a Mach 5 nozzle. The tests were performed for stagnation pressures from $p_{st} = 7 \cdot 10^5$ Pa to $p_{st} = 50 \cdot 10^5$ Pa which corresponds to unit Reynolds number from $Re_L = 5.95 \cdot 10^6$ to $Re_L = 42.5 \cdot 10^6$ with $T_{st} = 650$ K. The infrared thermography technique was used for the heat flux measurements. Successive thermograms were recorded at a frequency of 50 Hz and, for a known local heat capacity of the wall, the analysis of successive thermograms yields the heat flux on the investigated surface. In addition, four thermocouples implemented at the wall were used to check the infrared results.

A flat plate model with a sharp leading edge at 0° incidence was used for experiments. An exploded view of the set-up in the R2Ch test-chamber is shown in figure 1. On the left is the nozzle. The model may receive two inserts: one made out of steel (isotan) and one made out of ceramics represented in green on the picture. To ensure a blowing from inside to outside, the model was pressurized.

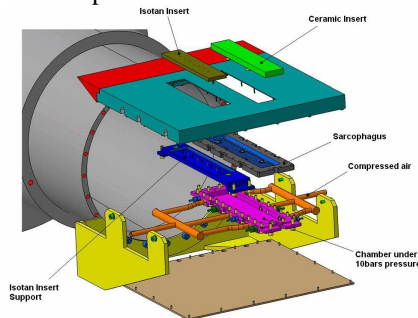


Figure1: Exploded view of the experimental set-up

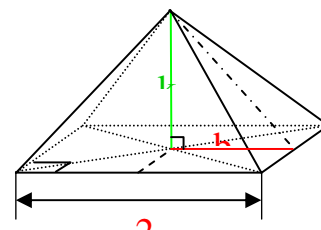


Figure 2: Sketch of a pyramid

An academic configuration (flat plate with regular roughness) was selected to permit easily numerical simulations. Indeed irregular roughness – as those obtained in reality during a re-entry flight - could not be taken into account by a model. The decision was made to reproduce a regular roughness pattern constituted by pyramidal elements such as shown in figure 2 (k-type roughness). The base of the pyramid is a square, each side being equal to $2b$. The height is k . The shape of the pyramid is defined by the ratio k/b fixed to 1, which leads to a theoretical angle of 45° .

A rough insert was manufactured

- a regular pattern constituted by pyramidal roughness ;
- the base of each pyramid is a square, each side around $2b = 550 \mu\text{m}$;
- the mean value of the height k of each pyramid is $176 \mu\text{m}$ with a standard error equal to $34 \mu\text{m}$

To simulate the effect of an ablating wall, pressurized air was blown through the porous wall from a tank located under the insert. The mass flow rate level was determined in order to have a simulation in agreement with the reality along a classical re-entry trajectory.

To remove the uncertainty due to transitional flows, transition was triggered in most of the runs using a rough band. This band had the following characteristics:

- location at $X = 30 \text{ mm}$ from the leading edge
- width along X-axis : 12 mm
- diameter of the carborandum spheres slied at the wall : 0.7 mm

Thirty-one documented runs were performed in the hypersonic R2Ch wind tunnel for various conditions (porous and rough wall, with and without blowing, different Reynolds numbers). The heat-fluxes were determined from the evolution of the temperature – detected by infrared thermography - during the first seconds of the run. The Stanton numbers have then been calculated from these values by the following formula:

$$St = \Phi / \rho_{\text{inf}} U_{\text{inf}} C_p (T_{\text{st}} - T_w)$$

where

- Φ is the heat-flux in W/m^2 ,
- ρ_{inf} and U_{inf} respectively are the density and the velocity delivered by the nozzle ;
- T_{st} is the stagnation temperature ;
- T_w is the wall temperature ;
- C_p is the calorific coefficient at constant pressure, equal to 1003 J/kg/K .

For each run, a Schlieren photograph of the flow was carried out. Figure 3a shows the case using a smooth insert in natural transition without blowing. Figure 3b is representative of experiments with triggered transition. One sees downstream the shock wave emanating from the sharp leading edge, a second shock wave which is not present in figure 3a. This shock is induced by the rough band located at 30 mm from the leading edge to trigger the transition. The following shock wave for the two visualisations is relative to the beginning of the insert at 140 mm from the leading edge.

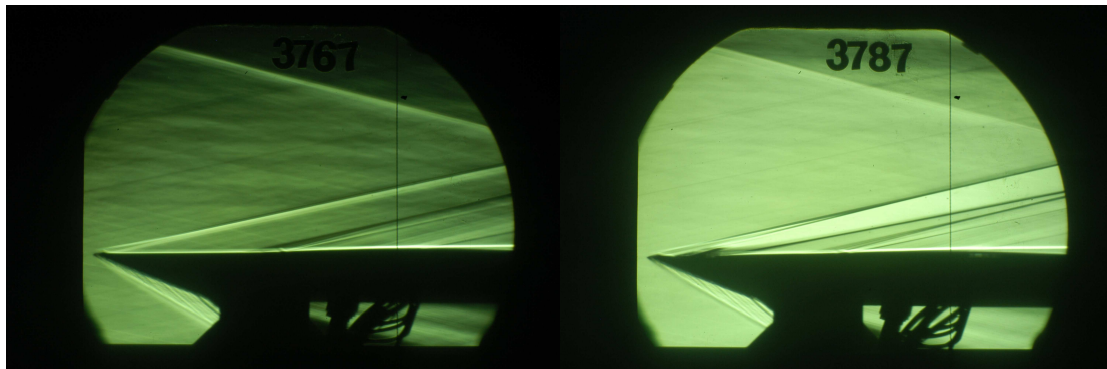


Fig . 3 Schlieren photograph for $p_{\text{st}} \sim 50 \cdot 10^5 \text{ Pa}$ on the smooth insert with blowing rate 4.8 g/s
a) natural transition run (3763) b) triggered transition (run 3787)

2) BOUNDARY LAYER ANALYSIS OF THE EXPERIMENTS

2.1 Foreword

Nearly all 31 runs were computed, with various hypotheses on the wall temperature, the transition location, the turbulence model, which led to a total of 244 cases, only some of them being reported here. The ONERA boundary layer code [3] has a large variety of transition and turbulence models, and an adaptive grid generation which ensures grid convergence. Transition can be either natural or tripped. For natural transition, Arnal [1] gives, for that wind tunnel and at Mach number five, a transition Reynolds number $\rho_e u_e x / \mu_e$ between $2 \cdot 10^6$ and $3.5 \cdot 10^6$. For tripped transition, Reda [8] criterion was used. Moreover, a lag between the trip location and the start of the transition region may appear at this Mach number. At last, the transition can be computed as abrupt or smooth, an intermittency function [1] being used to model the growth of turbulence for a smooth transition.

Several turbulence models were investigated:

- Mixing length models, with the classical van Driest [10] model and the CLIC model which is specific to the code and is a variant of the van Driest model with more elaborate wall treatments. Wall blowing and wall roughness can be accounted for in these models, by altering the wall damping. Moreover, both effects can be considered together.
- The one equation model by Spalart and Allmaras [9]. There is no wall blowing correction available but two roughness corrections by Boeing and ONERA [2].
- The $k-\omega$ BSL and SST models from Menter [7] and Wilcox [14] are available. Wall blowing and wall roughness corrections are available but cannot be used together. Moreover, these corrections are known to interact with the SST limiter (Hellsten and Laine [6]).

All roughness corrections are based upon the equivalent sand grain concept. Therefore, this equivalent sand grain height has to be determined. The real roughness elements can be viewed as truncated pyramids, with a basis of $550 \mu\text{m}$, a gap of $50 \mu\text{m}$ between them, slopes of 45° and an average height of $175 \mu\text{m}$. Using either Grabow and White [5] or Flack and Schultz [4] correlations, an equivalent sand grain roughness about $400 \mu\text{m}$ is obtained. The wall temperature is assumed to be 300K .

2.2 Smooth wall cases, without wall blowing for high stagnation pressure

These simple cases were used to check the ability to correctly account for the transition process and reproduce the flow physics. So determined transition settings will be used after.

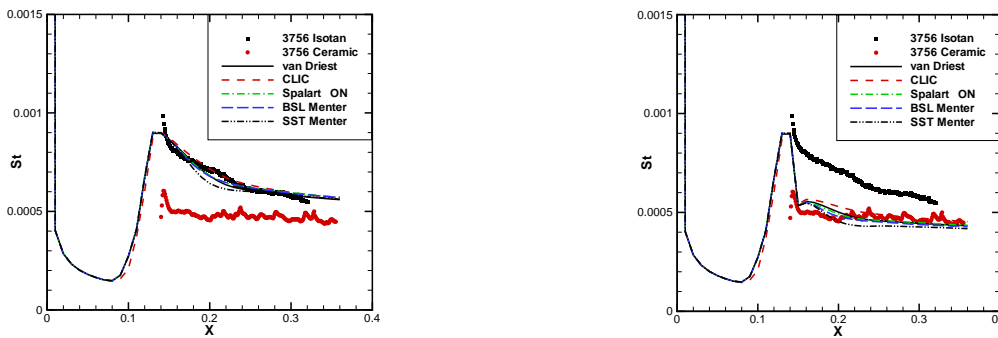


Figure 4 : Stanton number predictions for a smooth surface, $p_{st} = 50 \cdot 10^5 \text{ Pa}$, natural transition

a) calculations with : $T_w = 300\text{K}$,

b) calculations with : $T_w = 400\text{K}$

For natural transition conditions, the more upstream the transition point, the thicker the boundary layer in the measurement region and the lower the Stanton number. A fair agreement with the measurements on the Isotan is achieved for a transition location 70 mm downstream of the leading edge (Figure 4a). Moreover, little differences are observed between the various models predictions. For the ceramic insert, the wall temperature has to be increased to 400 K (Figure 4b), which is roughly its temperature at the end of the run, to achieve a fair agreement.

For tripped transition, Reda's criterion confirms that the wire is able to trip the transition. The best agreement with experiments is obtained assuming a smooth transition. Again, the wall temperature has to be increased to get fair predictions on the ceramic insert.

2.3 Smooth wall cases, with wall blowing

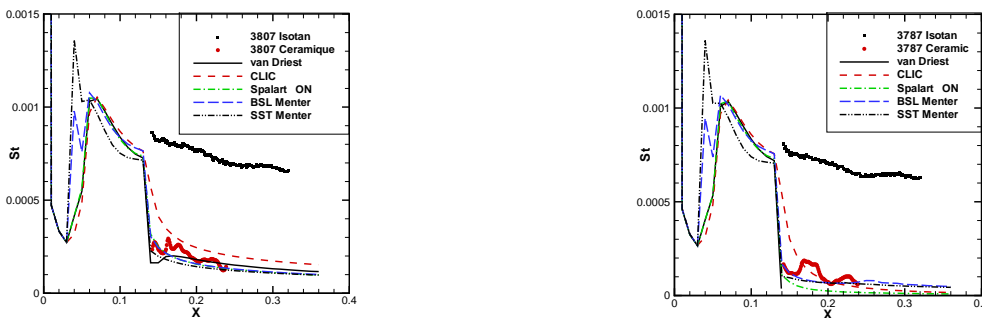


Figure 5: Stanton number predictions for a smooth surface, with wall blowing $p_{st} = 50 \cdot 10^5 \text{ Pa}$

a) blowing rate : $0.65 \text{ kg/m}^2/\text{s}$

b) blowing rate : $1.2 \text{ kg/m}^2/\text{s}$

The effect of wall blowing on the Stanton number is rather well reproduced by all models, for the two investigated blowing rates (Figures 5a and 5b). For these blowing cases, computations have to be compared only to measurements on the ceramics, the ones on the Isotan giving Stanton numbers without blowing. It can be noticed that the lag on wall blowing effects in the CLIC model deteriorates the prediction. For the highest blowing rate, the Spalart and Allmaras model, which accounts for wall blowing only through a change in the wall condition but without any enhancement of the near-wall turbulence due to the blowing, underpredicts the Stanton number. The primary blowing effect is thus due to the change in the wall normal velocity but a correct modelling of turbulence enhancement due to wall blowing is mandatory for significant wall blowing.

2.4 Rough wall, without wall blowing

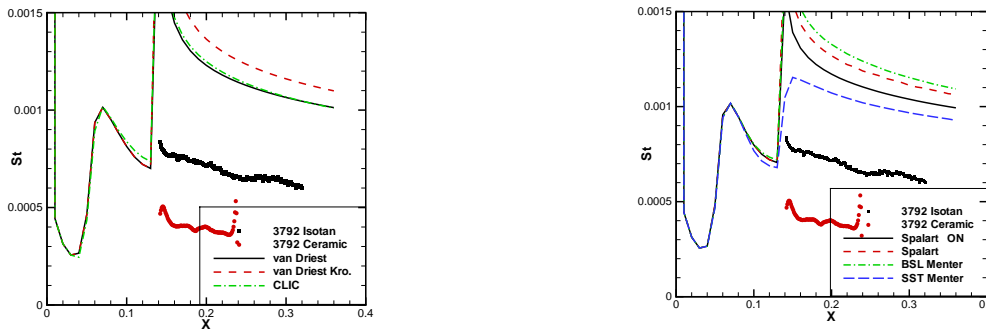


Figure 6 : Stanton number predictions for a rough surface, without wall blowing $p_{st} = 50 \cdot 10^5$ Pa

a) algebraic models

More models are now considered, as the van Driest model can be coupled with the Rotta's and Krogstad's (Kro.) roughness corrections, while Blanchard's correction is used in the CLIC model. Similarly, the ONERA (ON) and Boeing corrections are used for the Spalart and Allmaras model. This rough wall experiment corresponds to a reduced equivalent sand grain height $k_s^+ = \rho_w u_\tau k_s / \mu_w$ about 120, i.e. the flow is in the fully rough regime. Figure 6 shows that all models predict similar Stanton number increase on the rough ceramic, with a level about twice that on a smooth surface, while unexpectedly experiments show a decrease. Computations using a higher wall temperature and a smooth surface yet predict higher Stanton numbers than measured on the ceramics, so that this behaviour remains unexplained. Some scatter among roughness correction predictions can be evidenced, the SST model underpredicts the roughness effect thanks to interference between the roughness correction and the SST limiter.

b) transport equation models

2.5 Rough wall, with wall blowing

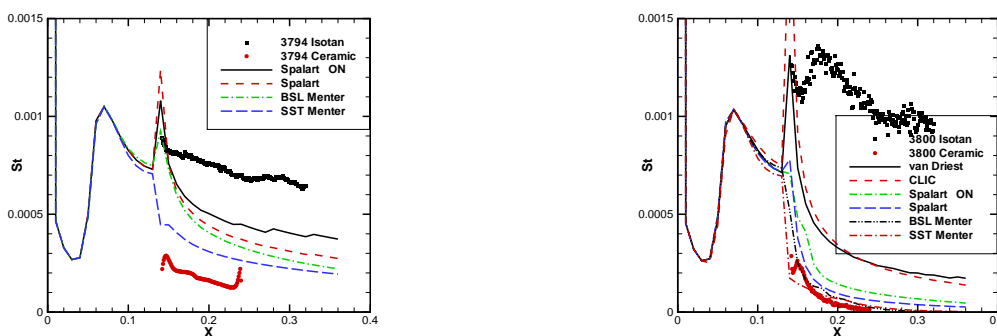


Figure 7: Stanton number predictions for a rough surface, with wall blowing $p_{st} = 50 \cdot 10^5$ Pa

a) blowing rate : 0.65 kg/m²/s

b) blowing rate : 1.2 kg/m²/s

Figure 7 evidences that the blowing effect is much stronger than the roughness effect so that the Stanton number is reduced compared to the smooth wall case. Depending upon the blowing rate and the model, the reduced equivalent sand grain roughness k_s^+ is now between 30 and 60, i.e. the flow is in the transition regime. For the lowest blowing rate (Figure 7a), trends are similar to those without blowing, i.e. the same scatter among models and an overestimation of the measured Stanton numbers. For the highest blowing rate (Figure 7b), algebraic models which account for both wall roughness and wall blowing effects on turbulence still overestimate the measured Stanton numbers while a better agreement is fortuitously achieved with the Spalart and Allmaras and $k-\omega$ models which cannot account for the enhancement of turbulence due to wall blowing in presence of wall roughness.

3) NAVIER STOKES SIMULATIONS OF THE EXPERIMENTS

3.1 Calculation Matrix and set-up

From the experimental results and the results of the boundary layer computations, six cases were selected at a stagnation pressure of $50 \cdot 10^5$ Pa for rebuilding using the NSMB (Navier Stokes Multi Block) CFD solver [12], see Table 1.

Case	1	2	3	4	5	6
Run #	3782	3807	3787	3792	3794	3800
Blowing rate (kg/m ² /s)	0	0.65	1.2	0	0.6575	1.15
Roughness (μ m)	smooth	smooth	smooth	176	176	176

Table 1: Experimental cases selected for Navier Stokes simulations.

The free stream conditions for each of these cases are summarized in Table 2, which are based on the actual measured values.

		Case 1	Case 2	Case 3	Case 4	Case 5	Case 6
Mach		5	5	5	5	5	5
P _{st}	Pa	4'870'956	4'854'826	4'9098'12	4'740'064	4'883'531	4'880'887
T _{st}	K	668	666	656	617	657	641
Reynolds	1/m	39'422'781	39'451'803	40'871'820	43'261'722	40'521'610	42'092'077
Tw	K	410	350	320	380	330	320

Table 2: Free stream conditions Navier Stokes simulations.

P_{st} and T_{st} are respectively the stagnation pressure and temperature, corresponding to the reservoir conditions. Due to the blowing of cold air through the porous wall, the wall temperature is lower for the cases with blowing.

In all calculations transition was imposed at a distance of 0.03 m from the leading edge of the plate. A distance of 0.00124 m was used to go from a laminar to a fully turbulent flow.

Two grids were used in the CFD simulations, a 19'200 cells grid used for all conditions, and a 76'800 cells grid to assess the influence of the grid on the results. The grid was clustered near the wall to obtain a y^+ value near the wall smaller than 0.2. The grid was made such that it was easy to impose roughness and blowing wall conditions. At the inflow boundary, the values of P_{st} and T_{st} were set to the values given in Table 2, at the outflow boundaries, boundary conditions were imposed using Riemann invariants, and at the wall a constant wall temperature was imposed. In the case of blowing the normal velocity component was imposed at the wall.

All calculations were made using the 4th order central space discretization scheme. The equations were integrated in time using the LU-SGS scheme. Convergence was judged by the reduction of L2-residual for the continuity equation. About 2'000 iterations were needed to obtain a reduction of 3 orders of magnitude in L2-residual which is sufficient for convergence. In practice all calculations were performed until 10'000 iterations.

3.2 Rebuilding the Wind Tunnel Experiments

This section presents the results of the rebuilding of the experiments. Results of the NSMB CFD calculations (solid lines with symbols) are compared with experimental results and with results from boundary layer solver calculations (solid lines). In the boundary layer solver calculations the transition from a laminar to a turbulent flow is done using an intermittency function, which explains the large differences in Navier Stokes and boundary layer solver Stanton numbers in the region until the ceramic insert (between $x=0.03$ m and $x=0.15$ m).

3.2.1 Case 1: Smooth Insert, No blowing

Figure 8 shows the Stanton number for the case with a smooth insert without blowing. As can be seen in this figure, the computed Stanton number using NSMB for both turbulence models are very close. Differences in Stanton number exist

mainly in the transition region (around $x=0.03$ m) where the computed results obtained using the $k-\omega$ Menter Shear Stress model show some oscillations. Comparing the computed results with the experimental results on the ceramic insert shows a good agreement. The computed results are also in good agreement with the results of boundary layer calculations.

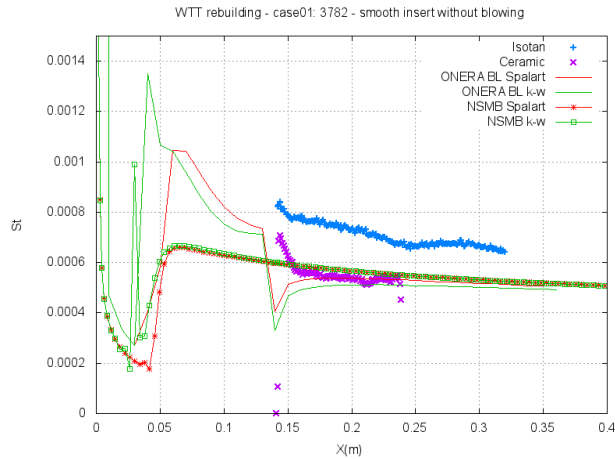


Figure 8 : Stanton number for case1: smooth insert, no blowing.

3.2.2 Case 2 and 3: Smooth Insert, blowing $0.6 \text{ kg/m}^2/\text{s}$ and blowing $1.2 \text{ kg/m}^2/\text{s}$

Figure 9 shows the Stanton number for this case. Until the start of the ceramic insert (at $x=0.138\text{m}$) the computed Stanton number is very close to the results for the case without blowing, as was to be expected. On the Ceramic insert the computed Stanton number using the Spalart Allmaras turbulence model is slightly higher than the one computed using the $k-\omega$ Menter Shear Stress model. For the Spalart Allmaras turbulence model there is also a good agreement between the Navier Stokes and boundary layer calculations. Both Navier Stokes and boundary layer calculations slightly underestimate the measured Stanton number in the middle of the ceramic insert.

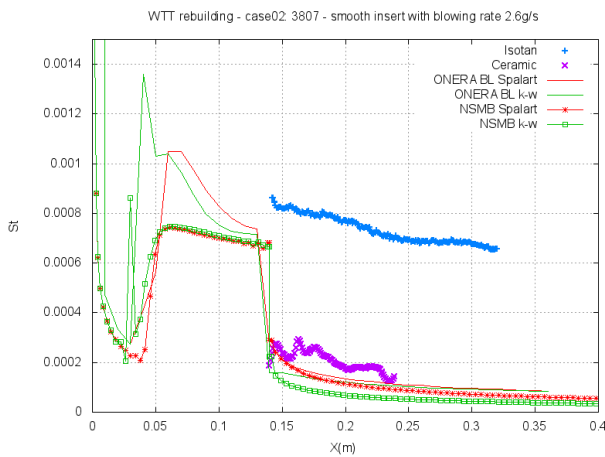


Figure 9 : Stanton number for case 2

smooth insert, blowing rate: $0.6 \text{ kg/m}^2/\text{s}$

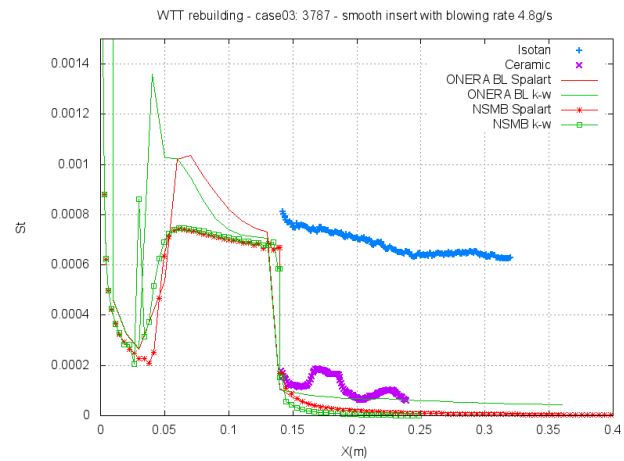


Figure 10: Stanton number for case 3

smooth insert, blowing rate: $1.2 \text{ kg/m}^2/\text{s}$

Figure 10 shows the Stanton number for the case with a smooth insert with blowing at 4.8g/s , and the same observations as for the case with lower blowing rate can be made. The computed Stanton number on the ceramic insert using the Navier Stokes and boundary layer calculations with the Spalart Allmaras turbulence model are almost equal. For the Navier Stokes calculations the computed Stanton number using the $k-\omega$ Menter Shear Stress model is slightly lower than the results obtained using the Spalart Allmaras turbulence model, but the opposite behavior is found for the boundary layer calculations. The best agreement with the measured Stanton number is obtained with the boundary layer solver using the $k-\omega$ Menter Shear Stress model.

3.2.3 Case 4: Rough Insert, no blowing

Figure 11 shows the Stanton number for the case with a rough insert without blowing. Up to the Ceramic insert the Stanton numbers are equal to the results obtained for the smooth insert. The computed Stanton number using the Spalart Allmaras model obtained using the Navier Stokes and boundary layer solvers are very close, and the same observation can be made when using the $k-\omega$ model using the Knopp method (labeled model 1) to account for roughness. Using the Wilcox method (model 2) to account for roughness leads to slightly higher Stanton numbers compared to the results obtained with the Spalart Allmaras turbulence model.

Comparison of the computed Stanton number with the measured values shows large differences that are difficult to explain. It is expected that the Stanton number increases due to the surface roughness, and this is confirmed by the results from the boundary layer and Navier Stokes simulations. The experiments show an opposite trend: for the smooth insert the measured Stanton number is around 0.00057, while for the rough insert the measured Stanton number is lower and around 0.0004 (see Figure 11).

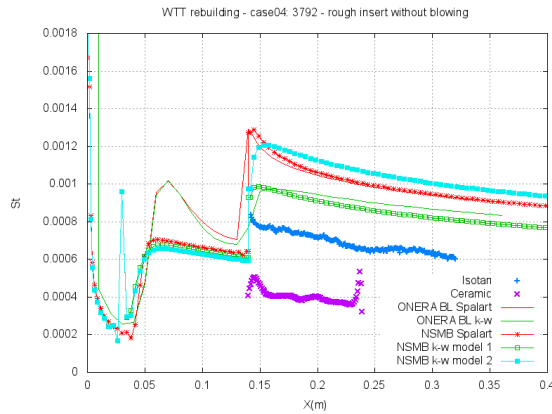


Figure 11 : Stanton number for case 4, rough insert, no blowing.

3.2.4 Cases 5 and 6 : Rough Insert, blowing $0.6575 \text{ kg/m}^2/\text{s}$ and $1.15 \text{ kg/m}^2/\text{s}$

Figure 12 shows the Stanton number for the case with a rough insert with blowing at $0.6575 \text{ kg/m}^2/\text{s}$. The computed Stanton number using the Spalart Allmaras model calculated with the Navier Stokes and boundary layer solvers are very close, and they yield higher Stanton numbers than the results obtained using the $k-\omega$ model and compared to the experimental results. A very good agreement with the measured Stanton number is obtained with the Navier Stokes simulations using the $k-\omega$ Menter Shear Stress model and model 1 (Knopp method) to account for roughness. Using the Wilcox method (model 2) to account for roughness leads to higher Stanton numbers, which are comparable to the results of the boundary layer calculations using the $k-\omega$ Menter Shear Stress model.

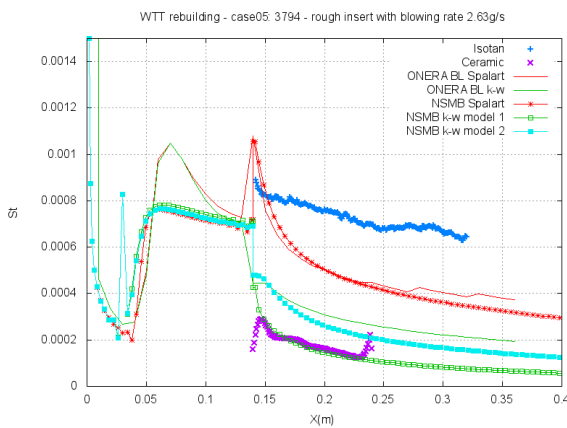


Figure 12 : Stanton number for case 4
rough insert, blowing rate : $0.6575 \text{ kg/m}^2/\text{s}$

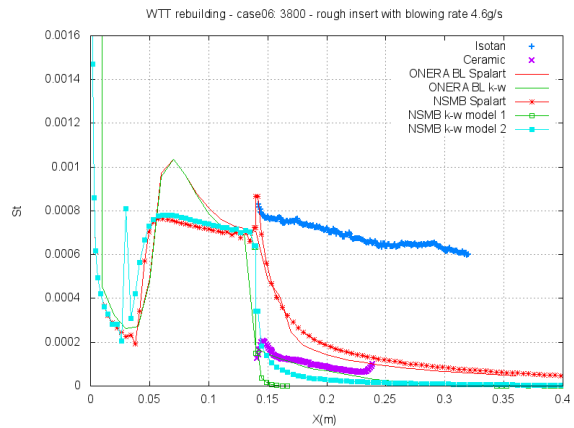


Figure 13 : Stanton number for Case 6
rough insert, blowing rate : $1.15 \text{ kg/m}^2/\text{s}$

Figure 13 shows the Stanton number for the case with a rough insert with blowing at $1.15 \text{ kg/m}^2/\text{s}$. Again the computed Stanton number using the Spalart Allmaras model obtained using the Navier Stokes and boundary layer solvers are close, and they yield higher Stanton numbers than the results obtained using the $k-\omega$ model and compared to the experimental results. A very good agreement with the measured Stanton number is obtained with the boundary layer

simulations using the $k-\omega$ Menter Shear Stress model. The Navier Stokes simulations using the $k-\omega$ Menter Shear Stress model show a reasonable agreement with experimental results when using the Wilcox method to account for roughness (and blowing).

CONCLUSION

The objective of the research presented here was to analyze in detail the coupling between surface roughness and blowing in the turbulent flow regime. It was expected that the roughness effect tends to increase the turbulent heating whereas the blowing effect tends to decrease the heating. Unfortunately an essential point of interrogation concerns the experimental results obtained without blowing in the case of the rough insert versus the smooth insert. An abnormal decrease of heat-flux in the presence of the rough wall was observed compared to the similar case with the smooth wall, while one expected on the contrary an increase of heat-flux with roughness.

A total of 31 experimental runs were made on flat plate inserts for three stagnation pressure (7, 28 and $50 \cdot 10^5$ Pa), with natural and tripped transition and a large quantity of valuable experimental data have been acquired. The approach employed to reach massive blowing was validated. The blowing effect on smooth insert leads to a huge decrease of heat flux.

The rebuilding of the runs was performed thanks to boundary layer approach which allows a large parametric investigation. Three turbulence model families were tested: algebraic, one transport and two transport equations among popular turbulence models employed for industrial applications.

A good agreement between the different solvers (Boundary Layer technique – ONERA) and NSMB (CFSE) was found. The intermediate blowing mass flow cases are rather well predicted by all models and engineering methods. The strong blowing mass flow run points out the need for a blowing correction in the Spalart and Allmaras model. Cebeci's correction for wall blowing seems to be too strong. The $k-\omega$ model predicts Stanton number in agreement with experiments. For rough wall, models predict heat flux increase as expected, while experiments show heat flux decrease. The roughness and blowing effects are more complicated to simulate and a large scattering between experimental data and the computations predictions is observed. Since high levels of blowing are obtained during this campaign there is need to have lower levels of blowing to fully describe the blowing effect.

Author names appear in alphabetic order

REFERENCES

- [1] D. Arnal, 1988, *Laminar-turbulent transition problems in supersonic and hypersonic flows*, Special Course on Aerothermodynamics of Hypersonic Vehicles, AGARD Report No. 761.pp 8-1 - 8-45, VKI Institute
- [2] B. Aupoix and P.R. Spalart, 2003, *Extensions of the Spalart-Allmaras turbulence model to account for wall roughness*. International Journal of Heat and Fluid Flows, Vol. 24, pp 454-462
- [3] B. Aupoix, 2010, *Couches limites bidimensionnelles compressibles. Descriptif et mode d'emploi du code Clicet - version 2010*, Technical Report RT 1/117015 DMAE, ONERA
- [4] K.A. Flack and M.P. Schultz, 2010, *Review of hydraulic roughness scales in the fully rough regime* Journal of Fluid Engineering, Vol. 132, pp. 041203-1 - 041203-10
- [5] R.M. Grabow and C.O. White, 1975, *Surface roughness effects on nosetip ablation characteristics*. AIAA Journal, Vol. 13, N° 5, pp. 605-609
- [6] A. Hellsten and S. Laine, 1998, *Extension of the $k-\omega$ shear-stress transport turbulence model for rough-wall flows*. AIAA Journal, Vol. 36, pp. 1728-1729
- [7] F.R. Menter, 1994, *Two-equation eddy-viscosity turbulence models for engineering applications*. AIAA Journal, Vol. 32, N° 8, pp. 1598-1605
- [8] D.C. Reda, M.C. Wilder, D.W. Bogdanoff, and D.K. Prabhu, 2007, *Transition experiments on blunt bodies with distributed roughness in hypersonic free flight*. AIAA Paper 2007-306, 45th Aerospace Sciences Meeting and Exhibit, Reno, Nevada,
- [9] P.R. Spalart and S.R. Allmaras, 1992, *A one-equation turbulence model for aerodynamic flows*. AIAA Paper 92-0439, 30th Aerospace Sciences Meeting and Exhibit, Reno, Nevada
- [10] E.R. van Driest, 1956, *On turbulent flow near a wall*. Journal of Aeronautical Sciences, Vol. 23, N° 11, pp. 1007-1011 & 1036
- [11] D.C. Wilcox, 1988, *Reassessment of the scale-determining equation for advanced turbulence models*. AIAA Journal, Vol. 26, N°11, pp. 1299-1310
- [12] Vos J. B., Rizzi A. W., Corjon A., Chaput E., and Soenne E.; *Recent Advances in Aerodynamics inside the NSMB (Navier Stokes Multi Block) Consortium*. AIAA 36th Aerospace Sciences Meeting, January 1998.
- [13] T. Knopp, B. Eisfeld, J.B. Calvo, *turbulence A new extension for k- models to account for wall roughness*, International Journal of Heat and Fluid Flow, Vol. 30, pp. 54-65, 2009.
- [14] D.C. Wilcox, 1988, *Reassessment of the scale-determining equation for advanced turbulence models*. AIAA Journal, Vol. 26, N°11, pp. 1299-1310

Radiation-Shapes-Thermal Protection Investigations
*for High **Speed Earth Re-entry***

High-speed entry ablation-flight mechanics coupling effects

7th European Workshop on TPS & Hot Structures - Noordwijk (NL)
2013, April 8-10 - Session "Modelling of Ablation and Gas- Surface Interaction
(part 2)"

N. de CHAMPVALLINS (speaker) - EADS Astrium Space Transportation, Les Mureaux, France
A. BOURGOING - EADS Astrium Space Transportation, Les Mureaux, France



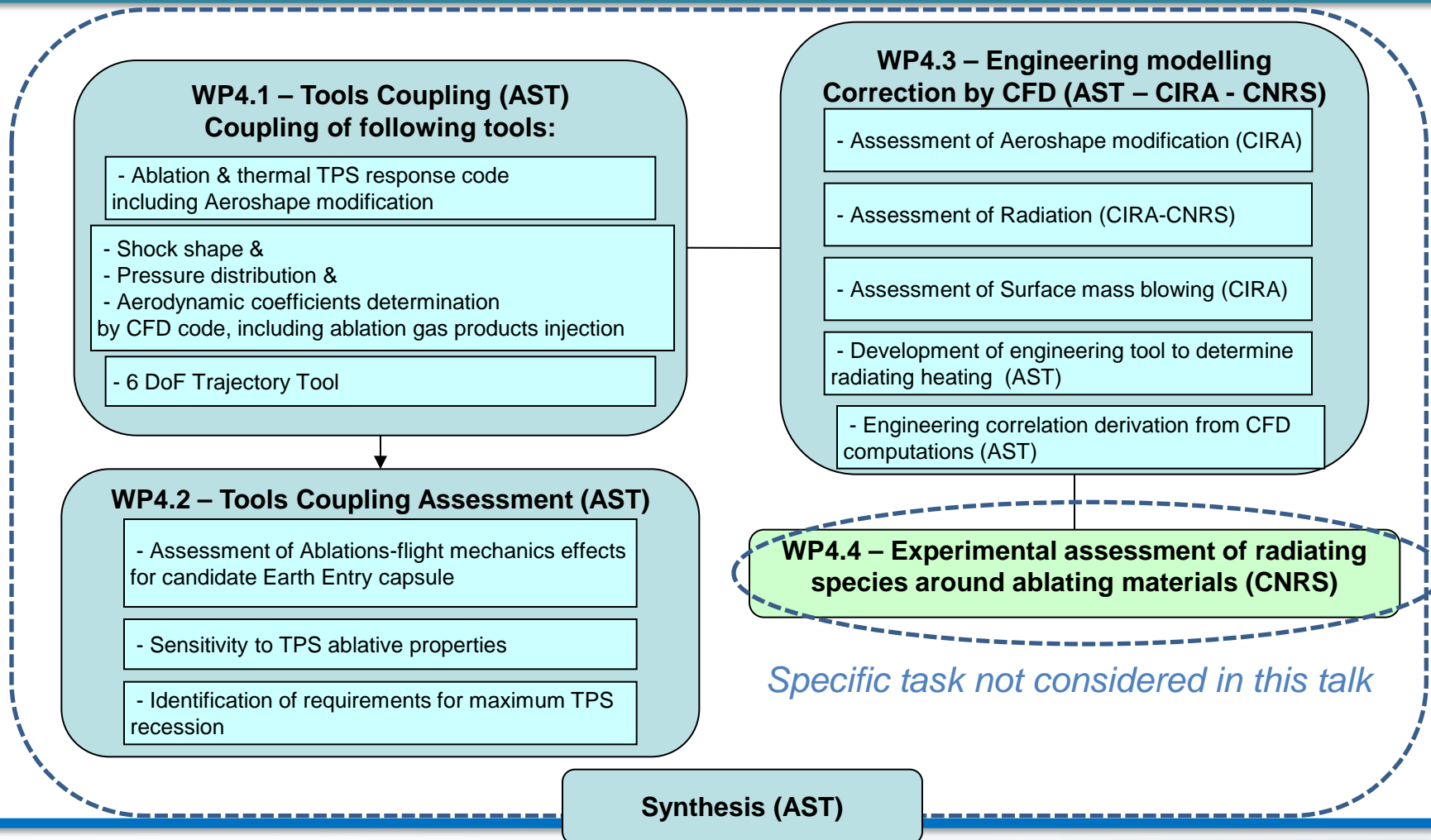
Summary

- Main objectives
- Work Logic Breakdown
- Tools coupling presentation
- Tools coupling assessment
- Engineering modelling correction by CFD
- Conclusion and Future Works

Main Objectives

- ↪ To assess impact of massive ablation on aerodynamics performances and stability
- ↪ To identify of recession level that could be tolerated with respect to capsule aerodynamic performances and stability requirements.
- ↪ To Elaborate and validate an engineering tool that couples
 - Aeroshape aerodynamic,
 - Trajectory and stability,
 - Aerothermal environments,
 - TPS material thermal response,
 - and then recession determination resulting in aeroshape modification.
- ↪ To translate these results into criteria for maximum recession requirements in relation with usual landing accuracy, g-loads, heating and incidence profile issues

Work Logic Breakdown

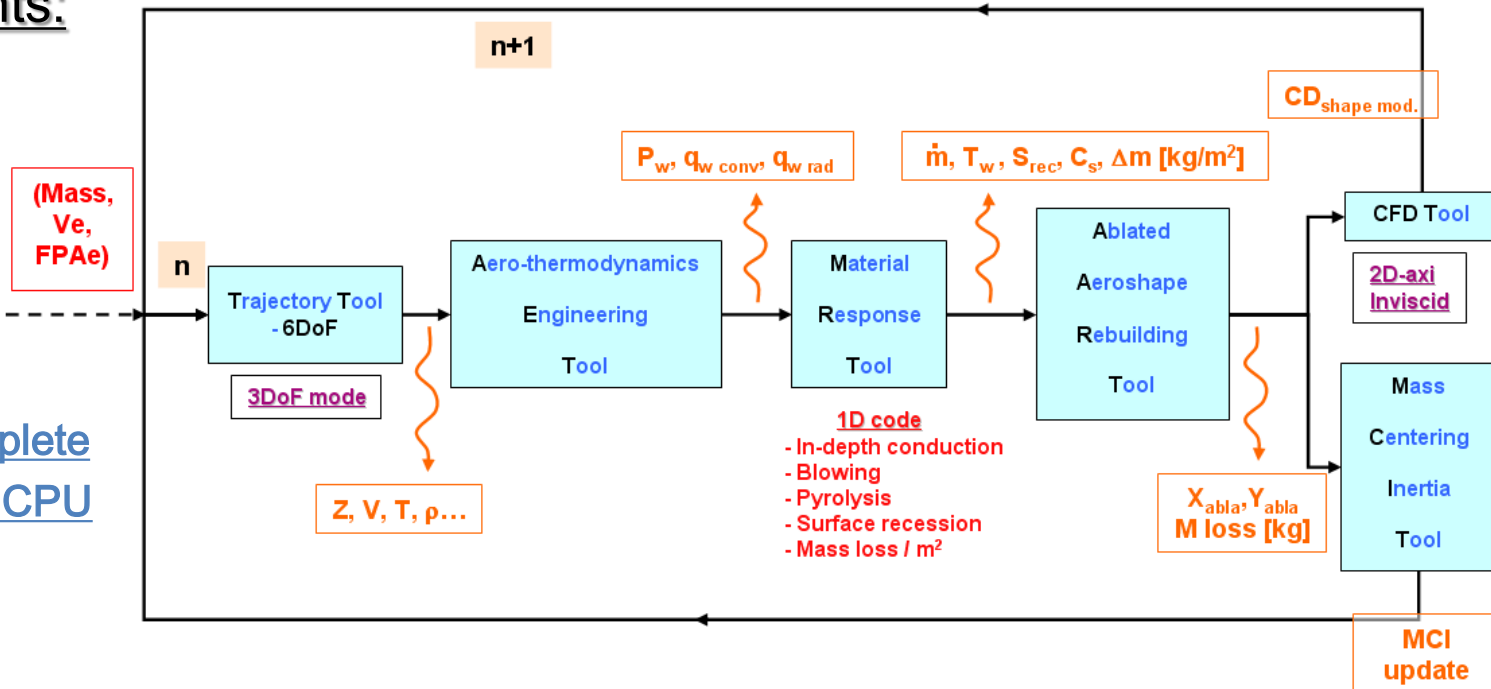


Tools coupling presentation (AST)

Initial inputs:
 - Initial profile
 - Trajectory (Ve, FPAe, Mass)
 - AEDB on initial profile

Main requirements:

- ↳ Modular tool
- ↳ Robustness
- ↳ Evolutionary tool
- ↳ To perform a complete trajectory within 12h CPU



Tools coupling assessment (AST)

- Trajectory Tool: 6DoF in 3DoF mode
- Aero-thermodynamics Engineering Tool:
 - Table of Kp
 - Convective heat flux – Engineering correlations along the profile
 - Radiative heat flux – Sutton-Graves
 - Transition criteria – post flight ARD
- Material Response Tool: Heat transfer + pyrolysis + charring-ablation 1D code
 - Pyrolysis : Arrhenius Laws of PICA
 - Ablation : Chemical tables
 - Boundary conditions: Convection + Radiation
 - Blockage effect : on convective heat flux $f(M_{\text{gas inj}}/M_{\text{air}}, T, P, \text{regime})$
- CFD Tool:
 - 2D-axi – Inviscid Real gas at equilibrium
 - Hypersonic/supersonic ($2 < M_{\infty} < 42$)
- Mass Centering Inertia Tool: Mass loss update and ΔX_{CoG} evolution

At this step no update of CD on ablated aeroshape has been made for $M < 2$

Tools coupling assessment (AST)

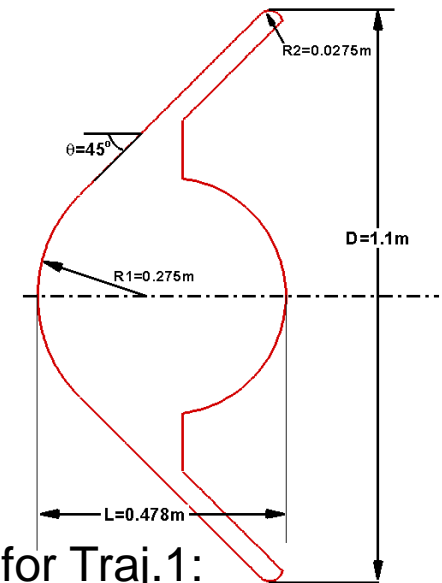
INPUTS AND ASSUMPTIONS

• Aeroshape characteristics:

R_1/D	0.25
θ° (Half cone angle)	45
R_2/D	0.025
Lref [m]	1.1
Sref [m ²]	0.95

Mass = 66.7kg

AoA=0°



• Trajectories:

	Traj. 1	Traj. 2
Entry Velocity at 120km	12.3km/s	12.3km/s
Flight path angle (FPAe)	-12.5°	-16.8°

FPAe effect

Parametric study on CD for Traj.1:

- 1st loop nominal: CD modified by shape change

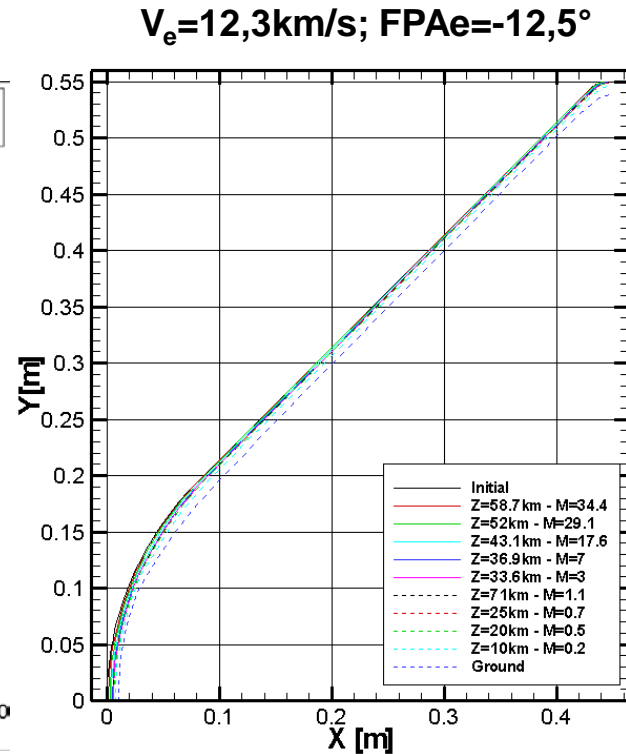
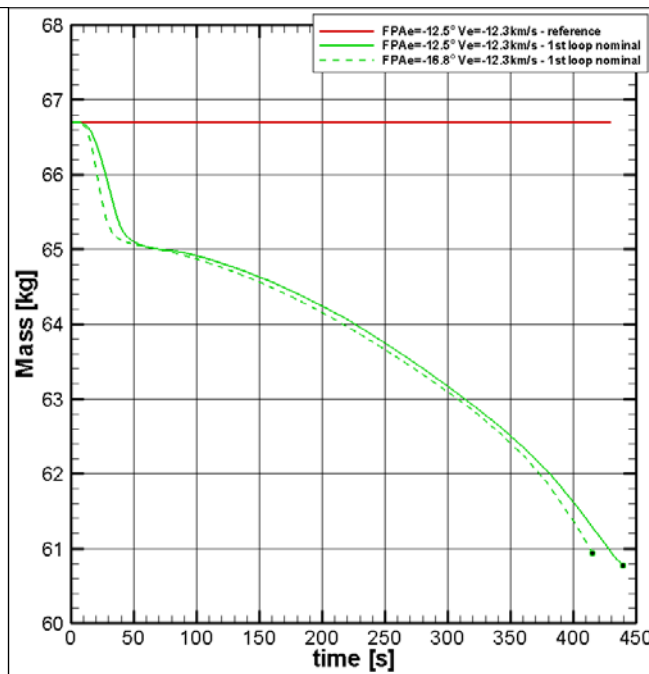
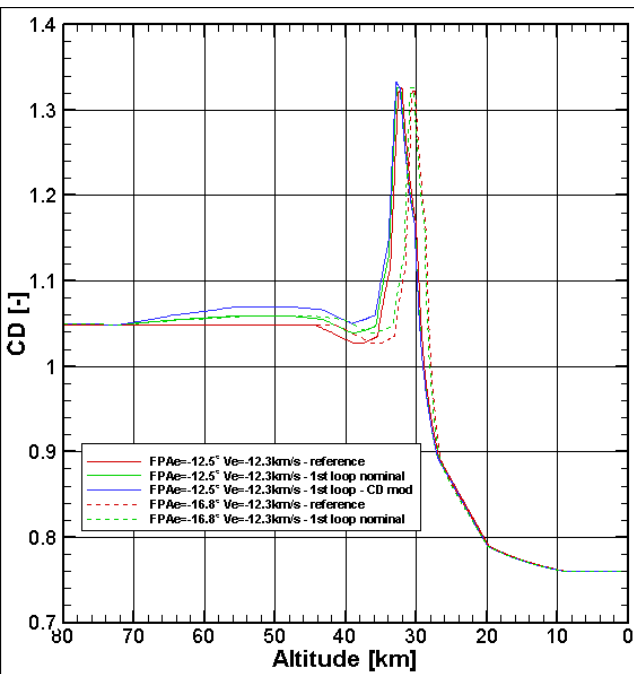
$$CD = CD_{AEDB} (1 + (CD_{abla} - CD_{non\ abla}) / CD_{non\ abla})$$

- 1st loop CDmod: $CD = CD_{AEDB} (1 + 2x \Delta CD_{shape\ mod.})$

(Pure aeroshape mod. effect (w/o additional mass loss))

Tools coupling assessment (AST)

- Trajectory analysis



↪ Shape change effect on Drag

↪ Mass loss evolution

↪ Front shield profile evolution

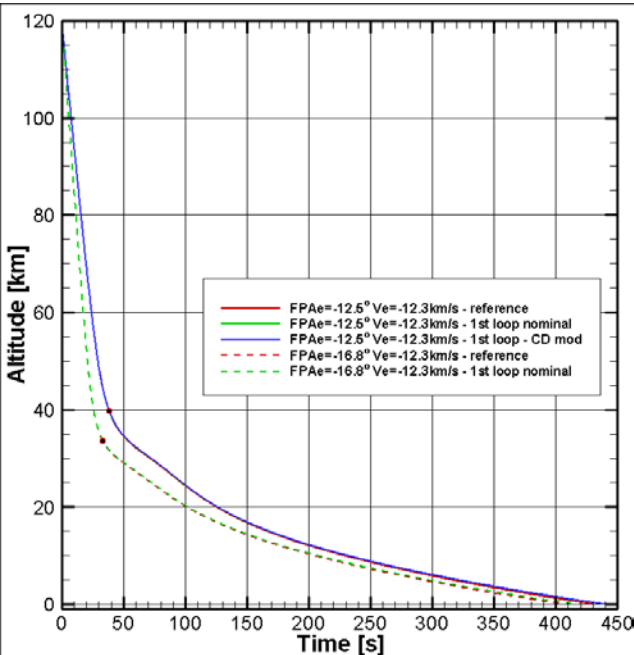
$(\Delta M \sim 5,7\text{kg})$

Total of 10mm recession at stag. Point (5mm in hyp/sup regime)

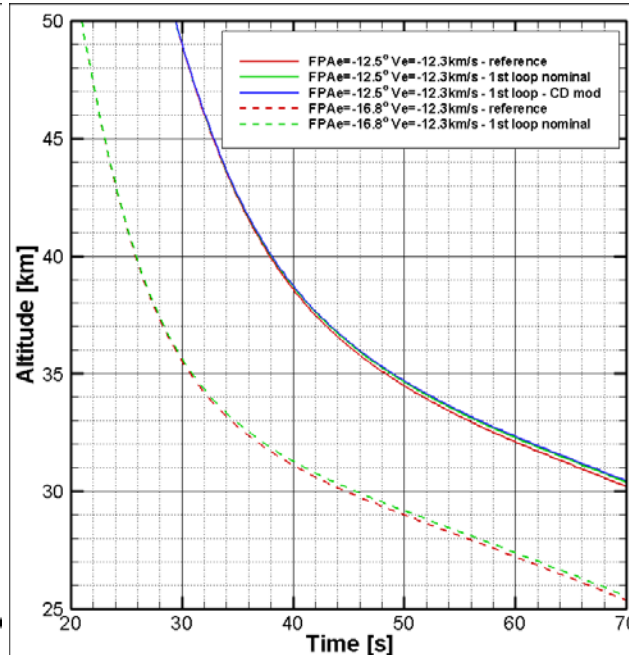
Tools coupling assessment (AST)

- Trajectory analysis – Altitude vs. time

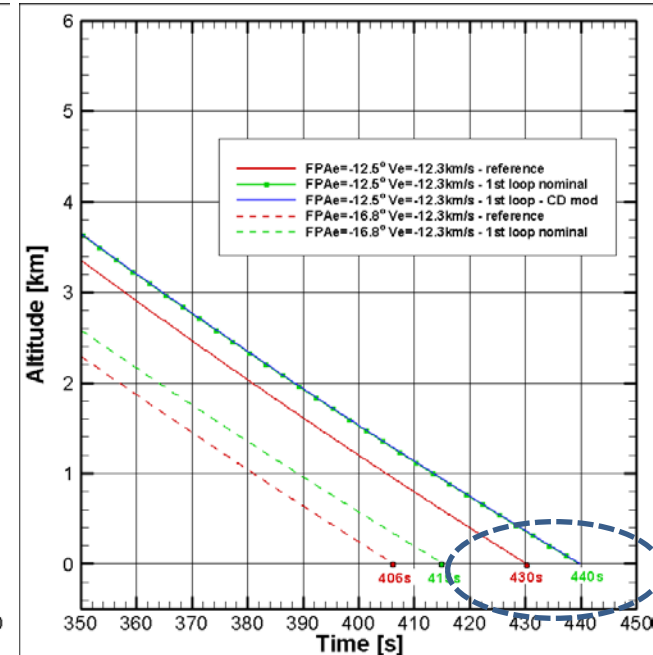
Full Domain



High Velocity Domain



Final Domain



↳ 10s longer

Tools coupling assessment (AST)

- Trajectory analysis – Summary

Parameters	Effects compared with nominal case	Maximum levels difference	% vs nominal case	Criticality
Velocity	↘	50 ⇔ 75m/s	~1 %	Low
Mach	↘	0.15 ⇔ 0.25	~1 %	Low
Deceleration	↗	-0.5 ⇔ 1g	1 % ⇔ 1.5 %	Low
Dynamic pressure	↘	0.9 ⇔ 1.3kPa	3 % ⇔ 3.5 %	Medium
Stagnation pressure	↘	2 ⇔ 3kPa	2.5 % ⇔ 4 %	Medium
Heat Fluxes	↘	<100W/m ²	~0 %	Negligible
Heat Load	↘	1.5 ⇔ 2.5MJ/m ²	1 % ⇔ 2 %	Medium
Range	↘	0.8 ⇔ 1.4km	~0.3 %	Low

↳ **Assessment of tools coupling:**

On the considered Rastas Spear trajectories (12.3 km/s), the aeroshape modification due to ablation is limited, and hence a low influence is observed on trajectory, heat fluxes and MCI

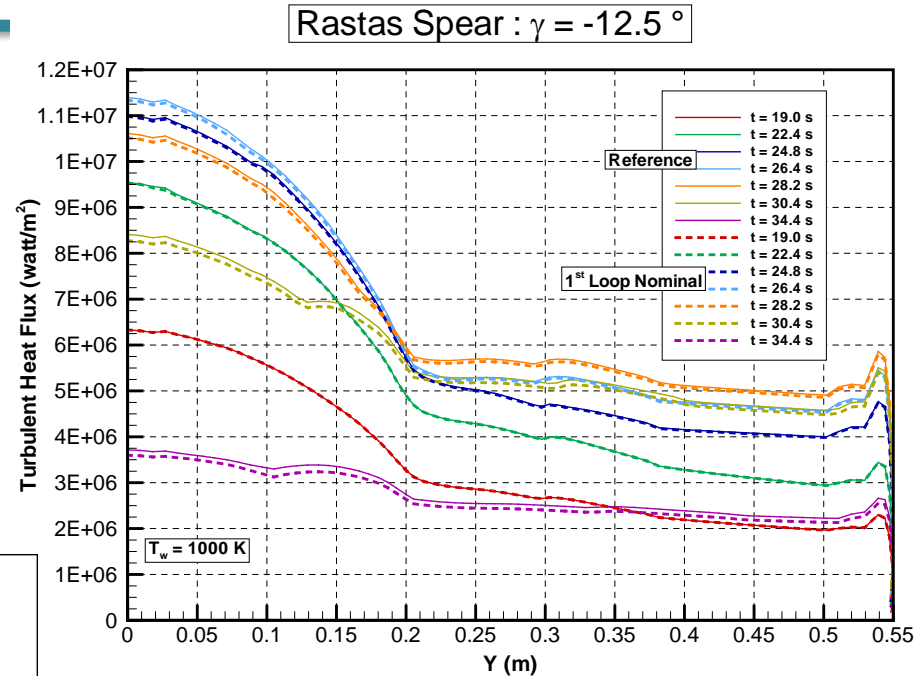
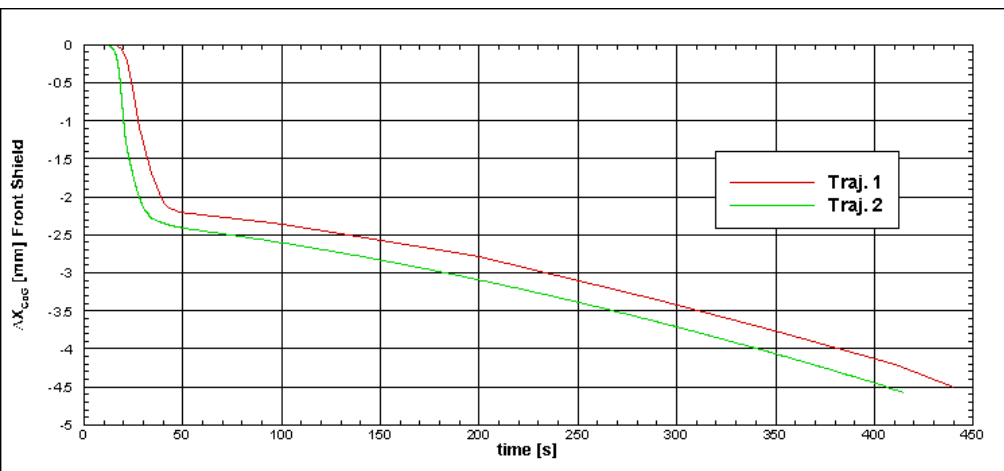
Tools coupling assessment (AST)

- **Aero-thermodynamics analysis**

↪ Convective heat fluxes along the profiles

↪ Low impact on convective heat flux
(same conclusion for $FPA_e = -16.8^\circ$ traj.)

- **MCI Analysis**



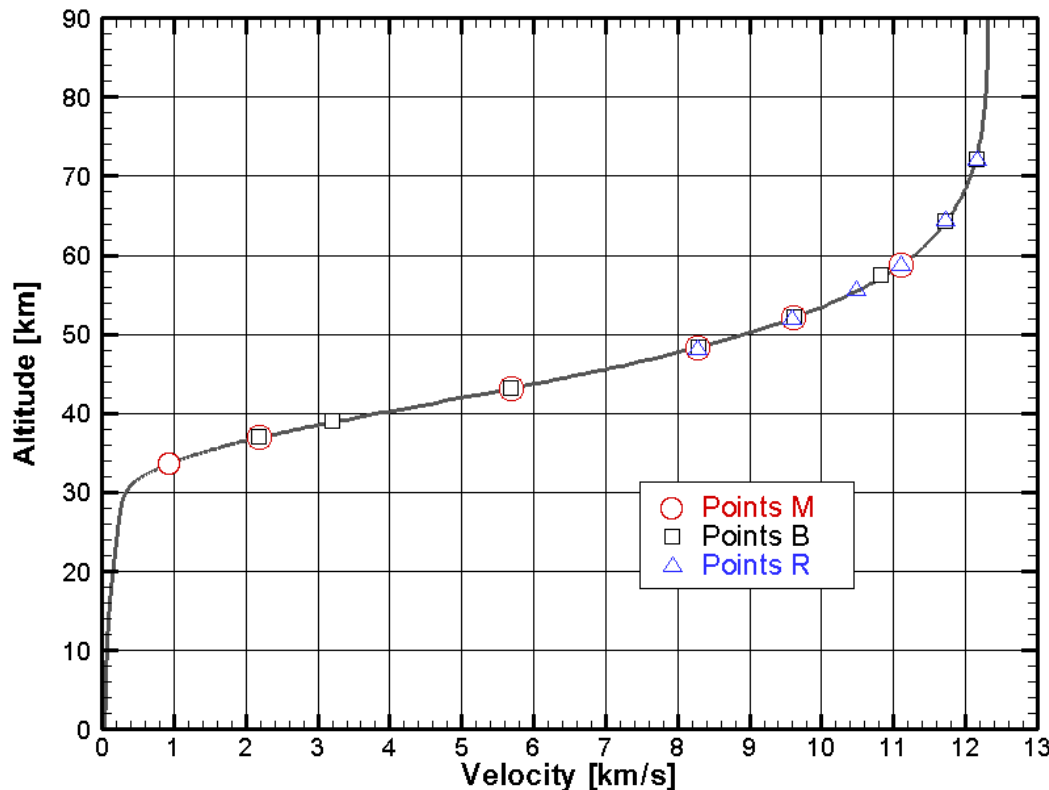
↪ Max 4.5mm displacement of the X_{CoG} on the front shield towards rear part

Engineering modelling correction by CFD

Task 1: Assessment of Aeroshape modification (M) ⇒ ablated/non ablated profiles on 6 traj. points

Task 2: Assessment of Radiation Coupling (R) ⇒ 6 traj. points

Task 3: Assessment of Surface Mass Blowing (B) ⇒ 8 traj. points



Computations performed in 2D-axisymmetric mod (AoA=0)

Engineering modelling correction by CFD

- Summary

		Current Model	NS CFD	Comments
Aerodynamics	Shape change	Inviscid chem@eq.	Viscous chem@neq. for Air (13species)	Low effect → Current model not updated
	Blowing	Not taken into account	Viscous chem@neq. for abla.+pyro. products (32sp.)	Low effect TBC for High speed → Current model not updated
Convective heat flux	Shape change	Engineering correlations	Viscous chem@neq. for Air (13species)	Further consolidation needed → Current model not updated
	Blowing	$f(M_{\text{gas inj}}/M_{\text{air}}, T, P, \text{regime})$	Viscous chem@neq. for abla.+pyro. products (32sp.)	Further consolidation needed for High speed → Current model not updated
Radiative heat flux	Engineering correlation	Tauber-Sutton	Viscous chem@neq. for Air (13species)	Reduction of Shock stand-off distance → correlation can be updated

Conclusion and future works

- Tools coupling:
 - A first version of the coupling tool is available and has been used for assessment tasks in WP4.2 activities
 - All the requirements are completed
 - Further work needed on following points
 - The aeroshape modification in Transsonic/Subsonic domain cannot be taken into account in this version \Rightarrow the use of NS computations seems to be the best way \Rightarrow strong investment on mesh activities, CPU time \nearrow and impact on robustness
 - Rarefied domain must be examined
- Assessment of tools coupling:
 - Low influence observed on considered trajectories
 - High interest to evaluate the tool for more severe trajectories

Conclusion and future works

- Engineering modelling correction by CFD:
 - Complex and very challenging CFD computations were run to assess shape change, blowing effects (on aerodynamics and convective blockage) and radiatif
 - Not all results were satisfactory, and consolidation is required for several points
- ⇒ Aerodynamic coefficient
 - CFD computations show that current correlations are valid (to be consolidated for high velocities)
- ⇒ Convective heat flux
 - Correlations used for coupling tool are kept by conservatism
 - No firm trend may be derived from current CFD computations, which require further consolidation
- ⇒ Radiative heat flux
 - Engineering Correlation can be updated (confirmed reduction of shock stand-off distance on stagnation line)
 - Reduction of radiative heat flux level is expected
 - To be extended for a larger range of entry velocities

Thank you for your attention

More at www.rastas-spear.eu

Ground to Flight Investigations of Hayabusa with Ablation Effects

8-10 April 2013

ESA/ESTEC, Noordwijk, The Netherlands

Elise Fahy⁽¹⁾⁽²⁾, Nikhil Banerji⁽²⁾, Valentin Marguet⁽²⁾, Jeremy Mora-Monteros⁽²⁾, Daniel Potter⁽³⁾, Fabian Zander⁽¹⁾,
Pénélope Leyland⁽²⁾, Richard Morgan⁽¹⁾.

⁽¹⁾*Centre for Hypersonics*

The University of Queensland

Brisbane 4072

Australia

Email: e.fahy@uq.edu.au

⁽²⁾*Interdisciplinary Aerodynamics Group*

Ecole Polytechnique Federale de Lausanne

1015 Lausanne

Switzerland

⁽³⁾*Institute of Aerodynamics and Flow Technology*

DLR Göttingen

Germany

1. INTRODUCTION

Thermal protection systems (TPS) are imperative to the survival of space vehicles especially during superorbital re-entry to Earth. The design of thermal protection systems requires in-depth knowledge of the thermal loading experienced during re-entry. The thermal loading data is mostly determined using ground testing and can be backed up by numerical modelling including computational fluid dynamics (CFD). The verification of this data with flight data is invaluable and a recent, rare example of an opportunity for comparison was the Hayabusa asteroid sample return mission, which landed in Australia in 2010. During this re-entry a team of international scientists collected spectral data which can now be used for comparison and verification of ground test and modelling data.

Ground testing of subscale models at flight equivalent hypervelocity flow conditions (8 - 12 km/s) can be performed in hypersonic impulse facilities such as the X2 expansion tunnel at The University of Queensland. A recently developed method at The University of Queensland (UQ) enables heated reinforced carbon-carbon (RCC) models to be tested at temperatures representative of those experienced in flight (2000 - 3000 K), in addition to testing with cold-wall metallic models. Hot wall testing allows more realistic simulation of re-entry flow characteristics including important thermal surface effects (surface chemistry, catalycity) which has previously not been possible due to the short testing time scales compared to Plasma Wind Tunnel facilities (PWT).

The *eilmer3* compressible flow CFD code is used extensively for simulating atmospheric re-entry vehicles at flight and laboratory conditions. Simulations of the Hayabusa aeroshell incorporate heated walls, as well as surface catalycity, to accurately model the conditions experienced by the TPS. These simulations can be coupled with SACRAM, a 1D thermal response ablation modelling code, to include the effects of ablation and pyrolysis at critical points on the model surface. The modelling of these effects in *eilmer3* and the coupling with SACRAM is in early stages and the development is progressing with a current European Space Agency (ESA) TRP project on Ablation-Radiation Coupling (ARC), led by EPFL.

Current work is investigating the effects and validity of heat flux scaling correlations applied to a range of scaled models with the Hayabusa geometry and flight equivalent flow conditions. This will be achieved through results of CFD simulations, coupled to radiation and ablation modelling, and expansion tunnel testing with hot and cold wall models. Increased understanding of scaling methods will allow higher fidelity heat loading data to be acquired allowing more efficient and effective design of TPS.

This paper will discuss preliminary results from *eilmer3* CFD simulations with ablation modelling and the development towards modelled surface chemistry and solver coupling. An outline of planned experiments in the X2 expansion tunnel, including background on the RCC heating method and test conditions, will also be presented.

2. EXPERIMENTS AND TEST CONDITIONS

X2 Expansion Tunnel Experiments

Expansion tunnels are very good at reproducing hypervelocity flow conditions experienced by flight vehicles during re-entry, but the use of cold wall metallic models coupled with the extremely short test times in the X2 facility (on the order of 100 μ s) results in negligible temperature increase of the model surface, and therefore a different thermal response to flight. A new technique developed by Zander [1] allows the use of hot wall models in X2 by resistively heating reinforced carbon-carbon (RCC) to temperatures on the order of 2000 - 3000 K, which are representative of temps experienced in flight [2]. The presence of CN was the metric selected to show surface reactions were taking place during the very short test times. Preheating of the RCC is necessary for X2 testing so that the model reaches a sufficient temperature prior to the test, and through this process any remaining resin is burnt off, leaving just the carbon to ablate during the test. Small pieces of material can be seen ablating off the cylindrical model surface in the high speed camera image shown in Fig. 1, recorded 50 microseconds into a test. Experiments for the ARC project are currently underway and results will be compared to the modelling, as described in the following sections. Goals for future testing include developing methods to identify surface chemistry in spectra and determine an experimental mass flow rate due to ablation, and extend to testing with carbon phenolic-type materials in order to achieve pyrolysis effects, as well as ablation.

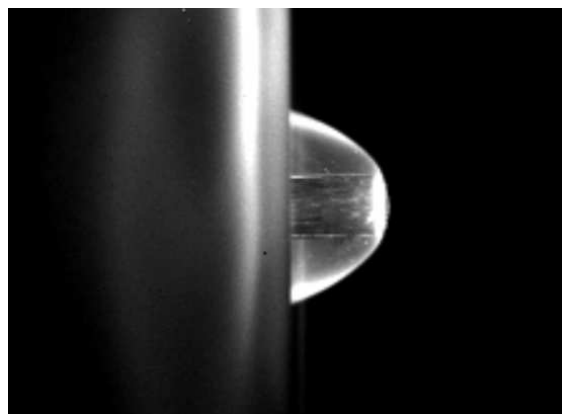


Fig. 1: A high speed camera image of a heated RCC model 50 μ s into a test (Image courtesy F. Zander).

Test Conditions for Expansion Tunnel Experiments and CFD Simulations

Test conditions corresponding to crucial points on the Hayabusa trajectory have been identified for the ESA-ARC project [3]. These include full-scale conditions taken from Hayabusa flight data and tunnel scale conditions that have been adapted from the full scale conditions to closely approximate flight stagnation enthalpy and flight equivalent speeds. The fast90A and medium90A conditions from Table 1 are the expansion tunnel test conditions for the ESA-ARC project, and medium90B has been selected for use in simulations as an extra point of comparison, even though not a condition for current X2 tests.

Table 1: Test conditions for experiments and simulations derived for the ESA-ARC project.

Condition	<i>H1</i> (peak total heating)	<i>H2</i> (peak radiative heating)	<i>fast90A</i> (X2 condition)	<i>medium90A</i> (X2 condition)	<i>medium90B</i> (X2 condition)
Flight equivalent speed [m/s]	10520	10770	10990	10060	10425
Total enthalpy [MJ/kg]	59.3	60.4	60.4	50.6	54.4

3. FLOWFIELD SIMULATIONS

Numerical simulation of the flowfield around an aeroshell provides detailed analyses of the flowfield chemistry and physics, as well as a good comparison to flight and experimental data. The *eilmer3* code has been used for the full-scale and sub-scale Hayabusa simulations in this work, with a number of assumptions and simplifications made in the modelling at this stage in the ARC project. A brief overview of the structure of *eilmer3* is presented along with selected preliminary results.

Computational Fluid Dynamics with *eilmer3*

eilmer3 is a compressible flow computational fluid dynamics (CFD) code developed by The University of Queensland, in partnership with the Interdisciplinary Aerodynamics Group (IAG) at EPFL and several other partners. The main code collection consists of a pre-processor, the main simulation program and a post-processor, and libraries for thermochemistry, radiation, geometry and numerical methods [4]. *eilmer3* can simulate a specialised range of compressible flow problems, including aeroshells at re-entry and ground test conditions. Compressible flow solutions (in two dimensions for this work) are obtained by applying a cell-centred, finite-volume approach to the integral form of the compressible Navier-Stokes equations, given in (1).

$$\frac{\partial}{\partial t} \int_V U dV = - \oint_S (\bar{F}_i - \bar{F}_v) \cdot \hat{n} dA + \int_V Q dV \quad (1)$$

S represents the bounding surface and \hat{n} the outward-facing normal of the control surface, and in 2D axisymmetric flow, V represents the volume and A the area of the cell boundary per unit radian in the circumferential direction [4]. The conserved quantities for the thermal non-equilibrium model are density (ρ), x - and y -momentum per volume, total energy per volume, vibrational energy for mode m , electron-electronic energy and mass density of species s , provided in vector form in (2).

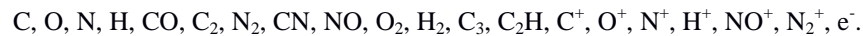
$$U = [\rho \quad \rho u_x \quad \rho u_y \quad \rho E \quad \rho e_{v_m} \quad \rho e_e \quad \rho f_s] \quad (2)$$

The flux is separated into inviscid, \bar{F}_i , and viscous, \bar{F}_v , components. In 2D, the viscous components are calculated from the axisymmetric viscous stresses and viscous heat fluxes and the source term, Q , is a combination of geometry,

chemistry, thermal energy exchange and radiation terms. A full discussion of the flux vector and source term formulations, as well as solution methods, is provided in the *eilmer3* user guide [4].

3.2 Models Chosen, Assumptions and Simplifications

Models need to be chosen for the thermal non-equilibrium of the air plasma as well as for the ablation species interaction within the boundary layer. Assumptions and simplifications have been made in work to date in order to obtain preliminary results and perform verification tests. Present simulations use the Park [5] chemistry model for air and ablative species, and the 20 species included are:



There are 24 reactions in Park's model: 12 exchange reactions, 5 dissociation reactions 4 electron impact ionisation reactions, and 2 associative ionisation reactions. The low number of reactions, although making the model numerically faster, ignores some potentially important mechanisms. The Abe model, comprising 26 species and 50 reactions, is being created for *eilmer3* by means of chemical species data, reaction files and collision integrals [6].

Simulations have been designed to replicate both flight and expansion tunnel conditions and therefore have to take into account different surfaces that could be used. At present, the available material data comes from the NASA test case material TACOT (Theoretical Ablative Composite for Open Testing) [7], however, acquisition of carbon phenolic data will enable more realistic heat shield simulations. Full-scale simulations can currently utilise a user-defined boundary condition for pyrolysis gas injection only, and without ablation, mass flow rates of injected species are low and the gases will remain close to the wall. Modelling surface reactions and char mass flow module is under development as part of the ESA-ARC project. At the boundary, an energy balance takes place whereby the energy coming into the surface from the flowfield, in the form of convective and radiative heat flux, is balanced by the energy re-radiated into the flowfield and carried by mass entering the flowfield. This surface energy balance is controlled in the boundary condition by total mass, momentum, energy and species mass fluxes.

Wall catalycity can be included in modelling to compare to ground test results to simulations with mass injection. At present there are two options available in *eilmer3*: non-catalytic, where the wall has no influence on reactions, or super-catalytic, where the wall forces recombination to freestream concentrations. The latter effect is sometimes prevalent in expansion tunnel tests with cold-wall metallic models.

Preliminary Results

The results presented are preliminary results from simulations at full-scale and subscale, to show what is currently achievable with the code. Important parameters to consider from simulation results are the stagnation line temperature profiles, species concentrations, especially when including pyrolysis and ablation, and convective, radiative and total heat flux, especially with different wall effects.

An example stagnation line temperature profile plot has been provided in Fig. 2 for a full-scale Hayabusa model at the H2 condition. A two-temperature model splits the modes into two sets: translational-rotational, and vibrational-electron-electronic. Across the shock there is a large region of non-equilibrium as the translational-rotational modes rise sharply in temperature and relax through the shock layer to meet the vibrational-electron-electronic modes in equilibrium closer to the wall. The shape of the temperature profile is expected to change near the wall when a finite-rate catalytic wall or mass injection boundary condition is used. The reasons for the curves lacking smoothness in areas around the peaks is entirely within the code, and since the production of these plots, the code has undergone improvements in energy exchange modelling to improve these features.

The stagnation line temperature profiles compare well in magnitude to Winter et al [8], however, *eilmer3* pairs the temperature modes differently to Winter et al and so a larger region of non-equilibrium can be seen in Fig. 2. The shape of the temperature profiles meets the work of Potter [9], as expected through similar use of the *eilmer3* code.

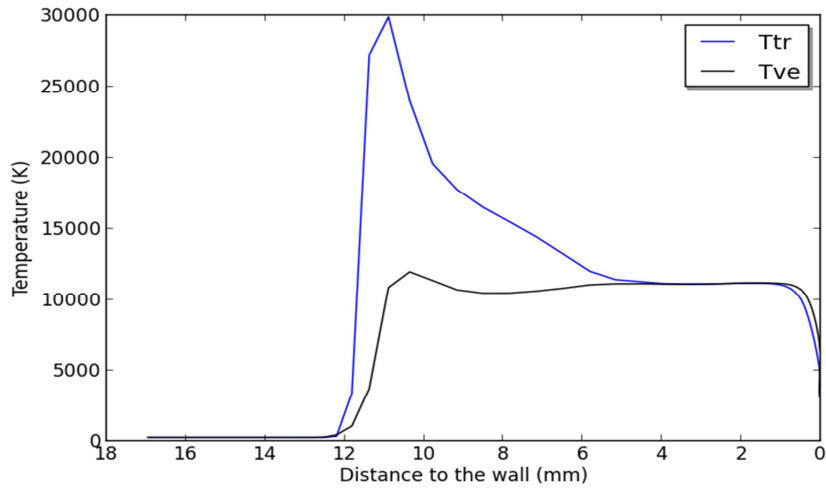


Fig. 2: Stagnation line temperature profile for the H2 full-scale condition, non-catalytic case.

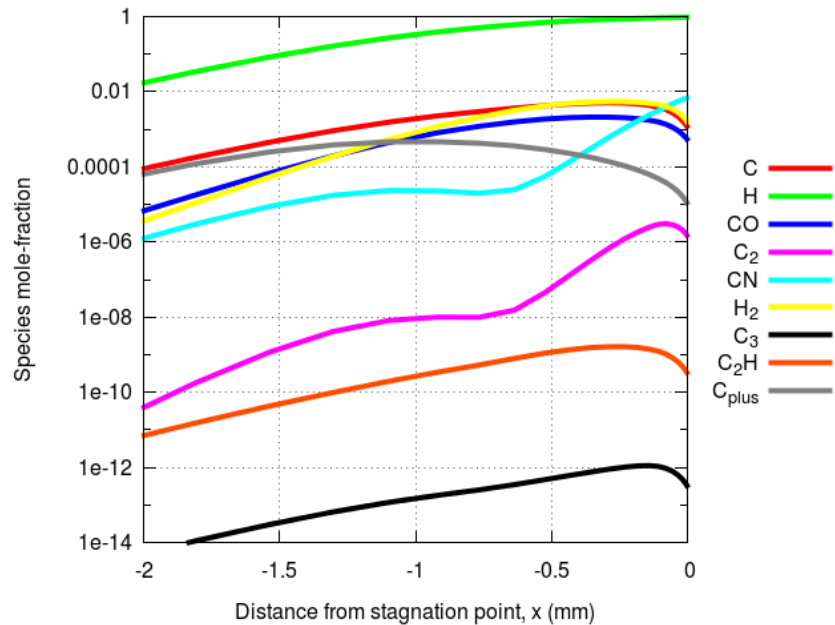


Fig. 3: Concentrations of pyrolysis gas species near to the wall, H2 condition.

The species concentrations are important to observe in simulations to gain an understanding of the chemical processes that are occurring in the shock and boundary layers, and at the surface. Spectra can then be created through *eilmer3*'s inbuilt radiation solver or codes such as Fluid Gravity's PARADE to compare to flight or experimental data. Fig. 3 illustrates the pyrolysis gas species concentrations in the region close to the wall for a full-scale simulation at the H2 condition. Since this simulation has pyrolysis gas injection only, without ablation from the surface, species such as C_3 have very low concentrations. The species that result from reactions in the pyrolysis gas at equilibrium wall temperature and pressure conditions (as in [5]) have the highest concentrations. There is a sharp drop-off of all pyrolysis species concentrations beyond this region, as the mass flow rate is very low and the species do not traverse further into the flowfield. The mass flow rate has been computed in SACRAM, a 1D material response solver discussed in the next section, and will increase approximately ten-fold with the inclusion of ablation, assuming the trends in Park [5] are followed. The results in this plot have are in the process of validation as the coupling is still in development to include surface reaction effects: this is a goal for future work within the ARC project.

Heat flux is a parameter of interest for the influence of radiation, diffusion and ablation, as well as scaling analysis using empirical correlations, and results at full-scale are presented in Fig. 4 as an example of heat flux analysis for the ESA-ARC project. The points $Q_{conv_h1_ARC}$ and $Q_{conv_h2_ARC}$ are the Hayabusa flight convective heat flux values, and Q_{cond_h1} and Q_{cond_h2} are the corresponding conductive heat flux values. It is assumed that convective

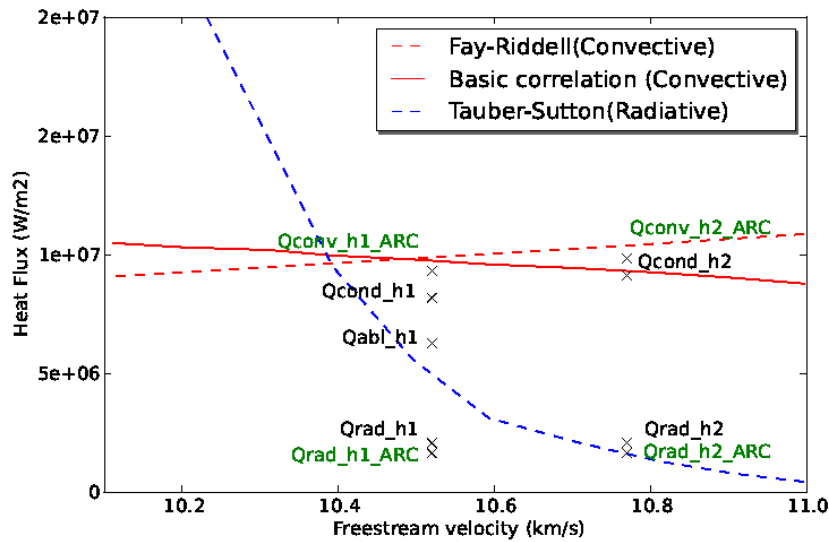


Fig 4: Various heat fluxes compared with empirical correlations.

heat flux is the sum of a conductive heat flux term and a diffusive heat flux term, and upon improvements to the diffusion modelling, it is hoped that the diffusive heat flux will provide the difference between the numerical and flight data points. The inclusion of ablation lowers the conductive heat flux (Q_{abl_H1}) for the H1 condition, and it is predicted that the extra difference to the flight point could be made up by a larger diffusive heat flux, due to mass injection. These convective/conductive heat fluxes match reasonably well with the relevant scaling correlations, as do the H2 radiative heat fluxes, but a larger difference can be seen between the H1 data points and the Tauber-Sutton correlation.

4. ABLATION CODE AND COUPLING DEVELOPMENT

Modelling Material Response

Heat loading will influence the thermal response of the TPS and the mechanisms of pyrolysis (gas formed from resin) and ablation (surface reactions with fibres) need to be modelled accordingly. Pyrolysis gases are treated using SACRAM, a one-dimensional thermal response code developed by Joshi et al [10] and based on the work of Amar [11]. SACRAM solves the mixture energy, gas phase continuity and solid phase continuity equations using Fourier's law to model conduction, Darcy's law to model porous flow and the ideal gas law to model states of the pyrolysis gases. The governing equations are solved through a control volume finite element spatial discretisation method (CVFEM), an Euler implicit time integrator and a contracting grid scheme. A Newton iterative method is applied to solve the series of non-linear equations. Fig. 5 illustrates the operation of SACRAM, taking heat flux and temperature values from the flowfield to calculate the pyrolysis gas mass flow rate, and new species concentrations through the user-defined boundary condition back to the flowfield.

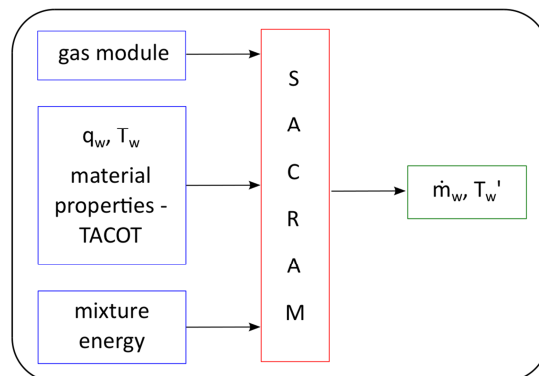


Fig. 5: Operation of 1D material response code SACRAM.

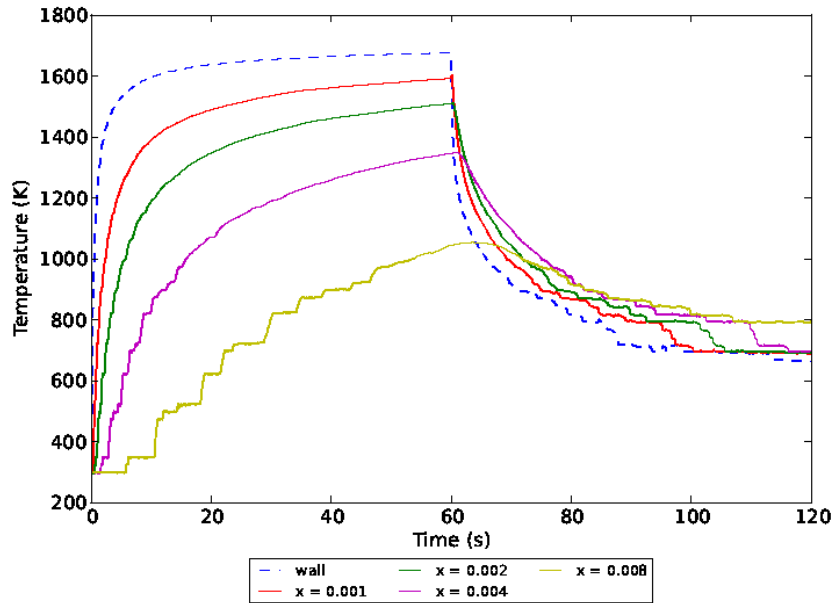


Fig. 6: Temperature profiles for SACRAM test case.

The SACRAM solver has been verified using the TACOT data [7] and the following response test case:

- Ramp up the flux from 0 - 0.45MW/m² in 0.1s;
- Hold constant at 0.45MW/m² from 0.1s - 60s;
- Ramp back down from 0.45-0MW/m² from 60s - 60.1s;
- Hold constant at 0MW/m² until 120s.

The results presented in Fig. 6 and Fig. 7 are similar to those presented by Joshi et al [10] but have been updated by the authors after development of the SACRAM code. The behaviour of the temperature profiles at different points through the surface (where x is the distance from the surface in metres) meets the test case specifications in Fig. 6. The pyrolysis gas mass flow rate, or blowing rate, \dot{m}_g calculated by SACRAM is shown in Fig. 7.

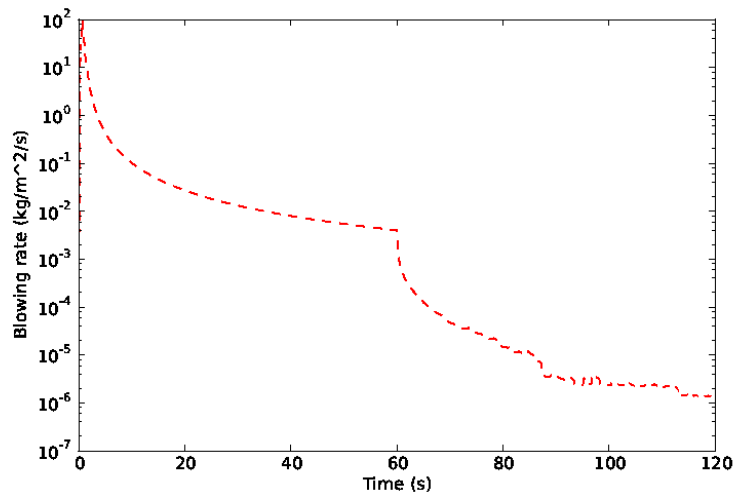


Fig 7: Blowing rate of pyrolysis gases over test time.

Flowfield and Material Response Coupling

The partnering of SACRAM with *eilmer3* is illustrated in Fig. 8. The material response solver and CEA (NASA's Chemical Equilibrium with Applications solver) provide pyrolysis gas parameters to the user defined ablation boundary

condition. This boundary condition interacts with the flowfield throughout the simulation until convergence is reached, usually after a prescribed number of body lengths of flow.

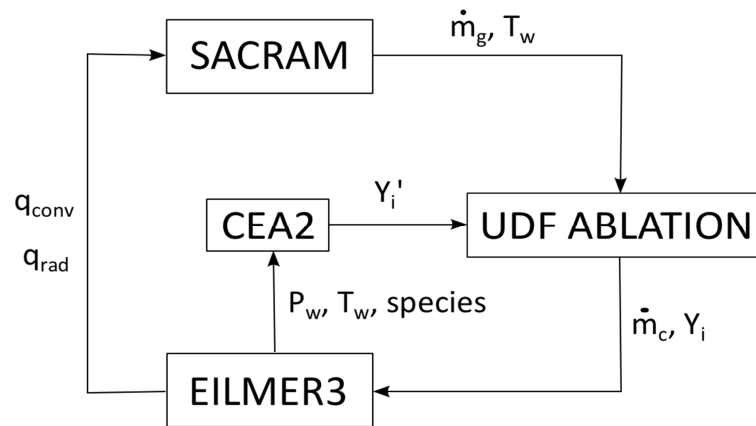


Fig. 8: Coupling of SACRAM and *eilmer3*.

The coupling between material response and flowfield through this iteration loop can be loosely or strongly coupled. A loosely coupled approach runs the flowfield simulation to convergence, executes the material response solver with required flowfield values, returns a new set of values to re-run the flowfield simulation, continues this process until convergence of a shared metric between material and flowfield solvers. A strongly coupled approach achieves a converged flowfield result in one run of the flowfield simulation, executing the material response solver at certain time intervals during the flowfield simulation. The interface for loose coupling of the flowfield and material response solvers is a shell script that executes each solver, passing values as required, and using a python script to evaluate the convergence of a metric. For stronger coupling, the material response solver is executed within the boundary condition script at specified time steps, automatically updating the required parameters. This interface is still in early stages of development, as work focuses on how to optimise the running of both the flowfield and material response solvers and minimise computational expense.

5. CONCLUSIONS AND FUTURE WORK

The comparison of flight data to experimental and computational results is of great importance in the development of ground testing methods, enabling greater understanding of thermal loading experienced during atmospheric re-entry and improving future design of thermal protection systems. The Hayabusa mission has provided a rare set of flight data that is a focus for the ARC project and its continuing expansion tunnel testing and computational simulations. The potential for simulating subscale and full-scale models at expansion tunnel and flight conditions, respectively, has been shown through use of the *eilmer3* code. Linking with SACRAM, the ability to model ablation effects is under development, as demonstrated by preliminary results; however, these are yet to be validated.

Future work for the ARC project that follows the work presented in this paper includes:

- X2 testing with heated RCC aeroshell models, for direct comparison with CFD;
- Development of *eilmer3*, including improved diffusion and catalycity models, and improvements to radiation modelling, including polyatomic species;
- Development of ablation boundary conditions, including combined pyrolysis and ablation modelling;
- Improvements to SACRAM, including coupling to *eilmer3* and expansion to more material data sets;
- Inclusion of other chemistry models.

REFERENCES

- [1] Zander, F., 'Hot Wall Testing in Hypersonic Impulse Facilities', *PhD Thesis*, The University of Queensland, 2013.
- [2] Abe, S., Fujita, K., Kakinami, Y., Iiyama, O., Kurosaki, H., Shoemaker, M.A., Shiba, Y., Ueda, M. and Suzuki, M., 'Near-Ultraviolet and Visible Spectroscopy of Hayabusa Spacecraft Re-Entry', *Publications of the Astronomical Society of Japan*, Vol. 63, No. 5, 2011.
- [3] Leyland, P. et al., 'TN 1.6: Definition of Experimental Backup Solutions', *ESA Ablation-Radiation Coupling (ARC) Project*, 2012.
- [4] Jacobs, P. A. et al., 'Eilmer's Theory Book: Basic Models for Gas Dynamics and Thermochemistry', *The University of Queensland Mechanical Engineering Report* 2010/09.
- [5] Park, C., Jaffe, R. L. and Partridge, H., 'Chemical-Kinetic Parameters of Hypersonic Earth Entry', *Journal of Thermodynamics and Heat Transfer*, Vol. 15, No. 1, 2001.
- [6] Suzuki, K., Fujita, K. & Abe, T., 'Chemical Nonequilibrium Viscous Shock-Layer Analysis over Ablating Surface of Superorbital Re-entry Capsule', *The Institute of Space and Astronautical Science Report SP No. 17*, 2003.
- [7] Lachaud, J., Martin, A., Cozmuta, I. and Laub, B., 'Ablation Workshop Test Case', *4th Ablation Workshop*, Albuquerque, USA, 2011.
- [8] Winter, M.W., McDaniel, R.D, Chen, Y., Liu, Y., Saunders, D. and Jenniskens, P. M., 'Radiation Modeling for the Re-entry of the Hayabusa Sample Return Capsule', *50th AIAA Aerospace Sciences Meeting*, Nashville, USA, 2012.
- [9] Potter, D. F. 'Modelling of Radiating Shock Layers for Atmospheric Entry at Earth and Mars', *PhD Thesis*, The University of Queensland, 2011.
- [10] Joshi, O., Duffa, G. and Leyland, P., 'Development and Validation of SACRAM: A Swiss Approach to the Computational Response of an Ablative Material', *5th Ablation Workshop*, Lexington, USA, 2012.
- [11] Amar, A. J., Blackwell, B. F., and Edwards, J. R., 'One-Dimensional Ablation Using a Full Newton's Method and Finite Control Volume Procedure', *Journal of Thermophysics and Heat Transfer*, Vol. 22, No. 1, 2008.

A numerical comparison of high- and low-fidelity radiation models for conduction-radiation coupling in (charring) ablators

G. Pinaud, Astrium Space Transportation
T. van. Eekelen, LMS Samtech

7th European Workshop on Thermal Protection Systems and Hot Structures
8-10 April 2013
Noordwijk, The Netherlands

All the space you need



A Siemens Business



CETHIL
UMR 5008



ASTRIUM
AN EADS COMPANY

Thermal radiation heat transfer in hypersonic shock layers is currently widely studied...

... But the counterpart in solid medium that can absorb, emit and scatter radiation is not straightforward.

... Moreover,

- current space exploring missions generally involve low density TPS material (PICA, ASTERM...)
- due to increasingly heat flux for typical sample return mission, wall temperature can reach more than 3000 K
- radiation heat transfer mode in the vicinity of the wall is the main contributor

... The need of a better understanding of the non intrusive temperature measurements (pyrometer, spectro-radiometer...) is obvious

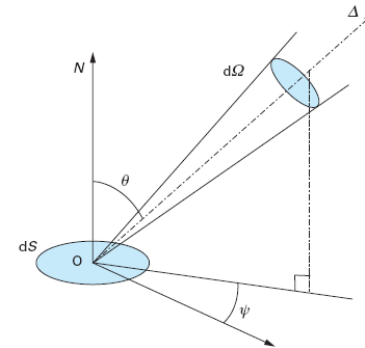
... Further needs in multifunction TPS lead to the development of radio-electrical transparent material

- Radiation phenomena in solid media and governing equations
- Part 1:
 - Astrium's 1D semi-transparent & ablation tool (BE04)
 - Semi-transparent glassy material (3DSiSi) thermal model
 - Plasma wind tunnel rebuilding
- Part 2:
 - Development of a volume radiation module in Samtech/Amaryllis code
 - Application to charring and ablative TACOT (*Theoretical Ablative Composite for Open Testing*) under:
 - plasma wind tunnel
 - High speed Earth entry mission
- Conclusions & perspectives

- Radiation intensity is a convenient quantity for use in problem dealing with radiative transfer and is defined by:

The energy per unit time, per unit of projected surface area normal to the traveling direction and per unit elemental solid angle centered around the traveling direction

$$d\phi(O, \Delta, \lambda) = L_{\lambda}(O, \Delta, \lambda) dS \cos(\theta) d\Omega d\lambda$$



- We consider a full participating media meaning that a radiation impinging on a layer of material can be:

- absorbed
- scattered

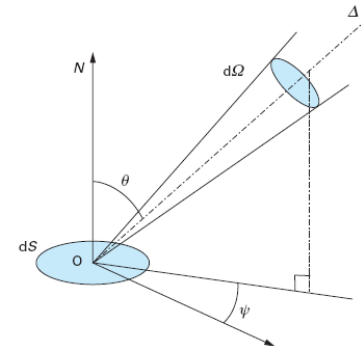
... and due to energy exchange mode and coupling, radiation is also:

- emitted

- Radiation intensity is a convenient quantity for use in problem dealing with radiative transfer and is defined by:

The energy per unit time, per unit of projected surface area normal to the traveling direction and per unit elemental solid angle centered around the traveling direction

$$d\phi(O, \Delta, \lambda) = L_\lambda(O, \Delta, \lambda) dS \cos(\theta) d\Omega d\lambda$$



- We consider a full participating media meaning that a radiation impinging on a layer of material can be:

- absorbed
- scattered

... and due to energy exchange mode and coupling, radiation is also:

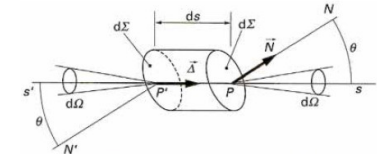
- emitted

- The attenuation of energy is a consequence of:

Absorption: the change in intensity of radiation passing through the layer is found experimentally to depend on the magnitude on the local intensity.

$$d\phi'_a(s, \vec{\Delta}) = -k_v(s) d\phi'(s, \vec{\Delta}) ds$$

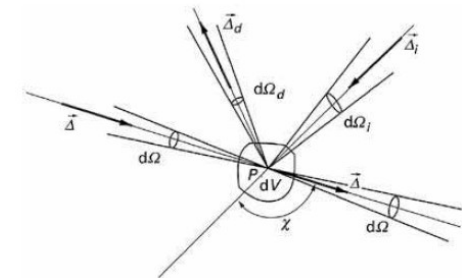
k_v is the true absorption coefficient (assuming no induced emission)



Scattering: is the encounter between photon and one or more other particles during which the photon does not lose its entire energy but may undergo a change in direction. The scattering coefficient σ_v is the inverse of the mean free path that a photon travel before been scattered.

The phenomenon can be characterized by 4 types of events:

- Elastic scattering (energy, wavelength do not change)
- Inelastic scattering (energy is changed)
- Isotropic scattering (any direction is equally likely)
- Anisotropic scattering (direction changes are not equally distributed)



- The emission of energy :

Considering an isothermal elementary volume of a medium in equilibrium with its surroundings, the radiation emitted by this volume is:

$$d\phi'_e(s, \vec{\Delta}) = k_v n_v^2 L_v^0(s, \vec{\Delta}) dV d\Omega dv$$

L_v^0 is the black body spectral emissive power

n_v is the index of refraction of the medium

- Finally, for a absorbing, emitting and scattering medium, the equation of radiative transfer is given by:

$$\frac{dL'_v(s, \vec{\Delta})}{ds} = \underbrace{k_v n_v^2 L_v^0(s, \vec{\Delta})}_{\text{Emission}} - \underbrace{[k_v(s) + \sigma_v(s)] L'_v(s, \vec{\Delta})}_{\text{Extinction}} + \underbrace{\frac{\sigma_v(s)}{4\pi} \int_{\Theta} L'_v(s, \vec{\Delta}_i) p_v(\vec{\Delta}_i \rightarrow \vec{\Delta}) d\Omega_i}_{\text{Scattering - Phase function}}$$

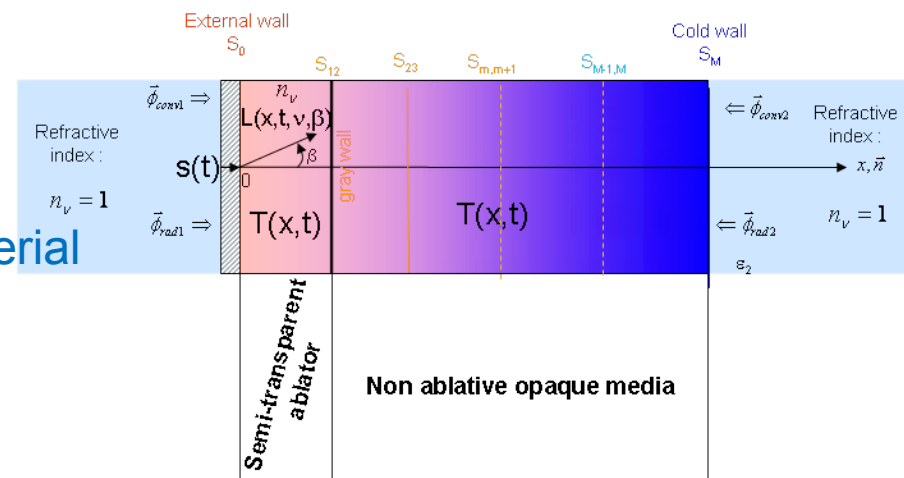
Part 1: BE04 / 3DSiSi

This document is the property of Astrium. It shall not be communicated to third parties without prior written agreement. Its content shall not be disclosed.



■ Astrium's code BE04 is accounting for:

- conduction-radiation coupling
- non-charring semi-transparent material
- chemical oxydation
- mechanical recession



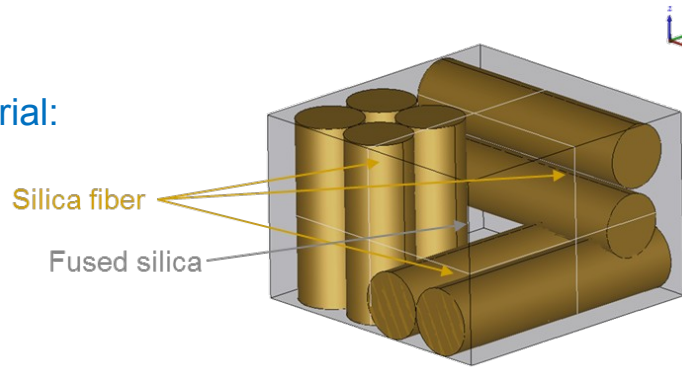
■ The conduction-radiation coupling problem is solved using 1D finite difference zonal approach, iteratively in a staggered scheme:

- $[T(x,t), S(t)]$ system
- $L(x,t,v,\beta)$ for a converged $[T(x,t), S(t)]$

■ BE04 was used as a reference for the inter-comparison exercise for SAMCEF module development and validation

■ Rebuilding of plasma arc-jet test on a quartz-silica fiber (3DSiSi) semi transparent material :

● 3DSiSi material:



- Elementary characterizations of the 3DSiSi media provide spectral absorptivity, scattering coefficient, refractive index, and extinction coefficient:

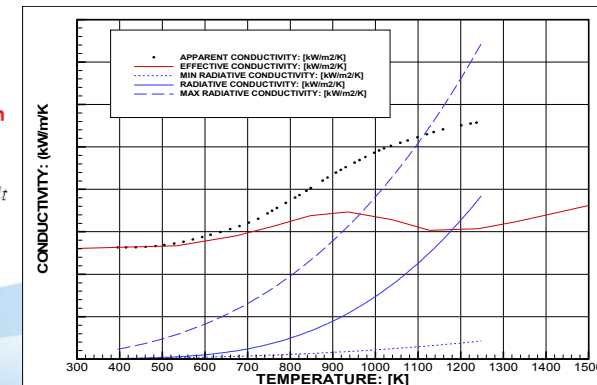
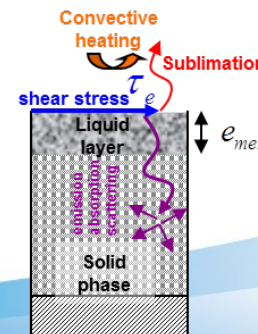
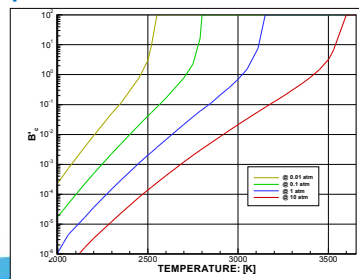
- The scattering phase function is supposed uniform $\beta_v = \alpha_v + \sigma_v$

- From the measurement of the total conductivity, assessment of the effective thermal conductivity using Roseland radiation diffusion model:

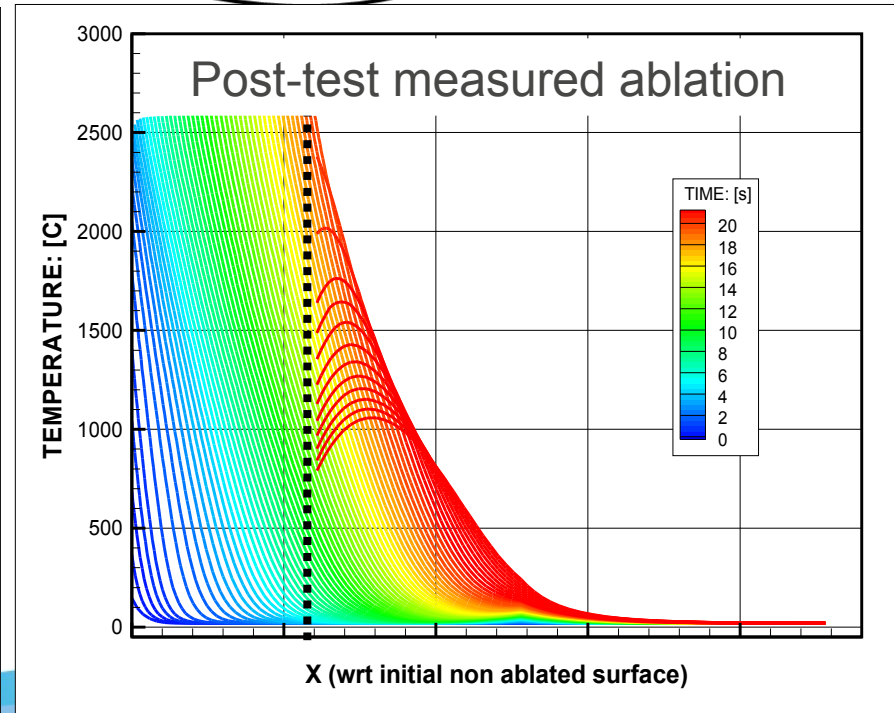
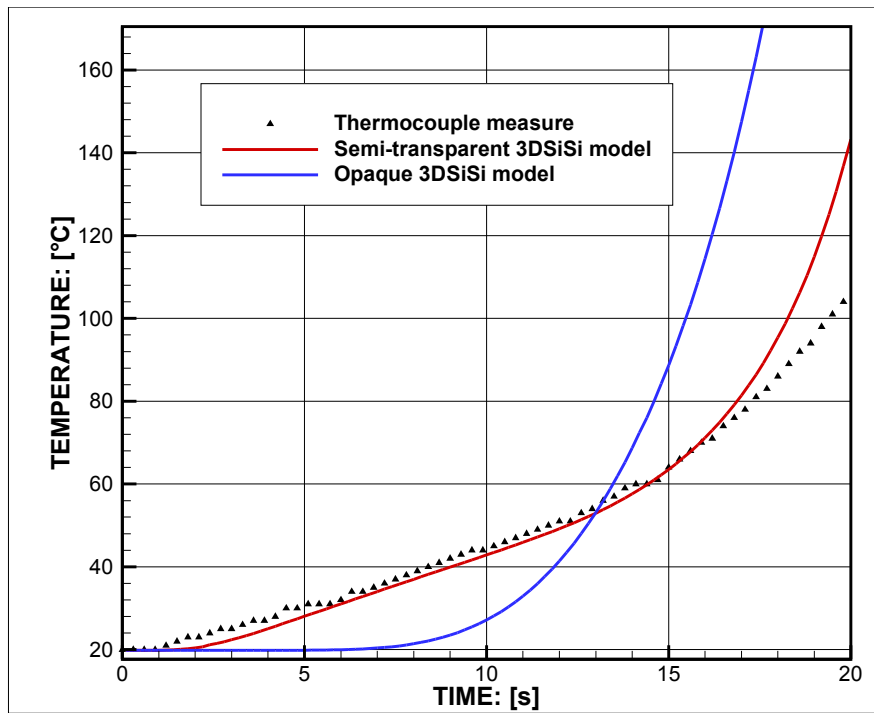
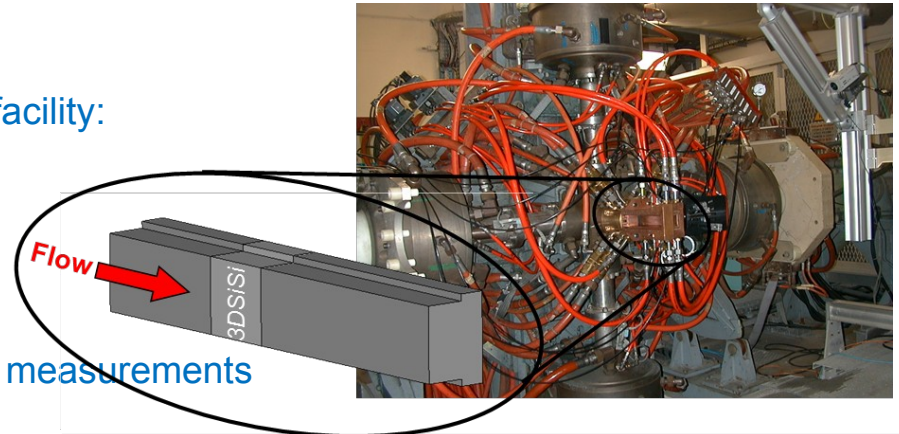
$$k^R = \frac{4\pi}{3} \int_0^\infty \frac{1}{\alpha_v + \sigma_v} \frac{\partial}{\partial T} (n_v^2 L_{b,v}(T)) dv$$

- Both chemical ablation (sublimation) and mechanical (liquid removal under aerodynamic stress) are taken into account

- Chemical ablation is expressed as standard equilibrium B'c table:



- Rebuilding of plasma arc-jet test on a quartz-silica fiber (3DSiSi) semi transparent material :
- High pressure-enthalpy arc-jet plasma Astrium facility:
 - Plan, square cross section configuration, supersonic tangential flow
 - Steady state heat flux at 10 MW/m²
- Comparaisons with temperature and recession measurements



This document is the property of Astrium. It shall not be communicated to third parties without prior written agreement. Its content shall not be disclosed.

Part 2: SAMCEF / TACOT

This document is the property of Astrium. It shall not be communicated to third parties without prior written agreement. Its content shall not be disclosed.

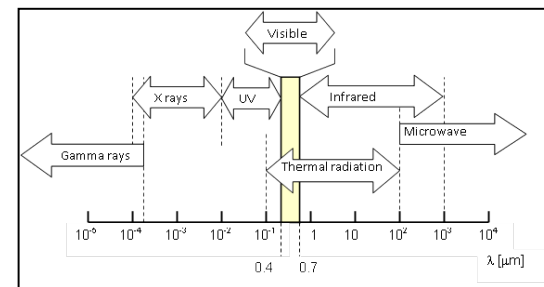
- A conduction-radiation coupling algorithm has been implemented in SAMCEF Amaryllis

- To the charring-conduction equation a radiation source term is added

$$\dot{\rho} = \sum_i \Delta \rho_i A_i \rho_v^{N_i-1} (\rho_v - \rho_c)^{N_i-1} (1 - \alpha_i)^{N_i} e^{-E_i/RT}$$

$$\nabla \cdot (K_p \nabla P) = \dot{\rho}$$

$$-\dot{\rho} H_p + \rho c \dot{T} = \nabla \cdot (\lambda \nabla T) - \bar{m}^g \nabla h^g - \int_0^{\infty} \nabla (\phi_{rv}) dv$$



- The radiation problem is solved for a given density and temperature field

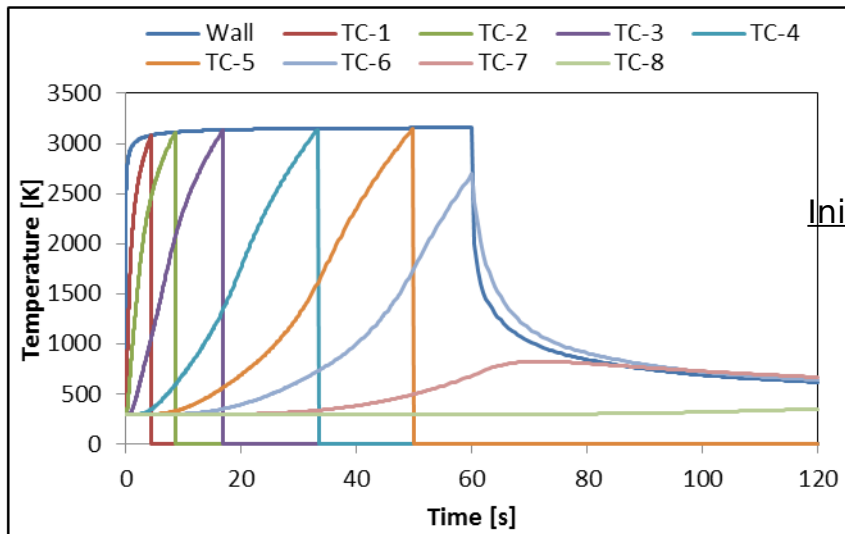
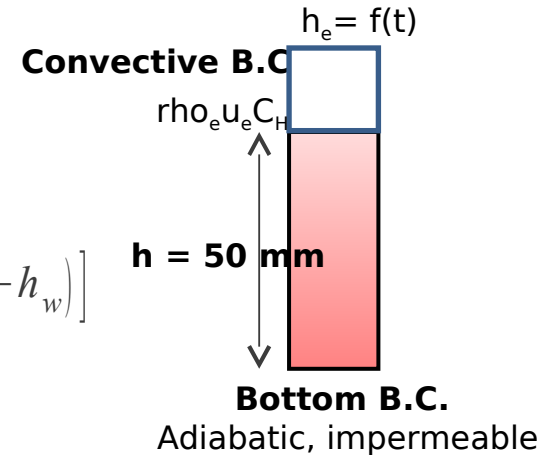
$$\frac{\partial L_v}{\partial \vec{s}} = -(\alpha_v + \sigma_{sv}) L_v + n^2 \alpha_v L_{bv} + \frac{\sigma_{sv}}{4\pi} \int_{\Omega=4\pi} \Phi(\vec{s}, \vec{s}') L(\vec{s}') d\Omega$$

- A Monte-Carlo ray-tracer is used to calculate the “view-factors”:
 - At very iteration/time step
 - Properties are wave-length dependent
 - The conduction mesh is used as a finite volume mesh with “constant” properties
 - Thermo-optical properties depend on temperature and density
 - The outer surface can be a participating medium

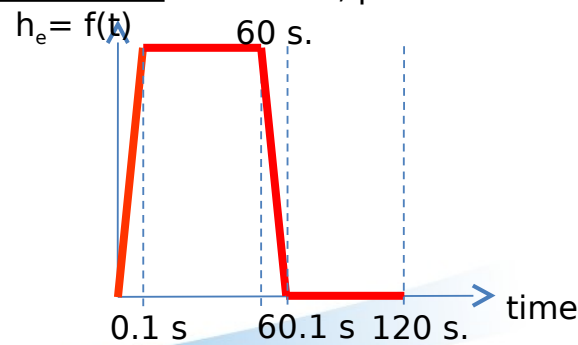
Test-case 2.3 of the ablation test-case series.

- A 1D test specimen
- The test-specimen is made of TACOT (PICA like material)
- Applied external radiation + convection (plasma test like profile)

$$q = \sigma \varepsilon (T_{\infty}^4 - T_w^4) + \rho_e u_e C_h (h_e - h_w) + \rho_e u_e C_h [B'_c (h_c - h_w) + B'_g (h_g - h_w)]$$



Initial conditions: **T=300 K**, $p = 101325 \text{ Pa}$ (1 atm), air.



This document is the property of Astrium. It shall not be communicated to third parties without prior written agreement. Its content shall not be disclosed.

- Classically the radiation term is added as a temperature dependent conductivity

- Optically thick medium → Rosseland assumption

$$\lambda_r = \frac{16 \cdot n^2 \cdot \sigma \cdot T^3}{3 \cdot (\alpha + \sigma_s)} = \frac{16 \cdot n^2 \cdot \sigma \cdot T^3}{3 \cdot \beta}$$

- Compare Rosseland approximation with full conduction-radiation problem for TACOT

- Remove radiation contribution from the conductivity

- For PICA¹ material (n=1):

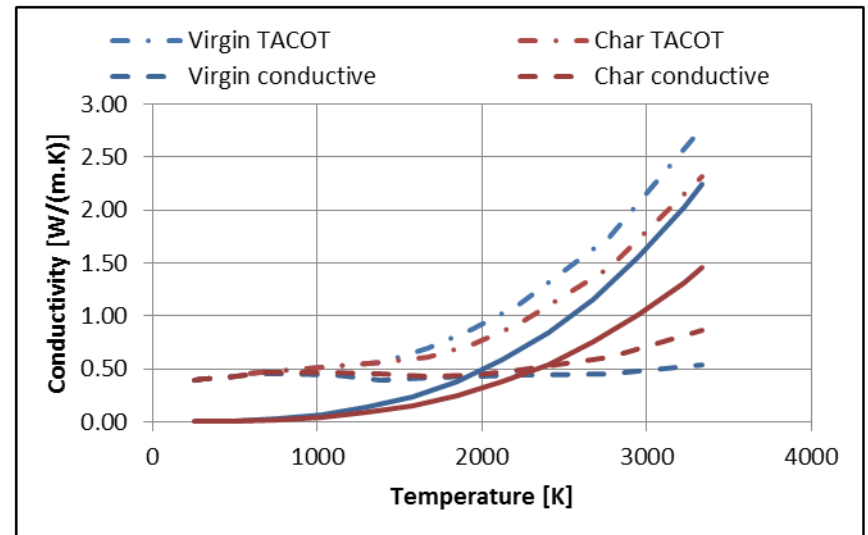
$$\beta_c = 7300 \quad [m^{-1}]$$

$$\beta_v = 5000 \quad [m^{-1}]$$

- Keep diffuse outer surface

$$q = \sigma \varepsilon (T_\infty^4 - T_w^4)$$

- Also diffuse inner surface !!!



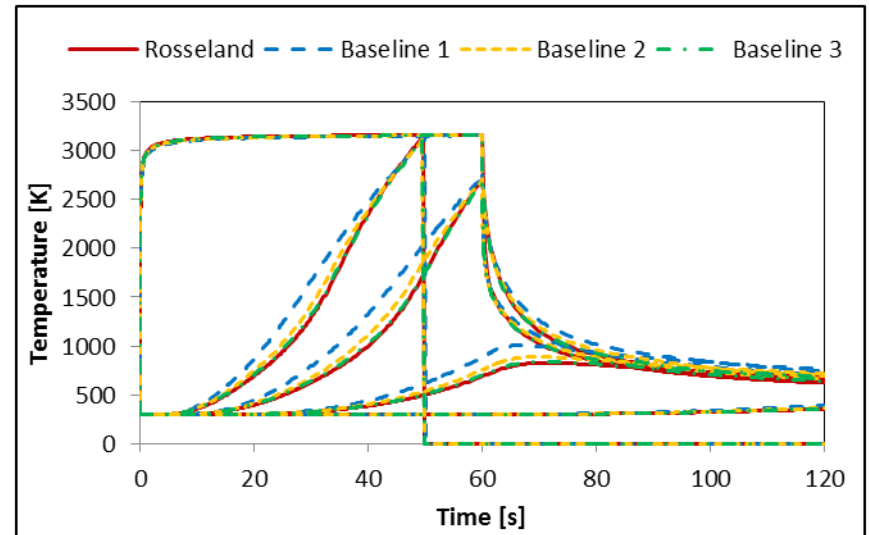
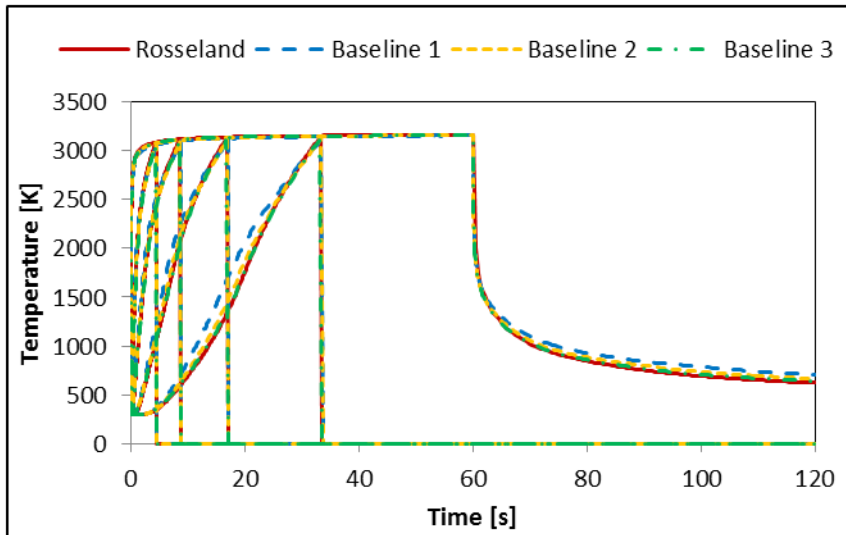
¹Susan White, Radiation Testing of PICA at the Solar Power Tower, AIAA 2010-4665

- Comparison with “constant” thermo-optical properties (interpolate properties between virgin and charred state)

Four different test-cases are run:

- Rosseland: Identical to original Test-case 2.3
- Baseline 1: albedo coefficient 0.0
- Baseline 2: albedo coefficient 0.68 (realistic estimate)
- Baseline 3: albedo coefficient 0.90

$$\Omega_{\text{albedo}} = \frac{\sigma_s}{(\alpha + \sigma_s)} = \frac{\sigma_s}{\beta}$$

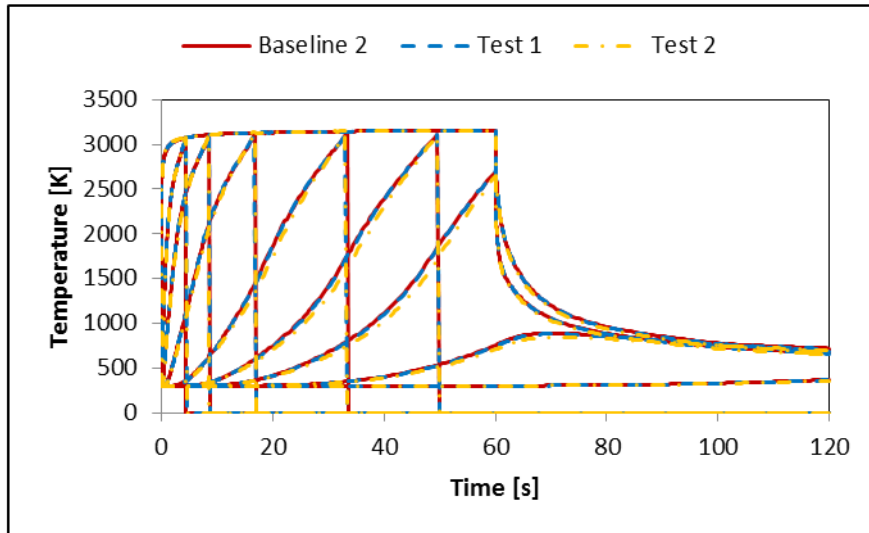
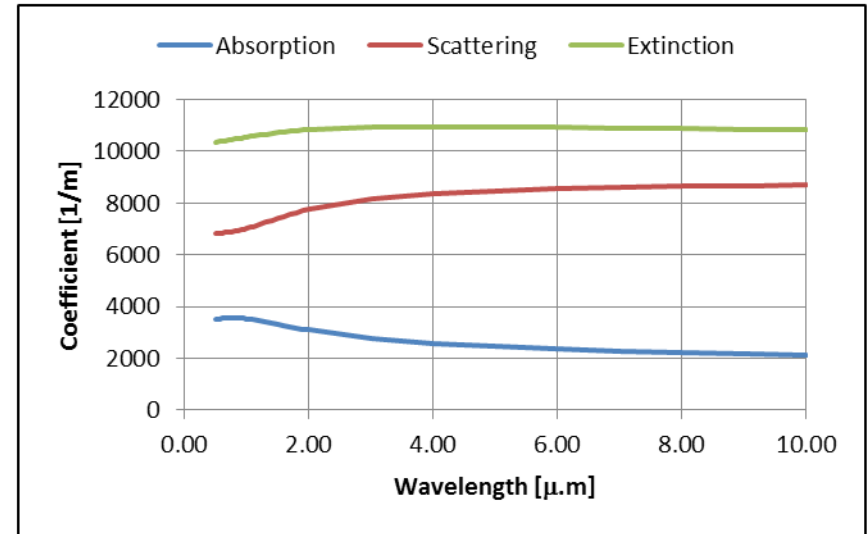


This document is the property of Astrium. It shall not be communicated to third parties without prior written agreement. Its content shall not be disclosed.

- Estimated carbon fibre preform properties (charred) – Mie theory for infinite cylinders homogenised for the material.

Three examples are compared:

- Baseline 2: albedo coefficient 0.68
- Test 1: Scaled wave length dependent properties
- Test 2: wave-length dependent properties



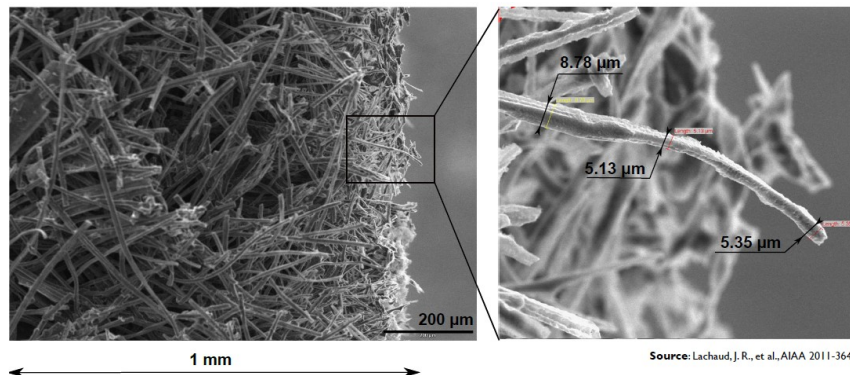
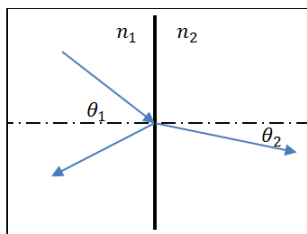
- Estimate virgin properties using PICA extinction coefficients and Mie theory value at 1.4 μm

$$\beta_{\text{Mie theory}} = 10.561 \quad [m^{-1}]$$

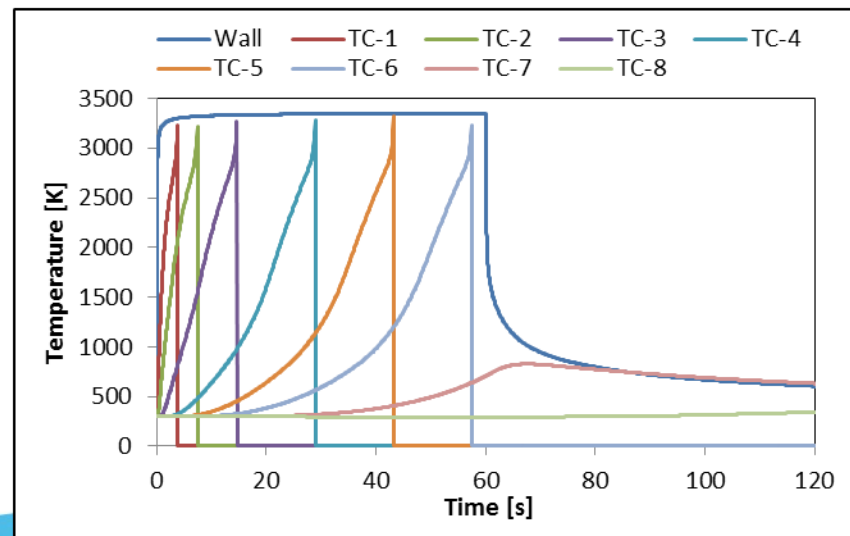
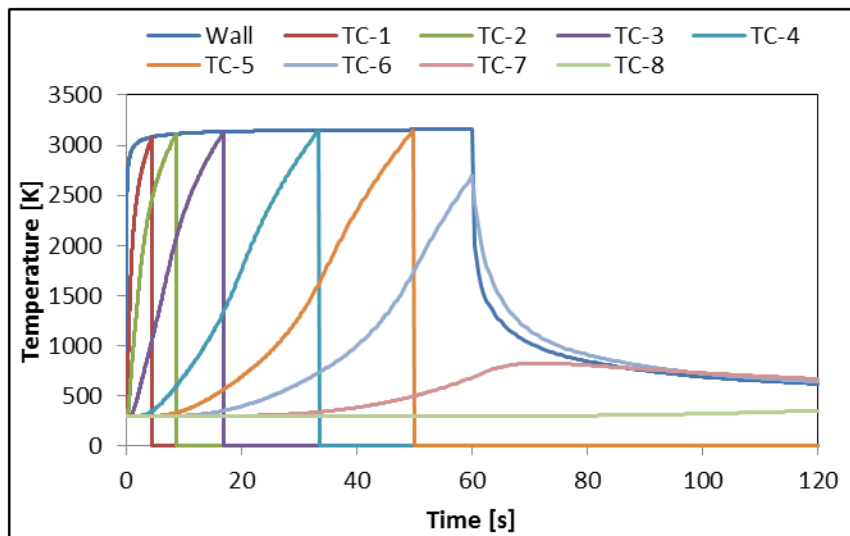
$$\beta_c = 7300 \quad [m^{-1}]$$

$$\beta_v = 5000 \quad [m^{-1}]$$

- More realistic radiation type boundary for the radiation problem (Fresnel type) – we assume that $n_1 = n_2 = 1$



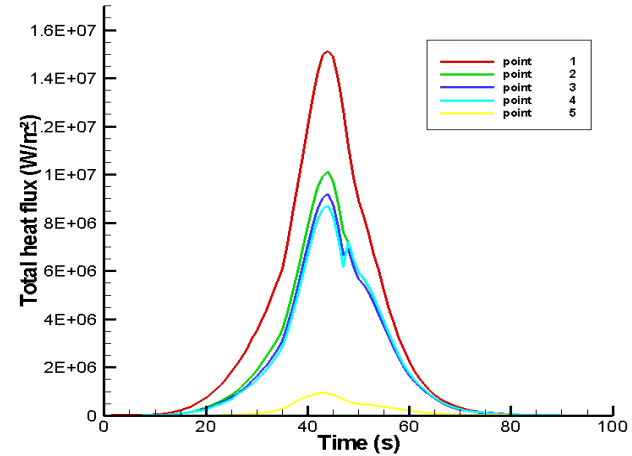
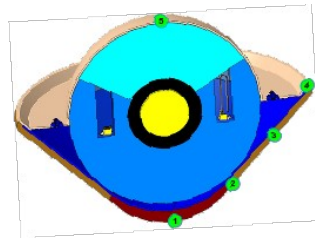
- Reduced “effective” surface emissivity
- Thermo-couples show “non-Rosseland” response – Optical thick assumption at outer surface not valid



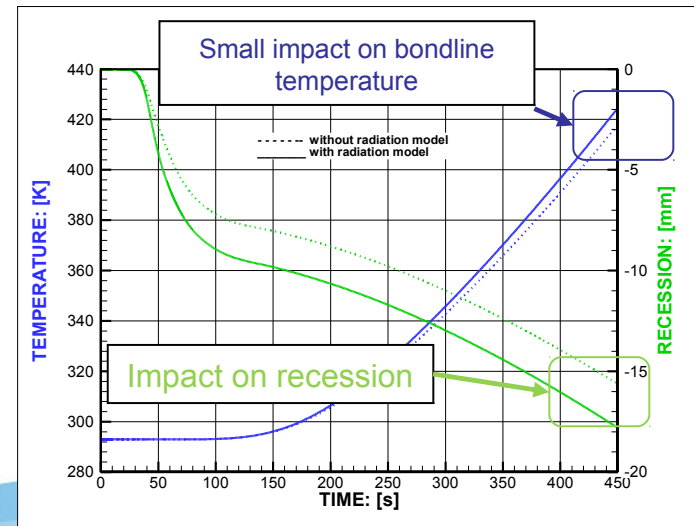
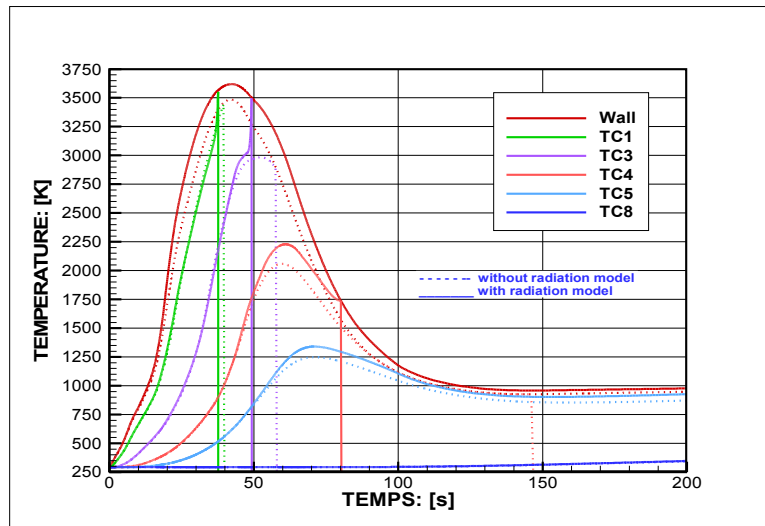
- Compare TACOT material with and without radiation model on High Speed Earth entry like mission and impact on bond-line temperature with heat-shield structure.



1D representative heat shield stack material



- Thermo-couples show “non-Rosseland” response – Optical thick assumption at outer surface not valid



This document is the property of Astrium. It shall not be communicated to third parties without prior written agreement. Its content shall not be disclosed.

- Conduction-radiation coupling in full participating (charring) and ablative material has been successfully implemented in 2 different code BE04 and SAMCEF relying on 2 different numerical solver method.
- A semi-transparent thermo-ablative model has been built on existing quartz-silica material (3DSiSi) which appeared relevant to rebuild ground plasma test.
- On low density C/R PICA like material (TACOT), numerical experiments demonstrate the interest of high fidelity conduction-radiation coupling compared to standard Rosseland radiation diffusion model in order to capture the near outer wall temperature distribution.
- But confidence on thermo-optic properties of low density C/R material must be increased.
- Optical elementary characterization of carbon felt are on progress at the CETHIL laboratory.
- Consistency of these parameters will be assessed at a macro-scale homogenized thermo-optical model

This document is the property of Astrium. It shall not be communicated to third parties without prior written agreement. Its content shall not be disclosed.

Thank you for your attention

This document is the property of Astrium. It shall not be communicated to third parties without prior written agreement. Its content shall not be disclosed.



*Radiation-Shapes-Thermal Protection Investigations
for High Speed Earth Re-entry*

Gas surface interaction modeling

B. Aupoix¹, A. Bourgoing², B. Chanetz¹, D. Coponet¹,
B. Rey³, J.B. Vos³

¹Onera – ²Astrium – ³CFS Engineering

7th European Workshop on TPS & Hot Structures, April 8-10, 2013, Noordwijk NL



The research leading to these results has received funding from the European Union Seventh Framework Programme (FP7/2007-2013) under grant agreement n° 241992

Contents

- Background
- Experimental studies
- Numerical rebuilding
- Conclusions

Background: RASTAS SPEAR FP7 Project

Main objective EU funded FP7 RASTAS SPEAR Project:

*increase Europe's knowledge in high speed re-entry vehicle
technology to allow for planetary exploration missions in the
coming decades*



Earth Re-Entry Capsule shape

Background WP5 Gas Surface Interaction Modeling

Main objective of RASTAS SPEAR WP5

to analyze in detail the coupling between surface roughness and blowing and to identify possible savings in design margins

Activities:

- Turbulence modelling (roughness + blowing)
- **Wind Tunnel Experiments and Numerical rebuilding**
- Earth Re-entry capsule simulations
- Synthesis

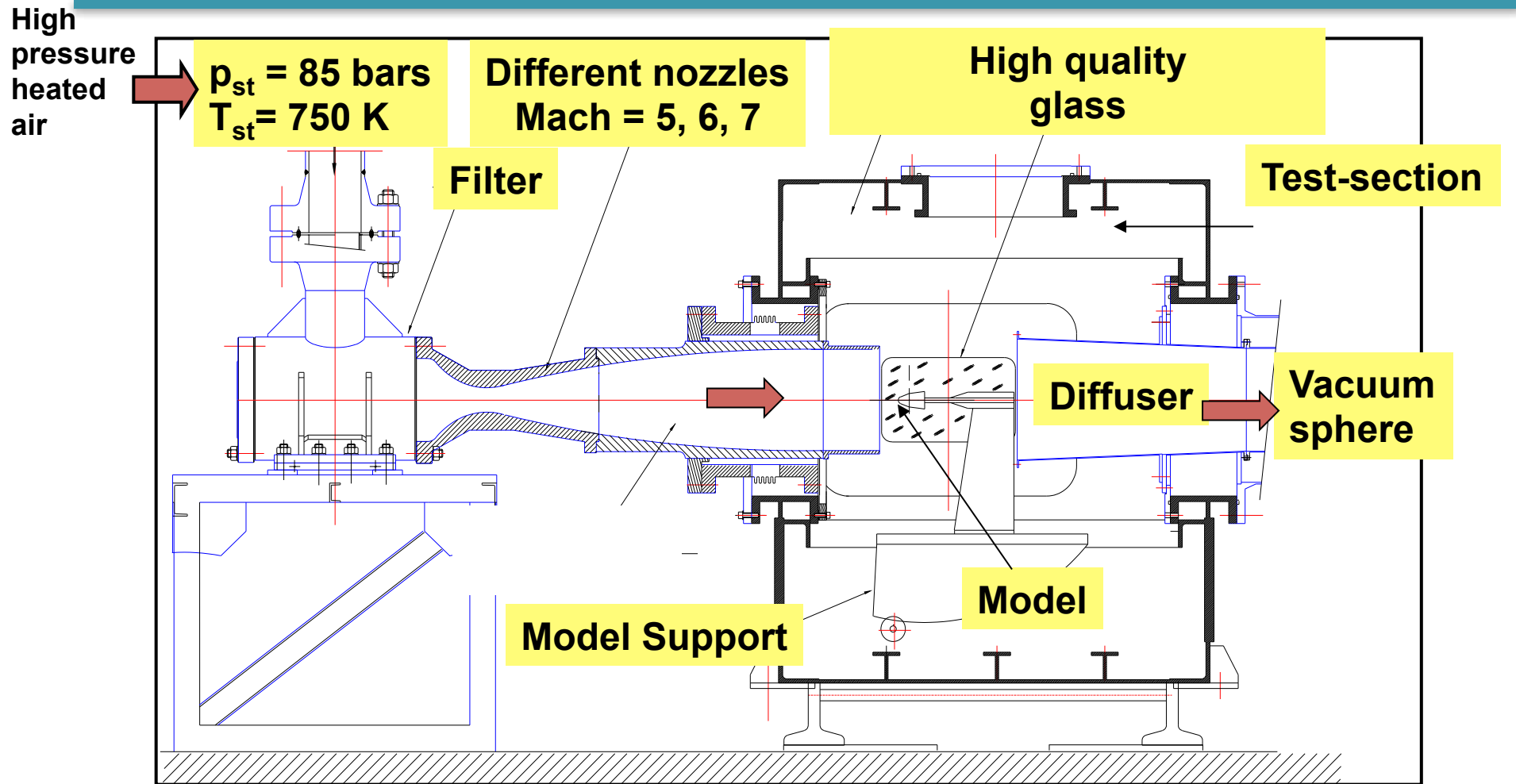
Wind Tunnel Experiments

Objective

determination of the wall heat-flux with and without roughness and with and without mass blowing

- Wind tunnel facility: Onera R2Ch blow-down WT
- Wind tunnel model : flat plate with a sharp leading edge

R2Ch Wind Tunnel Characteristics (I)



R2Ch Wind Tunnel Characteristics (2)

Nozzle exit diameter :

326 mm

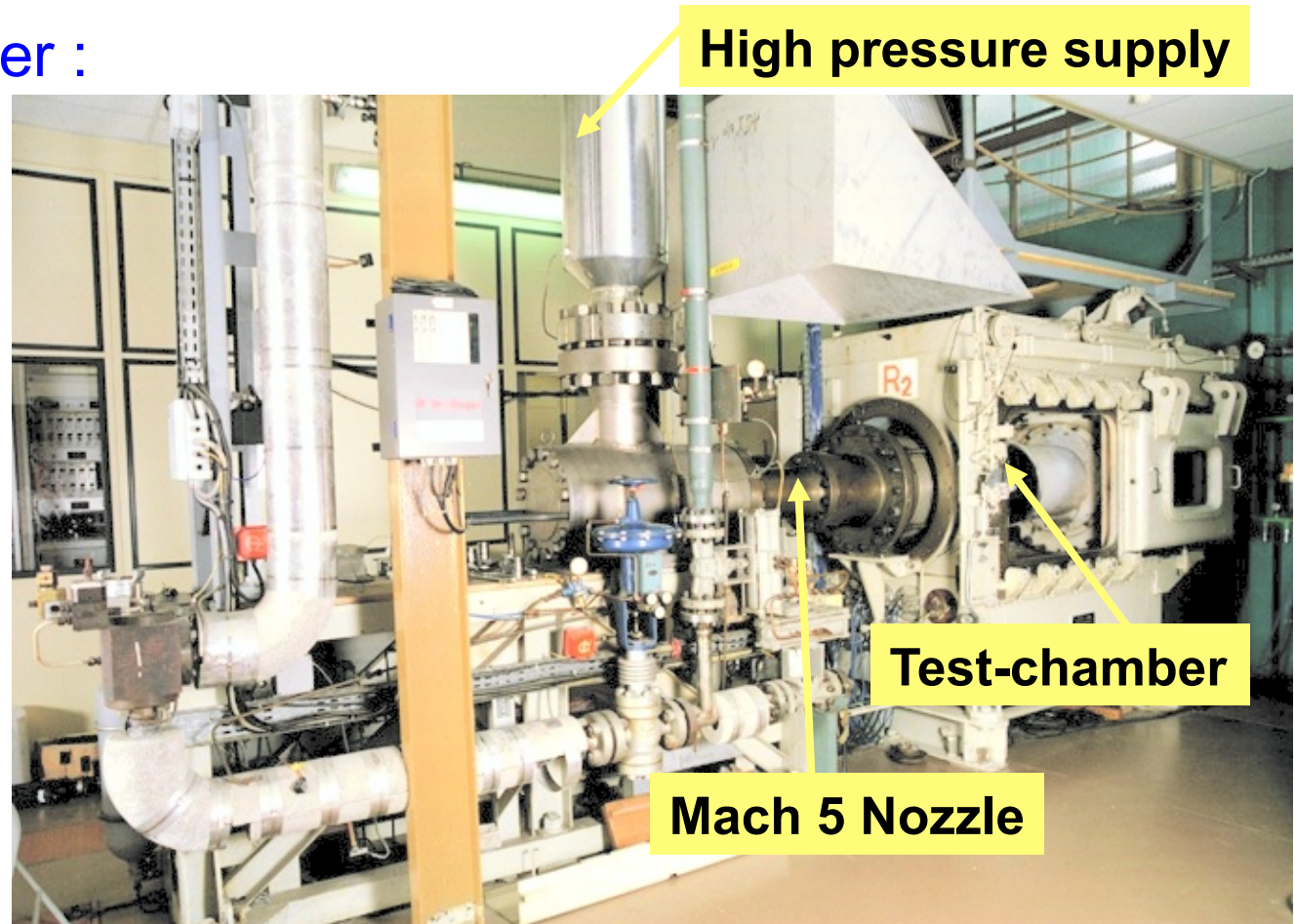
p_{st} :

from $5 \cdot 10^5$ Pa
to $50 \cdot 10^5$ Pa

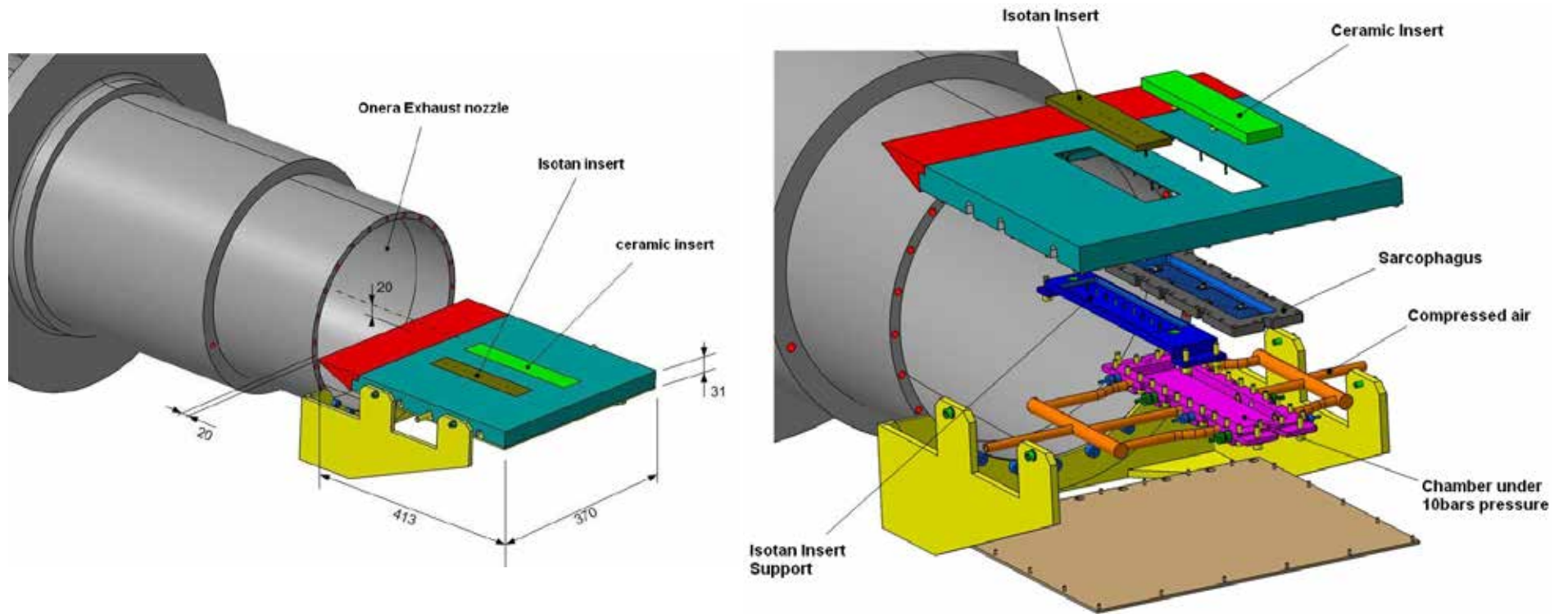
$T_{st} = 650$ K

Re_u (L=1 m) :

from $4.25 \cdot 10^6$
to $42.5 \cdot 10^6$

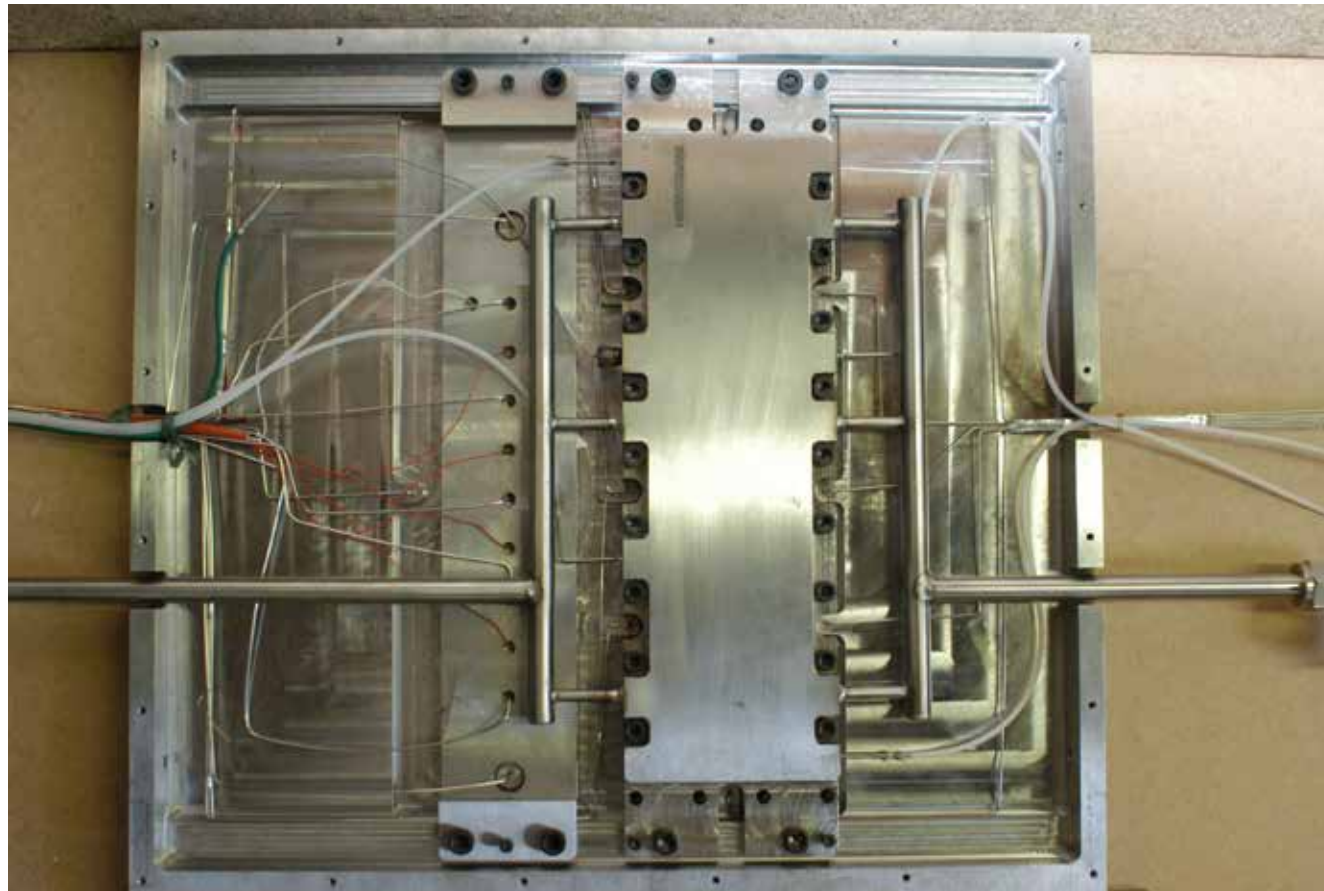


View of the experimental set-up



Two inserts:
 isotan (smooth)
 porous ceramic inserts (smooth/rough)

View of the pressurized circuit



R2Ch Measured data

measurements:

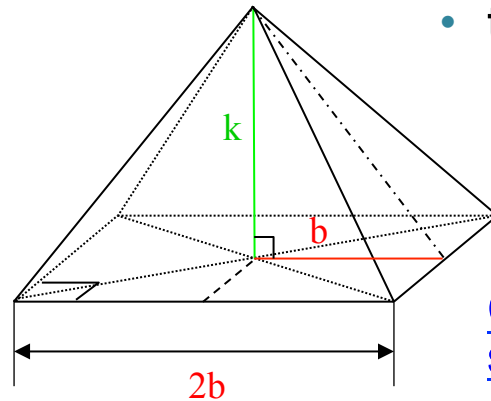
- heat-flux through infrared thermography
- temperature (thermo couples)

visualization :

- Schlieren photographs



Roughness characteristics (I)



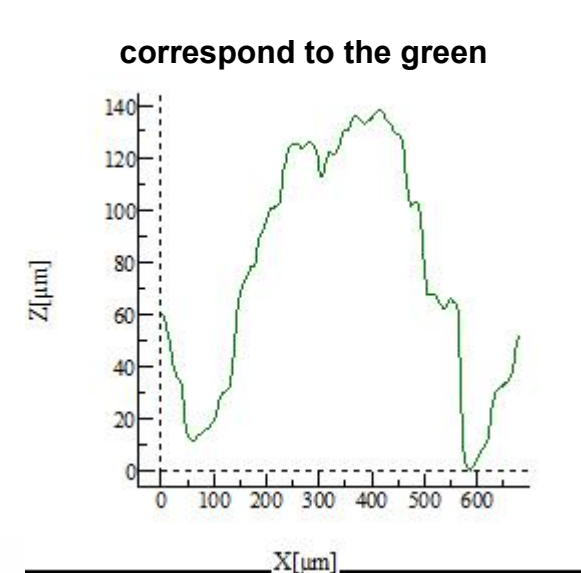
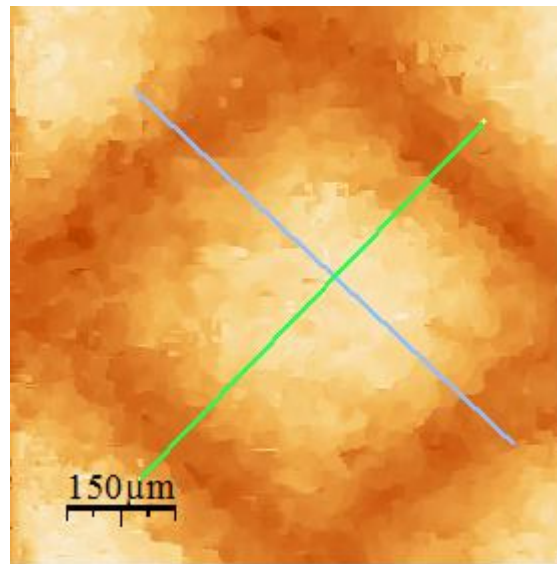
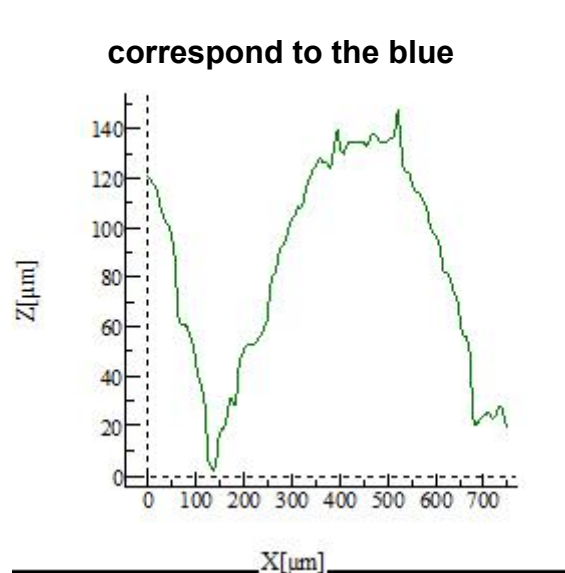
- two porous ceramic inserts (porosity 48 %)
 - without roughness
 - with roughness

Characteristics of the roughness : pyramids joined and in staggered rows

- a regular pattern constituted by pyramidal roughness ;
- the base of each pyramid is a square, each side around $2b = 550 \mu\text{m}$
- the mean value of the height k of each pyramid is $176 \mu\text{m}$ (standard error = $34 \mu\text{m}$)
- the shape of the pyramid is defined by the ratio k/b , which leads to a theoretical angle of 30°
- these pyramids are in alternate rows

Roughness characteristics (2)

determination using an electron microscope: **truncated pyramids**



Height : 146 μm
 Base (L) : 522 μm
 Base (l) : 562 μm



Equivalent sand roughness height $k_s \sim 400 \mu m$

Triggered transition

Characteristics of the rough band

- located at $X = 30$ mm from the leading edge
- length along X-axis : 12 mm
- diameter of the carborandum spheres : 0.7 mm

Blowing rates

Characteristics of the reduced ceramic insert

- located at 140 mm from the leading edge
- length along X – axis : 100 mm
- length in spanwise along Y – axis : 40 mm

Connection between the mass flow rates

- 1.2 kg/m²/s equals 4.8 g/s through the insert
- 0.6 kg/m²/s equals 2.4 g/s through the insert

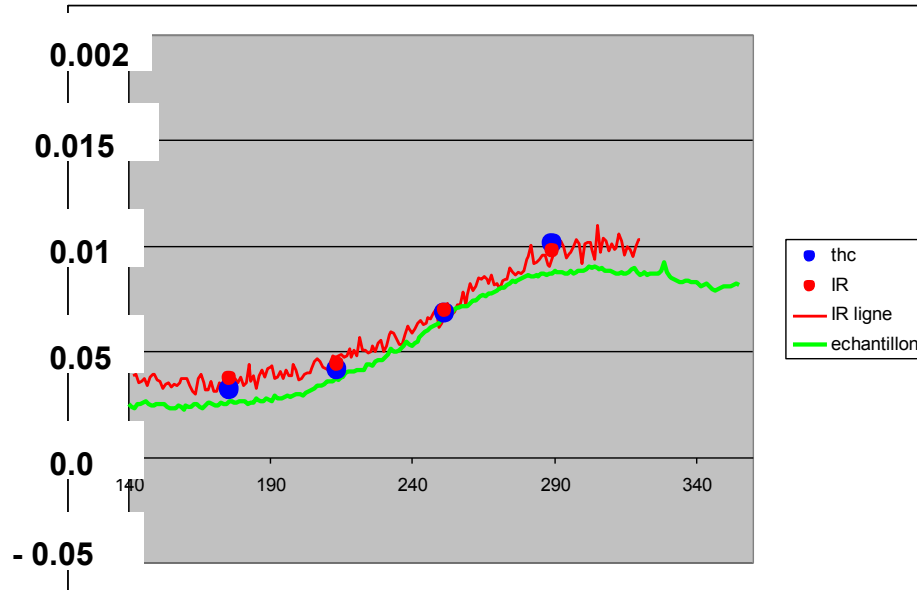
Stanton number definition

$$St = \Phi / \rho_{inf} U_{inf} Cp (T_{st} - T_w)$$

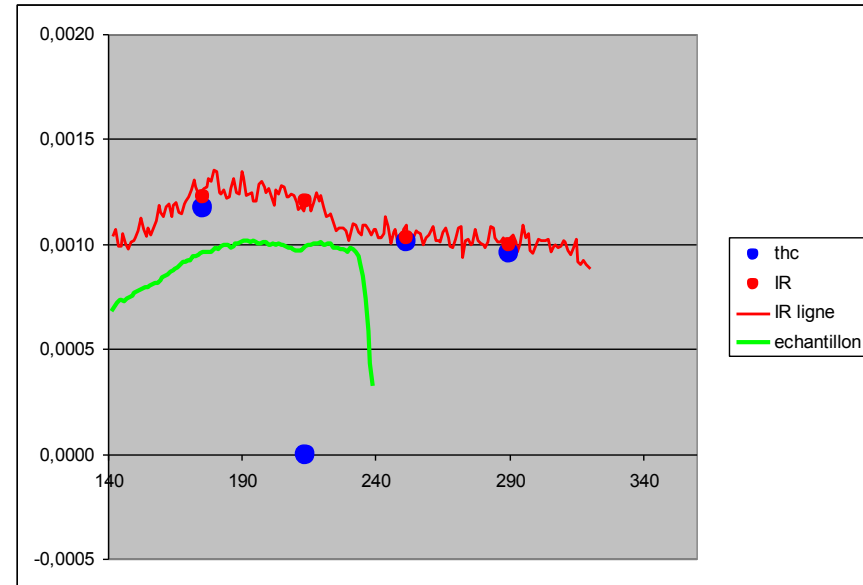
- Φ wall heat-flux in W/m²,
- ρ_{inf} the density in the nozzle
- U_{inf} the velocity in the nozzle
- T_{st} the stagnation temperature
- T_w the wall temperature
- Cp the calorific coefficient at constant pressure equal to 1003 J/kg/K.

Natural and triggered transition $7 \cdot 10^5$ Pa

natural transition



triggered transition

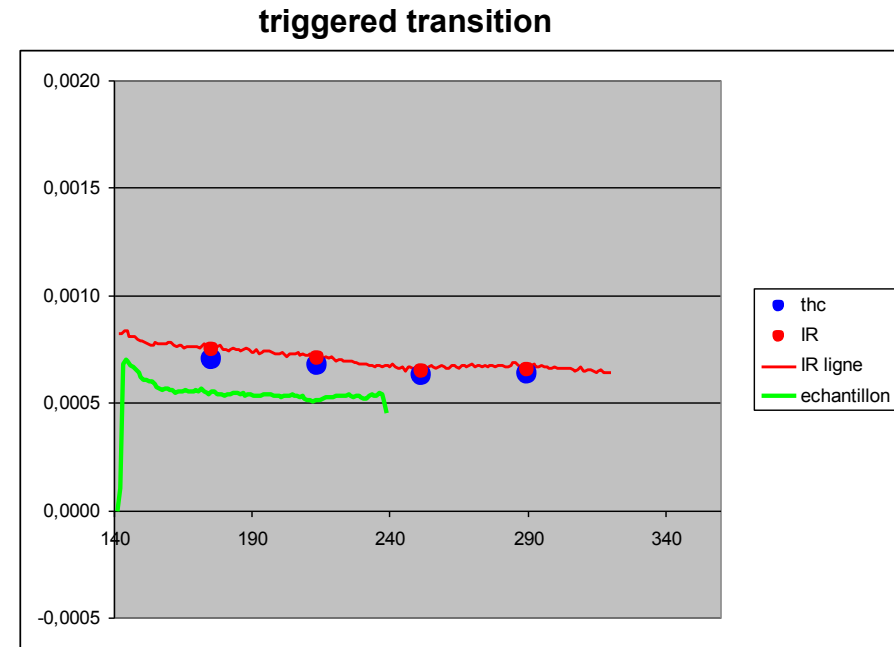
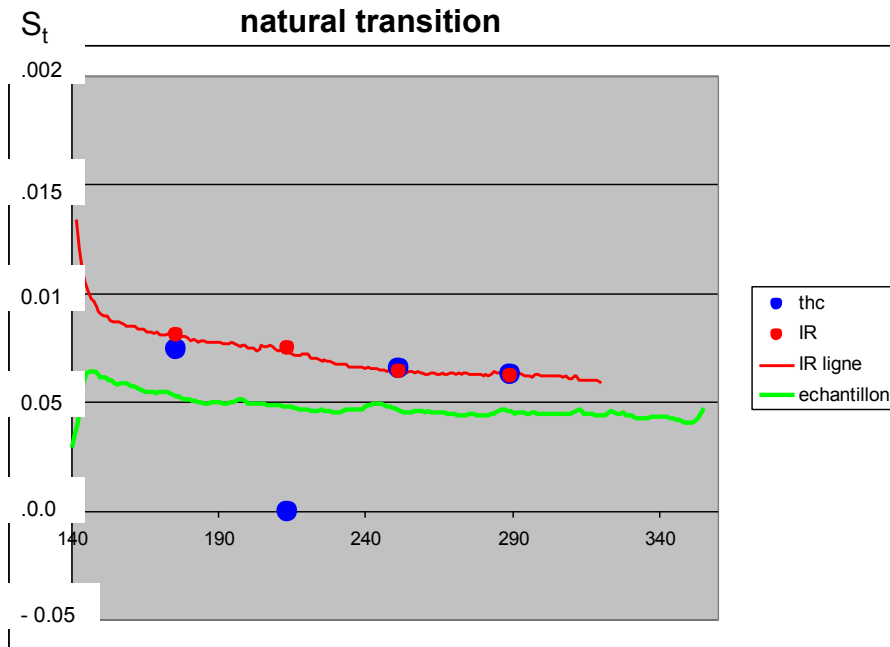


Evolution of the Stanton number along the X-axis for $p_{st} = 7 \cdot 10^5$
on the smooth insert without blowing
natural and triggered transition - run 3757 and 3780

Green = ceramic insert

Red = Isotan insert

Natural and triggered transition $50 \cdot 10^5 \text{ Pa}$

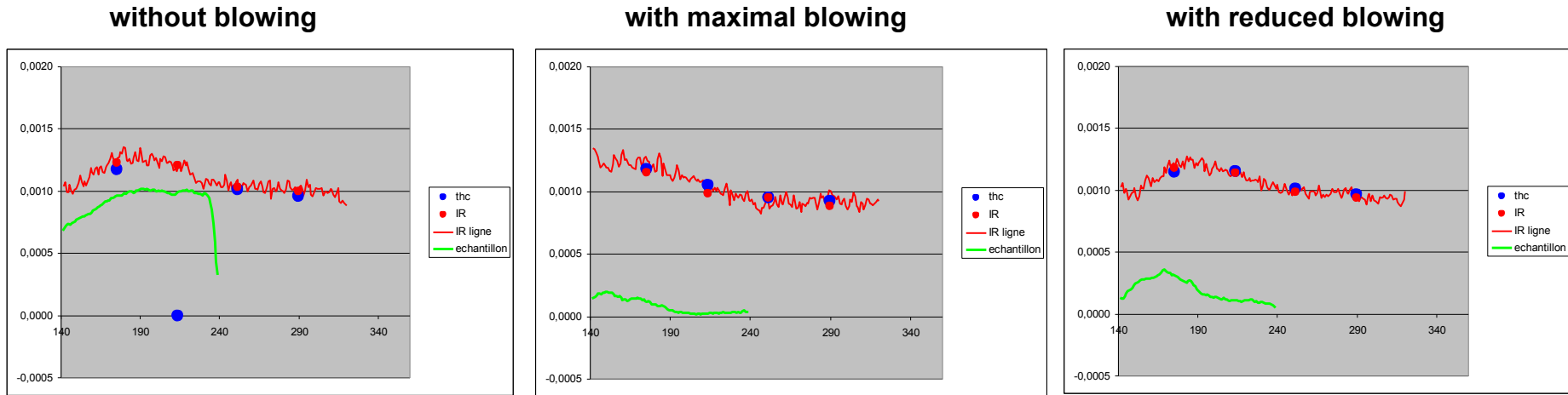


Evolution of the Stanton number along the X-axis for $p_{st} = 50 \cdot 10^5$ on the smooth insert without blowing in natural and triggered transition - run 3763 and 3782

Green = ceramic insert

Red = Isotan insert

Effect of blowing at $7 \cdot 10^5$ Pa

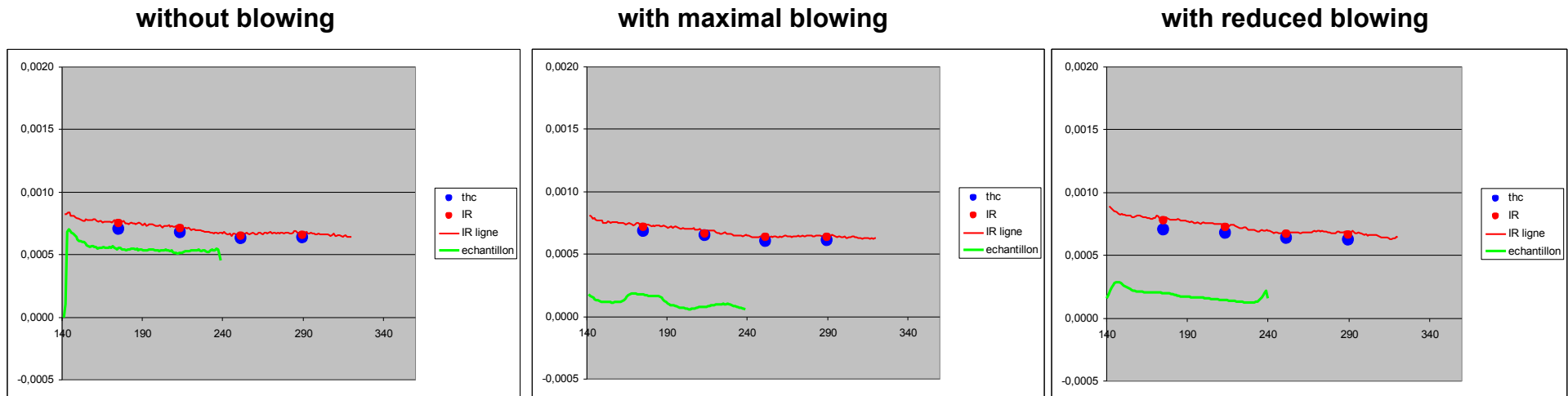


Evolution of the Stanton number along the X-axis for $pst = 7 \cdot 10^5$ on the smooth insert without blowing and with a blowing rate equal to 4.8 g/s then of 2.4 g/s with triggered transition - run 3780 , 3781 and 3784

Green = ceramic insert

Red = Isotan insert

Effect of blowing at $50 \cdot 10^5 \text{ Pa}$



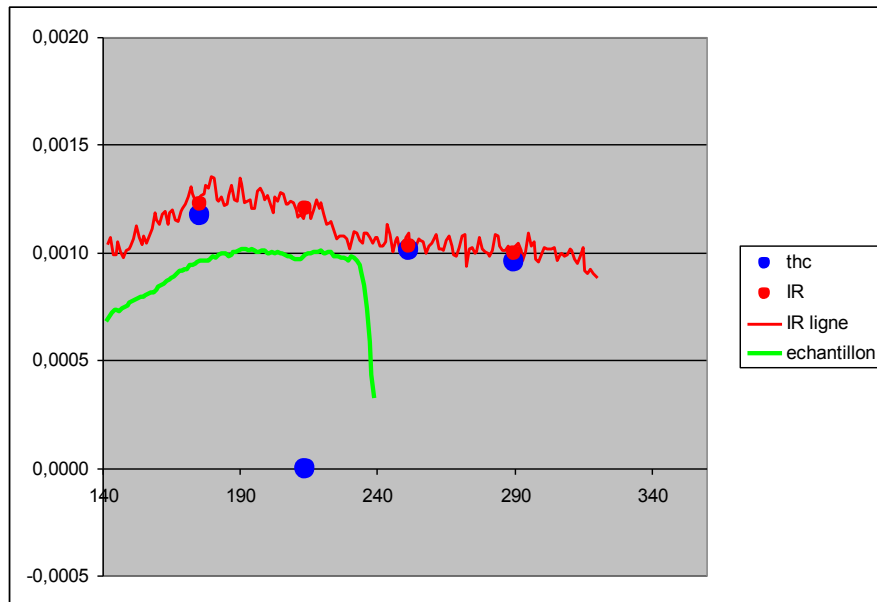
Evolution of the Stanton number along the X-axis for $p_{st} = 50 \cdot 10^5$ on the smooth insert without blowing and with a blowing rate equal to 4.8 g/s then of 2.6 g/s with triggered transition - run 3782 , 3787 and 3794

Green = ceramic insert

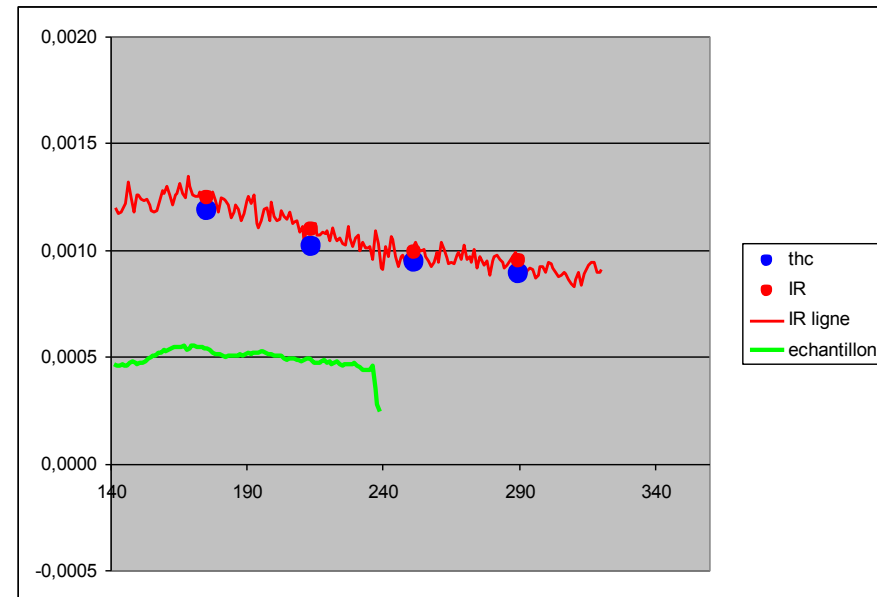
Red = Isotan insert

Effect of roughness $7 \cdot 10^5$ Pa

smooth



rough

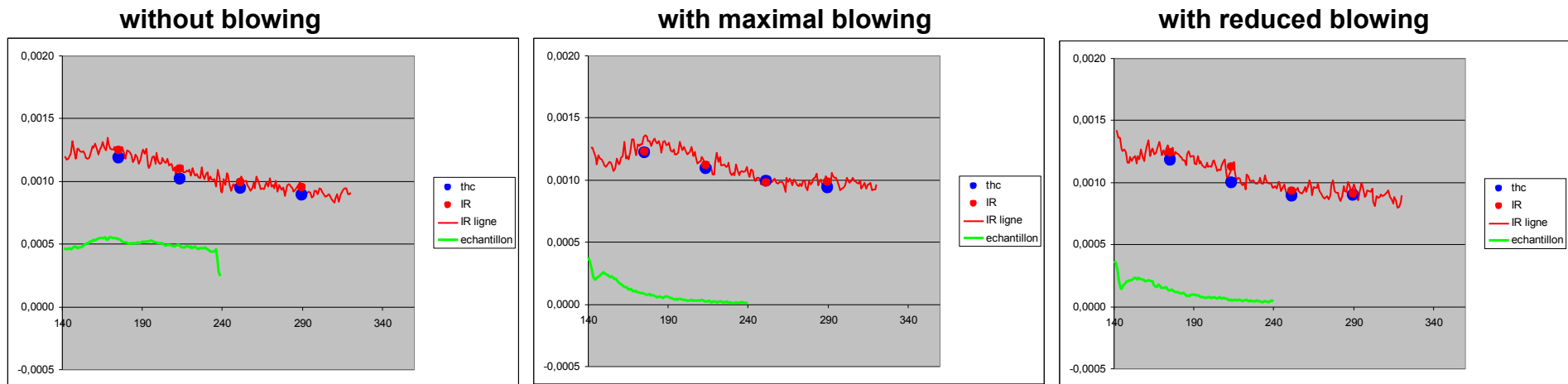


Evolution of the Stanton number along the X-axis for $p_{st} = 7 \cdot 10^5$ on the smooth and rough insert without blowing in triggered transition - run 3780 and 3790

Green = ceramic insert

Red = Isotan insert

Effect of blowing on the rough insert $7 \cdot 10^5$ Pa

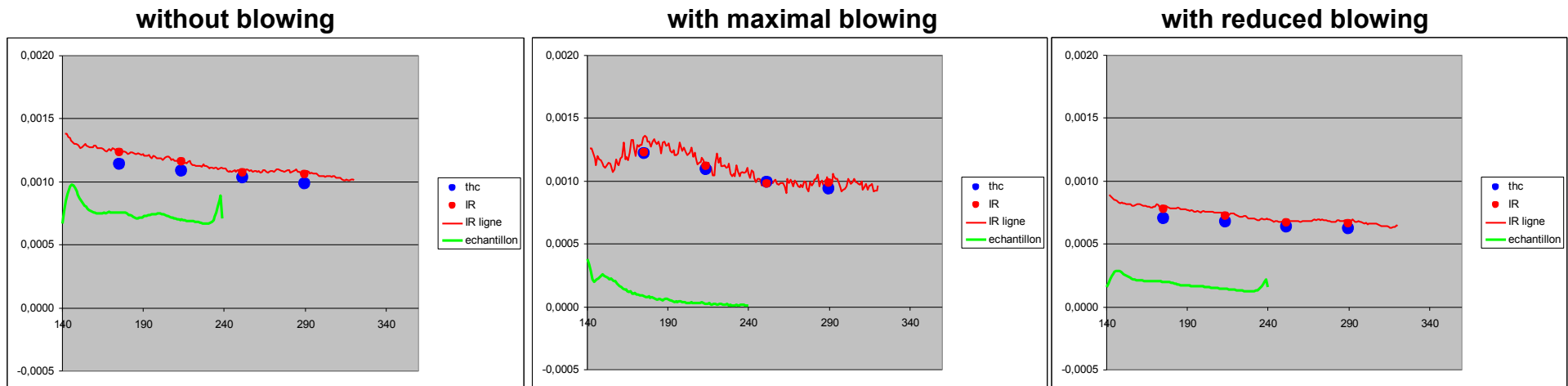


Evolution of the Stanton number along the X-axis for $p_{st} = 7 \cdot 10^5$ on the rough insert without blowing and with 4.6 g/s and 2.6 g/s in triggered transition - run 3790 , 3799 and 3798

Green = ceramic insert

Red = Isotan insert

Effect of blowing on the rough insert $50 \cdot 10^5 \text{ Pa}$



Evolution of the Stanton number along the X-axis for $pst = 50 \cdot 10^5$ on the rough insert without blowing and with 4.6 g/s and 2.6 g/s in triggered transition – runs 3791, 3794 and 3800

Green = ceramic insert

Red = Isotan insert

Conclusions experiments

- 31 experiments were made
- good repeatability of the runs
- transition triggered in most of the cases
- **no increase of the heat flux with roughness**
- very important effect of blowing on Stanton number

Numerical Rebuilding ONERA WTT Experiments

Two approaches

1. Boundary layer simulations using the ONERA Clicet code
2. Navier Stokes simulations using the NSMB CFD code

Boundary Layer Computations of the Onera-Meudon Experiments

Aims

- Assess the performances of turbulence models to predict hypersonic flows with wall roughness and wall blowing effects
- Get a deeper insight into the flow physics (transition process...)

Choice of a boundary layer approach

- Nearly all 31 experimental runs were computed
- Parametric investigation
 - Transition location and process
 - Turbulence model ⇒ 244 computations
 - Wall temperature
- Need an efficient solver ⇒ boundary layer approach
 - Justified as no entropy swallowing, shock/B.L. interaction, separation...
 - ONERA code CLICET
 - large set of transition, turbulence, roughness models
 - adaptive grid...

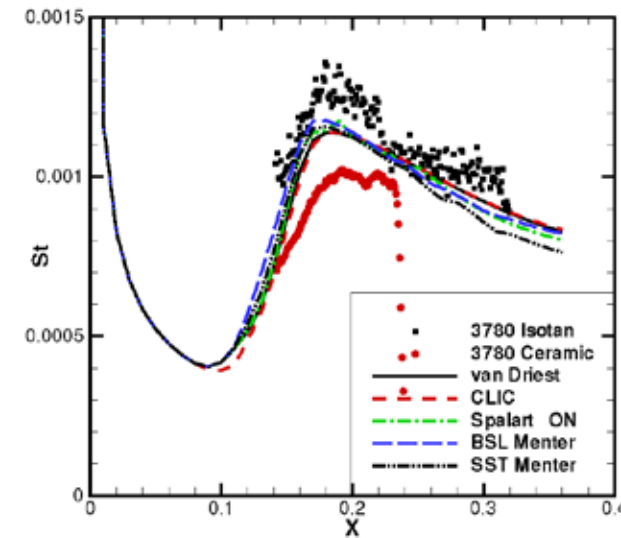
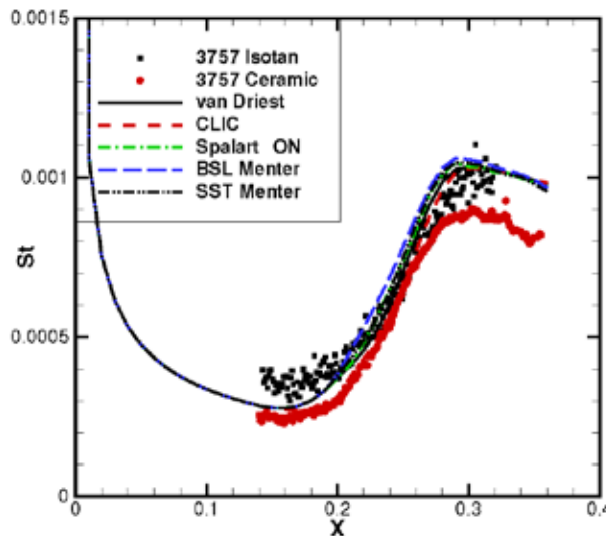
Transition Modelling

- Arnal (1988)
 - R2Ch wind tunnel, Mach 5: transition location $2 \cdot 10^6 < \rho u_e x / \mu_e < 3.5 \cdot 10^6$
- Tripped transition
 - Reda (2004) criterion
 - Can account for lag behind the trip
- Transition can be computed as abrupt or smooth (intermittency function)

Turbulence Modelling

- Wall roughness and blowing \Rightarrow turbulence increase in the wall region
- Wall blowing at least accounted for via change of wall normal velocity
- Investigated models
 - Mixing length models: van Driest and “CLIC” (blend Michel & Cebeci mod.)
 - Wall roughness and blowing corrections can be used together
 - Spalart and Allmaras:
 - Boeing and ONERA wall roughness corrections (Aupoix and Spalart, 2003)
 - No wall blowing correction
 - $k-\omega$ models : BSL and SST (Menter)
 - Wilcox’ wall roughness and blowing corrections (cannot be used together, cure developed for CFSE)
 - Interference of wall corrections with SST limiter (cure now available, BSL models more reliable)

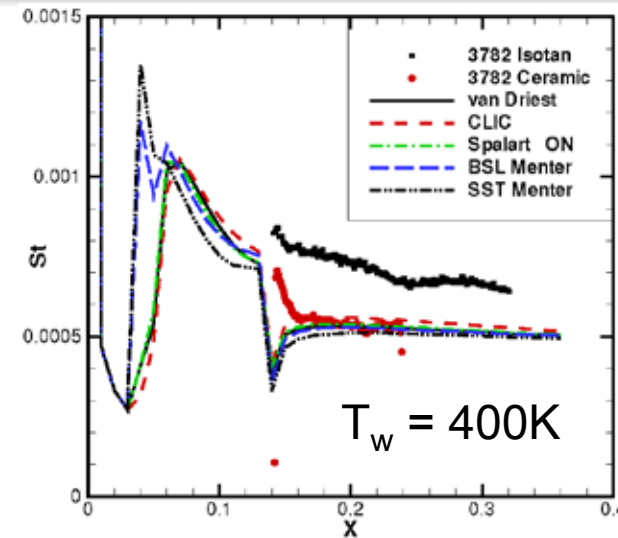
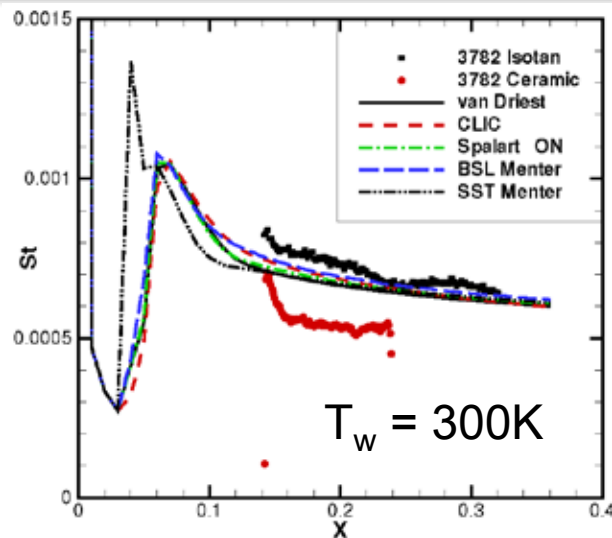
Smooth Wall Cases – No Blowing



- 7 bar, natural transition
- Trip 3 cm from leading edge : significant transition lag behind the trip
- In all cases, measurements in the transition regime \Rightarrow not relevant
- Smaller heating: reduced differences between measurements on isotan and ceramic insert

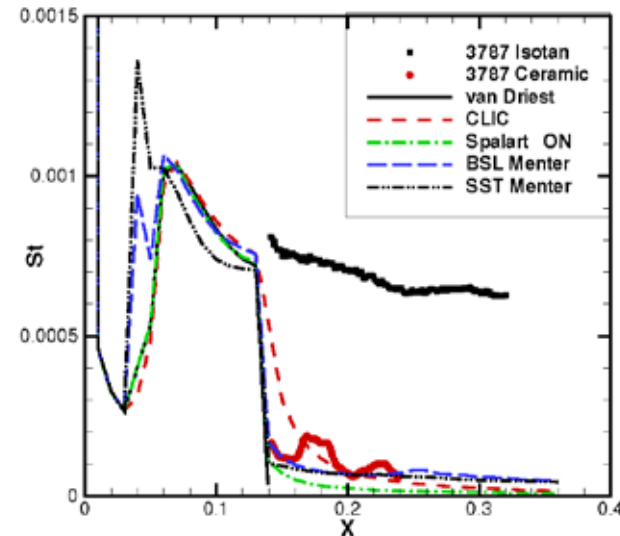
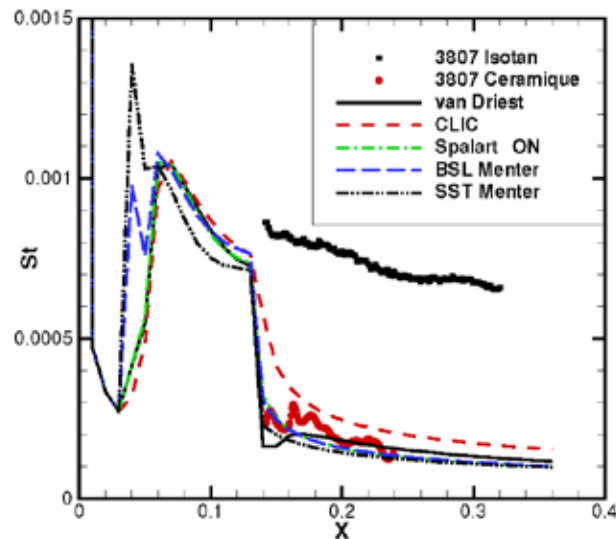
Tripped transition

Smooth Wall Cases – No Blowing



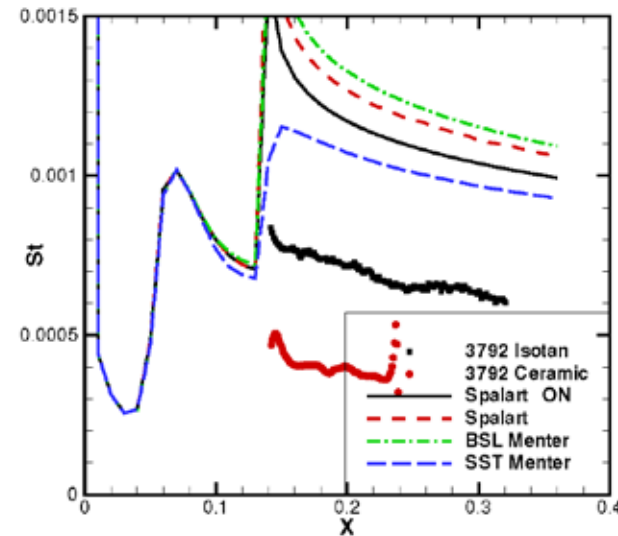
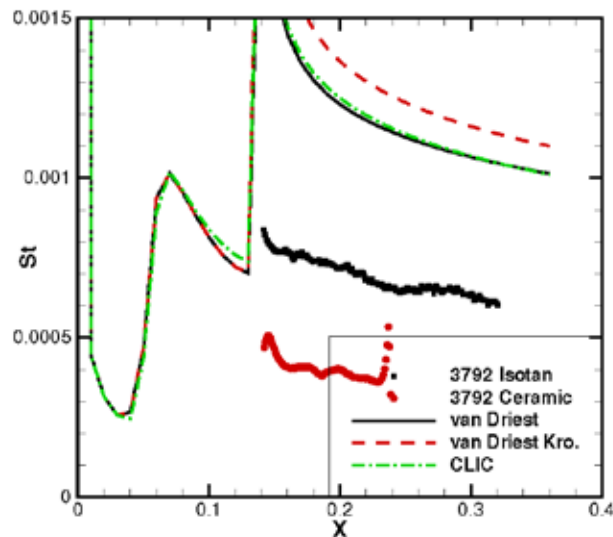
- 50 bar, tripped transition
- Reda's criterion confirms trip efficiency
- Best predictions assuming smooth transition (different model behaviours in the transition region)
- Change of T_w still needed to get good agreement with isotan and ceramic insert

Smooth Wall Cases – Wall Blowing



- 50 bar mass flow rate 2.6 gs^{-1} 4.8 gs^{-1}
- Models fairly reproduce the heat flux reduction on the ceramic insert
- CLIC: lag effect which deteriorates the prediction
- Highest blow rate: Spalart model underpredicts (lacks turbulence enhancement)

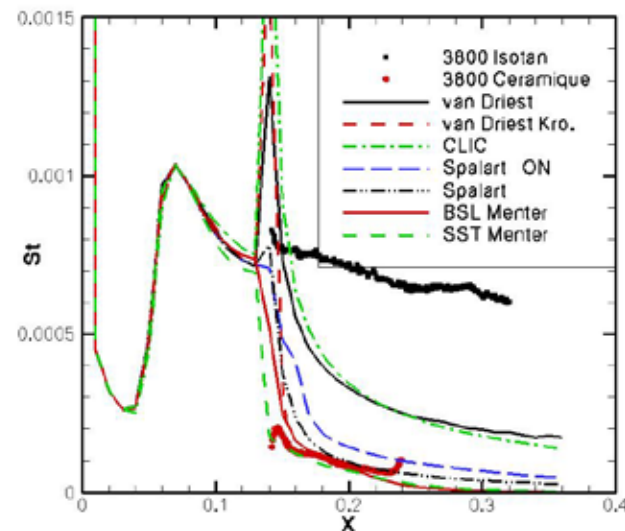
Rough Wall cases – No Wall Blowing



- 50 bar Algebraic models
- $k_s^+ \sim 120$ Fully rough regime
- All models predict Stanton number in agreement with Isotan upstream of rough insert and a heat flux increase on the rough insert while measurements give opposite trend!

Transport equation models

Rough Wall – Wall Blowing



- Blowing mass flow rate: 4.6 gs^{-1}
- Main effect is heat flux reduction by blowing
- Same model ranking (accounting or not for turbulence enhancement by blowing)
- Agreement with experiment fortuitous ?

Conclusions boundary layer simulations

- Boundary layer approach allowed a large parametric investigation at a reasonable cost
- Smooth surface
 - Importance of transition
 - Tripping required to have transition upstream of the inserts
 - Fully turbulent on the insert only for the 50b test cases
 - Wall heat flux determination on the ceramic insert: wall temperature has to be increased
- Wall blowing
 - Small blowing mass flow case well predicted by all models
 - Strong blowing mass flow case evidences the lack of a blowing correction for the Spalart and Allmaras model

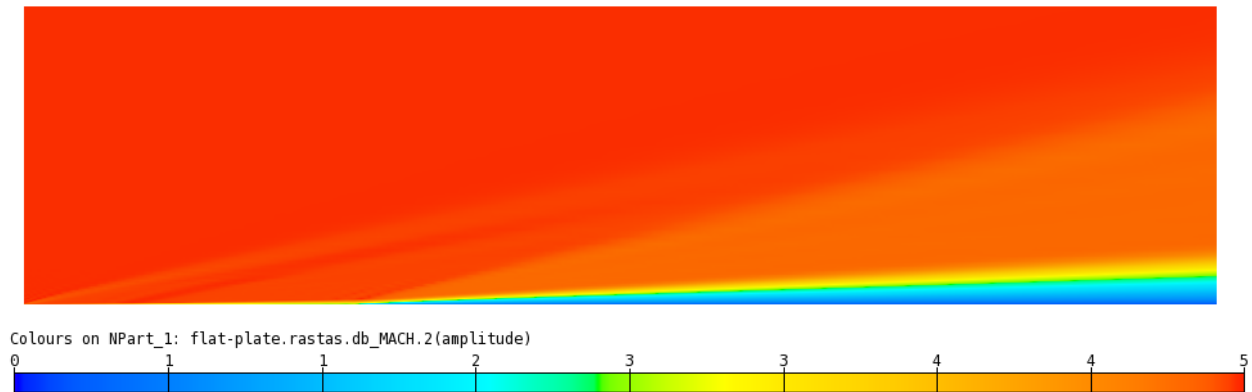
Conclusions boundary layer simulations

- Wall roughness
 - Evidences some discrepancies among models
 - Key issue: models predict heat flux increase, experiment heat flux decrease. Remains unexplained.
- Wall roughness and blowing
 - Models which cannot account for wall blowing (Spalart, $k-\omega$) predict lower (too low?) levels
 - Still problems with experiment?
- Analysis allowed to select test case for CFSE and provides reference computations for validation

Navier Stokes simulations

WTT rebuilding

- Mach: 5
- **Tripped transition**
- Imposed:
 - wall temperature
 - total pressure
 - total temperature
 - Reynolds number
 - Mach number
 - Blowing rate
 - Roughness height



Navier Stokes simulations

WTT reconstruction and validation

- Focus on 6 experiments at $50 \cdot 10^5$ Pa

Runs	1	2	3	4	5	6
code	3782	3807	3787	3792	3794	3800
Blowing rate	0 g/s	2.6 g/s	4.8 g/s	0 g/s	2.63 g/s	4.6 g/s
Roughness	smooth	smooth	smooth	rough	rough	rough

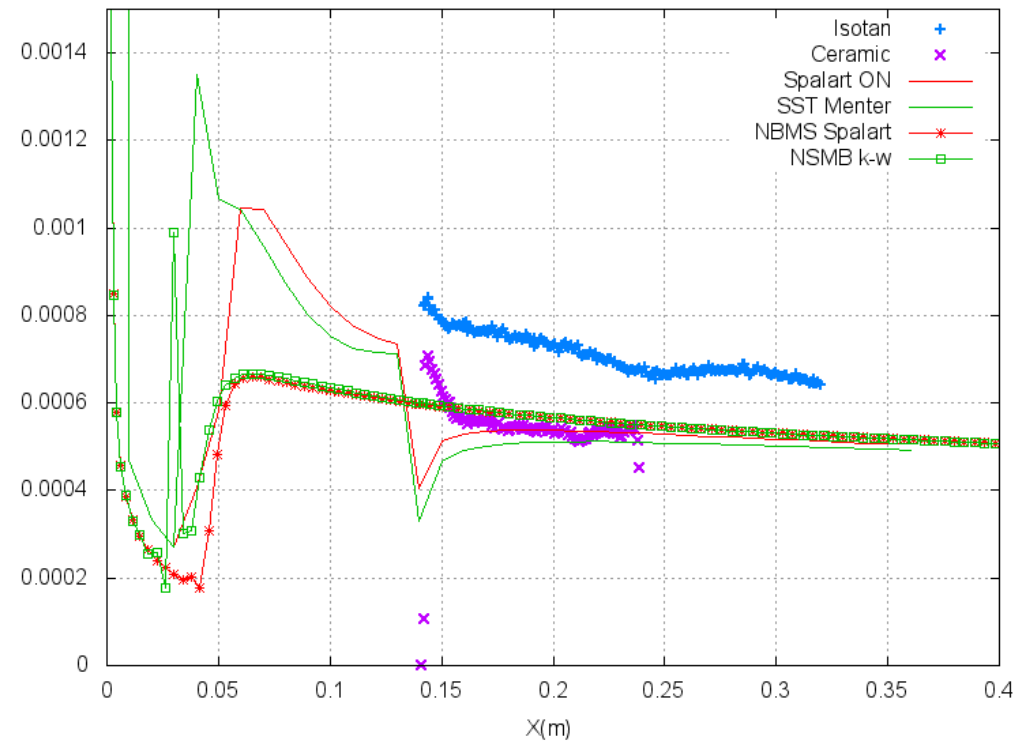
Navier Stokes simulations

WTT reconstruction and validation

Stanton number comparison for:

- **WTT Isotan insert**
- **WTT Ceramic insert**
- **Onera Spalart solver**
- **Onera SST Menter solver**
- **NSMB with Spalart (with points)**
- **NSMB with k-w (with points)**

WTT rebuilding - case01: 3782 - smooth insert without blowing

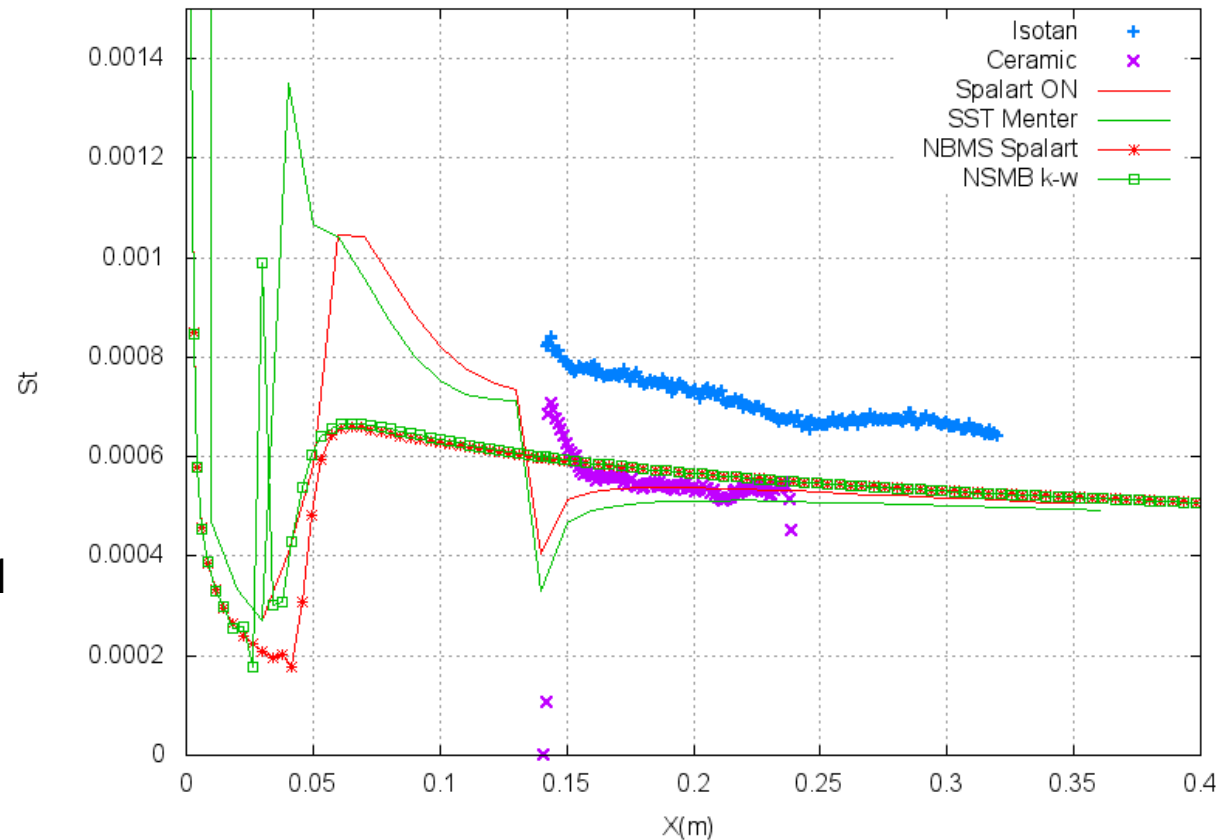


Navier Stokes simulations

WTT reconstruction and validation

Run 1: no blowing
no roughness

- $P_{st} = 4'870'956\text{Pa}$
- $T_{st} = 668\text{K}$
- Reynolds = 39'422'781
- $T_w = 410\text{K}$

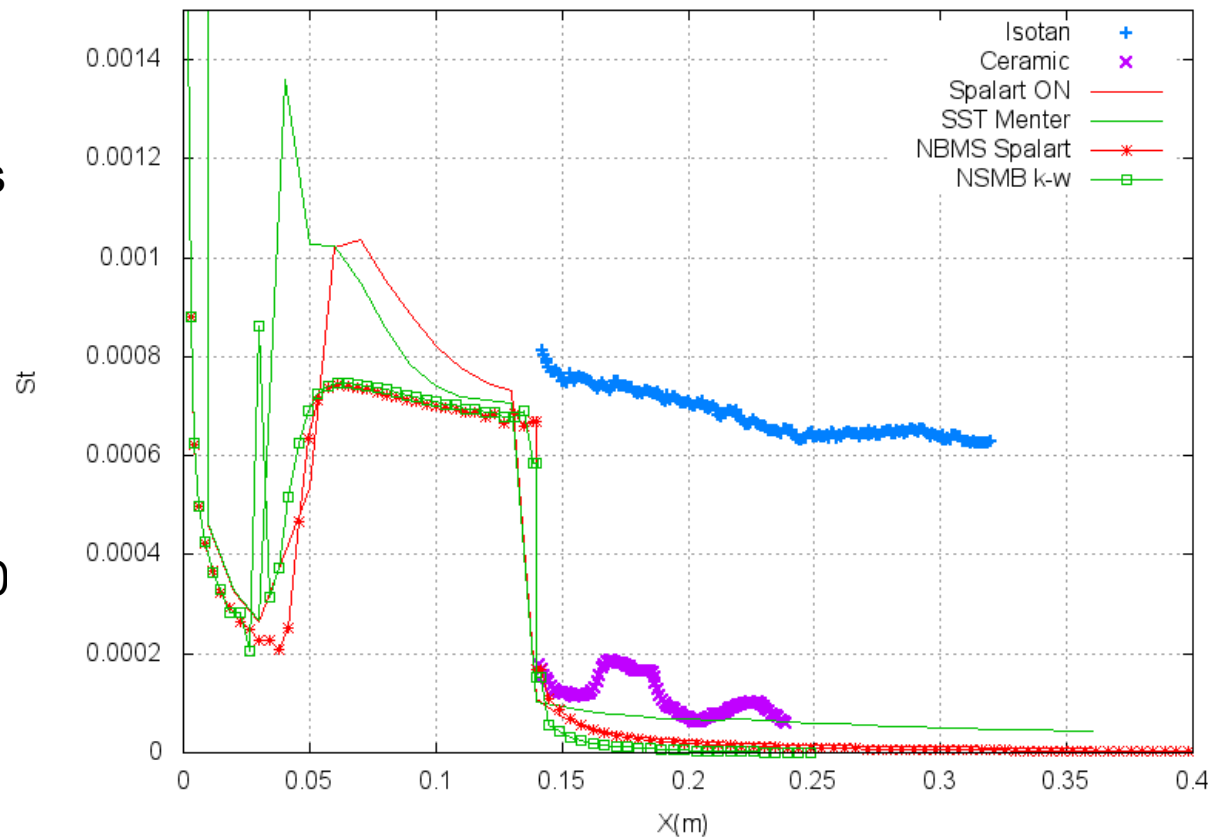


Navier Stokes simulations

WTT reconstruction and validation

Run 3: blowing rate: 4.8 g/s
no roughness

- $P_{st} = 4'909'812\text{Pa}$
- $T_{st} = 656\text{K}$
- Reynolds = 40'871'820
- $T_w = 320\text{K}$

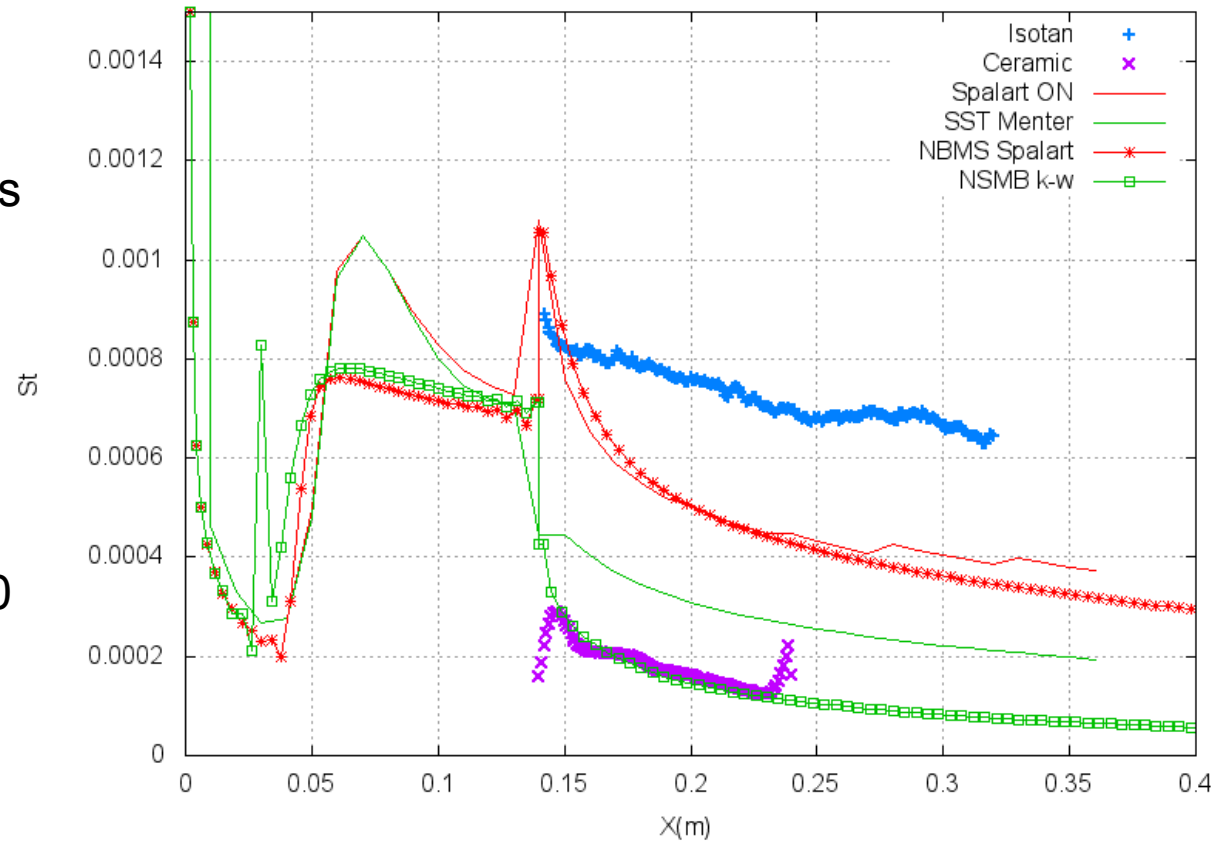


Navier Stokes simulations

WTT reconstruction and validation

Run 5: blowing rate: 2.63g/s with roughness

- $P_{st} = 4'883'531\text{Pa}$
- $T_{st} = 657\text{K}$
- Reynolds= 40'521'610
- $T_w = 330\text{K}$

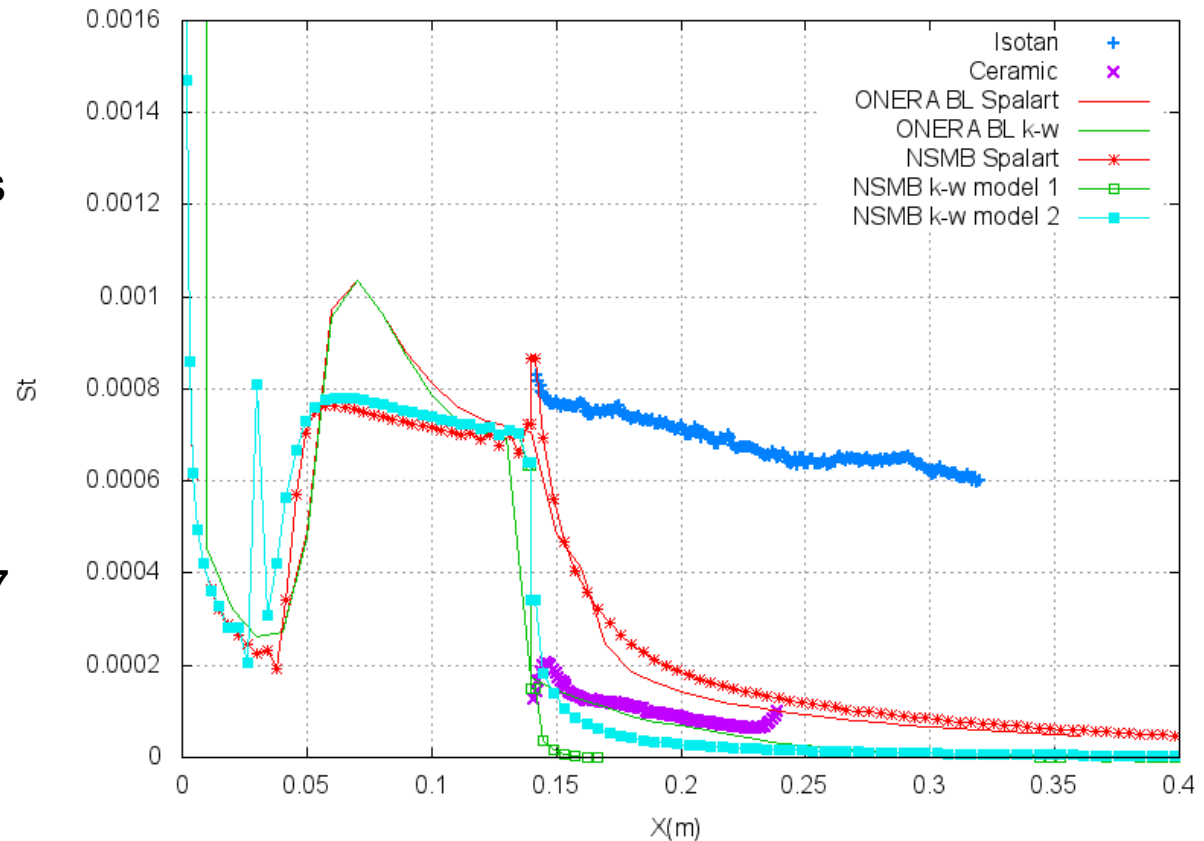


Navier Stokes simulations

WTT reconstruction and validation

Run 6: blowing rate: 4.6 g/s with roughness

- $P_{st} = 4'880'887\text{Pa}$
- $T_{st} = 641\text{K}$
- Reynolds = 42'092'077
- $T_w = 320\text{K}$



Conclusions Navier Stokes simulations

- Good agreement between results obtained using the ONERA boundary layer solver and the NSMB Navier Stokes solver
- Fair agreement of CFD simulations on blowing tests
- Blowing + roughness cases are more complicated to simulate
- No obvious best choice between Spalart and k-w models

Possible Future Work

- Investigate the large differences in Stanton number on Isotan and Ceramic inserts
- Investigate further why the experiments showed a reduction in Stanton number for a rough wall (compared to a smooth wall). Experiments using Isotan with roughness?
- Further improvements in the turbulence modeling is needed, in particular for the case of both roughness and blowing

*Thank you for your attention
Questions?*

for more info on RASTAS-SPEAR: www.rastas-spear.eu

OXIDATION BEHAVIOR OF LAMINATE CERAMICS BELONGING TO SiC-ZrB₂ SYSTEM

C. Badini⁽¹⁾, E. Padovano⁽¹⁾, J. Barcena⁽²⁾, M. Lagos⁽²⁾, I. Agote⁽²⁾, C. Jimenez⁽²⁾, X. Hernandez⁽²⁾, S. Gianella⁽³⁾, D. Gaia⁽³⁾, V. Liedtke⁽⁴⁾, K. Mergia⁽⁵⁾, S. Messoloras⁽⁵⁾, P. Yialouris⁽⁵⁾, Y. Panayiotatos⁽⁵⁾, A. Ortona⁽⁶⁾, C. D'Angelo⁽⁶⁾, and C. Wilhelmi⁽⁷⁾

⁽¹⁾*Politecnico di Torino
Department of Applied Science and Technology
Corso Duca degli Abruzzi, 24. 10129, Torino, Italy
Email: claudi.badini@polito.it*

⁽²⁾*Tecnia Research & Innovation.
Industry and Transport Division
Mikeletegi Pasealekua, 2, Donostia-San Sebastian, Spain
Email: jorge.barcena@tecnalia.com*

⁽³⁾*Erbicol SA
Porous Ceramic Department
Viale C.Pereda 22. 6828 Balerna, Switzerland
Email: sandro.gianella@erbicol.ch*

⁽⁴⁾*Aerospace & Advanced Composites GmbH
Institute of Nuclear Technology and Radiation Protection
Viktor-Kaplan-Straße 2.A-2700 Wiener Neustadt, Austria
Email: volker.liedtke@aac-research.at*

⁽⁵⁾*N.C.S.R. "Demokritos"
Institute of Nuclear Technology and Radiation Protection
Aghia Paraskevi, 15310 Athens, Greece
Email: kmergia@ipta.demokritos.gr*

⁽⁶⁾*University of Applied Sciences (SUPSI)
The iCIMS Research Institutien
Galleria 2, CH 6928 Manno, Switzerland
Email: alberto.ortona@icimsi.ch*

⁽⁷⁾*EADS Innovation Works
Dept. TCC 2 / CTOIWMS. 81663 Munich, Germany
Email: Christian.Wilhelmi@eads.net*

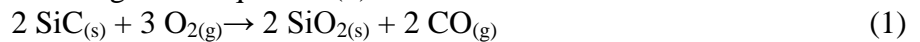
Abstract

In this work the oxidation behavior at high temperature of SiC has been compared to that of ZrB₂ and SiC-ZrB₂ composite. Ceramic laminates consisting of several ceramic layers have been produced by tape-casting, layer stacking, de-binding and pressureless sintering. Laminates with different composition were prepared. Their oxidation resistance was investigated by thermal gravimetric analysis (TGA): temperature scans under flowing air up to 1600°C were performed repeatedly on the same specimen in order check the possible formation of a passive surface layer. Isothermal oxidation treatments in calm air were carried out at 1600°C for 24 hours. The microstructure changes resulting from oxidation were investigated by microscopy, X-ray diffraction and microanalysis techniques. A thin oxide scale (15-30 µm thick) quickly grew on the SiC

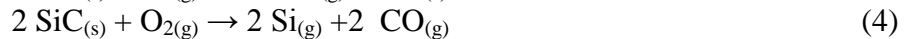
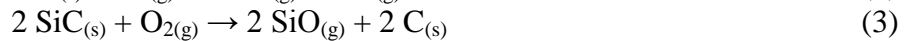
laminar surface; this silica layer granted passivation in a very effective manner since the underlying material was found practically unchanged also after an oxidation treatment 24 hours long. On the contrary oxidation of both ZrB₂ laminate and composite laminate resulted in a rather thick oxide layer showing a complex microstructure. The full oxide scale, consisting of three zones with different compositions, grew rather quickly and reached the thickness of several hundreds of micrometers. Nevertheless TGA showed that also in this case the complex oxide layer is able to slow down the oxygen diffusion towards the sample core.

Introduction

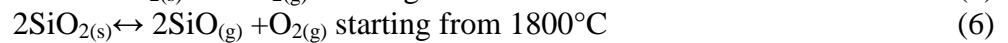
Ultra high temperature ceramics (UHTCs) are considered very promising materials for application in re-usable thermal protection systems as oxidation resistant materials. Among UHTCs SiC and ZrB₂ have been widely investigated for this kind of application owing to their properties. Silicon carbide and zirconium diboride show high thermal stability and high melting temperatures (2545°C with decomposition for SiC and 3245°C for ZrB₂ respectively) because of the presence of covalent bonds in their crystalline structure. In addition they show rather high strength and stiffness, very high hardness and erosion resistance, and fairly good corrosion resistance. Actually SiC can undergo oxidation according to different mechanisms depending on the temperature and the oxygen partial pressure in the oxidizing atmosphere. The most common oxidation mechanism of SiC is passive oxidation that occurs according to the equation (1):



In this case a thin, but not porous, layer of crystalline silica forms on the surface; the layer grants protection against further oxidation since oxygen diffusion through this layer is very slow. When the temperature greatly increases (over 1400°C) and contemporaneously the oxygen partial pressure greatly decreases (below 10⁻² atm) active oxidation of SiC can occur according to the equations (2), (3) and (4):



When this happens mainly gaseous species result from oxidation and then SiC is quickly consumed. Finally, also when passive oxidation happens the recession of SiC can be observed if the temperature increases up to the silica melting point. Starting from 1723°C the molten silica undergoes volatilization; vapors of SiO₂ or of SiO (above 1800°C) are in equilibrium with molten silica according to (5) and (6) :



Nevertheless at temperatures lower than 1700°C silicon carbide can provide very good protection against oxidation. Thin layers of SiC have been deposited on the surface of conventional CMCs by CVD for this purpose, but such a kind of SiC coating suffers damage because of the thermal mismatch with the substrate and this limits the re-usability of TPS containing SiC coatings. Alternatively SiC laminates (about two mm thick) have been tested under simulated re-entry conditions (according to HERMES study, previously adopted in ESA study "OLCHOS") [1,2]. Temperature (up to 1550°C) and oxygen pressure profiles adopted for this test can cause the alternation of passive and active oxidation conditions. Passive mechanism conditions prevailed since a thin silica layer was found on the SiC surface after 100 re-entry simulations; in addition only negligible variation of laminate thickness occurred and the material retained most of the original strength and stiffness after the re-entry cycles.

Slurry components		Composition of SiC slurry (wt%)	Composition of 20%SiC-80%ZrB ₂ (wt%)	Composition of ZrB ₂ slurry (wt%)
Solvents	Ethanol	19,9	16,1	15,3
	Buthanol	30,5	24,6	23,5
Dispersant	Fish oil	0,1	0,1	0,1
Powders	SiC	33,6	5,4	-
	Boron	0,3	0,1	-
	Carbon	1,0	0,2	-
	ZrB ₂	-	41,7	49,8
Binder	Polyvinyl Butyral	9,6	7,8	7,4
Plasticiser	Polyethylene Glycol	5,0	4,0	3,9

Tab. I Composition of the slurries

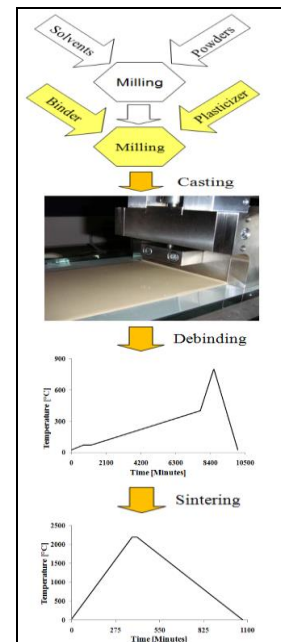
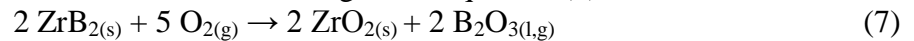


Fig.1 Processing steps for ceramic laminate production.

The ZrB₂-based ceramics have been also investigated for TPS applications since they can offer some advantages over SiC, even though ZrB₂ density is higher than that of SiC (3.2 g/cm³ for SiC and 6.1 g/cm³ ZrB₂). Oxidation of ZrB₂ occurs according to the equation (7):



Boria melts at about 500°C and then it suffers of evaporation (which becomes rather quick over 900°C) while zirconia remains in the solid state up to 2677°C (ZrO₂ melting point). Even if the ZrB₂-SiC system has an eutectic melting temperature near 2300°C, ZrB₂-SiC composites containing from 10 to 30% vol SiC have been proposed for application in TPS (as coating of conventional CMCs or as thicker ceramic layer). The addition of SiC to the ZrB₂ matrix is believed to provide some advantages: SiC improves the sintering behavior of ZrB₂ and the oxidation of this composite results in the formation of a molten borosilica layer which slows down the oxygen diffusion with respect to zirconia (diffusivity at 1550°C: 10⁻¹⁰ m²/s for zirconia and 1.7 10⁻¹⁴ m²/s for borosilica glass). In addition the composites are believed to show better toughness than monolithic ceramics. Unfortunately the diffusivity of oxygen through molten borosilica still remains much higher than that through silica at 1550°C (1.7 10⁻²¹ m²/s); in addition the borosilica layer is progressively depleted of boria owing to its quick evaporation. Nevertheless ZrB₂-SiC composite proved to be able to grant oxidation protection at very high temperature (around or over 2000°C) because of the formation of a solid zirconia oxidation product. Preliminary ground test of re-entry simulation performed by using plasma wind tunnel and plasma torch gave encouraging results [3- 6]. However recent investigations about the oxidation behavior of monolithic ceramics belonging to ZrB₂-SiC system showed their poor oxidation resistance below 1700°C and suggested that the best content of SiC for oxidation protection should be better investigated [7]. At present, it seems that SiC and ZrB₂ can display their best in terms of oxidation protection under very different temperature conditions, as a consequence it seems there is not a single material that can provide oxidation resistance in TPS under every possible environmental condition. Generally speaking, the

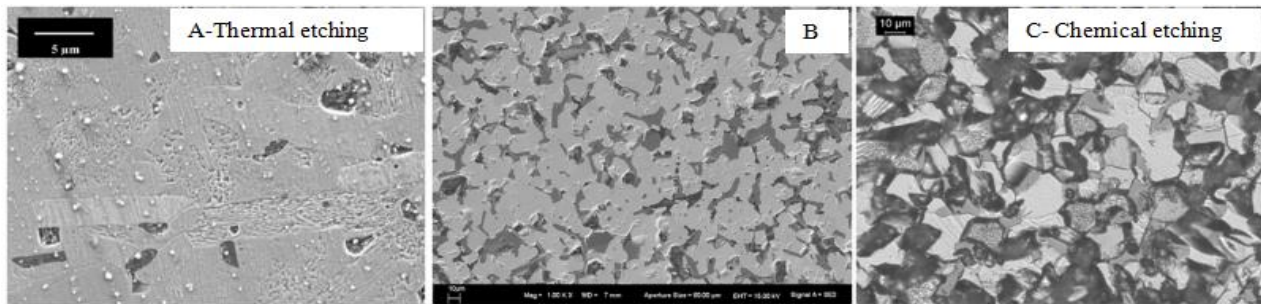


Fig. 2 Microstructure of laminates cross section: A= 100% SiC; B= 80%ZrB₂-20%SiC; C= 100% ZrB₂.

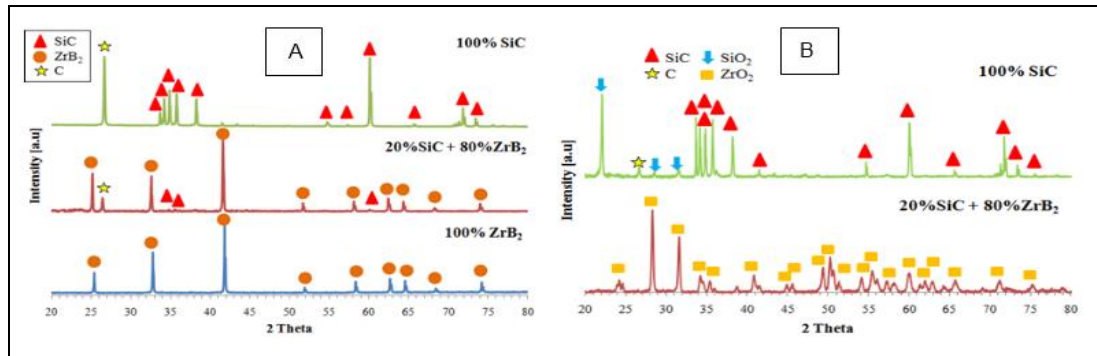


Fig. 3 XRD patterns of the sample surfaces: A= before oxidation; B= after oxidation

main lack of both SiC and ZrB₂-based ceramics still remains their poor toughness. On the other hand the toughness of ceramics can be improved by using ceramic fibers; but, unfortunately, the integration of fibers in the ceramic matrix generally causes residual matrix porosity and then the worsening of oxidation resistance (which is the main requirement for the external part of TPS). Another way to improve toughness deals with the adoption of laminate structures. The presence of interfaces between the layers and of residual stresses favor phenomena of crack deviation that result in toughness improvement [8-10].

In this paper ceramic laminates based on SiC and ZrB₂ have been prepared and compared in terms of oxidation resistance.

Experimental part

Materials and methods

Ceramic laminates were produced according to the following processing path: preparation of a slurry containing the ceramic powders, tape casting and slow solvent evaporation at room temperature to obtain green ceramic sheets 200-250 μm thick, stacking green tapes in a multilayer structure (ten layers), de-binding under flowing argon up to 800°C, sintering at 2200°C (Fig. 1).

The slurries were obtained by mixing the ceramic powders and the sintering aids in solvents; firstly the powders were mixed for 12 hours in an alumina jar containing alumina milling bodies then a plasticizer and a binder were added and the slurry was mixed for additional 24 hours. The composition of the slurries designed to obtain SiC, ZrB₂ and 80%ZrB₂-20%SiC laminates are reported in table I.

Zirconium diboride powder (Grade B, H.C. Starck, Germany, with an average particle size of 2.25 μm), α-SiC powder (H.C. Starck UF-15, Germany, with a mean particle size of 0.55 μm), C (Alfa

Samples composition [% Vol.]	Geometrical density [% of theoretical]	Elastic modulus [Gpa]	Bending strength [MPa]	Microhardness [GPa]
100% SiC	89.0 ± 2.6	339 ± 19	324 ± 24	21.2 ± 0.6
20%SiC-80%ZrB ₂	92.9 ± 1.0	444 ± 10	277 ± 29	17.5 ± 1.5
100% ZrB ₂	83.0 ± 1.8	337 ± 15	165 ± 14	10.4 ± 0.6

Tab. II Properties of laminates

Aesar flakes 7–10 μm), B (H.C. Starck amorphous grade I, 1–2 μm), polyethyleneglycole (Bisoflex 102 Cognis) and polyvinilbutyral (Butvar B76 Solutia) were use for slurry preparation.

The slurries were poured by tape casting on a movable Mylar support (advance speed 100 mm/min, height of doctor blade 1 mm). The green tapes were stacked to obtain the green laminates that were then de-binded and sintered. Pressureless sintering was performed (T.A.V. Cristalox oven) under argon (99.99% purity, pressure around 550 mbar) according to the cycle depicted in figure 1 with a final step of 30 minutes at 2200°C. The flat bars thus obtained (55X12X1.8 mm³ in size) were used for microstructure characterization, mechanical and oxidation tests. Three-point bending test was performed adopting 40mm outer span and a cross-head speed of 0.1 mm/min. Elastic modulus was measured by using a method based on impulse excitation technique and analysis of transient natural vibration on RFDA MF basic instrument (IMCE n.v. Belgium). Vickers microhardness measurements were performed on the cross section of the specimens with a test load of 300g. Very small specimens were used for Thermal Gravimetric Analysis (TGA Mettler Toledo); two temperature runs were carried out in consecutive sequence up to 1600°C under flowing air (heating rate 10°C/min). Isothermal oxidation test was performed at 1600°C under calm air for 24 hours. The microstructure of specimens was investigated before and after oxidation by using SEM-EDS (SEM-FEG Assing SUPRA 25 equipped with EDS Oxford analyzer), optical microscope observations on specimen cross-section after etching (thermal etching at 1600°C or chemical etching with 1:1:1 HF:HNO₃:H₂O solution) and X-ray diffraction (Philips PW 1710, CuK α radiation).

Results and discussion

The microstructure of laminates under investigation is shown in figure 2. The microstructure of SiC multilayer consists of smaller polygonal and bigger elongated crystals, these last frequently longer than 100 μm and with an aspect ratio of 6 or even more. Much smaller polygonal crystals (few tenth of μm in size) can be observed in case of both 100%ZrB₂ and 80%ZrB₂-20%SiC laminates. In this last multilayer ceramics the white phase is ZrB₂, the grey one is SiC and the black zones belong to carbon added as sintering aid (as in the case of SiC laminate too). XRD patterns (Fig. 3) confirm that only these three phases can be found in the as-processed laminates and then that no reaction between the material components occurred during sintering, but only grain growth (particularly in the case of SiC laminate). After oxidation for long time at 1600°C the XRD patterns show the formation of crystalline silica on the surface of SiC laminate and the presence of a glassy phase mixed with crystalline zirconia on that of 100%ZrB₂ and 80%ZrB₂-20%SiC .

The physical characteristics of ceramics laminates are compared in table II. Rather good strength, stiffness and hardness were achieved in case of both SiC and composite laminate (produced with the help of sintering aids) while ZrB₂ laminate shows lower densification and consequently worse mechanical features.

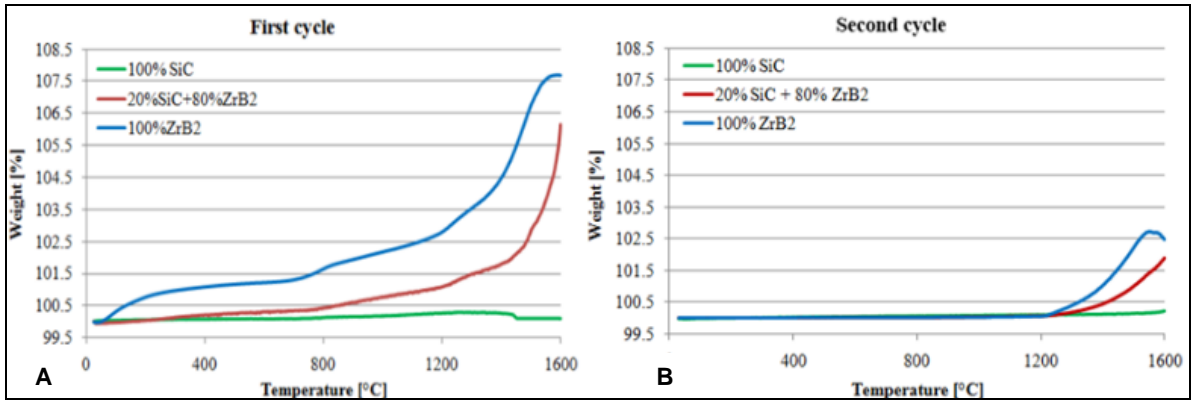


Fig. 4 Comparison of TGA curves of SiC, ZrB₂ and 80%ZrB₂-20%SiC laminates under oxidizing atmosphere: A = first TGA run; B= second TGA run showing formation of passive surface layers

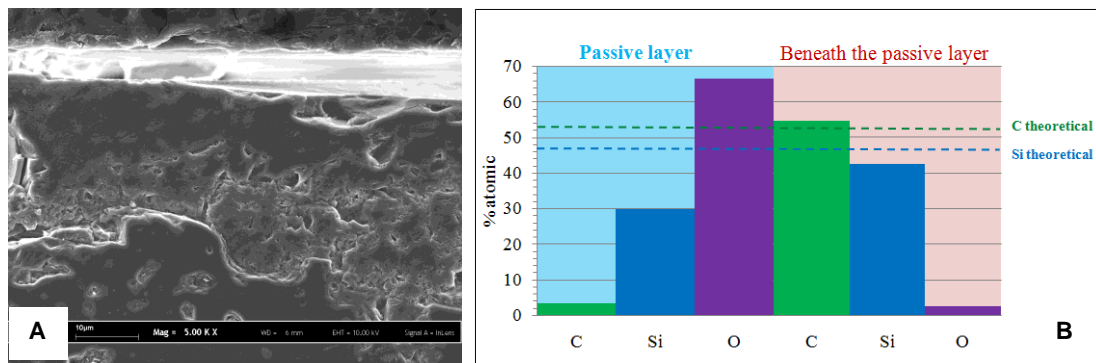


Fig. 5 A= Cross section of SiC laminate after 24 h oxidation in air at 1600°C; passive silica layer; B= EDS analysis of passive layer and the zone beneath the passive layer

TGA run under oxidizing atmosphere results in appreciable weight gain (6-8%) in case of both ZrB₂ and 80%ZrB₂-20%SiC, while the mass of SiC laminate increases less than 0.5% (Fig. 4). If the same specimen is cooled and then re-heated during a second oxidation cycle in the TGA more flat curves are obtained in every case, showing that the oxidation products formed on the sample surface during the first run can exert some passivation effect. In particular any mass change was observed for SiC laminate, while ZrB₂ and 80%ZrB₂-20%SiC suffered of limited mass gain (2-3%) starting from 1200°C.

The formation of passive layers can be better appreciated after long term oxidation treatment at 1600°C. The passive layer grown on SiC (20-30 μm thick) is shown in figure 5A; EDS analysis shows that this layer consists of SiO₂ with some carbon inclusions (Fig. 5B), while below the passive layer the material is almost unaffected by oxidation and it mainly consists of SiC.

Solid state diffusion of oxygen through the passive layer occurs during the 24 h oxidation treatment since few percent of oxygen were found beneath the silica layer.

On the contrary most of the 80%ZrB₂-20%SiC laminate was affected by oxidation during the long term oxidation test since only the core of the laminate (a zone in the centre about 640μm thick) was found to show the original material microstructure and composition. The growth of a very complex oxidation layer occurred. This oxidation layer (Fig. 6) consisted of: an external glassy layer (borosilica) with some ZrO₂ crystals, a very thick (more than 1 mm thick) intermediate and two-phase layer made of columnar grains of zirconia embedded in a borosilica glass, a porous layer arising from the active oxidation of SiC and then containing less than 2% of Si (but more than 40% of C in addition to ZrO₂ and ZrB₂).

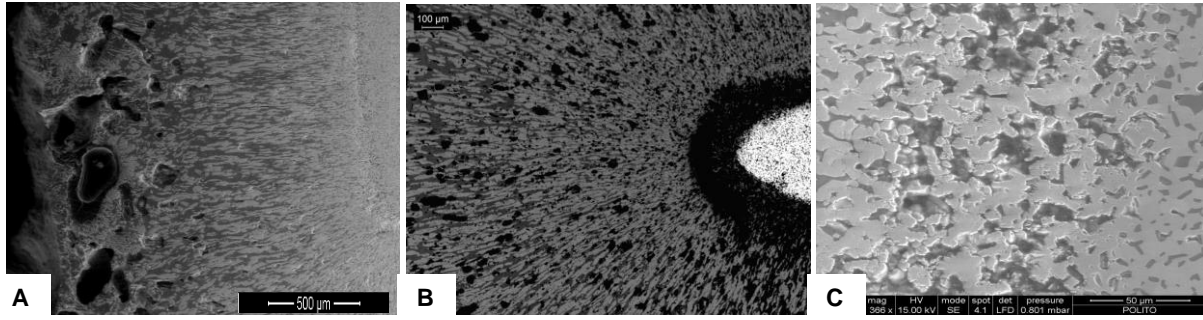


Fig. 6 A= Overview of 80%ZrB₂-20%SiC cross section after oxidation; B= Interface between the core (not oxidised), the porous layer and the two-phases oxide layer; C = interface between the sample core (on the right side) and the porous layer.

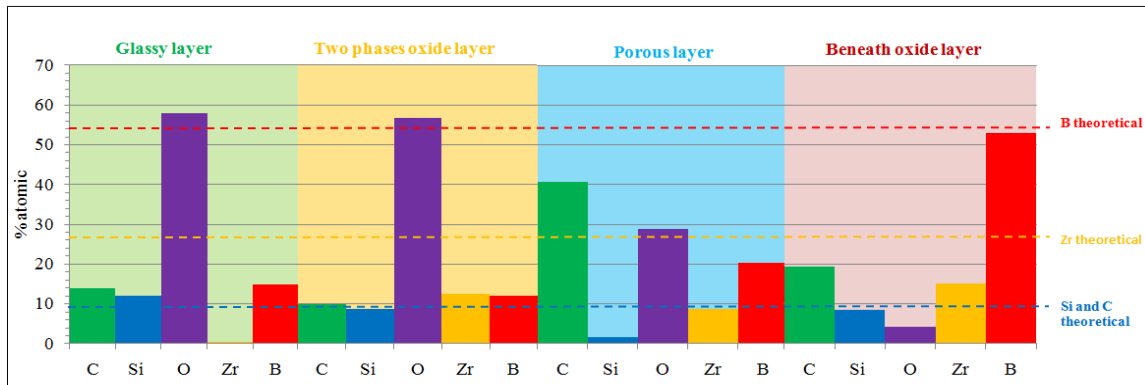
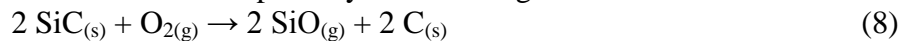


Fig. 7 EDS analysis of the zones constituting the 80%ZrB₂-20%SiC laminate after oxidation.

This specimen blistered during oxidation treatment because of the outward growth of the glassy layer and the emission of gaseous reaction products (boria, carbon dioxide). The surface glassy layer showed the presence of very large pores that very likely were left by gas bubbles (Fig. 6A). The EDS analysis performed after oxidation on the cross section of 80%ZrB₂-20%SiC laminate allows to assess the composition of the different zones constituting the oxidized laminate (Fig. 7). Within the glassy external layer the oxygen content is well consistent with the formation of a borosilica glass. Beneath this layer the average composition in figure 7 results from the two-phase structure: the elongated crystals contain about 27% at Zr and 60% at O and then they can be attributed to ZrO₂; the zone surrounding these crystals (containing 20% at Si, 8% at B and 69% at O) can be attributed to borosilica glass.

The porous layer contains Zr, B, O and C, but only little Si; the thick oxide layer grown on the core slows down the oxygen diffusion and allows only little amount of this element to reach this area, then conditions for active oxidation occur and the porosity forms owing to the reaction:



Just below the porous layer also the sample core contains a not negligible amount of oxygen and then its composition is not completely consistent with a mixture of ZrB₂ and SiC crystals.

Conclusions

The oxidation behavior of SiC, ZrB₂ and 80%ZrB₂-20%SiC laminates was investigated in the temperature range between room temperature and 1600°C. Under these conditions the laminates containing ZrB₂ showed very poor oxidation resistance compared to SiC, which takes advantage from the formation of a passive silica layer.

Nevertheless, also on the surface of the laminate containing ZrB₂ an oxide layer, able to slow down oxygen diffusion and then oxidation progress, forms. This layer shows a complex structure and it is more effective in the case of 80%ZrB₂-20%SiC composite laminate.

On the other hand, the passive silica layer is expected not to be effective any longer when the temperature increases over 1700°C because of the volatilization of molten silica.

Under these last temperature conditions 80%ZrB₂-20%SiC composite should behave better as its surface should be covered by solid zirconia.

Since the external part of a TPS during the re-entry in the earth atmosphere experiences temperatures progressively changing with the time (from low temperature up to a maximum value, depending on the different TPS zones and sometimes as high as 2000°C or more) neither of these two materials (SiC and 80%ZrB₂-20%SiC) can be considered as the ideal one for this application.

Reasonably, improved oxidation behavior in a wide range of temperature (up to about 2000°C) could be achieved by optimizing the ZrB₂-SiC ratio in the composite or adopting a laminate structure comprising stacked layers with different composition.

Acknowledgements

This work has been performed within the framework of the European Project “SMARTTEES (G.A. n. 262749) with the financial support By the European Community. The paper only reflects the view of the authors and the European Community is not liable for any use of the information contained therein.

References

- [1] S. Biamino, V. Liedtke, C. Badini, G. Euchberger, I. Huertas Olivares, M. Pavese and P. Fino, Multilayer SiC for thermal protection system of space vehicles: Manufacturing and testing under simulated re-entry conditions. *J Eur Ceram Soc* 2008; 28:2791-2800.
- [2] C. Badini, V. Liedtke, G. Euchberger, E. Celasco, S. Biamino, S. Marchisio, M. Pavese and P. Fino, Self passivating behavior of multilayer SiC under simulated atmospheric re-entry conditions. *J Eur Ceram Soc* 2012;32:4435-45.
- [3] F. Monteverde and R. Savino, Stability of ultra-high-temperature ZrB₂-SiC ceramics under simulated atmospheric re-entry conditions. *J Eur Ceram Soc* 2007;27:4797-4805.
- [4] F. Monteverde, R. Savino, M. De Stefano Fumo and A. Di Maso, Plasma wind tunnel testing of ultra-high temperature ZrB₂-SiC composites under hypersonic re-entry conditions. *J. Eur. Ceram. Soc* 2010; 30: 2313-2321.
- [5] F. Monteverde, R. Savino and M. De Stefano Fumo, “Dynamic oxidation of ultra-high temperature ZrB₂-SiC under high enthalpy supersonic flows”, *Corrosion Science* 2011;53:922-929.
- [6] A.L. Chamberlain, W.G. Fahrenholtz, and G.E. Hilmas and D. Ellerby, Oxidation of ZrB₂-SiC ceramics under atmospheric and reentry conditions. *Refractories Applications Transactions* 2005; 2:2-8.
- [7] Williams PA, Sakidja R, Perepezko JH, Ritt P. Oxidation of ZrB₂-SiC ultra-high temperature composites over a wide range of SiC content. *J Eur Ceram Soc* 2012; 32:3875-3883.
- [8] W.J. Clegg, K. Kendall, N.McN. Alford, T.W. Button and J. Birchall, A simple way to make tough ceramics. *Nature* 1990;347:455
- [9] W.J. Clegg, The fabrication and failure of laminar ceramic composites, *Acta Metall. Mater.* 1992;40:3085-3093
- [10] J. B. Davis, A. Kristoffersson, E. Carlstrom and W.J. Clegg, Fabrication and crack deflection in ceramic laminates with porous interlayers. *J. Am. Ceram. Soc.* 2000;83: 2369-2374



OXIDATION BEHAVIOR OF LAMINATE CERAMICS BELONGING TO SiC-ZrB₂ SYSTEM

C. Badini, E. Padovano



J. Barcena, C. Jimenez, M. Lagos, I. Agote 

P. Yialouris, K. Mergia, Y. Panayiotatos, S. Messaloras



V. Liedtke



C. Wilhelmi



7th European Workshop on Thermal Protection Systems and Hot Structures
Noordwijk 8-10 April 2013

OXIDATION BEHAVIOR OF LAMINATE CERAMICS BELONGING TO SiC-ZrB₂ SYSTEM

Aim of the present work: to compare materials to be used in TPS for protection against oxidation

The external part of a re-usable TPS facing the atmosphere is required to operate for several re-entry missions under very severe environmental conditions including:

- Oxidizing atmosphere at very high temperatures
 - High thermal fluxes and temperatures
- Mechanical loads due to thermal gradients, pressure gaps and vibrations
 - Friction forces
 - Accidental collisions

UHTCs and composites are believed to be the best choice for this application, some UHTCs entail the greatest interest:

- SiC
- ZrB₂
- ZrB₂-SiC composites

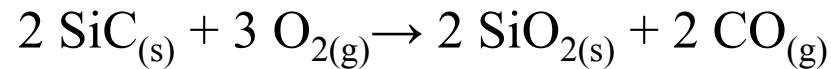
In order to assess which is the best solution their oxidation behavior and thermal stability must be compared

OXIDATION BEHAVIOR OF LAMINATE CERAMICS BELONGING TO SiC-ZrB₂ SYSTEM

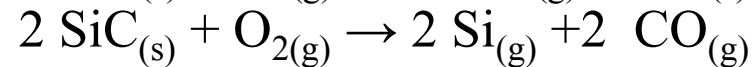
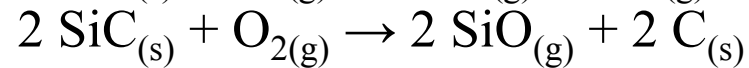
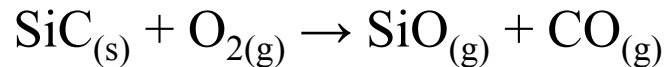
SiC characteristics

- It melts with decomposition at 2545°C
- It undergoes oxidation according to two possible mechanisms

a) Passive oxidation:



b) Active oxidation ($T > 1400^\circ\text{C}$, $P_{\text{O}_2} < 10^{-2} \text{ atm.}$):



- The silica passive layer melts at around 1700°C and then can undergo volatilization:



OXIDATION BEHAVIOR OF LAMINATE CERAMICS BELONGING TO SiC-ZrB₂ SYSTEM

SiC characteristics and state of the art for TPS

- CVD SiC is currently used as surface coating giving protection against oxidation to conventional CMCs (C_f/C and C_f/SiC)
- SiC laminates successfully sustained 100 re-entry simulation tests (maximum temperature 1550°C) without suffering important damage thanks to the formation of a passive silica layer on the surface

Ref.

1. Biamino S, Liedtke V, Badini C, Euchberger G, Huertas Olivares I, Pavese M, Fino P. Multilayer SiC for thermal protection system of space vehicles: Manufacturing and testing under simulated re-entry conditions. J Eur Ceram Soc 2008; 28:2791-2800
2. Badini C, Liedtke V, Euchberger G, Celasco E, Biamino S, Marchisio S, Pavese M, Fino P. Self passivating behavior of multilayer SiC under simulated atmospheric re-entry conditions. J Eur Ceram Soc 2012;32:4435–45)

OXIDATION BEHAVIOR OF LAMINATE CERAMICS BELONGING TO SiC-ZrB₂ SYSTEM

ZrB₂ and ZrB₂-SiC (20% vol SiC) characteristics

- ZrB₂ melts at 3250°C
- It easily undergoes oxidation according to the reaction:
$$2 \text{ZrB}_{2(s)} + 5 \text{O}_{2(g)} \rightarrow 2 \text{ZrO}_{2(s)} + 2 \text{B}_2\text{O}_{3(l,g)}$$
- Boria melts at around 500°C and zirconia at 2677°C
- Molten boria quickly undergoes evaporation above 900°C leaving a ZrO₂ porous skeleton
- The ZrB₂-SiC system has an eutectic melting temperature near 2300°C
- Also ZrB₂-SiC composites suffer oxidation giving : zirconia plus borosilica glass
- Borosilica glass provides passivation effect since the oxygen diffusion through it is lower than through zirconia (1000 times lower at 1550°C)
- Unfortunately the oxygen diffusion in borosilica is 10⁷ higher than in pure silica
- ZrB₂-SiC composites (10-30%vol SiC) were tested under simulated atmospheric re-entry conditions and are believed to behave better than SiC at around 2000°C

Ref.

Monteverde F, Savino R. Stability of ultra-high-temperature ZrB₂-SiC ceramics under simulated atmospheric re-entry conditions. J Eur Ceram Soc 2007;27:4797–4805

PROCESSING OF MULTILAYER CERAMIC BASED ON ZrB_2/SiC COMPOSITES

Ceramic laminates were prepared according to the following processing path:

- Preparation of a slurry by mixing in an alumina jar: ceramic powders, sintering additives, solvents, binders and plasticizers
 - Tape casting and slow solvent evaporation in air
- Layer stacking to obtain a ten layer green laminate (about 2.2 mm thick)
 - De-binding under argon flow (up to 800°C)
- Sintering under inert atmosphere and low pressure (up to 2200°C)

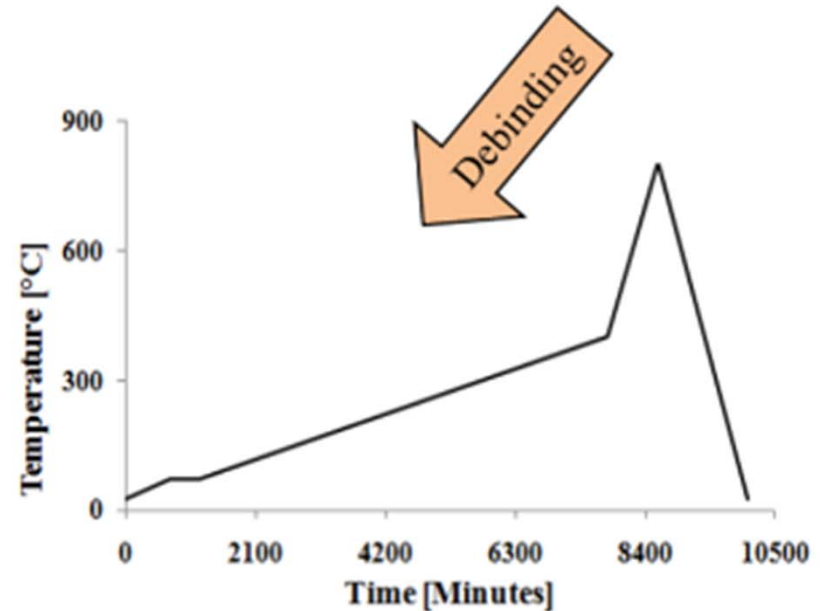
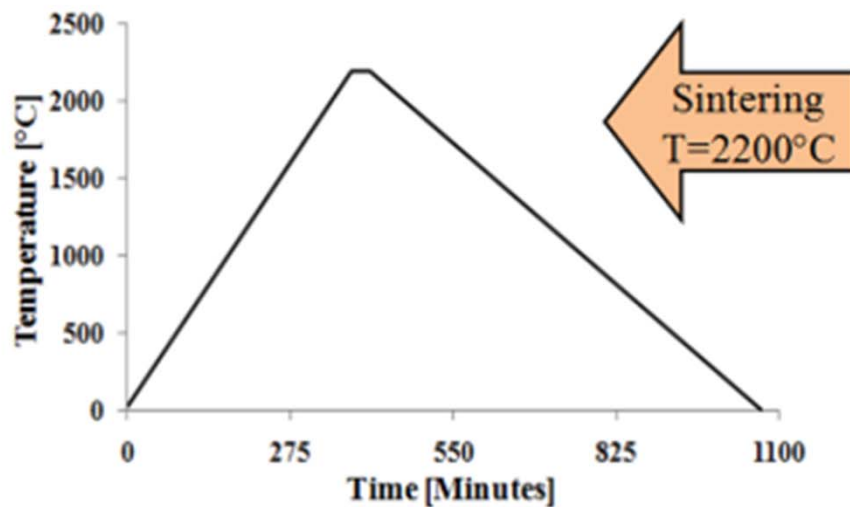
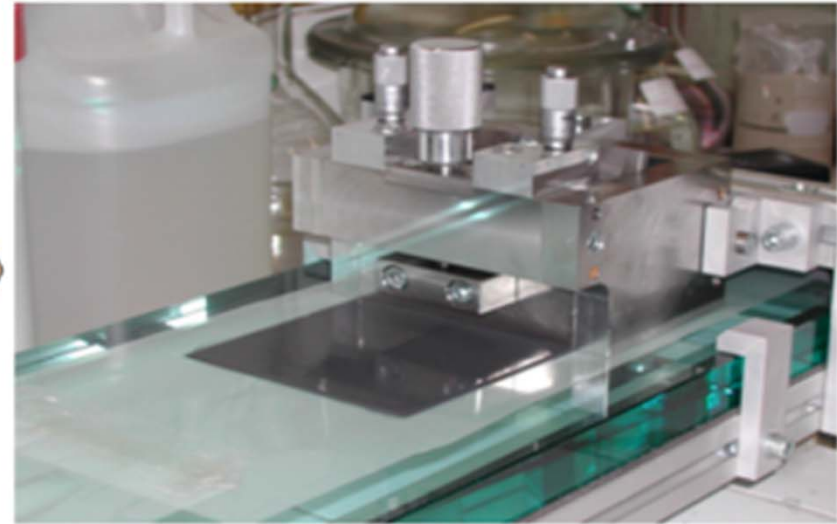
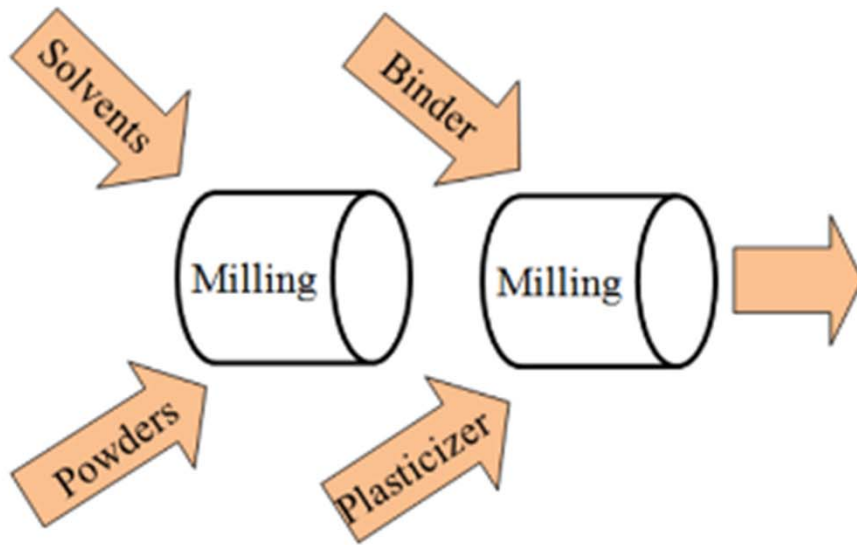
Three kinds of ceramic laminates were prepared(around 1.8 mm thick):

- Every layer made of 100% SiC
- Every layer made of 100% ZrB_2
- Every layer made of 80% ZrB_2 -20%SiC

SLURRY COMPOSITION

Slurry components		Composition of SiC slurry (wt%)	Composition of 20%SiC-80%ZrB ₂ (wt%)	Composition of ZrB ₂ slurry (wt%)
Solvents	Ethanol	19,9	16,1	15,3
	Buthanol	30,5	24,6	23,5
Dispersant	Fish oil	0,1	0,1	0,1
Powders	SiC	33,6	5,4	-
	Boron	0,3	0,1	-
	Carbon	1,0	0,2	-
	ZrB ₂	-	41,7	49,8
Binder	Polyvinyl Butyral	9,6	7,8	7,4
Plasticiser	Polyethylene Glycol	5,0	4,0	3,9

PROCESSING OF MULTILAYER CERAMIC BASED ON ZrB_2/SiC COMPOSITES



OXIDATION TREATMENTS

Oxidation by Thermal Gravimetric Analysis equipment

- Heating runs performed under flowing air
 - From 25°C to 1600°C
 - Heating rate 10°C/min
- After the first run the sample was cooled and the heating run was repeated

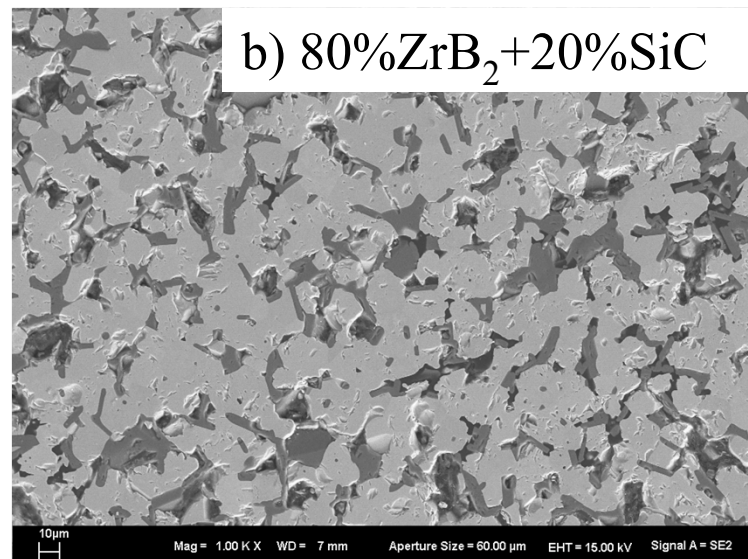
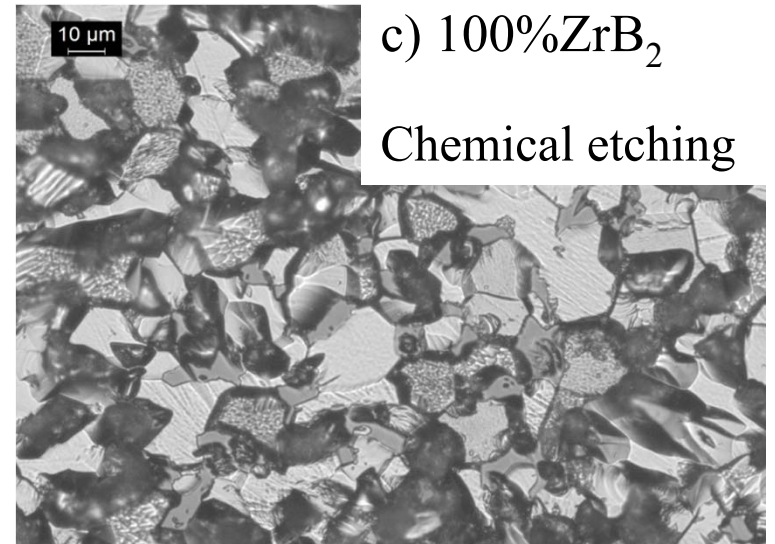
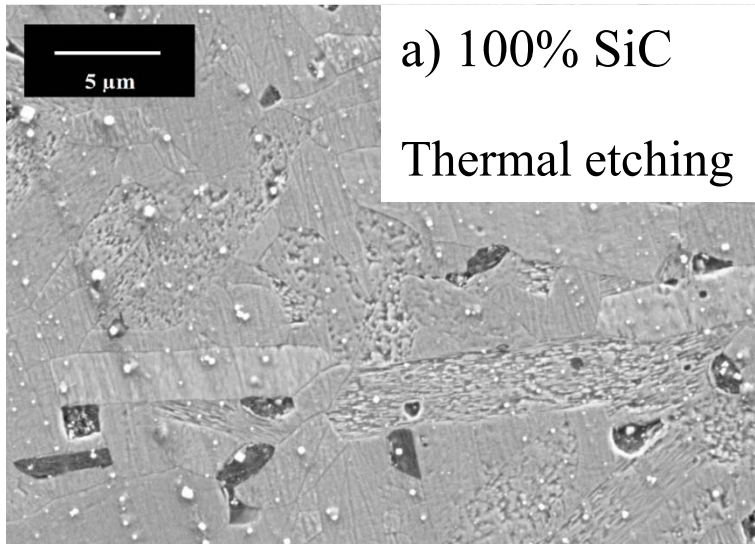
Isothermal long term oxidation treatment

Temperature: 1600°C
Holding time: 24 hours
Atmosphere: calm air

CHARACTERIZATION METHODS

- **X-Ray Diffraction** of the sample surface before and after oxidation
- **Optical microscope**: microstructure of the specimen cross sections (after polishing and thermal or chemical etching)
- **Density, bending strength, modulus and hardness measurements**
- **SEM-EDS** microanalysis of the oxide layers (on the specimens cross section)

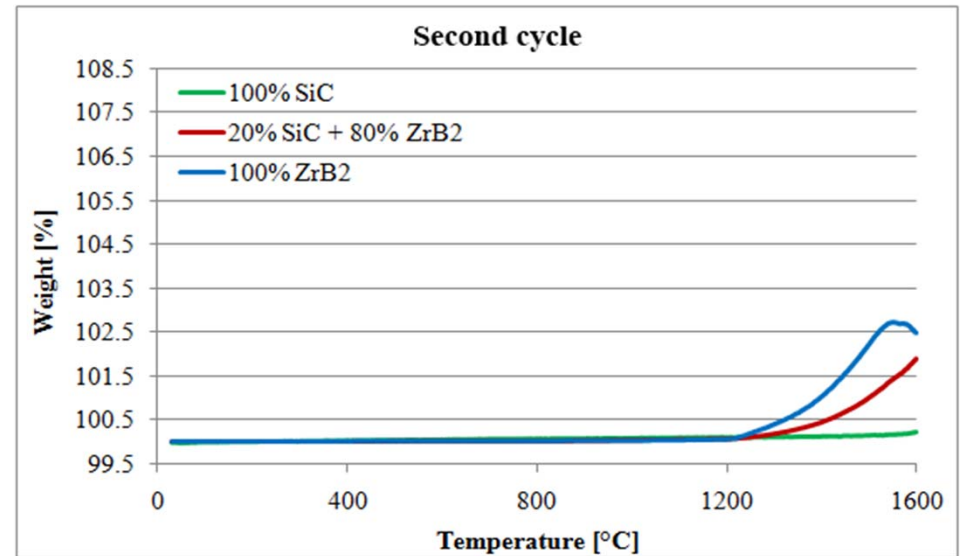
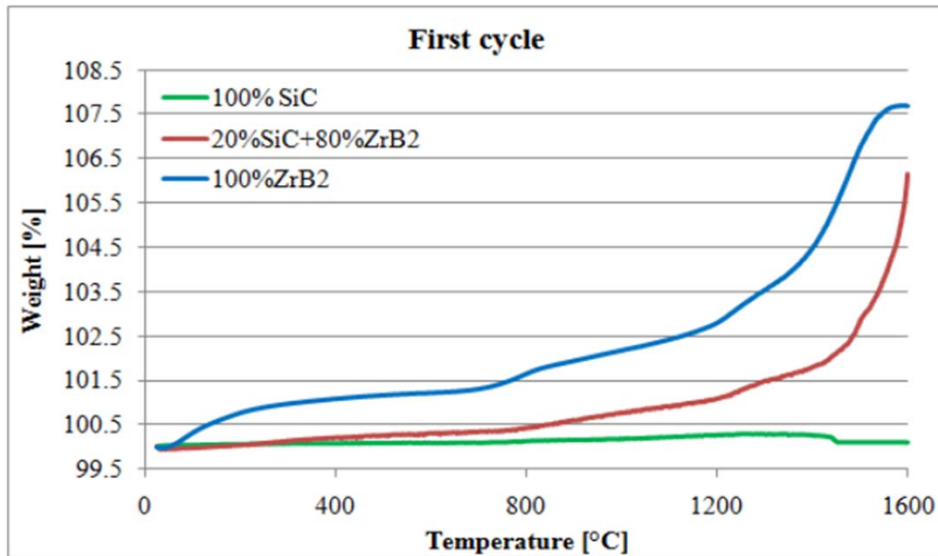
MICROSTRUCTURE OF SINTERED LAMINATES



LAMINATE PHYSICAL PROPERTIES

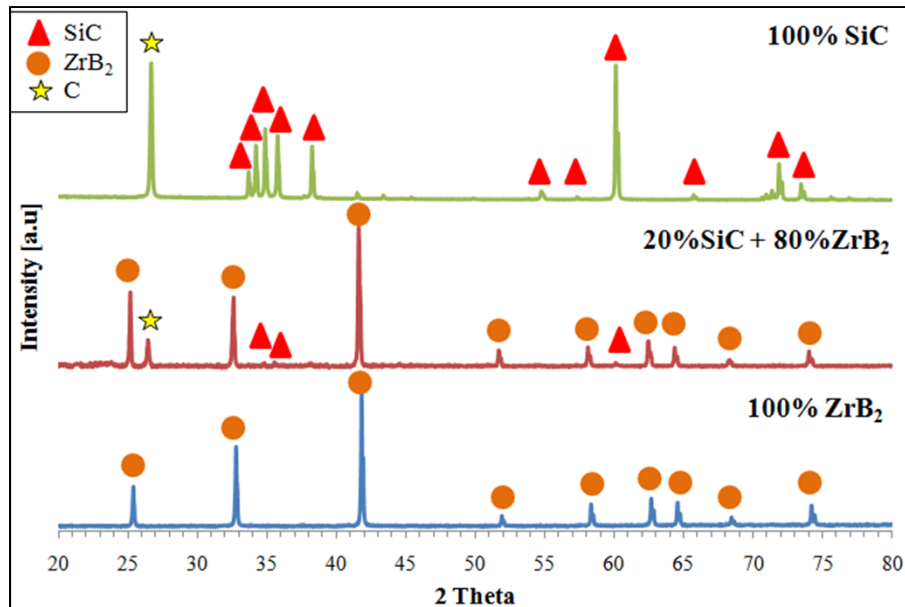
Samples composition [% Vol.]	Geometrical density [% of theoretical]	Elastic modulus [Gpa]	Bending strength [MPa]	Microhardness [GPa]
100% SiC	89.0 ± 2.6	339 ± 19	324 ± 24	21.2 ± 0.6
20%SiC-80%ZrB ₂	92.9 ± 1.0	444 ± 10	277 ± 29	17.5 ± 1.5
100% ZrB ₂	$83,0 \pm 1.8$	337 ± 15	165 ± 14	10.4 ± 0.6

Oxidation resistance by TGA: PASSIVATING BEHAVIOUR

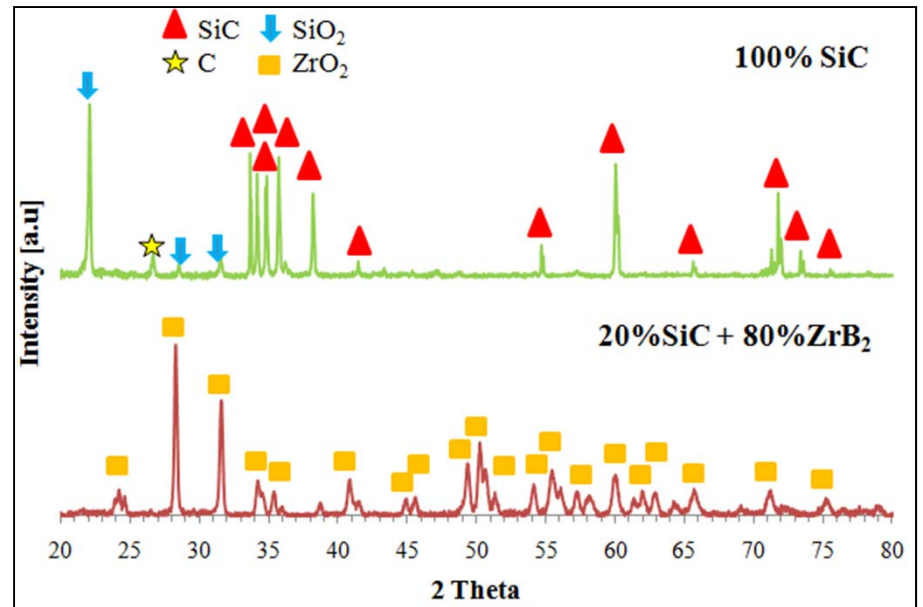


Comparison of TGA curves obtained during the first and second run for three different kinds of ceramic laminates: pure SiC; 80%ZrB₂ - 20%SiC; pure ZrB₂

XRD BEFORE AND AFTER OXIDATION

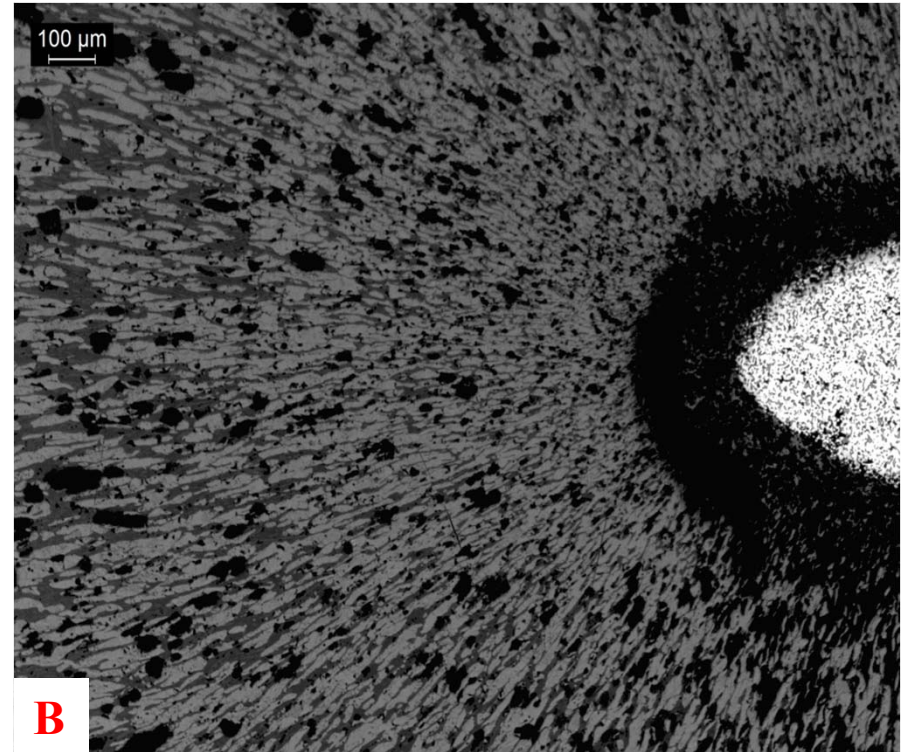
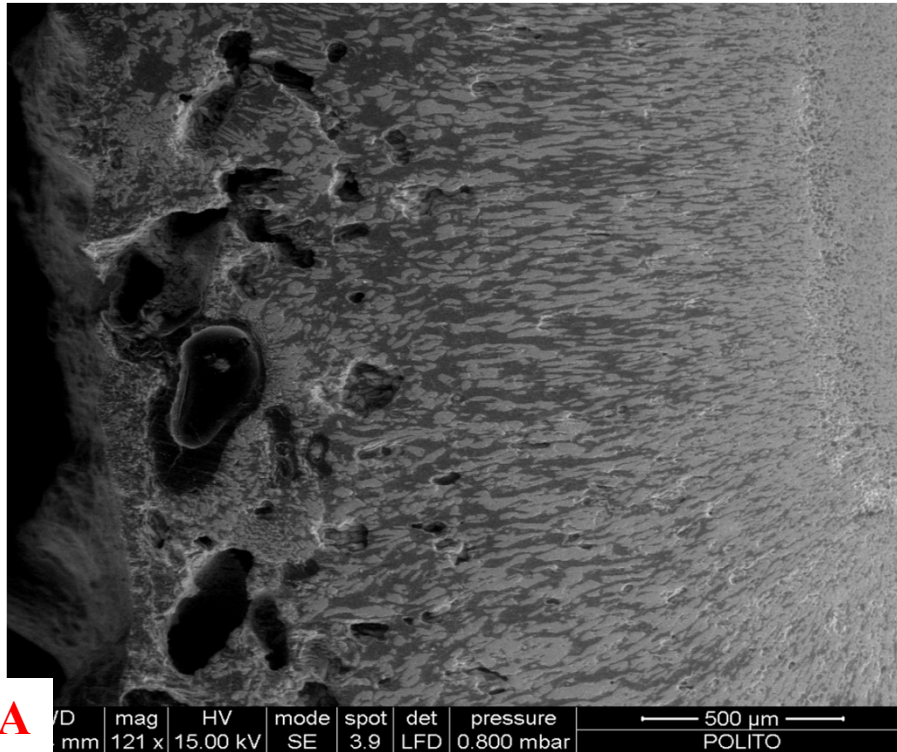


XRD of surface of as-sintered laminates



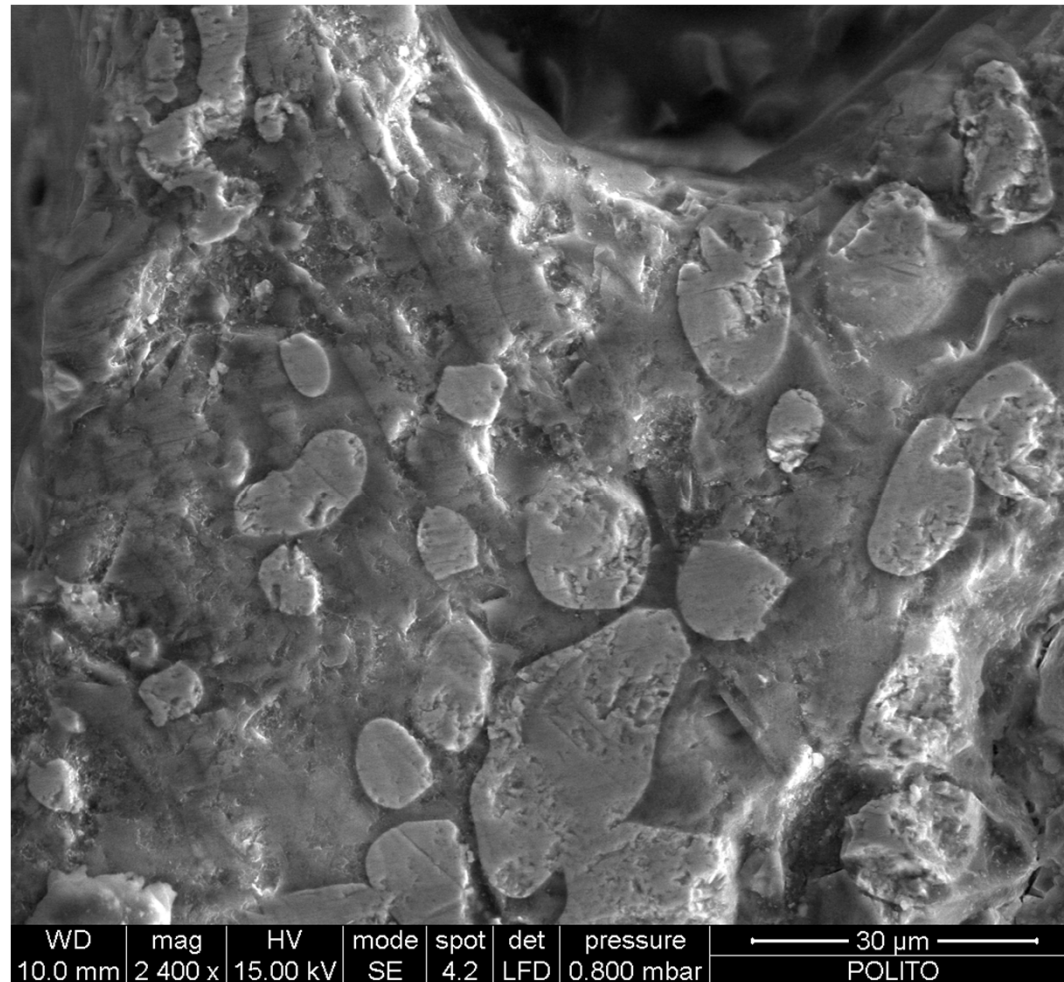
XRD of laminate surface after oxidation at 1600°C for 24 h

Oxidation of 80%ZrB₂+20%SiC laminate: MICROSTRUCTURE



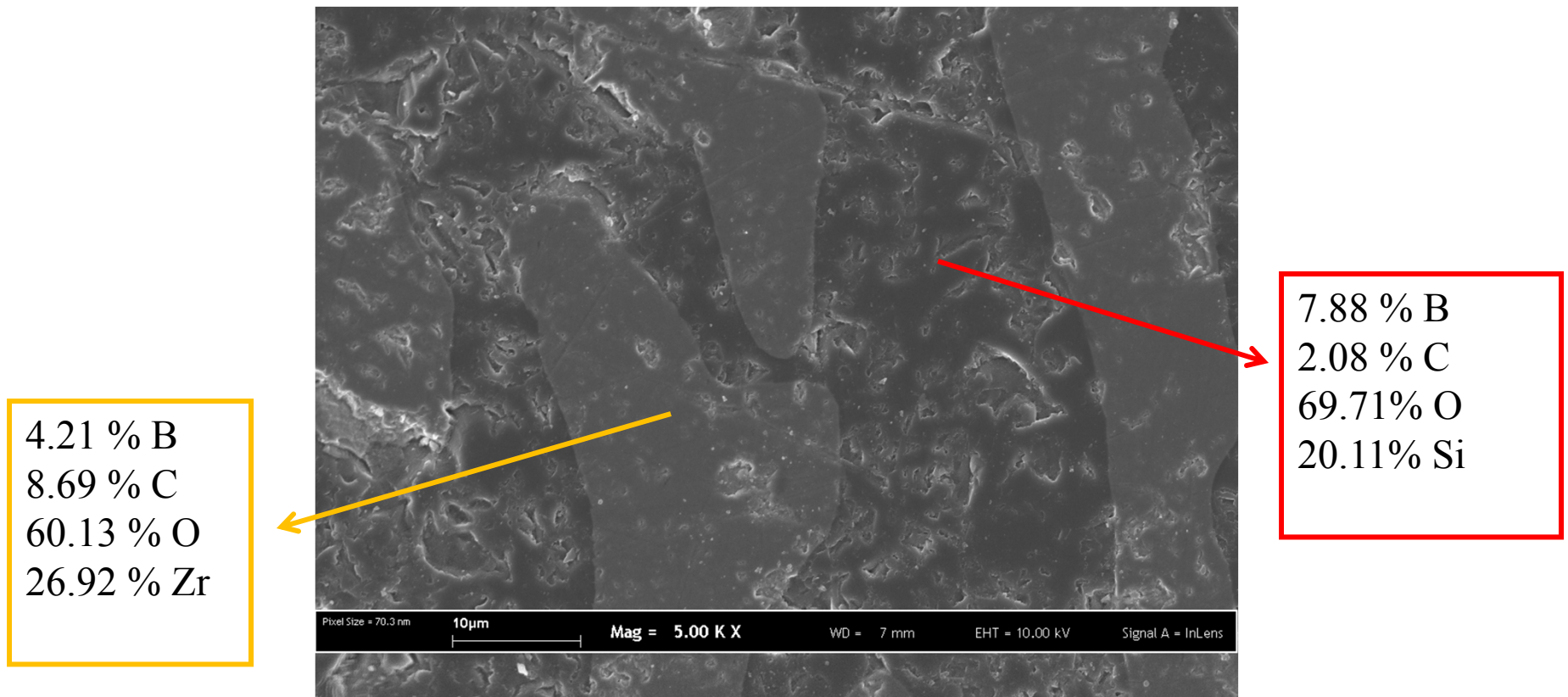
- Microstructure of 80%ZrB₂ - 20%SiC laminate after oxidation in air at 1600° C for 24 hours:
- A) Overview of oxidised layers;
 - B) Interfaces between the core (not oxidised), the porous layer and the two-phases oxide layer.

Oxidation of 80%ZrB₂+20%SiC laminate: EXTERNAL GLASSY LAYER



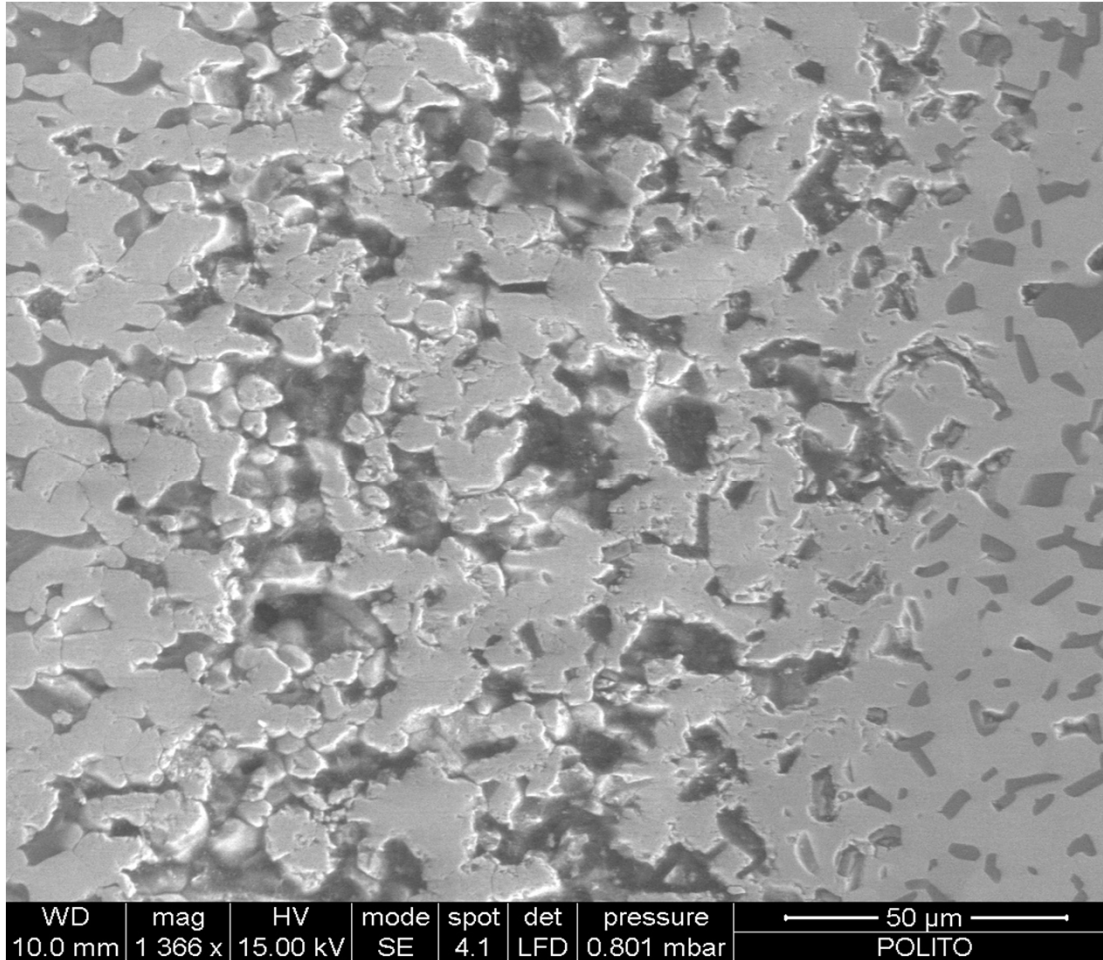
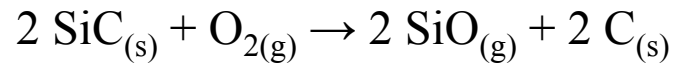
External glassy layer grown on 80%ZrB₂ - 20%SiC laminate after oxidation in air at 1600° C for 24 hours

Oxidation of 80%ZrB₂+20%SiC laminate: TWO-PHASES OXIDE LAYER



Differences in composition in two-phases oxide layer, formed in 80%ZrB₂ - 20%SiC laminate after oxidation in air at 1600° C for 24 hours

Oxidation of 80%ZrB₂+20%SiC laminate: POROUS LAYER



EDS analysis

At. %

Si = 1.51 % at.

O = 28.74

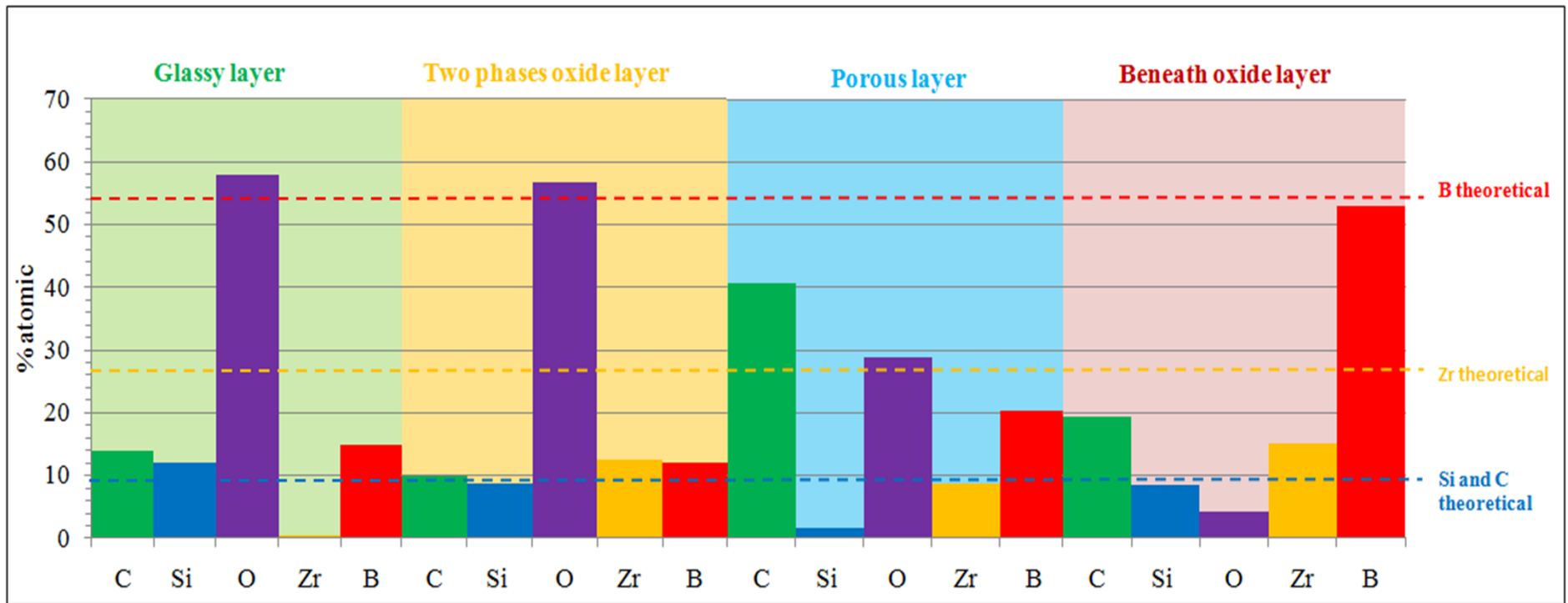
C = 40.47

Zr = 8.55

B = 20.82

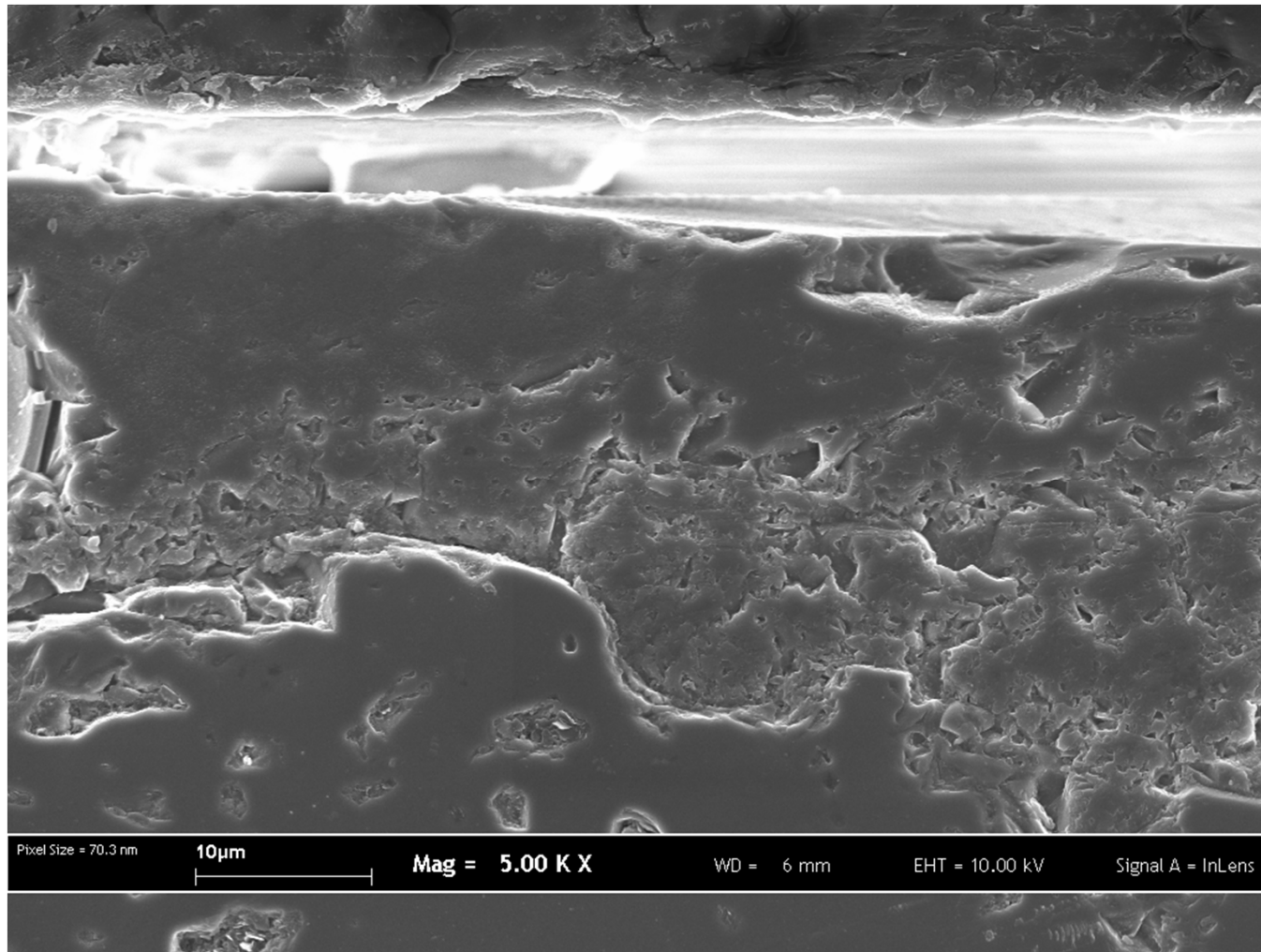
Porous layer formed in 80%ZrB₂-20%SiC laminate after oxidation in air at 1600° C for 24 hours

ZrB₂-SiC laminate: COMPOSITION VARIATION THROUGH THE THICKNESS



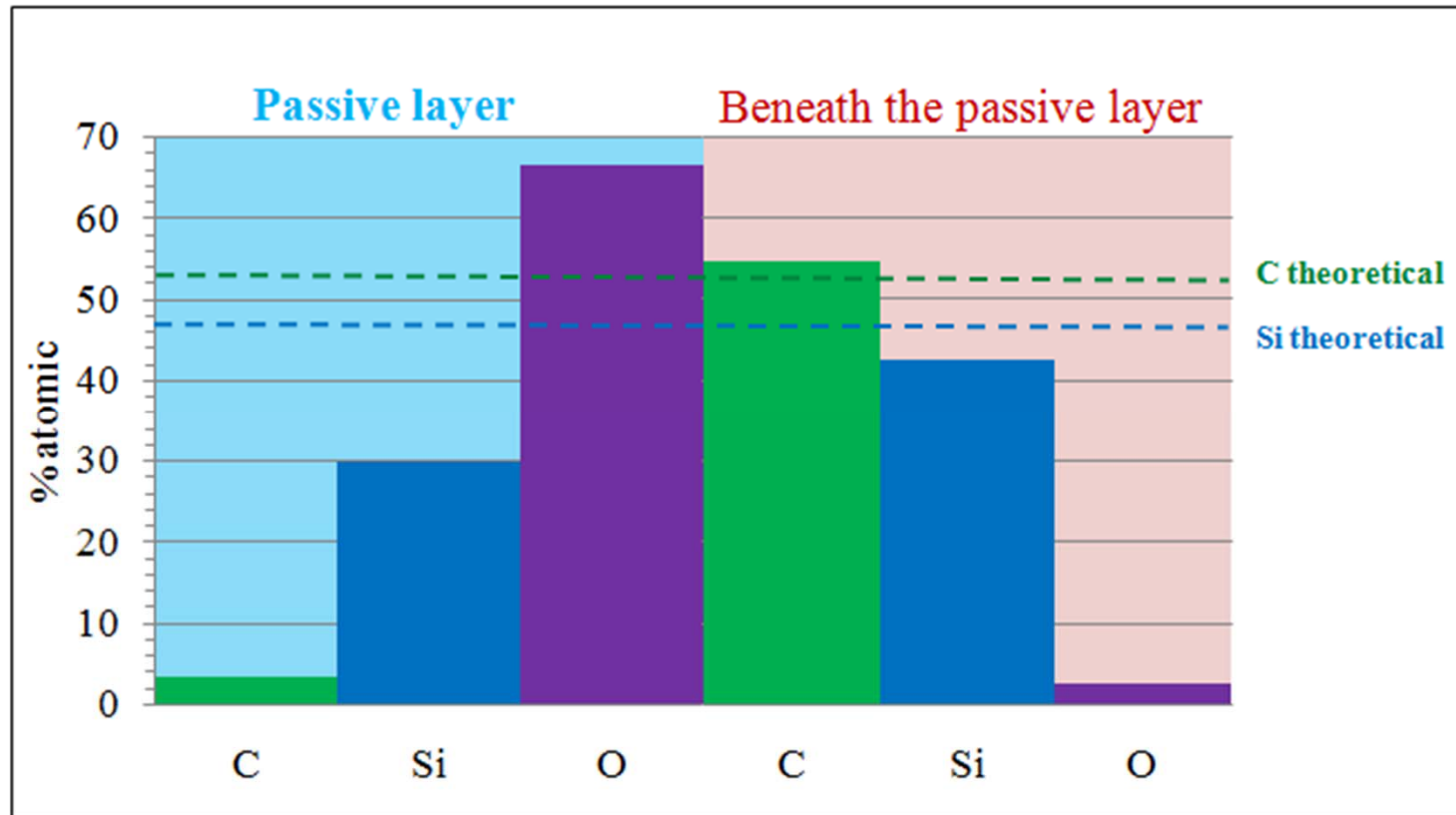
EDS composition of different parts of 80%ZrB₂ - 20%SiC specimens after oxidation in air at 1600°C for 24 hours.

Oxidation of SiC laminate: MICROSTRUCTURE



Microstructure of SiC laminate after oxidation in air at 1600° C for 24 hours

SiC laminate: COMPOSITION VARIATION THROUGH THE THICKNESS

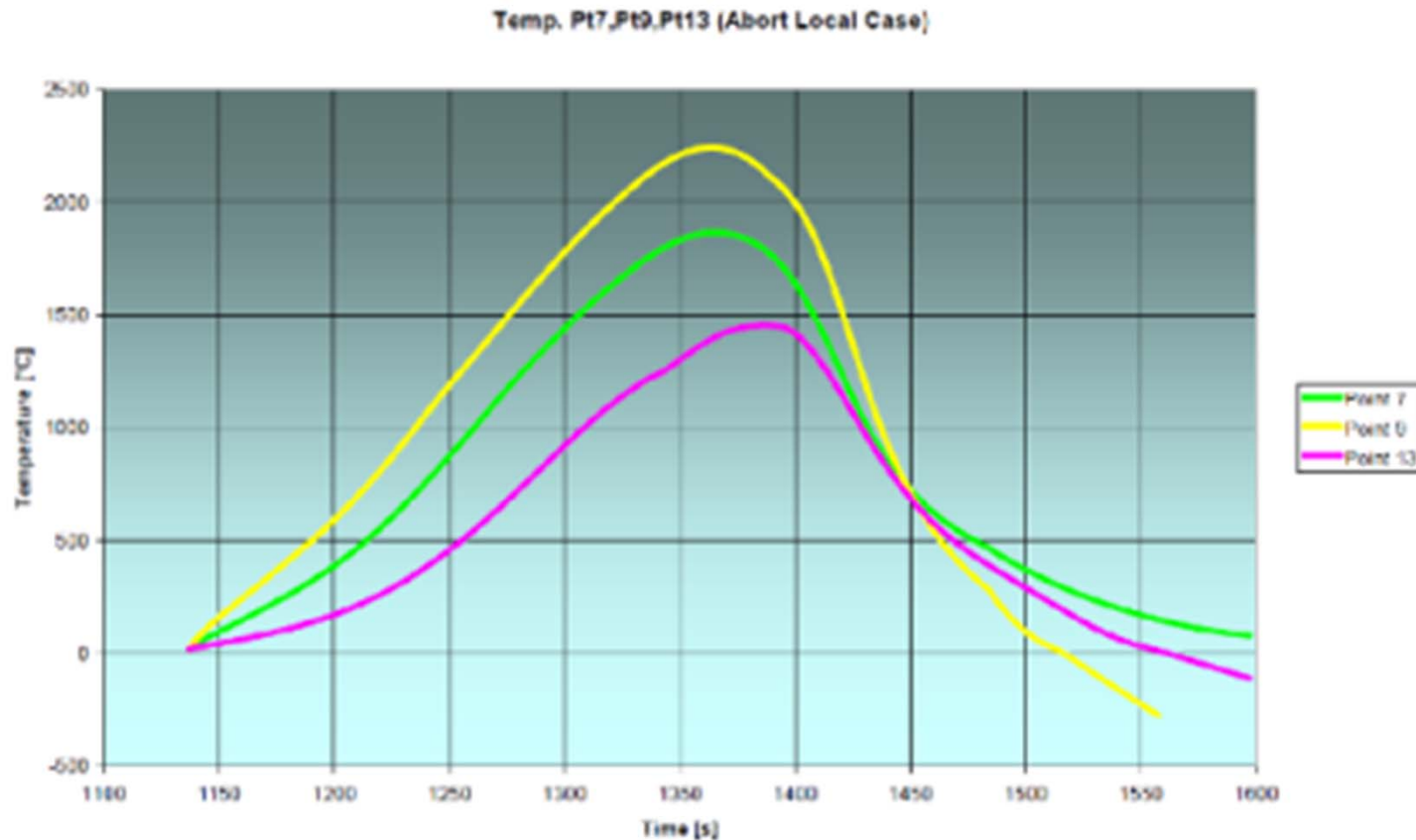


EDS composition of different parts of SiC specimens after oxidation in air at 1600°C for 24 hours.

THICKNESS OF LAYERS AFTER OXIDATION IN AIR FOR 24 h AT 1600°C

Material composition	Layer thickness (μm)			
	External glassy layer	Oxide layer	Porous layer	Sample core
80%ZrB ₂ -20%SiC	600-700	1200-1300	140-200	640
SiC	-	21-36	-	1750

TEMPERATURE PROFILE DURING RE-ENTRY AT THE MOST CRITICAL POINTS OF TPS (from ARV data base and SMARTTEES)



Yellow curve (200 s spent over 1000°C): 41% of time between 1000°C and 1600°C and 59% over 1600°C

Green curve (200 s over 1000°C): 64% between 1000°C and 1600°C and 36% over 1600°C

CONCLUSIONS

- 1) The present investigation confirmed that SiC laminate shows passivating behavior up to 1600°C
- 2) SiC laminate grants high protection against oxidation, provided that during re-entry passive oxidation prevails on active one (simulated re-entry test performed up to 1550°C showed that passive layer is consumed under active oxidation conditions but it is promptly restored under passive oxidation and then it still stands at the end of the test)
- 3) 80%ZrB₂-20%SiC composite laminate suffers strong oxidation between 1000-1600°C that involves boria evaporation
- 4) Very thick and complex oxide layer grows under these conditions; it comprises:
 - An external borosilica glassy layer
 - An intermediate layer consisting of ZrO₂ crystals embedded in glass matrix
 - A porous zone of Si depletion

FUTURE INVESTIGATIONS

- Investigation about oxidation behavior below 1600°C of ZrB₂-SiC composite laminates with different ZrB₂:SiC ratios
- Comparison of oxidation resistance of SiC and ZrB₂-SiC laminates at around 2000°C under re-entry simulated conditions (scheduled in SMARTTEES project)
- Development of alternative concepts suitable for providing protection against oxidation in a wide range of temperature (at least between 1000°C and 2000°C): laminates integrating alternate layers with different composition

**THANK YOU FOR YOUR
ATTENTION**

Active/passive oxidation transition and active oxidation kinetics for C/SiC composites in IXV re-entry conditions – Explanation of temperature jump observed in high enthalpy facilities

M. Balat-Pichelin ⁽¹⁾, L. Charpentier ⁽¹⁾, O. Chazot ⁽²⁾, F. Panerai ⁽²⁾, B. Helber ⁽²⁾

⁽¹⁾ PROMES-CNRS, 7 rue du four solaire, 66120 Font-Romeu Odeillo (France) marianne.balat@promes.cnrs.fr

[#] VKI, 72 chaussée de Waterloo, 1640 Rhode St Genèse (Belgium) o.chazot@vki.ac.be

INTRODUCTION

C/SiC composites (CMC) coated by a CVD β -SiC layer will be used for the hottest parts of the IXV vehicle that are localized on the nose, front part of the windward and on the flaps. Two materials, one from Herakles (France) and one from MT Aerospace (Germany) have been selected and tested in order to precisely determine the transition between active and passive oxidation to know their re-usability limits and to study the oxidation kinetics in some of the worst conditions of the trajectory (active oxidation up to 2250 K).

The complementary characteristics of the two facilities - MESOX and VKI Plasmatron - lead to a wide range of temperatures and pressures covering the whole trajectory of the IXV with some cross-checking. The domain investigated in details covers the partial oxygen pressure range of 40-1200 Pa leading to a total air pressure range of 200-6000 Pa and a temperature range of 1700-2300 K.

The transition between passive and active oxidation regimes was determined on both facilities and materials, and an agreement was found for the results obtained on both facilities and on both materials. SEM micrographs of the surface and of the cross-section of the samples were carried out in order to plot the transition limit that was finally defined by a single law. The mass loss rate in active oxidation conditions was also studied to know the evolution with time of the recession of the materials in critical conditions that can be encountered during the IXV reentry.

The sudden temperature jump at constant free-stream conditions was observed for samples exposed to very high enthalpy dissociated flow in the Plasmatron facility. This phenomenon occurred at wall temperature near 2100 K whatever the pressure. A high mass loss exceeding 30% of the initial values was found, one order of magnitude higher than that experienced during active oxidation condition, and a full modification of the surface, which a strong reduction in thickness, was observed. This jump is explained by strong active oxidation reactions that would lead to the complete erosion of the superficial SiC layer and expose the carbon fiber preform to oxidation. Optical emission spectroscopy methods were implemented in order to provide information on spatially and temporally resolved species volatilization during plasma flow exposure of the test samples that confirm the temperature jump origin.

IXV PEAK TEMPERATURES IN REENTRY CONDITIONS

The material that will be used for the hottest parts of the IXV vehicle will be based on silicon carbide. The IXV thermal protection system is composed of a C/SiC nose, C/SiC shingles on the windward area and ablative materials on the leeward. The control of the vehicle during re-entry is made using C/SiC flaps. As shown in Fig. 1, the hottest parts will be localized on the nose (points noted N), the front part of the windward and on the flaps (points noted W). Two materials, one from Herakles (HER or SPS) and one from MT Aerospace (MTA) have been selected and were tested in order to precisely determine the transition between active and passive oxidation and to study the oxidation kinetics in some of the worst conditions of the trajectory (active oxidation up to 2250 K). Taking into account the data given by ESA for the IXV trajectory in terms of flux, temperature on the walls and total air pressure, several points were identified on the surface of the vehicle as critical being during few seconds in the active oxidation zone. Fig. 1 reports the trajectory points selected together with the transition line determined by Balat on the C/SiC materials from SPS in 1996 [1]. The trajectory points reported in Fig. 1 show that the main part of the IXV would remain in the passive region, except for the nose point N10, for the windward points W17 and W8, and for the flaps points W10, W20 and W21, that will undergo active oxidation for short duration during the re-entry procedure.

TEST CONDITIONS FOR PASSIVE/ACTIVE OXIDATION OF CMC

A test plan for the oxidation study in the two plasma facilities was implemented. The complementary characteristics of the two facilities lead to a wide range of temperatures and pressures covering the whole trajectory of the IXV with some cross-checking, as for example for total air pressures in between 2000-5000 Pa. This test plan includes the experimental determination of the passive/active oxidation transition on the MESOX facility and then confirmed for some points on

the VKI Plasmatron. The domain that will be investigated in details for this study will mainly cover the partial oxygen pressure range of 40-1200 Pa leading to a total air pressure range of 200-6000 Pa and a temperature range of 1700-2300 K. Active oxidation at high temperature levels will be performed on both the MESOX and Plasmatron facilities to evaluate the recession rate as it have been done on the MESOX facility for the cladding materials of the Gas-cooled Fast Reactor (GFR), one reactor of the Generation IV program for nuclear fission [3-5].

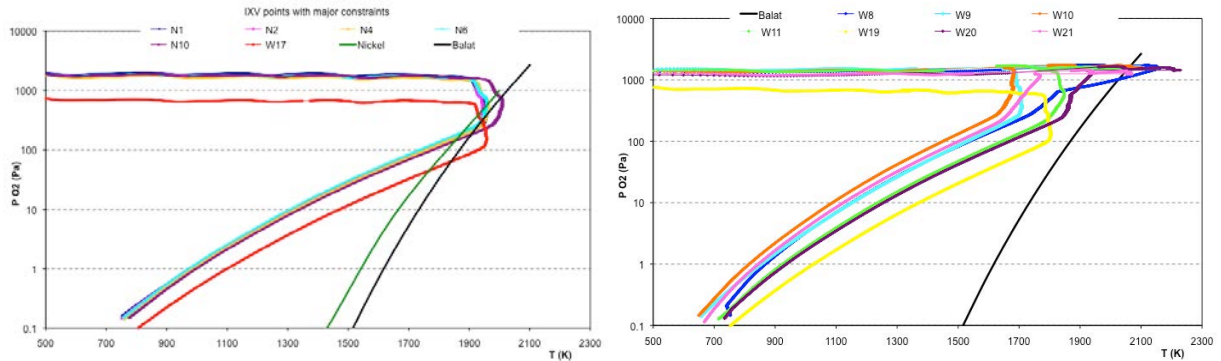


Fig. 1. Oxygen partial pressures as a function of temperature for some hot points of the IXV trajectory with the transitions reported by Balat, in black [1] and Nickel, in green [2].

TEST FACILITIES AND MATERIALS

MESOX and VKI Plasmatron facilities were already described in several papers [3-9] and are not reported here.

Two Ceramic Matrix Composites (CMC) based on a carbon perform and a matrix of silicon carbide have been retained for this study. They present also a SiC coating to increase the protection for high temperature oxidation. These two materials will be used on the IXV vehicle for the nose, leading edges and flaps.

One of these composite materials is Sepcarbinox[®] L6, from Herakles. The L6 CMC material is made from a Guipex[®] carbon fibre preform. This type of texture is a multi-layered weave, well adapted to the manufacturing of thin, delamination-resistant parts. The pre-preg is moulded directly to the part shape on a specific mould, and then cured in order to provide the part with the required stiffness for further processing. The cured preform is then densified with a SiC matrix obtained by Chemical Vapor Infiltration (CVI). The final CVI cycle ensures that the SiC matrix is deposited on the entire surface, fibers included. This resulting seal-coat acts as a protective layer against oxidation of the carbon fibers.

The manufacture of MT Aerospace Keraman[®] C/SiC ceramic composites is realized by an improved near-net shaped lay-up technique of carbon fabric layers combined with an optimized SiC matrix infiltration via gradient CVI process. The process allows the fabrication of complex and integrally shaped CMC parts. The technique as well as ceramic components' properties have been verified and qualified under several former programs and during flight hardware manufacture (leading edges, body flap and chin panel) for the NASA vehicle X38. A process is disclosed for producing a high temperature stable fiber composite ceramic by CVI with a silicon carbide precursor in a suitable carrier gas on carbon fiber performs or silicon carbide fiber performs.

DETERMINATION OF THE ACTIVE/PASSIVE TRANSITION

SiC is oxidized according to two regimes, mainly depending on the oxygen partial pressure and temperature. During passive oxidation (Eqs. 1 and 2) – often at low temperature and high partial pressure of oxygen – a silica layer is formed on the surface of SiC and this layer is protective slowing down the oxidation process (passivation):



During active oxidation (Eq. 3) – often at high temperature and low partial pressure of oxygen – gaseous SiO is produced and consequently, no passive layer is formed and significant mass loss is observed:



Previous studies had given theoretical and/or experimental transitions between passive and active oxidation, according to total pressure, oxygen partial pressure and temperature. The huge discrepancy between the results can be explained

by the difference in the parameters taken for the study and mainly by the nature of the gaseous atmosphere surrounding the sample: standard, dissociated in low enthalpy facilities and dissociated in high enthalpy facilities.

In this study, the classification in passive conditions is determined by a relative mass loss lower than almost 0.5-1 % and by a mass loss rate lower than $0.7 \text{ mg cm}^{-2} \text{ min}^{-1}$. The confirmation is obtained through the SEM images performed on the surface of the samples. The transition was found for 200 Pa air total pressure between 1760 and 1853 K, for 500 Pa, between 1843 and 1883 K, for 2000 Pa, between 1922 and 2006 K and for 5000 Pa, between 2003 and 2033 K. Fig. 2 reports the transition determined for Herakles material (SPS) with the points representing the several experiments with green diamonds for samples under passive oxidation and red diamonds for the active ones and Fig. 3 clearly shows the difference between active and passive oxidation for SPS L (2003 K) and SPS 2 (2033 K) at 5000 Pa for samples tested in the MESOX facility (300 W microwave power, 4l/h air flow rate). In passive conditions, there is a thin silica layer on the oxidized samples (L) compared to the reference sample. For sample 2, the silicon carbide layer is broken and in the hole, the carbon fibers are clearly visible. Oxygen is highly reactive with carbon at these temperature levels and the mass loss rate increases a lot in these conditions. The Plasmatron tests were also performed in air plasma at a mass flow of 16 g/s.

The transition obtained, taking into account that the temperature measurement carried out at PROMES-CNRS using the optical pyrometer working at $5 \mu\text{m}$ was done with a value of 0.90 for the spectral normal emissivity, leads to the following expression: $p_{\text{O}_2}(\text{SPS}) = 10^{15} \exp(-5585/T)$ with a correlation factor of 0.99994 with the oxygen partial pressure p_{O_2} expressed in Pa and T in K. This transition is very close to the one previously obtained by Balat [1] on same materials (reported in blue in Fig. 2); at that time, the value chosen for the spectral ($5 \mu\text{m}$) normal emissivity was 0.87 that explains the difference between the two curves of around 20 to 30 K, but the activation energy of the process is the same and equal to around 46 kJ/mol.

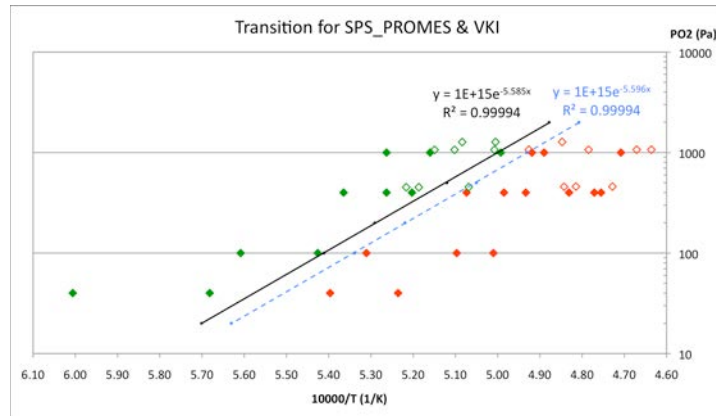


Fig. 2. Experimental transition determined at PROMES-CNRS (solid dots) and VKI (open dots) for Herakles material.

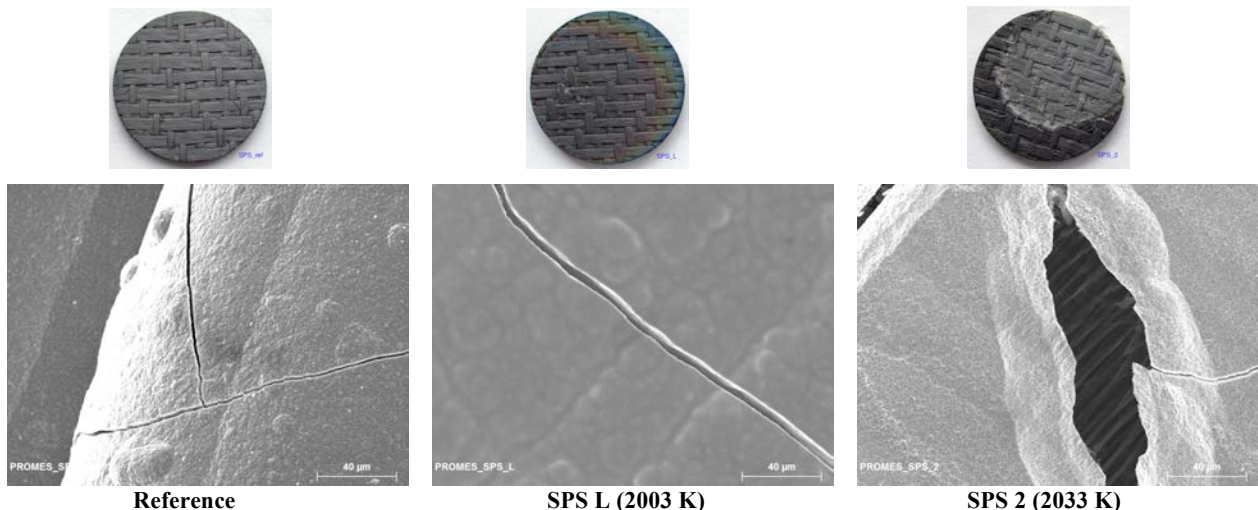


Fig. 3. Optical and SEM images of SPS samples: reference, L passive (2003 K) and 2 active (2033 K) at 5000 Pa.

For the MTA samples, the transition was found for 200 Pa air total pressure between 1776 and 1822 K, for 500 Pa between 1841 and 1906 K, for 2000 Pa between 1927 and 1957 K and for 5000 Pa between 2008 and 2052 K. The

transition is reported in Fig. 5 together with the points representing the several experiments with light green dots for samples under passive oxidation and orange dots for the active ones. As before, the transition obtained, taking into account that the temperature measurement carried out at PROMES-CNRS, leads to the following expression:
 $p_{O_2}(\text{MTA}) = 10^{15} \exp(-5614/T)$ with a correlation factor of 0.99991 with the oxygen partial pressure p_{O_2} expressed in Pa and T in K. As previously, this transition is very close to the one obtained by Balat (reported in blue in Fig. 5). Fig. 6 also shows the difference between active and passive oxidation for MTA 11 (2008 K) and 12 (2052 K) at 5000 Pa. In passive conditions, there is a thin silica layer on the oxidized samples (11) compared to the reference sample. For sample MTA12, the silicon carbide layer is broken and absent in some parts, and in the hole, the carbon fibers are clearly visible.

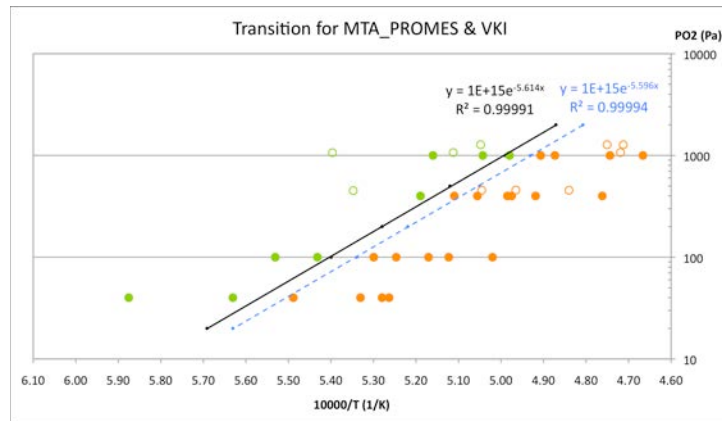


Fig. 5. Experimental transition determined at PROMES-CNRS (solid dots) and VKI (open dots) for MTA material.

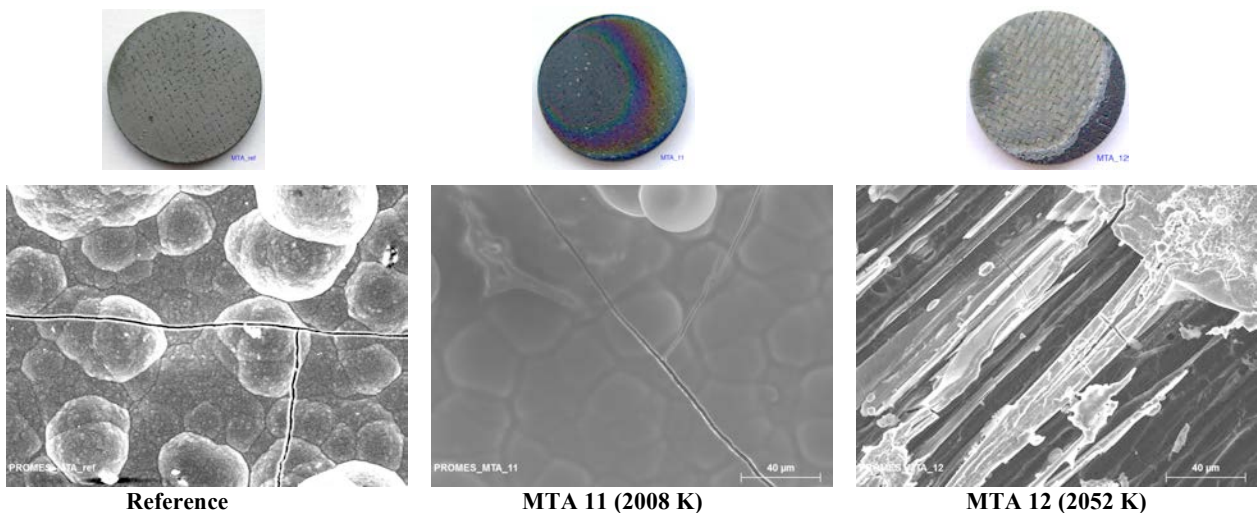


Fig. 6. Optical and SEM images of MTA samples: reference, 11 passive (2008 K) and 12 active (2052 K) at 5000 Pa.

MASS LOSS RATES IN ACTIVE OXIDATION CONDITIONS

The mass loss rates (MLR) obtained in active oxidation conditions are given, for example, for the SPS samples and reported in Fig. 7. These mass loss rates are calculated from the mass difference before and after oxidation taking into account the surface corresponding to a diameter of 25 mm and the duration of the temperature plateau. It is possible to find some correlation, for the experiments performed on the MESOX facility, taking into account only the samples in active oxidation conditions plus the last passive point at the highest temperature and it seems that linear fits are correct and that the slope is the same for all the pressure levels studied, the preliminary laws obtained being:

- for 500 Pa total air pressure: MLR = 0.0253 T - 46.83 R²= 0.94
- for 2000 Pa total air pressure: MLR = 0.0263 T - 50.37 R²= 0.93
- for 5000 Pa total air pressure: MLR = 0.0264 T - 51.26 R²= 0.88

Nevertheless, more experiments would be necessary to find better correlation for the mass loss rates in active oxidation conditions particularly for the lowest pressures and they will be carried out soon on smaller samples in order to have homogeneous temperature on all the surface.

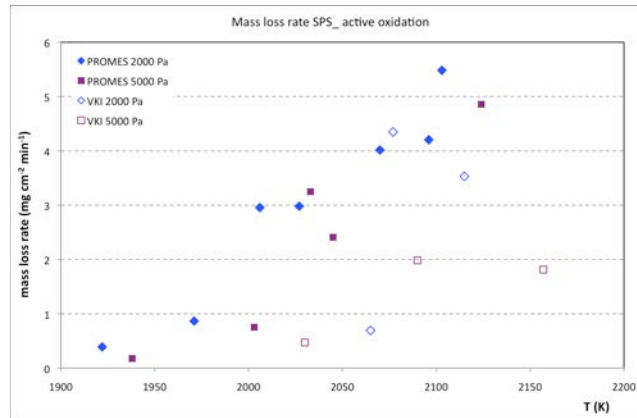


Fig. 7. Evolution of the mass loss rate versus temperature for the Herakles samples for experiments performed at PROMES-CNRS and at VKI

TEMPERATURE JUMP

The sudden temperature jump at constant free-stream conditions was observed for samples exposed to very high enthalpy (> 26.5 MJ/kg) dissociated flow in the Plasmatron facility, rich of atomic oxygen and nitrogen reactants. This phenomenon occurred at wall temperature near 2100 K. A high mass loss exceeding 30% of the initial values was found, one order of magnitude higher than that experienced during active oxidation condition, and a full modification of the surface, which a strong reduction in thickness, was observed. The jump is explained with strong active oxidation reactions which would lead to the complete erosion of the superficial SiC layer and expose the carbon fiber perform to oxidation and/or nitridation reactions.

Many authors experienced a severe jump in surface temperature of several hundred K during exposure of silicon carbide specimens to high heat flux, low pressure environments and associated this phenomenon with a passive-active oxidation transition in plasma wind tunnels. Lacombe and Lacoste [10] first described this phenomenon on C/C-SiC specimens in the arc-jet plasma facility at NASA JSC. Marschall et al. [11] recently performed Plasmatron experiments on Ultra-High Temperature Ceramics and observed a strong rise in surface temperature for ZrB₂-SiC specimen after they reached a steady-state surface temperature, forming stable silica on the surface. This stable phase was followed by a sudden increase of cold wall heat flux, induced by the Plasmatron ICP torch, which triggered the temperature jump.

We can propose here that the previous explanation of the temperature jump were not correct and cannot be attributed to the passive/active transition or to a catalycity effect as it was stated by several authors.

The test performed on sample HER 17 represents a unique test case in the experimental campaign (Figs. 8, 9). Several attempts were performed in order to obtain a similar phenomenology for different pressure conditions. Nevertheless a sudden failure of the SiC holder was experienced during each run at very high heat flux and significant data could not be retrieved. Therefore graphite specimens holders were adopted in place of SiC for tests at different pressure conditions with both HER and MTA samples. Graphite offers better performances than sintered SiC when exposed to sharp heating rates, nevertheless presents the inconvenient of being subjected to a rapid recession due to ablation processes. Such erosion phenomena are likely to occur at the graphite edges surrounding the C/SiC specimens, resulting in highly reactive hot zone transferring side-heating to the test samples in addition to the incoming heat flux from the dissociated flow. Consequently, as it can be observed in Fig. 8 for sample HER 23 (left) and samples MTA 11-13 (right), the initial temperature rise is significantly accelerated for heat flux level consistent to that used with sample HER 17. As result, a steady state temperature cannot be achieved and the temperature jump is observed during the fast heating of the specimen surface. The progress is: a bright front propagates from the edges to the center of the C/SiC sample until the full surface is covered and the models turns into unique bright image. Due to the ablation of the cover the phenomenon is faster (~ 30 s for HER 17) and a front propagation rate of 1.5 mm/s can be calculated.

Fig. 10 presents the SEM images of the samples HER 17 after the temperature jump where one can see the matrix made of carbon fibers eroded like needles and no SiC is anymore visible.

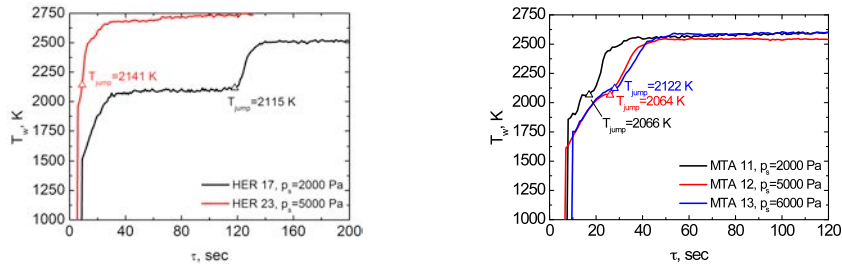


Fig. 8. Temperature histories during standard model testing: Herakles (left) and MTA (right) samples

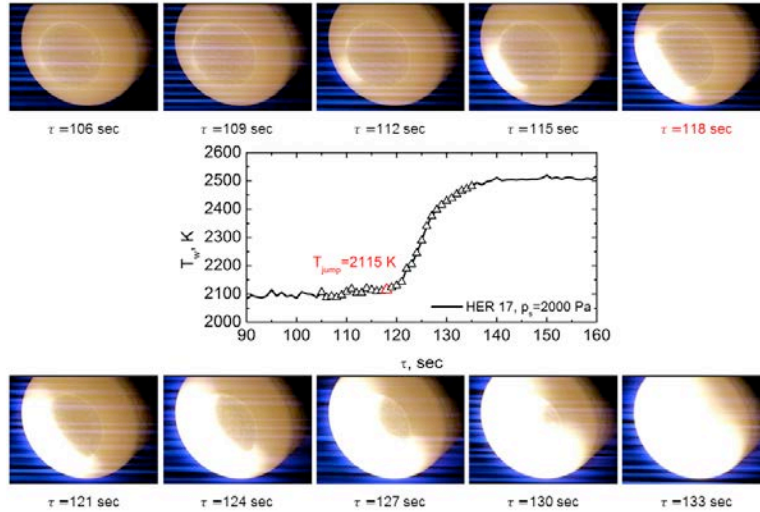


Fig. 9. Details of the temperature jump phenomenon observed during test for sample HER 17. The temperature plot is an enlargement of Fig. 8 (left) around the jump region. The images are frames extracted from the HD video recording, each 3 s starting at the onset of the jump phenomenon. The total duration of the process is 27 s.

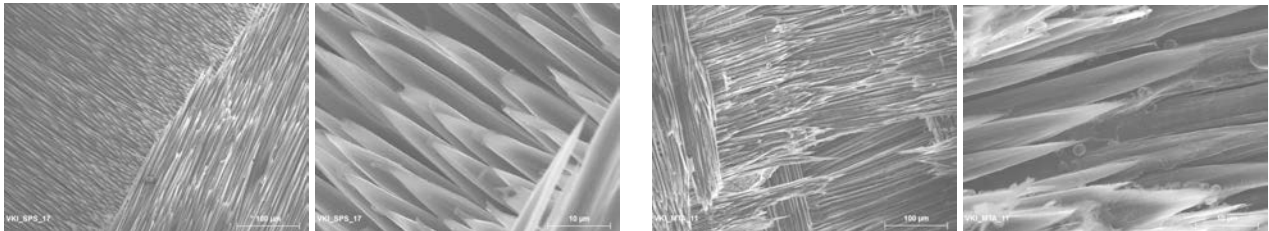


Fig. 10. SEM images for HER 17 (left) and MTA 11 (right) after the temperature jump for 2000 Pa total air pressure.

Optical emission spectroscopy methods were implemented in order to provide information on spatially and temporally resolved species volatilization during plasma flow exposure of the test samples. Three low resolution spectrometers were focused at a distance of 2, 5.5 and 9 mm in front of the test sample in the Plasmatron facility, covering a broad wavelength range in order to record excited free-stream species (O, N) as well as products coming from gas-surface interaction and material erosion such as silicon (Si) and cyanogen (CN).

Below certain heat flux levels, the specimens heated up and reached a steady-state surface temperature level suggesting a passive oxidation regime due to the production of a silica layer. No Si emission was recorded by the spectrometers for conditions where a passive oxidation regime was expected. At higher heat flux, the surface temperature still remained stable but Si emission was detected in the boundary layer, suggesting removal of the silica layer through active oxidation reactions. A further heat flux increase, or for experiments where the test sample was directly injected into the high target heat flux, a temperature jump occurred from near 2100 up to 2500 K. HD-camera movies showed that the jump was triggered at a point of the specimen edge, progressed along the circumference and spread over the whole sample like in Fig. 9. Emission intensities of both species, CN violet and Si (multiple atomic lines) sharply rose during this phenomenon, proving the volatilization not only of an existing silica layer but also reactions of the carbon fibers by oxidation and/or nitridation. The emission of CN violet was delayed by a few seconds compared to that of Si and furthermore, the Si emission peaked during the temperature jump before reaching lower, steady emission intensity.

Such an emission peak was not observed for CN violet, which rather leveled off simultaneously with Si reaching constant emission. We assume that silica volatilization leads to the high radiative signal of Si during the jump followed by a steady consumption of the SiC matrix. Simultaneously, carbon fiber nitridation might lead to CN violet radiation, increasing during the temperature jump as more and more fibers are being exposed to the hot boundary layer. Oxidation reactions are probably more dominant for such test conditions in atmospheric air plasmas, leading now to the destruction of the sample (Fig. 10), but the strong radiative signature of the CN molecule helped to identify the onset of carbon fiber degradation. Regarding a spatial analysis of the radiative signature, it was found that CN violet emission strongly dropped throughout the boundary layer between 2 and 5.5 mm and vanished at a distance of 9 mm ahead of the test specimen. Contrary to CN violet, a higher Si emission was recorded by the spectrometer focused 5.5 mm ahead of the sample compared to that one focused at 2 mm. It seems that the dissociation of SiO, produced by active oxidation of the SiC matrix and the sublimation of SiC, leads to a higher concentration of Si farther away from the surface. Temporally and spatially resolved emission spectra of characteristic erosion products are shown in Fig. 11. Left-panel plots show the range 240-290 nm where most of Si emission can be identified and plots on the right-panel show CN violet emission in the range of 340-440 nm. Spectra shown in the upper plots are collected close to the sample surface with increasing distance to bottom plots (lowest plot taken at 9 mm distance from target). Strong Si emission at 243, 252, 263 and 288 nm is clearly evident and increased after the first 20 s of sample exposure to plasma flow. We assume that this strong Si emission is an evidence for the volatilization of silicon containing species such as SiO₂ and SiC. An emission peak of all Si lines can be distinguished before the intensity dropped to a steady-state value. This emission peak occurred 40 s after sample injection and was recorded by all three spectrometers. It can further be observed that Si emission collected by the spectrometer pointing 5.5 mm ahead of the specimen was stronger than Si emission close to the specimen wall (2 mm ahead), with the weakest emission collected at the farthest probing volume (9 mm). Opposed to an increase of Si emission throughout the boundary layer, CN violet emission sharply decreased from the 2 mm to 5.5 mm probing locations and almost vanished at 9 mm distance. Furthermore, an emission peak such as recorded for Si emission during the occurrence of the temperature jump could not be detected for CN emission. To summarize, the observations suggest that initial Si production was started by active oxidation, which leads to consumption of an existing silica layer that could rapidly form during sample injection, but did not induce a temperature jump. The state of the SiC coating after such tests would be of high interest to further confirm active oxidation. If locally the SiC coating could be removed, e.g. at a point on the sample edge at higher heat flux, and carbon fibers were exposed to the hot plasma flow, oxidation reactions of the carbon fibers may trigger the temperature jump and lead to a fast consumption of the silica layer and SiC coating (Fig. 10).

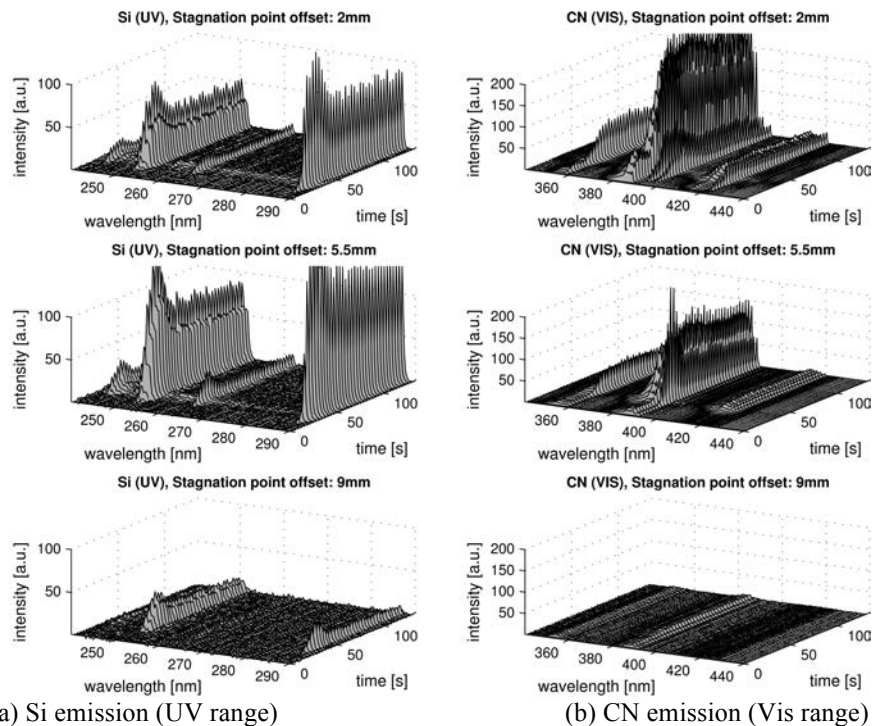


Fig. 11. Temporally and spatially resolved radiative signature of characteristic emission lines of Si (a) and CN violet (b) band systems; Spectra are shown from sample injection (time=0) until test end along three distances from sample stagnation point (MTA 12: 1.4 MW/m², 5000 Pa)

SUMMARY

The transition between passive and active oxidation regimes was determined on both facilities (MESOX and Plasmatron) and materials (SPS/HER and MTA) and an agreement was found. The transition limit can be finally defined by the following law, with p in Pa and T in K: $p_{O_2} = 10^{15} \exp(-5600/T)$ with $E_a = 46$ kJ/mol.

Same transitions were obtained experimentally at PROMES-CNRS and at VKI for both the CMC samples from Herakles (ex SPS) and MT Aerospace, not surprising as the composition is nearly the same, together with a CVD β -SiC coating on the top surface. This transition is very close to the one previously obtained by Balat [1]: difference of around 20 to 30 K in the pressure range, due to the chosen spectral (5 μ m) normal emissivity value. The mass loss rate kinetics in active oxidation conditions was partially studied showing some differences between SPS and MTA samples and more experiments are scheduled to find better correlation.

The temperature jump observed at VKI was explained and can be attributed to carbon combustion after the disappearance of the SiC (layer and matrix) and additional testing, refinement of the measurement methods and further analysis of the microstructure are required to better understand the chemical and physical mechanisms arising at the surface during the temperature jump.

Acknowledgments

The authors acknowledge the European Space Agency ESA-ESTEC for the support of this work carried out in the frame of the TRP on *Passive/Active Oxidation of CMC Structural Materials*, contract n°4000103145/11/NL/CP, and the two manufacturers Herakles and MT Aerospace.

REFERENCES

- [1] Balat M.J.H., Determination of the active-to-passive transition in the oxidation of silicon carbide in standard and microwave-excited air, *J. Europ. Ceramic Society* 16 (1), 1996, 55-62.
- [2] Nickel K.G., The role of condensed silicon monoxide in the active-to-passive oxidation transition of silicon carbide, *J. Europ. Ceramic Society*, 9, 1992, 3-8.
- [3] Charpentier L., Balat-Pichelin M., Audubert F., High temperature oxidation of SiC under helium with low-pressure oxygen – Part 1: sintered alpha-SiC, *J. Europ. Ceramic Society*, 30, 2010, 2653-2660.
- [4] Charpentier L., Balat-Pichelin M., Glénat H., Bêche E., Laborde E., Audubert F., High temperature oxidation of SiC under helium with low-pressure oxygen – Part 2: CVD beta-SiC, *J. Europ. Ceramic Society*, 30, 2010, 2661-2670.
- [5] Dawi K., Balat-Pichelin M., Charpentier L., Audubert F., High temperature oxidation of SiC under helium with low-pressure oxygen – Part 3: betaSiC-SiC/PyC/SiC, *J. Europ. Ceramic Society*, 32, 2012, 485-494.
- [6] Balat-Pichelin M., Badie J.M., Berjoan R., Boubert P., Recombination coefficient of atomic oxygen on ceramic materials under Earth re-entry conditions by Optical Emission Spectroscopy, *Chem. Phys.* 291 (2), 2003, 181-194.
- [7] Chazot O., Krassilchikoff H.W., Thoemel J., TPS Ground testing in plasma wind tunnel for catalytic properties determination, *46th AIAA Aerosp. Sci. Meeting & Exhibit*, Reno, Nevada, January 7-10, 2008, AIAA-2008-1252.
- [8] Panerai, F., Chazot, O., Tagliaferri, E., Rossi, G., Testing of the EXPERT Thermal Protection System Junction in a Plasma Wind Tunnel, *16th AIAA/DLR/DGLR Int. Space Planes & Hyperson. System & Technol. Conf.*, AIAA 2009-7243, October 2009, Bremen, Germany.
- [9] Vérant J.L., Perron N., Balat-Pichelin M., Chazot O., Kolesnikov A., Sakharov V., Gerasimova O., Omaly P., Microscopic and macroscopic analysis for TPS SiC material under Earth and Mars reentry conditions, *Int. J. Aerodynamics*, 2 (2-4), 2012, 152-192.
- [10] Lacombe A., Lacoste M., Investigation of C/SiC breaking point under arc-jet environment at NASA-JSC, *High Temp. Chem. Processes*, 3, 1994, 285-296.
- [11] Marschall J., Pejaković D.A., Fahrenholtz W.G., Hilmas G.E., Panerai F., Chazot O., Temperature jump phenomenon during Plasmatron testing of ZrB₂-SiC Ultra High Temperature Ceramics, *J. Thermophys. Heat Transfer*, 26(4), 2012, 559-572.

Catalycity and emissivity of ZrB₂-SiC based UHTC in air plasma flow at high temperatures

M. Balat-Pichelin⁽¹⁾, E. Bêche⁽¹⁾, J.L. Sans⁽¹⁾, V. Flaud⁽²⁾, D. Sciti⁽³⁾, D. Alfano⁽⁴⁾

⁽¹⁾ PROMES-CNRS, 7 rue du four solaire, 66120 Font-Romeu Odeillo (France)

marianne.balat@promes.cnrs.fr eric.beche@promes.cnrs.fr jean-louis.sans@promes.cnrs.fr

⁽²⁾ ICGM, Place Eugène Bataillon, CC1701, 34095 Montpellier (France) valerie.flaud@univ-montp2.fr

⁽³⁾ ISTECCNR, 64 via Granarolo, 48018 Faenza (Italy) diletta.sciti@istec.cnr.it

⁽⁴⁾ CIRA, via Majorise, 81043 Capua (Italy) d.alfano@cira.it

INTRODUCTION

Ceramic compounds based on metal borides such as ZrB₂ and HfB₂ have been commonly referred to as Ultra High Temperature Ceramics (UHTCs). UHTCs represent a class of promising materials for use in extreme applications because of their high melting point (around 3500 K), solid state stability, good thermo-chemical, and thermo-mechanical properties [1] and relatively good oxidation resistance in re-entry conditions. These extremely promising high performance materials are also characterized by hardness above 20 GPa, high wear resistance, high emissivity, high electrical conductivity, excellent corrosion resistance, and good thermal shock resistance [2, 3]. Leading applications are currently found in aerospace, more specifically in the possibility to employ them to realize sharp-shaped hot structures like wing leading edges and nose caps able to withstand the severe thermal requirements of next generation of hypersonic re-entry vehicles. The highly thermal demanding trajectories foreseen for future space planes like winged re-entry vehicles dictate the need for base materials able to sustain operating temperatures approaching 2500 K, to resist sublimation, erosion and oxidation in the harsh re-entry environment. The research on this class of materials began in the 60's in the frame of Air Force contracts and the early works were devoted to the production of dense materials by mean of pressure assisted sintering, and to investigate the influence of a variety of additives, including carbon and silicon carbide, on the processing and oxidation resistance of Hf and Zr diborides. These works showed that the addition of SiC as secondary reinforcing phase provides significant enhancements to the oxidation resistance of UHTCs [4]. Moreover the SiC addition was also found to improve the processing by lowering sintering temperatures [5-7]. An important parameter such as the upper limit of the service temperature is strongly related to the characteristics of secondary phases. NASA started in 1990 a research program on UHTCs and ended up in 1997 and 2000 demonstrating the use of ZrB₂ and HfB₂ for sharp leading edge in the Sharp Hypersonic Aero-thermodynamic Research Probe Ballistic experiments (SHARP-B1 and B2) [8]. During the 90s, a wide range research activity on UHTC materials was conducted in Italy, mainly by the Institute of Ceramic Materials (CNR-ISTEC) that investigated new processing routes based on pressure assisted sintering, on the adoption of sintering aids and secondary reinforcing phases in order to obtain dense bodies characterized by superior oxidation resistance and mechanical properties [5, 7]. Since 2000, the Italian Aerospace Research Centre (CIRA) has studied, developed in collaboration with CNR-ISTEC, and tested massive UHTCs in the frame of the Unmanned Space Vehicle (USV) National Program [9-11]. The poor fracture toughness of UHTCs can be still considered the main limitation of this class of materials for aerospace applications. In these last years, the activities of several research groups on UHTCs have been focused on the improvement of the fracture toughness by using SiC whiskers or SiC chopped fibers as reinforcing aids [12-14].

The objective of this paper is to present and discuss the experimental results of emissivity and atomic oxygen catalytic efficiency properties of different UHTCs materials based upon the ZrB₂ composition with different sintering additives (Si₃N₄, ZrSi₂, MoSi₂) and with SiC chopped fibers as reinforcing aids. Micro-structural analyses by SEM, EDS, XRD and XPS have shown oxidation-induced surface modifications with oxide layers composed of silica with trace amounts of boron oxide and zirconia if the maximum reached temperature is lower than about 1800 K and mainly zirconia for higher temperature values. The differences in the oxide layer composition may account for the different thermal radiative properties and catalytic behavior.

MATERIALS PREPARATION AND CHARACTERIZATION

Ceramic billets were prepared using the following commercial powders: SiC chopped fibers (HI Nicalon, COI Ceramics Inc., Magna, Utah, USA), ZrB₂ Grade B (H.C. Starck, Germany). As for the sintering aids Si₃N₄ Baysind (Bayer, Germany) and ZrSi₂ F (Japan New Metals Co., LTD, Osaka, Japan) were used. The following compositions were produced (vol%): ZrB₂ + 15% SiCf + 5% Si₃N₄, labeled as ZS and ZrB₂ + 15% SiCf + 10% ZrSi₂, labeled as ZZ.

Powders and fiber mixtures were ball-milled for 24 hours. After solvent removal, the powder mixture was uniaxially pressed at 15 MPa to form 45 diameter green pellets. Prior to sintering, the pellets underwent a debonding cycle at 773 K to remove organic species. The pellets were subsequently hot-pressed with a load of 40-50 MPa. Since the reinforcing fibers tend to react with the matrix and secondary phases during the high temperature thermal treatment, the sintering temperature should be kept as low as possible. ZrSi₂ allowed densification to be completed at 1923 K, Si₃N₄ at 1973 K (Table 1). The maximum temperature was dwelt as long as no further shrinkage was observed. The bulk densities were measured by Archimedes' method. To identify the crystalline phases present, all samples were examined using X-ray diffraction (Bruker D8 Advance, Germany). The microstructure was analyzed on fractured and polished surfaces using scanning electron microscopy (SEM, Cambridge S360, Cambridge, UK) and energy dispersive spectroscopy (EDS, INCA Energy 300, Oxford instruments, UK). Grain size, residual porosity and amount of secondary phases were determined through image analysis on SEM micrographs of polished surfaces using the commercial software Image Pro-Plus 3.0 (Media Cybernetics, Silver Spring, MD). ZrB₂ matrices were nearly fully dense at the selected sintering temperatures with limited residual porosity. The fiber dispersion was homogeneous, since no agglomeration was observed. As expected, the fibers showed the tendency to align their longest axis perpendicular to the direction of applied pressure. Residual ZrO₂ particles and secondary phases were observed in all the sintered microstructures, the nature of which was dependent on the sintering aid used. For the composites with Si₃N₄ (ZS), they were isolated pockets of BN, Zr-Si phases, SiO₂ and a borosilicate glass containing Zr-Si-B-N-O distributed along grain boundaries. For the material densified with ZrSi₂ (ZZ), Zr-Si with various stoichiometries were concentrated at triple points and along the grain boundaries. The fibers showed a multilayered core-shell morphology: the inner part is constituted by stoichiometric SiC, the surrounding shell is partially amorphous Si-C-O embedding crystalline ZrB₂ grains and the outermost jagged layer is a re-crystallized SiC phase. In the ZZ system, it can be noticed that despite the lower sintering temperature the extent of fiber/matrix interaction was greater than the system containing Si₃N₄ (ZS): the fiber surface appeared rough with little porosities and the interface region was very irregular. Often, faceted ZrB₂ grains were incorporated in the fiber. The reaction interface is constituted by Si-C-O phases, Zr-Si with various stoichiometries and traces of B, C, and O [15].

Mechanical Properties

The thermo-mechanical properties of the composites ZS and ZZ are reported in Table 1. For the sake of comparison, mechanical properties of unreinforced ZrB₂ (reference) are also reported. The addition of SiC fiber was effective in improving the fracture toughness that passed from 3.8 to 5.3-5.4 MPa m^{1/2}.

Table 1. Composition, sintering conditions, final density and thermo-mechanical properties of reinforced compositions and reference unreinforced ZrB₂: K_{Ic} fracture toughness, σ 4-pt bending strength at room temperature

Sample name	Composition (vol%)	Sintering conditions (K/MPa/min)	Density (g/cm ³)	Relative density (%)	K _{Ic} (MPa·m ^{1/2})	σ _{RT} (MPa)
reference	ZrB ₂ + 5% Si ₃ N ₄	1973/30/10	5.85	99.9	3.8 ± 0.1	600 ± 90
ZS	ZrB ₂ + 15% SiCf + 5% Si ₃ N ₄	1973/50/10	5.38	98.7	5.3 ± 0.1	453 ± 19
ZZ	ZrB ₂ + 15% SiCf + 10% ZrSi ₂	1923/50/10	5.50	99.9	5.4 ± 0.1	385 ± 13

Actually, no fiber pullout was observed on fracture surfaces and crack propagated straight through the fibers with little or no deflection. Considering the high fracture strength of the fibers, crack bowing was considered the dominant toughening mechanisms for these composites rather than crack deflection or bridging, as previously outlined [14]. For all the composites, the room temperature flexural strength values resulted lower compared to typical ZrB₂-SiC particle composites. Very likely the incorporation of large elements as the fibers adversely affected flexural strength by changing the defect population.

TOTAL HEMISPHERICAL EMISSIVITY

Emissivity measurement performed at PROMES-CNRS laboratory is based on a direct method where the temperature and the total or spectral radiance of the sample are measured [16, 17]. The total or spectral directional emissivities are the ratio of the measured radiances to the part of the blackbody radiance in the same conditions of temperature and wavelength according to the formula:

$$\varepsilon' = \frac{L'_{0.6-40}}{L_{0.6-40}} \quad (1)$$

with ϵ' the directional emissivity, L' the material radiance, L_0 the blackbody radiance and in subscripts the wavelength ranges expressed in μm . The hemispherical emissivity is then calculated by integration of the directional values acquired from normal direction 0° up to 80° .

All the measurements were performed using the MEDIASE (Moyen d'Essai et de Diagnostic en Ambiance Spatiale Extrême) facility, developed in collaboration with CNES, detailed in previous papers [16-18] and briefly described here taking into account the specific configuration for emissivity measurements. The set-up is placed at the focus of the 1MW solar furnace (fig. 1). A hemispherical quartz window, placed in front of the chamber, allows the heating of the sample with concentrated solar radiation. For these experiments, the pressure was fixed at 200 Pa air using vacuum pumps. The temperature of the material is measured using a pyro-reflectometer, equipped with an optical fiber and developed at PROMES-CNRS laboratory [19, 20]. The radiance measurements are performed using a Heimann KT4 bolometer equipped with Cassegrain optics through a window. The window quality is adapted to the wavelength range and for these measurements the window used is made of thallium iodobromide (KRS 5) in order to perform measurements from 0.6 to 40 μm . The measurements are performed using a specific three-mirrors goniometer developed at PROMES-CNRS laboratory in order to cover the whole angular range from normal incidence to 80° incidence, without moving nor the radiometer nor the sample. The whole system (radiometer + optical window + three-mirrors goniometer, and the pyro-reflectometer) is calibrated before and after each measurement series on a blackbody. Depending on the wavelength range of interest, the radiometer can be used without filter (0.6-40 μm), with narrow spectral filters (2.7; 5; 5.5 μm) or with band-pass filters (0.6-2.8; 7-10; 8-14 μm).

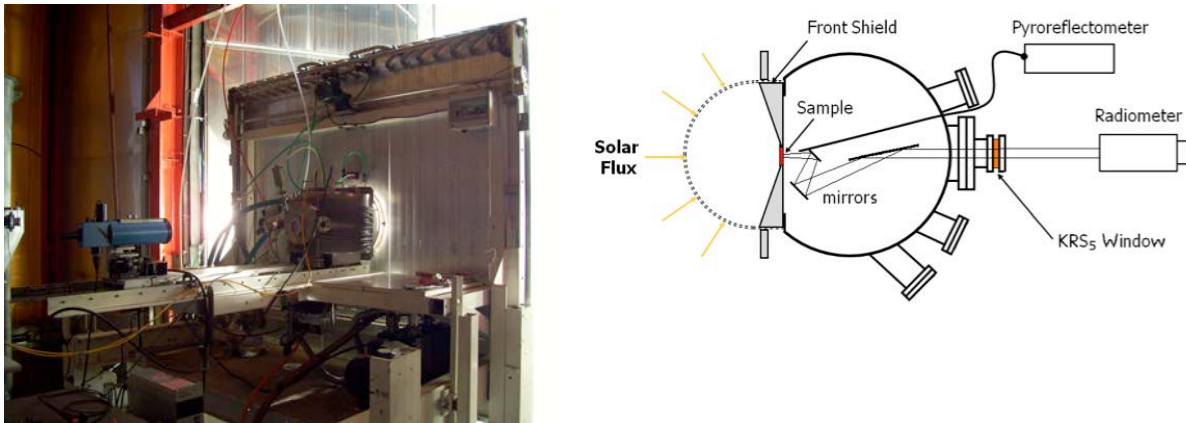


Figure 1. Picture and scheme of the experimental set-up MEDIASE at the focus of the 1 MW solar furnace for the measurement of thermal radiative properties

Experimental results obtained for the materials ZS and ZZ are reported in fig. 2 and compared with previous results obtained on $\text{ZrB}_2\text{-SiC-MoSi}_2$ [21, 22]. Looking at the results, it appears that the sample containing Si_3N_4 (red diamonds) presents a higher emissivity all along the temperature range, with value around 0.75 at 1200 K up to 0.90 at 1750 K. Emissivity were not measured at higher temperature than 1800 K due to the volatile oxides formed during measurement at 200 Pa air that leads to the dirtiness of the optical fiber used for temperature measurement.

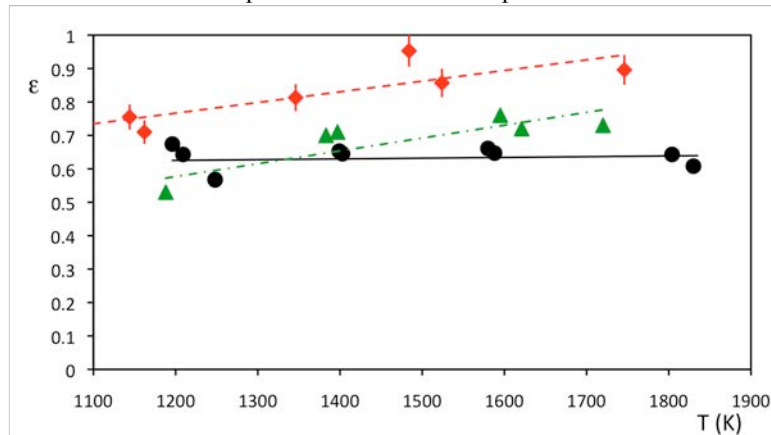


Figure 2. Total hemispherical emissivity of ZS (red diamonds), ZZ (black dots) and $\text{ZrB}_2\text{-SiC-MoSi}_2$ (green triangles) samples versus temperature at 200 Pa total air pressure (standard air)

RECOMBINATION COEFFICIENT OF ATOMIC OXYGEN

The actinometry technique is used to follow the relative atomic oxygen concentration profile along the discharge. A low and known quantity of argon is introduced in the flow and the evolution of the intensities ratio I_{O}/I_{Ar} of an oxygen line to an argon line is measured along the discharge zone. To determine the spatial variation of the relative concentration of atomic oxygen, we use its most reliable transition at 844.6 nm. For the actinometer line, we choose the argon transition at 842.4 nm that presents a similar energy threshold (13.1 eV) than for the atomic oxygen transition (11 eV). Thus, it is reasonable to assume that the ratio of the intensities of the two lines is proportional to the oxygen atom concentration. Moreover, the lines 842.4 and 844.6 nm can be recorded simultaneously that increasing the accuracy of the intensities ratio measurements. We have chosen to work at a constant microwave power of 300 W, a total air pressure of 200 Pa and a total flow of $10^{-6} \text{ m}^3 \text{ s}^{-1}$ with 5 % argon. Recently, we have used fiber-optics catalytic probe to measure the absolute density of neutral oxygen atoms in our reactor in collaboration with Vesel from the Jozef Stefan Institute (Ljubljana, Slovenia). The degree of the dissociation of oxygen molecules in our 2450 MHz air plasma is around 80% for the above conditions of flow rate [23].

A cylindrical volume corresponding to the discharge zone is considered, every point being represented by the coordinates (r, x) . As the mean free path of the atoms (0.043 cm at 200 Pa) is less than the diameter of the reactor (5 cm), the atom diffusion is given by the diffusion equation written in cylindrical coordinates that describes the variation of the concentration C_O of an oxygen atom O versus time for a fixed point in the cylinder (r, x) . In steady state conditions, the equation is reduced to:

$$D \cdot \left(\frac{\partial^2 C_O}{\partial x^2} + \frac{\partial^2 C_O}{\partial r^2} + \frac{1}{r} \frac{\partial C_O}{\partial r} \right) + \omega = 0 \quad (2)$$

with ω the variation of the concentration due to the recombination in the gaseous phase and on the reactor walls.

We suppose that the convective transfer is negligible. The radial gradient in the reactor is negligible compared to the axial one, so the concentration is only function of x . Moreover, the stability of the ratio I_O/I_{Ar} in the reactor allows neglecting the recombination in volume and on the reactor wall. Thus, equation (2) can be simplified in:

$$D \cdot \frac{\partial^2 C_O}{\partial x^2} = 0 \quad (3)$$

This equation has two limit conditions:

- the ratio I_O/I_{Ar} is constant along the discharge, thus, far from the sample, the concentration has a known fixed value: $C_O(x = L) = \text{constant}$
- at the surface sample ($x = 0$), the mass balance in oxygen atoms is established by the equality between the oxygen arriving at the surface by diffusion and the atomic oxygen recombined at the surface:

$$-D_{O, \text{air}} \cdot \frac{\partial C_O}{\partial x} \Big|_{x=0} - C_O(x=0) \cdot \frac{\gamma \cdot V}{4} = 0 \quad (4)$$

with V the mean square velocity of oxygen atoms.

The evolution of the atomic oxygen concentration is given by the solution of equation (3). Finally, the intensities ratio obtained by actinometry leads to the determination of the recombination coefficient γ by the following equation:

$$\gamma = \left(\frac{\frac{I_O}{I_{Ar}} \Big|_{x=L} \cdot \frac{T_S}{T_L} - 1}{\frac{I_O}{I_{Ar}} \Big|_{x=0}} \right) \cdot \frac{4 \cdot D_{O, \text{air}}}{V \cdot L} \quad (5)$$

with I_O/I_{Ar} the ratio of the intensities respectively at the entrance of the reactor ($x = L$) and at the surface sample ($x = 0$), $D_{O, \text{air}}$ the binary diffusion coefficient of atomic oxygen in air, V the mean square atomic velocity and L the thickness of the recombination boundary layer.

The experimental measurement of the recombination coefficient was carried out on several samples from 1000 K to 2250 K for ZS and ZZ materials. The pictures of the samples are shown in fig. 3 with the maximum temperature reached and the results of the recombination coefficient are presented in fig. 4.

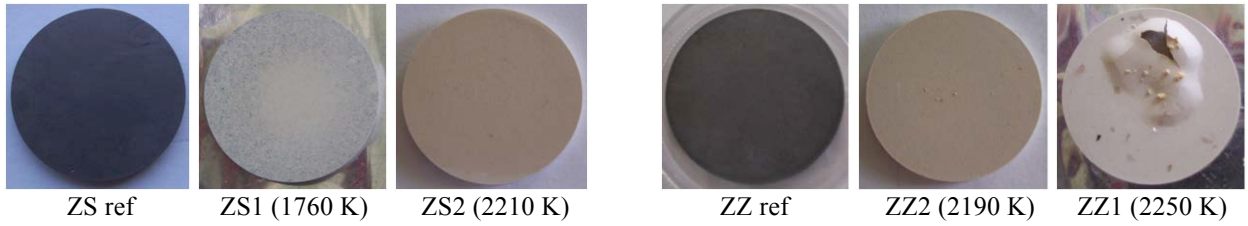


Figure 3. Pictures of the samples tested with the maximum temperature reached during the measurement of the recombination coefficient of atomic oxygen

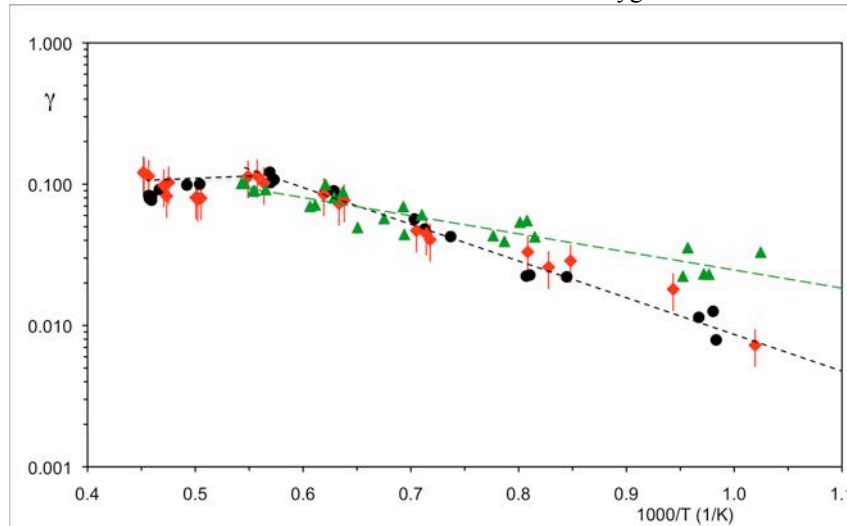


Figure 4. Recombination coefficient of atomic oxygen on ZS (red diamonds), ZZ (black dots) and $ZrB_2-SiC-MoSi_2$ (green triangles) samples versus reciprocal temperature.

The recombination coefficient is increasing following an Arrhenius fit with temperature for both the samples ZS and ZZ up to 1820 K and is lower than the one previously measured on samples containing $MoSi_2$. This coefficient is then constant and equal to 0.1 at higher temperatures up to 2250 K when the surfaces are mainly composed of zirconia. The values of the recombination coefficient are close for the materials with the two different sintering aids Si_3N_4 or $ZrSi_2$ (ZS2 and ZZ2) and from 1000 K to 1820 K, the law of the evolution of the recombination coefficient is $\gamma = 2.359 \exp(-5412/T)$ with $R^2 = 0.98$. If the emissivity parameter is taken into account in order to choose the best material, then the ZS material seems more interesting than the ZZ one due to its higher emissivity in the whole temperature range. Due to the bubbles formation on ZZ1 that was quickly heated up to 2250 K, the results obtained from 1820 K to 2250 K were not taken into account.

MICROSTRUCTURAL CHARACTERIZATION BY SEM AND XPS

The sections and surfaces of all specimens were examined by Scanning Electron Microscopy (SEM). Microscopy images were obtained by using a FeiCo Philips-Electroscan FEG XL-30 Environmental Scanning Electron Microscope (ESEM) and operating in conventional SEM mode. Each SEM observation was carried out without any surface deposition process.

Morphologies of ZS and ZZ before and after catalycity and emissivity tests are shown in figs. 5, 6 and 7 respectively. The surfaces of tested samples appear severely damaged with the formation of many microcracks and holes that were principally due to loss of surface SiC chopped fibers. Oxidation processes, which become active during catalycity measurements, modify the chemical composition of sample surface causing, probably, the reduction of adhesion between SiC fibers and ceramic matrix. The opening of cracks and holes can help in diffusion of gaseous oxidant species (molecular and atomic oxygen) toward the interior of ceramic matrix. In any case, as confirmed by the micrographs in figs. 5 and 6, the sample surface appeared covered by a vitreous layer that is particularly concentrated in the holes and fractures left empty by SiC fibers. XRD analysis has confirmed that the external layer is characterized by crystalline zirconia and boria and moreover presented a fraction of amorphous phase probably based on silica (borosilicate) for the samples tested up to 1800 K only. Thickness of the oxidized external layer estimated by SEM analysis is about 50-65 μm . After emissivity measurement, the surfaces of ZS and ZZ samples are mainly composed of zirconia as confirmed by XRD and XPS analyses.

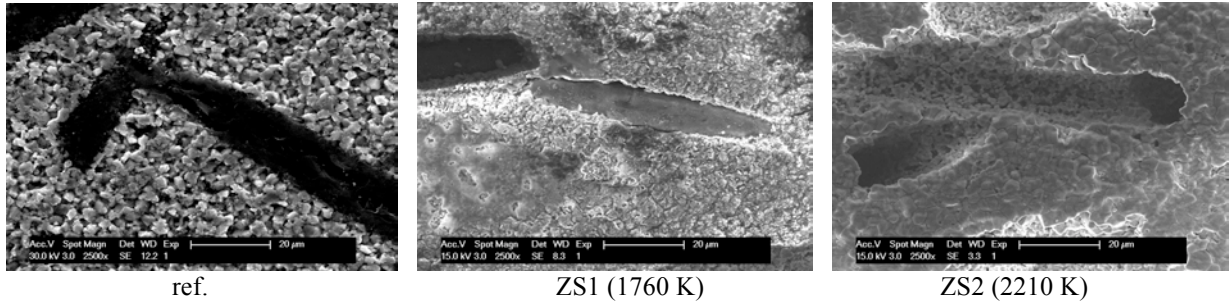


Figure 5. SEM images of the ZS samples before (ref) and after catalycity measurement at 1760 K and 2210 K

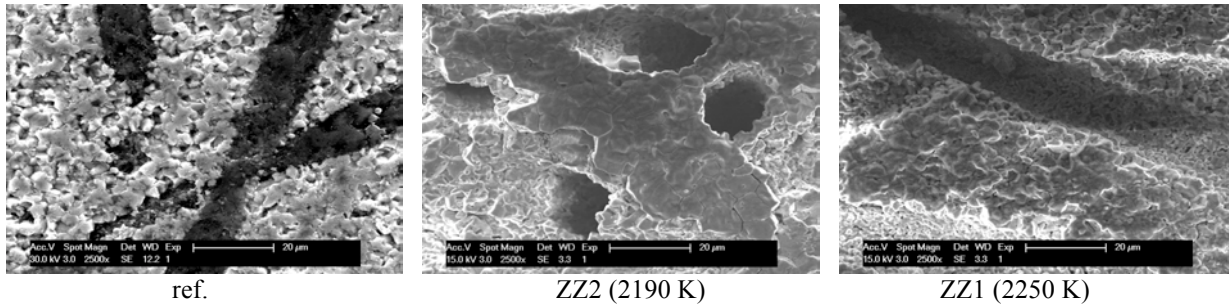


Figure 6. SEM images of the ZZ samples before (ref) and after catalycity measurement at 2190 K and 2250 K

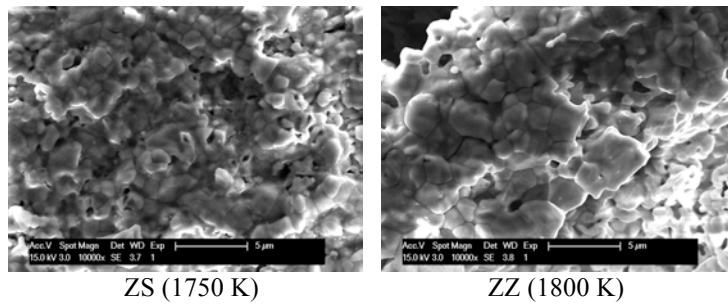


Figure 7. SEM images of the ZS and ZZ samples after emissivity measurement at around 1800 K

XPS analysis was performed using a Thermoelectron ESCALAB 250 device. The photoelectron emission spectra were recorded using Al-K α radiation ($h\nu=1486.6$ eV) from a monochromatized source. XPS analyses were performed in order to deeper qualify the surface chemistry of the ZS and ZZ samples after catalycity (fig. 8) and emissivity measurements (fig. 9). The surfaces of the ZS1 and ZS2 samples after catalycity evaluation (fig. 8) are characteristic of oxidized compounds: higher the temperature, lower the amount of SiO₂ and higher the amount of ZrO₂. For the ZS1 surface, the amount of silica is 71%, the difference being zirconia (29%); for the ZS2 sample, the composition is opposite: 94% zirconia and 6% silica. This is clearly visible on the Zr 3d and O 1s photoelectron peaks: the Zr 3d^{5/2} and Zr 3d^{3/2} peaks located at 182.6 and 185.0 \pm 0.1 eV are characteristic of O-Zr bonds in oxide compounds and the O 1s spectra were mainly deconvoluted into 2 components, the one located at 530.4 \pm 0.1 eV being attributed to O-Zr bonds and the one at (532.4 \pm 0.1 eV) attributed to Si-O bonds.

Under two different gas conditions (air plasma or standard air) and the same heating temperature (about 1750 K), the surface composition is very different; the amount of silica measured for the ZS1 surface (fig. 8 upper) is higher than for the ZS surface after emissivity measurement (fig.9) where zirconia is the main species (93%). The ZZ sample surface after emissivity evaluation is only composed of 100% zirconia.

CONCLUSION

Thermal radiative properties and catalycity measurement were performed on two UHTC materials based upon ZrB₂-SiC fibers differing by their sintering aids Si₃N₄ or ZrSi₂, and compared to previous results obtained on the one with MoSi₂ aid, and have shown surface modifications after high temperature air plasma exposure relative to the maximum temperature reached. For temperatures lower than 1820 K, mainly borosilicate and few zirconia were present on the surface of the tested materials. When higher temperatures were reached, up to 2250 K, only zirconia was detected on

the surface due to the high volatilization rate of silica and boria. Finally, these samples present a low catalytic activity, about 0.01, when a borosilicate glassy layer with some zirconia was formed on the surface up to 1820 K. When zirconia is present in higher concentration, the recombination coefficient increases by one order of magnitude up to about 0.1 and it is constant up to 2250 K.

The evolution of the total hemispherical emissivity with temperature was nearly constant and equal to 0.65 for the ZZ material and goes from 0.72 at 1100 K to 0.90 at 1750 K for the ZS material.

This study highlighted the extreme complexity of UHTC oxidation behavior, as well as the need of an exhaustive knowledge of the phenomena regulating surface oxidation in order to explain the surface properties of this class of materials.

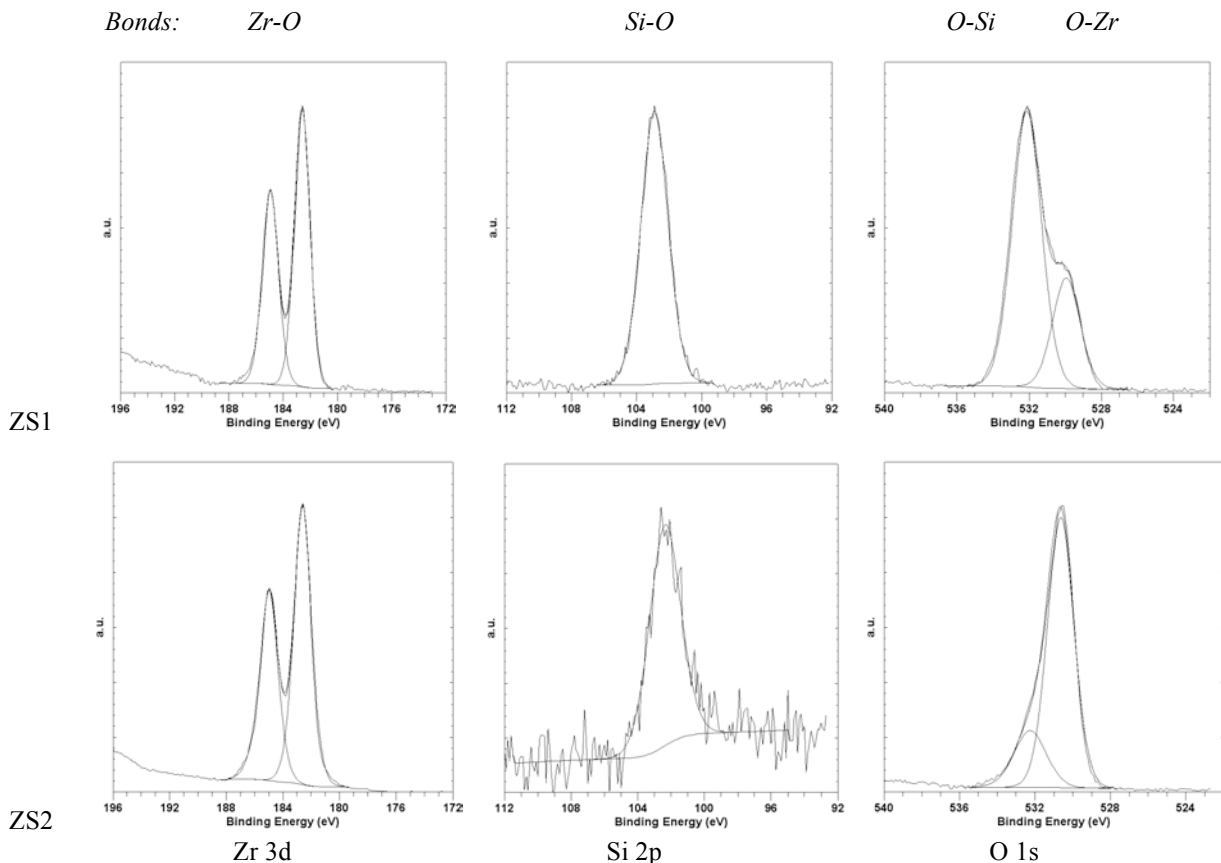


Figure 8. XPS photoelectron peaks of the ZS samples after catalicity measurement at 1760 K (ZS1, upper spectra) and 2210 K (ZS2, lower spectra)

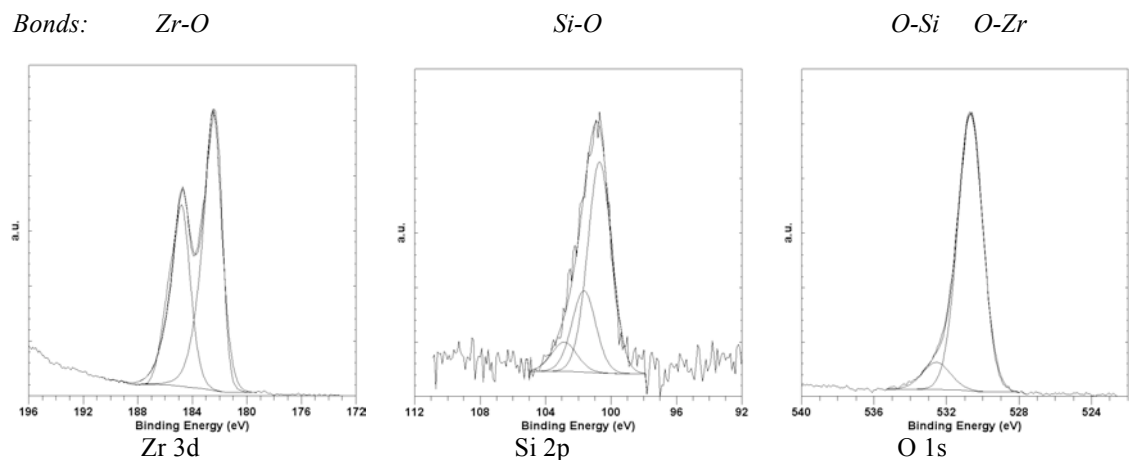


Figure 9. XPS photoelectron peaks Zr 3d, Si 2p and O 1s for the ZS sample after emissivity measurement at 1750 K

REFERENCES

- [1] Schneider S.J., *Engineered Materials Handbook: Ceramics and Glasses, Vol. 4*, ASM International, 0-87170-282-7, Ohio.
- [2] Mroz C., Zirconium diboride, *Amer. Ceram. Soc. Bull.*, 73(6), 1994, 141-142.
- [3] Fahrenholtz, G., Hilmas, G.E., Talmy, I.G., Zaykoski, J.A., Refractory diborides of zirconium and hafnium, *J. Amer. Ceram. Soc.*, 90(5), 2007, 1347-1364.
- [4] Tripp W.C., Davis H.H., Graham H.C., Effect of SiC addition on the oxidation of ZrB₂, *Amer. Ceram. Soc. Bull.*, 52(8), 1973, 612-616.
- [5] Monteverde F., Guicciardi S., Bellosi A., Advances in microstructure and mechanical properties of zirconium diboride based ceramics, *Mater. Sci. Engin.*, 346(1-2), 2003, 310-319.
- [6] Chamberlain A., Fahrenholtz W., Hilmas G., High-strength zirconium diboride-based ceramics, *J. Amer. Ceram. Soc.*, 87(6), 2004, 1170-1172.
- [7] Monteverde F., Beneficial effects of an ultra-fine α -SiC incorporation on the sinterability and mechanical properties of ZrB₂, *Appl. Phys. A: Mater. Sci. Process.*, 82(2), 2006, 329-337.
- [8] Rasky D.J., Salute J., Kolodziej P., Bull J., The NASA Sharp Flight Experiment, *Proceed. 3rd Europ. Workshop on Thermal Protection Systems*, Noordwijk, The Netherlands, 25-27 March 1998, ESA-ESTEC, WPP-141, 1998.
- [9] Russo G., Marino G., The USV Program & UHTC development, *Proceed. 4th Europ. Workshop on Thermal Protection Systems for Space Vehicles*, pp. 157-163, Palermo, Italy, 26-29 November 2002, ESA, Paris.
- [10] Scatteia L., Del Vecchio A., De Filippis F., Marino G., Savino R., PRORA-USV SHS: Development of sharp hot structures based on ultra high temperature metal diborides current status, *Proceed. 56th Int. Astronaut. Congress*, Fukuoka, Japan, 17-21 Nov. 2005, IAC-05-C2.3.05, Curran Associates Inc, Ohio.
- [11] Scatteia L., Alfano D., Cantoni S., Monteverde F., De Stefano Fumo M., Di Maso A., Plasma Torch Test of an Ultra-High-Temperature Ceramics Nose Cone Demonstrator, *J. Spacecraft & Rockets*, 47(2), 2010, 271-279.
- [12] Chen D., Xu L., Zhang X., Ma B., Hu P., Preparation of ZrB₂ based hybrid composites reinforced with SiC whiskers and SiC particles by hot-pressing, *J. Refract. Metals Hard Mater.*, 27(4), 2009, 792-795.
- [13] Guicciardi S., Silvestroni L., Nygren M., Sciti D., Microstructure and toughening mechanisms in spark plasma-sintered ZrB₂ ceramic reinforced by SiC whiskers or SiC chopped fibers, *J. Amer. Ceram. Soc.*, 93(8), 2010, 2384-2391.
- [14] Silvestroni L., Sciti D., Melandri C., Guicciardi S., Toughened ZrB₂-based ceramics through SiC whisker or SiC chopped fiber additions, *J. Europ. Ceram. Soc.*, 30(11), 2010, 2155-2164.
- [15] Sciti D., Guicciardi S., Silvestroni L., SiC chopped fibers reinforced ZrB₂: effect of the sintering aid, *Scripta Materialia*, 64, 2011, 769-772.
- [16] Balat-Pichelin M., Robert J.F., Sans J.L., Emissivity measurements on carbon-carbon composites at high temperature under high vacuum, *Appl. Surf. Sci.*, 253(2), 2006, 778-783.
- [17] Balat-Pichelin M., Eck J., Sans J.L., Thermal radiative properties of carbon materials under high temperature and vacuum ultra-violet (VUV) radiation for the heat shield of the Solar Probe Plus mission, *Appl. Surf. Sci.*, 258, 2012, 2829-2835.
- [18] Eck J., Sans J.L., Balat-Pichelin M., Experimental study of carbon materials behavior under high temperature and VUV radiation: application to Solar Probe+ heat shield, *Appl. Surf. Sci.*, 257(8), 2011, 3196-3204.
- [19] Hernandez D., A concept to determine the true temperature of opaque materials using a tricolor pyroreflectometer, *Rev. Scientific Instruments* 76, 2005, 024904-1- 024904-7.
- [20] Hernandez D., Sans J.L., Netchaieff A., Ridoux P., Le Sant V., Experimental validation of a pyroreflectometric method to determine the true temperature on opaque surface without hampering reflections, *Measurement* 42 (2009) 836-843.
- [21] Scatteia L., Alfano D., Monteverde F., Sans J.L., Balat-Pichelin M., Effect of the machining method on the catalycity and emissivity of ZrB₂ and ZrB₂-HfB₂-based ceramics, *J. Amer. Ceram. Soc.*, 91(5), 2008, 1461-1468.
- [22] Alfano D., Scatteia L., Monteverde F., Bêche E., Balat-Pichelin M., Microstructural characterization of ZrB₂-SiC based UHTC tested in the MESOX plasma facility, *J. Europ. Ceram. Soc.*, 30(11), 2010, 2345-2355.
- [23] Balat-Pichelin M., Vesel A., Neutral oxygen atom density in the MESOX air plasma solar furnace facility, *Chem. Phys.*, 327(1), 2006, 112-118.

**EPOSIL® high performance structural composite
TOUGH CERAM® high temperature structural composite**

7th European Workshop on Thermal Protection Systems and Hot Structures

8-10 April 2013

ESA/ESTEC, Noordwijk, The Netherlands

Author Dr Max SARDOU⁽¹⁾, Co-Author Mad. Patricia SARDOU⁽¹⁾,
Mad. Arantxa MARTINY⁽¹⁾, Mr Kais RIANIS⁽¹⁾,
Affiliation ⁽¹⁾ **SARDOU SA**
Address 18 rue du Sauvoy 77165
SOUPPLETS France
Email: info@sardou.net

SARDOU SA has developed highly stressed composites for 31 years. For intense, for three dimensional shear loading fatigue, we have had to concentrate our research on epoxy matrix in order to improve their life expectancy.

- **This work has led us to develop a unique matrix which is a compound of organic epoxy and “mineral micro-reinforcing fasteners epoxy” called EPOSIL®. Thanks to EPOSIL® it is now possible to produce damage tolerant structures and to improve by ten times their life expectancy.**
- **This concept has led us to develop a tough matrix for high temperature applications which is a compound of ceramic matrix and “mineral micro reinforcing fasteners” called TOUGH CERAM®**

NOMENCLATURE

UD =	unidirectional
US =	ultrasound
PREPREG =	pre impregnated yarn
RTM =	resin transfer molding
BMC =	bulk molding compound
OEM =	original equipment manufacturer = car manufacturer
TPS =	thermal protection system
LDN =	low density network
HDN =	high density network

I. INTRODUCTION

SARDOU SA is involved since 1980 in ground transportation development. Now the overall situation is to improve materials mechanical performances, to save weight, to increase available working temperature domain well beyond metal capacity.

On Cars:

A lot of OEM are now planning to reduce weight of their vehicles up to 350 kg by using carbon fibers and epoxy composite.

The target is to save:

- 1.2 litter/100 km of fuel consumption ,
- 3 g of CO₂/km.

On Railways, and especially in subway:

The weight of the structure cost a lot of energy and damage track.

On aeronautic:

The weight of the structure is a recurrent operational cost and performance problem, so now, for instance, helicopter Tiger is at 80% of composite, and aircrafts are reaching 53%, Boeing 787, Airbus 350.

On astronautic:

The weight and , now, cost of the structure are the main drivers, so, new VEGA and future ARIANE VI will use composite solid thruster elements.

Ground transportation Strategy:

In order to save weight a lot of car manufacturers are considering replacing metal by a composite carbon fibers epoxy.

Replacing metal by a composite is a smart solution:

- Offering the capacity to address all metal parts on a car and for instance to split by two the weight of expensive aluminum forged suspension components.
- Offering the capacity to produce light high pressure vessels for hydrogen and NGV storage tanks.

Drawback:

But classic epoxies are not tough enough:

- When a lot of shear stress are applied to composite, especially in springs and suspension systems.
- When the part are exposed to road stoning with high energy.

Solutions:

EPOSIL®:

- Is a compound of classic organic epoxy and of mineral epoxy.
- Is REACH compliant.
- Can be put in practice using all techniques of standard composite manufacturing.
- Can be reinforced with all kind of fibers, like glass, carbon and silica.
- Polymerization is exactly the same way than pure epoxy resin.
- Can be used between “minus 40 and plus 250 °C”.

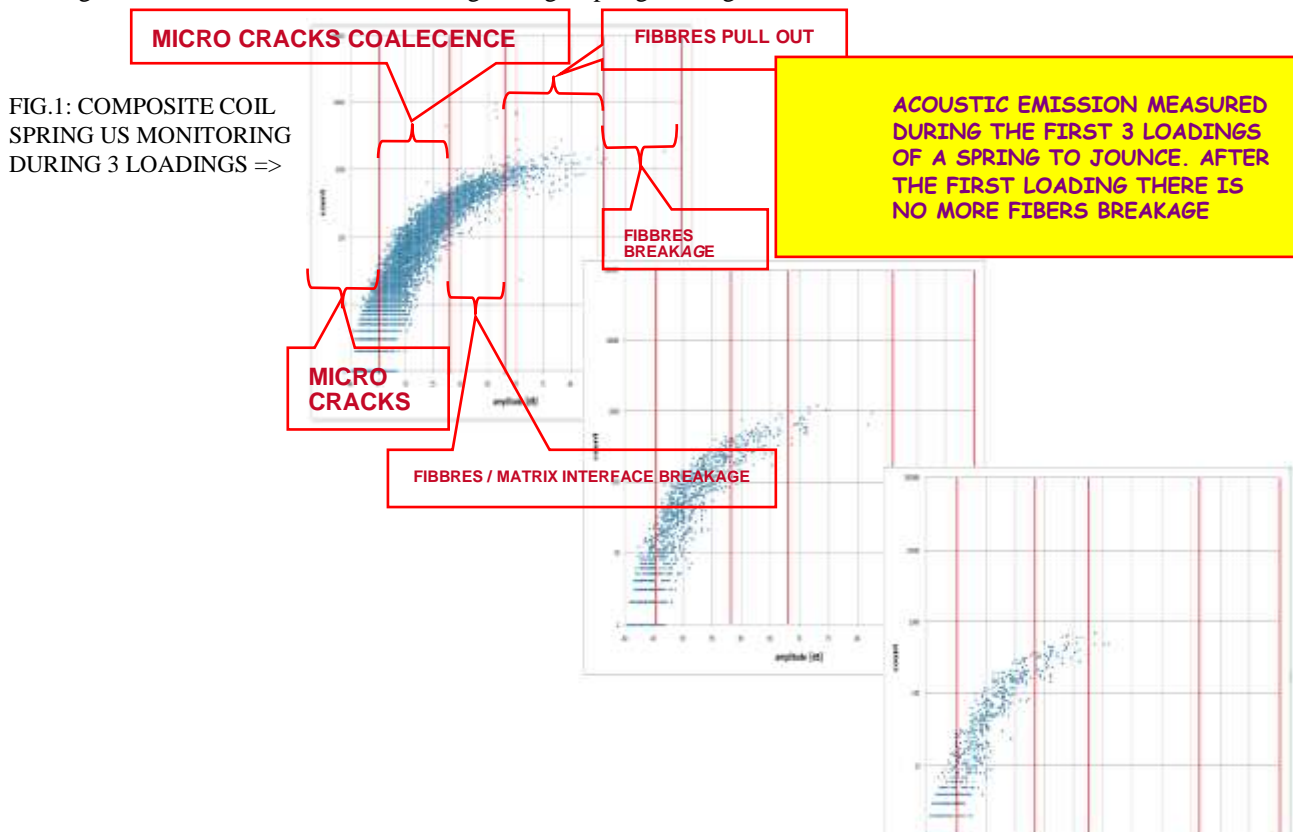
TOUHCERAM®:

- Is not derived from the carbon chemistry.
- Its chemical components are easily available elsewhere in Europe.
- Cost is very low compared to all known thermoset & thermoplastic matrix.
- Is fully recyclable, is REACH compliant, it does not burn and do not smoke.
- Is compatible with all techniques of composite manufacturing like PREPREG, RTM, BMC....
- Can be reinforced with all kind of fibbers like, glass, carbon and silica.
- Its polymerization uses much less energy than epoxy resin.
- Offer a density of 1.45 and mechanical properties equivalent to epoxy matrix.
- Can be used between “**minus100 and +1400°C**” (**plus ABLATIVE regime**) for ROCKET NOZZLE & TPS.

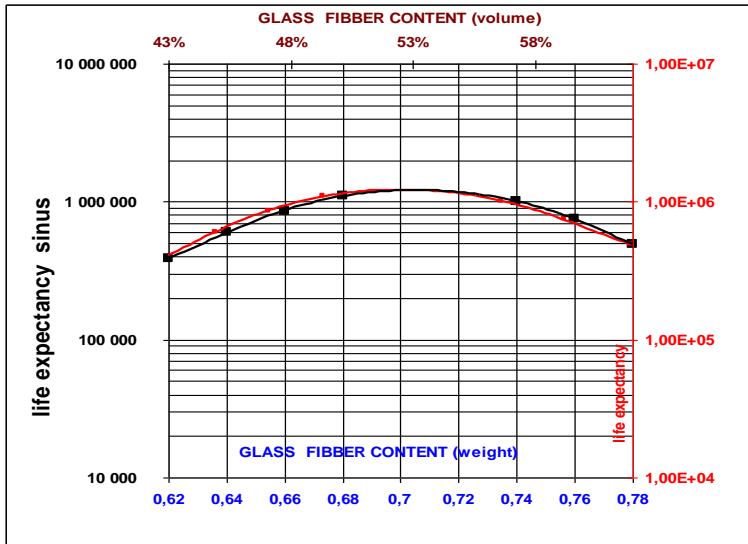
II. DEVELOPMENT MOTIVATIONS OF EPOSIL®

During the development of composite coils springs, we have observed a rapid degradation of the matrix in the interface between two plies of UD fibers. Under load the degradation mechanism was the apparition of micro cracks .Then, under fatigue, propagation and merging of the micro-cracks. So, after a certain number of cycles, the matrix was transformed in powder and ruined the structure.

The Fig. 1 shows this mechanism, occurring during a spring loading.



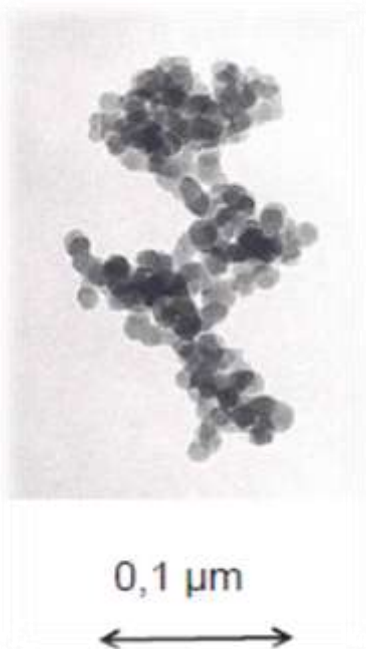
State of the art is to add “little loading particles” in order to reinforce a matrix. But the Fig. 2 shows that the composite life expectancy, versus composite loading, has an optimum for 50 % in volume of loading particles. As can be seen in Fig. 2 it is clear that if we wish high macro mechanical performances, of the structure, we have to use all available loading in the form of “UD” working fibers. So, if we want to reinforce the matrix, we have to find a solution which is not a “classic loading”!



<=FIG.2: COMPOSITE FATIGUE POTENTIAL VERSUS “UD” LOADING

III. DEVELOPMENT OF EPOSIL®

After evaluation a lot of potential loading candidate, we have selected a dendritic silica micro particle. This silica is the aggregate, by covalent bonding, of a lot of silica nano-pearls of around 0.020 µm diameter. The typical aggregate length is around 0.200 µm to 1 µm Fig.3 shows the “staple morphology” of the selected silica aggregate. We have developed a solution in order to transform the silica in an “epoxy with silica aggregate structure”. Using a patented process, we apply, on the silica aggregate, a perfectly controlled monomolecular surfactant layer offering epoxy function on the outer surface of the silica. On a single “silica aggregate epoxy” we can gang up to 100 000 epoxy functions. This big number, of epoxy functions, gives a high density crosslinking and a huge reinforcing potential of “silica epoxy” with the organic network. The young modulus of the silica, being 30 times the one of the organic epoxy, act as a matrix reinforcing and crack retarding agent.



<= FIG. 3: MICRO-REINFORCING STAPLE CONCEPT

Fig.4 show the micro-cracks blocking mechanism; “silica aggregate epoxy” act as a micro reinforcing staple!
 So,as illustrated, in Fig. 6, we end up with a three stage composite structure arrangement made of an organic matrix containing fonctionalized micro-reinforcing particles and macro reinforcing structure , like yarn or UD fibers .

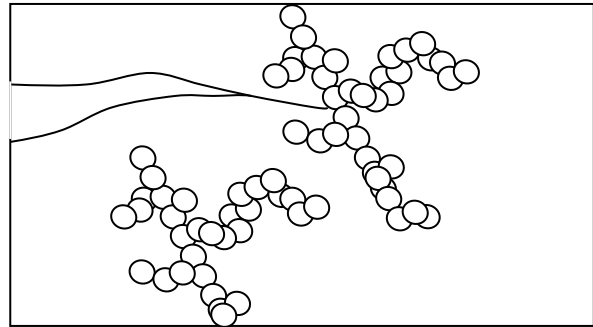


FIG. 4: MICRO-REINFORCING STAPLE
 BLOCKING MECHANISM =>

We can disperse in any organic resin our “silica aggregate epoxy”, in order to achieve any concentration that we need, aiming to match a targeted performance. The organic resin can be any kind of structural one, epoxy bisphénol A, epoxy bisphénol F, epoxy novolac, Cyanate esters etc.

IV. EPOSIL® TYPICAL PROPERTIES & TYPICAL APPLICATIONS

Dispersed in low cost DGEBA @ 9%, in weight proportion, compared to standard DGEBA we get:

- A shear improvement of: 23% in stress & 6% in strain
- A Young modulus improvement of: 32%
- A thermal dilatation reduction of: 22%
- A fatigue life expectancy multiplied by: 10 times!

EPOSIL® gives toughness & damage tolerance to structural parts.

Thanks to EPOSIL®, it is possible to produce a lot of structural parts like:

- composite springs,
- wishbones,
- solid rocket structure,
- fans blades etc.

Thanks to EPOSIL®, it is also possible to block solid borne noise propagation using difference of refraction indices between pure epoxy matrix & EPOSIL® matrix, see FIG 5.

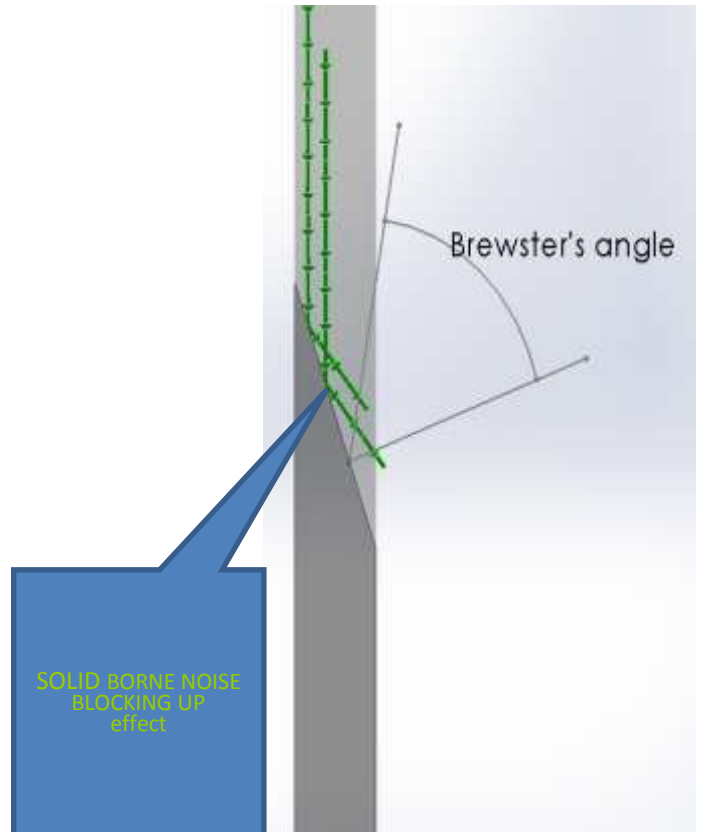


FIG. 5: SOLID BORNE NOISE BLOCKING CONCEPT =>

V. DEVELOPMENT MOTIVATIONS OF TOUGH CERAM®

During the development of, car weigh saving concept, it's appeared, due to EUROPEAN regulation that OEM must consider to have 85% of recyclable materials.

OEM has to reduce the weight of their vehicles and to improve the recyclability.

OEM considers using more and more thermoplastic. The drawbacks of thermoplastic are the cost the poor creep properties and the poor fire behavior.

Classic organic composites, in addition, are limited in temperature below 400 °C for the bests.

There are a lot of potential applications exceeding such temperature; in automotive, air craft and space applications.

Its appear, to us, at this point, that we have to search in another direction.

Ceramics are the way to go. The **huge drawback of ceramics is their brittleness.**

So it is an interesting, and full of applications, challenge to develop a tough ceramic.

VI. DEVELOPMENT OF TOUGH CERAM® LDN (low density network)

We have approached the TOUGH CERAM® LDN patented concept, with the same philosophy that what we have done successfully with EPOSIL®.

As illustrated, in FIG. 6, a three stage composite structure arrangement is applied .

This structure is made of a ceramic matrix containing functionalized micro-reinforcing particles and macro-reinforcing structure like yarn or UD fibers .

The ceramic matrix of TOUGH CERAM®, can be made of a lot of non-organic materials. The more handy to use is the Geopolymer. Geopolymer is a matrix which polymerize at only 60°C.

The functionalized micro-reinforcing particles can be made of a lot of materials. The more handy to use is the dendritic silica.

The functionalized macro-reinforcing structure can be made of a lot of materials. The more handy to use is the silica fiber. Note that, in order to help the comprehension of the all the below drawings, the dimensions of the real fibers have been reduced by 100 time, compared to the micro-reinforcing particles.

It is possible to get masive or foamed structure , as illustrated in FIG 7 . Interface, between foamed an masive structure, can be very progresive and strong.

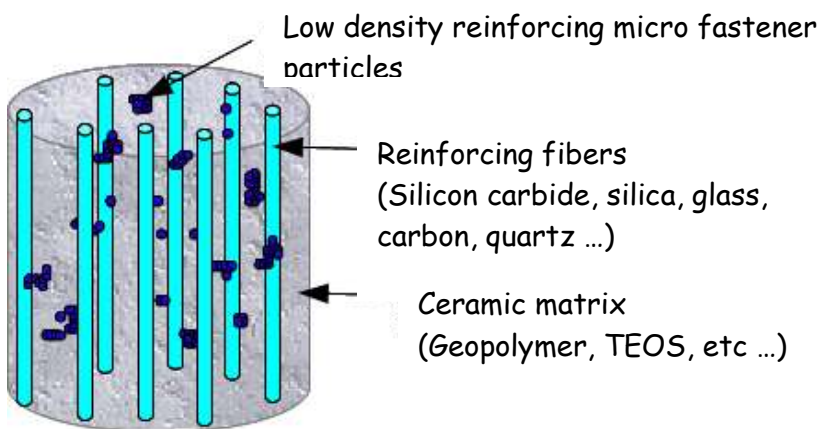


FIG. 6: THREE STAGE LDN COMPOSITE STRUCTURE CONCEPT

FIG. 7: PARTIALLY OR FULLY FOAMED STRUCTURE

VII. DEVELOPMENT OF TOUGH CERAM® HDN (high density network)

TOUGH CERAM® HDN patented concept, is using exactly the same kind of micro and macro reinforcing materials than the TOUGH CERAM® LDN, but then the matrix is now "just a binder" only used in order to keep in place the structure during a pressure less sintering.

Pressure less sintering is done at a reasonable 1 100°C with very little dimensional evolution.

We can use a lot of micro-reinforcing particles, best are the dendritic one, if we wish to get an ultra-low density structure.

We have evaluated Zirconium dioxide and Silicon dioxide for our applications, other materials could be considered. It is also possible to mix different materials together.

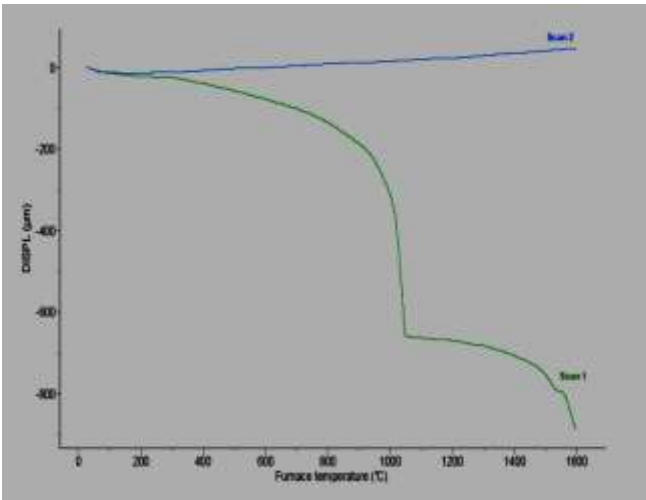
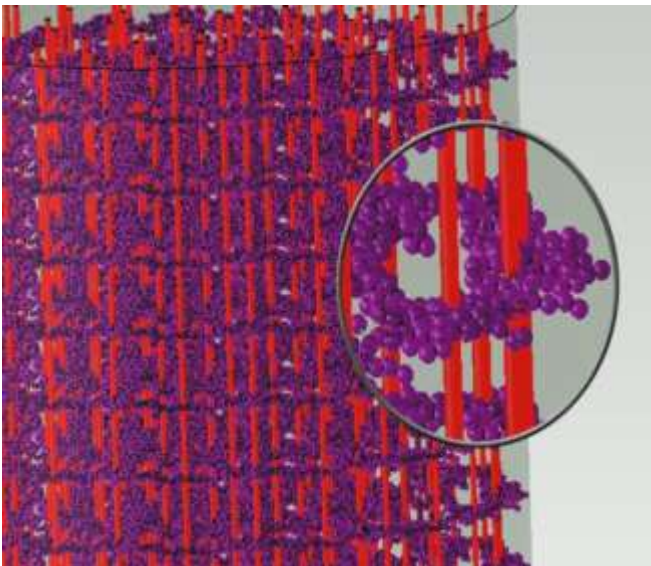


FIG. 8 shows the thermal dilatation measurement of the Silicon dioxide. We observe a pressure-less sintering occurring at 1 047°C during the first run (green curve) and the very linear dilatation, after sintering, during the second run (blue line). So, after sintering, we get a three dimensional ultra-high density and tough network of Nano-reinforcing structures.

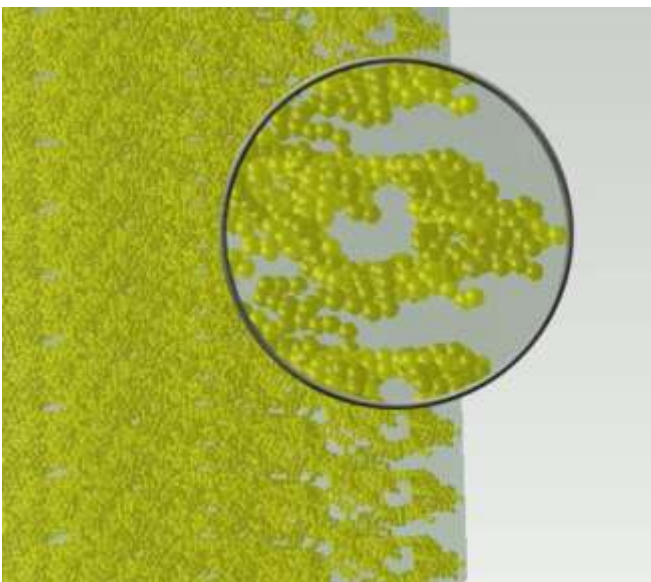
<= FIG. 8: SILICON DIOXIDE THERMAL DILATATION

FIG. 9 shows the HDN structure. As there is no more matrix we get a very low density and very low thermal conductivity material. Silica or SiC macro reinforcing structure help micro-reinforcing network in order to get high mechanical performances.



<= FIG. 9: THREE STAGE HDN COMPOSITE STRUCURE CONCEPT

FIG.10 show that we can also produce a TOUGH CERAM® HDN with only the micro-reinforcing particles and binder.



<= FIG. 10: TOW STAGE HDN COMPOSITE STRUCURE CONCEPT

VIII. TOUGH CERAM® TYPICAL PROPERTIES

At different scales ,we observe in FIG 11 that TOUGH CERAM® LDN looks exactly like the Geopolymer

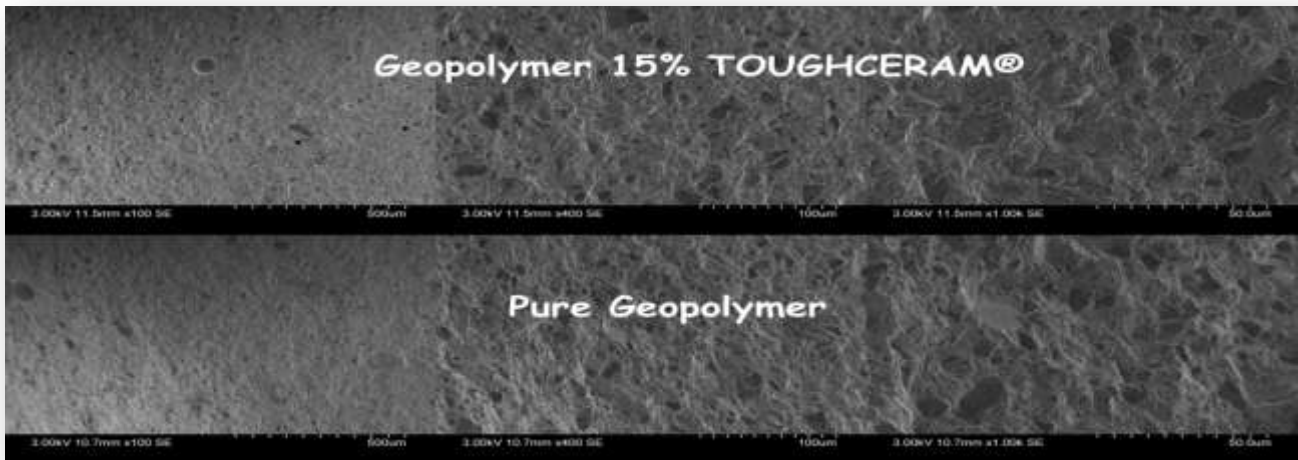


FIG 11 Geopolymer & TOUGH CERAM® LDN SEM pictures

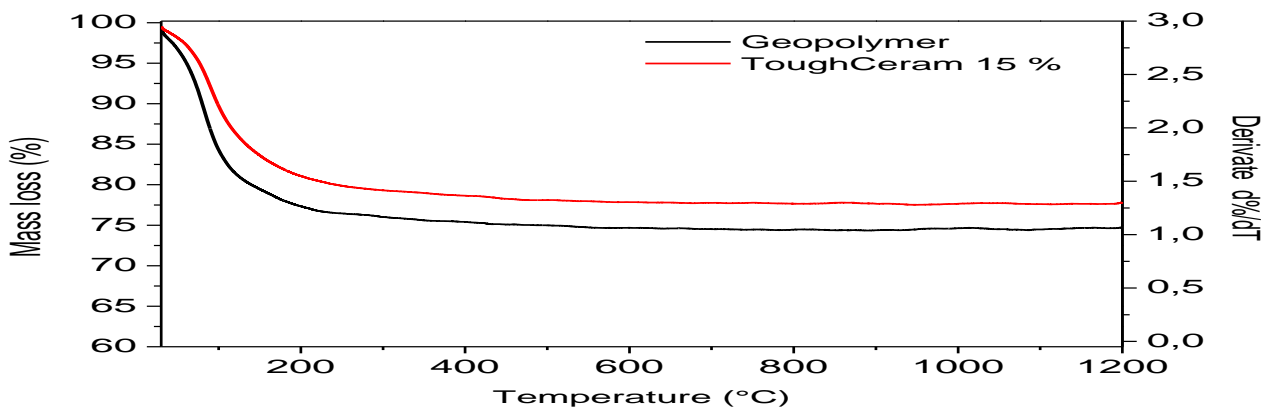


FIG 12 Geopolymer & TOUGH CERAM® LDN thermal stability

TOUGH CERAM® LDN density is 1.47 . Up to 1400°C TOUGH CERAM® LDN is stable .
The FIG 12 show that after expelling 20 % of water , TOUGH CERAM® LDN encounter no degradation .

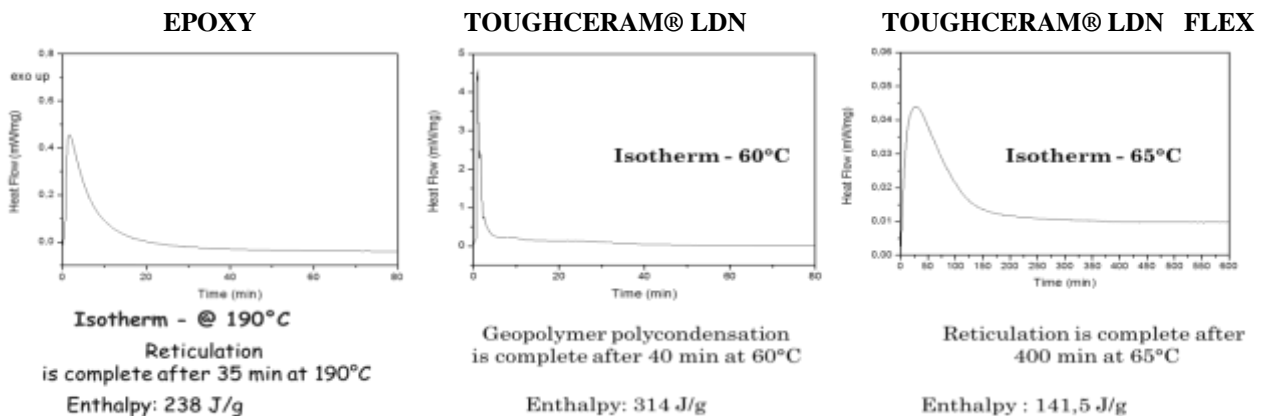


FIG. 13 = DSC comparizon: standard epoxy , TOUGH CERAM® LDN & FLEXIBLE TOUGH CERAM® LDN.

The FIG 13 clearly show that the polymerisation of epoxy resin compare well with TOUGH CERAM® LDN , we observe that TOUGH CERAM® LDN FLEX has 60 % of the enthalpy of the epoxy & only 45 % of the TOUGH CERAM® LDN .

TOUGH CERAM® LDN against geopolymer in infrared analysis is shown in FIG 14
 We observe that the Si-O-R (cm-1) pic move with TOUGH CERAM® concentration this is due to INTERCONNECTION BETWEEN SILICA AND GEOPOLYMER STRUCTURE

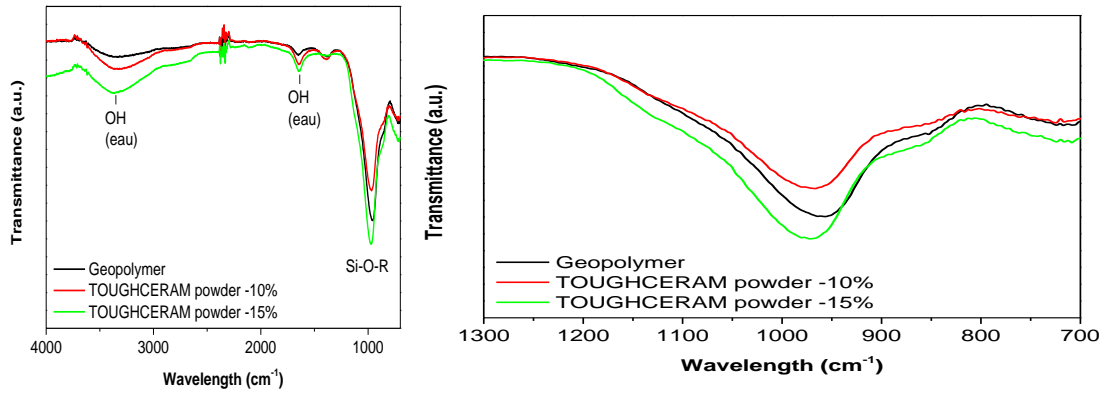


FIG. 14 INFRARED ANALYSIS

TOUGH CERAM® LDN against geopolymer in compression test we observe, FIG 15, a big reinforcing effect due to TOUGH CERAM® technology =

- TOUGH CERAM® ultimate stress improvement =166% compared to geopolymer
- TOUGH CERAM® ultimate strain improvement =133% compared to geopolymer
- TOUGH CERAM® Young modulus improvement =120% compared to geopolymer (FIG 16) we observe that TOUGH CERAM® Young modulus is also 120 % better than pure epoxy

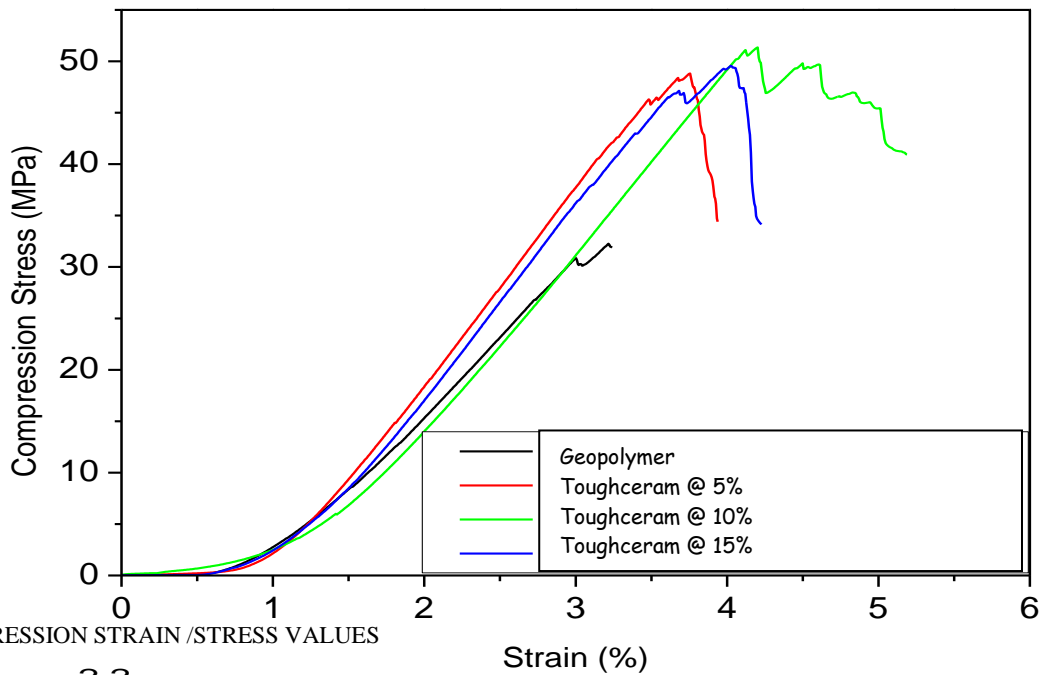


FIG. 15 COMPRESSION STRAIN /STRESS VALUES

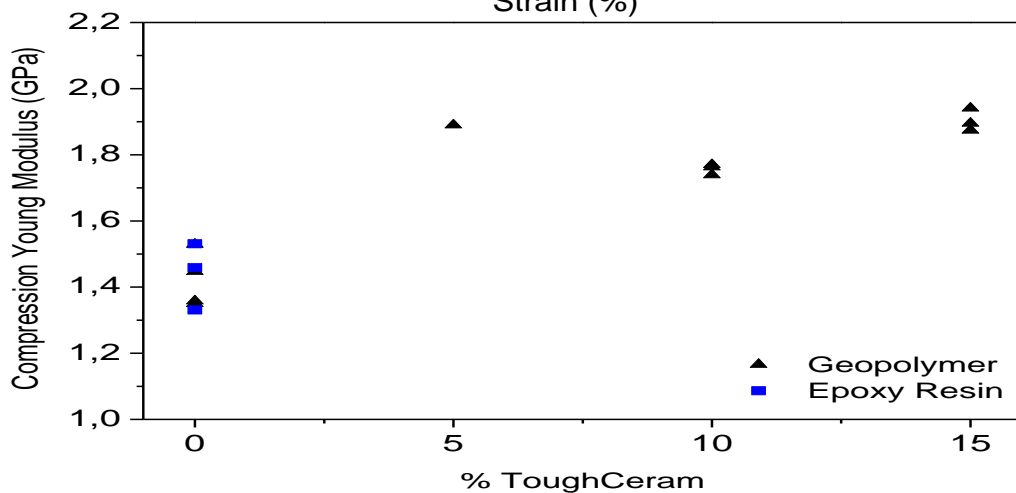


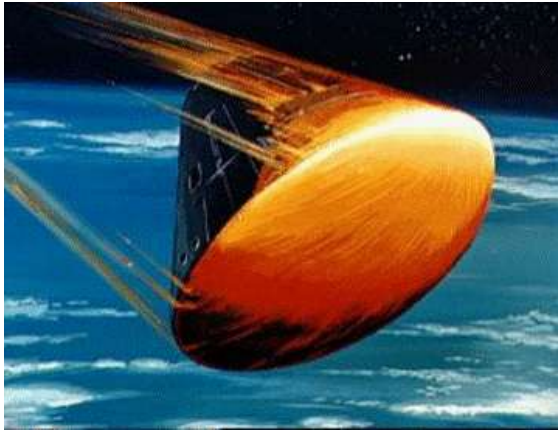
FIG. 16 COMPRESSION YOUNG MODULUS

FIG 17 FLEXUAL PROPERTIES OF FLEXIBLE TOUGH CERAM® LDN=>

FLEXIBLE TOUGH CERAM® LDN is no more brittle and can be bended as classic epoxy as illustrated in FIG 17.

IX . TOUGH CERAM® TYPICAL APPLICATIONS FIELD

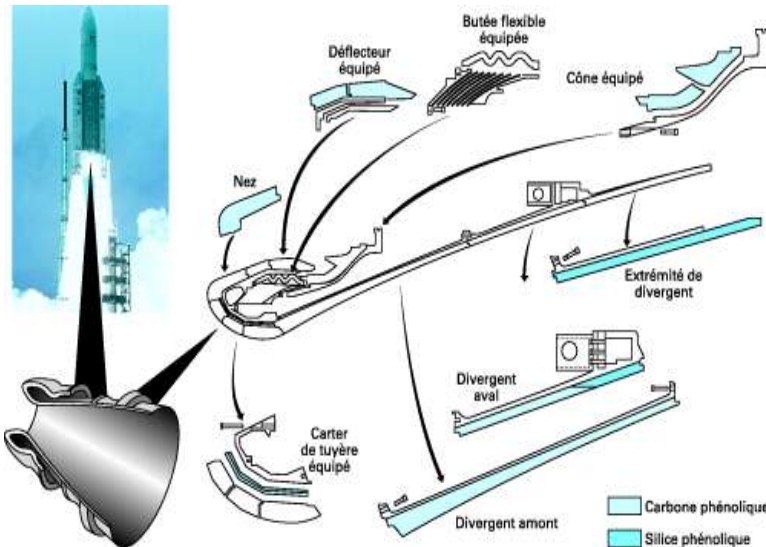
TOUGH CERAM® LDN & HDN APPLICATIONS



<= TPS application



We can accurately impregnate the HDN micro-reinforcing staples network, with an optimized thin layer of phenolic resin.



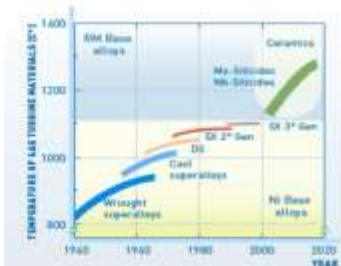
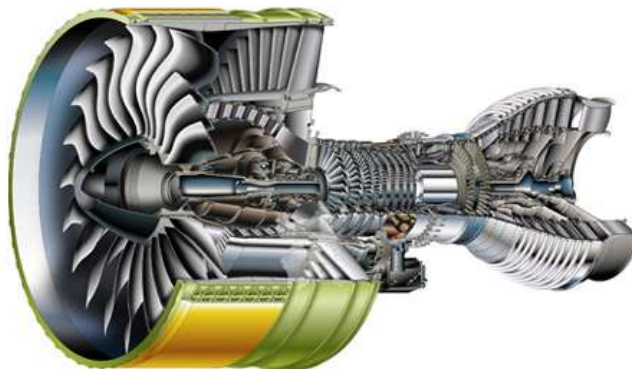
Layer thickness depending the ABLATIVE PROPERTIES we are targeting. This smart wetted HDN solution can replace advantageously carbon phenolic structure.

Monitoring ,carefully, the amount of applied phenolic resin on the HDN avoid a too big gaz emission (burst) during a NOZZEL high speed temperature rize. The controled gaz emission , cool the HDN, AVOID DELAMINATION AND DESTRUCTION OF THE NOZZEL. This solution can be very efficient for big SOLID ROCKET NOZZEL.

<= ROCKETS NOZZEL application

<= ROCKET MAIN STRUCTURE application

TURBOJET APPLICATIONS =COMBUSTION CHAMBER .FLAME STABILISATOR .HIGH TEMPERATURE ROTOR BLADES . EXHAUST DUCTS





SMARTEES FP7 Space Project – Towards a New TPS Reusable Concept for Atmospheric Reentry From Low Earth Orbit

J. Barcena¹, M. Lagos¹, I. Agote¹, C. Jimenez¹, C. Badini², E. Padovano², S. Gianella³, D. Gaia³, V. Liedtke⁴, K. Mergia⁵, S. Messoloras⁵, P. Yialouris⁵, Y. Panayiotatos⁵, A. Ortona⁶, C. D'angelo⁶, and C. Wilhelmi⁷

¹Tecnalia (Spain), ²Politecnico di Torino (Italy), ³Erbicol (Switzerland), ⁴Aerospace & Advanced Composites (Austria),
⁵National Center for Scientific Research "Demokritos" (Greece) ⁶SUPSI (Switzerland), ⁷EADS (Germany)



The research leading to these results has received funding from the European Union Seventh Framework Programme (FP7/2007-2013) under grant agreement n° 283797

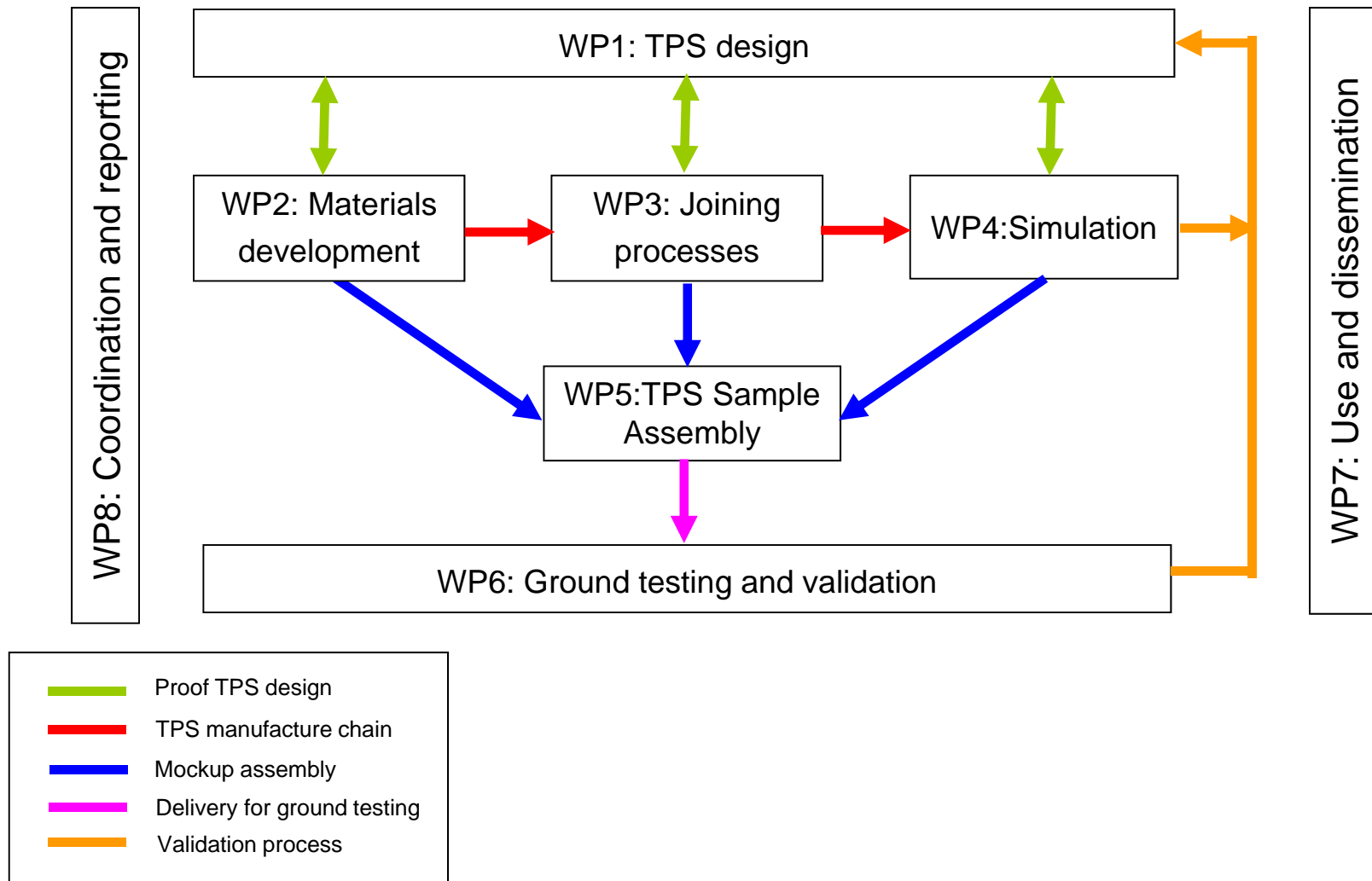
- INTRODUCTION AND MOTIVATION OF THE WORK
- CONSORTIUM
- RESULTS
- CONCLUSIONS, LESSONS LEARNT AND FUTURE WORK
- ACKNOWLEDGMENTS

- There is a strong interest in the development of reusable systems to accessing and return from Space. I.e. reusable capsules.
- This reusable systems demands a huge effort, not only in the development of new materials but also in the integration of them into the subsystems.
- On the one hand, ESA's TPS technology are based on existing materials high TRL and mission oriented. On the other hand, **EC space** programmes allow the development of **critical/disruptive technologies** for **advanced materials** on TPS. On this context SMARTTEES proposes innovative TPS concepts for ISS return systems and future launchers. Space tourism are potential candidate uses as well.
- **Future space transportation**, equipped with re-usable components will greatly **reduce the cost of launching a payload into space**. This issue is of great importance, i.e. ESA technology strategy and long term plan.
- SMARTTEES addresses the development of advanced ceramic composites structures for reusable thermal protection systems. The solution will be based on a novel reusable TPS architecture which can withstand the extreme environment conditions

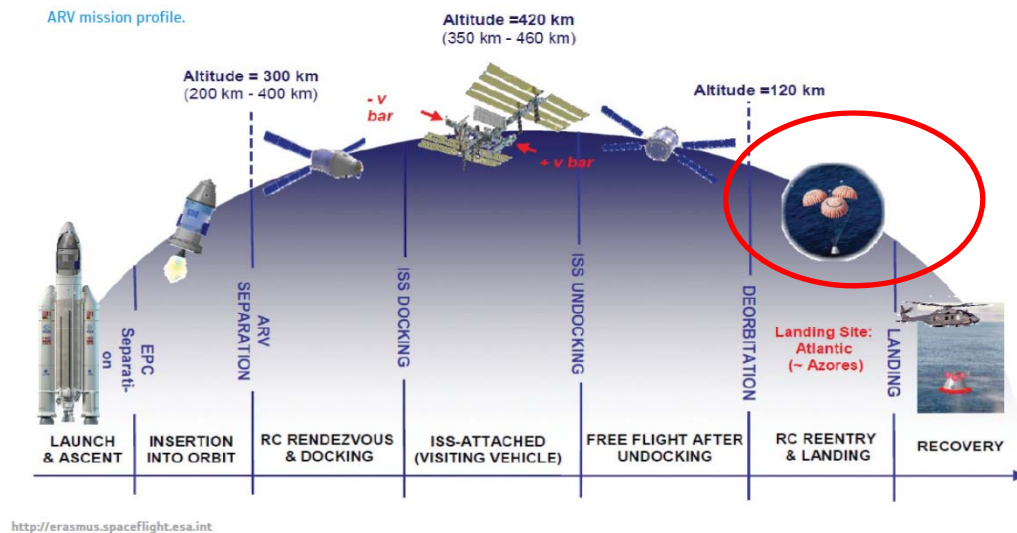
CONSORTIUM MEMBERS LOCATION

The core group of SMARTEES project is composed of **7 public and private organisations** coming from **6 different European countries**: Spain, Italy, Greece, Switzerland, Germany and Austria.





- A current Mission is selected based on the **Advanced Re-entry Vehicle***:

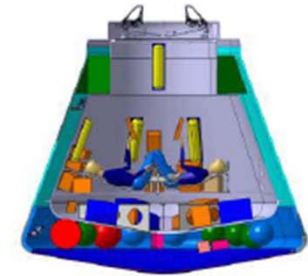
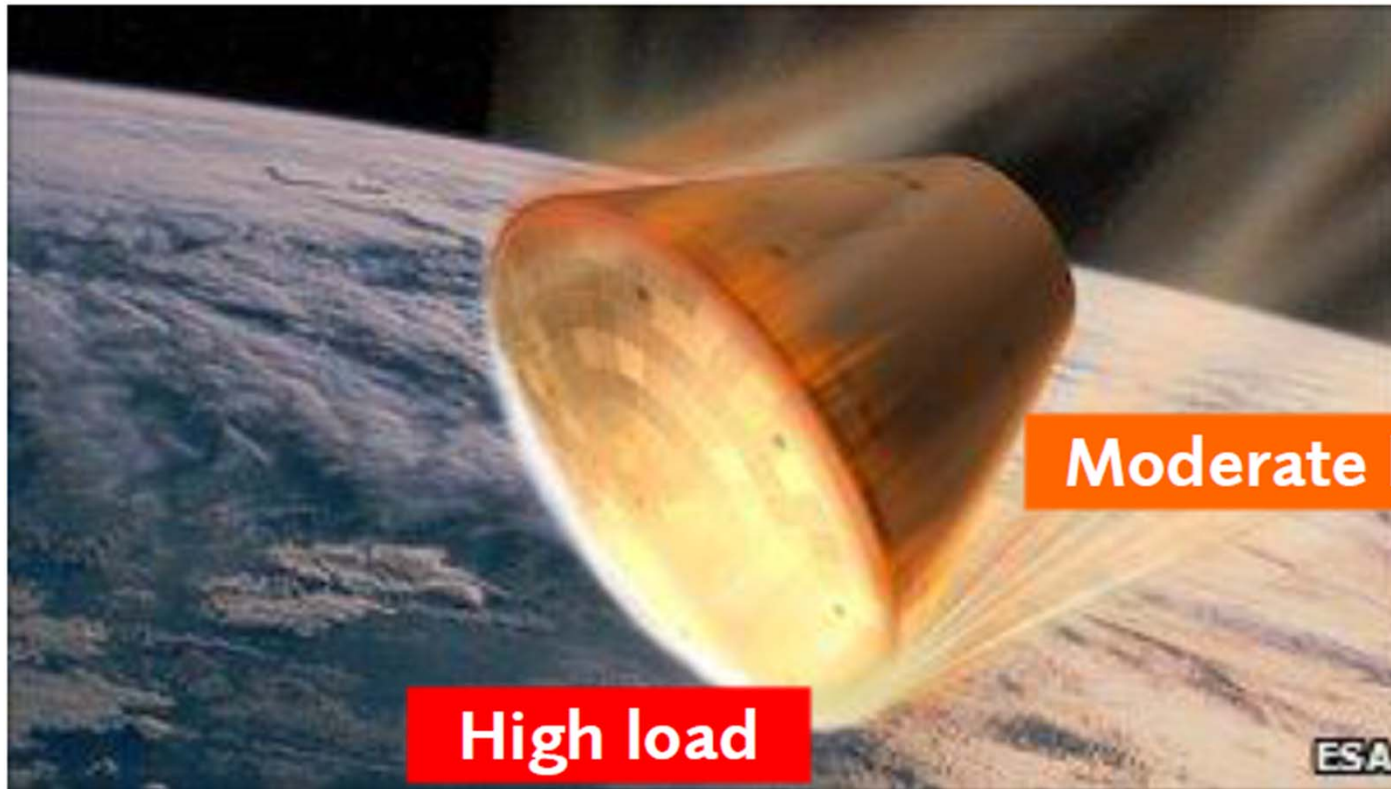


- Re-entry module evolved from ATV. It is a real mission owned by ESA and developed by Astrium GmbH, which consist of a capsule-like concept for a service module to the ISS.
- There are two versions for cargo or crew system. The re-entry will be from LEO (500 km). The first flight will be not reusable and currently there is a trade-off of designs (the currently favoured one is similar to Apollo).

For more details go to ARV's webpage: http://www.esa.int/esaMI/ATV/SEMNFZOR4CF_0.html

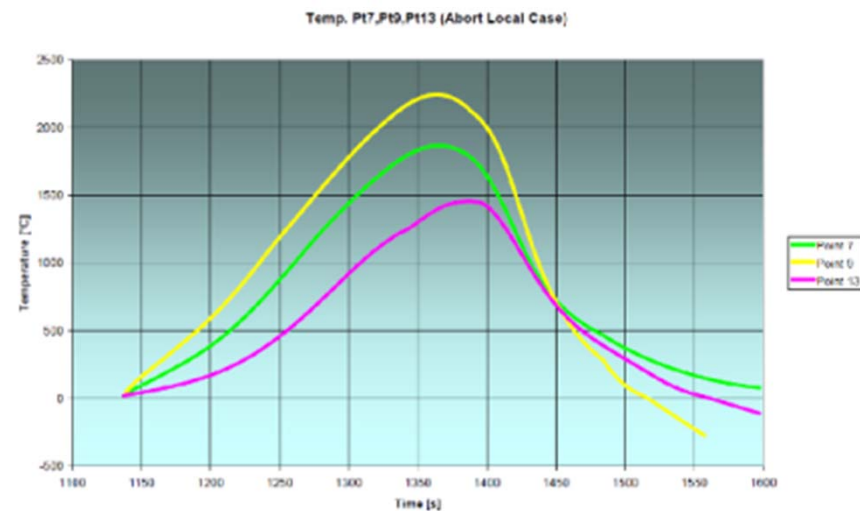
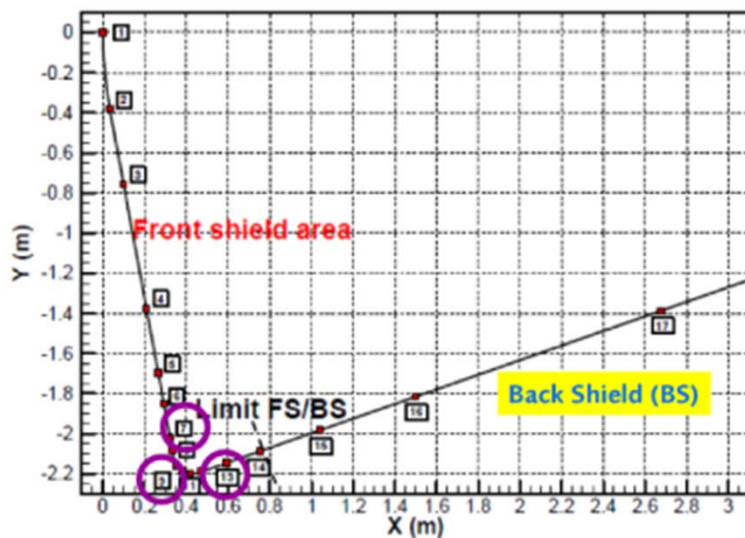
*ARV data have been produced by Astrium GmbH in the frame of a Contract with ESA

ARV capsule with heat shield locations

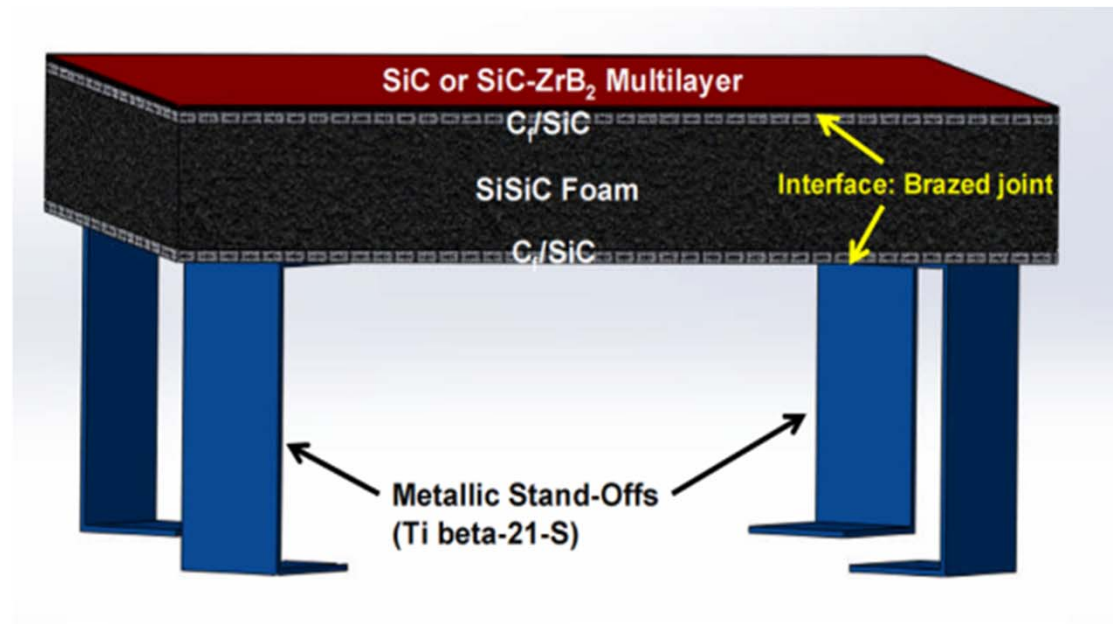


- ❖ The heat shield for such vehicle shape has been subdivided in to parts, the **front shield** with thermally high loaded areas and the **back shield** which is thermally moderately loaded

- The following specifications have been collected:
 - Heatfluxes
 - Time (during peak & total)
 - Pressure profile
 - Mechanical load
 - 3 different scenarios have been envisaged

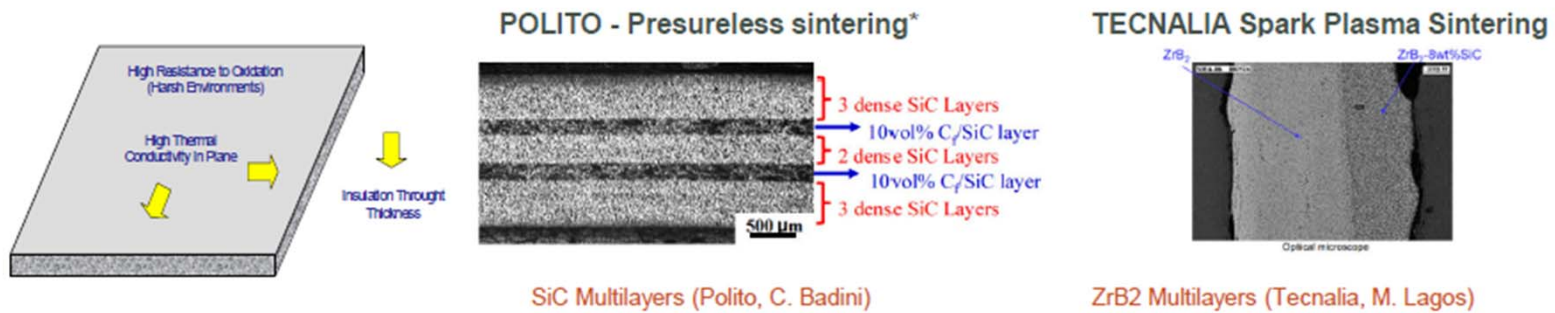


- A preliminary TPS design is ready and detailed design is on-going:
 - Materials & structure levels
 - Shape and thicknesses
 - Joining definition
 - Stand-off attachments



Schematic concept design (as an example)

- External protective multilayers based on high and ultrahigh temperature ceramics:
 - High temperature (SiC based) suitable for environments for temperatures below 1700 °C.
 - Ultrahigh temperature ceramics (ZrB₂ based) suitable for temperatures above 1700 °C.



* Progress under the framework of the PhD dissertation of E. Padovano (POLITO)

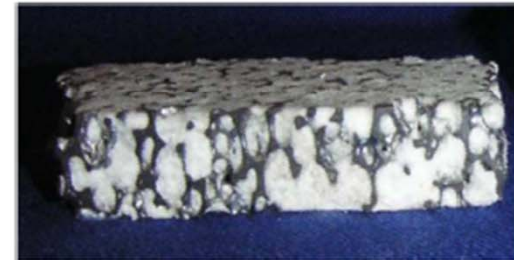
- Integration of advanced CMC structures and ceramic foams.



ERBISIC ceramic foams (Erbicol S. Gianella)

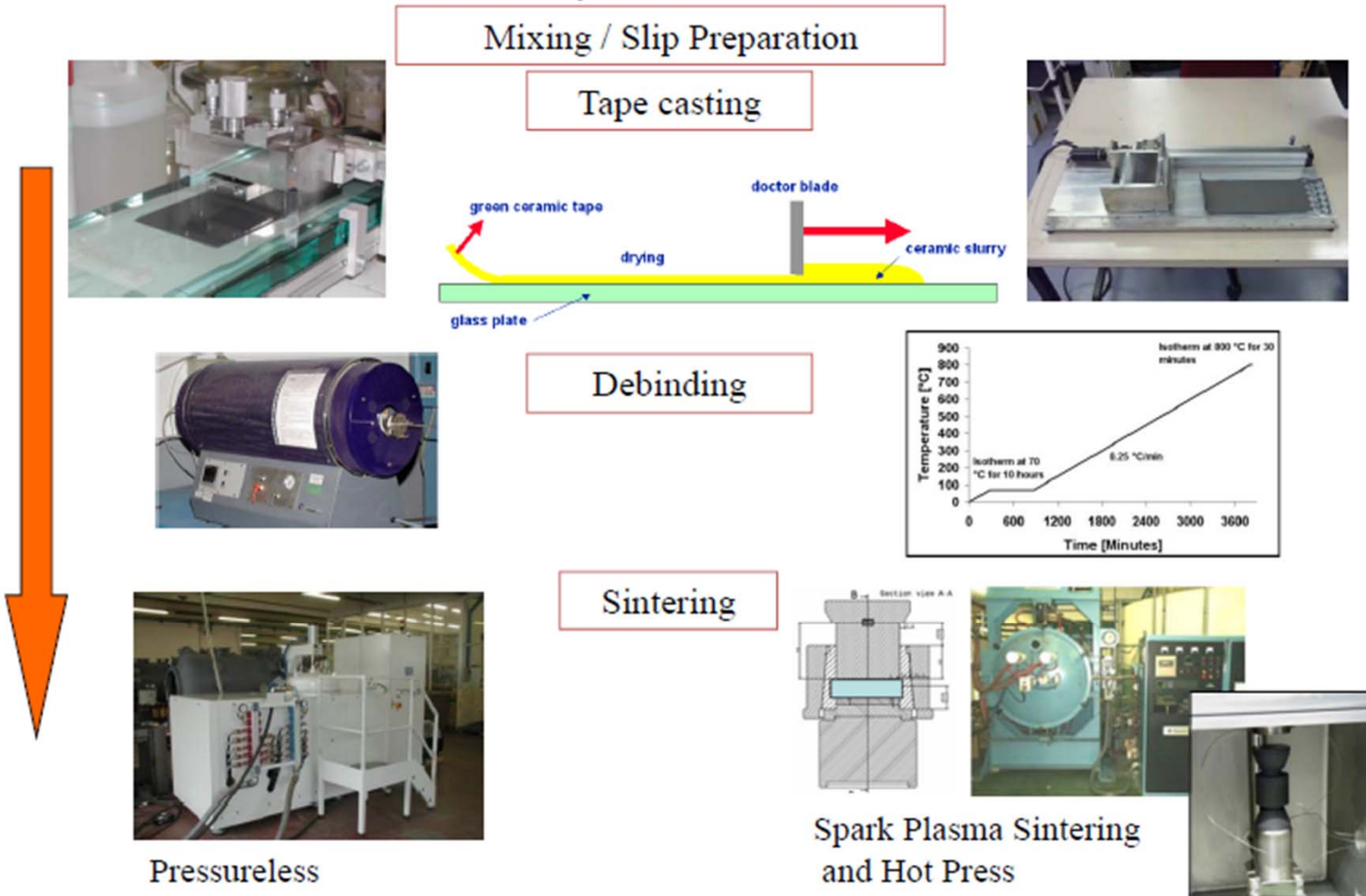


CMC/Foam sandwich progress (EADS-IW, C. Wilhelmi)

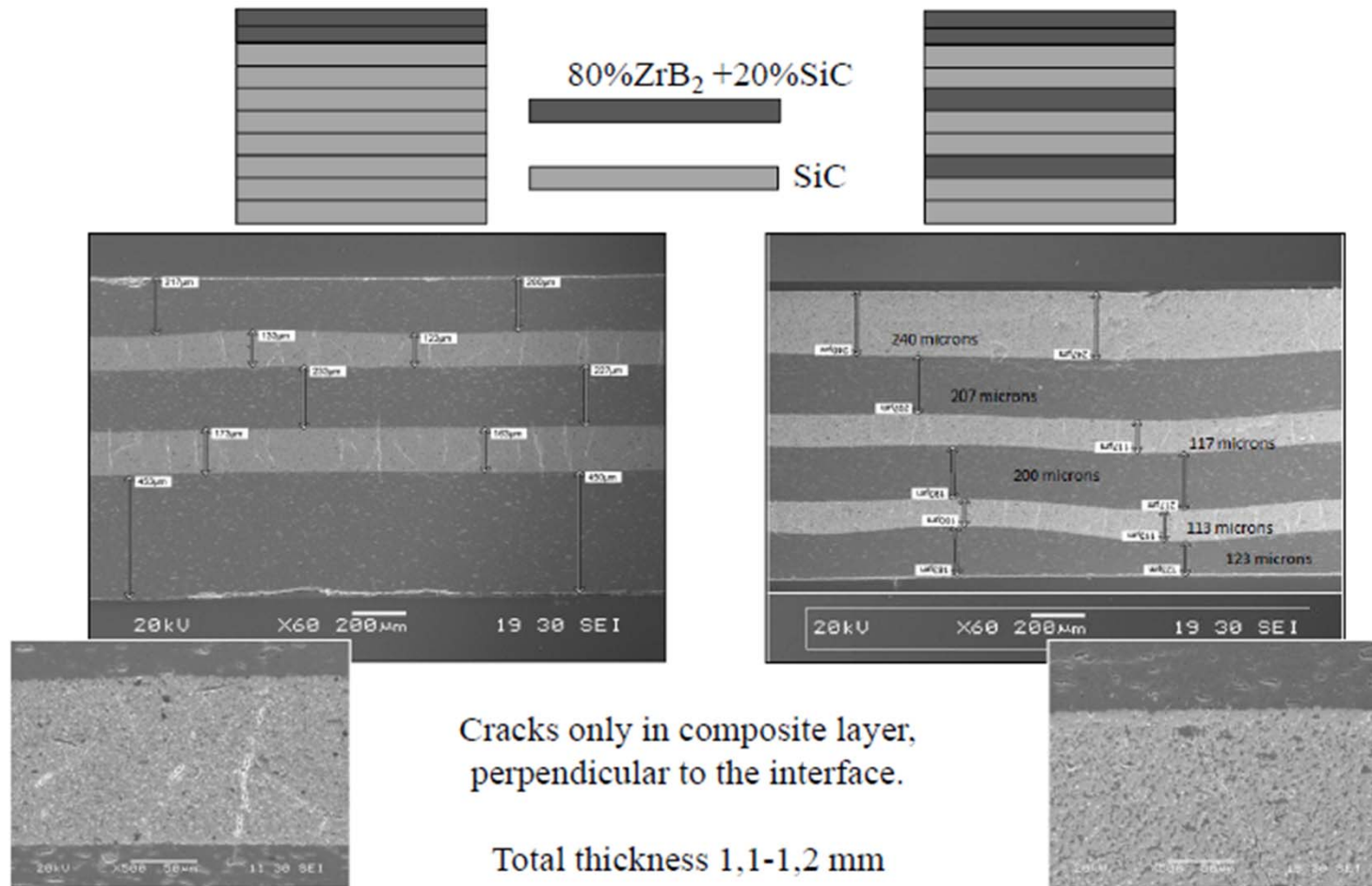


Heteroporous heterogenous ceramics (SUPSI, A. Ortona)

External protective multilayers



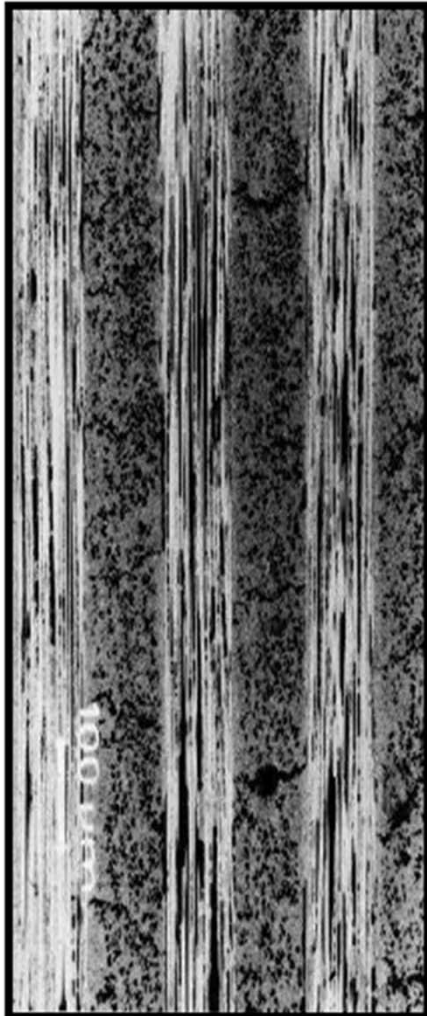
External protective multilayers. UHTC based



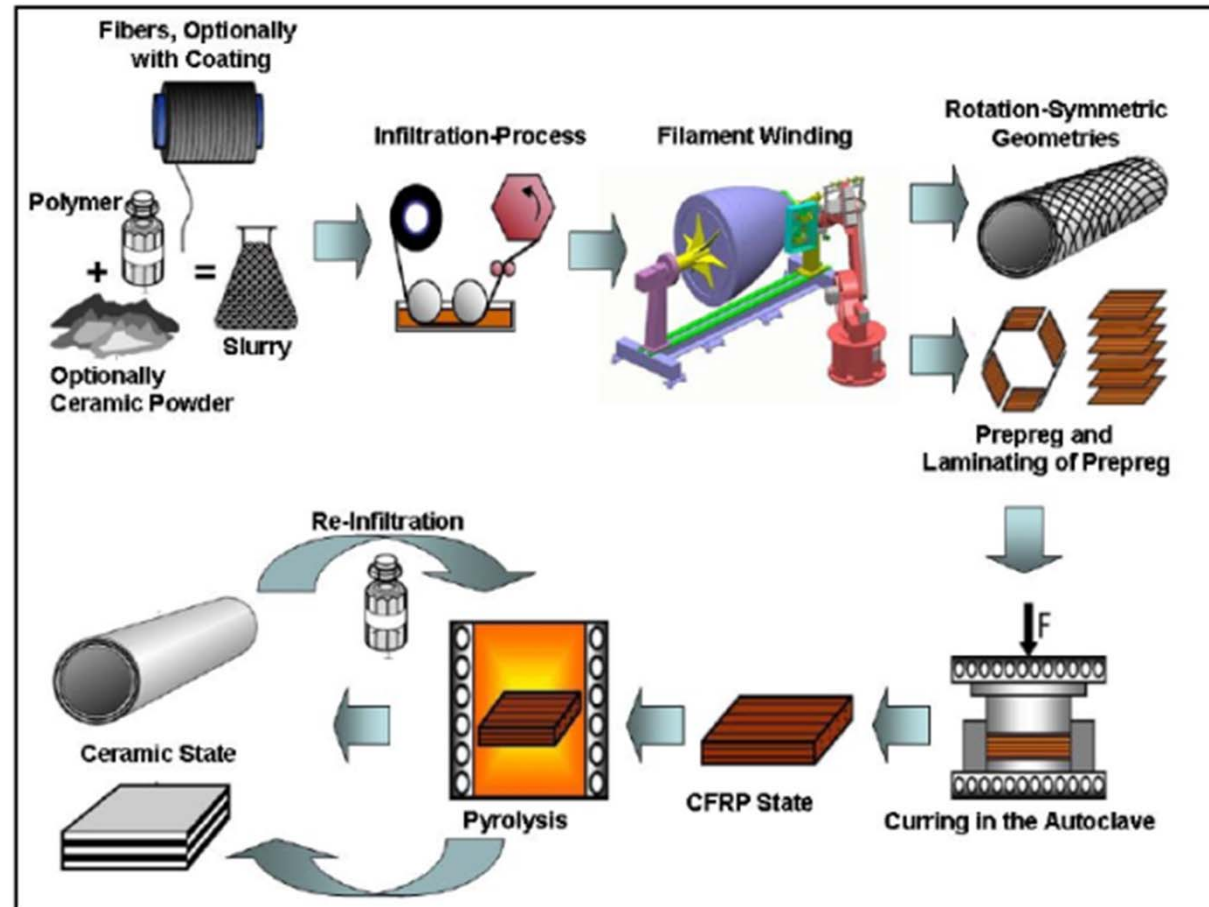
More details given under the presentation by Prof. Badini (Tuesday 9th at 9.25, Newton)

CMC External skins

SiCARBON™

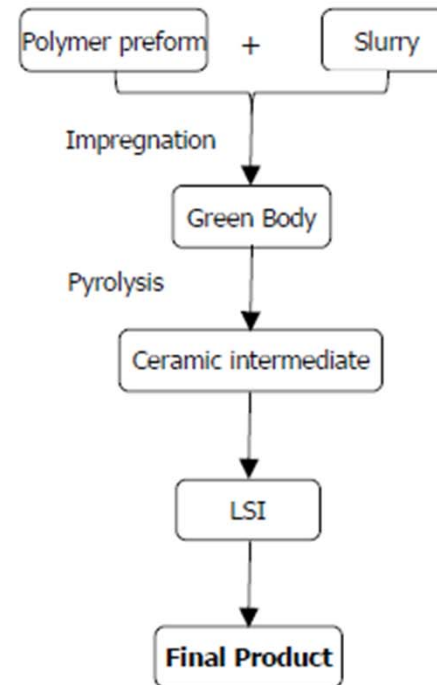


CMC (C_f/SiC) from EADS (PIP Process)



SiSiCFoams: TPS Insulating Core

Schwarwalder production method

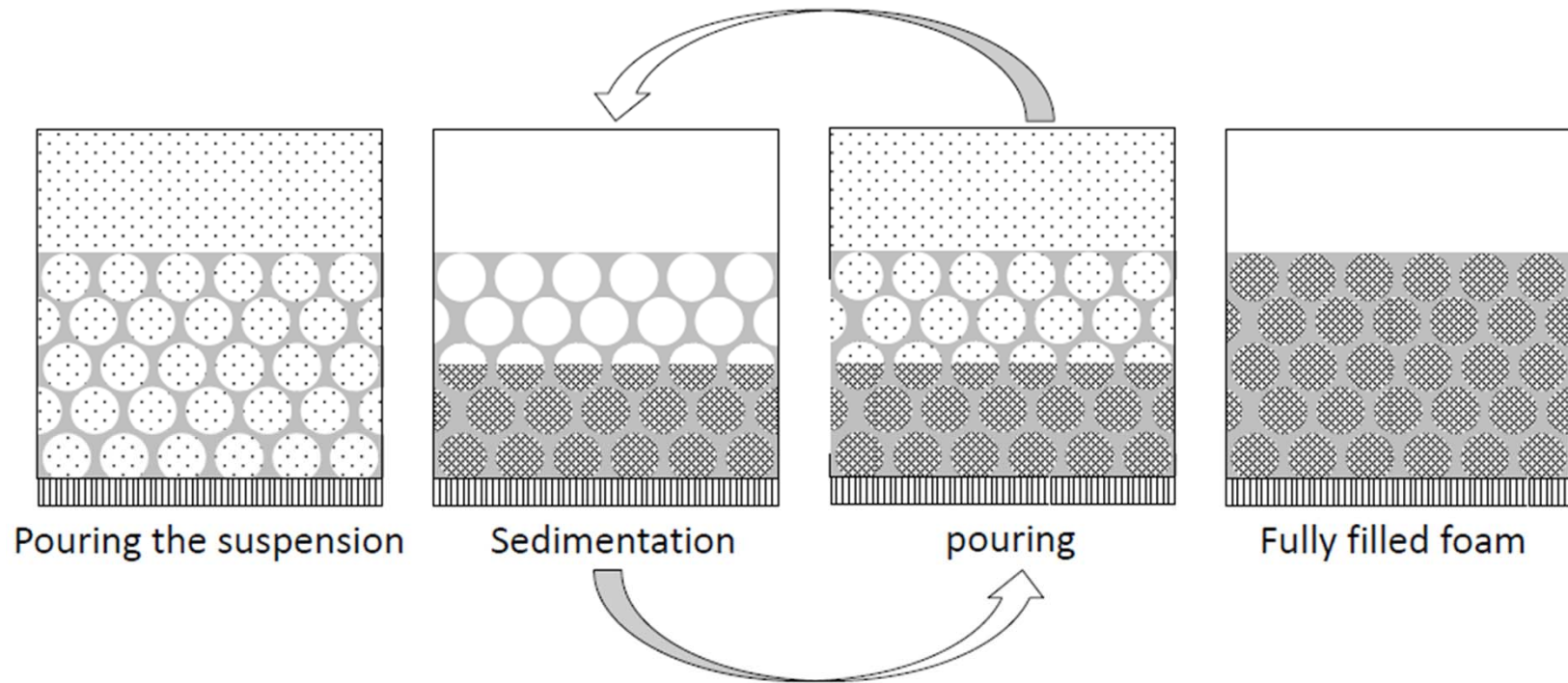


SiSiCFoams: TPS Insulating Core

Property		Value
Foam Density	[gcm ⁻³]	0.323
Normalized Density		0.114
Macroporosity	[%]	88.6
Surface Area	[m ² m ⁻³]	~ 500
Av. Strut Thickness	[mm]	0.9
Flexural Strength (3 point)	[MPa]	4
Compression Strength	[MPa]	3
Thermal Conductivity	[Wm ⁻¹ K ⁻¹]	~ 7
Young module (computed)	[GPa]	2-3

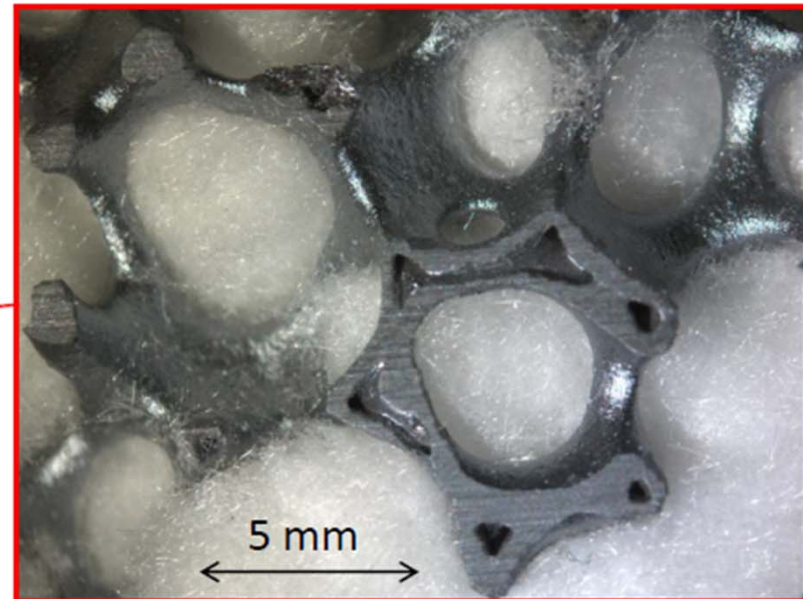
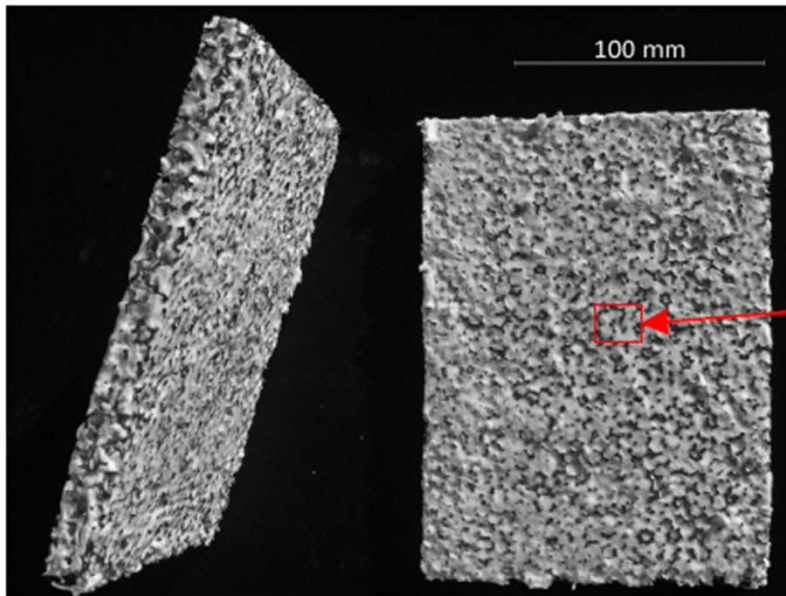
10 PPI ErbiSiC foam (Erbicol SA, Balerna, CH)

SiSiCFoams: TPS Insulating Core



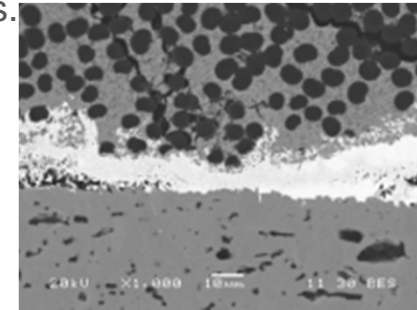
Nannetti, C.A., et al., *Manufacturing SiC-Fiber-Reinforced SiC Matrix Composites by Improved CVI/Slurry Infiltration/Polymer Impregnation and Pyrolysis*. Journal of the American Ceramic Society, 2004. **87**(7): p. 1205-1209.

SiSiCFoams: TPS Insulating Core

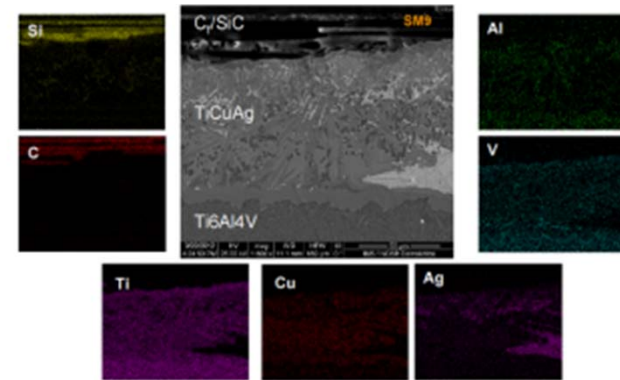


HHC close up

- Definition, selection and implementation of the bonding processes.
 - External hot-structure to CMC assembly
 - Assembly of stand-offs to the structure



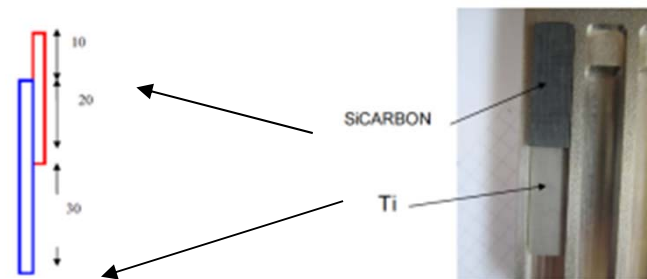
Multilayer/CMC Joining, Credit:NCRSD/TECNALIA



CMC/Stand-off Joining, Credit:NCRSD/TECNALIA

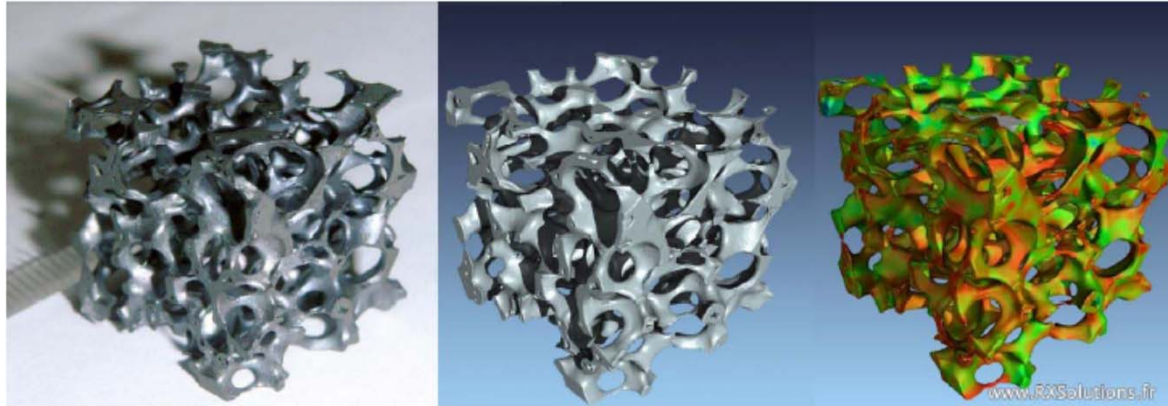
- Thermo-mechanical characterization and high temperature oxidation testing:

- Thermal conductivity
- Emissivity
- Mechanical loads
- Coefficient of thermal expansion
- Cataliticity



More details under the presentation by Dr. Mergia (Tuesday 9th at 11.25, Newton 2).

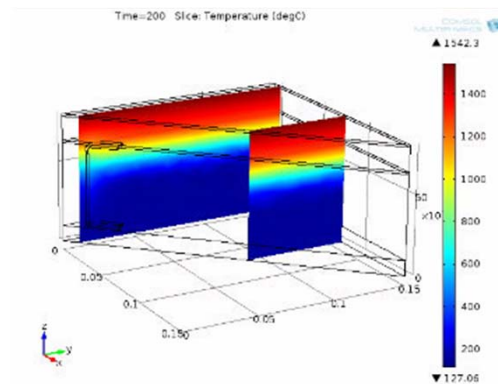
- Modelling of the different parts of the TPS (aided by computed tomography)



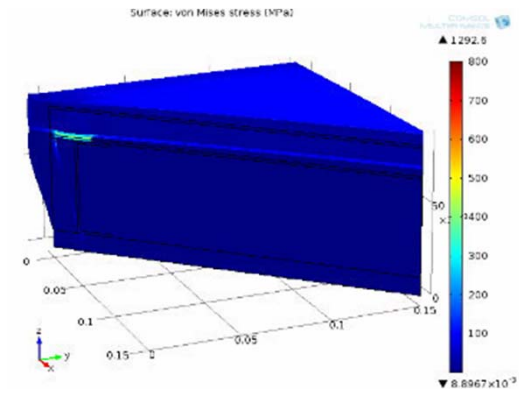
Credit: RX Solutions (France) made with ERBISIC ceramic foams (Erbicol S. Gianella)

- Thermo-mechanical analysis
 - Inputs for WP1 (specifications), WP2 (materials) and WP3 (processes)
 - Definition of temperature distribution
 - The output has allowed to calculate critical design parameters (WP1), such as aerial mass.

Simulation campaign					
Model	Standoff [mm]	CMC [mm]	Foam [mm]	UHTC [mm]	Arial mass [Kg/m ²]
1	1.5 (Ti)	1	10	-	20.04
2	1.5 (Ti)	1.5	15	-	27.12
3	1.5 (Ti)	1	10	2	25.53
4	1.5 (Ti)	1.5	15	2	32.61
5	1 (Ti)	1.5	15	-	21.69
6	2.5 (Ti)	1.5	15	-	27.48
7	1.5 (CMC)	1	10	-	19.66
8	1.5 (CMC)	1.5	15	-	26.75
9	Φ15/Φ12(CMC)	1.5	15	-	27.31
10	Φ8/Φ6(CMC)	1.5	15	-	26.76

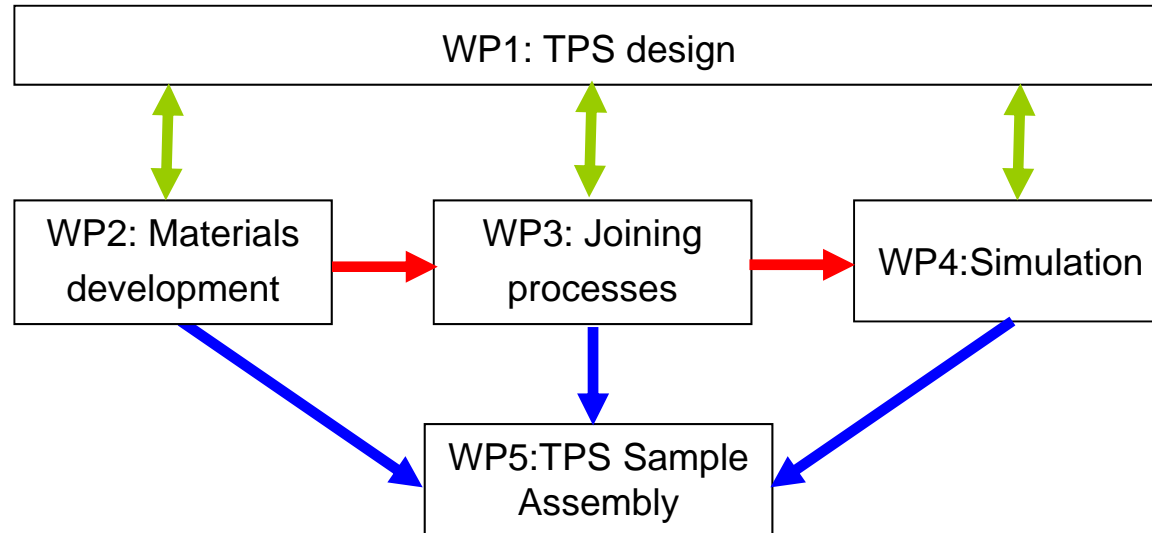


Temperature distribution
(C. D'Angelo, SUPSI)

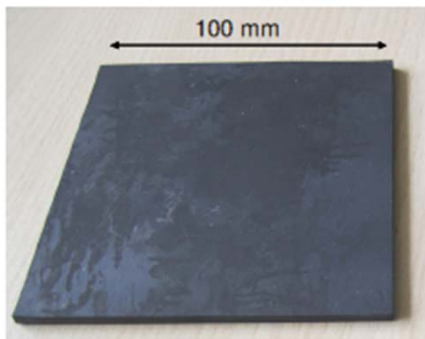


Stress distribution
(C. D'Angelo, SUPSI)

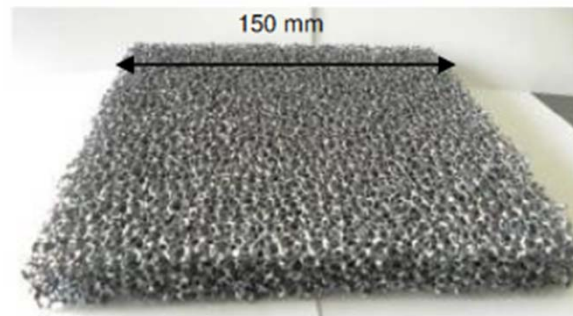
- Scale-up of materials and processes to build-up a technology sample



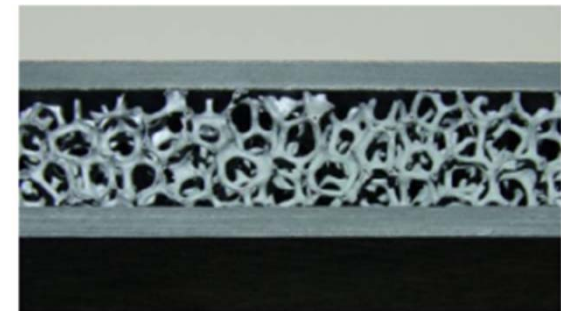
- This sample will be a TPS tile with functional properties -> First assembly trials
- Foreseen dimensions 150 x 150 mm.
- Full characterisation of the technological sample: mechanical and thermo-physical.
- Characterisation at the ground test re-entry rig.



Ceramic multilayers (POLITO E. Padovano)

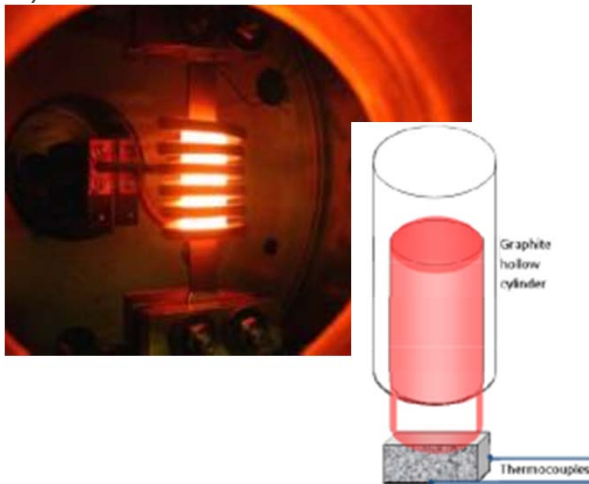


ERBISIC ceramic foams (Erbicol S. Gianella)

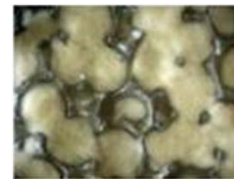


CMC/SiC sandwiches progress (EADS-IW, C. Wilhelmi)

- Bottom-up approach for testing in a ground facility simulating the re-entry conditions.
 - The testing is determining the fundamental performance and the degradation mechanisms.
 - This final step will give insight into the overall performance of the TPS, identify possible modes of failure, and assess the efficiency of the thermal insulation and the heat fluxes into the sub-structure of a spacecraft.
 - Testing outputs will be reviewed in comparison with the TPS requirements and specifications.
- Testing of foams (open vs. filled cells) -> Between 1400° C and 2100 ° C (vacuum, at equivalent heat flux)



Test Rig Chamber & Set-up
Credit:V. Liedtke (AAC)



1613 ° C



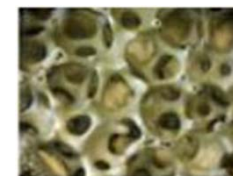
1794 ° C



2053 ° C



2053 ° C (10 cycles)



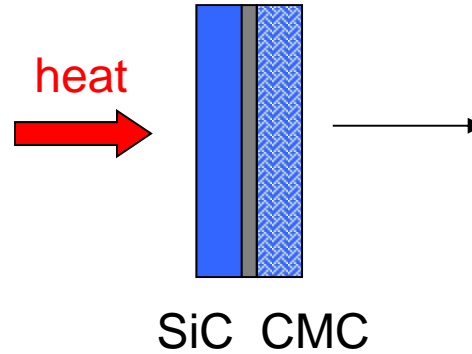
2163 ° C



2163 ° C (10 cycles)

High insulation capability is maintained until the foam degradation starts (at 2100 ° C, after 10 cycles) !

- Testing of Multilayer/CMC joints.



Recording of the temperature at the back side

Aspect after test:

Profile #12

T_{max} 1,392 C



Profile #11

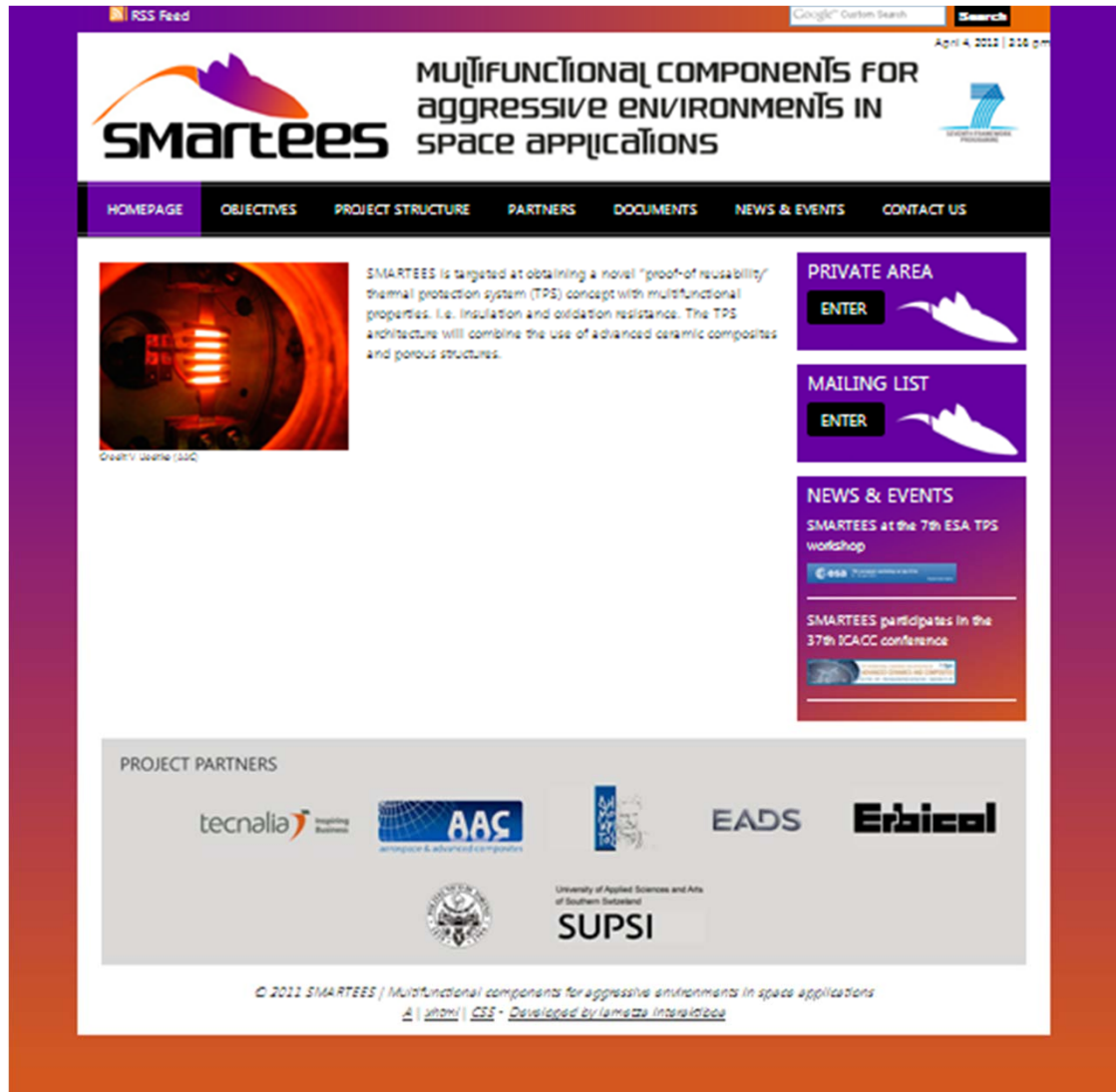
T_{max} 1,794 C

Initial tests did not result in catastrophic failure, but more detailed investigations are necessary.

Testing of CMC/foam sandwich and further Multilayer/CMC joints in air are planned for 2013

- SMARTeES aims at obtaining a novel “proof-of reusability” of a thermal protection system (TPS) concept with multifunctional properties. i.e. insulation and oxidation resistance. The TPS architecture will combine the use of advanced ceramic composites and porous structures.
- The project is in its final year and is progressing towards the final design and the technological sample assembly. There is a big challenge as the project deals with the development of new materials, but also new joining technologies and further testing.
- Future work, outside the scope of the project, has to be focused to the sample integration for a whole TPS concept for a re-entry vehicle, capsule or exploration probe.
- Positive effects of European Cooperation:
 - Europe will benefit from the results of SMARTeES by improving its access to space critical technologies. The next generation launcher (NGL) will take advantage of this concept. Another important asset is the contribution to the creation of an independent industrial supply chain and open new doors for collaboration with space fairing nations.
 - Space exploration in general may take advantage of the novel reusable TPS technologies. Potential for its use in cargo and crew space return vehicles. I.e. for a cost effective, safe and reliable return from the international space station (ISS), future launchers, space tourism.

- Astrium GmbH (W. Fischer)
- European Space Agency (M. Bottacini and B. Jeusset)
- European Commission
- Research Executive Agency (C. Ampatzis)
- EADS-Innovation Works (C. Wilhelmi, F. Meistring).
- NCSR D (S. Messoloras, K. Mergia and P. Yialouris).
- ERBICOL SA (D. Gaia and S. Gianela)
- Aerospace and Advanced Composites GmbH (V. Liedtke)
- SUPSI (C. D'Angelo and A. Ortona)
- Politecnico di Torino (E. Padovano and C. Badini)
- Tecnalia Research & Innovation (X. Hernandez, C. Jimenez, M. Lagos and I. Agote)



The screenshot shows the SMARTEES project website. At the top left is the SMARTEES logo. The main header reads "MULTIFUNCTIONAL COMPONENTS FOR aggressive ENVIRONMENTS IN SPACE APPLICATIONS". A navigation menu includes: HOME PAGE, OBJECTIVES, PROJECT STRUCTURE, PARTNERS, DOCUMENTS, NEWS & EVENTS, and CONTACT US. The main content area features a large image of a thermal protection system component with the text: "SMARTEES is targeted at obtaining a novel 'proof-of-reusability' thermal protection system (TPS) concept with multifunctional properties. I.e. insulation and oxidation resistance. The TPS architecture will combine the use of advanced ceramic composites and porous structures." To the right are buttons for "PRIVATE AREA" and "MAILING LIST". Below these are news items: "SMARTEES at the 7th ESA TPS workshop" and "SMARTEES participates in the 37th ICACC conference". A "PROJECT PARTNERS" section lists: tecnalia, AAC (Aerospace Advanced Composites), EADS, Erbicor, and SUPSI (University of Applied Sciences and Arts of Southern Switzerland). The footer contains copyright information: "© 2011 SMARTEES / Multifunctional components for aggressive environments in space applications" and credits: "A | sitem | CSE - Developed by lametta interlabio".

For more details visit the Project webpage: www.smartees-project.eu

END OF PRESENTATION

**Many thanks for your
attention**

**Please visit the showcase at
the exhibition!**

SMARTTEES FP7 Space Project – Towards a New TPS Reusable Concept for Atmospheric

Reentry from Low Earth Orbit

J. Barcena⁽¹⁾, M. Lagos⁽¹⁾, I. Agote⁽¹⁾, C. Jimenez⁽¹⁾, X. Hernandez⁽¹⁾, C. Badini⁽²⁾, E. Padovano⁽²⁾, S. Gianella⁽³⁾, D. Gaia⁽³⁾, V. Liedtke⁽⁴⁾, K. Mergia⁽⁵⁾, S. Messoloras⁽⁵⁾, P. Yialouris⁽⁵⁾, Y. Panayiotatos⁽⁵⁾, A. Ortona⁽⁶⁾, C. D'Angelo⁽⁶⁾, and C. Wilhelmi⁽⁷⁾

⁽¹⁾*Tecnalia Research & Innovation.
Industry and Transport Division
Mikeletegi Pasealekua, 2, Donostia-San Sebastian, Spain
Email: jorge.barcena@tecnalia.com*

⁽²⁾*Politecnico di Torino
Department of Materials Science and Chemical Engineering
Corso Duca degli Abruzzi, 24. 10129, Torino, Italy
Email: claudi.badini@polito.it*

⁽³⁾*Erbicol SA
Porous Ceramic Department
Viale C.Pereda 22. 6828 Balerna, Switzerland
Email: sandro.gianella@erbicol.ch*

⁽⁴⁾*Aerospace & Advanced Composites GmbH
Institute of Nuclear Technology and Radiation Protection
Viktor-Kaplan-Straße 2.A-2700 Wiener Neustadt, Austria
Email: volker.liedtke@aac-research.at*

⁽⁵⁾*N.C.S.R. "Demokritos"
Institute of Nuclear Technology and Radiation Protection
Aghia Paraskevi, 15310 Athens, Greece
Email: kmergia@ipta.demokritos.gr*

⁽⁶⁾*University of Applied Sciences (SUPSI)
The iCIMS Research Institutes
Galleria 2, CH 6928 Manno, Switzerland
Email: alberto.ortona@icimsi.ch*

⁽⁷⁾*EADS Innovation Works
Dept. TCC 2 / CTOIWMS. 81663 Munich, Germany
Email: Christian.Wilhelmi@eads.net*

INTRODUCTION

There is a strong interest in the development of reusable systems to accessing and return from Space. I.e. reusable capsules. These reusable systems demand a huge effort, not only in the development of new materials but also in the integration of them into the subsystems. On this context the FP7 project SMARTTEES proposes innovative TPS concepts for ISS return systems and future launchers. Space tourism are potential candidate uses as well. In addition, future space transportation, equipped with re-usable components will greatly reduce the cost of launching a payload into space. This issue is of great importance, i.e. ESA technology strategy and long term plan. SMARTTEES addresses the development of advanced ceramic composites structures for reusable thermal protection systems. The solution will be based on a novel reusable TPS architecture which can withstand the extreme environment conditions

SCOPE OF THE PROJECT

The aim of this project is the development of a reusable ceramic shield structure, such as hot parts of space vehicles for orbital re-entry, which are needed for applications in extreme space environments where oxidative and high temperature resistant components are required. The proposed thermal protection systems (TPS) solution is based on a novel reusable and Proof-of TPS architecture which can withstand the extreme environment conditions during ten earth atmospheric re-entries. SMARTTEES, along a three year schedule, aspires to impel a strong collaboration among the seven partners (coming from six different European countries) that compose the consortium. Special consideration will be taken as a result of the relationship among the industrial partners: EADS, ERBICOL and AAC (as end users and

SMEs respectively) to create a European supply chain of the TPS component. The project is composed of six different technical workpackages for the selection of a mission profile, definition of specifications and requirements of that mission, procurement and manufacture of the different parts of the TPS, characterisation of materials, thermo-mechanical modelling and simulation, final TPS design and re-entry testing. An iterative process among the outputs of each workpackage is being followed to obtain a proof-of final design.

PRELIMINARY RESULTS

Mission specifications and requirements

A current Mission is selected based on the Advanced Re-entry Vehicle or ARV [1]. It includes a Re-entry module evolved from ATV. It is a real mission owned by ESA and developed by Astrium GmbH, which consist of a capsule-like concept for a service module to the ISS (see artistic impression in Fig. 1a). There are two versions for cargo or crew system. The re-entry will be from LEO (500 km). The first flight will be not reusable and currently there is a trade-off of designs (the currently favoured one is similar to Apollo). The heat shield for such vehicle shape has been subdivided in to parts, the front shield with thermally high loaded areas and the back shield which is thermally moderately loaded (see Fig. 1b)

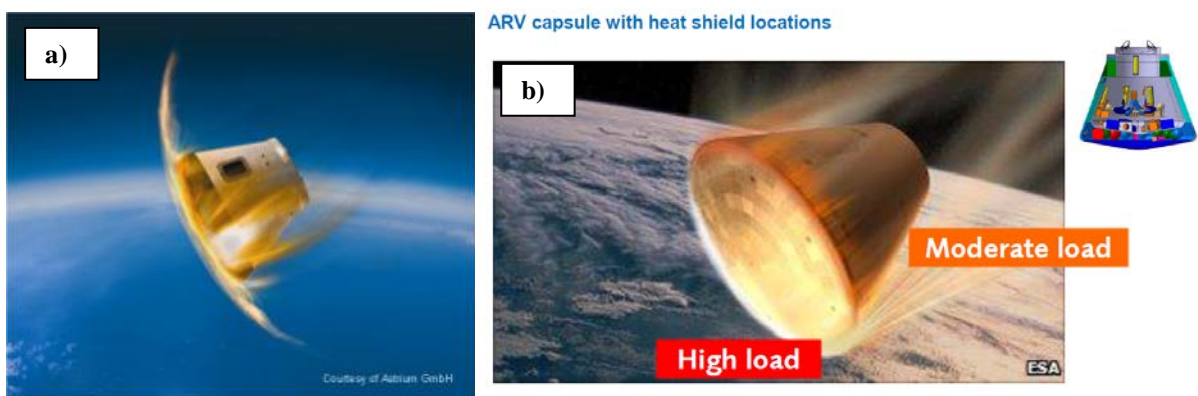


Fig. 1. Advanced Re-entry Vehicle: a) Artistic impression (courtesy of Astrium GmbH) and b) heat shield envisaged scenarios location.

Different specifications have been collected which concerns: heatfluxes vs.time (during peak & total), pressure profile, mechanical load.

Thermal protection system design

The TPS design is focused on the development of multilayer concept based on high temperature ceramics (HTCs) [2] and ultrahigh temperature ceramics (UHTCs) [3] with tailored properties. Their joining processes to conventional structural ceramic matrix composites (CMCs) or novel porous sandwich structures [4] and the final attachment to metallic structure. A proof-of TPS design is being provided within the project, having a real on-going re-entry mission as reference for the project.

The specifications have been correlated with the TPS design which concerns: heatfluxes vs.time (during peak & total), pressure profile, mechanical load. From this premise three different scenarios have been envisaged: (1) Scenario I: Back shield. For this area the heat fluxes and thermal loads (sizing trajectory) are moderate and therefore offer an interest for the Family 1 materials (SiC based). The selected point in this zone is leading to a max. temperature of approx. 1300 °C and heat flux around 0.3 MW/m². It is expected that SMARTEES materials can be designed to cover the loads with a certain margin and so fulfil the corresponding requirements. (2) Scenario II. Front shield. For this area the heat fluxes and thermal loads (sizing trajectory) are interesting and realistic for Family 2 materials (based on ZrB₂/SiC). The shape of the front shield is almost planar and therefore assembled with shingles. For the SMARTEES TPS development it is proposed to select a point front shield with corresponding temperatures of approx. 1800 °C and heat fluxes around 0.8 MW/m². (3) Scenario III. Corner area. In principle, for this area Family 2 materials (based on ZrB₂/SiC) could be suitable with respect to the thermal loads (sizing trajectory) but the challenge to fulfil the requirements is very high. For example a control point with a max. heat flux of approx. 1.6 MW/m² and temperature of approx. 2100 °C could be interesting but it has to be investigated and proofed whether SMARTEES materials can withstand the very severe loads at this point. Furthermore SMARTEES is addressed to planar shapes and this is not realistic for the corner area.

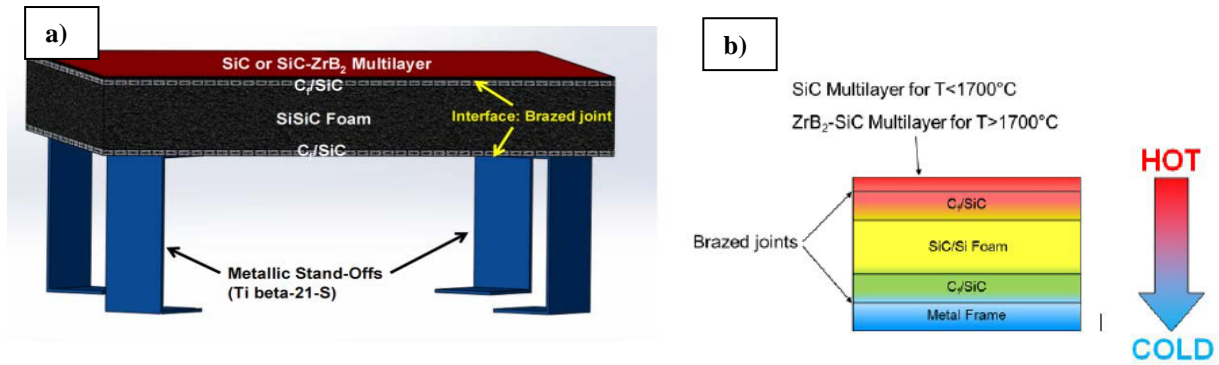


Fig. 2 TPS design: a) Example of schematic concept and b) heatflux through the proposed concept along its thickness

Materials development

The TPS solution involves the material development and integration at different levels, as depicted in Fig. 2: First of all external protective multilayers against oxidation, where high and ultrahigh temperature ceramics are being employed. High temperature (SiC based) are suitable for environments for temperatures below 1700 °C, while ultrahigh temperature ceramics (ZrB₂ based) suitable for temperatures above 1700 °C. These multilayers are manufactured through the tape casting technique and further sintered at temperatures above 1900 °C. Two sintering routes have been explored: (1) pressureless sintering and (2) spark plasma sintering. The first method is more mature and therefore easily scalable, but leads to high processing cycle. On the other hand, the second method is emerging and although the processing times are easily shortened and the levels of residual porosity are reduced, the uniaxial pressure aid is required and therefore the sizes and geometries are limited. The multilayer nature leads to high flexibility to tailor the composition of the tapes and has allowed obtaining unique layer combinations, such as the intercalation of SiC and mixtures of short carbon fibres with SiC layers, intercalation of high density and porous SiC layer and even alternation of SiC and ZrB₂/SiC composite layers. Few examples are given in Figure 3. The mechanical properties of these multilayers have been measured (mainly on the SiC based system) and collected in a database, to be later used as inputs for simulations. The bending strengths values are in the range of 250-300 MPa and elastic modulus in the range of 280-330 GPa [4], being the higher values when only pure SiC multilayer are used, or lower depending on the amount and number of carbon fibres and SiC intercalating layers. On the other hand the thermal properties are in the 60-100 W/mK at room temperature and decreases to 40-20 W/mK at 1500 °C [5].

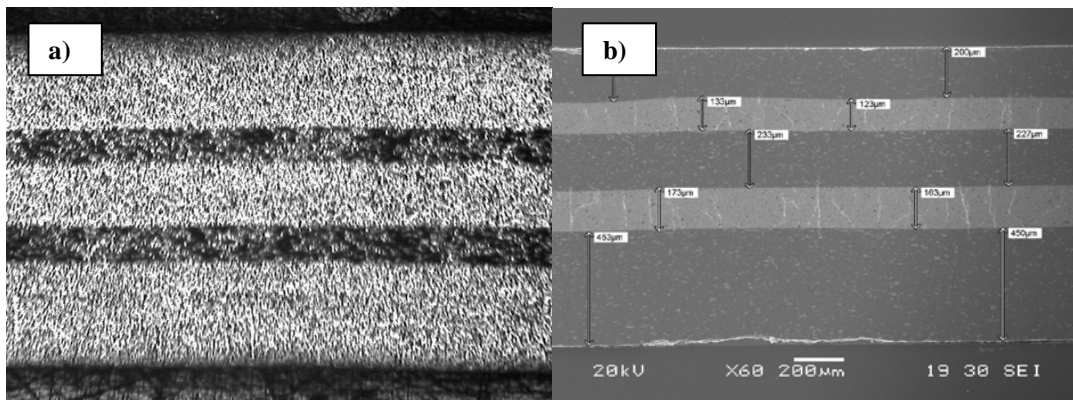


Fig. 3 Multilayer development examples: a) intercalation of SiC and C_f/SiC layers b) intercalation of SiC and ZrB₂/SiC

The second materials level consists of a ceramic sandwich with two CMC skins (C_f/SiC ceramic matrix composites, under the SICARBON[®] commercial name from EADS [6]) and a ceramic foams core (Si-SiC) from the small Swiss company ERBICOL [7]. A great effort has been carried out in order to integrate both parts in a single hot-structure. An example is depicted in Figure 4. In order to improve the thermal insulation performance of this subsystem the foams were infiltrated with short alumina fibres, as depicted in Fig. 4b, to create a so called “Heteroporous heterogeneous ceramics” structure.

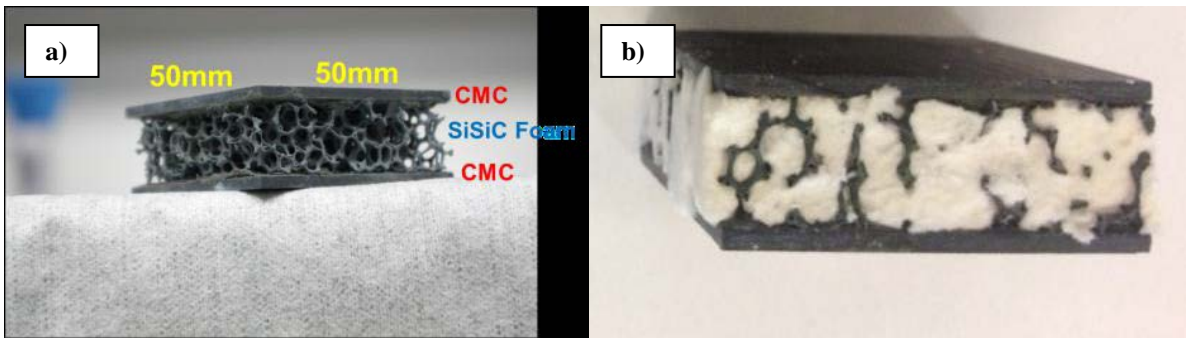


Fig. 4 C_f/SiC + SiSiC foam sandwich structures: a) after the assembly process by EADS b) after the short ceramic fiber infiltration by SUPSI.

The last material level consists of metallic stand-off, in order to allow the attachment of this novel TPS solution to the cold substructure of the vehicle. Two types of titanium alloys have been compared: Ti6Al4V and Beta 21s. Although the later alloy offers slightly better strength at temperatures above 600 °C, the former has been selected due to the temperature constructions during the integration of this part as it will be below explained in a greater detail.

Material and structures integration

All the materials, framed in the above described three levels, have been integrated by advanced joining methods based on brazing technologies [8]. The joining regions are depicted in Fig.2a above. For the integration of the 1st materials levels (multilayers) to the sandwich structures (2nd level) the use of ternary carbide (Ti_3SiC_2) has been investigated and different trials were performed using SiC multilayer on top of SICARBON plates. This is the so called “high temperature” joint. The ternary carbide is synthesized “in house” through the SHS (self-propagating high temperature synthesis) and the brazing process is carried-out at 1600 °C under uniaxial pressure to achieve a sound bond. The microstructure and the formed phases were intensively studied (see an example of the microstructure in Fig. 5a). For more details please find more detailed information in a separate paper under reference [8].

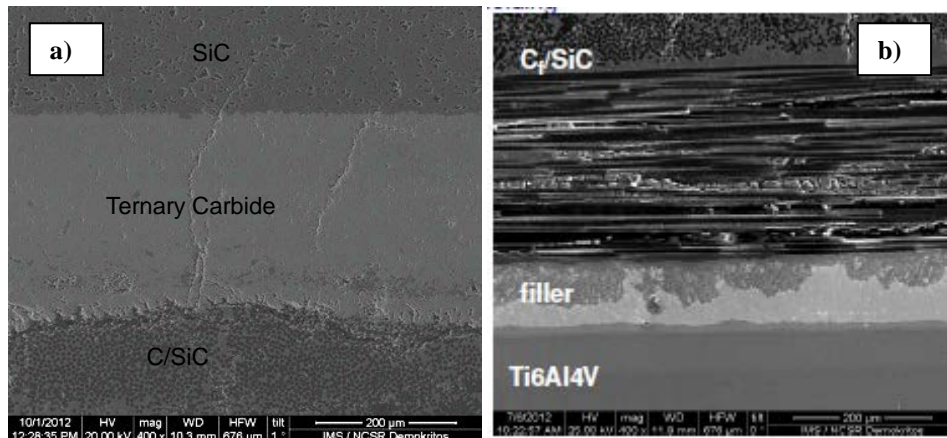


Fig. 5 Materials system joining by advanced brazing technologies: a) Multilayer/CMC joints b) CMC/Ti alloy joints

On the other hand, the materials assembly at the second (sandwich structures) and third level (stand-off) has been investigated by the use of a metallic alloys as filler. This is the so-called “low temperature” joint, where TiCuSi filler in different forms were investigated. The studied substrates were again the SICARBON CMC and two different Titanium alloys have been compared in view to select the proper material for the stand-off (third level). As above mentioned Ti6Al4V were compared vs. Beta 21s. The former were finally selected as the optimal brazing temperature was optimized to be 900 °C in view of microstructural aspects (see Fig. 5b as a typical example). Given this condition the Ti6Al4V alloy shows a higher beta transition threshold temperature rather than the Beta 21S alloy. The shear strength of this joint has been tested at 600 °C, providing an average value of 6MPa

TPS simulation under re-entry conditions and design refinement

SUPSI is in charge on the simulation activities in SMARTTEES, where they are progressing through a proper model reconstruction and simulation of the single parts of the TPS as well on the preliminary design of the whole TPS. For this purpose they have performed a digital reconstruction on the ceramic based sandwich (through X-ray computed tomography, see Fig. 6) and they have analytically studied the internal stress under bending load and furthermore a FE analysis on the crack propagation.

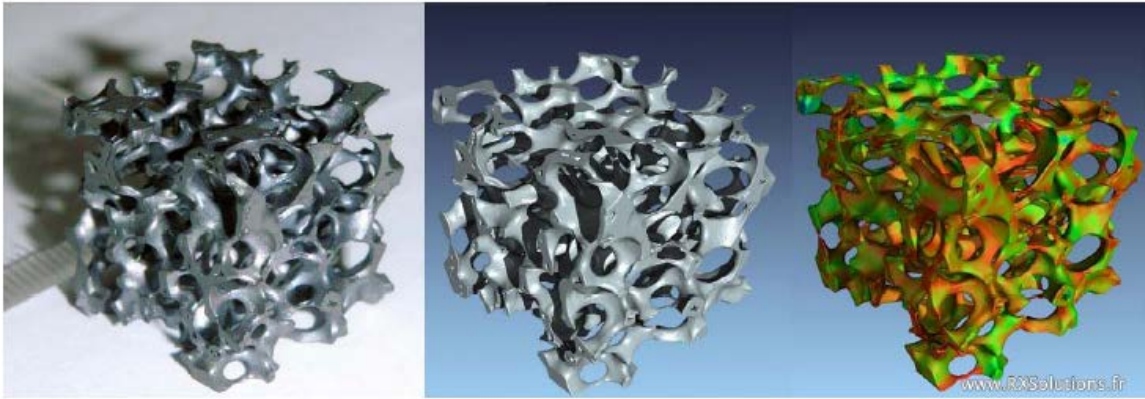


Fig. 6 SiSiC Foam reconstruction by RX Solutions (France) made with ERBISIC ceramic foams (Erbicol S. Gianella)

Concerning the TPS concept, a considerable progress thermal analysis and a thermo-mechanical analysis have been carried-out. Due to the time dependence nature of the re-entry profile a non linear (transient) approach has been necessary to perform. Brazing regions among the TPS parts have been taken into account for a realistic model reconstruction having as reference 3 different scenarios/control points (the most representative load cases as above described) from the profiles. The simulation of the thermal and mechanical internal loads is being requiring a large number of iteration to select the optimal thickness and geometries of each part in terms of a balance among aerial mass, thermal performance and feasibility for manufacture. The worse load case was found at the CMC/stand-off interface due to the largest CTE mismatch.

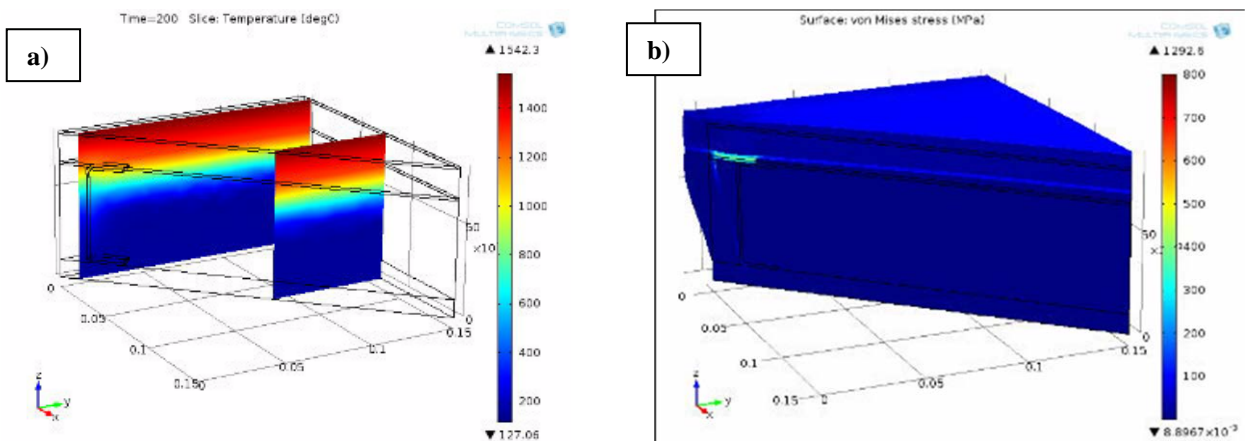


Fig. 7 Thermal analysis of the TPS solution a) Thermal distribution through thickness b) Mechanical stresses at critical areas (CMC/Stand-off Interfaces).

Up scaling and TPS technological sample assembly.

The development, manufacture and testing of a technological sample is on-going, in order to test its overall thermal performance and intrinsic thermo-mechanical behaviour. This technological sample consists of a TPS tile with functional properties. A full size tile of 150 x 150 mm has been agreed with Astrium GmbH (end user of the project).

The up-scaling activities is consisting not only on material manufacture: multilayers, foams, CMC plates and stand-offs (as seen in Fig. 8), but also on joining process for technology sample assembly and the characterisation of the technology sample. The results of the materials development and joining processes (both above described) have been inputs for this upscaling. A process chain is defined (compatible with the manufacturing limitations of each part) and a step-wise approach on subscale samples is being carried-out, being few of them already delivered for TPS re-entry characterization (see below), while a plan for full scale manufacturing to complete the verification is defined.

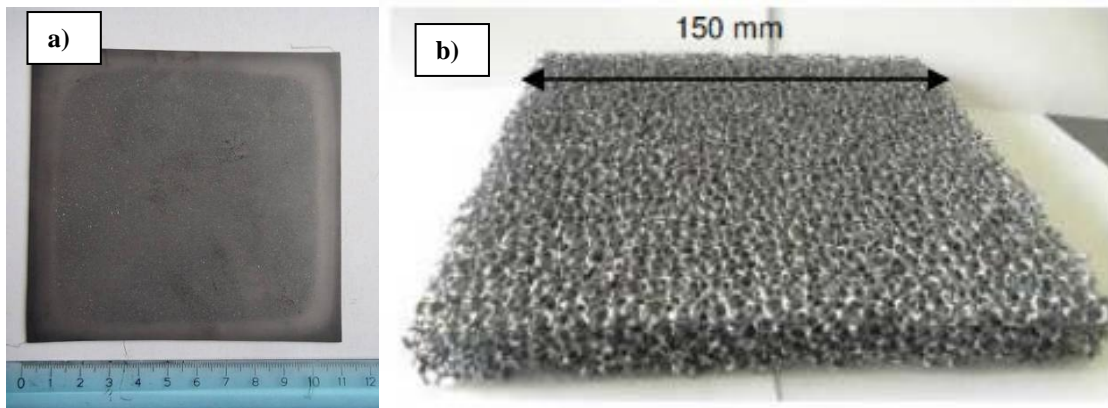


Fig. 8 Materials up-scaling examples: a) SiC multilayers and b) SiSiC foams.

Re-entry characterisation

The Austrian small company, AAC, has made available for the project its ground testing facilities for representative load case for the selected flight application. This facility consists of an environmental chamber based on a black body radiator, heated by induction, where the representative heatfluxes from the mission requirements are reproduced. The facility and sample lay-out is depicted in Fig. 9a. The heatflux conversion into the temperatures at the blackbody radiator are shown in Fig 9b. The sample to be tested is placed very close to a radiator tube and the thermal performance is monitored with thermocouples inserted at the side and back region of the sample.

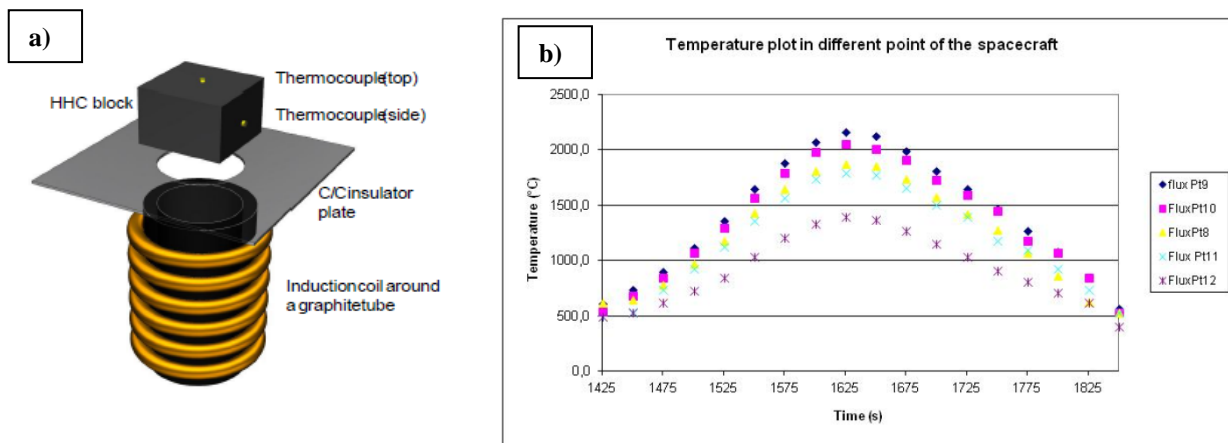


Fig. 9 AAC Environmental re-entry chamber facility: a) Radiator and sample set up b) Thermal profiles arising for the control points specifications.

On a first set of experimental test SiSiC based foams delivered by ERBICOL were tested under relevant thermal loads. The thermal performance of open pore and filled foam samples from ERBICOL was studied. For the foams, substantial decomposition of the ceramic filler and partial melting of the foam itself is observed at the 2 highest thermal loads (equivalent to 2,053 °C and 2,163 °C) only (see the degradation evolution in Fig.10).

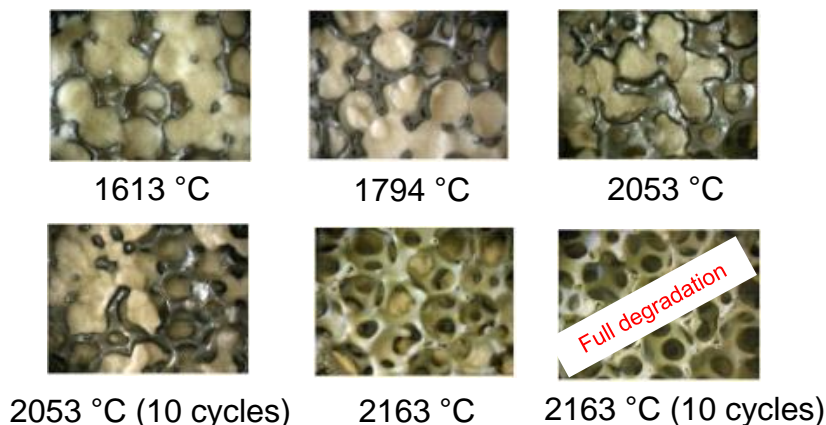


Fig. 10 Degradation evolution of filled foams at different thermal profiles

On a second set of experiments, joined C/SiC / Multilayer Plates were tested up to five cycles. As shown in Fig.11, regarding this joined plates, no damage could be observed after applying heat fluxes equivalent to 1,391 °C and 1,794 °C. Though the strength of the joints at higher temperatures is to be analysed further, the initial results look promising.

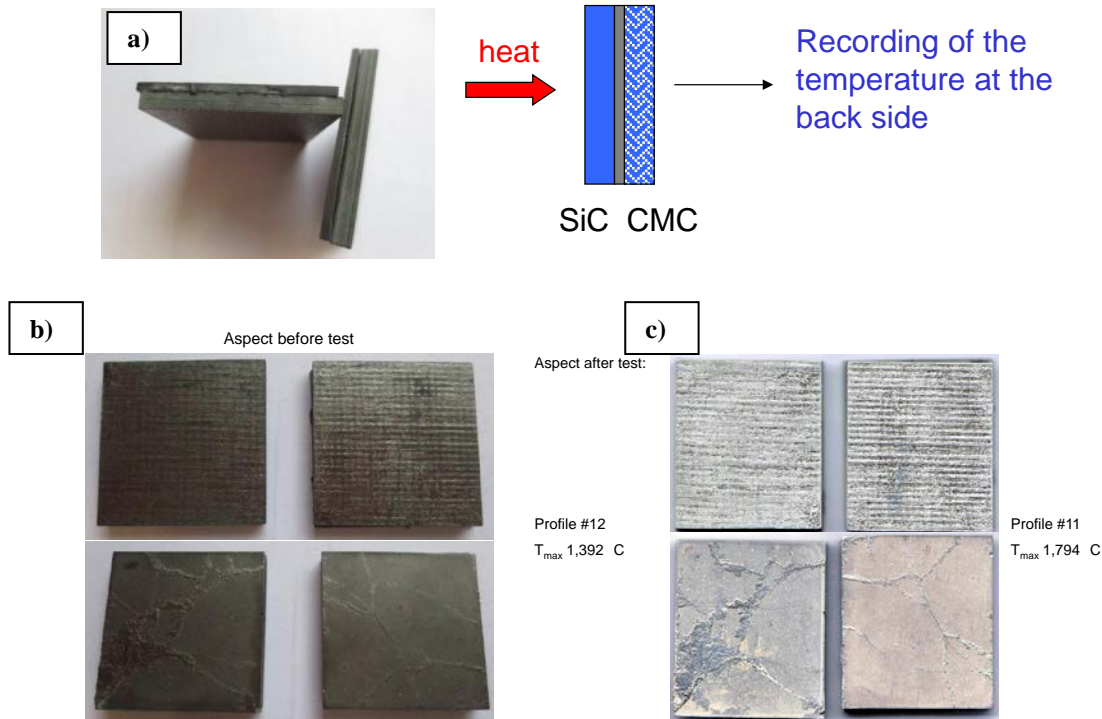


Fig. 10 Multilayer/CMC thermal test: a) Testing procedure, b) Aspect before test and c) Aspect after test.

MAIN CONCLUSIONS AND FUTURE WORKS

SMARTEES is addressed to a new TPS reusable concept and its further validation under a relevant environment. The current developments were addressed to the compilation of a reference mission (ARV), TPS design, material manufacture, characterisation and the assembly of the different parts (external multilayer, CMC/Foam core sandwich and metallic stand-offs). The design its being aided by a tailored transient thermal model and iterative loops have led to dimension the TPS. Sub-elements of the TPS have been tested in an re-entry characterisation environmental chamber.

The project is in its final year and is progressing towards the final design and the technological sample assembly. There is a big challenge as the project deals with the development of new materials, but also new joining technologies and further testing. Future work, outside the scope of the project, has to be focused to the sample integration for a whole TPS concept for a re-entry vehicle, capsule or exploration probe.

The results of SMARTEES will improve the access to space critical technologies. The next generation launcher (NGL) will take advantage of this concept. Another important asset is the contribution to the creation of an independent industrial supply chain and open new doors for collaboration with space fairing nations. Space exploration in general may take advantage of the novel reusable TPS technologies. Potential for its use in cargo and crew space return vehicles. I.e. for a cost effective, safe and reliable return from the international space station (ISS), future launchers and even space tourism.

ACKNOWLEDGMENTS

This work has been performed within the framework of the European Project ‘‘SMARTEES’’ (G.A. n. 262749) with the financial support by the European Community. The author specially thanks the strong support received from Wolfgang P.P. Fischer (Astrium GmbH). The support from ESA (M. Bottacini and B. Jeusset) is appreciated.

REFERENCES

- [1] T. Salmon, X. Vo and M. Bottacini, "TPS Architecture on ARV" Proceedings of the 7th European Symposium on Aerothermodynamics, by Ouwehand, L. Noordwijk, Netherlands: European Space Agency, 2011, id.120.
- [2] S. Biamino, V. Liedtke, C. Badini, G. Euchberger, I. Huertas Olivares, M. Pavese, P. Fino, "Multilayer SiC for thermal protection system of space vehicles: Manufacturing and testing under simulated re-entry conditions", *J. Eur. Ceram. Soc.*, 28, pp. 2791-2800, 2008.
- [3] J. Barcena, J. Coletto, S.C. Zhang, G.E. Hilmas and W.G. Fahrenholtz. "Processing of Carbon Nanofiber Reinforced ZrB₂ Matrix", *Composites for Aerospace Applications*, *Advanced Engineering Materials* 12, pp. 623-626, 2010.
- [4] S. Gianella, D. Gaia and A. Ortona, "High Temperature Applications of SiSiC Cellular Ceramics", *Advanced Engineering Materials*, Volume 14, Issue 12, pp.1074–1081, December 2012
- [5] W.S Yang, L. Fuso, S. Biamino et al, "Microstructures and mechanical properties of short carbon fibre/SiC multilayer composites prepared by tape casting", *Composites Science and Technology*, vol. 72, pp. 675-680.
- [6] W.S Yang, S. Biamino, E. Padovano et al. "Thermophysical properties of SiC multilayer prepared by tape casting and pressureless sintering", *Composite structures*, Volume 96, pp. 469-475, February 2013.
- [7] G. Motz, S. Schmidt and S. Beyer, "The PIP - process: Precursor Properties and Applications" in: "Ceramic matrix Composites, edited by Walter Krenkel, Wiley, pp. ,165-186, 2008
- [8] A. Ortona, C. Badini, V. Liedtke, C. Wilhelmi, C. D'Angelo, D. Gaia and W. Fischer, "Heteroporous heterogeneous ceramics for reusable thermal protection systems", *Journal of Materials Research*, available on CJOMay 2013. doi:10.1557/jmr.2013.70.
- [9] K. Mergia, C. Jimenez, M.A. Lagos, "Joining of ceramic matrix composites to high and ultra high temperature ceramics for thermal protection systems" 7th European Workshop on Thermal Protection Systems and Hot Structures, 8 – 10 April 2013, ESA-ESTEC, Noordwijk, The Netherlands.
- [10] V. Liedtke, Ground Testing of Re-Entry Materials – Methods, Challenges, and Significance for Application, ExtreMat Workshop "Space Materials for High Temperature Applications", Politecnico di Torino (I), 26th/27th June 2007.

Joining of ceramic matrix composites to high and ultra high temperature ceramics for thermal protection systems

K. Mergia⁽¹⁾, C. Jimenez⁽²⁾, P. Yialouris⁽¹⁾, M. Lagos⁽²⁾, I. Agote⁽²⁾, Y. Panayiotatos⁽¹⁾, L. Volker⁽³⁾, E. Padovano⁽⁴⁾,
C. Badini⁽⁴⁾, C. Wilhelmi⁽⁵⁾, S. Messoloras⁽¹⁾, J. Barcena⁽²⁾

⁽¹⁾*N.C.S.R. "Demokritos"*
Institute of Nuclear and Radiological Science, Energy, Technology and Safety
Aghia Paraskevi, 15310 Athens, Greece
Email: kmergia@ipta.demokritos.gr

⁽²⁾*Tecnalia Research & Innovation.*
Industry and Transport Division
Mikeletegi Pasealekua, 2, Donostia-San Sebastian, Spain
Email: cristina@tecnalia.com

⁽³⁾*Aerospace & Advanced Composites GmbH*
Viktor-Kaplan-Straße 2.A-2700 Wiener Neustadt, Austria
Email: volker.liedtke@aac-research.at

⁽⁴⁾*Politecnico di Torino*
Department of Applied Science and Technology
Corso Duca degli Abruzzi, 24. 10129, Torino, Italy
Email: claudi.badini@polito.it

⁽⁵⁾*EADS Innovation Works*
Dept. TCC 2 / CTOIWMS. 81663 Munich, Germany
Email: Christian.Wilhelmi@eads.net

INTRODUCTION

Advanced Ceramic Matrix Composite (CMC) based on SiC matrix reinforced with carbon fibers (C_f/SiC) materials are key materials for aerospace applications since they present superior mechanical properties and resistance against high temperatures and at the same time they are lightweight and cost effective. For the application of these bulk ceramics in hostile environments appropriate coatings have to be developed that will prevent the oxidation of the carbon fibers. The current thermal protection systems are based on the use of ceramic matrix composite materials coated with SiC [1] or other carbide based materials. SiC exhibits excellent oxidation resistance at high temperatures, because the formed glassy silica films prevent oxygen diffusion very efficiently and thus serve as protection against further oxidation. However, the amorphous silica at temperatures above 1200 °C crystallizes to cristobalite causing surface cracking and also reacts with water or Na/K vapor, resulting in severe degradation of the silica film [2].

On the other hand, ultra high temperature SiC based multilayer ceramics can be employed in combination with CMCs in order to provide systems with enhanced performance under the most severe re-entry conditions. The advantages in using multilayered ceramics stems from the capability of adjusting its architecture and its chemical composition. e.g. by incorporating ZrB_2 layers at the outer structure, and thus tuning the functionality of these protection layers to specific re-entry conditions i.e. the required service temperature and the oxidative environment these structures have to withstand. Therefore, advances in joining science and technology of CMC-ultra high temperature and oxidation resistant ceramics to SiC based multilayer ceramics are important in order the benefits of these advanced materials in aerospace applications to be realized.

The current work reports on a approach for the integration of external protective ceramic SiC based multilayers (SiC ML) with a thermostructural ceramic matrix composite (C_f/SiC), as part of a more complex system under a reference mission (Advanced Re-entry Vehicle). The integration method is based on diffusion brazing bonding. As a joining agent a filler metal based on a MAX-Phase Ti_3SiC_2 produced by self propagating high temperature synthesis has been employed. Ti_3SiC_2 has good stability at elevated temperatures, it presents both metallic and ceramic properties and plastic behaviour. It has a melting point higher than 3000 °C and a coefficient of thermal expansion (CTE) $9.12 \times 10^{-6}/K$ between 25 and 1200 °C [3]. It has been used in the past for the joining of SiC based ceramics in the temperature range 1200 to 1600 °C [4].

The process parameters of the joining method and their effect on the microstructure of the integrated structure are discussed. The structure and microstructure of the assembly has been investigated by optical microscopy, scanning

electron microscopy with energy dispersive analysis and X-ray diffraction measurements. Results from thermomechanical tests under re-entry conditions are presented and discussed with respect to envisaged applications.

EXPERIMENTAL PROCEDURES

The C_f/SiC (SICARBON) ceramic composites were supplied by EADS Innovation Works [5]. They consist of carbon fibers embedded in a silicon carbon matrix. The production process of this material is based on the Polymer Infiltration Pyrolysis process (PIP). The infiltration of the carbon fibers with a pre-ceramic polymer-based and powder-filled slurry system is performed by Liquid Polymer Infiltration (LPI) via filament winding. From the supplied material samples of 40×40 mm² were cut and used for all the experiments.

The SiC multilayers were fabricated by the tape casting technique followed by pressureless sintering [6]. The processing method involved several steps: SiC slurry preparation; tape cast-ing; stacking, debinding and pressureless sintering. The SiC multilayers used in the current study consist of eleven dense SiC layers.

For the joining of the SiC the ternary compound Ti₃Si_{1.5}C₂ was used as a filler metal which was produced by self propagating high temperature synthesis in a reaction furnace and in argon atmosphere using Ti, Si and C powders. The crystal structure of the filler was assessed by X-ray diffraction (XRD) measurements. The joints were fabricated employing the diffusion brazing technique in a high vacuum hot press furnace at 1600 °C. The pressures used were 2.7, 15 and 25 MPa. For the joints fabricated at 2.7 and 7 MPa the pressure was applies at room temperature and kept constant during the thermal cycle. For the joint fabricated at 25 MPa at the beginning of the thermal cycle and up to 1400 °C a lower pressure of 15 MPa was applied up and for the rest of the thermal cycle during heating and cooling the pressure of 25 MPa was applied. A heating rate of 15 °C/min up to 1400 °C, followed by a heating rate of 10 °C/min up to 1600 °C and a slow cooling rate of 5 °C/min were applied.

The XRD patterns were measured using a Bruker D8 diffractometer equipped with a Cu K α radiation, a parallel beam stemming from a Göbel mirror and a Văntec position sensitive detector with 9 degrees angular acceptance. The microstructure of the joints was examined using FEI Quanta Inspect scanning electron microscopy (SEM) coupled with energy dispersive X-ray spectroscopy (EDS).

Tests of the SiC-ML/CMC under re-entry conditions, i.e. temperature profiles under vacuum, were carried out at AAC's ground re-entry test rig [7] at a maximum temperature of 1794 and 1391 °C for each 5 cycles. The tests were performed under vacuum and the thermal profiles used correspond to two control points of the Advanced Re-entry vehicle (ARV) [8].

RESULTS AND DISCUSSION

The Ti₃Si_{1.5}C₂ filler metal crystallizes in the hexagonal P63/mmc space group and the XRD pattern of the compound produced by self propagating high temperature synthesis is depicted in Fig.1. The minority phases are TiC which crystallizes in the fcc cubic Fm-3m space group and Si₂Ti which crystallizes in the orthorhombic face-centered Fddd space group.

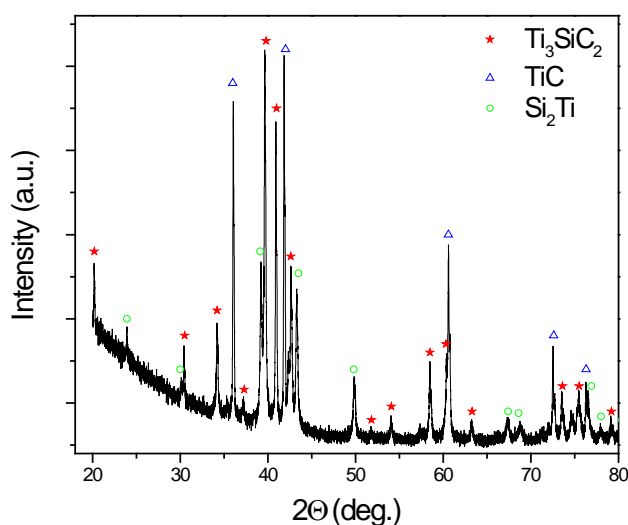


Fig.1. XRD pattern of Ti₃Si_{1.5}C₂.

Microstructure and Phase Analysis of the Joints

Fig.2a depicts, at a magnification of $\times 100$, the overview of the SiC ML- C_f /SiC joined structure fabricated at 25 MPa. The C_f /SiC consists of eleven SiC based interlayers reinforced with carbon fibers of an average thickness of 300 μm . The fiber orientation is at 90 degrees between the alternate interlayers. The top interlayer of the C_f /SiC has its carbon fibers vertical to the surface. The vertical to the SiC ML- C_f /SiC interface cracks that are observed in the C_f /SiC material are inherent in the material and are not produced during the joining process. Also few cracks appear in the filler vertical to the interface and in some cases they extend in the SiC multilayer up to its free surface. A more detailed micrograph of the same joint is presented in Fig.2b at a magnification of $\times 600$. It is observed that the filler wets properly both base materials and the joint is sound. The black dots at the lower part of Fig.2b in the region of the C_f /SiC are the carbon fibers that reinforce the composite ceramic material.

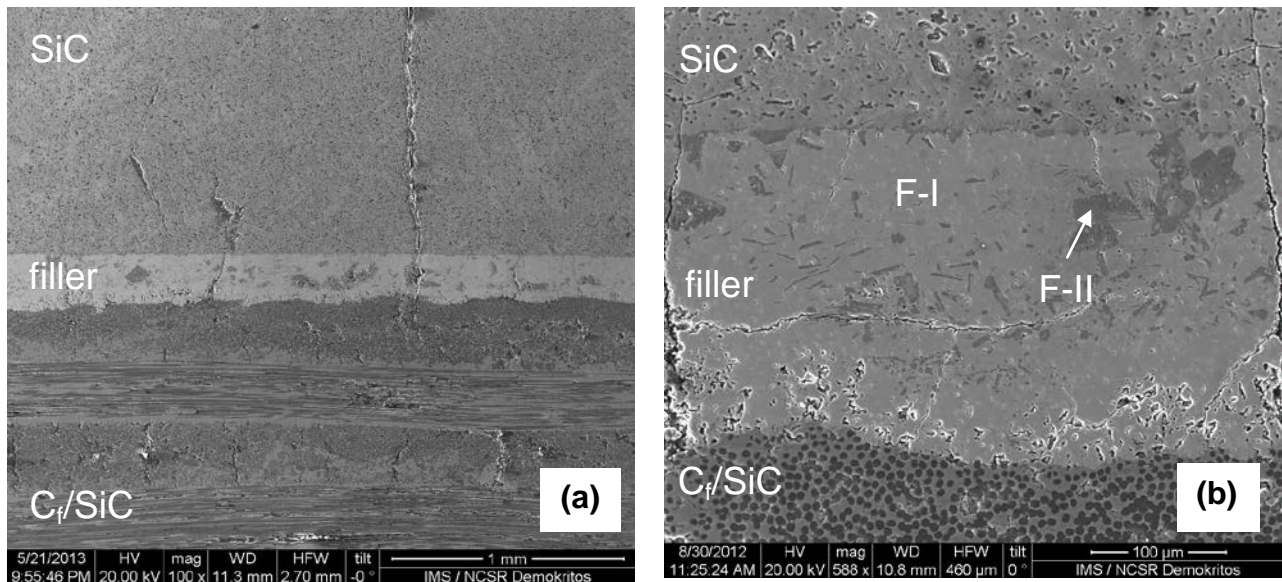


Fig.2. SEM micrographs of the SiC ML- C_f /SiC joint fabricated at 25 MPa at magnification $\times 100$ (a) and $\times 600$ (b).

The presence of cracks (Fig.2a, 2b) is attributed in the release of stresses, accumulated during the cooling of the joining process, due a) to the difference in the CTE between the base material and the filler and b) lack of flatness of the SiC ML. In general the vertical to the interface cracks are not expected to have a detrimental effect on the shear strength of the joint.

In the filler region two main areas are observed, a) the light grey area F-I and b) the dark grey area F-II (Fig.2b). The results from the EDX analysis of these two areas are presented in Table 1. The light grey area corresponds to phases of TiC and Ti_3SiC_2 whereas the dark grey area to the SiC or SiC+ Si_2Ti phase. The dispersion of the SiC phase in the filler region is quite inhomogeneous with a large scattering in the size of the SiC islands. The part of the joint adjacent to the C_f /SiC is characterized by a finer dispersion of this phase.

Table 1. EDX analysis of the filler area in the SiC ML- C_f /SiC joint fabricated at 25, 7 and 2.7 MPa pressure.

Pressure (MPa)		C (at%)	Si (at%)	Ti (at%)	Main Phases
25	F-I	46.0 - 49.0	1.4 - 3.0	48.0 - 52.0	TiC, Ti_3SiC_2
	F-II	47.3 - 48.4	46.8 - 52.7	0 - 4.8	SiC, Si_2Ti
7	F-I	38.0 - 42.0	12.0 - 15.0	46.0 - 47.0	Ti_3SiC_2
	F-II	41.0 - 49.0	35.0 - 40.0	11.0 - 24.0	SiC, Ti_3SiC_2
2.7	F-I	49.0 - 51.0	1.0 - 2.0	47.0 - 50.0	TiC, Ti_3SiC_2
	F-II	49.0 - 51.0	46.0 - 50.0	1.0 - 4.0	SiC

Fig. 3 depicts the SiC ML-filler and the filler- C_f /SiC interfaces. Both interfaces are continuous and sound. The black areas in the SiC are pores inherent in the SiC material.

The results, concerning the microstructure of the joints, are similar for the other pressures of 7 and 2.7 MPa used in the joining of SiC-ML to C_f /SiC as can be seen in Fig. 4. Whereas for both pressures the interface of the filler with the SiC

is continuous and sound, the interface with C_f/SiC is, on average, less continuous compared with the joint fabricated at 25 MPa pressure (Fig.3b).

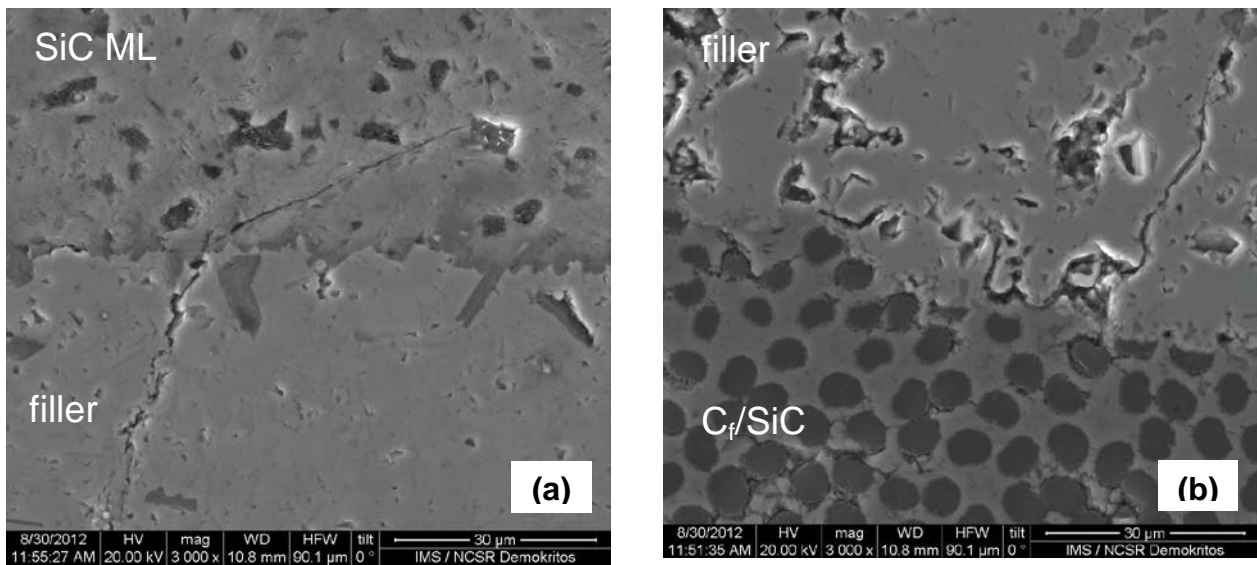


Fig.3. SiC ML-filler (a) and filler- C_f/SiC (b) interfaces of the SiC ML- C_f/SiC joint fabricated at 25 MPa pressure.

The results of the EDX analysis of the filler area for the joints fabricated at 7 and 2.7 MPa is presented in Table 1. In both joints we observe two main areas, the light grey one, F-I, and the dark grey one, F-II, as in the joint fabricated at 25 MPa. The chemical composition of these two areas is similar for the joints fabricated at 25 and 2.7 MPa pressure. The ternary phase Ti_3SiC_2 is the majority phase only for the 7 MPa joint. Since this cannot be an effect of the pressure used it must be due to different stoichiometries of the $Ti_3Si_{1.5}C_2$ powder used. It is also observed that as the applied pressure decreases the number density of the cracks decreases.

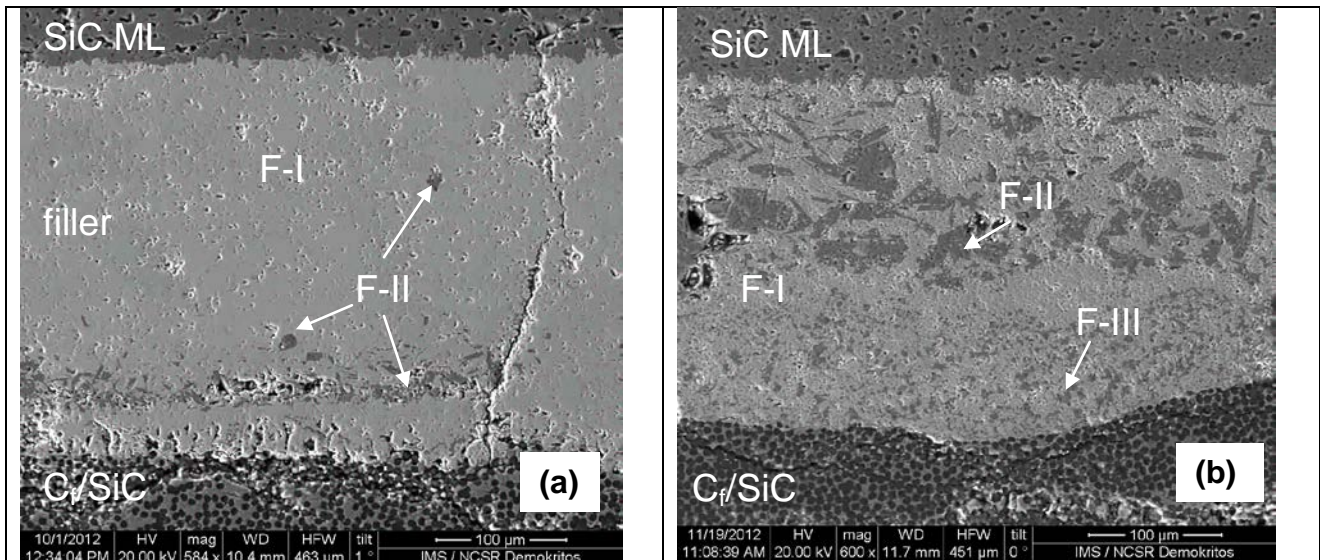


Fig.4. SEM micrographs of the SiC ML- C_f/SiC joints fabricated at 7 MPa (a) and 2.7 MPa (b) pressure.

Thermal Tests

SiC ML- C_f/SiC joints fabricated with an applied pressure of 2.7 MPa were subjected to preliminary re-entry tests up to 5 cycles under vacuum. The tests were performed using two different temperature profiles of the ARV, profile (a) with a peak temperature at 1391 °C (fig 5a) and profile (b) with a peak temperature at 1794 °C (fig 5b).

During the test the backside temperature of the joint, i.e. the back side of the C_f/SiC is monitored using a K-type thermocouple.

The temperature profiles of the two control points used in the tests are presented with the blue line in Fig.5. The red line in Fig.5 depicts the thermocouple temperature attached at the back side of the C_f/SiC . During the 2nd cycle of the test at

1794 °C the thermocouple was detached from the back surface of the C_f/SiC and the monitoring of the temperature is interrupted.

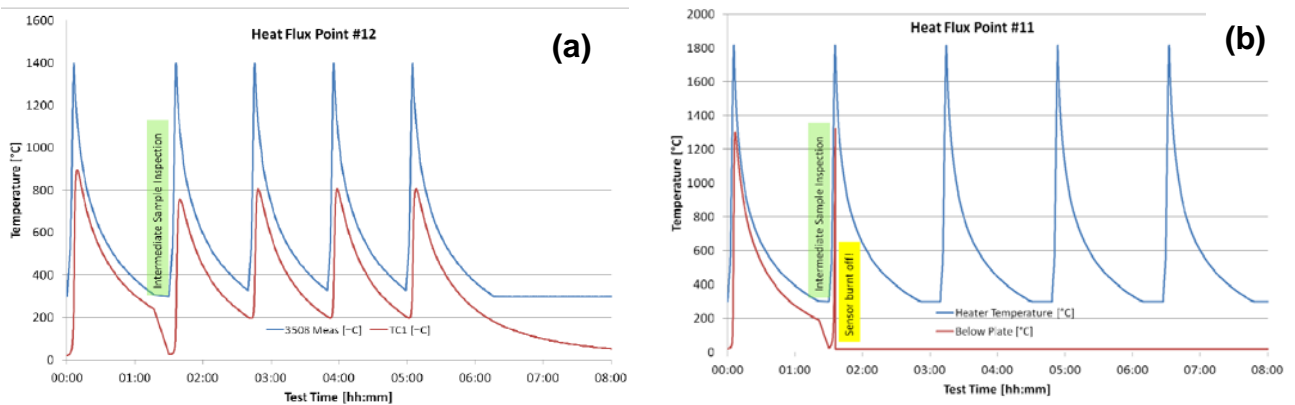


Fig.5. Temperature profiles used in the thermal tests.

The optical microscopy examination of the joints after the tests showed no detectable defects. The surface of the SiC that was subject to the thermal load was examined by SEM and XRD measurements. Figs.6a and 6b presents the surface of the SiC after the test at 1391 and 1794 °C, correspondingly. The results from the EDX analysis of the two surfaces are shown in Table 2. A high content of graphite is found on the surface of SiC which is not related with the re-entry tests and it stems from the fabrication of the SiC multilayers. The high graphite content is confirmed by XRD measurements on the SiC surface of the tested joints presented in Fig. 7 which show the presence of hexagonal graphite (P63/mmc space group). The dark areas in Fig. 6b is carbon and it comes from the graphite tiles that was used to place the structure to be joined in the hot press and remained on the surface of the SiC after the joining.

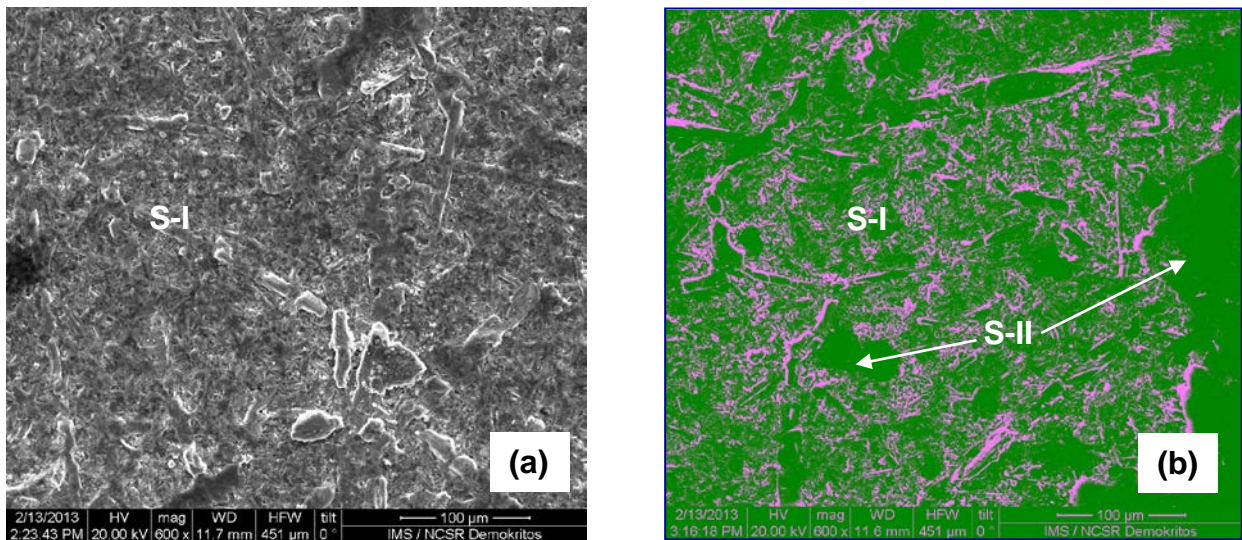


Fig.6. The surface of the SiC ML-Cf/SiC joint tested at 1391 (a) and 1794 °C (b).

Table 2. EDX analysis of the SiC ML surface and cross section of the SiC ML-C_f/SiC joints after the thermal tests.

Temperature (°C)			C (at%)	Si (at%)	O (at%)	Ti (at%)	Main phases
1391	surface	S-I	79 - 85	15 - 19	0 - 1	-	SiC, C
		F	19 - 51	17 - 26	3 - 7	29 - 48	Ti ₃ SiC ₂
	Cross section	F-I	49 - 50	3 - 4	-	47	Ti ₃ SiC ₂ , TiC
		F-II	34 - 47	52 - 64	-	0 - 7	SiC, Si ₂ Ti
1794	surface	S-I	67	31.5	0.1 - 1	-	SiC, C
		S-II	94	4	2	-	C
	Cross section	F-I	38 - 43	13 - 17	-	44 - 45	Ti ₃ SiC ₂
		F-II	45 - 51	47 - 50	-	2 - 8	SiC, Si ₂ Ti

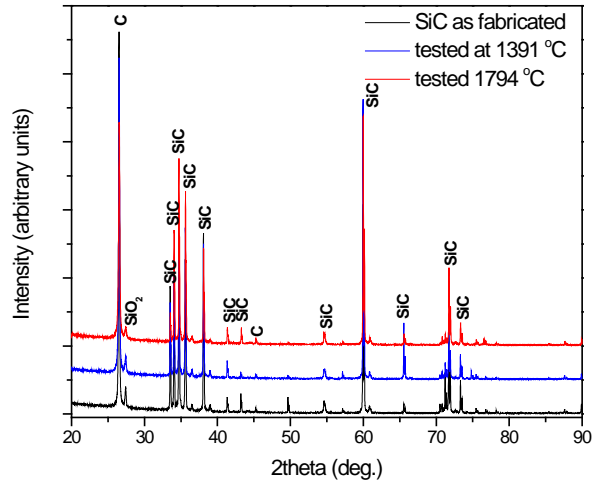


Fig.7. XRD spectra of the SiC surface as fabricated (black line), tested at 1391 °C (blue line) and at 1794 °C (red line).

The SEM examination of the areas of the SiC surface that present cracks show the presence of Ti₃SiC₂ grains from the filler that was used in the joining of the two ceramic parts. The cross section of the joints after the thermal test at both temperatures remain unaffected as depicted in Fig.9 showing that the thermal shock that these joints underwent did not influence their microstructure and their integrity. Table 2 presents also the results from the EDX analysis of the two areas, the light grey (F-I) and the dark grey (F-II), observed in the filler region, showing the presence of SiC islands in the TiC and or Ti₃SiC₂ matrix.

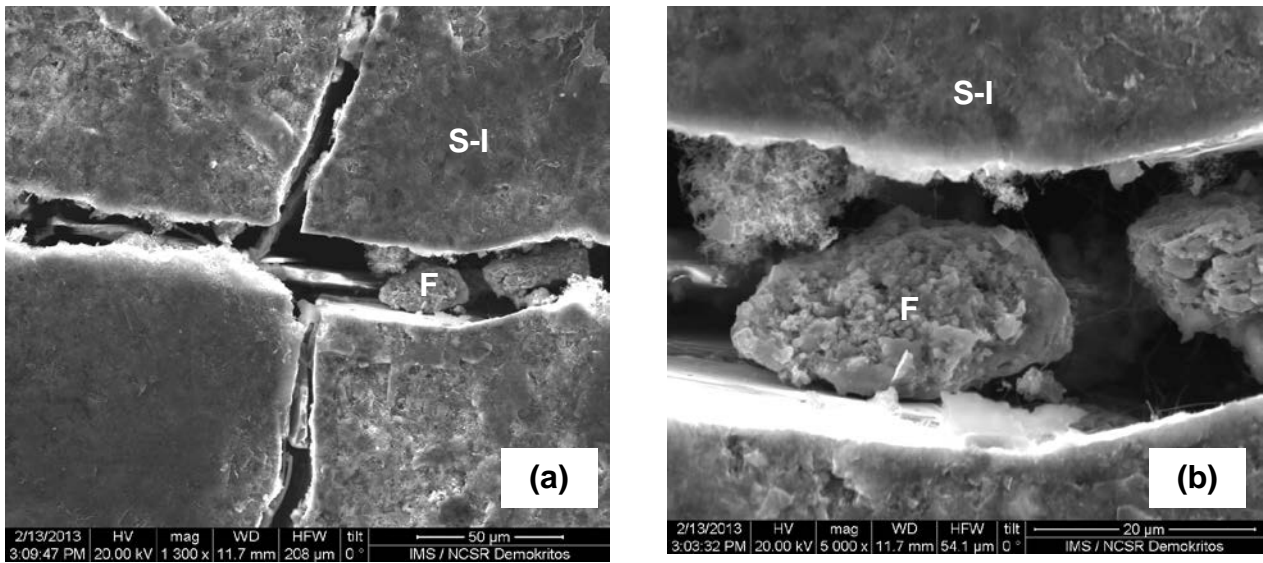


Fig.8. SEM micrographs of the SiC surface after the thermal test at 1391 °C at magnification ×1300 (a) and ×5000 (b).

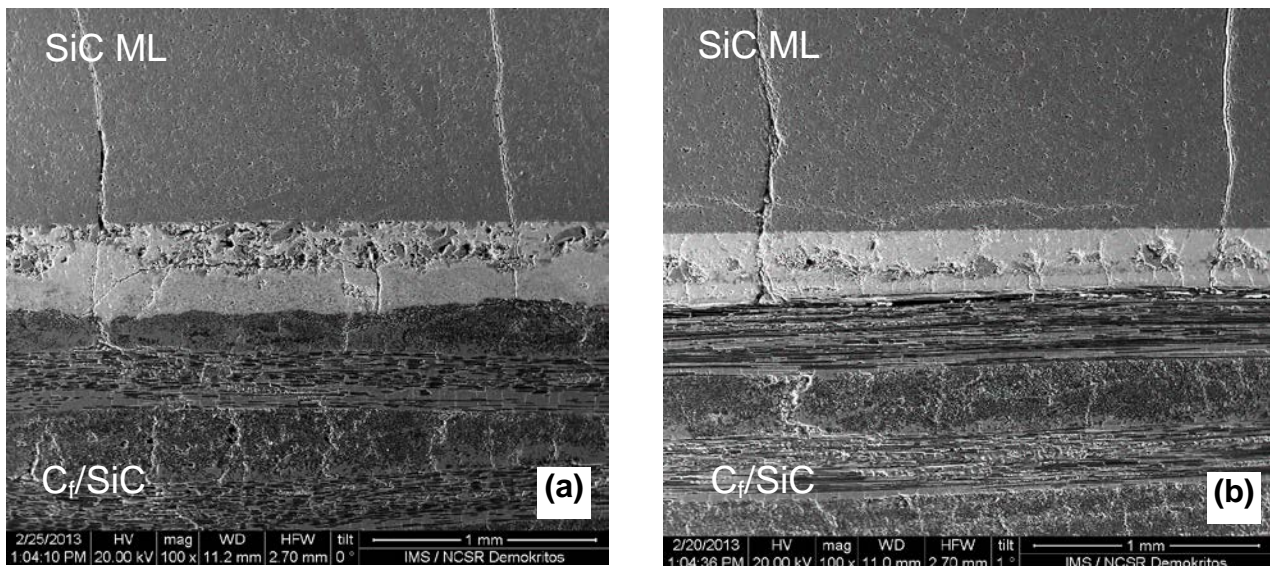


Fig. 9. SEM micrograph of the SiC ML-C_f/SiC cross section after the thermal test at 1391 (a) and 1794 °C (b).

CONCLUSIONS

Successful joining of SiC multilayers to C_f/SiC ceramic composite materials using the ternary carbide Ti₃Si_{1.5}C₂ and employing diffusion brazing bonding and pressures in the range 2.7 to 25 MPa was accomplished. Cracks appear in the filler area and few of them can extend up to the free surface of the SiC multilayer. The cracks are attributed to the brittle behavior of the filler, the CTE mismatch between the parts to be joined and the filler and to the lack of flatness of the SiC specimens. These cracks are vertical to the SiC ML-C_f/SiC interface and are not detrimental to the shear strength of the joint. Thermal tests under two re-entry conditions, in vacuum, have shown no detectable defects in the joints.

ACKNOWLEDGEMENTS

This work has been performed within the framework of the European Project “SMARTEES (G.A. n. 262749) with the financial support By the European Community. The paper only reflects the view of the authors and the European Community is not liable for any use of the information contained therein.

REFERENCES

- [1] I. Sakraker and C.O. Asma, “Experimental investigation of passive/active oxidation behavior of SiC based ceramic thermal protection materials exposed to high enthalpy plasma” *Journal of the European Ceramic Society*, vol. 33, pp. 351–359, 2013.
- [2] H. Kiyono, S. Shimada, and K.J.D. MacKenzie, “Kinetic and Magic Angle Spinning-Nuclear Magnetic Resonance Studies of Wet Oxidation of Beta-Sialon Powders”, *Journal of the Electrochemical Society*, vol. 148 pp.B86-B91, 2001.
- [3] M.W. Barsoum, T. El-Raghy, C.J. Rawn, W.D. Porter, H. Wang, E.A. Payzant, and C.R. Hubbard, “Thermal properties of Ti₃SiC₂” *Journal of Physics and Chemistry of Solids*, vol. 60, pp.429-439, 1999
- [4] H. Dong, S. Li, Y. Teng, and W. Ma, “Joining of SiC ceramic-based materials with ternary carbide Ti₃SiC₂”, *Materials Science and Engineering: B*, vol. 176(1), pp. 60–64, 2011.
- [5] G. Motz, S. Schmidt, and S. Beyer, “The PIP-process: Precursor Properties and Applications, Ceramic Matrix Composites”, W. Krenkel Ed., Germany, Wiley-VCH, pp. 165-186, 2008
- [6] W.S. Yang, S. Biamino, E. Padovano, M. Pavese, S. Marchisio, G. D’Amico, S. Ceresa MioX. Chen, P. Fino, and C. Badini, “Thermophysical properties of SiC multilayer prepared by tape casting and pressureless sintering” *Composite Structures*, vol. 96, pp. 469–475, 2013
- [7] J. Barcena, M. Lagos, I. Agote, C. Jimenez, X. Hernandez, C. Badini, E. Padovano, S. Gianella, D. Gaia, V. Liedtke, K. Mergia, S. Messoloras, P. Yialouris, Y. Panayiotatos, A. Ortona, C. D’Angelo, and C. Wilhelmi, “SMARTEES FP7 Space Project – Towards a New TPS Reusable Concept for Atmospheric Reentry from Low Earth Orbit”, 7th European Workshop on Thermal Protection Systems and Hot Structures, 8 – 10 April 2013, ESA-ESTEC, Noordwijk, The Netherlands.
- [8] T. Salmon, X. Vo, and M. Bottacini, “TPS Architecture on ARV” Proceedings of the 7th European Symposium on Aerothermodynamics, by Ouwehand, L. Noordwijk, Netherlands: European Space Agency, 2011, id.120



Joining of ceramic matrix composites to high and ultra high temperature ceramics for thermal protection systems

C. Jimenez¹, M. Lagos¹, I. Agote¹,
P. Yialouris², K. Mergia², Y. Panayiotatos², S. Messoloras²,
L. Volker³, E. Padovano⁴, C. Badini⁴, C. Wilhelmi⁵ and J. Barcena¹

¹Tecnalia Research and Innovation (Spain)

²National Center for Scientific Research "Demokritos" (Greece)

³ Aerospace & Advanced Composites (Austria)

⁴ Politecnico di Torino (Italy)

⁵ EADS Innovation Works (Germany)



7th european workshop on tps & hs
8 - 10 april 2013

European Space Agency



The research leading to these results has received funding from the European Union Seventh Framework Programme (FP7/2007-2013) under grant agreement n° 283797



Outline



- Introduction & motivation
- Materials to be joined
 - SiC multilayer
 - Ceramic matrix composites
- Joining procedure
- Structural characterization of the joints
- Thermomechanical characterization of the joints
- Conclusions
- Acknowledgments

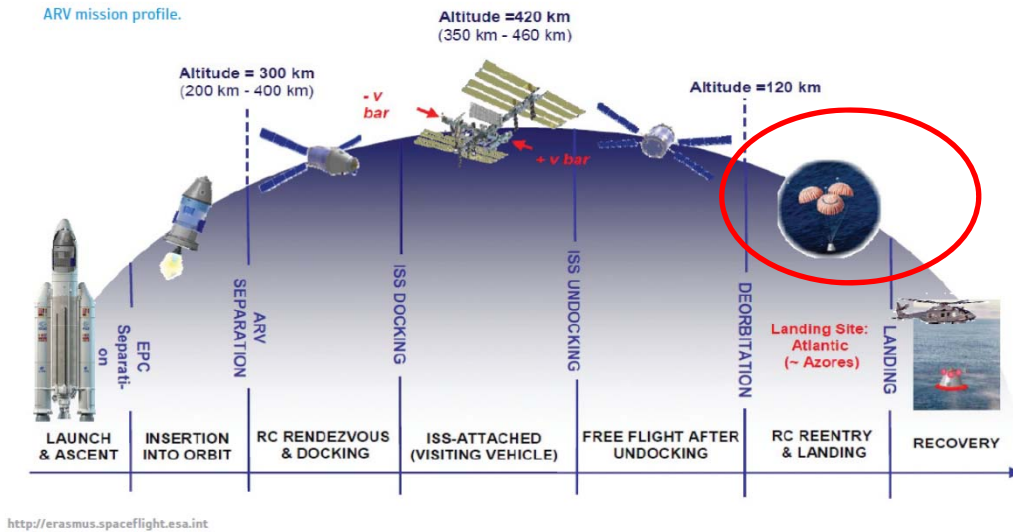


Introduction & Motivation



- There is a strong interest in the development of reusable systems to access and return from Space, i.e. reusable capsules.
- These reusable systems demand a huge effort, not only in the development of new materials but also in the integration of them into the subsystems.
- Current state-of-the-art protection materials is mainly based on bulk ceramics or on CMCs coated by i.e. HfC, ZrC, SiC CVD.
- Through SMARTees project a new approach has been proposed based on bulk ceramic multilayer design. This allows a higher flexibility for design (i.e. complex gradient layers) but integration with composite ceramic substrate and subsystems is a big challenge!
- In the current work we report on the integration of ceramic SiC based multilayers with a thermostructural ceramic matrix composite (CMC) as part of a Thermal Protection System (TPS).

The Mission selected is based on the **ARV/CTV***:



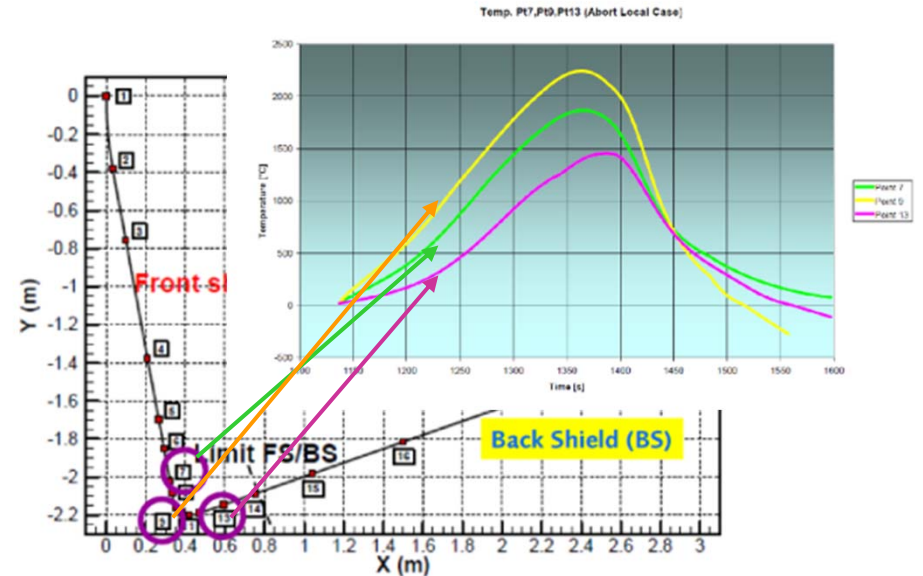
- Re-entry module evolved from Automated Transfer Vehicle (ATV). It is a real mission owned by ESA and developed by Astrium GmbH, which consists of a capsule-like concept for a service module to the International Space Station (ISS).
- ARV will provide a valuable service to the ISS in payload upload and download. There are two versions for cargo or crew system. The re-entry will be from LEO (500 km). The first flight will not be reusable and currently there is a trade-off of designs (the currently favoured one is similar to Apollo).

For more details visit ARV's webpage:

http://www.esa.int/Our_Activities/Human_Spaceflight/ATV/ATV_evolution_Advanced_Reentry_Vehicle_ARV

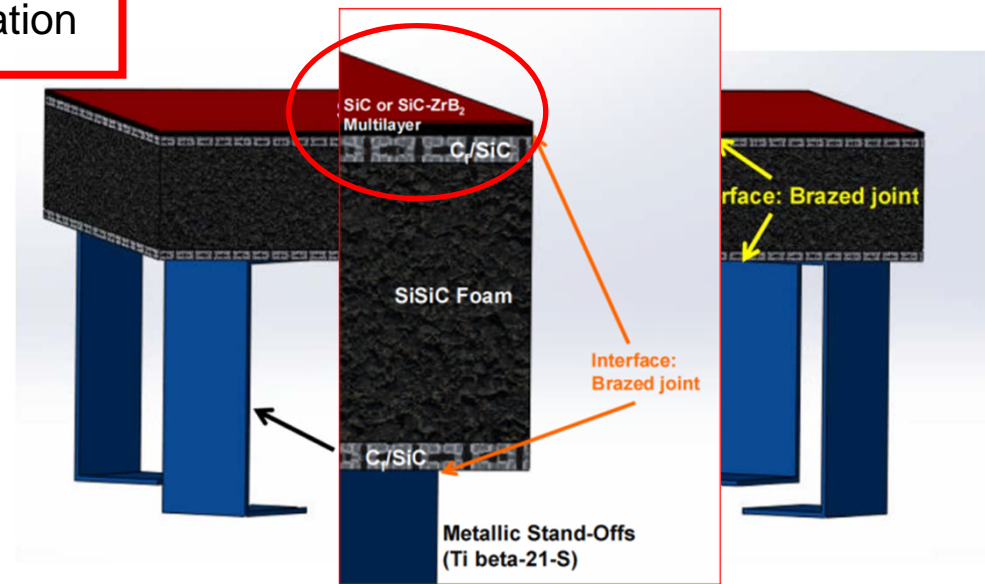
The following specifications have been collected:

- Heat fluxes profiles
- Pressure profile
- Mechanical load
- Aerial mass
- 3 different scenarios have been envisaged



The conceptual TPS design is based:

- SiC based multilayers to CMCs integration
- &
- CMCs to Ti alloy stand-offs integration



Schematic conceptual design

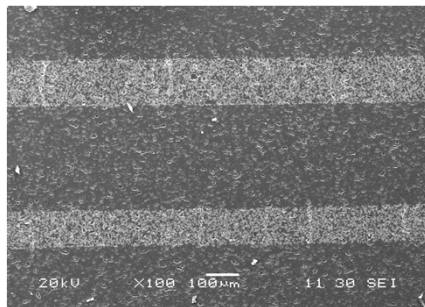
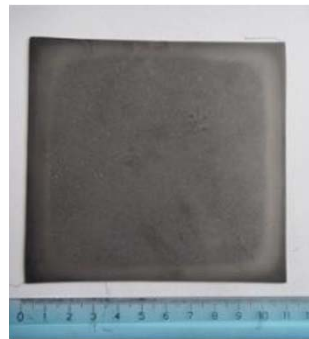
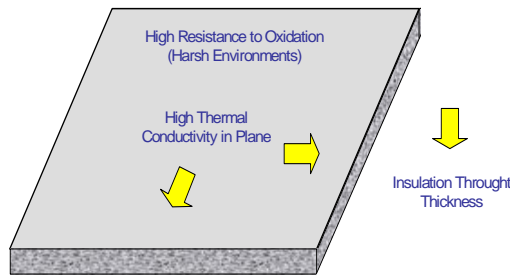


External protective structure: SiC based multilayers



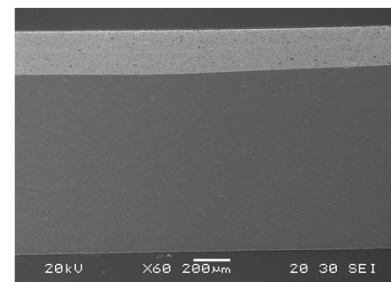
External protective multilayers based on high and ultrahigh temperature ceramics:

- High temperature (SiC based) suitable for temperatures below 1700 °C.
- Ultrahigh temperature ceramics (SiC-ZrB₂ based) suitable for temperatures above 1700 °C.
- Two manufacturing routes are employed: **tape casting** followed by **pressureless sintering** and **spark plasma sintering**



- 2 SiC layers
- 1 50vol%ZrB₂ + 50vol%SiC
- 2 SiC layers
- 1 50vol%ZrB₂ + 50vol%SiC
- 4 SiC layers

Politecnico di Torino (C. Badini) - Pressureless sintering



- 2 80vol%ZrB₂ + 20vol%SiC
- 8 dense SiC

TECNALIA (M. Lagos)- Spark Plasma Sintering

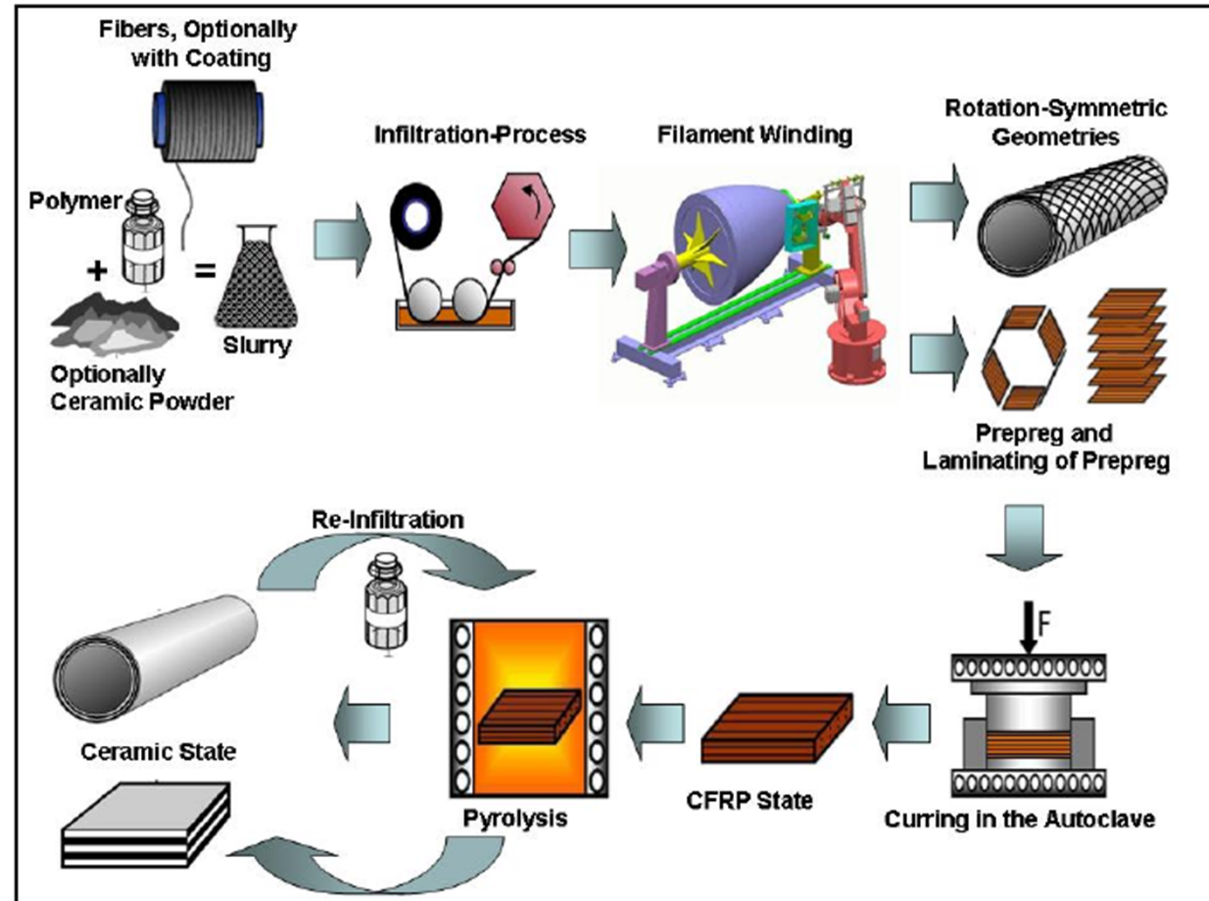
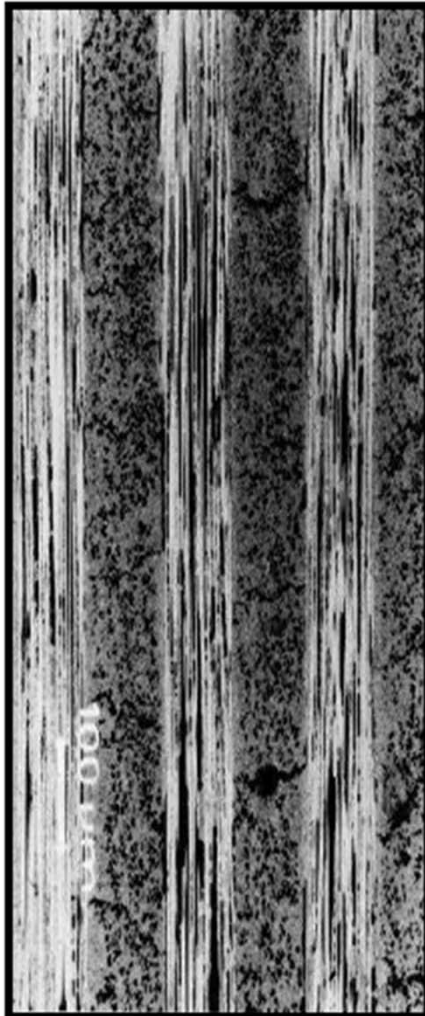


Materials: Ceramic Matrix Composites



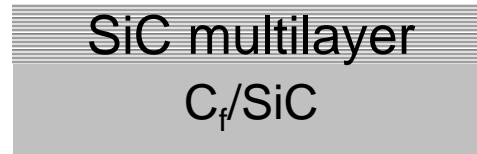
CMC (C_f/SiC) from EADS (PIP Process)

SiCARBON™





Joining process



The joining process is based on diffusion brazing using $\text{Ti}_3\text{Si}_{1.5}\text{C}_2$ filler at 1600 °C and pressure in the range 2 to 50 MPa.

A hot press furnace is employed for the fabrication of the joints.

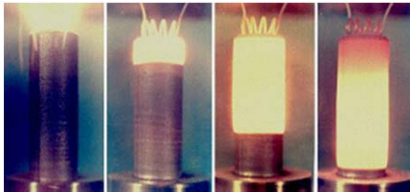
The joints were microstructurally investigated as a function of the **applied pressure** using optical and scanning electron microscopy with EDX analysis and X-ray diffraction.

Thermal tests under re-entry conditions are used to validate their performance.

Ti₃SiC₂ filler

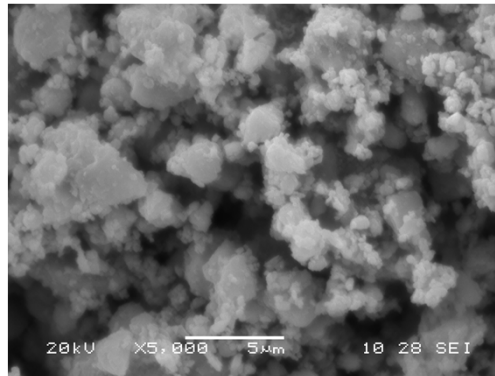
Ti₃SiC₂ possesses a combination of metallic and ceramic properties:

- Good stability at elevated temperatures
- CTE $7-9 \times 10^{-6} \text{ K}^{-1}$
- Young modulus 322 GPa
- $T_{\text{melting}} > 3000 \text{ }^\circ\text{C}$
- Plastic behavior



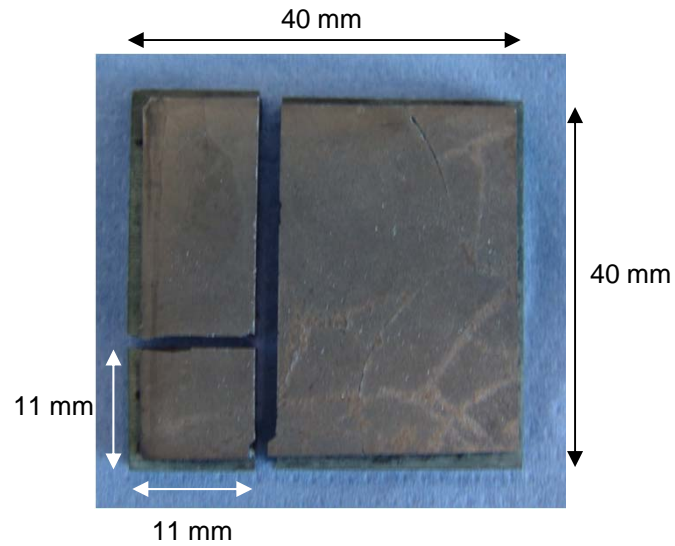
Self-propagating reaction

The filler Ti₃SiC₂ was produced by **Self-propagating High-temperature Synthesis (SHS)**. In this technique, the exothermic reaction between the elements is initiated by heating the sample locally. Once initiated, the reaction is self-sustained.

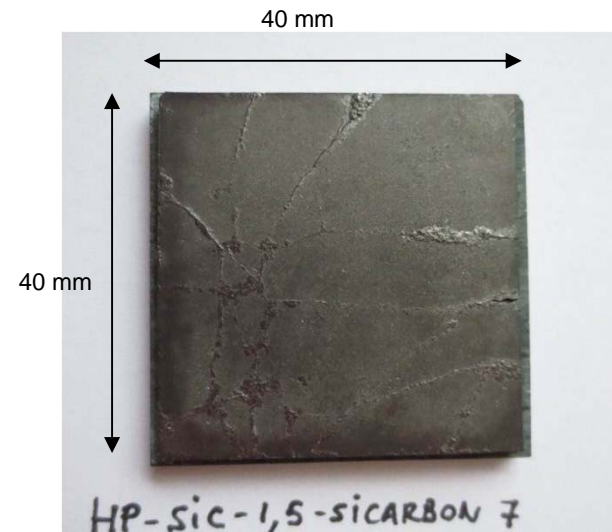


XRD: main phase Ti₃SiC₂,
Secondary phases TiC, Ti₅Si₃

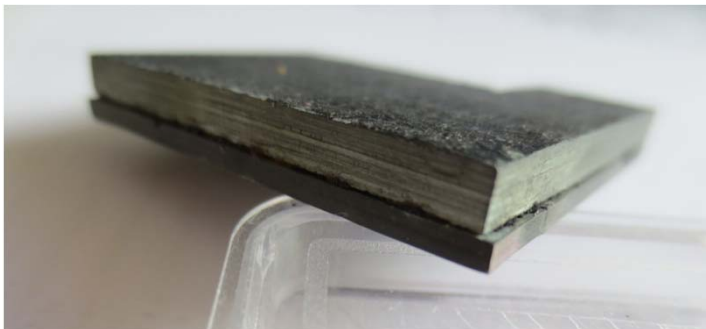
25 MPa pressure



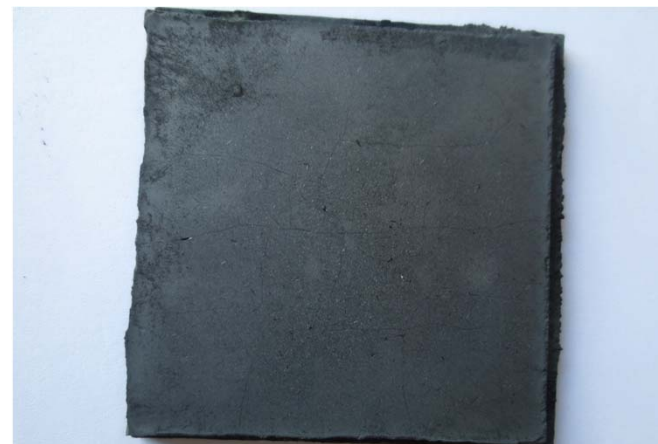
7 MPa pressure



3 MPa pressure



2 MPa pressure





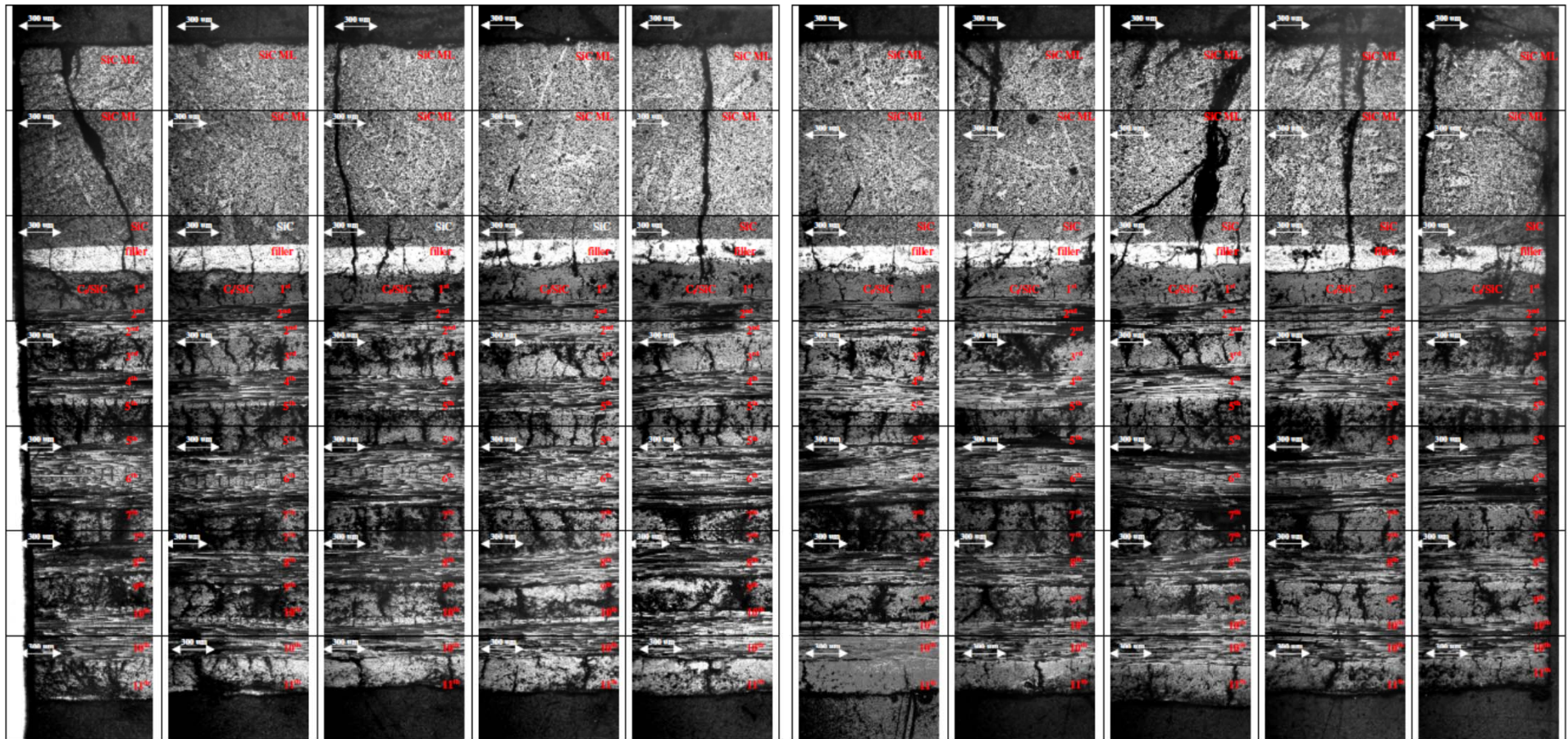
Joint characterization: Overview of joint cross sections



25 MPa pressure

40 mm

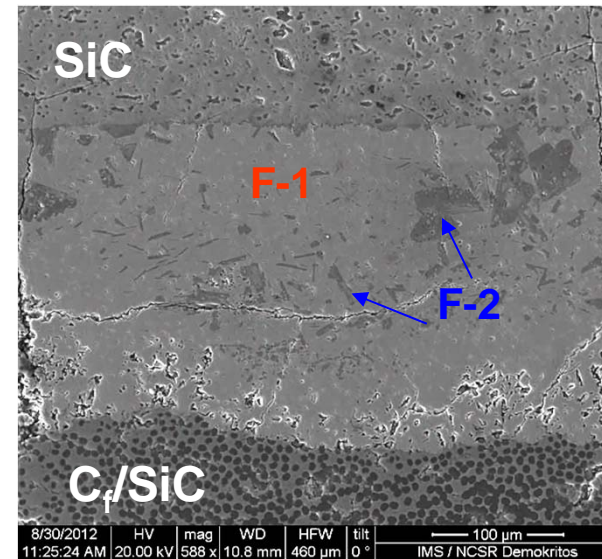
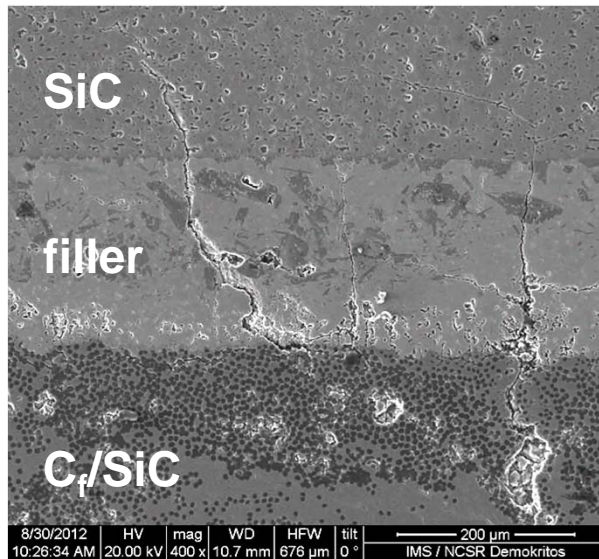
Mapping of the joint along cd direction



11 mm

25 MPa pressure

Cross sections - SEM investigation



	C (at%)	Si (at%)	Ti (at%)	Main Phases
F-1	46.0 – 49.0	1.4 - 3.0	48.0 – 52.0	TiC + Ti ₃ SiC ₂
F-2	47.3 - 48.4	46.8 – 52.7	0 – 4.8	SiC

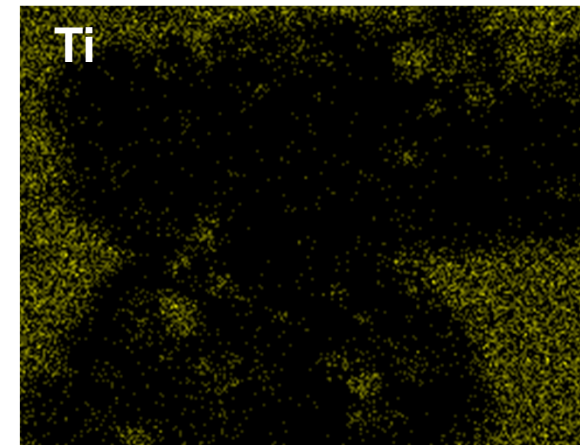
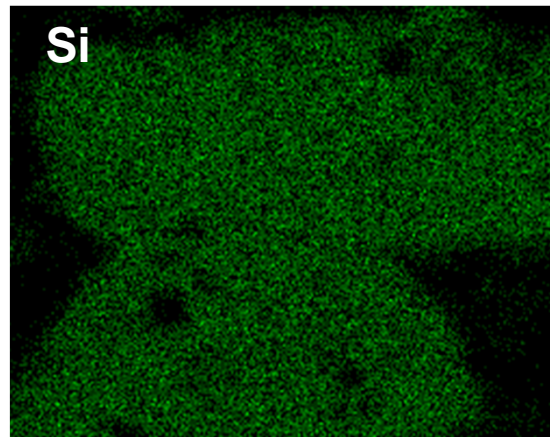
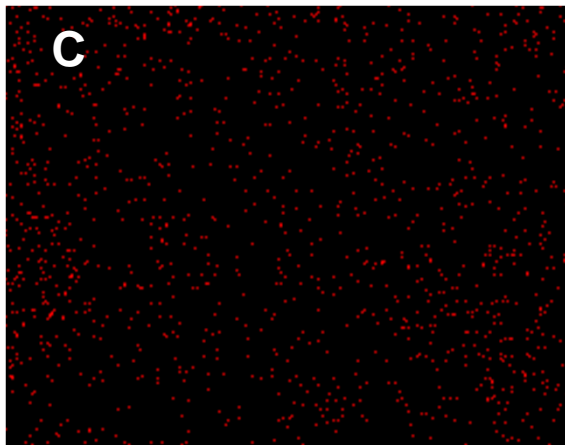
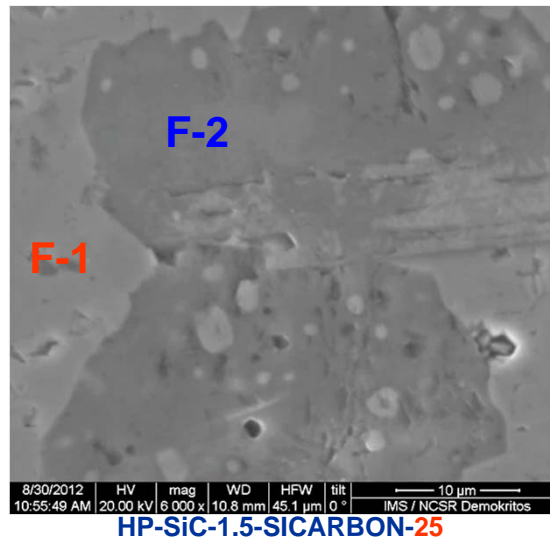
The filler wets properly both base materials and the joint is in general sound.

The cracks are generally attributed to:

- Release of internal stresses during specimen cutting
- Lack of flatness of the SiC multilayer
- CTE mismatch of the filler with the materials joined

25 MPa pressure

Elemental mapping in the filler area



	C (at%)	Si (at%)	Ti (at%)	Main Phases
F-1	46.0 – 49.0	1.4 - 3.0	48.0 – 52.0	TiC + Ti₃SiC₂
F-2	47.3 - 48.4	46.8 – 52.7	0 – 4.8	SiC

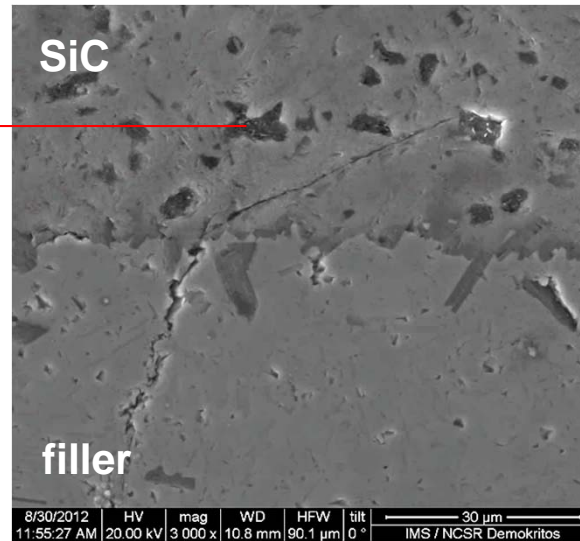


Joint characterization: interfaces

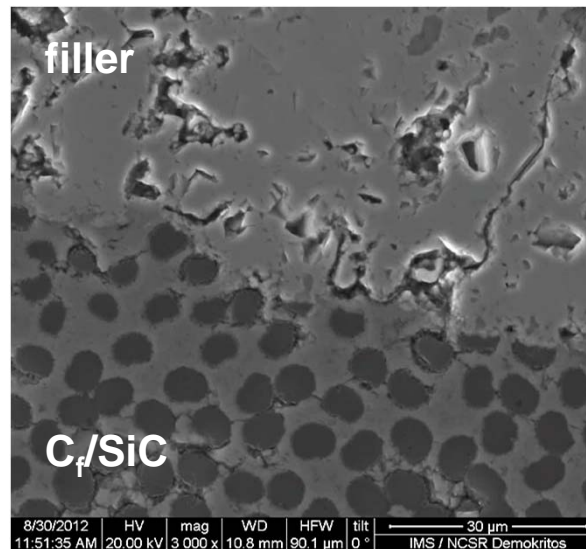


25 MPa pressure

Pores



SiC/CMC interface



SiC/CMC interface

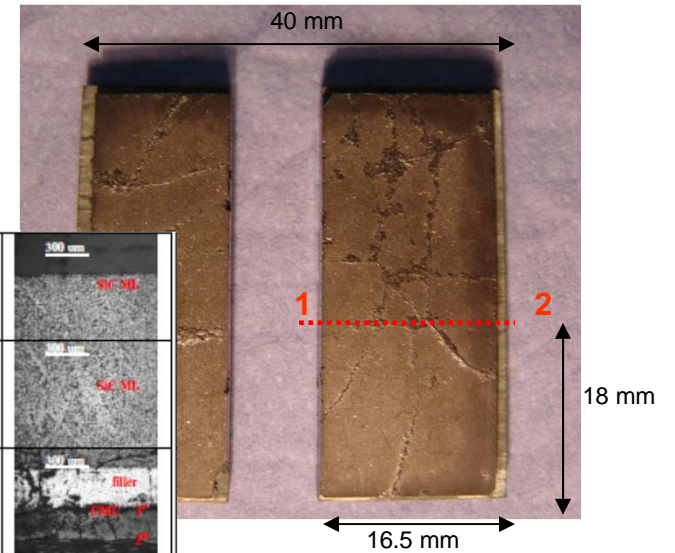
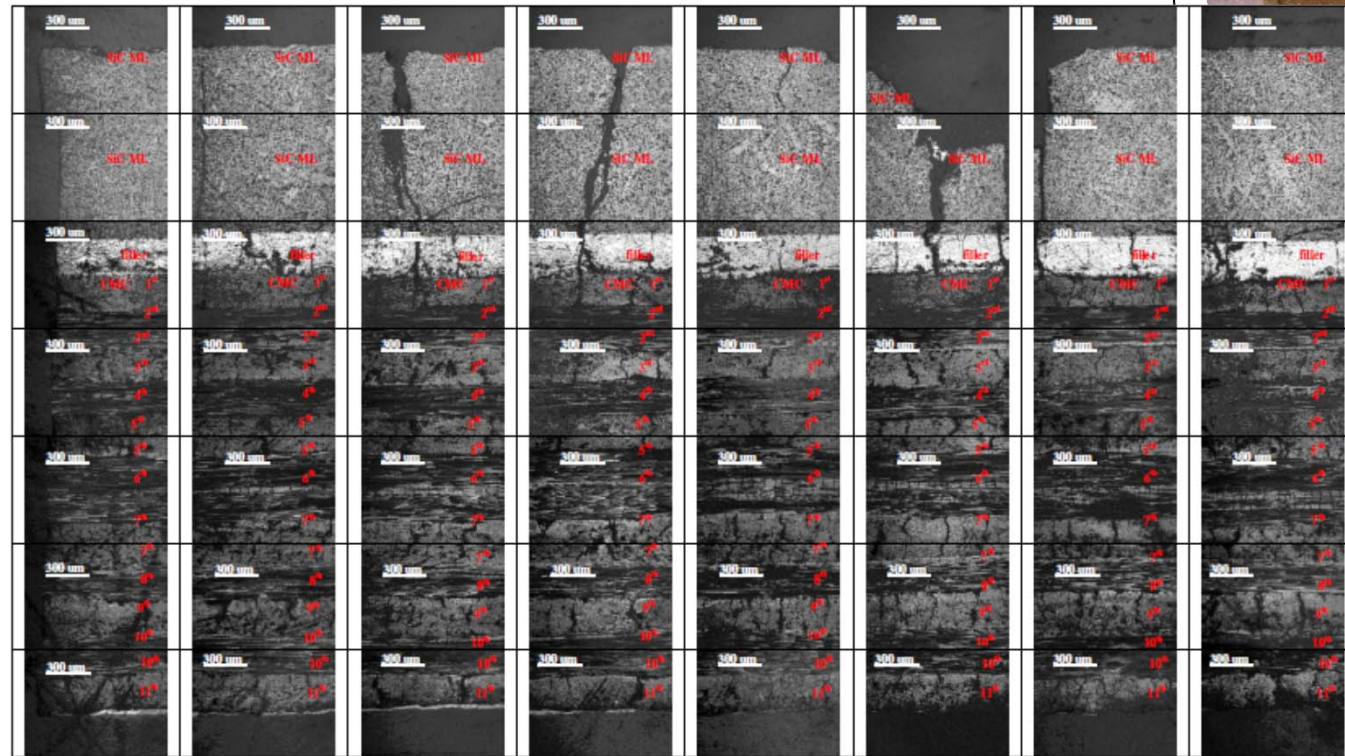


Joint characterization: Overview of joints

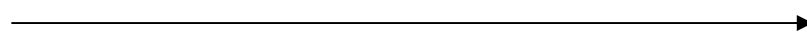


7 MPa pressure

Mapping of the joint along 1-2 direction



Left edge



center

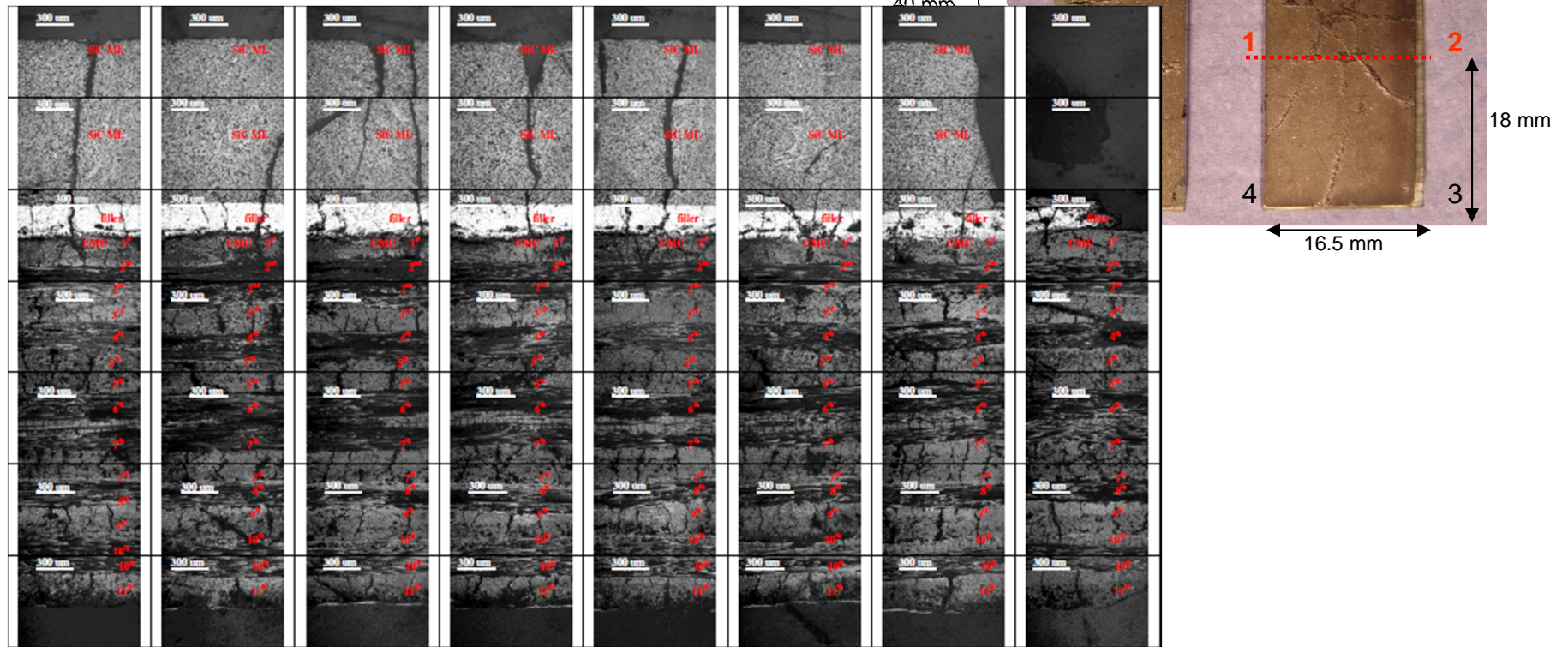


Joint characterization: Overview of joints



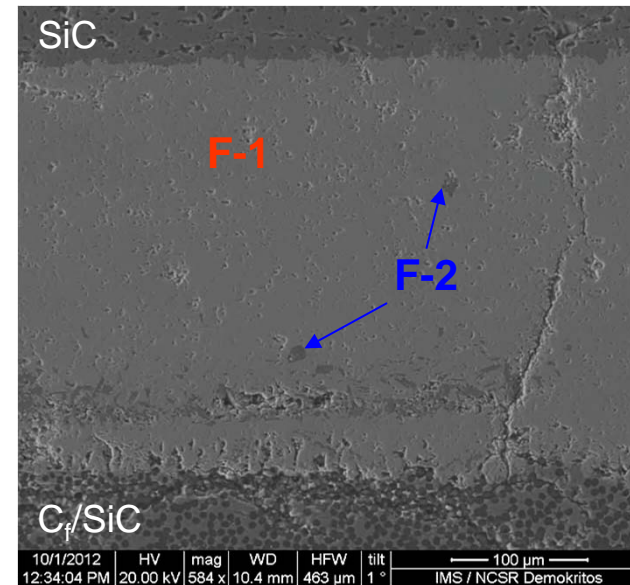
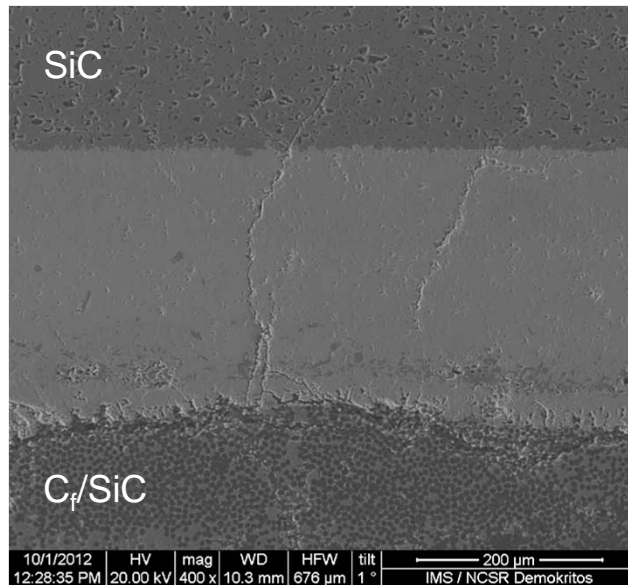
7 MPa pressure

Mapping of the joint along 1-2 direction



Center → Right edge

7 MPa pressure

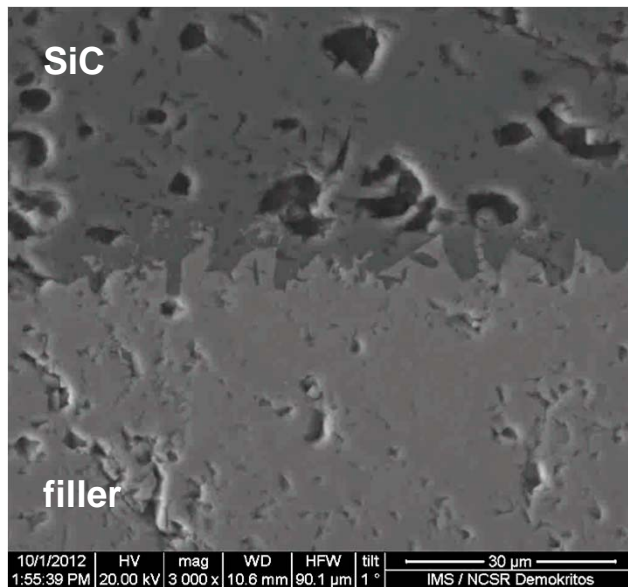


	C (at%)	Si (at%)	Ti (at%)	Main Phases
F-1	38.0 – 42.0	12.0 – 15.0	46 – 47	Ti₃SiC₂ + TiC
F-2	41 – 49	35 – 40	11 – 24	SiC+Ti₃SiC₂

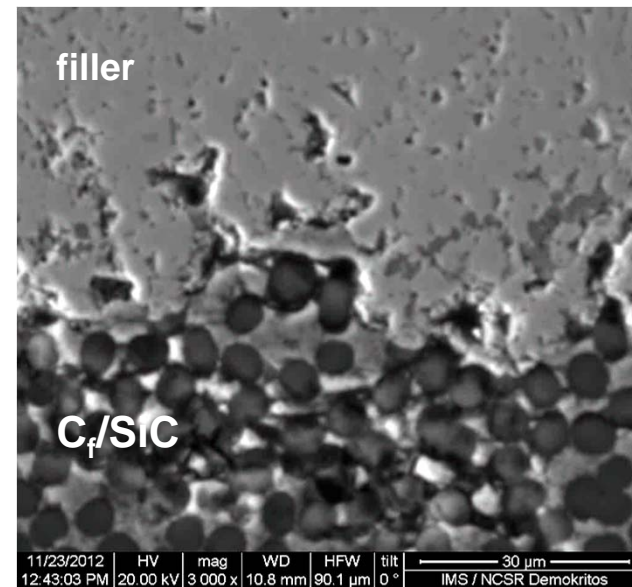


Joint characterization: interfaces

7 MPa pressure



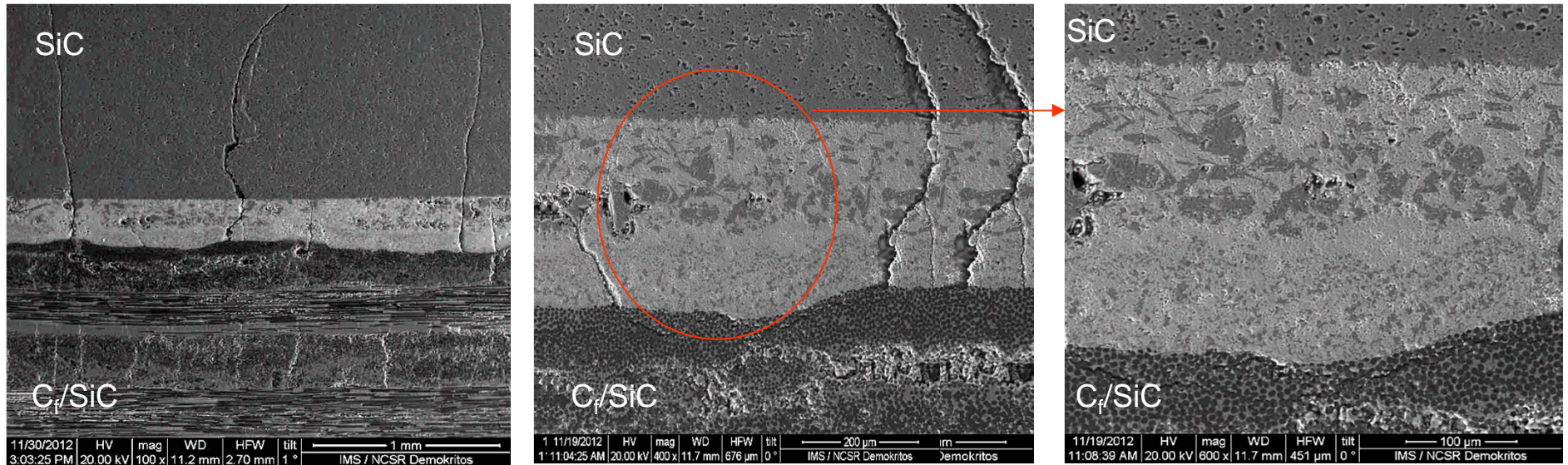
SiC/filler interface



filler/CMC interface

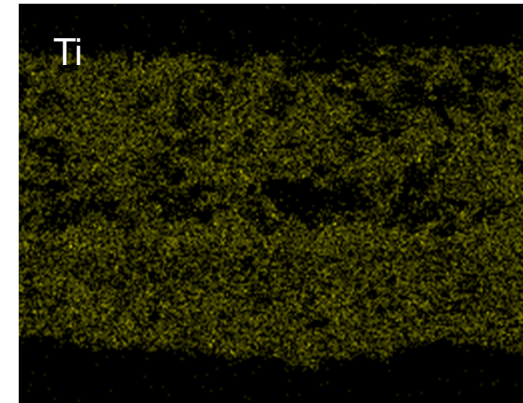
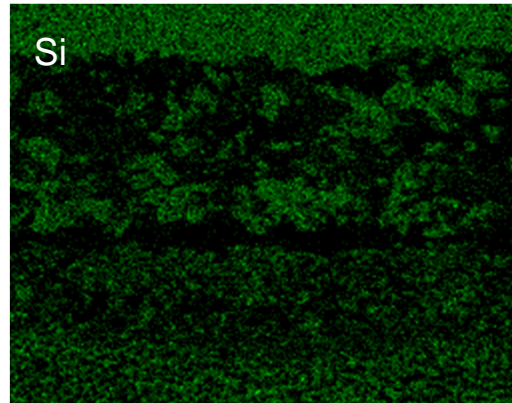
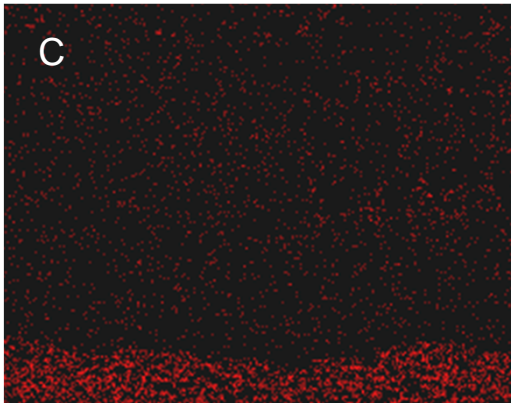
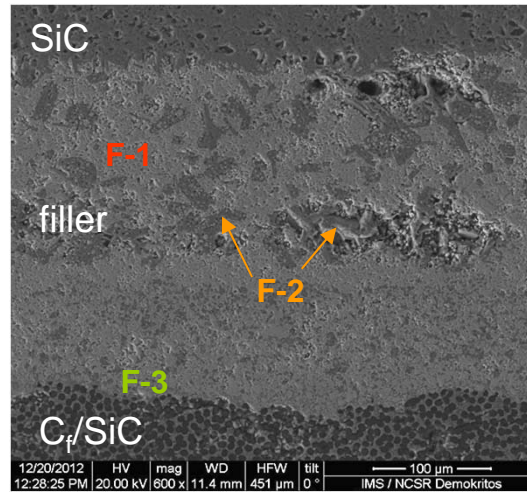
The bonding between the CMC and the filler is not as sound as in the case of 25 MPa pressure

3 MPa pressure



Fewer vertical to the interface cracks appear compared with the joints of 25 and 7 MPa

3 MPa pressure



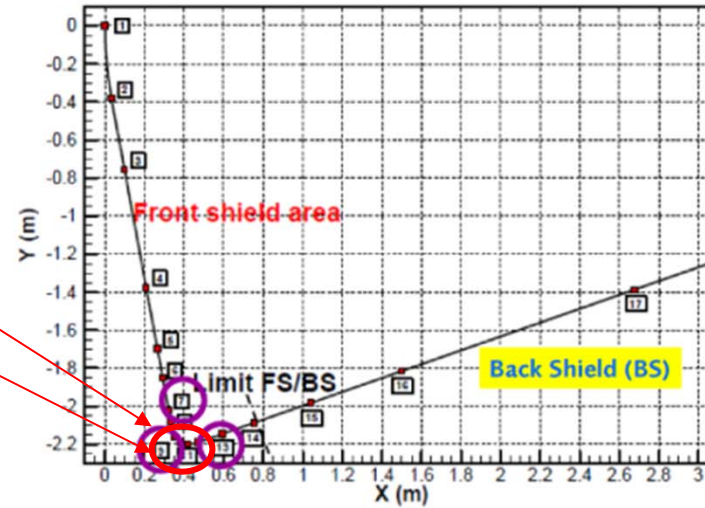
Joint zone	C (at%)	Si (at%)	Ti (at%)	Main Phases
F-1	50.4	1.5	48.1	TiC
F-2	49.6 -54.4	44.6-48.3	1.0-2.1	SiC
F-3	48.7	20.0	31.3	TiC, SiC



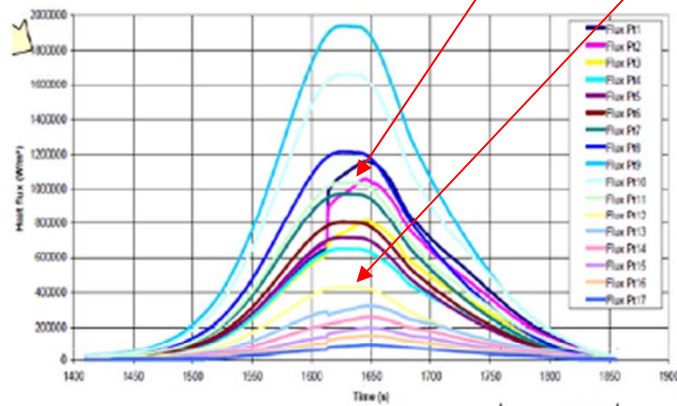
Joint thermal tests – temperature profiles



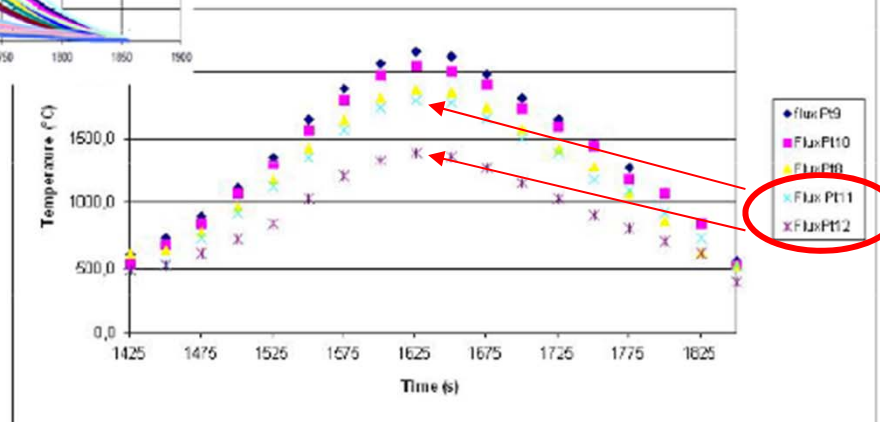
Points 11 and 12 were used



Heating profiles of #11 & #12



Temperature plot in different point of the spacecraft

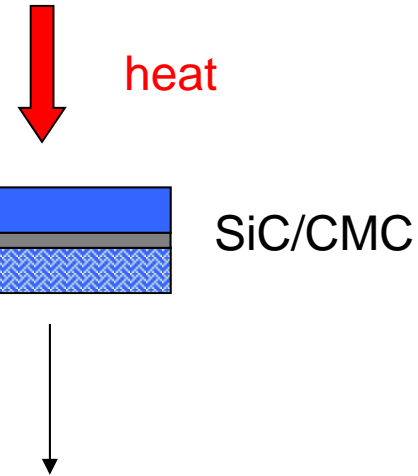
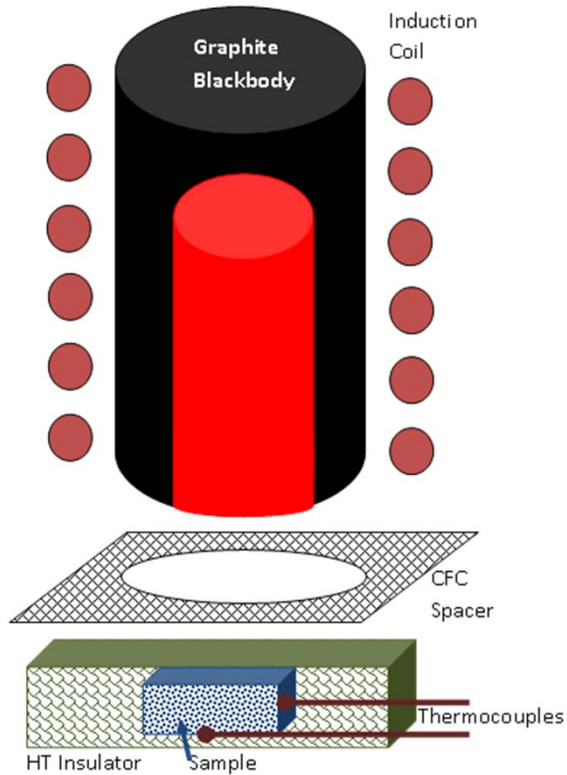




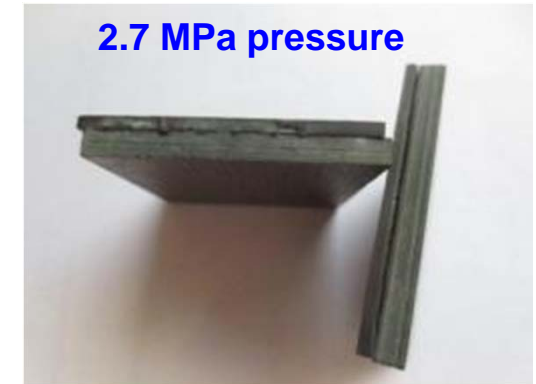
Joint thermal tests – Experimental Setup



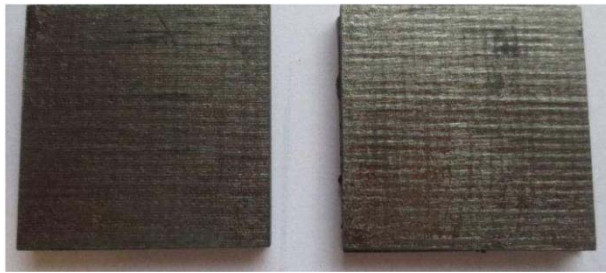
Experimental set-up



Recording of the temperature at the back side



Before the re-entry tests

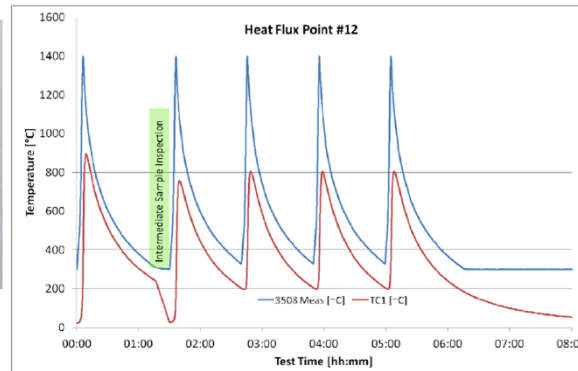
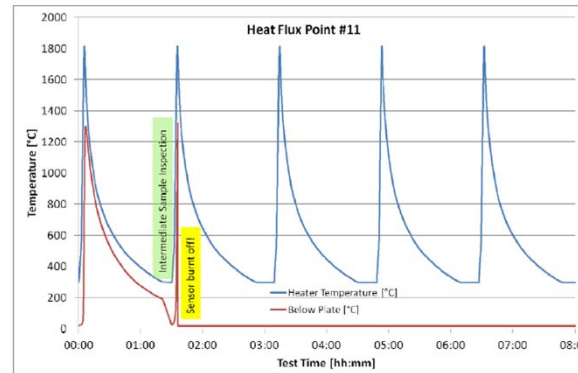


CMC surface



SiC multilayer surface

Re-entry profiles



After the re-entry tests



CMC surface



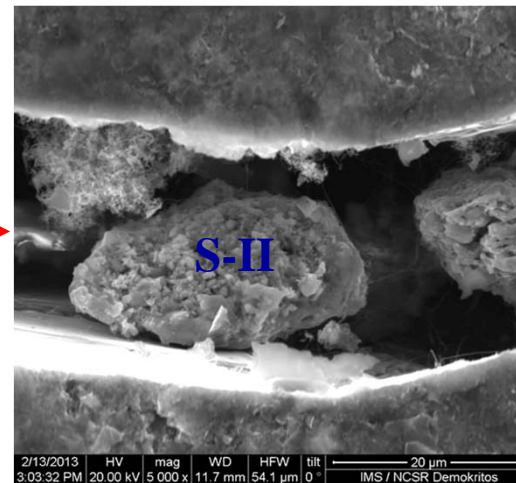
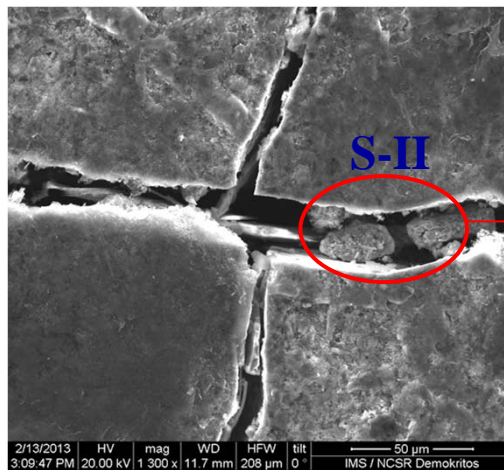
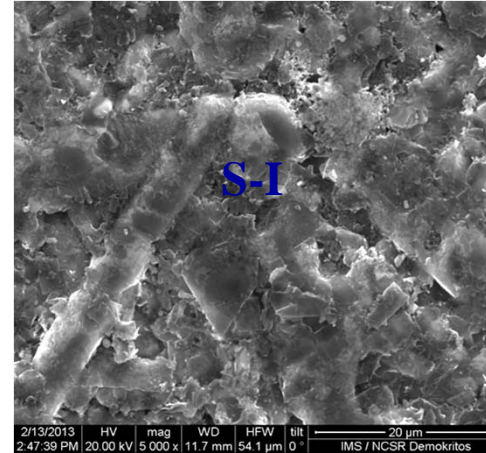
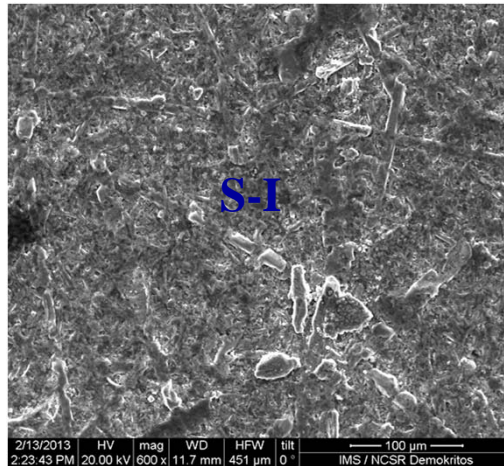
SiC multilayer surface

High heat flux

Lower heat flux

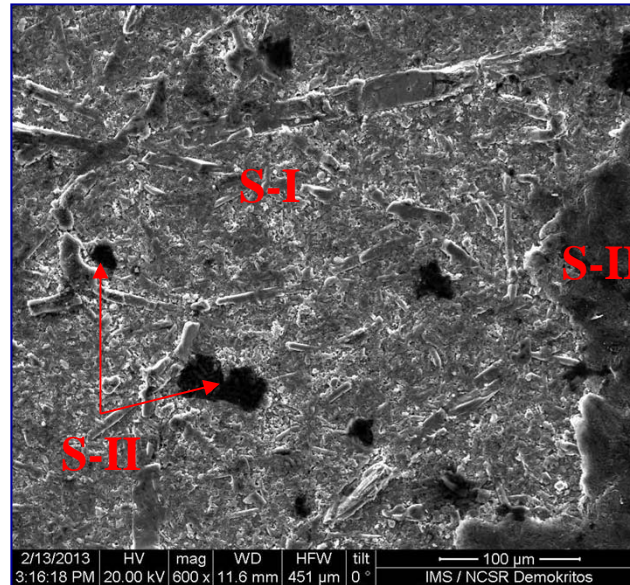
- Thermal tests SiC/CMC joints (size 40 ×40 mm²) under two re-entry conditions showed no detectable defects on the joints.
- The joints survived 5 cycles with maximum temperature of 1800 and 1400 °C

SiC surface after thermal tests at 1400 °C



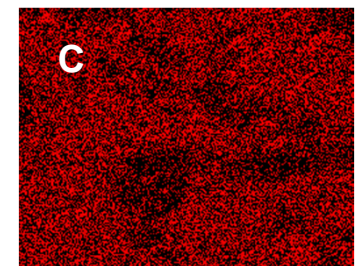
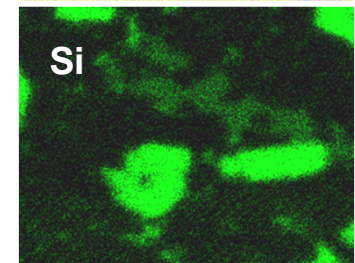
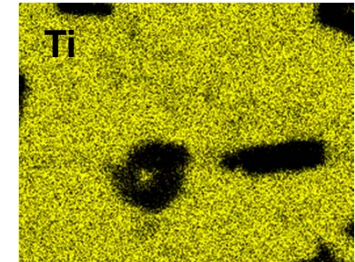
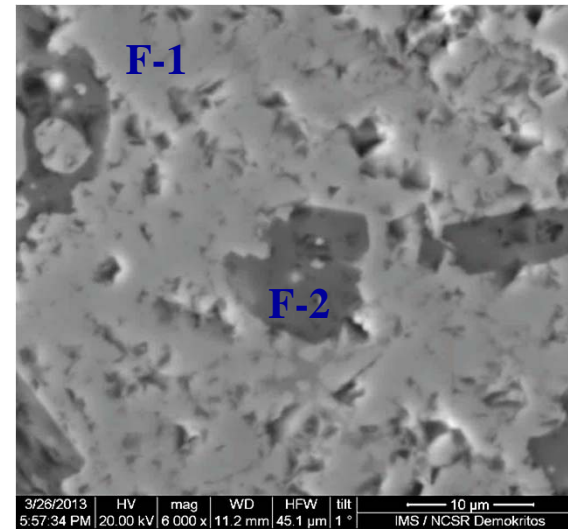
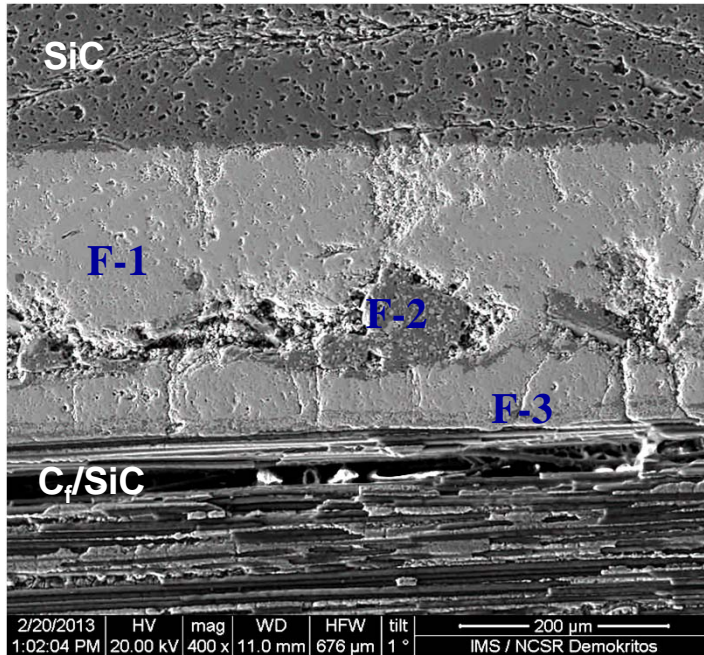
	C	Si	O	Ti	Main phases
S – I	79.0 – 85.0	15.0 – 19.0	0.0 – 1	-	SiC, C
S – II Material in crack	19.0 – 51.0	17.0 – 26.0	3.0 – 7.0	29.0 - 48.0	Ti ₃ SiC ₂

SiC surface after thermal tests at 1800 °C



	C (at%)	Si (at%)	O (at%)
S – I	67.0	31.5	0.1 – 1
S – II Dark grey area	94.0	4	2.0

Cross section of the joint tested at 1800 °C



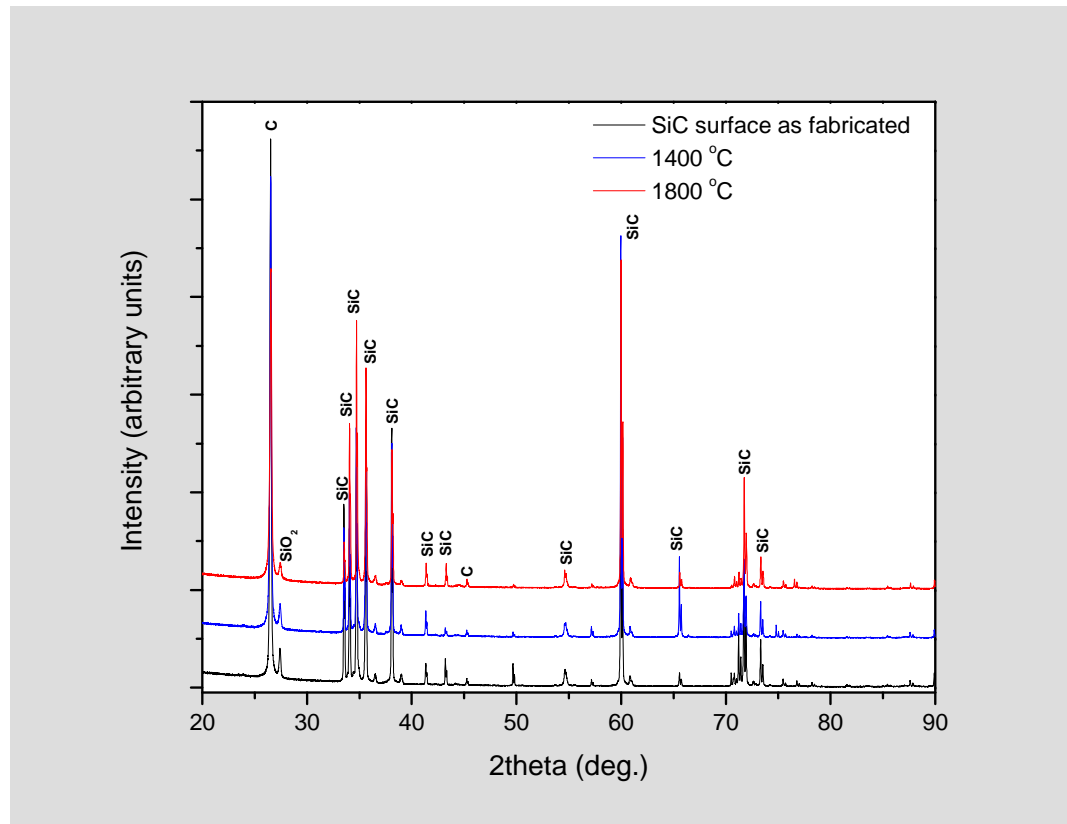
	C (at%)	Si (at%)	Ti (at%)	Main phases
F-I	38.0 – 43.0	13.0 – 17.0	44.0 – 45.0	Ti ₃ SiC ₂
F-II	45.0 – 51.0	47.0	2.0 – 8.0	SiC
F-III	46.0 – 52.0	34.0 – 42.0	11.0 – 16.0	Ti ₃ SiC ₂ + SiC



Joint thermal tests – joint structure integrity



X-ray diffraction measurements of the SiC surface that underwent the thermal re-entry tests



Structural stability of the SiC multilayer joined to CMC after 5 re-entry cycles



CONCLUSIONS AND FUTURE WORK



MAIN CONCLUSIONS:

- Successful joining of CMC to SiC multilayer using $\text{Ti}_3\text{Si}_{1.5}\text{C}_2$ powder employing diffusion brazing bonding and pressures in the range 3 to 25 MPa
- Cracks appear on the surface of the SiC multilayer and are attributed partly to the lack of flatness of the SiC specimens and partly to the brittle behavior of the filler. These cracks are vertical to the SiC/CMC interface and are not detrimental to the shear strength of the joint.
- First thermal tests under two re-entry conditions (in vacuum) have shown no detectable defects in the joints.

FUTURE WORK:

- Further tests under re-entry conditions (more cycles, oxidizing atmosphere)
- Upscaling of the samples to technological demonstrator of size $150 \times 150 \text{ mm}^2$.
- Mechanical (shear strength) tests are underway



ACKNOWLEDGMENTS



- European Commission
- Astrium GmbH (W. Fischer)
- EADS-Innovation Works (C. Wilhelmi, F. Meistring)
- Politecnico di Torino (E. Padovano and C. Badini)
- Aerospace and Advanced Composites GmbH (V. Liedtke)
- Tecnalia Research & Innovation (C. Jimenez, M. Lagos and I. Agote)
- NCSR Demokritos (P. Yialouris, S. Messoloras, Y. Panayiotatos)



Thank you for your attention

Morphological Study and Characterization of Carbon Composites for Hot Structures

M.Albano⁽¹⁾, O.M.Alifanov⁽²⁾, S.A.Budnik⁽²⁾, M.Marchetti⁽¹⁾, R. Bueno Morles⁽¹⁾, A.V.Nenarokomov⁽²⁾, D.M.Titov⁽²⁾

⁽¹⁾ *Sapienza University of Rome, DIAEE department, SASLab
Via Eudossiana 18 00184 Rome Italy
Email: marta.albano@uniroma1.it*

⁽²⁾ *Moscow Aviation Institute (Technical University), Dept. of Space System Engineering
4 Volokolamskoe Hgw., Moscow, 125993, Russia
Email: aleksey.nenarokomov@mai.ru*

INTRODUCTION

The key role played by carbon composites in re-entry environment is due to their high stability at high temperature, preserving their mechanical properties. However, most of these applications involve extended time periods in oxidizing environments. Unfortunately, carbon reacts rapidly with oxygen at temperatures as low as 770K and the composites are subjected to oxidation degradation. From this point of view C/C has to be modified in order to improve its thermal and oxidative resistance. [1] The most common solutions are firstly to use silicon carbide into the carbon composites matrix (SiC composites) to make the thermal properties increase and secondly to make a deposition of coating on the surface in order to protect the composite from the space plasma effects.

These solutions change the properties of C/C thermal protection composites. Here coated and non coated C/C and C/SiC composites thermal behaviour is studied and Thermal Expansion Coefficient (CTE) is determined. Moreover by the use of the inverse method heat capacity and thermal conductivity are also analyzed. A robust numerical approach, such this inverse method, is one of the best for this problems as many parameters concur for the determination of properties. Such approach permits to perform the parametric and structural identification of the model. These procedures are presented including both experimental investigation and methodical-numerical aspects. Special test equipment and the regularizing algorithm for solving the ill-posed inverse heat conduction problem are briefly described.

COATING AND SUBSTRATE DESCRIPTION

CARBON/CARBON

C/C composites are composed by carbon fibers and carbon matrix. The thermal resistance combined with the capacity to maintain high mechanical performance at high temperatures, makes this kind of material unique. The key factor respect to the CSiC composites is the higher performances [2][3].

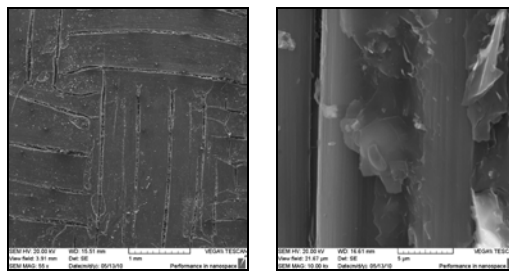


Fig.1. Carbon carbon SEM analysis. On the right: composite surface, on the left: study of matrix adhesion on fibers. The carbon carbon here analyzed is commercial ones.

C/SiC COMPOSITE

This composites are composed by carbon fibers and a silicon carbide matrix.

At higher working temperature the use of this kind of composite is more suitable for its capacity to better resist to oxidation although this does not eliminate the necessity of a coating. Many are the applications in hypersonic vehicles as thermal protection system and also as leading edges.

The key factor for this material is the excellent adhesion of the coating to the substrate. In Figure 2 it is shown a SEM Picture of a coated CSiC. Microcracks of the coating are natural and they come from the manufacturing process, but they don't influences the coating performances, as demonstrated by plasma tests on this kind of material [4]. The material here analyzed are commercial CSiC. As it is possible to see from the diagram the CTE values are lower and more stable than the no-coated samples. A possible cause can be the thermal cycle which occur during the coating deposition which can stabilize the matrix components, as for example it occurs with carbon foams, and this bring to a lower expansion of

the sample. The samples do not show any modifications after the tests and the coating remain on the surface without visible damages.

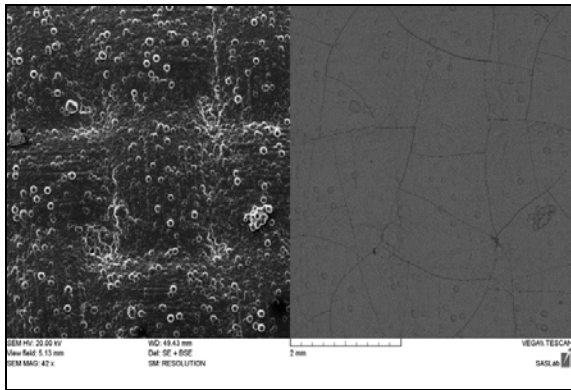


Fig.1. SEM analysis on coated CSiC

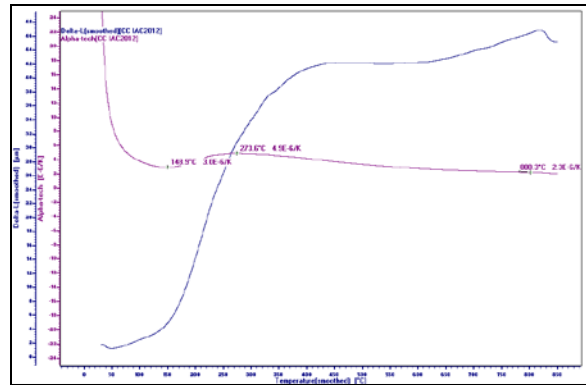


Fig.2a C/C CTE and dL-rel.

THERMAL ANALYSIS OF THE SAMPLES

Dilatometer tests have been performed by the means of a LINSEIS push rod dilatometer, L75H. All the test follows the ASTM C1470. CARBON CARBON

C/C samples tested with the dilatometer are:

- 1) C/C_A
- 2) C/C with a SiC coating(C/C_B);

C/C_A

In Figure 2 C/C CTE and dL-rel is reported. The test has been performed till 820°C. The CTE is not so variable between 2.3E-6/K and 4.9E-6/K.

These values are justified by theory as they are in the 1-10E-6/K range.[5]

SiC coated C/C

Nowadays C/C materials have a high strength, hardness and thermal conductivity but for these characteristics the C/C is subjected to erosion by hydrogen and atomic oxygen at the high temperatures. To protect the C/C is necessary to introduce a SiC coating on C/C surface. The SiC is made with a mix of carbon, powdered coke and clay. It is chemically stable because it does not react with nitric acid, sulfuric and hydrochloric acid.[6]. As it is possible to see from the diagram the CTE values are lower and more stable than the no-coated samples. A possible cause can be the thermal cycle which occur during the coating deposition which can stabilize the matrix components, as for example it occurs with carbon foams, and this bring to a lower expansion of the sample. The samples do not show any modifications after the tests and the coating remain on the surface without visible damages.

CARBON SILICON CARBIDE

C/SiC composites manufactured by two different companies have been tested by L75H dilatometer. Sampels which have been tested are:

- 1) C/SiC ;
- 2) SiC Coated C/SiC

C/SiC



Fig. 2. Coated C/C

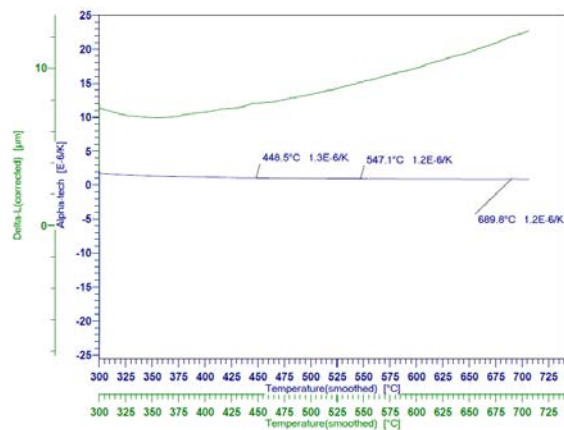


Fig.3. Thermal Expansion coefficient and dL-rel of coated C/C

CTE result are regular and about $1.70E-6/k$, so nearer the expected values. The trend is regular and the CTE values increase smoothly. The material is stable and after the test there are no variations in length and weight

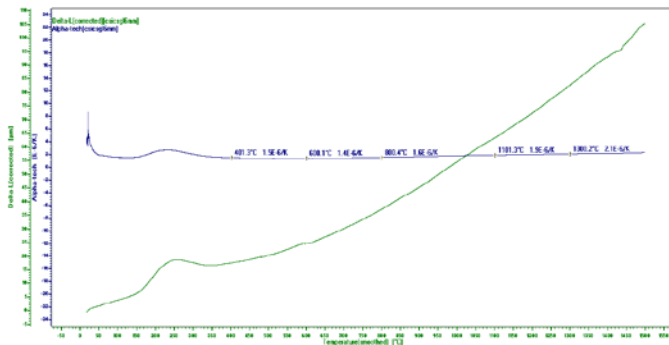


Fig.4. Thermal Expansion Coefficient and dL-rel of CSiC_2

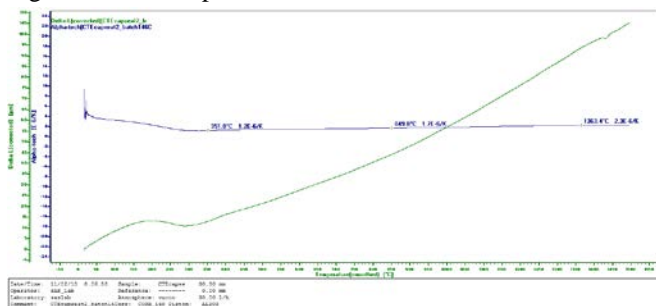


Fig.5. CTE and dL-rel of SiC coated CSiC_1

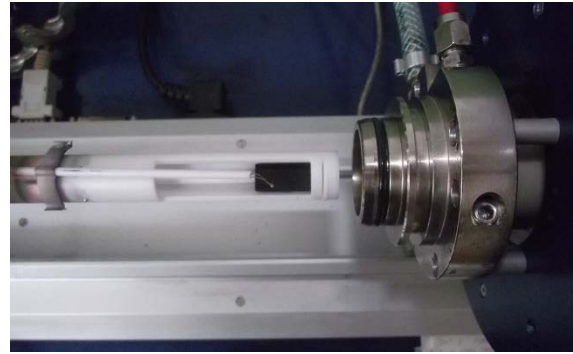


Fig. 6. SiC coated C/SiC sample



Fig.6. Non-tested sample (on the left) and tested sample (on the right)

The diagram shows the CTE of the sample during the heating phase. The CTE trend is similar to the non coated sample, in fact it has a decreasing trend. However a similar behavior with the coated C/C samples took place, in fact the CTE values are lower than the non coated samples, of about $0.1 \times 10^{-6}/K$. This is similarly can due to the stabilization of the matrix morphology during the heating cycle of the CVD coating deposition run. Looking at the sample after the test it is possible to see that the coating is partially oxidized, in fact the color of the sample is more black than a non-tested sample.

MORPHOLOGICAL STUDY

The specimens which has been tested with the dilatometer facility has been analyzed by SASLab with SEM facility.

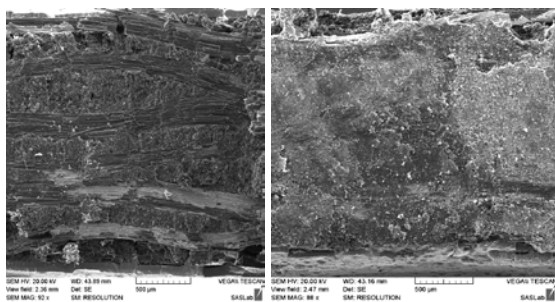


Fig.7. C/C before (right) and after dilatometer test

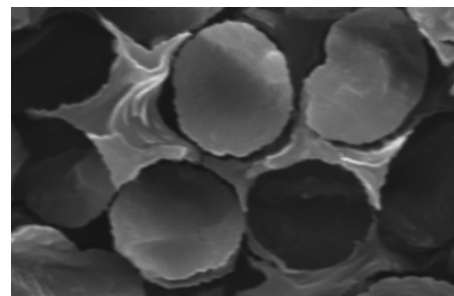


Fig.8.C/SiC before the test

As it is possible to see from the pictures, after the test the matrix of the C/C is much more dense, it is no possible to distinguish fibers from matrix. This can due to the permeation of the coating into the composite due to the high temperature and long exposure time.

As it is possible to observe from the pictures and comparing the sample before and after the tests, it is possible to understand that:

- Particles are well visible and their presence is much higher in the tested samples. The non coated sample matrix is more degraded
- The matrix is visually decomposed
- As for the tested coated C/C, the coated sample after the test has a more dense matrix and fibers are not well visible.

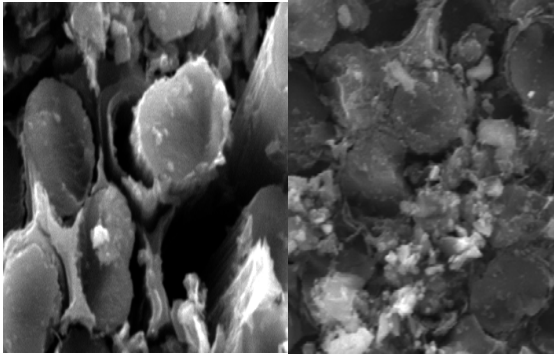


Fig.9. Not coated C/SiC (right) and coated C/SiC (left) sample after the test



Fig.12. C-C material specimens

ESTIMATION OF THE THERMAL PROPERTIES BY INVERSE METHOD

The problem of carbon-carbon material characterization (in fact determining the thermal properties by inverse problems technique [7]) is considered in this section. The two specimens of C-C material were submitted for thermal tests. (140×140×40mm). The two specimens designed for final tests, which have the form of rectangular plane with the following size 140×100×4mm, were manufactured from original specimens (Fig.12). The remnants of the material (140×38×4mm) were used for preliminary tests. The weight and size of specimens are presented in the Table 1.

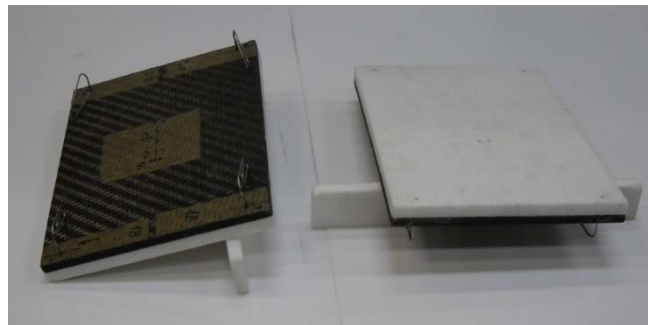


Fig.12. C-C material specimens

Table 1. The parameters of specimens A and B

Specimen	Length, mm	Width, mm	Thickness*, mm	Weight, kg	Density, kg/m ³
A, B	140,0	140,0	4,0	0,10695	1364,16

During the thickness measurement the estimation of surface irregularity was carried out with the help of dimples depth measurements of salient surface with the help of micrometer detector. The value of irregularity was equaled to $\pm 3\text{mm}$ and wasn't taken into account during the density calculation. The photos of heating and front specimens surfaces before and after test are shown in the Fig.14. with optical zoom $\times 5$ and $\times 20$.

The thermocouples were installed only on the heating and back surfaces of A and B specimens since the analyzed material is electrically conductive (Fig.15). The thermocouples with the wires thickness 0,05mm were used. The thermocouples T1 and T5 on the specimens heating surfaces were installed into the thin dimples in surface with isothermal area of 6mm length and were fixed by high-temperature adhesive. Thermocouples wires were output in specimen back surface throughout the specimen slots. The thermocouples T2 and T6 on the specimens back surfaces were fixed with the help of high-temperature adhesive. The heat flux sensors in the form of rectangular slab made from SiO₂ fibers with the following size 140×100×5,8 mm were positioned on the specimens back surfaces to provide inverse problems unique solution [7]. The temperatures on the heating and back surfaces of specimens were measured by thermocouples T3, T4 (specimen A) and T7, T8 (specimen B). The sensor thickness was selected during the process of pilot tests with the help of obtainment condition of essential (measured) temperature reaction on the back surface.

The experimental facilities TVS-2M and experimental module with heating element (HE) made from stainless steel stripe with thickness 0,1mm were used for tests execution. The automatized system AS based on PXI tools were used for heating manipulation, measurements and data collecting. At the first step the pilot tests were carried out. The aim of these tests were: estimation both of physical properties and material behavior during tests execution; selection and verification of constructive and technological solution to tests scheme; realization possibility verification of the given heating mode and heating mode specification; preliminary selection of control program for heating mode realization.

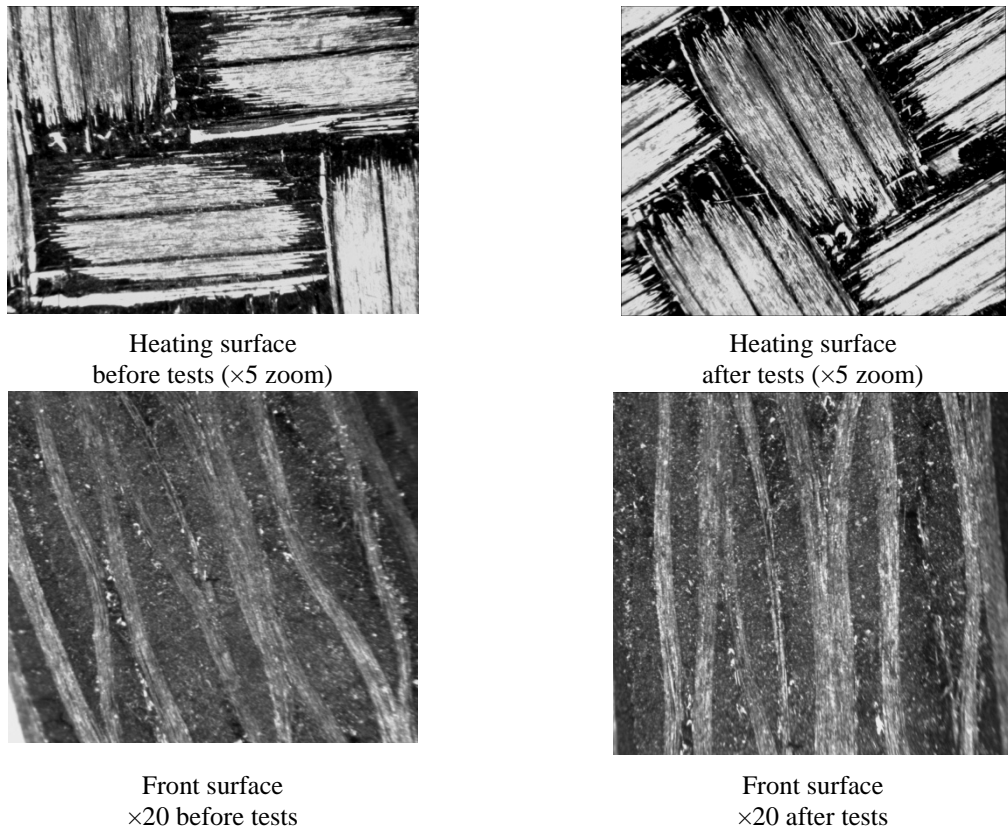


Fig.13. Photos of specimens surfaces before and after tests with optical zoom

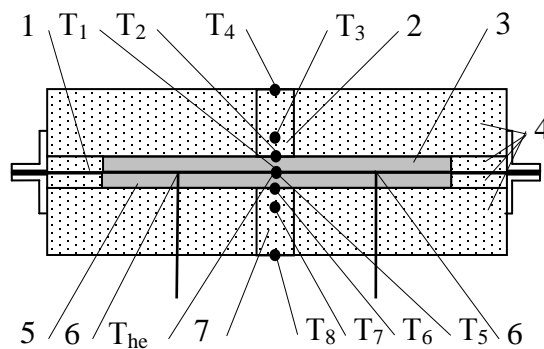


Fig.14. A testing scheme for specimens: 1 – heating element of module EM-3D; 2 - heat flux sensor on the upper specimen; 3 – upper specimen (A); 4 – thermoinsulating slabs; 5 – lower specimen (B); 6 - voltage measuring points on the heating element; 7 - heat flux gage on lower the specimen; T he- thermocouple on the heating element; T1, T2 - thermocouples on upper the specimen; T5, T6 - thermocouples on lower the specimen; T3, T4, T7, T8 - thermocouples on heat flux sensors

The pilot tests have shown that analyzed material has great electrical conductivity, which arises during the temperature increasing, and at temperature more than 120°C it is practically comparable with the electrical conductivity of HE material. This property creates serious problems during the realization of chosen thermal tests scheme and it demands electrical isolation both of HE and thermocouples wires from HE material. The usage of covering fiber-glass fabric allowed obtaining the sufficient temperatures and heating rates on the specimens heating surface. Thermocouple THE installed (welded) on experimental module HE was used as control thermocouple. The symmetric scheme of heating of two similar specimens A and B by steel HE was chosen for tests execution.

Major measurements, which were carried out during the optional test:

$$T_i(\tau), 0 \leq \tau \leq \tau_e - \text{temperature measurements of specimen } X_i, i = 1, \dots, M$$

$$T_i(\tau), 0 \leq \tau \leq \tau_{e1} - \text{temperatures measurements of thermal flux sensors } X_i, i = M + 1, \dots, M1.$$

Additional measurements:

$T_{HE}(\tau)$, $0 \leq \tau \leq \tau_{e1}$ - temperature measurement of heating element (HE);

$I(\tau)$, $0 \leq \tau \leq \tau_{e1}$ - current measurement in HE and $U(\tau)$, $0 \leq \tau \leq \tau_{e1}$ - voltage measurement in HE. These characteristics are used for estimation of electrical power generated on HE.

Temperature measurements scheme is presented in Table 2.

Table 2. Thermal measurements schemes in specimens

Coordinate, mm	Specimen A	Specimen B	Note
Thermocouple			
X_1	0,0	0,0	Heating surface of specimen
T_i	T_1	T_5	
X_2	4,0	4,0	Back surface of specimen
T_i	T_2	T_6	

Table 3. Temperature measurements scheme in thermal flux sensors

Coordinate, mm	Sensor on specimen A	Sensor on specimen B	Note
Thermocouple			
X_1	0,0	0,0	Sensor heating surface
T_i	T_3	T_7	
X_2	5,8	5,8	Sensor back surface
T_i	T_4	T_8	
X_3	28,8	28,8	Back surface of thermal isolating
T_i	$T_A(\tau) = T_4(\tau = 0) =$ $= const$	$T_B(\tau) = T_8(\tau = 0) =$ $= const$	

Heating program of specimens was chosen during the pilot tests process based on the achievement of given maximum temperature of specimen heating surface $T_{1max}(\tau) \sim 330 \div 350^\circ\text{C}$ and $T_{5max}(\tau) \sim 330 \div 350^\circ\text{C}$; ensuring of acceptable temperature measurement at specimens back surfaces; not exceedance of HE temperature ($T_{HEmax} = 470^\circ\text{C}$), which is critical to electrical isolation covering of HE and thermocouples. The final tests of C-C material were carried out in the air with pressure 1 bar. In accordance to tests scheme the specimens were placed in experimental module of stand. Thermocouples wires were output throughout specialized slots in thermal isolated mandrels (Fig.15-16).

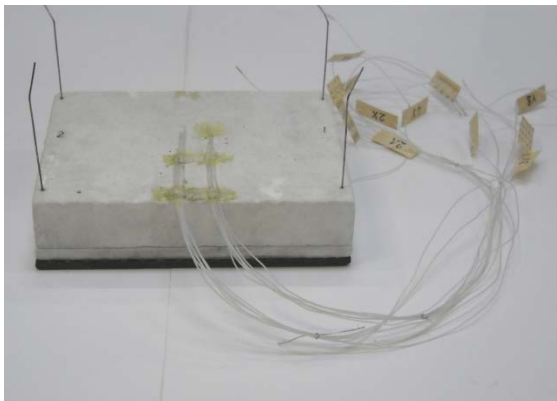


Fig.15. Specimen with thermal flux sensor and thermal isolating



Fig.16. Assemblage made from two specimens A and B into experimental module.

Two tests of specimens A and B were carried out. The temperature measurements results in specimens A and B, which were obtained in tests №1, №2 and №3 $T_i(\tau)$, $0 \leq \tau \leq \tau_e$ are presented in Fig.17-18.

The carried out tests have shown, that:

- After three tests execution the surfaces of experimental specimens didn't have visible markings of heating and destructions.
- In the tests the temperature values on back and heating surfaces of specimens A and B, as well as on sensor back surfaces were negligibly differ from each other, and with taking into account the previous point it allows to talk about good heating symmetry of specimens in realized tests scheme.

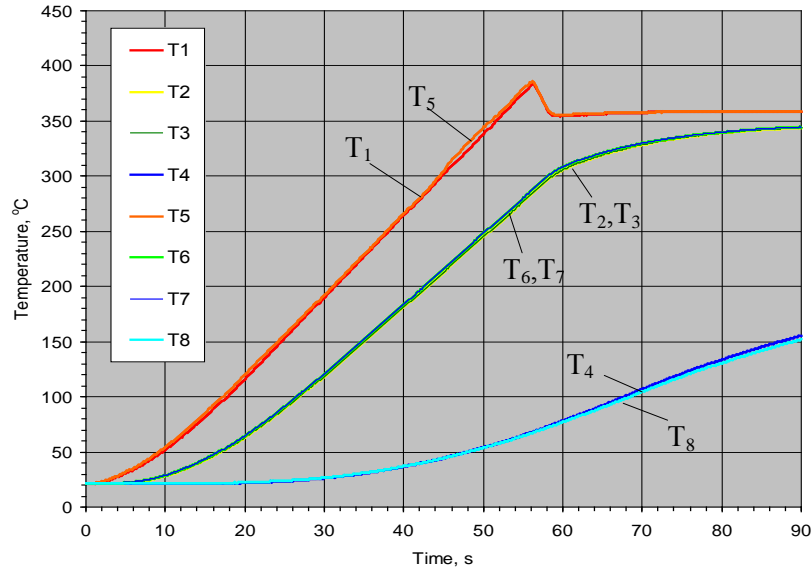


Fig.17. Temperature measurements results in test №2 (specimens A and B)

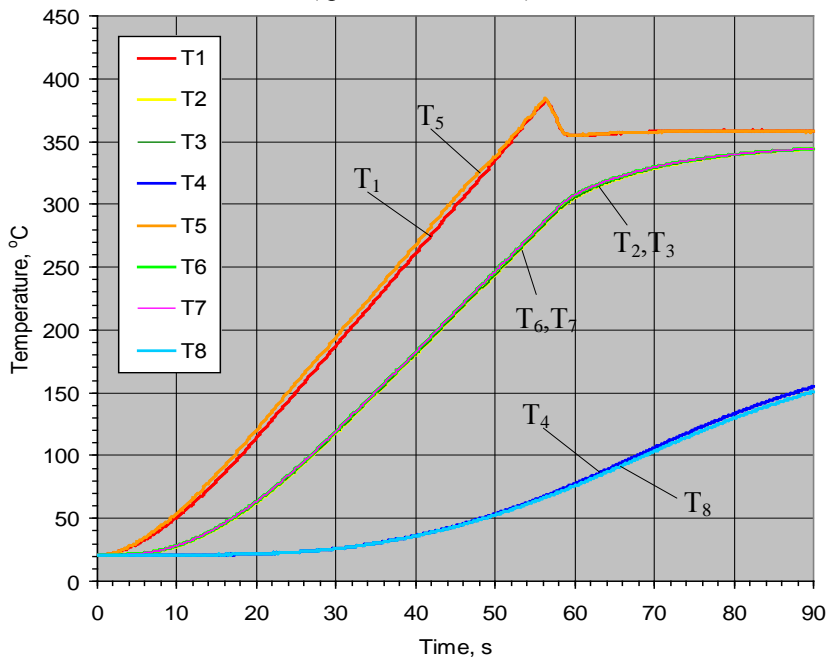


Fig.18. Temperature measurements results in test №3 (specimens A and B)

Based on the given physical model, a mathematical model of heat transfer process in the material's specimen (infinite plate of known thickness) can be presented as follows

$$C(T) \frac{\partial T}{\partial \tau} = \frac{\partial}{\partial x} \left(\lambda(T) \frac{\partial T}{\partial x} \right), \quad x \in (X_0, X_1), \quad \tau \in (\tau_{\min}, \tau_{\max}] \quad (1)$$

$$T(x, \tau_{\min}) = T_0(x), \quad x \in [X_0, X_1] \quad (2)$$

$$-\lambda(T) \frac{\partial T(X_0, \tau)}{\partial x} = q_1(\tau), \quad \tau \in (\tau_{\min}, \tau_{\max}] \quad (3)$$

$$-\lambda(T) \frac{\partial T(X_1, \tau)}{\partial x} = q_2(\tau), \quad \tau \in (\tau_{\min}, \tau_{\max}] \quad (4)$$

In models (1) – (4) the coefficients $C(T)$ and $\lambda(T)$ are unknown. The heat flux in (4) is determined from boundary inverse problems for heat flux sensor on the back surface of specimen. The additional information needed for solving the inverse problem prescribed are the results of the temperature measurements

$$T^{\text{exp}}(x_m, \tau) = f_m(\tau), \quad m = \overline{1, 2}, \quad x_1 = X_0, \quad x_2 = X_1 \quad (5)$$

The least- square residual of computational and measured temperatures at points of the thermocouple installation is given

$$J(C(T), \lambda(T)) = \sum_{m=1}^2 \int_{\tau_{\min}}^{\tau_{\max}} (T(x_m, \tau) - f_m(\tau))^2 d\tau \quad (6)$$

where $T(x_m, \tau)$ is defined from a solution of the boundary-value problem (1) – (4). Proceeding from the principle of iterative regularization, the unknown function can be determined through the minimization of the functional (6) by gradient methods of the first-order prior to the fulfilment of the condition [7]

$$J(\bar{p}) \leq \delta_f \quad (7)$$

$$\delta_f = \sum_{m=1}^M \int_{\tau_{\min}}^{\tau_{\max}} \sigma_m(\tau) d\tau$$

To construct the iterative algorithm for this inverse problem, the solution of a conjugate gradient method is used. The details of this algorithm can be found at [7,9]. Comparisons of the calculated and measured temperatures on the specimens' surfaces are presented in Fig. 19. The results of estimating the functions $\lambda(T)$ and $C(T)$ for material are presented in Fig.20-21. Table 4 includes the obtained values of the least squares and the maximum deviation of the calculated temperatures from that measured in the experiments.

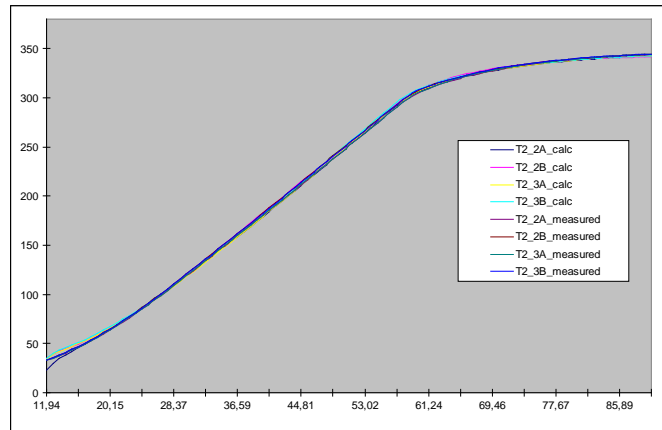


Fig.19. Comparison of the calculated in the thermocouples positions and measured temperatures on the surface of the specimen

Table 4. The deviation of the calculated temperatures

Specimen	Least-squares temperature deviation, K	Maximum temperature deviation, K
2A	2.61	11.2
2B	3.35	14.1
3A	2.11	10.0
3B	2.33	10.8

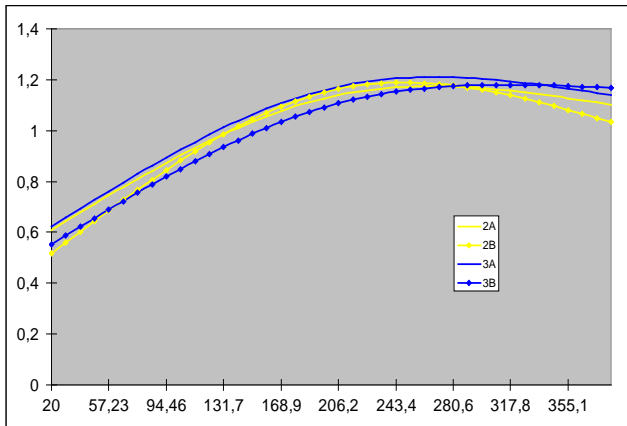


Fig.20. Estimated value of the thermal conductivity

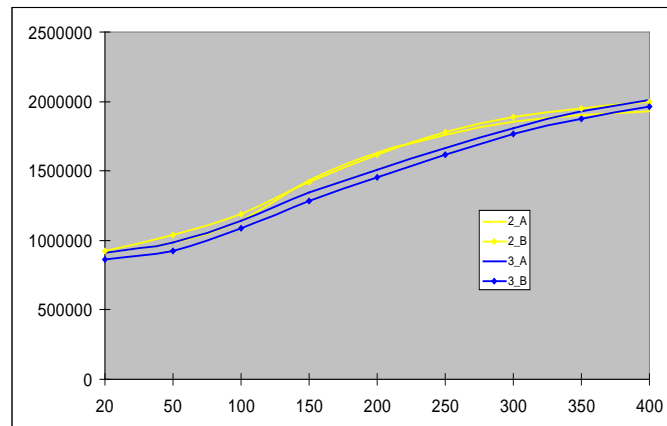


Fig.21. Estimated value of the volumetric heat capacity

CONCLUSIONS

Coated and non coated materials have been compared. Coating does not influence the substrate in general and there is a good adhesion on the material. SiC coating is really suitable. Strong differences come from the manufacturer and are probably due to the infiltration grade of the composite matrix. Coating protects the matrix and after a heating cycle the matrix becomes more dense: it is necessary to understand the grade of coating infiltration into the composites before and after thermal cycles. The executed thermal testing provided the solving of the above formulated problems to study the heat transfer in the specimens and to estimate the thermal properties of the carbon-carbon materials. The deviations of the calculated temperatures (using thermal property estimations) from the temperatures measured in the experiments are insignificant showing sufficient accuracy in the estimations of thermal properties of the analyzed materials.

ACKNOWLEDGEMENTS

This work was supported by RBRF in the framework of the International grant No 3871. The specimens were manufactured and tests were executed by Mr. Anatoliy N. Ivanov and Mr. Aleksey G. Mednov.

REFERENCES

- [1] *Re.entry and hypersonic vehicles thermal protection systems-ceramic matrix composite*, Snecmaphamlet
- [2] *Microstructure and mechanical properties of three dimensional carbon silicon carbide composites fabricated by chemical vapor infiltration*, Yongdong Xu, Litong Zhang, Laifei Cheng, Dantao Yan, Carbon vol.36, no.7-8, pp.1051-1056
- [3] *C/C-SiC composites for space applications and advanced friction systems*, W.Krenkel, F. Brendt, Materials Science and Engineering, pp177-181
- [4] *Emissivity characterization of carbon silicon carbide composites for TPS thorough plasma wind tunnel tests: experimental validation*, Panerai F., Vassalli C., Albano M., Agostinelli F. Delfini A., Chazot O., Marchetti M., Coluzzi P., IAC-12,C2,9,9,x14181
- [5] *Carbon Carbon Composite*, G. Savage, Chapman and Hall, 1993
- [6] *Stabilità Dimensionale di Materiali Compositi per Applicazioni Spaziali*, F.Cioeta F., Mazza F., Marchetti M., Rivista Italiana di Compositi e Nanotecnologie - Volume 4 - n°1 - Maggio 2008
- [7] Alifanov O.M., et. al. "Identification of thermal properties of materials with applications for spacecraft structures", Inverse Problems in Science and Engineering, Vol. 12, 579-594, 2004.
- [8] Muzylev N.V., "Uniqueness of simultaneous determining of coefficients of thermal conductivity and volumetric heat capacity", USSR Comput. Math. and Math. Phys., Vol. 23, 102-108, 1983.
- [9] Artyukhin E.A., Ivanov G.A. and Nenarokomov A.V., "Determination of a complex of materials thermophysical properties through data of nonstationary temperature measurements", High Temperature, Vol. 31, 235-241, 1993.

Radiation-Shapes-Thermal Protection Investigations

for High Speed Earth Re-entry

RASTAS SPEAR :

Radiation-Shapes-Thermal Protection Investigations for High Speed Earth Re-entry

Overview of the TPS activities

A MARINOU¹, G VEKINIS¹ and J-M BOUILLY²

¹Institute of Advanced Materials PPNM, NCSR "Demokritos", 15310, Aghia Paraskevi Attikis, Greece

²EADS Astrium Space Transportation - BP 20011, 33 165 Saint-Médard_en-Jalles Cedex, France

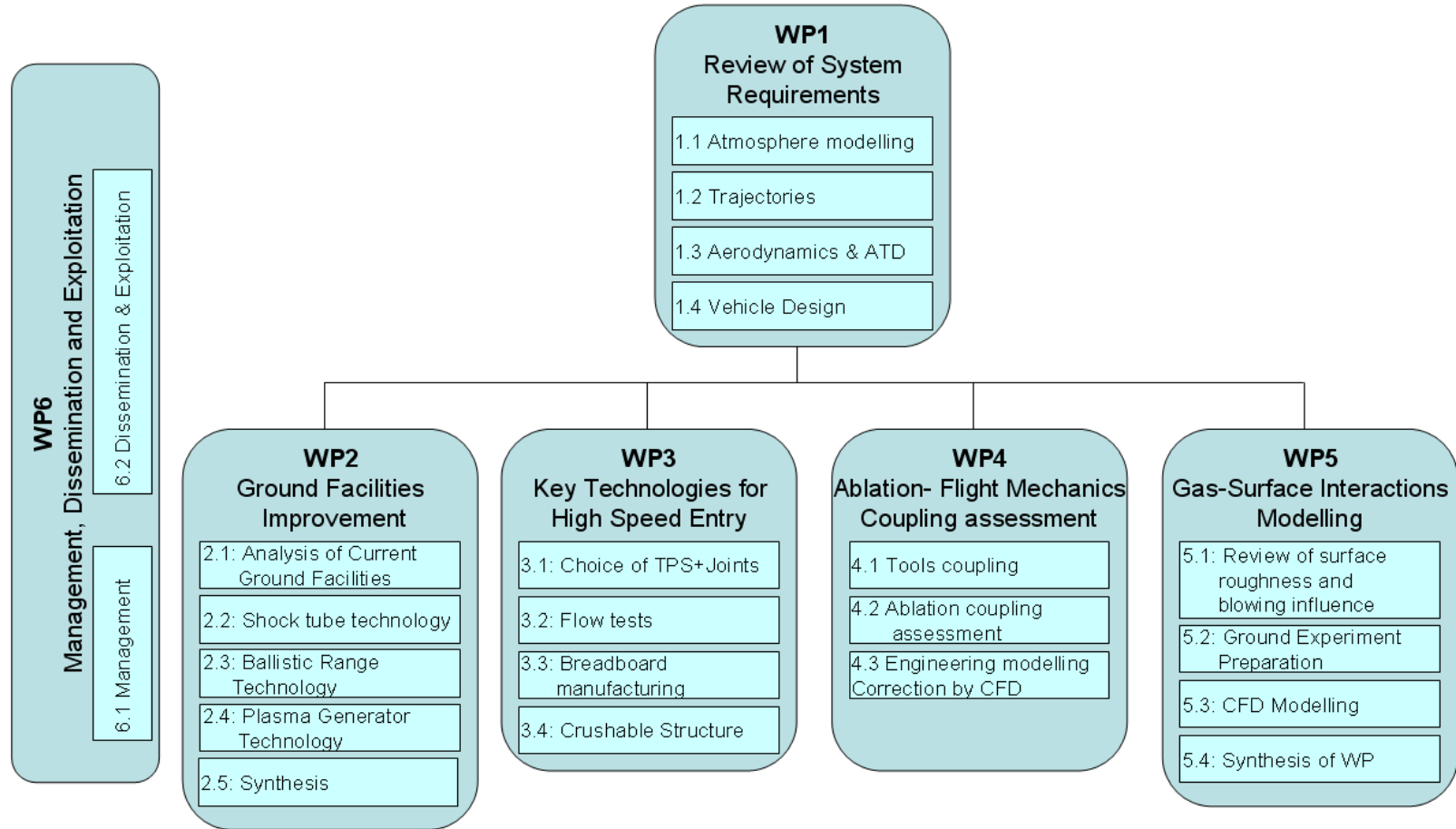
7th European Workshop on TPS-HS – ESA/ESTEC, 8-10 April 2013

www.rastas-spear.eu



The research leading to these results has received funding from the European Union Seventh Framework Programme (FP7/2007-2013) under grant agreement n° 241992

Rastas-Spear – Review and development of necessary technologies for sample-return missions



Rastas Spear Consortium




Von Karman Institute for Fluid Dynamics
<https://www.vki.ac.be/>





Astrium SAS
<http://www.astrium.eads.net/>


CNRS/EM2C
<http://www.em2c.ecp.fr/>


Office National d'Etudes et de Recherches Aéropatiales
<http://www.onera.fr/english.php>



Centro Italiano Ricerche Aerospaziali
<http://www.cira.it/it>



Lomonosov Moscow State University
<http://www.msu.ru/en/>



Institute of Aviation
<http://ioa.edu.pl/>



Kybertec
<http://kybertec.cz/>



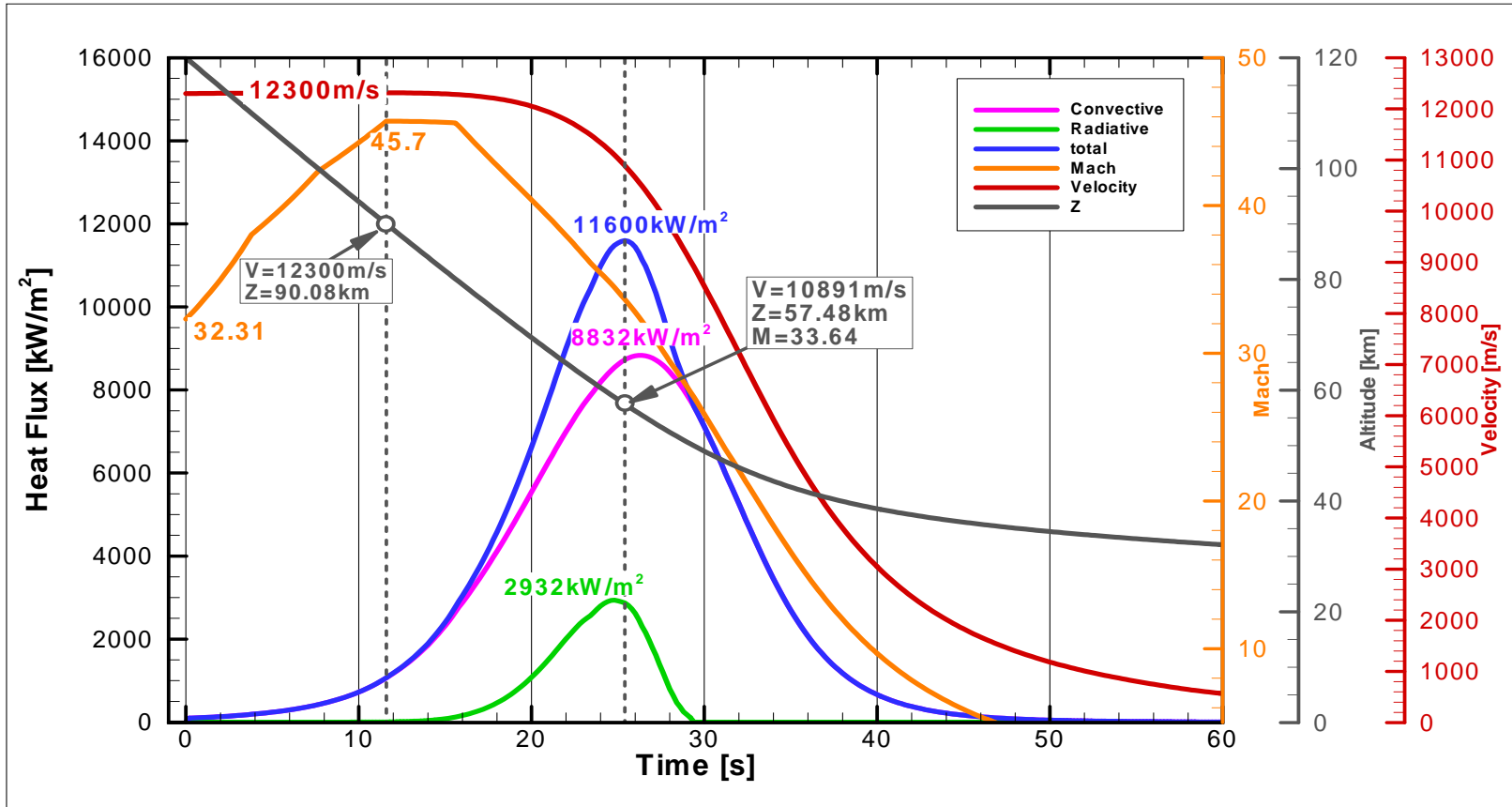
CFS Engineering
<http://www.cfse.ch/cfse/site/home.php>



NCSR Demokritos
<http://www.demokritos.gr/default.aspx?lang=en>

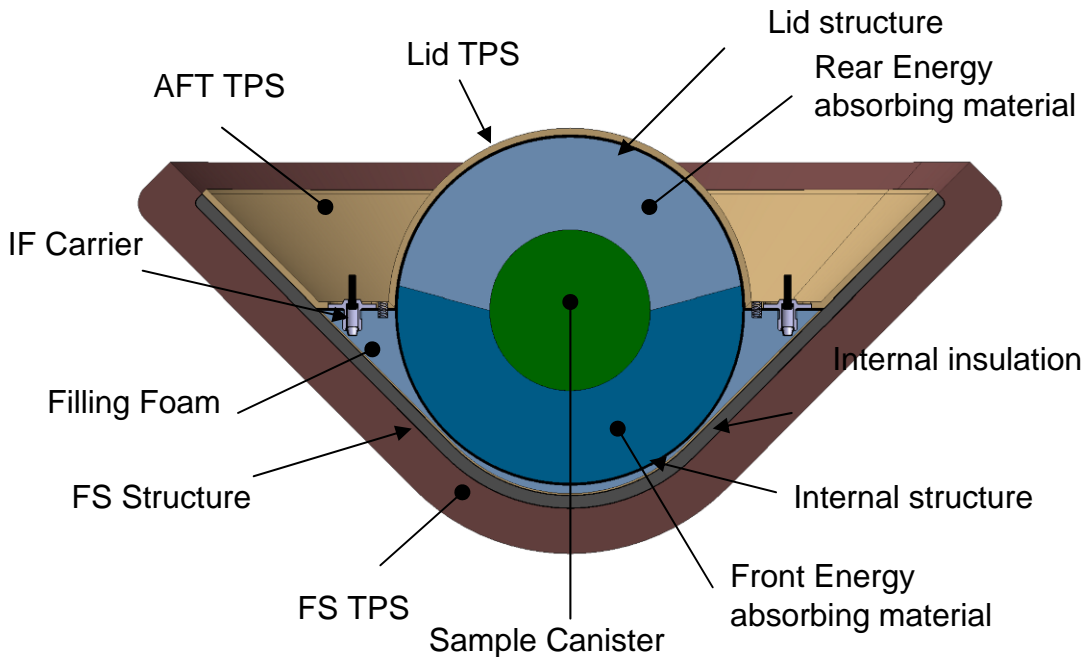



Rastas-Spear – Characteristics of the passive re-entry



Main characteristics of the RS passive re-entry. Effective max. total heat flux is about 11.6MW/m², max. velocity 12.3km/sec (47.5Mach), total heat energy about 250MJ/m².

Passive Earth Re-entry Capsule – Hayabusa design



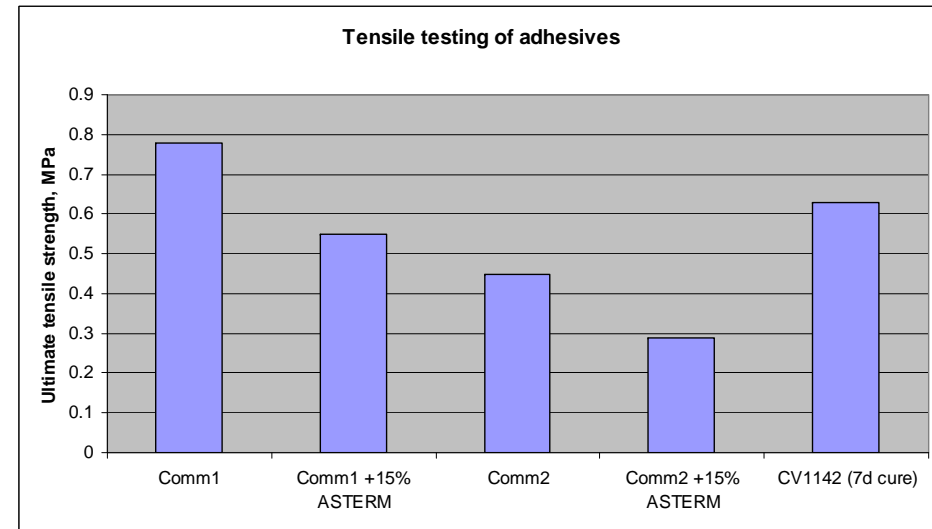
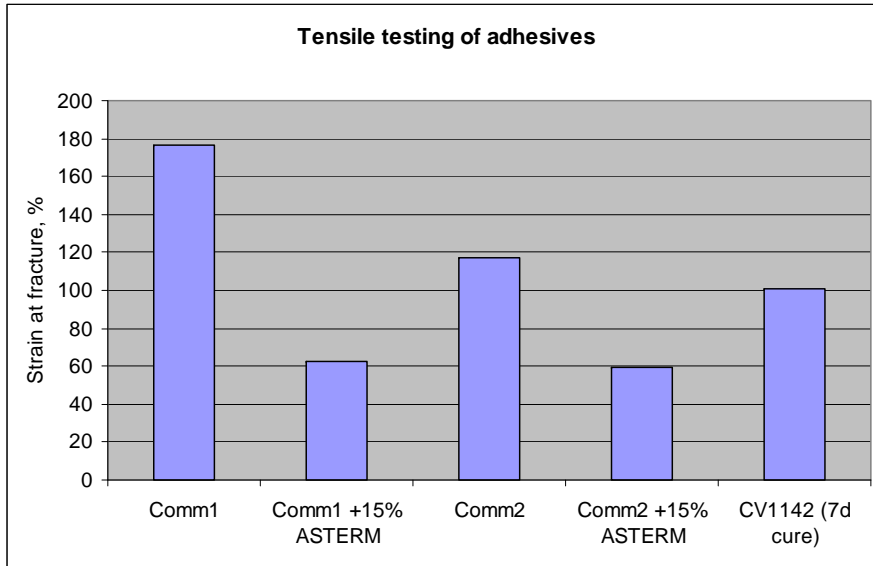
A 45° cone, spherical nose design for 12.3km/sec re-entry.

Maximum diameter 110cm, front radius of curvature 27.5cm and front HS TPS thickness of 56mm.

Main TPS activities in Rastas-Spear

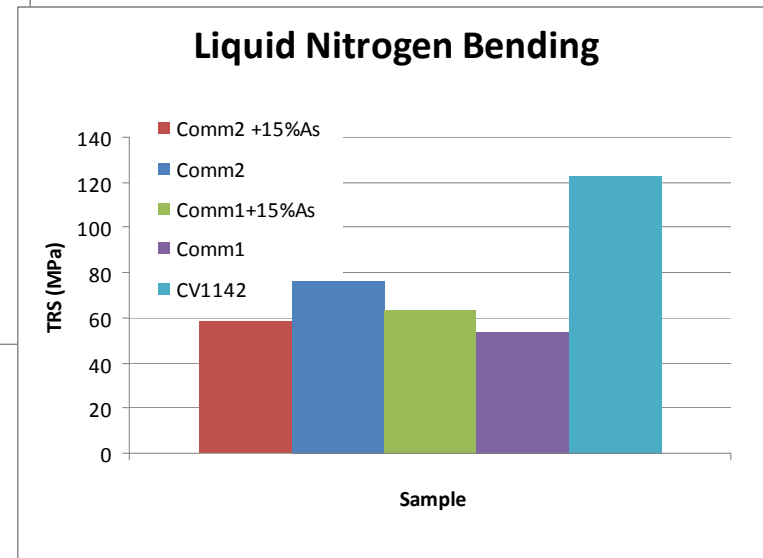
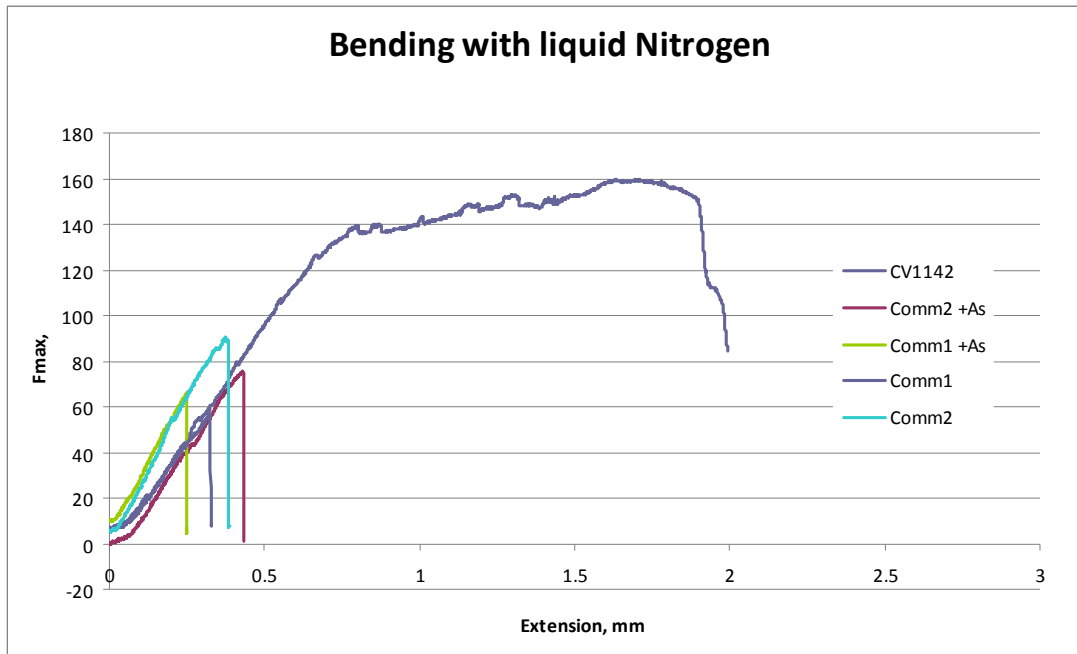
- Adhesive tests and shield development based on the ASTERM carbon-phenolic ablator, made by EADS/Astrium
- Screening and testing of a range of commercial adhesives for joining of ASTERM and bonding with various substrates. Main screening parameters: outgassing, curing behaviour and remanent elasticity at -196°C
- Two commercial adhesives selected and compared with CV1142 heritage adhesive (and with ESP495 for the DLR plasma tests).
- Comparison tests carried out included: mechanical strength of ASTERM joints and bonds, plasma-jet tests (CIRA/Scirocco and DLR/L3K at 5MW/m² and 6.1MW/m² / 13.6MW/m² respectively) up to about 200MJ/m²
- Manufacturing of a front heat shield demonstrator breadboard using an alternative low-cost, manual method.

Mechanical behaviour of adhesives at RT



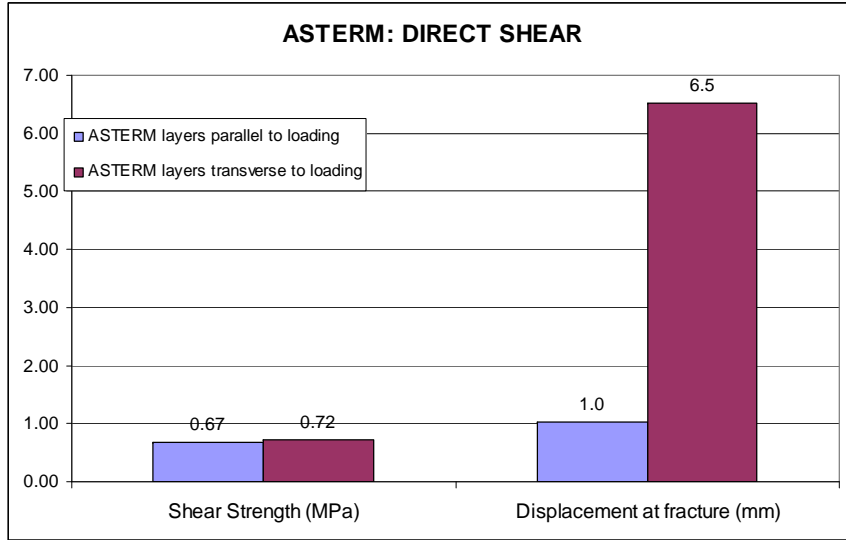
Mechanical behaviour in tension at RT is comparable for all adhesives, including those containing some Asterm powder. In all cases all adhesives are stronger than the Asterm ablator.

Mechanical behaviour of the adhesives at -196°C

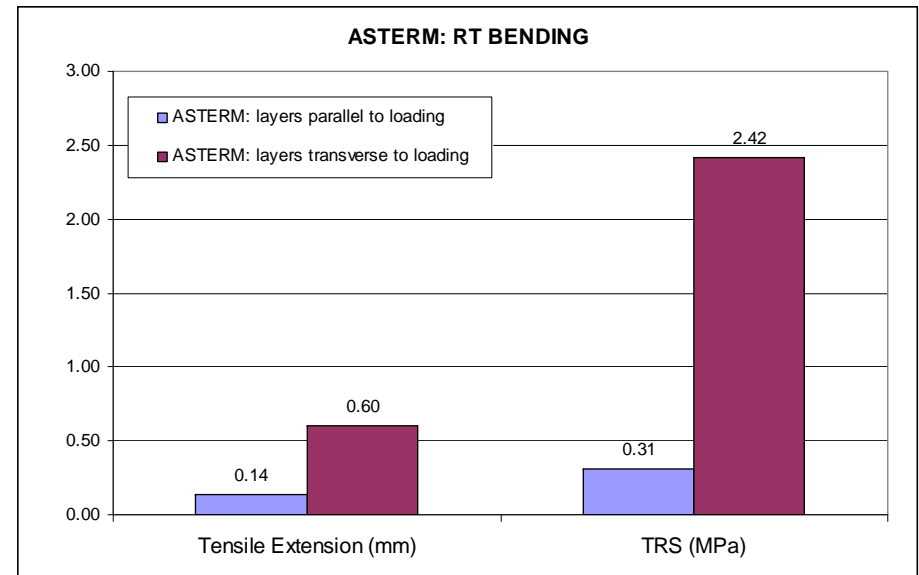


All adhesives tested show remanent elasticity at -196°C but CV1142 is much stronger in bending

ASTERM: Shear and bending strength

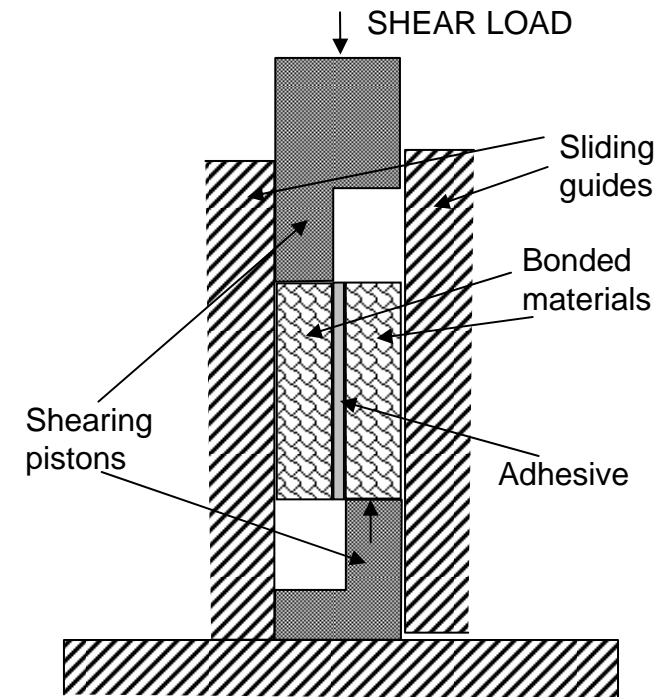
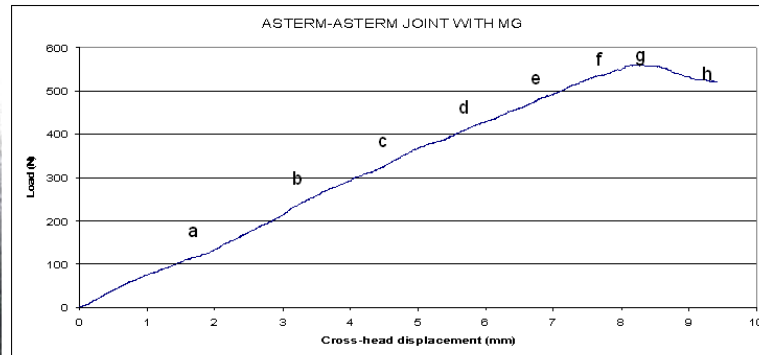
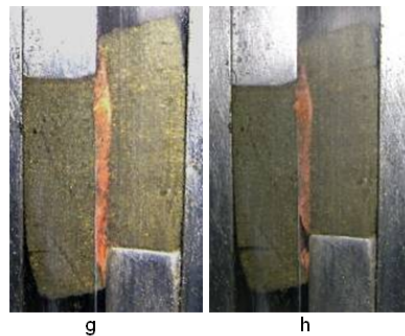
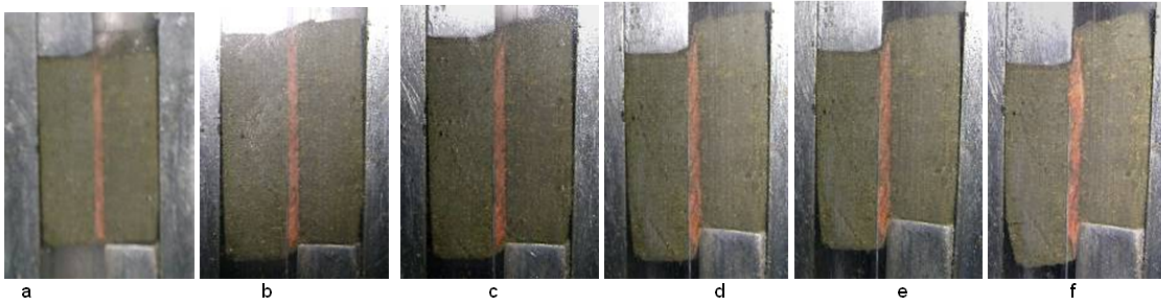


Shear strength in shear is independent of fibre direction but bending strength is highly dependent on it. Displacement at fracture is always much larger when the fibre layers are parallel to loading direction

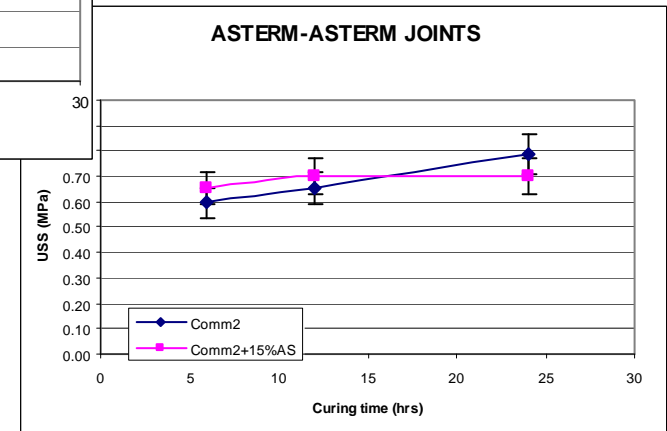
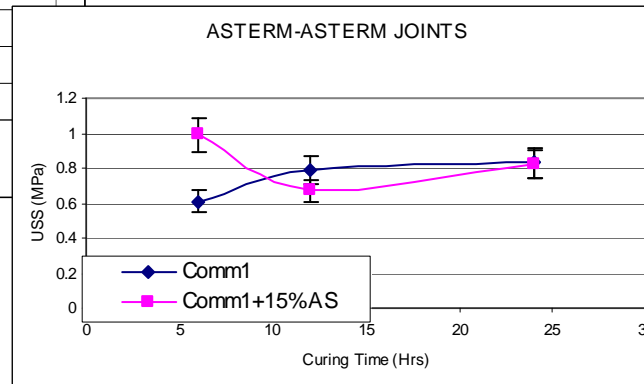
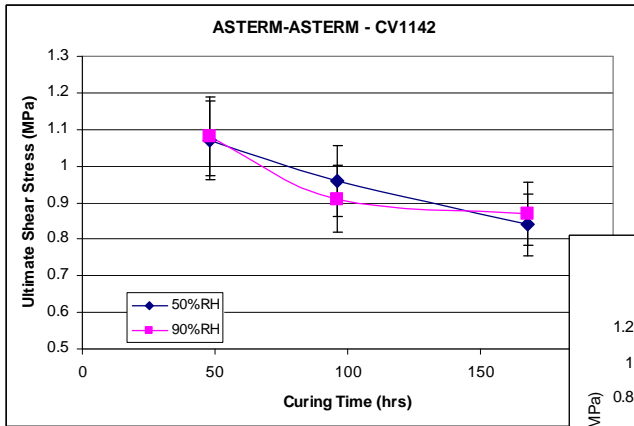


ASTERM-ASTERM joints: Mechanical properties

Shear strength and fracture behaviour of joints and bonds

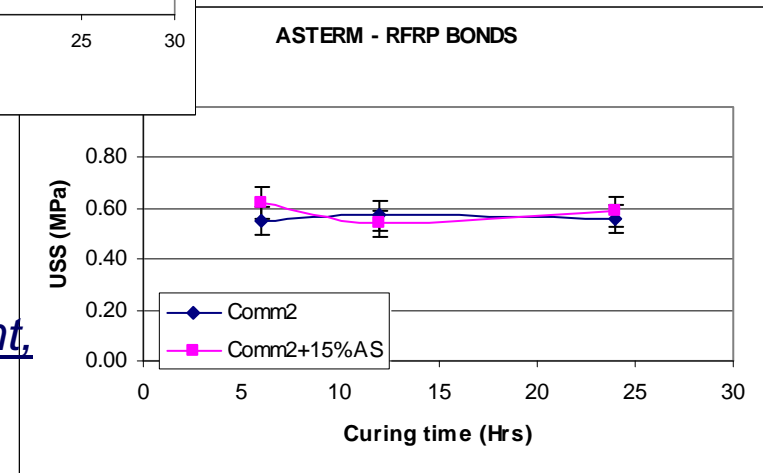
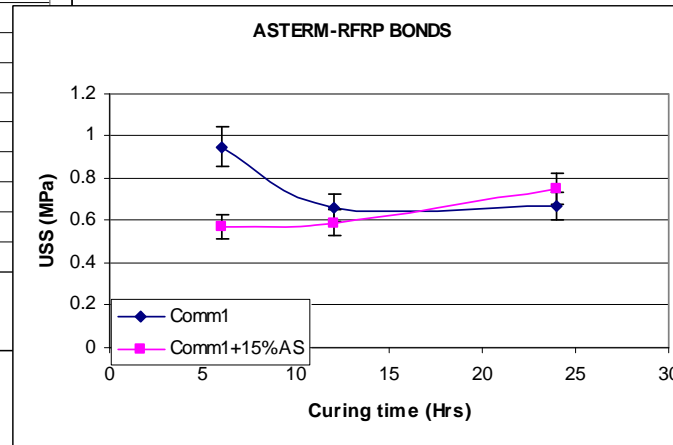
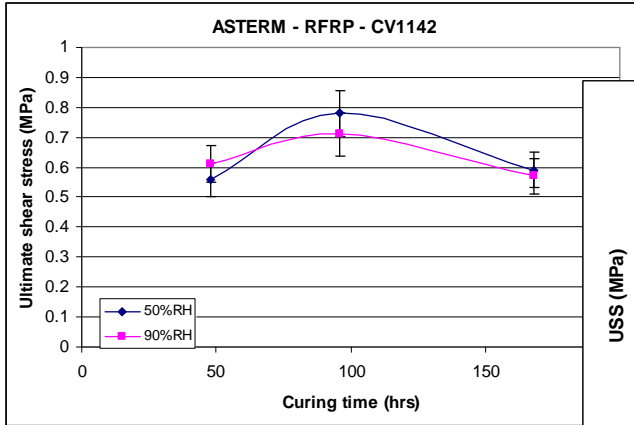


ASTERM-ASTERM joints: Shear strength



Shear strength and fracture behaviour of joints were similar for all adhesives tested.

ASTERM-CFRP bonds: Shear strength



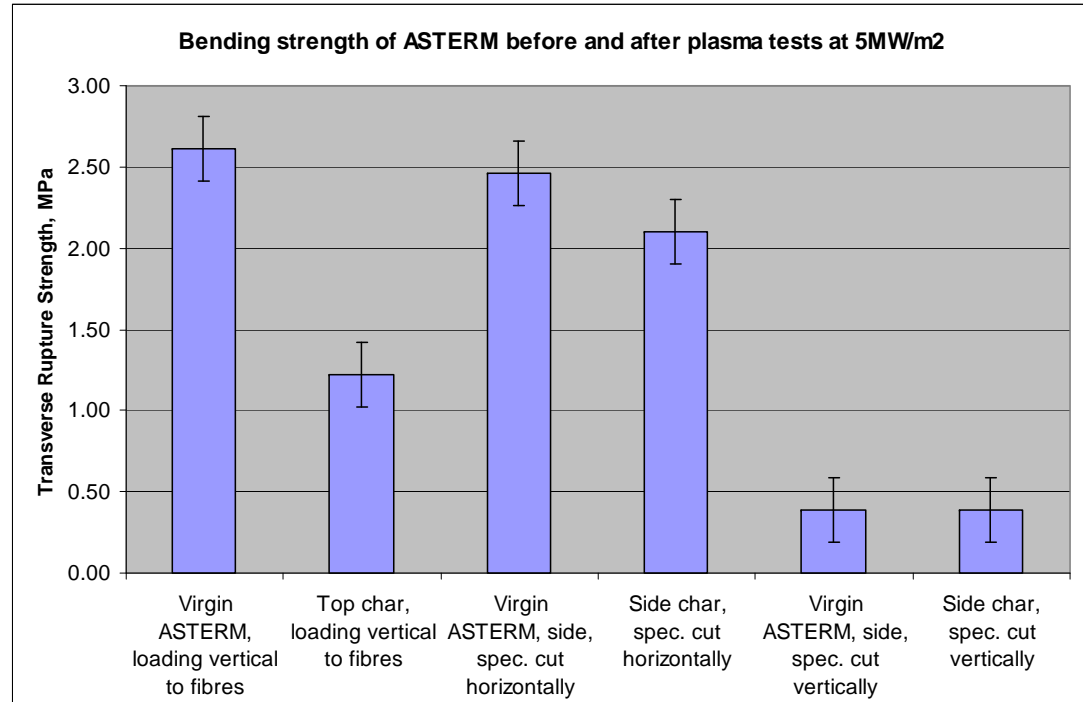
For both joints and bonds, beyond a certain minimum strength and strain at failure, the mechanical behaviour of the adhesive is irrelevant, since the weak link is the ablator in every case.

ASTERM joints: Plasma jet tests – CIRA/Scirocco

CIRA/Scirocco test:
5Mw/m², 12 seconds, 4Mach



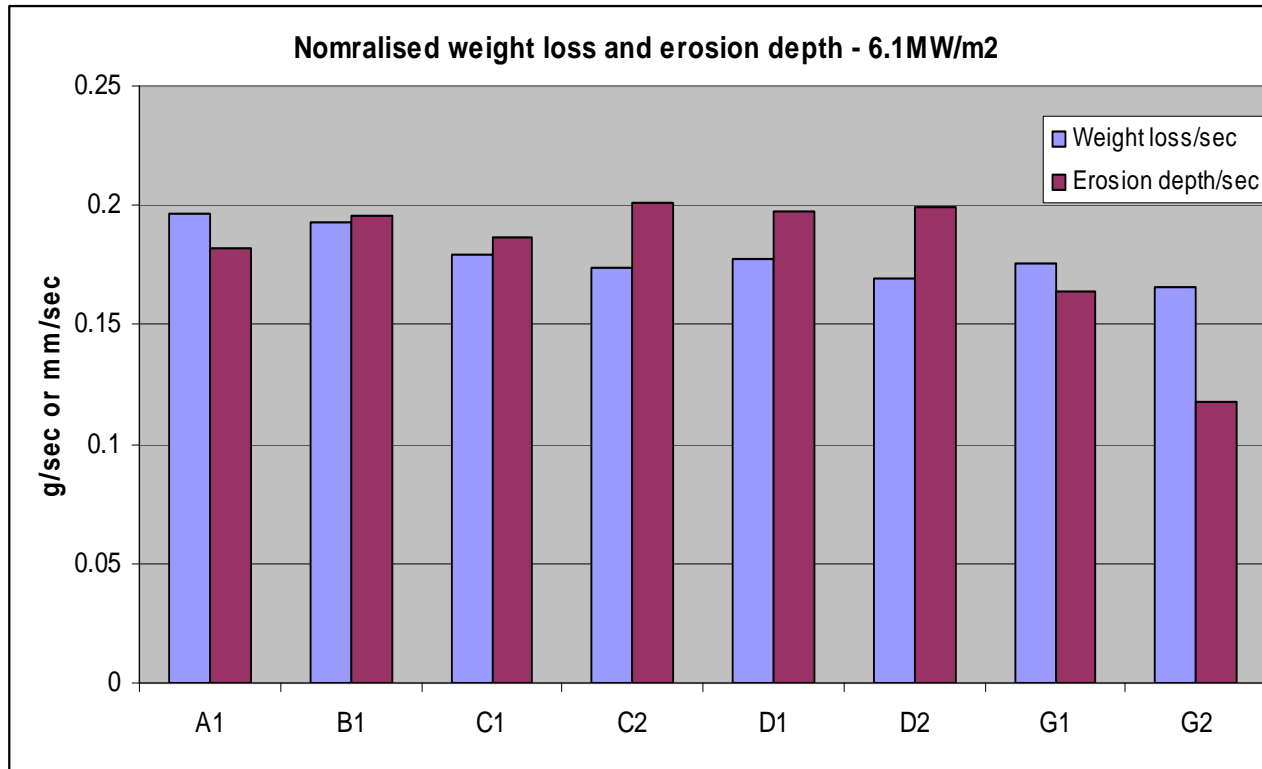
Total uniform recession about 2mm,
top char 12mm, side char about
6mm.



Good remanent strength after plasma-jet test

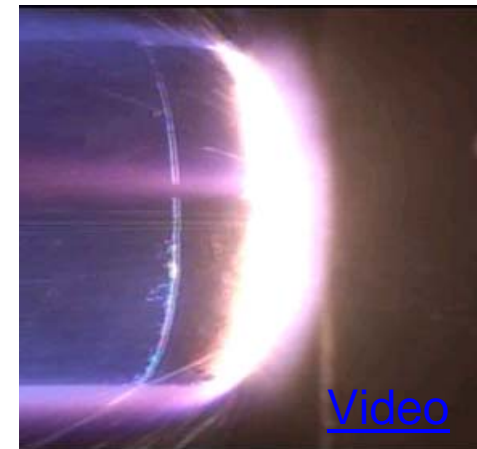
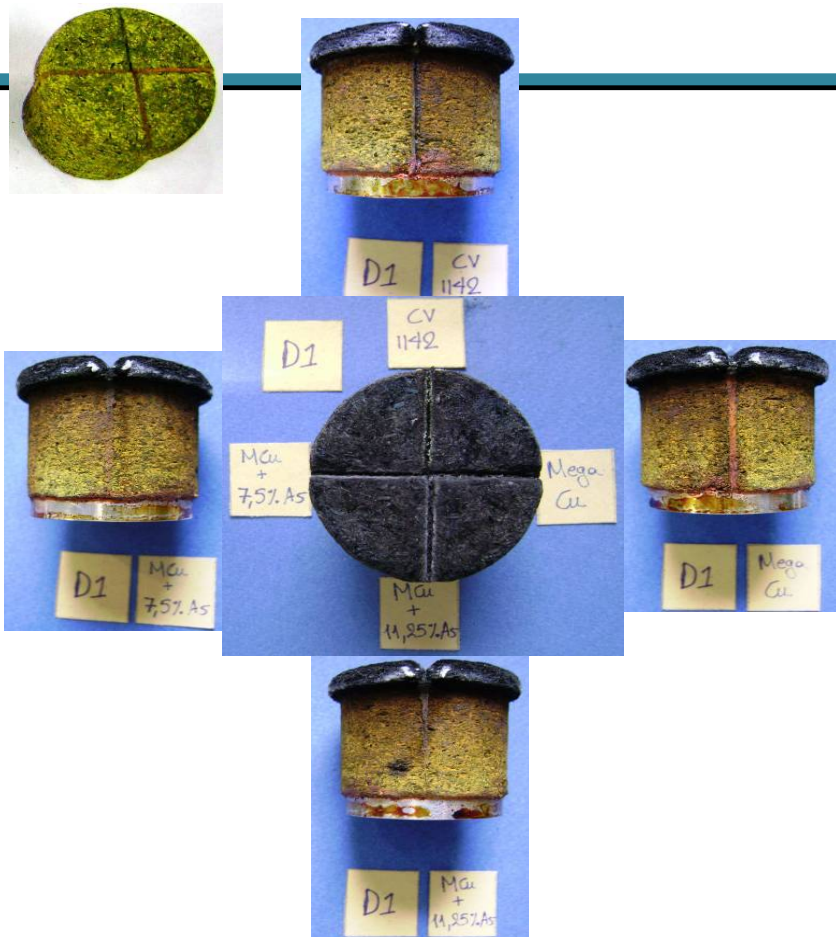
ASTERM joints: Plasma jet tests – DLR/L3K

DLR/L3K tests at 6.1Mw/m², 25-31 seconds



All adhesives eroded deeper than ablator.
 Average erosion rate 0.12-0.2mm/sec.

ASTERM joints: Plasma jet tests – DLR/L3K



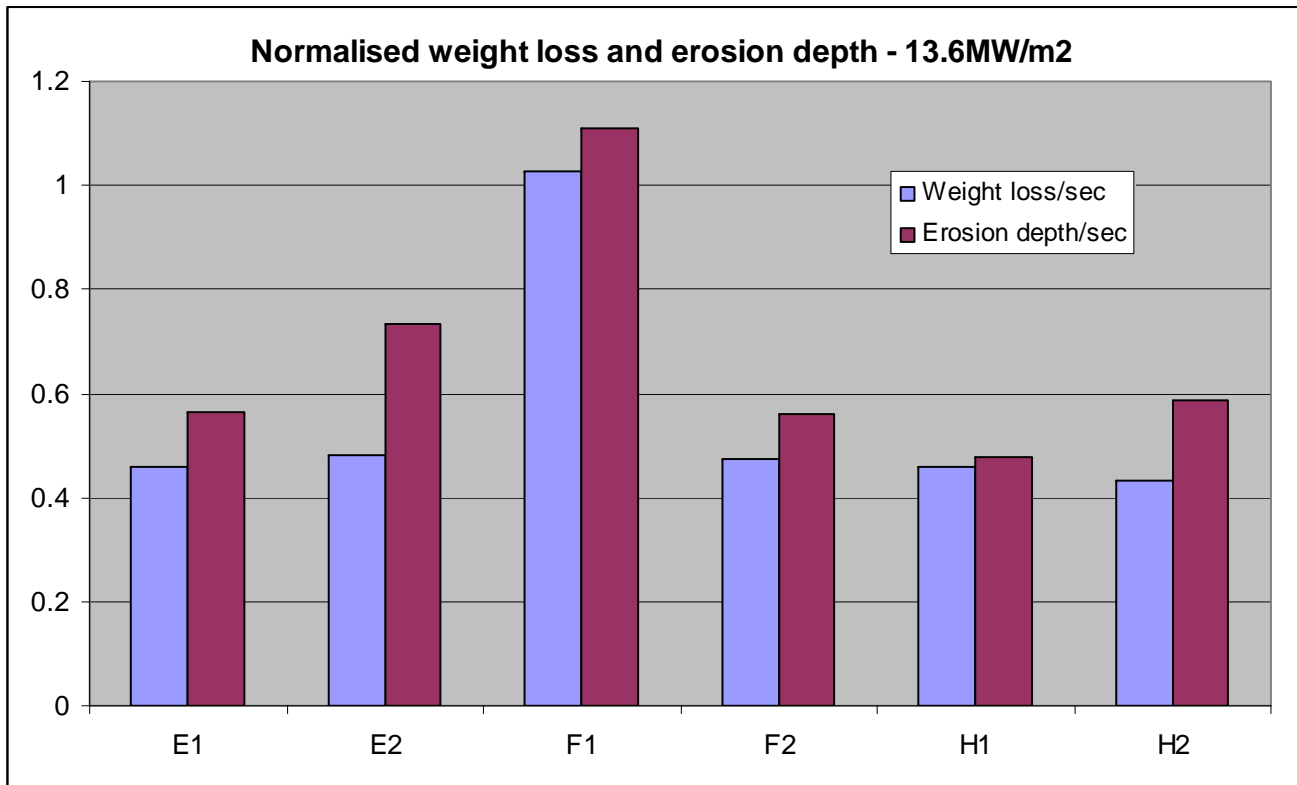
[Video](#)

Video of the D1 test at
6.1MW/m² for 25.3 seconds

All adhesives eroded more than ablator. Average erosion rate about 0.12-0.2mm/sec.
Mixing ASTERM powder with adhesive increases erosion resistance.

ASTERM joints: Plasma jet tests – DLR/L3K

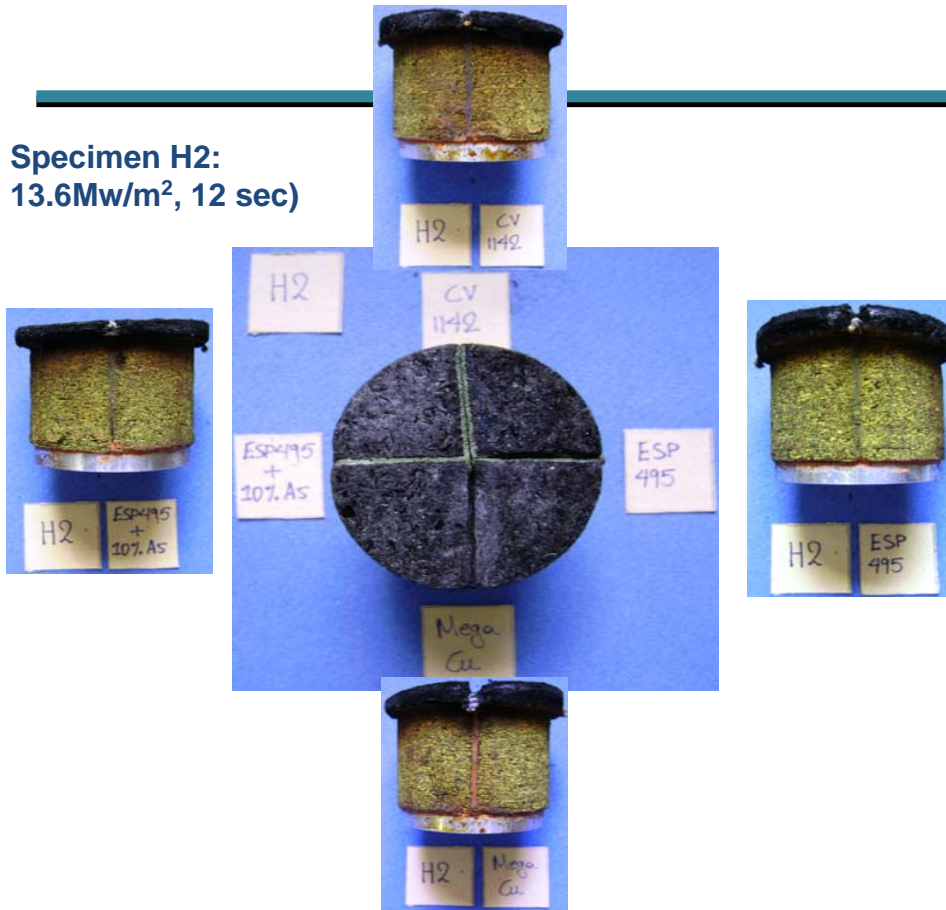
DLR/L3K tests at 13.6Mw/m², 9-14 seconds



All adhesives eroded deeper than ablator. Mostly uniform erosion with an average rate of about 0.6mm/sec for the ablator and about 0.8mm/sec for the adhesives.

ASTERM joints: Plasma jet tests – DLR/L3K

Specimen H2:
13.6Mw/m², 12 sec)



Video of the H2 test at
13.6MW/m² for 14 seconds

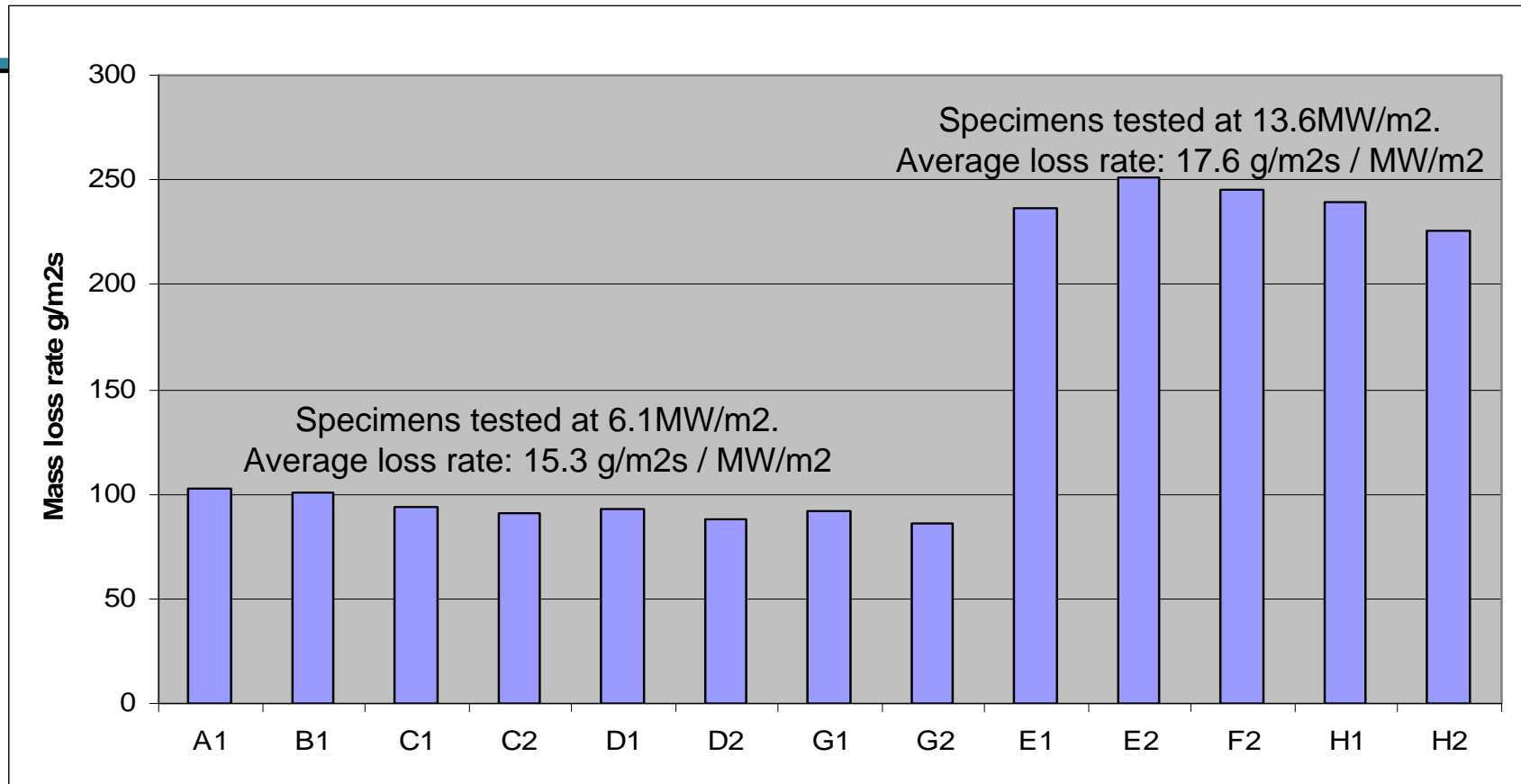
Heritage adhesives CV1142 and ESP495 displayed about 30% less erosion than the commercial adhesive tested. Mixing ASTERM powder with any adhesive increases erosion resistance.

ASTERM joints: Plasma jet tests – DLR/L3K

Sample	Joint 1				Joint 2				Joint 3				Joint 4			
	ASTERM		Gap		ASTERM		Gap		ASTERM		Gap		ASTERM		Gap	
	1a	1b	1a	1b	2a	2b	2a	2b	3a	3b	3a	3b	4a	4b	4a	4b
A1	4.5	5.6	5.5	6.3	4.5	5.5	6	7.9	4.6	6	6.5	8.5	4.6	6.1	6.2	8.3
B1	4.5	5.5	5.3	7.1	4.3	5.3	5.6	6.9	4.3	5.6	5.6	8.2	4.5	6	5.4	8.3
C1	4.6	5.5	5.4	7.1	4.4	5.2	6.2	8.5	4.5	5.6	6.2	8.4	4.5	5.6	6.3	9.5
C2	6	6.8	7	8.2	5.9	6.8	7.1	9.3	6.1	7.4	8.1	10.7	6	7.5	8.1	10.1
D1	4.4	5.1	4.9	7.1	4.4	5.5	6.1	7.5	4.7	5.8	5.9	8.8	4.6	5.6	5.8	9.3
D2	5.8	6.5	6.5	8.1	5.7	6.8	7.1	9.3	5.8	6.9	6.6	10.4	5.8	6.9	7.1	10.1
G1	4.2	4.9	5	6.5	4.5	5.2	4.9	6	4.5	5.8	5.3	8.1	4.4	5.4	4.5	6.1
G2	5.6	6.6	6.8	9.2	5.6	6.4	6.1	7.5	5.8	6.9	7.5	10.1	5.5	7	5.6	7.4
E1	7.7	6.8	9.6	10.9	8.1	6.6	12	13.5	8.6	8.6	12.8	15.5	8.5	9.1	10.7	12.4
E2	4.9	4.2	8.5	5.2	5.6	4.7	12	8.8	6	6	9.5	13.9	6.6	6.2	7.5	8.9
F2	7.6	5.4	11.5	8.7	8.1	6.5	10.8	12.2	8.3	7.7	10.7	13.1	8	7.5	13.1	12.7
H2	6.8	6.7	7.1	7.5	5.3	4.7	8.6	6.5	6.5	5.5	10.1	8.6	6.9	7.7	8.3	8.6
H1	5.4	5.2	5.4	5.9	4.6	4.2	8.5	6.9	5.4	5.1	8.4	8.5	5.9	6.7	6.8	7.8
X	5.5	6.9	5.8	8.5	6	6.4	6.4	8	6	6.4	8	11	5.8	7.4	6.8	9.8

CV1142 displayed least erosion wrt ASTERM followed by ESP495 and the commercial silicones with ASTERM powder.

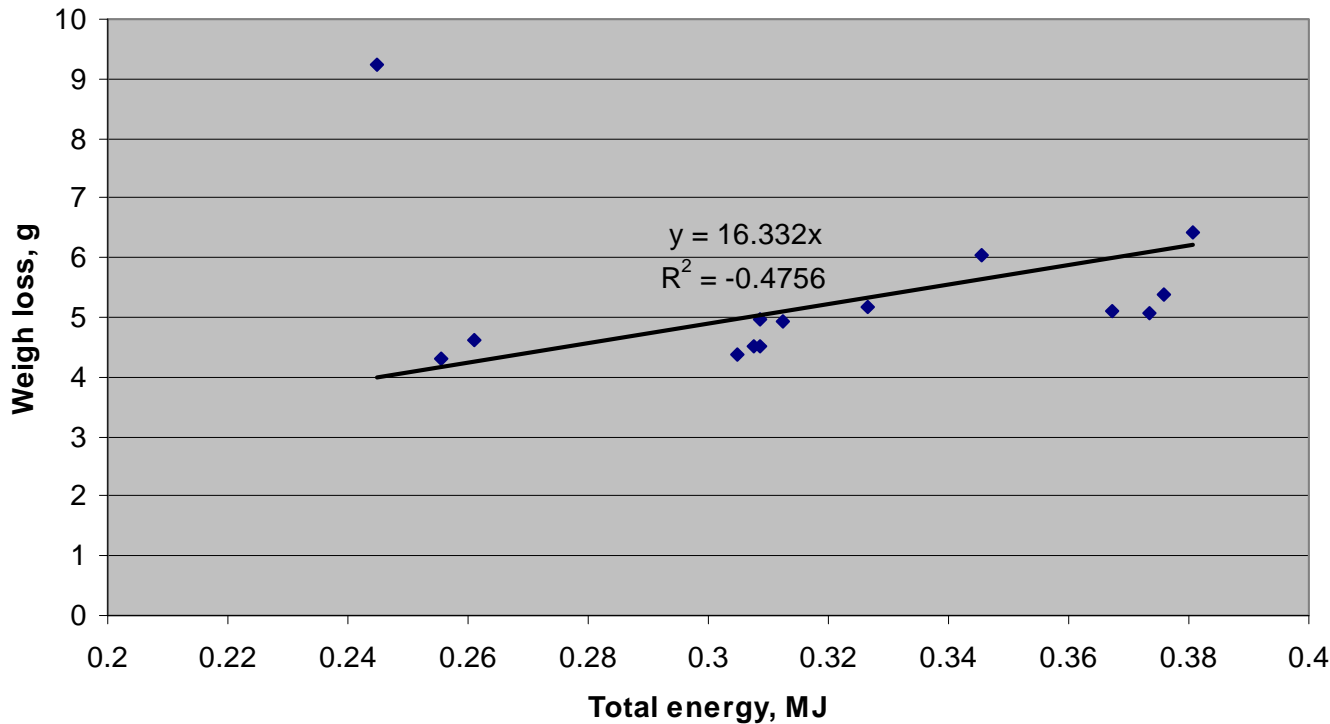
ASTERM joints: Plasma jet tests – DLR/L3K



The apparent acceleration of the mass loss rate with increasing heat flux level is possibly related to the plasma jet encroaching onto the sides of the specimen at extreme levels of erosion (aberrant result for F1 not shown).

ASTERM joints: Plasma jet tests – DLR/L3K

Weight loss against total energy for all specimens



Linear relationship of weight loss vs total plasma energy. Gradient gives 60kJ per g of material removed mainly by ablation, agreeing with independent plasma torch tests.

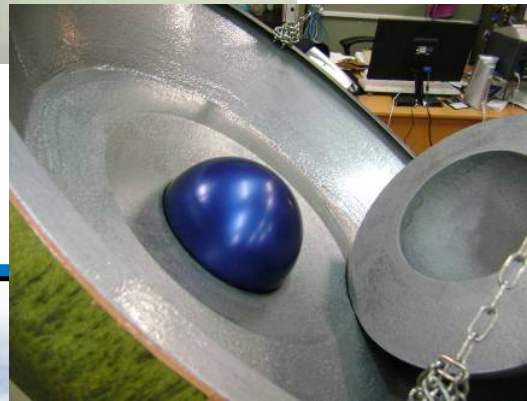
Rastas Spear: Front Heat Shield Breadboard



A front Heat Shield Breadboard Demonstrator was constructed with ASTERM and a commercial adhesive by a mainly manual, low-cost method, with a single, top surface finishing operation.

Maximum diameter 92.5cm, ablator thickness 56mm, joint and bond thickness about 1-1.2mm.

The method is flexible and can be adapted for any symmetric shape. It can be used to produce actual heat shields as long as the current dimensional tolerances are relaxed to some extent.



The inside of the breadboard Demo with the sample canister demonstrator in the crushable material made of rigid PU foam(made by IoL)

Rastas Spear: Main conclusions of the TPS tasks

- Space-qualified RTV silicone CV1142 as well as low-outgassing, low-cost, commercial RTV silicones were used for producing ASTERM joints and bonds with various substrates.
- Mechanical properties of joints and bonds were measured in shear and bending at -196°C
- ASTERM joints and bonds loaded in shear always failed through the ASTERM for all silicone adhesives examined and in both parallel and transverse loading directions.
- CV1142 displayed higher strength but similar elasticity at -196°C to commercial silicones. However, the higher strength cannot be leveraged as failure occurs through the ablator.
- Plasma-jet testing of various joints at 5.0 - 13.6MW/m² for up to 30 and 14sec respectively showed that ASTERM always displayed less recession than all joints tested, including CV1142 and ESP495 joints which were however better than commercial silicones.
- The use of ablator powder mixed-in with all silicones increases erosion resistance closer to that of ASTERM, potentially reducing irregularities on the charred surface.
- A tiled demonstrator front heat shield was manufactured satisfactorily using an alternative flexible manual method at much lower cost – this may be applicable for producing low-cost heat shields if the geometric tolerances on production method can be relaxed somewhat.

Thank you for your attention

Any questions?

More info at www.rastas-spear.eu

TPS Design, Development and Verification Approach for IXV Program

Elena Brach Prever⁽¹⁾, Maria Teresa Signorelli⁽¹⁾, Flavio Camarri⁽¹⁾, Angelo Denaro⁽¹⁾, Gandolfo Di Vita⁽²⁾

⁽¹⁾*Thales Alenia Space, Strada Antica di Collegno, 253 – 10146 Torino, Italy*

elena.brachprever@thalesaleniaspace.com

mariateresa.signorelli@thalesaleniaspace.com

flavio.camarri@thalesaleniaspace.com

angelo.denaro@thalesaleniaspace.com

⁽²⁾*ESA/Launchers Directorate – ESA HQ, Paris, France*

gandolfo.divita@esa.int

1. ABSTRACT

The need to validate through an in-flight experience re-entry systems and technologies led in the past years to design and develop several experimental vehicles.

In this context, the Future Launchers Preparatory Programme (FLPP) has been conceived by the ESA Member States to collect and harmonize the know-how gained by the European Space Community and to direct the technical effort and the necessary funds relevant to this matter on the development and the manufacturing of the Intermediate eXperimental Vehicle (IXV), a re-entry demonstrator.

Among the various technological challenges of the IXV project, there are the demonstration of the feasibility of using Hot Structures (HS) for re-entry vehicles and the need to gain information on in-flight behaviour of Thermal Protection System (TPS) materials like ceramic and ablative ones, insulations, attachments, seals. For this scope, the TPS parts are properly instrumented to perform the investigation of the material behaviour in conjunction with critical aerodynamic and aero-thermodynamic phenomena such as pressure and thermal gradients, laminar-to-turbulent transition, material catalysis, shock wave/boundary layer interactions.

The in-flight verification of TPS&HS performance built on past studies and ground verification, and aims at maturing of the technologies for operational space applications.

The main capabilities to be provided by the TPS&HS are to withstand the heat loads foreseen during the re-entry reference trajectory and to provide the adequate stiffness against the dynamic pressure to maintain the required aerodynamic shape.

Different assemblies are then foreseen in order to demonstrate different technologies and to optimize the materials involved, since different zones on the IXV surface experience different levels of thermal heat fluxes and loads.

A dedicated development and qualification program for all the TPS&HS components and technologies before the flight appears as essential.

2. INTRODUCTION

Since several years significant importance was given to the development of the critical re-entry technologies through several basic research and technology preparatory programs. Today, the in-flight verification of such technologies is considered an important European programmatic objective to be pursued within the short-term undertakings.

IXV (Intermediate eXperimental Vehicle) was conceived as a technology platform that, building on a series of technology investments and achievements, would perform the step forward with respect to the ARD demonstration, by increasing its in-flight manoeuvrability and verifying the involved technology performance.

Among the various technological challenges of the IXV project, the demonstration of the feasibility of using HS for re-entry vehicles, the need to gain information on in-flight behaviour of TPS materials like ceramic and ablative ones, insulations, attachments, seals, as well as the opportunity to enable in-flight measurements of critical aerodynamic and aero-thermodynamic phenomena such as laminar-to-turbulent transition, material catalysis, shock wave/boundary layer interactions, etc., are considered the primary objectives.

Different on-ground experimental activities at equipment, assemblies and subsystem level were executed or are planned in order to demonstrate the maturity of the different technologies involved to withstand the aerothermal loads foreseen during the re-entry.

3. IXV MISSION PHASES BREAKDOWN

The IXV TPS&HS verification activity is aimed at verifying that the TPS&HS is able to sustain the environments encountered during the entire IXV mission that, for TPS&HS sizing and verification purposes, can be subdivided in:

- Lift-off, Ascent
- Separation
- Re-entry
- Parachute Opening, Descent
- Landing

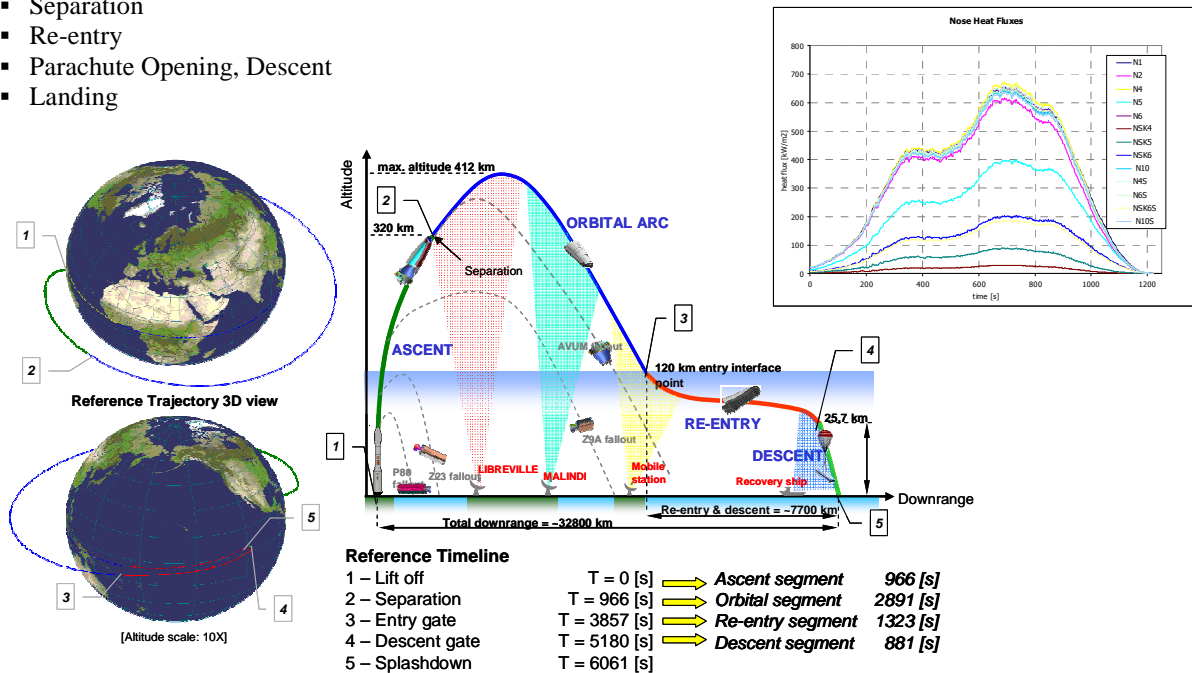


Figure 1. IXV mission phases

During lift-off and ascent phase, the TPS&HS will be subjected to dynamic, quasi-static and static loads. Shock loads are experienced during launcher stages separation and parachute opening at the beginning of descent phase. Re-entry phase represents the most critical environment for sizing of TPS&HS subjected to severe thermal and thermo-mechanical loads.

Deceleration is to be sustained during re-entry and descent phases.

At landing very demanding splashdown loads will be encountered; these loads are not taken into account for sizing: only recoverability in exploitable state is required.

4. TPS&HS ARCHITECTURE

The TPS&HS subsystem consists of the following assemblies:

- Nose Assembly HS (developed by Herakles)
- Windward C/SiC Assembly (developed by Herakles)
- Body Flap Assembly (developed by MT Aerospace)
- Leeward, Lateral and Base Assemblies (developed by Avio)

All the interfaces between different TPS&HS assemblies and between TPS&HS assemblies and different IXV subsystems are designed and developed by Thales Alenia Space. TPS&HS assemblies location on the IXV external surface is reported in Figure 2.

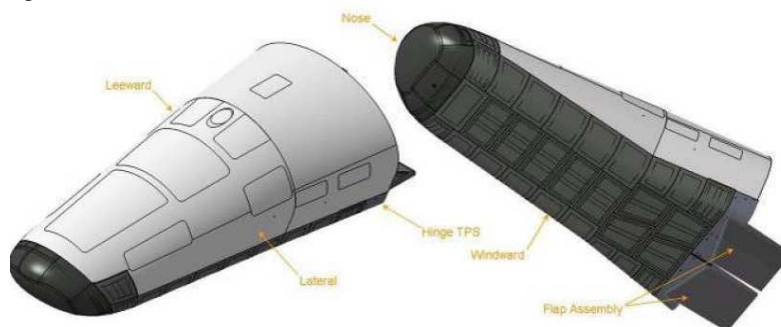


Figure 2. IXV TPS&HS layout

4.1. Nose Assembly HS

The Nose Assembly HS consists of a CMC nose filled with internal insulation held in place by an Aluminum nose dome. The nose cap has one periphery stiffener to avoid any large thermal expansion. Out of this stiffener, sixteen attachment legs link the nose cap to an Aluminum attachment ring via sixteen stand-offs. The ring is linked to the cold structure front bulkhead thanks to brackets.

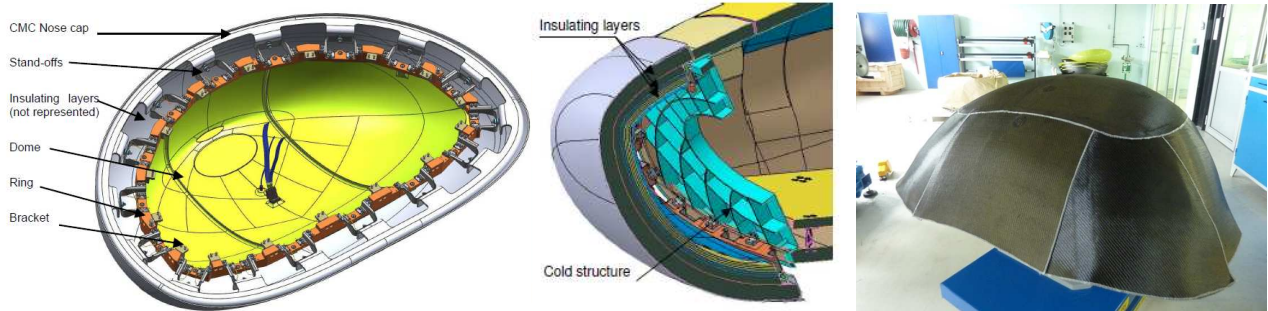


Figure 3. Nose Assembly HS design (left side) and QM part on early manufacturing stage (right side)

4.2. Windward C/SiC Assembly

The Windward C/SiC Assembly is characterized by the innovative shingle technology, which is able to dissociate mechanical functions and thermal insulation functions. This is profitable as it allows benefiting from the use of optimized materials for both functions.

This concept is divided into two sets of elements:

- the ones with mechanical functions (mechanical shell, fasteners, and stand-offs);
- the ones with thermal functions (inner insulation layers, seals and insulating washers).

Each shingle is composed of C/SiC panel made of SPS Sepcarbinox® L6® C/SiC material peripheral stiffeners and internal stiffeners (two for flat shingles and one for curved shingles); attachment system, ceramic fibre internal insulation stack-up and ceramic fiber seal placed around the peripheral stiffeners of the C/SiC panel.

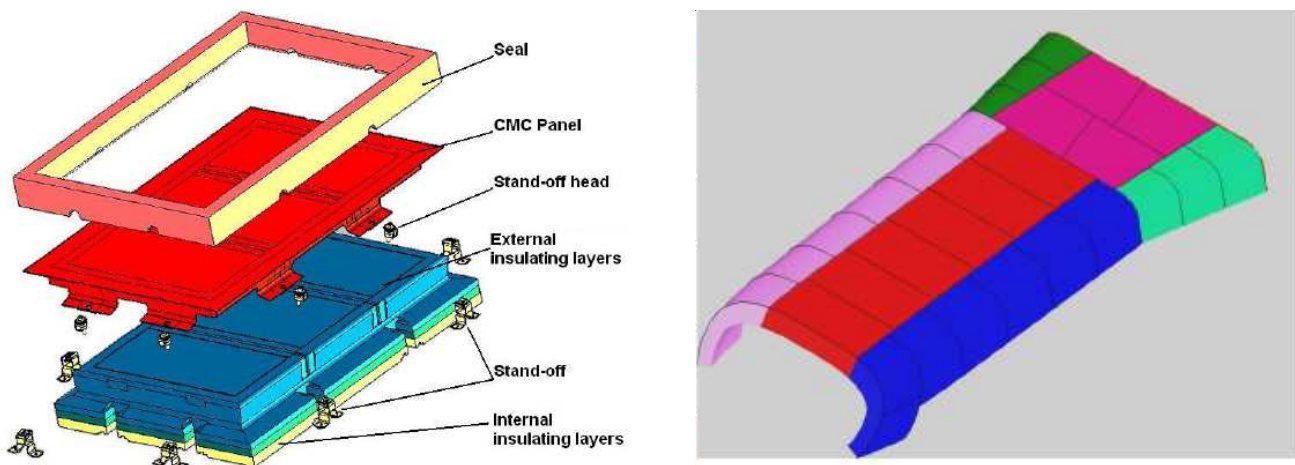


Figure 4. Shingle exploded view (left side) and Windward C/SiC Assembly pattern (right side)

4.3. Body Flap Assembly

The Body Flap Assembly is a Hot Structure designed to contribute to the aerodynamics and to the manoeuvrability of the IXV through the re-entry and the descent mission phases by providing a pair of movable, load bearing, geometrically defined, stiff and heat resistant control surfaces. The Body Flaps Assembly and its interfaces comprise the following main constituents (see Figure 5):

- a pair of control surfaces
- a rod-like between the Electro-Mechanical Actuator (EMA) and each of the body flaps to deflect the flap for flight control
- ceramic bearings installed at the attachment points
- flexible Nextel-Saffil hinge seals used to close the gaps between the leading edge of each flap and the opposing surface of the windward TPS of the IXV vehicle at the hinge line
- Hinge TPS that forms the TPS interface between the body flap and the windward shingles
- EMA TPS, that provides the interface with bulkhead, hinge TPS and flap rod.



Figure 5. Body Flap Assembly design (left side) and QM manufactured parts (right side)

4.4. Leeward, Lateral and Base Assembly

The Ablative TPS consists of different materials, each fulfilling a dedicated function:

- an external insulating material providing the heat absorption and removal by means of thermo-ablative phenomena: **P50 cork** on the majority of the IXV surface (22mm thickness on leeward and lateral areas and 18mm thickness on base area) and a silicone elastomer based material **SV2-A** on antennas
- an antistatic paint coating on the external ablative surface, avoiding electrostatic charge accumulation and providing known thermo-optical properties to the outer insulator surface, as well as avoiding moisture absorption
- an adhesive layer that provides the bonding of the insulating material on IXV cold structure (EA9394 for P50, siliconic adhesive for SV2-A)
- a filler (based on EA9394 and P50 for P50, siliconic for SV2-A) that provides a continuum insulating mean in correspondence of gaps present between the insulating material tiles.

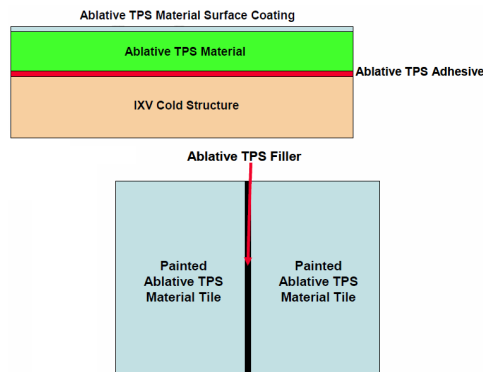


Figure 6. Ablative TPS materials functional scheme

4.5. TPS&HS Interfaces

Each single TPS assembly is designed to properly interface with the vehicle cold structure, the adjacent components, the launcher adapter, the sensors foreseen for in-flight experimentation, and the MGSE. In the present section a brief description of interfaces between the different TPS assemblies is reported.

4.5.1. Ablative TPS / Shingle Interface

Windward shingles are designed with the already described attachment system. The ablative TPS is directly glued to the cold structure. At the boundary between windward/leeward and windward/lateral, respectively a cold structure step is required in order to host both assemblies due to the different thicknesses. An interface solution between these two different types of TPS shall therefore protect the cold structure wedge surface from the heating arising from the shingle side.

The I/F ablative side design solution adopted consider Saffil-Nextel seals. In this configuration, the Saffil-Nextel seal is placed into a recess of structure wedge (see Figure 7) in order to guarantee a maximum temperature of 160°C at the interface with the cold structure (both aside and underneath the seal itself). The shingle CMC overlaps the ablative in order to drop the sneaking flow occurring through sealing and insulating material.

4.5.2. Ablative TPS / Nose Interface

The interface between nose and leeward ablative TPS adopts a configuration similar to that described for the shingle to ablative I/F. The same materials are involved, thus a similar solution has been proposed and then validated by analysis.

4.5.3. Ablative TPS / Hinge TPS Interface

The interface between lateral ablative and hinge TPS assemblies is illustrated in Figure 7. Hinge CMC overlaps the ablative in order to drop the sneaking flow occurring through sealing and insulating material. Ablative side seal is composed by Saffil-Nextel seal similarly to the hinge side seal.

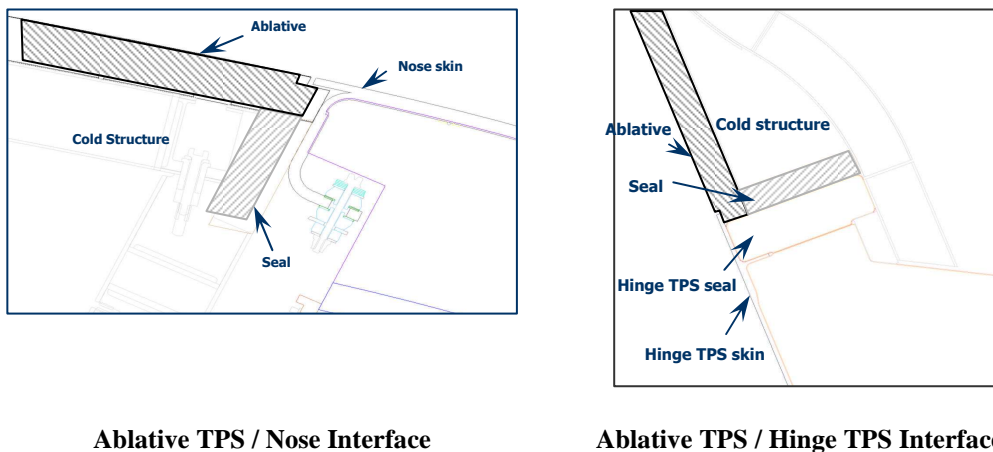


Figure 7. Interfaces between different TPS&HS assemblies

5. DEVELOPMENT AND QUALIFICATION APPROACH FOR TPS&HS ASSEMBLIES

The TPS&HS development and qualification phases consist of several activities following a bottom-up approach from equipment development level to subsystem and system qualification. The definition of these activities relies on an iterative process involving many engineering disciplines i.e. the aerothermodynamics, structures, thermal control, operations, AIT from subsystem point of view and on the cooperation between the prime contractor and the different subcontractors responsible for each subassembly.

Considering the complexity of the IXV TPS&HS S/S based on different materials and technologies involved, some criticalities arose, in particular the design and development of the CMC nose and the qualification for re-entry applications of the Avio ablative materials usually applied on launchers, and therefore subjected to aerothermal loads very different.

On the other side the Windward Assembly based on CMC shingles has been developed by Herakles in past programs funded by CNES and ESA and during the early phase of IXV Program and FLPP Materials & Structures1 (M&S1) achieving a TRL 5/6. Anyway, given the complexity of the TPS elements a large number of development tests have been carried out in phase C2 and in early phase D in order to cover the specific issues of IXV program. Many of these activities cover also the Nose Assembly development that is characterized by the same materials and similar attachments, insulation and sealing systems.

The Body Flap Assembly maximize the experience and the background acquired in past programs (e.g. X-38 and EXPERT) dealing with the TPS for atmospheric re-entry.

5.1. Nose and Windward Assembly

An extensive development campaign was conducted during phase C2. Material characterization in terms of oxidation behaviour and catalycity has been performed exposing CMC coupons to the plasma environment at VKI; particular effort has been devoted to the identification of active-to-passive oxidation transition that has been considered a critical constraint for the mission. CMC samples were subjected to mechanical tests (tensile, compression, shear) and thermal tests (thermal diffusivity, thermal expansion, specific heat).

In the frame of the development activities, the mechanical and thermo-mechanical performances of CMC shingles have been conducted through detailed FE analysis. The thermal insulation capability has been verified by means of numerical analysis and development tests are carried out in ISQ facility on representative insulation layers. Permeability, venting and sneak flow tests have been carried out at ISQ to assess the assumptions made in the analysis. Different tests have been carried out to verify the design of the attachment system design by mechanical and thermal point of view of both metallic and CMC components. The pressure port was subjected to mechanical, dynamic and thermal tests.

A dedicated assembly test was conducted to verify shingle components mountability/dismountability (and to check operation duration), insulation cutting, no damage on CMC and seal, shimming between adjacent shingles, together with sensors installation feasibility (see Figure 9).

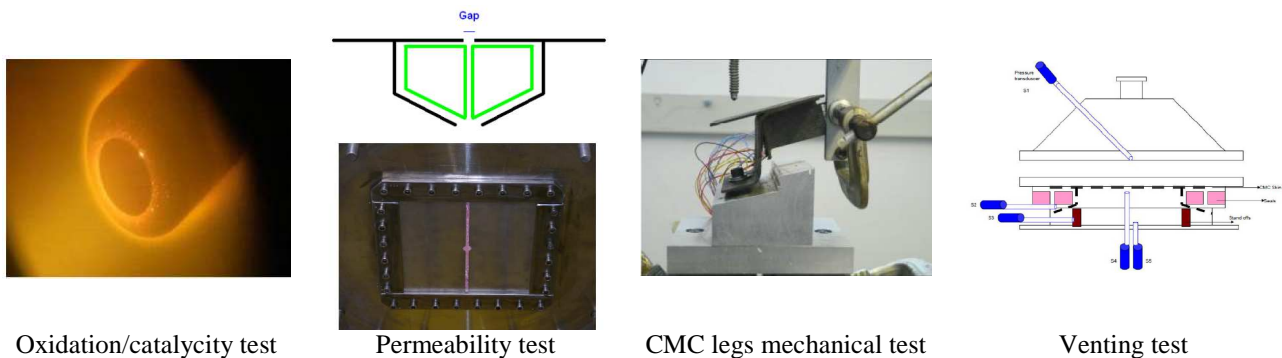


Figure 8. Figures and/or sketches of Nose and Windward C/SiC Assembly development tests campaign

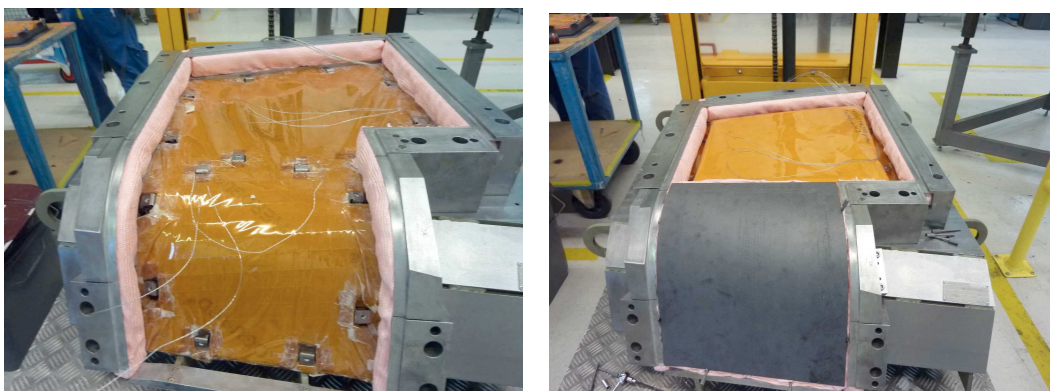


Figure 9. Shingles assembly test

Qualification tests during phase D comprise a Plasma Wind Tunnel Test of an array of shingles equipped with singularities (e.g. instrumentation interface ports) at the SCIROCCO PWT facility (CIRA). A thermo-mechanical test under representative thermal loads will be performed at ISQ facility.

Moreover a dedicated dynamic qualification test campaign is planned to verify compatibility of nose and shingles under the launch dynamic environment in ISQ facility.

5.2. Leeward, Lateral and Base Ablative Assembly

Ablative SV2-A provided by Avio has been subjected to thermal characterization (thermal properties evaluation) before ablation phenomena occurs. Thermo-gravimetric analysis has been performed to identify thermo-chemical behaviour during pyrolysis reactions. Plasma tests on small coupons at SPES (University of Naples) and at VKI have been performed to complete the characterization in representative environment and to assess the capability of the material to sustain the re-entry heat loads.

A number of tests was conducted on P50 material: thermo-physical tests (specific heat, enthalpy of formation, for both virgin and charred material, thermal conductivity, TGA, mass spectrometry, CTE), mechanical characterization (ultimate elongation, Young modulus, hardness, density, ultimate pull and shear strength, peeling), interface bonding shear tests, humidity, ageing and outgassing tests, torch tests, technological tests (for full scale application for 22 mm thickness) and thermo-ablative tests (in VKI Plasmatron).

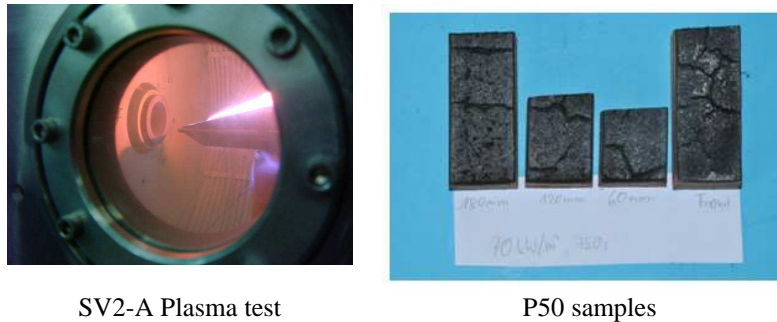


Figure 10. SV2-A and P50 development tests

The assembly qualification test on the ablative TPS will be performed in “full scale” configuration and will be mainly dedicated to the testing of P50 different bonding strategies: vacuum bag (already qualified in the frame of Vega program), weights, adhesive tape; additional test objectives are the SV2-A bonding qualification the mortar cap bonding and the unglued area verification. Furthermore the PWT S/S qualification test will allow verifying the behaviour of a ablative TPS panel in re-entry representative environment and to verify the I/F between P50 and SV2-A materials.

Ablative TPS tiles are/will be made available by Avio and implemented into the IXV test model to be utilized for the following test activities:

- DRS drop test
- In-Flight Experimentation tests (performed by RUAG, to verify the correct thermocouples installation design)
- Antenna + Fiberglass + Ablative TPS compatibility test
- DRS panels separation test
- Full-scale bridle extraction test.

5.3. Body Flap Assembly

Considering the sufficient high TRL (≥ 5) of the body flap reached during X-38 and EXPERT programs and of the hinge TPS, no development test were performed in phase C2. For what concerns the EMA TPS, the increase of the development status of this equipment by means of ground tests has been considered unfeasible and therefore the development has been carried out only by analysis. Catalycity and emissivity tests have been carried out on Keraman samples at VKI.

The qualification by similarity of the body flap assembly design towards the combined thermo-mechanical environment during re-entry can be pursued by using the thermo-mechanical model used for X-38 project and extrapolate the results to temperatures above 1600°C. Qualification by similarity of bearing performances with what available from X-38 project can be also pursued even accounting the restrictions concerning the X-38 test conditions with respect to the IXV application (mainly due to different deflection range, different number of deflection cycles, thermal test performed without mechanical load). The correlation of applied deflection cycles, applied deflection angle and involved surface for X-38 with IXV BFA bearings requirements shows that wear path accumulated by the X-38 bearings exceeds IXV requirements (5500 mm versus 2600 mm).

A thermal qualification test was conducted on a QM consisting of the EMA TPS including the seal sliding on the EMA rod, with the scope to qualify the BFA with respect to the thermal barrier performance, the kinematics of the rod under exposure to thermal and pressure environments occurring during re-entry and the integrity of the hardware with respect to the thermal environment (material degradation due to high temperature loads). Body flap and hinge TPS dynamic tests have been performed to qualify the BFA to the harmonic, random and shock loads expected during IXV mission and to assess the first eigenmode of hinge TPS and body flap. A pressure test is planned on body flap and hinge TPS.

6. QUALIFICATION TESTS OF TPS&HS AT S/S AND SYSTEM LEVEL

Qualification tests at TPS&HS S/S level are related to the necessity of verifying:

- the design of the interfaces between the adjacent TPS Assemblies (critical TPS technology) in terms of capability to comply with the requirements relevant to the allowed sneak flow (overheating) and the steps and gaps displacements coming from the aerothermodynamics discipline in “hot conditions”;
- the design of the interfaces between the TPS and other IXV Subsystems (e.g. DRS, RCS).

6.1. TPS&HS S/S Verification

The areas where different materials are interfacing can be critical elements of the TPS&HS S/S in terms of behaviour under exposure to the aerothermal fluxes also in consideration of possible singularities as gaps and steps. Their verification under PWT condition can be considered as complementary to the PWT test foreseen at shingles level. The test will be carried out to evaluate the TPS behaviour in correspondence of the TPS interfaces most critical concerning aerothermal flux levels of the complete IXV TPS.

The chosen areas are the four reported in Figure 11.

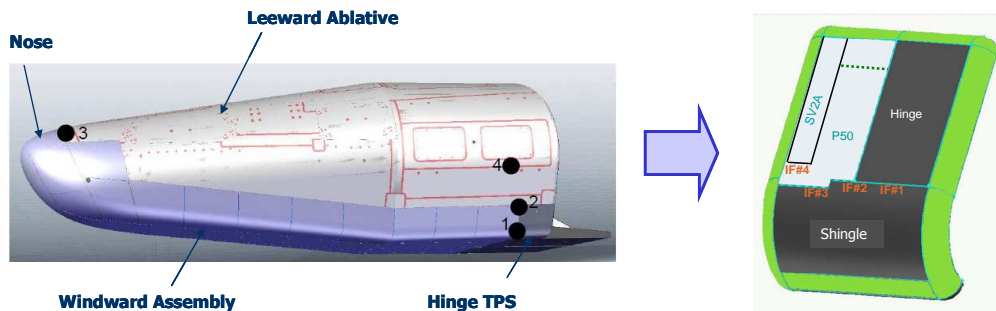


Figure 11. Adjacent TPS I/Fs

The Test Article to be tested in SCIROCCO PWT facility (CIRA) is an assembly of 4 different panels, one curved and three flat panels, supported by a test holder interfacing with the test facility. The overall projected are 600 x 500 mm, in agreement with the maximum dimensions compatible with the facility.

The front face directly exposed to the incident plasma flow is by consequence defined by:

- Three flat surfaces forming an overall flat surface of about 400 x 400 mm. For the test of IF#2, IF#3, IF#4, performed as first run, one of them is made of MT Aerospace Keraman (Hinge TPS) and the other of Avio P50 and SV2-A. At the interface between the ablative and hinge panel a gap of 2 mm is foreseen. For the test of IF #1 (second run), due to the largest heat fluxes, the ablative materials tile are substituted by a flat shingle.
- One Herakles CMC curved panel with a cylindrical surface. Its length is 400 mm and its radius is 200 mm. At the interface with the MT Aerospace flat panel a gap of 3 mm is foreseen, while at the interface with Avio flat panel a gap of 2 mm is foreseen.
- All the interfaces and the attachments will be as close as possible to the flight configuration. The hardware will be equipped with thermocouples and pressure transducers to achieve a large number of experimental data for numerical rebuilding and experiments evaluation.

6.2. Body Flap Assembly Chain

A joint test to verify the complete FlaPs Control System (FPCS), i.e. the combined EMA/Body Flap Assembly performances, will be performed.

The test will re-use the test bench developed by MT Aerospace to test the body flap under load. After the end of MT Aerospace activities, the actuator used on the test bench will be replaced by the qualification model of SABCA. Aim of the test is to validate and calibrate the multi-body model of the body flap chain, and to run a final set of cases to have the final prediction of the body flap chain during flight.

DEVELOPMENT AND QUALIFICATION OF THE THERMAL PROTECTIVE SEAL OF IXV'S HOT STRUCTURE CONTROL SURFACE ACTUATOR ROD

Farid Infed, Harald Lange, Armin Steinacher, Karin Handrick

MT-Aerospace, Franz-Josef-Strauß-Straße 5, 86153 Augsburg, Germany
farid.infed@mt-aerospace.de, harald.lange@mt-aerospace.de, armin.steinacher@mt-aerospace.de,
karin.handrick@mt-aerospace.de

Carlos Pereira

RUAG Space Switzerland, CH- 8052 Zürich, Schaffhauserstrasse 580, Switzerland
carlos.pereira@ruag.com

Abstract

For the Intermediate eXperimental Vehicle (IXV) the deflection of the highly loaded body flap is performed by an actuator system which is connected to the body flap by a rod. Beside the thermal and mechanical loads the sealing of the inner vehicle against possible leaking hot plasma is an important issue whereby the special challenge for the design results from the spatial movement of the rod. This requires a design consisting of different parts and various materials in order to satisfy the mechanical flexibility and the resistance to the thermal and mechanical loads under the aspect of reusability. The first part of the paper describes the MT Aerospace (MT) approach for the thermal protection system for the actuator as currently realized for the flight hardware of IXV. The design will be presented and described, including all necessary performed analysis steps towards such special layout.

The second major of the paper is to explain the qualification approach and its realization with the RUAG testing facilities. Finally, the results of the successfully performed qualification campaign will be presented and discussed in context with the goals of the qualification and the design layout assumptions, reflecting the robustness of the design with respect to the expected loads during IXVs flight.

1. INTRODUCTION

In continuation of the Future Launchers Preparatory Program (FLPP), which has been initialized by the ESA Member States to collect and harmonize the know-how gained by the European Space Community and to direct the technical effort and the necessary funds relevant to this matter on, the development with the aim of manufacturing and launching, a European re-entry demonstrator, has emerged.

One of the technological challenges to be mastered during the IXV program is the layout, manufacturing and qualification of a reusable Thermal Protection System (TPS), which will be tested in real flight returning from Low Earth Orbit (LEO). The realization, as for the TPS, of Hot Structure (HS) in shape of body flaps as a control surface sustaining very high temperatures and

significant mechanical loads arises from the vehicles concept and its navigation and guidance control concept, is also a great challenge.

MT Aerospace is in charge of developing and manufacturing both kinds of high temperature application parts namely the Hinge TPS, which can be considered as part of the TPS and the Body Flap Assembly (BFA), which are the control surfaces of the vehicle. The common strategy of ESA, Thales Alenia Space Italia (TASI), as a prime for the vehicle, and MT Aerospace is to apply as much as possible of the experience by the successful development and qualification of CMC body flaps, leading edges and chin panel of the X-38 vehicle .

The control concept of the vehicle and executing the control movements of the body flap by a rod, which is connected with inner vehicle at the Electro-Mechanical Actuator (EMA) on one side and with the body flap on the other side, requires the design of a sealing in order to prevent the entrance of hot air flows into the vehicle. Considering the share of radiative heating emitted in the region and its great contribution to the temperatures governing the same region, the sealing, which we call 'Bellow', fulfills also the function of radiation protection device.

After all, beside the heat protection qualities of the Bellow, this part should be mainly build by flexible materials in order to keep its sealing function during the body flap and therefore the rods movements. The fixation and attachment to the main vehicle of such flexible and protective element requires the combination of non-flexible materials in shape of rings and bolts, which has not only to sustain thermal loads caused by the re-entry of the vehicle, but also mechanical loads in terms of vibrations, pressure differences and acceleration vectors at different stages of IXVs mission. The temperatures requirements of the so called Cold Structure (CS) with a limiting temperature of 433 K (160°C), on which the protective seals have to be fixed, makes the use of isolative materials absolutely necessary.

The combination of all attachments parts, Rod, Bellow and insulations gives the EMA TPS. This paper describes as main issue the development of such TPS. From the thermal, pressure and mechanical requirements given by IXVs mission profile, in combination with the geometrical design concept and the used materials, the layout process will be described showing the

design optimization process reached by means of final element simulations. Finally, a qualification test was performed at RUAG Space to verify the EMA TPS CDR design hardware and to prove the functionality and the integrity of all components after exposure to re-entry loads.

2. DESIGN DESCRIPTION

For the BFA Ceramic Composite Material (CMC) hot structure technologies developed and qualified in X-38 and related programs are applied [R1]. The product depicted in Fig. 1 and Fig. 2 concerns the assembly of two symmetrically identical Body Flaps, to be integrated at the rear part of the IXV vehicle for the purpose of active control during re-entry. Furthermore, two adjacent TPS elements – called Hinge TPS – representing the cavity for Body Flaps accommodation and the EMA TPS that closes the opening between the actuation rod and the rear TPS of the vehicle are part of the BFA. Both elements ensure the thermal protection of the aft vehicle directly facing to the body flaps.

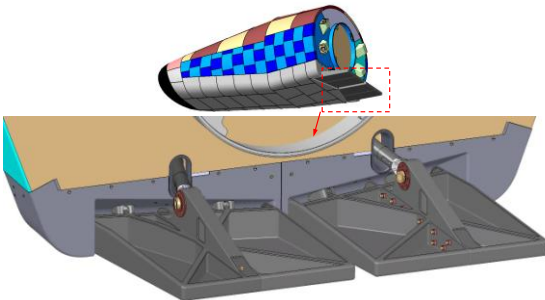


Fig. 1: Body Flap Assembly of the IXV vehicle

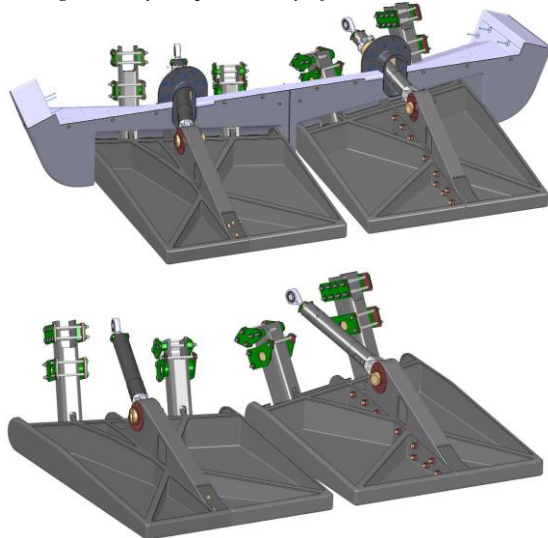


Fig. 2: BFA main items (Body Flaps, Hinge TPS and EMA TPS)

The detailed description of the components has been published in the past [R2].

3. ANALYSIS AND VIRTUEL DESIGN VERIFICATION

The IXV experiences during its different mission phases a variety of complex loads and interacting thermal and mechanical loads pre-defined by the prime TASI. All requirements were summarized in a set of assessment criteria. Considering all load scenarios, the design of the components had to take into account the following main criteria:

- Limit temperature of materials
- Avoiding the occurrence of active oxidation
- Avoiding occurrence of first eigenmode
- Achieving positive margins of safety wrt. stress and reaction forces at I/Fs, bearings and fasteners
- Step and gap requirements
- Limitation of the surface bowing

This design status was achieved after several design and analysis loops starting on an initial design without precursor from previous phases and leading to a stepwise improvement. This optimization process was dedicated mainly to the requirement on allowable max. temperature at the cold structure. Other requirements turned out to be already fulfilled by the initial design solution. A summary of the analysis subjects are collected in *Table 1*. The computations were performed according to following methodology and considerations:

- Due to the selected design, the specified environmental and load conditions, the thermal loading of the EMA TPS was the design driving parameter, especially wrt serviceable materials for the flexible bellows. Thus, firstly a thermal FE model was established with all constituents of the EMA TPS and realistic thermal boundary conditions. Analysis runs considered the most critical heating conditions, i.e. specified thermal load cases for the re-entry phase. Main outputs were the max. temperatures of the different materials and I/Fs as well as the temperature distribution in the non-flexible components.
- Secondly, a simplified structural FE model was established on which the temperature distributions at distinct instants from thermal analysis results were mapped in order to determine the thermally induced stresses in the non-flexible structural parts and the I/F connection.
- Thirdly, the heat input by gas-flow through the bellows from the leeward side into the vehicle's aft compartment was estimated on conservative assumptions in order to preliminarily justify the sealing function of the EMA TPS.
- Fourthly, the integrity of the Bellows is demonstrated wrt to mechanical loading by simplified analytical calculations.
- The simplifications concerning the third and fourth item are justified by the rather low mechanical load levels, the vague specifications concerning

the pressure environment in the vicinity of the EMA TPS and by the early development state.

type of analysis	subject	Analyzed?
thermal	T-distribution	x
	max. T at I/F	x
	occurrence of active oxidation	x
gas flow	heat input into vehicle's aft structure by hot air penetration	x
structural	frequency of first dynamic mode	no
	stresses/strength	x
	deformations	no
	bearing forces	n/a
	forces in fasteners	x
	I/F forces	x
	steps and gaps	n/a
	buckling	x

Table 1 : Analysis scope for the EMA TPS

The thermal load cases for the Body Flap and the Hinge TPS are compiled in Table 2. With the exception of load case No. 3, that concerns the temperature evolution after splash-down, only load conditions relevant for the re-entry and descent phase of the IXV were considered in the layout computations. The heat loads during ground, ascent and induced by the thrusters were comparatively low and not explicitly assessed, however part of the analysis runs of LC1 and LC2 which start with the instant of begin of re-entry

LC No.	phase	α	Thermal Load Definition	criteria
1	re-entry	-5°	Aerothermal heating environment of case "maximum heat flux"	limit temp. (material, CS), P/A transition
2	re-entry	-5°	Aerothermal heating environment of case "maximum heat load"	maximum cold structure temperature
3	splash-down	-	calculated temperatures decay at the instant of splash-down, $T_{water} = 25^{\circ}C$	Thermal shock

Table 2 : Thermal load cases for the BF and HTPS

For the EMA TPS only load conditions relevant for the re-entry and descent phase of the IXV were taken into account. Loads induced by the thrusters and resulting

from splash-down were assumed not to be applicable. The focus was on the geometrical configuration, where the BF with a deflection α of -5°. Table 3 summarizes the load cases.

LC No.	phase	α	Thermal Load Definition	criteria
1	re-entry	-5°	Aero-thermal heating and Pressure environment (Max Heat Load)	limit temp. (material, CS)
2	re-entry	-5°	Aero-thermal heating and Pressure environment (Max Heat Flux)	limit temp. (material, CS) P/A Oxidation
3	re-entry	-5°	Aero-thermal heating, pressure environment and max.pressure difference 0.1 bar (Max Heat Load)	heat input by gas-flow through EMA bellows

Table 3 : Thermal load cases for the EMA TPS

The thermal loads cases account for two separate cases or re-entry scenarios:

- maximum heat load trajectory (MHL) (relevant for sizing of components in order to maintain given cold structure limit temperatures)
- maximum heat flux trajectory (MHF) (relevant for demonstrating CMC limit temperatures and analysis of passive/active oxidation phenomena).

Both trajectory scenarios differ in loading and duration. The time line is given in Fig. 3.

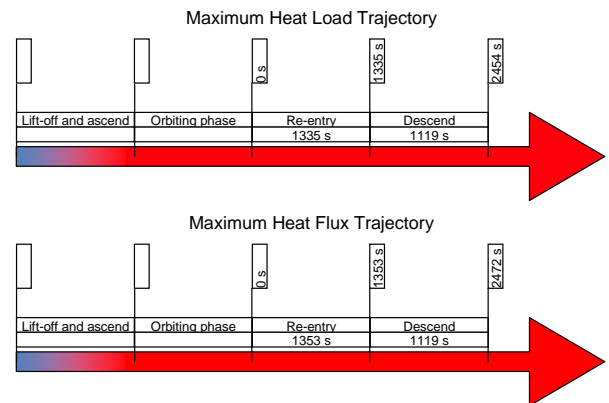


Fig. 3: Time lines for MHL and MHF

The applicability of thermal loads during the different flight phases was defined in a load applicability matrix. The matrix contains the source (convective loads, solar flux, Albedo, earth shine and radiation sink) of the thermal loads relevant for the particular mission phase. The convective loads were defined only for the re-entry phase but not for the subsequent descend phase. Thus, no release of heat to the surrounding atmosphere was taken into account during the descend phase.

The convective loads for the body flap and the hinge TPS are defined in technical specification and further detailed in Excel spreadsheets, which were delivered

along with the specification. As an example, the time evolution of the magnitudes for some Aerothermal Dynamics (ATD) controls points is given in Fig. 4 and Fig. 5.

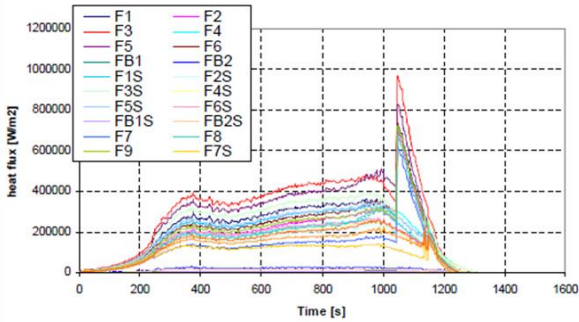


Fig. 4: MHL convective loading

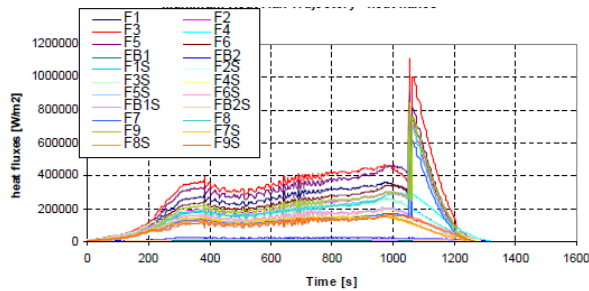


Fig. 5: MHF convective loading

For the complex geometrical surface of the vehicle with few ATD control points, heat flux distributions taken directly from the aero-thermodynamic computation have been applied. These flux maps have been delivered for the maximum heat load and the maximum heat flux case for Flap and Hinge as TECPLOT files (see Fig. 6). The porting of spatial and time dependent flux values has been done in a subroutine that utilized a nearest neighbor search algorithm for assigning the correct flux value for each of the concerned nodes in the thermal mathematical model.

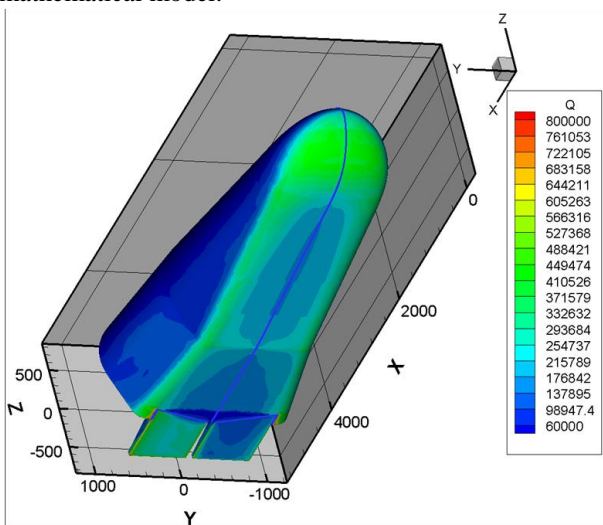


Fig. 6: Tecplot data of heat flux (max heat flux, $t = 1057s$) Same applies to the extraction of the pressure data.

Fig. 7 shows the time dependent pressure for the prementioned ATD control points.

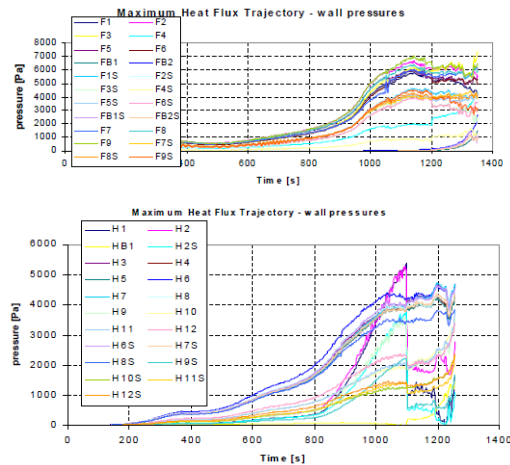


Fig. 7: Wall pressure evolution during re-entry

The relevant structural load cases are summarized in Table 4

LC No.	phase	mech. design limit load	subject
1_1	lift-off	harmonic vibration at f_1 with spec. sine or QSL = sine equivalent: 8gx, 20gy, 19.6gz	bellows, fixations, structure
1_2 ¹⁾	lift-off	$\Delta p = 100\text{mbar}$ internal overpressure	bellows, fixations, structure
1_3	lift-off	$\Delta p = 100\text{mbar}$ internal overpressure + LC1_1	bellows, fixations, structure
2 ²⁾	Re-entry	Δp , QSL=6g, T@1080 s	bellows, fixations, structure

Table 4 : Structural load cases for the EMA TPS

Maximum Temperature:

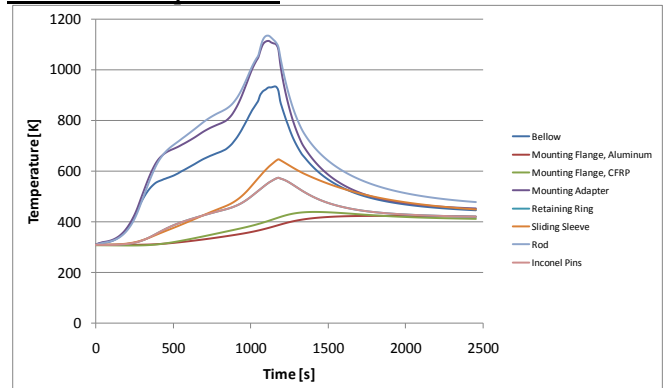


Fig. 8: Maximum temperatures of the EMA TPS parts during re-entry, MHL

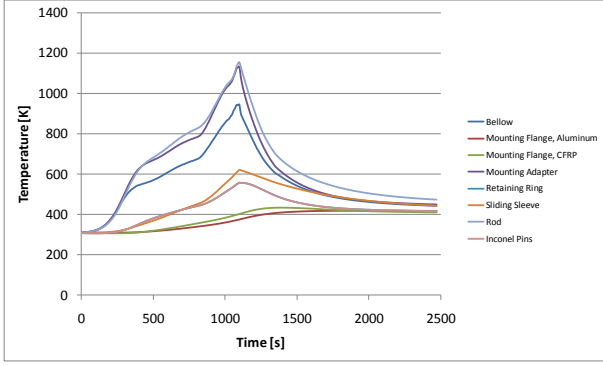


Fig. 9: Maximum temperatures of the EMA TPS parts during re-entry, MHF

Fig. 8 shows the evolution of the maximum temperature of the EMA TPS parts during re-entry for maximum heat load. The maximum Bellow temperature at the peak heating, which occurs 1160 sec after the beginning of the re-entry phase, is about 933 K and thus significantly lower than the allowed material temperature of 1473 K. The CMC parts (Mounting Adapter, Mounting Sleeve and the Rod) are in the range between 650 K and 1140 K, which is far away from the maximum possible operational temperature of CMC (2000 K). The optimized insulation layout keeps the temperature of the aluminum part of the Mounting Flange under the required maximum temperature of 433 K. The maximum temperature for 3 mm thick aluminum interface is about 430 K. The CFRP part of the Mounting Flange reaches 415 K. The Retaining Ring and Pins are in an acceptable range of 575 K for Inconel alloy. Even for the MHF load case, see Fig. 9, which is only relevant for the dimensioning of the non cold structure parts regarding the maximum temperatures for the EMA-TPS parts are within secure range of the maximum material operating temperatures. The Bellow reaches temperatures of 950 K, CMC parts are within 625 K and 1160 K and the Inconel parts have a maximum temperature of 560 K. The Mounting Flange reaches 433 K. At the aluminum part of the Mounting Flange and at the CFRP part a maximum temperature of 416 K, respectively 410K is expected. The following table summarizes the expected temperatures w.r.t. allowable material temperature range.

Part	Material	Expected Temperature	Allowable Temperature
Bellow	Nextel/Saffil	950 K	1475 K
Mounting Flange	CFRP	415 K	433 K
Mounting Flange	Aluminum 7075-T6	430 K	433 K
Mounting Adapter	KERAMAN© C/SiC	1160 K	1950 K
Retaining Ring	KERAMAN© C/SiC	650 K	1950 K
Rod	KERAMAN© C/SiC	1160 K	1925 K
Sliding Sleeve	KERAMAN© C/SiC	650 K	1925 K
Screws→Pin	Inconel 718	575 K	1100 K

Table 5 : EMA TPS maximum expected part temperatures and the allowable material temperatures

PA Oxidation:

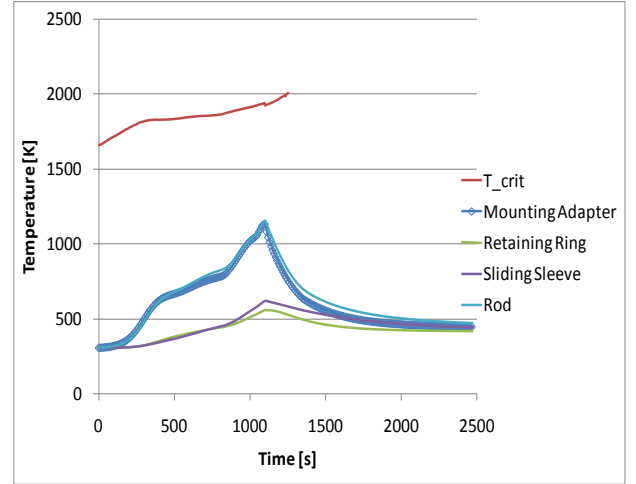


Fig. 10: Temperature vs. pressure evolution along the MHF trajectory for the CMC parts

Fig. 10 shows that the CMC parts of the EMA TPS are clearly far away from the PA oxidation transition line and definitely within the passive oxidation region. The danger of active oxidation can definitely be excluded.

Leak flow through Bellow:

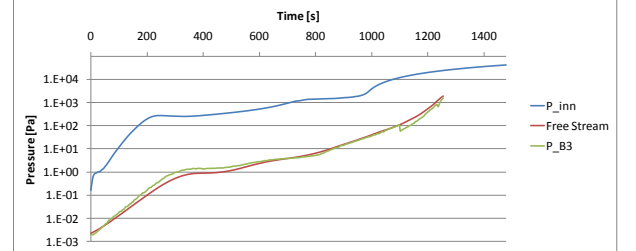


Fig. 11: Pressure evolution inside and outside the vehicle near EMA

Taking into account the pressure outside the vehicle (but within the EMA TPS region) and the inner vehicle pressure as shown in Fig. 11, one can see that the pressure in the vehicle during the hot re-entry phase is permanently higher than the one outside the vehicle. Therefore, a heat flow into the vehicle cannot be assumed. However, for safety reasons, a pressure difference driving the flow through the Bellow into the vehicle has been considered. For calculating the Δp , the inner vehicles pressure has been set to 0 Pa.

$$\Delta p = P_{B3}, \quad (1)$$

The mass flow through the Bellow into the vehicle was calculated using the simplified 1-dimensional Darcy equation, which describes leakage mass flow through porous media:

$$\dot{m} = \frac{\rho}{\mu} \cdot A_{Flow} \cdot L_{Flow}^{-1} \cdot k \cdot \Delta p \quad (2)$$

where Δp is the pressure difference through the Bellow, $k=10^{-10} \text{ m}^2$ the combined permeability of Saffil and Nextel Material, $L_{\text{Flow}}=8\text{mm Saffil} + 1 \text{ mm Nextel}$ the flow length through the seal, A_{Flow} the cross section flow, μ the dynamic viscosity of the air flow and ρ the density of the air flow. With the given gas flow temperature profile, the total heat input into the vehicle and the heat leak flow is according to Fig. 12.

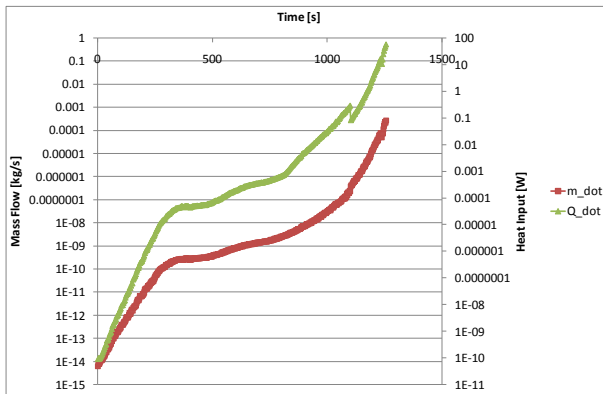


Fig. 12: Mass flow and heat input for leak flow consideration

The figure shows that the heat input at its peak is about 60 W. By performing a thermal simulation, where the very near surrounding of the Bellow in the vehicle is defined by an aluminum box with a wall thinness of 12 mm, the mentioned heat input barely changes the maximum location temperatures by less than 0.2 K. However, for this case the influence of potential thermal degradation of the Bellow toward permeability changes has not been considered. In order to track this effect, the situation was considered, in which we assume that the combined permeability of Saffil and Nextel changes by a factor of 10. Taking the Darcy equation into account, the resulting heat input would be 590 W. This would increase the maximum temperature of the defined surrounding by 1 K w.r.t. the temperature level for the virgin permeability. If the permeability would be influenced by the temperature in a way that the permeability will be getting worse by a factor of 100, then the heat input of 6000W would increase the maximum temperature by 12 K.

In addition to the leak flow heat input, the radiative heat input into the vehicle - due to the heating of the Bellow during re-entry - should be considered. The peak average temperature is 460 K at 1260 sec. This corresponds to a heat source of 70W. The heat inputs through the Bellow (convective heating) and the heat input due to the heating of the Bellow (radiative heating) will be at its maximum 130 W. This in combination with the very short duration of an effective exposing to the heating mechanisms can be considered as negligible side effects, which do not require special counter measurements.

Interface temperature to Lever:

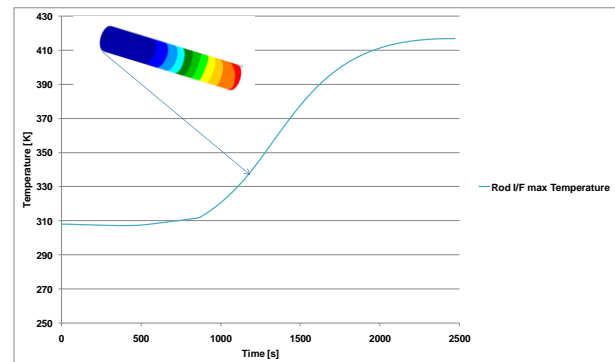


Fig. 13: Rod to actuator interface temperature

Fig. 13 shows the temperature of the cold end of the rod assuming adiabatic boundary conditions. The maximum temperature at this interface is 413 K. Due to the thermal properties of the rod material, the peak will be reached at the end of the descent phase. The cold end interface is the lever, which is made by iron. Therefore the interface temperature can be considered as uncritical for the lever. In addition, the boundary condition at this interface is considered to be adiabatic, which gives more safety regarding the temperature loading. The thermo-mechanical analysis showed acceptable MoS for all components.

4. EXPERIMENTAL VERIFICATION AND QUALIFICATION

After the virtual qualification up to the CDR status of the EMA TPS, a qualification test was performed to verify the EMA TPS CDR design hardware and to prove the functionality and the integrity of all components after exposure to re-entry loads. Most important issues to be verified by the test were:

- The thermal protection performance against sneaking flows (permeability)
- the moveability of the rod during re-entry (kinematics)
- the integrity of the hardware wrt thermal and kinematic environment (material degradation due to high temperature loads)

The expected results are:

- permeability of the EMA TPS
- identifying possible obstacles for the kinematics caused by the EMA TPS
- identifying possible degradation of the EMA TPS used materials, especially the flexible materials Nextel and Saffil used for the Bellow.

The qualification sequence consisted of two main tests: the permeability test and the moveability test. Prior the moveability test, an exposure of the EMA TPS consisting of

- Bellow,
- Mounting Adapter,
- Retaining Ring,

- Clip Collar and
- Inconel attachments (Bushes and Screws)

to thermal re-entry conditions has been performed. For simplicity, from now on the above mentioned configuration will be referred as EMA TPS. The herein described EMA TPS qualification test approach was directly linked and adapted to the test center RUAG and their test capabilities. The EMA TPS hardware was identical to the CDR design, only the rear side of IXV is a dummy device, which has been adapted to the test facility. The EMA Rod was not part of the qualification campaign for the EMA TPS and therefore, it was not qualified within the frame of this test. As a consequence, the I/F to the Body Flap side of the Rod was not made by CMC, since the Rod was not thermally loaded. The EMA ROD will be qualified during a future Load and Kinematic Qualification Test. For this test, the EMA Rod was only providing the appropriate friction for the EMA TPS degradation. However, for this test, the goal was to observe the change in the resistance of the motion by monitoring the power of the moveability test driving unit. By evaluating the power add-on for the kinematics the integral resistance and afterwards the integral friction of the entire EMA TPS has been determined. There was a single test device unit for all tests and test sequences. Flexibility in changing the testing facilities according to the test needs was given by RUAG Space facilities. One thermal test cycle covered the re-entry period of IXV (1353 sec) based on the MHF Trajectory. Kinematics of the EMA Rod has been rebuilt during the tests under room temperature and 1 atm pressure conditions. The EMA Rod has to be removed (simple out sliding) from the test unit for the exposure to the temperature environment and afterword added to the complete testing unit for the moveability and permeability test. Two sub-tests were distinguished –gas flow and moveability test. The qualification test comprised a sequence of several gas-flow and moveability tests. Prior the moveability test, a preconditioning of the EMA TPS by exposing it to a temperature profile as expected for the re-entry phase was performed. The order of the test cycles was selected wrt to increasing criticality of the loading condition, i.e. risk that test sample degradation is initiated and to control of EMA TPS performance by intermediate gas-flow tests.

4.1. Test Sample

The test sample has been manufactured according to the same procedure and materials as well as with the same design as planned for the flight hardware. The test article provided by MT, as a proband unit, consisted of

- the EMA TPS ,
- a CMC Rod with metallic I/F structure

RUAG contributed prior to the testing by design and manufacturing:

- a dummy structure having realistic thermal properties as the flight hardware vehicle’s rear side
- a dummy adapter for mounting the angled EMA TPS on the rear side dummy

The dimensions of the dummy rear side structure, the dummy adapter and necessary insulation and sealing have been adapted to the geometry of the testing facilities.

4.2. Load Parameters

The following loading have been applied

- Permeability test (gas-flow test)
 - A pressure difference along both sides of the EMA TPS was applied, while $p_0=1\text{atm}$ and RT
 - The resulting mass flow was measured
 - The adjustment magnitude was p
- Preconditioning for the moveability test
 - The heat loads will be rebuilt by HT oven at 1 atm pressure.
 - The loading was applied to rebuild the temperature profile acting on the Bellows as predicted by the thermal analysis
 - The duration of the preconditioning was 1353 sec
- Moveability test
 - The test was performed at RT and 1 atm pressure.
 - A duty cycle was defined by 331 body flap movements from -21° to $+19^\circ$ with a angular speed of $\omega_1=331 \times 40^\circ / 1353\text{s}=9.79^\circ/\text{s}$ for the first three cycles,
 - $\omega_2=15^\circ/\text{s}$ for the fourth and last cycle

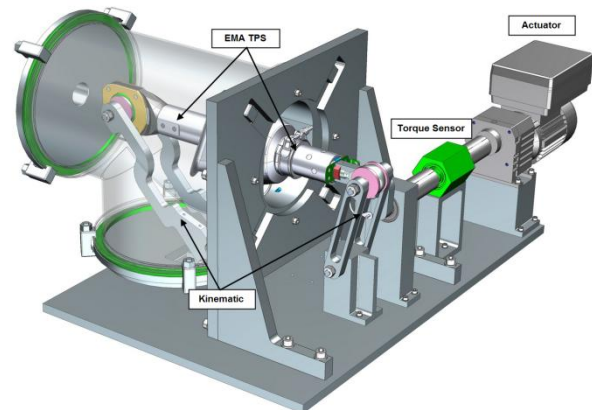


Fig. 14: Moveability and permeability test set-up

5. TEST RESULTS

The qualification campaign has been performed according to the scheme given in Fig. 15

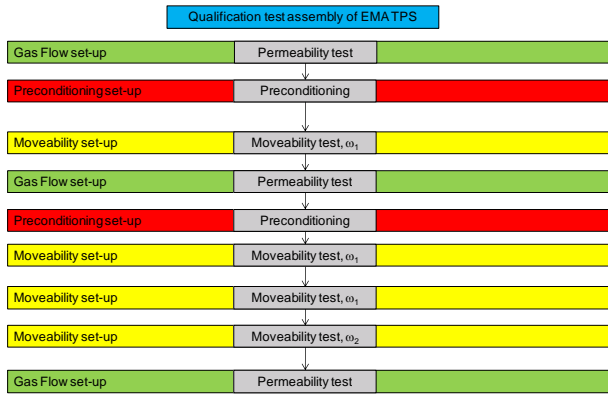


Fig. 15: Qualification test sequence.

5.1. Permeability Test

The permeability was determined by the following Darcy equation:

$$k = \frac{c_{pipe} \cdot A_{pipe} \cdot \mu \cdot L_{flow}}{A_{flow} \cdot \Delta p} \quad (3)$$

A_{pipe} , A_{flow} , L_{flow} are geometrical values constant over all measurements. μ is the dynamic viscosity value for air. By measuring the velocity c_{pipe} inside the pipe and Δp one can determine the permeability. This test was performed for different velocities with different angular settings of the Rod (-21deg, -10deg, 0deg, +10deg, +19deg) wrt the EMA TPS. The measurement has been performed on a large velocity range between 10 to 25 m/s in order to reliably determine the permeability. For the evaluation the value of the different measurements variables were averaged over 10 seconds between the different angle positions. Fig. 16 shows a typical plot of the recorded signals. The red marked zones are the intervals where the signal values have been averaged for the evaluation

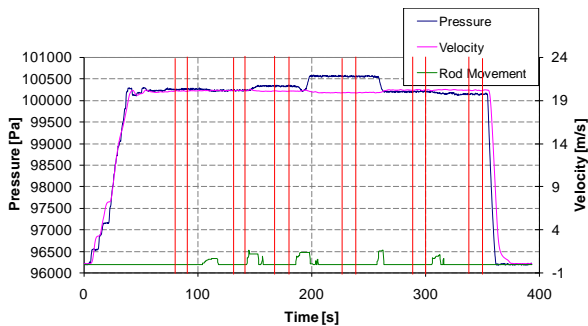


Fig. 16: Recorded signals during the first permeability measurement for $v = 20$ m/s

According to this method, the permeability for the entire test campaign has been determined.

All measured results over the entire test campaign confirm that the permeability is significantly under the requirement of 2.10^{-9} m^2 . The worst measured value is approximately 6.10^{-11} m^2 while the best value is with the range of 3.10^{-11} m^2 .

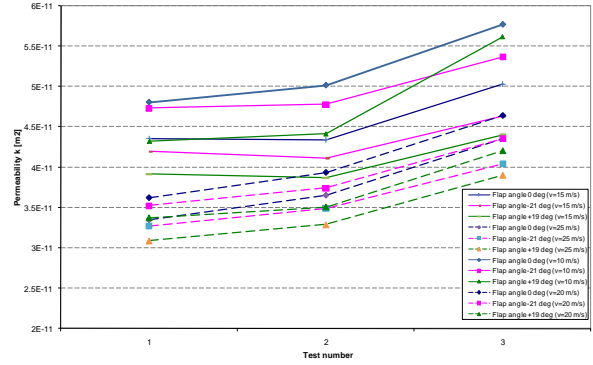


Fig. 17: Permeability change during test campaign

Fig. 17 reveals that the test campaign led to a degradation of the permeability performance of the EMA TPS. This has been expected since it is well known that thermal aging reached by the two very hard preconditioning tests, which were very intensive in terms of gradients, peak temperature and duration, will stiffen the Nextel and Saffil material and make it more brittle. The four moveability cycles with 1324 complete BF deflections over the maximum span of 40° also put the device through extreme mechanical loading, which had to influence the permeability. Due to the applied loading, the very small degradation wrt permeability can be neglected, since the absolute values are still fulfilling the requirements by more than one magnitude of order. Secondly, the position of the Rod and thus the body flap deflection causes more deviations in the permeability coefficient than the degradation caused by a qualification process.

A more significant observation is the decreasing of the permeability - and thus an increase of the permeability performance against sneak flows- of the EMA TPS with increasing airflow speed and pressure difference. The measured pressure difference dependency on the velocity reveals a linear correlation of these magnitudes, in which with increasing air flow speed an augmentation of pressure difference can be observed, as one can see from Fig. 18

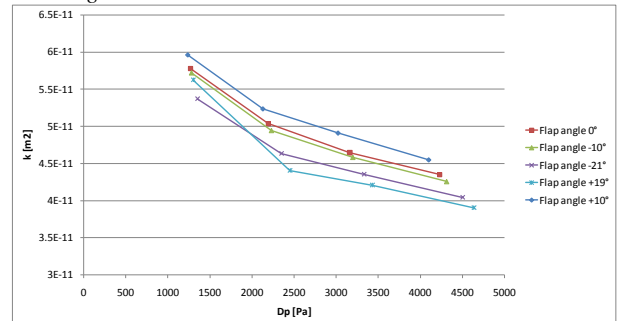


Fig. 18: Pressure difference vs. permeability

The permeability coefficient decreases with increasing pressure difference. As it can be seen for the different Rod positioning, the assumption of the higher compress-

sion of the Saffil inside the Bellow becomes more reasonable and can therefore be confirmed. The compression leads to a more compact material with lower permeability.

2.2 Preconditioning

According to the given temperature measurements, both Preconditioning Tests delivered the same results, which indicates a reliable application of the loads and a constancy in the thermal properties of the EMA TPS test article. This is of great relevance, since it can be excluded that the used materials have had experienced a significant degradation during the first thermal exposition, as the thermal response is identical.

Fig. 19 demonstrates that the CMC Mounting Adapter experienced during both tests a temperature peak over 1200 °C. The hot side of the Bellow reached - as prescribed - a temperature of 1100°C. The thermal sealing performance is excellent. The smallest gradient between cold and hot side of the Bellow is about 500 °C at peak heating. The average gradient can be quantified by 600 °C.

The comparison of the test results with the expected temperature profiles during real flight, i.e. MHL and MHF trajectories is also given in Fig. 19.

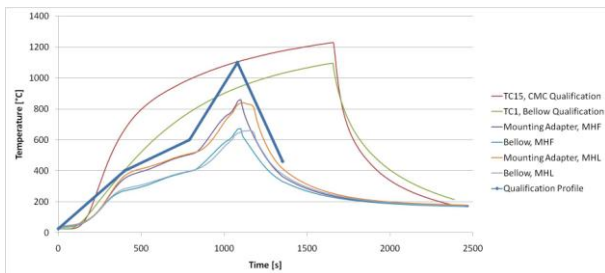


Fig. 19: Comparison of second Preconditioning Test results with temperature predictions for MHL and MHF

The comparison demonstrates that the EMA TPS has been exposed in both tests by far to higher

- heating up gradients
- maximum temperature peaks
- heating duration
- cooling down gradients

However, the Precondition Test post inspection (after the complete cooling down of the test device) showed that no damage was observed. In summary

- all screws were tight
- the Bellow was still highly flexible and undamaged
- no signs of thermal degradation or lost tightness
- no cracks
- no rupture
- no melting of metallic parts



Fig. 20: CMC Adapter after second Preconditioning Test

Some visible changes could be observed. The CMC material and inner hot screws showed some colorization. The Sliding Sleeve showed some white colorization as a sign of flush coloring on Si/C surfaces. No P/A oxidation occurred, no harm to coating or/and components occurred. All these effects were expected and are standard behavior. It can be stated that the article survived all temperature tests with no degradation. The temperature control worked well. The thermal functionality concept can be confirmed. As stated for the Permeability Test evaluation, the thermal loading did not lead to significant changes in the sealing performance of the Bellow.

2.2 Moveability Test

The number of performed cycles per test was calculated from the recorded torque signal. The peaks were used as reference, since they allowed an accurate time definition. The actual speed value was averaged over 5 cycles, while the total number of performed cycles was calculated from the total time and the speed value. The first and the last cycle were not taken into account, because of inaccurate speed setting due to the ramp up. Prior to the main measurements of the EMA TPS with the Rod, a momentum recording of the kinematics with only the Rod for both maximum speeds was taken in order to compute out the resistance influence of the EMA TPS. The performed cycles are summarized in Table 6. For each test 331 cycles were requested.

One aim of the Moveability Test was to apply the requested cycles on the EMA TPS in order to observe the lifetime aging of the test device and the integrity of the flexible part in it. The other purpose was to determine the resistance of the EMA TPS in the EMA kinematics and to prove that the CDR design maintains the resistance requirement of less than 10 N. For this purpose a moveability measurement at the beginning and at the end of the qualification campaign has been performed with just the Rod and without the bellow. This measurement contained the friction and the mass signal of the kinematic chain of the test set up and is called M_{zero}

in the following. For the calculation of the EMA TPS resistance, M_{zero} was extracted from the measured momentums $M_{measured}$ during test. However, the measured torque had to be transformed into a force response as the requirement is defined.

Test	Test id #	Performed cycles under full speed
1 st Moveability, ω_1	3	337
2 nd Moveability, ω_1	6	343
3 rd Moveability, ω_1	7	353
4 th Moveability, ω_2	8	353
Σ		1386

Table 6 : Summary of complete full cycles

Putting $M_{lever} = M_{measured}$, the resistance force of the EMA TPS perpendicular to the lever can be calculated as:

$$F_{rod} = \frac{M_{measured} - M_{zero}}{L_{lever}} \quad (4)$$

The absolute values of the resistance for ω_1 sequences are shown in Fig. 21. For ω_2 , the resistance values are shown in Fig. 22.

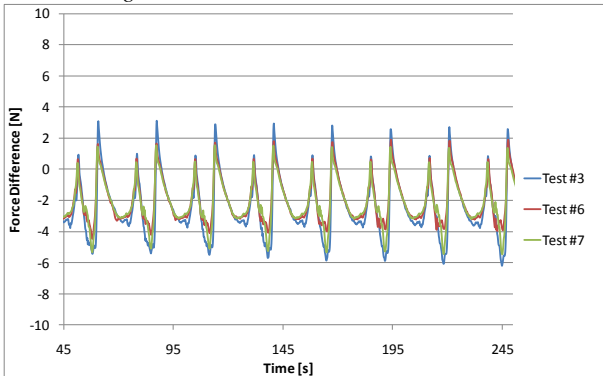


Fig. 21: Resistance for ω_1 movements

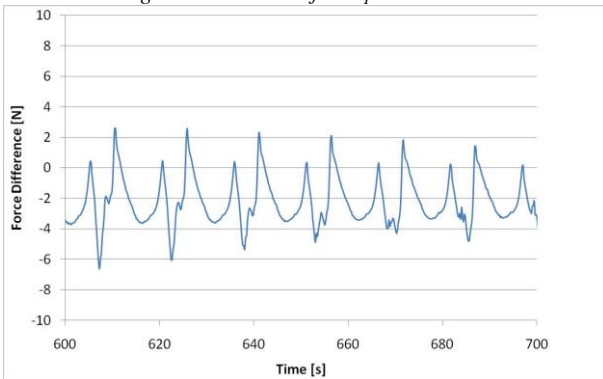


Fig. 22: Resistance for ω_2 movements

The resistance evaluation clearly confirms that the force is less the required 10 N for both speed set ups. An

increase of the force during each moveability sequence was not observed. The small deviations between test beginning and test end can be explained by synchronization errors, which could not be avoided, since each test had a different ramp up and the accuracy of the measurement in time was 0.2 seconds. Furthermore, it can be observed that the resistance of the EMA TPS is independent from the speed, since all tests show identical characteristics and values.

Therefore, EMA TPS passed therefore successfully the Moveability Tests

6. SUMMARY AND CONCLUSION

The test has been successfully performed according to the test procedure. The test exposed the article for more than 993 movements with a maximum angular speed of 9.79 °/s and more than 331 with a speed of 15.1°/s. So a total movement loading of more than 1324 complete BF deflections over the maximum span of 40° could have been proven. In addition, the EMA TPS has been loaded twice by a temperature profile which largely exceeded the expected thermal loading during re-entry for both trajectory scenarios. The thermal loading during the qualification procedure exceeded by far the expected heating gradients, the expected maximum temperature, the duration of the exposure to high loading and cooling down gradients. During the qualification campaign three permeability measurements have been performed. Each measurement covered the total BF deflection of 40° in 5 steps. The permeability measurements clearly demonstrated that the sealing performance is better than assumed for the design layout and the development activities up to CDR. The layout activities have been performed with a permeability factor of 10⁻⁹ m². The measurements prove that the sealing performance of the EMA TPS is within a range 10⁻¹¹ m². Therefore the sealing performance against sneak flows through the EMA TPS can be considered as proven. The recorded momentum evaluation showed that the mechanical resistance of the EMA TPS is at its maximum about 6 N, which is significantly lower than the requirement of 10 N. The post examination of the test article did not indicate any functionality endangering damages. All recorded and well documented experimental traces are considered as minors, not affecting the functionality. Nevertheless, the main critical part of the EMA TPS is the Bellow which functionality is to provide a low permeability wrt sneak flows and high movement flexibility (flexible sealing). Considering the last permeability measurement and the resistance force evaluation, which fully confirmed the intended functionality, any observation considering the appearance changing of the EMA TPS during the qualification process, was by measurement proven to be negligible. All requirements can be considered to be successfully fulfilled. The application of the load and the measured responses, especially the

high sealing performance against sneak flows, lead to the conclusion, that the functionality of EMA TPS can be considered to be proven.

7. REFERENCES

- [R1] Handrick, K., Lange, H.; Steinacher, A.; Progress in CMC control surface development. 4th Int. Symp. on atmospheric re-entry vehicles and systems, Arcachon, France 2005.
- [R2] F. Infed, K. Handrick, H. Lange, A. Steinacher, S. Weiland, C. Wegmann, Development of thermal protective seal for hot structure control surface actuator rod, *Acta Astronautica*, Vol. 70(2012), pp. 122–138.

Qualification of In-Flight Experimentation for the IXV Vehicle Re-entry

C. Pereira, E. Jaramillo, T. Roesgen
ESTEC, April 9, 2013

IXV-IFE

Agenda

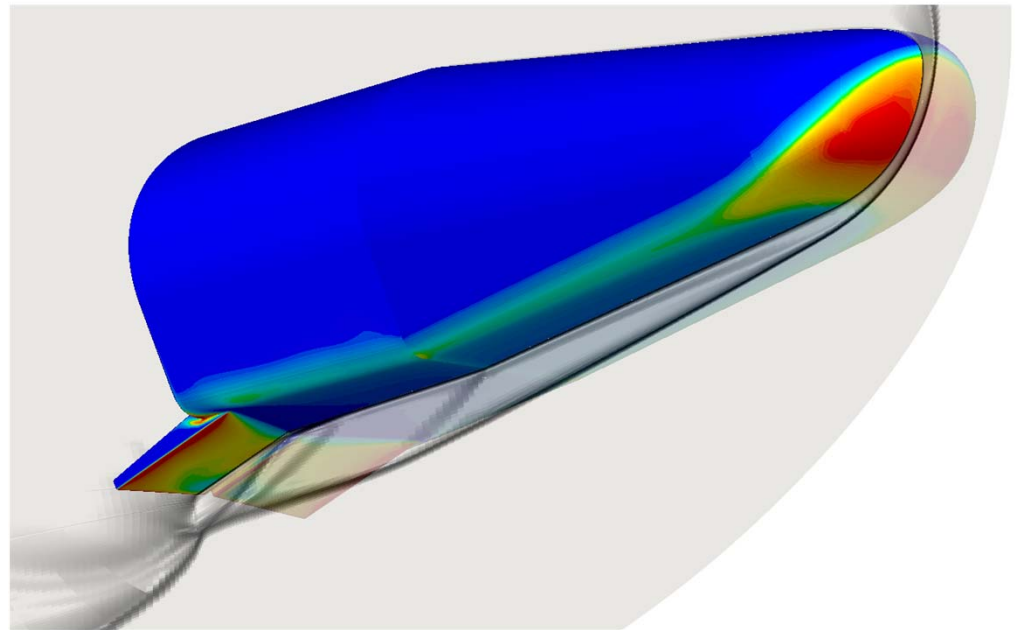
- Overview IFE
 - Objectives
 - Architecture
- Pre-Qualification Testing
- Qualification Testing

IXV- IFE

Intermediate eXperimental
Vehicle

In-Flight Experiments

- Launch: 2014 in Vega
- Guided re-entry at Mach 20
- Re-entry temperatures up to 1700° C



Objective: *Measure Thermal Protection System (TPS) Performance and Aero-thermodynamic Phenomena during Atmospheric Re-Entry*

Objectives



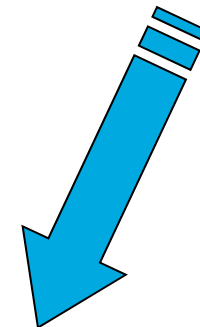
In-Flight Experimentation

Aerodynamics and Aerothermodynamics (ATD)

- Validation of the numerical tools used to estimate **Re-entry heat fluxes**

Thermal Protection Systems (TPS)

- Verification and characterization of **TPS performance**



Optimize Re-entry Vehicle Design

IXV-IFE Objective

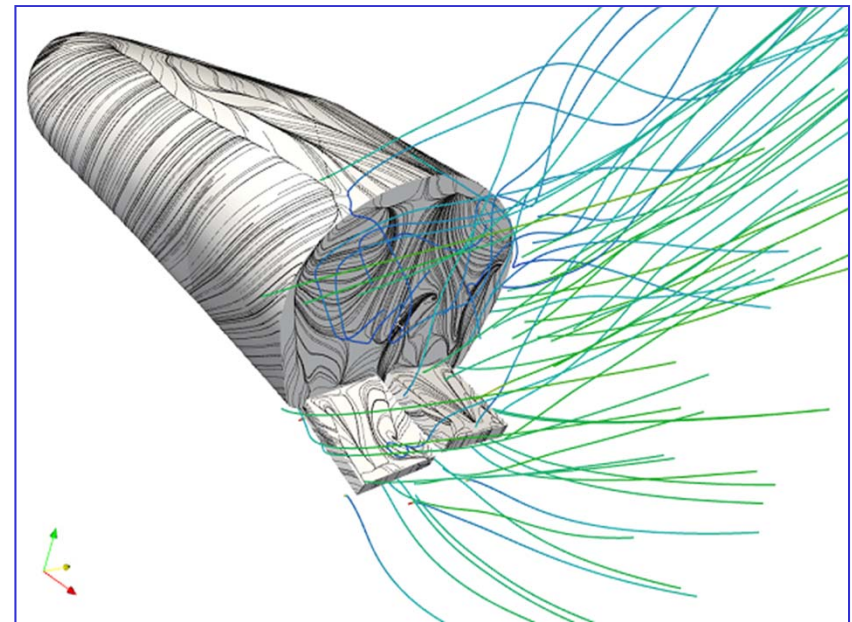
Measurement of Phenomena during Atmospheric Re-entry:

Aerothermodynamic (ATD)

1. Real-gas effects
2. Shock-wave-boundary-layer interaction
3. Shock-shock interaction
4. Laminar-to-turbulent transition
5. Transitional separation
6. Turbulent heating
7. Flap surface efficiency
8. RCS efficiency
9. Rarefied and continuous aerodynamics
10. Base aerodynamics and aerothermodynamics

Thermal Protection System (TPS)

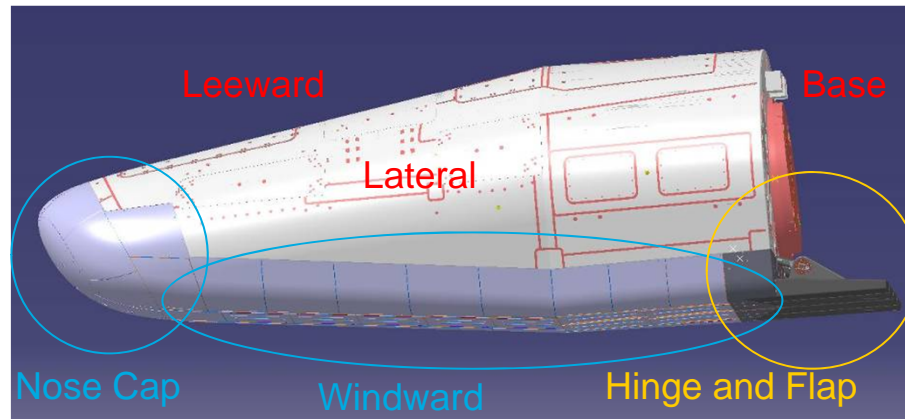
- a. Cavity heating
- b. Materials catalytic behavior
- c. Materials oxidation effects



Thermal Protection Systems

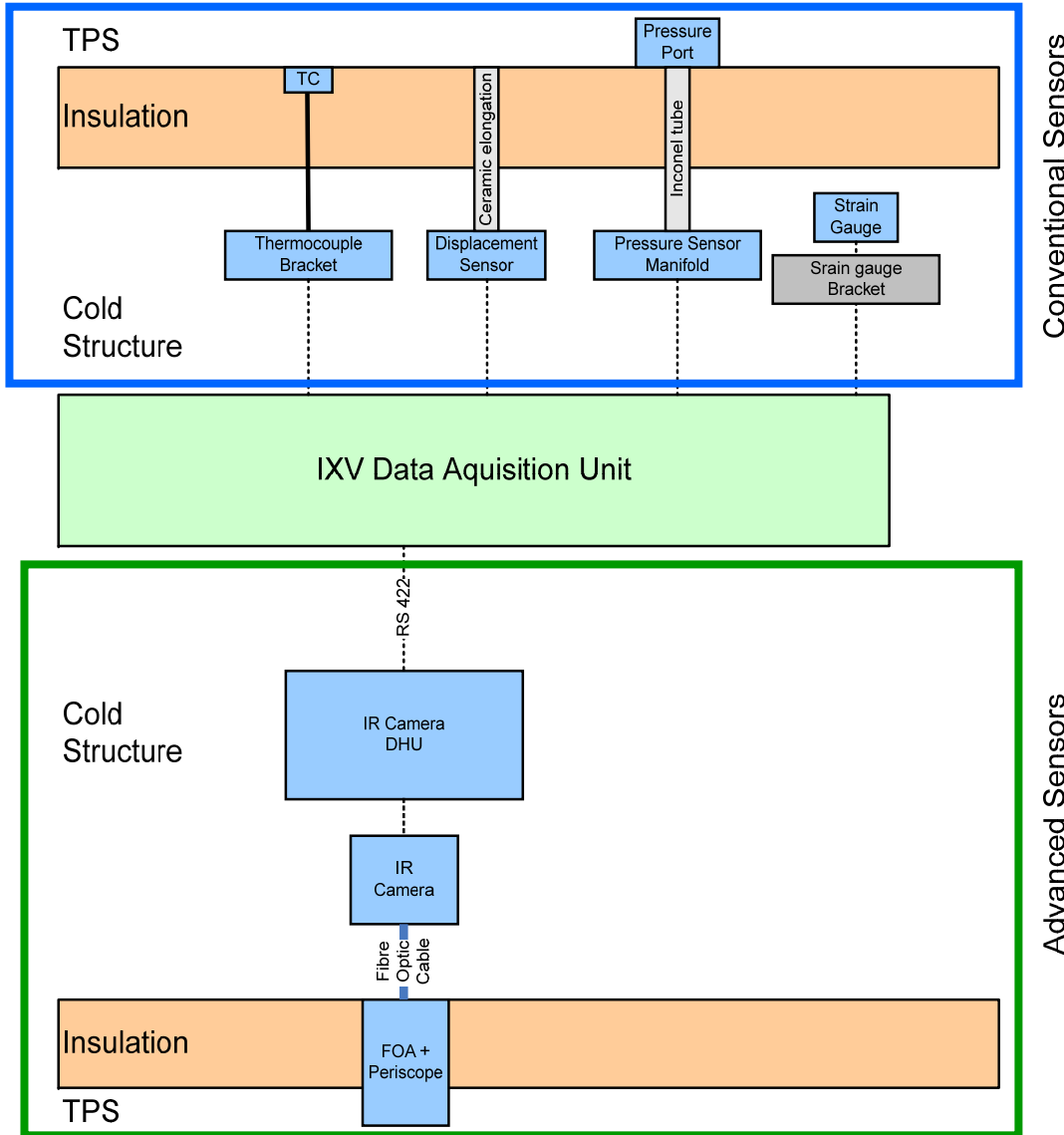
Three TPS :

- Sepcarblnox® C-SiC from Herakles, SAFRAN Group
- Keraman ® C-SiC from MT Aerospace
- Ablative P50 ® from Avio SpA



- ❖ Effects at TPS interfaces
- ❖ Thermal loads on TPS
- ❖ Steps and gaps in windward
- ❖ Strains on the nose
- ❖ Deflection and gradients in flap

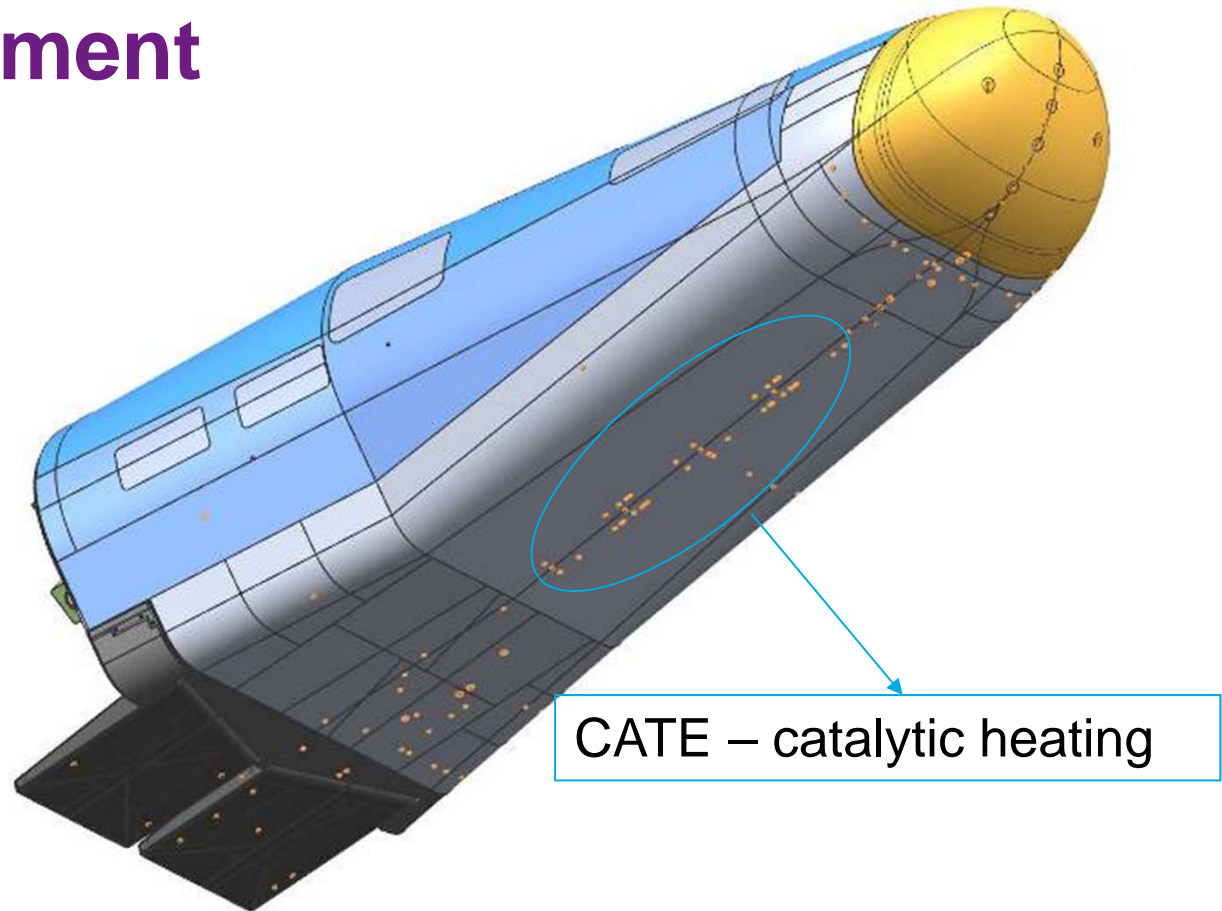
IXV-IFE Architecture



- Distinction between conventional and advanced sensors

General Heating Experiment

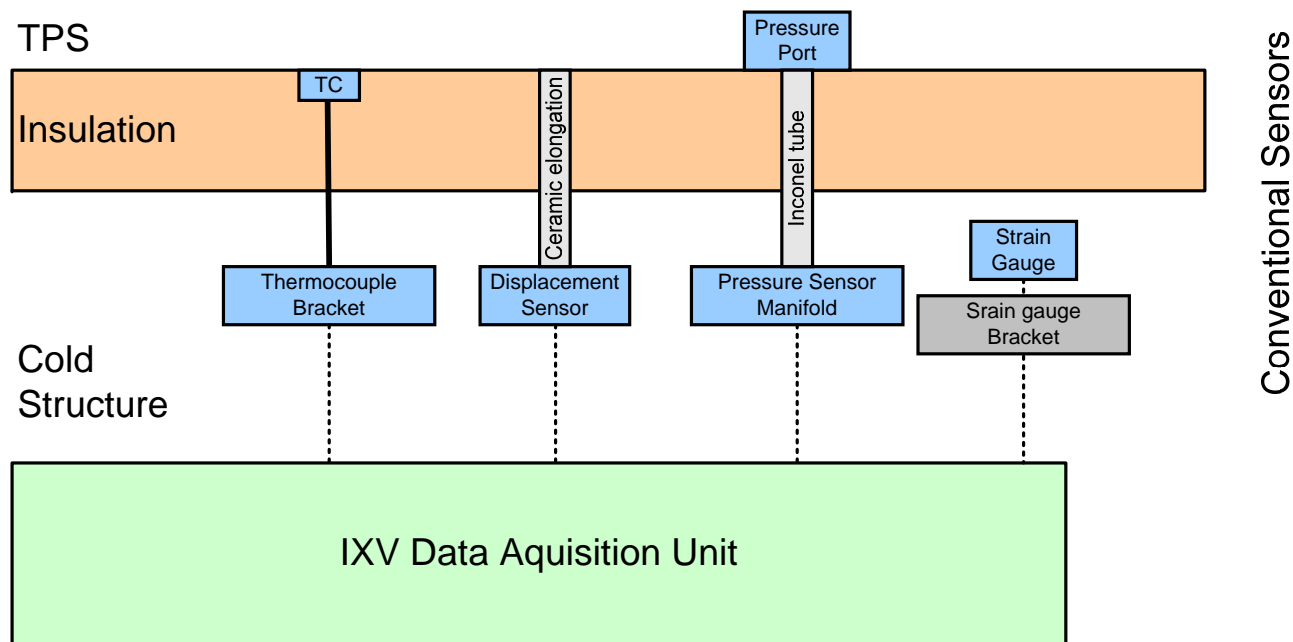
CATE Experiment



- 190 Thermocouples in three types of TPS
- Thermocouples on cold structure and manifolds

IFE Conventional Sensors

- Temperature sensing system – ca. 200 thermocouples
- Pressure sensing system – 37 pressure sensors
- Mechanical displacement - 52 strain gauges and 12 displacement sensors



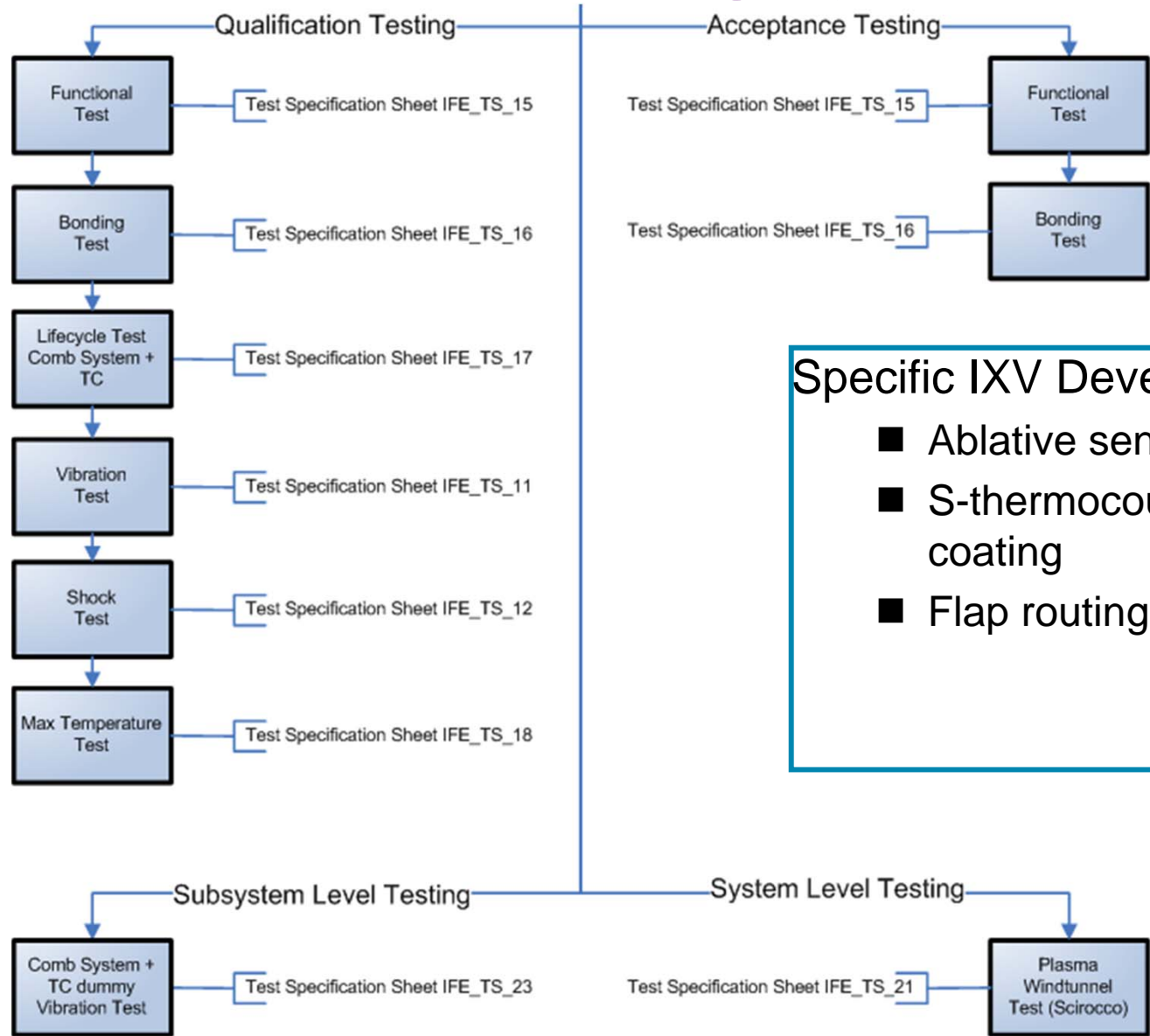
IXV-IFE



■ Qualification

- EQSR in 2011
- Test Specification defined at S/S CDR
- Test readiness review for qualification held in October
- Qualification Review in April 2013
- Environmental testing includes two Scirocco Plasma Wind Tunnel tests on representative TPS samples in September 2013

Temperature Sensing System

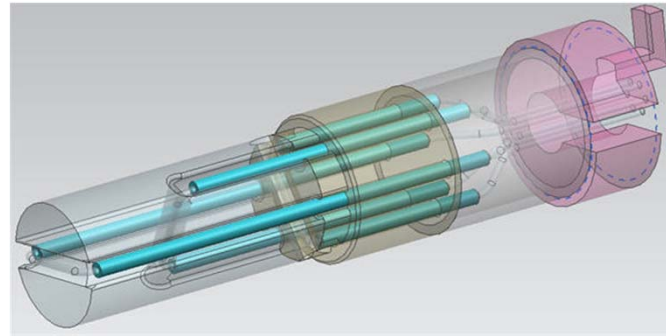


Specific IXV Developments

- Ablative sensor
- S-thermocouple ceramic coating
- Flap routing

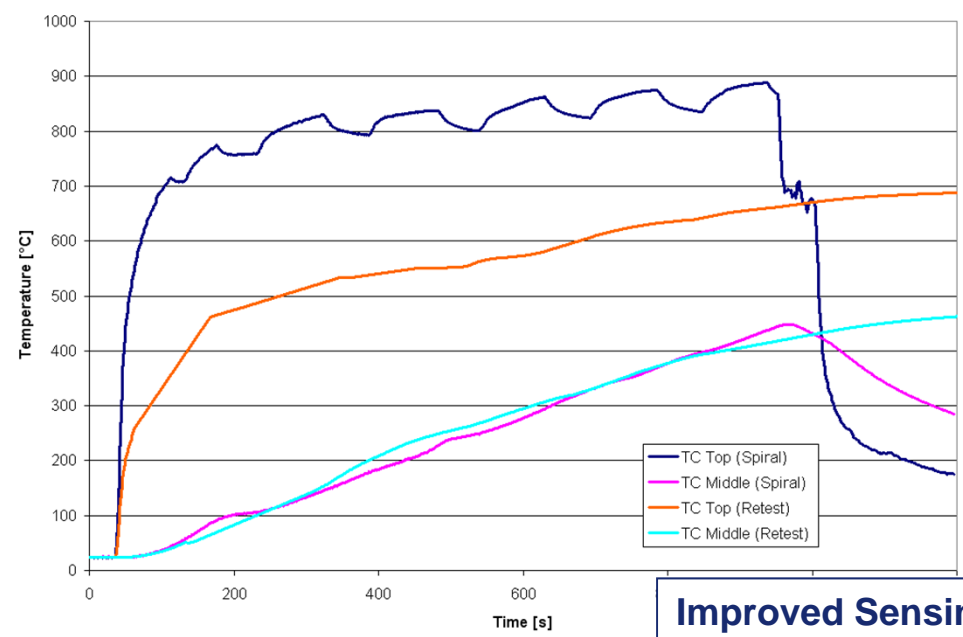
Temperature Sensing System

Ablative Sensors



■ Achievements :

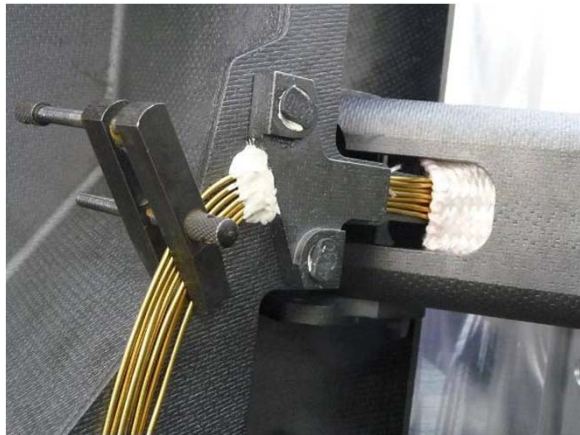
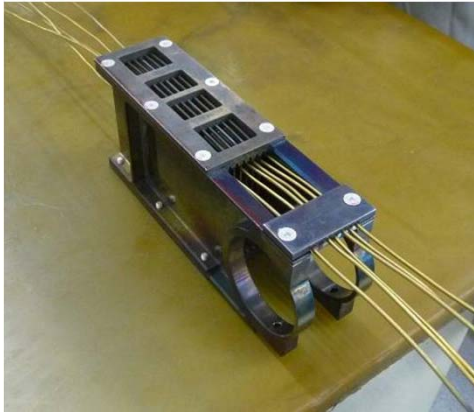
- Redesign and Test of Sensing System for Ablative



Improved Sensing at 900° C



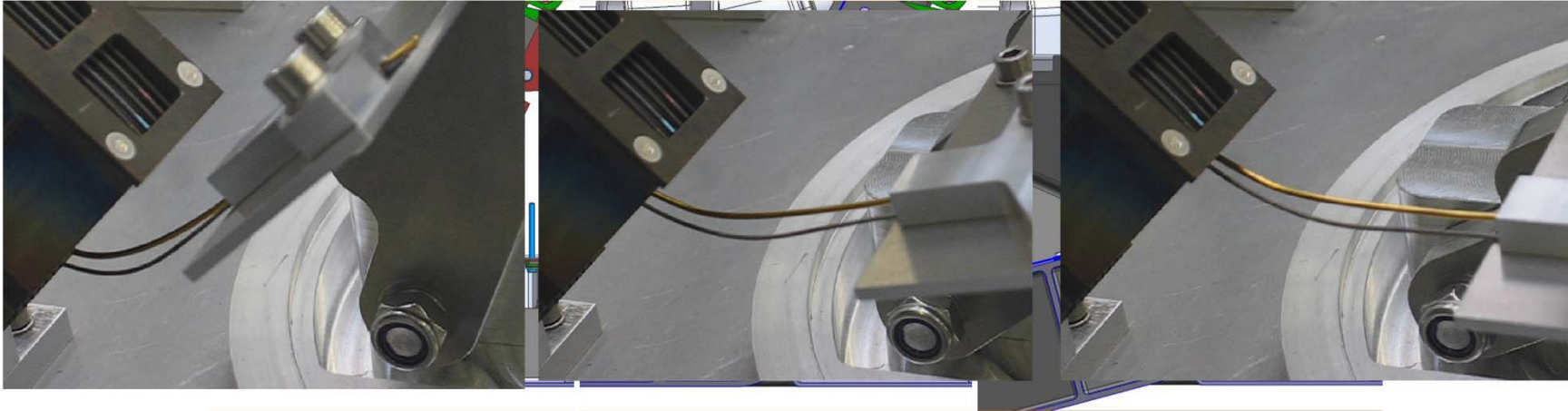
Flap Routing



- Vibration and Shock Tested

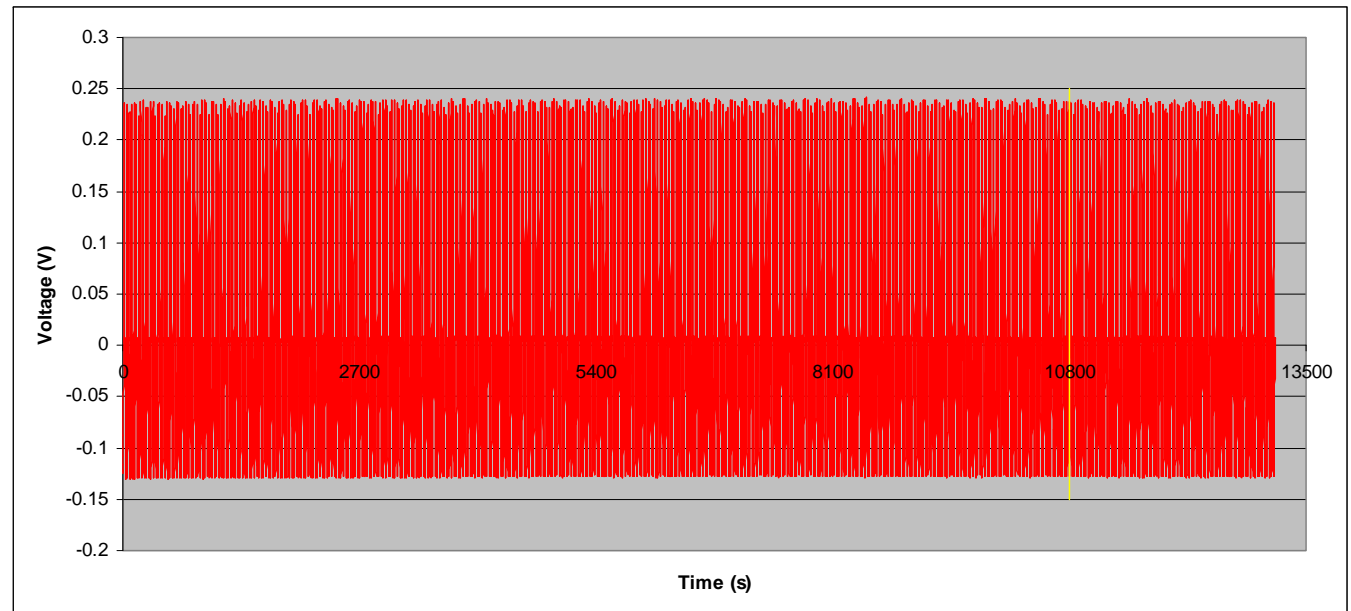


Temperature Sensing System – Flaps

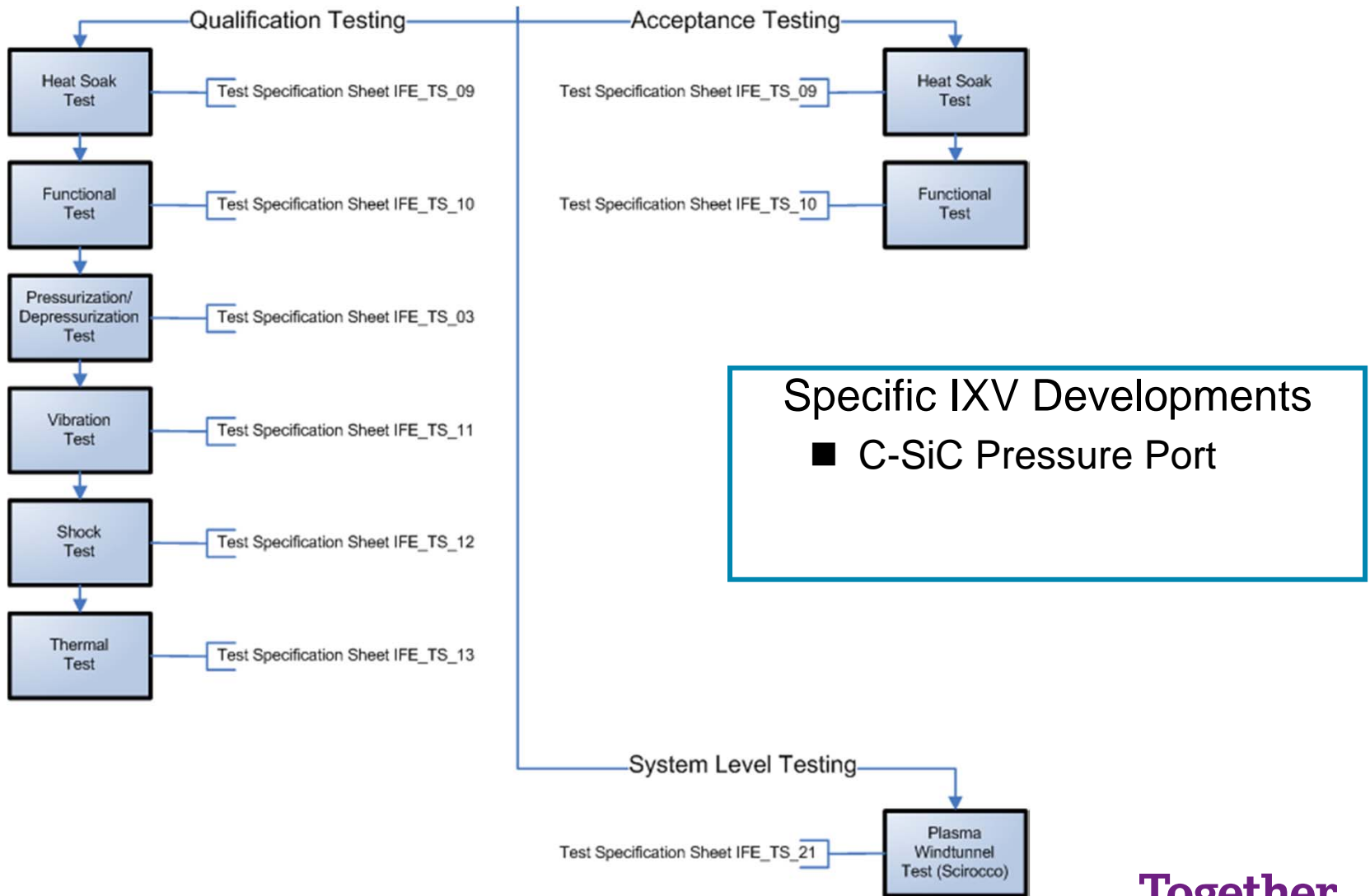


■ Fatigue Testing

1260 cycles



Pressure Sensing System

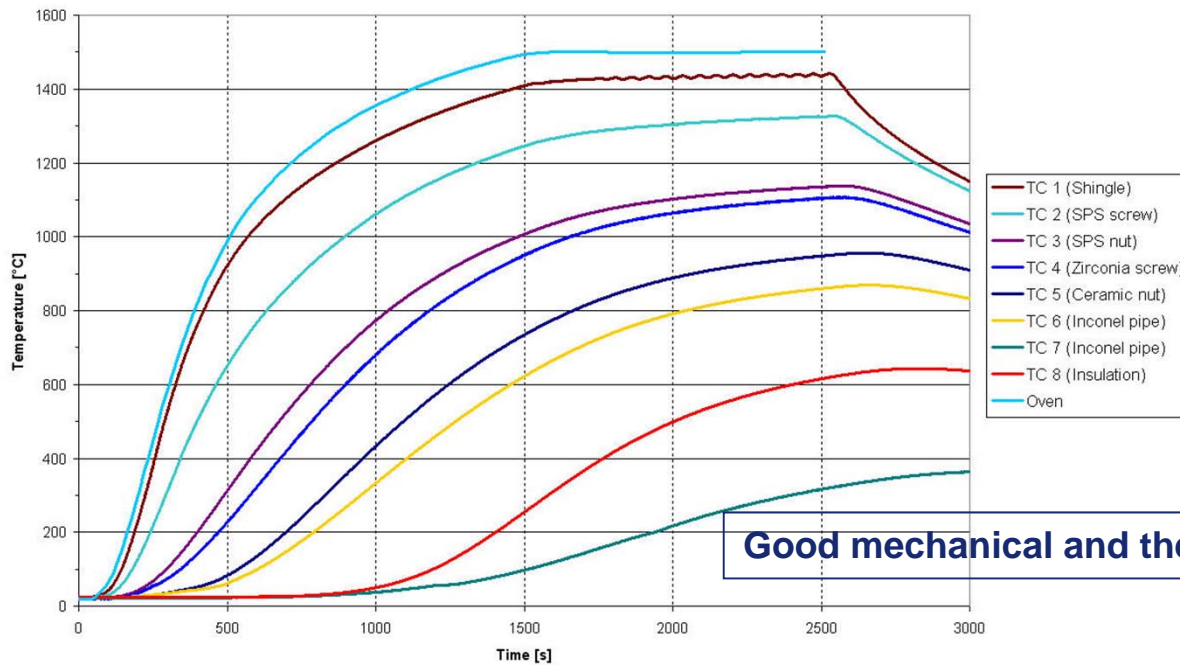
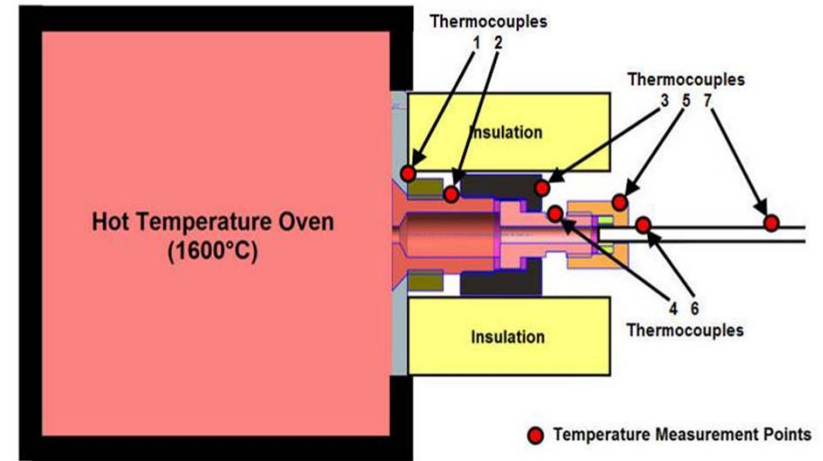


Conventional Sensors

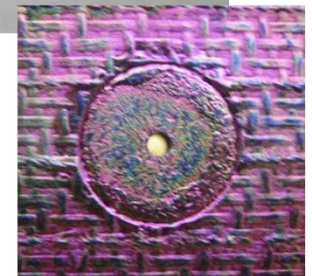
Pressure Sensing System

■ Achievements:

■ Successful Thermal Test @ 1500° C



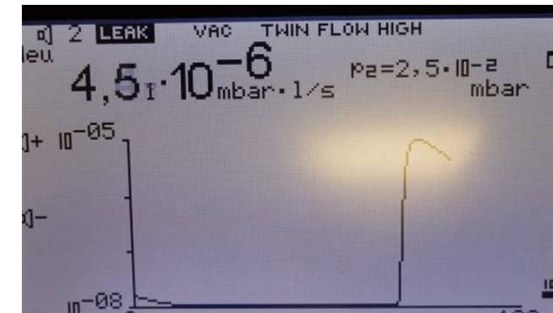
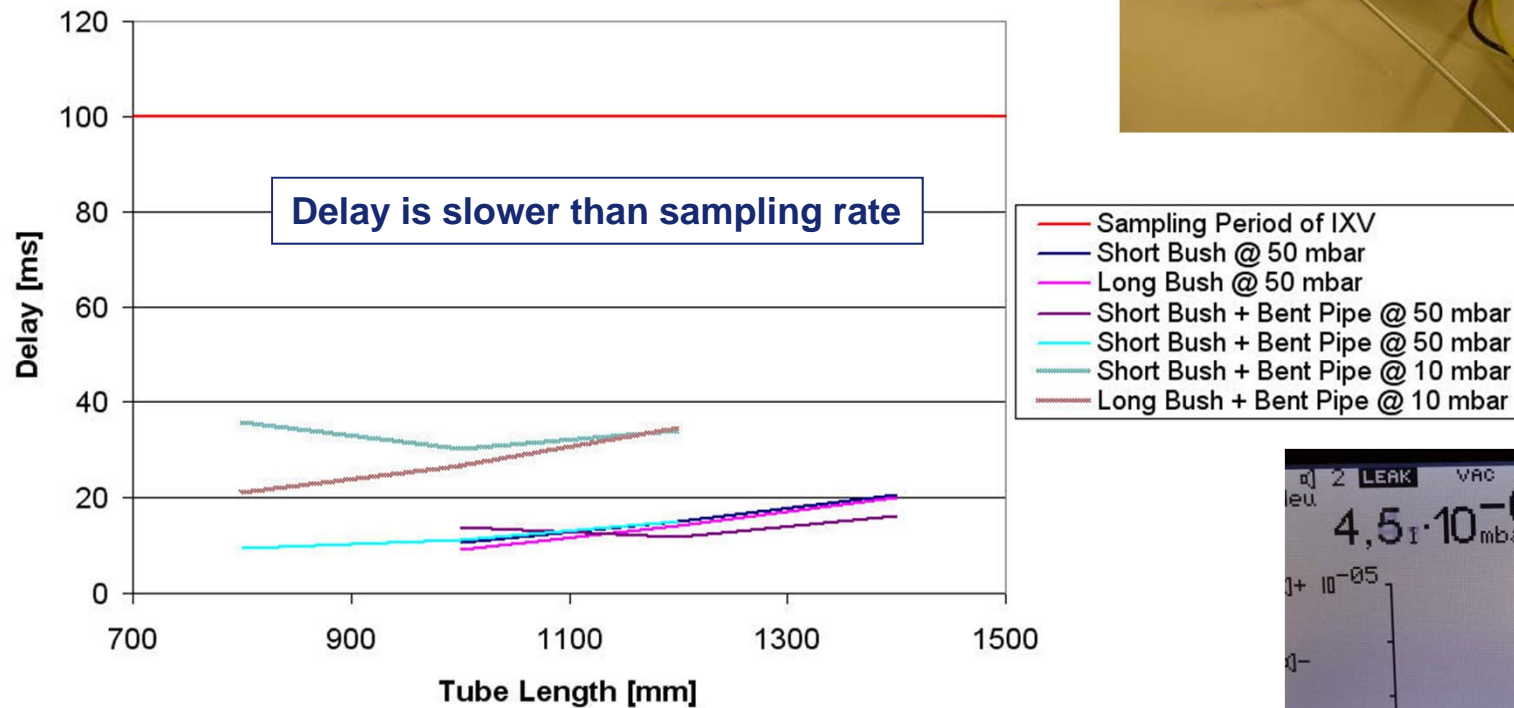
Good mechanical and thermal behaviour



Together ahead. **RUAG**

Pressure Sensing System

Pneumatic Delay and Leakage



Together
ahead. **RUAG**

Mechanical Sensing System

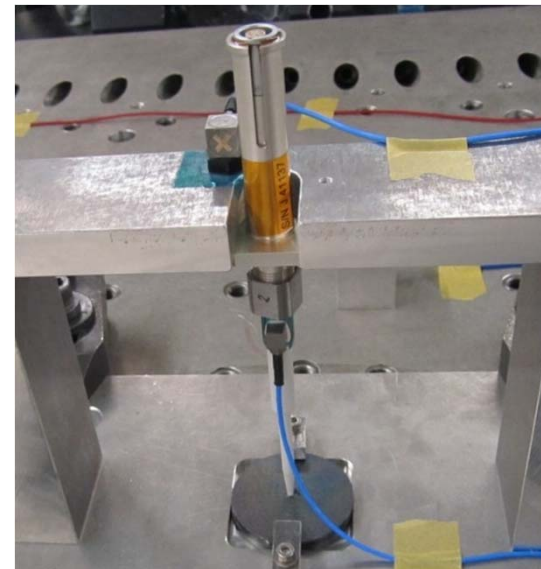
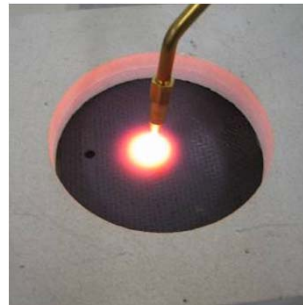


Displacement Sensors

Thermal, mechanical and functional testing performed

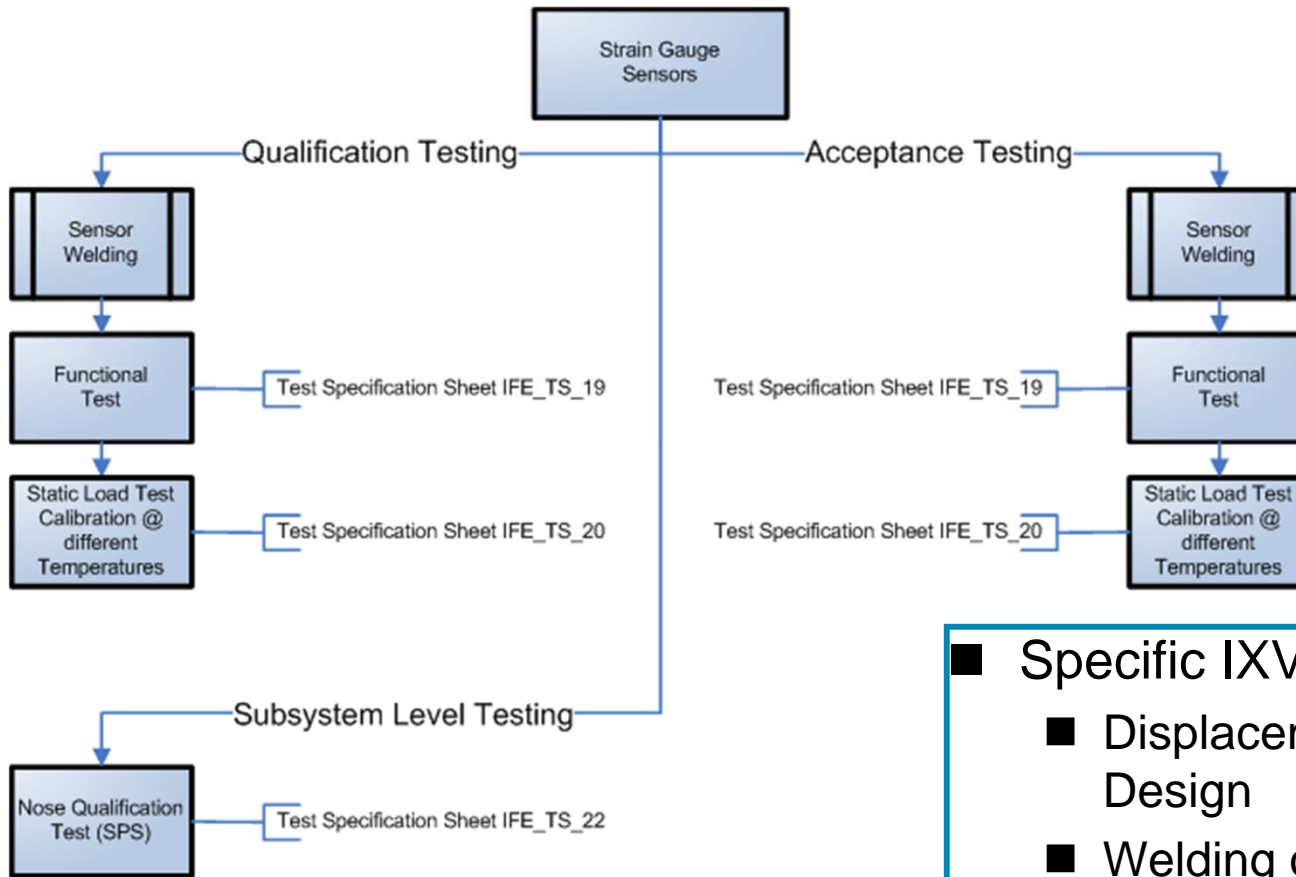


Change of ceramic tip



Together
ahead. **RUAG**

Mechanical Sensing System



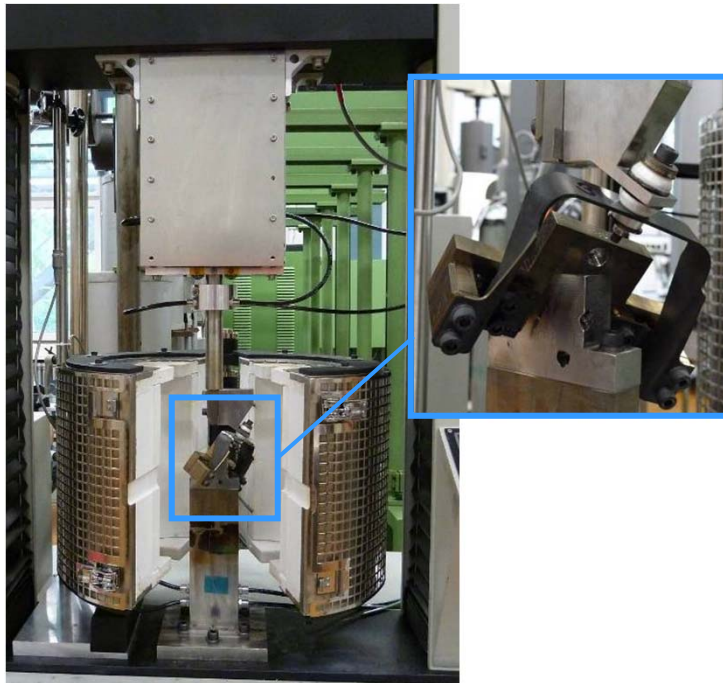
- Specific IXV Developments
 - Displacement Sensor Design
 - Welding of strain gauges

Mechanical Sensing



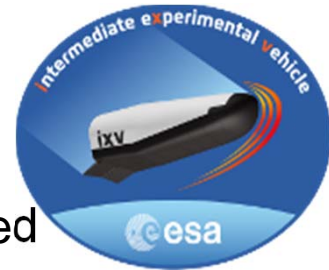
Strain Gauge Sensors

- Thermo-Mechanical Tests in Nose Stand-off and Tensile Coupons

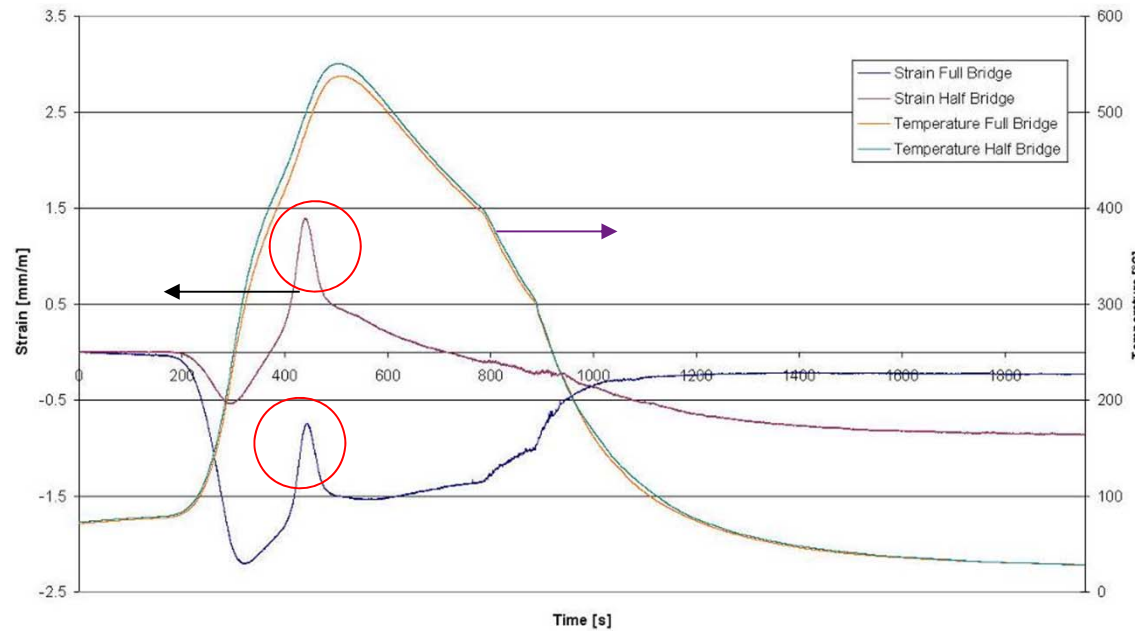


- Quarter bridge sensors do not allow temperature compensation
- Half bridge sensors show good correlation with theory

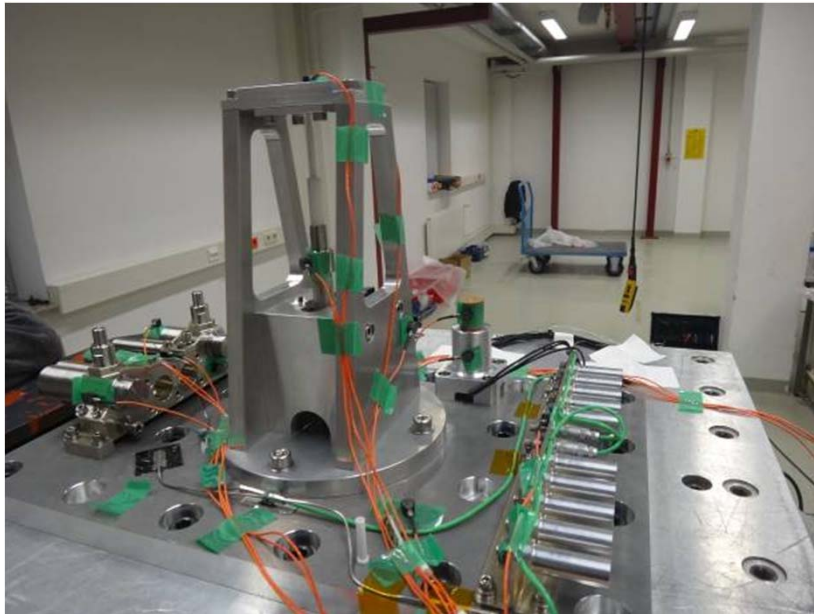
Conventional Sensors



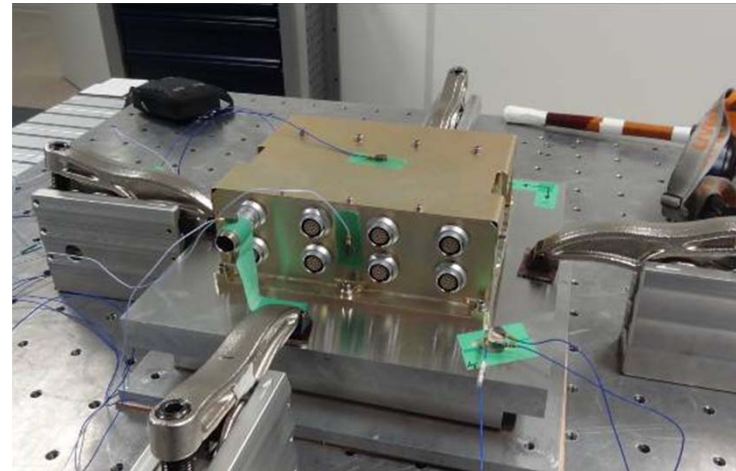
- Nonlinearity observed during heating transients - unloaded



Qualification Testing

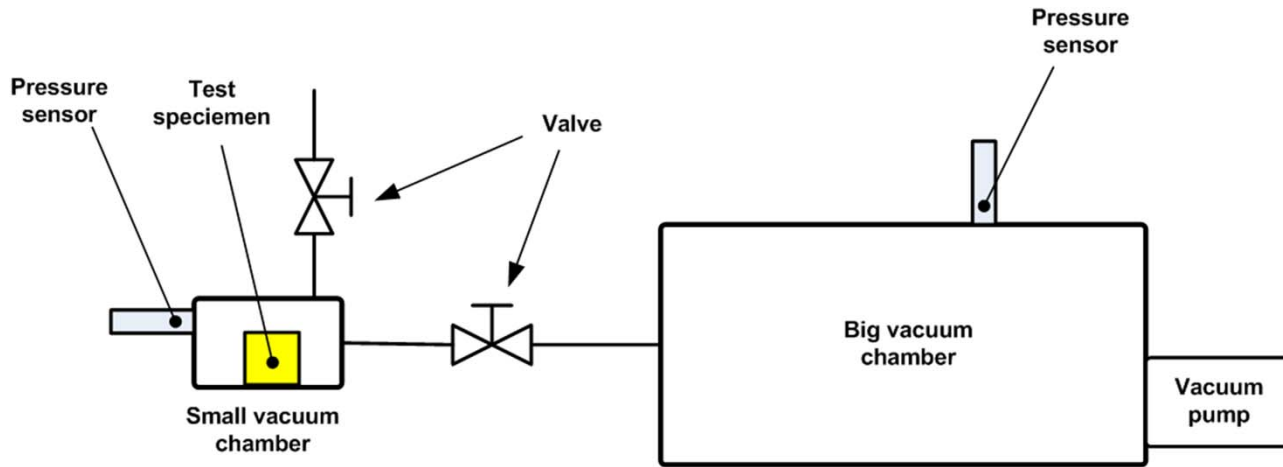


Shock and Vibration of Sensors



- All functional, thermal and mechanical tests passed

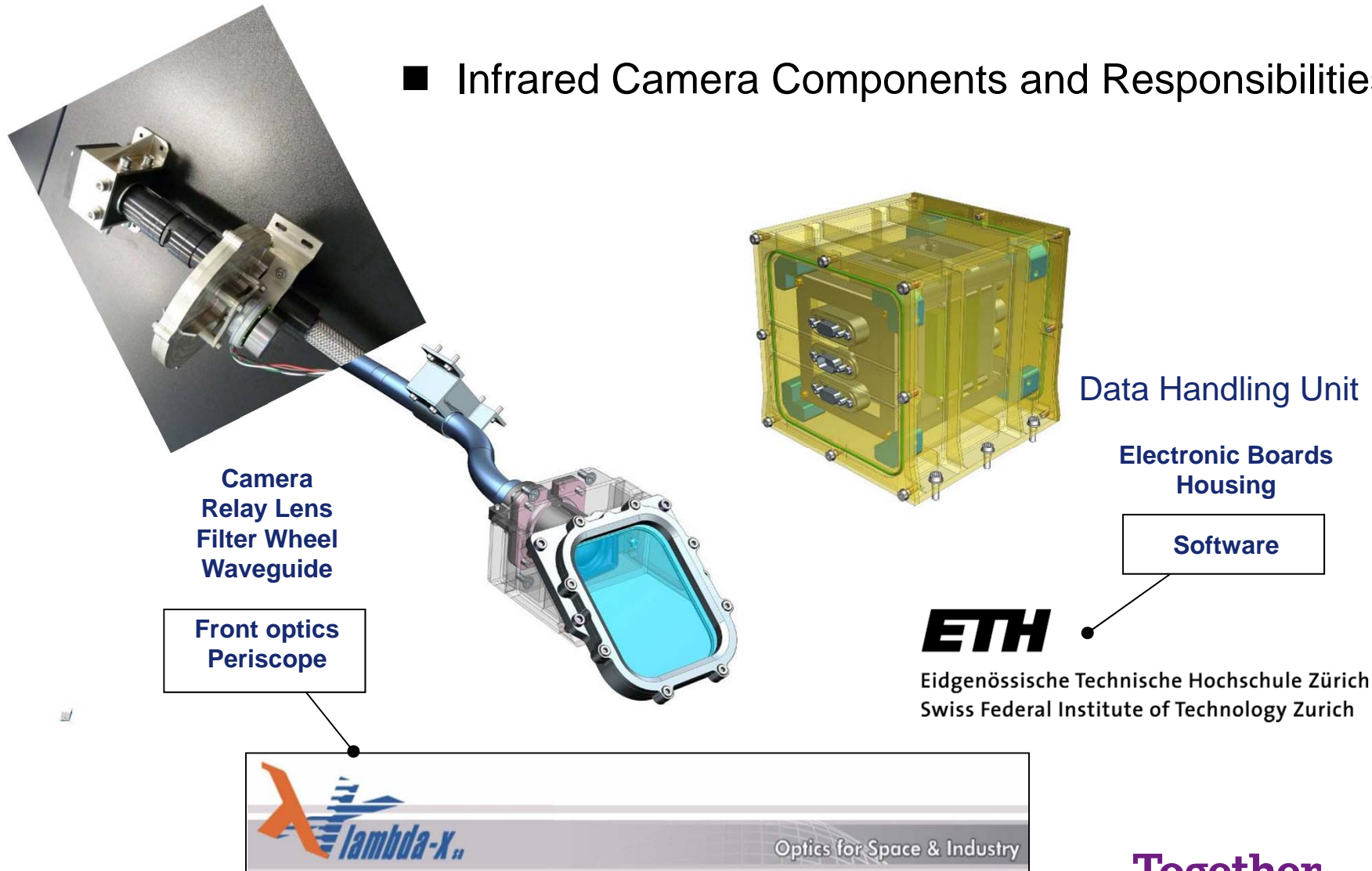
De-pressurization/Re-pressurization



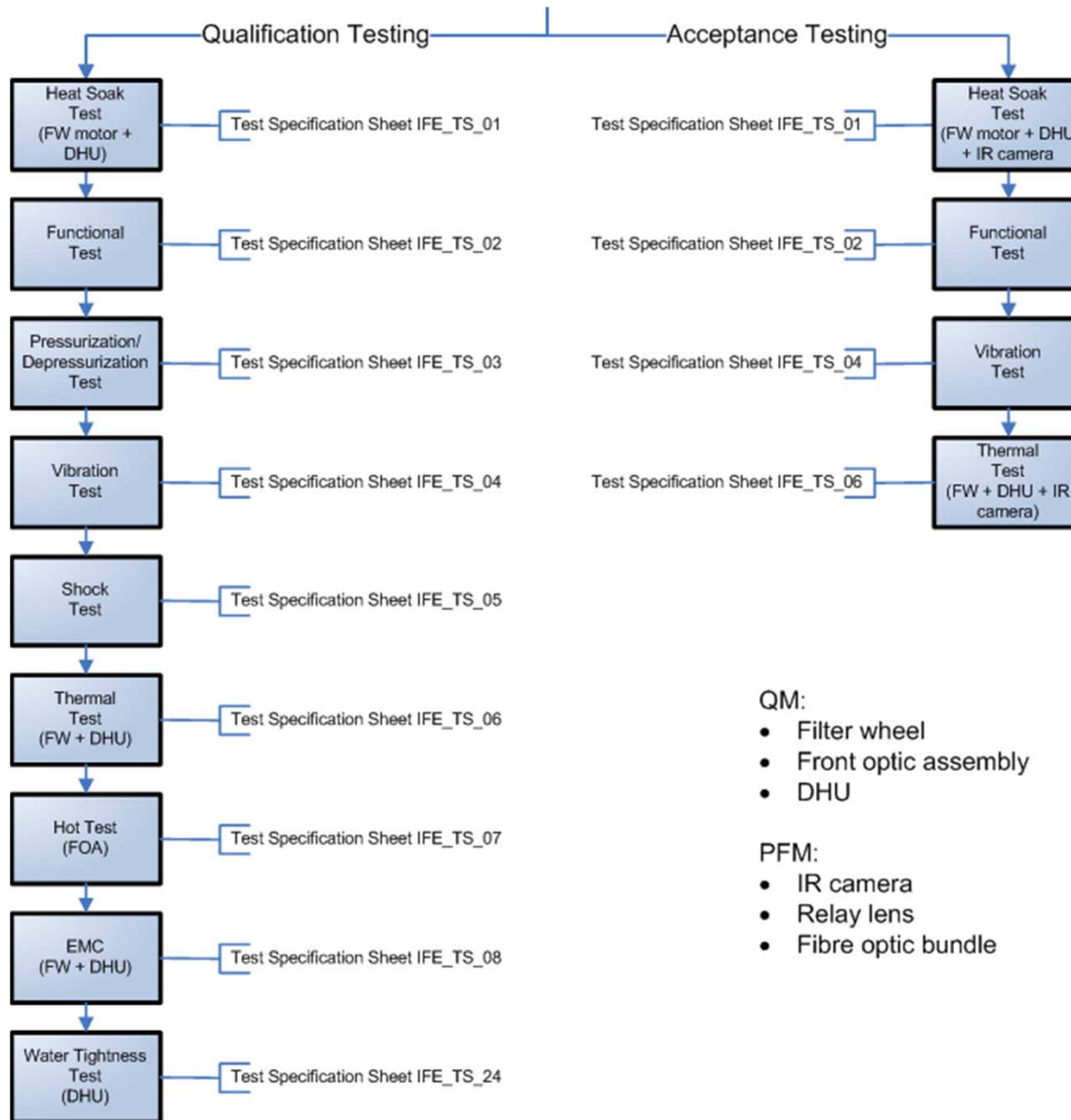
Specimen	Depress rate (Pa/s)	Repress rate (Pa/s)
Filter wheel assembly	~100000	~285000
Front optic and fibre optic	~130000	~283000
Data handling unit	~125000	~315000
Displacement sensor	~119000	~476000
Strain Gauge bracket	>200000	~175000
Differential pressure sensor	~200000	>250000
Absolute pressure sensor	~150000	~200000

Infrared Camera Experiment

■ Infrared Camera Components and Responsibilities



Infrared Camera Experiment



QM:

- Filter wheel
- Front optic assembly
- DHU

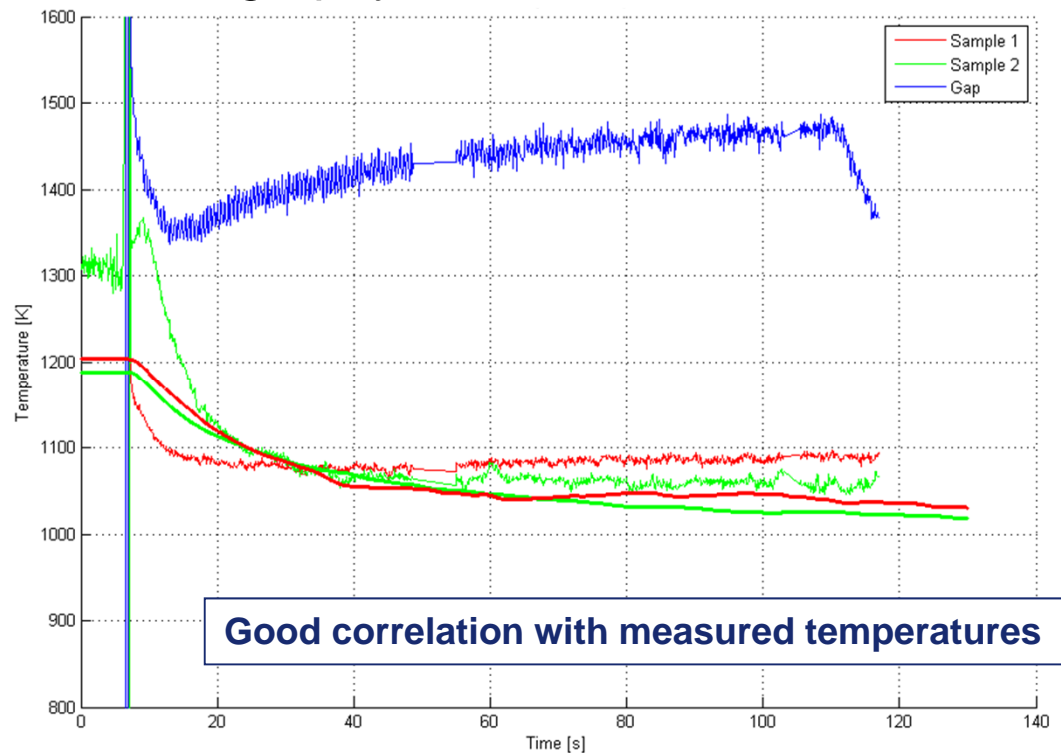
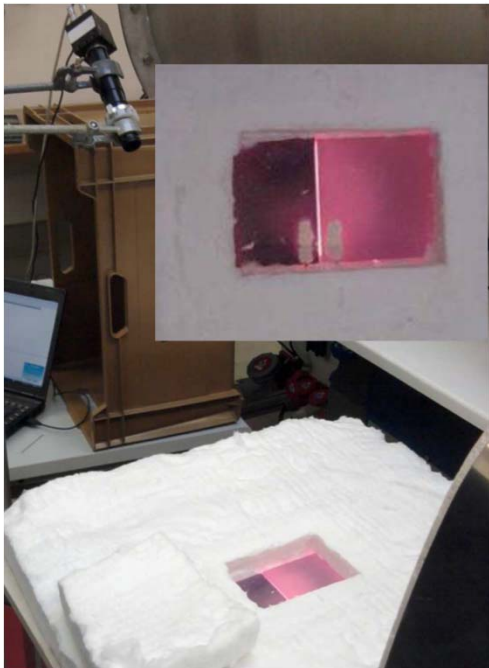
PFM:

- IR camera
- Relay lens
- Fibre optic bundle

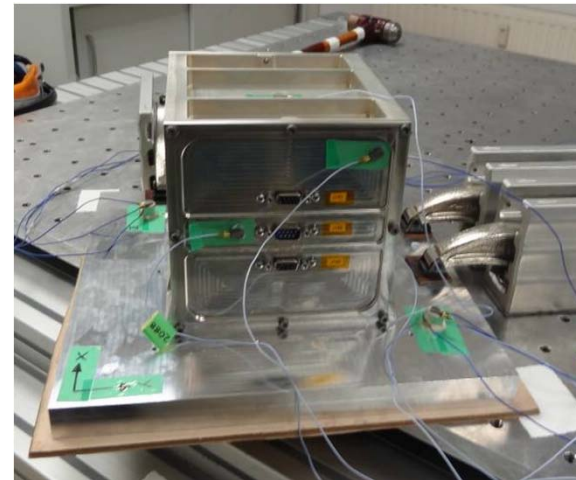
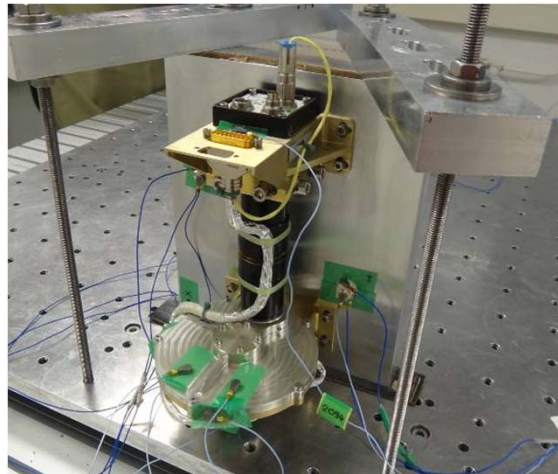
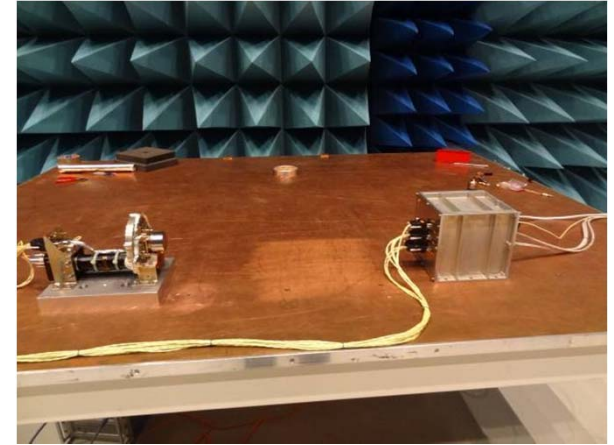
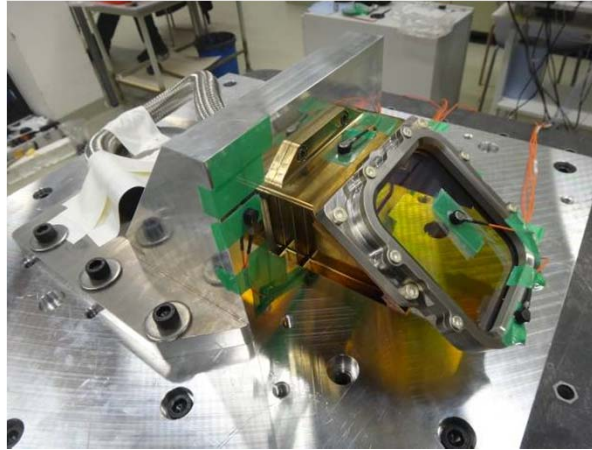
Together
ahead. **RUAG**

Infrared Camera Experiment

- Software Testing at ETH Zurich
- Optical performance at L-X
- Testing of Multispectral Thermography at 1000° C



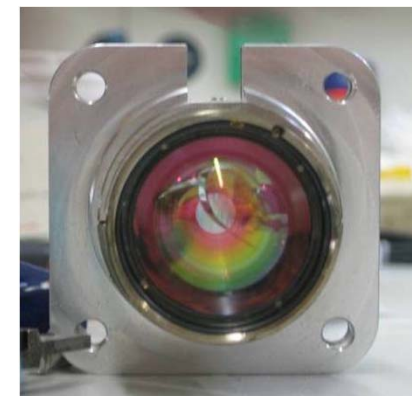
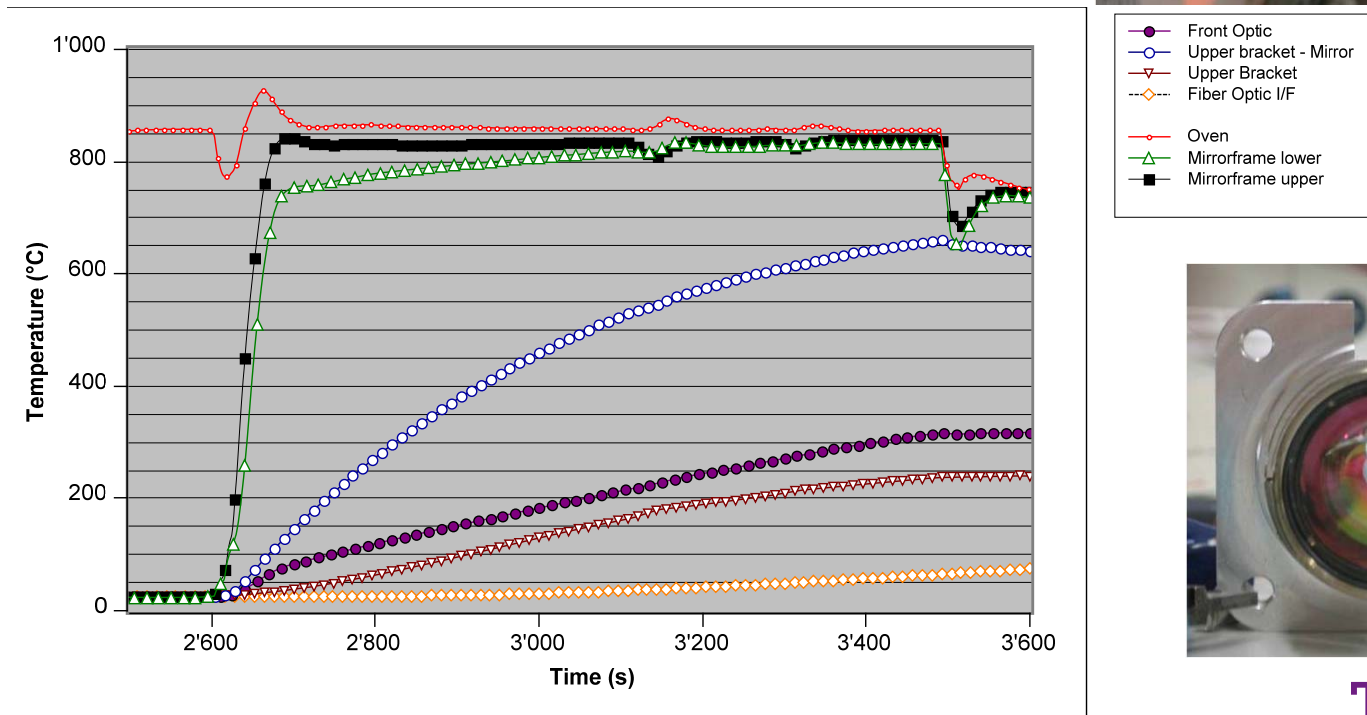
Qualification Testing – Nov. 2012



- EMC, Mechanical and Thermal cycling

Infrared Experiment

- Thermal Test at 900° C
 - Mirror survived shock and hot test
 - Major NCR – Lens damage



Together
ahead. **RUAG**

Conclusions

- All Qualification Tests Performed
 - Minor NCRs on electrical bonding of displacement sensors
 - 1 NCR during TC installation (sheath damage) –
 - Major NCR on shock envelope violation of front optics

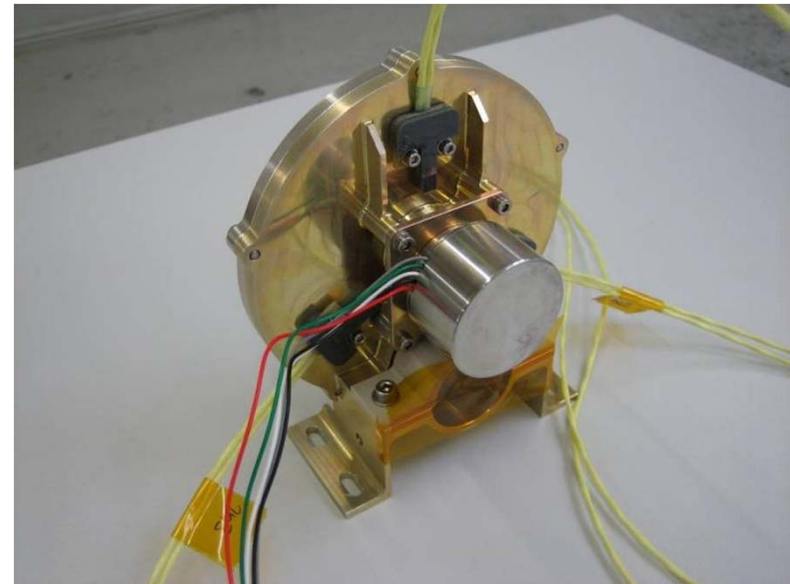
- Tests repeated
 - Conducted Emissions of Infrared Experiment
 - Thermal test of front optics
 - Shock of front optics

Acknowledgements

The authors wish to thank following organizations:

- Lambda-X for optical testing
- Prime – Thales Alenia Spazio for their support
- ESA HQ for technical supervision
- Swiss Space Office for support and funding

Thanks for your attention



Design Solutions for Integration of TPS Assemblies on IXV

7th European Workshop on Thermal Protection Systems and Hot Structures

8 – 10 April 2013

ESA-ESTEC, Noordwijk, The Netherlands

M.T. Signorelli⁽¹⁾, E. Brach Prever⁽¹⁾, V. Ancona⁽¹⁾, V. Damiani⁽¹⁾, G. Pippia⁽²⁾

⁽¹⁾Thales Alenia Space, Strada Antica Di Collegno 253, 10146, Turin (TO), Italy

mariateresa.signorelli@thalesaleniaspace.com

elena.brachprever@thalesaleniaspace.com

vittorio.ancona@thalesaleniaspace.com

vincenzino.damiani@thalesaleniaspace.com

⁽²⁾Sofiter System Engineering, Corso Francia 35, 10138, Turin (TO), Italy

gianni.pippia@external.thalesaleniaspace.com

1. ABSTRACT

Different types of advanced thermal protection technologies have been developed within the frame of IXV Program, aiming to demonstrate their suitability for re-entry applications.

Ceramic shields and attachment components constitute the main technology for the most loaded areas from an aerothermodynamics standpoint, together with proper stack-ups of insulating materials. Less stressed areas are protected by ablative materials directly bonded to the structure aeroshell.

Beside the attachment to cold structure aeroshell, the TPS assemblies interface with different assemblies and in correspondence of other IXV subsystems, in particular Descent System and Recovery System items, In-Flight Experimentation sensors, antennas. Hence, the design implementations of such technologies deal with complex interface requirements, ranging from geometrical and thermo-mechanical constraints to the need to limit sneak flow of the hot plasma inside the vehicle. Furthermore, several integration constraints needed to be defined and taken into account throughout the definition of the TPS design, in some cases deeply driving its implementation, in order to guarantee the possibility to incorporate within the vehicle the different items.

Focus of this paper is illustrate the implementation of a number of design solutions defined in order to comply with the integration flux, and the tailoring of such flux to optimise the TPS integration in accordance to the design constraints and the different facilities involved.

2. IXV TPS&HS OVERVIEW

The IXV TPS&HS (Thermal Protection System & Hot Structure), designed to protect the cold vehicle structure and other subsystems from the harsh re-entry environment, is based on different advanced technologies and mainly consists of the following assemblies:

- Ceramic Nose Assembly (design by Herakles)
- Ceramic Windward Assembly (design by Herakles)
- Ceramic Body Flap Assembly (design by MT Aerospace)
- Ablative TPS Leeward, Lateral and Base Assemblies (design by AVIO)

All the interfaces between different TPS&HS assemblies and different IXV sub-systems are designed and developed by Thales Alenia Space. The IXV TPS&HS configuration is shown in Fig. 1.

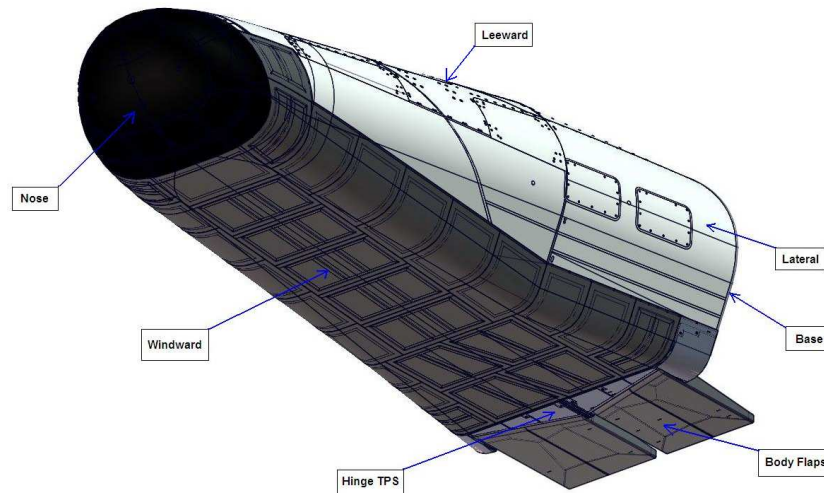


Fig. 1 IXV TPS & HS Architecture (Vehicle Configuration)

3. IMPACTS OF INTEGRATION CONSTRAINTS ON TPS DESIGN

Besides Cold Structure aeroshell panels and rear bulkhead, TPS assemblies interface with a number of different subsystems, in particular Descent & Recovery System (parachute panel and parachute extraction bridles, mortar cover, floatation balloons panels), In-Flight Experimentation (infra-red camera, thermocouples, pressure sensors), GPS and TM antennas, Reaction Control System.

This implies different needs to be fulfilled at system level, resulting in complex interface requirements; among them, geometrical, thermo-mechanical, sneak flow resistance, and integration requirements are the ones most demanding.

A major constraint is represented by the TPS top-level integration flux, mainly responding to needs of the ceramic assemblies because of their complex cold structure attachment systems, which are integrant part of their design and were defined in an early phase of the Programme. On the basis of ceramic attachment systems needs, the TPS has to be integrated according to the following sequence:

- Ablative TPS integration on removable panels, to be performed off-line
- Nose I/F ring pre-installation fit-to-check
- Nose integration
- BFA Pre-integration & demounting
- Windward integration
- On-line Ablative TPS integration
- Hinge TPS integration
- Body flap final integration
- Aeroshell (with Ablative TPS already integrated) final integration
- TPS integration completion (Ablative sealing tiles and overall Ablative TPS sealing)

The Ablative TPS is the assembly with the simplest attachment system, basically relying on direct adhesion on the cold structure; combined with the capability of being manufactured with complex shapes, this awards a high flexibility in terms of design that can be exploited to fulfil the demanding integration needs resulting from CMC TPS integration constraints. Furthermore, it is worthy noticed that the Ablative Assemblies, because of their huge distribution on leeward, lateral, and base sides of the vehicle, are the ones most involved by interfaces with other subsystems, in particular Descent and Recovery System (DRS), Reaction Control System (RCS), and antennas, besides Cold Structure and In-Flight Experimentation (IFE) sensors. Hence, integration requirements and flux of related activities (ranging from top- to bottom-level) mostly impact on Ablative Assembly.

For similar reasons (complex shapes obtainable with limited manufacturing effort and simple fixation systems), also flexible TPS Sealing are able to be specifically designed for guaranteeing the fulfilment of integration needs.

The following sections illustrate some of the design solutions which have been adopted to optimize the TPS design facing different major integration constraints.

4. DESIGN SOLUTIONS FOR INTEGRATION OF ABLATIVE TPS ASSEMBLIES

The first constraint here discussed regards the need to avoid the correspondence of Ablative TPS filler paths with respect to **gaps between aeroshell panels**, while at the same time the dismounting of aeroshell panels has to be guaranteed after the bonding of ablative tiles and until the AIT activities at launch site.

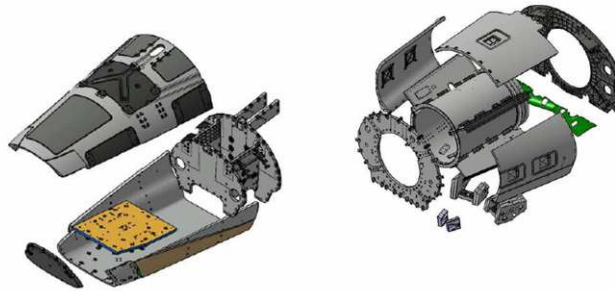


Fig. 2 Cold Structure Aeroshell Panels

In order to guarantee the dismounting of cold structure panels, a number of ablative sealing tiles have been defined in correspondence of aeroshell interfaces, as illustrated in Fig. 3. These tiles are foreseen to be integrated in latter integration phase at launch site, after all activities requiring disassembly of aeroshell panels are completed.

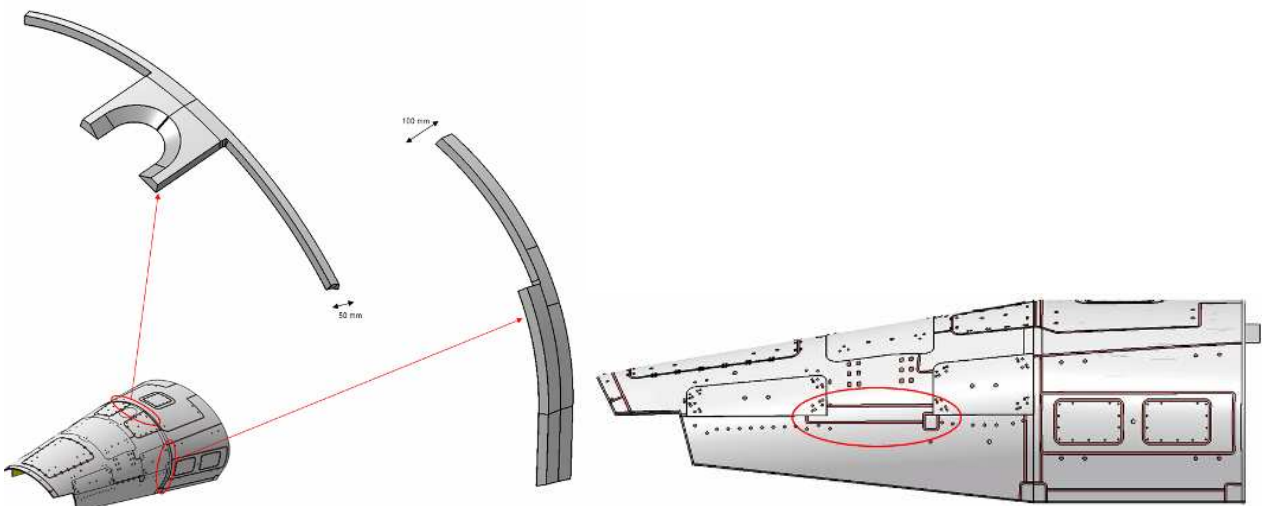


Fig. 3 Ablative Sealing Tiles Interfacing in Correspondence of Aeroshell Gaps

As presented before, a number of ablative tiles have to be integrated after the installation of **Ceramic TPS**. This is due to different constraints: the Nose TPS needs full clearance in the forward region of the upper aeroshell panels for its installation; mating of lateral rear aeroshell panels (protected by Ablative TPS) with the lower rear panel (protected by leading edge shingles) in the aft part of the vehicle requires a handling clearance not achievable in case of ablative tiles already in place; interface between ceramic and ablative assemblies is preferable to be finalized after the results of TPS&HS Plasma Wind Tunnel Test, whose schedule is currently superimposed to the AIT activities.

For these reasons, a number of Ablative TPS sealing tiles to be installed after CMC TPS have been introduced in correspondence of interface with Windward, Nose, and Hinge TPS, as illustrated in Fig. 4 and Fig. 5.

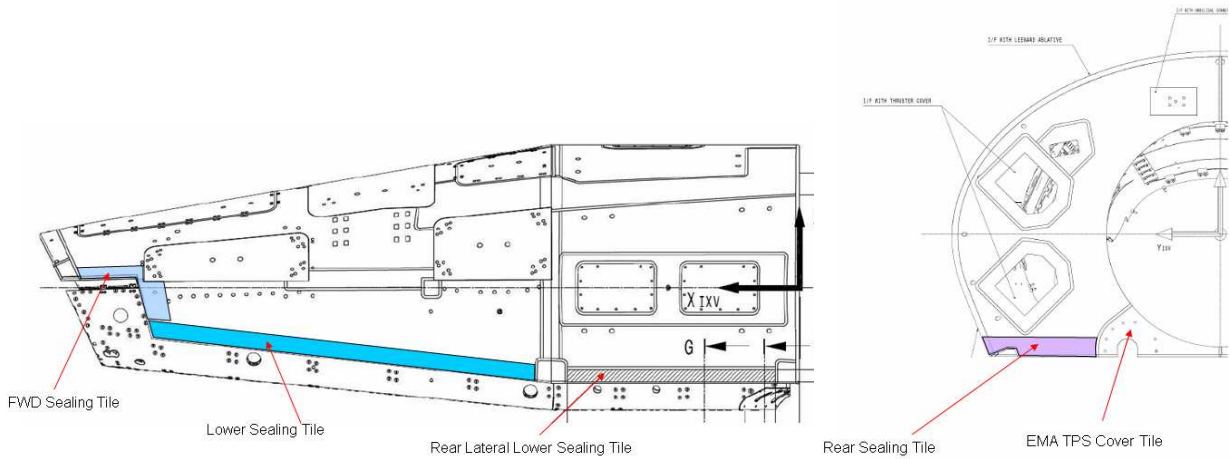


Fig. 4 Ablative Sealing Tiles Interfacing with Windward and Hinge TPSs

For allowing the installation of such sealing tiles, the integration process of ablative materials on cold structure substrate, initially foreseen to be performed via vacuum bag application, needed to be deeply reviewed. After the installation of larger ablative panels (indicated as “1” in Fig. 6), the portion of sealing tile in contact to CMC (“2”) is installed below the ceramic overlapping segment by means of weight application; then, the integration of a second portion of sealing tile (“3”) re-establishes the assembly continuity; finally, gaps between ablative tiles are filled.

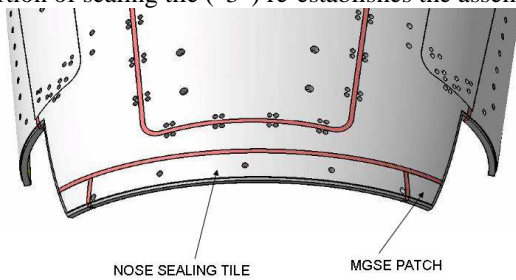


Fig. 5 Ablative Sealing Tiles Interfacing with Nose TPS

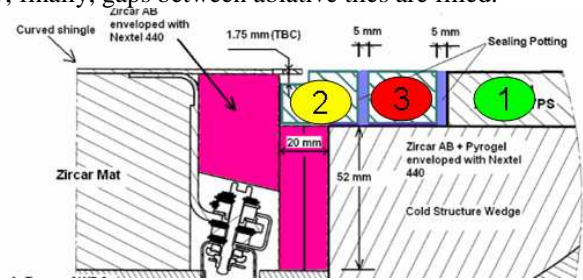


Fig. 6 Sealing Tiles Installation Sequence

Another constraint concerns the need to install a critical item as the **TPS covering the mortar cover**. The cover TPS has to be installed with proper clearance on surrounding sides, in order to ensure that no glue has percolated towards the mortar tube and hence putting at risk the correct ejection of pyro-activated mortar cover. At the same time, the integrated mortar tube/cover/TPS has to be installed from the external side of the vehicle, being the internal side not accessible due to fixation points to the internal structure; therefore, the tiles surrounding the mortar cover TPS tiles need to be bonded after the installation of mortar system. For these reasons, the TPS around Mortar Cover features a dedicated split design (shown in Fig. 7) able to guarantee its integration after mortar cover has been installed.

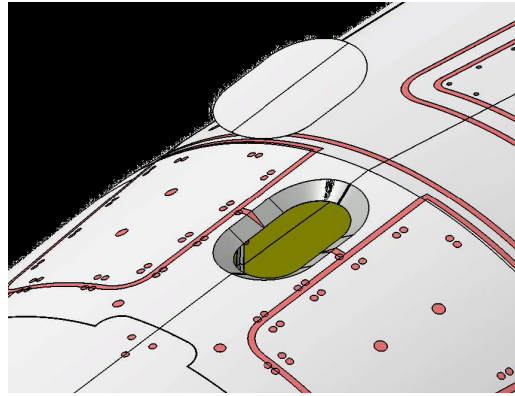


Fig. 7 Ablative TPS Surrounding Mortar Cover

A further major constraint is related to the access to **MGSE lifting points**, which shall be guaranteed up to the very late integration phases. Since lifting points are all distributed across lateral and leeward sides of the IXV, the needed clearance has to be provided by Ablative TPS.

After handling manoeuvres are finished and the vehicle is mated to its launcher, the cold structure surface is refurbished by aluminium brackets substituting the hoisting points. To allow the installation of brackets, dedicated ablative patches have been designed and are foreseen to be installed directly on the aluminium surface during the very late integration phases.

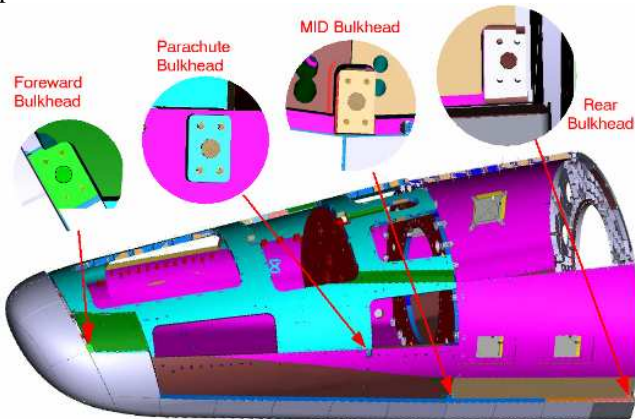


Fig. 8 Distribution of MGSE Lifting Points

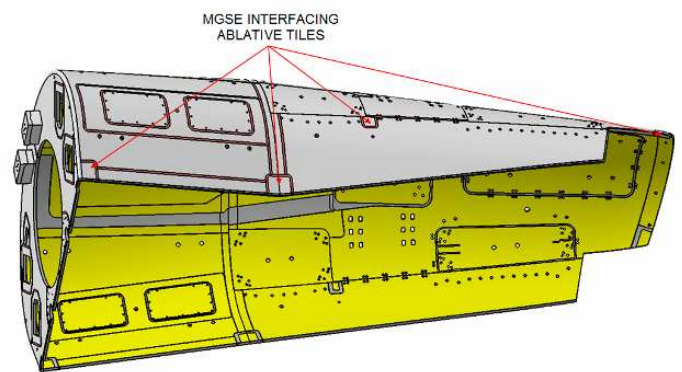


Fig. 9 Ablative TPS Covering MGSE Brackets

RCS thrusters are encapsulated within a titanium case, which is protected by mattresses made of Saffil-Nextel fabric. Mattresses interface with Ablative TPS bonded on the rear bulkhead; resistance to sneak flow is ensured by labyrinth design.

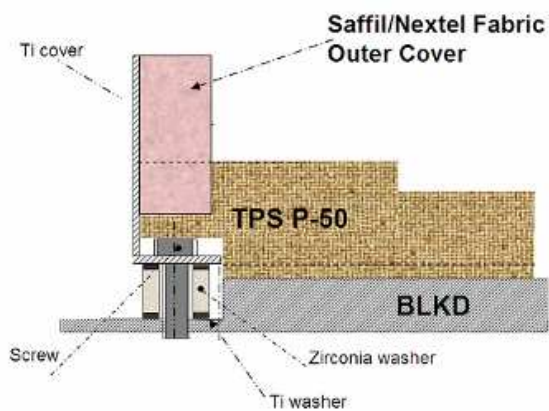
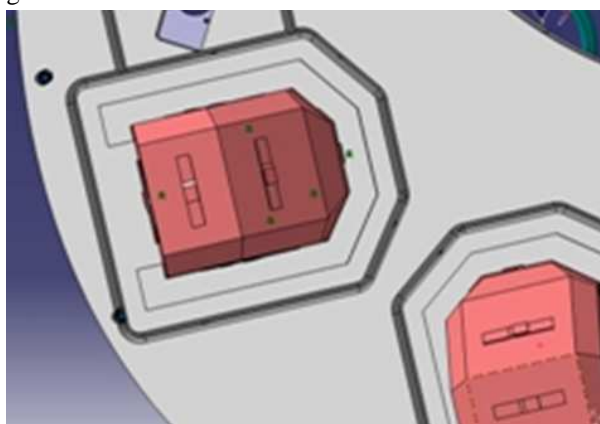


Fig. 10 Saffil-Nextel and Ablative TPS Protecting RCS Thruster Covers

This design has to be compatible with different constraints regarding the integration of the different items: titanium case, Saffil-Nextel mattresses, and P50 tiles. First, accessibility to flexible mattresses has to be ensured; however, they cannot be installed before the Ablative TPS tile attached onto rear bulkhead. Furthermore, the mattresses protecting the nozzle-side of the thrusters have to be integrated on launch site, for late operations on RCS.

For these reasons, a dedicated patchwork has been implemented, in order to split the integration activities of TPS on RCS in five steps (depicted in Fig. 11):

- On three side of thrusters covers, a first portion of ablative tiles (Cover Tile 1, CT1) are first bonded to the rear bulkhead;
- On the same sides, Saffil-Nextel mattresses are then installed on thrusters cover, with the needed clearance for fixing operations;
- The second portion of ablative tile (CT2) is then bonded on the first one;
- Finally, on the nozzle-side of the thrusters, the flexible mattresses are first integrated at launch site;
- The installation of last tile of ablative tile (CT3) completes the integration activities.

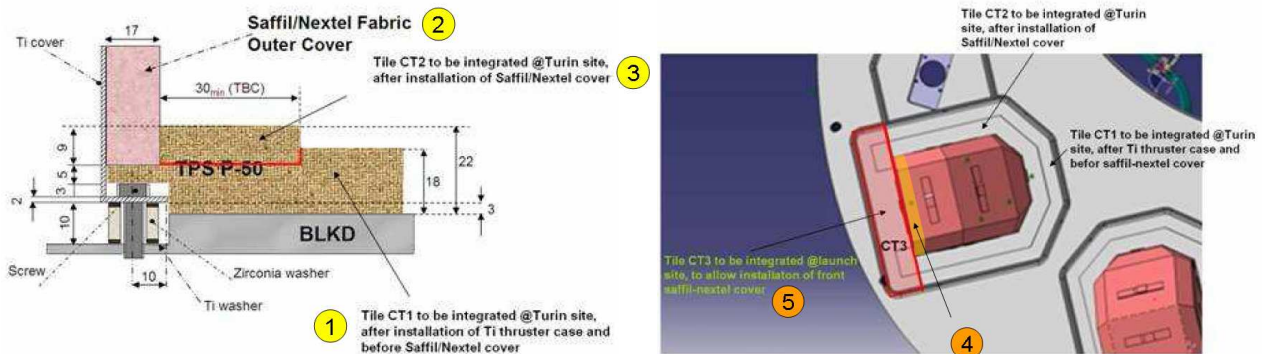


Fig. 11 Design and Integration Sequence of Ablative TPS Tiles Interfacing RCS

TPS protecting the **umbilical mechanisms case and cover**, which is another critical item from thermo-fluidic standpoint, shows a design particularly complex, both for ensuring a labyrinth-like shape and for guaranteeing the correct kinematics. A further complication is due to the need of providing access to the internal side to the security pin, which avoids the mechanism closure during on-ground activities.

The pin access is provided by the mechanisms TPS design highlighted in Fig. 12.

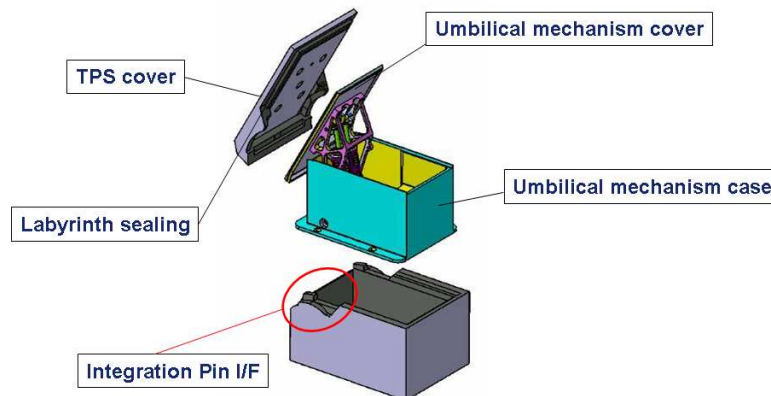


Fig. 12 TPS on Mechanisms Cover and Interface with Security Pin

The **In-Flight Experimentation thermocouples** within Ablative TPS feature a design elaborated after the failure of initial concept, based on “conventional” stick thermocouples with that proved to be not compatible with ablative behaviour. The ultimate design, shown in Fig. 13, uses “U” shape thermocouples, able to not impact the structural integrity of ablative holder; hence, beside providing accommodation for thermocouples, the ablative holder needed to be coupled with an interface cylinder for enabling its integration and refurbish the mechanical continuity with the surrounding tiles. Henceforth, as described in Fig. 14, the holder is installed by press-fitting within the interface cylinder, which features a gap with respect to surrounding tile to be filled by conventional mean.

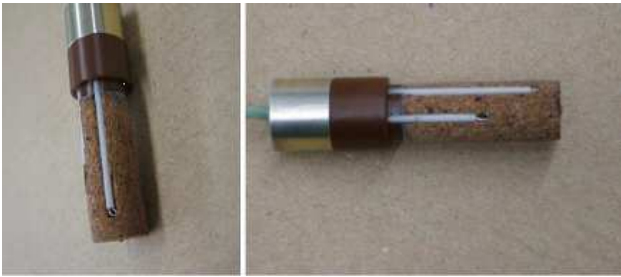


Fig. 13 IFE Ablative Thermocouples Holder

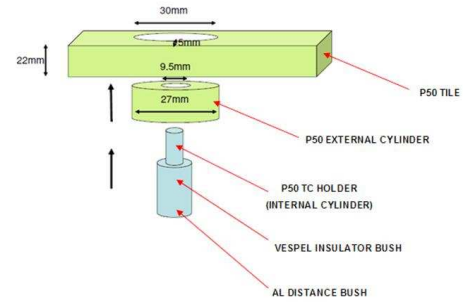


Fig. 14 IFE/Ablative Overall Interface Design (right)

5. DESIGN SOLUTIONS FOR INTEGRATION OF FLEXIBLE SEALING TILES

One of the major constraints for of the Flexible Sealing tiles design definition has been the requirement of removability of the IXV AFT lateral panels and the accessibility to the underneath screws without removal of Shingle tiles.

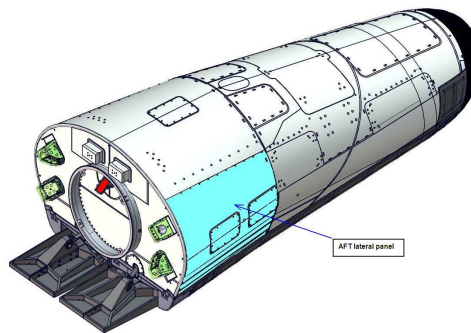


Fig. 15 IXV AFT Lateral Panel

Therefore, in order to easy the integration activity avoiding use of special tools and fixing screws, the design of Shingle insulations (Aeroguard and Pyrogel both encapsulated with Kapton HN) has been changed and part of the insulation in correspondence of the screws has been removed.

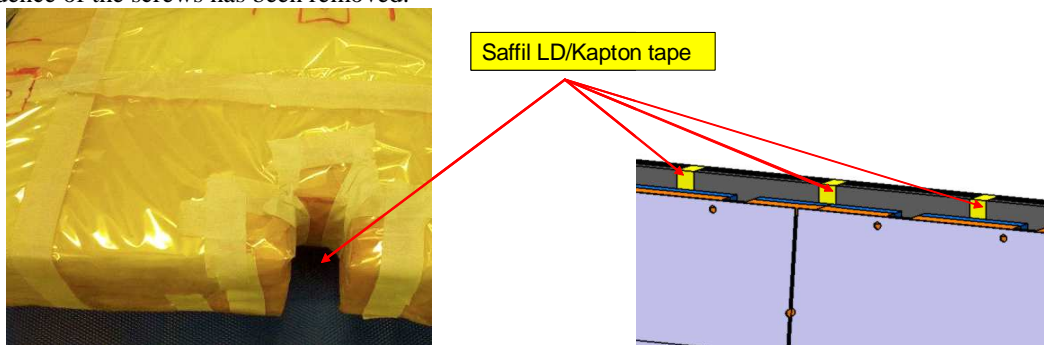


Fig. 16 Shingle Insulation design

Once the integration activities are completed, the missing insulation is restored with Saffil LD (not encapsulated); then, the final closure is provided by Kapton tape. Finally, the I/F cavity between Shingles and Ablative TPS is filled with seals of Saffil LD MAT encapsulated with Nextel 312 (Saffil/Nextel density=96kg/m³).

The selection of Saffil-Nextel, lighter than previously baselined material ((Superwool VF 607 HT), has been possible thanks to the better insulation properties of ablative P50 with respect to the former, siliconic-based SV2-A material. Typical length of each seal segment is about 350mm. The dimension has been defined to comply with AIT request in order to ease the late integration of the seal corresponding to the aft lateral panels.

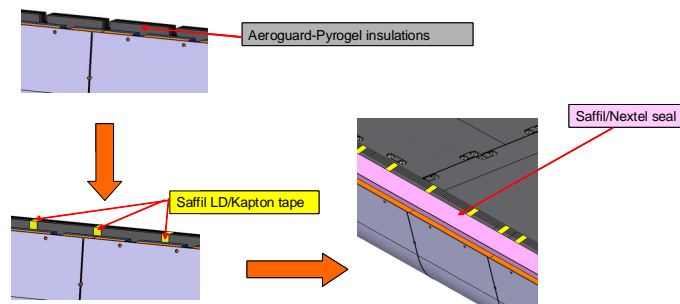


Fig. 17 Shingle Insulation design

6. IMPACTS OF ABLATIVE TPS DESIGN ON INTEGRATION FLOW

Whereas integration constraints have driven large areas of design, the integration flow has been also tailored in order to account for major design needs. As major examples, bridle covers TPS, needing to be manufactured in single pieces to allow their rupture during the parachute extraction and ranging from forward to rear aeroshell panels, have to be integrated on the late integration phase at launch site, in order to allow aeroshell panels dismounting during integration activities. Mortar Cover and Parachute Panel cannot be integrated off-line, since their installation has to follow the bridle routing; for this reason, their integration, together with the intermediate tile, has to be performed during the late AIT activities.

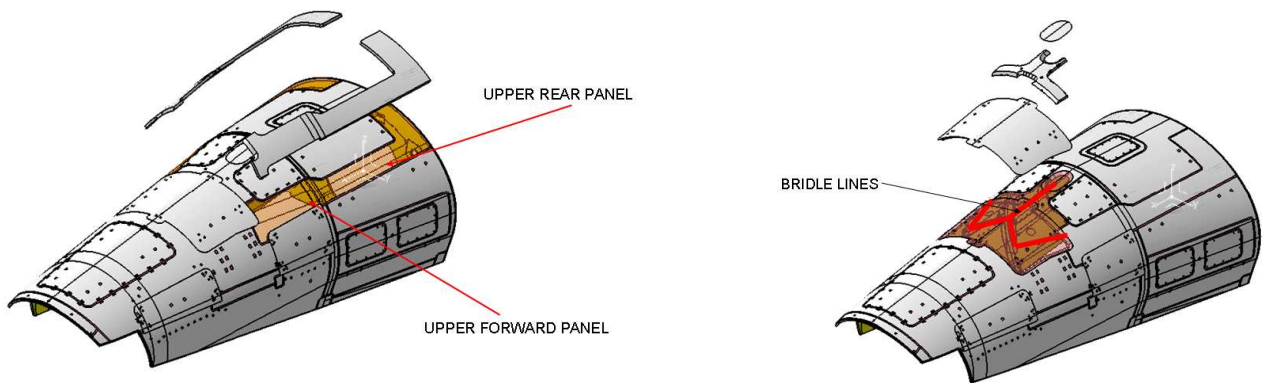


Fig. 18 Installation of Bridle Covers (left) and Parachute/Mortar/Intermediate Tile (right) TPS

Because of the number of activities to be performed on-line and on not rigid surfaces (such as porous seals), the former bonding strategy based on vacuum bag application cannot apply and will be partially substituted with different strategies, based on the application of mechanical loads. Innovative bonding means and tools are currently under definition within the frame of Ablative TPS Full-scale Validation Tests.

7. CONCLUSIONS

Besides thermal, thermo-mechanical, and thermo-fluidic requirements, the design of TPS assemblies, constituted by ceramic and flexible items, is deeply related to integration needs. Ceramic TPS have been specifically designed for being integrated onto the IXV cold structure, by means of complex attachment systems that mainly drive the definition of integration flux at different levels. Featuring Ablative TPS and sealing tiles a high level of flexibility, both in terms of manufacturing and bonding standpoints, they are able to take in charge a number of different integration needs at TPS subsystem and system level. Henceforth, their design is deeply driven by integration constraints.

The most representative integration constraints and related design solutions have been briefly illustrated in this paper, in particular concerning interfaces with cold structure panels, DRS, IFE, RCS, mechanical mechanisms, as well as contiguous TPS. An outlook of the major impacts of design implementation on integration flux (and in particular on Ablative TPS bonding strategy) has been also given.

PREPARATORY ACTIVITIES FOR THE IXV TPS&HS SUBSYSTEM PWT TESTS (LESSON LEARNED)

7th European Workshop on Thermal Protection Systems and Hot Structures

8 – 10 April 2013
ESA-ESTEC, Noordwijk, The Netherlands

M.T. Signorelli⁽¹⁾, E. Brach Prever⁽¹⁾, D. Francesconi⁽¹⁾, A. Di Maso⁽²⁾, G. Rufolo⁽³⁾, D. Cinquegrana⁽⁴⁾, E. Trifoni⁽⁴⁾

⁽¹⁾Thales Alenia Space ~~Italy~~, strada Antica Di Collegno 253, 10146, Turin (To), Italy

⁽²⁾Altran Italia, strada Del Drosso 33/19 pal. C, 10135, Turin (To), Italy

⁽³⁾ESA-HQ, Paris, France

⁽⁴⁾CIRA, Italian Aerospace Reserach Center, Capua, Italy

1. ABSTRACT

In the frame of IXV (Intermediate eXperimental Vehicle) program, developed by the European Space Agency (ESA), one of the most challenging tasks is represented by the definition and the verification of the interfaces among different Thermal Protection System (TPS) assemblies. In order to better understand and predict the thermo-mechanical and thermo-chemical behaviour of this complex subsystem, PWT ~~(Tests in SCIROCCO (PWT plan, t-CIRA- - (Centro Italiano Ricerche Aerospaziali); the tests are planned for late 2013. This paper presents the preparatory activities performed to define the experimental set-ups and TAs (Test Articles) design, as well as the chamber hypersonic flow conditions representative of IXV TPS re-entry phase. The Test Articles-TAs are composed by different ablatives and CMC (Ceramic Matrix Composite) panels provided with seals and flight sensors; the geometry is a flat plate with a cylindrical leading edge able to reproduce the flux on most critical IXV TPS IF (interfaces). The tests will be performed in high-enthalpy hypersonic, non-equilibrium flow conditions; in particular the CMC materials will undergo temperatures up to 2000_K for several minutes experimenting also the oxidation resistance in extreme conditions. A glance on numerical experimental predictions carried out by computational fluid-dynamics is given. The methodology to evaluate the catalytic efficiency and the emissivity of the materials at different temperatures needed are considered for test rebuilding is finally described.~~

2. THE IXV HEAT SHIELD MATERIALS AND REQUIREMENTS

The TPS&HS (Thermal Protection System & Hot Structure) is one of the most complex assemblies of a re-entry vehicle [1]. The main capabilities to be provided by the TPS&HS are to withstand the heat loads foreseen during the re-entry reference trajectory and to provide the adequate stiffness against the dynamic pressure to maintain the required aerodynamic shape.

The TPS&HS Subsystem consists of the following assemblies:

- Ceramic Nose Assembly (design by Herakles)
- Ceramic Windward Assembly (design by Herakles)
- Ceramic Body Flap Assembly (design by MT Aerospace)
- Ablative TPS Leeward, Lateral and Base Assemblies (design by AVIO)

All the interfaces between different TPS&HS assemblies ~~and between TPS&HS assemblies~~ and different IXV subsystems are designed and developed by Thales Alenia Space. The IXV TPS&HS ~~distribution configuration~~ is shown in Fig. 1.

The presence of so different TPS&HS types generates ~~possible~~ interface problems, so that the interfaces became the most complex part of the TPS&HS. For this reason PWT (Plasma Wind Tunnel) tests to be conducted at the SCIROCCO facility ~~were has been~~ planned. In Fig. 1 are indicated the selected points ~~on~~ the interfaces, indicated as

Formatted: Justified

IF#1...4; these points have been chosen because of the worst heat flux conditions. In Fig. 2 the sections of the four TPS interfaces are shown.

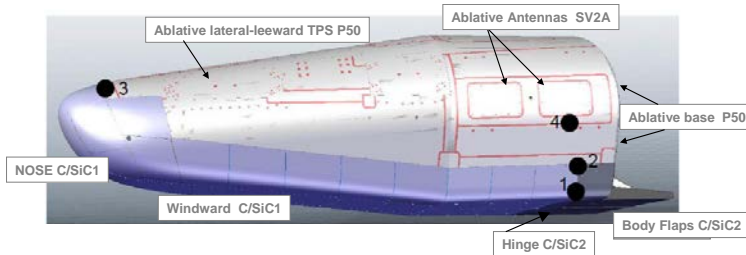


Fig. 1 The IXV TPS & HS Architecture (Vehicle Configuration) and the selected interface positions named (IF#1, IF#2, IF#3, IF#4)

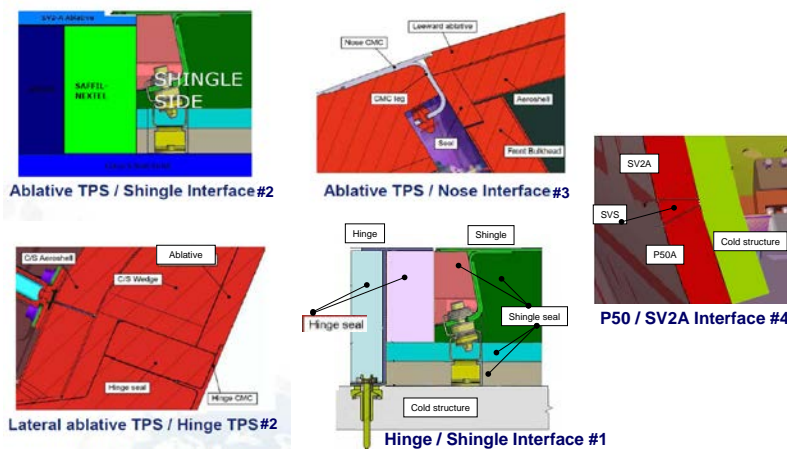


Fig. 2 Interface sketch sections with the materials indications (note: the IF#2 is a triple point interface where ablative, hinge and shingle are in contact united)

3. THE IXV MISSION

- ☐ The IXV will perform one single mission and will be launched from Kourou by the ESA/VEGA Launcher.
- ☐ It will perform a ballistic sub-orbital equatorial elliptic orbit with final sea landing in Pacific Ocean, with Apogee \approx 500 km, and flight duration of about 5200 s.
- ☐ The atmospheric re-entry will be representative of LEO re-entry conditions:
- ☐ Re-entry Duration \approx 19 min (1126 s considering the re-entry trajectory from 130 km, 3700 s after the launch)
- ☐ Entry velocity \approx 7.5 km/s
- ☐ Entry AoA (Angle of Attack) \approx 45°
- ☐ Max Dyn Pressure \approx 6 kPa
- ☐ Max Heat Flux \approx 800 kW/m² (at the stagnation point)
- ☐ Max Mach during re-entry \approx 27
- ☐ Mach 20 and Re \approx 20000 at the maximum heat flux

The fundamental data trajectory can be found in [1] and [2]. Since the TPS is the fundamental part of a re-entry vehicle [3] [4], it is important to test the TPS most critical parts i.e. the junctions in the worst flight conditions. A similar test on the ground it is possible could be made only with a in-a-PWT test.

Formatted: Bullets and Numbering

4. TEST ARTICLE DESCRIPTION

The TA (~~Test Article~~) has to implement the four interfaces (Fig. 1) among the IXV TPS (~~they have~~ to be tested in one assembly). Several designs have been evaluated taking into account the following parameters:

- ⊕ the overall maximum dimensions;
- ⊕ the 4 TPS interfaces, between the TPS attachment systems;
- ⊕ past experience acquired in the former program M&S1 (Future Launcher Preparatory Programme, Phase I) Materials and Structures Phase 1).

The TA for the IF#2, 3, 4 test is an assembly of 4 different panels, one curved and three flat (Fig. 3 and 4). The TA is supported by a test holder interfacing with the test facility, ~~the holder has a thermal protection frame with the only aim to protect the metallic parts~~. The whole item constituted by the TA ~~assembly plus~~ the holder and lateral thermal protection will be identified as TAA (Test Article Assembly-). The overall projected front surface is about 600 x 500 mm.

The edges and the lateral sides (brown panels in Fig. 3) of the TAA will be protected by thermal protection frame (high-density carbon-phenolic material) able to withstand the high heat fluxes foreseen on these areas.

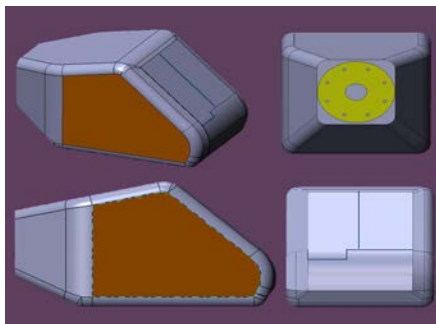


Fig. 3 Test Article Assembly layout

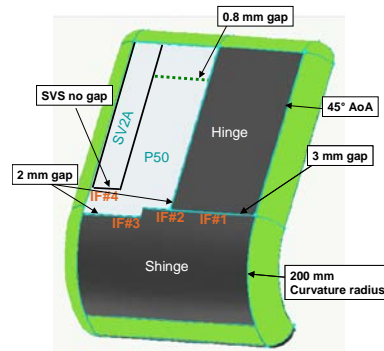


Fig. 4 Test Article description

The TAA design includes a flange interface compatible with the test facility. In the TAA ~~are will be foreseen installed~~ about 60 TCs (Thermocouples) and two pressure ports.

The front face of the TAA for the test of IF#2, #3 and #4 is depicted in Fig. 4. In the second run, dedicated to test the IF#1, the ablative tiles are replaced by a dummy panel able to withstand the higher heat fluxes w.r.t. first run.

The TA (Fig. 3 and 4) is representative of all the IXV TPS interfaces design.

5. THE FACILITY SCIROCCO

The tests will be conducted in the CIRA PWT facility called SCIROCCO. The installation is located in south Italy at Capua. A 70 MW segmented arc heater brings the compressed air flow up to temperature above 10000_K, then the plasma flow is expanded through a converging-diverging nozzle where the thermal and pressure energy is turned into kinetic energy and is accelerated up to hypersonic speed [3], the effective Mach number at the exit nozzle depending on the area ratio of the nozzle, in fact is possible to install 4 different nozzles. The hypersonic air flow arrives in the test chamber, a cylindrical vessel, where the model is placed on a mobile arm.

For the present tests the "D" nozzle will be used, with a nominal Mach of 7.5 and an exit diameter of 1.1 m.

6. THE TESTING METHODOLOGY

The PWT tests requirements have been defined on the basis of a conservative assumption, in fact the maximum heat flux value is relevant to the steep trajectory of IXV re-entry flight, while the heat load value is derived from the shallow one. The heat fluxes are calculated at radiative equilibrium [3] (i.e. approximating that the convective heat flux arriving from the gas is rejected completely as radiation) by means of CFD (Computational Fluid-Dynamics) analysis on the whole vehicle OML. The heat fluxes and pressure foreseen in the steep trajectory for the reference points are indicated in Fig. 5.

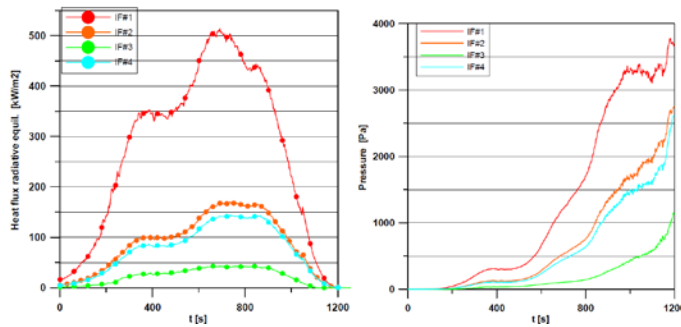


Fig. 5 Heat fluxes and pressure at I/Fs locations along IXV re-entry

From the plots of heat fluxes (above figure) is clear the impossibility to perform the exact heat flux required for every IF in one test, and the big difference between IF#1 and the other IFs. For this reason two different tests have been planned, one for IF#1, and the other for the remaining IF#2,3,4. For the test of IF#2,3,4 the reference heat flux is the IF#2 one i.e. the highest among the control points 2,3,4; this means the testing of IF#4 at value substantially higher than the flight one, ~~this can be partially overcome by the TA configuration as it will be explained in the next paragraph.~~ In the PWT testing the energy developed from the electric arch can be used to obtain heat or momentum [3] [4] (the two are mutually kept out), this means that usually it is impossible to reproduce both the flight surface pressure and shear load together with the flight heat flux; in this case, ~~as since~~ is a TPS test, the heat flux has the priority. In any case, for the pressure standpoint, it is possible to choose a value range.

The test reference pressure has been selected at 1000 s, as can be seen from Fig. 5. This is a conservative value with respect to the sneak flow even if ~~that this~~ is not the maximum value (as for the heat flux), but the pressure has reaches the maximum only at the zero altitude where the heat flux is close to zero.

The reference values for the tests are resumed in the following table:

ID	Heat Flux	Pressure	Shear load [Pa] Flight/test	Duration
Run #1 (IF#2 & IF#3)	170 +/- 5% kW/m ²	1750 +/-10% Pa	30/19	706 s (Heat load 120 MJ/m ²)
Run #2 (IF#1)	514 +/- 5% kW/m ²	3250 +/-10% Pa	90/38	710 s (Heat load 365 MJ/m ²)

Tab. 1 Test reference values

The shear stress has been also taken in ~~to~~ account to compare the test conditions to the flight ones. The shear is important only for the ablative test.

7. THE TEST PREDICTIONS

CFD test prediction activities have been conducted to understand:

- ⊕ the feasibility of the test reference values
- ⊕ the related PWT plant settings
- ⊕ if the temperature exceeds the materials limits (active oxidation occurrence)

First of all a forecast has been conducted by TAS (Thales Alenia Space) on the basis of past experiences for similar TA (M&S1) and then by calculating the heat flux by approximating semi empirical formulas for the cylinder and flat plate [4]. In a second step the heat flux distribution along the longitudinal section has been calculated by means of 2D (two dimensional ~~analysis~~) CFD analysis.

The analyses have been conducted by simulating the PWT test by means of experimental data to obtain far field conditions to be imposed at the TA as a free stream. The data taken into account are the Mach (depending only from the nozzle), the exit nozzle pressure (can be measured), the total enthalpy at the exit nozzle (can be measured or indirectly obtained), the chamber pressure (can be measured), and the fundamental chemical species (usually at the exit nozzle the oxygen is all dissociated [4], while the nitrogen dissociation can be neglected, in every case the chemical composition is not important to obtain full catalytic heat flux). As proposed by CIRA, the 2D results on the TA have been extrapolated

to 3D (three dimensional analysis) values on the basis of a former similar test (M&S1 test), in particular scaling coefficients have been defined by comparing the M&S1 2D simulations with the 3D one performed by CIRA [6]. This approach allowed to assess preliminarily the 3D analysis results before performing the simulations of the 3D OML that require some week of CPU calculations.

The exit nozzle conditions have been imposed to the 2D model by neglecting the presence of the chamber and of the expansion waves at the nozzle exit. In the frame of 2D analyses several SCIROCCO setting points have been evaluated in order to meet the required test conditions on the TA.

First of all the effect of curvature radius has been evaluated. Fig. 6 shows the 2D wall heat flux predictions by TAS on the 2D model for two different curvature radii (200 mm and 250 mm). The SCIROCCO test conditions at the reservoir are an average total enthalpy value of 18.5 MJ/kg and a total pressure of 8 bar.

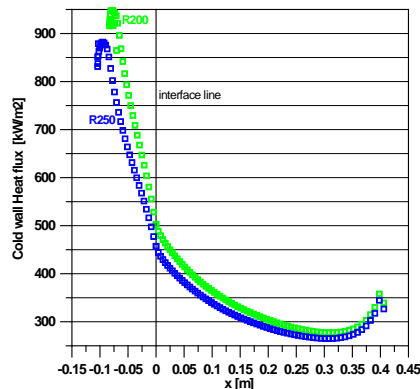


Fig. 6 Wall heat flux at radiative equilibrium on the 2D model (SCIROCCO test conditions 18.5MJ/kg, 8 bar)

The curved panel in 2D approximation can be approximated to a 2D cylinder. The heat flux is proportional to $1/\sqrt{R}$ where R is the curvature radius of the cylinder [5]. As shown in Fig. 6, the reduction of the curvature radius leads to a heat flux increase not only on the curved panel but also on the flat part of TA because the whole TAA becomes sharp. The radius value of 200 mm has been selected because it meets the required condition for test IF#1 shown in Tab. 1. Because of extreme test condition of test IF#1 it has been necessary to assess the real-actual temperature experienced by the ceramic material during the test to verify if active oxidation phenomenon occurred. For this reason, CIRA has performed 2D CFD analysis with VKI (Von Karman Institute) PC (Partial Catalytic) model for two different reservoir conditions. The wall heat flux distribution has been evaluated for FC (Fully Catalytic), PC (Partial Catalytic), and NC (Non Catalytic) wall conditions. The figures show a heat flux reduction of about 50% respect to the FC value on the stagnation point. The green plot has been obtained using the VKI model in the CIRA 2D model.

Formatted: Font: 10 pt
 Formatted: Font: 10 pt
 Formatted: Font: 10 pt, English (U
 Formatted: Font: 10 pt
 Formatted: Font: 10 pt
 Formatted: Font: 10 pt

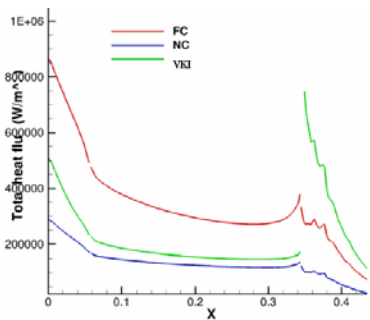


Fig. 7 wall heat flux distributions at 8 bar, 18.5 MJ/kg reservoir conditions, with FC, NC, and VKI PC wall condition

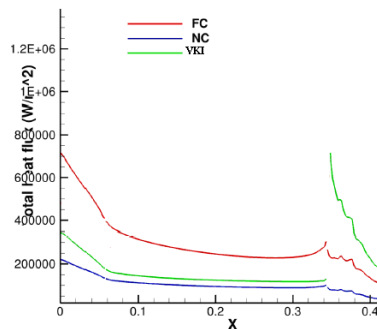


Fig. 8 wall heat flux distributions at 4.2 bar, 19.7 MJ/kg reservoir conditions, with FC, NC, and VKI PC wall condition

The AoA effect has been evaluated for reservoir conditions of 4.3 bar, 10.4 MJ/kg. The FC and NC heat flux distribution at radiative equilibrium ($\epsilon = 0.8$) along the TA surface are in Fig. 9 and Fig. 10.

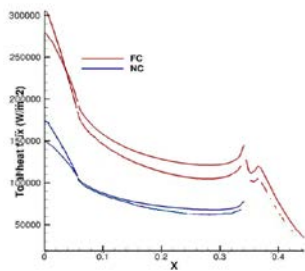


Fig. 9 The FC and NC heat flux at radiative equilibrium ($\epsilon = 0.8$) along the TA surface, 4.3 bar, 10.4 MJ/kg reservoir conditions, for AoA 45° and 55°

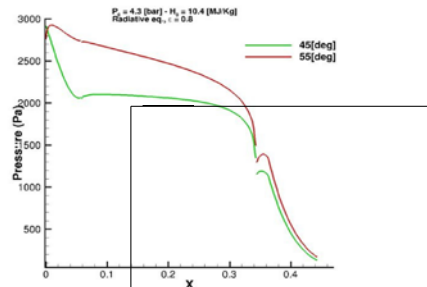


Fig. 10 wall pressure distribution at 4.3 bar, 10.4 MJ/kg reservoir conditions for AoA 45° and 55°

In the 2D 55° configuration there is an improvement of about 8 kW/m² at IF position and a reduction on the SP (stagnation point) of about 25 kW/m². The increasing of AoA leads to a reduction of the heat flux ratio between the SP and the flat part of the TA, this could be useful to uniform the heat flux on the TA surface.

Formatted: Superscript

The ablative thermal protection around the TAA can have influence on TA leading edge heat flux. In particular in the Fig. 12 based on TAS-I analysis, it is shown the effect of the design of the ablative frame covering the TAA edges. The analysed profiles are indicated, in the Fig. 11, as A* (R = 20 mm) and B* (R = 40 mm), and in Fig. 12 it is shown the heat flux along a transversal section of the TAA. The CMC is present between the abscissa 0 and 0.2 m, while between 0.2 and 0.25 m there is the ablative frame. The Fig. 11 shows that the profile A* leads to two beneficial effects: the reduction of maximum heat flux, and move the heat flux peak from the CMC leading edge to the ablative frame, thus reducing the risk of active oxidation. The heat flux on the profile B* shows two peaks, the first (the highest) is due to the 10° angle in the ablative shape, the second is due to curvature radius.

The analysis of the ablative frame shape has shown the difficulty to predict the heat flux jump on the geometrical discontinuities such gaps and steps, in particular numerical data in correspondence of 3 mm steps have a very high heat flux jump.

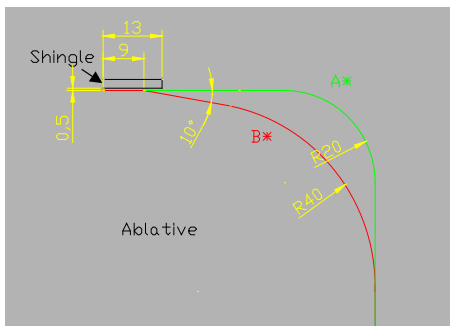


Fig. 11 TAA ablative frame profiles

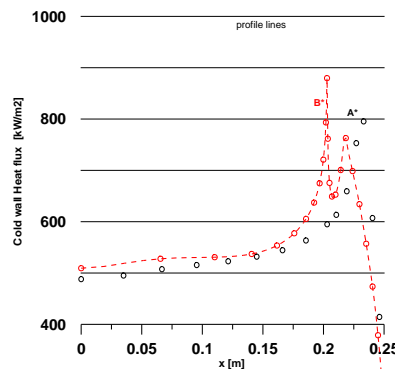


Fig. 12 Heat flux along the transversal section of the TAA, the abscissa zero corresponds to the symmetry of TAA

7.1 Differences between 2D and 3D model

In 2D analysis, TAA model is approximated by an infinite profile, leading to a shock wave more detached from the TAA surface than the 3D one [6]. This results in a lower heat flux on the top and bottom edges while around the stagnation point the heat fluxes are representative of the real values. Fig. 13 by TAS shows the different shock waves calculated with 2D and 3D model with the same PWT settings.

Another limitation of 2D model is the impossibility to predict the heat flux values on the lateral edges because not modelled. Unfortunately in this region the heat flux achieves the maximum value due to the expansion waves and therefore a lower pressure than in the symmetry axis. Only with a 3D analysis it is possible to predict the heat flux and pressure on the whole TAA correctly. Comparing 3D analysis with a 2D one, scaling coefficients can be derived to obtain approximated 3D heat flux and pressure from 2D solutions. This approach allows to analyse different working points, avoiding a large amount of numerical calculations. Fig. 14 based on TAS-I analyses shows the scaling coefficients for the defined TAA geometry.

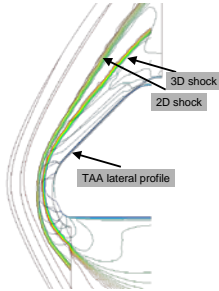


Fig. 13 2D-3D shock wave comparison

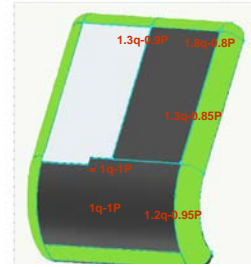


Fig. 14 2D-3D scaling coefficients for heat flux and pressure

7.2 3D analysis

The 3D analysis has been run by TAS for the FC case at 18.5 MJ/kg and 8bar reservoir conditions.

Fig. 15 shows a grid used for 3D model and the heat flux behaviour along three transversal lines on the TAA surface. The transversal lines are indicated on the grid. The heat flux along the stagnation point (SP) line shows oscillation around an average value of 900 kW/m² due to numerical errors typical of the stagnation point solutions. Fig. 15 shows also that the heat flux is quite constant for most of the part of transversal lines on the CMC except in the last five centimetres where the border effect on the heat flux becomes not negligible. The picture in the middle of Fig. 15 shows the heat flux contours, the heat flux plots along the symmetry axis of the TAA and along the borderline are in the plot at right of Fig. 15.

Errore. L'origine riferimento non è stata trovata. The borderline is positioned at the interface between the CMC panel and the ablative TPS covering the holder frame. In this line the ~~f.e.~~FC heat flux reaches the maximum value at which the CMC will be exposed. The heat flux reduction in correspondence of $x = -0.07$ m is relevant to the area below the stagnation point.

From the contours appears that the ablative frame will be exposed to a heat flux of about 1200 kW/m².

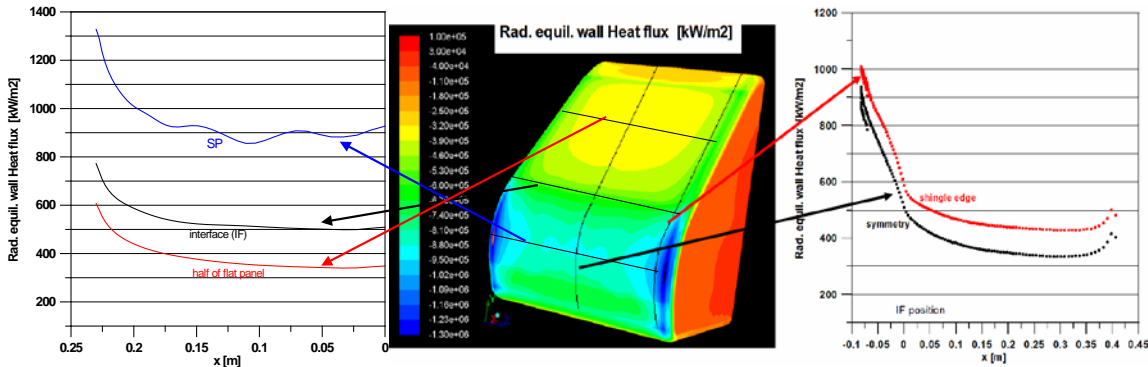


Fig. 15 FC. heat flux along the z axis (transversal lines) of the TAA, the FC heat flux contours, and on the right the FC heat flux along the x axis (longitudinal lines) midline and borderline

The heat flux has been evaluated also for the PC case of CMC materials with both the recombination coefficient and emissivity as a function of the temperature and the ablative frame modelled as FC.

Fig. 16 shows the heat flux contour. The heat flux value is less than half of the FC one and should be close to the NC value, because generally the SiC is a non catalytic material [7] and the air in the PWT is strongly dissociated already at the exit nozzle. In fact, the order of magnitude of the recombination coefficients γ (ratio of recombined atoms to impinging atoms at a wall) is about 10^{-3} .

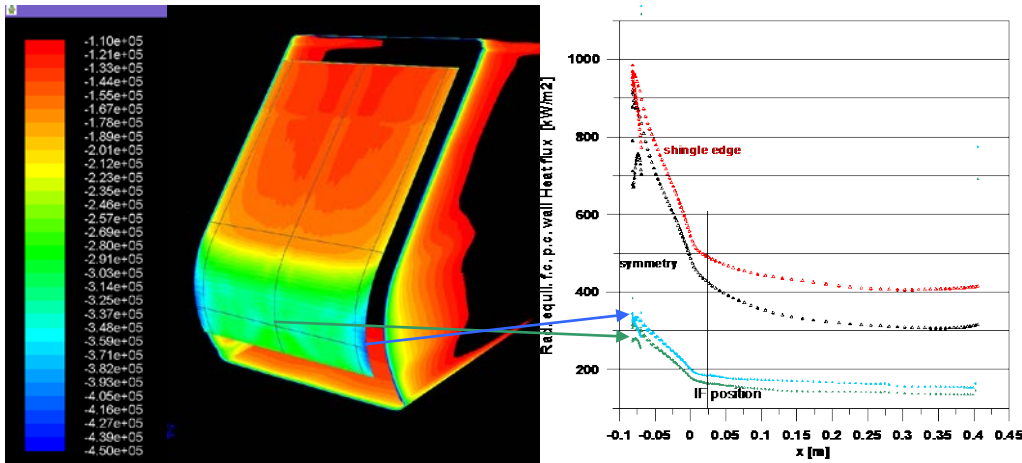


Fig. 16 PC heat flux contour on the TA surface, and on the right FC heat flux in comparison with the PC heat flux along the midline and borderline of CMC materials

In the Fig. 16, the contour on the ablative frame in the edges is not visible because is out of the range, the heat flux calculated on the ablative is higher than the one FC case of CMC materials of **Errore. L'origine riferimento non è stata trovata.** Fig. 15. In particular have been evaluated values above 2 MW/m^2 due to catalytic jump at the interface with the CMC. Probably the real values during the test will be lower respect to the predicted one because the ablative frame could be not FC and the numerical model could amplify the heat flux jumps. A jump due to catalytic difference of the adjacent TPS materials is expected also in the test for IF#2_3_4 where CMC will be close to an ablative panel.

8. CONCLUSIONS

The numerical models limits as, for example, the difficulty to predict the heat flux jump on the geometrical discontinuities such gaps and steps and at the interface between materials with different catalycity values, can be overcome by using test results and semi empirical formula.

Also past experience on PWT tests, literature data and CFD simulations can provide useful information and data.

A complex TAA has been designed. The complexity was due to the four TPS interfaces to be tested in an unique test article with overall dimensions of about $500 \times 600 \text{ mm}$ and, in addition, the need to implement the TPS underneath structure representative of the cold structure of the IXV.

The performed preparatory activities allowed to define the design of the test article and the need to plan two test runs in order to achieve the test objectives.

References

- [1] J.C. Bastante, R. Haya, J.Senna, "End to End Optimization of IXV Trajectory via Multiple Subarc Sequential Gradient Restoration Algoritm"; IAC 2010
- [2] R. Haya-Hamos, D. Bonetti, J. Senna, J. C. Bastante, J. Frexia, C. Parigini, A. Caramagno, "Mission Analysis and Flight Mechanism", 3^o International ARA Days
- [3] J.D. Anderson, "Hypersonic and High Temperature Gas Dynamic", *McGraw-Hill*, 1989.
- [4] A. Di Maso, "Plasma wind tunnel testing of Ultra High Temperature Ceramics: experiments and numerical correlation", published on the University of Naples web library, December 2009
- [5] M. Tauber, "A Review of High-Speed, Convective, Heat-Transfer Computation Methods", *NASA technical paper*, 1989.
- [6] S. Di Benedetto, et al "Rebuilding and Analysis of a SCIROCCO PWT test", *Intech Open Journal* 2008.
- [7] J. V. Rakich et al., "Catalytic Efficiency of Space Shuttle Heat Shield", NASA Ames research center, AIAA conference paper 1982.

AEROFAST : Development of Innovative Thermal Protections

7th European Workshop on TPS & Hot Structures - Noordwijk (NL)
2013, April 8-10 - Session "Ablative Materials"



J-M. Bouilly¹, G. Pinaud¹ / J. Carvalho², A. Coelho²

¹EADS Astrium, e-mail: jean-marc.bouilly@astrium.eads.net

²Amorim Cork Composites, e-mail : jcarvalho.acc@amorim.com



Funded under Seventh Framework Programme



Overview

- AEROFAST project objective & organization
- Existing cork TPS & status
- Ablative Thermal Protections development
 - Development strategy
 - Innovation ways
 - Preliminary characterization tests and selection
- Plasma test
 - Description of test campaign on COMETE facility
 - Main Results
 - Evidence of swelling effect
- 3D thermal and ablative analysis
- TPS Demonstrator manufacturing
- Conclusion

AEROFAST project objective & organization

- European Union R&D project aiming at increasing the TRL of *Aerocapture* technology for efficient Mars Exploration missions

⇒ 30-month project – 2009/2011

⇒ 12 European partners, ASTRIUM SAS prime, 6 workpackages:



⇒ AEROFAST top 5 objectives:

- Obj1: Define a project of aerocapture demonstration
- Obj2: Increasing TRL planetary relative navigation and aerocapture algorithm up to 5.
- Obj3: Build a breadboard to test in real time the pre-aerocapture and aerocapture GNC algorithms.
- **Obj4: Demonstrate/prototype the thermal protection system.**
- Obj5: Define on-board instrumentation for aerocapture phase recovery.

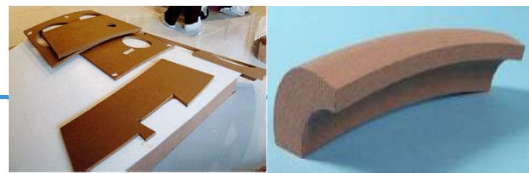
Existing cork TPS & status



⇒ Norcoat Liège©

Used on:

- Launchers (Ariane 5, M51)
- ARD cone & back-cover
- Beagle 2 (assembly process)
- ExoMars (CO₂ qualified)



AMORIM
Amorim Cork Composites

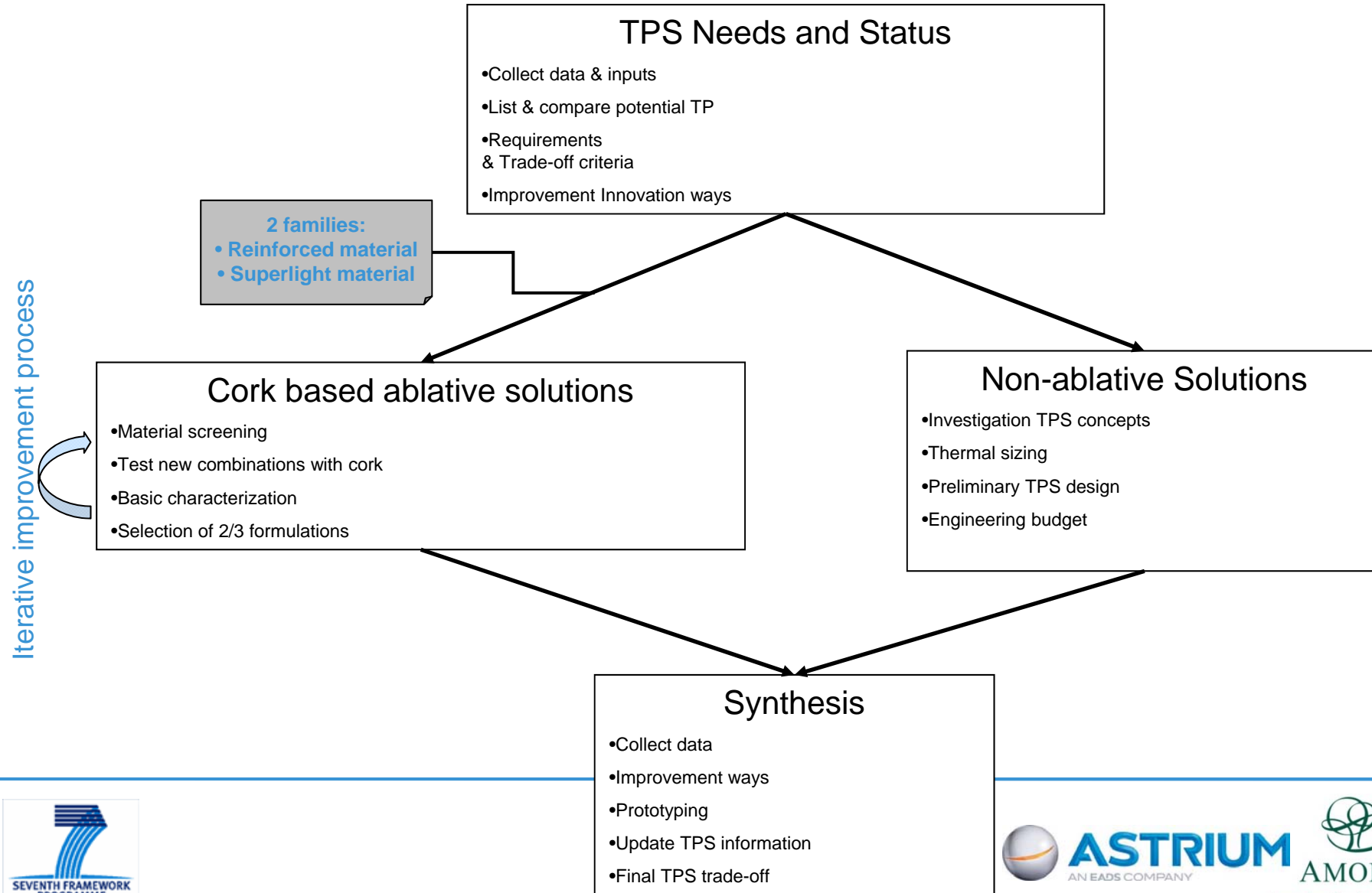
P45-P50 ←

Used on:

- SRB of Space Shuttle
(booster nose cone, forward and aft skirt...)
- Delta rockets (booster nose cone, frustum ...)

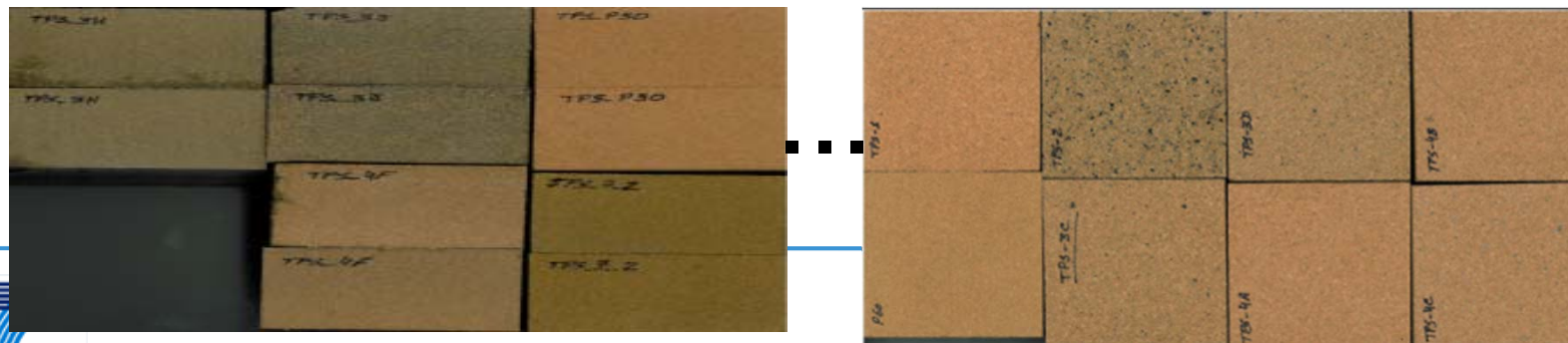
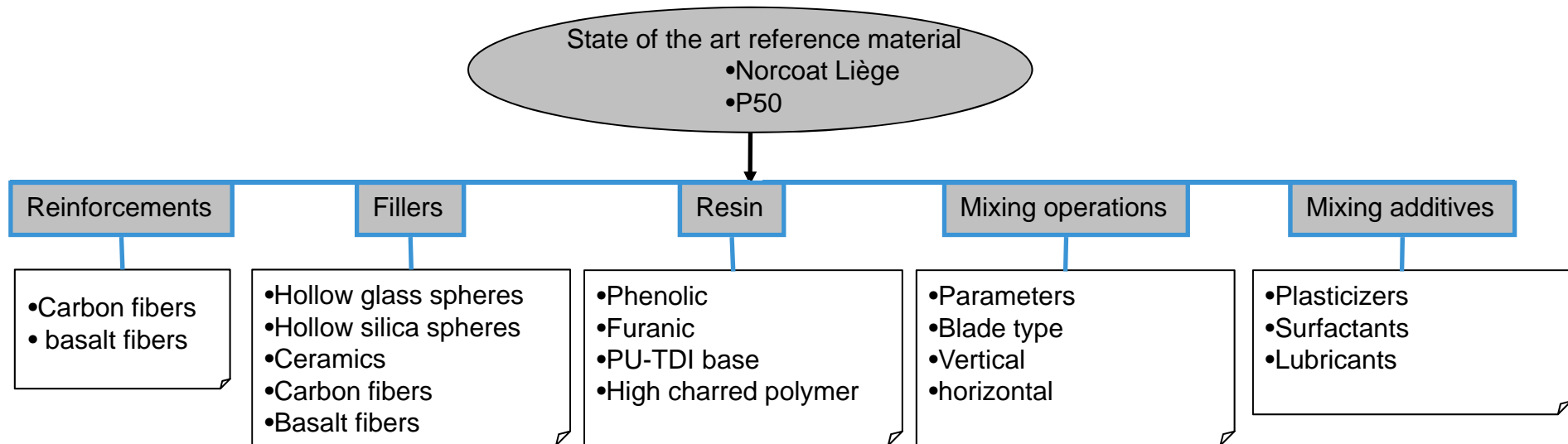


Development strategy



Innovation ways

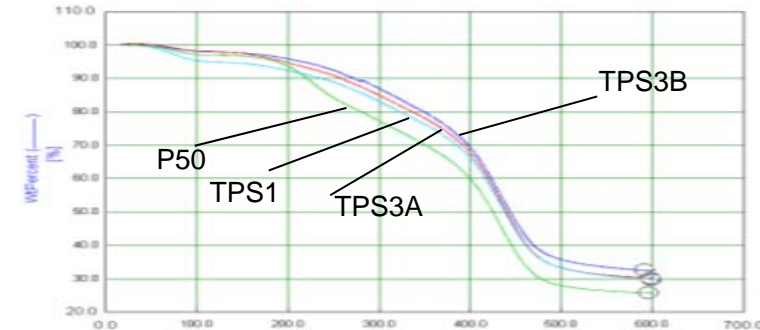
New formulations were proposed (up to 25) based on a "development road map":



Preliminary characterization tests & selection

- Basic characterization perform for all formulations & ref material

- Density
- Hardness
- Tensile
- Elongation
- Compression
- Flexibility
- Mass loss @ 1000°C (TGA)



- For the most interesting samples fire tests were performed

- Test conditions : 75 kW/m² during 300 s
- Calorimetric measurements
- Mass loss



- Selection of the 4+3 best candidates based on:

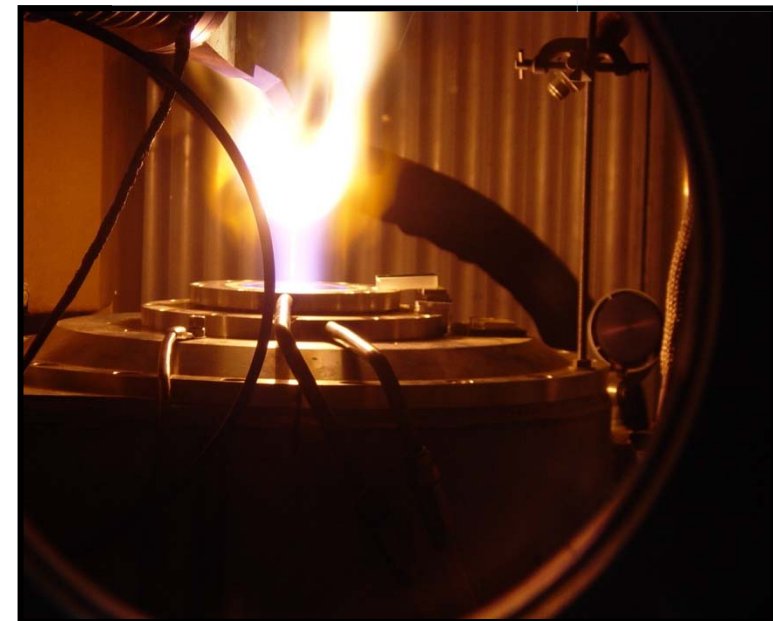
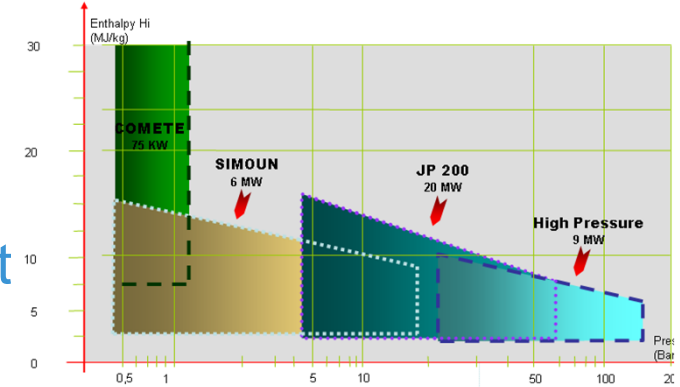
- Material recession (mass loss under fire test)
- Material mechanical integrity (disaggregation, ash)
- Surface roughness
- Cracks (number, depth, width)



- Deeper thermal investigation followed on the most promising formulations (TGA, *k*, *C_p*...)

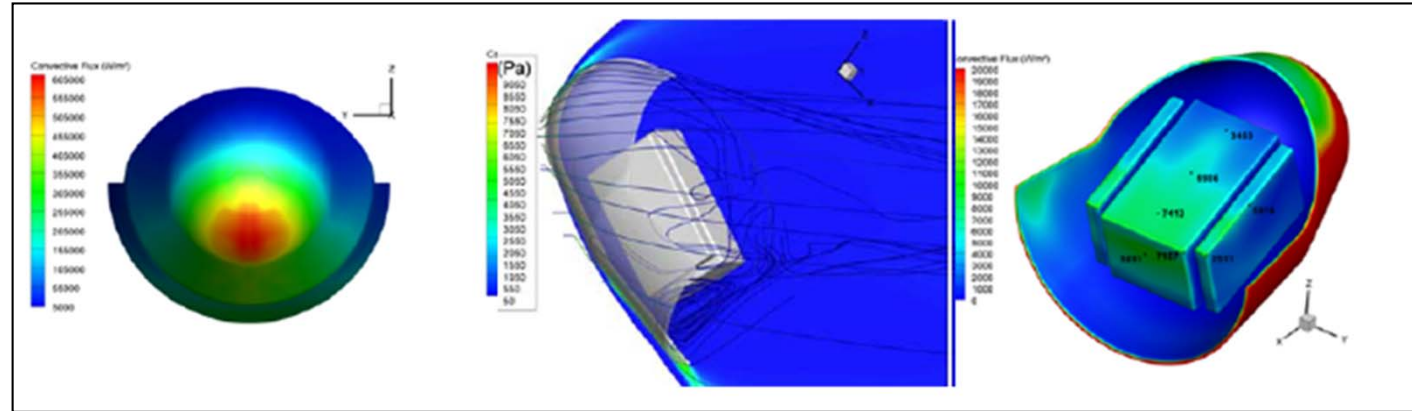
Plasma test : COMETE facility

- Stagnation point configuration
- 300 to 7000 kW/m²
- Duration : few seconds to 30 minutes test
- Non polluted flow
- Air atmosphere



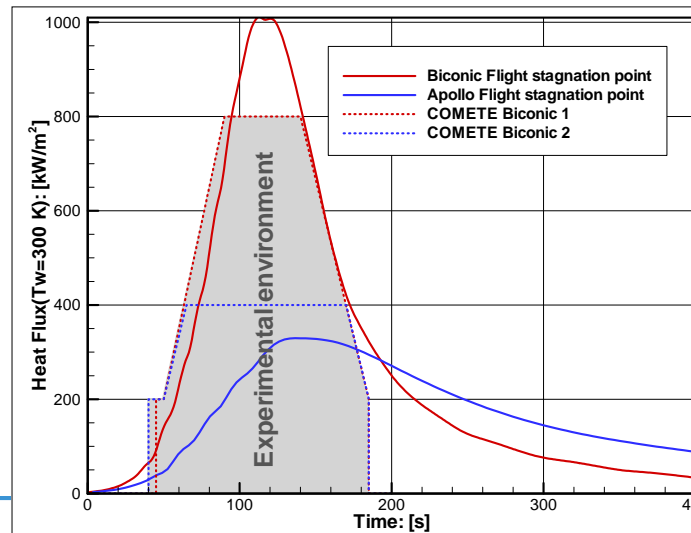
Plasma test : Aerothermal environment

- 2 representative ground missions derived from maximum energy flight conditions :



COMETE Biconic 1

$$\begin{aligned} \phi_{\max} &= 800 \text{ kW} / \text{m}^2 \\ E_{\max} &= 84 \text{ MJ} / \text{m}^2 \\ P &\sim 100 \text{ mbar} \end{aligned}$$

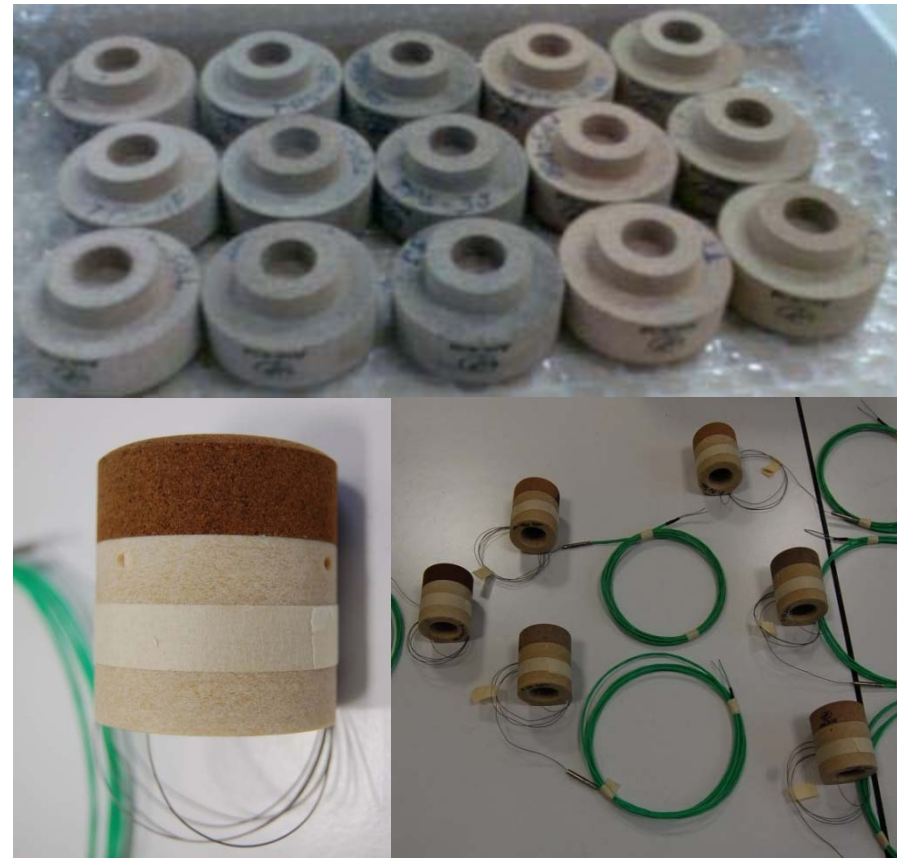


COMETE Biconic 2:

$$\begin{aligned} \phi_{\max} &= 400 \text{ kW} / \text{m}^2 \\ E_{\max} &= 53 \text{ MJ} / \text{m}^2 \\ P &\sim 100 \text{ mbar} \end{aligned}$$

Test campaign on COMETE facility

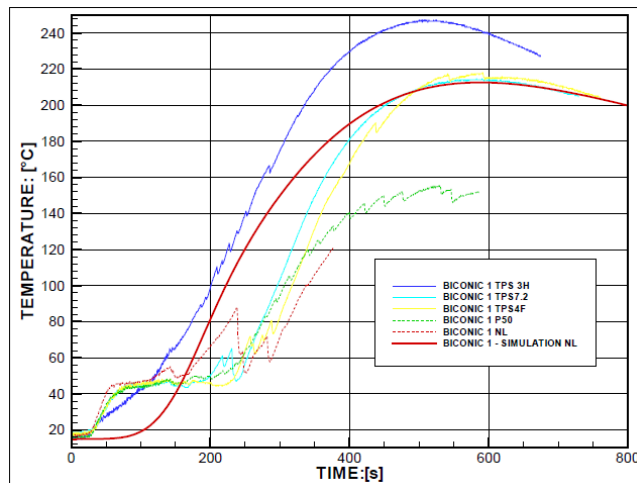
Heat flux	1 series of runs for each mission <ul style="list-style-type: none"> • Biconic 1 : Max 800 kW/m² • Biconic 2 : Max 400 kW/m² 	
Materials	1 run for each material	
	1	Norcoat-Liege (reference 1)
	2	P50 (reference 2)
	3	TPS 3H (Phenolic + carbon fibres)
	4	TPS 4F (Phenolic + basalt fibres)
	5	TPS 7-2 (Furanic + basalt fibres)
	6	TPS 3J (Phenolic + carbon fibres)



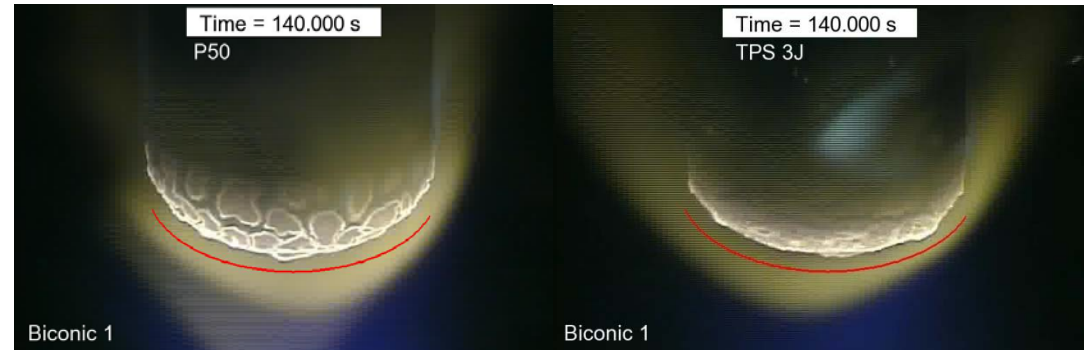
COMETE Plasma tests : Main Results

Exploitation based on comparisons of measured parameters

- Back face Temperature
- Surface recession profile
- Material mass loss



Temperatures comparison between real and simulated thermocouples



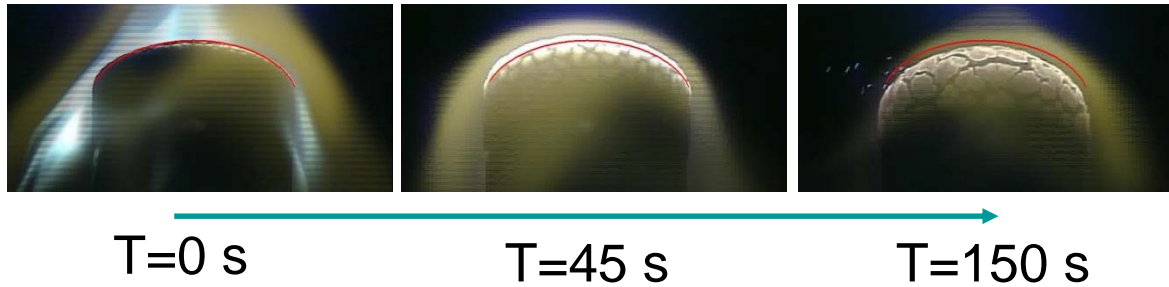
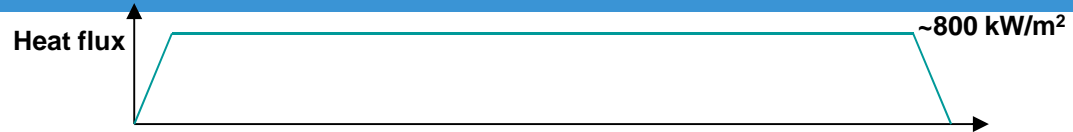
Final selection of the most promising formulations based on thermal and integrity criteria

- Good surface aspect observed on variant reinforced with carbon fibres (TPS3J)
- Confirmed the first observations following preliminary / screening tests
- Complementary investigations required for thermal performance

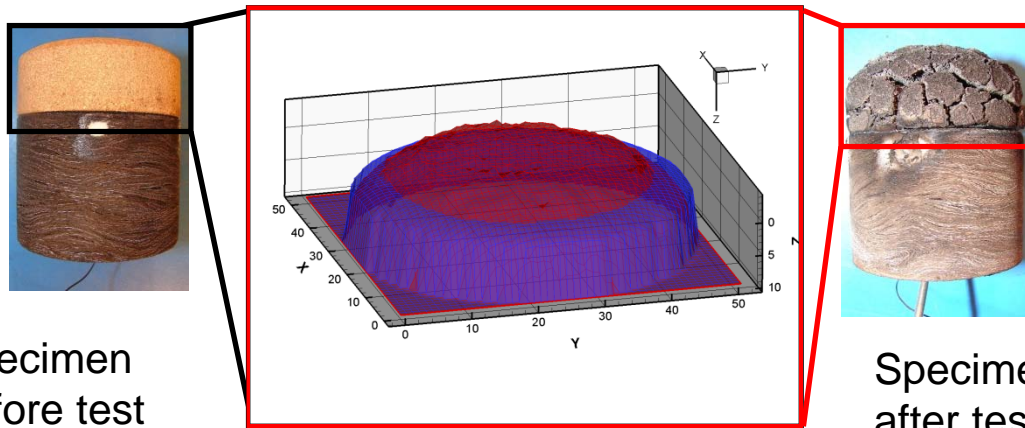


COMETE Plasma tests : Main Results

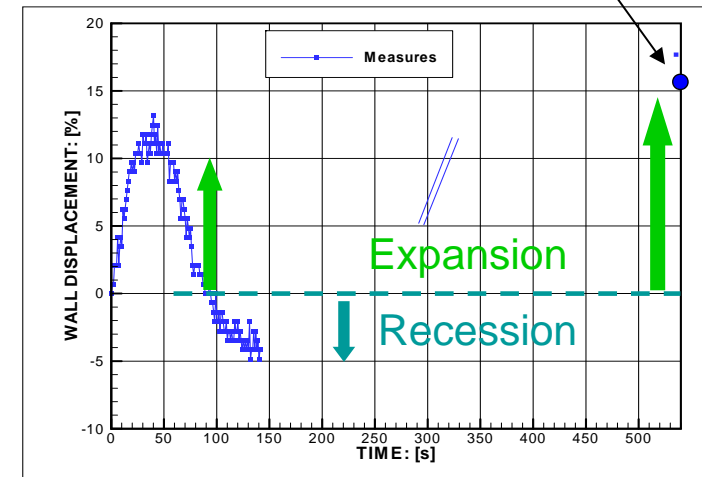
Evidence of swelling effect



Post-test direct axial measurements

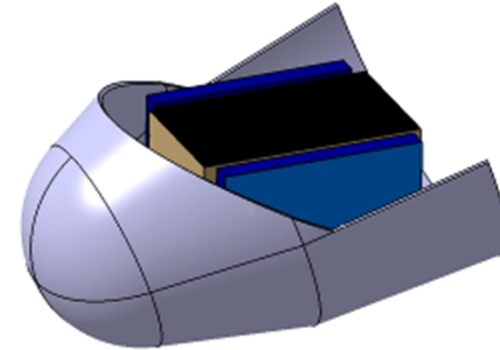
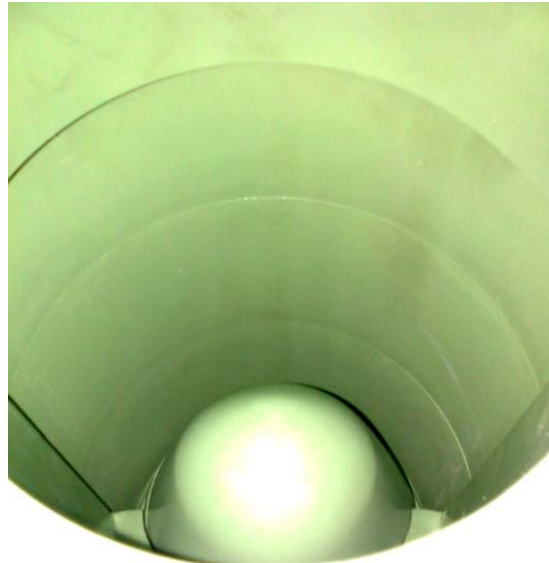


Comparison of surface scanned geometry before/after test



⇒ Strong lagged swelling effect on thickness

Demonstrator manufacturing

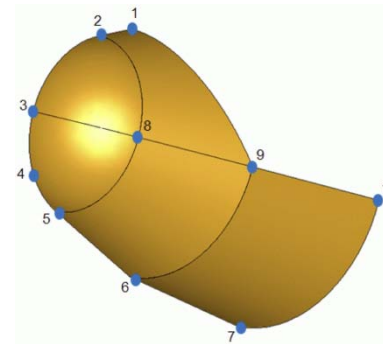


- A representative prototype mould was made
 - Reduced scale for shape, scale 1 for thickness
- Initial trials made using P50 as reference
- Moulding procedure optimized and new pieces made with the final selected TPS material : TPS3J
- Good homogeneity obtained for simple shapes, still to be improved for complex shapes

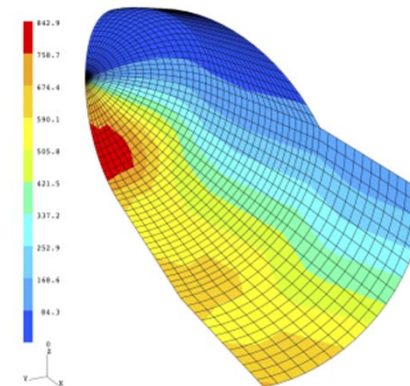


3D thermal and ablative analysis

- The 3D ablation module of the SAMCEF Amaryllis code was developed in the frame of the AEROFAST project
- First application on AEROFAST mission
 - Biconic heat shield
 - Maximum heat load trajectory
 - (undershoot); dimensioning for support structure temperature
 - 3D heat flux data base from ONERA
 - Max 842.9 kW/m²
 - Norcoat Liege TPS
 - Pyrolysis and ablation
 - Constant thickness first, then optimised



Point number	S/D [-]	ϕ [°]	TPS #1 [mm]	TPS #2 [mm]
1	0.520	0.00	6	8
2	0.381	0.00	6	8
3	0.000	180.0	15	15
4	0.212	180.0	19	19
1	0.381	180.0	16	19
6	0.798	180.0	16	16
7	1.325	180.0	16	16
8	0.381	90.0	8	10
9	0.798	90.0	8	10
10	1.325	90.0	7	10



3D thermal and ablative analysis

Model characteristics

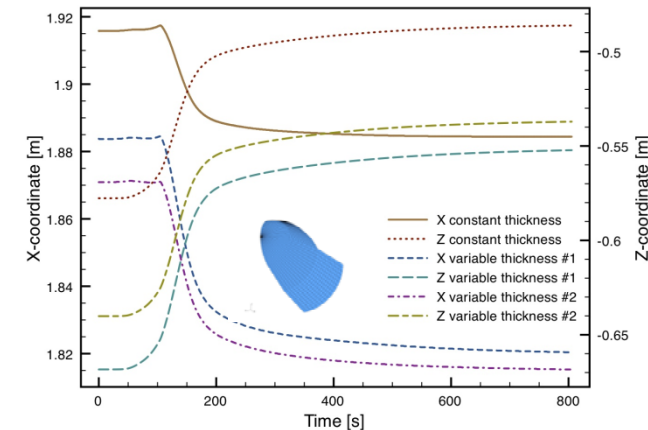
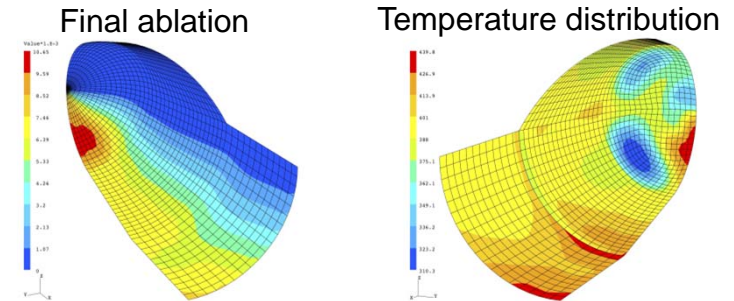
- 190.448 doff CPU 29 h 30 m (598 time steps)

Variable thickness biconic

- Linear interpolation of thickness between points
- Final ablation: 10 mm max
- Inner temperature at end of trajectory
 - TPS #1: maximum 468 K
 - TPS #2: maximum 439 K
- Geometry update procedure not optimal

C.o.g position for Biconic

- Z-coordinate moves upward
- X-coordinate moves backward before moving forward
 - Stabilizing effect pitching moment
 - Ablation has largest contribution to mass loss



Heat Shield	Mass [kg]	Mass-loss [kg]	$\frac{x_{c.o.g.}}{D}$ [%]	$\frac{z_{c.o.g.}}{D}$ [%]
Apollo	133.5	25.6	-0.083	0.12
Const. thickness	295.4	56.1	-0.88	2.54
Var. thickness #1	201.6	55.8	-1.76	3.20
Var. thickness #2	235.1	55.8	-1.55	2.86

Conclusion

- A 3D charring/ablation code has been implemented and tested
 - A first sizing of a 3D TPS has been successfully performed within Aerofast
 - 3D Amaryllis now available for general application
- Ways for enhancement of cork-based TPS have been demonstrated
 - Reinforced and lighter solutions demonstrated promising behaviour under near aerocapture thermal environment
- Demonstrator manufacturing
 - Reduced scale prototype of the whole front heat shield
 - Such a geometry is a bit too complex to reproduce the good homogeneity usually obtained by moulding of simple shapes
- Unfortunately, lack of continuity after the Aerofast project
 - Tests results were obtained at the very end of the project
 - Opportunities were missing for immediate analysis of improvement ideas
- Interest to extend evaluation testing of developed formulations to various type of missions
 - Mars entry probes, back shell of Earth entry vehicles...
 - Contribution to technology maturation studies...

THANK YOU
FOR YOUR ATTENTION

More at www.aerofast.eu

AEROFAST: Development of Innovative Thermal Protections

References

1. A.J.van Eekelen, G. Pinaud, J.-M. Bouilly, AEROFAST: Thermal/Ablation analysis of the front heatshield for a Martian aerocapture mission - 7th International Planetary Probe Workshop, June 14-18, 2010.
2. J-M. Bouilly, A. Pereira - AEROFAST: Development of Innovative Thermal Protections – 4th International ARA Days - May 2 – 4, 2011 – Arcachon, France
3. G. Pinaud and A.J. van Eekelen, AEROFAST: Development of Cork TPS Material and a 3D comparative Thermal/Ablation Analysis of an Apollo & a Biconic sled shape for an Aerocapture Mission, 8th International Planetary Probe Workshop, June 6-10, 2011.
4. F. Bonnefond, T. Salmon, AEROFAST: Aerocapture for Future Space Transportation, 4th European Conference for Aerospace Sciences (EUCASS), July 4-7, 2011
5. G. Pinaud, Thermo-chemical and mechanical coupled analysis of swelling charring and ablative materials for re-entry application, 5th AF/SNL/NASA Ablation Workshop, Lexington (KY), Feb 28-March 1, 2012

ASTERM : Maturation of a new low density ablative material

7th European Workshop on TPS & Hot Structures - Noordwijk (NL)
2013, April 8-10 - Session "Ablative Materials"

Jean Marc Bouilly, Astrium Space Transportation

e-mail : jean-marc.bouilly@astrium.eads.net

Cedric Plaindoux, Astrium Space Transportation

All the space you need



Overview

■ Introduction

- Missions : heritage and perspective
- Requirements
- Development history : key dates

■ Materials features

- Heritage
- Process

■ Achievements

- Manufacturing
- Tests
- Modelling

■ Perspectives

- Astrium R&D approach
- Next steps

■ Conclusion

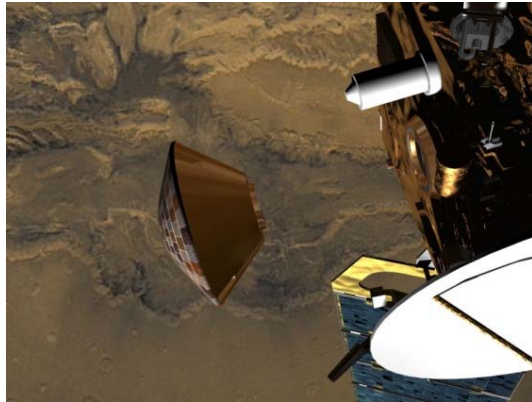
All the space you need



Missions : Heritage & Perspectives

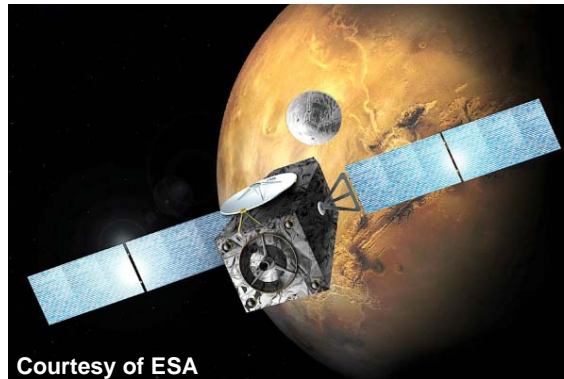


ARD (1998)

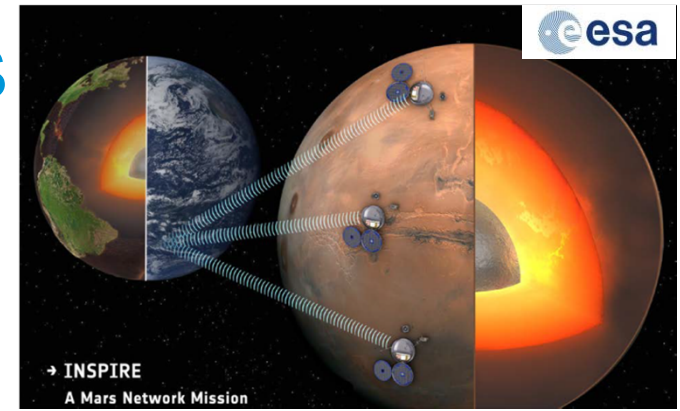


Mars Express/
BEAGLE 2 (2003)

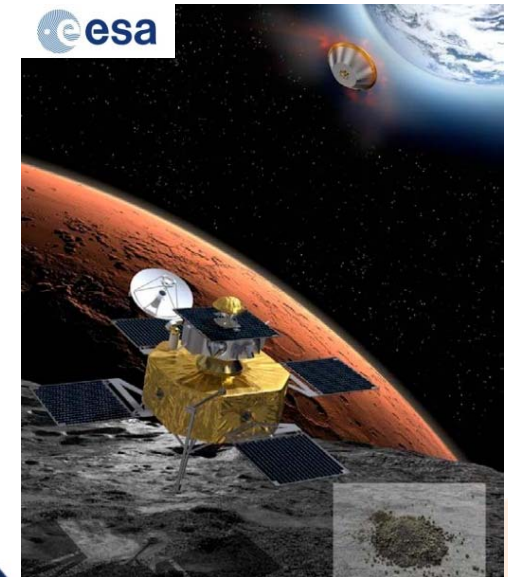
ExoMars EDM (2016)
EDL Demonstrator Module



Courtesy of ESA



→ INSPIRE
A Mars Network Mission



Phootprint : Phobos
Sample Return



HUYGENS (2005)



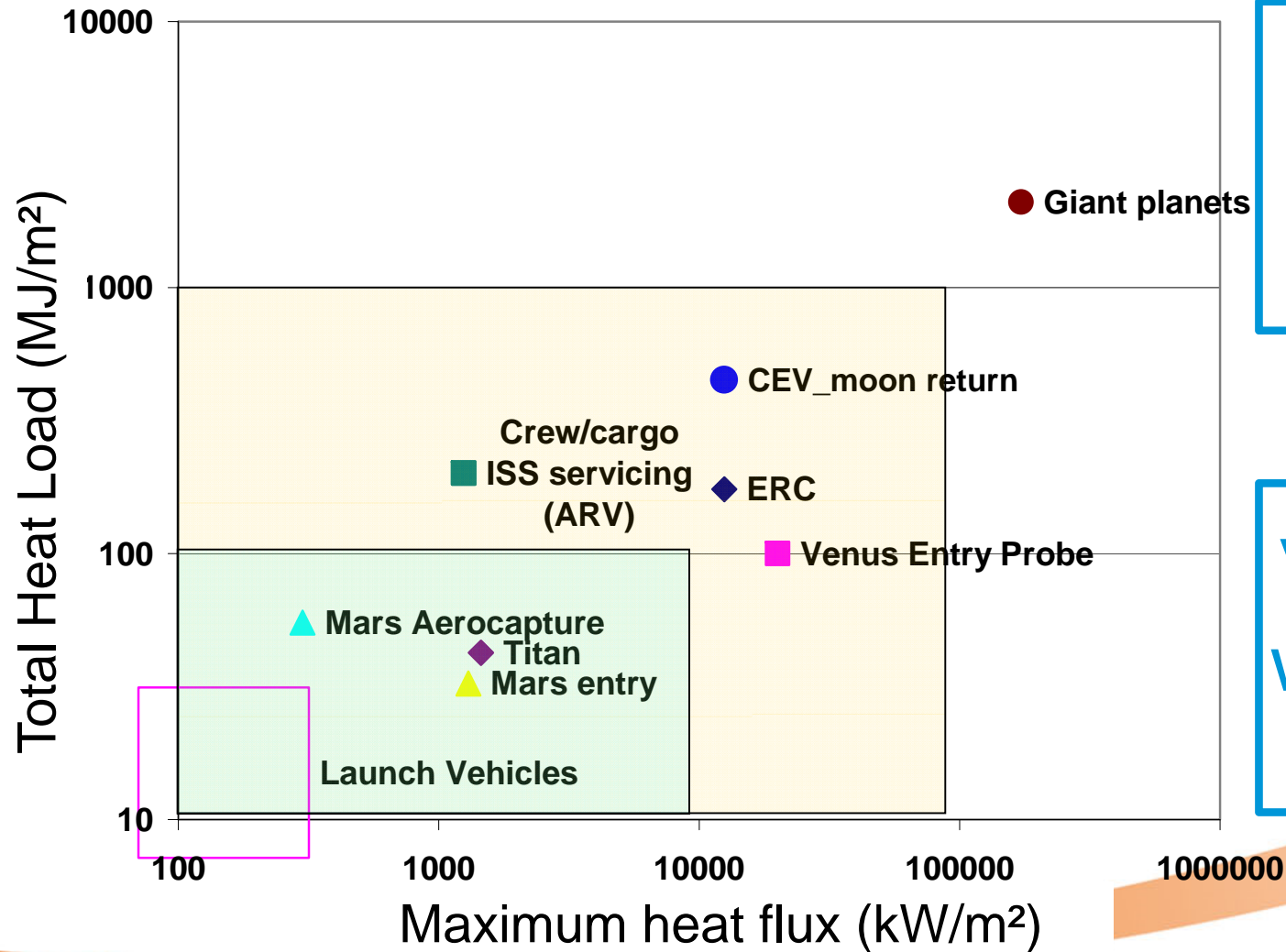
All the space you need



This document and its content is the property of Astrium [Ltd/ASAS/GmbH] and is strictly confidential. It shall not be communicated to any third party without the written consent of Astrium [Ltd/ASAS/GmbH].

Different categories of possible missions

→ different classes of materials required



Optimised solution for each mission

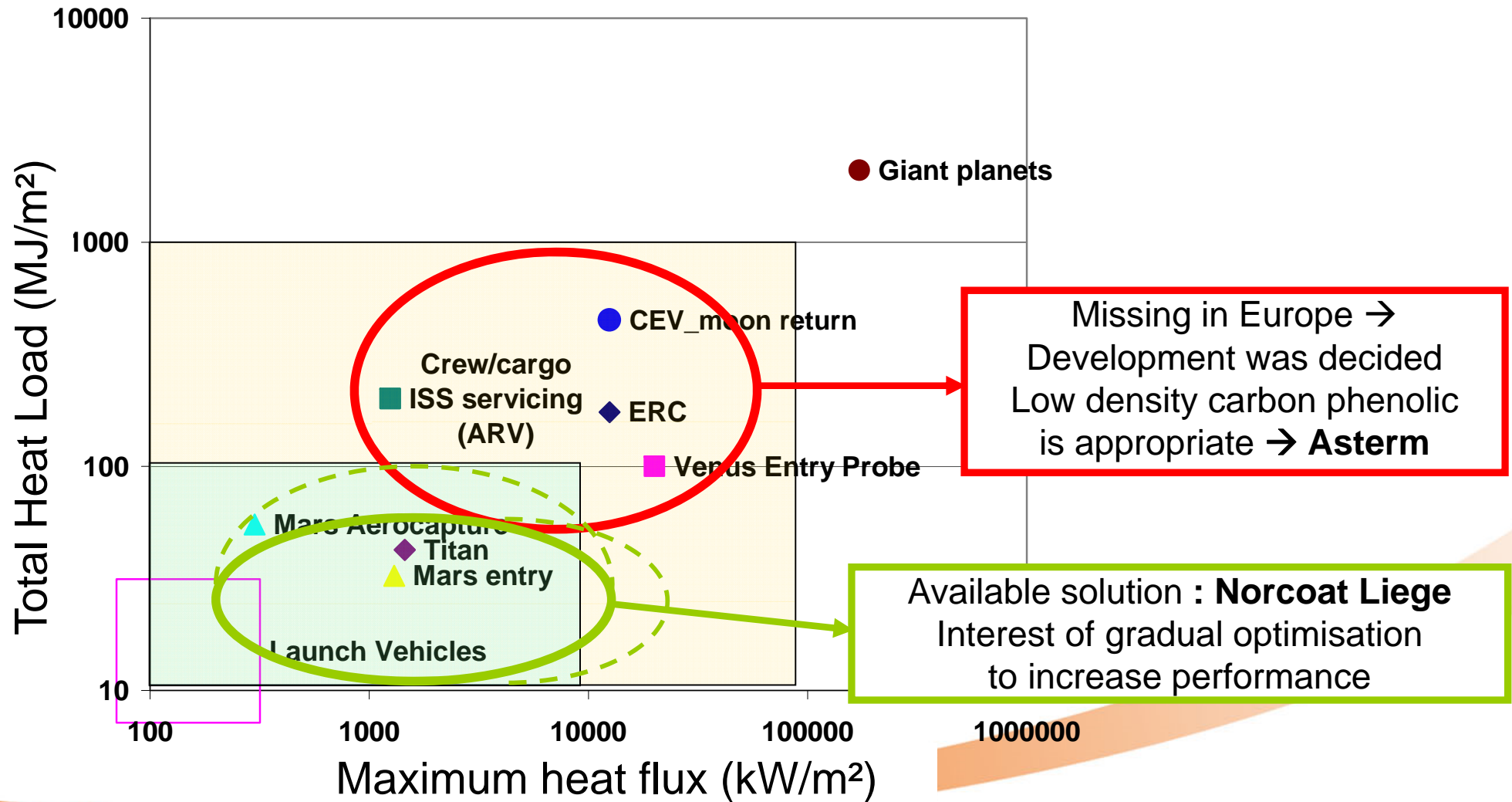


Versatile family with wide range of application



This document and its content is the property of Astrium [Ltd/SAS/GmbH] and is strictly confidential. It shall not be communicated to any third party without the written consent of Astrium [Ltd/SAS/GmbH].

Different categories of possible missions → different classes of materials required



This document and its content is the property of Astrium [Ltd/SAS/GmbH] and is strictly confidential. It shall not be communicated to any third party without the written consent of Astrium [Ltd/SAS/GmbH].

ASTERM Development approach and history



ESA TRP AURORA-DQA (2004-2005)
 → *evidence of need of a new material*

TRL 5 (evaluation based on Marco Polo)

Initial background + Continuous and significant internal R&T effort

Astrium R&T ARER (Ablator for Rapid Earth Re-entry)
 → *confirmed interest of low density carbon resin*

Astrium R&T ASTERM (2008-2012)
 → *anticipated exploration of various versions*
 → *elaboration and validation of development process*
 → *capability to adapt and propose relevant options*
 → *offers mature solutions for agency contracts*

ESA TRP DEAM (2009-2011)
 → *characterisation of standard & dense versions*

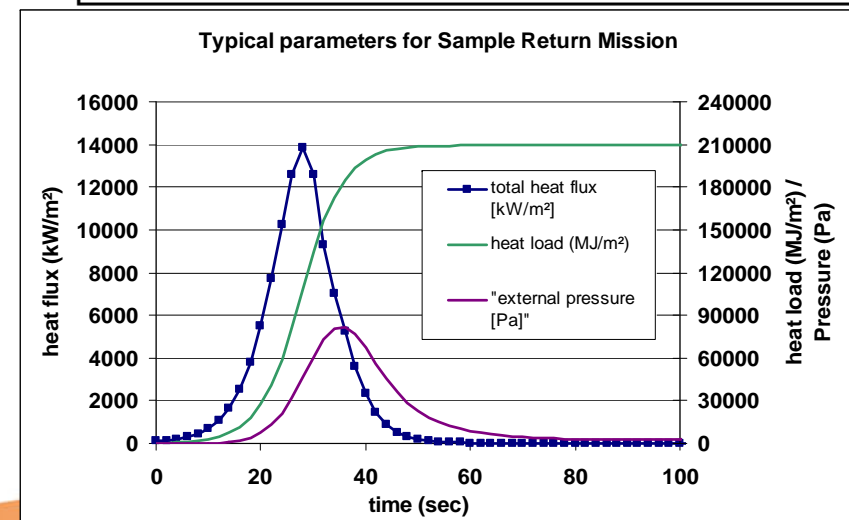
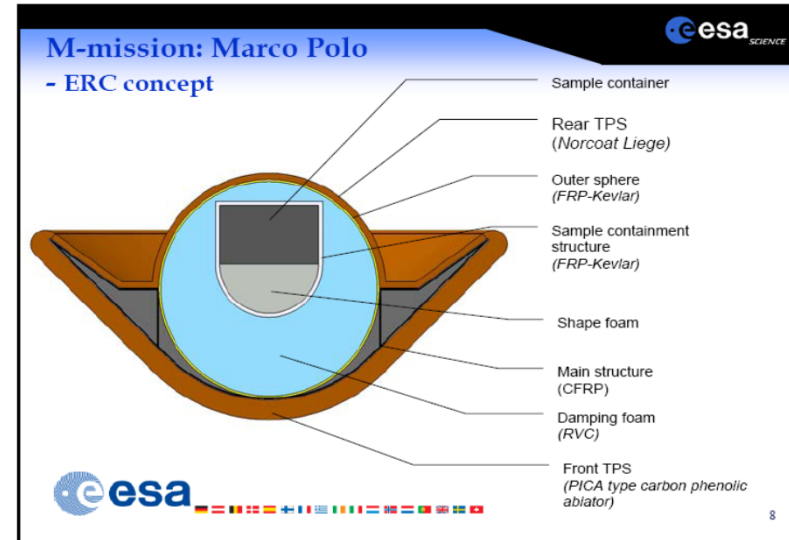
DEAM continuation (2012-2014)
 → *TRL6 in 2014*

FP7 Rastas Spears (2010-2013)
Assembly and joints

This document and its content is the property of Astrium [Ltd/SAS/GmbH] and is strictly confidential. It shall not be communicated to any third party without the written consent of Astrium [Ltd/SAS/GmbH].

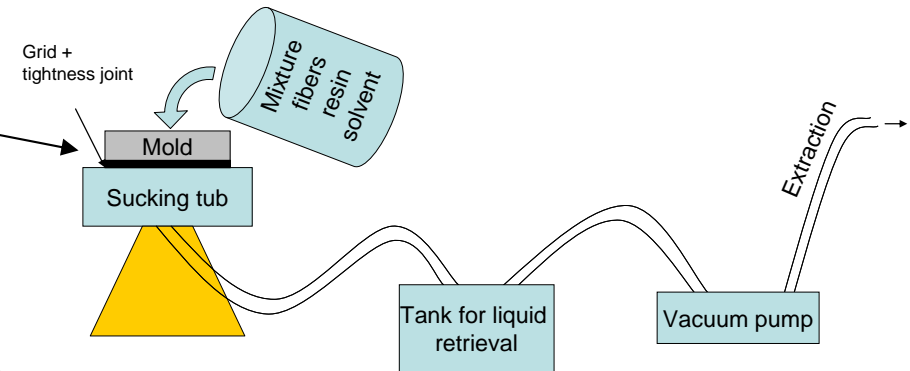
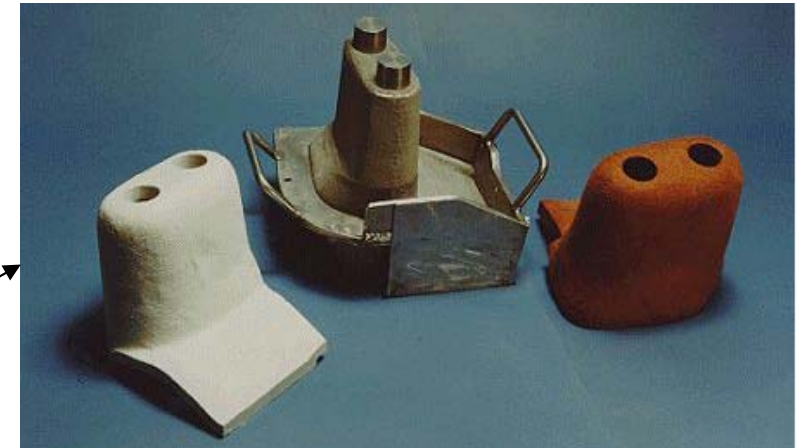
Requirements Review (general)

- Main initial orientation :
Sample Return Missions (e.g. from Mars, asteroids...)
 - Marco Polo
 - Phootprint
- Several potential other applications
 - Mars Sample Return MSRO
 - ARV (Advanced Return Vehicle)
 - European Venus Exploration (EVE)
- Technical drivers:
 - 14-15 MW/m²
 - 170°C
 - 15 kg/m²



Heritage

- General background
 - elaboration of relevant spec
- Technology
 - AQ60 : low density silica phenolic
 - AQ61 : low density carbon/phenolic
 - General : impregnation of large pieces of carbon felt used as tooling (e.g. Hermes nose, mandrels)
- Modelling and characterisation approach
- System consideration and assembly process
 - incl. singularities, instrumentation,...

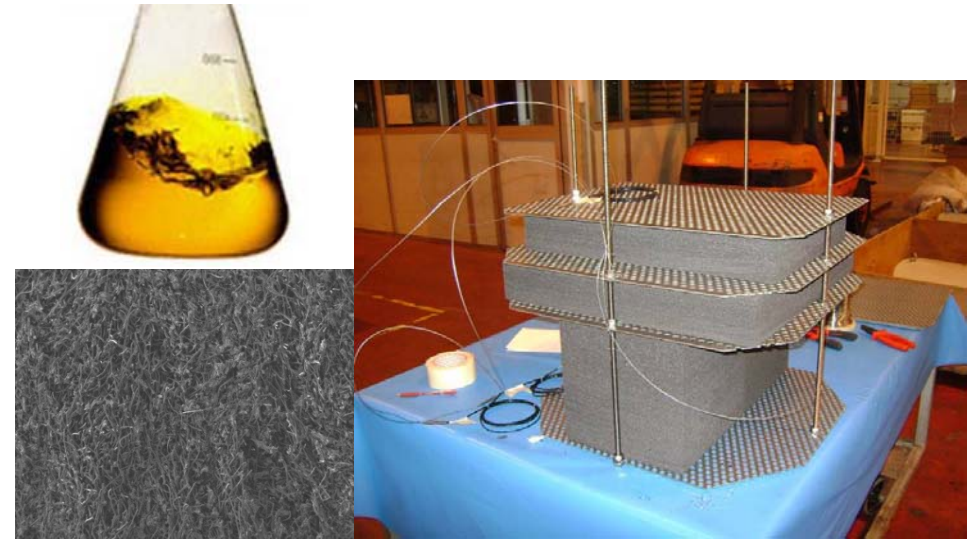


This document and its content is the property of Astrium [Ltd/SAS/GmbH] and is strictly confidential. It shall not be communicated to any third party without the written consent of Astrium [Ltd/SAS/GmbH].

ASTERM

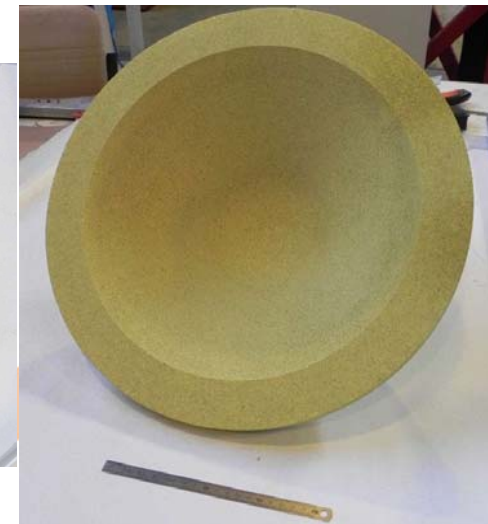
■ PROCESS SUMMARY

- Produced by impregnation of a rigid graphite substrate by phenolic resin



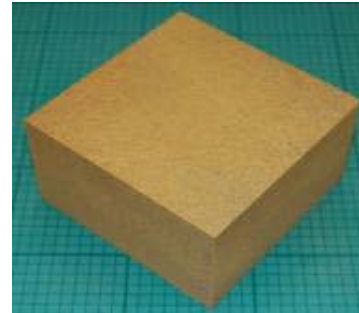
■ KEY DRIVERS

- Standard European raw materials
- Available Astrium facilities
- TRL6 in 2014

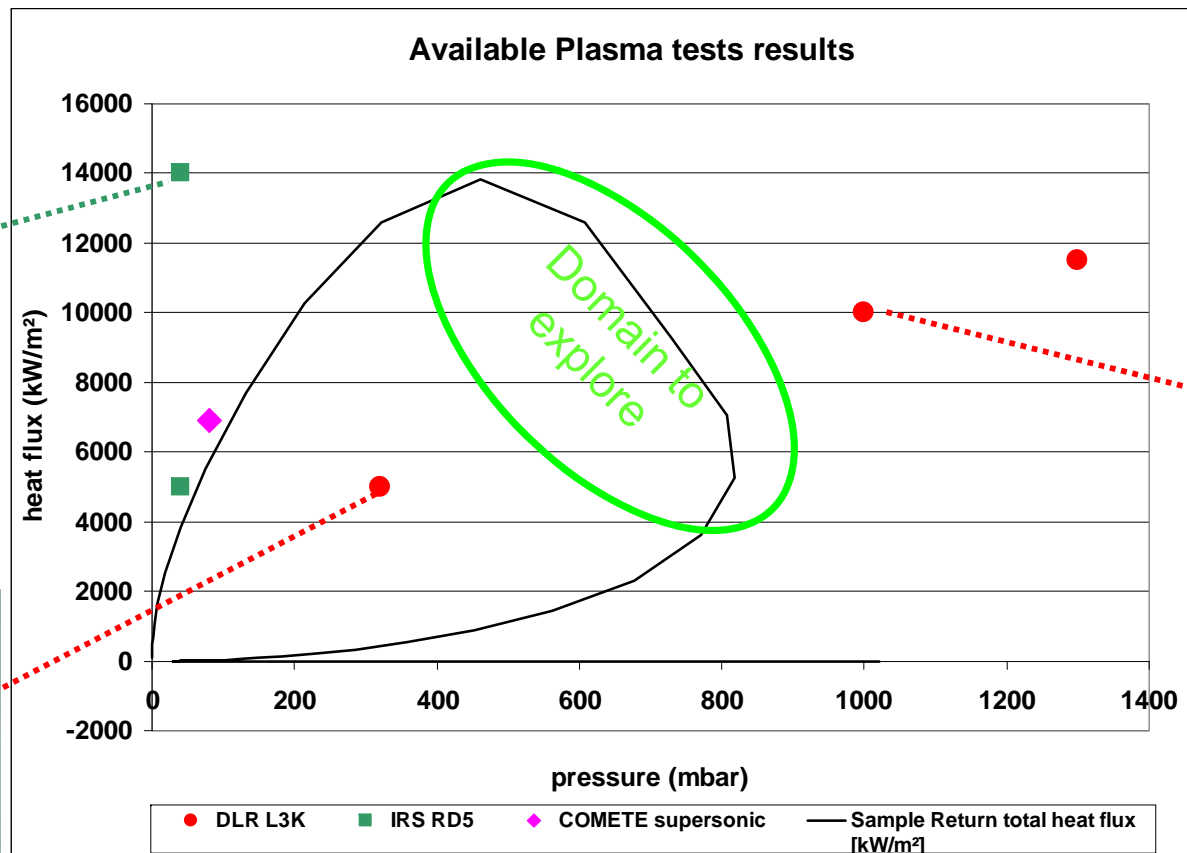


ASTERM manufacturing : summary of achievements (2008-2010)

- Evaluation of different substrates
 - Tuning of manufacturing parameters
 - Manufacturing trials, with increasing dimensions
 - Laboratory facilities
 - Then, production facilities
 - Large range of densities achievable
 - Standard: 0.28 g/cc
 - Possible tuning from 0.24 to 0.55
- Global validation of process and facilities
- Samples for characterisation

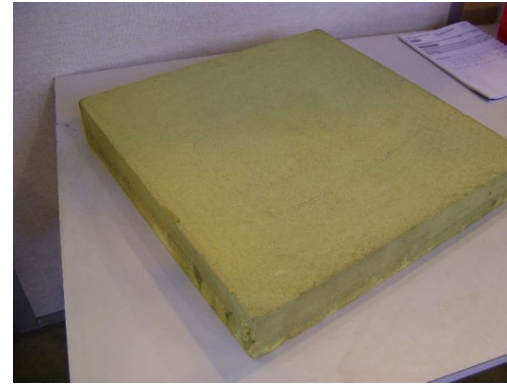
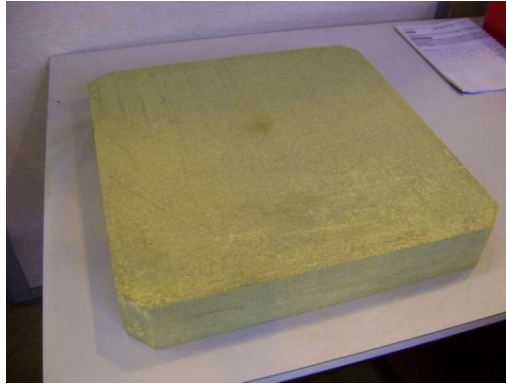


Plasma tests results (mid 2010) (DEAM + Astrium R&T)



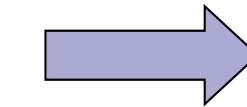
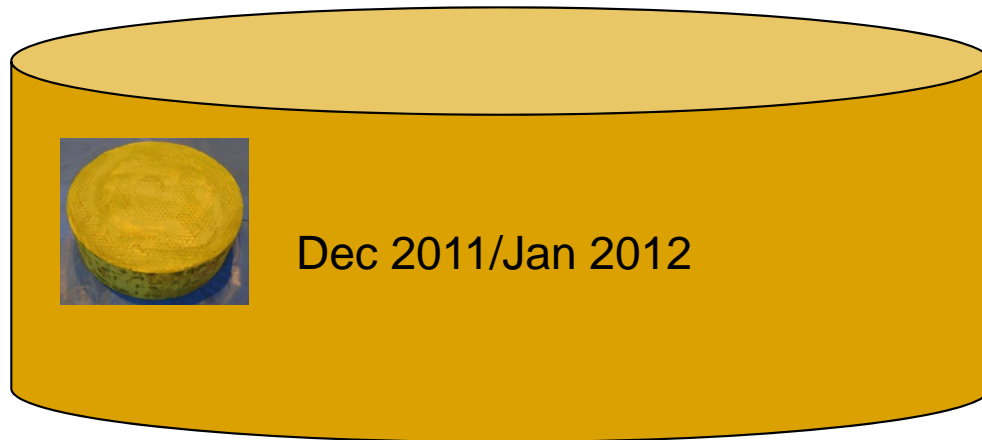
**Objective to extend as much as possible
the successfully explored domain,
and to identify the limits**

ASTERM manufacturing : summary of achievements (2011-2012)



+ 10 blocks manufactured
for Rastas Spear
ASTERM standard version
(Q1 2012)

Nov 2011 blocks for DEAM : $\sim\text{Ø}500 \times 500 \times 70 \text{ mm}$ - $\sim 6.0 \text{ kg}$

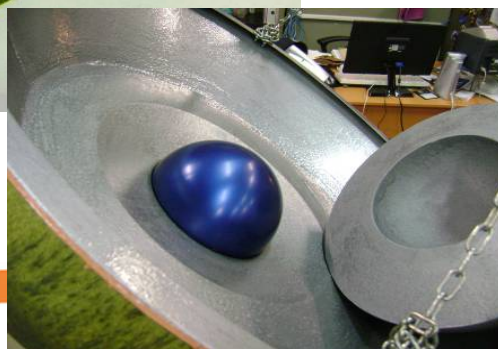


2011-12 demonstrator block for DEAM: $\sim\text{Ø}600 \times 200 \text{ mm}$ - $\sim 19.0 \text{ kg}$

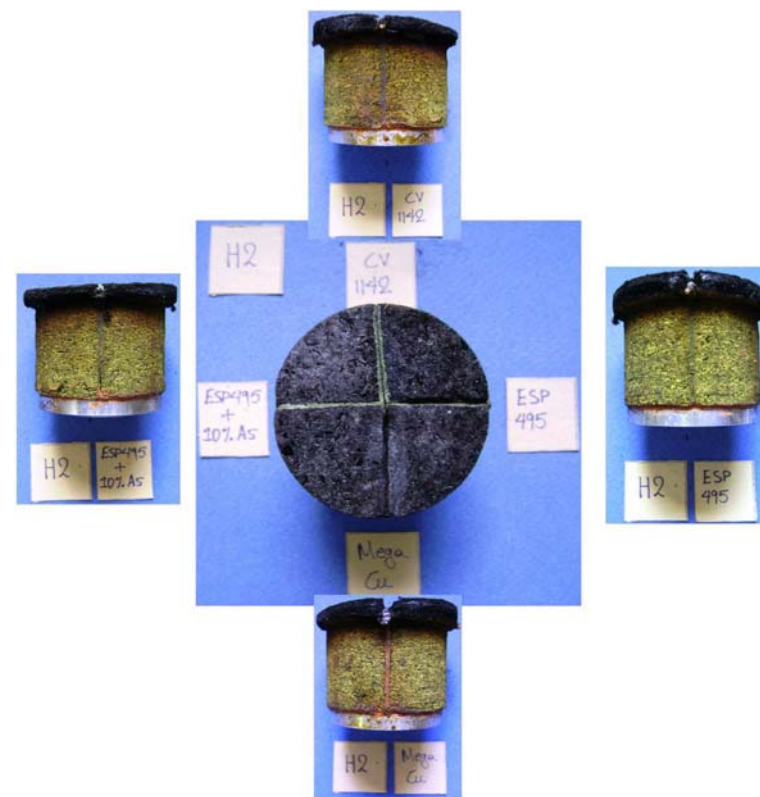
Achieved demonstrator : $\sim\text{Ø}450 \text{ mm}$ (0.8 x Marco Polo)



Rastas Spear: Assembly and joints



After DLR/L3K test at 13.6Mw/m², 9-1



Heritage adhesives CV1142 and ESP495 displayed about 30% less erosion than the commercial adhesive tested.

"Overview of the TPS Activities within the RASTAS SPEAR Project" - G. Vekinis, NCSR Demokritos - 7th European Workshop on TPS & Hot Structures - Noordwijk (NL) - 2013, April 8-10 - Session "Advanced joining techniques"



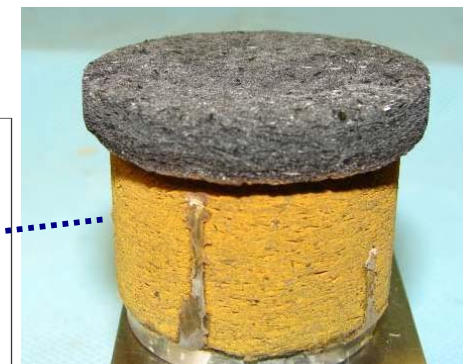
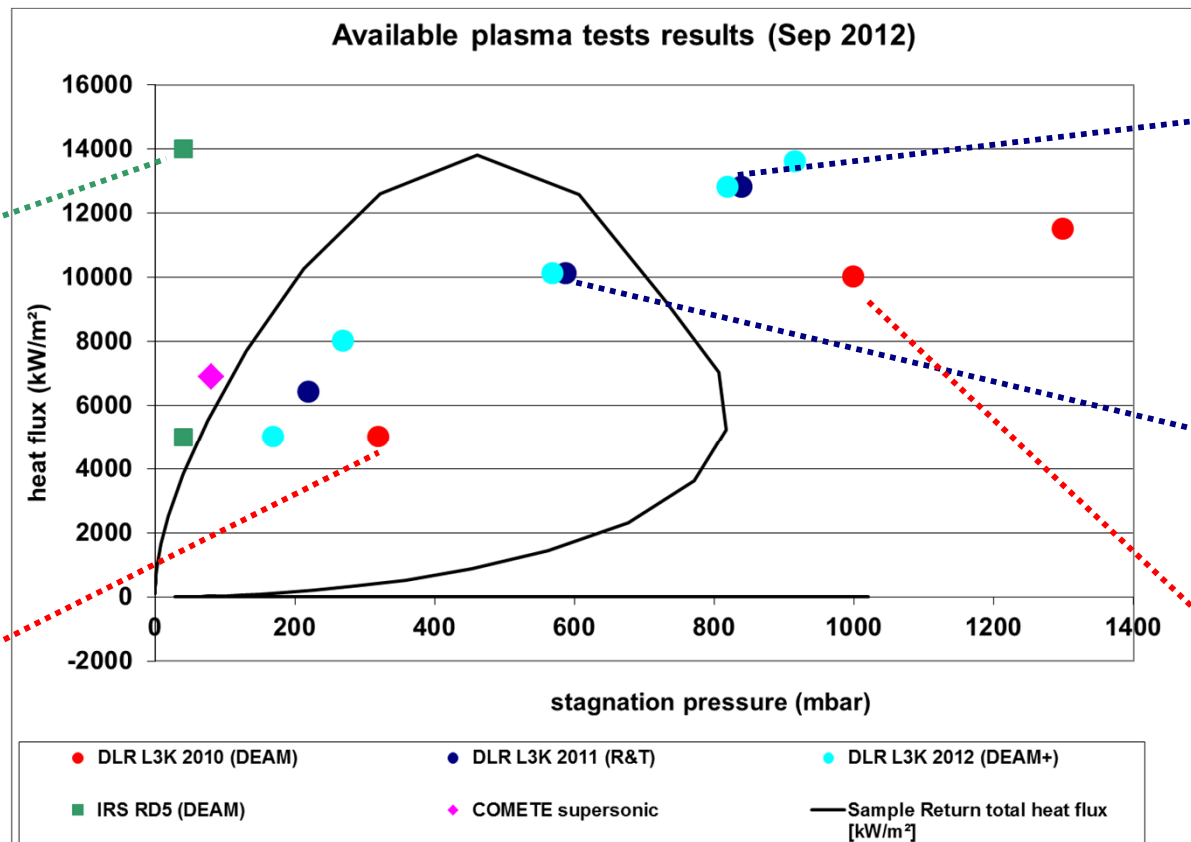
Plasma tests results (DEAM + Astrium R&T)



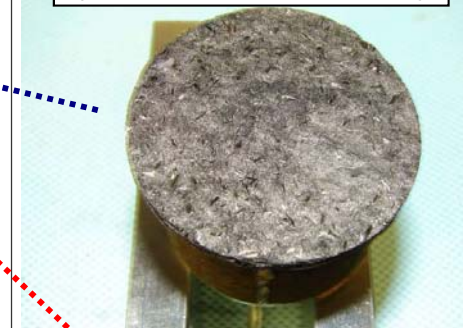
d = 280 kg/m³
(350 also tested)



d = 280 kg/m³
(350 also tested)



d = 280 kg/m³
(350 & 420 also tested)



d = 350 kg/m³

Material performance validated through a successful coverage of the flight domain (~50 tests on different variants & test points)
Objective for next step 2013-2014: to extend as much as possible the successfully explored domain, including repeatability, and to identify the limits

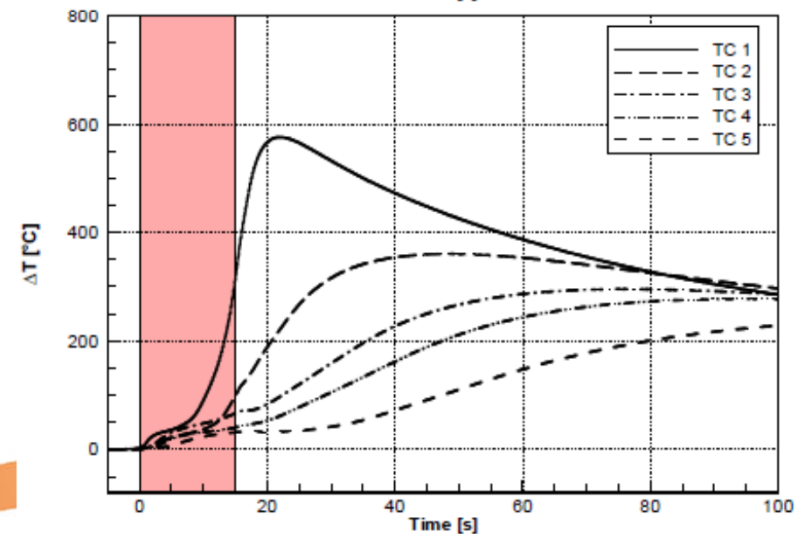
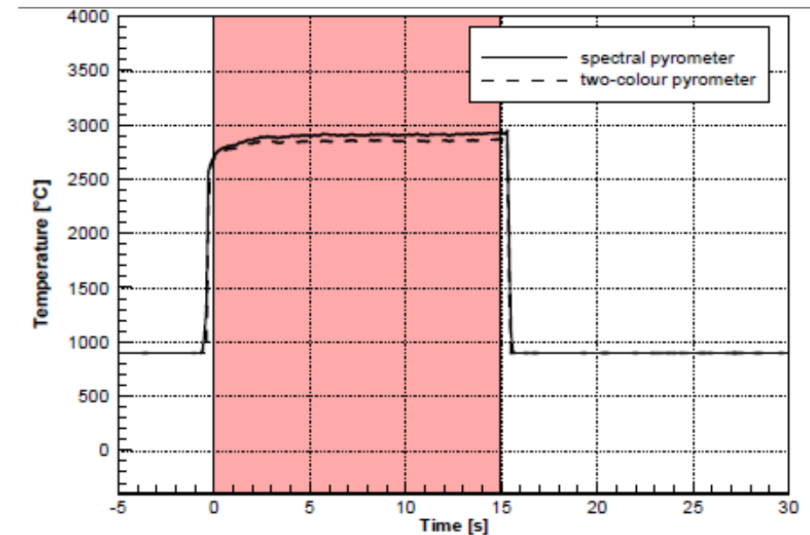
All the space you need



This document and its content is the property of Astrium [Ltd/SAS/GmbH] and is strictly confidential. It shall not be communicated to any third party without the written consent of Astrium [Ltd/SAS/GmbH].

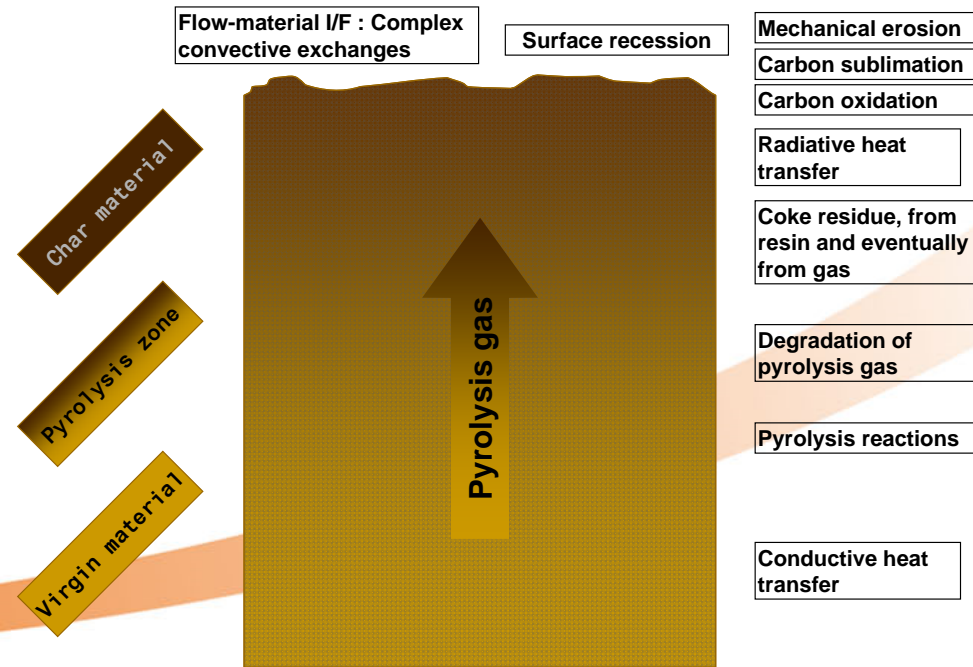
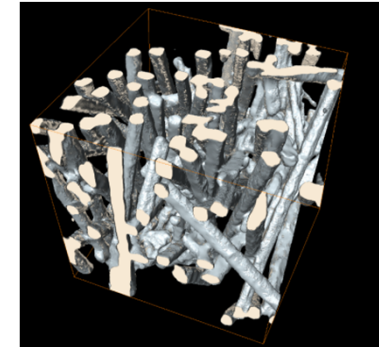
Thermal performance and material modelling

- Excellent thermal performance is observed
- Typical test result
 - Test 15 sec @ 10 MW/m²
 - TC: 11, 14, 16, 18, 22 mm
 - Recession : ~6.1 mm
- Numerical restitution of test data
 - Several questions after first comparisons
 - Not a simple 1D heat transfer
 - Other phenomena ?

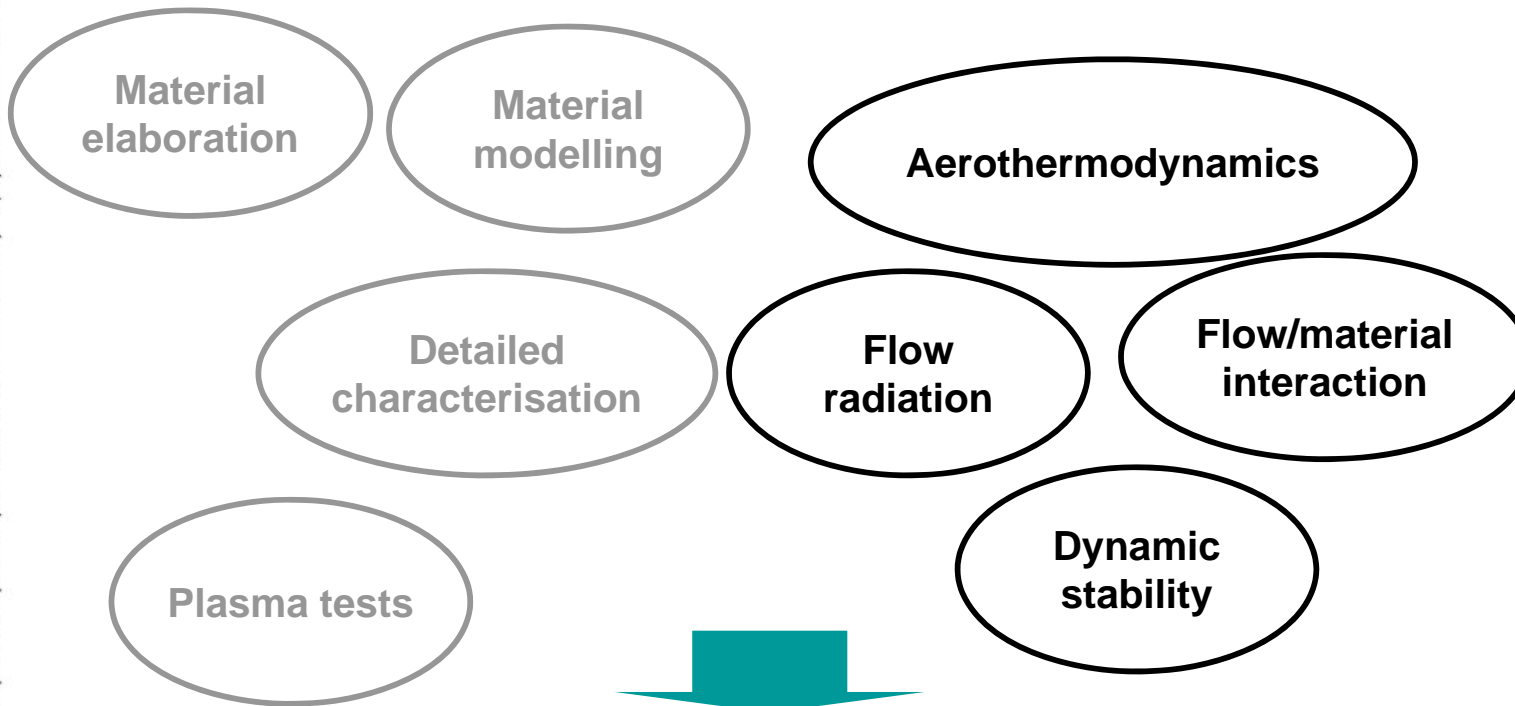


General rationale on material modelling

- Available engineering codes
 - Are we solving the right equations ?
- Modelling of elementary bricks
 - Methodological / academic approach (detailed observation / characterisation → model)
 - Multi-scale consideration (Complex model → applicable only on micro-models)
 - Open for publications
- Identification of dominating phenomena
 - Surface or volume ablation
 - Radiative heat transfer, ...
- Introduction in engineering codes
 - Simplified correlations applicable on global models
 - The most effective, even though not with the most refined physics
- Derivation of guidelines for optimisation
 - e.g. Search for optimal density, resin/fibers mass fraction,...



Development needs : not only material



Astrium R&T 'Re-entry Technologies'
Foster scientific and international cooperation

Re-entry Technologies

Goals and Objectives

This project aims at developing key technologies needed to enable future atmospheric entry projects. Various types of missions are targeted: Sample Return (Marco Polo), Planetary Exploration (Mars, Venus, Titan), Crew/cargo transportation from ISS (Advanced Return Vehicle ARV), experimental vehicles (SHEFEX). It is comprised of several complementary topics that are mandatory for Astrium as prime company in this domain:

- Aerothermodynamics tools and methods
 - Consolidation of TPS portfolio with enhanced solutions (lightweight carbon phenolic ASTERM, advanced cork-based, SPFI)
- This project also provides resources to play a role in agencies technology developments in this field (e.g. ESA Technology Programs).

Technology Challenges

- The essential technical developments are presented
- Development of ASTERM, in order to reach TRL 5 (manufacturing + validation + modeling) in 2011 for Marco Polo (15MW/m²), then for other missions (e.g. ARV)
 - Technology maturation / validation & theoretical modeling of advanced cork-based TPS, in order to reach TRL 3/4 in 2011, then TRL 5 in 2013 (for application to Mars Exploration)
 - Increase TRL on key aspects: gas/surface interaction for high speed entry (TRL3 -> 5), low speed aerodynamics of planetary capsules (TRL4 -> 6), Aerodynamic & Aerothermodynamic databases (TRL 4 -> 6)
 - Increase TRL to 5-6 by end 2010 for SPFI (Surface Protected Flexible Insulation)
 - Perform flight demonstration of TPS technologies on SHEFEX II for metallic TPS, SPFI and C/SiC panel TPS.

Project Facts

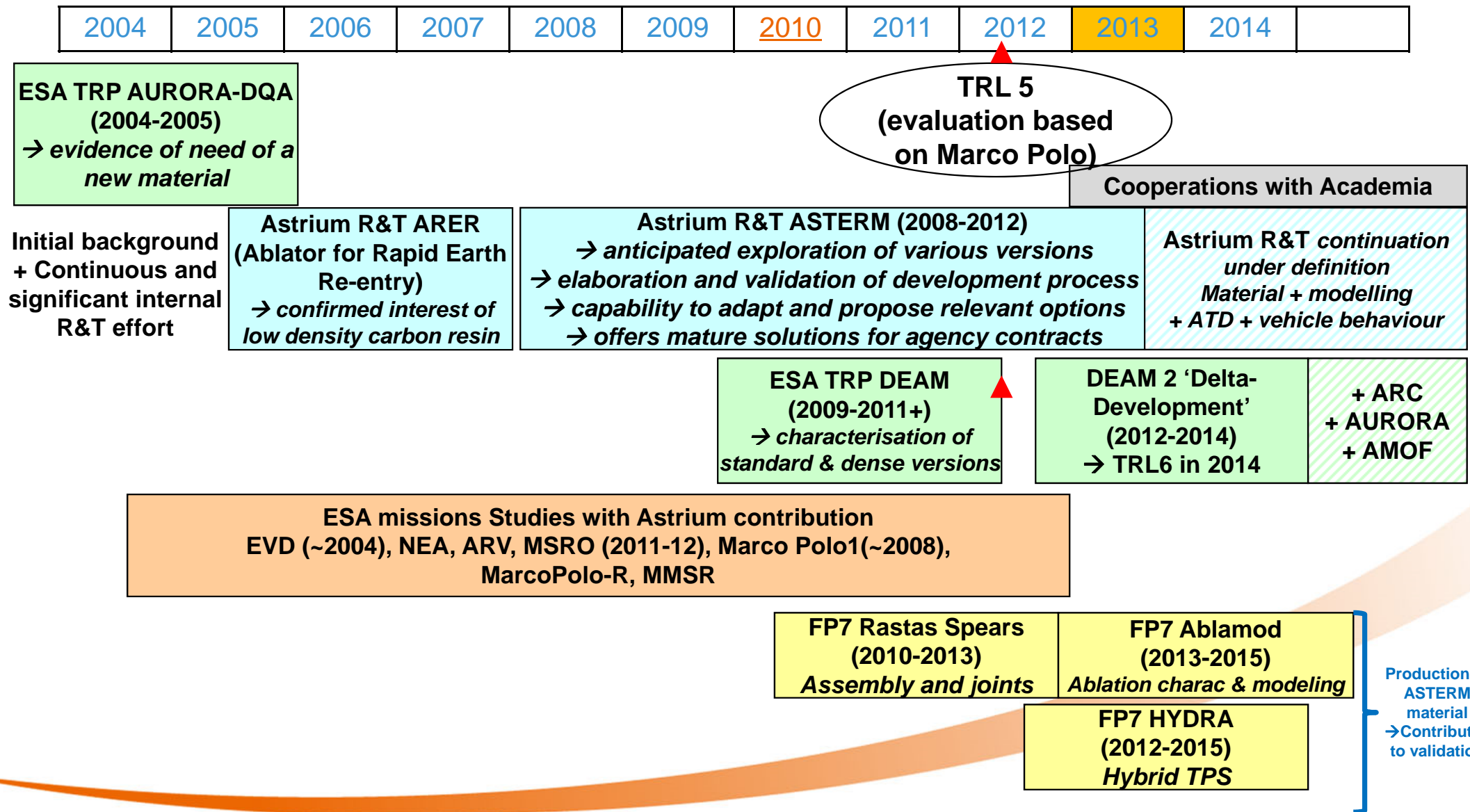
Lead/Team:	Astrium Space Transportation
Location:	Aquitaine / Bremen / Les Mureaux
Partners:	Amovim, LCPD, Surrey Univ, INSA, VKI, + potential
Product:	Thermal Protection System
Customers:	ReEntry Programs of Space Agencies
Funding:	90 % self-funded activity
Budget:	3.6 M€
Duration:	4 years (2009 - 2012)
TRL:	Evolution 3 to 5 for TPS, 4 to 6 for ATD tools
Contact:	jean-marc.bouilly@astrium.eads.net wolfgang.fischer@astrium.eads.net

Milestones:

Key point for phase 2 of ASTERM development	2010
ASTERM validated for Sample Return mission (incl. Demonstrator, characterisation & modelling)	2011
SHEFEX II Flight	2011
SPFI Demonstrator final presentation	2010
Completion of AEDB tool	2010
Enhanced formulations of cork-based TPS	2011
Enhanced model for cork-based TPS	2011
Huygens and ExoMars rebuilding with FLUSEPA	2011
Validation Aerochemistry: Earth Entry reconstruction	2011

www.astrium.eads.net

ASTERM Development approach and history



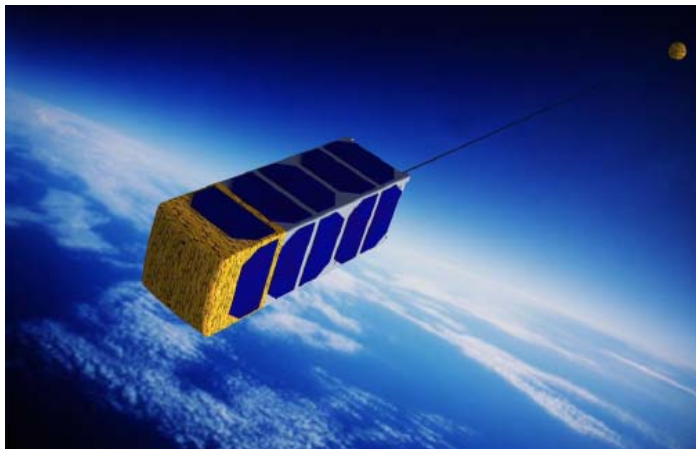
Next Steps

- A lot of activities planned in 2013-2014
 - DEAM2
- Process refinement
- Characterisation tests
- Modelling

QARMAN



QubeSat for Aerothermodynamic
Research and Measurements on
AblatioN



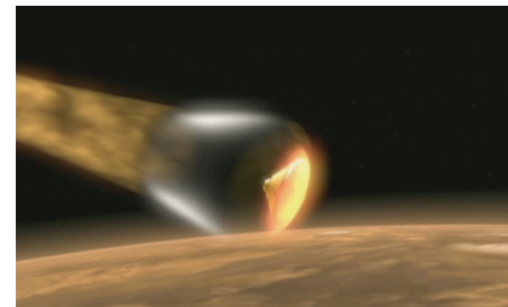
- PhD theses
 - Radiative and Ablative Studies for In-Flight Validation on Reentry Platforms
 - Comprehensive characterization of the material response of innovative ablators in plasma flows
 - Modelling of radiative heat transfer in hot fibrous materials

HYDRA



- Characterisation and modeling activities about Astern

ABLAMOD

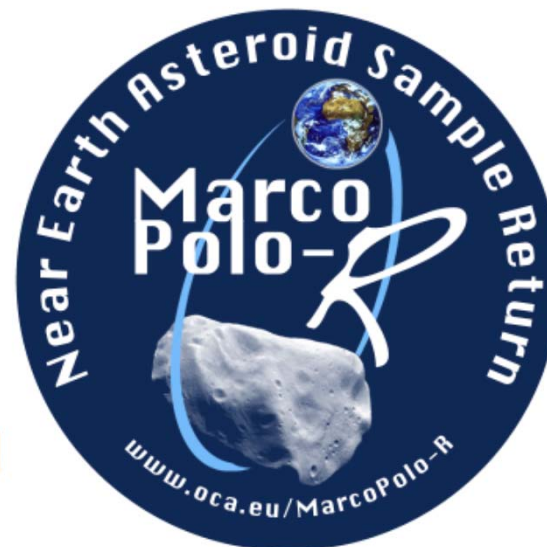


- "Advanced Ablation Characterization and Modelling"
- 3-year project led by DLR



Conclusions

- After successful initial development, maturation of ASTERM is ongoing
- TRL 6 in 2014
→ a fully realistic objective
- Then, time for actual missions
 - MarcoPolo-R, Phootprint,...



THANK YOU
FOR YOUR ATTENTION

Coming soon

4th International ARA Days,
to be held in Arcachon, France
May 27 to 29, 2013



ASTERM : Maturation of a new low density ablative material

References

1. Ongoing European developments on entry heatshields and TPS materials, Heiko Ritter et al., 8th International Planetary Probe Workshop, 2011
2. ESA TPS Activities for Sample Return Missions - H. Ritter, D. Agnolon, L. Ferracina - 9th International Planetary Probe Workshop, IPPW9, 2012, Toulouse (F)
3. ASTERM : a new low density ablative material, J-M Bouilly, C. Plaindoux, 3rd International ARA Days, May 2 – 4, 2011 – Arcachon, France
4. RASTAS SPEAR: Radiation-Shapes-Thermal Protection Investigations for High Speed Earth Re-entry - J-M. Bouilly et al - 7th European Workshop on TPS & Hot Structures - Noordwijk (NL) - 2013, April 8-10 - Session "Heatshield Concepts"
5. "Overview of the TPS Activities within the RASTAS SPEAR Project" - G. Vekinis, NCSR Demokritos - 7th European Workshop on TPS & Hot Structures - Noordwijk (NL) - 2013, April 8-10 - Session "Advanced joining techniques"

Ablative Materials Thermal Properties Estimating

Aleksey V. Nenarokomov⁽¹⁾, Oleg M. Alifanov⁽¹⁾, Sergey A. Budnik⁽¹⁾, Andrey V. Netelev⁽¹⁾

⁽¹⁾ *Moscow Aviation Institute (Technical University), Dept. of Space System Engineering
4 Volokolamskoe Hgw.
Moscow, 125993, Russia
aleksey.nenarokomov@mai.ru*

INTRODUCTION

In many practical situations it is impossible to measure directly thermal and thermokinetic properties of analyzed composite materials. The only way that can often be used to overcome these difficulties is indirect measurements. This type of measurements is usually formulated as the solution of inverse heat transfer problems. Such problems are ill-posed in mathematical sense and their main feature shows itself in the solution instabilities. That is why special regularizing methods are needed to solve them. The general method of iterative regularization is concerned with application to the estimation of materials properties. The objective of this paper is to estimate thermal and thermokinetic properties of advanced materials using the approach based on inverse methods. An experimental-computational system is presented for investigating the thermal and kinetics properties of composite materials by methods of inverse heat transfer problems and which is developed at the Thermal Laboratory of Department Space Systems Engineering, of Moscow Aviation Institute (MAI). The system is aimed at investigating the materials in conditions of unsteady contact heating over a wide range of temperature changes and heating rates in a vacuum, air and inert gas medium. In estimating temperature-dependent properties of modern composite destructive materials the most effective are methods based on solution of the coefficient inverse heat transfer problems. The most promising direction in further development of research methods for destructive composite materials using the procedure of inverse problems is the simultaneous determination of a combination of material's thermal and kinetic properties (thermal conductivity, heat capacity, heat capacity of charring gas, thermokinetics and some other parameters). Such problems are of great practical importance in the study of properties of composite materials used as destructive surface coating of spacecrafts [1-8].

The experimental equipment and the presented method could be applied for estimating of material's seven characteristics; the availability of a few specimens of the material allows us to provide uniqueness of the solution. The application of the considered technique for real thermoprotective materials is presented. The results of temperature measurements inside the specimen are assigned as necessary additional information to solve an inverse problem. To construct an iterative algorithm of the inverse problem solving a conjugate gradient method was used. In the approach being developed the methods of calculus of variations are used for calculation of the minimized functional gradient. For partially decomposed materials the model of heat conduction with temperature-dependent thermal characteristics is approximate, and characteristics are effective, since the heat transfer in such material is provided not only by heat conduction but also by different transformation processes depended on conditions of heating. A deviation of calculated and experimental temperature values in the experiments did not exceed 8 K, that confirms the possibility of using, for the given material, a model of heat conduction with the effective thermal characteristics. But the presented method can be used only for determining the effective thermal characteristics of composite materials for particular heating conditions.

At the present paper the problem of parametric identification of the mathematical model of the internal thermokinetics is considered. And all coefficients of mathematical model (thermal and thermokinetic properties of considered materials) are estimated by computational-experimental method based on inverse problems technique. The flexible thermal protective materials used in the thermal protection of IRDT are considered as example of implementation of developed method.

EXPERIMENTAL STUDY

By the way of experimental study of the material specimens the results of experiments on the thermo-vacuum stand (TVS-2M) at the Department of Space System Engineering of MAI are used. The test stand (Fig. 1) consists of units and systems, described below. A horizontally set vacuum chamber 1 of 0.1 m³ volume is a cylinder with double walls between which the cooling water is circulating. A cylinder is sealed at both ends by spherical covers, the rear cover is set fixed, the front cover is hinged and provided with the quick-opening locks. Both covers are water-cooled too. A vacuuming system consists of a mechanic vacuum pump, a diffusion pump, a vacuum seal and valves. A power supply system includes a control desk, a thyristor voltage regulator, a control unit and a power transformer. A control unit is for voltage control fed to a heater. The control can be in manual mode or in automatic mode from a computer. Two couples of specimens D1A, D1B and D2A, D2B made of the same test material (Fig. 2) were located symmetrically about the heating element on a thermoinsulating base made of thermal insulation material so that its heating surface is parallel to

the heater and at a certain distance from it ($\delta = 4-5$ mm). The other surfaces of specimens were heat-insulated by a layer of heat-insulating material. A heating element from a tantalum foil with dimensions $80 \times 70 \times 0.1$ mm allowed: 1) to increase the specimen heating rate till the desired values; 2) to avoid destruction of heating elements till the completion of specimen tests, this having occurred sometimes in attempting to provide a corresponding heating rate. Control of the specimen heating condition is performed by temperature on the heated surface measured by a thermocouple, made from a thermocouple wire BP5 - BP20 of 0.1 mm diameter in accordance with a prescribed regime. A control system of the heating regime includes a thermocouple, set up on the specimen surface, a control-point setting device, operating jointly with a self-balancing electronic potentiometer, an analogy regulator device in the set with the control units. Control over the heating regime was maintained in the experiment by the results of three trial starts with specimens from test materials, the structure of which is similar to the structure used in tests. In making the trial starts a criterion in choosing the suitable heating regime is the coincidence of the specimen external surface temperature measured with a prescribed temperature. Measurement and recording of non-steady temperatures in the test specimen are made by means of an automatic system for experimental information gathering and processing based on PC.

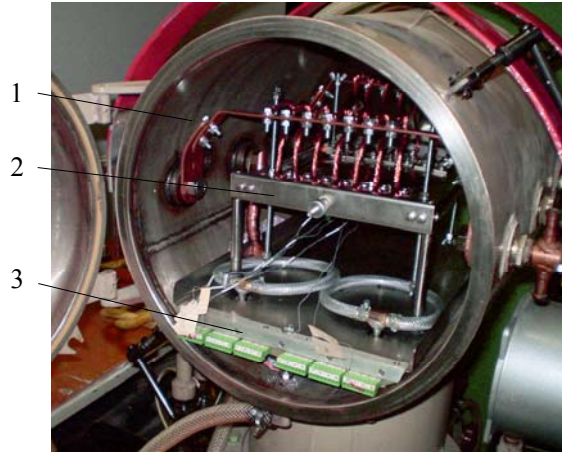


Fig.1. Experimental module EM-3D installed in vacuum chamber of stand TVS-2M1 – vacuum chamber, 2 – module EM-3D, 3 – connector blocks of thermocouples

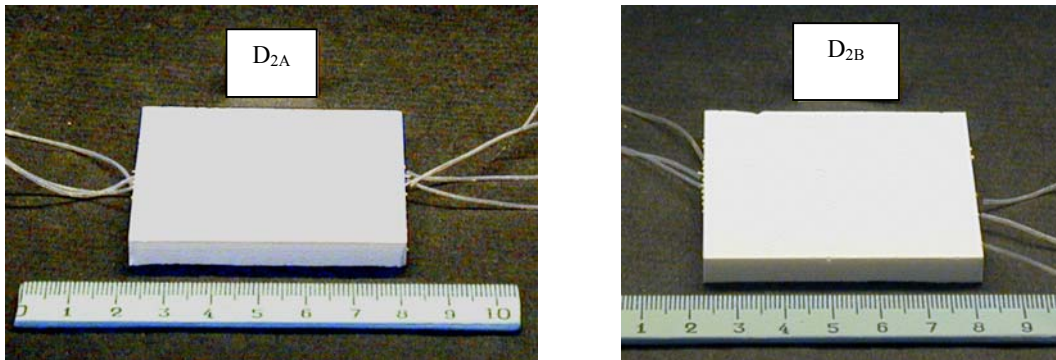


Fig.2. Experimental samples of sensor prototype for execution of optional tests with the help of stand TVS-2M

The temperature measurements schemes (schemes of thermocouples installation into sensors) are given in Table 1. The coordinates of measurement points $X_m, m = 1, \dots, M$ are measured from sensor heating surface. The real coordinates of inner thermocouples junction installation were controlled by the X-ray examination.

Table1. The real coordinates of measurements in sensors D2A and D2B.

Sensor	X1, [mm]	X2, [mm]	X3, [mm]	X4, [mm]	X5, [mm]
D2A	0,0	1,10±0,1	1,70±0,05	2,20±0,05	6,20-0,1
D2B	0,0	2,30-0,1	3,60-0,2	5,00-0,2	6,10±0,05

The symmetric scheme of contact heating of two samples was used in tests. The scheme is shown in Fig.3.

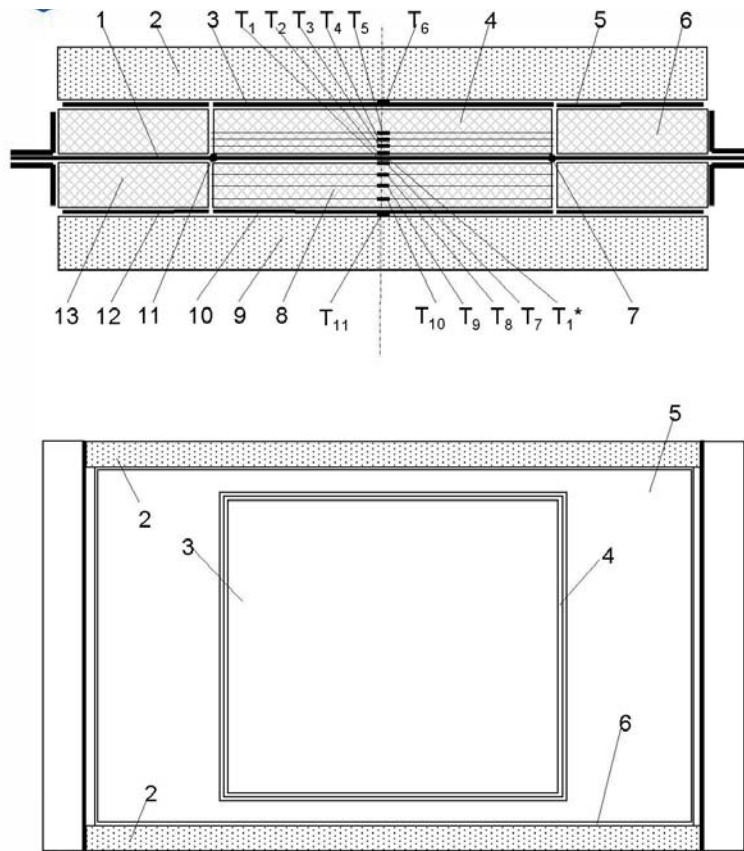


Fig. 3: A testing scheme for specimens: 1 – heating element; 2 –thermal insulated slab; 3 – sensitive element (SE) of heat flux on the upper specimen; 4 – upper specimen (1a/2a); 5 –mask of the upper (SE); 6– siding thermoinsulated slab; 7 – voltage measuring point on the heater element; 8 –lower specimen (B); 9-thermo insulate slab; 10 – SE on lower element specimen (B); 11- voltage measuring points on the heating element; 12- mask of the lower SE; 13- siding thermoinsulated slab; T_1, T_1^* - thermocouples on the heater ; $T_2, -T_6$ - thermocouples on the upper specimen (A).
 $T_2, -T_6$ - thermocouples on the lower specimen (B)

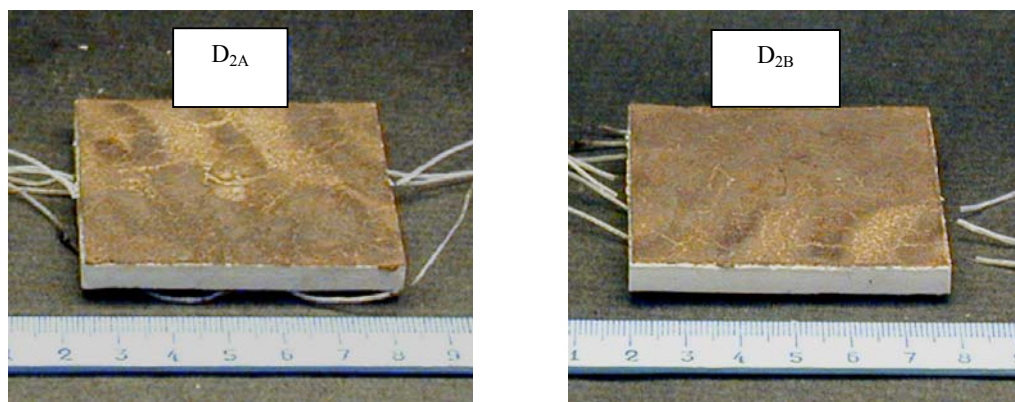


Fig.4. Experimental specimens after tests

The tests were carried out in the air in condition of decreased pressure 1×10^{-3} bar into vacuum chamber. The pilot tests of specimens D1A and D1B were carried out for verification of heating manipulation subsystem, measurement and data collection and for selection of heating mode as well as the verification of chosen temperature measurement scheme. The final tests of sensor samples D2A (A - upper) and D2B (B – lower) were prepared and carried out with taking into account results of pilot test. The heating program includes several stages:

- primary stage with duration of 4 seconds and constant temperature value $T_0 = 25,5^{\circ}\text{C}$, which equals to temperature into the vacuum chamber in the moment of tests beginning, which is necessary for manipulation system becoming on operative mode;
- the first stage is heating by linear behavior from set temperature T_0 to maximum temperature $T_{\text{max}} = 680^{\circ}\text{C}$ with the given heating mode $32,7^{\circ}\text{C}/\text{sec}$;
- the second workable stage with constant temperature $T_{\text{max}} = 680^{\circ}\text{C}$ during the 32sec;
- the third stage is decreasing of temperature from $T_{\text{max}} = 680^{\circ}\text{C}$ to 80°C in accordance with the given heating mode.

The heating program is given in Fig.5 ($T_{pr}(\tau)$).

The measured results, which were obtained $T_m(\tau), 0 \leq \tau \leq \tau_e$ after primary data processing, are given in Fig.5-6.

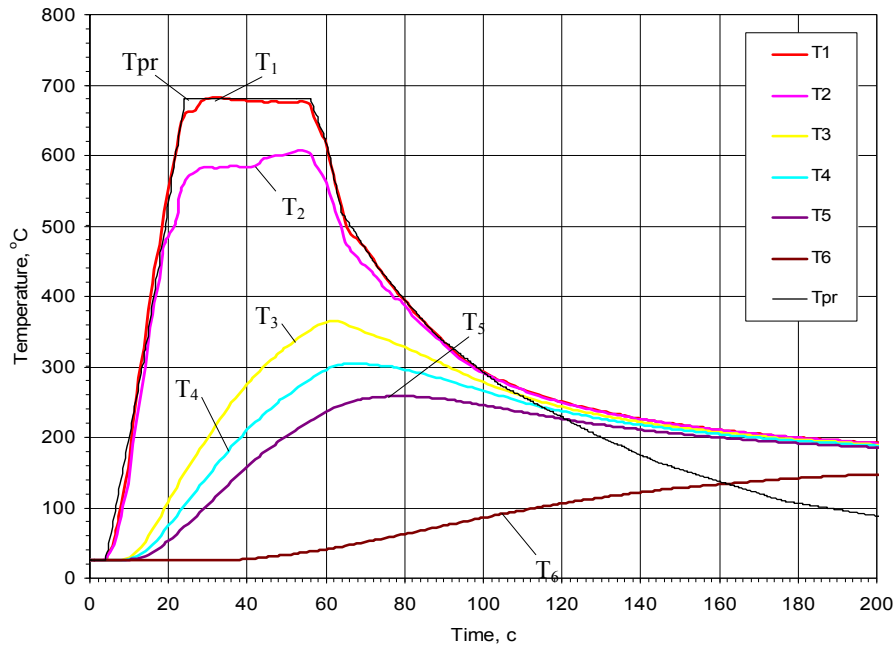


Fig.5. The results of temperature measurement into sensor D2A

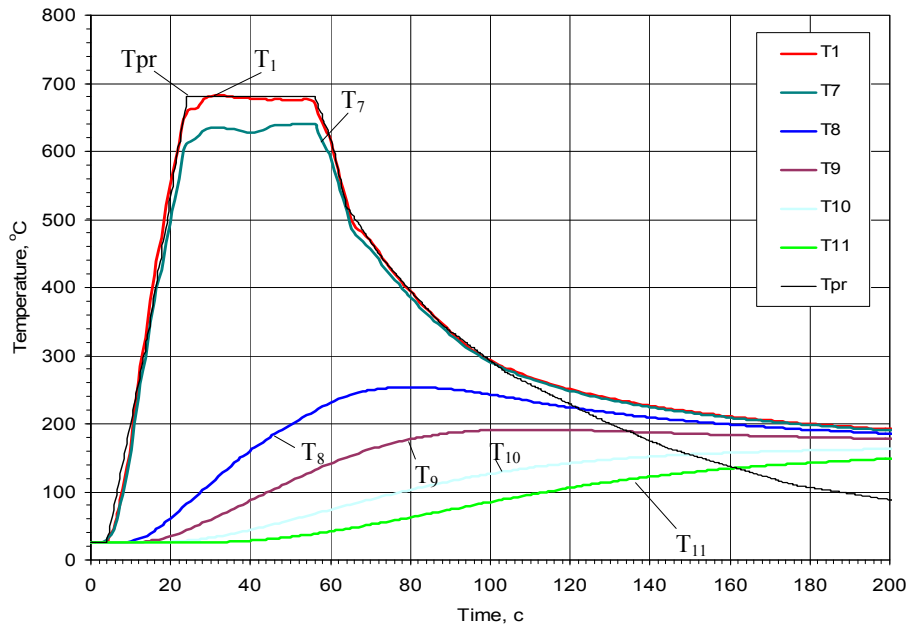


Fig.6. The results of temperature measurements into sensor D2B

The experimental module EM-3D is implemented to provide a determining of the heat flux into the specimens from the heater to provide the uniqueness of the inverse problem solution by simultaneous determining of full set of mathematical models coefficients. In the process of non-steady heating of specimens, recording of temperatures inside the specimen in the points of thermocouples positioning, heater's temperature and also electric power released on it. Therefore the electrical power at the heater can be calculated as

$$Q_{electr} = U * I \quad (1)$$

where U - r.m.s. voltage on the heater, I - r.m.s. strength of current, transmitted through the heating element. The heat flux (Fig.7) supplied to a specimen due to symmetry is determined as

$$q_2(\tau) = Q_{electr} / (2A) = U * I / (2A) \quad (2)$$

EXPERIMENTAL DATA PROCESSING

The mathematical model of heat transfer in specimen is

$$C(T(\tau, x)) \rho \frac{\partial T(\tau, x)}{\partial \tau} = \frac{\partial}{\partial x} \left(\lambda(T(\tau, x)) \frac{\partial T(\tau, x)}{\partial x} \right) + C_g(T(\tau, x)) \int_{x_n}^x \frac{d\rho(x, \tau)}{d\tau} d\xi \frac{\partial T(\tau, x)}{\partial x} + H(T(\tau, x)) \frac{d\rho(x, \tau)}{d\tau} \quad (3)$$

$$0 < x < L, \quad 0 \leq \tau < \tau_{\max}$$

where the second term on the right hand side covers the effect of convective heat transfer by the filtration of the gas arrived inside the material in the process of thermal kinetics (we make assumption that temperatures of the gas and the destructed material are equal), and the third term covers the specific heat of thermal kinetics.

$$T(0, x) = T_0(x) \quad (4)$$

$$-\lambda(T(0, \tau)) \frac{\partial T(0, \tau)}{\partial x} = q_1(\tau) \quad (5)$$

$$T(L, \tau) = T_2(\tau) \quad (6)$$

$$\frac{d\rho(x, \tau)}{d\tau} = F(x, \tau) = \begin{cases} 0, T(x, \tau) < T_r \\ -\rho^n A \exp\left(\frac{-E}{RT(x, \tau)}\right) \\ 0, \rho(x, \tau) \leq \rho_c \end{cases} \quad (7)$$

$$\rho(x, \tau) > \rho_c, T(x, \tau) \geq T_r$$

$$T(x, \tau_r) = T_r, \rho(x, \tau_r) = \rho_0, \rho(x, \tau_c) = \rho_c$$

In model (3)-(6) the coefficients $C(T)$, $\lambda(T)$, $C_g(T)$, $H(T)$ as well as A , E and n are unknown. The experimental equipment and the method described below could be applied for estimating of materials seven characteristics; the availability of a few specimens of the material allows us to provide uniqueness of the solution.

The results of temperature measurements inside the specimen are assigned as necessary additional information to solve an inverse problem

$$T^{\exp}(x_m, \tau) = f_m(\tau), \quad m = \overline{1, M} \quad (8)$$

The inverse problem is solved by iterative regularization method [9-12].

THERMOKINETIC PARAMETERS ESTIMATING

It is impossible to estimate all parameters of mathematical model (3)-(7) just by temperature measurements. The kinetics parameter have been determined by using facility STA Jupiter 449C manufactured by NETZSCH-Geratebau GmbH

(Fig.7-8). Experimental data processing has been made by software Netzsch Thermokinetics. Data of thermo-gravimetric analysis and differential scanned calorimetric are presented in Fig.9-10.

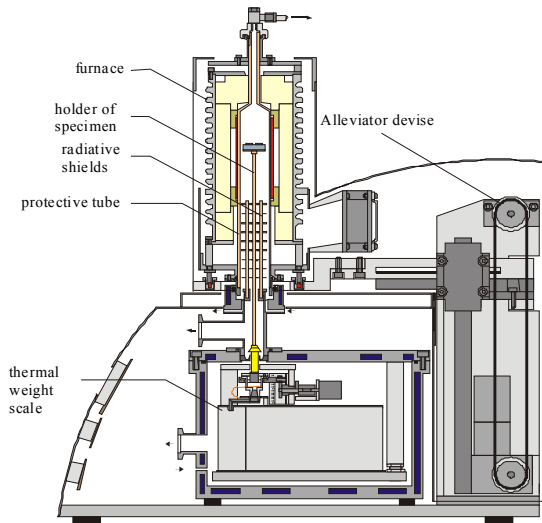


Fig.7.STA 449 Jupiter measuring facility

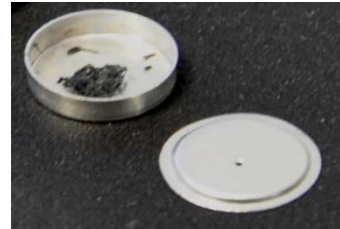


Fig.8. Specimens before and after experiment

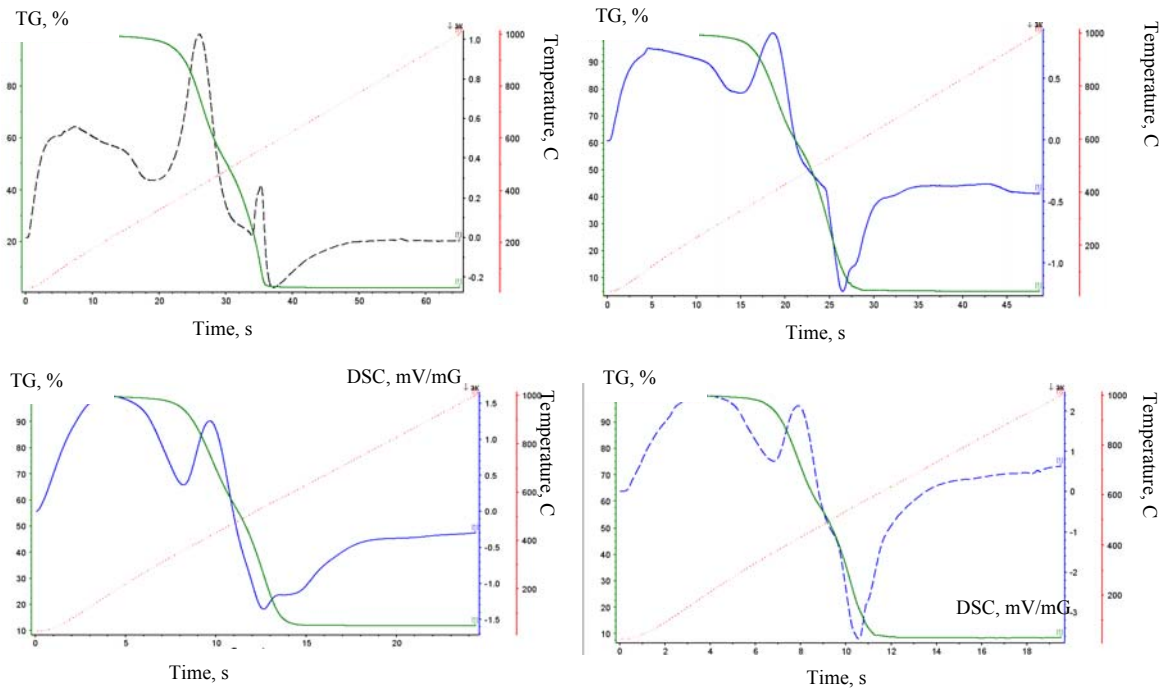


Fig.9. Data of thermo-gravimetric experiments

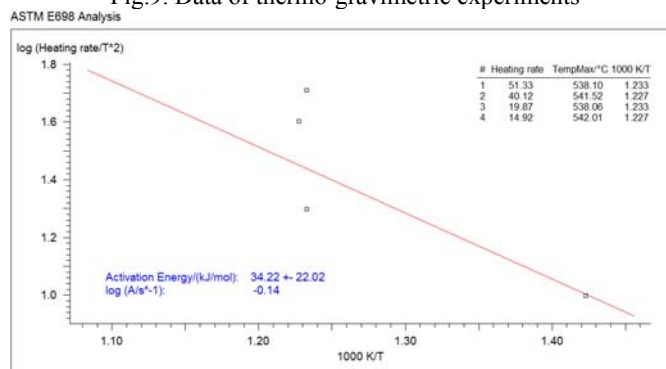


Fig.10. Estimated values of the energy of activation and pre-exponential coefficient

DATA PROCESSING BY INVERSE PROBLEMS TECHNIQUE

The inverse problems is solved by iterative regularization method. Comparisons of the calculated and measured temperatures on the specimens' surfaces for testing material presented in Fig.11. The result of estimating the functions $C(T)$, $\lambda(T)$, $C_g(T)$, $H(T)$ for material are presented in Fig.12-15. Table 2 includes the obtained values of the least squares and the maximum deviation of the calculated temperatures from that measured in the experiments.

Table 3. The deviation of the calculated temperatures and measured temperature

experiment	Least-squares temperature deviation (K)	Temperature deviation (%)	Maximum temperature deviation (K)	Maximum temperature deviation (%)
D1A	5.64	3.3	27.5	12.1
D1B	6.46	4.7	33.5	13.5
D2A	8.41	5.9	41.2	14.2
D2B	4.98	2.4	20.8	10.3

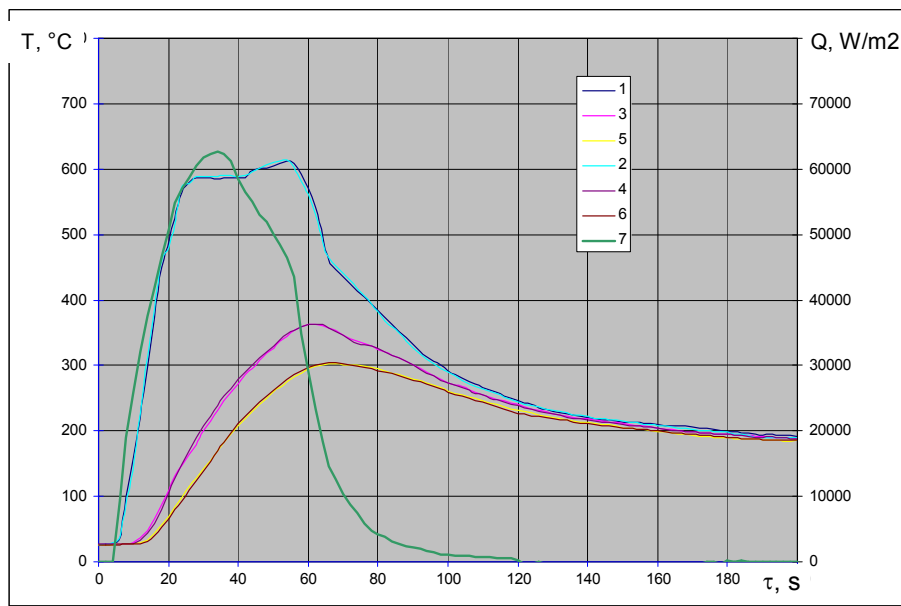


Fig.11. Comparing of calculated in positions of T2 (1), T3 (3) and T4 (5) and measured T2 (2), T3 (4) and T2 (6) temperatures (TestsD2A) and heat flux (7) calculated by equations (2)

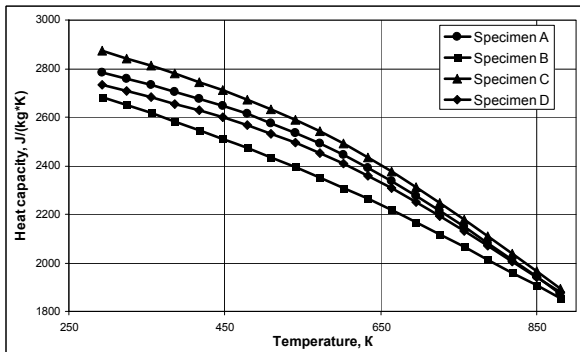


Fig.12. Estimated value of the heat capacity

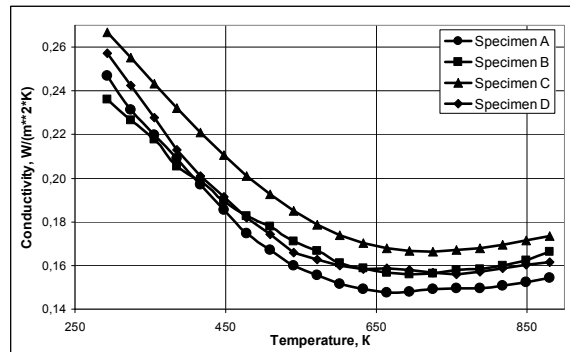


Fig.13. Estimated value of the thermal conductivity

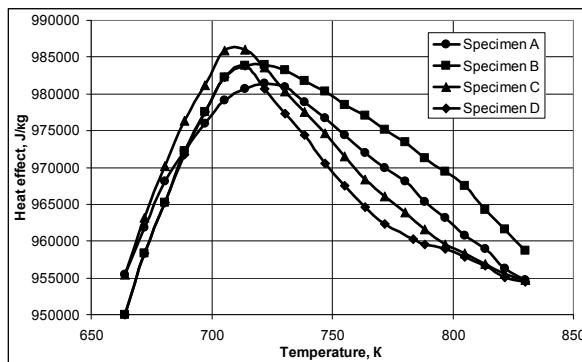


Fig. 14. Estimated value of the gas heat capacity (specimens #1 and #2)

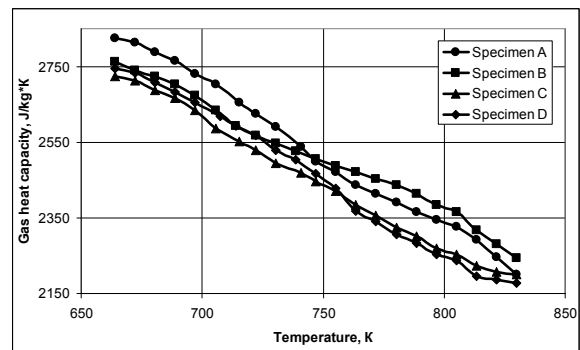


Fig. 15. Estimated value of the heat effect (specimens #1 and #2)

CONCLUSIONS

The paper seeks to describe the algorithm developed to process the data of unsteady-state thermal experiments. The algorithm is suggested for determining these unknown characteristics of a slab specimen as a solution of the nonlinear inverse heat conduction problem in an extreme formulation.

The following main factors have an influence on the accuracy of the inverse heat conduction problem (in sequence of significance): the errors in coordinates of thermosensor positions; the errors in values of different characteristics; the errors in estimating the residual level. For partially decomposed materials the model of heat conduction with temperature-dependent thermal characteristics and one-stage is approximate, and characteristics are effective, since the heat transfer in such material is provided by heat conduction and a few different transformation processes depended on conditions of heating. A deviation of calculated and experimental temperature values in the experiments did not exceed 42 K, that confirms the possibility of using, for the given material, a model of heat conduction with the effective thermokinetics. But the presented method can be used only for determining the effective thermal characteristics of composite materials for partial heating conditions.

ACKNOWLEDGMENTS

This work was done with the financial support of RBFR (grant # [11-08-00952 -a](#)).

REFERENCES

- [1] J.G. Hansel, R.F. McAlevy "Energetics and chemical kinetics of polystyrene surface degradation in inert and chemically reactive environments," *AIAA Journal*, vol.4, N5, pp. 529-551, 1966.
- [2] J.H. Lundell, R.R.Dickey, J.W. 'Jones Performance of charring ablative materials in the diffusion - controlled Surface Combustion regime' *AIAA Journal*, , vol, 6, pp. 1329-1341,1968
- [3] R.C.Pfal Jr., B.J. Mitchel "Simultaneous measurement of six thermal properties of a charring ablator," *Int. Journal Heat and Mass Transfer*, vol.13, No.2, pp.275-281, 1970.
- [4] R.L. Potts "Hybrid integral/quasi-steady solution of charring ablation," *AIAA Pap.*, No.1677, 20p. ,1990.
- [5] Reinikka E.A., Wells P.B. Charring ablators in lifting reentry.- *AIAA Pap.* No.63-181, 15p.
- [6] N.S. Vojvodich, R.B. Pope "Effect of gas composition on the ablation behavior of a charring material," *AIAA Journal*, vol.2, No.3, pp.536-542, 1964.
- [7] D.B.Adarkar, L.B. "Hartsook An integral approach to transient charring ablator problems," *AIAA Journal*, vol.4, No.12, pp.2246-2248,1966.
- [8] B.L. Clark "A parametric study of the transient ablation of Teflon," *Trans. ASME. Journal of Heat Transfer*, vol.94,pp.347-354, 1972/
- [9] O.M.Alifanov, *Inverse Heat Transfer Problems*, Springer-Verlag, Berlin \ Heidelberg, 1994, p. 348.
- [10] O.M.Alifanov, E.A.Artyukhin and S.V.Rumyantsev "Extreme Methods for Solving Ill-Posed Problems with Applications to Inverse Problems". Begell House, New York, p. 306, 1995.
- [11] E.A. Artyukhin, G.A.Ivanov and A.V.Nenarokomov "Determination of a complex of materials thermophysical properties through data of nonstationary temperature measurements" *High Temperature*, vol.31, pp.235-247, 1993.
- [12] E.A.Artyukhin and A.V. Nenarokomov "Coefficient Inverse heat conduction problem," *Journal of Engineering Physics*, vol. 53, pp. 1085-1098, 1987.

CARBON-PHENOLIC ABLATORS

Industrial status and potential applications

R. Barreteau – T. Pichon – M. Lacoste

7th European Workshop on TPS & HS
8-10th April 2013

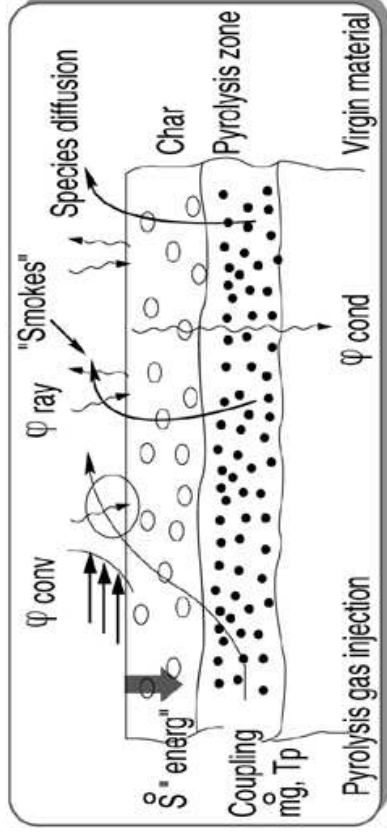
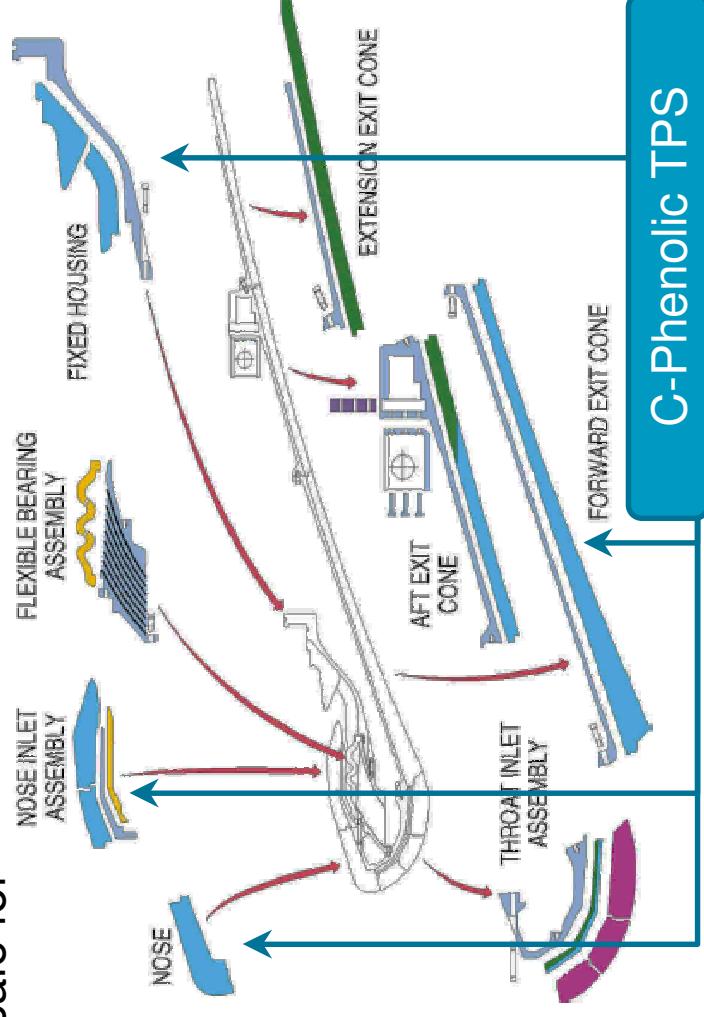
/01/ C-PHENOLIC ABLATORS DESIGN AND MANUFACTURING AT HERAKLES



CARBON-PHENOLIC HERITAGE IN HERAKLES

→ Large heritage from solid rocket motors (SRMs) application of fibre-reinforced polymers TPS

- Started in the 60's for solid rocket propulsion (military application)
- Technology matured through several generations of rocket engines and extended to larger scale for Ariane 5 SRMs
- Continuous development effort of sizing tools (incl. thermo-chemical ablation models) and manufacturing processes



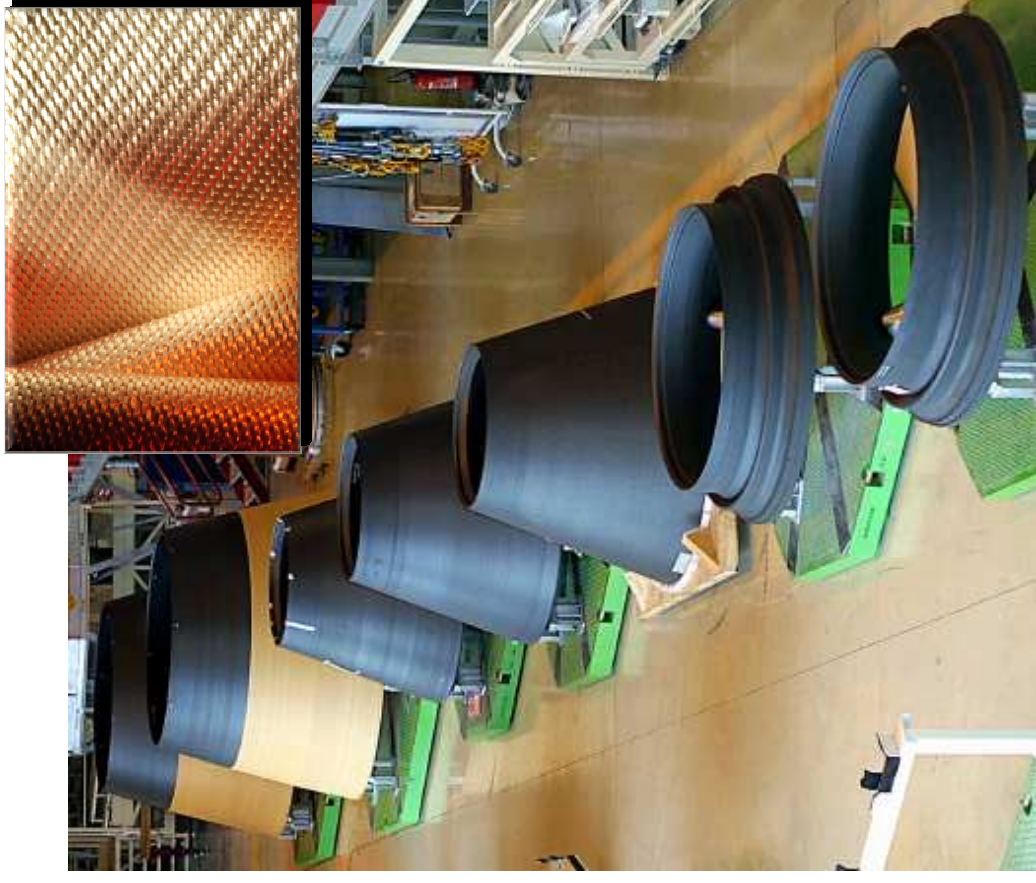
CURRENT PRODUCTION : “STANDARD” 2D C-PHENOLIC

→ C-phenolic ablators based on 2D reinforcement are still widely manufactured :

- Large existing database and flight experience
- High thermal insulation performance in harsh environments ($> 10 \text{ MW/m}^2$)

→ Sustainability of carbon-phenolic has been consolidated

- Up to end of 1990s, use of US (NARC) rayon as precursor of carbon fabric
- After shutdown of US production, alternative sources identified, focusing on sustainable rayon grade (e.g. high tenacity rayon used in automotive industry)
- Dedicated production tool invested by Herakles : carbon fabric Raycarb® C2 is now under production ($>20\text{-}30$ tons per year)



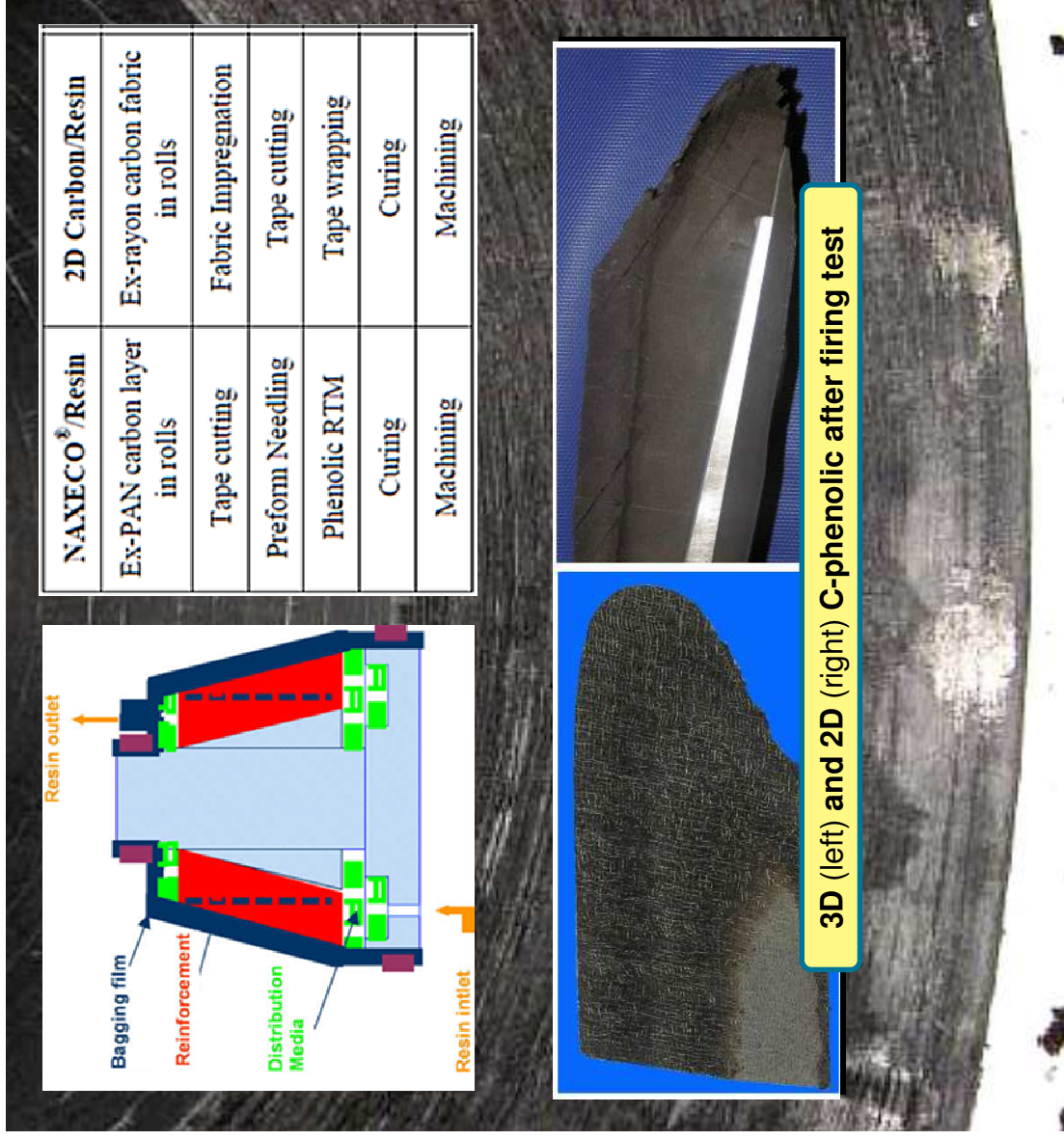
CURRENT PRODUCTION : “ADVANCED” C-PHENOLIC

→ Improvements developed from beginning of 2000s

- Replacement of ex-rayon by ex-PAN tape
- Replacement of pre-preg wrapping process by 3D (needed) carbon reinforcement

→ Main benefits :

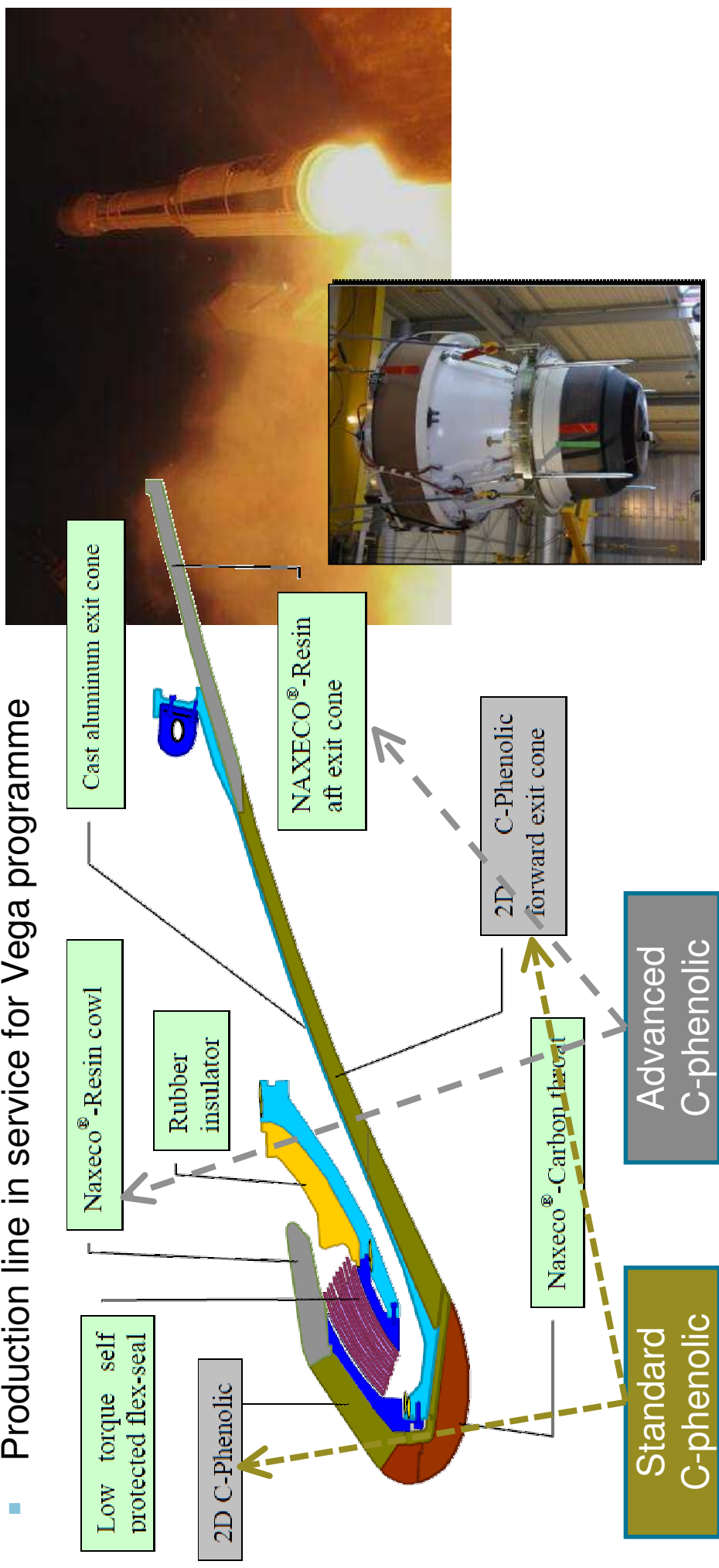
- Increased delamination resistance
- Decreased need for structural parts on the rear face of the ablator (metal housing for nozzles)
- Introduction of more economic manufacturing processes (precursor, RTM,...)



STATE OF THE ART FOR ROCKET ABLATORS

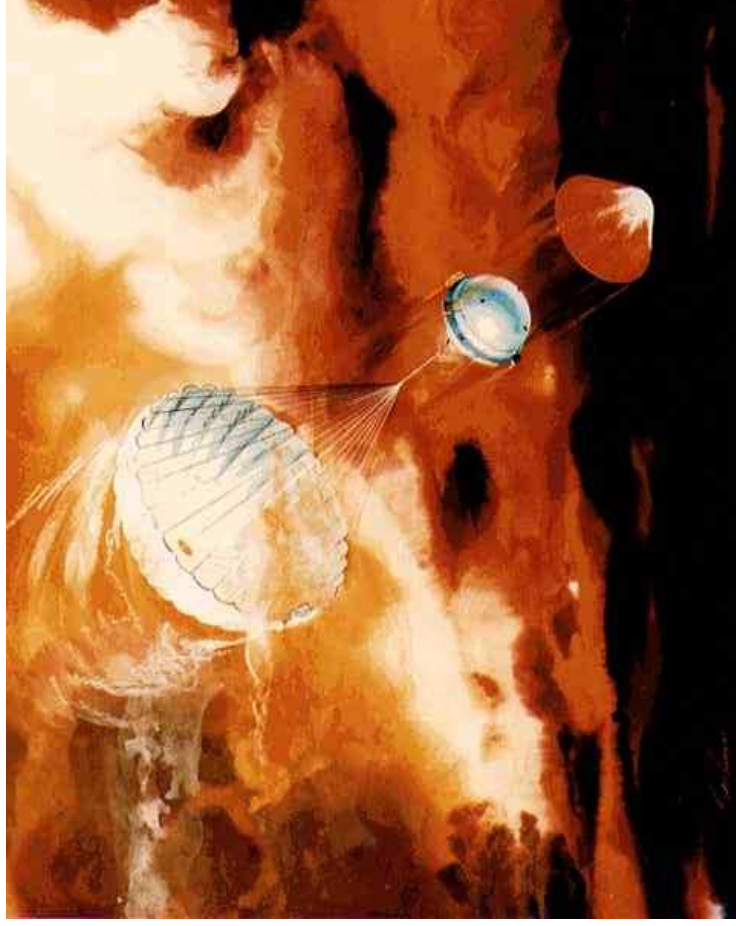
→ Advanced C-phenolic material (NAXECO®-Resin) developed for Vega P80

- Successful qualification through ground firing tests and launcher maiden flight
- Production line in service for Vega programme



/02/

C-PHENOLIC TPS FOR RE-ENTRY APPLICATIONS



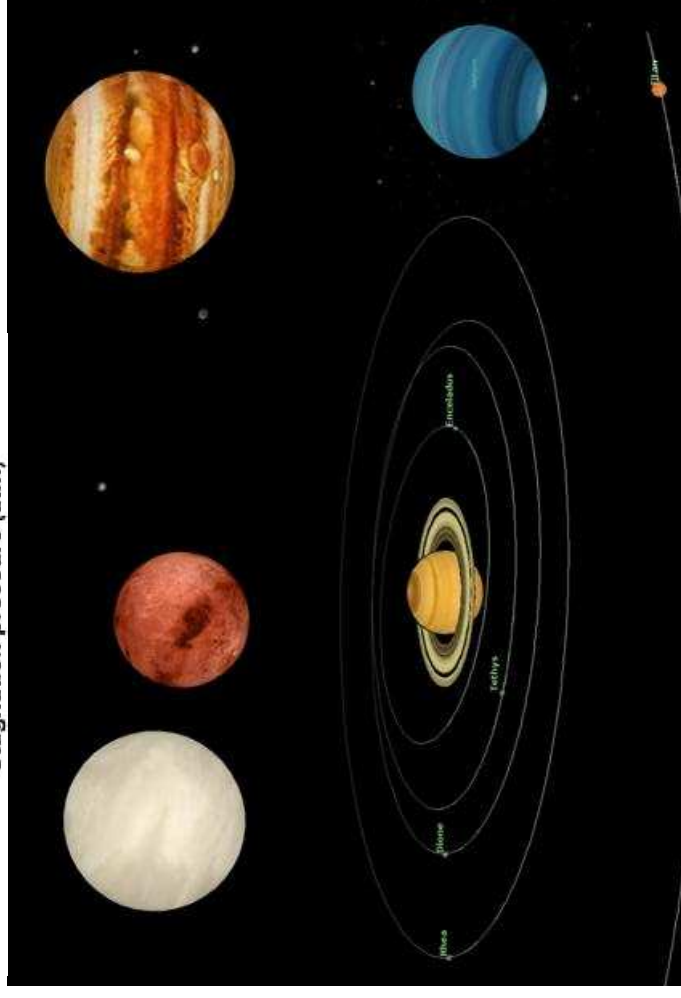
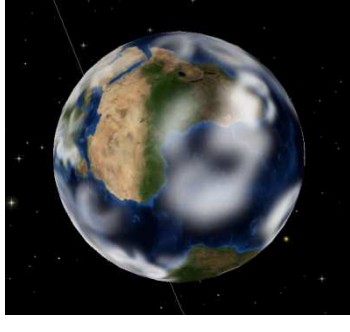
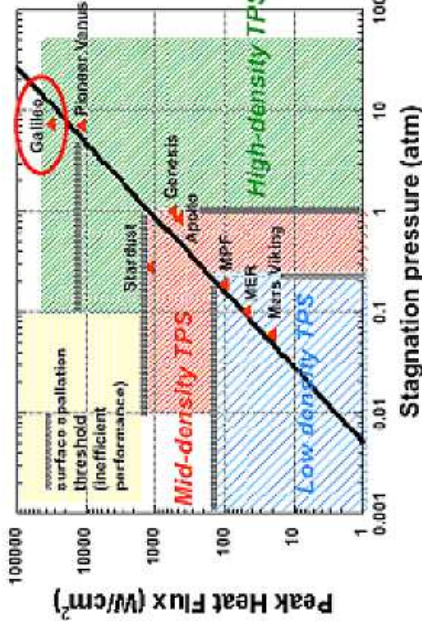
TPS NEEDS FOR EXPLORATION MISSIONS

→ Flight heritage shows that past re-entry heat shields used different categories of ablators

- **Light ablators** ($d < \sim 500 \text{ kg/m}^3$) for atmospheric entry in Earth : Moon return (Apollo), comet sample return (Stardust), Mars (various landers) and Titan (Huygens) atmospheres
- **Dense ablators** ($d \sim 1500 \text{ kg/m}^3$) for atmospheric entry in Venus (Pioneer Venus) and Jupiter (Galileo) atmospheres

→ Strong interest still present for scientific missions with atmospheric phase :

- **Entry** in Mars, Venus, Jupiter, Saturn, Titan, Neptune atmospheres for in-situ observations
- **Aero-capture** manoeuvres in Mars or giant planet atmospheres (Saturn Ring Observer)
- **Earth atmosphere re-entry** for return of samples : NEOs (MARCO POLO-R), Mars (Mars Sample Return), comets,...



SUITABILITY OF C-PHENOLIC FOR FUTURE PROBE MISSIONS IN THE SOLAR SYSTEM

→ Large agreement in TPS community that demanding missions such as Venus and giant planet entry / aero-capture can only use dense ablators, such as C-phenolic

Mission type	Planet	Entry velocity (km/s)	Peak heat Flux (kW/m ²)	C-phenolic suitability	Lightweight ablator suitability
Atmospheric entry	Venus	10 ^[a]	20000 ^[a]	Yes	No
	Mars	5,7 ^[a]	500 ^[a]	Yes (heavy)	Yes
	Jupiter	60 ^[a]	350000 ^[a]	Yes	No
	Saturn	28.6 ^[b]	45400 ^[b]	Yes	No
	Titan	6 ^[b]	650-950 ^[b]	Yes (heavy)	Yes
Aerocapture	Mars	4 ^[c]	160 ^[c]	Yes (heavy)	Yes
	Saturn	28.6 ^[b]	29850 ^[b]	Yes	No
	Neptune	30 ^[d]	50000 ^[d]	Yes	No
Sample return to Earth	Mars	12-13 ^[a]	1000-15000 ^[a]	Yes	to be confirmed
	NEO	12 ^[a] 11.5 - 15 ^[e]	5000 ^[a] 5000 - 16000 ^[e]	Yes	to be confirmed

^[a] Lacoste et al., Sustainable c-phenolic ablative material for the Ariane 5 SRM motor and application to TPS for entry probes, 5th TPS Workshop, 2006

^[b] Venkatapathy et al., Thermal protection system development, testing, and qualification for atmospheric probes and sample return missions - Examples for Saturn, Titan and Stardust-type sample return, Advances in Space Research, 2008

^[c] Requiston et al., AEROFAST: Aerocapture for future space transportation, International Planetary Probe Workshop (IPPW-7), 2010

^[d] Park, Stagnation-point radiative heat fluxes in Neptune aerocapture, International Planetary Probe Workshop (IPPW-7), 2010

^[e] Venkatapathy et al., Thermal Protection System Technologies for Enabling Future Sample Return Missions, White paper to the NRC decadal primitive bodies sub-panel, 2009

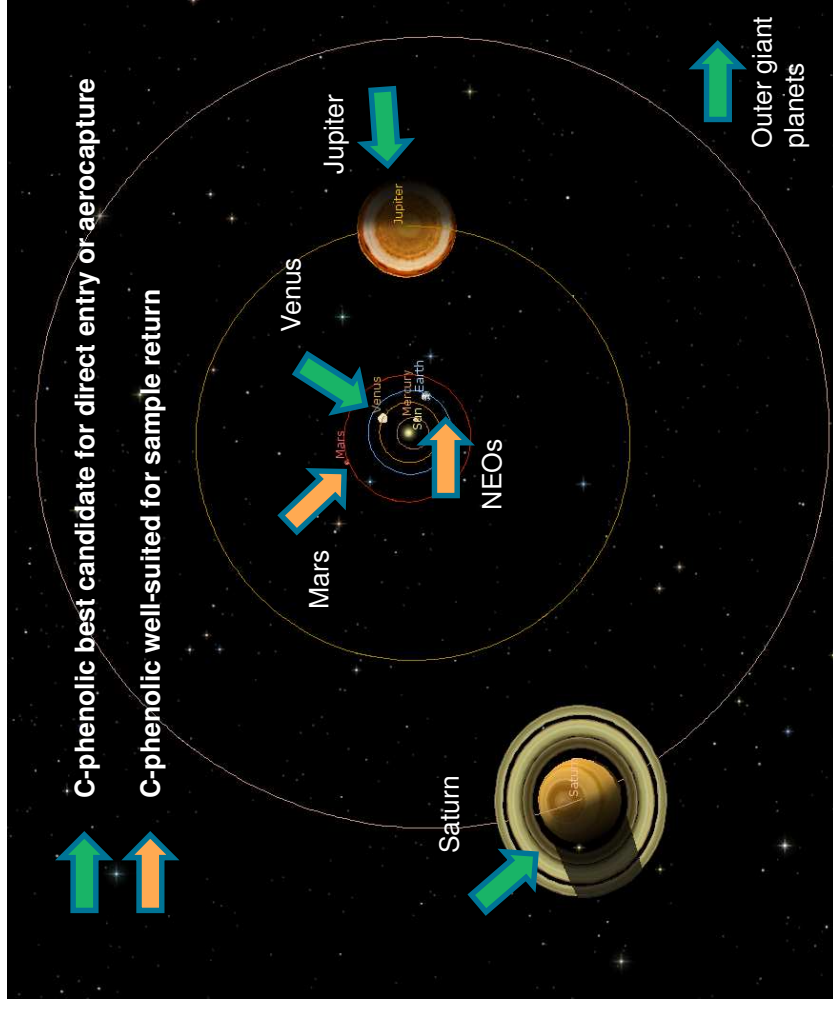
SUITABILITY OF C-PHENOLIC FOR FUTURE PROBE MISSIONS IN THE SOLAR SYSTEM (CONTINUED)

→ One main drawback...

- high density

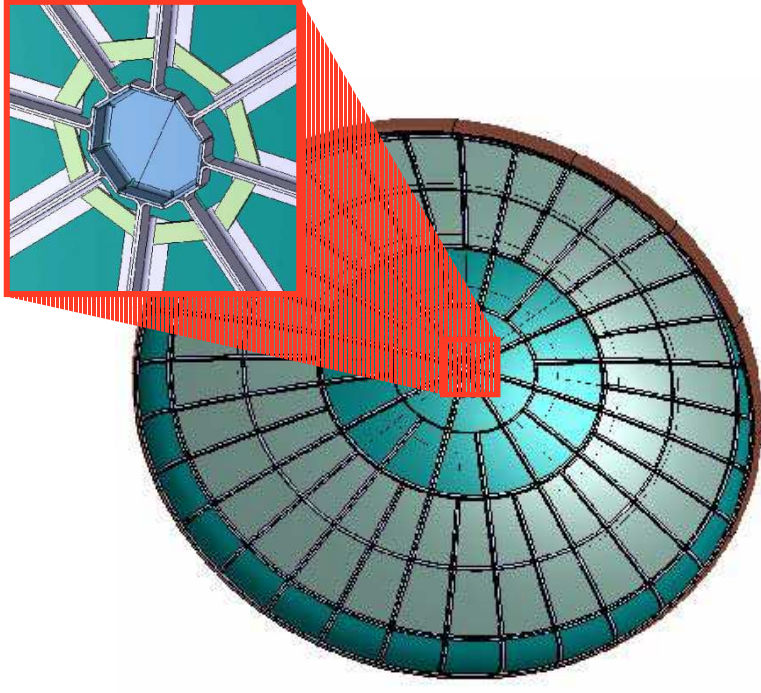
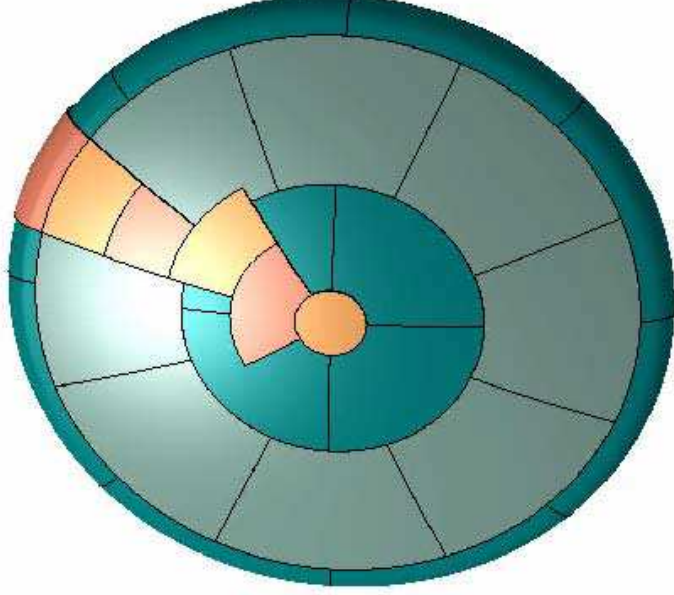
→ ... but many advantages :

- Good resistance to MMOD impacts
- Very high reliability due to large flight heritage (adapted to high value, complex exploration missions (e.g. return of samples to Earth))
- Availability, sustainability
 - C-phenolic will be applied on European launcher in the next decades,
 - Existing manufacturing facility in Herakles are compatible of most heat-shield sizes (typically from 1 to 2 m in diameter in foreseeable missions)
 - Numerous lightweight ablators, produced specifically for probe heat-shield application, have met disruption in manufacturing capacity, leading to long and costly re-qualification process



/03/

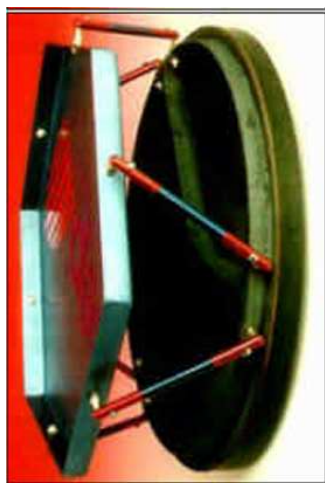
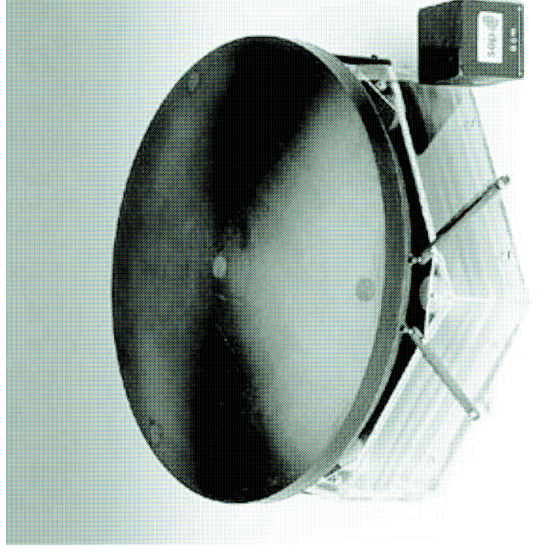
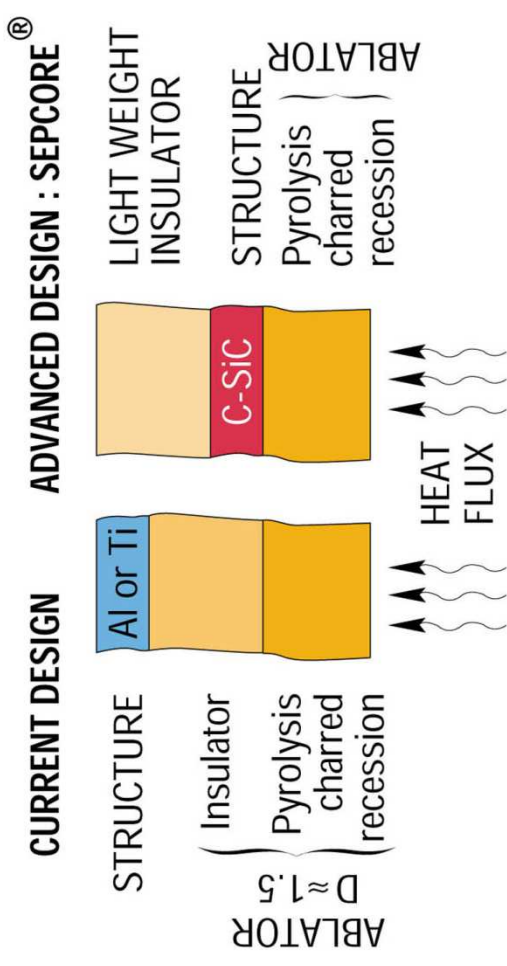
THE SEPCORE® ADVANCED TPS DESIGN



WHAT IS SEPCORE® ?

→ **Advanced TPS concept providing significant weight reduction by use of higher temperature-capable support structure :**

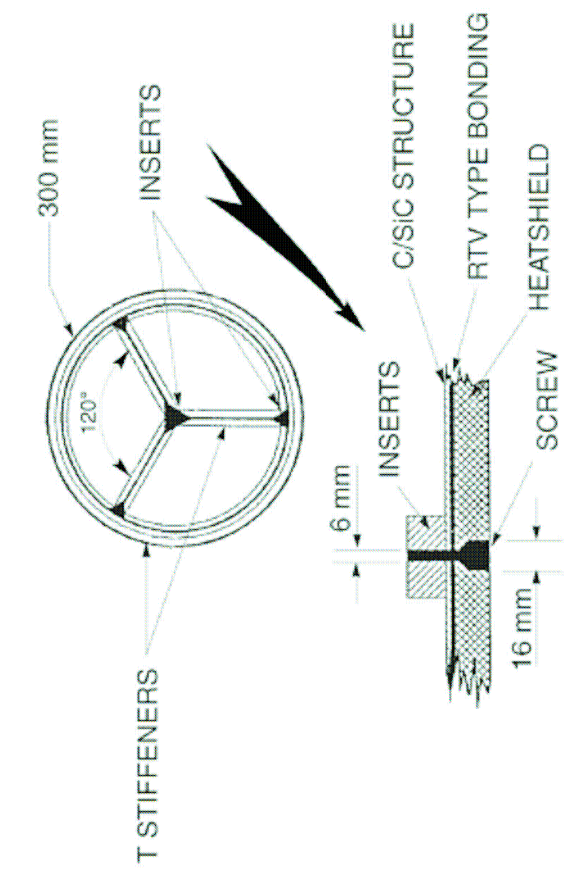
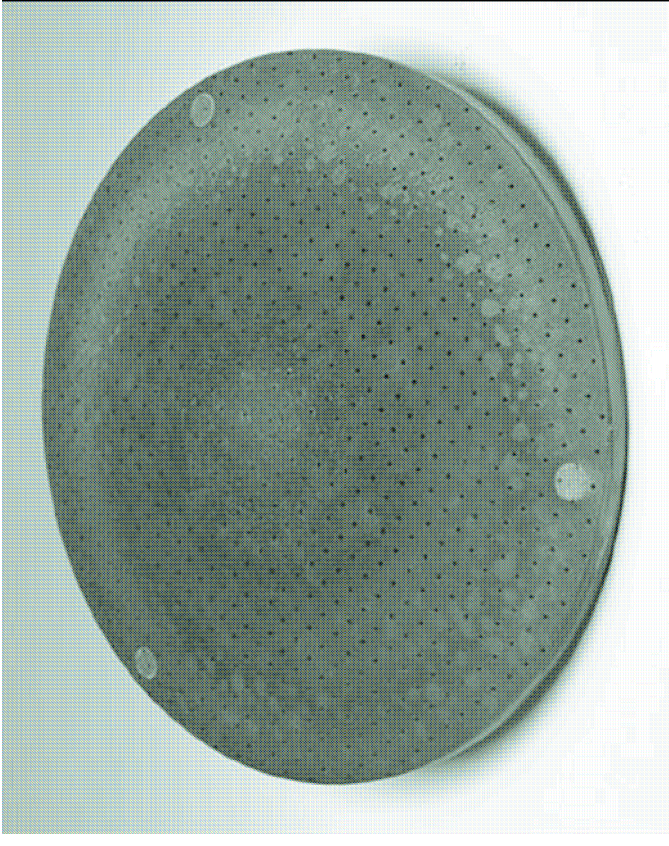
- Outer component made of C-phenolic (other types of ablators can be considered)
- Hot structure made of thermo-structural material (C-C or C-SiC) provide mechanical support, fastening being made through thermo-mechanical bolts
- Lightweight internal insulation (e.g. multilayer insulation)



SEPCORE® TESTING

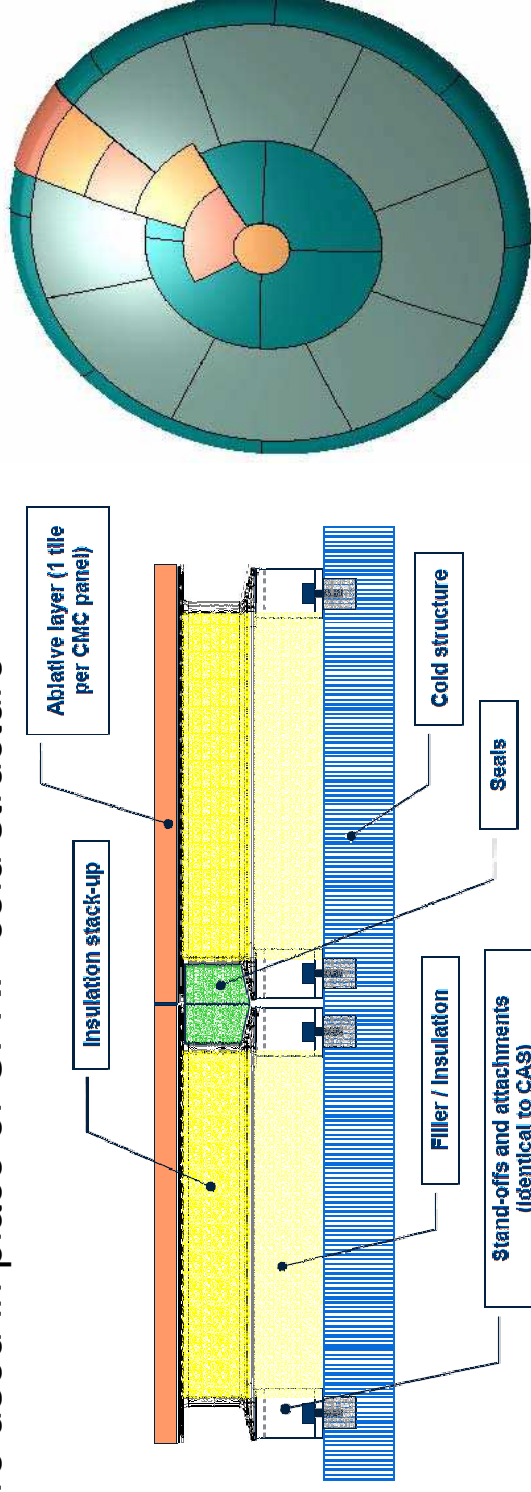
→ First design and PWT tests performed in 1990s within ESA TRP

- Mock-up manufactured with C-SiC structure
- PWT test in PWK1 facility in IRS : peak heat flux of 10 MW/m² at stagnation point
- Demonstrated satisfactory thermal and mechanical behaviour of both ablative and thermo-structural layer on a significant scale (Ø 300 mm)



SEPCORE® PERFORMANCE

- **Different conceptual designs performed for various TPS mission profiles**
- **ROSETTA probe** (peak heat flux $\sim 10 \text{ MW/m}^2$) : **-30% mass** reduction (taking into account C-phenolic, structure and internal insulation) compared to standard heat shield design (C-phenolic bonded on aluminium or CFRP structure)
 - **Jupiter entry probe** (peak heat flux $\sim 350 \text{ MW/m}^2$) : **>25% reduction** of C-phenolic mass necessary
 - **Apollo-like heat shield** for Moon return : **-40% mass** compared to standard design if C-phenolic ablator used on top of C-SiC shingles, **-50% mass** if integral C-SiC structure used in place of CFRP cold structure



HOT STRUCTURE TECHNOLOGY AT HERAKLES

- **Hot structures made of thermo-structural materials developed since 1980s**
- **Available materials comprise C-C and C-SiC, manufactured at industrial scale for aeronautics and space applications :**
 - C-SiC nozzle flaps for Rafale fighters
 - C-C and C-SiC nozzles for upper stage rocket engines (RL10-B2 and Vinci engines)
 - C-C nozzle throat for solid motors nozzle throats (incl. MPS and Vega stages)
 - Re-usable thermal protection system for entry vehicles (IXV) : significantly increased level of maturity through development and manufacturing of Qualification and Flight Models



CONCLUSION

- **Decade-long development and industrial production of C-phenolic ablators at Herakles for solid rocket propulsion components**
 - Up-to-date ablation modelling and ablator sizing capacity
 - Sustainable manufacturing chain established and qualified for C fabric (space grade), providing off-the-shelf European C-phenolic ablator
 - Continuous improvement of C-phenolic technical performance and reduction of costs through state-of-the-art processes
- **Wide range of C-phenolic potential applications in space exploration**
 - Direct entries or aero-capture in harsh atmospheric environment (Venus, Jupiter, Saturn, Neptune)
 - Samples return from Mars, comets or NEOs into Earth atmosphere
 - Any application where high reliability or low development cost is a major driver
- **Mass decrease of C-phenolic base heat shields can be reached through development of advanced TPS concepts (SEPCORE®)**
 - use of standard C-phenolic and CMC hot structures (high level of maturity through rocket nozzles and IXV TPS)
 - 30 to 50% mass reduction compared to standard C-phenolic heat shield concept can be reached, extending the mission range of potential missions for C-phenolic

HIGH SPEED GAS TURBINE EXHAUST FACILITY FOR THERMAL PROTECTION SYSTEMS MATERIALS TESTING

P. Bonfà⁽¹⁾, F. Morganti⁽¹⁾, F. Dolce⁽²⁾, W. Villadei⁽³⁾

*⁽¹⁾Aero Sekur S.p.A.
Via delle Valli 46, 04011 – Aprilia (Italy)
Email: bonfa@sekur.it*

*⁽¹⁾Aero Sekur S.p.A.
Via delle Valli 46, 04011 – Aprilia (Italy)
Email: morganti@sekur.it*

*⁽²⁾Italian Air Force – Flight Test Center - Chemistry Dept.
Structural Materials Group – Aeroporto Militare "M. De Bernardi"
Via Pratica di Mare 45, 00040 – Pomezia (Italy)
Email: ferdinando.dolce@am.difesa.it*

*⁽³⁾Italian Air Force Staff
3rd Department – Aerospace Plans and Transformation, Space Policy Office
Viale dell'Università 4, 00185 – Rome (Italy)
Email: walter.villadei@am.difesa.it*

ABSTRACT

The study and the experimental evaluation of aerospace materials is actually one of the most challenging and money demanding issues in the aerospace science. In particular the development of thermal protections materials (TPM) can be considered as a relevant goal. For this reason in 2010 Italian Air Force tasked (ItAF) Aero Sekur S.p.A. to develop a thermometric facility (Ground Support Equipment - GSE) able to test specimens of thermal protection materials immersed inside an high speed hot gas flux ejected by aircraft turbine. This ItAF facility has been successfully tested with the support of Flight Test Center of ItAF located in Pratica di Mare near Rome. The facility is able to evaluate flux enthalpy by measuring gas speed, stagnation point and free stream temperatures as well as front and back temperatures in the specimen in order to evaluate the evolution of the thermal flux versus the time.

The GSE has been firstly designed to test ablative materials, nevertheless it can be used also for testing different thermal protections materials as those used for hot structures (combustion chambers, nozzles, thermo-structural protections for hypersonic flight). The expected main advantages of this experimental method are: the reduction of the costs compared to arc jet and plasma tunnels, to be quick to use, flexible and adaptable to several applications with negligible impact in the test set up configuration. The drawbacks are mainly concerning the representativeness of the environment mainly for what the ablative materials are concerning, even if the enthalpies which can be achieved are sufficient to activate pyrolysis and to start ablation, therefore the method is considered effective whenever a comparison in performance of different materials is needed.

The test was concerning specimens of Silicone elastomer ablative material. The max front temperature achieved on the specimens was 1100 °C in a gas flux having speeds up to 270 m/sec (M=0.4).

The specimen started the ablation process which extended to about 1 mm of its exposed surface.

The GSE could potentially be used also to assess other materials performance used for aircraft support/protections.

INTRODUCTION

Since 2010 started the collaboration between Aero Sekur and ItAF because the study and the experimental evaluation of aerospace materials is one of the most challenging and money demanding issues in the aerospace science and in particular the development of thermal protection material for aerospace applications is considered as a relevant goal. The aim of this collaboration is the development of a thermometric facility that can test specimen of thermal protection material immersed inside an high speed hot gas flux ejected by aircraft turbine having enough energy to represent the application environment. This allow the possibility of evaluating the flux enthalpy by measuring gas speed, stagnation point and free stream temperatures, and front and back temperatures in the specimen in order to evaluate the evolution of the thermal flux versus the time; besides a characterization of material performance like chemical properties, physical properties and so on, it is also possible and it is an activity conducted in the ItAF laboratories after the tests.

Aero Sekur has started the study of thermal protection materials since 2004 proving the viability of an inflatable technology for thermal protection shield application (Inflatable Reentry Technologies – IRT); four years later (2008) it developed and tested successfully the inflatable thermal protection shield for planetary reentry (SPEM – Spacecraft Emergency Module) with a system level demonstrator designed to perform an assisted reentry mission for emergency spacecrew rescue. Now a facility for thermal material test have been designed (Ground Support Equipment for SPacecraft Emergency Module – GSE SPEM) and tested in collaboration with ItAF.

The ItAF is developing Space capability following several strategic guidelines. Basically the main topic concerning space is related to operational support: strategic military environment is rapidly changing and nowadays dynamicity and threat asymmetry are the main features of military operations; in this framework the space can be considered “a force multiplier” in most operational architectures and all its applications become “key enabling factors” for future operational capabilities. This new scenario needs to develop new concepts for Space component (assets and capabilities) in order to establish a new policy and a new doctrine. At the same time this process allows the ItAF to strengthen its environmental expertise and another important aspect is the duality of the Space. Astronautics component is the main feature of the Armed Force, and tends to combine the technological aspects, required for space "manned" flight, and the safety requirements and crew management aspects. ItAF has qualified professionals, both employed in the International context (ESA with 3 ESA Astronauts – European Space Agency), both employed in the internal Staff (three qualified doctors to support spaceflight operations and an aerospace engineer, qualified as cosmonaut and Soyuz Flight Engineer at the GCTC – Gagarin Cosmonaut Training Center). About the new technologies development, ItAF is interested in development of following initiatives: Air Launch Capability, with regard to Responsiveness of space operations; Nano and Micro Satellites Technology development with regard to Air Launch Capability; Hypersonic and Suborbital flights. The ItAF tasked Aero Sekur to develop this thermometric facility and supported Aero Sekur during the test in a scenario that is located between new technologies development and human spaceflight in terms of SPacecrew Emergency Module advanced material test.

DESIGN OF GSE

The GSE SPEM has been designed to test ablative and different thermal protection materials as those used for hot structures (combustion chambers, nozzles, thermo-structural protections for hypersonic flight). The expected main advantage of this experimental method, though with the facility design, is the possibility of comparing different ablative materials and thermal protection materials performances before deep test to be performed in dedicated facility (arc jet and plasma tunnels); this allow a reduction of cost, enhancing the effectiveness of the qualification test programme, and introduce a pre-qualification screening phase. This facility is quick to use, flexible and adaptable to several application and to different specimen size with negligible impact in the test set up configuration; besides there is the capability of achieving test duration of several minutes if needed.

However there are also drawbacks and these are mainly concerning the representativeness of the environment, mainly for what the ablative materials are concerning, even if the enthalpies which can be achieved are sufficient to activate pyrolysis and to start ablation process. In particular the environment is characterized by an high gas mass rate at lower speed and temperature compared to the plasma chamber, furthermore additional heat flux due to molecular recombination cannot be reproduced.

Therefore the method is cooperative and complementary to the standard facility that can represent the re-entry environment and it is effective whenever a comparison in performance of difference material is needed.

The design of the GSE SPEM started from the data of exhaust gas flux ejected by aircraft, known in terms of temperature, speed and composition; obviously temperature and speed increase as the distance from the aircraft decrease. With these data enthalpy of 1.6 MJ/kg, and heat flux of 0.4 MW/m² was calculated and they were the reference data for the test used in order to verify the performance of the facility, furthermore with the dummy sample configuration, the calibration set up, it was checked and validated the aircraft parameters.

The facility (Fig. 1 and Fig. 2) is composed by: the calorimeter (constituted by a pitot tube, K type thermocouples with exposed junction and grounded junction, and the specimen to be tested); the ground support structure for calorimeter support; the acquisition electronics with a thermistor; the aircraft and other tools like high speed cameras, a remote control facility, alignment tools and overall logistic supports.



Fig. 1. Facility for ablative and thermal protection materials test

The calorimeter is placed at the top of the ground support structure, about 2 meters high, and it was designed in two different configurations: the first one for the calibration set up, realized with a dummy sample; and the second one for the specimen set up, for the ablative materials test. In order to measure the temperatures inside the specimen, both for dummy sample and for ablative material, three K type thermocouples were inserted inside it at different distance from the hot gas flux exposed surface, 5 mm, 10 mm and 15 mm respectively. Besides two more thermocouples were installed on the calorimeter structure for hot gas flux characterization. Both the thermocouples and the specimen of ablative material were insulated with mullite tubes to avoid heat dispersion towards the calorimeter structure; mullite is a kind of ceramic material. Next to the calorimeter is installed the pitot tube for measurement of pressure and speed of flux ejected by aircraft.

The acquisition electronics, constituted by an acquisition board, a power supply, a pressure transducer, and a thermistor, is located in the middle of the ground support structure inside a dewar box and it is connected to the calorimeter; the thermistor is important for temperature monitoring inside the dewar box in order to check that temperature does not increase over the maximum temperature allowable for the electronic components.

The distance between the aircraft and the calorimeter can be modified as necessary in order to achieve the desired or requested value of temperature and speed and then enthalpy, mass rate, Mach number and heat flux. Alignment tools are useful for correct alignment of the calorimeter respect to the aircraft and a remote control facility is used to provide power supply to the electronics components, to monitor in real time the evolution of the tests and to store the data achieved during the tests.



Fig. 2. Ground Support Equipment for SPacecrew Emergency Module

TEST RESULTS

The test configuration considered the calorimeter (with the dummy sample or the ablative material specimen) placed at a known distance from the aircraft and at two meters high. The aircraft provided at least three steps of increasing power before the achieving of operative environment and the step at full power was about 80 seconds long (even if it can be increased if necessary). Before the real tests with the ablative material specimens, many calibration tests have been performed with the dummy sample configuration in order to define the correct distance between aircraft and calorimeter at the correct aircraft engine power.

During the test with the calibration set up that have been performed at 5.5 meters far from the aircraft engine nozzle, the maximum temperature reached for hot gas flux is about 900 °C, the maximum speed is about 270 m/s and as expected the temperatures measured inside the dummy sample are different and vary with the position of the thermocouples, in particular the first thermocouple (5 mm far from the hot gas exposed surface) measures higher temperature than the second one and the third one (respectively at 10 mm and 15 mm from exposed surface).

The ablative material specimens, in Fig. 3, had a diameter of 100 mm and a thickness of 50 mm and everyone were placed inside the mullite tubes to avoid heat dispersion; then they were installed in the calorimeter structure for the tests.

In Fig. 4, Fig. 5 and Fig. 6 are showed the values measured during the ablative material specimen test with the specimen placed at 4.5 meters far from the aircraft engine nozzle, respectively for temperature of flux, speed of flux and temperatures in the specimen. It is possible to see that the maximum temperature and speed of flux measured were respectively about 1100 °C and 470 m/s, besides also in this case the three temperatures measured inside the ablative material are different and vary with the position of the thermocouples (placed at 5 mm, 10 mm and 15 mm far from the exposed surface); in addition the behavior of temperatures and speed in the graphics follow the aircraft engine power variation.

In Fig. 7 it is possible to see the trend of Prandtl and Reynolds numbers obtained from values of temperature and speed of flux and from heat gas flux composition parameters while in Fig. 8 is showed the Nusselt number trend computed with the formulation in [1] and used for the comparative evaluation of the convection heat transfer coefficient calculation. In fact from the experimental data from the specimen test, the convection heat transfer coefficient h_s was calculated and this value was compared with the value obtained analytically from the Nusselt number frontal plate formulation, h_a . The maximum value are respectively $h_s=1030.4 \text{ W/ m}^2\text{K}$ and $h_a=1405.6 \text{ W/ m}^2\text{K}$.

After the tests performed with the specimen of ablative material and from data of temperature and speed measured, an enthalpy of 1.9 MJ/kg, an heat flux of 0.5 MW/m^2 , a Mach number of 0.6, and a mass rate of $120 \text{ kg/m}^2\text{s}$, have been calculated; these values are summarized in Table 1.

Besides, before the test the weight of the specimen of ablative material was 0,627 kg and the measurement performed after the test showed a weight 9.5 grams lower than before, furthermore the ablation process extended at about 1 mm from the exposed surface and the char has a maximum depth of about 5 mm as shown in Fig. 11. In Fig. 9 is showed the specimen before, during (with images taken with an high speed camera in Fig. 10) and after the test.

Table 1. Results of ablative material test

Parameters	Values	
Max temperature	1100	°C
Max speed	470	m/s
Enthalpy	1.9	MJ/kg
Heat flux	0.5	MW/m ²
Mach number	0.6	/
Mass rate	120	Kg/m ² s



Fig. 3. Ablative material specimen

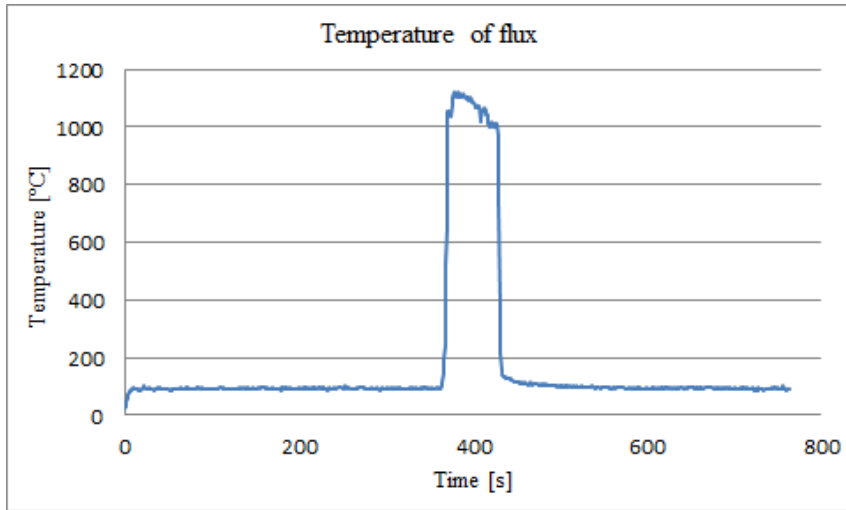


Fig. 4. Temperature of flux

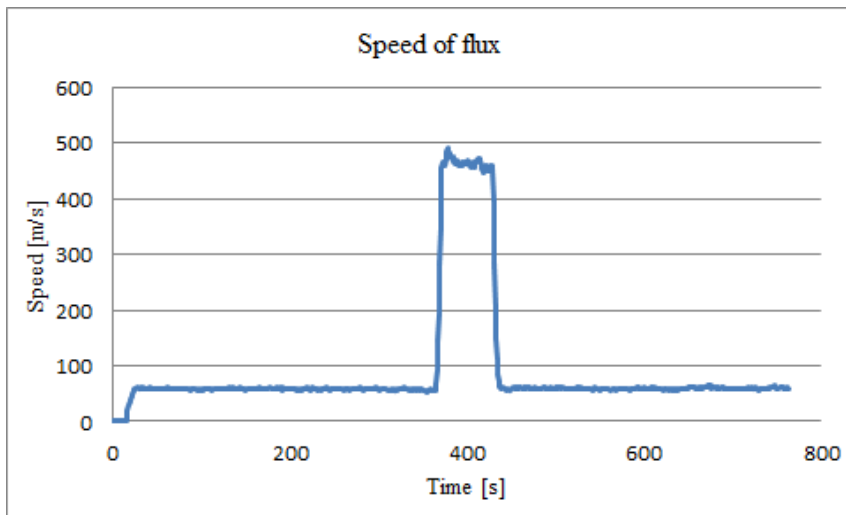


Fig. 5. Speed of flux

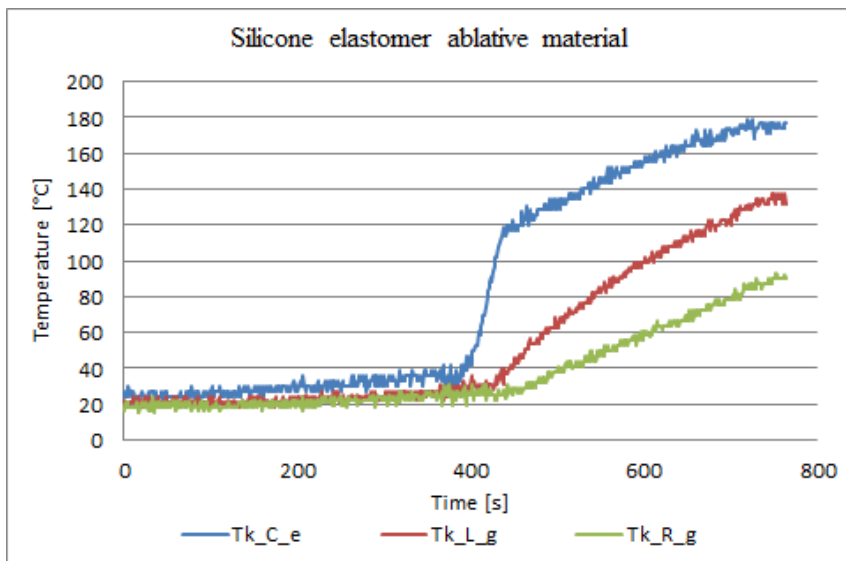


Fig. 6. Silicone elastomer ablative material

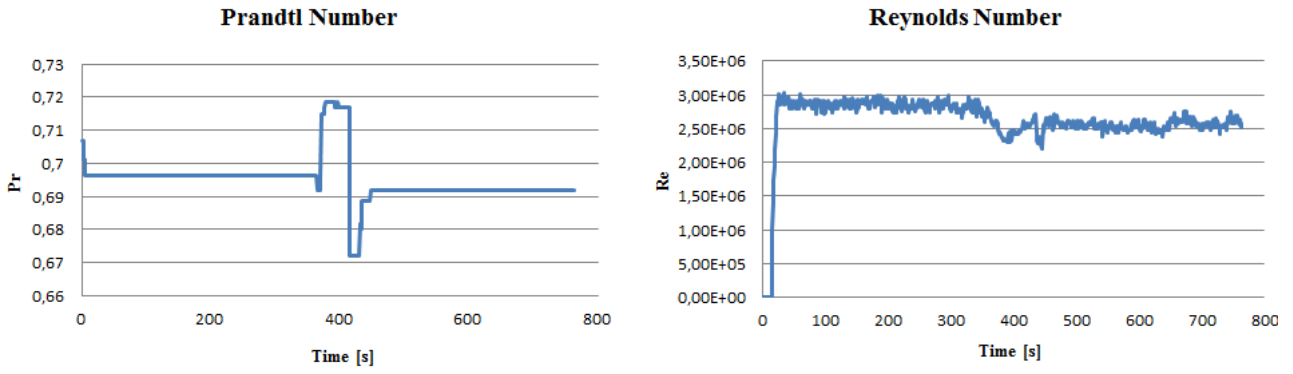


Fig. 7. Prandtl and Reynolds numbers

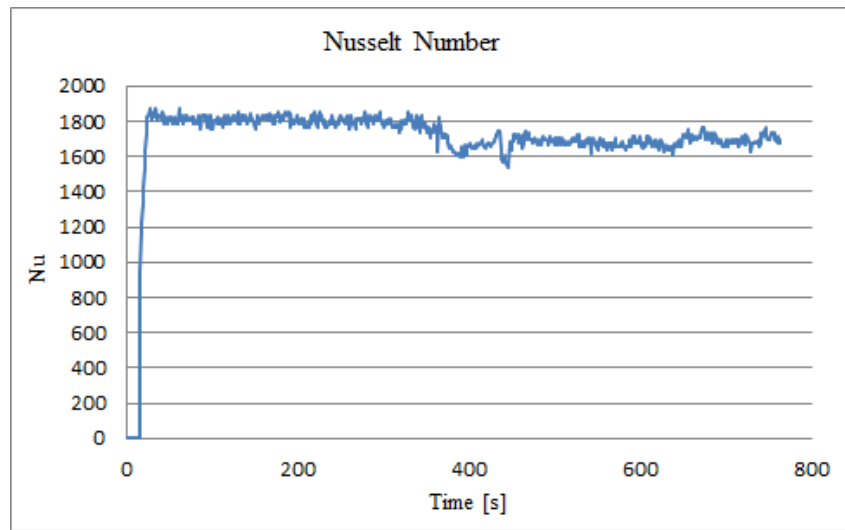


Fig. 8. Nusselt number



Fig. 9. Ablative material before, during and after the test

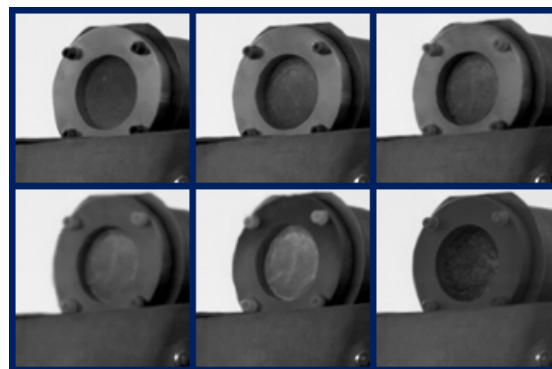


Fig. 10. High speed camera images of ablative material during the test

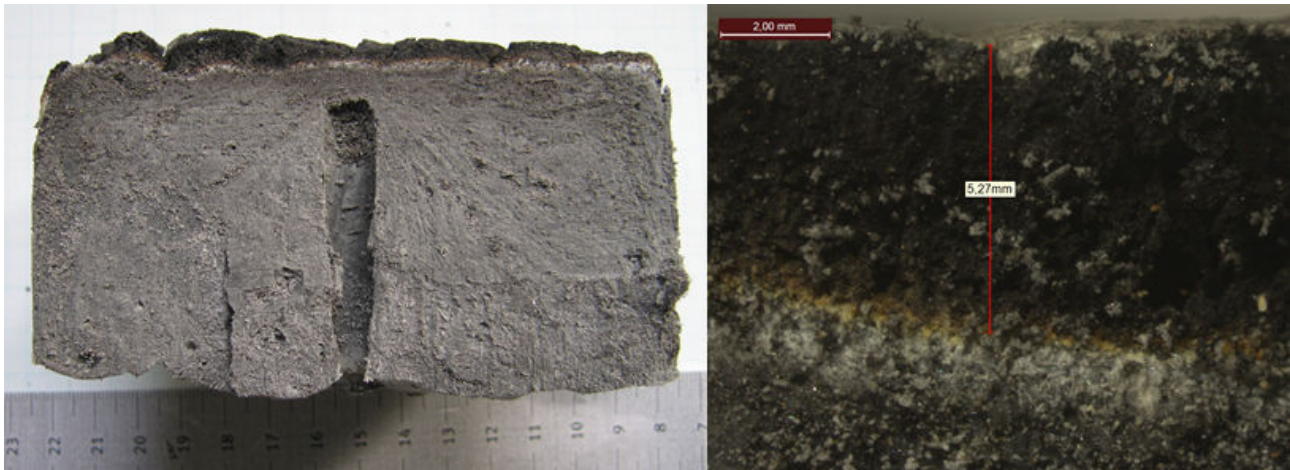


Fig. 11. Charred surface

CONCLUSION AND FUTURE DEVELOPMENT

The thermometric facility designed can test specimen of ablative and thermal protection materials in high speed hot gas flux ejected by aircraft turbine and the value of temperature, speed, enthalpy and heat flux reached are sufficient for comparison in performance of different materials. This because the screening of different materials is cost saving and useful before deep test to be performed in dedicated facilities. In addition the facility can be improved and easily adapted for different needs and configurations (materials tests, full scale and scaled models/systems tests, aircraft engine heat flux characterization, etc.) and it is conceived for dual uses applications covering either institutional aeronautical and also specific space applications. The maximum dimension of the specimen that can be tested is related to the dimension of the nozzle of the aircraft. Another possible application for the facility could be related to the thermo-mechanical test of full scale or scaled inflated/deployed system.

All tests performed were successful and the performance reached by the facility are sufficient to test ablative and thermal protection materials, then there are a lot of activities in progress and in particular they are related to the specimens chemical and physical characterization, the adaptation of the test facility to different aircrafts with ground fixed base analysis in order to decrease the logistic effort, and test activities on thermal protections for aeronautical application.

REFERENCES

- [1] Y.A. Cengel and A.J. Ghajar, *Heat transfer, a practical approach*, 2nd ed., McGraw Hill, chapter 7, 2002.
- [2] W.M. Rohsenow, J.P. Hartnett, Y.I. Cho, *Handbook of heat transfer*, 3rd ed., McGraw Hill, chapter 6, 1998.
- [3] R. Wiberg and N. Lior, "Convection heat transfer coefficients for axial flow gas quenching of a cylinder", Proceedings of the 4th International Conference on Quenching and the Control of Distortion, 20 - 23 May, 2003, Beijingin.
- [4] G.R. Ahmed and M.M. Yovanovich, "Analytical method for forced convection from flat plates, circular cylinders, and spheres", *Journal of thermophysics and heat transfer*, vol. 9, No. 3, July - September 1995.
- [5] F.P. Incropera and D.P. Dewitt, *Fundamentals of Heat and Mass Transfer*, 5th ed., John Wiley & Sons Canada, Ltd. 2001.
- [6] G. Giovangrossi and A. Piro, "SPEM: SPacecrew Emergency system", 3rd IAASS Conference, 21 - 23 October, 2008, Rome.
- [7] A. Esposito, F. De Rosa, V. Caso, F. Parente, "Design of slug calorimeters for re-entry tests", IPPW-7, 14-18 June, 2010, Barcelona.

**7th European Workshop on Thermal Protection
Systems and Hot Structures**

High speed gas turbine exhaust facility for TPS materials testing

8 – 10 April 2013

**ESA-ESTEC, Noordwijk, The Netherlands
Newton Room 1 and 2**

Pasquale Bonfà*
Aero Sekur SpA – Space BU

Maj. Ferdinando DOLCE, PhD
Italian Air Force – Flight Test Center

Index

- ✓ AS and ItAF overview
- ✓ Aim and context
- ✓ Set up overview and description
- ✓ Expected design environment
- ✓ Test configuration
- ✓ Test results
- ✓ On going activities
- ✓ Conclusion and future development

AS Overview

May, 2004

IRT
(Inflatable Reentry Technologies)

Tested at CIRA Scirocco Facility in order to prove the viability of the inflatable technology for Thermal Protection Shield application.

Sep, 2008

SPEM
(SPacecrew Emergency Module)

Project aimed to develop and test the inflatable Thermal Protection Shield for planetary reentry with a system level demonstrator designed to perform an assisted reentry mission for emergency spacecrew rescue; it was tested at CIRA Scirocco Facility.

2010 —→ In progress

GSE SPEM
(Ground Support Equipment for SPacecrew Emergency Module)

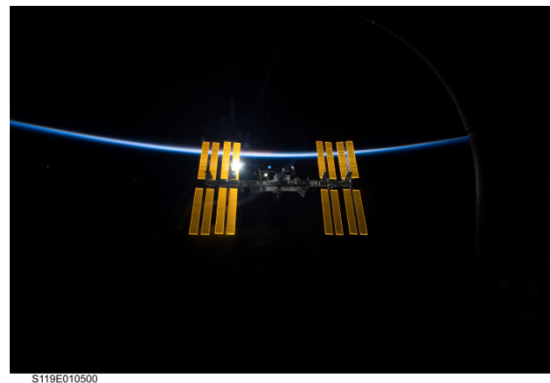
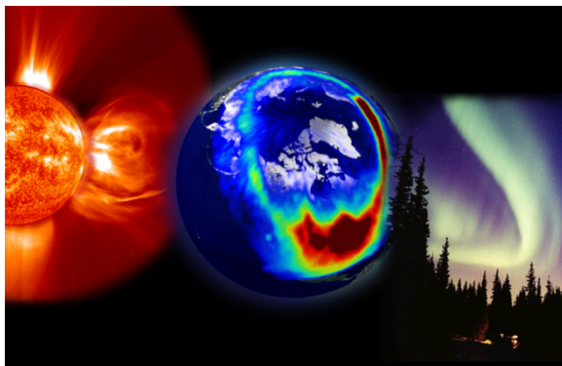
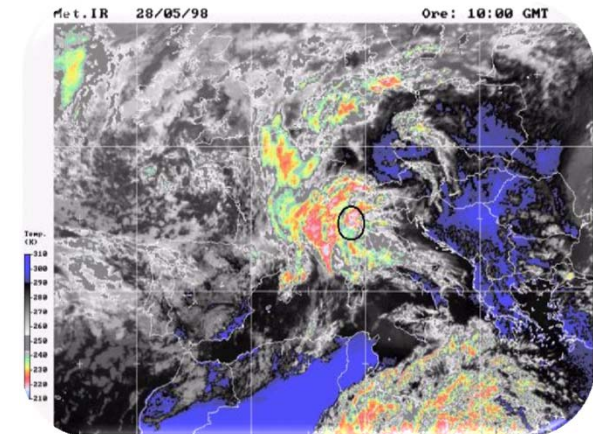
Facility for thermal material test



IT Air Force and Space

Strategic Guide Lines

- ✓ Support to Operational Capabilities
- ✓ Doctrine Evolution
- ✓ Human Spaceflight activities
- ✓ New technologies development



Aim and Context of the collaboration

Context of the collaboration:

- The study and the experimental evaluation of aerospace materials is actually one of the most challenging and money demanding issues in the aerospace science.
- In particular the development of thermal protections materials for aerospace applications can be considered as a relevant goal.
- In this context starts the collaboration between the ItAF (Italian Air Force) and AeroSekur, established since 2010.

Aim and Context of the collaboration

Aims of this collaboration are:

- developing a thermometric facility (Ground Support Equipment – GSE, property of ItAF) able to test specimens of thermal protection materials immersed inside an high speed hot gas flux ejected by aircraft turbine having enough energy to represent the application environment.
- evaluating flux enthalpy by measuring:
 1. gas speed;
 2. stagnation point and free stream temperatures;
 3. front and back temperatures in the specimen in order to evaluate the evolution of the thermal flux versus the time.
- characterizing material performance (chemical properties, physical properties, etc. ItAF)

Set-up overview

- **The GSE has been designed by Aero Sekur to test:**
 - ablative materials,
 - different thermal protections materials as those used for hot structures (combustion chambers, nozzles, thermo-structural protections for hypersonic flight).

- **Expected main advantages of this experimental method are:**
 - To be able to compare ablative and thermal materials performances before deep tests to be performed in a dedicated facility (arc jet and plasma tunnels); this allows a reduction of costs, enhancing the effectiveness of the qualification test programme, introducing, where necessary, a pre-qualification screening phase.
 - To be quick to use, flexible and adaptable to several applications with negligible impact in the test set up configuration.
 - Adaptability to different specimens sizes.
 - Capability of achieving test durations of several minutes.

Set-up overview

- **The drawbacks are mainly concerning:**
 - The representativeness of the environment, mainly for what the ablative materials are concerning, even if the enthalpies which can be achieved are sufficient to activate pyrolysis and to start ablation process.
 - In particular the environment is characterized by an high gas mass rate at lower speed and temperature compared to the plasma chamber.
 - Additional heat flux due to molecular recombination cannot be reproduced.

Therefore the method is considered cooperative/complementary to the standard facilities able to represent the re-entry environment, being effective whenever a comparison in performance of different materials is needed

Set-up description

The test facility is composed by:

- Calorimeter (GSE):

- Pitot tube;
- Thermocouples with exposed junction and grounded junction
- Specimen of ablative material insulated with mullite tube

- Calorimeter support (GSE);

- Thermistor for temperature control of the acquisition electronics (GSE);

- Acquisition electronics (GSE);

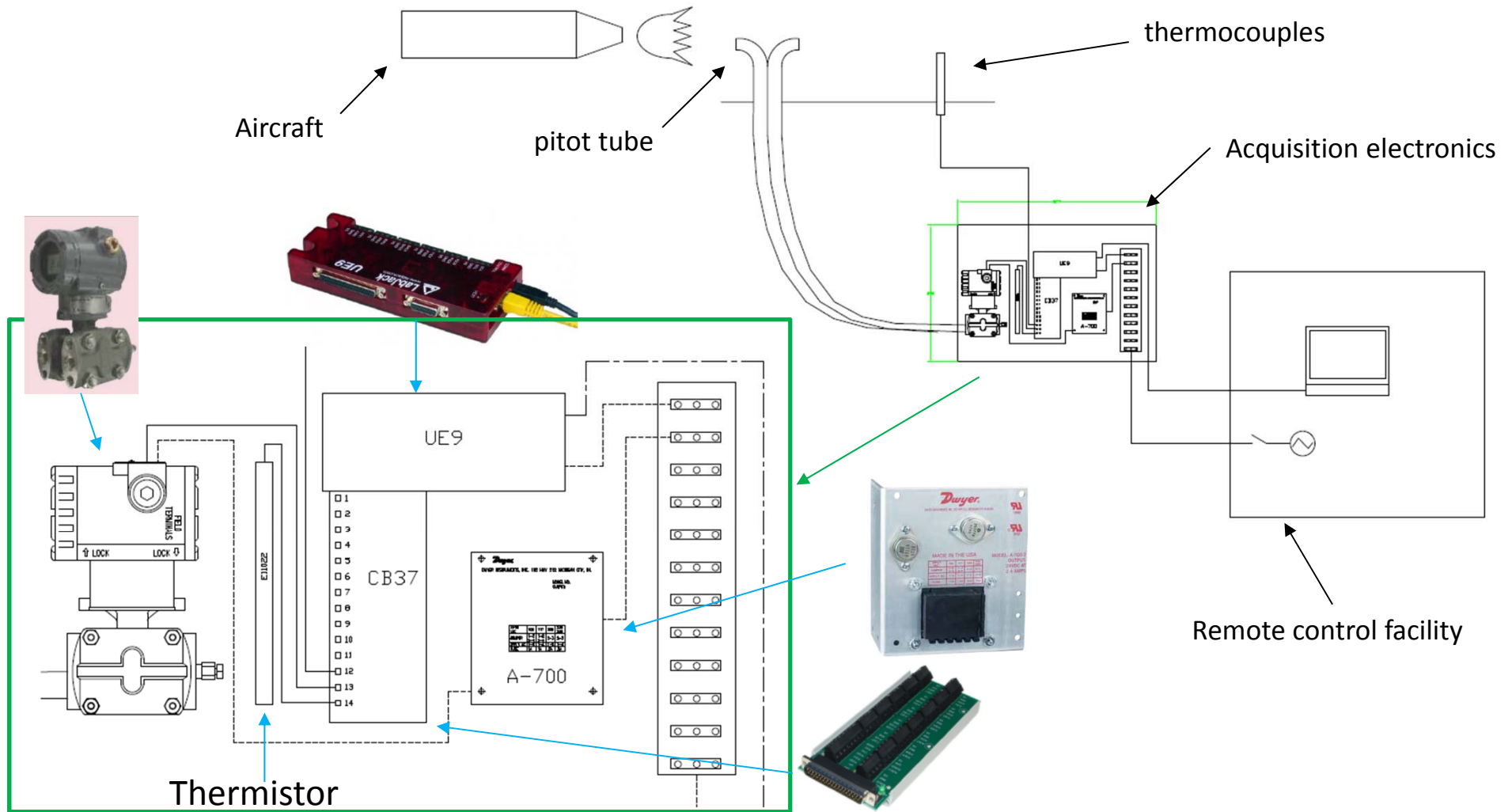
- Aircraft (provided by ItAF);

- Other tools (provided by ItAF):

- Remote control facility,
- Alignment tooling,
- High speed cameras,
- Overall logistic supports.



Set-up description



Set-up description - Calorimeter

Pitot tube

Specimen of ablative material insulated with mullite tube

Thermocouples:

- exposed junction (for flux characterization),
- grounded junction (for specimen characterization)

Both thermocouple types are insulated by mullite tubes.



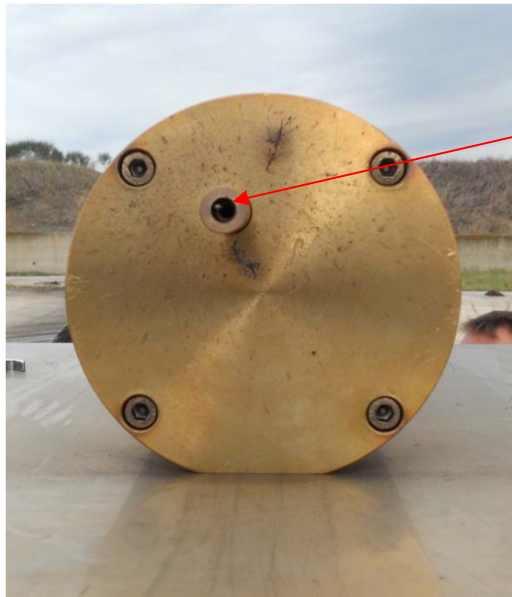
Calorimeter

Ground support structure

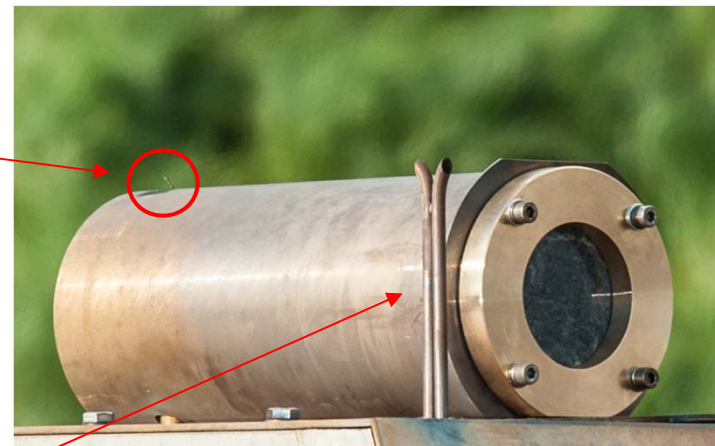
Calorimeter

Two different configurations

Calibration set up
Dummy sample



Specimen set up
Silicone elastomer ablative material



Exposed junction
thermocouple (for
flux characterization)

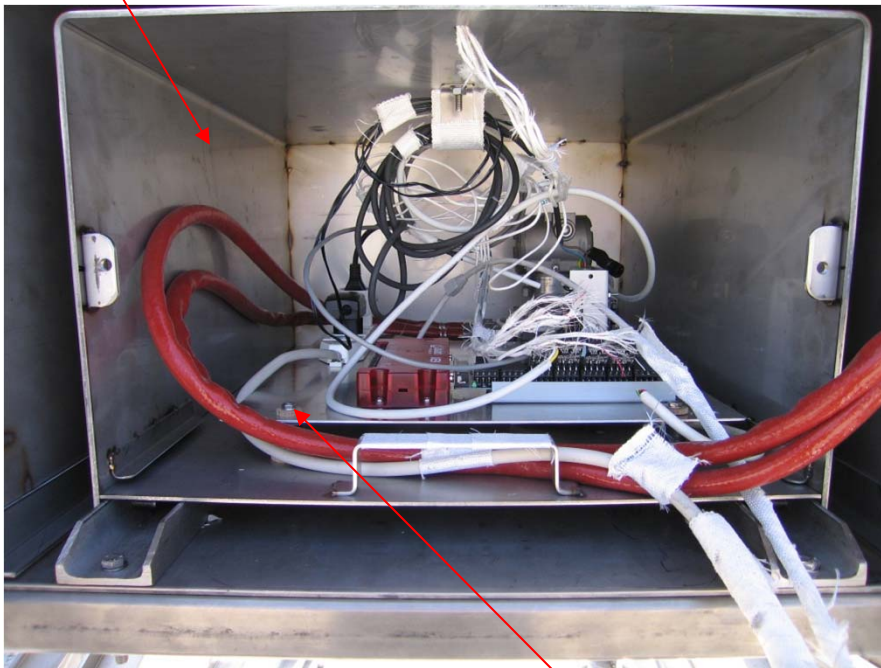
Pitot tube

Specimen with its mullite tube before
insertion in calorimeter structure



Set up description- Acquisition electronics

Dewar box to allocate acquisition electronics



Acquisition electronics protected by damped low conductance supports



Set-up description – Other tools



Remote control facility

Acquisition electronics



Aircraft

High speed cameras
(provided by ItAF)

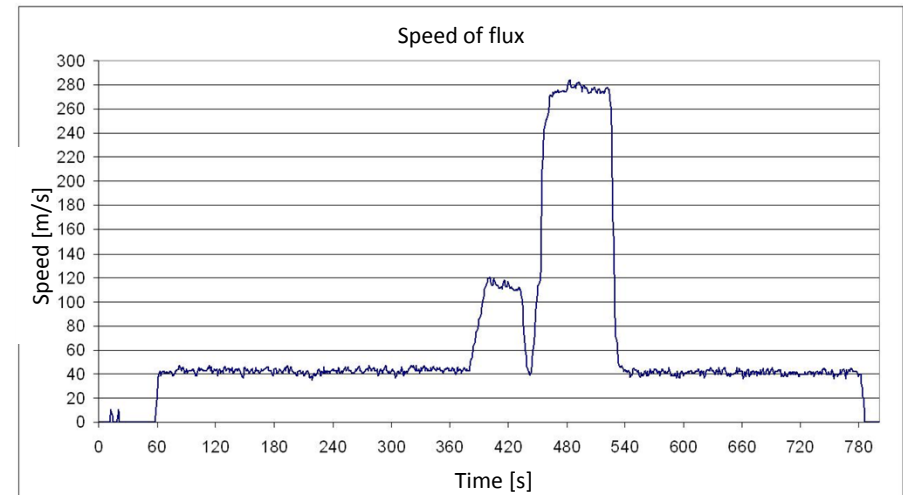
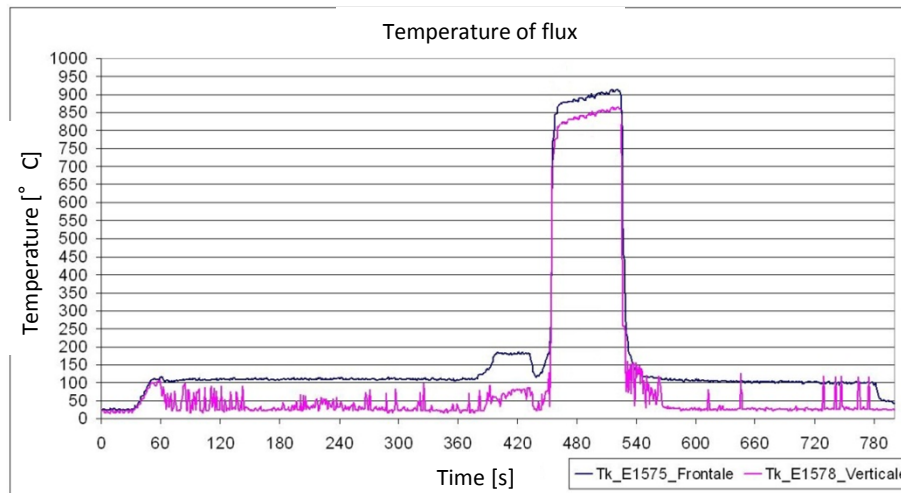
Expected Design Environment

- Aircraft environment characterization performed during test campaign (dummy sample), also in order to check and validate aircraft parameters like exhaust flux temperature and speed.
- The data obtained have been compared to the expected performance of the aircraft and used for the facility design.



- Reference Enthalpy to be achieved in the working point: $1,6 \text{ MJ/kg}$
- Reference heat flux: $0,4 \text{ MW/m}^2$
- Reference speed: $250\text{-}350 \text{ m/s}$
- Mach number: around 0,4
- Flow rate: $80 \text{ kg/m}^2\text{s}$

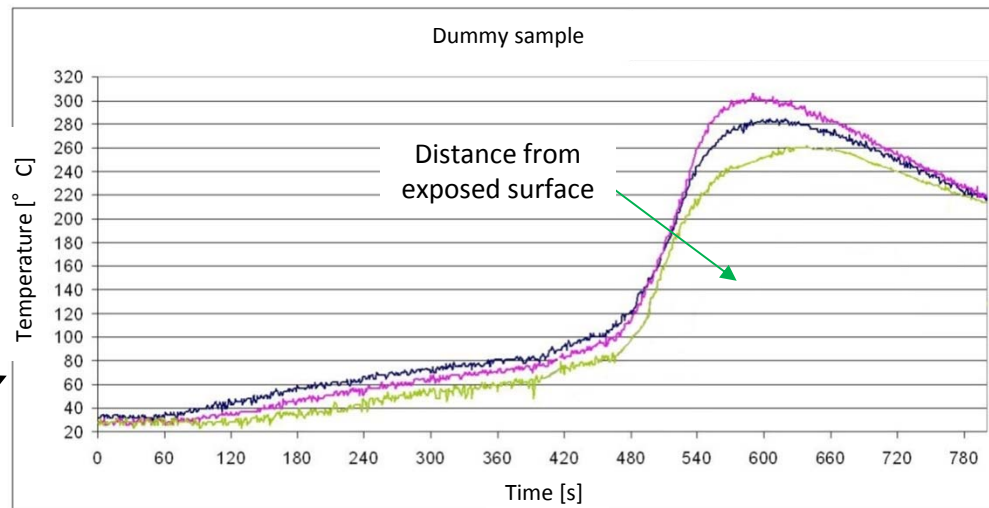
Test results – Calibration set up



Temperature of the hot gas flux

Speed of the hot gas flux

Temperature in the dummy sample

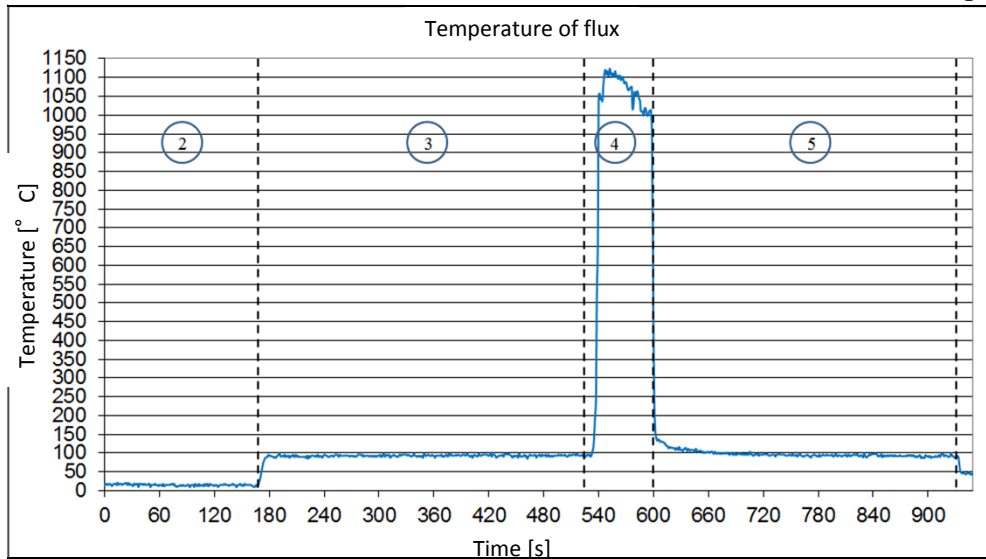


5.5 meters far from the aircraft engine nozzle

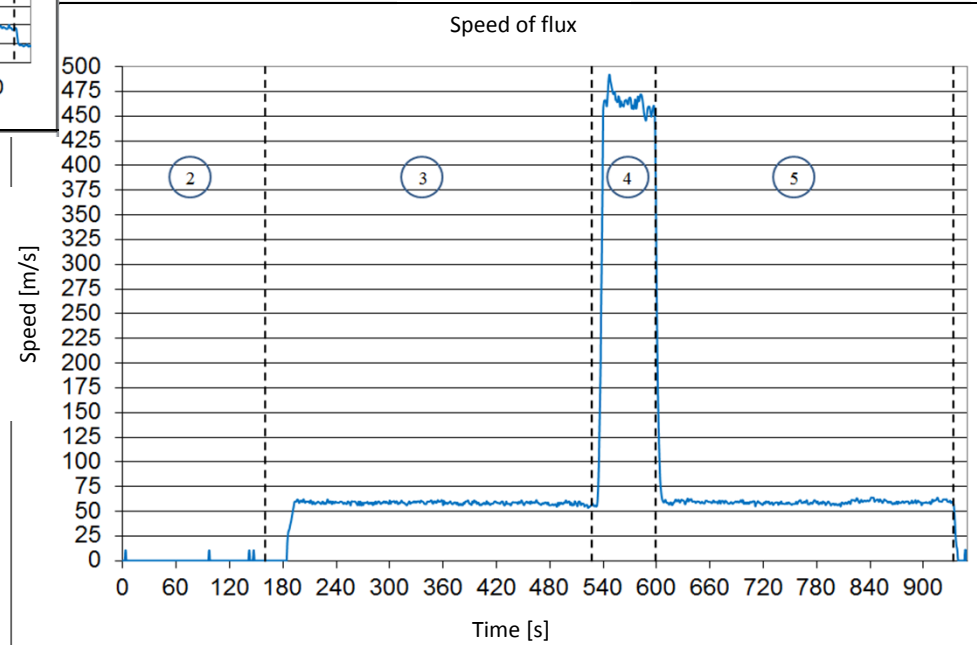
Test configuration

- The test was concerning two specimens of Silicone Elastomer (C/SiC) Ablative materials;
- The specimens have been placed at 4.5 meters from the aircraft engine nozzle at 2 meters height;
- The specimens have a diameter of 100 mm and a thickness of 50 mm;
- The specimens were inside mullite tubes to avoid heat dispersion;
- The aircraft provided at least three steps of increasing power before the achieving of the operating environment (this in order to reduce the transients);
- Full power test was about 80 secs long (it could be increased if necessary).

Test Results – Specimen set up



4.5 meters far from the aircraft engine nozzle

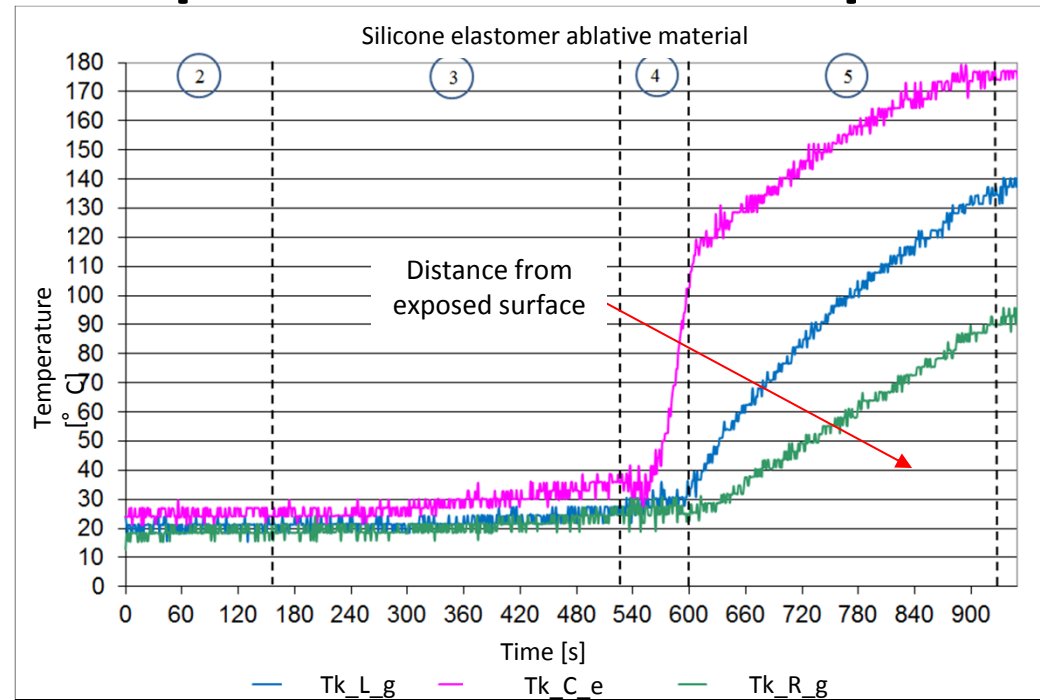


Temperature of the hot gas flux

Speed of the hot gas flux

Test Results – Specimen set up

Temperature in silicone elastomer ablative material measured respectively at 5mm from exposed surface (Tk_C_e), 10 mm (Tk_L_g) and 15 mm (Tk_R_g)



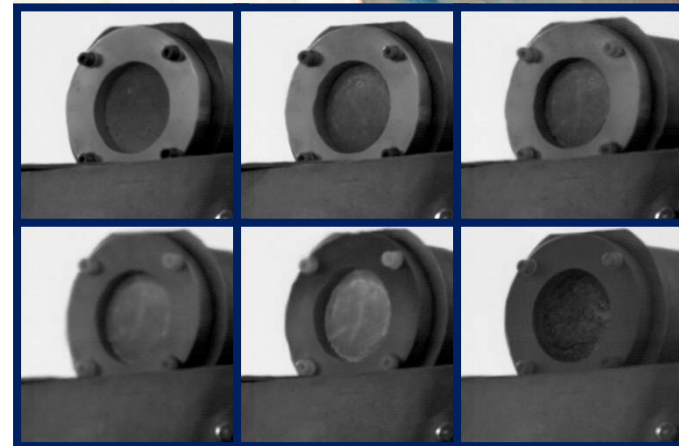
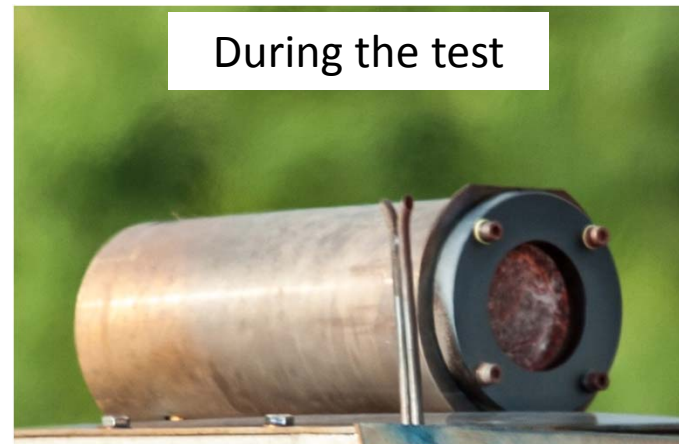
Parameter	Value	
Mach number	0,6	
Flow rate	120	Kg/m ² s
Enthalpy	1,9	MJ/kg
heat flux	0,5	MW/m ²

← Final values obtained

Test Results - Specimen



Test Results - Specimen



High speed camera results (up to 1800 fps)

Test Results - Specimen

The specimen started the ablation process which extended to about 2 mm of its exposed surface

Weight before the test	0,62735 kg
Weight after the test	0,61785 kg
Delta Weight	9,5 grams



On going activities

- Specimens chemical and physical characterization
- Adaptation of the test facility to different aircrafts
- Ground fixed base analysis in order to evaluate a logistic effort decreasing
- Test on thermal protections for aeronautical application

Conclusions and future developments

- The thermometric facility (Ground Support Equipment - GSE) designed is able to test specimens of thermal protection materials immersed inside an high speed hot gas flux ejected by aircraft turbine.
- Values of temperature, speed, enthalpy and heat flux reached during the test are sufficient for comparison in performance of different materials.
- Screening of different materials is useful and costs saving before deep tests in dedicated facility.
- The facility could be improved and easily adapted for different needs and configurations (materials tests, full scale and scaled models/systems tests, aircraft engine heat flux characterization,....).
- The facility is conceived to be used for dual uses applications, covering either institutional aeronautical and also specific space applications.

Thank you for the attention

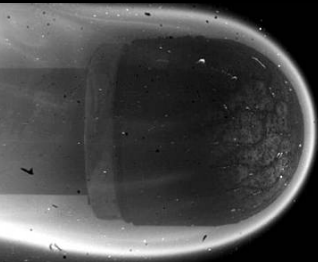
Any questions ?



Reference

Mr. Pasquale Bonfà
Aero Sekur S.p.A – Space BU
bonfa@sekur.it

Maj. Ferdinando DOLCE, PhD
Italian Air Force – Flight Test Center
ferdinando.dolce@am.difesa.it



TPS Testing in the Plasmatron Facility for Super-Orbital Re-Entry

7th European Workshop on TPS and Hot Structures



*ESA-ESTEC,
Noordwijk, The Netherlands*
8 - 10 April 2013



Vrije
Universiteit
Brussel

Bernd Helber^{1,2}, Thierry Magin¹, Olivier Chazot¹

¹Aeronautics and Aerospace Department, von Karman Institute for Fluid Dynamics, Belgium

²Research Group Electrochemical and Surface Engineering, Vrije Universiteit Brussel

Outline

- 1 Introduction: High Speed Re-entry
- 2 Ground testing in Plasmatron facility
- 3 Results Flow Field: Boundary Layer Chemistry
- 4 Results Material Field: Surface & Char Examination
- 5 Conclusions and Perspective

ACKNOWLEDGEMENTS

Funding and materials
supply:



In particular:

- Jean-Marc Bouilly (EADS Astrium ST)
- VKI Plasmatron team (P. Collin, I. Sakraker, Y. Babou, D. Lequang)
- VUB SURF research team (I. Vandendael, O. Steenhaut)

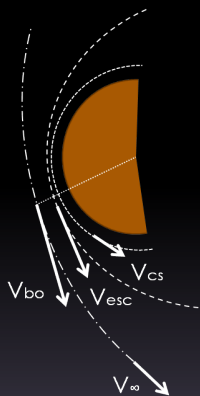
Outline

- 1 Introduction: High Speed Re-entry
 - Reentry Environment Overview
 - Strategy for High Speed Reentry & Material Response Characterization
- 2 Ground testing in Plasmatron facility
- 3 Results Flow Field: Boundary Layer Chemistry
- 4 Results Material Field: Surface & Char Examination
- 5 Conclusions and Perspective

Orbital Trajectories and Entry Velocities

Total energy conservation (vis-viva equation):

$$\epsilon = \frac{v^2}{2} - \frac{\mu}{r} \quad (1)$$



- Elliptic trajectory ($\epsilon < 0$): Orbital velocity

$$v_o \approx \sqrt{\frac{\mu}{r}} \quad (2)$$

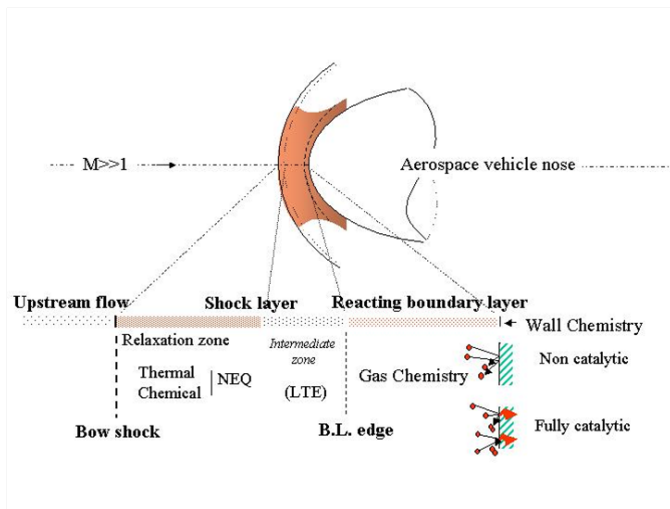
- Parabolic trajectory ($\epsilon = 0$): Escape velocity

$$v_{esc} = \sqrt{\frac{2\mu}{r}} \quad (3)$$

- Hyperbolic trajectory ($\epsilon > 0$): Escape + excess velocity

$$v^2 = v_{esc}^2 + v_{\infty}^2 \quad (4)$$

Reentry Environment Overview (1)



Reentry Environment Overview (2)

Complex Multiphysics - Multiscale Problem

Radiative and convective heating



Pyrolysis of phenolic resin
 C_6H_5-OH ($>200^\circ C$)

Ablation

Chemical mechanisms

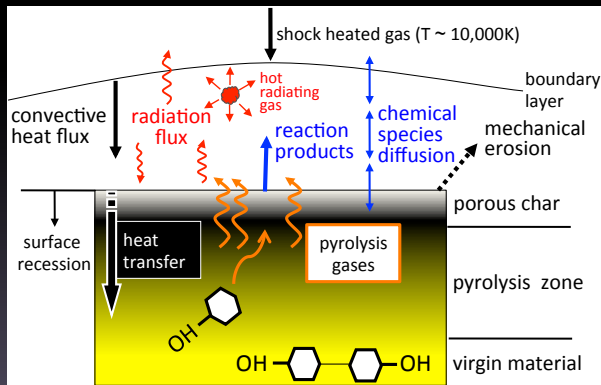
oxidation (CO , CO_2),
 nitridation (CN)

Phase changes

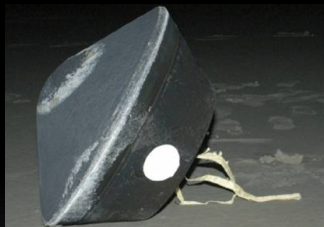
melting,
 sublimation (C , C_2 , C_3)

Mechanical removal

spallation, shear stress,
 melt removal



New Porous, Lightweight Ablators



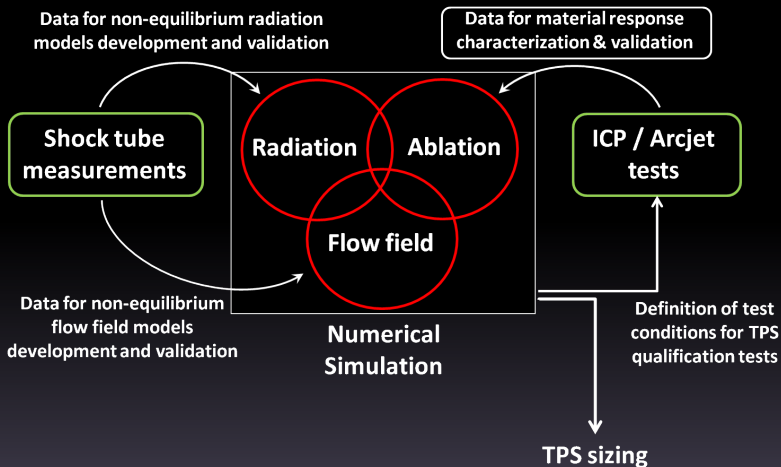
Stardust probe (2006, 12.9 km/s, [1])

- New low weight materials (PICA, ASTERM) [2, 3]
- New missions (Asteroid / Mars sample return)

Modeling tools inherited from Apollo program (1960s) [4]

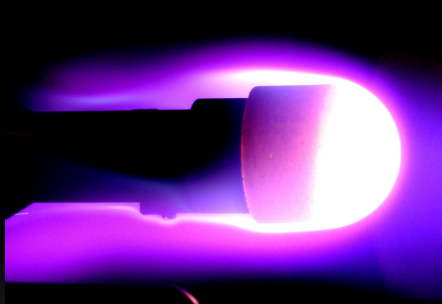
- new material response models [5]
- qualification of materials & validation of models required [6]

Strategy for High Speed Reentry Characterization

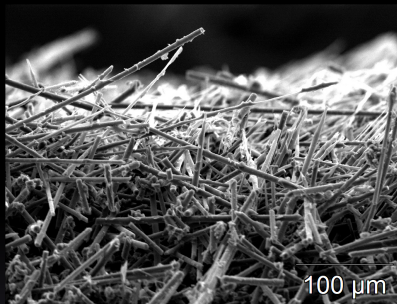


Material Response Characterization

Research Strategy and Objectives



VKI: Analysis in High-Enthalpy Plasma Flows



VUB: Multiscale Characterization

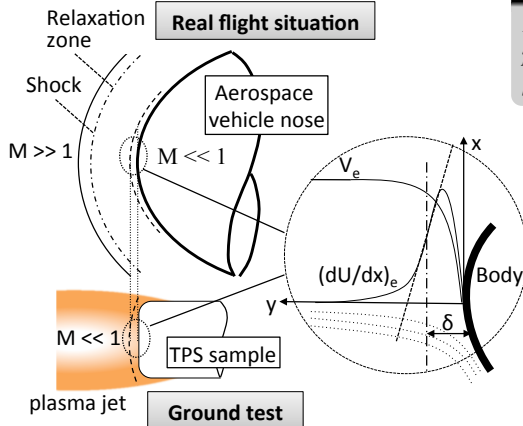
- Gas phase:
 - pyrolysis gas chemistry
 - transport phenomena & radiation in the boundary layer
- Material:
 - thermal performance and internal degradation
 - char ablation zone and degradation of carbon fibers

Outline

- 1 Introduction: High Speed Re-entry
- 2 Ground testing in Plasmatron facility
 - Local Heat Transfer Simulation: LHTS
 - Plasmatron Facility
 - Measurement techniques
- 3 Results Flow Field: Boundary Layer Chemistry
- 4 Results Material Field: Surface & Char Examination
- 5 Conclusions and Perspective

Local Heat Transfer Simulation (LHTS)

- Plasmatron design based on LHTS methodology
- Revision for high heat flux condition



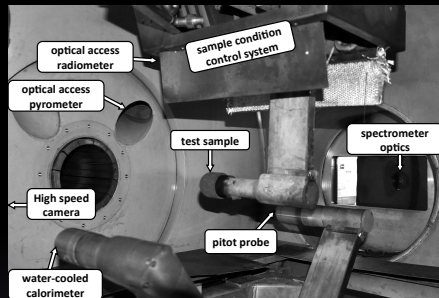
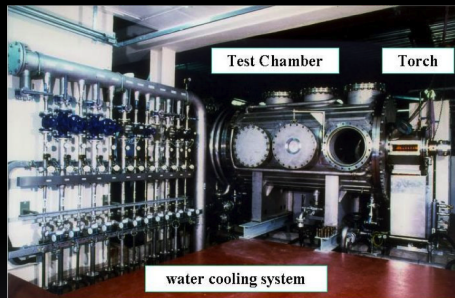
Stgn.pt. heat flux similarity:

$$H_f = H_{exp},$$

$$p_f = p_{exp},$$

$$\beta_f = \beta_{exp}, \beta = (dU/dx)_e \quad [7]$$

1.2 MW Inductively Coupled Plasmatron

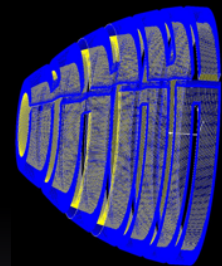


Plasmatron test chamber showing experimental setup and torch exit

- Gases: Air, N₂, CO₂, Ar
- Power: 1.2 MW
- Heat-flux: 90 kW/m² - >8 MW/m²
- Pressure: 10 mbar - 1 atm
- Water-cooled sample retention system

1.2 MW Inductively Coupled Plasmatron

High Heat Flux Condition



Subsonic jet with 80mm contraction and cooling channel computation

- Converging nozzle AR = 4
- Sufficient cooling of nozzle & probe holders
- Facility operational at full power

1.2 MW Inductively Coupled Plasmatron

High Heat Flux Condition

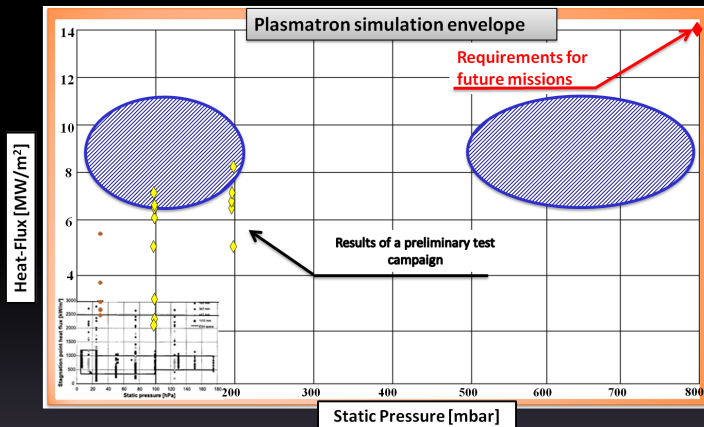


Subsonic jet with 80mm contraction and Gardon gauge

- Converging nozzle $AR = 4$
- Sufficient cooling of nozzle & probe holders
- Facility operational at full power
- Clean signals measured with Gardon gauge

1.2 MW Inductively Coupled Plasmatron

High Heat Flux Condition



- Extension of the operating envelope to 8.2 MW/m² (subsonic)
 - Extension of envelope to higher pressures (800mbar, moderate heat flux)
- Further increase of heat flux and extension to higher pressures

Materials of Investigation



Carbon fiber preform (Mersen Scotland Holytown Ltd.)

- chopped carbon fibers, fully carbonized no phenol content
 - density: 180-210 kg/m³, porosity: 90%
- cf. 3rd PhD Symposium, VKI [8]



AQ61 (EADS Astrium ST)

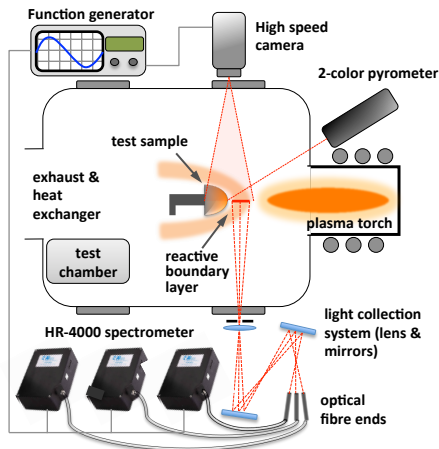
- low density carbon-phenolic
- made of short carbon fibers impregnated with phenolic resin
→ compacted & pyrolysed
- low resin content



ASTERM (EADS Astrium ST)

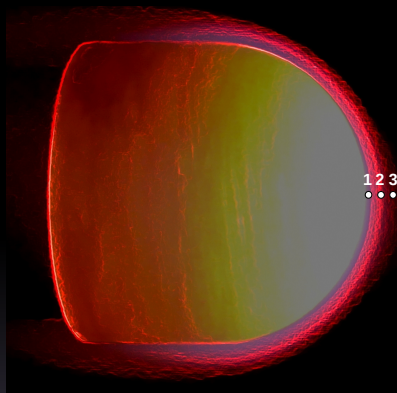
- low density carbon-phenolic
- rigid graphite felt impregnated with phenolic resin
→ polymerization
- precursor similar to carbon fiber reform

Experimental Techniques for Ablation Characterization



- Radiometry
surface temperatures & emissivity
- In-depth thermocouples
internal temperature histories
- High-speed-camera
 - in-situ recession analysis
 - in-situ determination of spectrometer probing locations
- Optical emission spectroscopy
temporally and spatially resolved radiation profiles in the boundary layer
 - chemical composition
 - temperature estimation

Experimental Techniques for Ablation Characterization



- Radiometry
surface temperatures & emissivity
- In-depth thermocouples
internal temperature histories
- High-speed-camera
 - in-situ recession analysis
 - in-situ determination of spectrometer probing
- Optical emission spectroscopy
temporally and spatially resolved radiation profiles in the boundary layer
 - chemical composition
 - temperature estimation

Experimental Techniques for Ablation Characterization

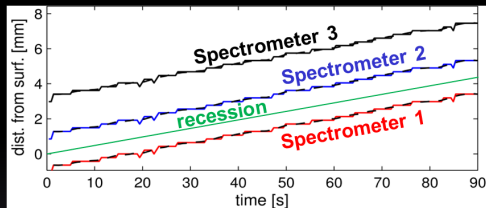
Determination of recession and spectrometer distances

movie loading...

Experimental Techniques for Ablation Characterization

Determination of recession and spectrometer distances

movie loading...

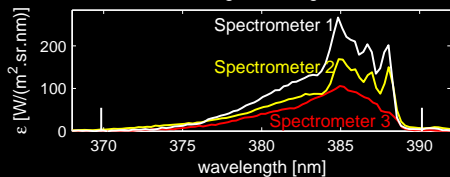


Outline

- 1 Introduction: High Speed Re-entry
- 2 Ground testing in Plasmatron facility
- 3 Results Flow Field: Boundary Layer Chemistry
 - Boundary Layer Radiation Profiles
 - CN Radiation Simulation for Temperature Estimation
- 4 Results Material Field: Surface & Char Examination
- 5 Conclusions and Perspective

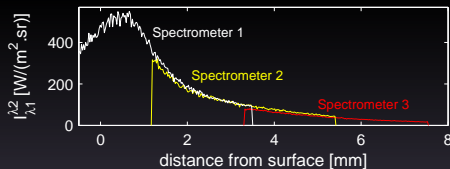
CN Spatial Radiation Profiles in Boundary Layer

Integration range

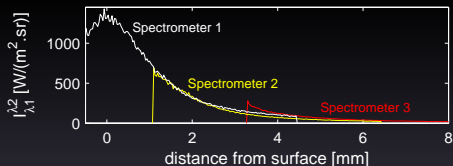


$$I_{CN}^{(t)} = \int_{370nm}^{390nm} \epsilon(\lambda) d\lambda \quad (5)$$

Carbon Preform (no phenol)

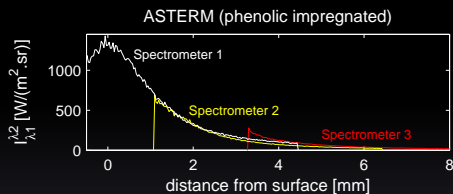
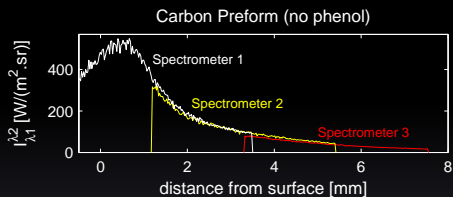


ASTERM (phenolic impregnated)



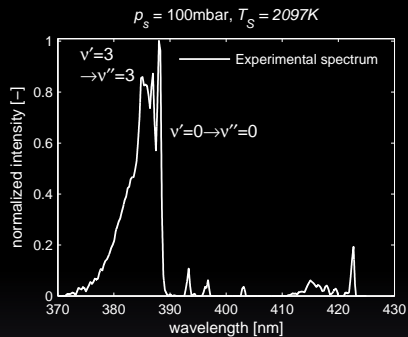
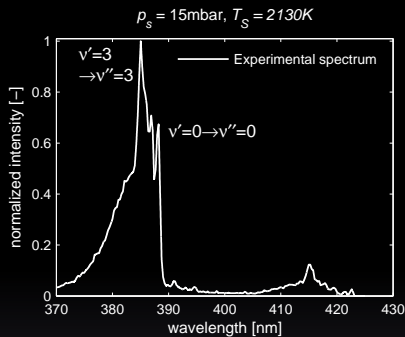
CN Spatial Radiation Profiles in Boundary Layer

- Correlation of 3 adjoin spectrometers → steady ablation process
- 2-times higher radiation for ASTERM
→ probably due to high reactivity of carbonized resin in char layer



We are interested in temperature and concentration profiles in the boundary layer
→ use molecular radiative signature of CN violet system

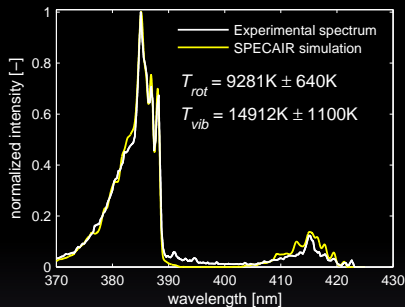
CN Radiation Simulation for Temperature Estimation



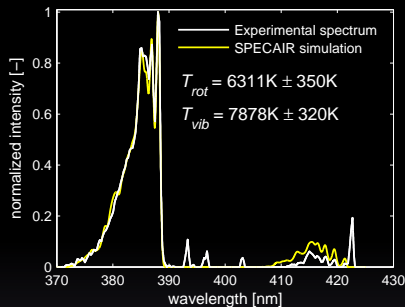
- Vibrational levels variations for different chamber pressures (close to wall)
→ temperature estimation using simulation tool SPECAIR [9]
- Simulated spectra reveal non-thermal vibrational level distribution of CN violet at low chamber pressure (higher deviation w.r.t. T_{rot} and T_{vib} using a Boltzmann distribution)
→ Check for various distances off the surface

CN Radiation Simulation for Temperature Estimation

$p_s = 15\text{mbar}$, $T_s = 2130\text{K}$

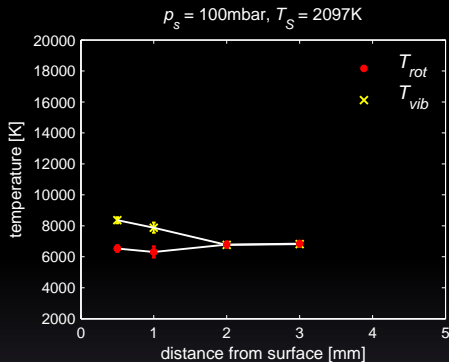
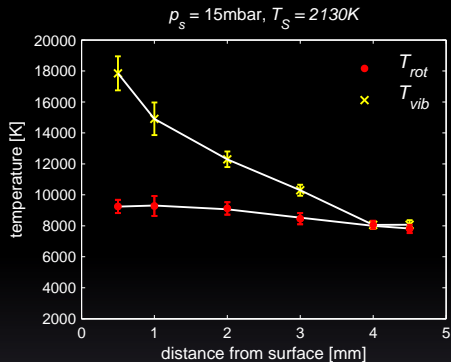


$p_s = 100\text{mbar}$, $T_s = 2097\text{K}$



- Vibrational levels variations for different chamber pressures (close to wall)
→ temperature estimation using simulation tool SPECAIR [9]
- Simulated spectra reveal non-thermal vibrational level distribution of CN violet at low chamber pressure (higher deviation w.r.t. T_{rot} and T_{vib} using a Boltzmann distribution)
→ Check for various distances off the surface

Boundary Layer Temperature Profile



- Deviation from thermal EQ close to the wall (low pressures)
- Equilibrating effect throughout BL
- Mainly equilibrium cond. at high pressure (right)

Boundary Layer Temperature Profile

Non-Equilibrium condition?

- Only electrically excited states are probed (CN B-X), not the ground state
only in equilibrium reliably related to total number densities

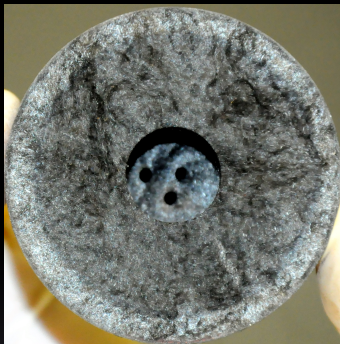
$$N_i = N \cdot \frac{g_i}{Q} \cdot \exp\left(\frac{-E_i}{k_B T}\right) \quad (3)$$

- SPECAIR based on Boltzmann distribution for equilibrium population N_i
→ possible deviation of excited populations from Boltzmann distribution yielding stronger excitation of higher vibrational levels
 - Thermal non-equilibrium at the reactive wall?
- ⇒ LIFBASE for simulation of spectra following a deviation from Boltzmann population
- ⇒ Results useful for comparison/validation of models including excited states

Outline

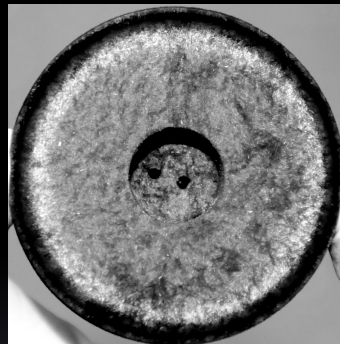
- 1 Introduction: High Speed Re-entry
- 2 Ground testing in Plasmatron facility
- 3 Results Flow Field: Boundary Layer Chemistry
- 4 Results Material Field: Surface & Char Examination
 - Macroscopic: Post-Test Inspection
 - Post-Test Microscopic Inspection
- 5 Conclusions and Perspective

Post-Test Visual Inspection



after ablation in air

- Macroscopic char identification
- Symmetric charring of AQ61

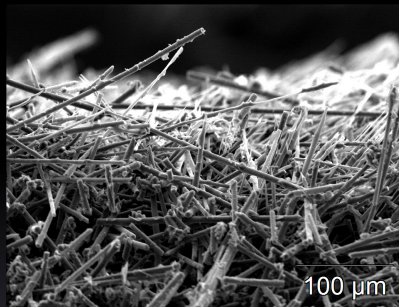


after ablation in N₂

- Black char over whole surface
- Symmetric charring of AQ61

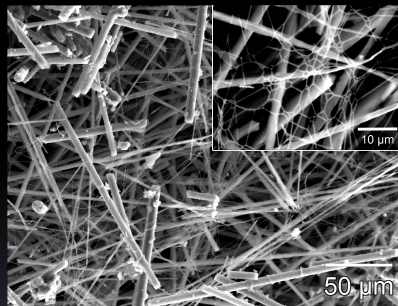
Post-Test SEM Inspection: Stagnation Point

AQ61 in air



- icicle shaped fibers & high porosity (charred resin sparsely identified)

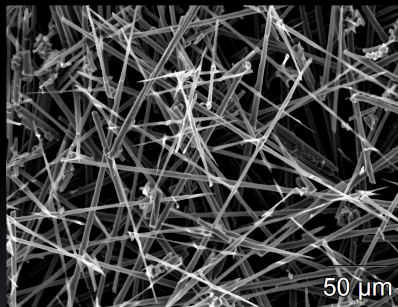
AQ61 in N₂



- 'cross filaments' found on the surface
- Catenation?: Strong carbon bounds formed from gas-phase

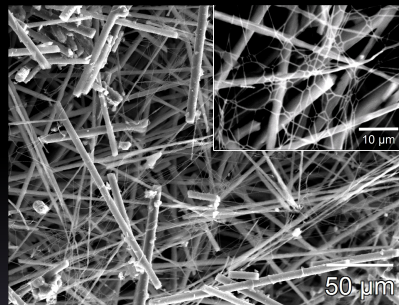
Post-Test SEM Inspection: Stagnation Point

AQ61 in air



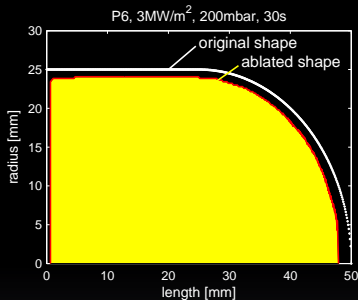
- icicle shaped fibers & high porosity (charred resin sparsely identified)

AQ61 in N₂



- 'cross filaments' found on the surface
→ Catenation?: Strong carbon bounds formed from gas-phase

Blowing Rate Determination



$$\dot{m}_{pg} + \dot{m}_c = \frac{m_{tot,exp}}{t_{exp}} \quad (5)$$

$$\dot{m}_{pg} = \dot{m}_{tot} - \frac{V_{abl} \cdot \rho_c}{t_{exp}} \quad (6)$$

Carbon Preform (no phenol):

$$\rightarrow \dot{m}_c = \dot{m}_{tot} = V_{abl} \cdot \rho_{cp}$$

$$\dot{m}_{meas} = 74.6 \pm 0.03 \text{ [mg/s]}$$

$$\dot{m}_{HSC} = 61.3 \pm 4.00 \text{ [mg/s]}$$

- char density required
- gas mass blowing rate
- experiment vs. num. model

Outline

- 1 Introduction: High Speed Re-entry
- 2 Ground testing in Plasmatron facility
- 3 Results Flow Field: Boundary Layer Chemistry
- 4 Results Material Field: Surface & Char Examination
- 5 Conclusions and Perspective

Conclusions and Perspectives

Plasmatron envelope: Extended to higher heat flux levels (converging nozzle)
Perspective: Campaign at supersonic flow regime

3 adjoin spectrometer: steady ablation process

Simulated spectra: deviation from LTE w.r.t. T_{rot} and T_{vib} (low chamber pressure) equilibrating throughout BL

Perspective:

→ Simulations with populations deviating from Boltzmann distribution

→ Simulation of other molecular emitter (e.g. C_2 Swan)

Post-test observation: Air: icicle shaped fibers w/ small ablation zone
 N_2 : strong corrosion & recombination of hydrocarbons
Estimation of gas blowing rate \dot{m}_{pg} (char layer density required)

⇒ Comparison with existing experimental data, stagnation line and material response codes (collaboration J.B. Scoggins, P. Schrooyen, A. Turchi (VKI), F. Panerai, J. Lachaud, N.N. Mansour (NASA ARC))

References

- [1] M. Stackpoole, S. Sepka, I. Cozmuta, Post-flight evaluation of stardust sample return capsule forebody heatshield material, in: AIAA 2008-1202, Reno, NV, USA, 2008.
- [2] H. Tran, C. Johnson, D. Rasky, F. Hui, M.-T. Hsu, T. Chen, Y. K. Chen, D. Paragas, L. Kobayashi, Phenolic Impregnated Carbon Ablators (PICA) as Thermal Protection Systems for Discovery Missions, in: NASA, TM 110440, 1997.
- [3] H. Ritter, O. Bayle, Y. Mignot, E. Boulrier, P. Portela, J.-M. Bouilly, R. Sharda, Ongoing european developments on entry heatshields and tps materials, in: 8th International planetary probe workshop, Portsmouth, Virginia, 6.-8. June, 2011.
- [4] R. Kendall, E. Bartlett, R. Rindal, C. Moyer, An analysis of the coupled chemically reacting boundary layer and charring ablator: Part i, NASA CR 1060, NASA (1968).
- [5] J. Lachaud, I. Cozmuta, N. Mansour, Multiscale approach to ablation modeling of phenolic impregnated carbon ablators, J. Spacecraft Rock. 47 (6) (2010) 910–921.
- [6] J.-M. Bouilly, L. Dariol, F. Leleu, Ablative Thermal Protections For Atmospheric Entry. An Overview Of Past Missions And Need For Future Programmes, in: Proceedings 5th European Workshop on Thermal Protection Systems and Hot Structures, Noordwijk, The Netherlands, 2006.
- [7] A. F. Kolesnikov, Conditions of simulation of stagnation point heat transfer from a high-enthalpy flow, Fluid Dyn. 28 (1) (1993) 131–137.
- [8] B. Helber, O. Chazot, T. Magin, A. Hubin, Ablation of carbon preform in the VKI Plasmatron, in: AIAA paper 2012-2876, 2012.
- [9] A. Cipullo, B. Helber, F. Panerai, O. Chazot, Experimental Characterization of the Free-stream Plasma Flow Produced by the VKI Plasmatron Facility using Optical Emission Diagnostics, in: RTO-EN-AVT-199, Paper 17, von Karman Institute, Rhode-Saint-Genèse, Belgium, 2012.

CHARACTERIZATION OF NEW HIGH HEAT FLUX TEST CONDITIONS IN L3K

Burkard Esser⁽¹⁾, Ali Gülhan⁽¹⁾

⁽¹⁾German Aerospace Center (DLR)
Supersonic and Hypersonic Technologies Department,
Linder Höhe, 51147 Köln, Germany
Email: Burkard.Esser@dlr.de, Ali.Guelhan@dlr.de

INTRODUCTION

When entering a planetary atmosphere, a space vehicle is subjected to severe heat loads caused by extremely high gas temperatures in the surrounding shock layer. While for reentries from low Earth orbit, reusable thermal protection structures are sufficient, ablator materials are required as a protective surface layer for entries into atmospheres of other planets as well as for Earth return missions. During the recent years, various sample return mission scenarios have been studied, considering e.g. a return from Mars, asteroids or comets. In general, an Earth return from an extraterrestrial object involves a hyperbolic trajectory resulting in atmospheric entry velocities around or above 12 km/s and resulting peak heat fluxes in the order of 10-18 MW/m².

DLR's arc heated facilities LBK, in particular the L3K test leg, had continuously been used for the characterization and qualification of ablative material during the last two decades. A principal sketch of the LBK facilities is shown in Fig. 1. In L3K, a segmented arc heater with a maximum electrical power of 6 MW is used to energise the working gas to high enthalpy conditions. Hypersonic free stream velocities are provided by a convergent-divergent nozzle. The nozzle's expansion part is conical with a half angle of 12°. Based on its conical geometry the nozzle could be designed modular. Different throat diameters from 14 mm to 29 mm are available and can be combined with several nozzle exit diameters. So, the facility setup can effectively be adapted to particular necessities of a certain test campaign. A more detailed description of the facility is given by Gülhan et al. [1,2,3].

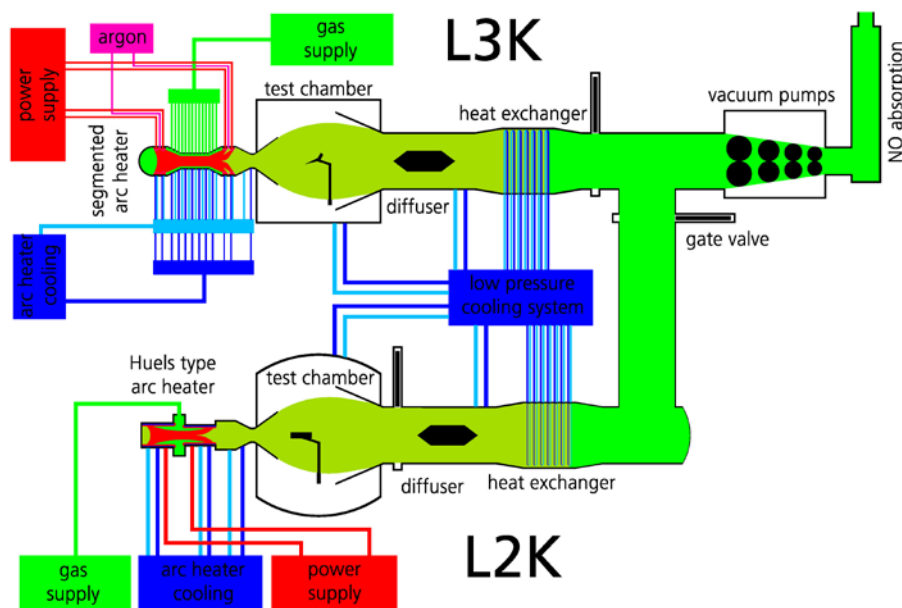


Fig. 1. DLR's arc heated facilities LBK with its test legs L2K and L3K.

Until 2009, the set of available nozzles included exit diameters of 100 mm, 200 mm, and 300 mm for L3K. Highest heat fluxes and stagnation pressures were obtained with the 100 mm nozzle exit. With this configuration, nevertheless, the test conditions were restricted to stagnation pressures up to 400 hPa and cold wall heat flux rates up to 6 MW/m² which is much below the above mentioned requirements for extraterrestrial Earth return.

HIGH HEAT FLUX TEST CONDITIONS

A new nozzle with an exit diameter of 50 mm was put into operation in 2009. The new nozzle was operated in combination with a 29 mm nozzle throat usually, and the arc heater was set up in 4-pack configuration with a total number of 64 constrictor segments. With the operating conditions listed in Table 1, the operational envelope of the L3K facility could be extended towards flight relevant heat fluxes and pressure levels with the 50 mm nozzle. Three test conditions were established for this configuration. All were obtained with the same operating condition, only test location was varied. Corresponding stagnation pressures and cold wall heat fluxes to a standard sample with 50 mm diameter are listed in Table 2. The maximal heat flux could be increased to 11.5 MW/m^2 at a pressure of 1294 hPa.

Table 1. Operating conditions for 4-pack configuration.

Gas mass flow rate [g/s]	180
Reservoir pressure [hPa]	6000
Reservoir temperature [K]	5775
Specific enthalpy [MJ/kg]	11.8

Table 2. Test conditions established for 4-pack configuration.

Distance from nozzle exit [mm]	150	85	70
Pitot pressure [hPa]	331	840	1294
Cold wall heat flux rate [mW/m^2]	5.0	10.0	11.5

These conditions were applied for ablator testing during several test campaigns, e.g. ESA's DEAM study. When comparing with the requirements for Earth return, the conditions, however, cover the lower range of required heat fluxes only, the while the achieved stagnation pressures are slightly above the requirements. Accordingly, additional considerations were initiated to further improve L3K's operating range towards higher heat fluxes at lower stagnation pressures.

In particular, an increase of total enthalpy was required and two methods were identified for realization. Firstly, the gas mass flow rate could be lowered, and secondly, the energetic efficiency of the arc heater could be improved by increasing the length of the arc. Eventually, both measures were applied in order to obtain maximal improvement. The arc heater was reconfigured to 5-pack configuration which increased the total number of constrictor segments to 80. By reducing the gas mass flow rate to 101 g/s it was possible to raise the total enthalpy to 15.9 MJ/kg. Additional operating parameters are listed in Table 3.

Table 3. Operating conditions for 5-pack configuration.

Gas mass flow rate [g/s]	101
Reservoir pressure [hPa]	3750
Reservoir temperature [K]	6462
Specific enthalpy [MJ/kg]	15.9

A detailed characterization of the hypersonic flow field has been performed for the 5-pack operating condition. Seven potential test conditions were identified, and the corresponding values of heat fluxes and stagnation pressures are listed in Table 4. The data indicate that the change of operating condition and arc heater configuration had the intended effects. The maximal cold wall heat flux could be increased to 13.6 MW/m^2 and the stagnation pressure could be decreased to 917 hPa.

Table 4. Test conditions for 5-pack configuration.

Test condition	FC-1				FC-2	FC-3	
Distance from nozzle exit [mm]	160	155	140	110	100	75	70
Pitot pressure [hPa]	210	225	290	516	588	840	917
Cold wall heat flux rate [mW/m^2]	6.1	6.4	7.2	9.3	10.1	12.8	13.6

The new test conditions were applied for the first time to thermal characterization of an ablative material in a test campaign on AQ61. AQ61 is an existing ablative material with a composition and thermal response behaviour very similar to the expected final product of the ongoing developments within DEAM. However, due to the specific

manufacturing process of AQ61, its production is not cost efficient. In particular, no cost efficient large scale production is feasible. For this reason there is no strategic interest in the material which makes it available as study material with the possibility to distribute the test results. The test campaign was initiated and supported by ESA, since plasma testing on AQ61 is expected to provide an important reference point for code assessment and improvement and might further help to fine-tune the right material combinations for the ongoing ablator developments.

The test results of the AQ61 campaign should be made available to the Ablation Working Group, which has been established on a European level under the lead of ESA and is aiming to assess the available numerical ablation codes towards their capability to reliably predict the behaviour of ablative material in order to assess the required ablator thickness on the heat shield of atmospheric entry vehicles. In the subsequent section the experimental setup, the test matrix and the achieved test results will be described in more detail.

EXPERIMENTAL SETUP

In total, 9 cylindrical samples made of AQ61 had been delivered for the test campaign. The samples were designed as flat-faced cylinders with a front diameter of 50 mm and a thickness of 40 mm. Photographs are shown in Fig. 2, a technical drawing is provided as Fig. 2c. The front surface has an edge radius of 4.4 mm and the rear surface was sharp-edged in order to provide a smooth and immediate transition to the model holder interfaces. On the backside the samples were glued to a 5 mm thick aluminium backing plate. 12 mm behind the front surface the cylinder's diameter is reduced to 43 mm in order to provide space for a ceramic shell that serves as a side protection. Four samples could be prepared with a slightly reduced front diameter of 47 mm only. All other details of these samples were identical to the nominal shape.

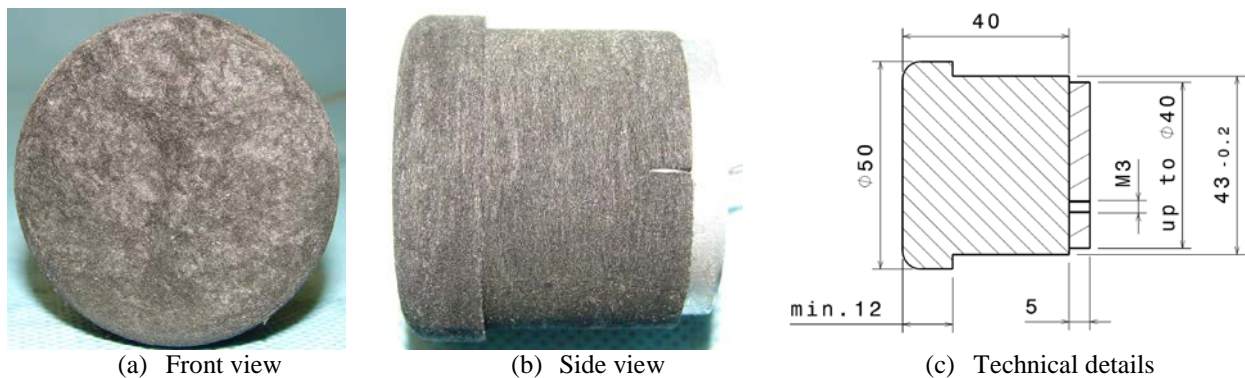


Fig. 2. AQ 61 sample.

The samples had been delivered pre-instrumented with 3 K-type thermocouples TC 1, TC 2, TC 3 to measure the temperature evolution at different locations inside the sample. The three measurement spots were located along the sample's axis. Thermocouple TC 1 was installed closest to the front surface, at a nominal distance of 10 mm. TC 2 and TC 3 were installed in a nominal depth of 15 mm and 25 mm, resp. All thermocouples were fed through a central bore hole in the backing plate and led along the backing plate to the sample's side wall, where they were directed upwards along the side wall and from there with a certain inclination to the measurement location. Preparation and instrumentation was performed by HPS Portugal.

In addition to the temperature measurements by integrated thermocouples the samples' surface temperature was measured by two pyrometers, a spectral pyrometer and a two-colour pyrometer. The pyrometers were aligned to the centre of sample in such a way that best front view could be realised. For the test campaign an emissivity value of 0.85 was set for the spectral pyrometer.

All samples were weighed before and after testing. Since the samples had been delivered ready for testing, these measurements include the backing plate as well as the thermocouples. To evaluate surface recession the samples' thickness was measured at three locations before and after the test.

TEST CONDITIONS AND TEST MATRIX

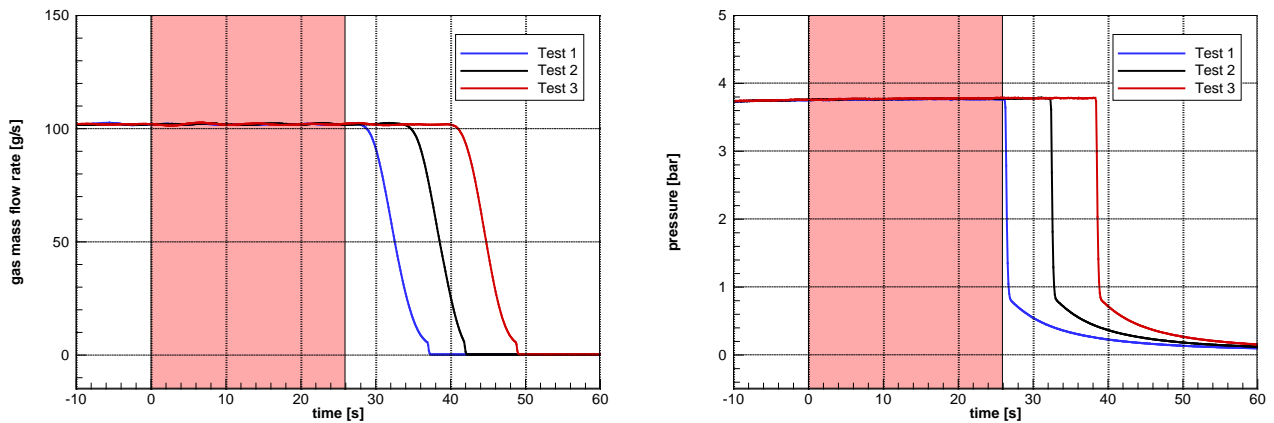
All tests of the campaign were performed in the L3K facility at the test conditions which are marked in Table 4 as FC-1, FC-2, and FC-3. The test campaign started with three tests at test condition FC-1. The test matrix in Table 5 indicates that the test duration was gradually increased from 26 seconds to 38 seconds. Test duration nominally started when the sample arrived at the test location on the axis of the flow field, and ended after the specified testing time by shutting down the arc heater.

Next three tests were performed at test condition FC-2. Due to the higher heat flux rate the test duration was reduced for these tests. The final three tests were carried out at test condition FC-3 with a heat load of 12.8 MW/m^2 . Test duration was again adjusted accordingly.

Table 5. Test matrix.

Test number	Sample diameter [mm]	Test condition	Heat flux rate [MW/m^2]	Test duration [s]
1	50	FC-1	6.1	26
2	47	FC-1	6.1	32
3	47	FC-1	6.1	38
4	47	FC-2	10.1	13
5	50	FC-2	10.1	16
6	50	FC-2	10.1	19
7	50	FC-3	12.8	10
8	50	FC-3	12.8	12
9	47	FC-3	12.8	14

The samples were tested in subsequent facility runs. Therefore, a good reproducibility of the test conditions is a fundamental prerequisite for a reliable comparison of measurements. In arc heated facilities the test conditions are directly related to the reservoir pressure and the gas mass flow rate. These two parameters must be well reproducible in order to achieve comparability of test results. Therefore, they are monitored continuously during facility operation. In Fig. 3 the time histories of gas mass flow rate and reservoir pressure are compared for the first three tests of the campaign. Within the testing period of the shortest test, which is indicated by the red background colour, the curves are almost identical indicating a good reproducibility of test conditions. During the tests with a longer duration the conditions remain constant until the facility is shut down.



(a) Gas mass flow rate

(b) Reservoir pressure

Fig. 3. Reproducibility of facility operating conditions.

TEST RESULTS

All tests could be run successfully as intended. The post-test photographs shown in Fig. 4 do not indicate any kind of damage or structural non-integrity. At all three test conditions the front surface of the samples appeared homogeneous after the test.

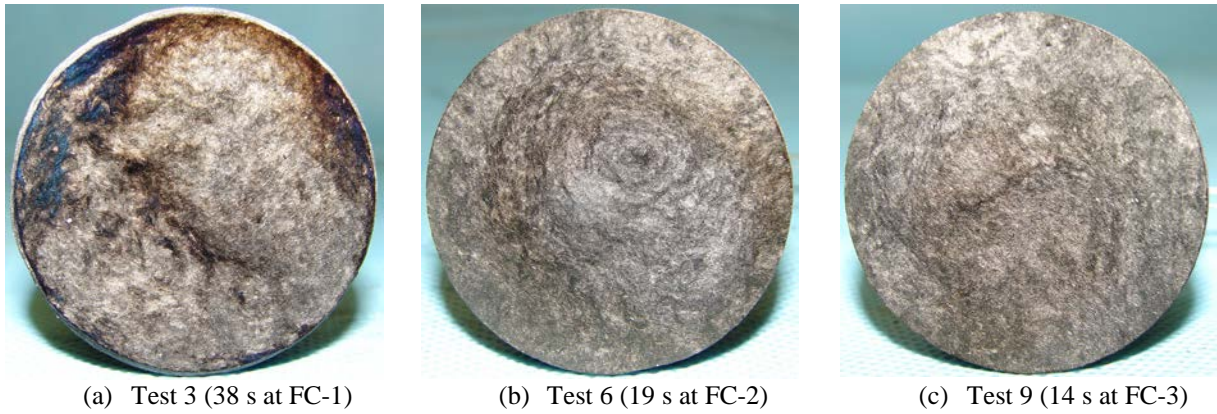


Fig. 4. Post-test appearance of the samples.

Tests at condition FC-1

In Fig. 5a the surface temperatures are plotted, which were measured with the pyrometers during test 1 at condition FC-1. In the figure the actual heating period is marked by a red background colour. Only within this period the reading of the pyrometers is physically relevant. At any other time the sample was placed outside the flow field and the pyrometers were not aligned to the sample's front surface providing an artificial reading of 900°C.

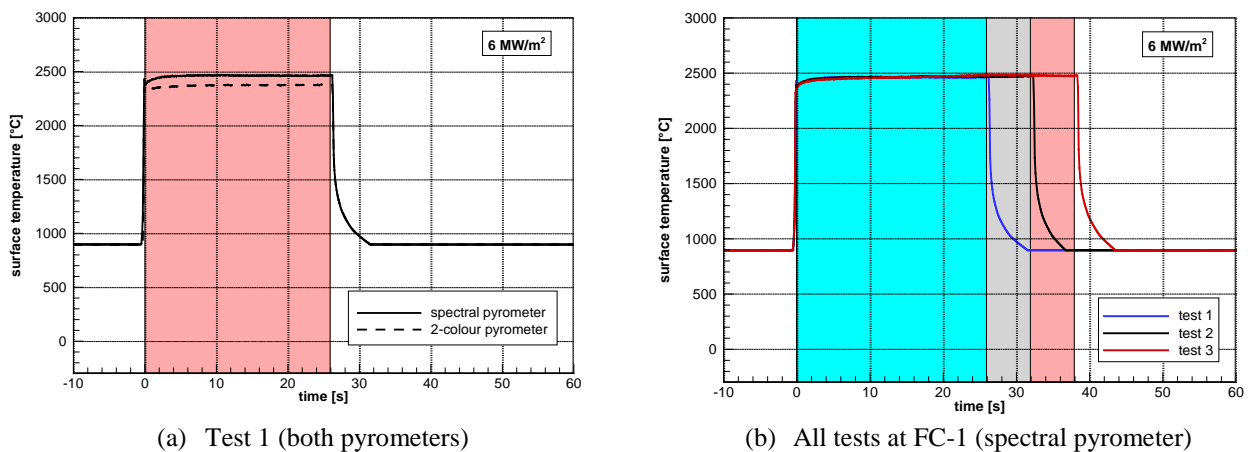


Fig. 5. Surface temperature measurements from tests at FC-1.

After having reached the test location the surface temperature immediately rises above 2300°C. Within the first five seconds the temperature further increases to nearly 2500°C. Afterwards, no significant temperature change is observed until the end of heating. There is a slight temperature difference of about 80 K between the measurements of the two pyrometers, with the spectral pyrometer indicating a higher surface temperature. There are two possible reasons for this difference. Firstly, there is an uncertainty in the emissivity value of 0.85 which was set for the spectral pyrometer. On the other hand, the measurement with a two-colour pyrometer is fundamentally based on the assumption that the AQ61 material behaves like a grey body in the pyrometer's sensitive wavelength regime.

A comparison of the surface temperatures measurements with the spectral pyrometer is shown in Fig. 5b for all three tests at condition FC-1. Except for the varying test durations, which are indicated by different background colours there are no obvious differences between the measurements. Even details of the time histories, e.g. the initial temperature jump as well as the slight subsequent increase, are well reproduced in all tests indicating an excellent repeatability at this test condition.

Thermocouple measurements from the tests at condition FC-1 are compared in Fig. 6. Again the heating periods are marked by a various background colours. The signals of the topmost thermocouple TC 1 are not included in the figure, because its readings were strongly irritated by a connector problem during all tests at condition FC-1. The other two

thermocouples, TC 2 and TC 3, provided similar results in all tests. During the first 20 seconds the measurements are very close. Afterwards the measurements differ, but the deviations can directly be related to the different test durations. Highest temperature increase is observed for test 3 with the longest duration, lowest for test 1 with shortest duration. This observation is in accordance with the fact that a larger total amount of heat is transferred to the sample with increasing test duration.

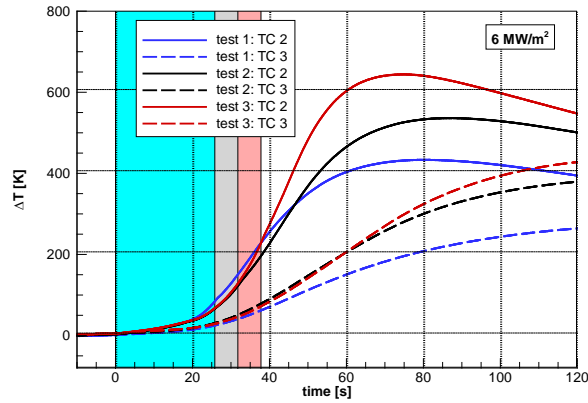


Fig. 6. Thermocouple measurements from tests at FC-1.

The erosion data, i.e. mass loss and surface recession, which were evaluated for the tests at condition FC-1, are listed in Table 6. Surface recession is given as an averaged value from the three thickness measurements. In addition to the absolute erosion data the corresponding erosion time rates are listed as well. According to the different test durations the rates provide a better basis for comparison. The mass loss rate also accounts for the different diameters of the samples' front surface.

Table 6. Erosion data from tests at FC-1.

Test	Duration [s]	Mass loss [g]	Mass loss rate [g/(m ² s)]	Surface recession [mm]	Recession rate [mm/s]
1	26.2	3.29	64.2	4.8	0.183
2	32.3	3.52	62.8	6.2	0.192
3	38.3	4.30	64.6	7.1	0.185

According to the increasing test duration mass loss and surface recession values increase from test 1 to test 3. The corresponding rates, however are similar. The mass loss rate is varying between 62.8 and 64.6 g/(m²s). In the relation to the mean value the variation is below ±2% for the mass loss rate and below ±3% for the recession rate.

Tests at condition FC-2

For the tests at test condition FC-2 the test duration was reduced to half the values, which had been used for condition FC-1, in order to obtain a roughly comparable total amount of heat. Again, three samples were tested at this condition. The surface temperatures measurements from the tests at condition FC 2 are compared in Fig. 7a. Except for the different test durations, the measurements are close with a slightly higher steady state temperature during test 6. The overall trend, however, is different to that observed at condition FC-1, since surface temperature reaches its final value immediately after the sample reaches the test position.

Thermocouple measurements from the tests at condition FC-2 are plotted in Fig. 7b. The problems with the signal line of TC 1 could be overcome for these tests. Therefore, TC 1 measurements are also included in the figure. Due to its position very close to the surface TC 1 reaches maximal reading during the hot testing phase during tests 4 and 6, nearly at the same time. During test 5, however, the temperature at TC 1 remains significantly lower and does not exceed above 950°C. From X-ray photographs that had been taken from all samples after thermocouple installation it was found that the different behaviour of TC 1 during test 5 was caused by a significantly larger installation depth of TC 1.

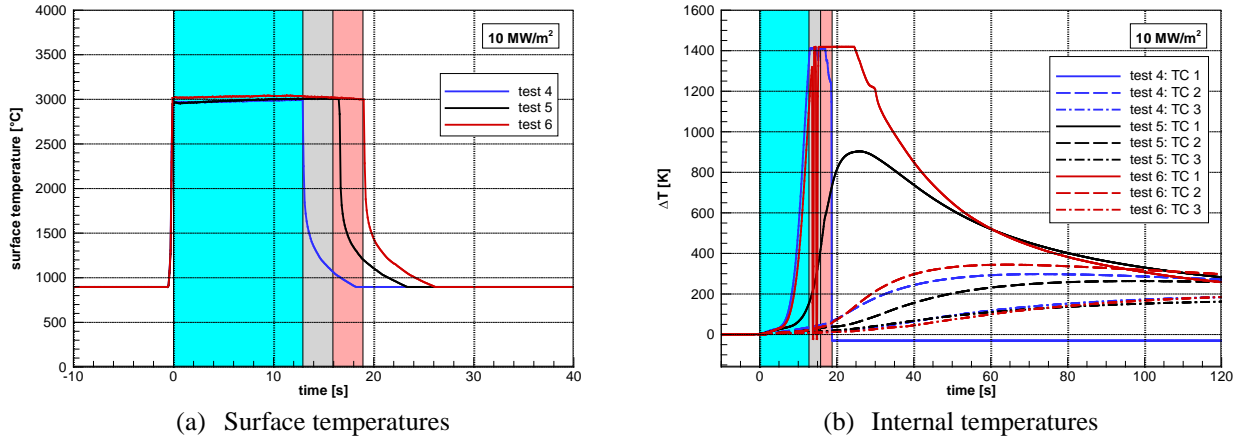


Fig. 7. Temperature measurements from tests at FC-2.

The erosion data of the tests at FC-2 are listed in Table 7. Mass losses and recession rates are comparable to the values measured at condition FC-1. The corresponding erosion rates are very close for tests 5 and 6. After test 4, however, mass loss rate as well as recession rate were measured about 10% higher. An explanation for the increase, however, could neither be found from the operational data nor from surface temperature measurements (see Fig. 7a).

Table 7. Erosion data from tests at FC-2.

Test	Duration [s]	Mass loss [g]	Mass loss rate [g/(m ² s)]	Surface recession [mm]	Recession rate [mm/s]
4	12.9	2.91	130.3	5.3	0.411
5	16.5	3.82	117.7	6.2	0.376
6	19.0	4.43	118.7	7.3	0.384

Tests at condition FC-3

The remaining three samples were tested at test condition FC-3. Test durations were reduced to 10, 12, and 14 seconds, resp. The surface temperatures measurements from the tests at condition FC-3 are compared in Fig. 8a. Again, a very good agreement between the three measurements is found. As for test condition FC-2, the initial temperature jump directly ends at the nearly constant level of about 3050°C. Different to condition FC-2, the surface temperature slightly decreases with time. With 30 K, the decrease is not substantial and might be explained by fact that due to surface recession the heat load slightly decreases.

Thermocouple measurements from the tests at condition FC-3 are plotted in Fig. 8b. As already observed for condition FC-2, TC 1 reaches maximal reading very soon after the sample's arrival at the test location. The curves are very close for tests 7 and 8. The sample used for test 9 had only two thermocouples installed, with TC 1 omitted. During the hot phase of testing the readings of TC 2 and TC 3 are close for all three tests. Afterwards the readings are directly related to the duration of the test, i.e. higher temperature increase is measured for longer tests.

The erosion data of the tests at FC-3 are listed in Table 8. Mass losses and recession rates are comparable to the values measured at conditions FC-1 and FC-2. The corresponding erosion rates are rather close for all three tests. Compared to the mean value the variation does not exceed $\pm 3\%$ for both, mass loss rate and recession rate.

Table 8. Erosion data from tests at FC-3.

Test	Duration [s]	Mass loss [g]	Mass loss rate [g/(m ² s)]	Surface recession [mm]	Recession rate [mm/s]
7	10.5	3.42	166.0	5.7	0.543
8	13.2	4.11	158.4	7.5	0.586
9	14.1	4.04	165.4	7.6	0.539

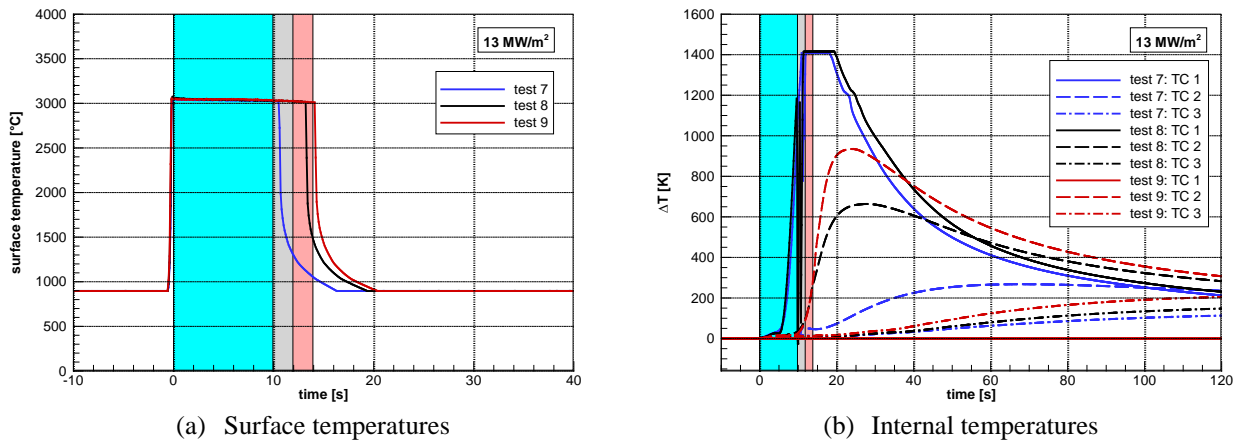


Fig. 8. Temperature measurements from tests at FC-3.

CONCLUSIONS

In several steps the capabilities for thermal testing of ablative materials at DLR's arc heated facility L3K had been improved towards the requirements for materials to be used for the heat shield of Earth return missions. It was found that the L3K segmented arc heater could stably be operated in 5-pack operation at a total enthalpy of 15.9 MJ/kg. Using the new 50 mm nozzle, cold wall heat fluxes up to 13.6 MW/m² could be achieved on standard flat-faced cylinder models with a diameter of 50 mm.

The new test conditions were applied during a test campaign aiming at the thermal characterization of AQ61, which is an available ablative material without strategic interest and whose thermal response is considered to be comparable to actually developed ablator materials. AQ61 samples were tested at three conditions in L3K. Three tests were performed at each condition providing a good reproducibility of test results, in particular surface temperature measurements and erosion data.

After the end of the AQ61 test campaign the considerations to further extend L3K's operating range were continued. Potential for improvement was identified in modifying the optical access to the interior of the test chamber in order to allow for testing at locations closer to the nozzle exit. By that, the maximal heat flux could be increased to 16.0 MW/m² enabled L3K to cover almost the complete range required for future Earth return missions.

REFERENCES

- [1] A. Gülhan, B. Esser, "Arc-Heated Facilities as a Tool to Study Aerothermodynamic Problems of Reentry Vehicles", in: Lu, F.K.; Marren, D.E. (Eds.): *Advanced Hypersonic Test Facilities*, Progress in Astronautics and Aeronautics, Vol. 198, p. 375-403, AIAA, 2002.
- [2] A. Gülhan, B. Esser, U. Koch, K. Hannemann, "Mars Entry Simulation in the Arc Heated Facility L2K", 4th European Symposium on Aerothermodynamics of Space Vehicles, October 2001, Capua, Italy, ESA SP-487, 2002.
- [3] Gülhan, A.; Esser, B.; "A Study on Heat Flux Measurements in High Enthalpy Flows", 35th AIAA Thermophysics Conference, Paper AIAA 2001-3011, Anaheim, CA, USA, June 11-14, 2001.

Characterization of new high heat flux test conditions in L3K

B. Esser, A. Gülhan
Supersonic and Hypersonic Technologies Dept.
DLR Cologne

7th European Workshop on Thermal Protection Systems and Hot Structures, April 8-10, 2013



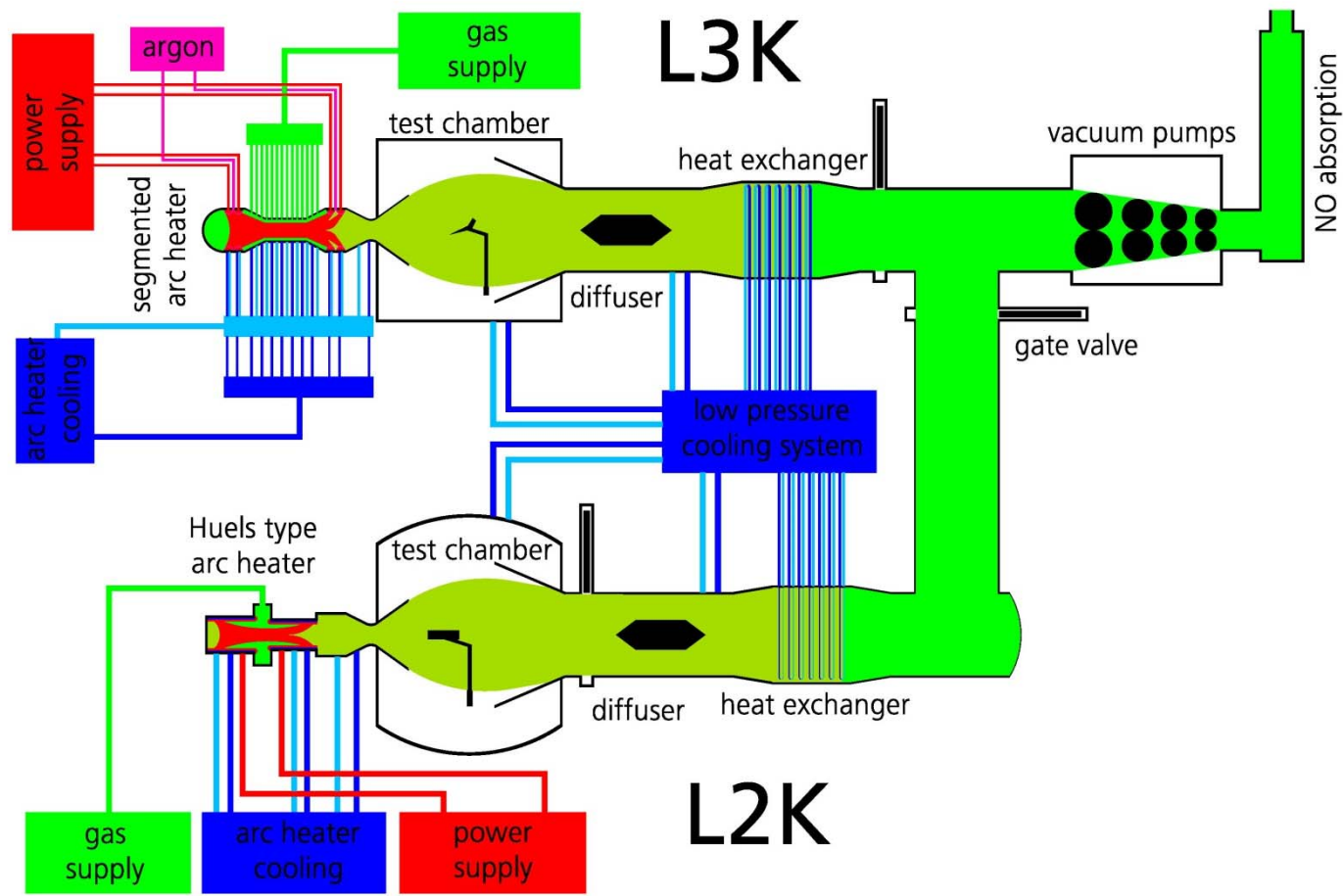
Knowledge for Tomorrow

Overview

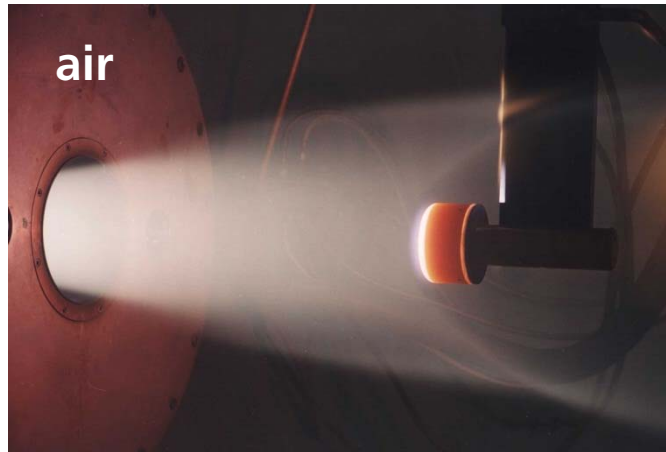
- Introduction
 - Ablation testing at arc heated facilities in Cologne
- Facility improvements towards higher heat loads
 - Short nozzle
 - New arc heater configuration
- Tests on AQ61 samples
 - Experimental setup
 - Test conditions and test matrix
 - Test results
- Summary and outlook



Arc Heated Facilities LBK

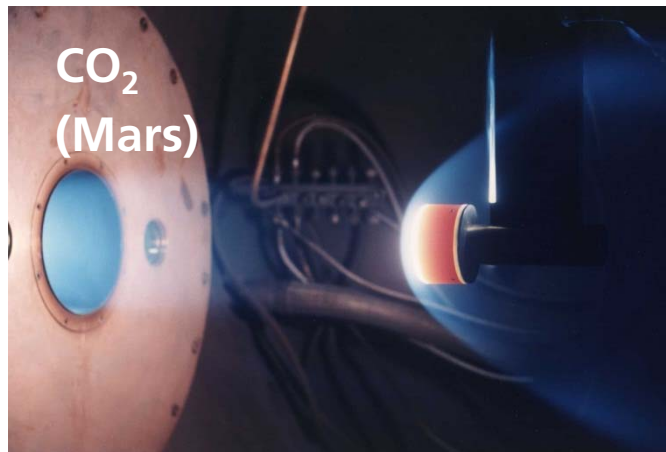


TPS Characterization for Planetary Entry



Test Environment

- Hypersonic flow
- High enthalpy
- Dissociated gas
- Long duration testing (max. 2h)



Working gases

- Air
- CO₂
- Martian mixture (CO₂/N₂)
- Titan mixture (N₂/CH₄)
- Argon



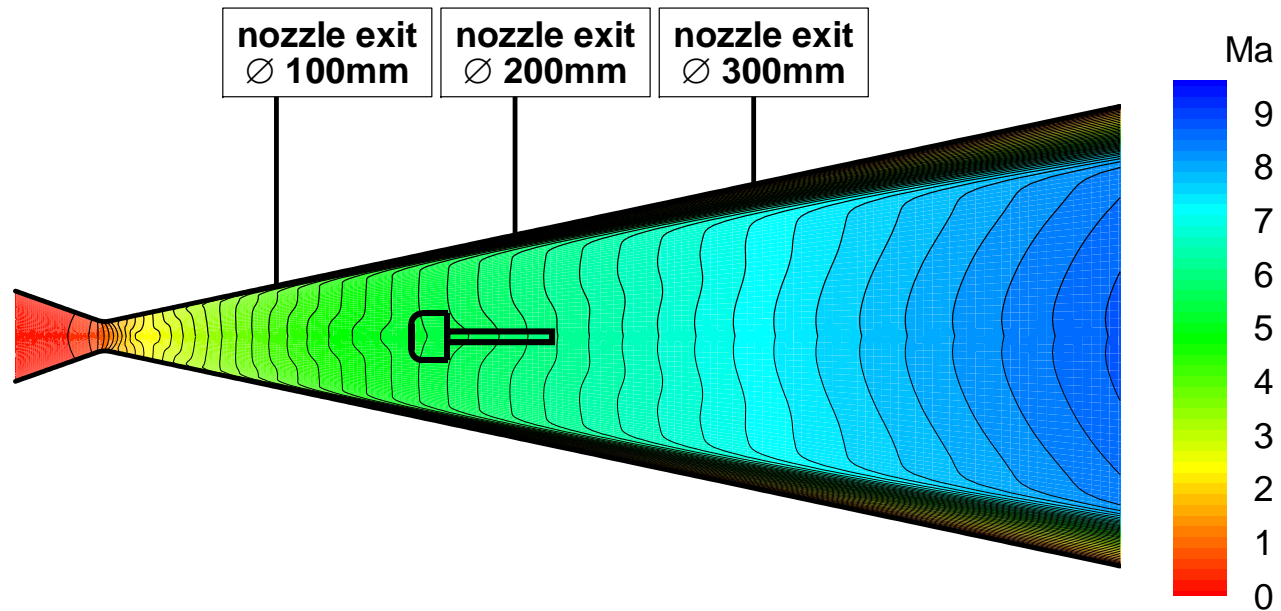
Test Campaigns on Ablative Materials

Overview

- MSTP Programme	(Dassault/ESA)	1995
- USERS Reentry Module	(USEF/Japan)	1998-1999
- Ablators for Martian Atmosphere	(SNECMA)	2001
- IRT Concept	(OHB/ESA)	2003
- TPS for Ariane 5	(Cryospace)	2005
- Characterization of LM Ablators	(FGE/LM)	2006,2009
- Dust Erosion in Martian Atmosphere	(ESA/CNES)	2007-2010
- TPS for Ariane 5	(Cryospace)	2008
- IMENS-3C	(DLR)	2008-2011
- Validation of Aerothermal Models (AMOD)	(VKI/ESA)	2009-2010
- Development of a European Ablator (DEAM)	(HPS/ESA)	2009-1010
- Tests on AQ61 samples	(ESA)	2012
- FP7 Project RASTAS SPEAR	(Astrium)	2013



L3K nozzle configuration before 2009

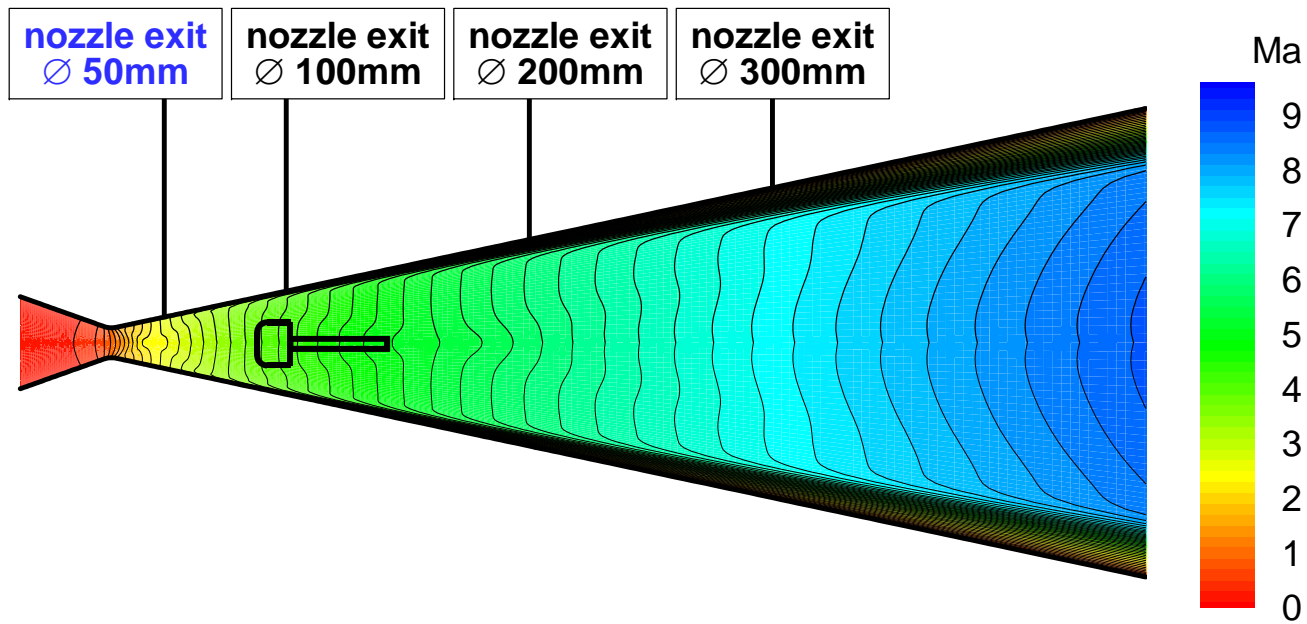


- Smallest nozzle exit diameter: 100 mm
- Most upstream test position: 120 mm behind nozzle exit



Facility Improvements

Short nozzle (D = 50 mm)



Objective

- Thermal testing of ablative materials at flight relevant heat flux levels



Facility Improvements

Short nozzle (D = 50 mm)

Test conditions on a 50 mm flat-faced cylinder sample

Sample distance from nozzle exit [mm]	70	85	105
Pressure p_{t2} [hPa]	1294	840	331
Cold wall heat flux rate [MW/m ²]	11.5	10	5

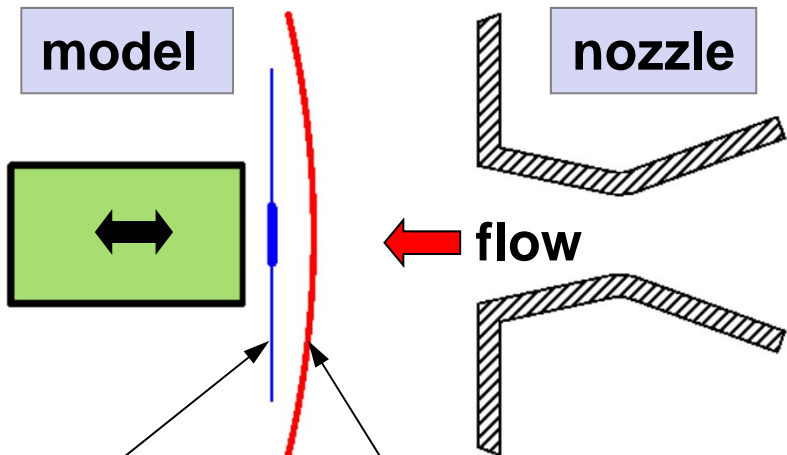
Operation and Application

- The short nozzle is in operation since 2009, and has been used for almost all recent testing activities on ablative materials and structures



Flow characterization

CARS campaign (DLR Institute of Propulsion)

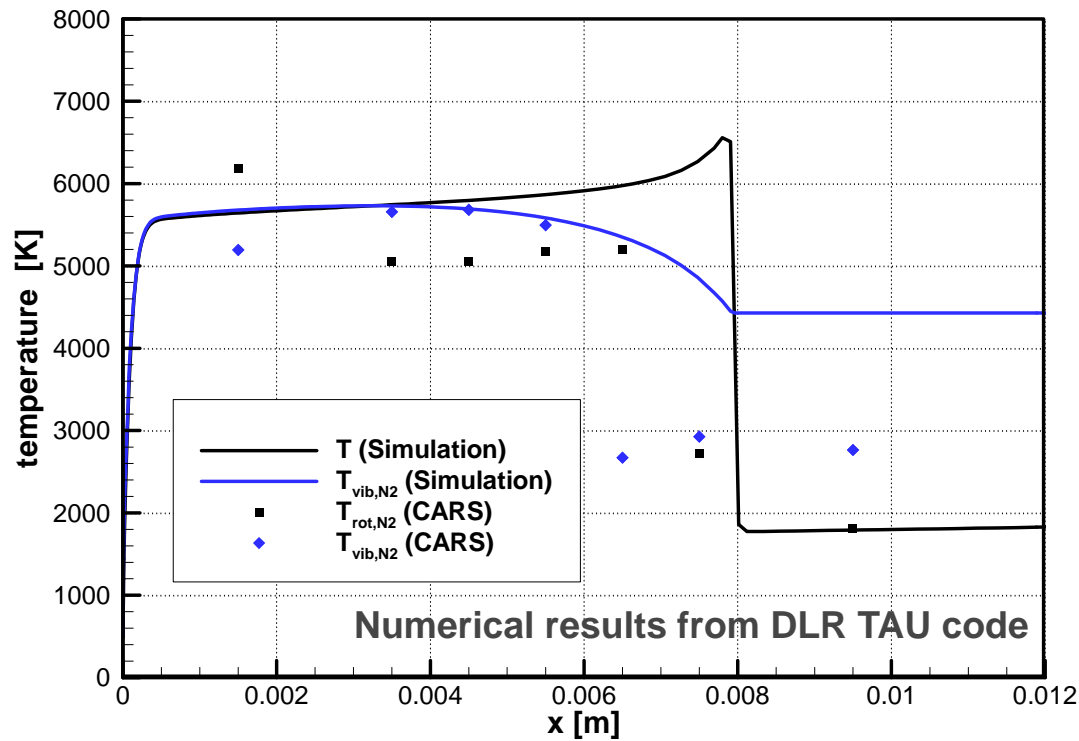
<p>Test setup</p>  <p>The diagram illustrates the test setup. A green rectangular model is positioned on the left, with a double-headed arrow indicating its movement. To its right is a nozzle, shown as a hatched L-shaped structure. A red arrow labeled 'flow' points from the nozzle towards the model. A red curved line represents the bow shock wave in front of the model. A blue vertical line represents the CARS beam, which is directed at the model. Labels 'model', 'nozzle', 'flow', 'CARS beam', and 'bow shock' are placed in light blue boxes with arrows pointing to their respective components.</p> <p>model: 50 mm flat faced cylinder nozzle throat/exit diameter: 29/50 mm</p>	<p>Test conditions</p> <ul style="list-style-type: none">• mass flow rate: 180 g/s• reservoir pressure: 6000 hPa• Pitot pressure: ~1000 hPa• specific enthalpy h_0: 11,8 MJ/kg• total temperature T_0: 5775 K• free stream velocity: 3435 m/s• free stream static pressure: 64 hPa
<p>Broadband CARS</p> <ul style="list-style-type: none">• spectra taken at 10 Hz• free stream measurements: ~60 s<ul style="list-style-type: none">• a few hundred spectra• measurements with model: 10 s<ul style="list-style-type: none">• 100 spectra• rotational and vibrational temperatures could be evaluated from spectra	



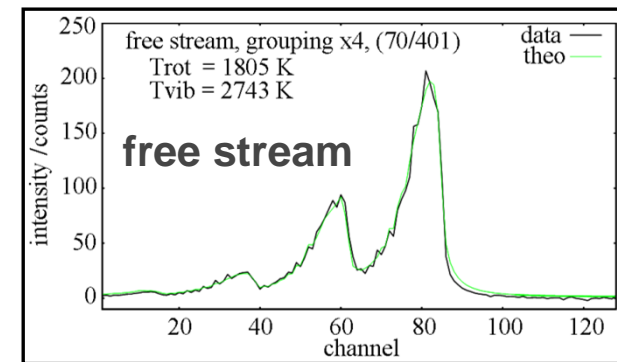
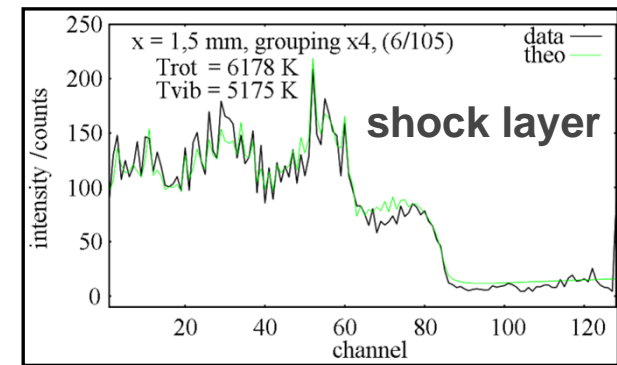
Flow characterization

CARS campaign

Temperatures along the stagnation line



Single spectra

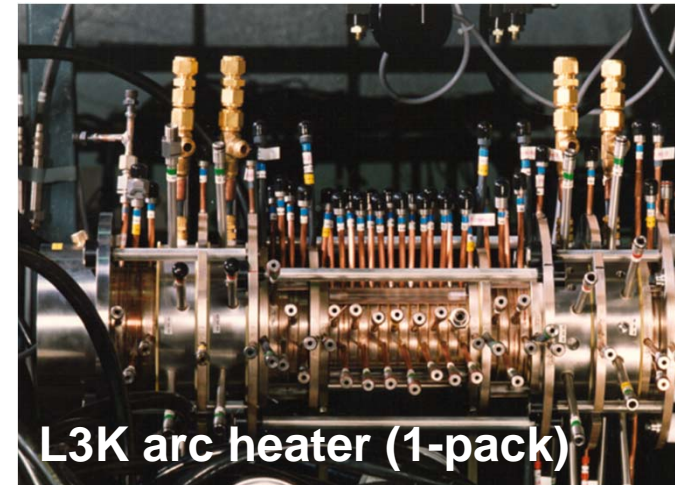


Facility Improvements

5-pack arc heater configuration

Objectives

- Operation at higher total enthalpies compared to 4-pack configuration
- Thermal testing of ablative materials at flight relevant
 - heat flux levels
 - stagnation pressures

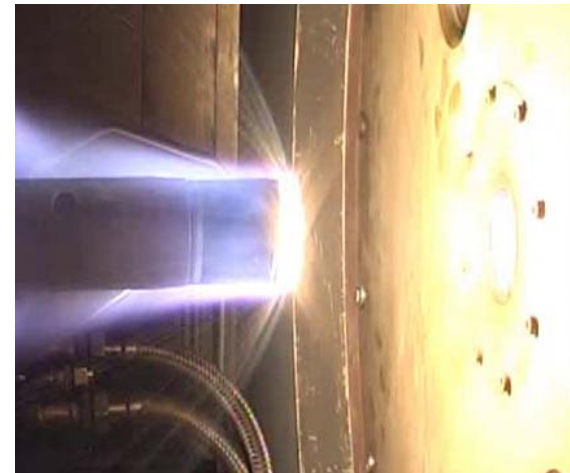


Facility Improvements

5-pack arc heater configuration

New operating condition

Gas mass flow rate [g/s]	101
Reservoir pressure [hPa]	3750
Reservoir temperature [K]	6462
Specific enthalpy [MJ/kg]	15.9
Nozzle throat diameter [mm]	29
Nozzle exit diameter [mm]	50



Test conditions on a 50 mm flat-faced cylinder sample

Sample distance from nozzle exit [mm]	70	75	100	110	140	155	160
Pressure p_{t2} [hPa]	917	840	588	516	290	225	210
Cold wall heat flux rate [MW/m ²]	13.6	12.8	10.1	9.3	7.2	6.4	6.1

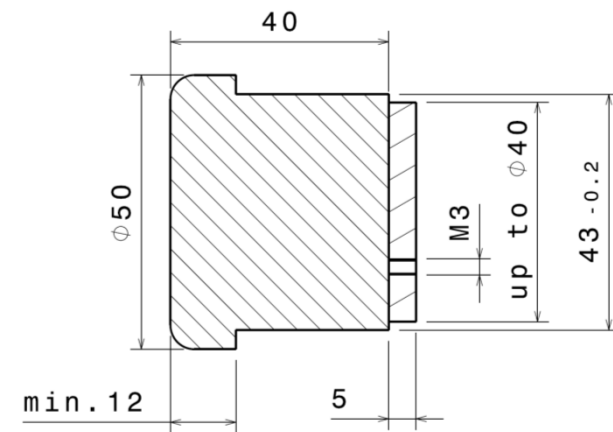
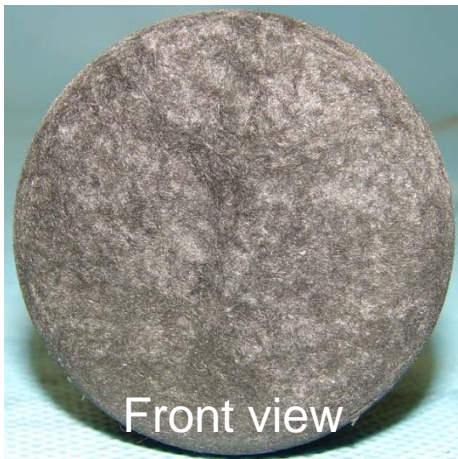
FC-3 FC-2

FC-1



Test Campaign on AQ61 Samples

Samples



- Flat-faced cylinder samples
- aluminium backing plate
- three thermocouples at 5, 10, and 20 mm depths
- material provided by Astrium
- Sample manufacturing and instrumentation by HPS Portugal



Test Campaign on AQ61 Samples

Test Matrix

Test No.	Sample	Sample diameter [mm]	Test condition	Heat Flux [MW/m ²]	Test duration
1	8	50	FC-1	6.1	26 s
2	6	47	FC-1	6.1	32 s
3	1	47	FC-1	6.1	38 s
4	9	47	FC-2	10.1	13 s
5	7	50	FC-2	10.1	16 s
6	4	50	FC-2	10.1	19 s
7	2	50	FC-3	12.8	10 s
8	3	50	FC-3	12.8	12 s
9	5	47	FC-3	12.8	14 s



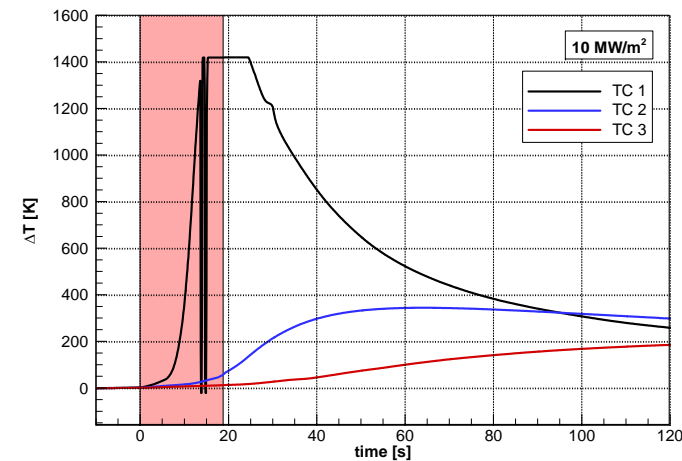
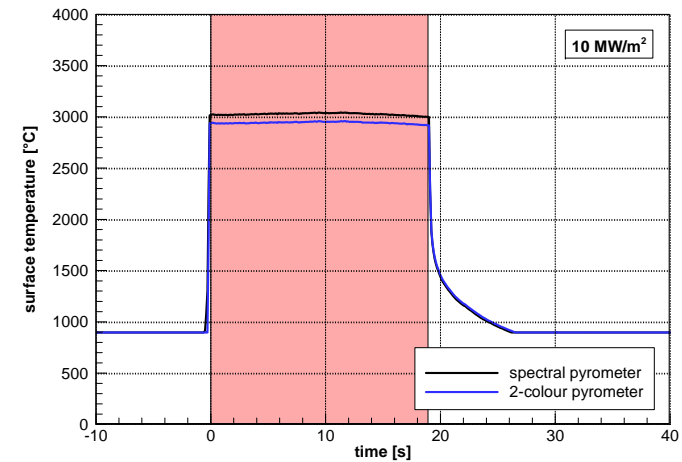
Measurements

Temperature measurements

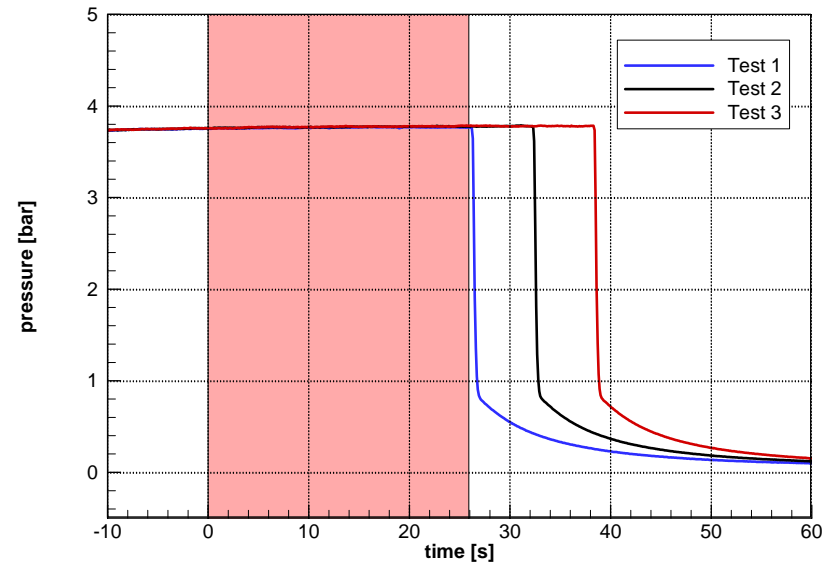
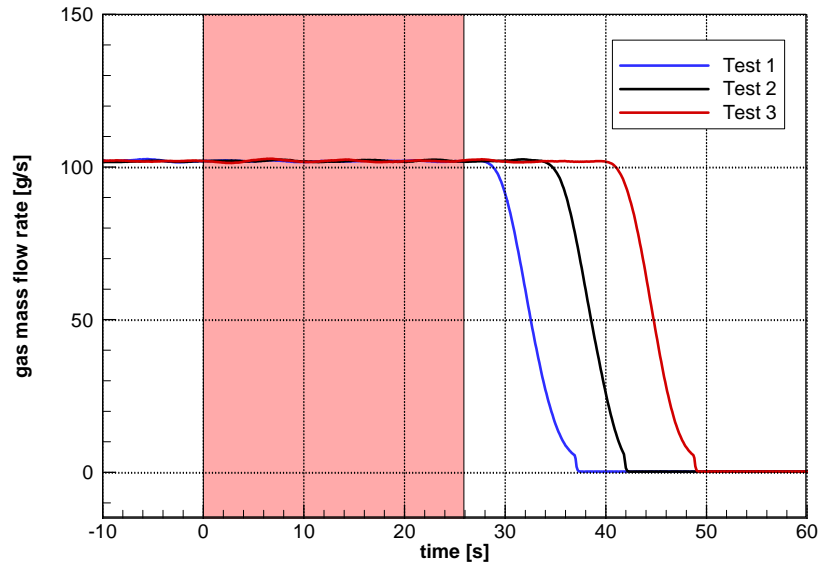
- Surface temperature
 - Spectral pyrometer
 - Two-colour pyrometer
- Internal temperature
 - 3 thermocouples

Pre-test and post-test measurements

- Sample weight
- thickness



Reproducibility of test conditions



- Test conditions are governed by geometry and operational parameters
- In subsequent tests the facility's operational parameters
 - gas mass flow rate and
 - reservoir pressurecan be reproduced very well



Post-test sample appearance



Test 3 (38 s)
6.1 MW/m²



Test 6 (19 s)
10.1 MW/m²



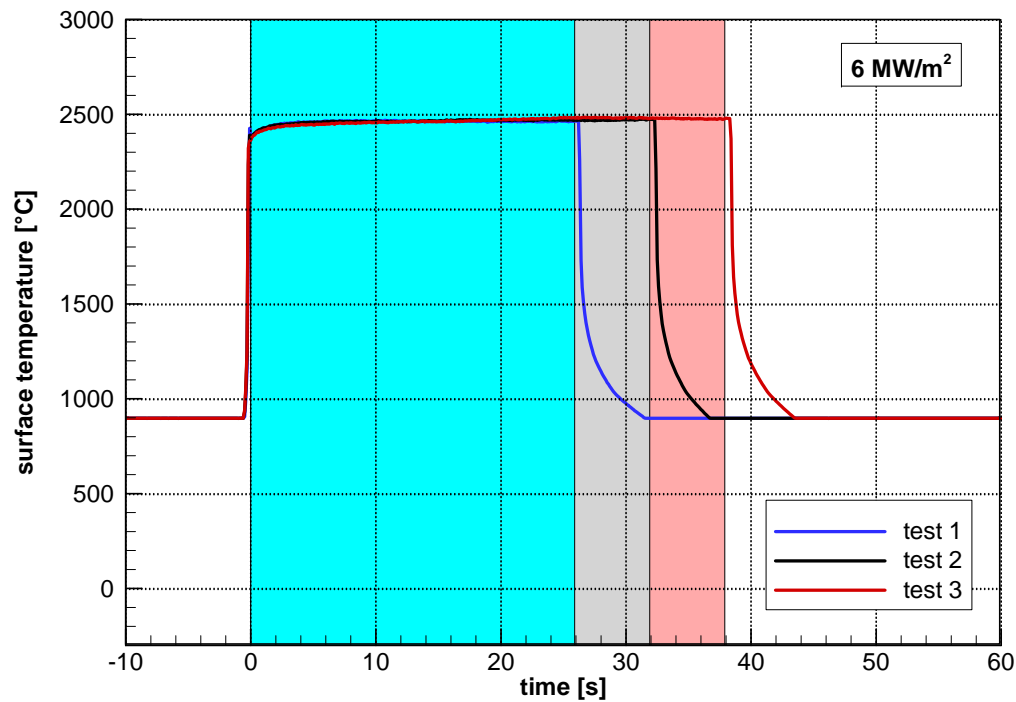
Test 9 (14 s)
12.8 MW/m²

- homogeneous appearance
- no local damages



Tests at condition FC-1 (6.1 MW/m²)

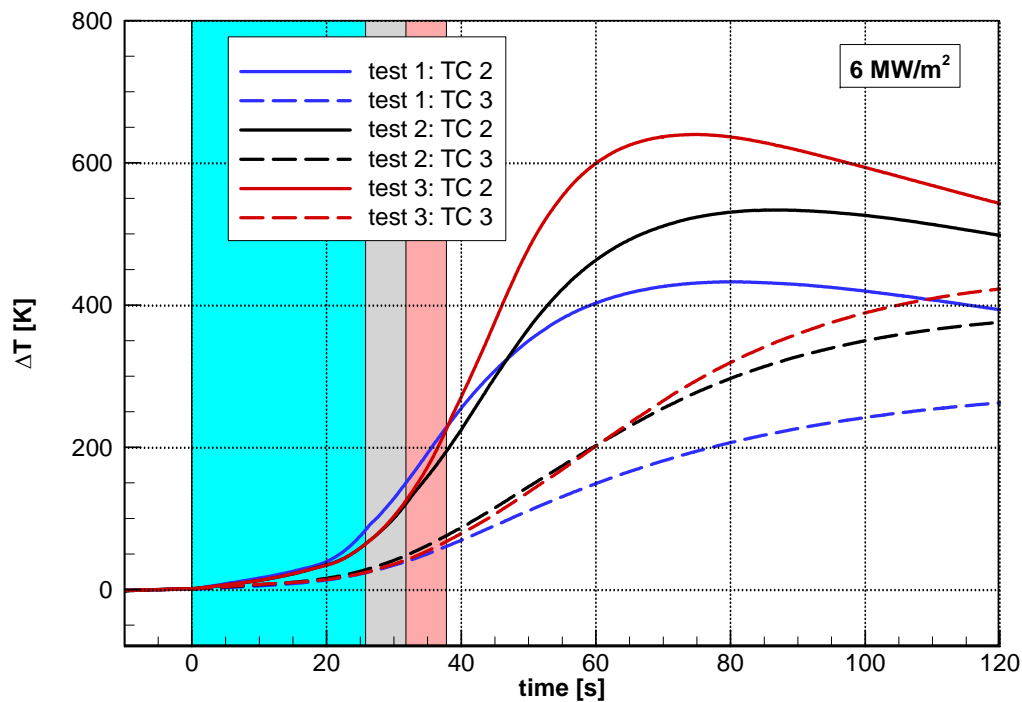
Surface temperatures



- Almost immediate jump to final surface temperature in the beginning



Tests at condition FC-1 (6.1 MW/m²) Thermocouple measurements



- TC 1 had problems with signal line
- Maximal temperatures correlated to test duration



Tests at condition FC-1 (6.1 MW/m²)

Erosion data

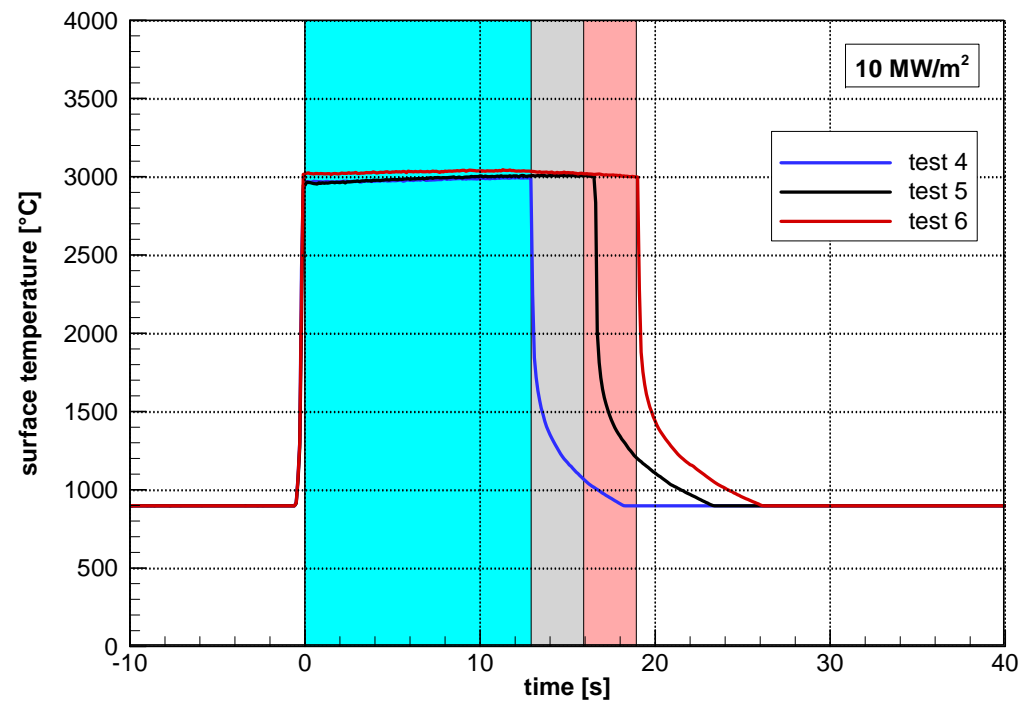
Test	Sample	Test duration	Mass loss	Surface recession	Sample diameter	Mass loss rate	Recession rate
		[s]	[g]	[mm]	[mm]	[g/(m ² s)]	[mm/s]
1	8	26.2	3.29	4.8	50	64.2	0.183
2	6	32.3	3.52	6.2	47	62.8	0.192
3	1	38.3	4.30	7.1	47	64.6	0.185

- good agreement in mass loss rate and recession rate

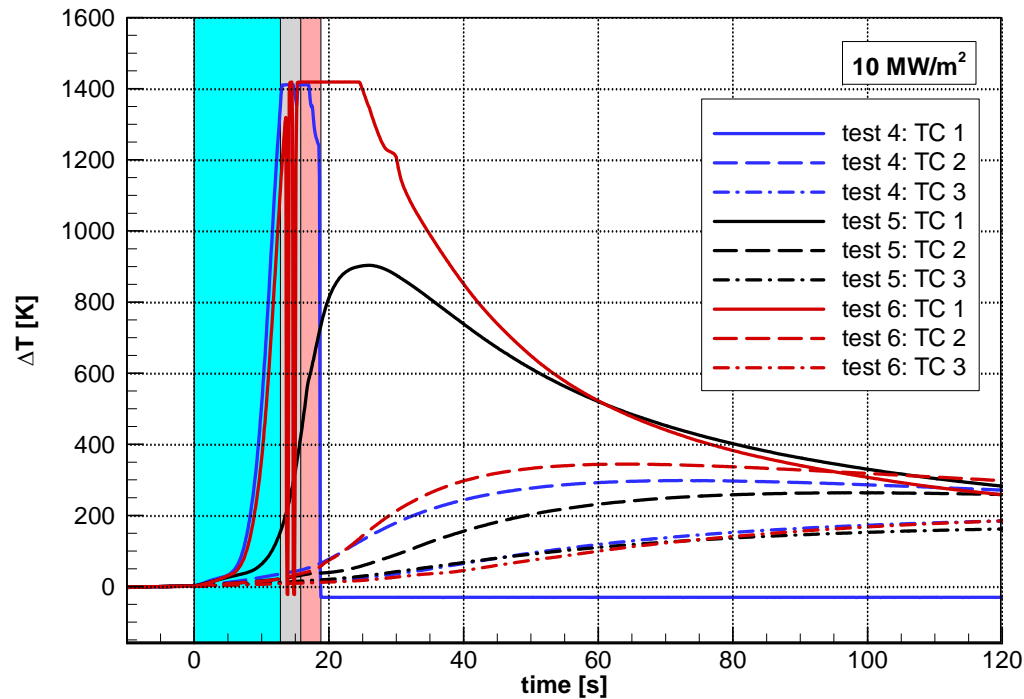


Tests at condition FC-2 (10.1 MW/m²)

Surface temperatures



Tests at condition FC-2 (10.1 MW/m²) Thermocouple measurements



- TC1 working
- in test 5 TC1 and TC 2 considerably lower than in tests 4 and 6
- not supported by erosion data, caused by thermocouple placement



Tests at condition FC-2 (10.1 MW/m²)

Erosion data

Test	Sample	Test duration	Mass loss	Surface recession	Sample diameter	Mass loss rate	Recession rate
		[s]	[g]	[mm]	[mm]	[g/(m ² s)]	[mm/s]
4	9	12.9	2.91	5.3	47	130.3	0.411
5	7	16.5	3.82	6.2	50	117.7	0.376
6	4	19.0	4.43	7.3	50	118.7	0.384

- higher erosion in test 4 is not supported by other measurements
- tests 5 and 6 show good agreement of erosion rates



Tests at condition FC-3 (12.8 MW/m²)

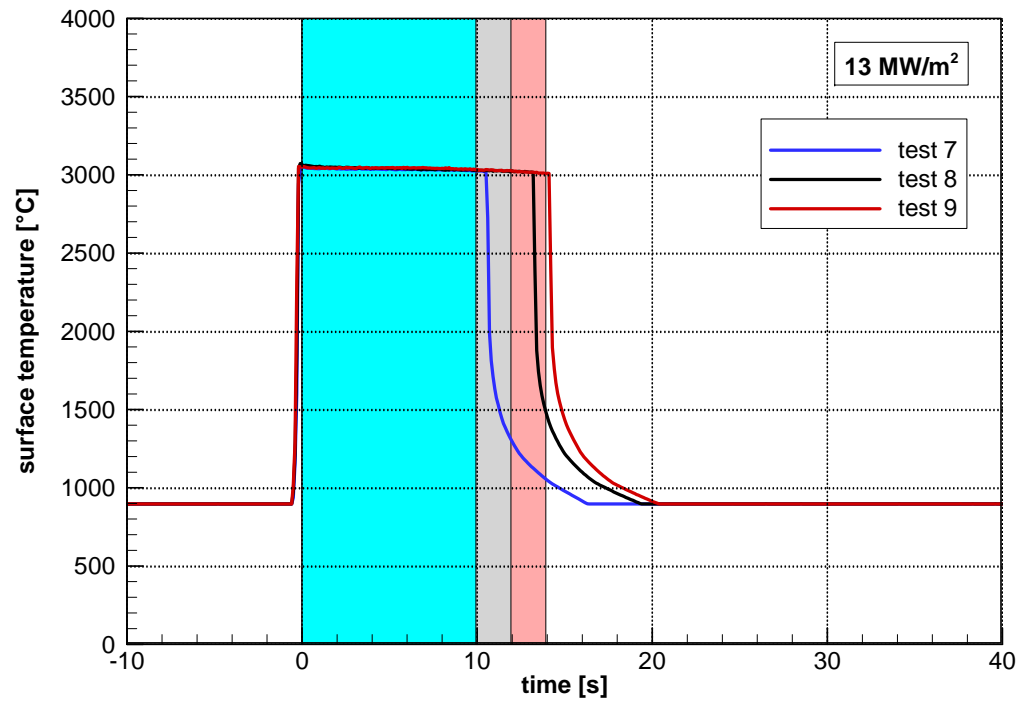
Erosion data

Test	Sample	Test duration	Mass loss	Surface recession	Sample diameter	Mass loss rate	Recession rate
		[s]	[g]	[mm]	[mm]	[g/(m ² s)]	[mm/s]
7	2	10.5	3.42	5.7	50	166.0	0.543
8	3	13.2	4.11	7.5	50	158.4	0.568
9	5	14.1	4.04	7.6	47	165.4	0.539



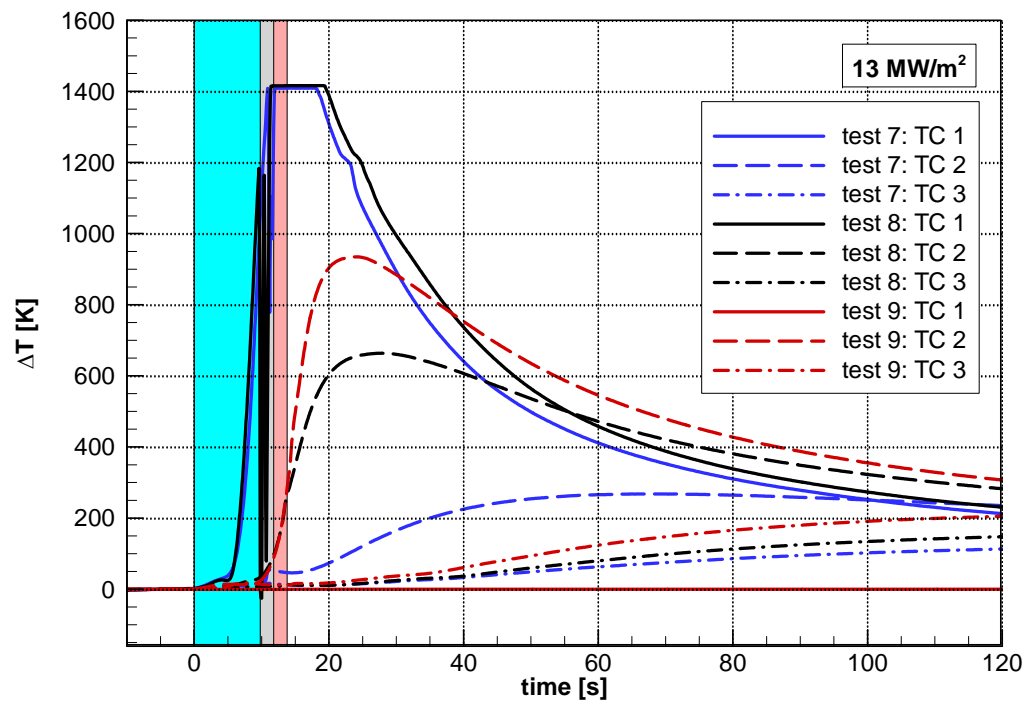
Tests at condition FC-3 (12.8 MW/m²)

Surface temperatures



Tests at condition FC-3 (12.8 MW/m²)

Thermocouple measurements



- only two thermocouples (TC2, TC3) in test 9



RASTAS SPEAR

Test at condition 13.6 MW/m²



Summary and Conclusions

- L3K arc heater and nozzle configurations had successfully been modified to establish test conditions with considerably higher heat loads up to 13.6 MW/m².
- To characterize the new conditions a test campaign was performed with ablative material samples made of AQ 61.
- Tests were performed at three test conditions with cold wall heat flux rates of 6.1, 10.1 and 12.8 MW/m².
- All samples survived the test in good shape without structural damage.
- The tests at 6.1 MW/m² showed an excellent reproducibility of test conditions, surface temperatures, and erosion rates on the samples.
- At 10.1 MW/m², the measured surface temperatures agreed very well between the three tests.
- At the highest heat load of 12.8 MW/m² surface temperatures above 3000° C were measured. The tests provided a good agreement in erosion rates and surface temperature measurements.



Outlook

- Continuous scientific and design effort is made to
 - further characterize the high heat flux test conditions
 - identify additional potential for further improvements of test conditions

- Recently the maximal heat flux for the 5-pack arc heater configuration could be extended to 16.0 MW/m².

Current set of test conditions on a 50 mm flat-faced cylinder sample

Sample distance from nozzle exit [mm]	50	70	75	100	110	140	155	160
Pressure p_{12} [hPa]	1143	917	840	588	516	290	225	210
Cold wall heat flux rate [MW/m ²]	16.0	13.6	12.8	10.1	9.3	7.2	6.4	6.1



Characterization of a 50 kW Inductively Coupled Plasma Torch for use in Testing of Ablative Materials

8-10 April 2013

ESA/ESTEC, Noordwijk, The Netherlands

Megan E. MacDonald⁽¹⁾, Carolyn M. Jacobs⁽¹⁾, Christophe O. Laux⁽¹⁾,
Fabian Zander⁽²⁾, Richard Morgan⁽²⁾

⁽¹⁾Laboratoire EM2C – CNRS UPR 288
Ecole Centrale Paris
Grande Voie des Vignes 92290 Chatenay-Malabry
Email: megan.mac-donald@ecp.fr

⁽²⁾University of Queensland
Center for Hypersonics
St. Lucia 4072, Australia

INTRODUCTION

In the field of atmospheric reentry, experimental studies of the interactions between atmospheric plasmas and ablative materials are of particular interest. Products ablated from the protective shield of a superorbital velocity re-entering vehicle may react with the incoming air plasma flow, thus producing chemical species that can couple with those contained in the incoming air flow field. These products may affect the absorption and emission properties of the boundary layer, thus potentially affecting the radiative heat flux to the surface of the superorbital velocity vehicle. This effect was previously demonstrated based on numerical simulations at a velocity of 10 km/s [1].

The first objective of this work was to add the capability of studying ablator materials in a recently recommissioned RF plasma torch facility. This included the manufacturing of an ablative layer holder to be placed in the hot air plasma produced by the torch and to implement systems to measure the heat flux delivered to the ablating sample and the surface temperature of the sample exposed to the plasma jet.

The second objective was to conduct optical emission spectroscopy measurements near the ablative layer exposed to the hot air plasma flow in order to determine whether it is possible to assess the influence of the coupling between the ablation products and the air plasma flow. As described here, this assessment was performed by optical emission spectroscopy in the spectral range extending from the ultraviolet to the near infrared.

FACILITY AND DIAGNOSTICS

50 kW Plasma Torch

The torch used for these experiments is a TAFE Model 66 inductively coupled plasma (ICP) torch powered by a radio frequency LEPTEL Model T-50-3 power supply operating at 4 MHz. This power supply can deliver up to 120 kVA of line power to the oscillator plates with a maximum of 12 kV DC and 7.5 A. The oscillator plates have in turn a maximum RF power output of 50 kW.

The temperature profile of the air plasma was measured at two flow conditions (7 cm and 5 cm plasma diameter) prior to conducting tests with the ablative materials, and these profiles are shown in Figure 1. The temperature measurement was the non-intrusive method based on emission from the strong oxygen triplet near 777 nm and is described in detail in [2].

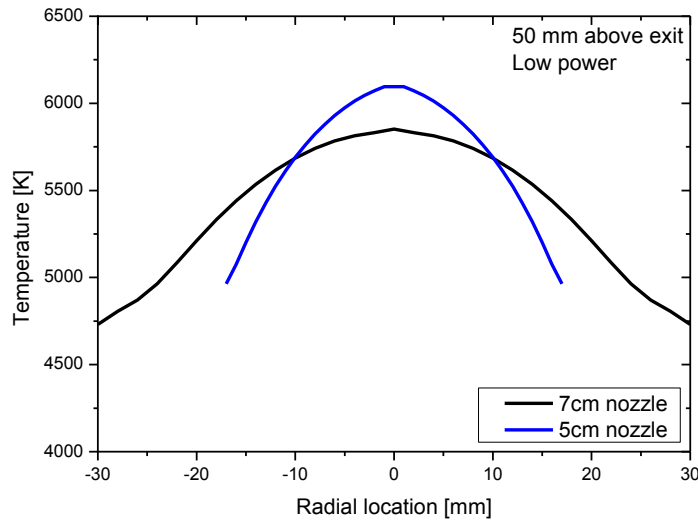


Figure 1. Measured temperature profiles 50-mm downstream of the nozzle exit for both the 5-cm and 7-cm diameter nozzles. Typical relative uncertainties are about 2 %.

Optical Emission Spectroscopy

Two spectrometers have been set up for the measurements conducted in this work, an Acton Research SpectraPro SP2750i for high-resolution measurements, and an Ocean Optics USB2000+ for broadband spectral measurements. The characteristics of these spectrometers are described below.

The Ocean Optics USB2000+ spectrometer was used to record emission spectra over a wide spectral range extending from the UV to the near infrared (280-870 nm). This spectrometer contains two spherical mirrors (focal length of 42 mm for the input mirror and 68 mm for the output mirror), a diffraction grating blazed at 300 nm with 600 grooves/mm, and a CCD linear array with 2048 pixels of dimensions 14 x 200 micron. The entrance slit of the spectrometer has a fixed width of 100 microns. The spectral resolution of this system is 2.45 nm. The spatial resolution is determined by the magnification of the optical train (here equal to 1) and the diameter (600 microns) of the optical fiber used to feed light into the spectrometer.

Also employed for these experiments was an Acton Research SpectraPro SP2750i spectrograph of focal length 750 mm. The current experiments utilized a 1200 g/mm grating blazed at 300 nm. The spectrometer is equipped with a VUV-enhanced intensified CCD camera (Princeton Instruments PI-MAX:1024RB-UV-18mm with 1024 x 256 pixels) with response from the VUV to the near-IR spectral range (140 - 930 nm). For an entrance spectrometer slit width of 25 microns (used in the present experiments), the spectral resolution of the spectrometer is approximately 0.075 nm (FWHM).

Calibration Sources

For absolute intensity calibration of the measured spectra, an Optronics Laboratory tungsten filament lamp was employed, which has a calibration curve traceable to NIST standard, for measurements in the UV/visible and near infrared (350 - 6000 nm).

Minolta Cyclops pyrometer measurements

The surface temperature of the ablator is monitored with the optical pyrometer (Minolta Cyclops Model 153A). The pyrometer measures the radiation emitted by an 11 mm diameter region of the observed material in the spectral range 800 - 1100 nm. This radiation can be converted into a temperature with knowledge of the emissivity of the observed material. Because the emissivity of the ASTERM material is not known, we have assumed that the mid-density ASTERM emissivity is 0.85 ± 0.15 . This value corresponds to the emissivity of a PICA material [3], which should have properties similar to those of the ASTERM material. For the tests with the higher density carbon material, an emissivity

of 0.8 was taken. The resulting surface temperature uncertainty is conservatively estimated to be $\pm 5\%$ due to unknowns in surface emissivity alone.

Two Color Ratio Pyrometry (TCRP)

In addition to the pyrometer measurements, detailed two dimensional surface temperature measurements were made across the surface using a technique known as called two-color ratio pyrometry (TCRP) that was recently modified at the University of Queensland [4,5] for use in impulse facilities. This procedure uses the magnitudes of the signals obtained from a commercial RGB digital SLR camera, and the ratios of the signals from adjacent R, G, and B pixels to infer a measure of surface static temperature.

This technique was developed for monitoring the temperatures of heated reinforced carbon-carbon (RCC) models in an expansion tube prior to the onset of hypervelocity flow, and was found to give a good overall accuracy and well defined surface distribution of the temperature. It assumes grey body radiation, and for the most accurate measurements requires independent spectral calibration of the RGB pixel receptivity across the full relevant wavelengths. This was carried out for the Canon EOS 400D DSLR used in the expansion tube set up at the University of Queensland. For the recent proof of concept tests in the plasma torch, a similar model camera was used (Canon 450D DSLR), and the same camera spectral response was assumed.

Data processing assumes a Planck distribution, and fits the temperature to best match the ratios recorded between the R/G, G/B, and R/B pixels. It does not rely on the absolute value of the emissivity of the surface under observation, but instead on the assumption of grey body radiation.

A tungsten ribbon lamp was used to calibrate the system. This ribbon had a uniform surface temperature of 2400 K, which was independently checked with a pyrometer. The surface temperature distribution of the calibration element is shown in Figure 2.



Fabian Zander

Figure 2. Temperature distribution across the tungsten ribbon, set at 2400 K, as processed by the three possible RGB ratio sets, and the optimized combination.

Video and Still Camera Monitoring

Direct imaging of the ablator placed in the plasma flow is obtained by means of two Canon Digital SLR cameras (450D and 1100D), one working to capture images for the TCRP and the other as a high resolution video, and a conventional

webcam (Hercules HD Exchange). Photographs for the TCRP were recorded every 10 to 30 s during the experiments, and the video clocked at 25 frames/s.

RESULTS

Measurements were completed at a “low power” condition (40 kW plate power) in order to begin quantification of the newly implemented ablator test capabilities in as safe a manner as possible. The results presented here correspond to this low power setting. All experiments were conducted at atmospheric pressure and in an air plasma with an undisturbed temperature profile as shown in Figure 1. Two flow conditions were studied, that with a 7 cm diameter air plasma, and that with a 5 cm diameter air plasma. Two materials were studied, ASTERM, developed by EADS Astrium ST as a low-density phenolic-impregnated ablative material, and carbon bonded carbon fiber (CBCF), a carbon preform representative of the virgin material utilized to produce ASTERM.

Emission spectra were recorded with the Ocean Optics spectrometer as a function of time throughout all four ablation experiments. The spectrometer was focused on a spot 600 micron in diameter, located initially about 2 mm above the lower surface of the ablator. Emission spectra obtained at times $t = 0$ s and 300 s are shown in Figure 3. The torch is started on argon, and then air is slowly substituted for argon over a period of approximately 100 s. Time zero is set at the beginning of 100% air plasma.

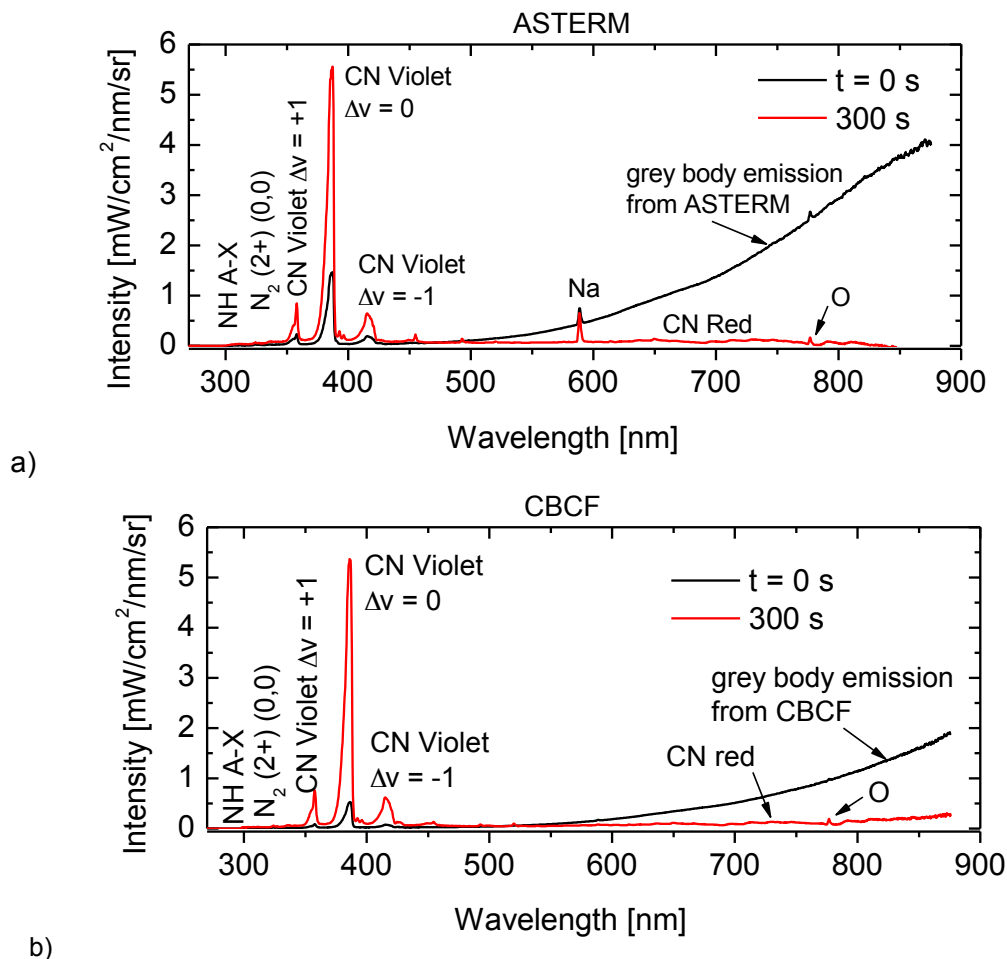


Figure 3. UV, visible and near infrared emission spectra measured at $t = 0$ and 300 s with the Ocean Optics spectrometer. Low power case (40.6 kW), 40 mm diameter/20 mm thick CBCF sample, surface located 50 mm above the plasma torch exit, air plasma exit diameter 7 cm. a) ASTERM, b) CBCF.

These four spectra contain a wealth of spectral features. In **Figure 3a**, the ASTERM experiment, we observe several spectral features common to both times, namely the emission bands of NH A-X, of the N₂ second positive system (in particular the (0,0) band at 337 nm), the CN violet band sequence between 350 and 415 nm, the atomic oxygen triplet line at 777 nm, as well as a spectral line at 588 nm that we have identified as sodium. There is, however, a major difference between the two times: the spectrum at 0 s contains a broadband emission feature from 500 to 900 nm, which is attributed to the grey body radiation of the ASTERM material. This is expected, since at time zero, the material is still in the field of view of the spectrometer. By contrast, at 300 s, we clearly see that this broadband feature is no longer present. Instead, we distinguish a molecular band structure that closely resembles the spectrum of the CN red system.

In **Figure 3b**, showing the emission measured during the CBCF experiment, we see many of the same features, notably the strong CN violet emission and the initial grey body radiation. However, the sodium lines present in the ASTERM experiment are clearly absent from the CBCF spectra. This observation rules out the possibility that the sodium seen in the ASTERM experiments could be due to contamination from the setup or handling of the samples as setup and experimental procedure in the two experiments was identical.

High-resolution spectroscopy was employed to identify the intense line observed around 588 nm with the Ocean Optics spectrometer in **Figure 3**. The high-resolution spectrum shown in **Figure 4** shows that this line is in fact a doublet of lines originating from two states very close in energy and having very similar transition probabilities. The only difference between the two lines is that the degeneracy of the emitting level is 4 for the line at 589.0 nm, and 2 for the line at 589.6 nm. Thus the line at 589 nm should be twice as intense as the one at 589.6 nm. This is clearly what we observe in the high-resolution spectrum shown in **Figure 4**, thus confirming that this is the sodium doublet.

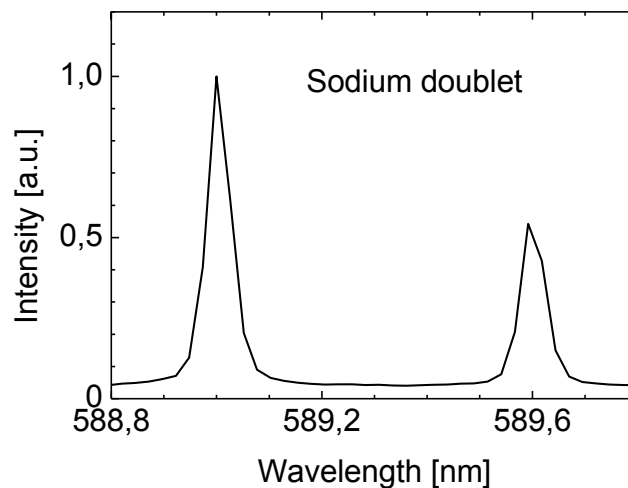


Figure 4. High-resolution spectrum taken with the SpectraPro spectrometer, showing the sodium doublet (589.0 and 589.6 nm).

Thermal images and recession rates were recorded for both materials at both flow conditions. The indicated surface temperature measured with a single-point optical pyrometer was between 1700 and 2000 K over test times of about 500 s. The TCRP temperature profiles for the case of an ASTERM sample in the 5 cm plasma are shown in **Figure 5**. It is clearly evident how uniform the spatial distribution of temperature is. It is also quite steady with time. The agreement of the Minolta pyrometer with the TCRP contours was very close, too, due to the absence of strong temperature gradients across the field of view.

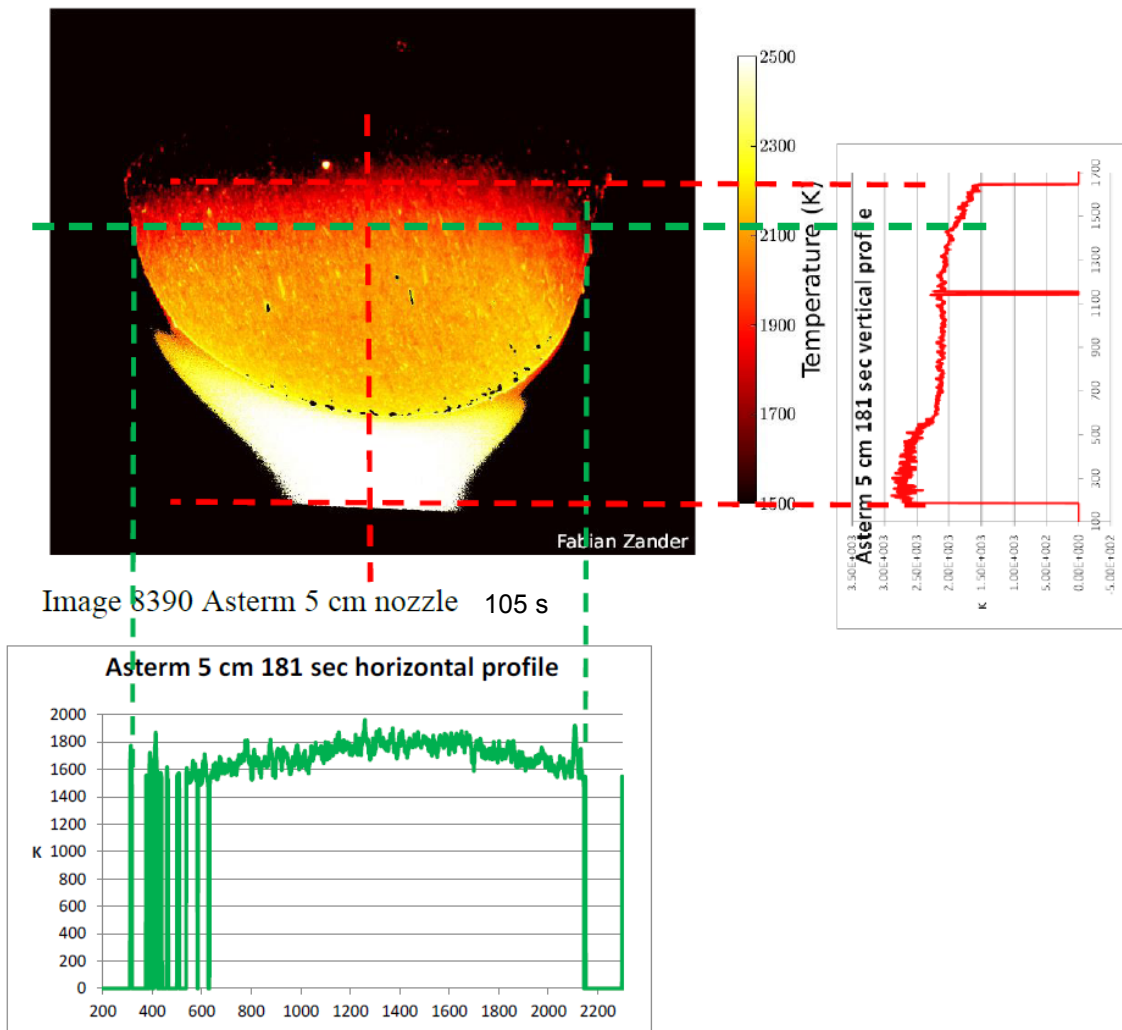


Figure 5. Thermography from ASTERM in 5 cm nozzle at 105 s after 100 % air test condition is reached, Minolta pyrometer indicated temperature, 2180 K.

Recession rates were measured with both the Acton SpectraPro spectrometer and the DSLR video. A comparison of the two methods showed good agreement, as is illustrated in Figure 6 for CBCF with the 7 cm diameter plasma flow.

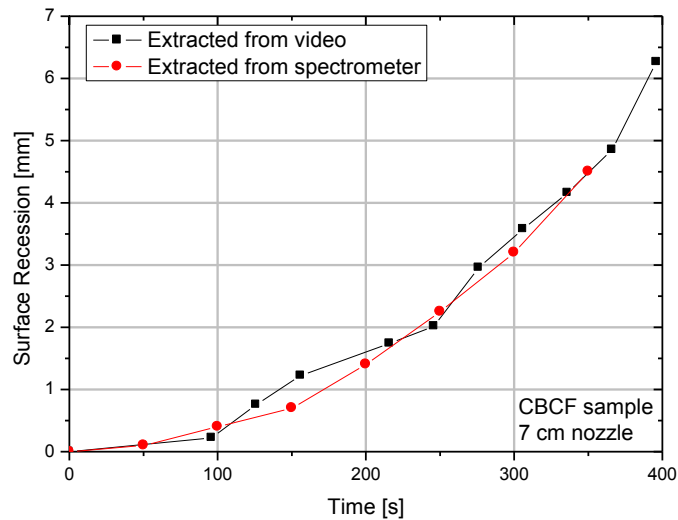


Figure 6. CBCF with 7 cm nozzle, recession rate comparison of video and spectral methods.

Preliminary measurements of CN, O, N₂, and Na species profiles have also been completed and are in the process of being analyzed.

CONCLUSIONS

The objective of this work was to provide a preliminary assessment of the interactions between an air plasma flow and an ablating material. To this end, a new plasma torch facility was commissioned and a characterization system including optical pyrometry, optical emission spectroscopy, and imaging for thermography and surface ablation measurement was developed.

The first tests were completed with ASTERM and CBCF ablating materials for an initial set of relatively low power conditions (40 kW plate power), providing an air plasma at atmospheric pressure with a torch nozzle diameter of 5 cm and 7 cm. The indicated surface temperature measured with the Minolta pyrometer was between 1700 and 2000 K.

The recession rates of ASTERM and CBCF were measured using two techniques: first, by imaging a local ablator surface element with an ICCD camera, and second using high-definition video imaging to continuously measure the shape of the exposed surface of the ablator in a plane normal to a selected line-of-sight. The recession rates deduced from these measurements agreed well and provided a recession rate of 1 to 2 mm/minute over the temperature range investigated.

Two-Color Ratio Pyrometry (TCRP) was used to give two-dimensional thermal imaging of the ablating surface. This technique provided results consistent with the bulk reading of the pyrometer. In addition, it provided detailed surface temperature distribution information from which the local heat transfer rate can be determined.

ACKNOWLEDGEMENTS

The research leading to these results received funding from the European Union Seventh Framework Programme (FP7/2007-2013) under grant agreement no. 241992. Support for M.E. MacDonald was provided by the United States National Science Foundation. Support for C.M. Jacobs was provided by the Centre National des Etudes Spatiales. The authors wish to thank Umar Sheikh for his assistance with the experiments.

REFERENCES

- [1] Laux, C.O. Winter, M., Merrifield, J., Smith, A., and Tran, P., "Influence of Ablation Products on the Radiation at the Surface of a Blunt Hypersonic Vehicle at 10 km/s," *AIAA 2009-3925, 41st AIAA Thermophysics Conference*, San Antonio, TX, June 22-25, 2009.
- [2] Laux, C.O., "Optical diagnostics and radiative emission of high temperature air plasmas," Ph.D. thesis, Stanford University, 1993.
- [3] Tran, H., Johnson, C., Rasky, D., Hui, F., Hsu, M.-T., Chen, T., Chen, Y.K., Paragas, D. and Kobayashi, L., "Phenolic Impregnated Carbon Ablators (PICA) as Thermal Protection Systems for Discovery Missions," NASA Technical Memorandum TM-110440, 1997.
- [4] Zander F. 'Hot wall testing in hypersonic impulse facilities', PhD Thesis under review, University of Queensland 2013.
- [5] Zander, F., Morgan, R.G., Sheikh, U.A., Buttsworth, D.R., Teakle, P.R., "Hot wall reentry testing in hypersonic impulse facilities," *AIAA Journal*, Vol. 51, No. 1, February 2013.

A New Calibration Based Inverse Method for Estimating Surface Heat Flux

Presented at:

European Space Agency

Thermal Protection Systems and Hot Structures Workshop

Noordwijk, Netherlands

10 April 2013

J.I. Frankel, Ph.D., Professor, Associate Fellow AIAA
Mechanical, Aerospace and Biomedical Engineering Department
University of Tennessee, Knoxville
Knoxville, TN 37996-2210

Acknowledgements:

NASA Cooperative Agreement: NNX10AN35A

NSF CBET-1137625

NSF CBET-1153476

NSF CBET-1234419

UTK Group: Dr. M. Keyhani

Present Graduate Students: D. Bottlaender, Y. Chen, H. Chen, A. Pande, K. Winstead, A. Hashemian

Past Graduate Students: B. Elkins, J. Plewa



Context: Hypersonics Heating Conditions (applications and materials)

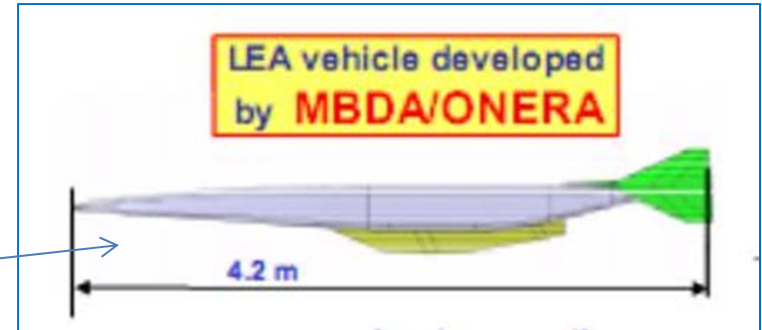
Mach 6-8 Sharp Edge
Nose Cones Germany's DLR

Bremen, DE October 2009,
Shefex II



Collaboration under development with MBDA (materials, ZrO₂)

Internal and External considerations



Translating cowl section

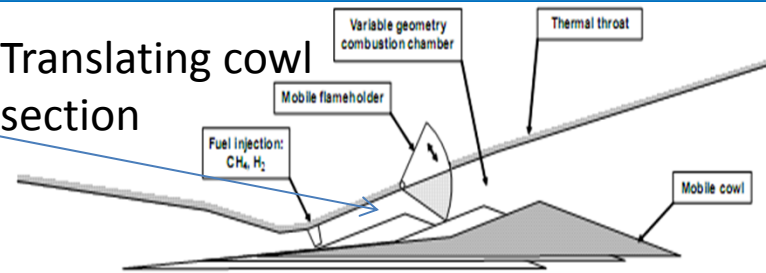
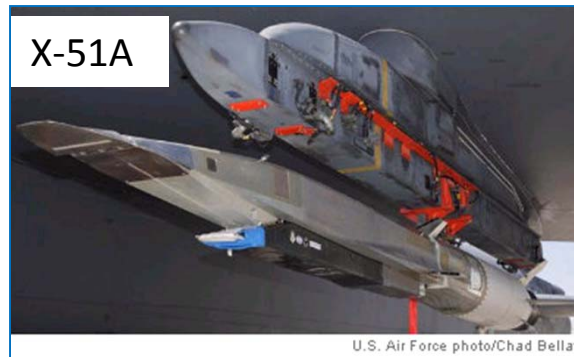
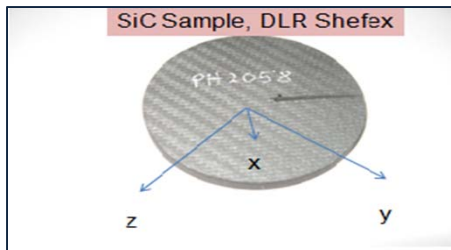


Fig 6-concept of translating cowl variable geometry engine

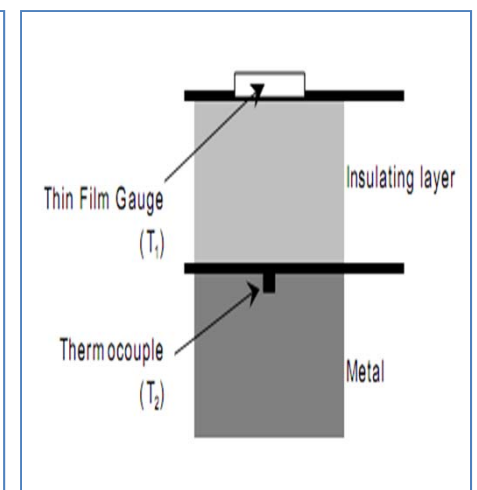
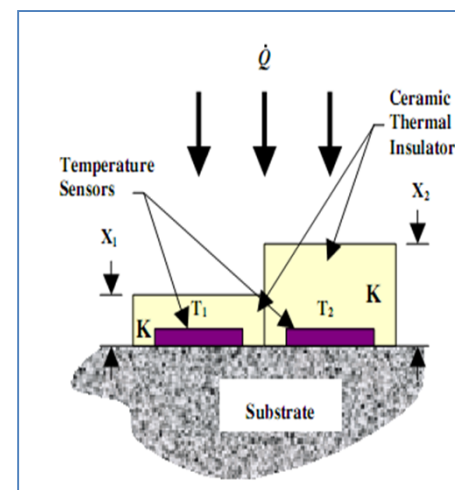
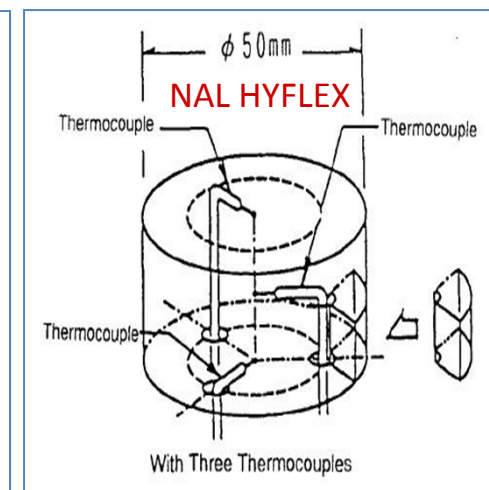
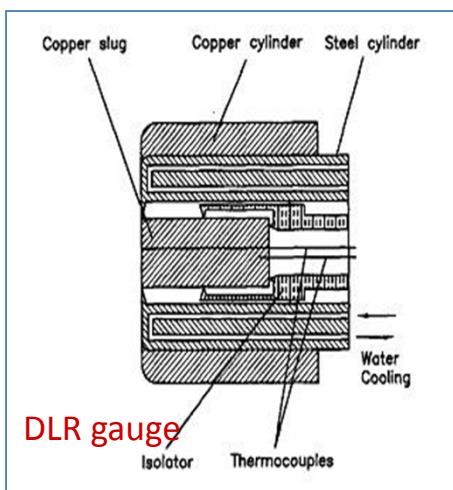
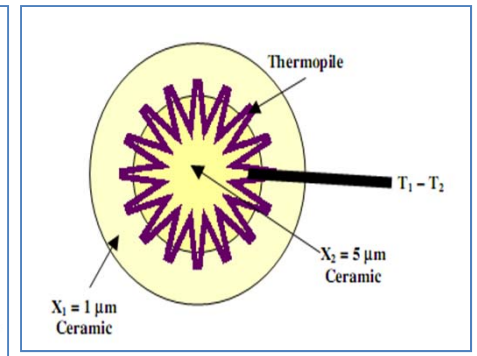
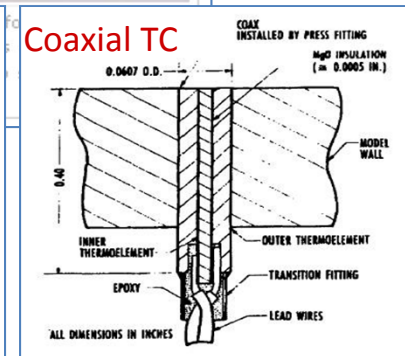
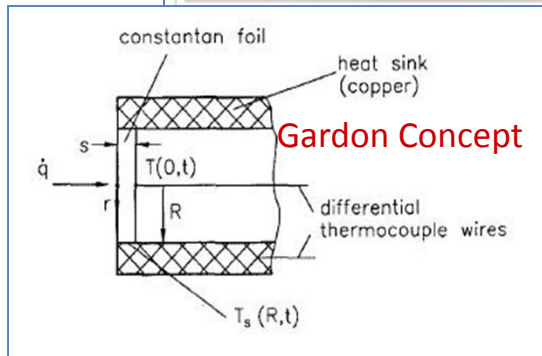
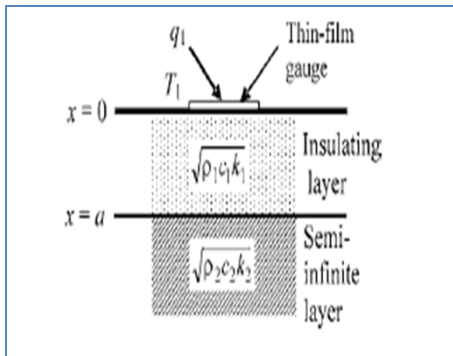
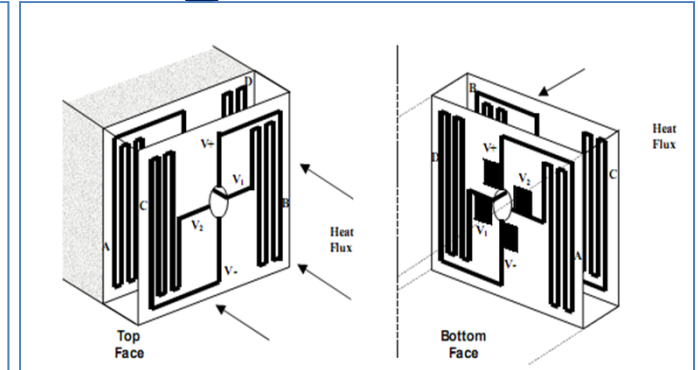
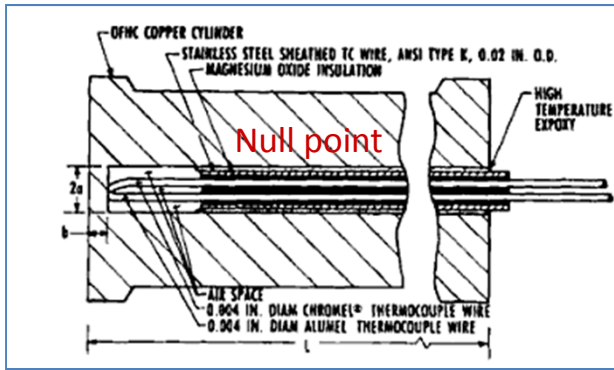


A New Calibration Approach for Predicting Surface Heat Fluxes Using In-Depth Sensors for Hypersonic Heating Applications

Objectives:

- ▣ Develop transformative calibration method and experimental test-beds for predicting surface heat fluxes (W/m^2) and total surface heat transfer (W) using in-depth temperature sensors with the intent of reducing systematic errors.
- ▣ Develop calibration methodology that possesses a fundamental and unified mathematical basis for generalization to multi-dimensions, multi-region, isotropic or orthotropic materials leading to a n-dimensional Volterra integral formulation.
- ▣ Develop regularized numerical method that produces stable and accurate heat flux predictions.

Common Heat Flux Sensor Configurations

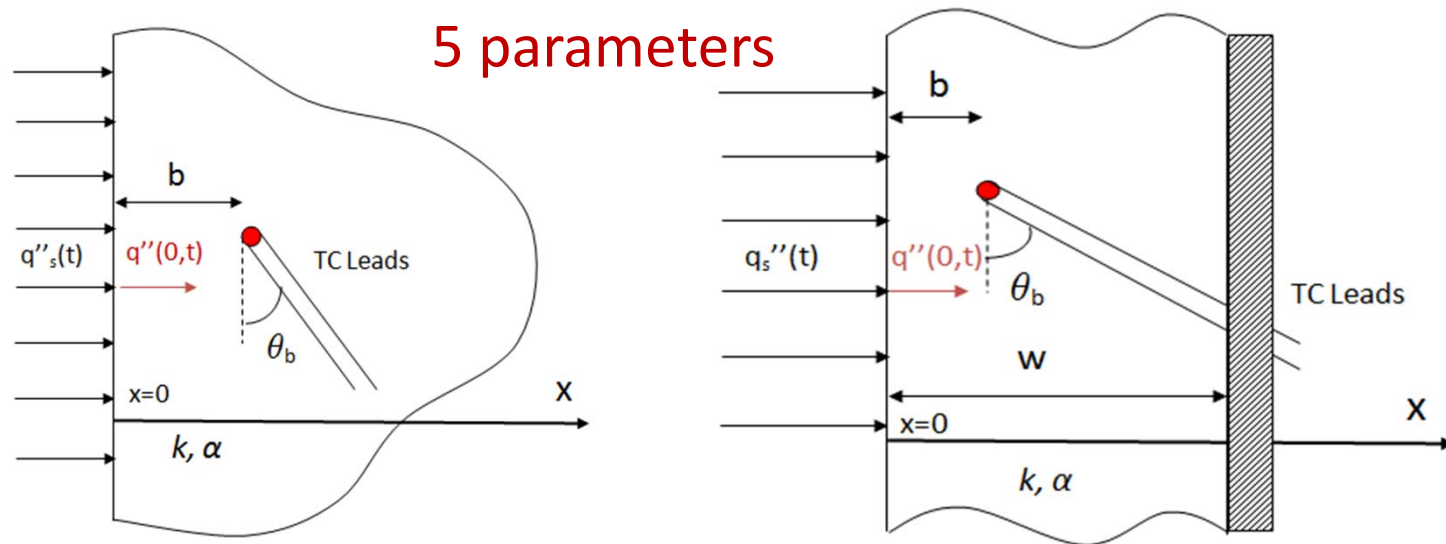


Concept Development: Use of In-Depth TC's in Through Plug Configurations

One-Dimensional Surface Heat Flux Calibration Integral Equations – Various Configurations (linear /nonlinear analyses)

- **Applications:**
 - Determine the surface heat flux in TPS's for material evaluation purposes
 - non-recessive surfaces (heat flux and/or surface temperature)
 - recessive surfaces associated with oxidation-chemical erosion processes (heat flux and recession rate)
 - Determine total heat (W) (ex., as needed in combustors)
- **Savings :**
 - Substantial reduction in systematic errors (no material properties, no positioning requirements)

I: Linear Analysis- (AIAA JTPHT (2, 2013),2013; Shock Waves, 2013)
 One-Region, One-Sided, One-Dimensional Calibration Integral Equation (surface heat flux and surface Temperature, $T_{oc}=T_{or}=0^{\circ}\text{C}$ for simplicity)



Surface Heat Flux Calibration (0 parameters required):

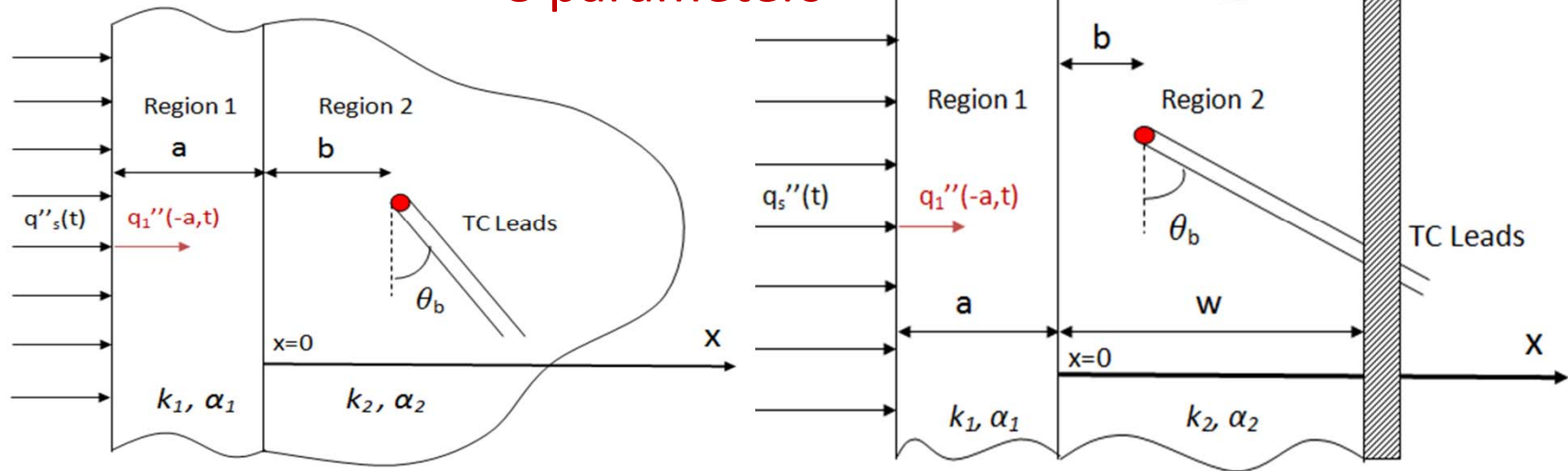
$$\int_{u=0}^t q''_r(0,u)T_{tc,c}(b,t-u)du = \int_{u=0}^t q''_c(0,u)T_{tc,r}(b,t-u)du, \quad t \geq 0$$

Surface Temperature Calibration:

$$\int_{u=0}^t T_r(0,u)T_{tc,c}(b,t-u)du = \int_{u=0}^t T_c(0,u)T_{tc,r}(b,t-u)du, \quad t \geq 0$$

Two-Region, One-Sided, One-Dimensional Calibration Integral Equation (surface heat flux and surface temperature)

8 parameters



Surface Heat Flux Calibration (0 parameters required):

$$\int_{u=0}^t q''_{r,1}(-a,u) T_{tc,c,2}(b,t-u) du = \int_{u=0}^t q''_{c,1}(-a,u) T_{tc,r,2}(b,t-u) du, \quad t \geq 0$$

Surface Temperature Calibration:

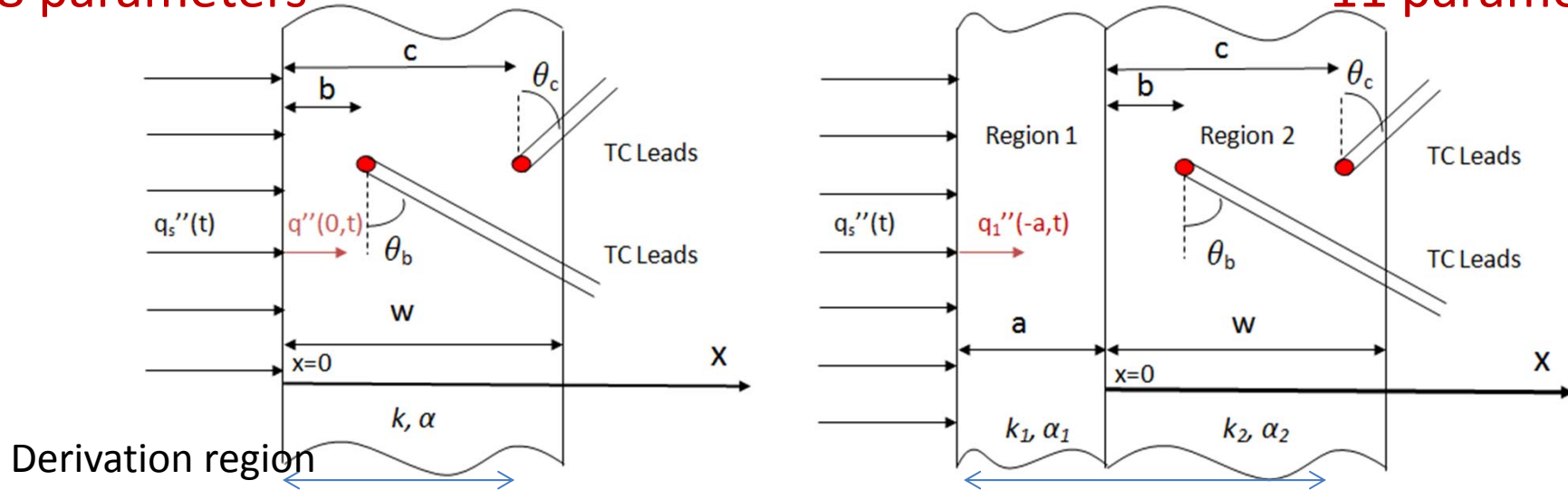
$$\int_{u=0}^t T_{r,1}(-a,u) T_{tc,c,2}(b,t-u) du = \int_{u=0}^t T_{c,1}(-a,u) T_{tc,r,2}(b,t-u) du, \quad t \geq 0$$

Two-Sided, One-Dimensional Calibration

Integral Equation (surface heat flux) – Option 1

8 parameters

11 parameters



Surface Heat Flux Calibration (one – region):

$$\int_{u=0}^t q_r''(0,u) \int_{r=0}^{t-u} \left(T_{tc,c_1}(c,r) T_{tc,c_2}(b,t-u-r) - T_{tc,c_2}(c,r) T_{tc,c_1}(b,t-u-r) \right) dr du =$$

$$\int_{u=0}^t T_{tc,r}(b,u) \int_{r=0}^{t-u} \left(q_{c_2}''(0,r) T_{tc,c_1}(c,t-u-r) - q_{c_1}''(0,r) T_{tc,c_2}(c,t-u-r) \right) dr du$$

$$- \int_{u=0}^t T_{tc,r}(c,u) \int_{r=0}^{t-u} \left(q_{c_2}''(0,r) T_{tc,c_1}(b,t-u-r) - q_{c_1}''(0,r) T_{tc,c_2}(b,t-u-r) \right) dr du$$

Several alternative formulations exist

Numerical Methodology

Regularization and Numerical Method

1. Define (First Kind Equation – exact) in context of one – region, semi – infinite geometry:

$$\int_{u=0}^t q_r''(0,u)T_{tc,c}(b,t-u)du = f(t), \quad t \in [0, t_{max}],$$

$$\text{where } f(t) = \int_{u=0}^t q_c''(0,u)T_{tc,r}(b,t-u)du, \quad t \geq 0$$

2. Time advancement by $t + \gamma$ ($\gamma =$ future time parameter):

$$\int_{u=0}^{t+\gamma} q_r''(0,u)T_{tc,c}(b,t+\gamma-u)du = f(t+\gamma), \quad t \in [0, t_{max} - \gamma]$$

3. Form approximate second kind equation (assume $q_r''(0,u) = q_r''(0,t)$ in $u \in [t, t + \gamma]$)

$$\int_{u=0}^t q_{r,\gamma}''(0,u)T_{tc,c}(b,t+\gamma-u)du + q_{r,\gamma}''(0,t) \int_{u=0}^{\gamma} T_{tc,c}(b,\gamma-u)du = f(t+\gamma)$$

$$\text{where } q_{r,\gamma}''(0,t) \approx q_r''(0,t).$$

4. Implement numerical method for estimating $q_{r,\gamma}''(0,t)$ for fixed future-time parameter, γ
5. Form residuals and running average for estimating γ_{opt} (also use additional metrics)

$$r_{\gamma}(t) = \int_{u=0}^t q_{r,\gamma}''(0,u)T_{tc,c}(b,t-u)du - f(t), \quad t \in [0, t_{max} - \gamma],$$

$$\bar{r}_{\gamma}(t) = \frac{1}{t} \int_{u=0}^t r_{\gamma}(u)du, \quad t \in [0, t_{max} - \gamma].$$

Expected Behavior of Residual Based on Theory

6. Expectations :

$$r_\gamma(t + \gamma) = -\frac{\partial q_r''}{\partial t}(0, t) \int_{u=0}^{\gamma} u T_{tc,c}(b, \gamma - u) du + \int_{u=0}^t (q_{r,\gamma}''(0, u) - q_r''(0, u)) T_{tc,c}(b, t + \gamma - u) du + \int_{u=t}^{t+\gamma} (q_{r,\gamma}''(0, u) - q_r''(0, t)) T_{tc,c}(b, t + \gamma - u) du + \dots + H.O.T.$$

From this, one would expect that the residual (near the optimal prediction) would behave proportionally to the time derivative of the heat flux, $q_r''(0, t)$.

Technical Issues:

I. Analytic Models:

- I.1) Heat Equation and properties
- I.2) Regularization model

II. Numerical Model:

- II.1) Integration method

III. Experimental Data Acquisition:

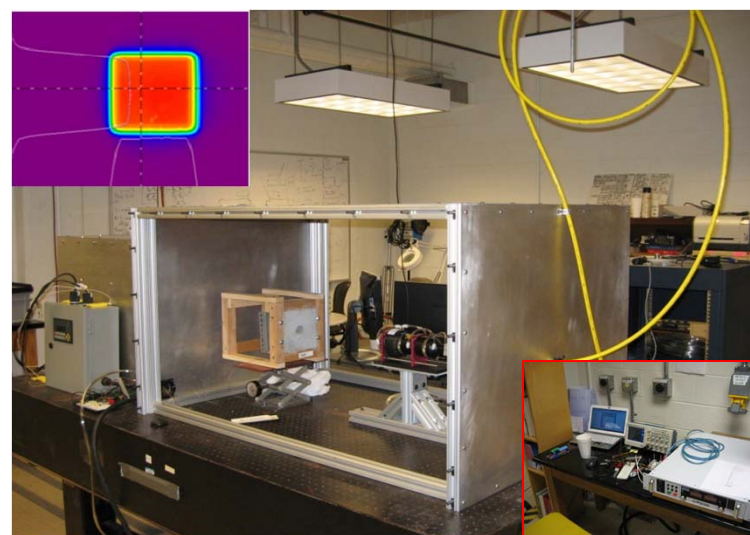
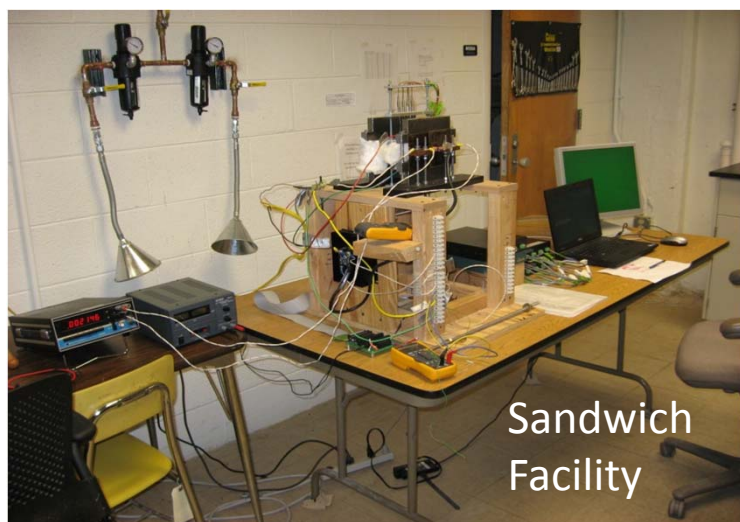
- III.1 DAQ on CAL and RUN

Base Residual (using 2 known fluxes)
views I.1 and II.1 with common III. DAQ

$$r_{base}(t) \square \int_{u=0}^t q_{c,2}''(0, u) T_{tc,c1}(b, t - u) du - \int_{u=0}^t q_{c1}''(0, u) T_{tc,c2}(b, t - u) du, \quad t \geq 0$$

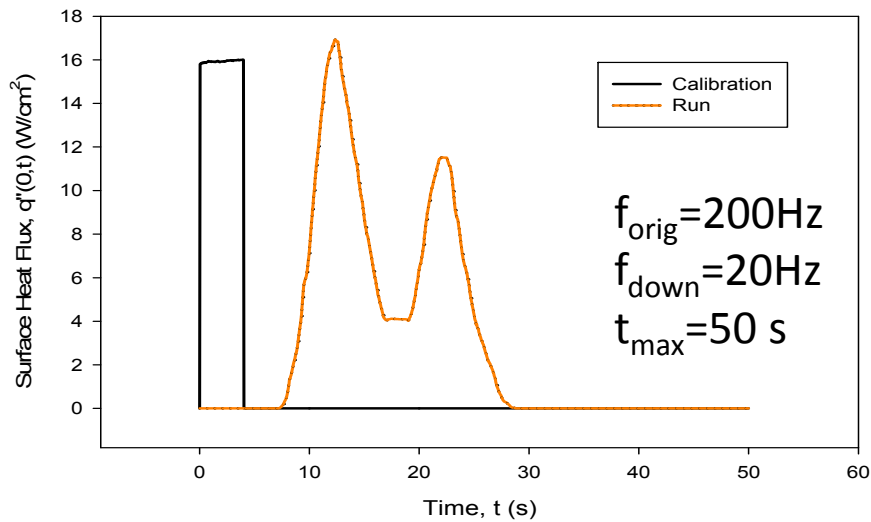
Conventional norms do not guarantee optimal results

UTK-Sandwich Heating Facility and Developing 500 W (0.91 μ m) laser Facility

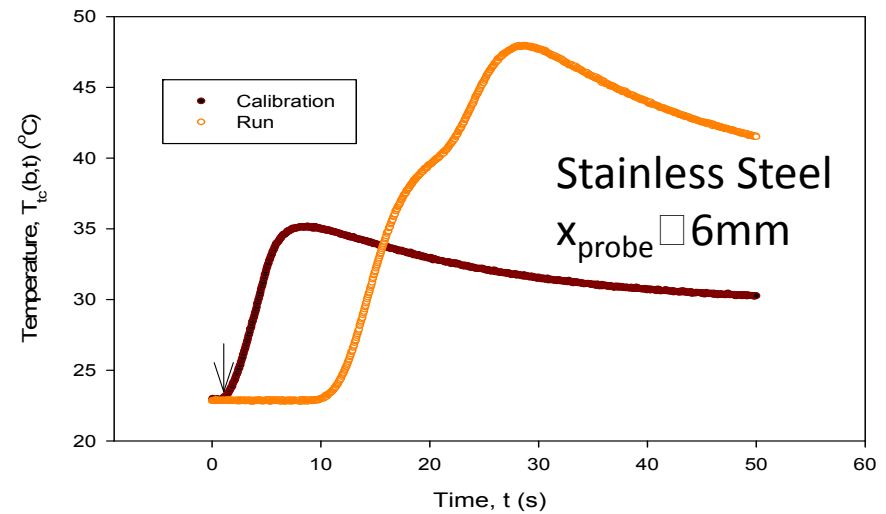


Sandwich Facility -Experimental Results for Verification of Theory- Stainless Steel (One-Probe Analysis) MK/JP Experiment-JIF Analysis

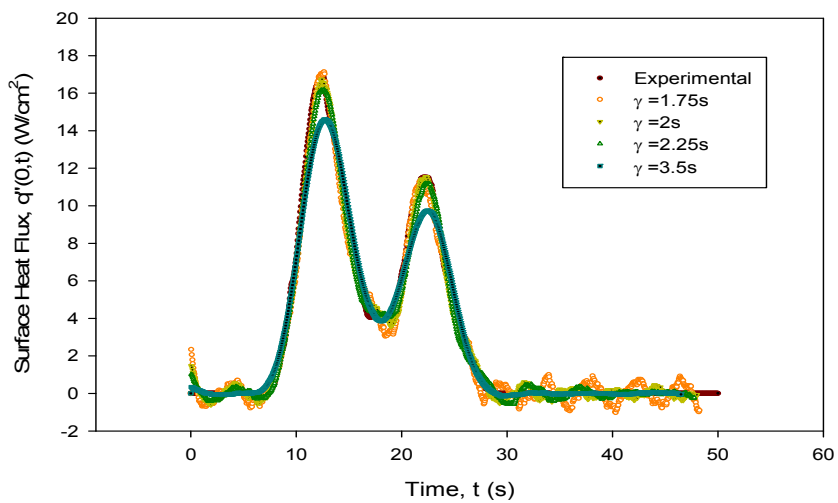
Heat Flux (experimental)



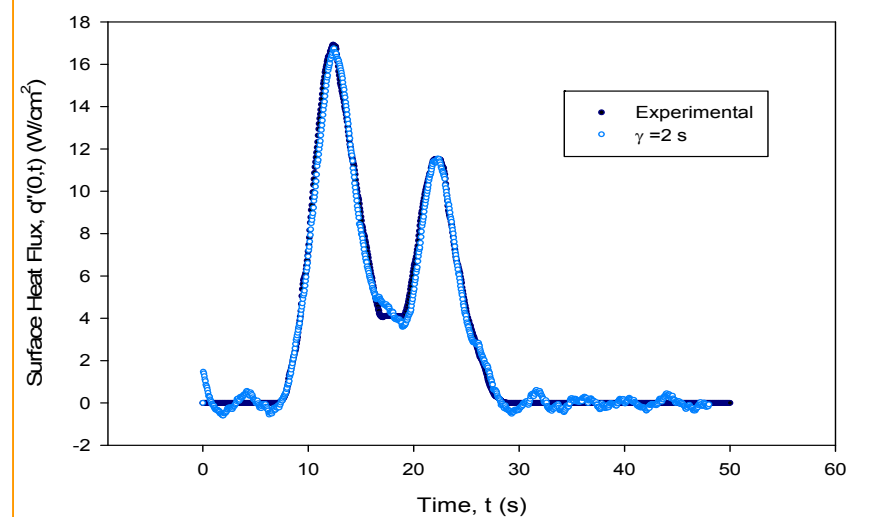
Thermocouple Temperature Data



Projected Surface Heat Flux

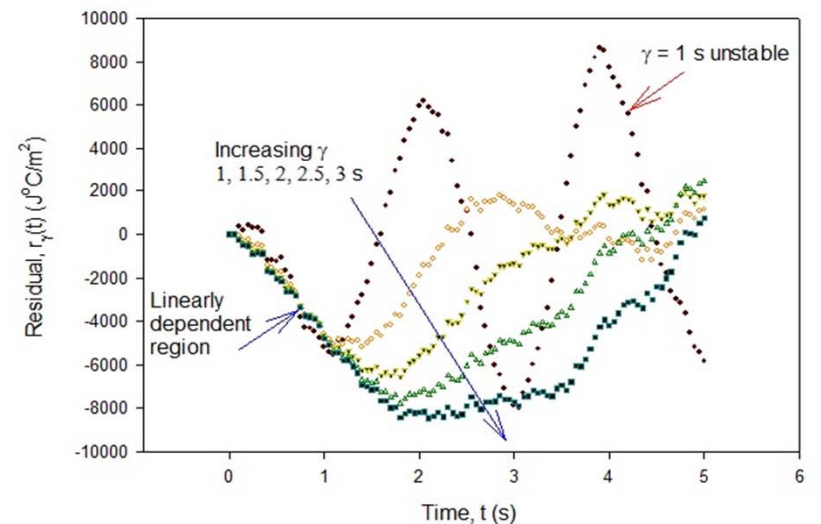
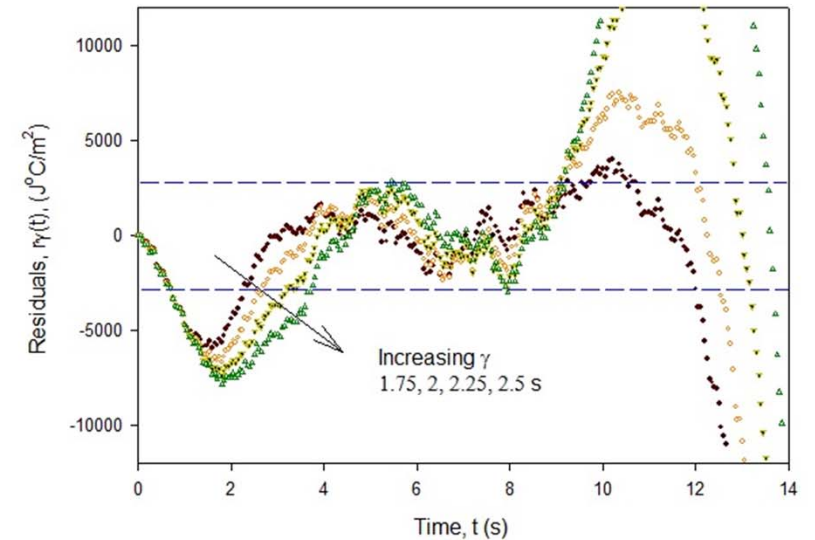
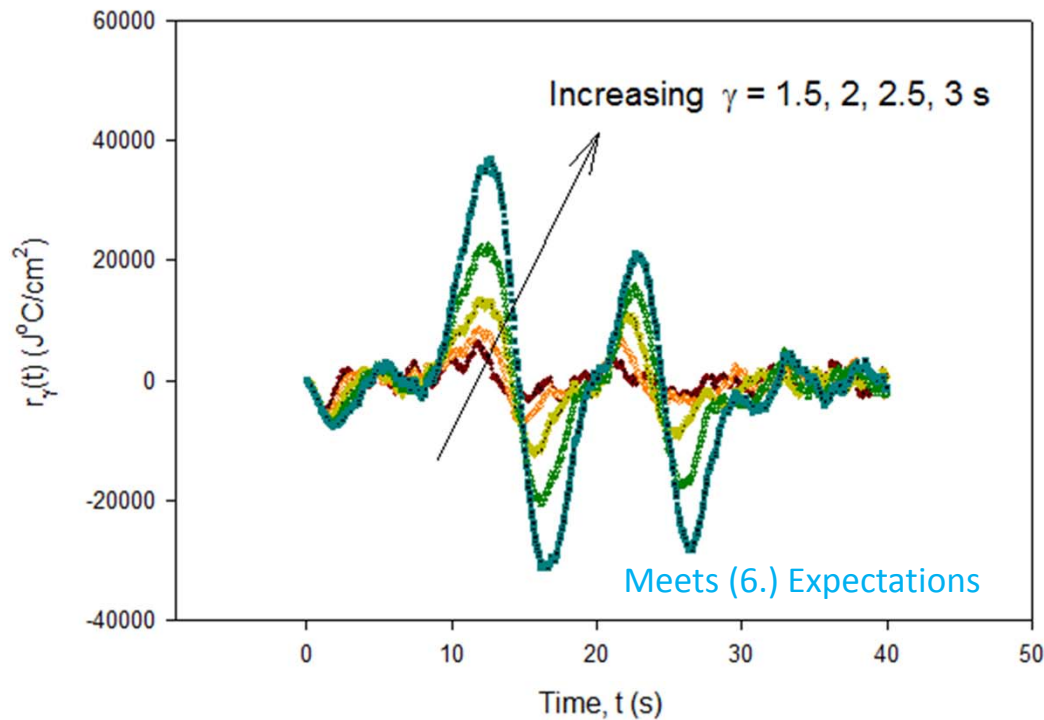


Optimal Prediction of Heat Flux



Residual Behavior

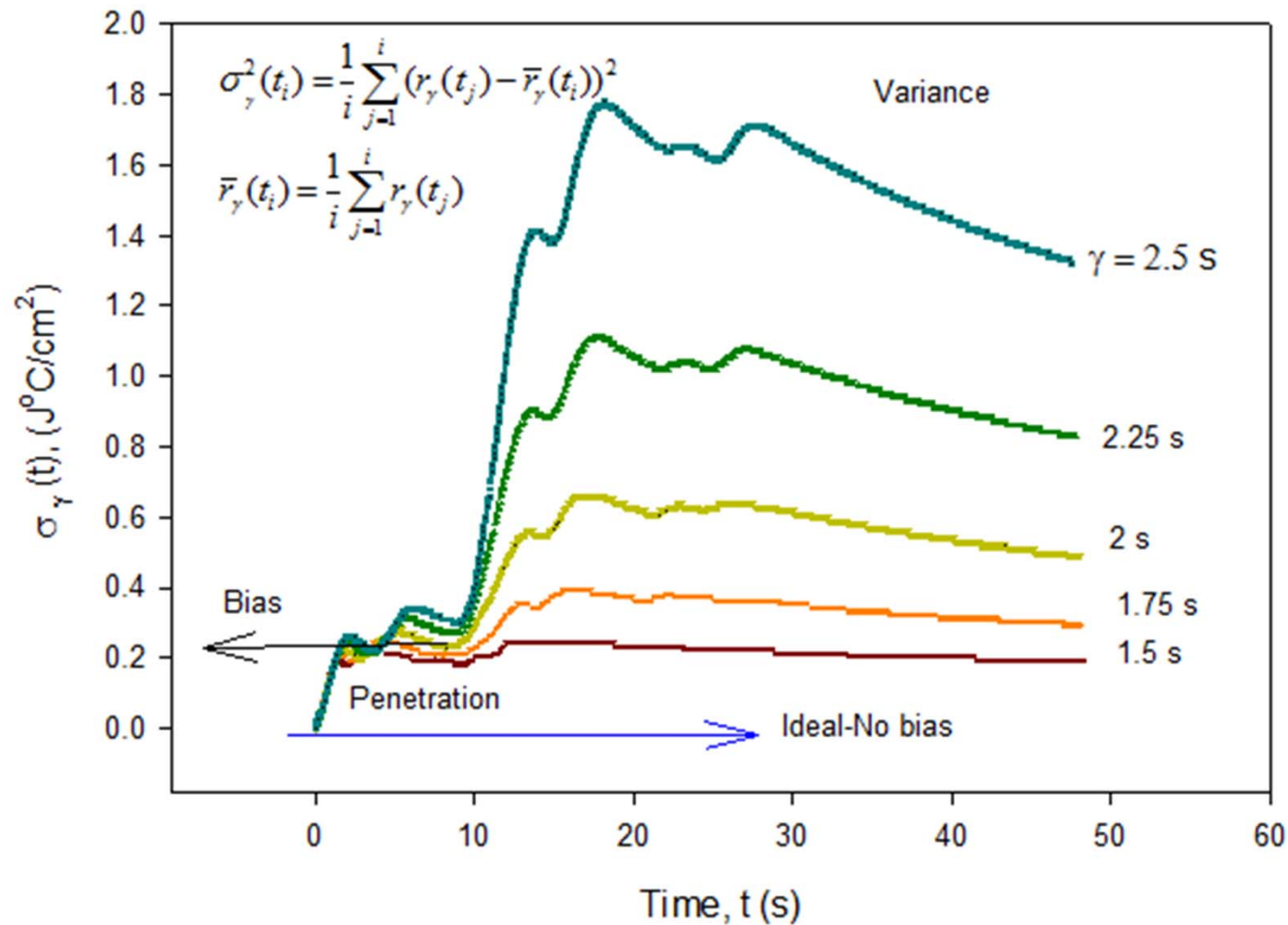
$$r_\gamma(t) \square \int_{u=0}^t q_{r,\gamma}''(0,u)T_{tc,c}(b,t-u)du - \int_{u=0}^t q_c''(0,u)T_{tc,r}(b,t-u)du, \quad t \geq 0$$



Over-smoothing occurs as \square increases beyond indicated values.

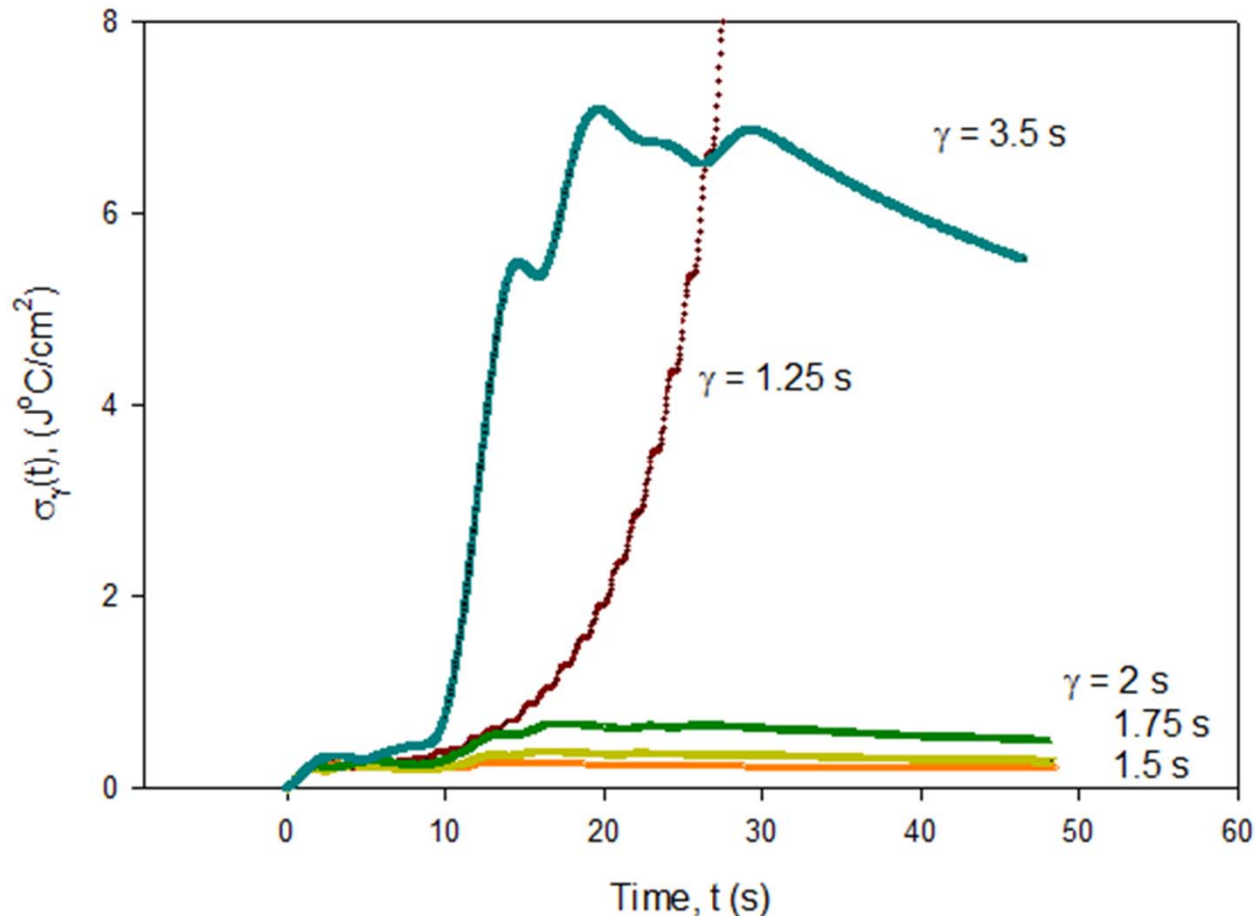
In this regularization methodology (local-future time), \square is robust.

SYSTEM Variance (S.D.) and Bias Control -System Performance: A New Measure-



We will come back to this fundamental plot for later considerations. Inverse analysis requires choosing an optimal solution. Purely norm based choices may not be the best indicator.

SYSTEM Variance (S.D.) and Bias Control -System Performance: A New Measure-



Four identifiable regions: early time, bias dominated, mixed bias-variance, variance dominated. Best physical representation should lie near instability (high frequency content).

II. Nonlinear Analysis-A **first step** based on the linearization of the nonlinear heat equation

Comment: Nonlinear problems are linearized. Linearization is normally thought to come from a numerical method. Here, we demonstrate linearization by choice of dependent variable and physical properties

One – dimensional, nonlinear heat equation

$$\rho c(T) \frac{\partial T}{\partial t}(x, t) = \frac{\partial}{\partial x} \left(k(T) \frac{\partial T}{\partial x}(x, t) \right), \quad (x, t) \geq 0,$$

subject to the boundary conditions

$$q_s''(t) = q''(0, t) = -k(T(0, t)) \frac{\partial T}{\partial x}(0, t),$$

$$\lim_{x \rightarrow \infty} T(x, t) = T_o, \quad t > 0,$$

and initial condition

$$T(x, 0) = T_o, \quad x \geq 0.$$

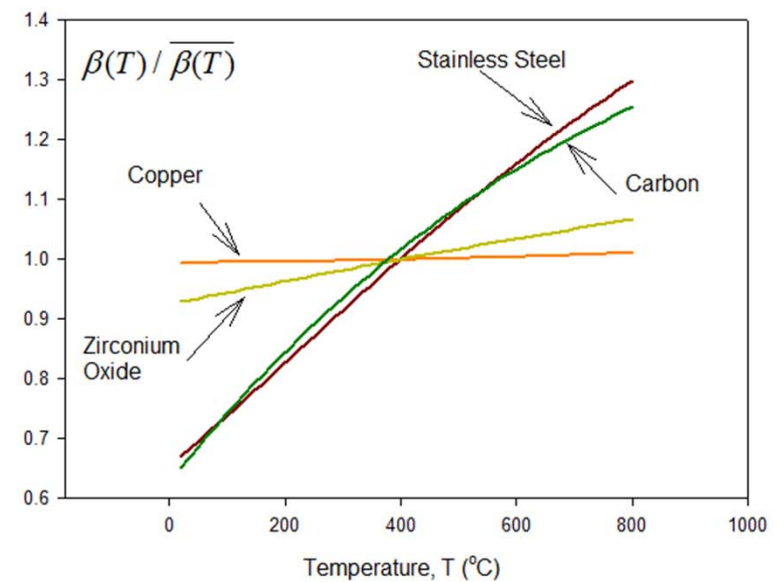
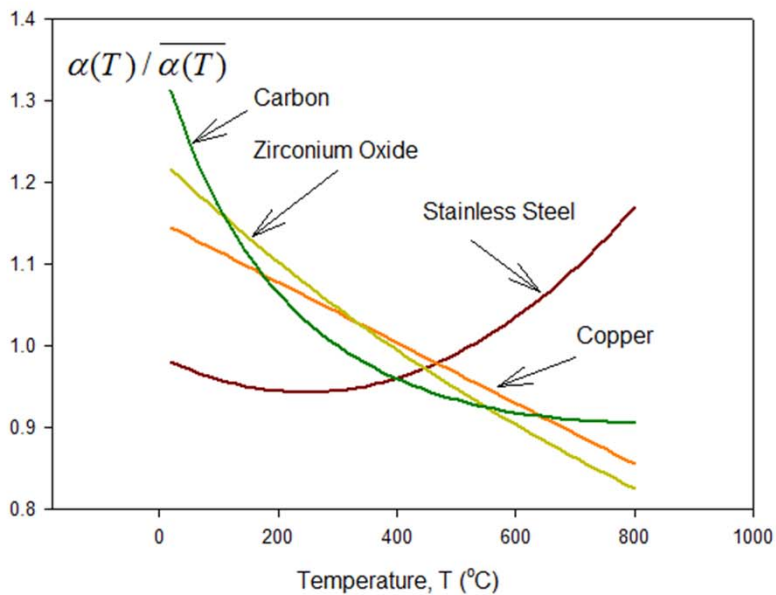
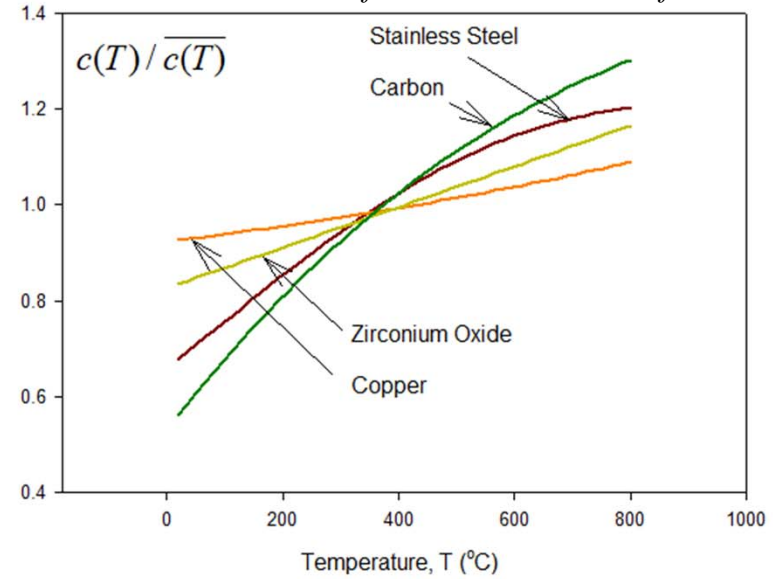
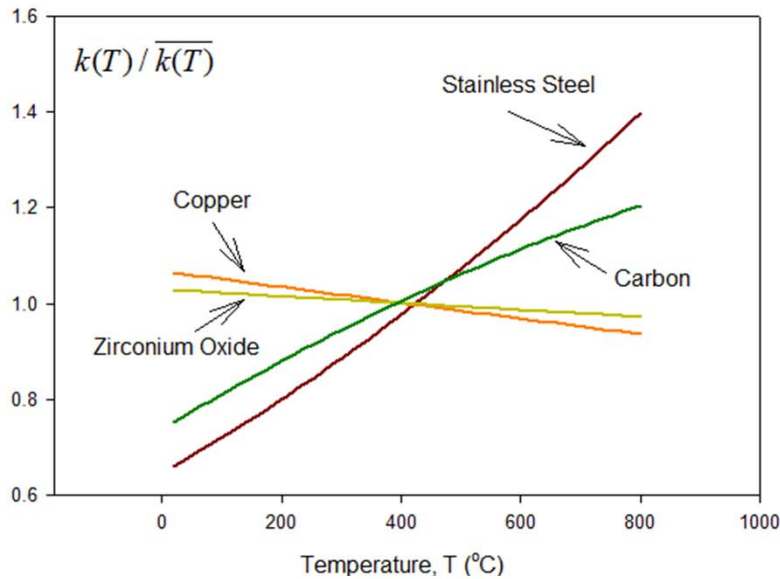
Primitive properties:
 $k(T), c(T), \alpha(T)$

First, Introduction of a novel abstraction or reformulation of the heat equation and its consequences

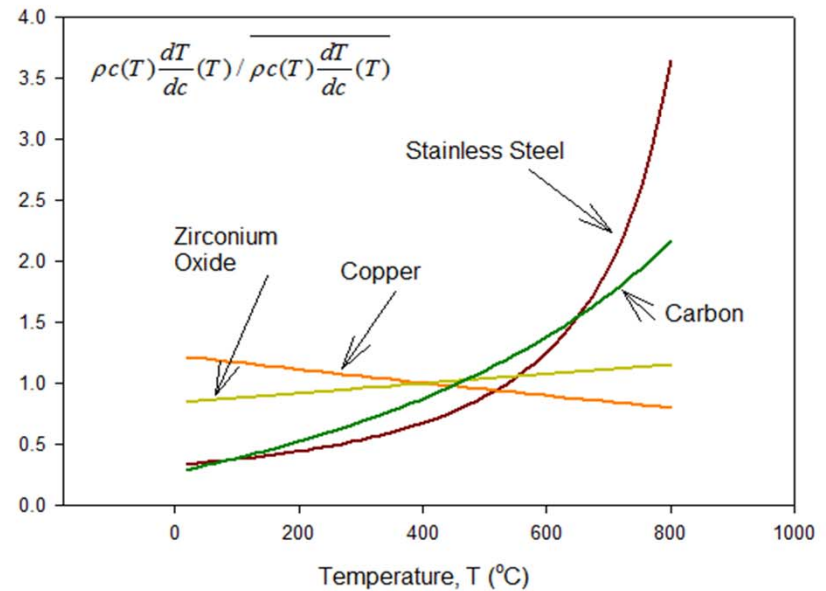
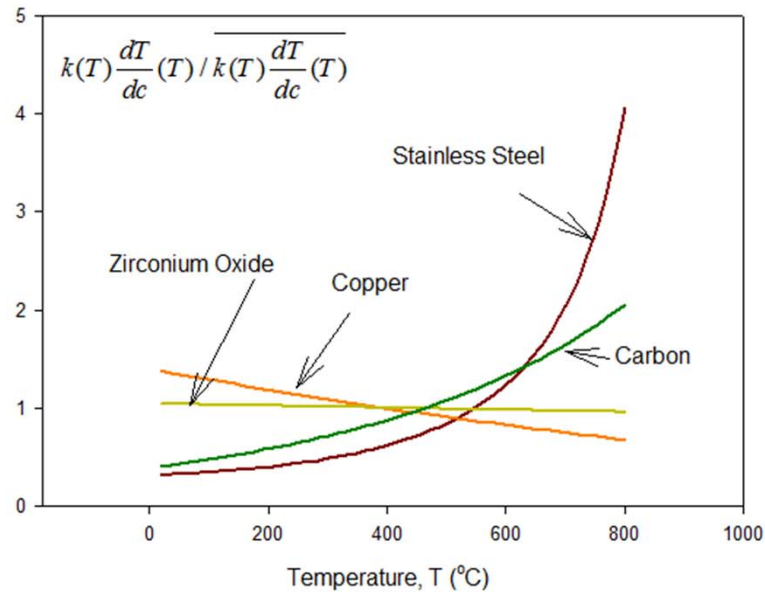
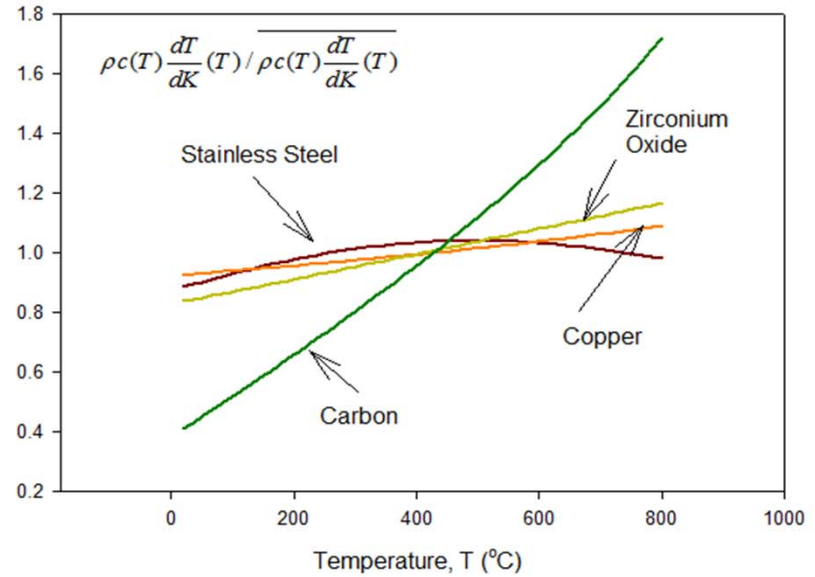
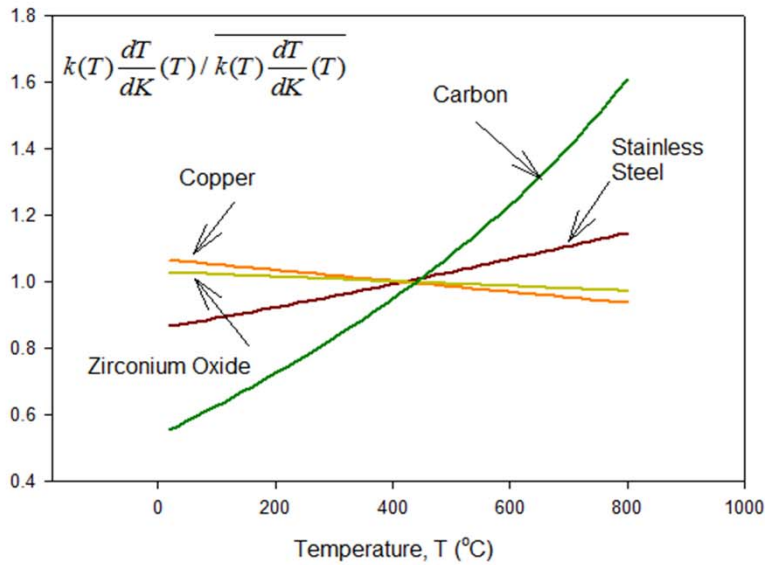
Representative Primitive Properties (correction zirconium di-oxide)

$$\bar{\psi} = \frac{1}{T_{\max} - T_{\min}} \int_{z=T_{\min}}^{T_{\max}} \psi(z) dz$$

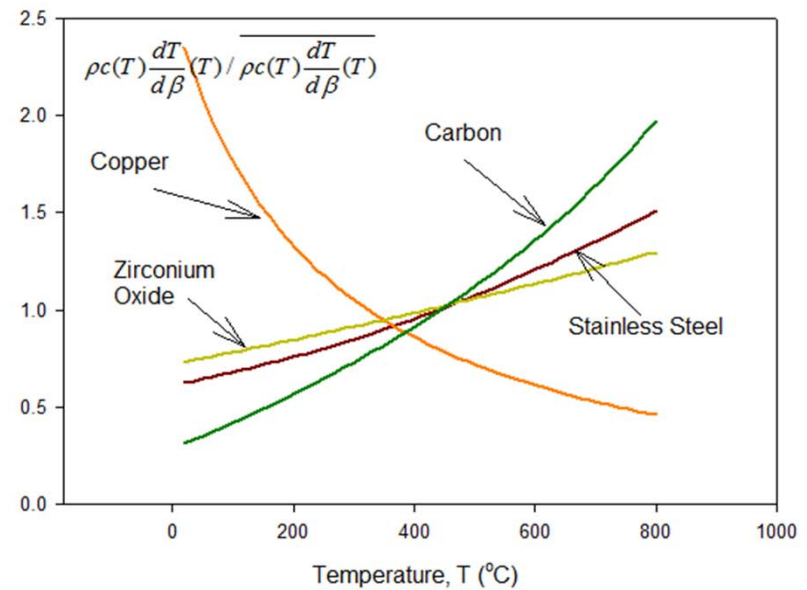
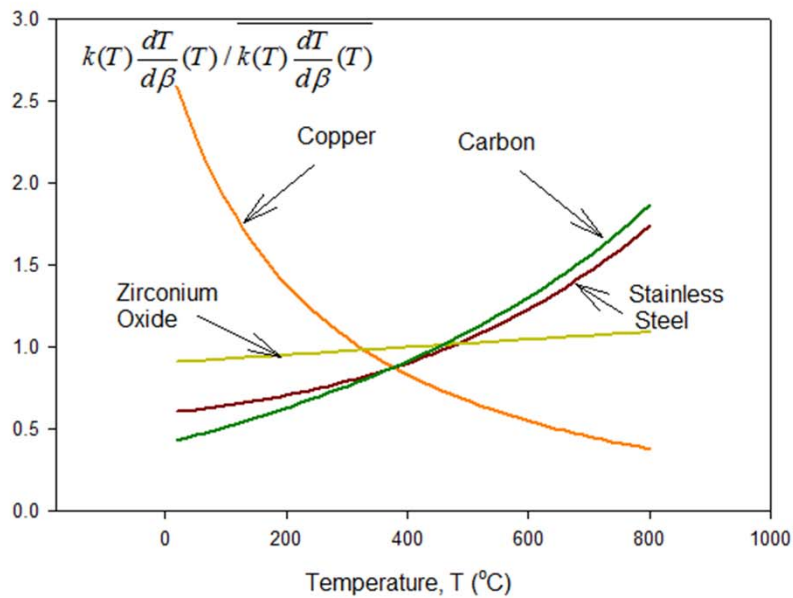
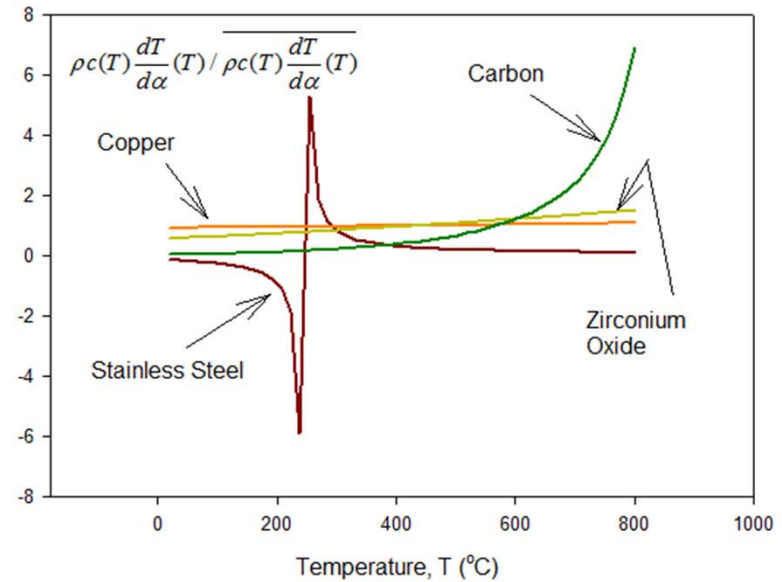
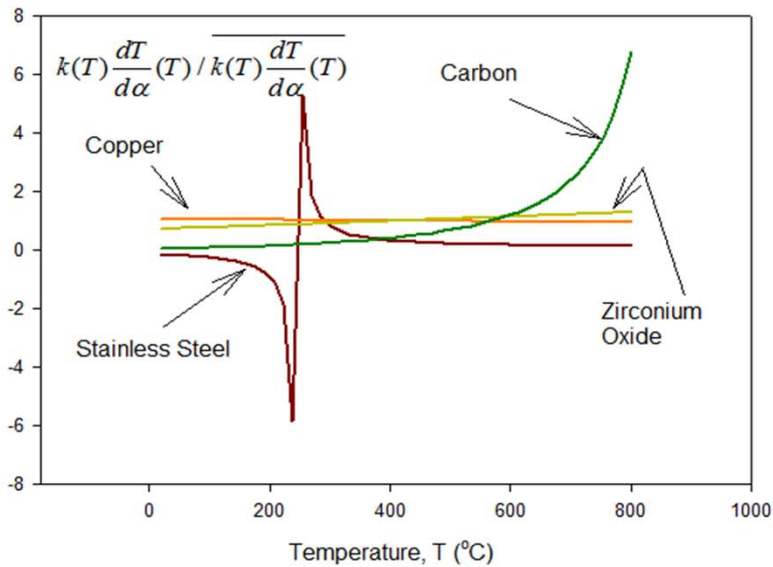
$$\psi(T) = \lambda_o + \lambda_1(T - T_{ref}) + \lambda_2(T - T_{ref})^2 + \dots$$



Alternative Property Selection based on Heat Equation Property Linearization



Alternative Property Selection based on Heat Equation Property Linearization



Kirchhoff and Alternative Property Transforms

Classical Kirchhoff (integral - based) Transform :

$$\Psi(T) = \frac{1}{k_o} \int_{z=T_o}^T k(z) dz = \Phi(x, t)$$

applied to the heat equation leads to

$$\frac{1}{\alpha(T)} \frac{\partial \Phi}{\partial t}(x, t) = \frac{\partial^2 \Phi}{\partial x^2}(x, t), \quad (x, t) \geq 0,$$

Auxiliary conditions: $q_s''(t) = q''(0, t) = -k_o \frac{\partial \Phi}{\partial x}(0, t)$, $\lim_{x \rightarrow \infty} \Phi(x, t) = 0$, $t > 0$,

and $\Phi(x, 0) = 0$, $x \geq 0$.

Assumption: If $\alpha(T)$ is relatively constant then we obtained the "linearized" equation

$$\frac{1}{\alpha} \frac{\partial \Phi}{\partial t}(x, t) = \frac{\partial^2 \Phi}{\partial x^2}(x, t), \quad (x, t) \geq 0.$$

General form for properties:

Note: $\lambda(T) = \lambda_o + \lambda_1(T - T_{ref}) + \lambda_2(T - T_{ref})^2 + \dots$ where $\lambda = k, c, \alpha$.

Differential Transforms (example)

Conductivity Transform:

$$\frac{\partial T}{\partial x}(x,t) = \frac{dT}{dk} \frac{\partial k}{\partial x}, \quad \frac{\partial T}{\partial t}(x,t) = \frac{dT}{dk} \frac{\partial k}{\partial t}, \quad k(T) = k(T(x,t)) = K(x,t)$$

∴ the N.L. heat equation becomes

$$\rho c(T) \frac{dT}{dk} \frac{\partial K}{\partial t}(x,t) = \frac{\partial}{\partial x} \left(k(T) \frac{dT}{dk} \frac{\partial K}{\partial x}(x,t) \right), \quad (x,t) \geq 0$$

for the moment, if

$$\beta_k = \rho c(T) \frac{dT}{dk} \approx \text{constant}, \quad \gamma_k = k(T) \frac{dT}{dk} \approx \text{constant then}$$

$$\frac{1}{\varepsilon_k} \frac{\partial K}{\partial t}(x,t) = \frac{\partial^2 K}{\partial x^2}(x,t), \quad (x,t) \geq 0 \quad \text{where } \varepsilon_k = \frac{\gamma_k}{\beta_k}$$

$$\text{Auxiliary conditions: } q_s''(t) = q''(0,t) = -\gamma_k \frac{\partial K}{\partial x}(0,t), \quad \lim_{x \rightarrow \infty} K(x,t) = k(T_o), \quad t > 0,$$

$$\text{and } K(x,0) = k(T_o), \quad x \geq 0.$$

Calibration Equations-Linearized Properties

Linear Heat Equation (T data):

$$\int_{u=0}^t q_r''(0,u) (T_{tc,c}(b,t-u) - T_{oc}) du = \int_{u=0}^t q_c''(0,u) (T_{tc,r}(b,t-u) - T_{or}) du, \quad t \geq 0$$

Kirchhoff Transform / $\alpha(T) \approx \alpha$ (T data):

$$\int_{u=0}^t q_r''(0,u) \Psi_c(b,t-u) du = \int_{u=0}^t q_c''(0,u) \Psi_r(b,t-u) du, \quad t \geq 0$$

Conductivity Transform (T data):

$$\int_{u=0}^t q_r''(0,u) (k_c(b,t-u) - k_{oc}) du = \int_{u=0}^t q_c''(0,u) (k_r(b,t-u) - k_{or}) du, \quad t \geq 0$$

Capacitance Transform (T data):

$$\int_{u=0}^t q_r''(0,u) (c_c(b,t-u) - c_{oc}) du = \int_{u=0}^t q_c''(0,u) (c_r(b,t-u) - c_{or}) du, \quad t \geq 0$$

Diffusivity Transform (T data):

$$\int_{u=0}^t q_r''(0,u) (\alpha_c(b,t-u) - \alpha_{oc}) du = \int_{u=0}^t q_c''(0,u) (\alpha_r(b,t-u) - \alpha_{or}) du, \quad t \geq 0$$

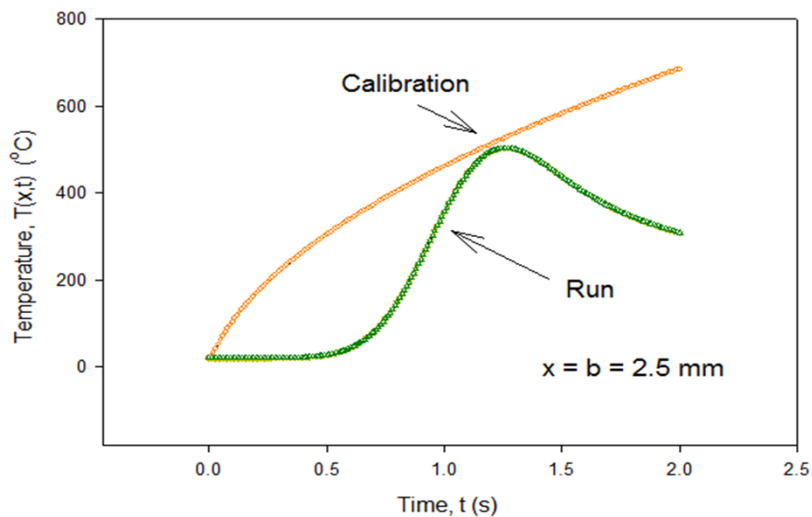
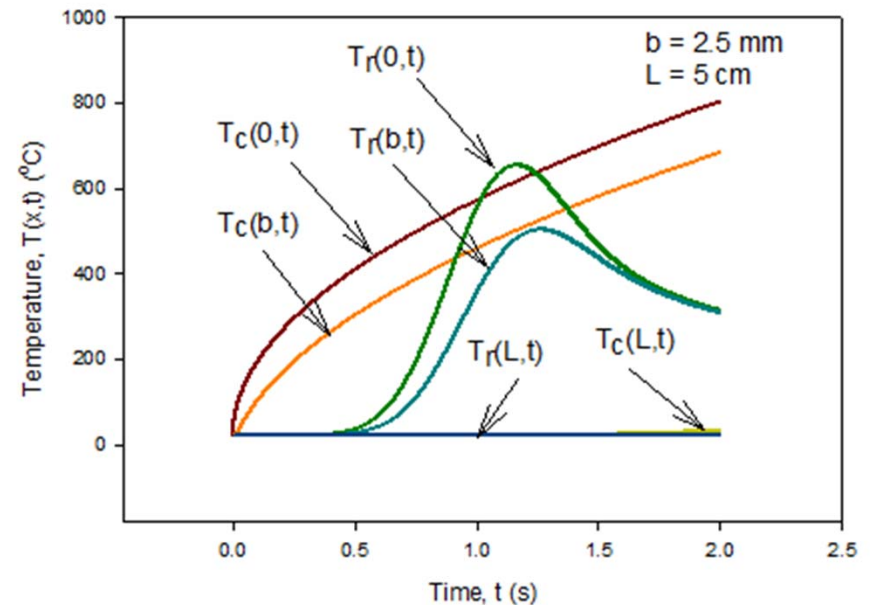
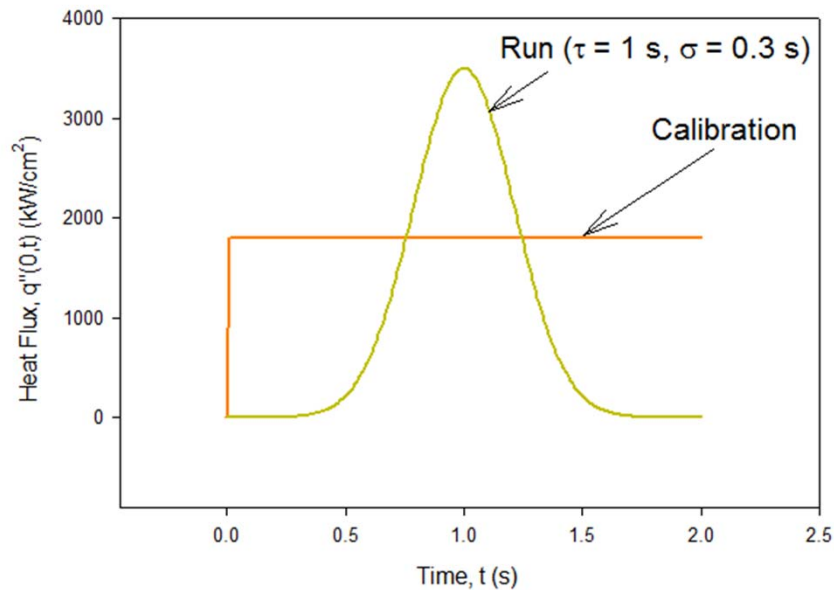
There exists others also

Max-Min of Properties-Metrics

Property Ratio (T ∈ [20,800]°C)	Copper Minimum	Copper Maximum	Stainless Steel Minimum	Stainless Steel Maximum
$k(T)/k_{avg}$	0.936	1.06	0.660	1.40
$c(T)/c_{avg}$	0.926	1.09	0.678	1.20
$\alpha(T)/\alpha_{avg}$	0.855	1.15	0.980	1.17
$\beta(T)/\beta_{avg}$	0.994	1.01	0.669	1.30
$(kdT/dk)/(kdT/dk)_{avg}$	0.934	1.07	0.867	1.15
$(\rho cdT/dk)/(\rho cdT/dk)_{avg}$	0.926	1.09	0.884	1.04
$(kdT/dc)/(kdT/dc)_{avg}$	0.676	1.38	0.317	4.07
$(\rho cdT/dc)/(\rho cdT/dc)_{avg}$	0.798	1.22	0.339	3.64
$(kdT/d\alpha)/(kdT/d\alpha)_{avg}$	0.936	1.07	5.84*	5.27*
$(\rho cdT/d\alpha)/(\rho cdT/d\alpha)_{avg}$	0.926	1.09	5.89*	5.31*
$(kdT/d\beta)/(kdT/d\beta)_{avg}$	0.378	2.59	0.605	1.74
$(\rho cdT/d\beta)/(\rho cdT/d\beta)_{avg}$	0.459	2.35	0.626	1.51

* Approximate

Numerical Simulations for Understanding Terms Copper-Errorless Data and Transforms



Copper- High k and used in many aero-tests ($b=2.5$ mm, $L=5$ cm)

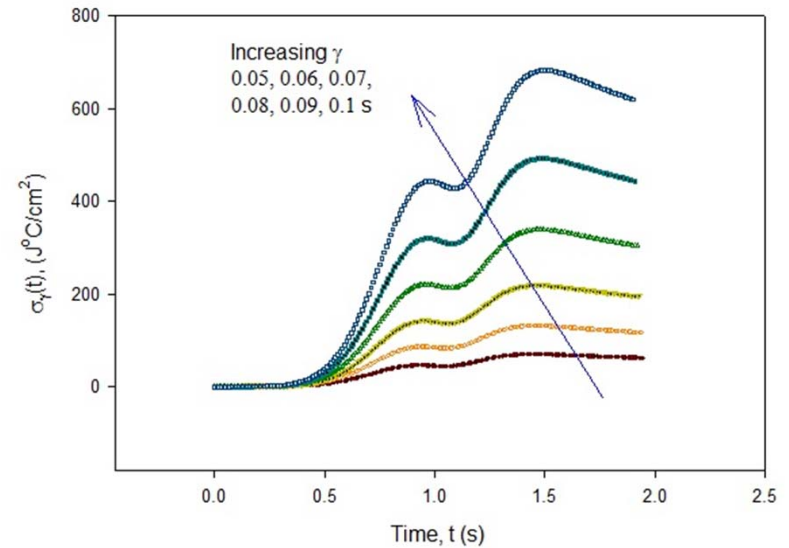
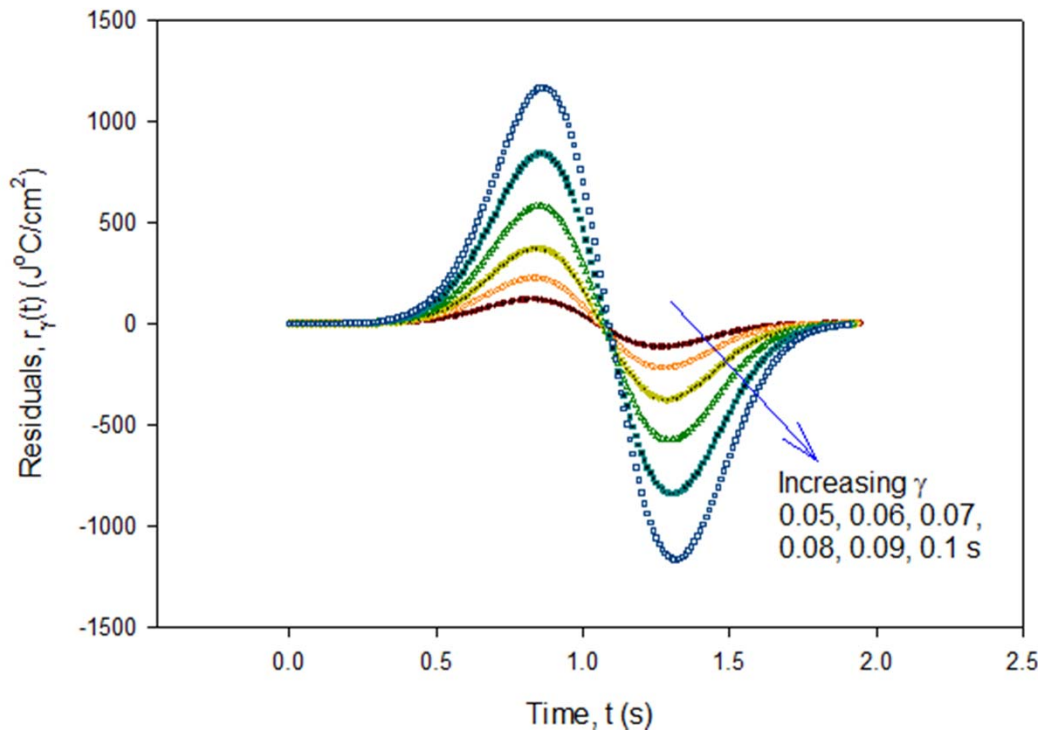
From previous primitive property slides, constant property assumption appears valid for 20-800°C range

Residuals-Cu

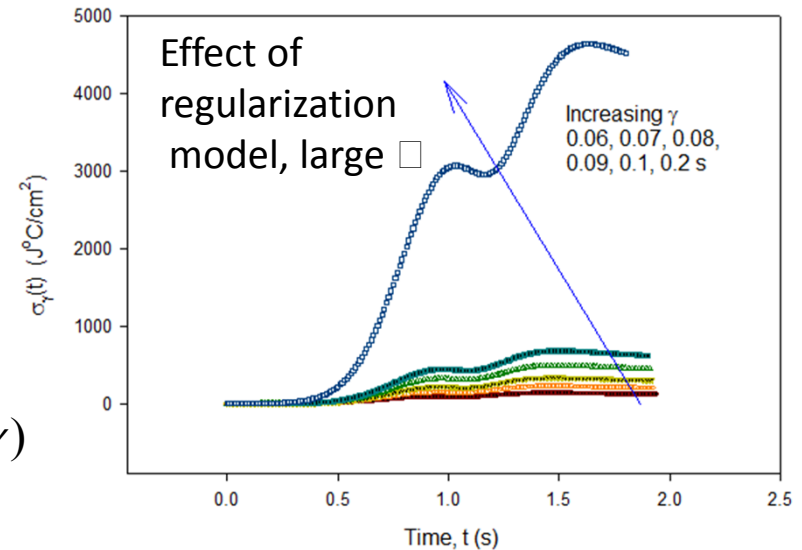
(down-sampling rate=100Hz from original FDM rate of 3kHz; $T_o=20^\circ\text{C}$)

Important-Try to keep bias as small as possible

Bias region (none-exact data)



Cannot see penetration time or bias when perfect data are used.



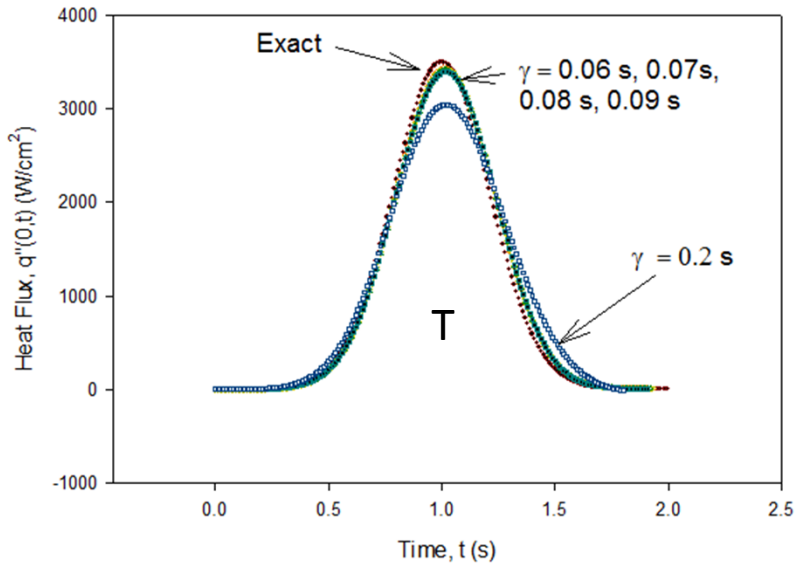
$$c_\gamma q_{r,\gamma}''(0,t) + \int_{u=0}^t q_{r,\gamma}''(0,u) T_{ic,c}(b,t+\gamma-u) du = f(t+\gamma)$$

where

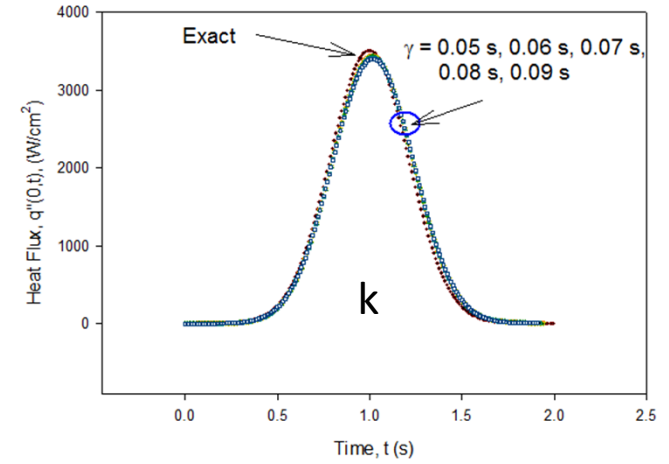
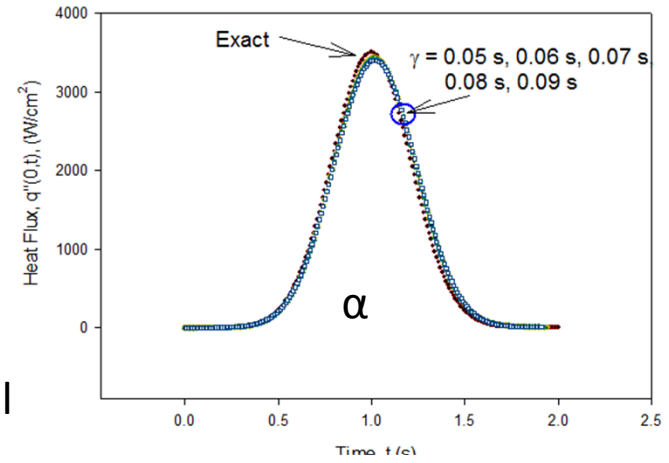
$$c_\gamma = \int_{u=0}^\gamma T_{ic,c}(b,\gamma-u) du$$

Artificial and used for regularization –Transforms 1st kind Volterra Integral equation into 2nd kind Volterra integral equation

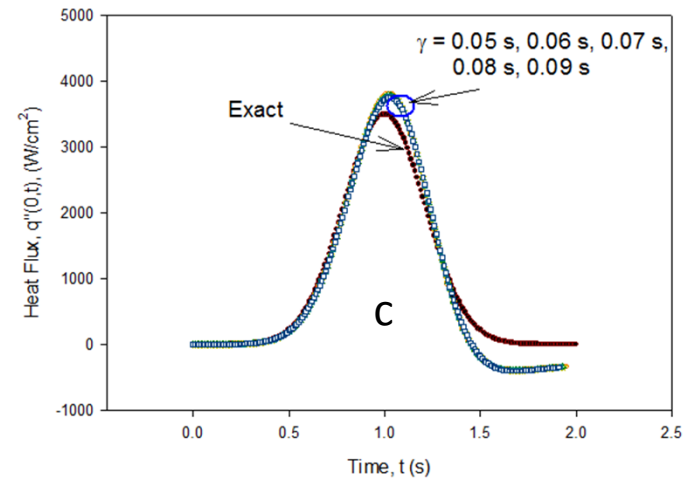
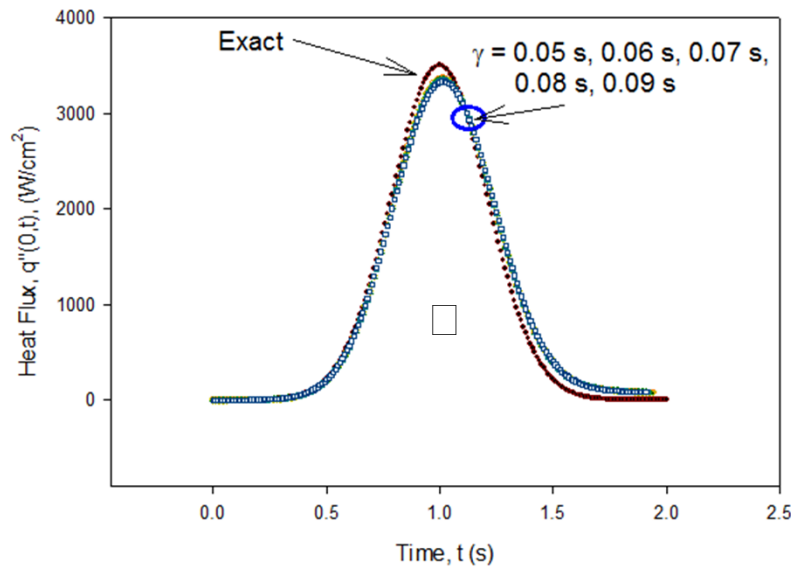
Heat Flux Predictions Based on Model



Various model equations



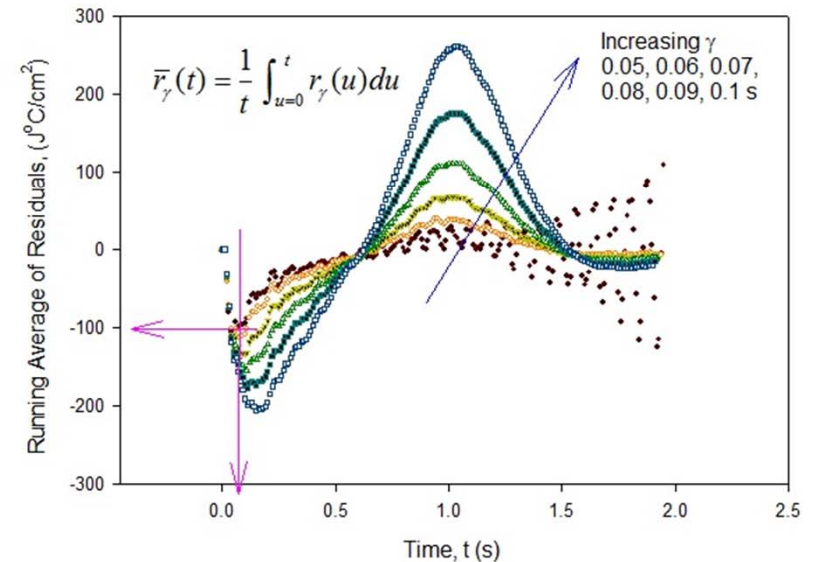
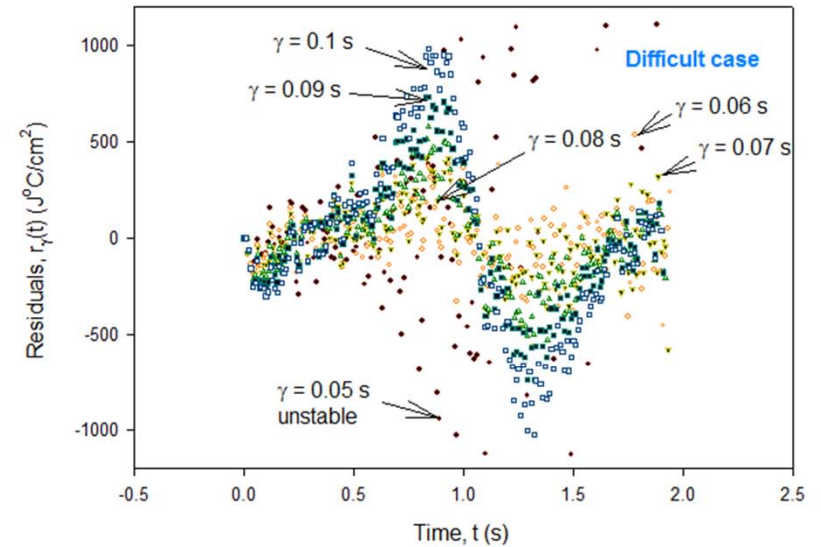
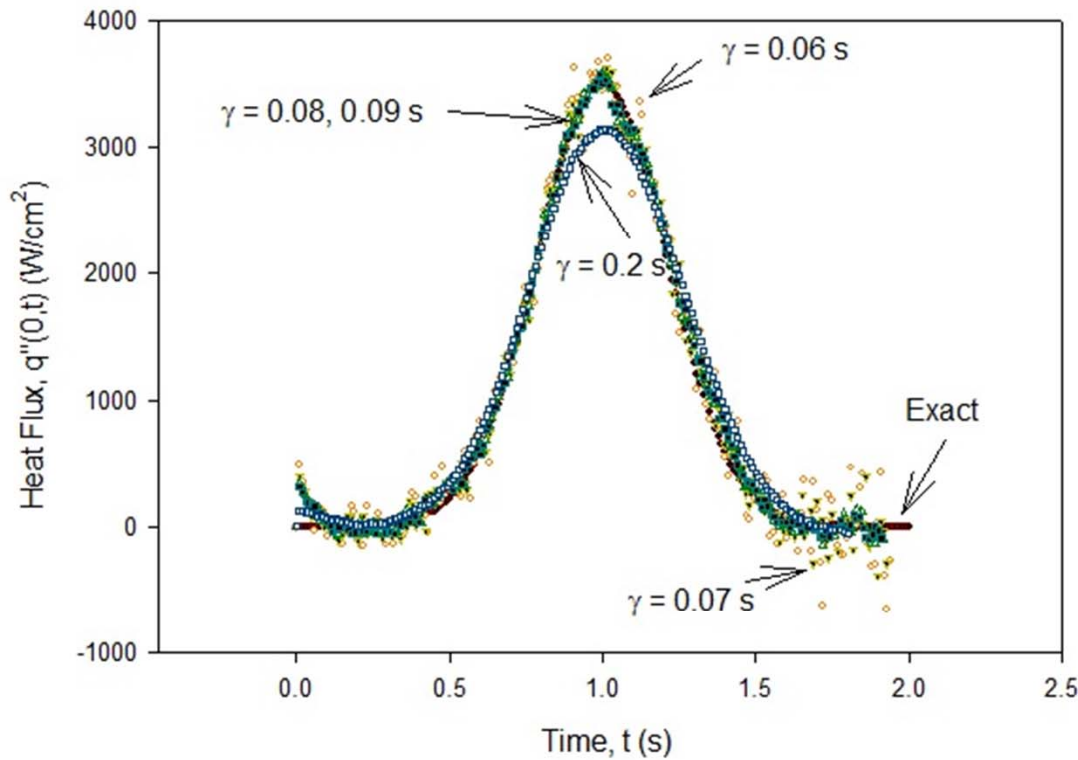
As expected Per Table



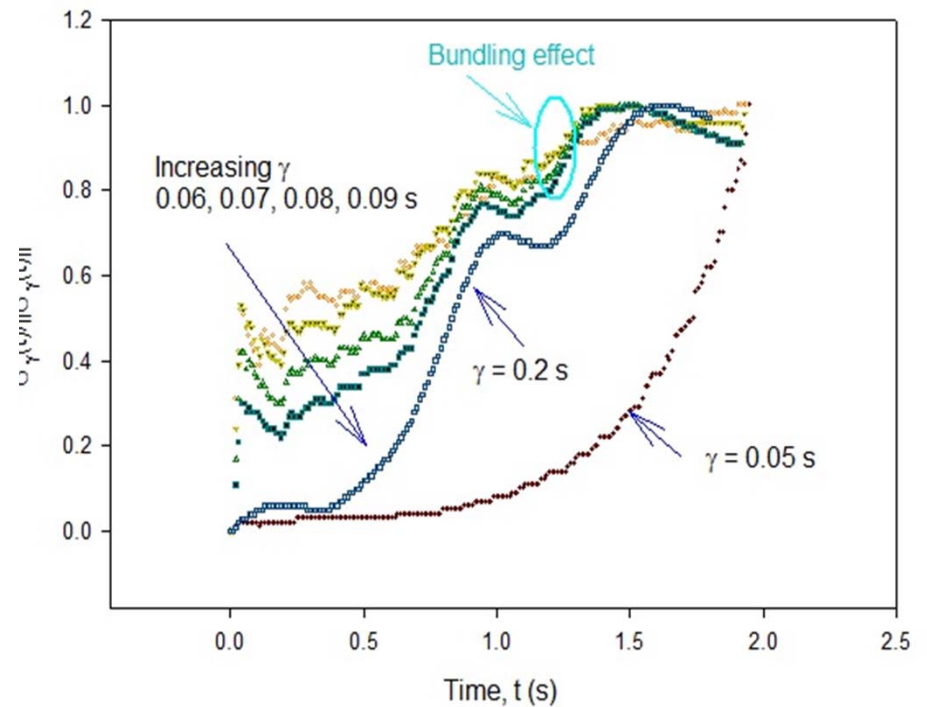
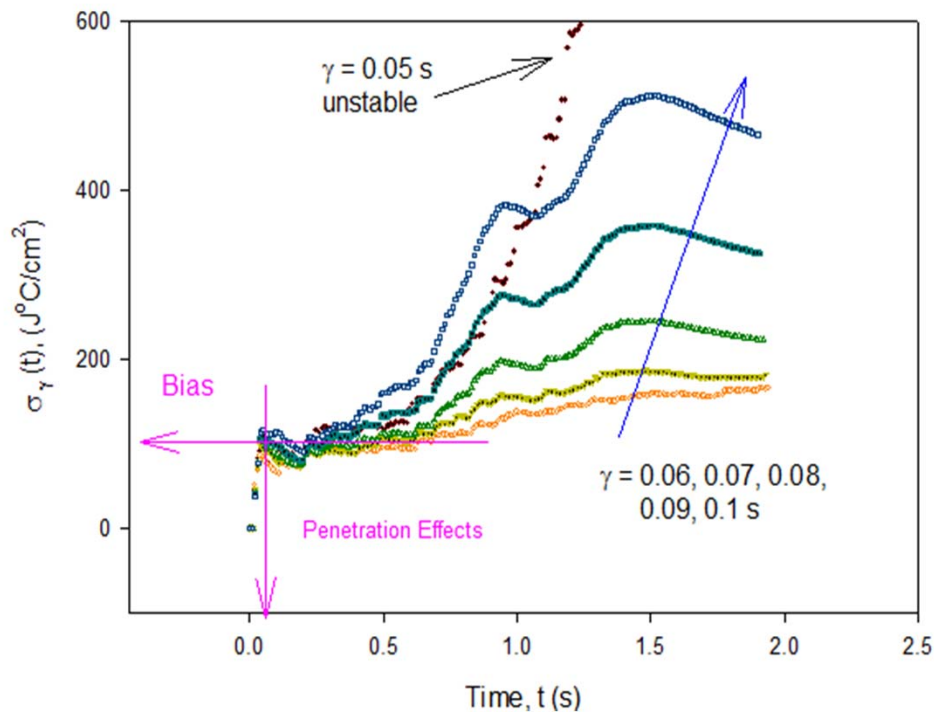
Noise-Copper (Noisy Data 2% max T, 5% max flux)

A challenging random set of numbers and alternative viewing of data

$$\phi_j = \phi(t_j) + \varepsilon_\phi \|\phi\|_\infty r_j \quad \text{where } r_j \text{ drawn from } [-1,1]$$

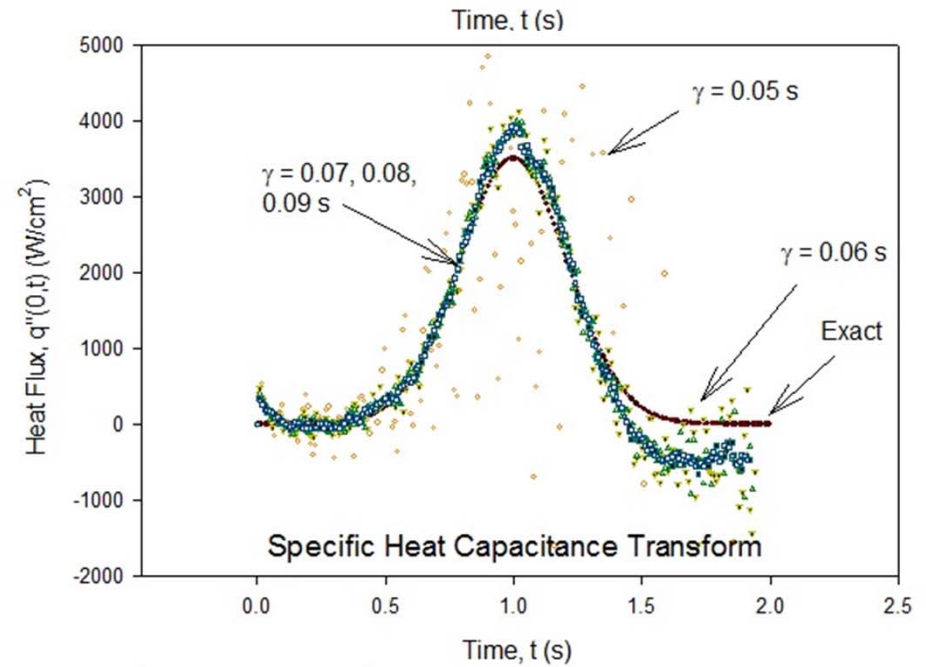
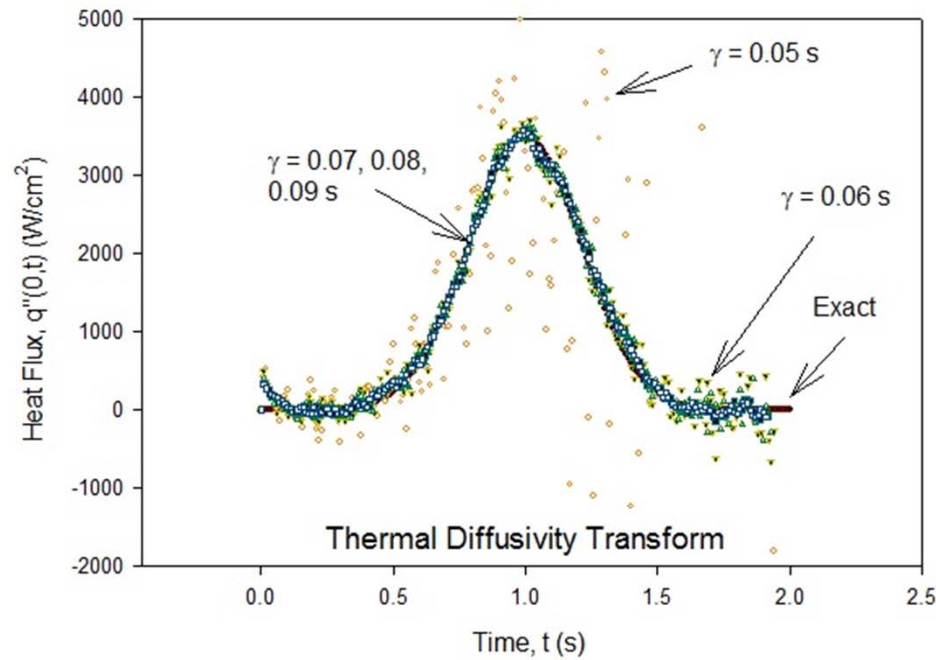
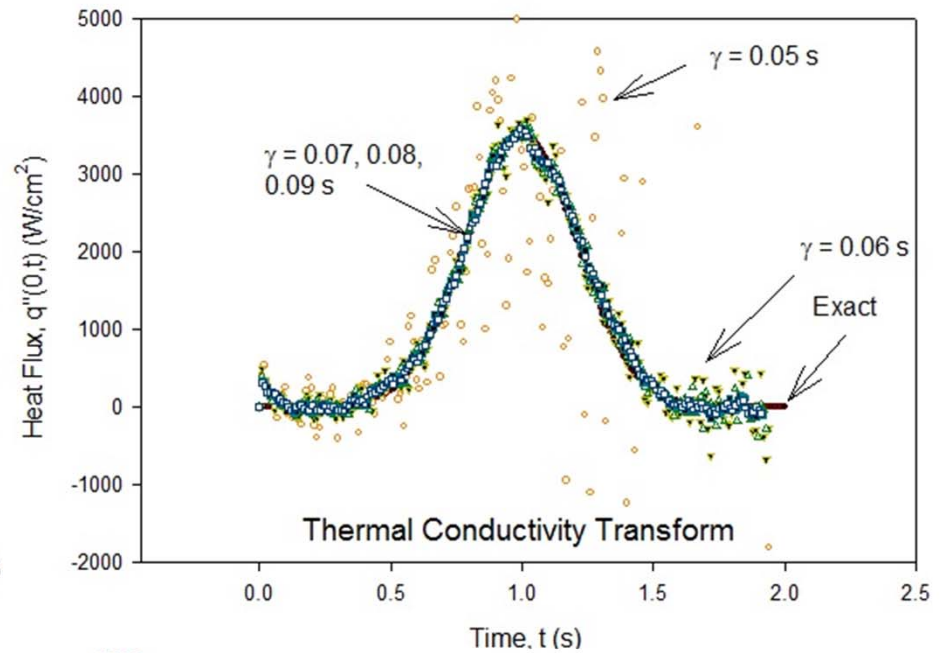
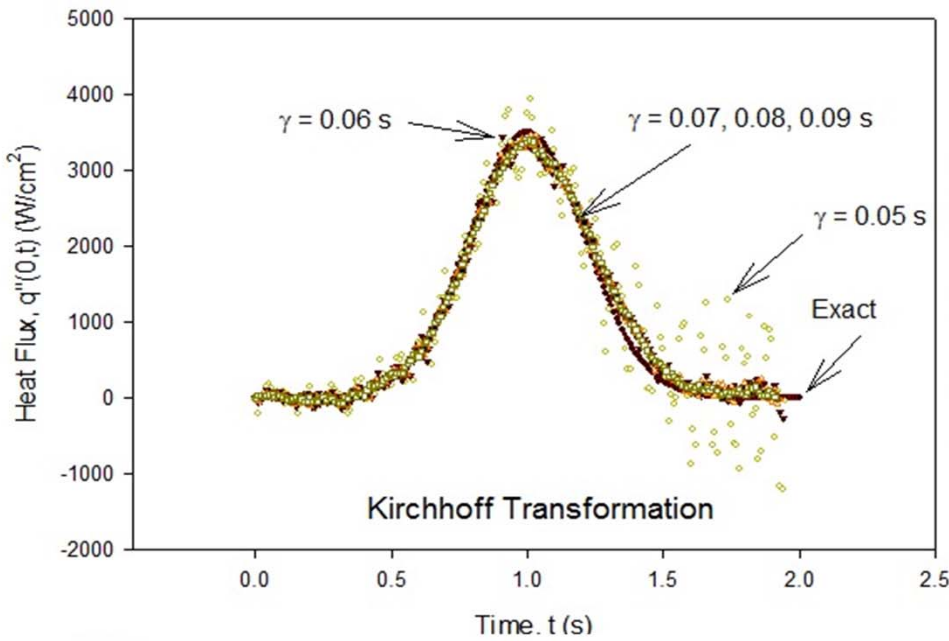


SYSTEM Variance (S.D.)-Copper

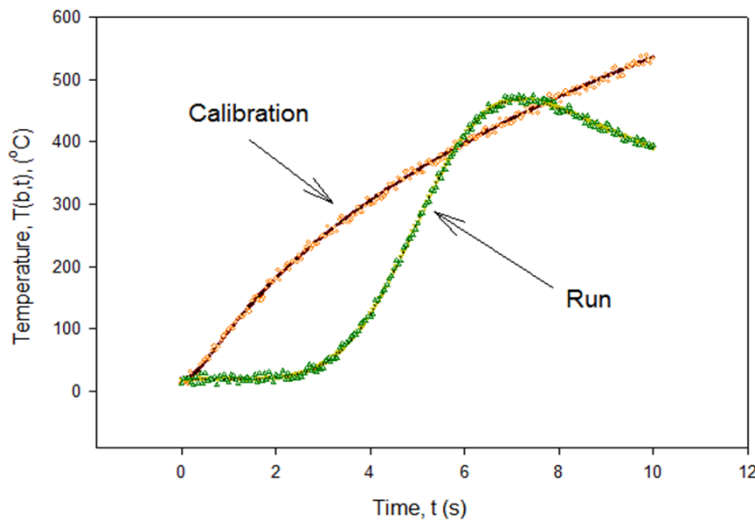
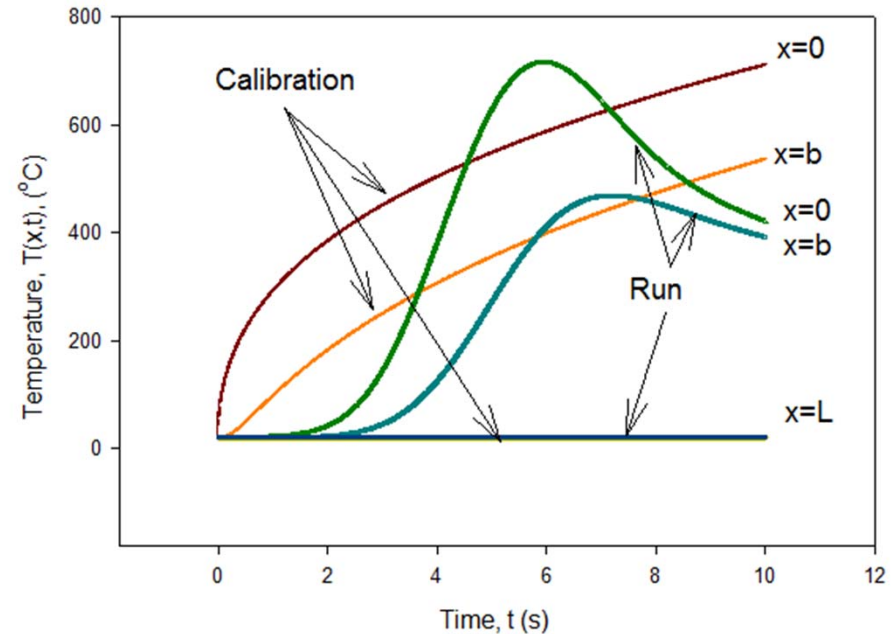
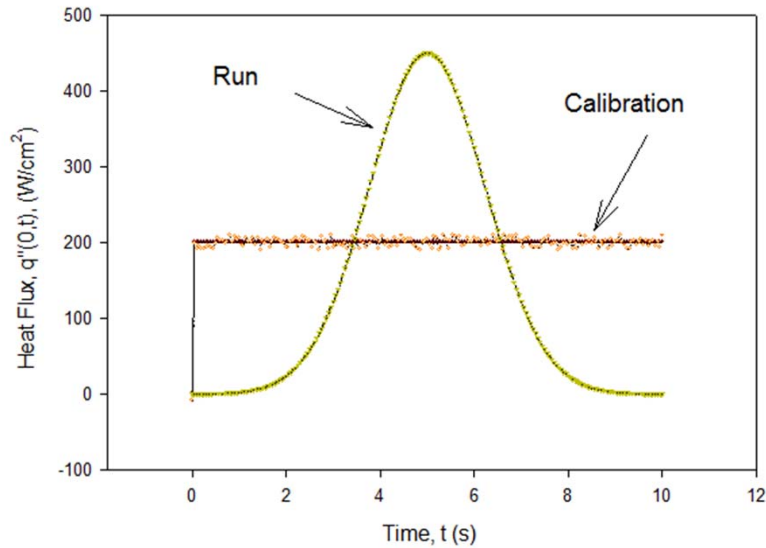


H. Chen suggested the normalization

Heat Flux Predictions – Alternative Formulations

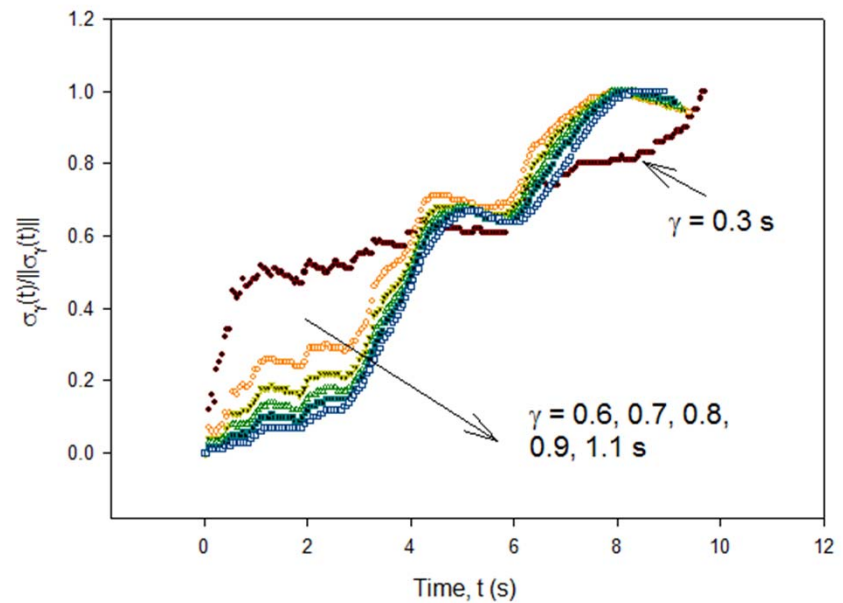
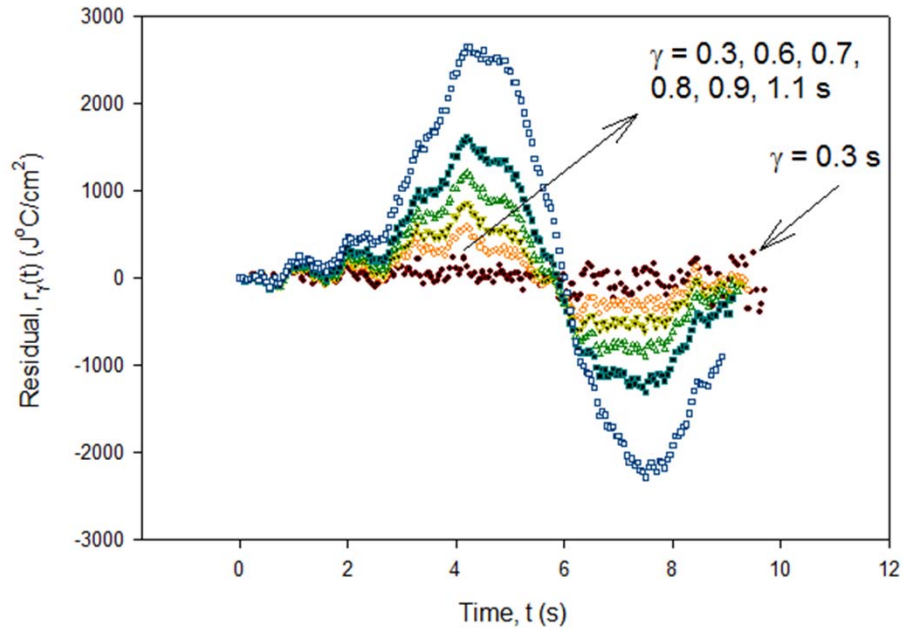
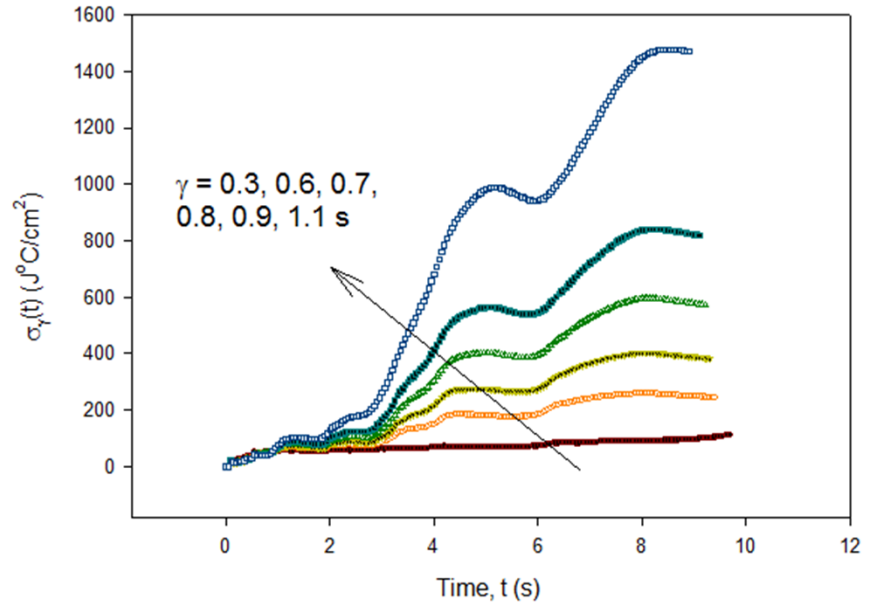
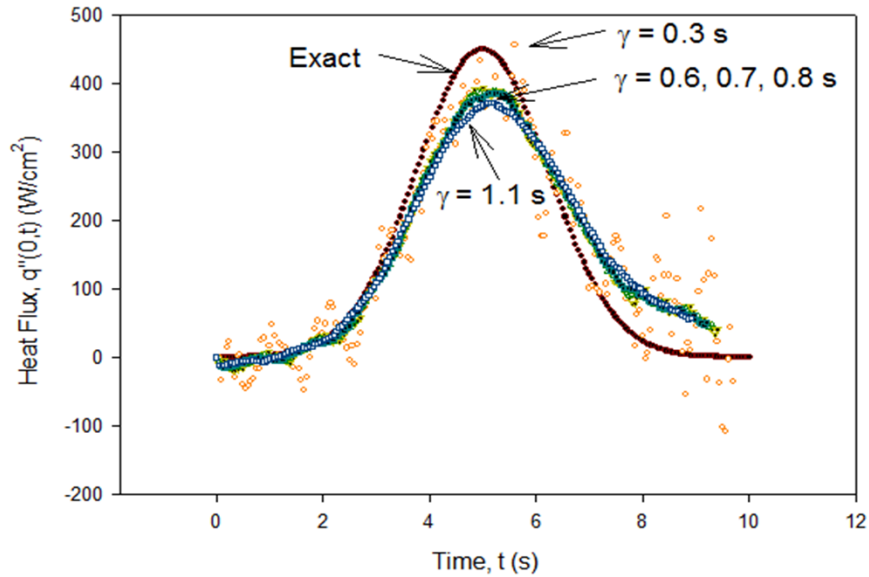


Stainless Steel with Noise

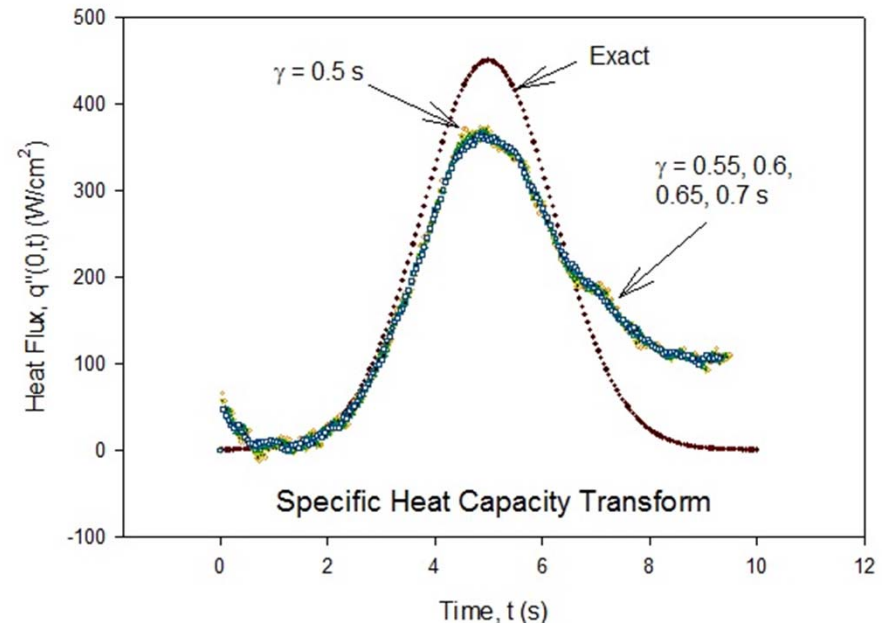
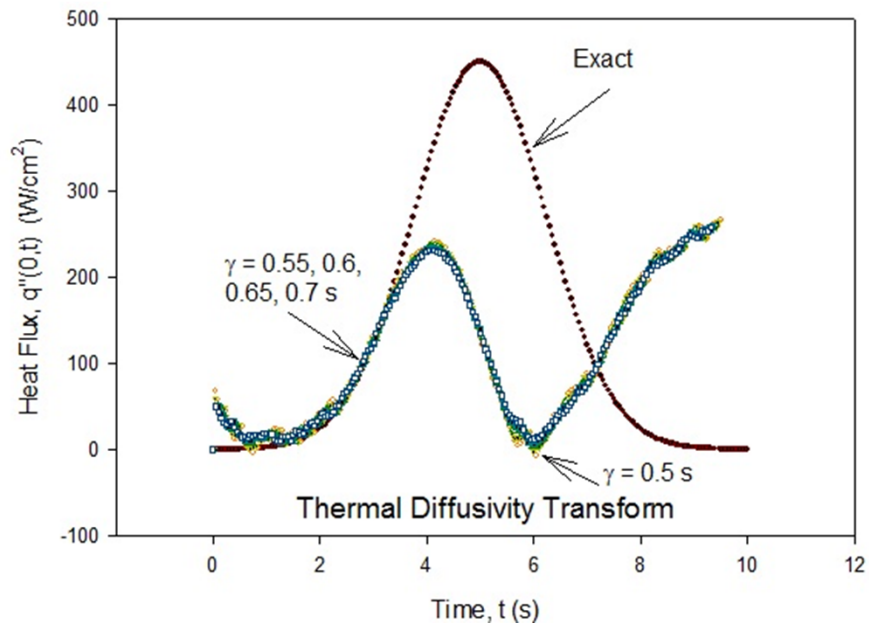
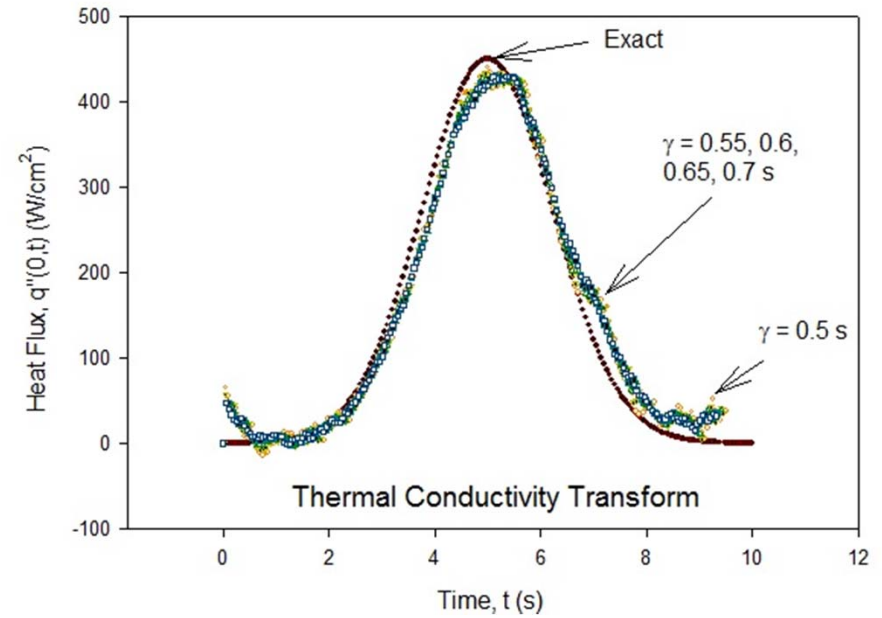
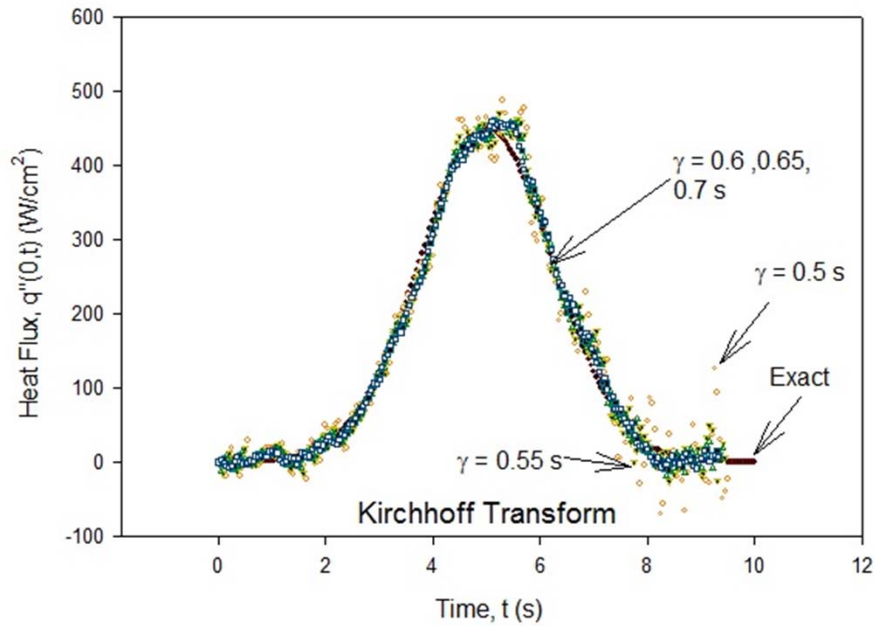


From Table 1, $\square(T)$ is relatively constant (hence, Kirchhoff transform prediction should be representative); and, k -transform properties are relatively constant. ($b=2.5\text{mm}$, $L=5\text{cm}$, $f=20\text{ Hz}$)

Residuals-Stainless Steel-T formulation (expect poor results) per previous table



Heat Flux Predictions Based on the Various Model Linearizations



Importance - Presentation of Data: Bprime Plots Analogy to Sigma Plots

“Investigation of Graphite Ablation at IRS”, Eswein, N., Herdrich, G, Fasoulas, S, Roser, H-P, AIAA 2011-3615, 42nd AIAA Thermophysics Conference, Honolulu, Hawaii, 27-30 June 2011. Below plots are from cited reference.

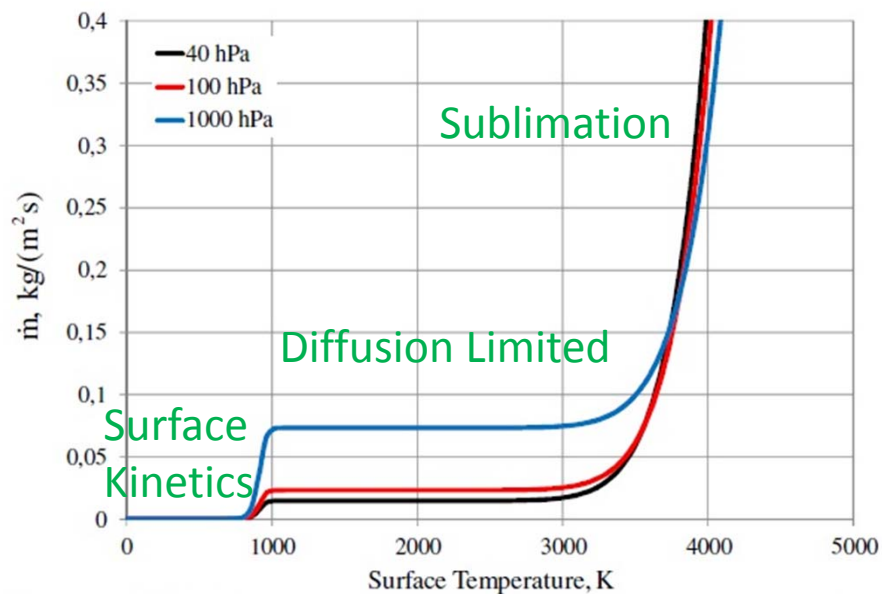


Figure 3. Mass loss rate for different stagnation pressure values (R=20mm)

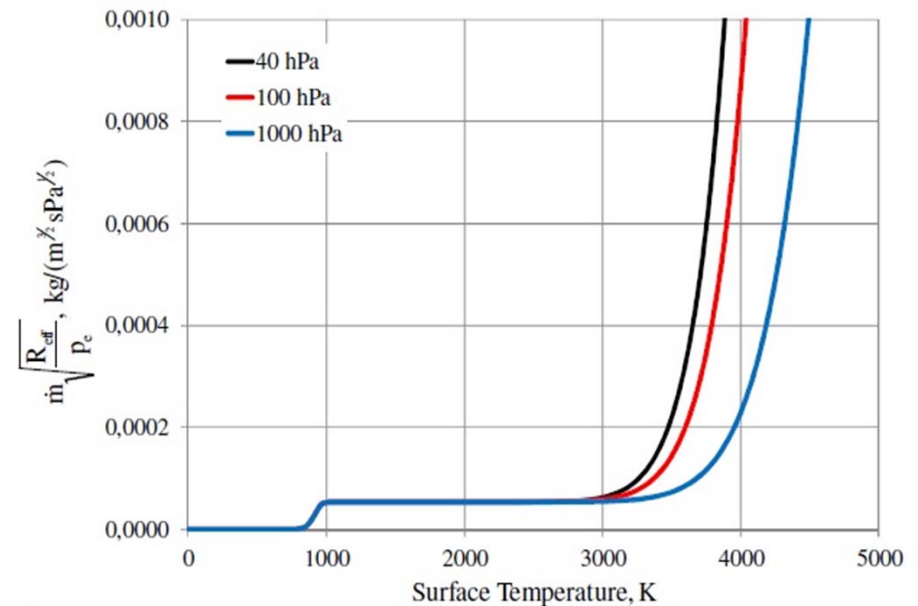


Figure 4. Normalized mass loss rate for different stagnation pressure values (R=20mm)

Integrating Theoretical Results Suggests Model for the One-Probe Nonlinear Calibration Integral Method

$$\int_{u=0}^t q_r''(0, u) (\varphi(T_c(b, t - u)) - \varphi(T_c(b, 0))) du =$$
$$\int_{u=0}^t q_c''(0, u) (\varphi(T_r(b, t - u)) - \varphi(T_r(b, 0))) du, \quad t \geq 0$$

where

$$\varphi(T(b, t)) = b_0 + b_1 T(b, t) + b_2 T^2(b, t) + \dots = \sum_{k=0}^N b_k T^k(b, t)$$

1. Introduce an additional calibration run. Use first two (calibration) runs to establish undetermined coefficients by least-squares method
2. Use first and third runs (third contains unknown heat flux) to determine surface heat flux and optimal regularization parameter

Conclusions and Direction

- New calibration approach for resolving inverse heat conduction problems possesses merit, performs well and is robust.
- Large class of one- and multi-dimensional problems can make use of this approach. (Also, quasi-one-dimensional)
- Calibration equations for heat flux (W/cm^2), total heat transfer (W) and temperature can be formulated.
- Calibration equations involving orthotropic materials can be formulated.
- Methodology may be applicable to oxidation-ablation studies
- Methodology possesses strong mathematical/physical basis for application and acquiring optimal predictions
- Potential exists for developing alternative regularization models.
- *Suggestive fully nonlinear calibration formulation appears possible by this study (for $b \in [0, L]$).*

Conclusions and Future

- Extension to chemical erosion (ablation/oxidation) for carbon-carbon based materials
- Potential integration of classical space-marching method with calibration approach to form hybrid method

Research Issues

- Surface temperature measurements for non-recessive and recessive cases? This could lead to potential means for estimating net surface heat flux, $q''(s(t),t)$; and, recession rates, ds/dt

Thank You

COMBINED SENSOR ASSEMBLY COMARS+ FOR EXOMARS EDM DEMONSTRATOR

A. Gülhan, T. Thiele, F. Siebe

*Supersonic and Hypersonic Technology Department of the Institute of Aerodynamics and Flow Technology,
German Aerospace Research Center (DLR), Linder Hoehe, D-51147 Cologne, Germany*

ABSTRACT

Based on experience gained during the successful hypersonic flight experiments SHEFEX-I and SHEFEX-II using a combined aerothermal sensor package, the DLR Supersonic and Hypersonic Technology Department developed a new aerothermal sensor called COMARS. In addition to static pressure, surface temperature and total heat flux rate the COMARS sensor is also able to measure radiative heat fluxes using two fibre optic based gas radiation detectors of CNES (called ICOTOM). In addition to the COMARS sensors, the overall payload for the ExoMars EDM (Entry, Descent, Landing Demonstrator Module), called COMARS+, also contains a broad band radiometer of DLR. Furthermore a new electronic box containing multiplexer and power distribution units has been designed for the ExoMars mission.

The performed thermo-mechanical analysis shows that all necessary system requirements can be satisfied. The aerothermal tests performed in Martian atmosphere in the arc heated facility L2K demonstrated the ability of the COMARS+ payload to collect data even at low aerothermal loads which are present during Mars entry.

1. INTRODUCTION

For the design margin of spacecraft structures the reliability of the aerothermal predictions and qualification tools is essential. Ground testing facilities are not capable to reproduce the exact flight environment of the ExoMars EDM capsule, which will enter the Martian atmosphere in 2016. The CFD codes have shortcomings in terms of correct physical modeling of some critical aspects like back cover heating. In the back cover region of the vehicle the Reynolds number of the flow is low and the flow itself has a highly transient character. This results in low convective heat fluxes on the back cover heat shield. Another very important parameter is the high radiative heating resulting from excitation of carbon dioxide molecules behind the strong bow shock. In the base region the radiative heat flux is even higher than the convective one. But neither ground test facilities nor numerical tools can simulate the radiation environment completely. Therefore the European Space Agency (ESA) decided to instrument the back cover of the ExoMars EDM to measure total and radiative heat flux.

Based on the flight instrumentation experience of the flight experiments SHEFEX-I and SHEFEX-II the Supersonic and Hypersonic Technology Department of the German Aerospace Center (DLR) in Cologne has developed the combined aerothermal sensor COMARS. A sensor similar in composition provided excellent data during the SHEFEX-II flight in 2012 [1], [2]. The COMARS sensor unit allows measuring the total heat flux rate, surface temperature and pressure in one plug. Furthermore, for the ExoMars EDM the COMARS sensor also contains two spectral radiometers to measure the gas radiation. These spectral radiometers based on fibre optics were developed by CNES (called ICOTOM). In addition to the spectral radiometers integrated in the COMARS sensor, a separate broad band radiometer of DLR measures the total radiative heat flux. The complete DLR payload including COMARS and radiometer sensors and the corresponding analogue data processing unit is called COMARS+.

This paper describes the main properties of the COMARS+ payload, mechanical and thermal design details and finally the results of aerothermal tests performed at DLR Cologne.

2. PAYLOAD LAYOUT

The following table presents an overview of the different parts of the DLR ExoMars EDM back cover instrumentation (COMARS+ payload). The payload consists of overall three COMARS sensors, one broad band radiometer, an electronic box and the corresponding harness between sensors and electronic box. The electronic box (multiplexing signal conditioner) is thereby used for sensor signal conditioning and multiplexing for acquisition by the EDM Remote Terminal Power Unit (RTPU). For the pressure measurement a Pirani-type pressure sensor is used. The total heat flux is measured by a heat flux microsensor from the VATELL company which also incorporates a temperature sensor. The radiative heat flux at two different spectral bands is measured by the ICOTOM sensors developed by CNES.

Unit name	Description
Multiplexing Signal Conditioner (MSC)	Electronic box
COMARS1 (COM 1)	Combined static pressure, total heat-flux, temperature and two CNES spectral radiometer sensors (ICOTOM)
COMARS2 (COM 2)	
COMARS3 (COM 3)	
Radiometer (RAD 1)	Broad band radiometer
Payload harness	Harness connecting the sensors to the electronic box

Table 1: COMARS+ payload instrumentation overview

The COMARS sensor is fixed to the ExoMars back cover (BCV) structure using a honeycomb insert to which the COMARS sensor is screwed with four M4 screws. Figure 1 and Figure 2 show exterior and interior views of the COMARS sensor with denomination of the different parts.

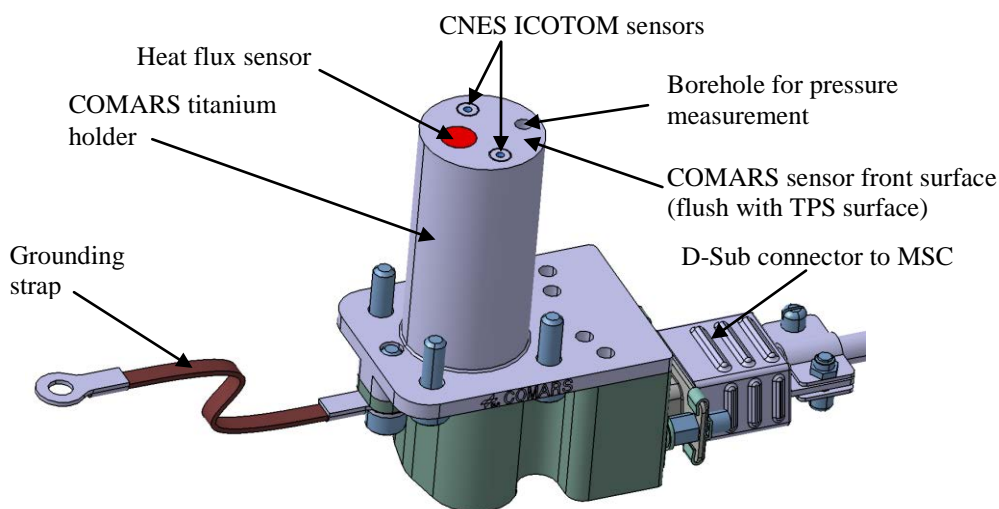


Figure 1: COMARS sensor assembly (top view)

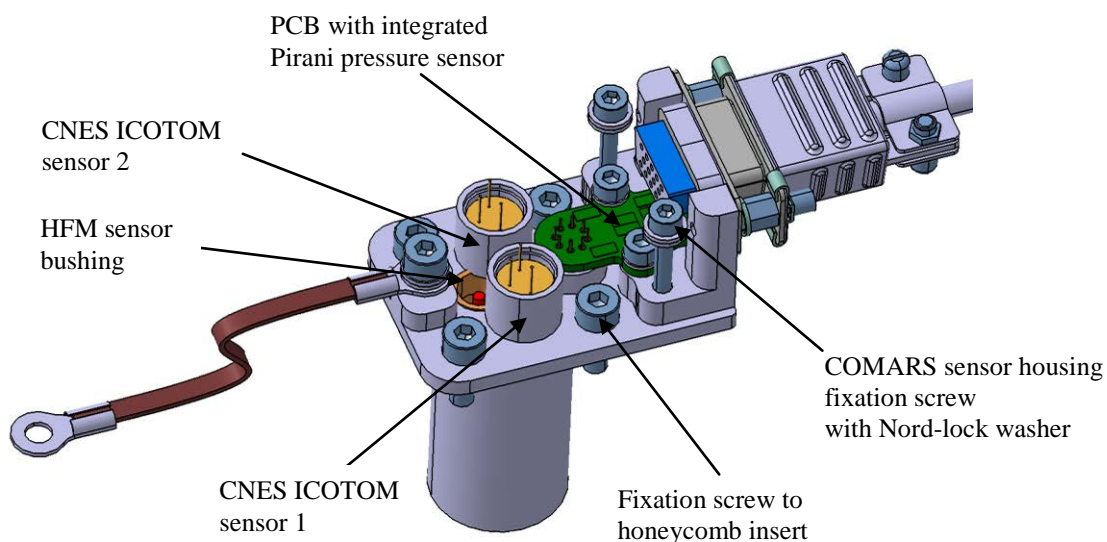


Figure 2: COMARS sensor assembly (bottom view with removed housing)

The multiplexing signal conditioner (COMARS+ electronic box) is used to amplify the signals of the sensors and to multiplex these signals on three analogue output lines for acquisition by the RTPU. It consists of one multiplexing board and one power board which generates the necessary voltage levels from the unregulated bus of the EDM using a DC/DC converter. The sensor signal multiplexing is controlled via clock and synchronisation signals coming from the EDM RTPU. Figure 3 shows an exterior and interior view (with removed cover plate) of the MSC box.

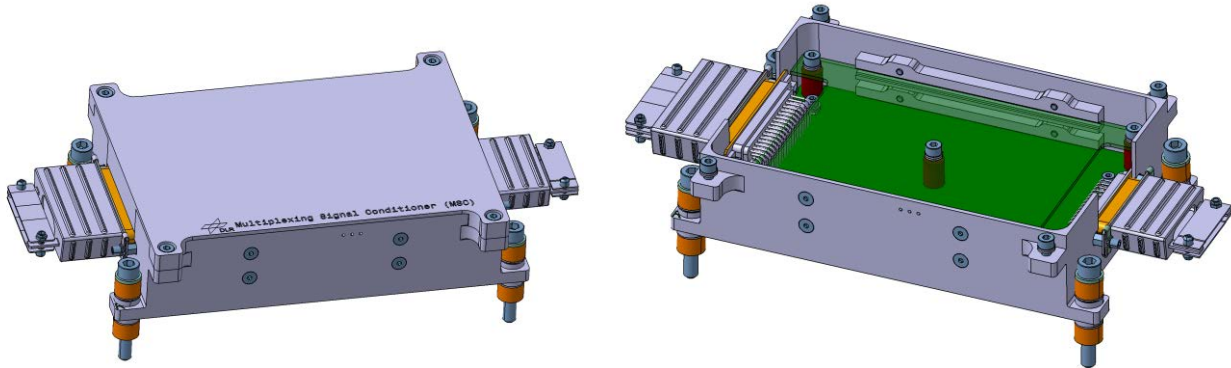


Figure 3: Electronic box of the COMARS+ payload

In Figure 4 the multiplexing layout for the COMARS+ payload is shown. The multiplexing board has three multiplexing units, one for each analogue channel (ChA-ChC). Each multiplexer handles the data of one sensor unit and one housekeeping signal (HK1-HK3).

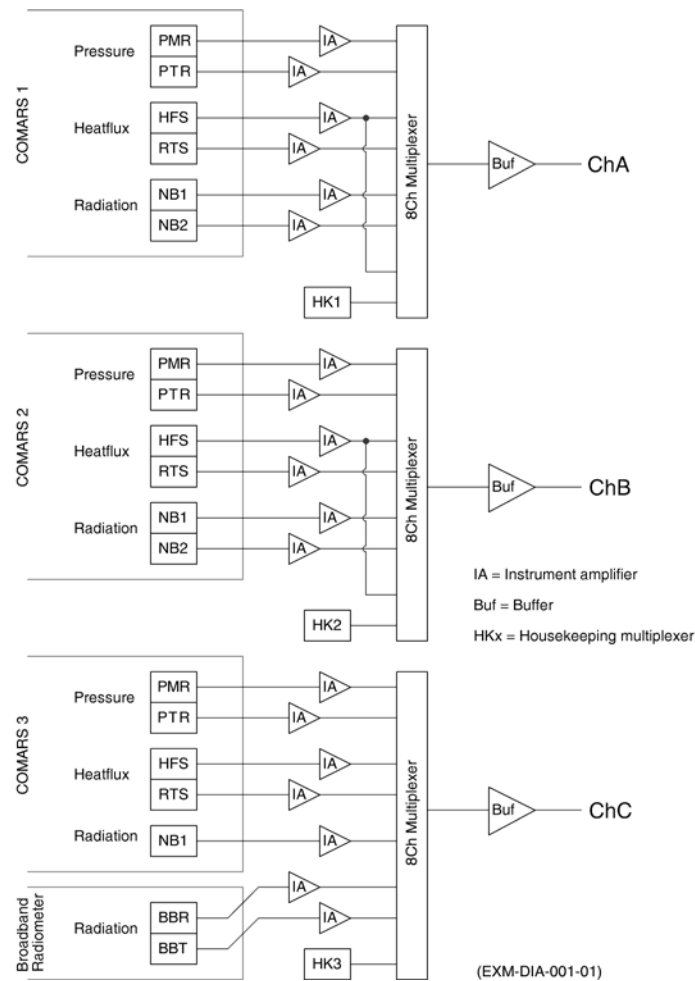


Figure 4: Data handling layout of COMARS+

The amplification of the sensor signals is thereby done before the multiplexing process (Instrument Amplifiers shown in Figure 4). The Pirani-pressure sensors provides two signals, the actual pressure signal (PMR) and the pressure sensor temperature (PTR) which is also used as temperature reference for the ICOTOM sensors. The Vatel heat flux sensors measure the heat flux rate (HFS) and surface temperature (RTS) of the sensor front surface. The ICOTOM sensors of CNES generate two signals corresponding to the radiative heat fluxes at the two wavelengths bands (NB1 and NB2). Since the third multiplexer has to process the radiation (BBR) and temperature signals (BBT) of the DLR broad band radiometer, only one ICOTOM signal (NB1) of COMARS sensor 3 is multiplexed. In the following figure the location of the COMARS+ components on the inner side of the ExoMars EDM back cover structure is shown.

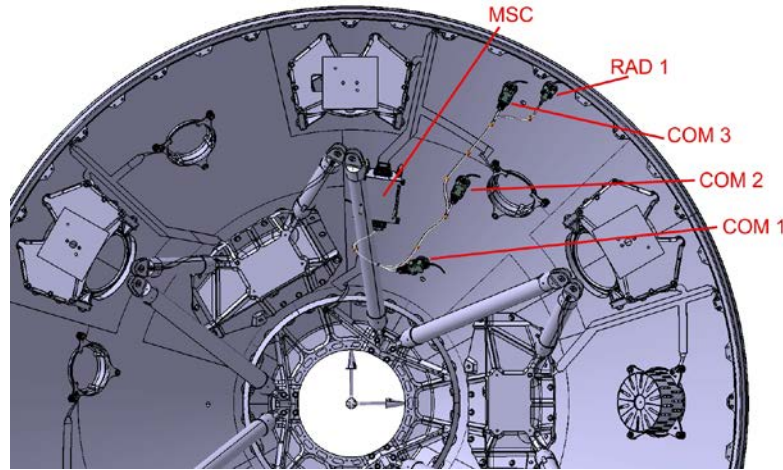


Figure 5: COMARS+ sensors and electronic box location on ExoMars back cover

3. STRUCTURAL ANALYSIS

To verify the structural integrity of the COMARS+ components during the launch phase several structural analysis were performed. In the following some results of the numerical analysis for the COMARS+ electronic box are shown. The electronic box is the heaviest part of the payload (about 800 grams) and is therefore exposed to the highest mechanical stresses acting on box structure and fixation devices (screws).

To evaluate the worst case vibration loads during launch and ascent, the random vibration spectra for the COMARS+ MSC is used (Figure 6). These random loads are converted into static loads using the Miles-equation. Using this equation a static load curve can be derived for the MSC which is also shown in Figure 6 with a maximum g-load of 182 g in out-of-plane (OOP) and 33 g in in-plane (IP) direction.

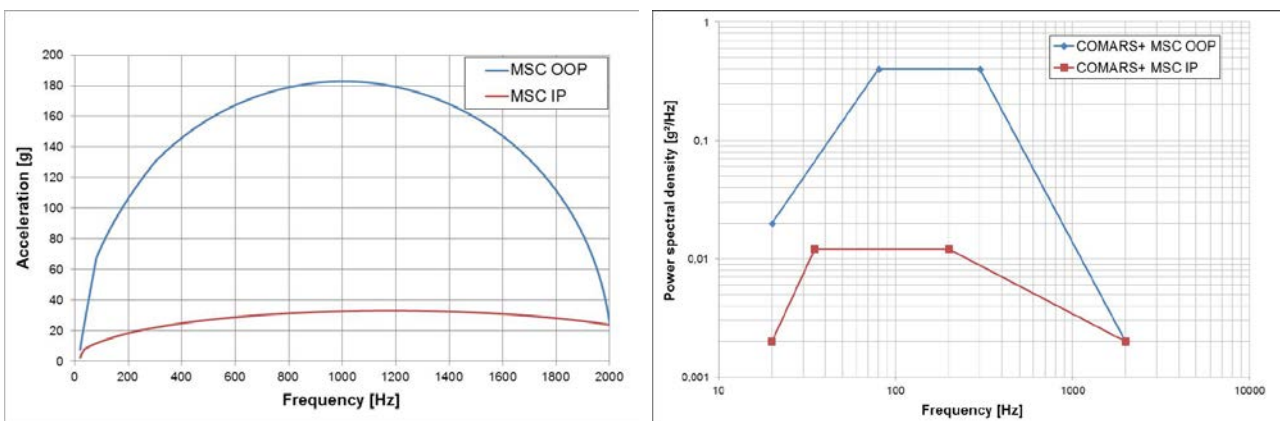


Figure 6: COMARS+ MSC static load curve (left) derived from random vibration loads (right) (taken from ExoMars EDM mechanical environment specification)

The FEM-model of the MSC is shown in Figure 7. For the FEM-model some simplifications were made but the overall mass of the box was kept constant:

- The geometry of the D-Sub connectors attached to the box was simplified but their mass was kept constant.
- Due to their small mass impact the harness cables attached to the connectors and the grounding strap of the box were neglected.
- All internal fixation screws (PCBs, connectors...) were removed to decrease the overall number of necessary mesh points. Although the overall mass of the internal fixation screws is small, the mass of the box structure was slightly increased to compensate for the missing weight.
- All contacts between different box parts are set to be bonded contacts.
- The multiplexing board and the power board are modelled as solid parts made of FR4 material (glass-reinforced epoxy laminate). The material density was increased to get the correct mass values for the boards. Therefore a uniform mass distribution is assumed on the PCBs.

A screw preload force of 6500 N (according to the used mounting torque, screw strength and thread friction coefficient) was applied to all four MSC fixation screws. To evaluate the static loads used for the simulation with a sufficient safety margin, a box mass of 1 kg and the maximum accelerations of 182 g and 33 g were used. This lead to an acceleration of 1820 m/s² in OOP direction and an acceleration of 330 m/s² in IP direction. The used FEM-mesh shown in Figure 7 consisted of 3506942 nodes and 1987165 elements.

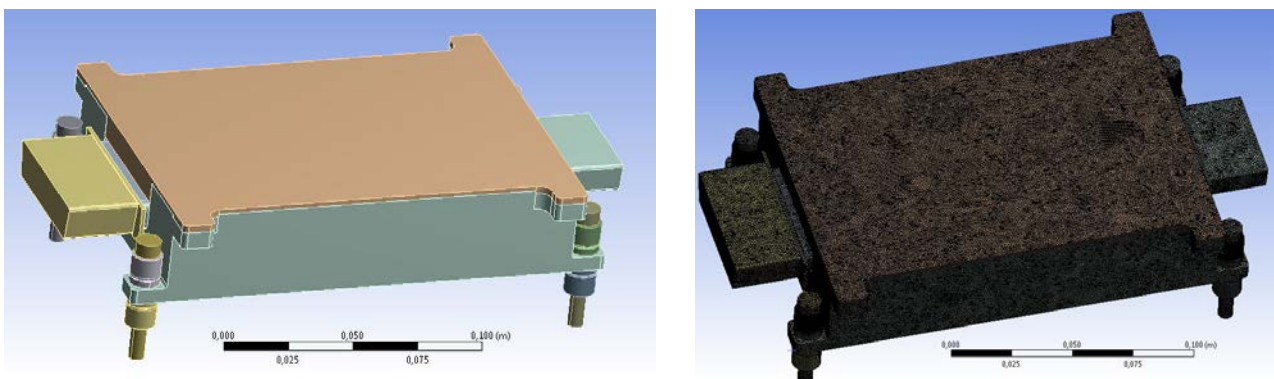


Figure 7: FEM-model and mesh

Figure 8 shows the von Mises equivalent stress for the MSC bottom part. The maximum stress of about 95 MPa occurs at the mounting feet. The MSC bottom part is manufactured from Aluminium material (7075 T7351) with yield strength (R_{p0.2}) of 380 MPa which ensures enough margin to prevent breaking or plastic deformation of the material. The maximum calculated stress inside the fixation screw shafts was calculated to 340 MPa. The yield strength for the used stainless steel screws (strength class 80) is 600 MPa which indicates sufficient margin to prevent plastic deformation of the MSC fixation screws.

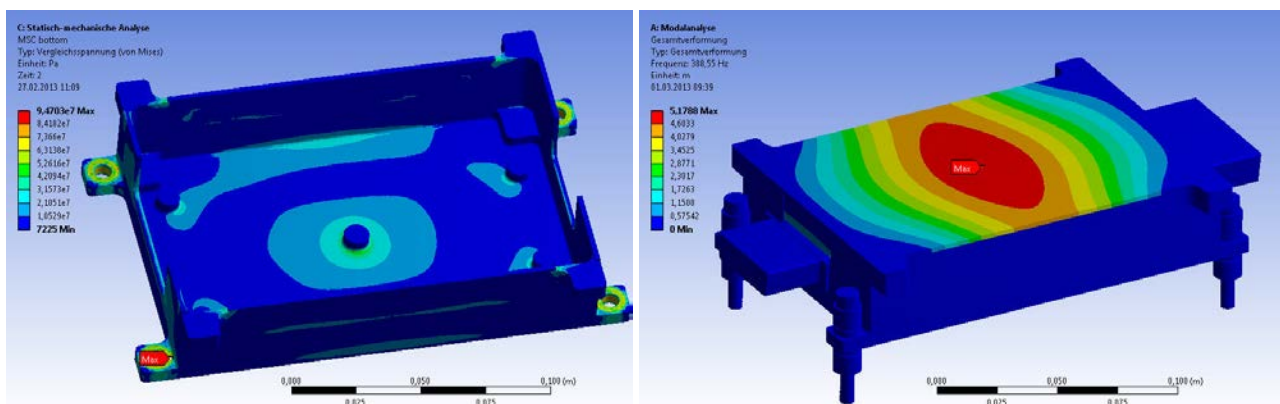


Figure 8: Von Mises equivalent stress at MSC bottom part (left) and modal analysis of MSC box (right)

The calculated stresses for the other fixation components (e.g. thermal washers) are also well inside the corresponding material stress limits. In addition to the structural analysis a modal analysis was also performed for the MSC to determine the first fundamental frequency. The result is also shown in Figure 8 with the first fundamental frequency at 388 Hz, which corresponds with the vibration of the MSC cover plate.

To determine the maximum deflection of the PCBs inside the MSC box a Power Spectral Density (PSD) analysis was performed using the random vibration loads shown in Figure 6. The result of the MSC modal-analysis was used as input for the PSD analysis. Figure 9 shows the deflection of the multiplexing and power board perpendicular to the board plane. A scaling factor of 3σ was used for the analysis leading to a result probability of 99.7%.

The maximum deflection of the multiplexing board occurs around the center of the board. As a fixation screw is placed in the center of the PCB, the deflection is very small with a maximum deflection of 0.11 mm. This is well inside the tolerable range to prevent damage or detachment of electronic components.

The maximum deflection of the power board is larger with a maximum of 0.36 mm at the short sides. This is because the power board is not fixed to the MSC structure by D-Sub connectors at these sides (like the multiplexing board). But this deflection is still inside the tolerable deflection range. In addition to the soldering, the components on the power board (DC/DC converter, voltage filter) are fixed to the PCB with epoxy adhesive. This is mainly done because of the quite severe shock loads that occur at the stage separations during ascent. Furthermore, these components are placed near the center of the board where the deflections are lower due to the fixation point (screw) in the center of the PCB.

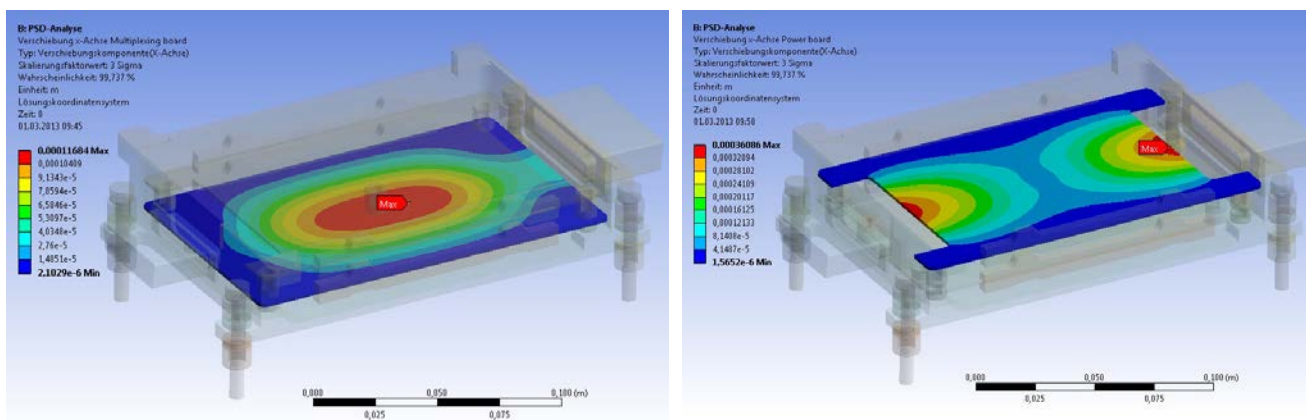


Figure 9: MSC PSD analysis, deflection of the multiplexing board (left) and power board (right)

4. THERMAL ANALYSIS

To verify the temperature resistance of the COMARS sensor assembly during Mars entry transient thermal analysis have been performed. The used thermal model is shown in Figure 10 and consists of a cut-out of the TPS with an area of 90x90 mm with integrated COMARS sensor. The components of the thermal model are (see Figure 1 and Figure 2)

- TPS with nominal thickness of 7.6 mm.
- Honeycomb structure with a thickness of 25 mm. The honeycomb structure was modelled as a solid structure with adjusted material properties (density, thermal conductivity, specific heat capacity).
- Honeycomb insert (to which the COMARS sensor is fixed) made of Aluminium material.
- Epoxy glue between honeycomb insert and honeycomb structure.
- COMARS titanium holder.
- Heat flux sensor (HFM).
- ICOTOM sensor without detector.

The glue between the TPS, carbon skins and honeycomb as well as the carbon skins themselves (at the upper and lower side of the honeycomb) were not included. These parts would normally increase the thermal resistance between TPS and sensor. Therefore the thermal environment for the COMARS sensor is even more severe if these parts are omitted. Furthermore, all other COMARS sensor parts were neglected because they are located at the back end of the sensor and do not influence the heat conduction from the TPS to the lower parts of the sensor along the sensor axis. All contacts between the different parts were assumed to be bonded contacts. The most susceptible parts of the COMARS sensor concerning temperature are the Pirani pressure sensor, the ICOTOM detectors and the heat flux sensor. To evaluate the

temperature of the Pirani pressure sensor and ICOTOM detectors, the temperature of the corresponding sensor contact surface to the titanium holder is calculated (see also Figure 10). The heat flux sensor consists of several parts. At the sensor front end the sensor substrate, on which the thermopile for the heat flux measurement is deposited, may be exposed to a maximum temperature of 200°C. Epoxy glue directly behind the substrate is used for the electric cable fixation, at which substrate and epoxy glue are encapsulated by a nickel housing.

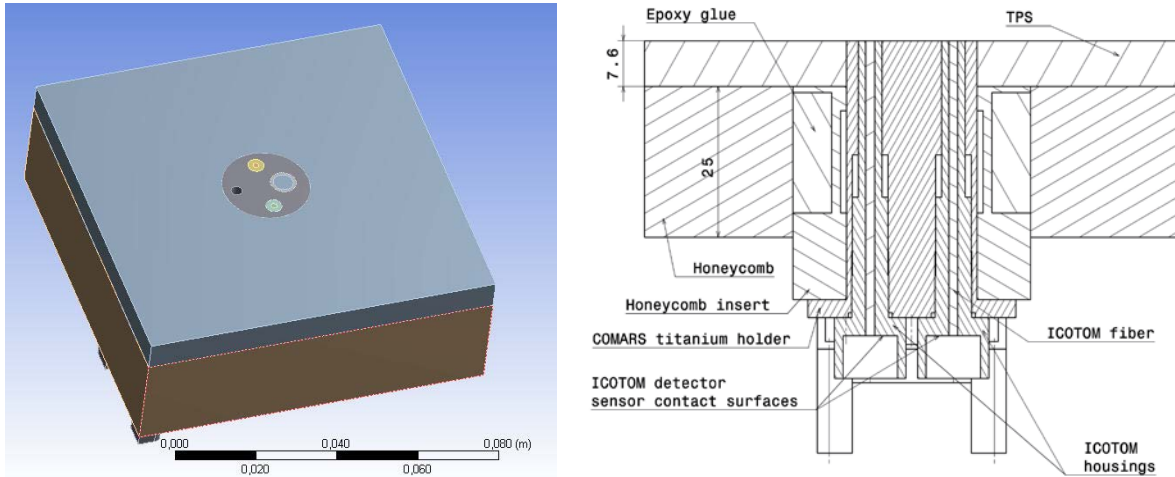


Figure 10: Simplified thermal model for COMARS sensor thermal analysis

The heat flux used for the thermal analysis can be seen in Figure 11 and was taken from the ExoMars EDM aerothermodynamic database. The COMARS and DLR radiometer sensors are thereby located in zones V and VI according to Figure 11. The shown heat flux profiles were computed with a wall temperature of 300 K and represent the worst-case heat fluxes to the TPS (sizing case). As the heat flux in zone VI is slightly higher than in zone V, the heat flux of zone VI was used for the thermal simulations.

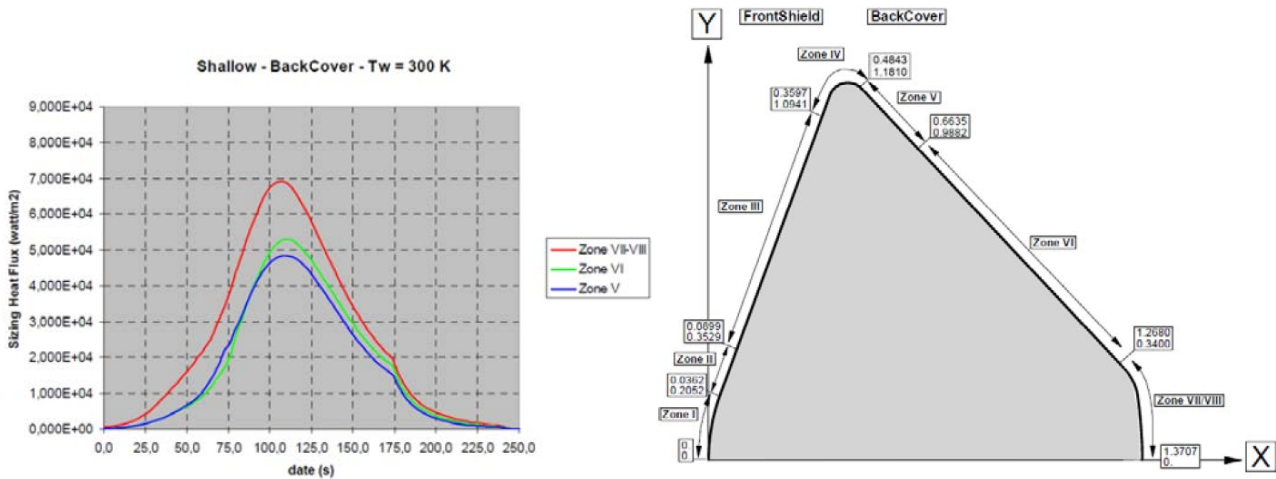


Figure 11: Sizing heat flux profile for EDM back cover TPS and EDM zone definition (taken from ExoMars EDM aerothermodynamic database)

The heat flux was applied to the upper TPS surface including the COMARS sensor surface. To simulate further heat conduction into the material after the heat flux becomes zero, the simulation time of the thermal analysis was extended to 450 seconds. A radiation to ambient space (temperature -120°C) with an emissivity of 0.9 was assumed for the TPS surface. Radiation of the COMARS sensor to ambient space was neglected. All other outer surfaces were set to be adiabatic. A uniform starting temperature of 300 K was used for the simulation to be compliant with the wall temperature assumption used for the heat flux calculation. In Figure 12 the used FEM mesh is shown in a sectional view

with overall 626065 knots and 281982 elements. The temperature distribution inside the sensor at the end of the simulation is also shown in Figure 12. As can be seen in the figure, the distribution inside the sensor is nearly homogeneous with a temperature of about 75°C.

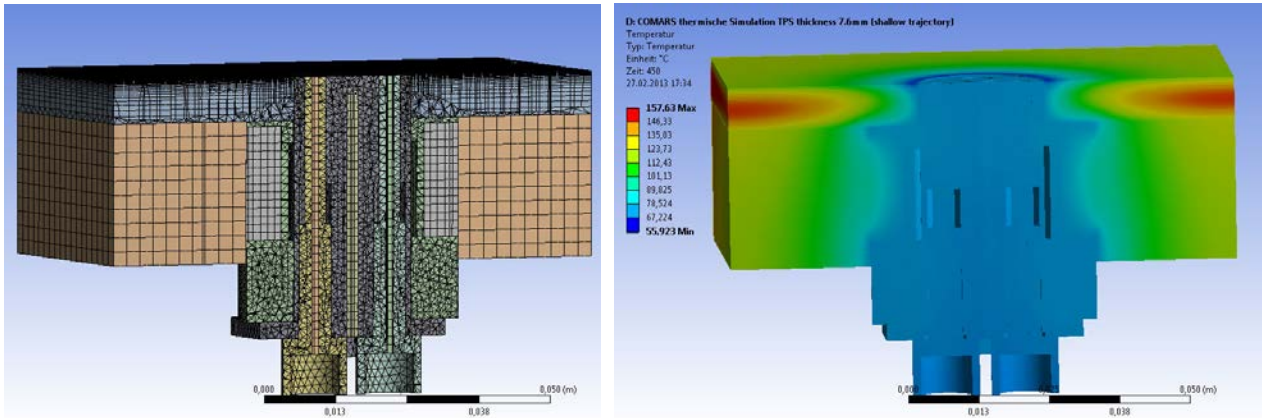


Figure 12: FEM mesh for COMARS simulation and computed temperature distribution at simulation end (t=450s)

The resulting maximum temperatures of the different parts are presented in Figure 13. The outer surface of the TPS reaches a maximum temperature of nearly 650°C, whereas the titanium holder of the COMARS sensor only heats up to a maximum of 126°C due to the heat sink effect of the metallic sensor components. As already shown in Figure 12, all sensor parts are at a nearly homogeneous temperature level at the end of the simulation time.

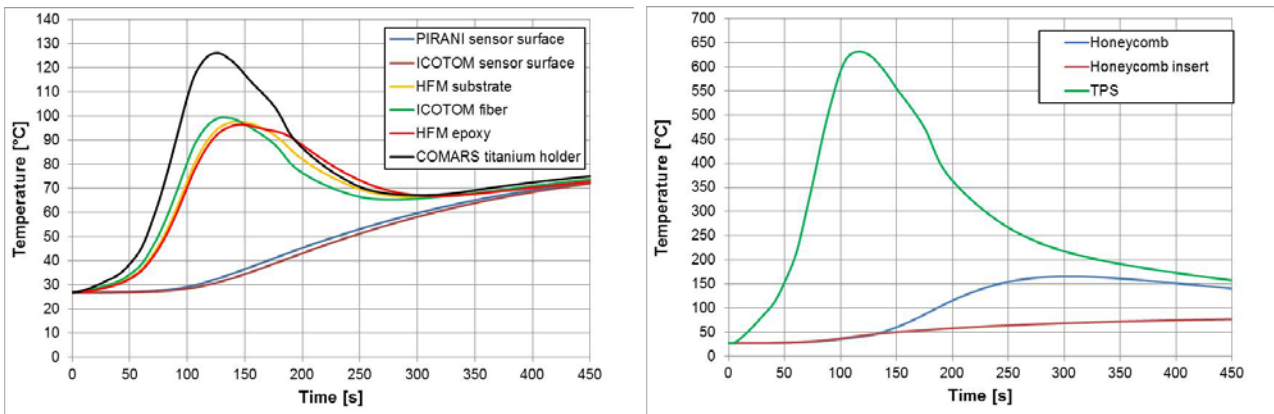


Figure 13: COMARS thermal simulation maximum temperatures

In the following table the important temperatures of the COMARS parts are summarized and compared with the maximum operative range. All calculated values are below the maximum operative temperatures which ensures, that the COMARS sensor is capable to withstand the thermal environment during Mars entry.

Part / surface	Maximum calculated temperature [°C]	Maximum operative temperature [°C]
Pirani sensor	72	90
ICOTOM detector	72	75
HFM substrate	98	200
HFM epoxy	96	200
ICOTOM fiber at TPS	99	> 120
COMARS titanium holder	126	400

Table 2: Calculation results compared with maximum operative temperatures of the different COMARS parts

As some of the calculated temperatures are very close to the corresponding maximum operative range, the following remarks should be considered:

- The used simulation time is longer than the measurement time of the sensor and therefore the temperatures at the actual end of the measurement will be lower.
- The starting temperatures of the different parts will be much lower than 300 K at the beginning of Mars entry leading to lower temperatures at the end of the measurement time.
- Some simplifications were made to the thermal model that would, in reality, decrease the calculated temperatures (e.g. omission of glue between TPS and honeycomb and assumption of overall bonded contacts between the different parts with perfect heat conduction).
- The used heat flux profile taken from the ExoMars EDM aerothermodynamic database represents the back cover TPS sizing case and therefore already includes a safety margin.

Considering all these points, the actual temperatures during Mars entry will definitely be lower than the calculated ones shown in Table 2 and therefore enough safety margin for the COMARS sensor is provided.

To verify that the implementation of the COMARS sensor into the TPS will not lead to local overheating of the TPS or honeycomb structure, a further simulation was performed only for the TPS structure using the same heat flux levels presented in Figure 11. A comparison of the TPS and honeycomb temperatures with and without COMARS sensor is shown in Figure 14. The curves show the maximum temperatures of the lower surface of the TPS (intersection to the honeycomb) and of the lower surface of the honeycomb structure (inner side of back cover). As can be seen in the figure, the maximum temperature of the lower TPS surface is higher without a COMARS sensor. The same is true for the lower surface of the honeycomb structure. Therefore the integration of the COMARS sensor into the TPS does not cause local overheating of the TPS or honeycomb structure. In fact, the temperatures are even lower with a COMARS sensor due to a local heat sink effect.

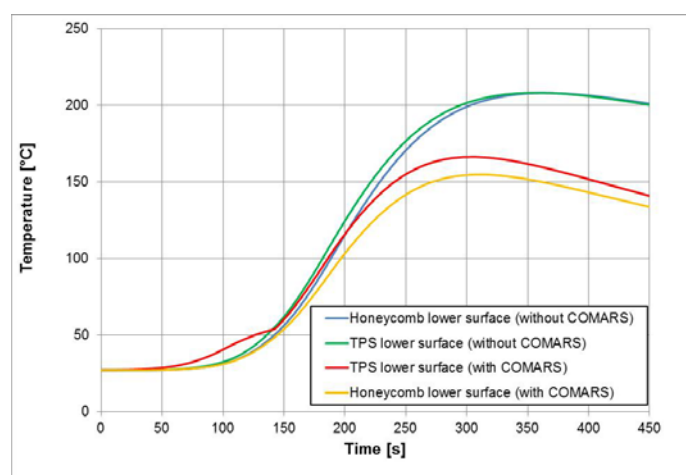


Figure 14: TPS temperatures with and without COMARS sensor

A thermal simulation was also performed for the DLR broad band radiometer. The thermal model consists of a cut-out of the TPS with an area of 90x90 mm with integrated radiometer sensor. For TPS and honeycomb structure the same simplifications were made as for the COMARS sensor. The only parts of the radiometer which were incorporated in the thermal model are the titanium holder and the thermopile sensor which is located at the lower end of the conical borehole, see Figure 15. The thermopile sensor was thereby replaced by a circular sensor dummy at the contact surface between titanium holder and thermopile. The temperature of the upper surface of this sensor dummy represents the temperature to which the thermopile sensor is exposed during Mars entry. All other parts (fixation screws, housing) were removed because they do not influence the heat conduction from the TPS to the lower parts of the sensor along the sensor axis and therefore have a negligible effect on the thermopile temperature calculation.

The temperature distribution inside the radiometer sensor at the end of the simulation is shown in Figure 15. As can be seen in the figure, the complete radiometer sensor has a nearly uniform temperature distribution of about 93°C.

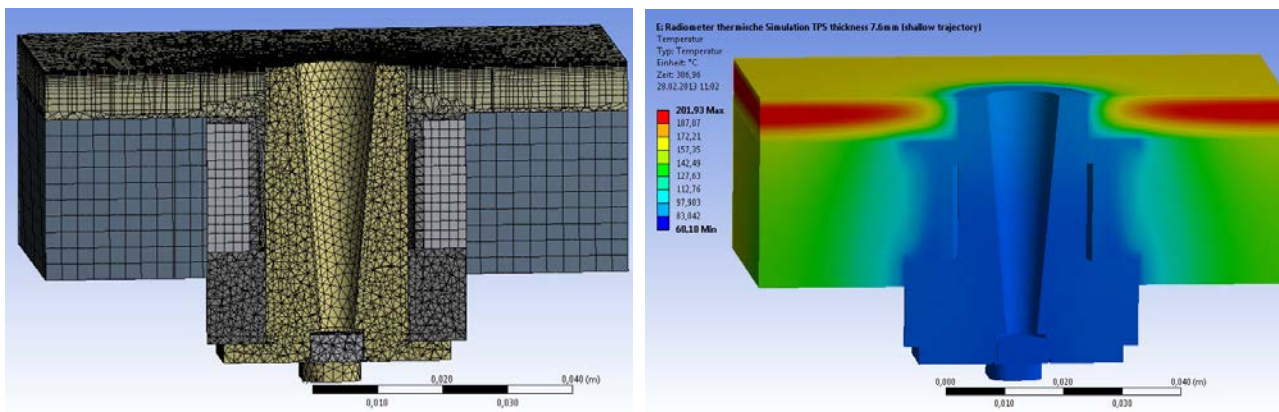


Figure 15: FEM mesh for radiometer simulation and computed temperature distribution at simulation end (t=450s)

Figure 16 shows the results for the radiometer computation. The diagrams show the maximum temperatures for the radiometer parts (thermopile sensor, radiometer titanium holder) and for the TPS parts (TPS, honeycomb, honeycomb insert). A maximum temperature of 93°C is reached for the thermopile sensor at the end of the simulation. With a maximum working temperature of 180°C, the calculated temperature is thereby well inside the operative temperature range of the sensor.

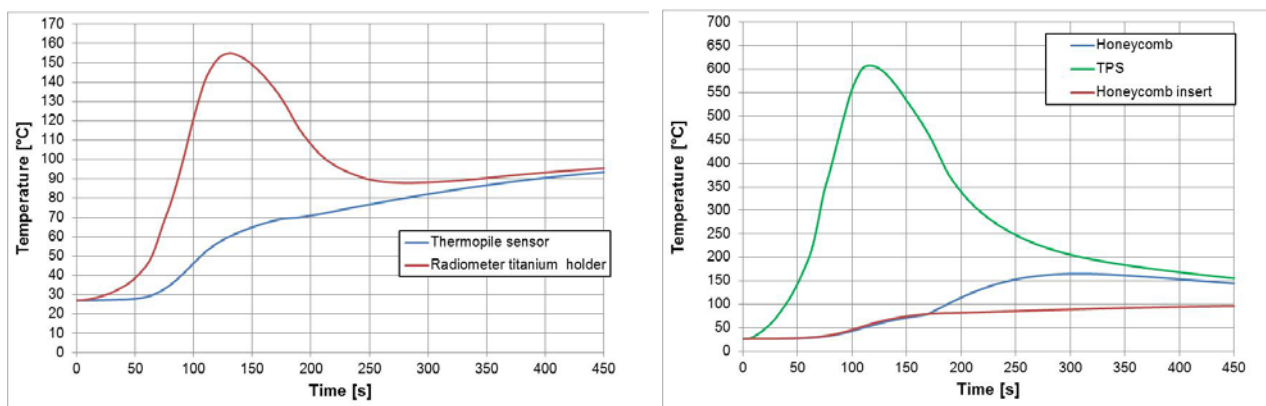


Figure 16: Calculated maximum temperatures for radiometer thermal simulation

5. AEROTHERMAL TESTS

All tests have been performed in the L2K facility of the Supersonic and Hypersonic Technology Department of DLR Cologne [3,4]. In contrast to preliminary stagnation point tests, these aerothermal tests were carried out in a flat plate configuration (Figure 17). The COMARS sensor and the broad band radiometer were integrated into the holder at the same distance from the model holder nose tip. This guarantees the same flow conditions on both sensors.

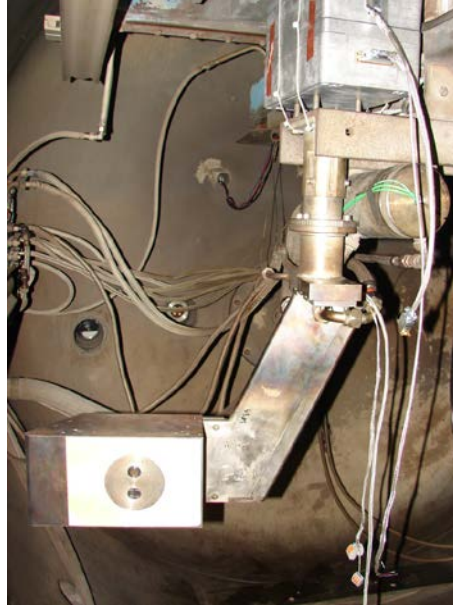


Figure 17: COMARS and radiometer sensors integrated in a flat plate model in L2K

The test conditions have been chosen in such a way, that the concentration of the CO₂ molecules, i.e. radiative heating, could be varied significantly. The enthalpy was varied from 5.6 MJ/kg to 9.2 MJ/kg leading to a CO₂ mole fraction change from 0.546 to 0.227 (Table 3).

Test condition	low enthalpy		high enthalpy	
	Stagn.	Wedge	Stagn.	Wedge
Configuration				
gas mass flow rate \dot{m} [g/s]	41.2		41.2	
reservoir pressure p_0 [hPa]	790		930	
specific enthalpy h_0 [MJ/kg]	5.6		9.2	
total temperature T_0 [K]	2815		3283	
nozzle throat/exit diameter D_1 / D_2 [mm]	29/100	29/200	29/100	29/200
distance from nozzle exit x_e [mm]	160	250	160	250
distance from nozzle throat x_t [mm]	329	654	329	654
free stream static pressure p_1 [hPa]	2.1	0.5	2.1	0.4
free stream static temperature T_1 [K]	1001	744	898	604
free stream density ρ_1 [kg/m ³]	$9.4 \cdot 10^{-4}$	$2.7 \cdot 10^{-4}$	$8.6 \cdot 10^{-4}$	$2.5 \cdot 10^{-4}$
free stream velocity v_1 [m/s]	2172	2306	2481	2611
mole fraction of CO ₂ n_{CO_2} [-]	0.546	0.546	0.227	0.227
mole fraction of CO n_{CO} [-]	0.277	0.277	0.459	0.459
mass fraction of O ₂ n_{O_2} [-]	0.122	0.122	0.162	0.162
mass fraction of O n_O [-]	0.027	0.027	0.126	0.126
mass fraction of N ₂ n_{N_2} [-]	0.022	0.022	0.016	0.016
mass fraction of NO n_{NO} [-]	0.005	0.005	0.009	0.009

Table 3: Flow parameters of the aerothermal tests in L2K facility

Figure 18 shows the measured total heat flux rate at both flow conditions in one run. At the beginning of the test the model was positioned outside the flow field and after achieving steady state conditions the model was injected into the flow. The heat flux peaks at the time points 172 and 185 seconds are caused by the heat flux sensor passing through the side shock of the free stream during model injection and removal. The constant heat flux rate between this transition points shows the quality of the flow and reliability of the sensor. The model was re-injected into the flow at a time of 216 seconds after adjusting the flow parameters for the second test condition. Since the total heat flux is proportional to the enthalpy and square root of the stagnation pressure it decreases at low enthalpy flow conditions.

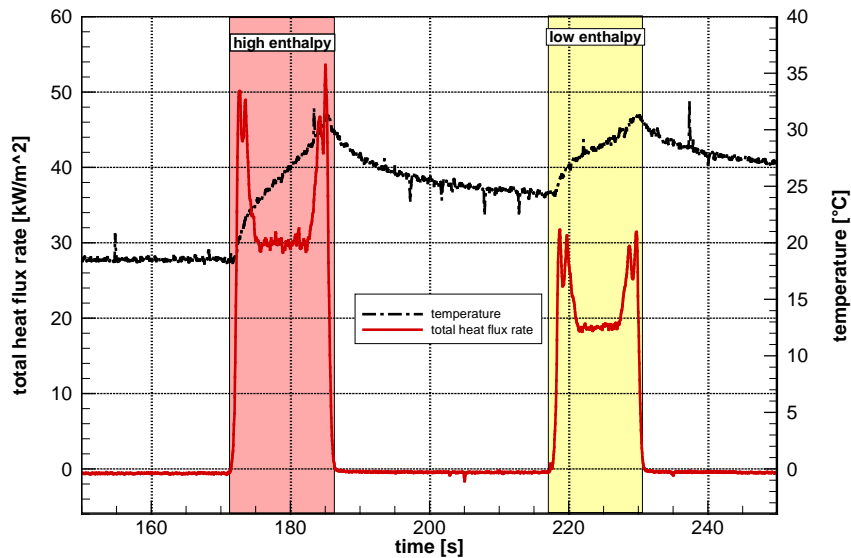


Figure 18: Measured total heat fluxes with the COMARS sensor at two different flow conditions

The situation is different for the radiative heat flux in Figure 19 measured by the DLR broadband radiometer sensor. The radiometer measured the radiative heat flux even without being inside the high enthalpy flow. Therefore the data up to 83 seconds represents the radiation of the free stream at low enthalpy condition. Then the facility parameters electrical current and mass flow rate were varied to reach the high enthalpy flow condition which was achieved at 150 s. Compared to the low enthalpy case the radiative heat flux is lower. This is related to the lower CO_2 concentration. The model was injected into the flow at 175 s. Due to the model leading edge shock the flow density increases and leads to higher radiation compared to the free stream case. After the model was removed from the flow the low enthalpy flow parameters were set again. The injection of the model into the flow at 221 s causes a slight increase in the measured radiative heat flux. But in contrast to the total heat flux, which is mainly convective, the radiative heat flux decreases by increasing the enthalpy due to the decreasing CO_2 concentration.

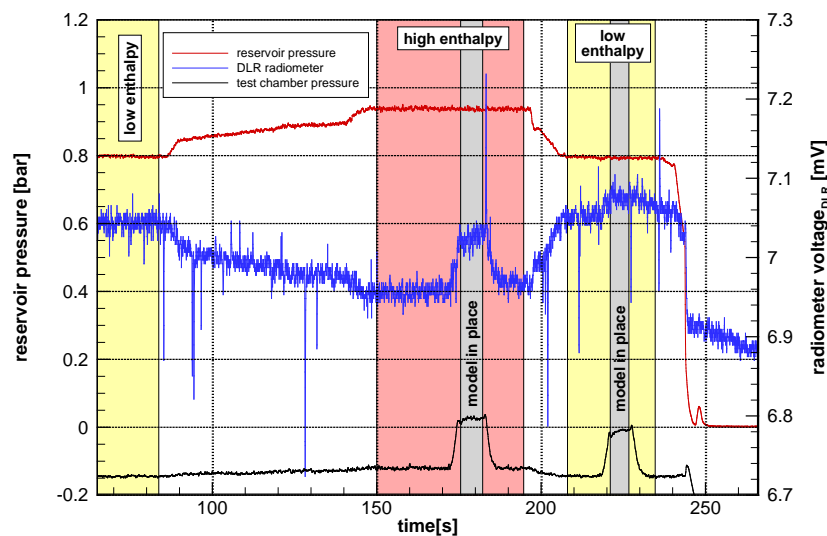


Figure 19: Measured radiative heat fluxes with the radiometer at two different flow conditions

6. CONCLUDING REMARKS

All components of the COMARS+ payload for the ExoMars mission in 2016 were designed and characterized by means of numerical simulations. Aerothermal tests performed at two different flow conditions with Martian atmosphere demonstrated the sensitivity of the COMARS+ sensors to low level total and radiative heat fluxes. The data of complementary spectroscopic measurements in the infrared range showed, that CO₂ molecules are the main contributors of radiation in Martian atmosphere. The qualification tests for the COMARS+ payload components including vibration, shock, thermal / vacuum cycling, EMC and planetary protection requirements are in preparation and will be completed around August 2013.

7. ACKNOWLEDGEMENTS

The authors express their special acknowledgement to the European Space Agency (ESA) and Thales Alenia Space Italy for their support.

8. REFERENCES

- [1] A. Gülhan, et al, *The Sharp Edge Flight Experiment SHEFEX I, A Mission Overview*, 5th European Workshop on Thermal Protection Systems and Hot Structures, Noordwijk, Netherlands, 17.-19.5.2006, ESA SP-631.
- [2] A. Gülhan, F. Siebe, T. Thiele, D. Neeb, J. Turner, J. Ettl, *Challenges of the SHEFEX-II Flight Instrumentation and Selected Flight Data*, Journal of Spacecraft and Rockets, (accepted, to be published).
- [3] A. Gülhan, B. Esser, U. Koch, *Experimental Investigation on Local Aerothermodynamic Problems of Re-entry Vehicles in the Arc Heated Facilities LBK*, AIAA Journal of Spacecraft & Rockets, Volume 38, Number 2, pp. 199-206, March-April 2001.
- [4] A. Gülhan, B. Esser, *Arc-Heated Facilities as a Tool to Study Aerothermodynamic Problems of Re-entry Vehicles*, in: Lu, F.K., Marren, D.E. (Eds.): *Advanced Hypersonic Test Facilities*, Progress in Astronautics and Aeronautics, Vol. 198, pp. 375-403, AIAA, 2002.

Experimental Investigation of Photogrammetric Surface Analysis of Heat Shield Materials during Plasma Wind Tunnel Testing

Stefan Löhle*,

*Universität Stuttgart, Institut für Raumfahrtssysteme
Pfaffenwaldring 29, D-70569 Stuttgart, Germany*

Thomas Reimer†,

*German Aerospace Center, Institute of ...
Pfaffenwaldring 38-40, D-70569 Stuttgart, German*

The paper presents first results of an experimental analysis of surface recession using advanced photogrammetric tools. Based on image pairs acquired with two DSLR cameras, classical photogrammetry has been tried, but pixelwise image analysis with corresponding matching algorithms show much better results and higher stability to image noise and radiation and reflection issues. A combination of open source tools for the analysis of camera positions and focal points, pixel matching analysis, and pixel cloud comparing, allows the recession to be measured with very high local resolution of $20\ \mu\text{m}$ of a 2D surface. The approach is analysed within this study with respect to window disturbance and experimental setup constraints. A first plasma wind tunnel experiment shows the applicability and an analysis of a central spot is comparable to laser recession measurements.

I. Introduction

Experimental investigation of the thermochemical performance of heat shield materials is usually conducted in plasma wind tunnels [1,3]. State of the art diagnostic tools concentrate on the measurement of surface temperatures, in-depth temperatures using thermocouples, and spectroscopic diagnostics to analyse the plasma layer in front of the tested materials [?,2].

A further crucial parameter to judge the performance of candidate materials is the surface change, i.e. recession of the surface and its deformation or shape change [7]. In particular for ablative thermal protection systems, where surface recession is an essential feature of the thermal protection, the design and layout of the TPS depends on the material's geometrical behavior (see e.g. Milos et al. and Park for the difference in analysis of the Galileo heat shield performance [4,5]). Furthermore, the rate of ablation even of very simple materials varies with time [7]. Therefore, a diagnostic tool is needed to observe the material's recession as a function of time. Finally, knowing the recession would allow to analyse its influence on the boundary layer. Pyrolysis gases lead to a cooling effect in the boundary layer and solid particles ablating can have a blocking effect to heat flux [5]. Knowing the recession can give first insight to the amount of material additionally present in the boundary layer.

Different approaches to measure the surface recession from embedded sensors have been published. The most recent development is the recession sensor developed for the Mars Science Laboratory (MSL) [?,?].

In ground testing environments, surface recession and surface changes can be observed using optical methods. Very simple approaches are based on the observation of laser spots on the surface that change its position when the material recesses [?]. This technology is also investigated by the authors in the plasma wind tunnels at IRS.

*Research Scientist

†Research Scientist

However, the main drawback of these systems is that the shape change is not observed due to the point measurement. Improvements could be made by using laser sheets or fast moving laser spots, but a much simpler approach is the direct observation of the surface and the application of photogrammetric tools to determine the three-dimensional surface geometry. This technology has been successfully demonstrated by Schairer et al. for arcjet tests at NASA Ames using CCD video cameras [6]. This system allows a maximum frame rate of 16 Hz and an accuracy of 0.3 mm.

The approach presented in this paper follows photogrammetric image analysis. Basically, two different open source software tools have been used to analyse simultaneously acquired photographs of the recessing surface. Modern photogrammetric software tools are based on a pixelwise analysis allowing a high geometrical resolution and a comparably high accuracy. In a first experimental part the principle feasibility of the approach was verified under lab conditions at room temperature with focussing on the equipment used and the types of materials to be tested. Two digital single lens reflex (DSLR) cameras were adapted for plasma wind tunnel purposes using fixed focal length (300mm or 420mm) lenses. The plasma radiation has been analysed with respect to photographic imaging of heated samples.

II. Methodology

The methodology presented here is the result of an extensive study of different hard- and software approaches. First, a commercially available photogrammetric analysis program named ARAMIS from GOM mbH has been applied [?]. First promising results were investigated in more detail in a laboratory setup in order to analyse the constraints of the program [?]. The main drawback of the commercial software was insufficient user information resulting in very problematic calibration issues. In cooperation with the Institute of Photogrammetry of the University of Stuttgart, an in-house code named AUSTRALIS which uses similar numerical tools for the calibration as ARAMIS does, showed that the main problem arises from the long focal lengths for comparably small objects and disadvantageous geometrical setup, i.e. view angle [?].

Meanwhile, there are many new developments for the calculation of three-dimensional sceneries using multiple 2D images. The invention of those tools comes with the three-dimensional analysis of aerial views and three-dimensional city maps, e.g. google street view citeFukuhara....

The approach that we are following in this paper is based on three different open source software solutions which will be described briefly in the following subsections [?]. The starting point are two images taken from the same situation with the two cameras (see section III for experimental details).

A. Bundler

The images taken with the two cameras are first analyzed with a software named BUNDLER [?]. This software allows to reconstruct several significant points in different images. Originally, it has been programmed to reconstruct the same scene from several viewpoints particularly interesting for applications with image searches on the internet [?].

In the present application, the software is used to analyse camera position and focal length. Unfortunately, the program does not allow to identify changes in any dimension of an image. Therefore it can not be used to measure the recession, i.e. the movement of a significant image pixel in on particular direction.

BUNDLER uses a pinhole camera model to position the camera with respect to the taken images

The BUNDLER software is restricted to 5 Megapixels. The images taken are usually 16 Megapixels. The resolution is reduced mainly by reducing the size of the images since only a small part of the picture contains the observed recessing sample.

B. Dense Matching and Cloud Compare

Using the so-called DENSE MATCHING method together with the visualization software CLOUD COMPARE, the acquired photographs are analysed. DENSE MATCHING has been developed at the Institute of Photogrammetry of the University of Stuttgart cite. Basically it uses the same approach as BUNDLER does. It reconstructs a 3D surfaces from at least two images identifying significant features in two or more images. Corresponding pixels between images are identified and possible positional changes of identified pixels from one pair of images to the next are analysed using the visualization software CLOUD COMPARE.

The dense image matching step determines a connection for every pixel in the image leading to a dense point cloud. A pixel $\vec{p} = [p_x p_y]^T$ with the intensity I_{lp} in the left image is suspected a correspondence to a

pixel \vec{q} in the right image with intensity I_{rq} . The pixel q is

$$q = e_{lr}(\vec{p}, d) \quad (1)$$

where e_{rm} is the epipolarline in the matching right image of the pixel \vec{p} in the left image. d is the disparity between \vec{p} and \vec{q} . In the present case with rectangular images e_{lr} becomes $e_{lr}(p\vec{p}, d) = [p_x - dP_y]^T$. In order to identify matching pixels, a matching cost function is defined [?]. It is based on the so-called *Mutual Information* which can be calculated from the entropy of the corresponding images. The entropy is defined by the probability distribution function of the pixel of interest. Geometrically, the matching right image has to be warped with a disparity D to become the base left image. Every pixel has to be treated separately. The unknown D image is searched iteratively with some additional boundaries, e.g. gradient conditions between adjacent pixels. Knowing D means to know the corresponding pixels in both images.

In the more classical photogrammetry calibration images are taken and transformations are calculated for certain corresponding windows. The camera's inner and outer orientation is identified from the calibration images and the most advanced method ... **Buendelblockausgleichung** ... is based on those calibrations. These methods are computationally rather expensive, but their main drawback is that these methods do not work at fine structures and discontinuities [?].

The drawback of a pixelwise analysis is that the calculation also needs high computing capacity. Furthermore, grey values are not unique in one image, so the connection between pixels from the first to the next image is not unique. Therefore, it uses an approximation of a global smoothness constraint of the observed surface over the image. This reduces the needed computing power and increases the probability for a useful correspondence. Noise can also be reduced with this method. Fig. 1 shows the result of the matching procedure. Both samples have been sprinkled with Keratin to improve the contrast and to assure clear comparable points. The left and right image are plotted next to each other and the lines point on the different features. Since the two images have been acquired at almost the same horizontal level, the lines

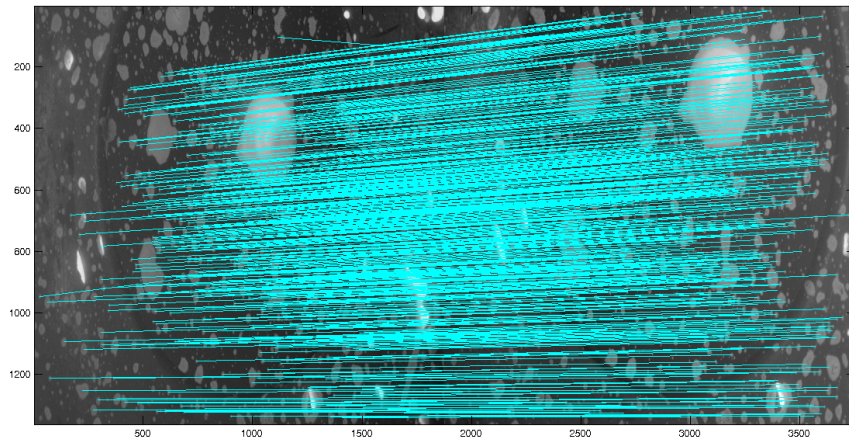


Figure 1. Result of feature matching.

should be almost parallel lines. It can be seen in Fig. 1 that some lines are warped significantly (e.g. the most top line). This indicates that an artificial feature has been identified. The higher the number of those wrong identifications the worse is the following triangulation process. In images with weak surface features, obviously the identification is more difficult. This motivated the investigation of different surfaces of interest in order to judge the performance of this method for recession measurement purposes.

The identified point clouds are analysed using the software CLOUD COMPARE. This is basically a tool to analyse various point clouds. The different image pairs of an experiment are loaded as a 3D point cloud which allows then to analyse possible pixel offsets. Fig. 2 shows the overlay of the first and the last acquired and analysed image pair of an experiment. As can be seen, there is a clear difference between the two images. In order to relate this to a recession, the scaling between pixels and mm has to be determined. One possibility is to use a known distance in one of the images or an image pair is used as a calibration distance.

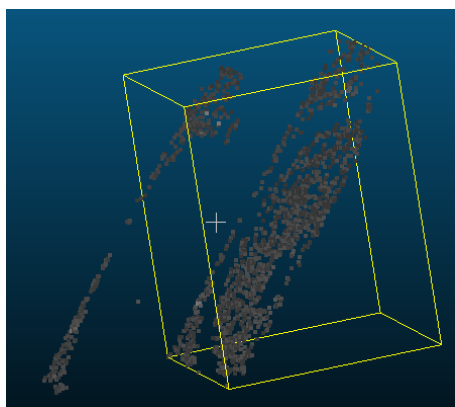


Figure 2. Raw image of two point clouds in Cloud Compare.

Finally, Fig. 3 shows a resulting surface image of the 3D cloud of the probe and the sample within a plasma wind tunnel test.

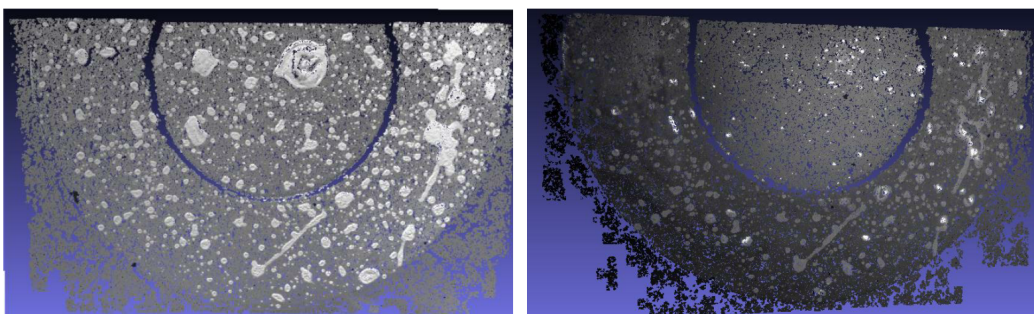


Figure 3. Perspective view of reconstructed point cloud.

III. Experimental Setup

The challenge to mount the photogrammetric setup at the plasma windtunnel facility is the limited access allowing an observation of the probe surface. The material tests within this study have been performed in the plasma wind tunnel PWK1. The probe is mounted on a moving platform inside a vacuum chamber with a diameter of 2 m and a length of 6 m. There are only small optical windows to observe the plasma flow and the probe. Fig 4 shows a photography and a sketch of the setup using two cameras. It has been decided that the best solution is to use the two inclined windows in the front lid of the vacuum chamber. Here, possible reflectivity issues are minimised and a comparably large part along the axial direction of the wind tunnel can be observed. The front lid has to be opened for sample installation, therefore, the camera setup has been mounted on separate tripods. This has the further advantage that vibrations of the vacuum chamber during evacuation do not affect the camera setup.

The images are acquired using two digital single lens reflex (DSLR) cameras of type Canon EOS 60D. Table 1 lists the parameters of the camera setup. Both cameras are released simultaneously radiocontrolled within < 100 ms. For the present investigation of the photogrammetric applicability, only few images were taken at a rate of one image per 30 s, the maximum rate of the camera being 6Hz. Figure 5 shows an example of a material probe in the plasma wind tunnel as seen through the side windows (left). On the right photo, a first photography of an ablation sample is shown. The plasma flow emission becomes fairly weak in the visible at very short exposure times which allows an observation of the sample's surface. For the surface photo an f-stop of $f/9$ at an exposure time of $1/500$ s has been set. Note that the bright spot in the center is a laser spot used for laser recession measurements.

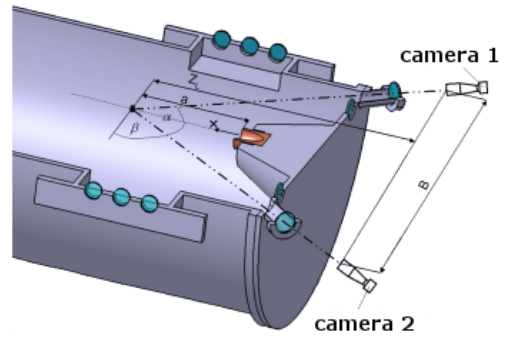
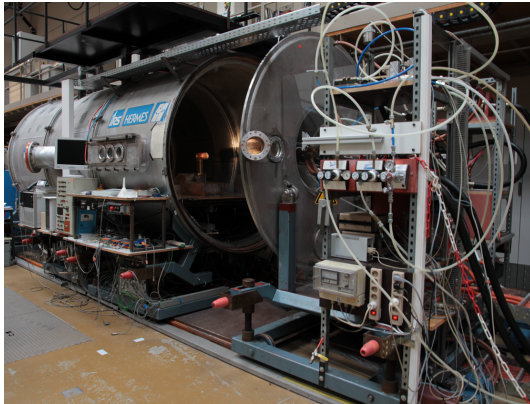


Figure 4. Plasma windtunnel PWK1 (left) and geometrical setup for the photogrammetry (right).

Table 1. Camera setup.

camera	Canon EOS 60 D
pixel	5184 x 3456 px ²
chip size	22.3 x 14.9 mm ²
pixel size	4.3 μm
aperture	22
ISO	100
exposure	automatic
focal length	420 mm
color depth	12 bit

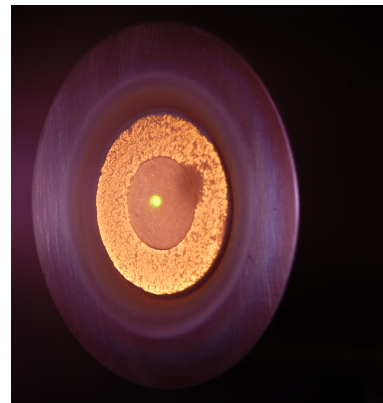
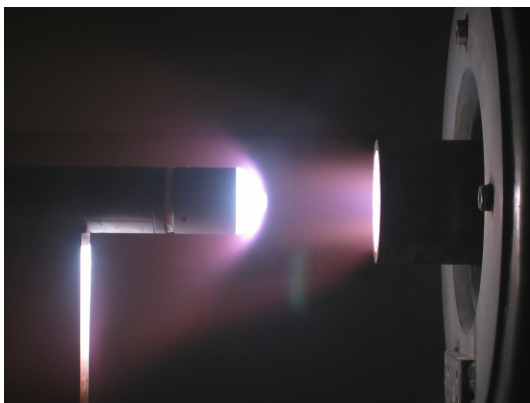


Figure 5. Material probe in the plasma wind tunnel (left) and photography of a material's surface (right).

IV. Results

The results section is divided in three main parts. First, an analysis of the setup's performance concerning observation angle is presented. Then, the analysis of different probe surfaces is presented. Here a generic setup has been used with an oxyacetylene torch for sample heating. The purpose was to investigate whether and how different surface reflectivities and surface structures affect the data analysis. Finally, first plasma wind tunnel testing has been performed and a first recession analysis has been conducted.

A. Setup performance

The camera setup has been installed in the DLR laboratory in order to investigate the problematic access through the chamber windows. As can be seen in Fig. 4 the windows do allow a certain view angle β with respect to the probe surface. If the probe is moved towards the generator to increase the heat load, the angle is becoming smaller, thus the photogrammetric approach becomes more complex. Fig. 6 shows the results of different base distances and apertures as an overview. These results have been acquired using the ARAMIS software. Distances between 870 mm and 3400 mm have been investigated. However, the maximum base distance for ARAMIS is 1500 mm. The facility, however needs a base distance of 3200 mm, which indicates the problem of using ARAMIS.

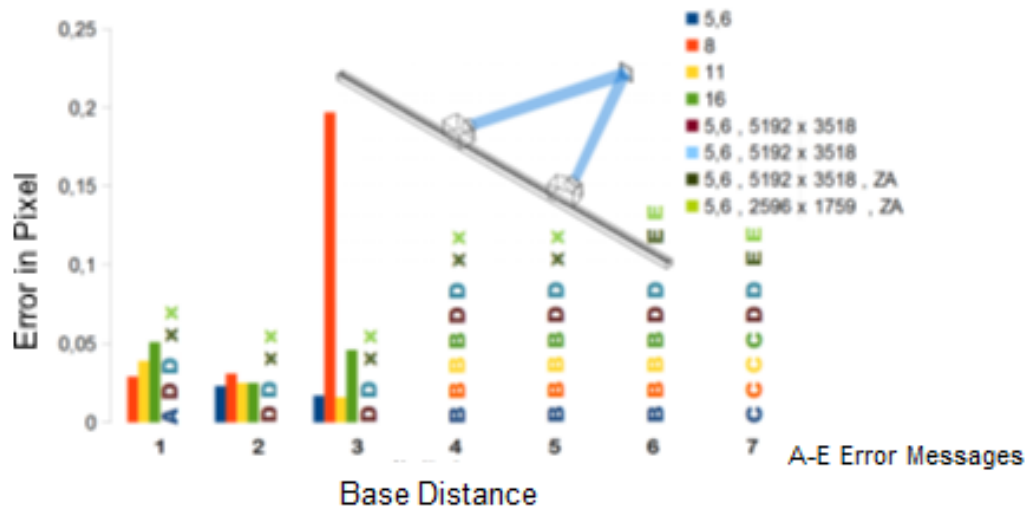


Figure 6. Increasing base distance error when using Aramis) [?].

B. Influence of the vacuum chamber windows

As described, the camera system is mounted outside the vacuum chamber for two main reasons: The camera system is not endangered to be damaged by hot gases and the camera setup can be modified during facility runtime.

The drawback of this setup is that the pictures are taken through the windows of the vacuum chamber. In order to minimize transmission losses, fused silica windows are mounted with high transmission between 200 nm and 900 nm. The cameras have been setup at the Institute of Photogrammetry of the University of Stuttgart in order to measure the difference with respect to recession accuracy for the windows. It has been shown that the window does not affect with respect to transmission (see Fig. 7). However, the reflections at the surfaces of the window do affect the measurements slightly. The most critical issue is a possible change in the setup during measurements. Therefore, the optical path between camera and window should be covered to avoid any random reflections and the camera adjustments have to be fixed with the appropriate set screws to avoid a change in focal length.

Comparing mirror setup similar to the one used by Schairer et al., the accuracy of the present study $20 \mu\text{m}$ instead of 0.2 mm .

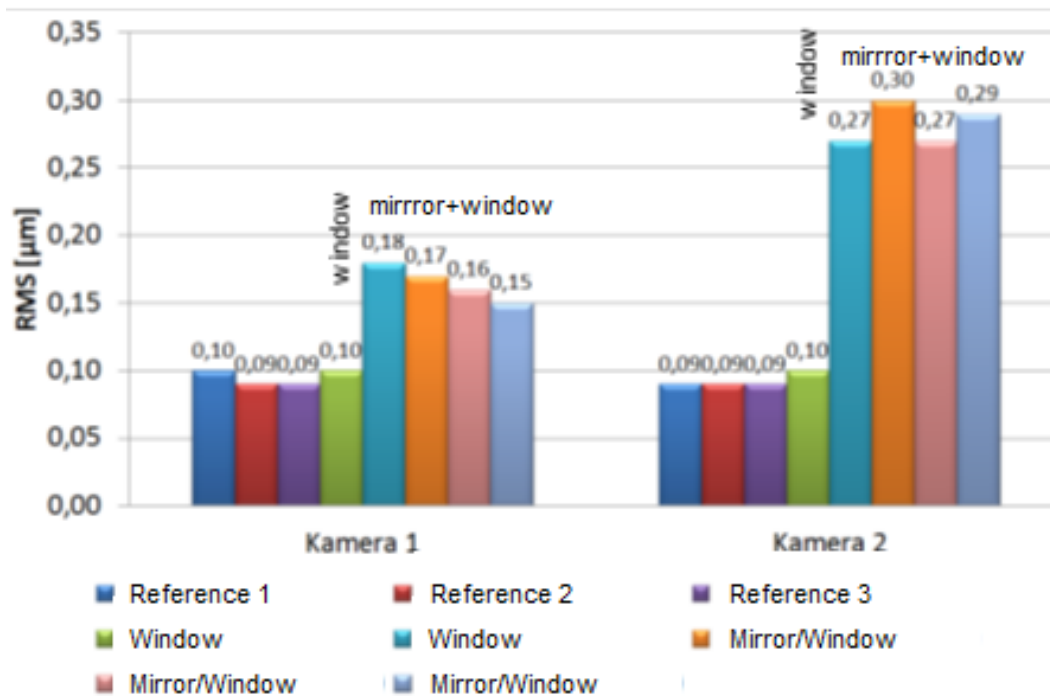


Figure 7. Influence of vacuum chamber windows and possible mirrors.

C. Surface condition and resolution

The data analysis strongly depends on the feature detection possible on the surface of interest. The two taken images have to be compared and therefore discrete features in every image pair are needed. Within the preparation of this approach, four different materials have been considered: pretreated carbon, virgin carbon, porous carbon, and a ceramic matrix composite C/C-SiC. The C/C-SiC material has furthermore a highly reflecting surface. All candidates are shown in Fig. 8. Using the approach with BUNDLER-DENSE

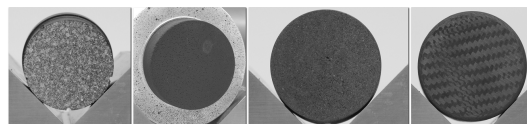


Figure 8. Different surfaces of common heat shield basic materials.

MATCHING-COULD COMPARE all material surfaces have been identified with high resolution. The higher reflectivity does not affect the number of identified features nor the accuracy of the triangulation. The surface discretization is very high (see Fig. 9). The scale is given in the lower right of the figure. The probe diameter has been 40 mm and there are about 1000 px in lateral direction, thus, there is about 1/400 mm per pixel. This high discretization means that the triangulation allows high accuracy. It can be clearly seen that there is an inhomogeneous recession, although the heat flux affecting the surface can be assumed to be rather constant across the sample surface. The recession is obviously also affected by the probe body and the highest recession is on the lower right side. Evaluating the center spot for different measurements with 300 s shows Fig. 10. The sample has been introduced into the flow at 0 s. The recession seems to reach a constant level after a higher beginning rate. The ablation processes seem to have a higher recession at the beginning. Wernitz et al. also observed a similar behavior when analysing emission spectra of the boundary layer [8]. In order to interpret further the resulting recession from the photogrammetric setup, Fig. 11 shows the recession of a similar sample measured with the laser pointing setup. The focused laser spot was about 5 mm in diameter. Therefore, the analysed recession is a mean value of a spot around the center pixel of Fig. 10. Furthermore, the heat flux was significantly higher. However, the basic result is similar. After the insertion of the probe recession rate is higher than the recession values after 5 s. The accuracy of the laser

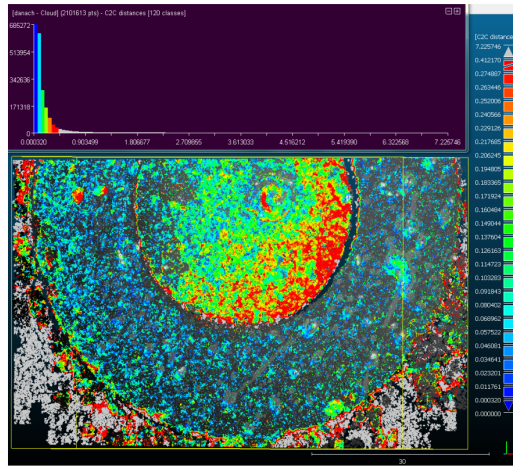


Figure 9. Resulting pixel cloud from photogrammetric measurement.

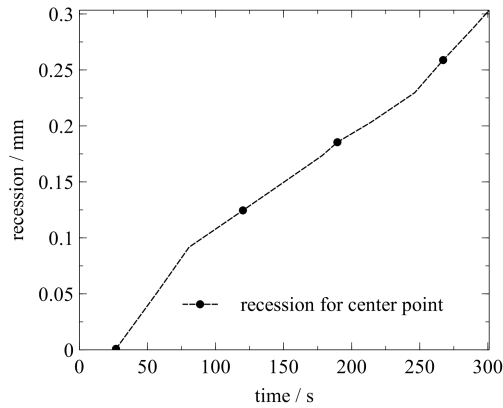


Figure 10. Quantitative recession measurement for one pixel.

recession, however, is by far lower than the photogrammetry. Laser recession with this setup gives about 0.2 mm, whereas the photogrammetry leads to 20 μm .

V. Conclusion and Outlook

In conclusion, the approach presented in this study, i.e. the application of pixelwise analysis of image pairs to analyse the 3D surface, is well applicable to plasma wind tunnel problems. Compared to classical photogrammetry technologies, significantly higher tolerance to image problems, as noise, radiation differences, is allowed and a considerably high resolution in the range of 20 μm is reached.. Compared to literature values this is a very promising result. An investigation of window effects and various camera positions has been investigated in this study, but do not influence the result significantly. A possible application of mirrors, however, reduces the accuracy by a factor of 2.

The main goal of future measurements is to analyse already mentioned issues of a high recession during beginning of ablation testing before reaching a rather constant recession rate. This observation affects a possible conclusion for a mission relevant material test with respect to safety margins.

In combination with optical emission spectroscopic analysis, the ablation process can be analysed in further detail towards better material performance prediction and thus lower possible safety margins and lightweight thermal protection systems.

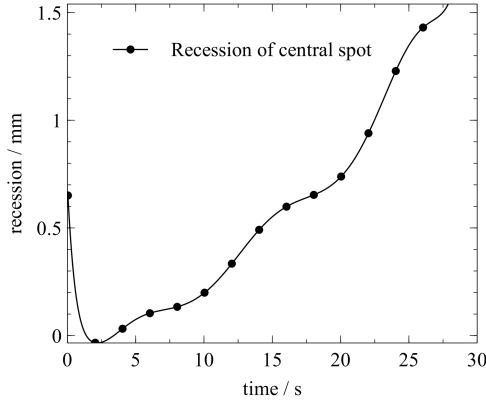


Figure 11. Quantitative laser recession measurement for central spot (diameter approx. 5 mm).

VI. Acknowledgments

The authors gratefully acknowledge the astonishingly interesting results Jens Marr, Mirko Zuber, Sebastian Hoerner, and Michael Wrasmann contributed. S. Löhle would like to thank the colleagues of the laboratory team for the support during testing. T. Reimer would like to thank Florian Hofmeister for his assistance in the basic laboratory testing.

References

- [1] M. Auweter-Kurtz and T. Wegmann. Overview of irs plasma wind tunnel facilities. *RTO Educational Notes*, 8, October 1999.
- [2] S. Löhle, C. Eichhorn, A. Steinbeck, S. Lein, G. Herdrich, H.-P. Röser, and M. Auweter-Kurtz. Oxygen plasma flow properties deduced from laser-induced fluorescence and probe measurements. *Applied Optics*, 47(13):1837–1845, 2008.
- [3] F. K. Lu and D. E. Marren, editors. *Advanced Hypersonic Test Facilities*, volume 198 of *Progress in Astronautics and Aeronautics*. AIAA, 2002. ISBN 1-56347-541-3.
- [4] F. S. Milos, R. A. Brewer, Y.-K. Chen, and T. H. Squire. Analysis of galileo probe heatshield ablation and temperature data. *Journal of Spacecraft and Rockets*, 36(3):298–306, May 1999.
- [5] C. Park. Stagnation-region heating environment of the galileo probe. *Journal of Thermophysics and Heat Transfer*, 23(3):417–424, 2009.
- [6] E. T. Schairer and J. T. Heineck. Photogrammetric recession measurements of ablative materials in arcjets. *Measurement Science and Technology*, 21, 2010.
- [7] G. W. Sutton. The initial development of ablation heat protection, an historical perspective. *Journal of Spacecraft and Rockets*, 19(1):3–11, February 1982.
- [8] R. Wernitz, C. Eichhorn, G. Herdrich, S. Löhle, S. Fasoulas, and H.-P. Röser. Plasma wind tunnel investigation of european ablaters in air using emission spectroscopy. In *42nd AIAA Thermophysics Conference*, 2011.

Experimental Investigation of Photogrammetric Surface Analysis of Heat Shield Materials during Plasma Wind Tunnel Testing

Thomas Reimer

DLR Stuttgart, Institute of Structures and Design

Dr. Stefan Löhle

Stuttgart University, Institute of Space Systems



Wissen für Morgen



Overview

- Motivation based on Re-entry and TPS needs
- Objective
- Photogrammetry
- Precursor work
- Experimental setup
 - Laboratory
 - Plasma wind tunnel application
- Results
- Outlook



Background

TPS performance optimization: mass reduction

TPS categories:

- Passive systems vs. active cooling

Passive systems

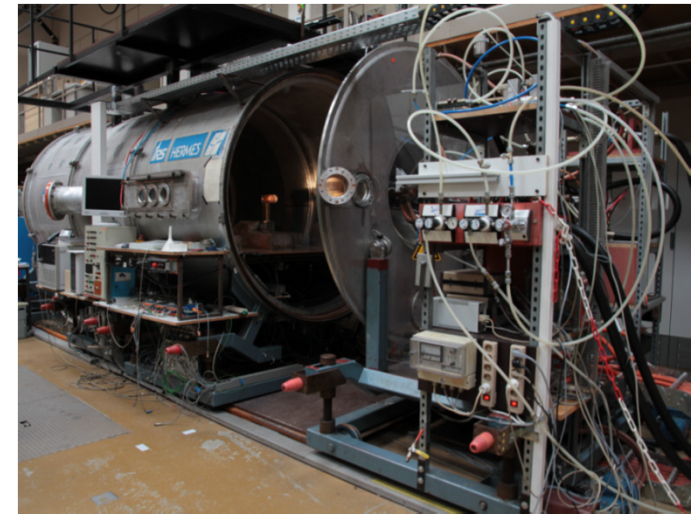
- Non-ablating with radiation cooling (re-usable, Shuttle)
 - Ablative systems with significant recession (capsules)
-
- LEO entry (lower energy): non-ablating or ablating systems
 - Hyperbolic entry (high energy): only ablating systems

Typical ablators: fiber-resin compounds of various density

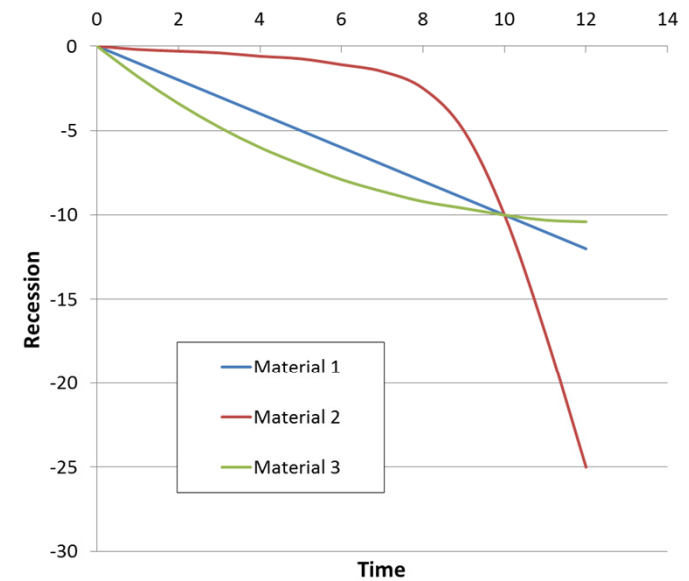
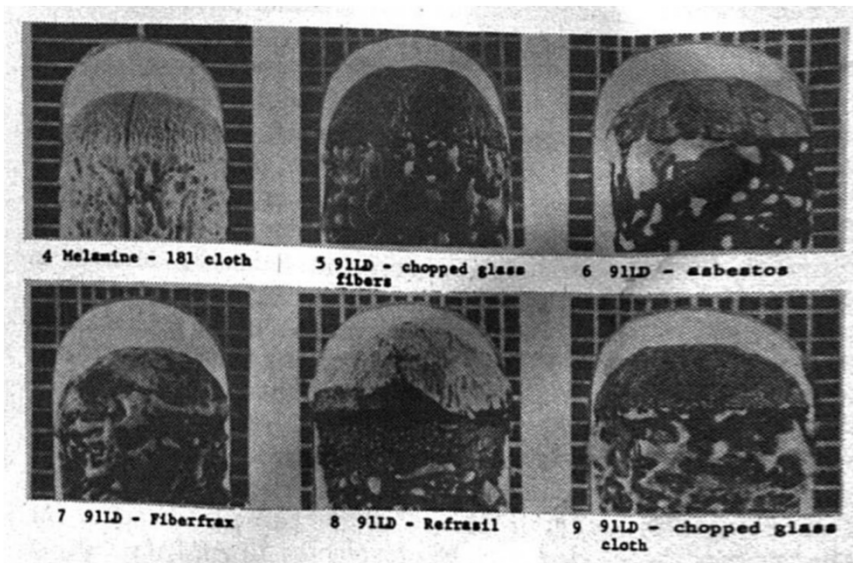


Motivation: Performance Improvement and Margin Reduction

- Ablator testing in plasma wind tunnels
 - Imperfect simulation of re-entry conditions
- Testing procedures
 - Steady-state load conditions
 - On-off testing
- Sample performance diagnostic
 - Thickness and mass
 - Before/after comparison



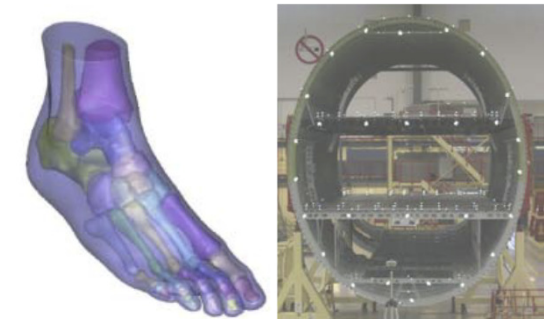
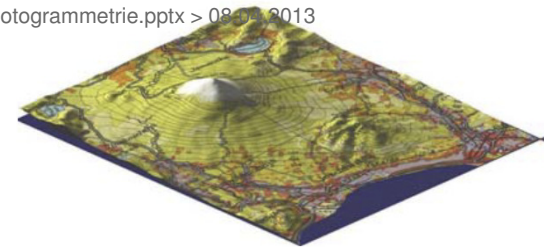
Transient 2-D in-situ thickness measurement



Photogrammetry

Photogrammetry

- Creation of a 3-D representation of a 3-D real-life object via processing of 2-D images
- Origin in geodesy
- Elevation maps from airborne images
- 3-D reconstruction and restoration
- Industrial application in quality assurance
- Medicine
- Movies



With regard to resection measurements:

- Ablators are fragile, embedded sensors disturb results
- Photogrammetry yields 2-D result vs. point data



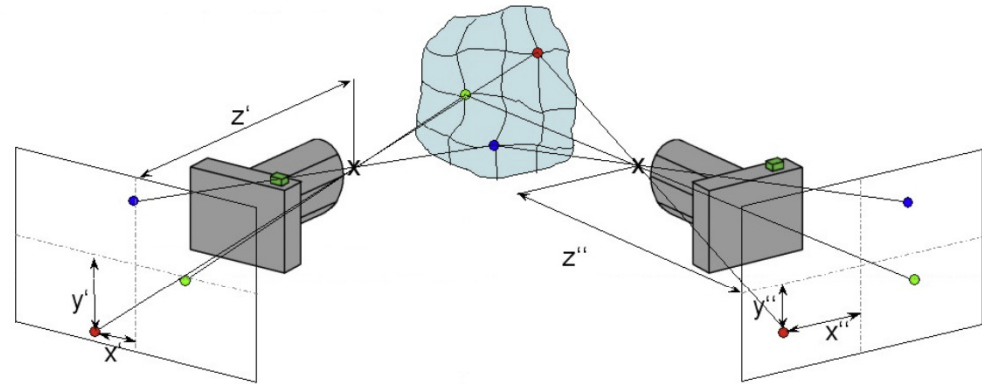
Stereo-Photogrammetry

Left Camera

$$\begin{bmatrix} X \\ Y \\ Z \end{bmatrix} = \begin{bmatrix} X_0^L \\ Y_0^L \\ Z_0^L \end{bmatrix} + m^L \cdot \begin{bmatrix} r_{11}^L & r_{12}^L & r_{13}^L \\ r_{21}^L & r_{22}^L & r_{23}^L \\ r_{31}^L & r_{32}^L & r_{33}^L \end{bmatrix} \cdot \begin{bmatrix} x' \\ y' \\ z' \end{bmatrix}$$

Right Camera

$$\begin{bmatrix} X \\ Y \\ Z \end{bmatrix} = \begin{bmatrix} X_0^R \\ Y_0^R \\ Z_0^R \end{bmatrix} + m^R \cdot \begin{bmatrix} r_{11}^R & r_{12}^R & r_{13}^R \\ r_{21}^R & r_{22}^R & r_{23}^R \\ r_{31}^R & r_{32}^R & r_{33}^R \end{bmatrix} \cdot \begin{bmatrix} x'' \\ y'' \\ z'' \end{bmatrix}$$



- Images from two perspectives
- Generation of surface with surface points
- Identification of a point in one image: 3 equations, 4 unknowns
- Identification of the same point in the second image: 6 equations, 5 unknowns
- X, Y, Z can be calculated
- Identification of remaining parameters (X_0, Y_0, Z_0, r_{ij}) via calibration



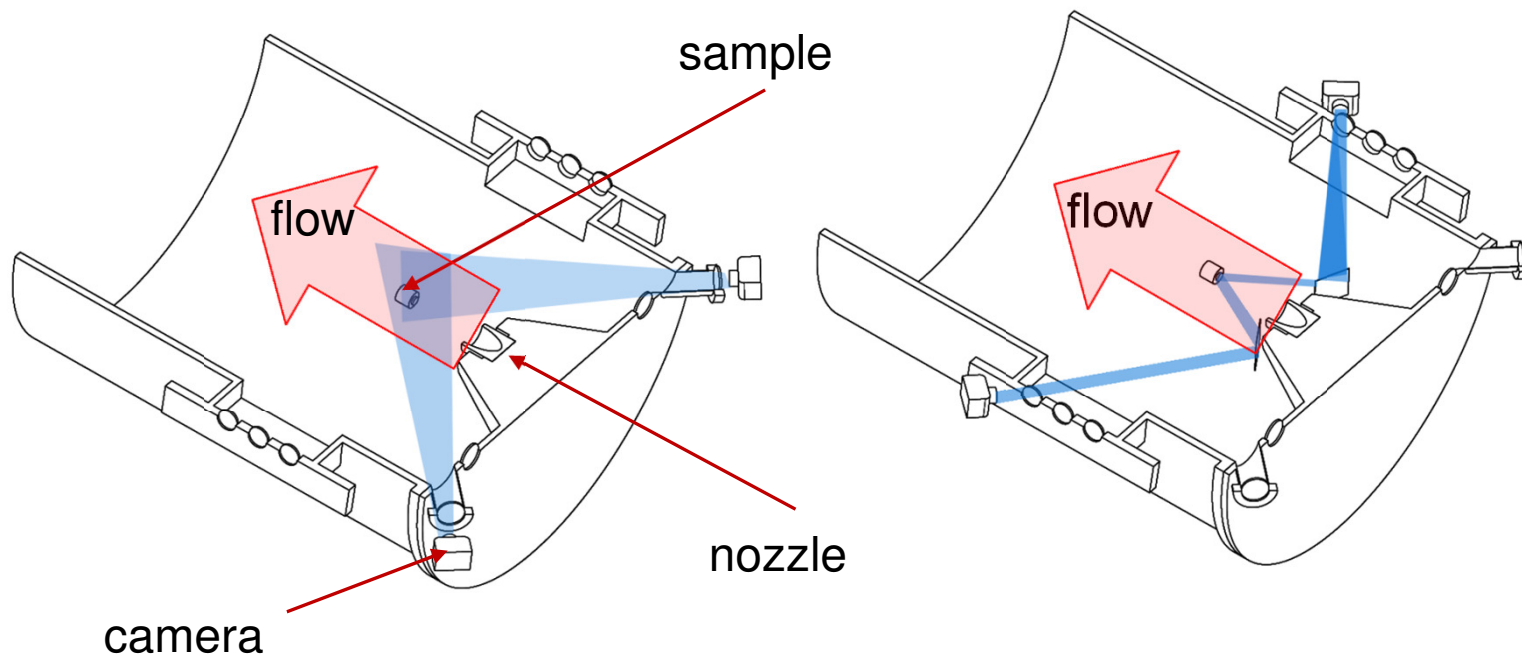
Precursor Work

- First study and application to arc jet testing by NASA: Schairer, Heineck
(E.T.Schairer, J.T. Heineck: **Photogrammetric recession measurements of ablative materials in arcjets**, Measurement Science and Technology 21, 2010, 025304)
- Results of Schairer and Heineck :
 - The PRM method was developed and demonstrated successfully in arc jet tests. The direct linear transformation method was used with the uncertainty/resolution in the range of 0.2 mm
- Feasibility studies at IRS/DLR/IFP by
 - Marr, Zuber, Hörner: First studies aimed at developing the basics in near-field photogrammetry using the ARAMIS software
 - Wrasmann, Pitzer: Parameter studies and identification of different approach using pixel comparison methods



Experimental Setup

- Experimental setup adapted to IRS plasma wind tunnel geometry
- Two basic variants: Direct vs. indirect observation due to limitations in visibility and software constraints
- Investigation of window and mirror influences



Imaging Hardware

- Cameras: DSLR cameras Canon EOS 60D (APS-C sensor 18MP)
- Lenses: Canon EF 300mm 1:4 L IS
- Optional: Canon Extender EF 1.4x III
- Total focal length 300 mm resp. 420 mm

Camera	Canon EOS 60D
Resolution	5184x3456 pixel
Sensor	22,3x14,9 mm
Pixel size	4,3 μm
Aperture	F 22
ISO	100
Exposure	Automatic
Lens	300 or 420 mm
Calibration target	50 x 40 mm
Convergence angle	73°
Distance sample-nozzle	350 – 400 mm



Image Data Processing

Two processing approaches have been investigated:

1. Available software ARAMIS (GOM) – established near field tool for measurements in material characterisation

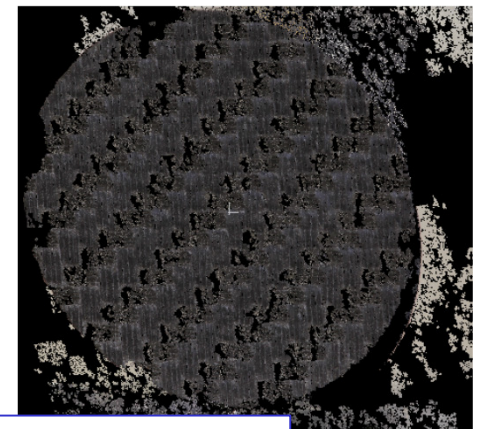
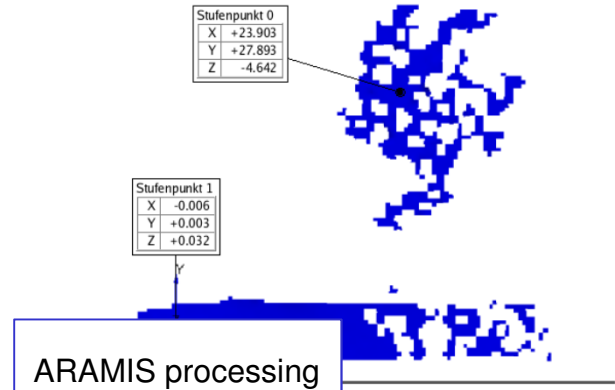
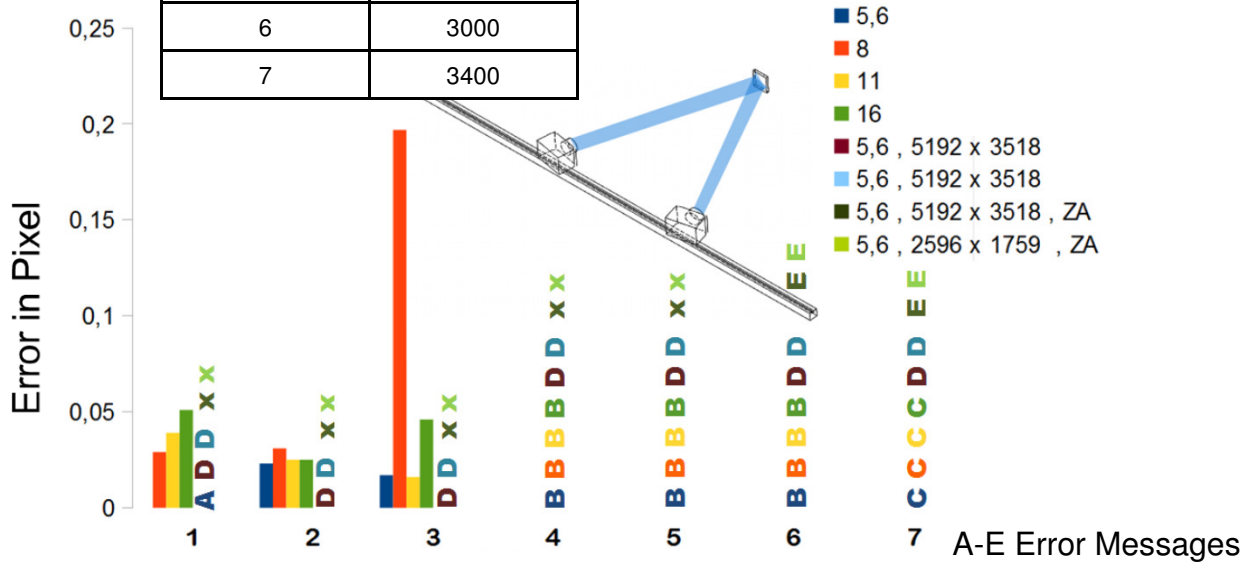
2. Alternative package of different tools
 - Calibration software AUSTRALIS (IFP Uni Stuttgart)
 - BUNDLER – reconstruction of the camera position (open source)
 - Dense Image Matching – reconstruction of the 3-D sample surface (IFP)
 - Cloud Compare – visualization and measurements in 3-D space upon calibration (open source)



Laboratory Results for ARAMIS

- Target application for ARAMIS is totally different
- Narrow geometric limitations mainly wrt. convergence angle
- Surface generation extremely difficult when no clear surface pattern is visible

Base Distance	Distance / mm
1	870
2	1000
3	1500
4	2000
5	2500
6	3000
7	3400



Dense Image Matching

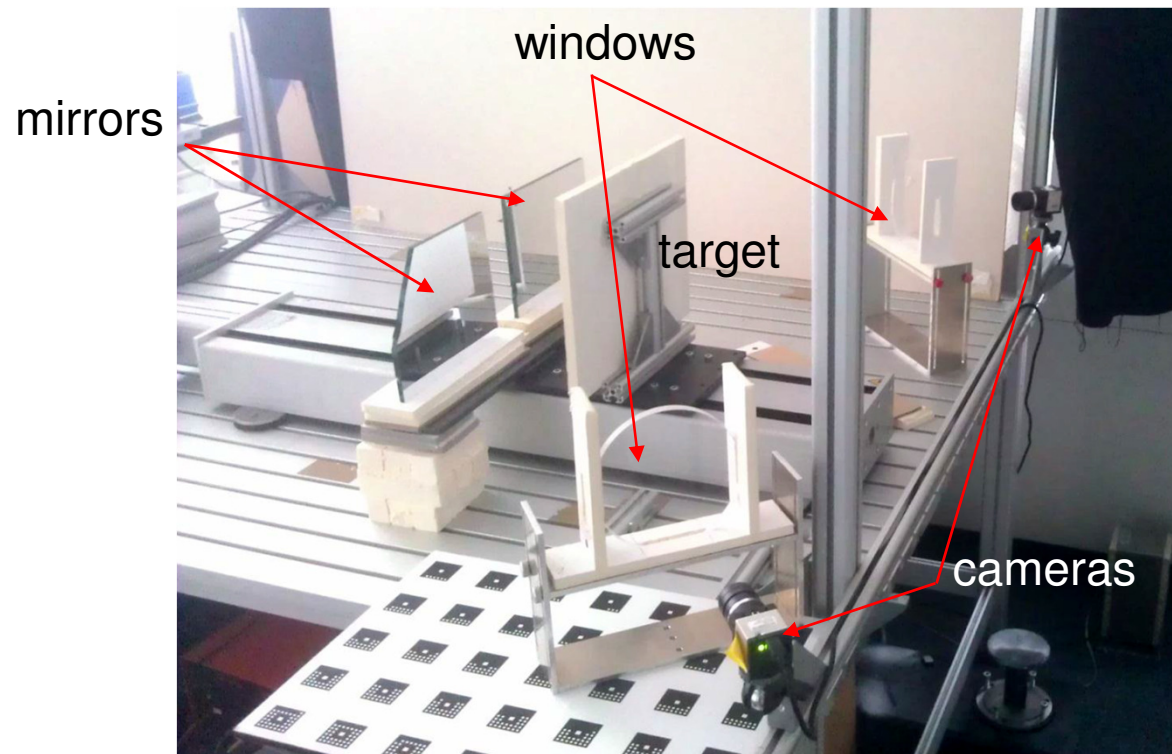


Base Distance



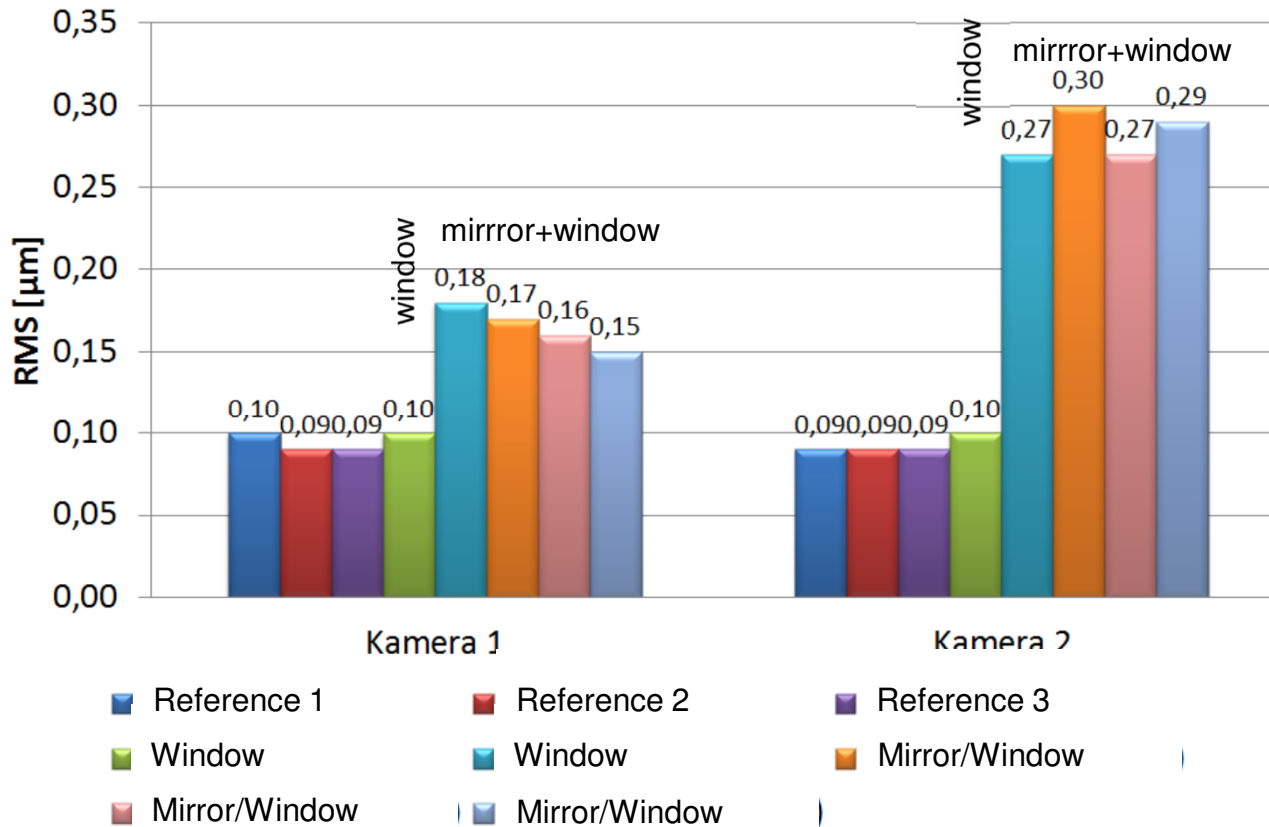
Experimental Setup Mirrors/Windows

- Experimental laboratory setup to determine window and mirror influences
- Alternative software package with AUSTRALIS



Results for Window and Mirror Influence

- Window influence is very small compared to mirrors (RMS increase in object space by factor 2-3)
- Front surface optical mirrors of lower quality were used



Result Comparison

Comparison of results for the two software approaches:

ARAMIS:

- Narrow limitations in test geometry
- Characteristic surface pattern required
- Very difficult to use mirrors

Alternative package:

- Calibration not required when BUNDLER is used
- Much better resolution
- Much weaker surface pattern sufficient
- Mirror use influences resolution but otherwise unproblematic

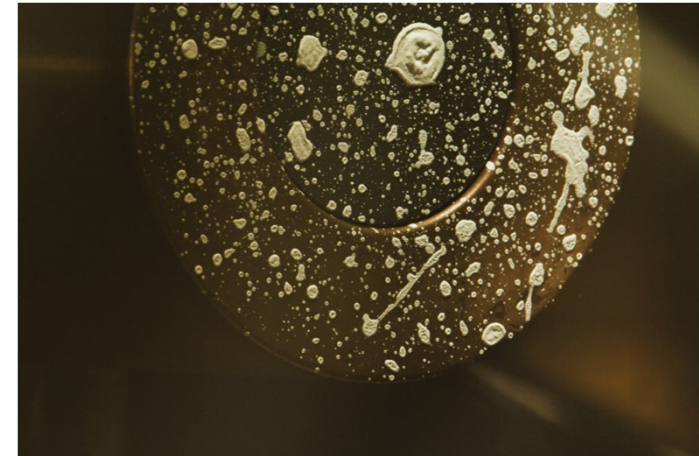
Conclusion

- Alternative package is the way to go

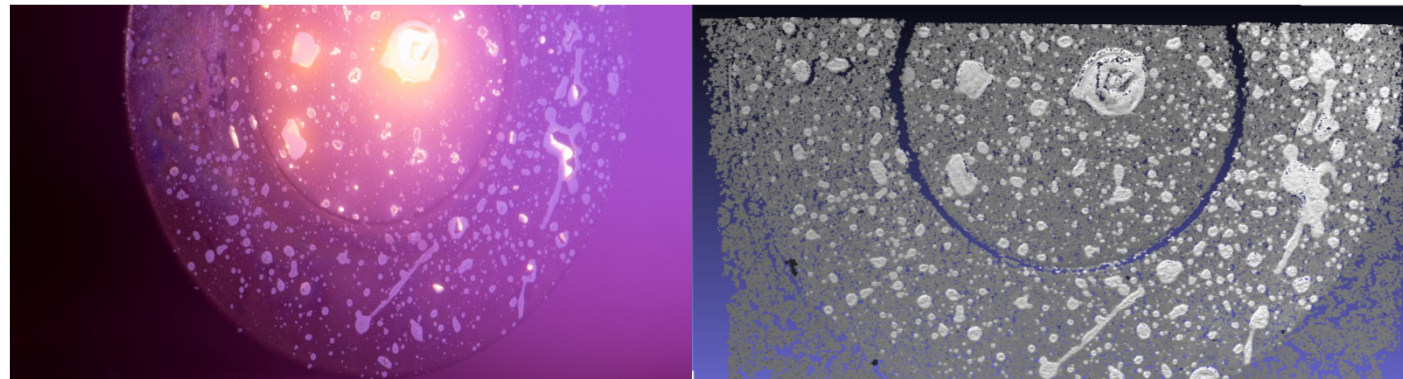


Results of PWK Test

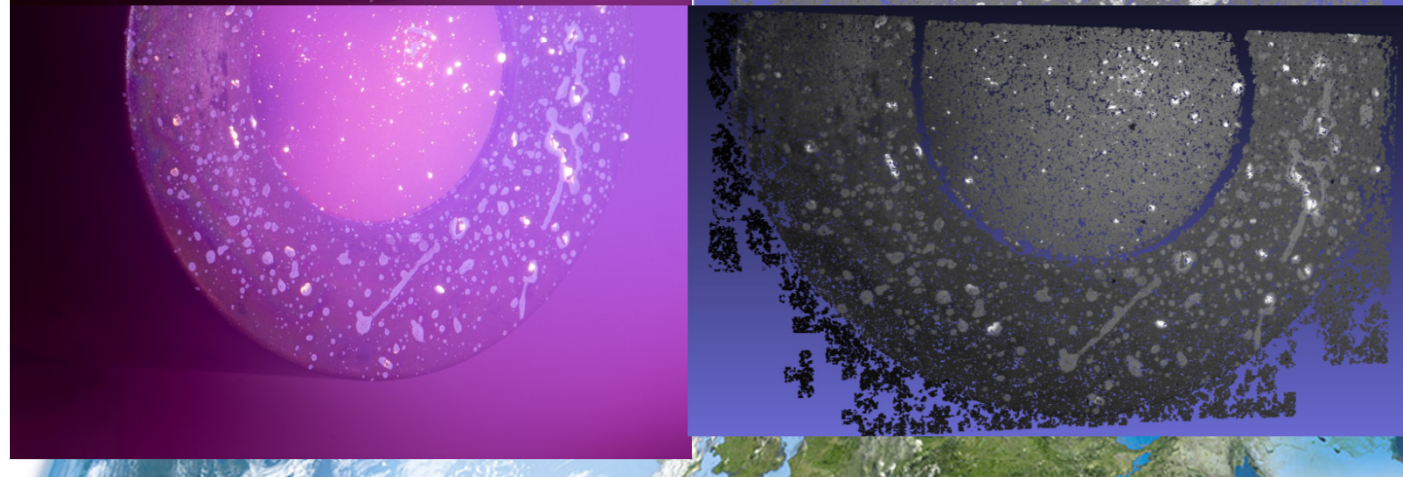
- Moderate condition, graphite sample
- Images of good quality can be acquired
- Processing with ARAMIS yields low quality results due to degradation of the surface pattern
- Alternative software bundle produces high quality data even with very little surface features (shown here)



Start of the test

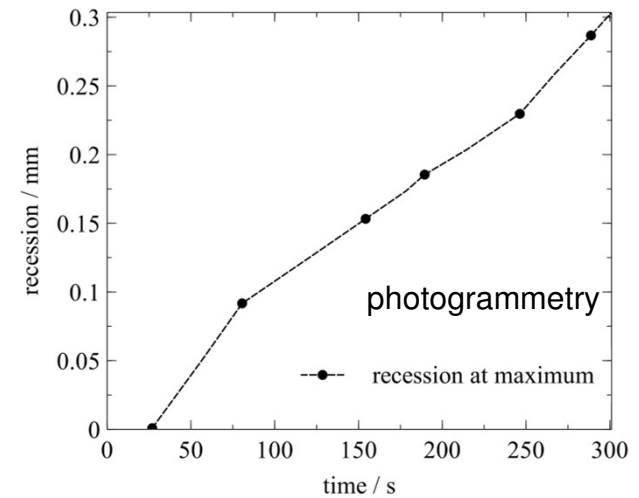
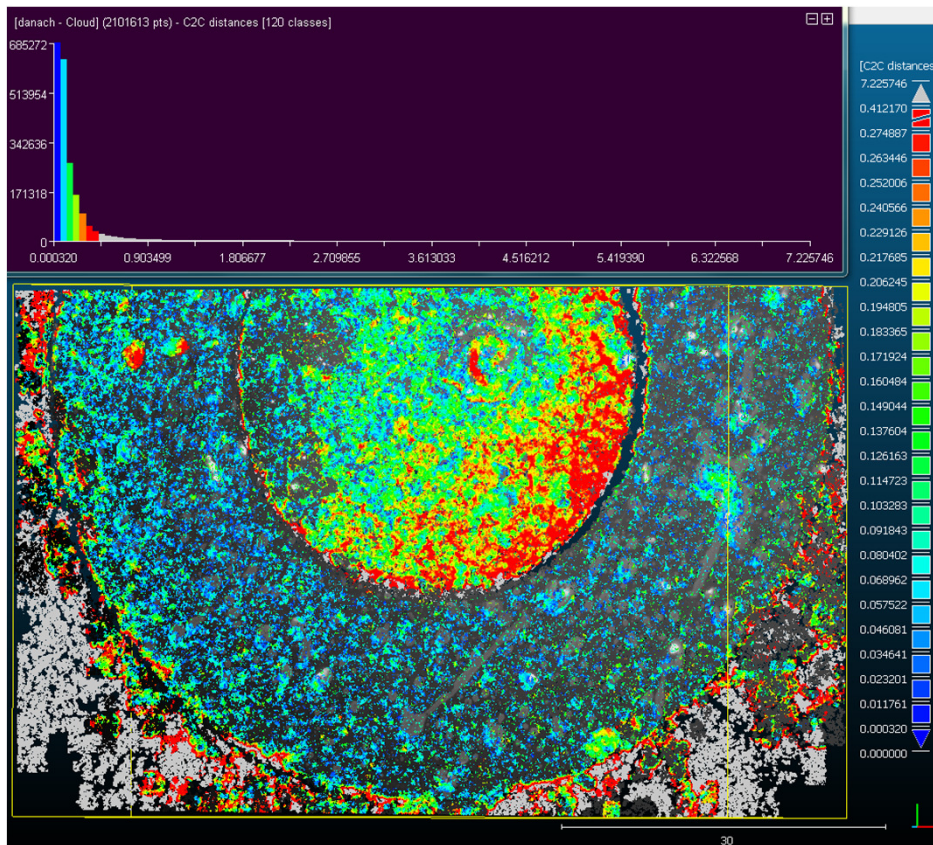


End of the test

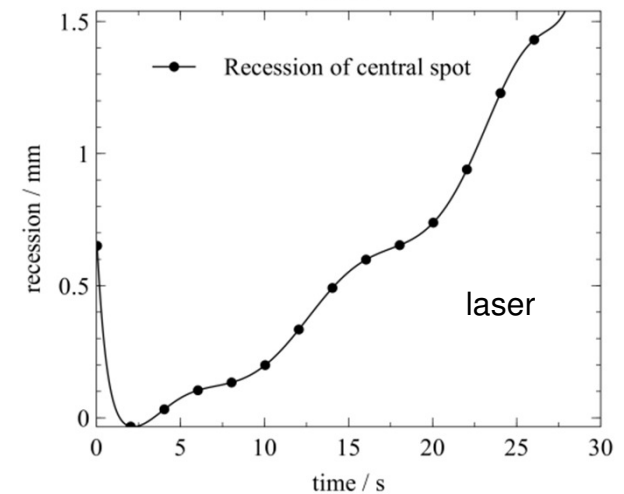


Results of PWK Test

- Images were processed with BUNDLER, DIM and Cloud Compare
- The transient recession can be measured with good accuracy
- The accuracy obtained in the PWK so far seems to be around 0,05 mm



Recession / mm



Conclusion

- An existing photogrammetry software was thoroughly checked for its applicability to plasma wind tunnel testing of ablator samples with negative result and an alternative software package was identified that can be used for the task
- Imaging hardware was procured according to the specifications of the measurement task at the plasma wind tunnel
- The influence of windows and mirrors of the test setup was investigated
- A successful measurement of the 2-D recession of a sample was performed in the plasma wind tunnel
- The laboratory accuracy is $20\mu\text{m}$ – wind tunnel $\sim 50\mu\text{m}$



MEASUREMENT OF TEMPERATURE AND HEAT FLUX IN ABLATIVE TPS

C. Pereira , E. Jaramillo , H. Bruggmann

RUAG Space
Schaffhauserstrasse 580
8052 Zurich
Email: carlos.pereira@ruag.com

INTRODUCTION

The measurement of thermal performance of ablative TPS systems is difficult due to the inherent characteristics of these systems: very low thermal diffusivity when compared to measurement instrumentation, conversion of the upper layer (charring), loss of material and thermal expansion of the material.

This paper shows the design and design evolution of a multilayer thermal measurement system for IXV which allows measurement of the thermal characteristics of ablative TPS as indicated by measurements on both glass filled silicone and cork based ablative systems.

DESIGN CONSIDERATIONS

The original design envisioned introducing pairs of sheathed thermocouples into the ablative so that the outermost thermocouple would be at the surface and a second at the interface to the vehicle structure. A test unit with K-thermocouples placed at varying depths in a glass filled silicone ablative sample was manufactured (Fig. 1).

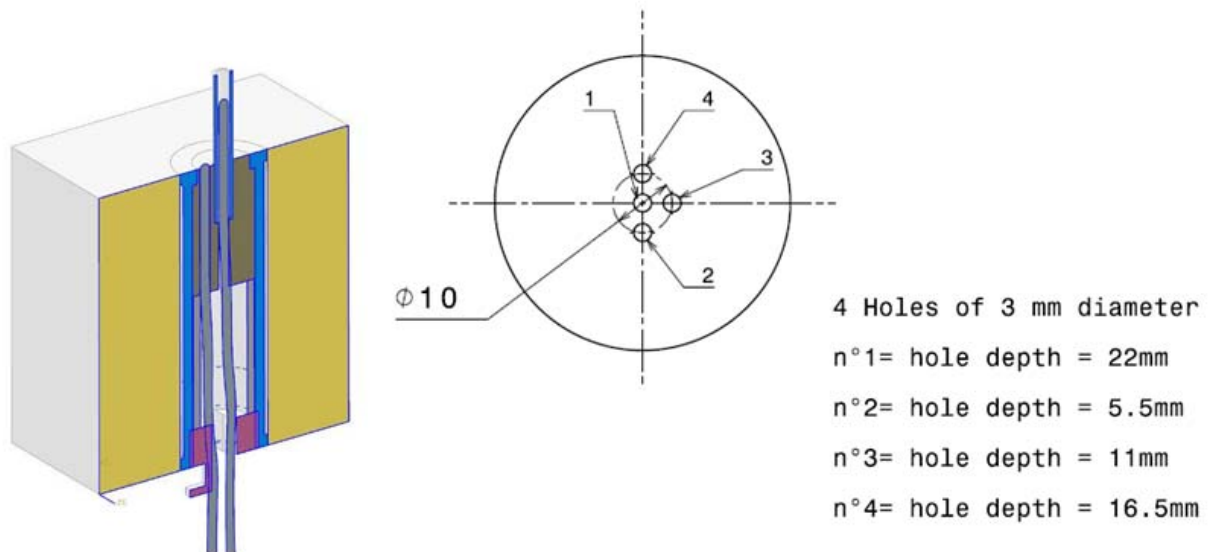


Fig. 1. Design concept for the vehicle (left) and placement of thermocouples in test sample (right)

Stagnation tests performed at the von Karman Institute with this sample show an expansion of the charred layer which covers the surface thermocouple and thus leads to a significant error in the measured temperature (Fig. 2). The image on the left of Fig. 2 shows the surface thermocouple covered with tape (removed before testing). Image on the right shows that this thermocouple disappears due to expansion of the charred layer.

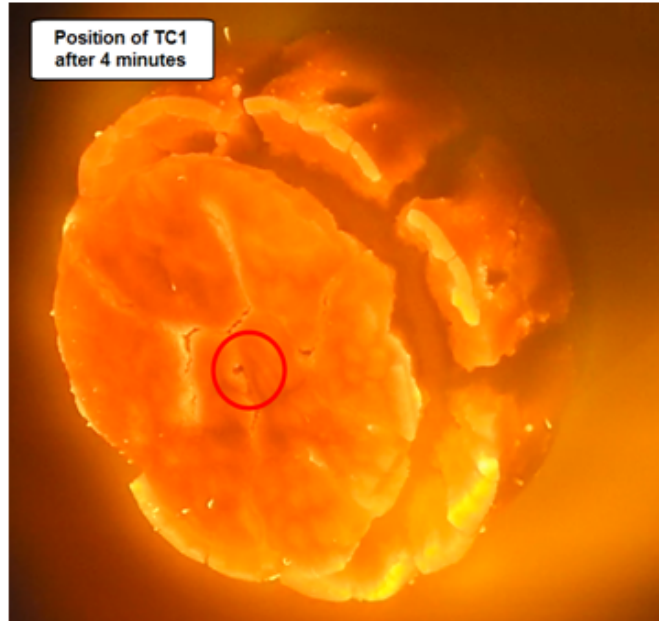
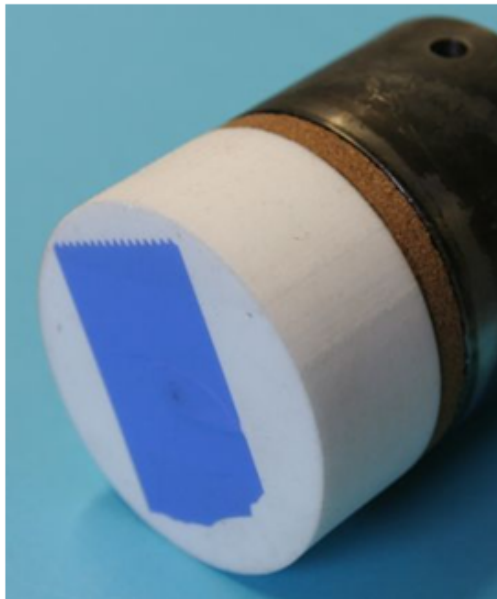


Fig. 2. Thermocouples in ablative stagnation test

Fig. 3. shows a very slow response of the front thermocouple and a very large discrepancy between the front thermocouple reading and the pyrometer measurement. The variations in TC-5 at the interface between ablative and holder are caused by improper grounding.

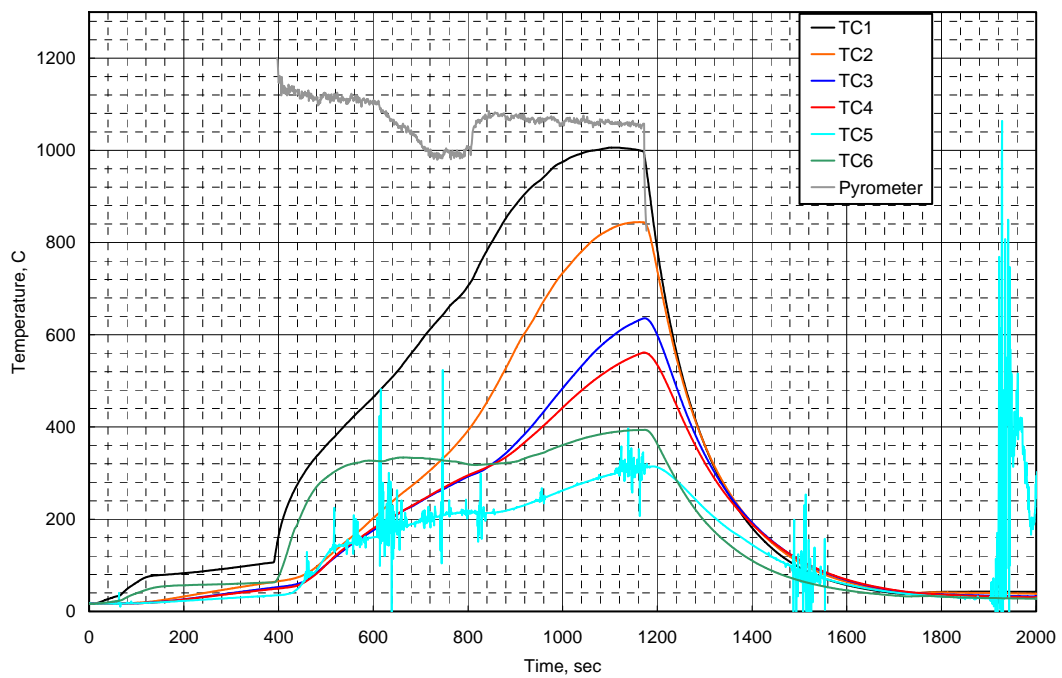


Fig. 3. Thermocouple reading of stagnation test

Although stagnation represents an extreme thermal loading of the ablative the main conclusion is that the thermal diffusivity of the sheath is too large and that therefore the design had to be modified.

The design was modified to include three exposed measuring elements with the first one embedded on the surface and a second one in the mid plane of the ablative. The third one remained at the interface between ablative and cold structure (Fig. 4).

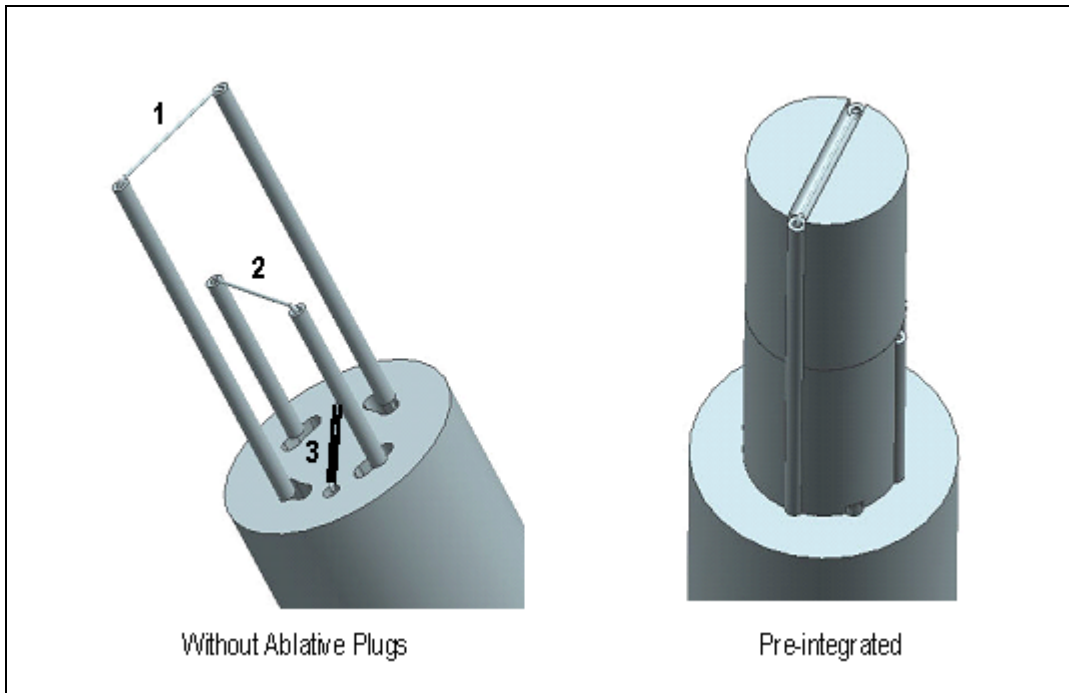


Fig. 4. Updated Design

Ablative plugs were used to complete the stack. The ceramic feed throughs were placed over the thermocouple wire and adhesive of silicone basis was used to seal all gaps (Fig. 5)

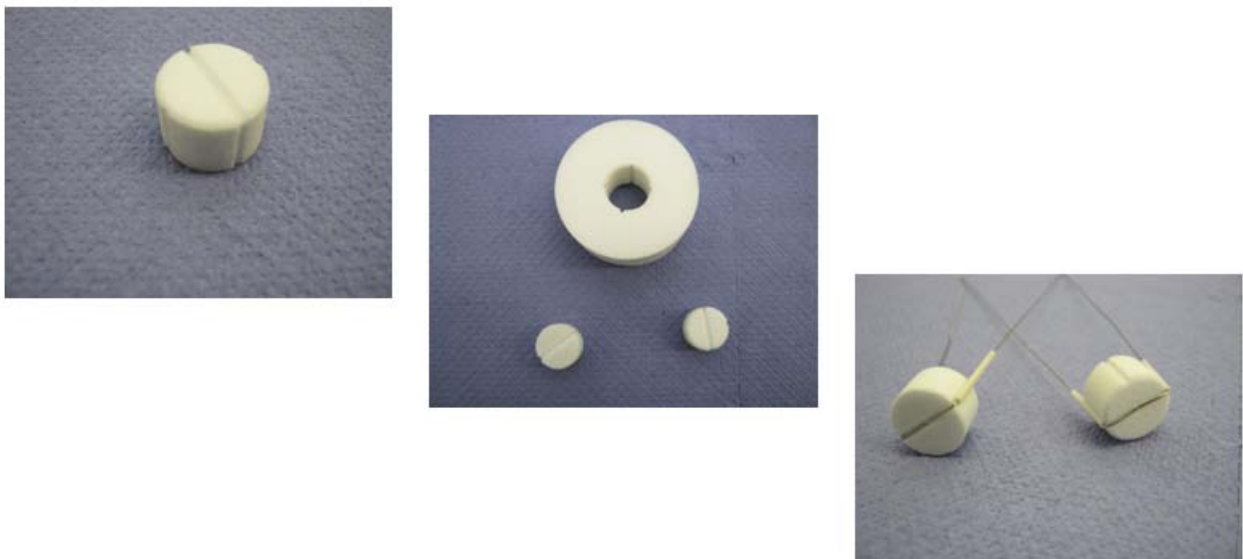


Fig. 5. Fabrication process of ablative detector

In order to quantify performance a comparative test was performed using an oven held at 1000°C and two ablative samples, the first with sheathed thermocouples placed at 5 mm depth intervals and a second using exposed measuring elements. The elements were placed in mullite tubes to avoid lateral impingement of the flames. As can be observed in Fig. 6. the redesigned sensor (right) is more sensitive to the temperature fluctuations at surface of the sample.

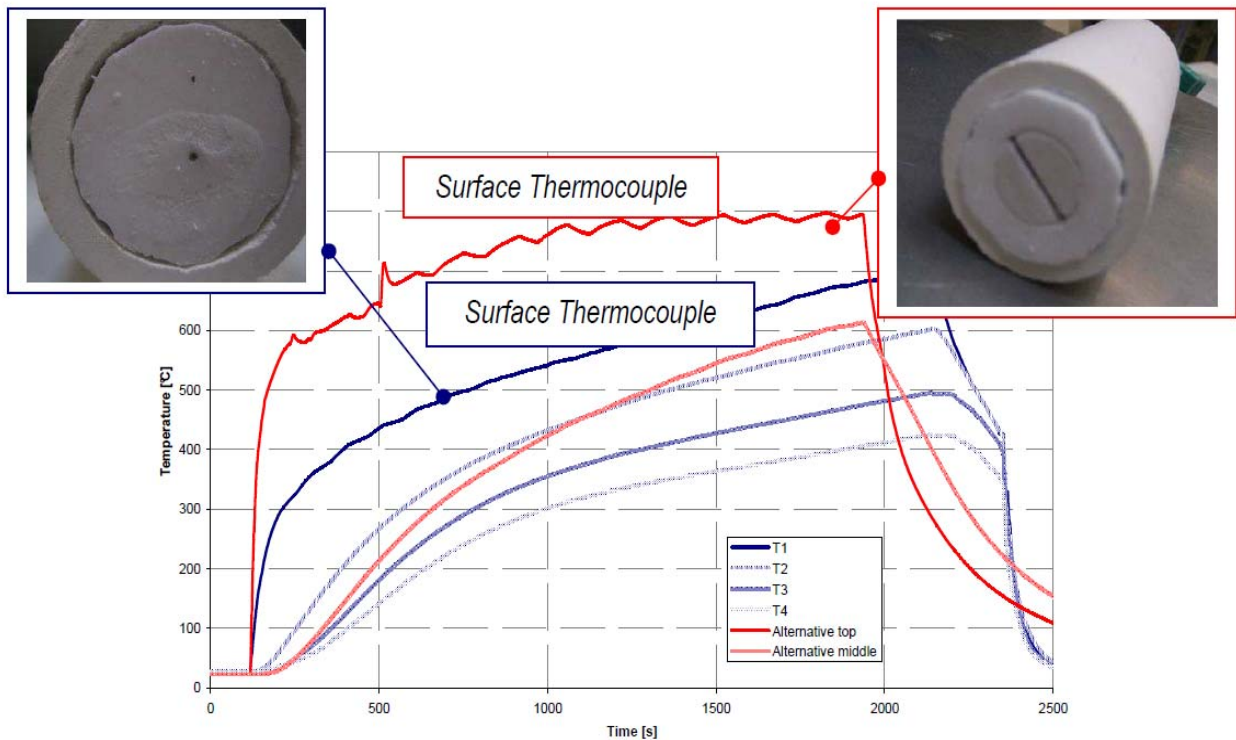


Fig. 6. Performance in hot test (left: original design, right: design of Fig. 4)

Unfortunately cutting a groove in the surface of an expanding ablative weakens it and the burn in pattern was very severe around the groove. A similar test was performed using a cork ablative. For this configuration the set-up was press fitted and no adhesive was used. Fig. 7. shows the performance of cork vs. the silicone ablative

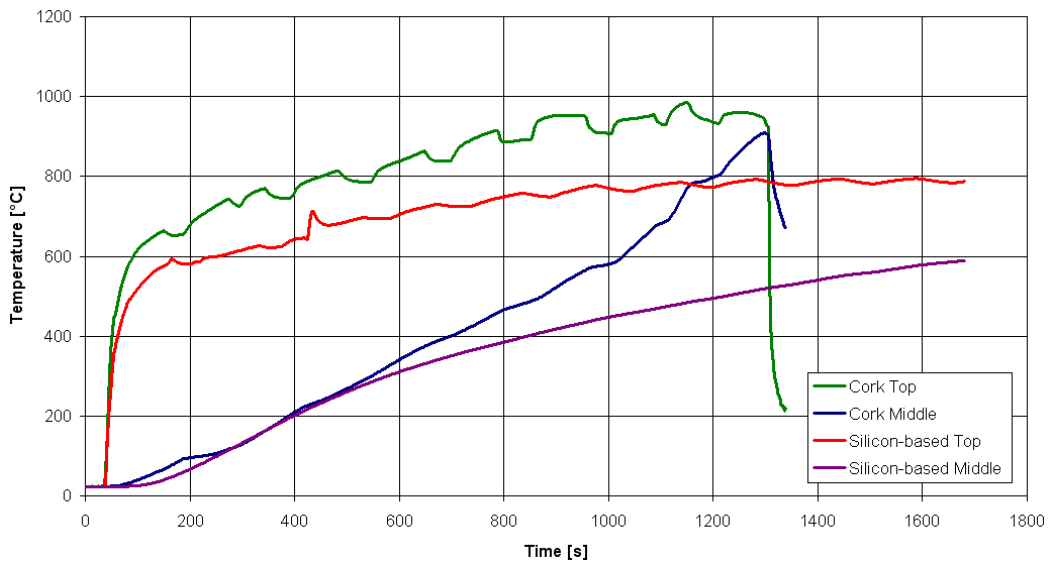


Fig. 7. Comparative performance: cork vs. silicone

Several observations can be made:

- Cork measured upper temperature exceeds that of silicone
- Surface thermocouple is sensitive to the oven control (variations in temperature in upper sensor)
- Middle temperature does not taper for the cork variant

The first observation that the measured temperature in cork is higher than silicone is explained by the fact that the cork is subject to recession, essentially leaving the upper thermocouple exposed whereas the silicone expands and chars thus covering the thermocouple. The steeper heating of the mid thermocouple was caused by lateral recession due to hot gas flow.

As it is unclear whether the surface thermocouple in Fig. 7 is measuring the air or the ablative temperature it was decided to place it below the surface. Two alternatives were considered: machining a 3 mm deep groove and covering it with a highly filled epoxy resin after laying the thermocouple or drilling lateral holes in the ablative 3 mm below the surface. In order to further minimize disruptions to the TPS the outer diameter of the plug was reduced by half.



Fig. 8. Comparative performance samples: grooved plug (left) and drilled plug (right)

In order to maximize the path through the ablative both legs of the thermocouple were spiralled and joined with a single weld point in the middle (Fig. 9). The plugs are pressed fit into the ablative precluding need for adhesives of any type.



Fig. 9. Wound Thermocouple and press fit plug

The two alternative designs were tested and their performance is shown in Fig. 10. In this case the behaviour of middle thermocouples is identical whereas the top thermocouple differs as result of combustion reaction of the adhesive at 350°C followed by charring. At 1500 seconds the grooved thermocouple showed very high recession resulting in heating of the mid thermocouple, whereas the drilled thermocouple showed a uniform recession .

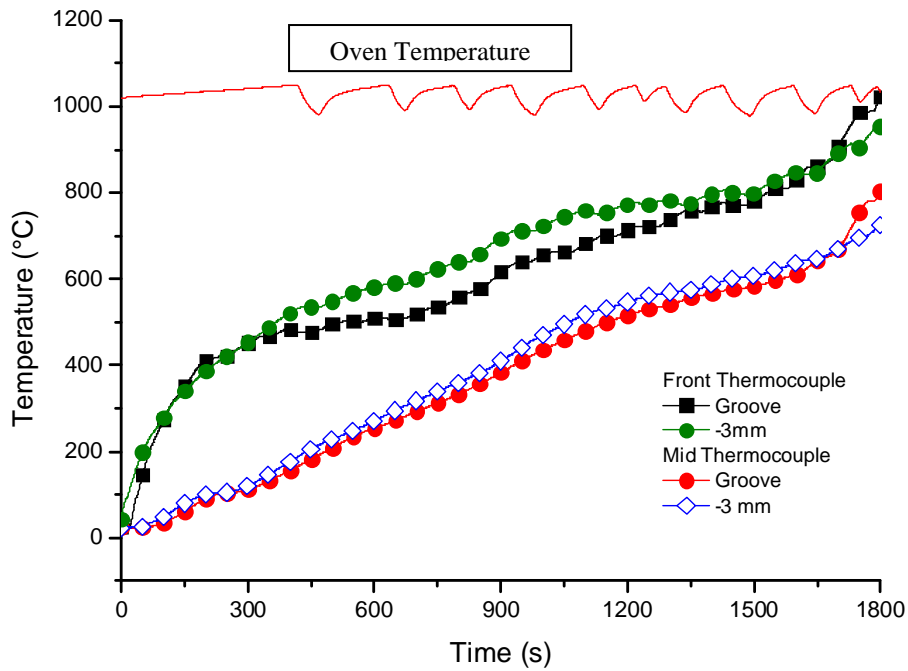


Fig. 10. Comparison between grooved and drilled thermocouples



Fig. 11. Ablation pattern of drilled thermocouple

The chosen design therefore considers the embedding of three spiraled thermocouples in a 15 mm diameter plug at different depths . As the thermocouples are not exposed to the receding front the heat flow through the ablative can be simply computed using the thermal diffusivity of the material and the exact position of the three thermocouple levels.

CONCLUSION

The design evolution of a temperature measurement system for the ablative TPS of the IXV vehicle has been reported in this paper. The final system involving tightly wound thermocouples placed at three depth levels (Fig. 12) has been tested using two kind of ablative materials: glass filled silicone TPS and cork based. The compact sensor can be manufactured in all of the geometries needed in the IXV vehicle.

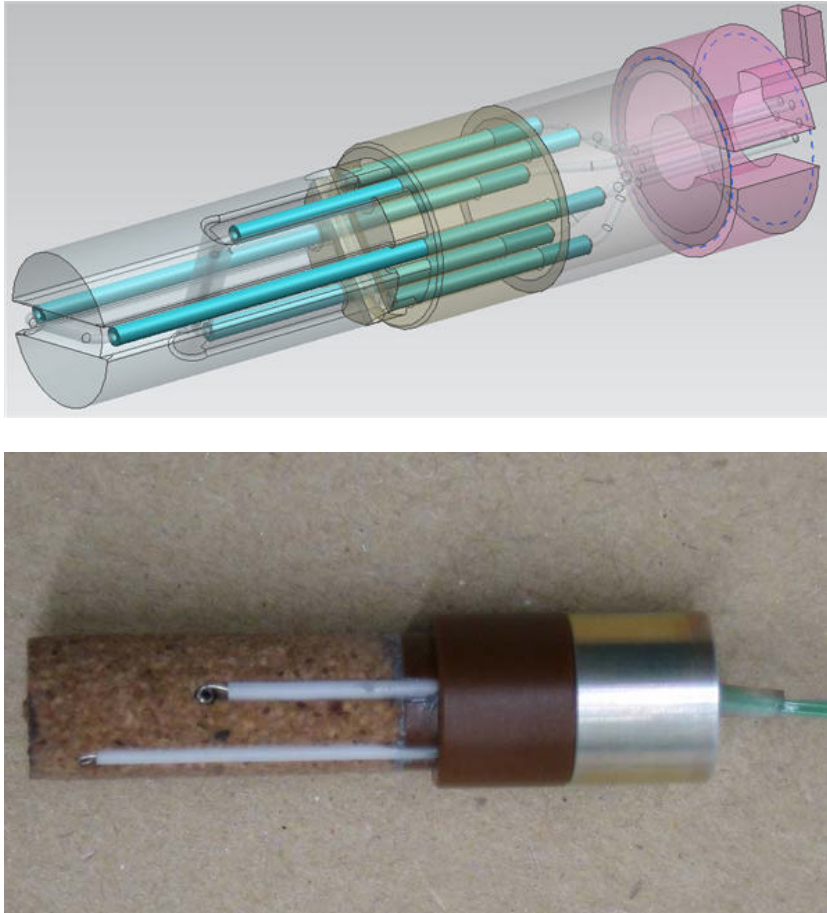


Fig. 12. Ablative sensor design

ACKNOWLEDGEMENTS

The authors wish to thank the Swiss Space Office and the European Space Agency for their support and funding, Thales Alenia Spazio for their technical guidance and both Avio SpA and Dassault Aviation for providing the materials and assisting in the design of the sensing system.

In-flight Experiment Design and Ground Testing for TPS Development

8-10 April 2013
ESA/ESTEC, Noordwijk, The Netherlands

Işıl Şakraker⁽¹⁾, Olivier Chazot⁽²⁾

⁽¹⁾PhD Candidate at von Karman Institute for Fluid Dynamics

Chaussée de Waterloo, 72, 1640

Rhode-St-Genese, Belgium

Email: isil.sakraker@vki.ac.be

⁽²⁾Professor at von Karman Institute for Fluid Dynamics

Chaussée de Waterloo, 72, 1640

Rhode-St-Genese, Belgium

Email: olivier.chazot@vki.ac.be

INTRODUCTION

The challenging physics of spacecraft's atmospheric entry require detailed investigation for reducing the conservative safety margins taken for thermal protection system design. In this study, the ground testing in VKI Plasmatron and a real flight experiment are elaborated. The mission is a small non-axisymmetric re-entry body called QARMAN (QubeSat for Aerothermodynamic Research and Measurements on AblatioN), a triple unit CubeSat with a new generation low density/high porosity carbon fiber perform ablative TPS with phenolic resin. QARMAN will fly with QB50 network and will be placed in an Earth orbit with 79 degrees inclination at altitude of 350 km. After almost 3 months lifetime, it will perform an atmospheric entry with 7.5 km/s at 120 km of altitude. The major scientific return of QARMAN project is the contribution of real flight data on an Earth re-entry trajectory by a very low cost mission compared to other similar missions and validation of the prediction and testing tools. The in-flight experiments on board of QARMAN consist of aerothermodynamic research on the ablative TPS as well as hypersonic flight dynamics and a passive aerodynamic drag control device for attitude stability and control.

GROUND TESTING AT VKI PLASMATRON

VKI Plasmatron

The Plasmatron facility is a high enthalpy wind tunnel in which plasma is generated by electromagnetic induction and blown in the form of a jet inside a test chamber at sub-atmospheric pressure (between 5 and 1 bar).¹⁷ The facility uses a high frequency, high power, high voltage (400 kHz, 1.2 MW, 2 kV) solid state (MOS technology) generator, feeding the single-turn inductor of the 160 mm diameter plasma torch.

The stagnation point temperature of the TPS samples during the test is measured by a 2-color pyrometer and Infrared (IR) broadband radiometer. Optical emission spectroscopy is used to qualitatively and quantitatively investigate the species formation effects in the free stream and in the boundary layer at the vicinity of the TPS sample. The tests are also recorded by a video camera focused at the surface of the samples. The recession of the TPS samples are monitored by high speed camera as well as inserted thermocouples at different depths inside the material.

The heat flux of the plasma is measured by a copper water cooled heat flux probe, which is injected into the plasma prior to the injection of the sample. The pressure of the test chamber is fixed to a constant value and is constantly monitored. The dynamic pressure is measured by a Pitot probe. It should be noted that the subsonic plasma jet has a very low dynamic pressure when compared to the static pressure. On the other hand during the hypersonic flight the dynamic pressure is the dominant contributor to the total pressure.

Methodology

The stagnation point heating of a vehicle flying at hypersonic velocities can be given by the following equation of Fay and Riddell[1]:

$$q_w = 0.763Pr^{-0.6}(\rho_e\mu_e)^{1/2}\left(\frac{dU_e}{ds}\right)_{edge}^{1/2}\left(\frac{\rho_w\mu_w}{\rho_e\mu_e}\right)^{0.1}(h_e - h_w) \quad (1)$$

The three independent parameters here are the density ρ , the velocity gradient dU/ds and the enthalpy h at the boundary layer edge. The density is a function of the pressure and the enthalpy therefore the three independent parameters are the pressure, enthalpy and the velocity gradient at the boundary layer edge. This is stated as the Local Heat Transfer Simulation (LHTS) by Kolesnikov [2]. If the same pressure, enthalpy and the velocity gradient at the boundary layer edge of the flight is reproduced in the ground facility, then the aerothermochemistry of the stagnation region is fully simulated. This approach is depicted in Fig. 1. The pressure is usually determined with high accuracy whereas the enthalpy and the velocity gradient are more complex and will be explained further in details in the coming sections.

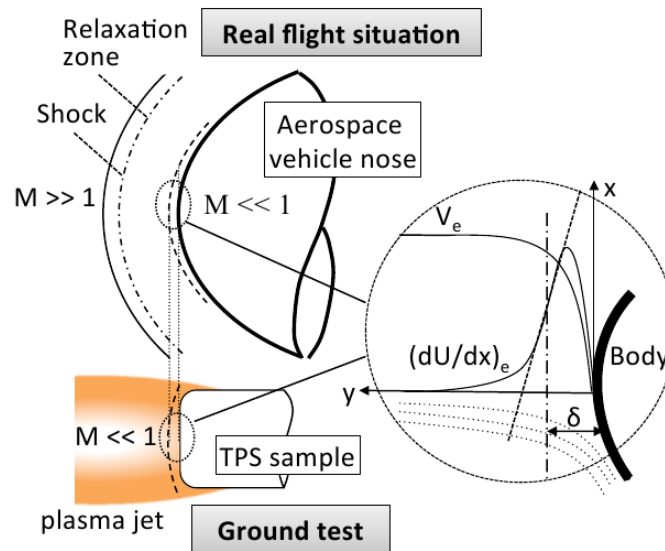


Fig. 1 : Local Heat Transfer Simulation at VKI Plasmatron.

Fig. 2 summarizes the steps of how to test a payload in a ground facility. The procedure is divided in four campaigns. The first campaign is related to establishing the testing conditions corresponding to the flight trajectory of the mission. This requires a series of tests, where the enthalpy and stagnation pressure are matched with the flight conditions, that the outputs will be the inputs of the second campaign. The second campaign is a combination of CFD simulations for flight conditions and numerical computations for ground tests. The important output of this campaign is the geometry of the test model which is equivalent to the vehicle flying at hypersonic velocities. The third campaign is a design and testing campaign where the probe with the geometry defined by the previous campaign is designed and manufactured. The probe is then tested in the plasma facility for verification and validation of the extrapolation. Once the probe concept is proven, the in-flight experiments can be tested to improve their Technology Readiness Levels (TRLs) as fourth campaign. For QARMAN, this last campaign includes the data acquisition unit testing in a full scale model as well, which is an ambitious concept for a CubeSat platform.

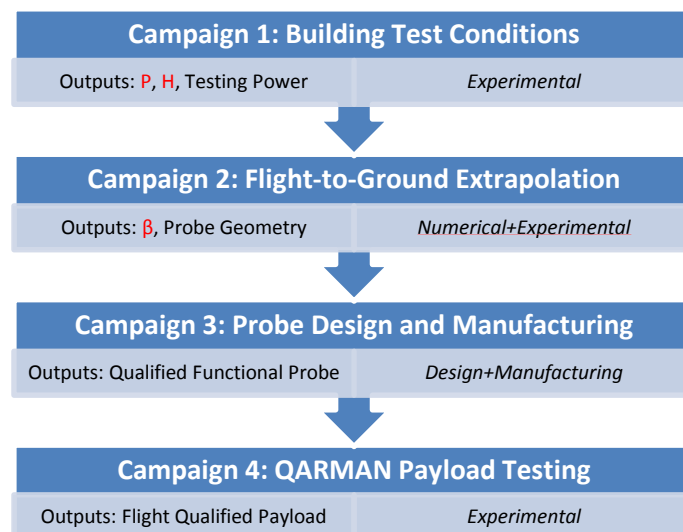


Fig. 2: Design of Payload Testing.

Duplicating Enthalpy

In Plasmatron, the free stream enthalpy is determined by rebuilding the heat flux measured by the water cooled copper calorimeter at a specific static and dynamic pressure condition. There is a considerable amount of error resulting from the lack of knowledge of the copper recombination efficiency behaviour. The overall procedure leads to an uncertainty of 20% and the aim is to reduce it down to 5%. Four independent enthalpy measurements are proposed here to reduce this high errors.

Enthalpy Probe

The enthalpy probe is in fact a calorimetric probe with a heat exchanger tube and an insulating cooling jacket. The plasma is sucked inside and its heat exchanged simply gives the enthalpy of the inlet by the following formula:

$$H_{inlet} = H_{outlet} + \frac{\dot{m}_{water}}{\dot{m}_{plasma}} C_{p,water} (T_{water,out} - T_{water,in}) \quad (2)$$

Finding the correct suction rate is very important so that the flow is not disturbed and the correct enthalpy is read. A lower suction will lead to high enthalpy reading and vice versa. The Fig. 3 shows how the flow can be disturbed at the incorrect suction rates.

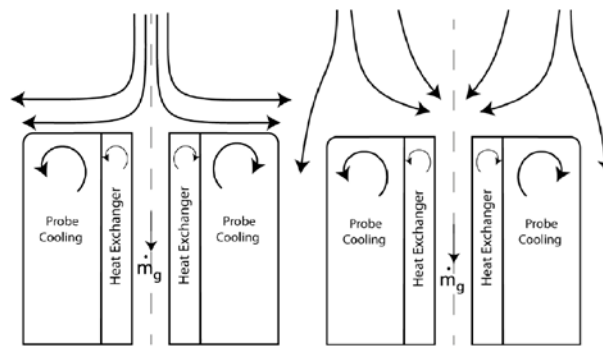


Fig. 3: Effect of plasma suction on the streamlines. Left: Low suction. Right: High suction.

The two unknowns; inlet enthalpy and plasma suction rate, are computed by an iterative approach in the post-processing which leads to a direct enthalpy measurement. The sensitivity of this measurement is expected to be 8% on enthalpy. The experimental campaign for validation is planned for the near future.

Optical Emission Spectroscopy: REDES

A real time temperature and enthalpy acquisition tool called REDES has been implemented to Plasmatron. REDES has two different modes. The first technique works with the method adopted by Fletcher [3] for generic air plasma. The method is based on the ratio of the integrated area or the peaks of N_2^+ first negative $\Delta v = 0$ and CN Violet $\Delta v = 0$. The theoretical spectrum at a given total pressure can be computed and the ratios are unique for a temperature under local thermal equilibrium conditions. The thermodynamic and transport properties for the species are extracted from the VKI in-house library Mutation and the temperature is converted to enthalpy in real time. This allows us to adjust the facility power, therefore the free stream enthalpy in real-time which come handy for rebuilding the mission's flight trajectory.

The second mode of REDES is the well known Boltzmann plot with 6 N, 4 N and 2 N spectral lines. The limitations of this method for VKI Plasmatron are still under investigation.

Damköhler Probes

Damköhler probes are basically three copper water cooled calorimeters inserted in three different probe geometries. Each of the cylindrical probes has the same corner radius but a different probe radius. Since all the three probes are made of the same material, the unknown copper catalyticity no longer poses a problem in the rebuilding. The difference of the three probes lies on the different Damköhler numbers. The Damköhler number is determining the chemical equilibrium of the flow and is given by the following expression:

$$Da = \frac{\tau_f}{\tau_c} \quad (3)$$

where the nominator is the characteristic time of the flow and the denominator is the characteristic time of the chemistry. One can conclude that low velocity gradient values promote chemical equilibrium while high velocity gradient values tend to 'freeze' the boundary layer. For given conditions, the probe radius drives the velocity gradient, then the Damköhler number in the boundary layer. Naturally, at the same free stream conditions all the probes will measure a different heat flux and if the copper catalyticity were known accurately enough, all the three measurements would lead to the same free stream enthalpy. VKI's rebuilding code is used to compute the enthalpy for a range of

catalycity values using the heat flux measurement and the radius of the probes. It should be noted that this method provides only a range of enthalpy and not an exact value however it still reduces the uncertainty on the enthalpy down to 10%.

Combined Calorimeter Method

This campaign includes three probes with the same geometry and all made of copper, but different calorimeters. The water cooled copper calorimeter measurements are combined with a copper slug calorimeter and a gardon gauge. Ideally, since they are all exposed to the same plasma flow, they should measure the same heat flux which is then converted to enthalpy. This campaign is currently being done at VKI Plasmatron for a range of pressure and powers to contribute to QARMAN experimental aerothermodynamic database.

Duplicating Velocity Gradient

The third independent parameter given in (1) is the velocity gradient at the boundary layer edge. The definition of the velocity gradient is depicted in Fig. 4; it is the derivative of the radial velocity component in the radial direction along the stagnation line at VKI Plasmatron (subsonic plasma). The challenge is to determine the boundary layer edge. For simplicity of the governing flow equations, the inflexion point of the velocity gradient is taken as the boundary layer edge in Plasmatron applications. However, the velocity gradient expression in the hypersonic flow does not look like the subsonic plasma case and it is depicted in Fig. 5. This difference is due to the difference in the modelling of the boundary layer. Therefore the correct way to match the velocity gradient is not directly equating the hypersonic case and the subsonic case in the ground facility. A new approach is proposed to correctly simulate the velocity gradient for a correct ground testing simulation.

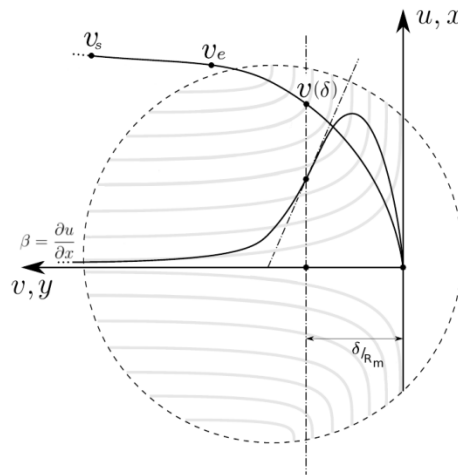


Fig. 4: Velocity profile and velocity gradient in front of the sample in subsonic plasma.

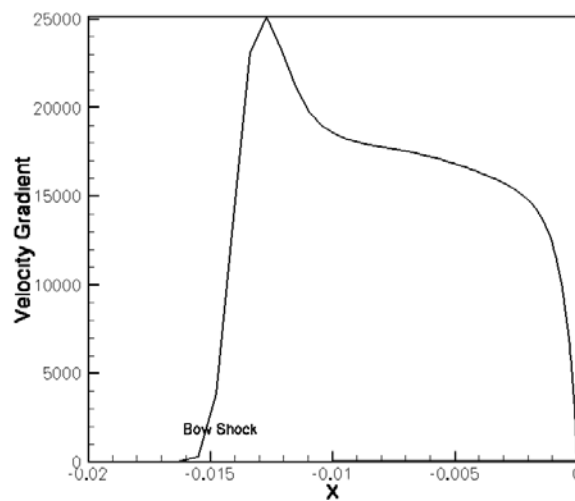


Fig. 5: Velocity gradient in hypersonic flow (CFD computation of QARMAN 50km).

The velocity gradient (a.k.a β) is a parameter that is driven by the geometry of the vehicle and the hypersonic flight conditions along the trajectory. Each point on the trajectory is defined by a different β and therefore can be simulated by a different probe in the ground facility. On the other hand, the geometry of the vehicle changes the pressure distribution

along the surface and therefore how the velocity is deviated. This is directly affecting the characteristic time of the flow as in the expression (3) of the Damköhler number. The characteristic time of the chemistry is then affected by the flow time since the chemical reactions might not find enough time to occur and the flow freezes or the flow is too slow that all the possible reaction occur and the flow reaches equilibrium. Therefore this parameter is important for duplicating the thermo-chemical environment behind the detached shock.

Here, two challenges appear separately: determining the β at the ground facility and at the hypersonic flight. As explained previously, the β in the Plasmatron is taken at the distance δ where there is the inflexion point. A bigger challenge is to determine the velocity gradient on the trajectory since no boundary layer edge is trivial as can be seen in Fig. 5. Scientists, since 50s, tried to figure out how to determine the velocity gradient in the boundary layer edge to correctly predict the stagnation point heating. The generic approach to determine the velocity gradient of axisymmetric spherical bodies is to define an “effective radius” which is a flying sphere giving the same pressure distribution in the stagnation region. However due to the unconventional geometry of QARMAN, a more detailed literature survey has been conducted. The famous study of Boison and Curtiss [4] compares experimental pressure measurements along the surface of axisymmetric blunt bodies at supersonic regime with the widely used Modified Newtonian (MNT) approach. They showed that bodies blunter than $x^*/r^* < 0.25$ the MNT no longer applies. The geometrical parameters x^* and r^* can be found in Fig. 1 of [4]. For QARMAN has $x^*/r^* = 0.101$, there is a need of determining the beta in the flight differently. More detailed reading can be found in [5][6][7][8][9].

The literature survey led to a decision that the velocity gradient for the QARMAN geometry should be extracted from CFD because it cannot be directly equated to an effective radius. An iterative approach is followed to match the equivalent subsonic hemispherical radii using the CFD computation along the trajectory and the CFD computation of the ground test. The β value is extracted from the CFD computation to give the radius at the hypersonic velocities, which can be converted to the subsonic equivalent by the similitude of the heat flux. On the other hand, the ground test with the enthalpy and the pressure of the point chosen on the trajectory is numerically simulated to define the non dimensional flow parameters which are then converted to the probe radius of a hemispherical probe. This conversion is simply given by the momentum equation assuming a finite thickness boundary layer. The two subsonic radii are then compared and a comparison success criterion of 2% is looked for.

QARMAN FLIGHT CHALLENGES

QARMAN is a standard triple unit CubeSat with two distinctive characteristics: an ablative TPS in the front unit and an aerodynamic drag augmentation device. The two mission objectives are: using aerodynamic drag to control the stability and de-orbiting for atmospheric entry; and performing an Earth atmospheric entry. The vehicle will be deployed at 350 km of altitude along with the other QB50 CubeSats.

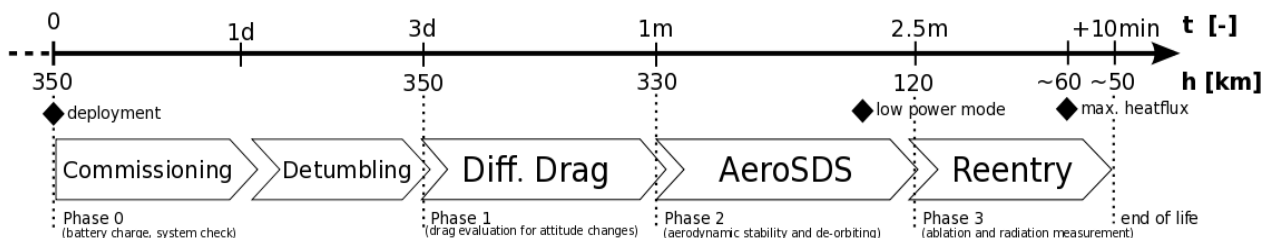


Fig. 6: QARMAN flight scenario.

The current mission operation plan of QARMAN is sketched in Fig. 6. After the deployment from the upper stage of the launch vehicle, QARMAN will automatically enter the commissioning and detumbling phase to reach a controlled flight condition (Phase 0). The AeroSDS (Aerodynamic Stability and De-Orbiting System) will be deployed in Phase 1 for aerodynamic stabilization and to speed up the orbital decay. During this period, measurements will be performed for the evaluation of the system’s performance and to get basic information on the atmospheric properties and the CubeSat trajectory. The AeroSDS will assure that QARMAN reaches 120 km of altitude with the desired entry conditions by reducing the speed down to 7.7 km/s. To guarantee fully charged batteries, the satellite will be put in a low power mode (no communication, less measurements) a short time before. During the re-entry (Phase 3), QARMAN will no longer have access to the ground station due to the telecommunications blackout because of the plasma sheet in front of the vehicle. Similar to Space Shuttle, it will send measurement results near real time via IRIDIUM transmissions to the ground. The maximal peak heating is expected to be between 2.5-2.6 MW/m² at around 61 km. At 50 km of altitude, QARMAN will start to disintegrate.

The ablative TPS will be a new generation low density /high porosity carbon fiber preform impregnated with phenolic resin. The vehicle is being designed to withstand the high aerodynamic heating down to 50 km altitude and then has to be disintegrated for safety issues.

There is a significant number of interesting physics to be experimented however the CubeSat platform has strict constraints on mass, volume, power and data link budget. Therefore specific design procedure has to be applied if one

wants to make a valuable aerothermodynamic experiment on CubeSat platform. It should be noted that the biggest advantage of such an experiment on a CubeSat platform is the reduced cost driven by standard subsystems, platforms and the lunch opportunities.

IN-FLIGHT EXPERIMENTS

Payloads

Even if a small platform is in consideration, all the experiments given in Table 1 are feasible. The total mass for all these in-flight experiments is 319 g with a safety margin of 1.2. The total power that will be consumed by all these experiments during the entire phase 3 is 0.556 W h or 3.34 W. Finally the total size of data to be transmitted is 21.57 KB with an acquisition frequency of 1 Hz for most of the payloads. How the payloads will be accommodated on board of QARMAN is shown in Fig. 7.

Table 1: Aerothermodynamic payloads on board of QARMAN.

Investigated Challenge	Parameter to measure	Sensor	Phase
TPS Efficiency	Temperature Distribution	12 x TC	3
TPS & Environment	Pressure	2 x Pressure Sensor	3
Stability	Pressure	2 x Pressure Sensor	2b
Rarified Flow Conditions	Low Pressure / Vacuum	1 x Vacuum Sensor	2a
			2b
Shear Force, Laminar to Turbulence Transition	Skin Friction	4 x Preston Tube	2b
			3
Off-Stagnation Temperature Evolution	Temperature	10 x TC	2b
			3
ATD Environment	Species	1 x Spectrometer	3
	Intensity	1 x Photodiode	3

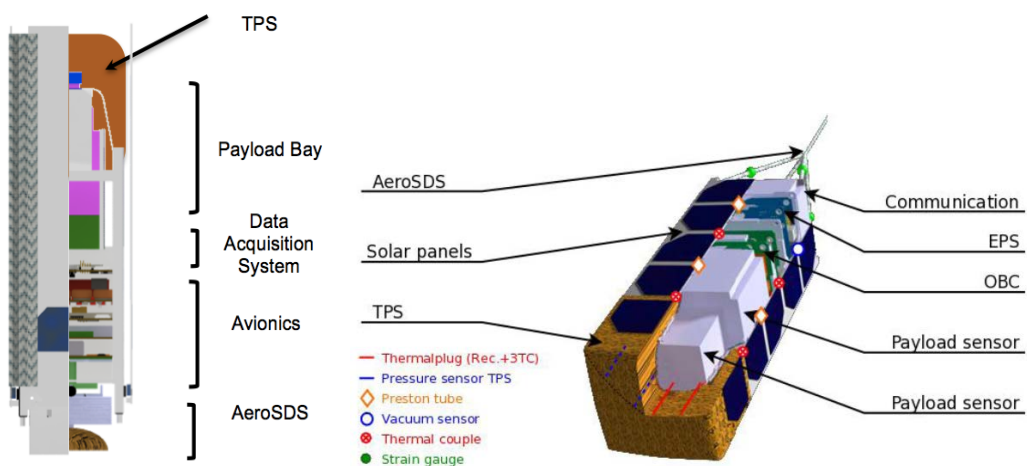


Fig. 7: Payload accommodation.

XPL01

Among the above mentioned payloads, the experimental payload XPL01 focuses on the TPS heating and recession. Two thermal plugs are planned in the diagonal direction of the TPS shown in Fig. 8 assuming zero angle of attack and symmetry. Six thermocouples type K and R will be inserted in U-shape as depicted in Fig. 9. The depths of the thermocouples are based on a qualitative analysis shown in Fig. 10 and will be at 2.5, 5, 10, 20, 30 and 40 mm. The data acquisition unit including the cold junction compensation is positioned at the back of TPS as shown in Fig. 7.

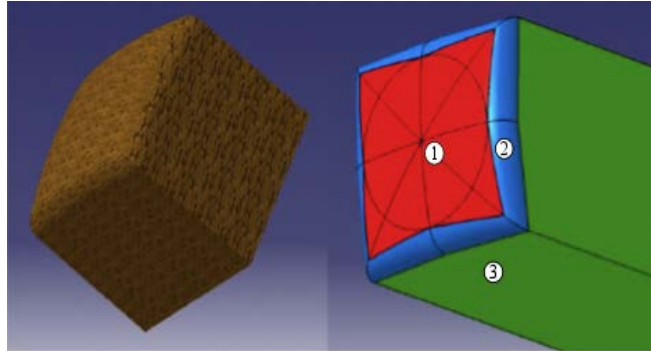


Fig. 8: QARMAN TPS [10].

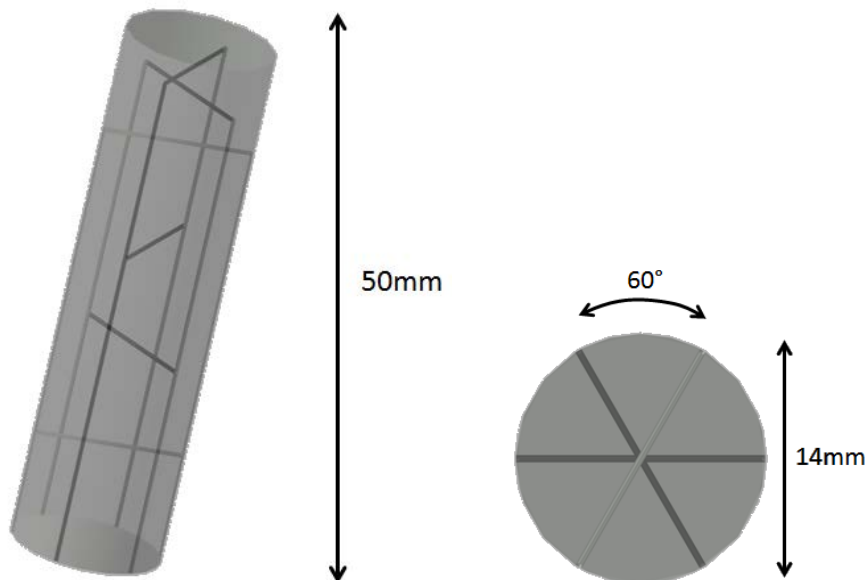


Fig. 9: Thermal plug design.

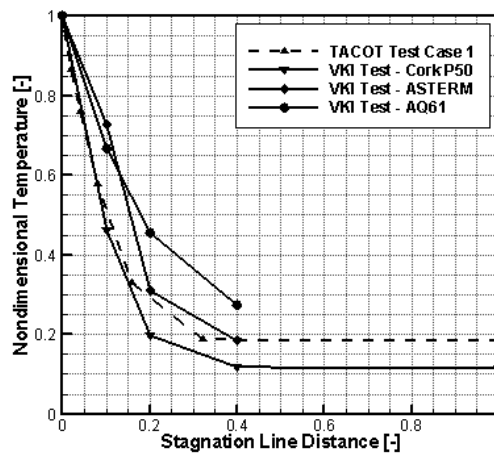


Fig. 10: Temperature evolution inside the TPS at an arbitrary time.

CONCLUSION

The challenging and complex physics of atmospheric entry are analyzed by numerical simulations and ground tests. These two important tools have to be validated by real flight tests which provide the most valuable information on the space transport technologies. However the real flight tests are also designed using ground tests and numerical simulations and flying a representative experimental vehicle comes with a very high cost. The aim of QARMAN is to provide an affordable platform, even if with strict mass, volume, power and data constraints, to make a real flight test on a representative trajectory and validate the ground test and numerical simulations. A flight-to-ground extrapolation methodology in terms of the velocity gradient is proposed for VKI Plasmatron facility to show how such rectangular blunt body can be correctly and accurately tested in a ground facility. Methods to make accurate free stream characterization in terms of enthalpy and pressure have been explained. The aerothermodynamic in-flight experiments of QARMAN have been presented and the thermal plugs for TPS heating and recession are detailed.

ACKNOWLEDGEMENTS

QARMAN project is partially supported by the European Community Framework Programme 7, Grant Agreement no. 284427 in the framework of QB50 Project.

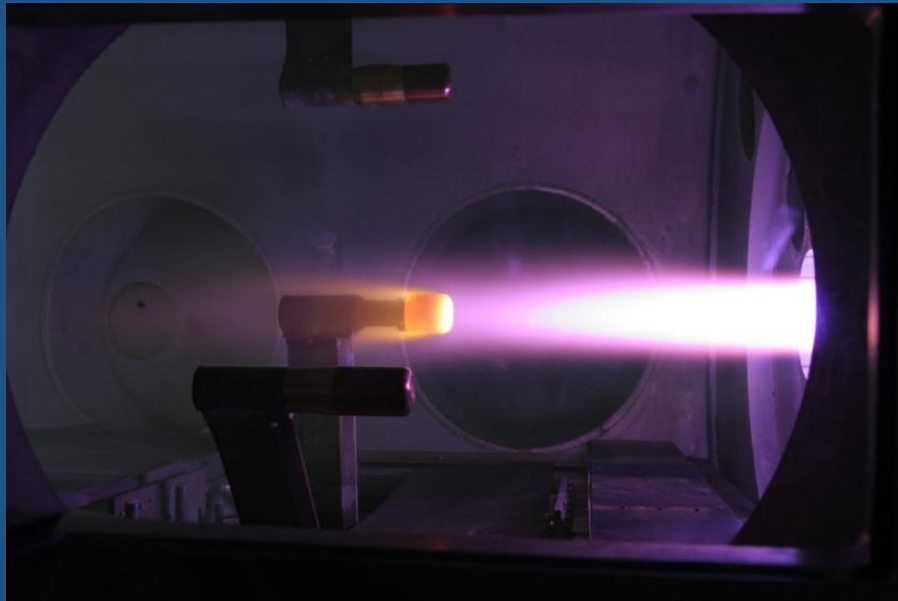
The authors are thankful to Dr. Cem O. Asma, Hyun Woo Krassilchikoff, Thorsten Scholz, Pablo Solano Lopez and Pascal Collin.

REFERENCES

- [1] J. A. Fay, F. R. Riddell, «Theory of stagnation point heat transfer in dissociated air,» chez *An Introduction to Hypersonic Aerodynamics*, VKI, 1958.
- [2] A. Kolesnikov, « Extrapolation from high enthalpy tests to flight based on the concept of local heat transfer simulation,» chez *RTO AVT Course on "Measurement Techniques for High Enthalpy and Plasma Flows"*, Rhode Saint Genese, Belgium, 1999.
- [3] D. G. Fletcher, «Nonintrusive diagnostic strategies for arcjet stream characterization,» chez *RTO AVT Course on Measurement Techniques for High Enthalpy and Plasma Flows*, Rhode Saint Genese, Belgium, 1999.
- [4] J. Boison, A. Curtiss, «An experimental investigation of blunt body stagnation point velocity gradient,» *ARS Journal*, pp. 130-135, 1959.
- [5] L. Lees, *Recent developments in hypersonics*, San Francisco, California: ARS Semi-Annual Meeting, 1957.
- [6] E. V. Zoby, E. M. Sullivan, «Effects of the corner radius on stagnation-point velocity gradients on blunt axisymmetric bodies,» Tech. Rep. NASA-TM-X-1067, 1965.
- [7] J. C. Ellison, «Experimental stagnation point velocity gradients and heat transfer coefficients for a family of blunt bodies at mach 8 and angles of attack,» Tech. Rep. TN D-5121, NASA Langley, 1969.
- [8] E. V. Zoby, «Empirical stagnation point heat transfer relation in several gas mixtures at high enthalpy levels,» Tech. Rep. TND-4799, NASA Langley, 1968.
- [9] H. Olivier, «Influence of the velocity gradient on the stagnation point heating in hypersonic flow,» *Shock Waves*, vol. 5, pp. 205-216, 1995.
- [10] G. Bailet, *Feasibility analysis and conceptual design of an atmospheric re-entry cubesat demonstrator*, von KArman Institute for Fluid Dynamics, Rhode Saint Genese: VKI PR2011-02, 2011.



In-flight Experiment Design and Ground Testing for TPS Development



Işıl Şakraker, Olivier Chazot

7th European Workshop on TPS & HS, 10 April 2013

Noordwijk, Netherlands



von Karman Institute



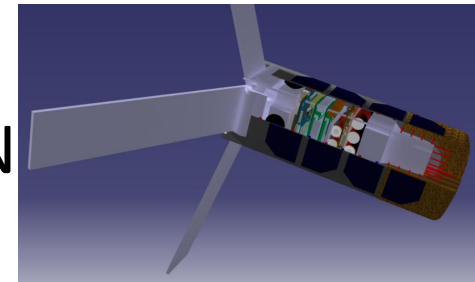
Université
de Liège

Objectives

Safe Manned/Unmanned Space Flights

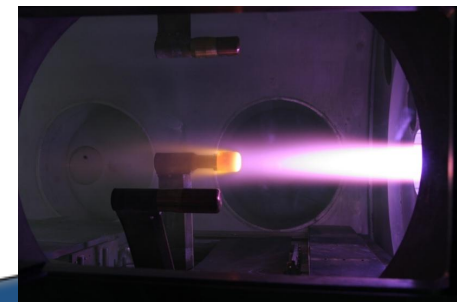
Real Flight Test Design

QARMAN



Accurate Ground Testing Methodology

VKI Plasmatron





QARMAN: Real Flight Testbed

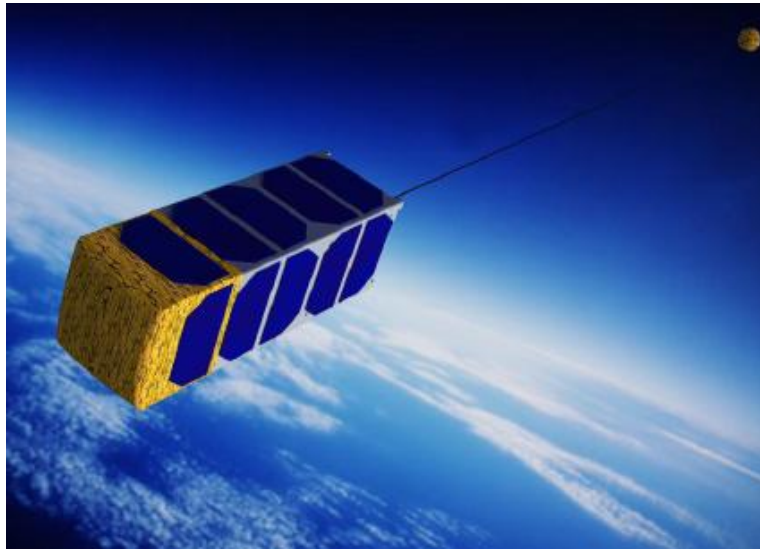
- Objectives
- **QARMAN**
- How to?
- Payload Design

QubeSat for Aerothermodynamic Research and Measurements on Ablation N

Platform: Triple CubeSat with Ablative TPS: 10x10x30 cm

Mission: Atmospheric Entry Demonstrator, Starting Altitude of 350 km

To be launched in 2015 with QB50 Network



Why a Re-Entry “CubeSat”?

→ Standardized small platform eliminates the only drawback: High Costs

→ Standard launch adaptors leading to highly flexible launch opportunities

→ If successful, it will be an affordable test platform for ablators, ceramics, sensors, trajectories, in-flight demonstrations, de-orbiting systems etc.



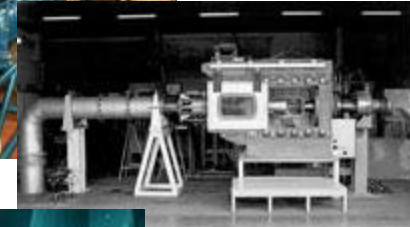


Ground Testing

Numerical Simulations

- Introduction
- Objectives
- QARMAN
- **How to:**
 - **design?**
 - simulate?
 - make sure?
- Payload Design

- Shock Tubes/Tunnels
- Expansion Tubes/Tunnels
- Blowdown Wind Tunnels
- Arcjets
- ICPs, etc..



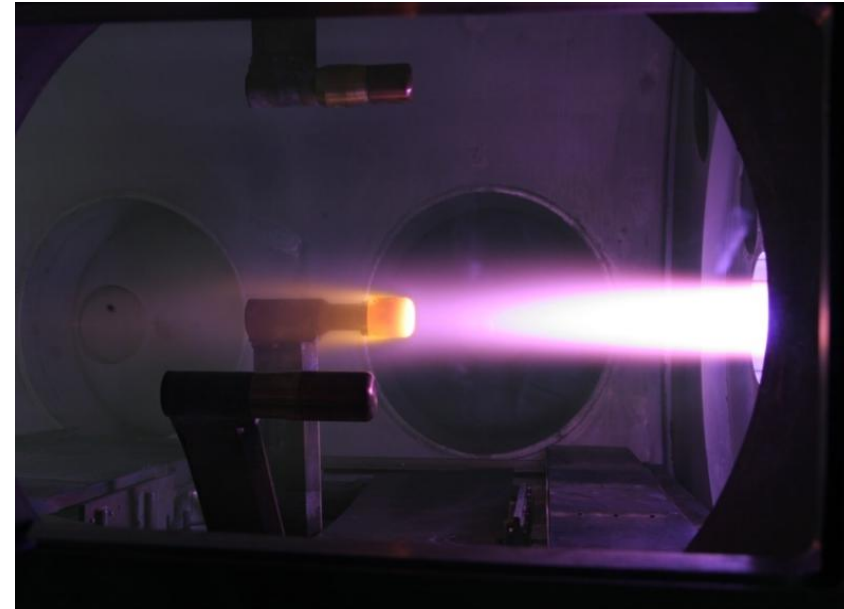
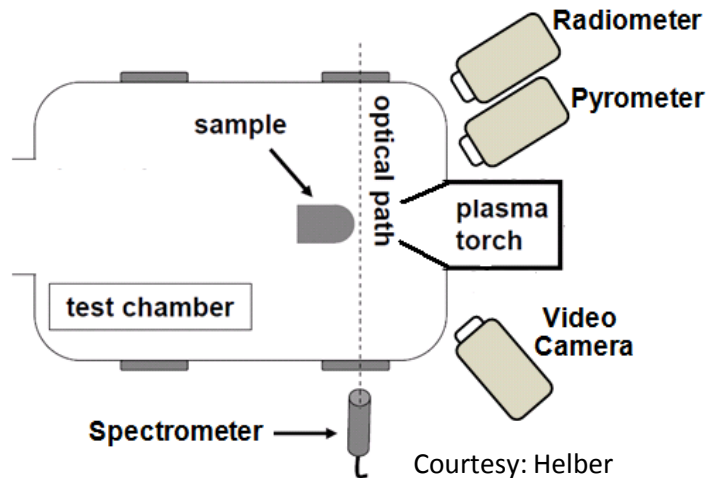
Focus: VKI Plasmatron : 1.2 MW, Inductively Coupled Plasma Generator





VKI Plasmatron

Measurement Techniques



Ablation Measurements

- **Pyrometer** : Temperature
- **Radiometer** : Temperature as $f(\epsilon)$
- **Spectrometer** : Species Detection
- **High Speed Camera**
- **Infrared Camera**
- **Thermocouples**

Free Stream Measurements

- **Cold Wall Heat Flux**
- **Static&Total Pressure**
- **Spectrometer**

- Introduction
- Objectives
- QARMAN
- **How to:**
 - **design?**
 - simulate?
 - make sure?
- Payload Design





Local Heat Transfer Simulation (LHTS)

Kolesnikov, 1993

- Introduction
- Objectives
- QARMAN
- **How to:**
 - design?
 - **simulate?**
 - make sure?
- Payload Design

$$q_w = 0.763 \text{Pr}^{-0.6} (\underline{\rho_e \mu_e})^{1/2} \left(\frac{dU_e}{ds} \right)_{edge}^{1/2} \left(\frac{\rho_w \mu_w}{\underline{\rho_e \mu_e}} \right)^{0.1} (\underline{h_e - h_w})$$

Thermo-chemical equilibrium at stagnation point:

Enthalpy:

$$H_e^f = H_e^t$$

Pressure:

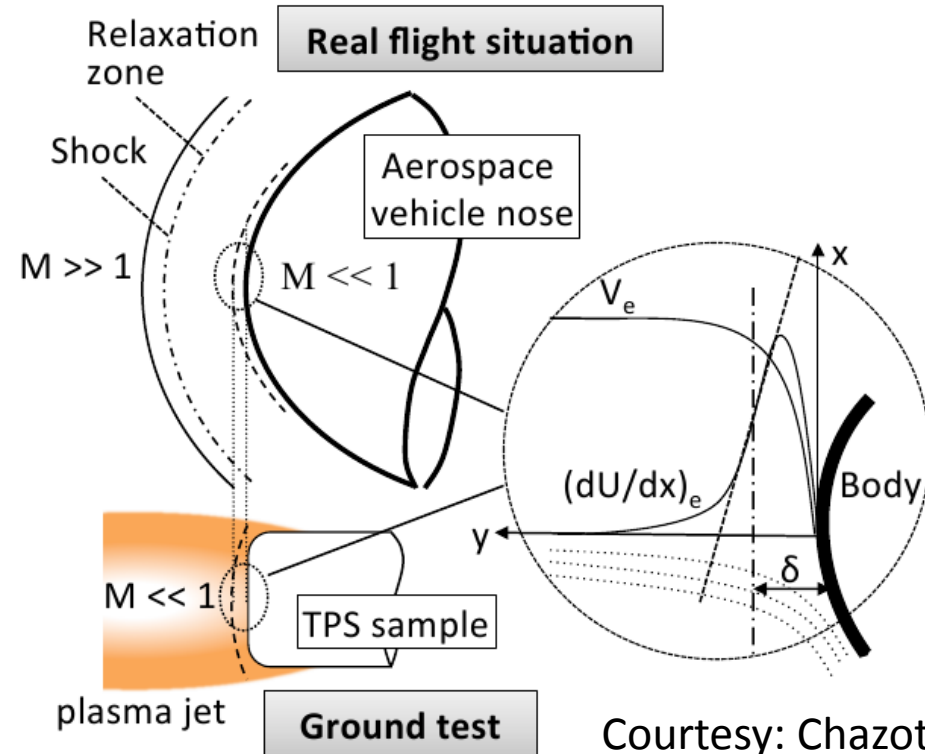
$$P_e^f = P_e^t$$

Velocity Gradient:

$$\beta_e^f = \beta_e^t$$

→ Subsonic plasma

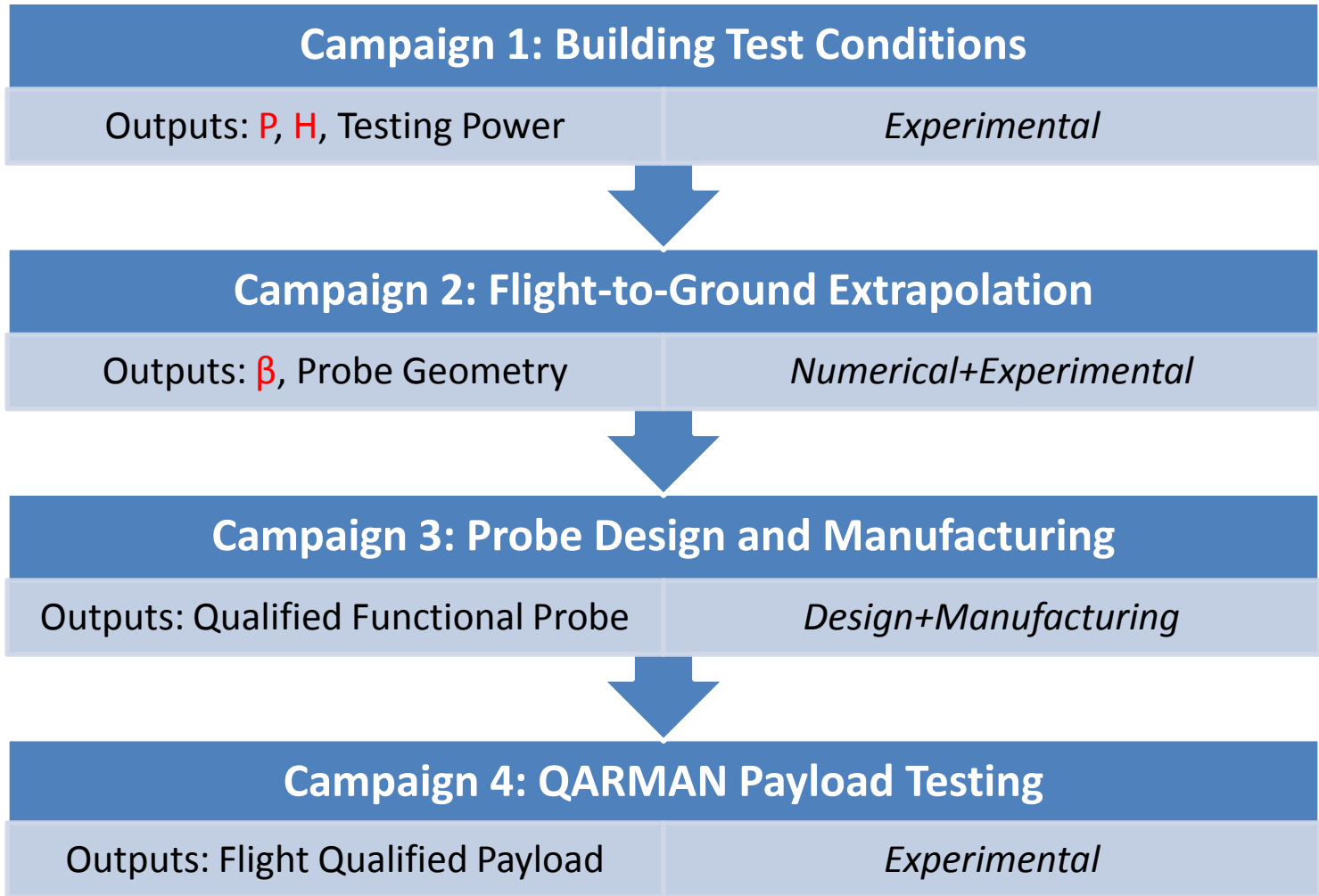
Full simulation of stagnation region



Ground Testing Methodology



- Introduction
- Objectives
- QARMAN
- **How to:**
 - design?
 - simulate?
 - make sure?
- Payload Design

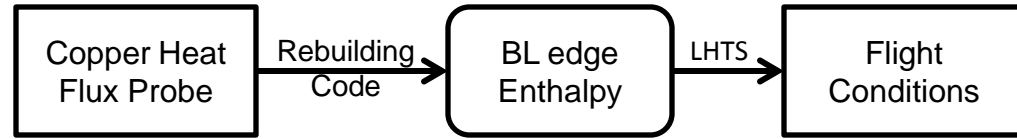




Duplicating Enthalpy

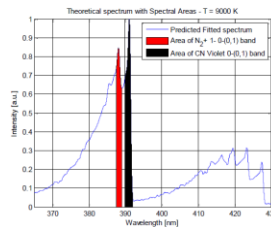
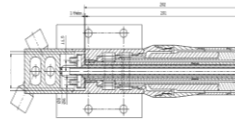
- Introduction
- Objectives
- QARMAN
- **How to:**
 - design?
 - simulate?
 - **make sure?**
 - h
 - β
- Payload Design

Current Method:

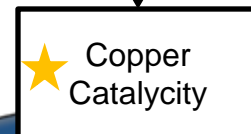


Y Unknown Copper Catalycity

Proposed Methods:



- + Damköhler Probes
- + Combined Heat Flux Probes



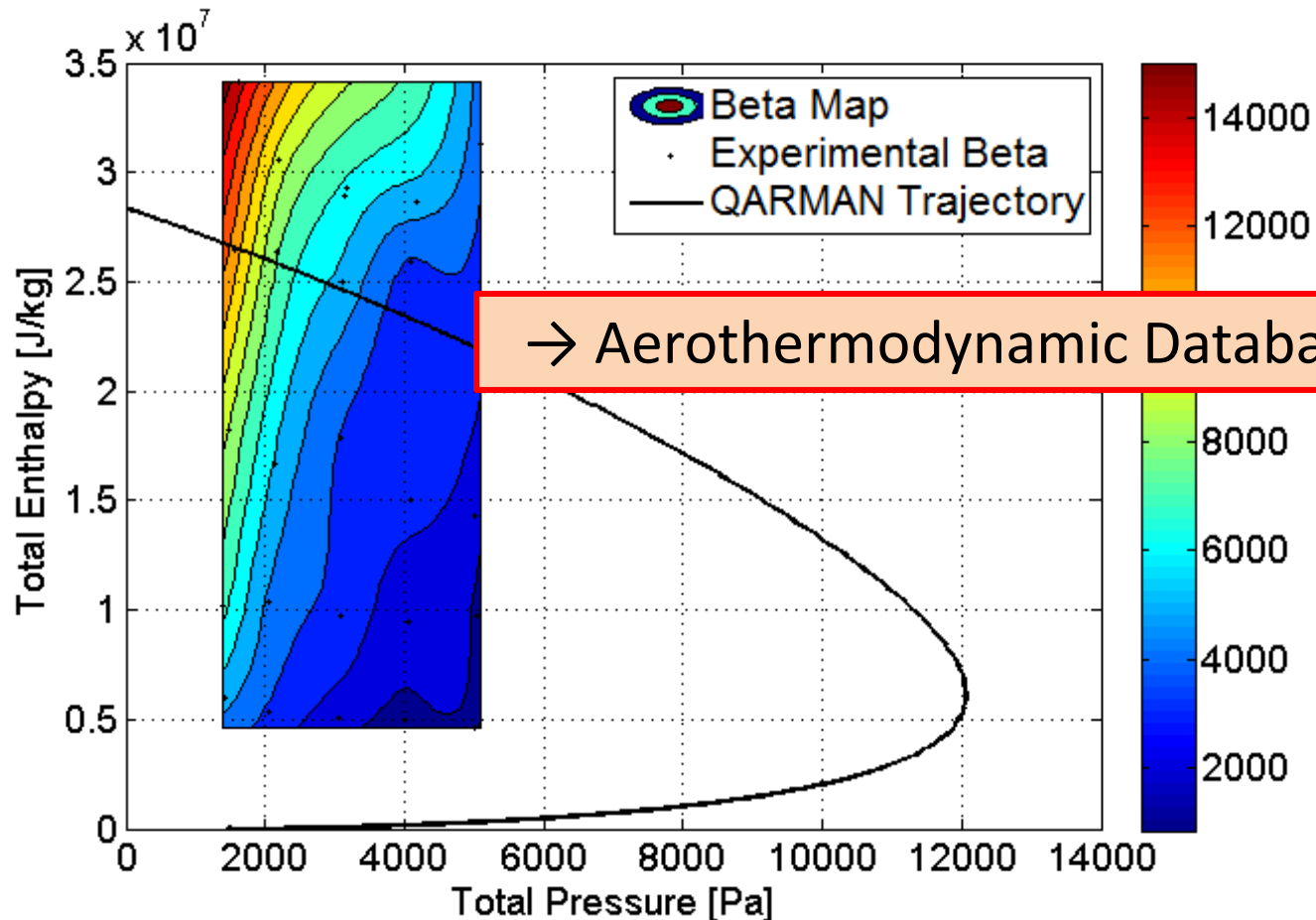


Velocity Gradient: β

- Introduction
- Objectives
- QARMAN
- **How to:**
 - design?
 - simulate?
 - **make sure?**
 - h
 - β
- Payload Design

Test Probe Geometry Unique to Mission

- Vehicle Geometry
- Trajectory





Defining Velocity Gradient: β

- Introduction
- Objectives
- QARMAN
- **How to:**
 - design?
 - simulate?
 - **make sure?**
 - h
 - β
- Payload Design

Conventional Method: Effective Radius

$$\beta^{flight} = \frac{1}{R_{eff}} \sqrt{\frac{8(p_e - p_\infty)}{3\rho_e}} \quad \text{Modified Newtonian Theory}$$

Spherical Bodies ✓

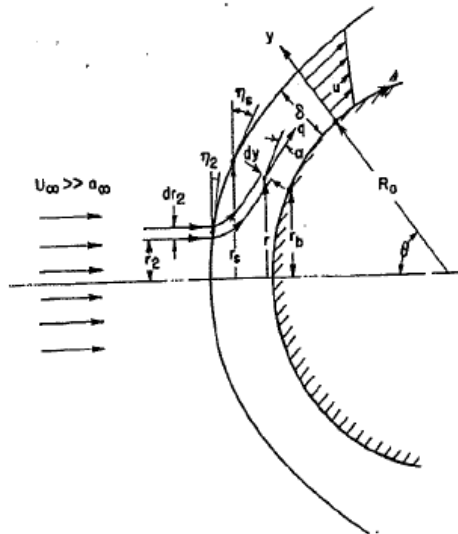


Fig. 1 Flow in the shock layer around a spherical nose
Ref: Lees1957

Blunt Bodies... ✗

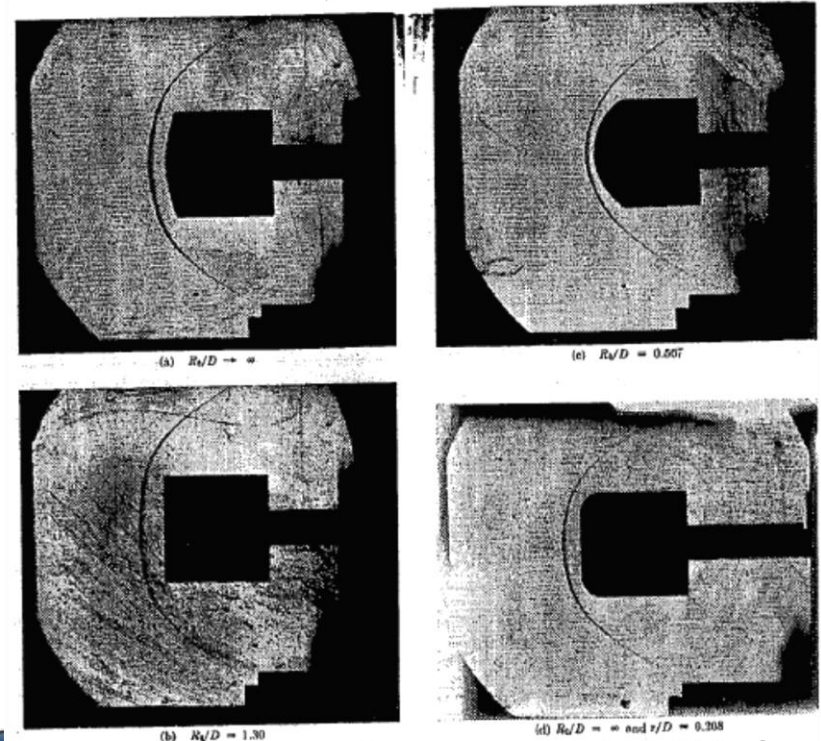


Fig. 3 Schlieren photographs of flow over a blunt-nosed body of revolution at $M_\infty = 5.8$ and $\alpha = 0$

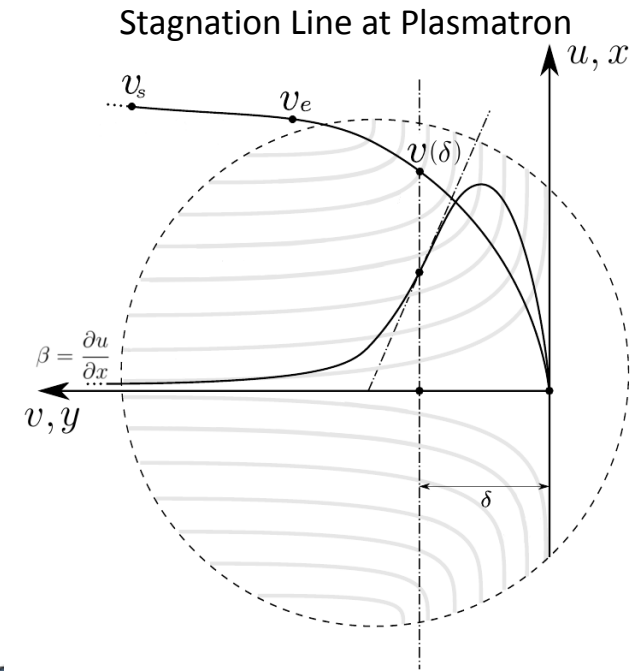
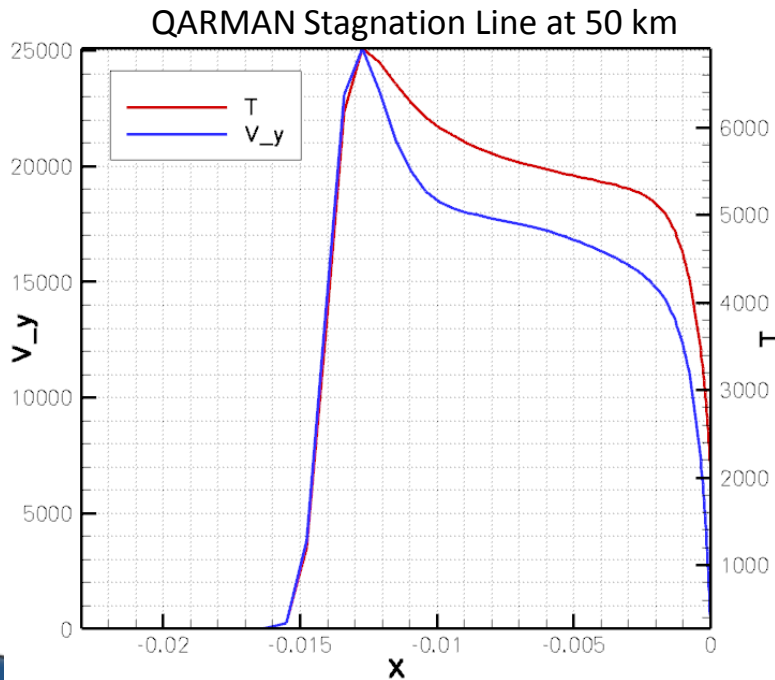
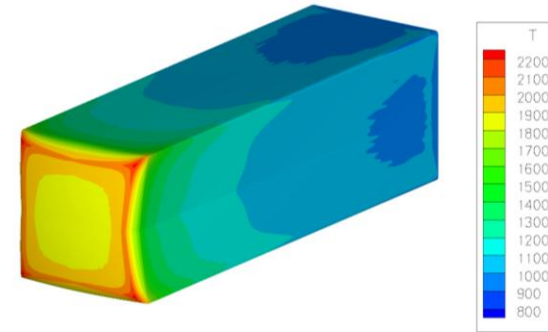
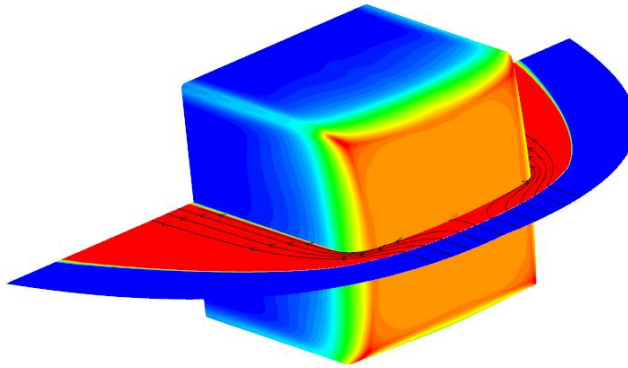




Flight to Ground Extrapolation

Combining: Experiments, CFD^{flight} and CFD^{ground}

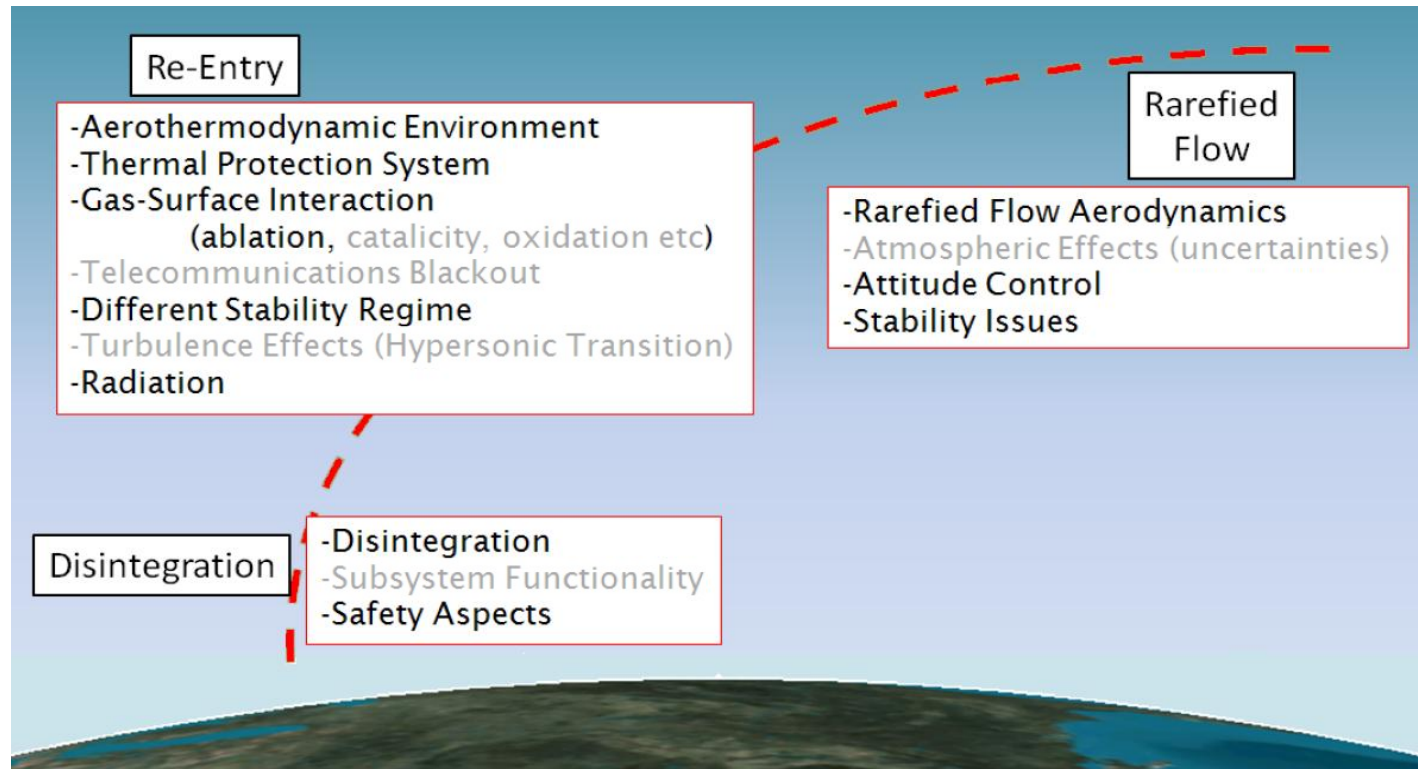
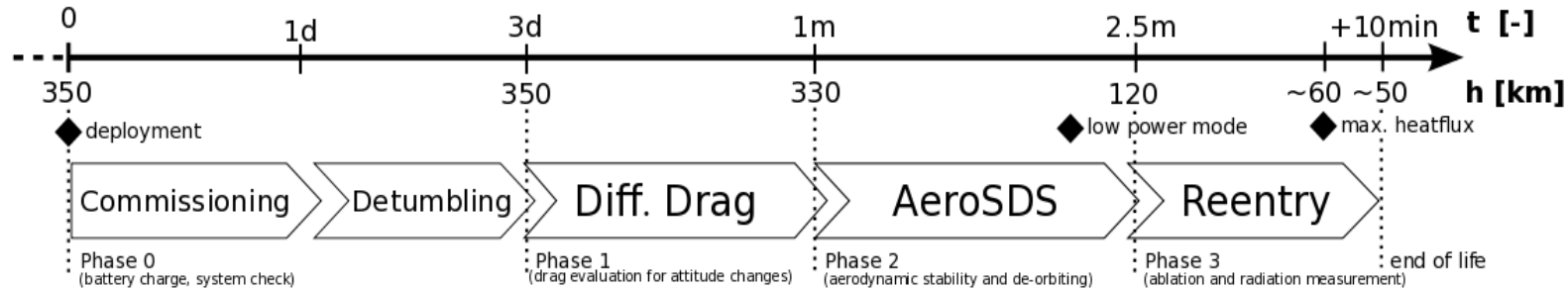
- Introduction
- Objectives
- QARMAN
- **How to:**
 - design?
 - simulate?
 - **make sure?**
 - h
 - β
- Payload Design





QARMAN Flight Challenges

- Introduction
- Objectives
- QARMAN
- How to?
- **Payload Design**
- **Scenario**
- Methodology
- Payloads





In-Flight Experiment Design

- Introduction
- Objectives
- QARMAN
- How to?
- **Payload Design**
 - Scenario
 - **Methodology**
 - Payloads

Payload Design Methodology

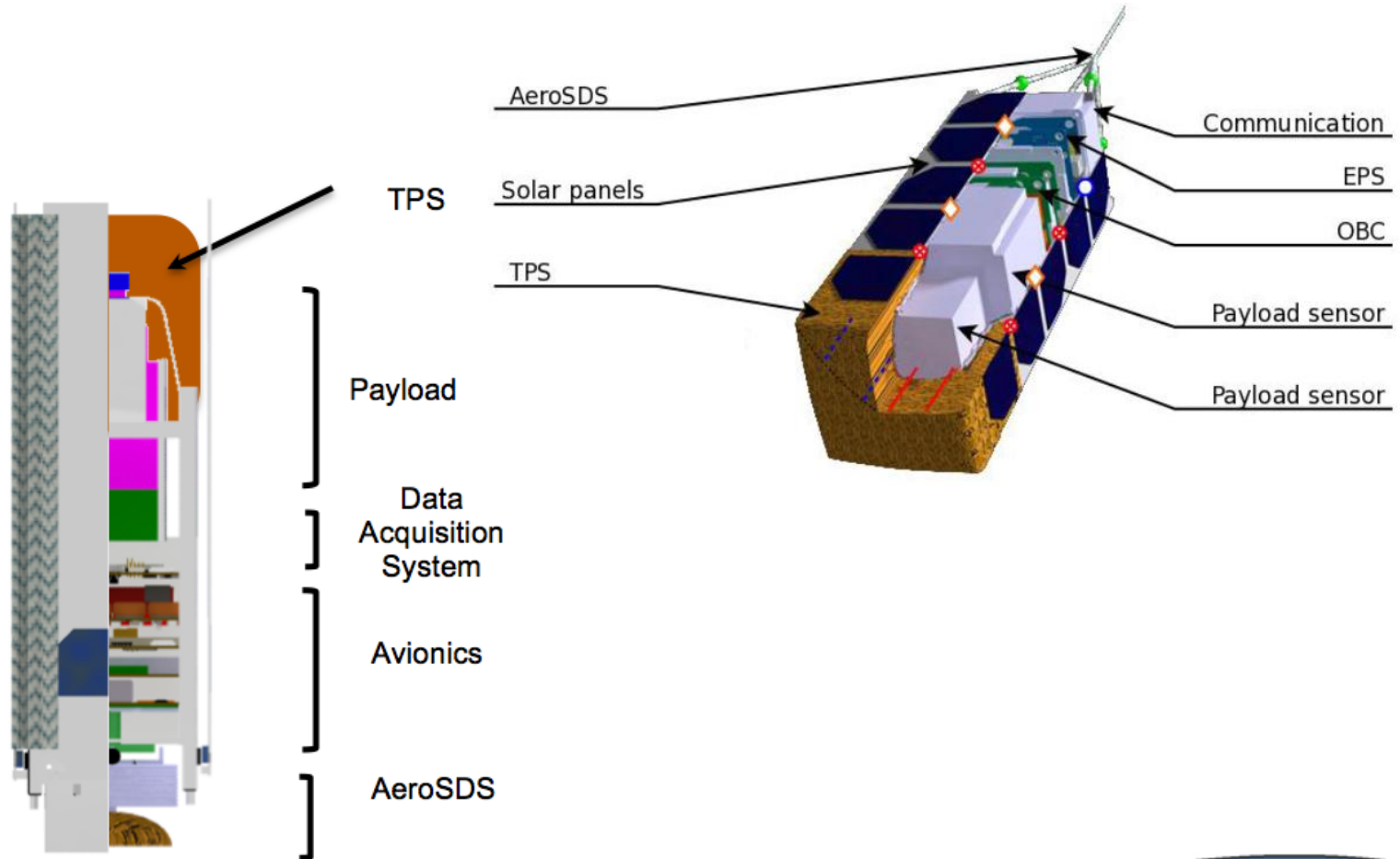
- Stating the Problem and Defining the Payload Objectives
- Subject Trades: Measurement Parameters/Magnitudes
- Preliminary Investigation: CFD, Experiments and Determining the 'Performance Thresholds'.
- Measurement Techniques: Mass, Volume, Power Consumption, Accuracy, Data Size, TRL, Cost and Feasibility in a CubeSat platform
- Preliminary Configuration and Operations Concept
- **Ground Testing Methodology and Extrapolation to Flight**
- Risk Analysis
- Success Criteria: Considering the previously defined 'performance thresholds'
- Document and Iterate





Payload Accomodation

- Introduction
- Objectives
- QARMAN
- How to?
- **Payload Design**
 - Scenario
 - Methodology
 - **Payloads**





Aerothermodynamic Payloads

Phase 3 Budgets

Total Mass: **319 g**

Total Energy Consumption: **0.556 W h**

Total Data Size: **21.57 KB**

- Introduction

- Objectives

- QARMAN

- How to?

- **Payload Design**

- Scenario

- Methodology

- **Payloads**

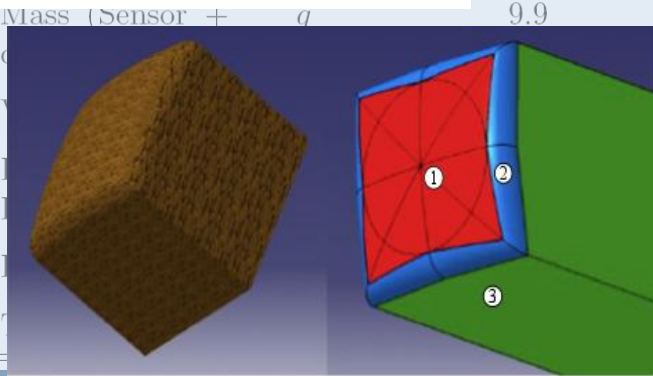
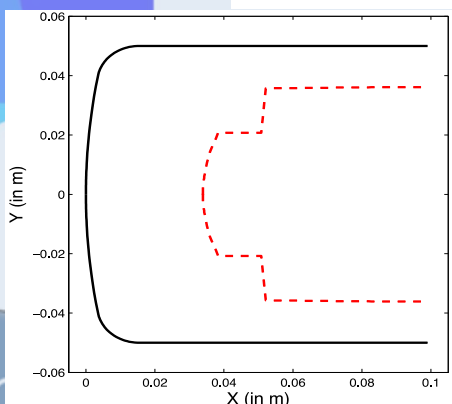
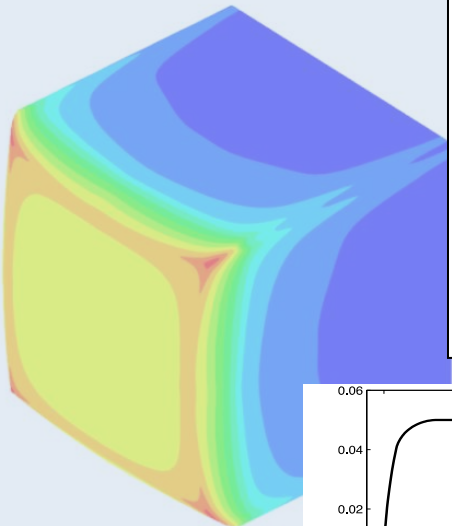
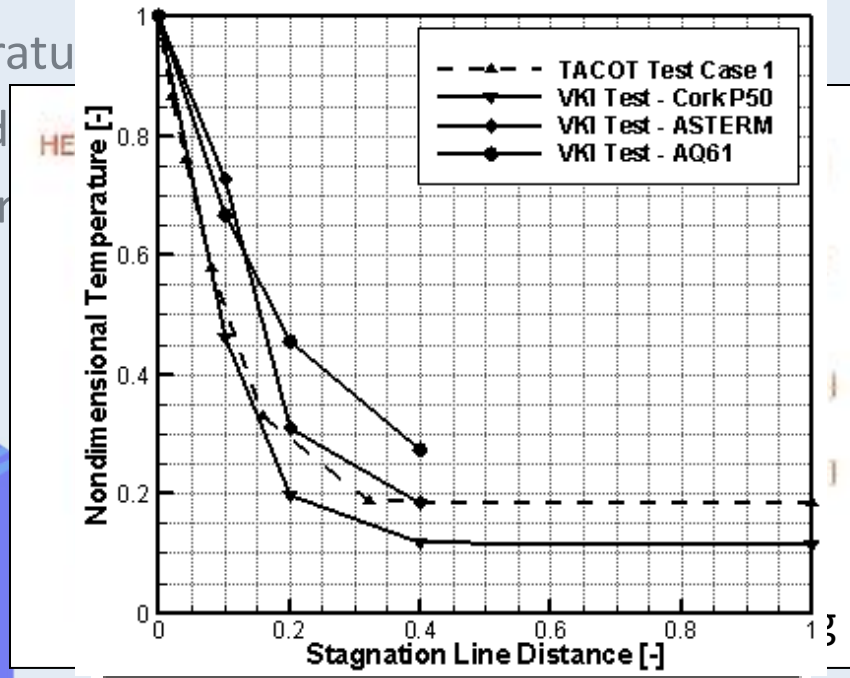
Investigated Challenge	Parameter to measure	Sensor	Phase
TPS Efficiency	Temperature Distribution	12 x TC	3
TPS & Environment	Pressure	2 x Pressure Sensor	3
Stability	Pressure	2 x Pressure Sensor	2b
Rarified Flow Conditions	Low Pressure / Vacuum	1 x Vacuum Sensor	2a
			2b
Shear Force, Laminar to Turbulence Transition	Skin Friction	4 x Preston Tube	2b
			3
Off-Stagnation Temperature Evolution	Temperature	10 x TC	2b
			3
ATD Environment	Species	1 x Spectrometer	3
	Intensity	1 x Photodiode	3
With safety margin 1.2			



Payloads

XPL01 – TPS Efficiency & Heating

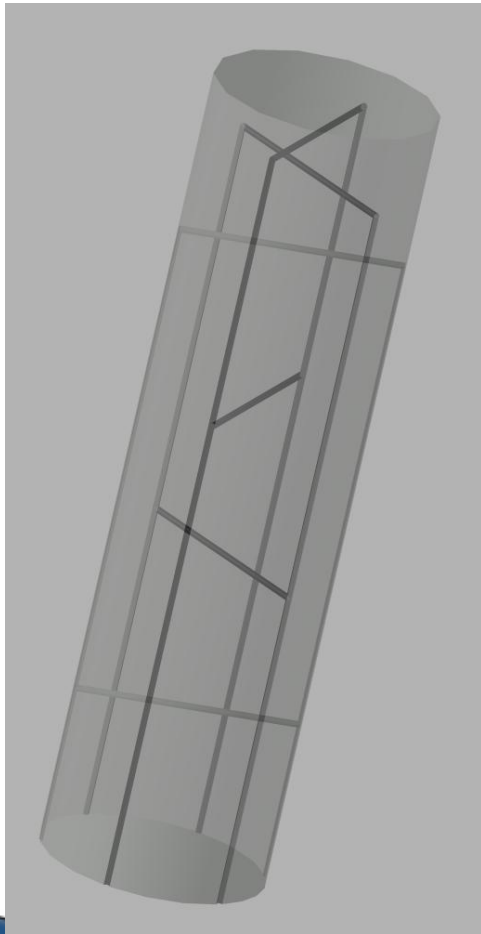
Subject Trades: Temperature
 Performance Threshold
 Meas. Techniques: Thermocouples



Desired	Acceptable
1700	273 – 1523
$(T) + 273.15$	$(0.0075 \times T) + 273.15$
60	1/240
1	0.5
1.1	0.5
9.9	16.8
Mass (Sensor + ...)	0.353
	11
	2.08
	4

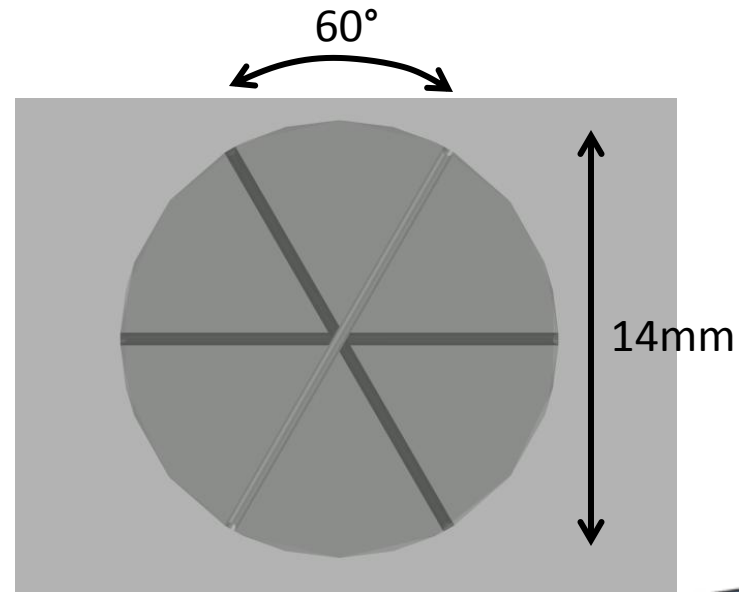
Payloads

XPL01 - Thermal Plugs



50mm

- 6 Thermocouples at 2.5, 5, 10, 20, 30, 40 mm
- At 60° apart
- 2 thermocouple per side trail
- TC Type K or R inserted in U-shape





Conclusion

- Introduction
- Objectives
- QARMAN
- How to?
- Payload Design

- Ground Testing
 - Building Test Conditions
 - Performing Accurate Tests
 - Flight to Ground Extrapolation
- Payload Design
 - CubeSat Platform Challenges
 - Aerothermodynamic Experiments
 - TPS Heating & Efficiency Payload XPL01

Acknowledgements: Cem O. Asma, Hyun Woo Krassilchikoff, Thorsten Scholz, Pablo Solano Lopez, Pascal Collin, QB50 FP7 284427.

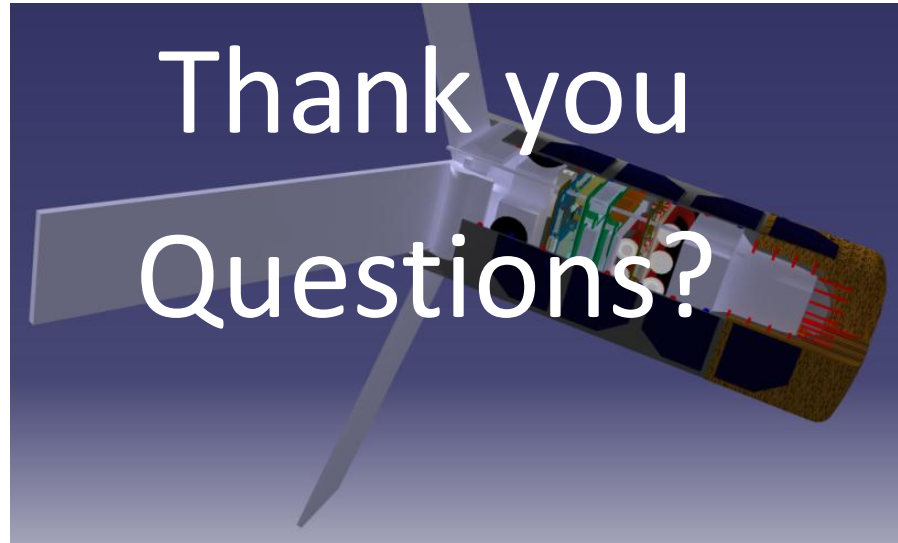




Université
de Liège



Thank you
Questions?



Isil.sakraker@vki.ac.be



QARMAN project is partially supported by the European Community Framework Programme 7, Grant Agreement no. 284427 in the framework of QB50 Project.



von Karman Institute

Université
de Liège¹⁹

